

Matt Allen · Randy Mayes · Daniel Rixen *Editors*

Dynamics of Coupled Structures, Volume 1

Proceedings of the 32nd IMAC, A Conference and Exposition on Structural Dynamics, 2014



Conference Proceedings of the Society for Experimental Mechanics Series

Series Editor

Tom Proulx

Society for Experimental Mechanics, Inc.,

Bethel, CT, USA

For further volumes:

<http://www.springer.com/series/8922>

Matt Allen • Randy Mayes • Daniel Rixen
Editors

Dynamics of Coupled Structures, Volume 1

Proceedings of the 32nd IMAC, A Conference and Exposition
on Structural Dynamics, 2014

Editors

Matt Allen
Engineering Physics Department
University of Wisconsin Madison
Madison, WI, USA

Randy Mayes
Sandia National Laboratories
Albuquerque, NM, USA

Daniel Rixen
Lehrstuhl für Angewandte Mechanik
Technische Universität München
Garching, Germany

ISSN 2191-5644 ISSN 2191-5652 (electronic)
ISBN 978-3-319-04500-9 ISBN 978-3-319-04501-6 (eBook)
DOI 10.1007/978-3-319-04501-6
Springer Cham Heidelberg New York Dordrecht London

Library of Congress Control Number: 2014932412

© The Society for Experimental Mechanics, Inc. 2014

This work is subject to copyright. All rights are reserved by the Publisher, whether the whole or part of the material is concerned, specifically the rights of translation, reprinting, reuse of illustrations, recitation, broadcasting, reproduction on microfilms or in any other physical way, and transmission or information storage and retrieval, electronic adaptation, computer software, or by similar or dissimilar methodology now known or hereafter developed. Exempted from this legal reservation are brief excerpts in connection with reviews or scholarly analysis or material supplied specifically for the purpose of being entered and executed on a computer system, for exclusive use by the purchaser of the work. Duplication of this publication or parts thereof is permitted only under the provisions of the Copyright Law of the Publisher's location, in its current version, and permission for use must always be obtained from Springer. Permissions for use may be obtained through RightsLink at the Copyright Clearance Center. Violations are liable to prosecution under the respective Copyright Law.

The use of general descriptive names, registered names, trademarks, service marks, etc. in this publication does not imply, even in the absence of a specific statement, that such names are exempt from the relevant protective laws and regulations and therefore free for general use.

While the advice and information in this book are believed to be true and accurate at the date of publication, neither the authors nor the editors nor the publisher can accept any legal responsibility for any errors or omissions that may be made. The publisher makes no warranty, express or implied, with respect to the material contained herein.

Printed on acid-free paper

Springer is part of Springer Science+Business Media (www.springer.com)

Preface

Dynamics of Coupled Structures, Volume 1 represents one of the eight volumes of technical papers presented at the 32nd IMAC, A Conference and Exposition on Structural Dynamics, 2014, organized by the Society for Experimental Mechanics, and held in Orlando, Florida, February 3–6, 2014. The full proceedings also include volumes on Nonlinear Dynamics; Model Validation and Uncertainty Quantification; Dynamics of Civil Structures; Structural Health Monitoring; Special Topics in Structural Dynamics; Topics in Modal Analysis I; and Topics in Modal Analysis II.

Each collection presents early findings from experimental and computational investigations on an important area within structural dynamics. Coupled structures, or substructuring, is one of these areas.

Substructuring is a general paradigm in engineering dynamics where a complicated system is analyzed by considering the dynamic interactions between subcomponents. In numerical simulations, substructuring allows one to reduce the complexity of parts of the system in order to construct a computationally efficient model of the assembled system. A subcomponent model can also be derived experimentally, allowing one to predict the dynamic behavior of an assembly by combining experimentally and/or analytically derived models. This can be advantageous for subcomponents that are expensive or difficult to model analytically. Substructuring can also be used to couple numerical simulation with real-time testing of components. Such approaches are known as hardware-in-the-loop or hybrid testing.

Whether experimental or numerical, all substructuring approaches have a common basis, namely the equilibrium of the substructures under the action of the applied and interface forces and the compatibility of displacements at the interfaces of the subcomponents. Experimental substructuring requires special care in the way the measurements are obtained and processed in order to assure that measurement inaccuracies and noise do not invalidate the results. In numerical approaches, the fundamental quest is the efficient computation of reduced order models describing the substructure's dynamic motion. For hardware-in-the-loop applications difficulties include the fast computation of the numerical components and the proper sensing and actuation of the hardware component. Recent advances in experimental techniques, sensor/actuator technologies, novel numerical methods, and parallel computing have rekindled interest in substructuring in recent years leading to new insights and improved experimental and analytical techniques.

The organizers would like to thank the authors, presenters, session organizers, and session chairs for their participation in this track.

Madison, WI, USA
Albuquerque, NM, USA
Garching, Germany

M. Allen
R. Mayes
D. Rixen

Contents

| | | |
|-----------|--|------------|
| 1 | Experimental-Analytical Dynamic Substructuring of Ampair Testbed: A State-Space Approach | 1 |
| | Mladen Gibanica, Anders T. Johansson, Anders Liljehrn, Per Sjövall, and Thomas Abrahamsson | |
| 2 | Experimental Dynamic Substructuring of the Ampair Wind Turbine Test Bed | 15 |
| | Jacopo Brunetti, Antonio Culla, Walter D’Ambrogio, and Annalisa Fregolent | |
| 3 | Are Rotational DoFs Essential in Substructure Decoupling? | 27 |
| | Walter D’Ambrogio and Annalisa Fregolent | |
| 4 | Validation of Blocked-Force Transfer Path Analysis with Compensation for Test Bench Dynamics | 37 |
| | D.D. van den Bosch, M.V. van der Seijs, and D. de Klerk | |
| 5 | Prediction of Forced Response on Ancillary Subsystem Components Attached to Reduced Linear Systems | 51 |
| | Sergio E. Obando and Peter Avitabile | |
| 6 | Towards Dynamic Substructuring Using Measured Impulse Response Functions | 73 |
| | M.V. van der Seijs, P.L.C. van der Valk, T. van der Horst, and D.J. Rixen | |
| 7 | Hybrid Modeling of Floating Raft System by FRF-Based Substructuring Method with Elastic Coupling ... | 83 |
| | Huang Xiuchang, Zhang Zhenguo, Hua Hongxing, and Xu Shiyin | |
| 8 | Experimental Based Substructuring Using a Craig-Bampton Transmission Simulator Model | 91 |
| | Mathew S. Allen, Daniel C. Kammer, and Randy L. Mayes | |
| 9 | Consideration of Interface Damping in Shrouded Mistuned Turbine Blades | 105 |
| | F. Schreyer, J. Gross, P. Reuss, M. Junge, and H. Schoenenborn | |
| 10 | Coupling Elements for Substructure Modelling of Lightweight Multi-storey Buildings | 113 |
| | Ola Flodén, Kent Persson, and Göran Sandberg | |
| 11 | Deformation Mode Selection and Orthonormalization for an Efficient Simulation of the Rolling Contact Problem | 125 |
| | Karim Sherif and Wolfgang Witteveen | |
| 12 | Towards a Parallel Time Integration Method for Nonlinear Systems | 135 |
| | Paul L.C. van der Valk and Daniel J. Rixen | |
| 13 | Efficient Model Order Reduction for the Nonlinear Dynamics of Jointed Structures by the Use of Trial Vector Derivatives | 147 |
| | Wolfgang Witteveen and Florian Pichler | |
| 14 | A Substructuring Method for Geometrically Nonlinear Structures | 157 |
| | Frits Wenneker and Paolo Tiso | |
| 15 | Craig-Bampton Substructuring for Geometrically Nonlinear Subcomponents | 167 |
| | Robert J. Kuether and Matthew S. Allen | |

| | | |
|-----------|--|-----|
| 16 | Parameterized Reduced Order Models Constructed Using Hyper Dual Numbers | 179 |
| | M.R. Brake, J.A. Fike, S.D. Topping, R. Schultz, R.V. Field, N.M. McPeck-Bechtold, and R. Dingreville | |
| 17 | Efficient Stochastic Finite Element Modeling Using Parameterized Reduced Order Models | 193 |
| | R. Schultz, M.R. Brake, S.D. Topping, N.M. McPeck-Bechtold, J.A. Fike, R.V. Field, and R. Dingreville | |
| 18 | Application of a Novel Method to Identify Multi-axis Joint Properties | 203 |
| | Scott Noll, Jason Dreyer, and Rajendra Singh | |
| 19 | Experimental Identification and Simulation of Rotor Damping | 209 |
| | Lothar Gaul and André Schmidt | |
| 20 | An Approach to Identification and Simulation of the Nonlinear Dynamics of Anti-Vibration Mounts | 219 |
| | A. Carrella, S. Manzato, and L. Gielen | |
| 21 | Test Method Development for Nonlinear Damping Extraction of Dovetail Joints | 229 |
| | C.W. Schwingshackl, C. Joannin, L. Pesaresi, J.S. Green, and N. Hoffmann | |
| 22 | Microslip Joint Damping Prediction Using Thin-Layer Elements | 239 |
| | Christian Ehrlich, André Schmidt, and Lothar Gaul | |
| 23 | Variability and Repeatability of Jointed Structures with Frictional Interfaces | 245 |
| | Matthew R. Brake, Pascal Reuss, Daniel J. Segalman, and Lothar Gaul | |
| 24 | Evaluation of North American Vibration Standards for Mass-Timber Floors | 253 |
| | Joshua A. Schultz and Benton Johnson | |
| 25 | Improving Model Predictions Through Partitioned Analysis: A Combined Experimental and Numerical Analysis | 261 |
| | Garrison Stevens, Sez Atamturktur, and Joshua Hegenderfer | |
| 26 | Model Reduction and Lumped Models for Jointed Structures | 273 |
| | G. Chevallier, H. Festjens, J.-L. Dion, and N. Peyret | |
| 27 | A Complex Power Approach to Characterise Joints in Experimental Dynamic Substructuring | 281 |
| | E. Barten, M.V. van der Seijs, and D. de Klerk | |
| 28 | Prediction of Dynamics of Modified Machine Tool by Experimental Substructuring | 297 |
| | Christian Brecher, Stephan Bäumlner, and Matthias Daniels | |
| 29 | Static Torsional Stiffness from Dynamic Measurements Using Impedance Modeling Technique | 307 |
| | Hasan G. Pasha, Randall J. Allemang, David L. Brown, and Allyn W. Phillips | |
| 30 | Full Field Dynamic Strain on Wind Turbine Blade Using Digital Image Correlation Techniques and Limited Sets of Measured Data from Photogrammetric Targets | 317 |
| | Jennifer Carr, Christopher Niezrecki, and Peter Avitabile | |
| 31 | Comparison of Multiple Mass Property Estimation Techniques on SWiFT Vestas V27 Wind Turbine Nacelles and Hubs | 329 |
| | Timothy Marinone, David Cloutier, Kevin Napolitano, and Bruce LeBlanc | |
| 32 | Overview of the Dynamic Characterization at the DOE/SNL SWiFT Wind Facility | 337 |
| | Bruce LeBlanc, David Cloutier, and Timothy Marinone | |
| 33 | Artificial and Natural Excitation Testing of SWiFT Vestas V27 Wind Turbines | 343 |
| | Timothy Marinone, David Cloutier, Bruce LeBlanc, Thomas Carne, and Palle Andersen | |
| 34 | Effects of Boundary Conditions on the Structural Dynamics of Wind Turbine Blades—Part 1: Flapwise Modes | 355 |
| | Javad Baqersad, Christopher Niezrecki, and Peter Avitabile | |

| | | |
|-----------|--|-----|
| 35 | Effects of Boundary Conditions on the Structural Dynamics of Wind Turbine Blades. Part 2: Edgewise Modes | 369 |
| | Javad Baqersad, Christopher Niezrecki, and Peter Avitabile | |
| 36 | Modal Testing and Model Validation Issues of SWiFT Turbine Tests | 381 |
| | Timothy Marinone, David Cloutier, and Bruce LeBlanc | |
| 37 | Development of Simplified Models for Wind Turbine Blades with Application to NREL 5 MW Offshore Research Wind Turbine | 389 |
| | Majid Khorsand Vakilzadeh, Anders T. Johansson, Carl-Johan Lindholm, Johan Hedlund, and Thomas J.S. Abrahamsson | |
| 38 | A Wiki for Sharing Substructuring Methods, Measurements and Information | 403 |
| | Matthew S. Allen, Jill Blecke, and Daniel Roettgen | |
| 39 | Novel Parametric Reduced Order Model for Aeroengine Blade Dynamics | 413 |
| | Jie Yuan, Giuliano Allegri, Fabrizio Scarpa, and Ramesh Rajasekaran | |
| 40 | Practical Seismic FSSI Analysis of Multiply-Supported Secondary Tanks System | 427 |
| | Nam-Gyu Kim, Choon-Gyo Seo, and Jong-Jae Lee | |
| 41 | DEIM for the Efficient Computation of Contact Interface Stresses | 435 |
| | M. Breitfuss, H. Irschik, H.J. Holl and W. Witteveen | |
| 42 | Amplitude Dependency on Dynamic Properties of a Rubber Mount | 447 |
| | C.B. Nel and J. van Wyngaardt | |
| 43 | Model Order Reduction for Geometric Nonlinear Structures with Variable State-Dependent Basis | 455 |
| | Johannes B. Rutzmoser and Daniel J. Rixen | |
| 44 | Stochastic Iwan-Type Model of a Bolted Joint: Formulation and Identification | 463 |
| | X.Q. Wang and Marc P. Mignolet | |

Chapter 1

Experimental-Analytical Dynamic Substructuring of Ampair Testbed: A State-Space Approach

Mladen Gibanica, Anders T. Johansson, Anders Liljerehn, Per Sjövall, and Thomas Abrahamsson

Abstract The Society for Experimental Mechanics (SEM) Substructuring Focus Group has initiated a research project in experimental dynamic substructuring using the Ampair 600W wind turbine as a testbed. In this paper, experimental as well as analytical models of the blades of said wind turbine are coupled to analytical models of its brackets. The focus is on a state-space based substructuring method designed specifically for experimental-analytical dynamic substructuring. It is shown (a) theoretically that the state-space method gives equivalent results to the second order methods under certain conditions, (b) that the state-space method numerically produces results equivalent to those of a well-known frequency-based substructuring technique when the same experimental models are used for the two methods and (c) that the state-space synthesis procedure can be translated to the general framework given by De Klerk et al.

Keywords Substructuring • Experimental-analytical dynamic • Modal analysis • Vibration testing • State-space • Component mode synthesis • Frequency based substructuring • Automatic system identification • Wind turbines

1.1 Introduction

The subject of substructuring has been an open research area ever since its advent in the 1960s [1]. Recently, often attributed to advances in computing capacity and experimental equipment, there has been a renewed interest in the subject. Substructuring builds on the idea that a complex structure can be decomposed into a number of simpler components, or substructures. The modeling approach of these substructures may vary, which allows creating mixed experimental and analytical models thereby increasing the modeling flexibility for complex mechanical structures such as cars, air planes, rocket launchers and wind turbines.

Although the main concept of substructuring is simple—a matter of enforcing compatibility and equilibrium at the interfaces between substructures—there are a number of different methods presented in literature. These are typically categorized, by the type of substructure models used, as Frequency Response Function (FRF) based and modal based (CMS—component mode synthesis) methods. Early works falling in the former category are e.g. [2, 3] while the Craig-Bampton method [4] is a well-known early representative of the latter. The paper by de Klerk et al. [1] is frequently cited as a well written overview of the field. This paper is based on the MSc thesis by Mr. Mladen Gibanica [5].

The structure under investigation here is the SEM Substructuring Focus Group testbed, the Ampair 600 wind turbine, further detailed by Mayes [6]. Since its introduction at IMAC XXX, several attempts at substructuring have been reported for this structure. A group from Sandia National Laboratories have worked with experimental substructuring using the Transmission Simulator Technique [7, 8], a method also employed at the Atomic Weapons Establishment in the UK [9],

M. Gibanica • A.T. Johansson (✉) • T. Abrahamsson
Department of Applied Mechanics, Chalmers University of Technology, SE-412 96 Göteborg, Sweden
e-mail: anders.t.johansson@chalmers.se

A. Liljerehn
AB Sandvik Coromant, R & D Metal Cutting Research, SE-811 81 Sandviken, Sweden

P. Sjövall
FS Dynamics, SE-412 63 Göteborg, Sweden

while a frequency-based method was used by a group from TU Delft [10]. Also, a group of Italian scientists have studied the role of interface degrees of freedom for the coupling of the structure [11].

The purpose of the test bed is to serve as a reference for researchers around the world. Data is shared online through a wiki [12]. This paper considers the blades and the brackets of the turbine only—the hub, tower and base are thus left for later studies. The dynamics of the joints has not been considered (a presentation on nonlinear effects from varying contact geometry at different load levels was given by Dr. Pascal Reuss at IMAC XXXI [13]). Components are coupled using the state-space synthesis method of [14]. (Similar methods have been proposed also by e.g. Su and Juang [15].) The results are compared to experimental measurements of the assembly as well as experimental-analytical FRF-based coupling techniques and analytical models coupled using CMS. The Ampair 600 wind turbine blades, consisting of a composite hull around a solid core, have been thoroughly tested in dynamic and static measurements as well as destructive tests to quantify the material parameters [16–21]. A calibrated FE model of the blades has been developed by Johansson et al. [20] which is used for comparison here. A new FE model of the bracket is created from geometry measurements made available by the TU Delft and using standard material properties.

The paper is structured as follows: Sect. 1.2 briefly introduces the theory behind the state space coupling technique and puts it into the framework of de Klerk et al. [1]. Section 1.3 describes the Finite Element models used. Section 1.4 elaborates on performed experiments and describes the experimentally derived models used. Section 1.5 relates results before the paper is rounded up by some conclusions in Sect. 1.6.

1.2 Theory

In linear system theory, systems are sometimes separated into *external* and *internal* descriptions, where the former offer information on the input-output relation only whereas the latter includes information on the *state* of the process [22, 23]. The typical external model in structural dynamics is the time domain convolution relation which gives rise to the Frequency Response Function in the frequency domain:

$$\mathbf{y}(t) = \mathbf{y}_0 + \int_0^{\infty} \mathbf{h}(t - \tau)\mathbf{u}(\tau)d\tau \quad (1.1)$$

$$\mathbf{Y}(\omega) = \mathbf{H}(\omega)\mathbf{U}(\omega) \quad (1.2)$$

While internal models are given in the usual first- or second-order forms [24]:

$$\begin{cases} \dot{\mathbf{x}}(t) = \mathbf{A}\mathbf{x}(t) + \mathbf{B}\mathbf{u}(t) \\ \mathbf{y}(t) = \mathbf{C}\mathbf{x}(t) + \mathbf{D}\mathbf{u}(t) \end{cases} \quad (1.3)$$

$$\mathbf{K}\mathbf{q}(t) + \mathbf{V}\dot{\mathbf{q}}(t) + \mathbf{M}\ddot{\mathbf{q}}(t) = \mathbf{f}(t) \quad (1.4)$$

where the matrices have the usual meanings and the forces in Eq. (1.4) relate to the input in Eq. (1.3) through a selection matrix such that $\mathbf{f}(t) = \mathbf{P}_a\mathbf{u}(t)$ [25]. A shaker or impact hammer testing campaign will thus result in an external model of the system, from which the analyst frequently attempts to derive an internal model. This process is often referred to as *modal parameter extraction* [26] in the structural dynamics community and *system identification* elsewhere [27].

1.2.1 System Identification

System identification is performed on experimentally obtained outer models in the frequency domain, Eq. (1.2), using the state-space subspace system identification algorithm implemented as `n4sid` in MATLAB's System Identification Toolbox [27, 28] to estimate a state-space model quadruple set $\{\mathbf{A}, \mathbf{B}, \mathbf{C}, \mathbf{D}\}$. In order to automate the system identification process a method for automatic model order estimation by Yaghoubi and Abrahamsson [29] is used along with the N4SID method.

All systems studied in this paper are considered to be linear time invariant (LTI) systems. By assumption they are also stable and passive. The systems are also assumed to be reciprocal (since the systems are non-gyroscopic and non-circulatory). As system identification is a general tool, these assumptions must be enforced explicitly (except for stability, which can be included as a condition on the system identification algorithm). Reciprocity is enforced through measuring using a limited

number of input nodes and applying Maxwell-Betti's reciprocity principle (see [5]). The passivity criterion states that the power supplied to the system is non-negative and can be zero only for components without damping. Models derived from first principles satisfy the passivity criterion implicitly, but this is not necessarily the case for experimentally identified models. The passivity problem for state space models is commonly known, for details see for example [14,30]. The passivity of a state space model is linked to the positive real (PR) lemma. In this paper, an engineering solution to the passivity optimization problem defined in [14] based on averaging of the \mathbf{B} and \mathbf{C} matrices has been used.

1.2.2 Substructuring

Substructuring is the process of coupling two structures together by enforcing two conditions at their common interface; compatibility and force equilibrium. This paper will treat only what de Klerk et al. [1] refers to as the primal formulation, which implies that the displacements are defined and interface forces are eliminated. For brevity, the explicit time dependency is dropped from the equations in the following.

For (analytically derived) internal models as in Eq. (1.4), enforcing compatibility and force equilibrium amounts to an assembly procedure parallel to that used for Finite Element Models, see further de Klerk et al. [1], such that synthesis of two systems 1 and 2 can be described by:

$$\begin{cases} \begin{bmatrix} \mathbf{K}_1 & \mathbf{0} \\ \mathbf{0} & \mathbf{K}_2 \end{bmatrix} \begin{Bmatrix} \mathbf{q}_1 \\ \mathbf{q}_2 \end{Bmatrix} + \begin{bmatrix} \mathbf{V}_1 & \mathbf{0} \\ \mathbf{0} & \mathbf{V}_2 \end{bmatrix} \begin{Bmatrix} \dot{\mathbf{q}}_1 \\ \dot{\mathbf{q}}_2 \end{Bmatrix} + \begin{bmatrix} \mathbf{M}_1 & \mathbf{0} \\ \mathbf{0} & \mathbf{M}_2 \end{bmatrix} \begin{Bmatrix} \ddot{\mathbf{q}}_1 \\ \ddot{\mathbf{q}}_2 \end{Bmatrix} = \mathbf{f} + \mathbf{g} \\ \mathbf{E}\mathbf{q} = \mathbf{0} \\ \mathbf{L}^T \mathbf{g} = \mathbf{0} \end{cases} \quad (1.5)$$

where \mathbf{E} can be thought of as a signed boolean matrix enforcing compatibility,¹ \mathbf{g} are the interface forces, and the matrix \mathbf{L} is the nullspace of \mathbf{E} . For details, refer to [1]. When coupling two structures, which are described by m_1 and m_2 degrees of freedom (DOFs), the assembled structure will consist of $m_1 + m_2 - m_c$ coordinates, where m_c is the number of coupling constraints. The de Klerk et al. paper [1] generalizes the formulation using the two matrices \mathbf{E} and \mathbf{L} to include also models using generalized coordinates and outer models (Eq. (1.2)), i.e. FRF coupling. In a following subsection, the state-space method [14] will be put into the same format.

1.2.3 State-Space Coupling

The state-space coupling used here is described in the paper by Sjövall and Abrahamsson [14]. At its core is the *coupling form* of Eq. (1.6), where the i :th first-order system to be coupled is rewritten to second-order form at the interface in order for the compatibility and force equilibrium conditions to be applicable

$$\begin{cases} \begin{bmatrix} \ddot{\mathbf{y}}_c \\ \dot{\mathbf{y}}_c \\ \dot{\mathbf{x}}_b \end{bmatrix} = \begin{bmatrix} \mathbf{A}_{vv}^i & \mathbf{A}_{vd}^i & \mathbf{A}_{vb}^i \\ \mathbf{I} & \mathbf{0} & \mathbf{0} \\ \mathbf{0} & \mathbf{A}_{bd}^i & \mathbf{A}_{bb}^i \end{bmatrix} \begin{bmatrix} \dot{\mathbf{y}}_c \\ \mathbf{y}_c \\ \mathbf{x}_b \end{bmatrix} + \begin{bmatrix} \mathbf{B}_{vv}^i & \mathbf{B}_{vb}^i \\ \mathbf{0} & \mathbf{0} \\ \mathbf{0} & \mathbf{B}_{bb}^i \end{bmatrix} \begin{bmatrix} \mathbf{u}_c \\ \mathbf{u}_d \end{bmatrix} \\ \begin{bmatrix} \mathbf{y}_c \\ \mathbf{y}_d \end{bmatrix} = \begin{bmatrix} \mathbf{0} & \mathbf{I} & \mathbf{0} \\ \mathbf{C}_{bv}^i & \mathbf{C}_{bd}^i & \mathbf{C}_{bb}^i \end{bmatrix} \end{cases} \quad (1.6)$$

Here, the subscript c refers to coupling degrees of freedom, b other degrees of freedom, v velocity outputs and d displacement outputs. Note that for state-space coupling there exist twice as many states as DOFs (a product of rewriting a second-order differential equation on first-order form) and thus if $n = 2m$, for two structures with n_1 and n_2 states and m_c coupling coordinates the coupled system will contain $n_1 + n_2 - 2m_c$ states.

¹This matrix is denoted \mathbf{B} in de Klerk et al. The notation cannot be adopted here as the \mathbf{B} matrix is strongly associated to the state-space formulation in Eq. (1.3).

1.2.3.1 General Framework

Here, the coupling procedure derived in [14] is recast into the general framework established by de Klerk et al. [1], thus using the \mathbf{E} and \mathbf{L} matrices defined above.

Starting from a general state-space formulation (Eq. (1.3)), a transformation matrix \mathbf{T} is introduced which takes the system to the coupling form of Eq. (1.6) [14]. Let the system on coupling form be:

$$\begin{cases} \dot{\tilde{\mathbf{x}}} = \tilde{\mathbf{A}}\tilde{\mathbf{x}} + \tilde{\mathbf{B}}\mathbf{u} \\ \mathbf{y} = \tilde{\mathbf{C}}\tilde{\mathbf{x}} \end{cases} \quad (1.7)$$

where $\tilde{\mathbf{A}} = \mathbf{T}^{-1}\mathbf{A}\mathbf{T}$, $\tilde{\mathbf{B}} = \mathbf{T}\mathbf{B}$, $\tilde{\mathbf{C}} = \mathbf{C}\mathbf{T}^{-1}$ and $\tilde{\mathbf{x}} = \mathbf{T}\mathbf{x}$. \mathbf{B}_{vv} of Eq. (1.6) is the inertia at the interface DOFs [31]. By forming of a new matrix denoted \mathbf{M}_B , the system can be rewritten such that the first block row is pre-multiplied by \mathbf{B}_{vv}^{-1} . The matrix \mathbf{M}_B will then be:

$$\mathbf{M}_B = \text{diag}(\text{diag}(\mathbf{B}_{vv}^{1-1}, \mathbf{I}, \mathbf{I}), \dots, \text{diag}(\mathbf{B}_{vv}^{h-1}, \mathbf{I}, \mathbf{I})) \quad (1.8)$$

Such that the system can now be written as:

$$\begin{cases} \mathbf{M}_B \dot{\tilde{\mathbf{x}}} = \mathbf{M}_B \tilde{\mathbf{A}}\tilde{\mathbf{x}} + \mathbf{M}_B \tilde{\mathbf{B}}\mathbf{u} \\ \mathbf{y} = \tilde{\mathbf{C}}\tilde{\mathbf{x}} \end{cases} \quad (1.9)$$

Introducing the \mathbf{E} and \mathbf{L} matrices such that compatibility is described by $\mathbf{E}\tilde{\mathbf{x}} = \mathbf{0}$ and equilibrium by $\mathbf{L}^T \mathbf{u}_{c,g} = \mathbf{0}$, where subscript g is used to denote interface forces, the matrix \mathbf{L} is formed as $\mathbf{L} = \text{null}(\mathbf{E})$ such that the following is satisfied: $\mathbf{E}\tilde{\mathbf{x}} = \mathbf{E}\mathbf{L}\tilde{\mathbf{z}} = \mathbf{0}$ and $\tilde{\mathbf{x}} = \mathbf{L}\tilde{\mathbf{z}}$. The new state vector $\tilde{\mathbf{z}}$ represents the new states after coupling. The synthesised state-space model is then formed as follows:

$$\begin{cases} \mathbf{L}^T \mathbf{M}_B \mathbf{L} \dot{\tilde{\mathbf{z}}} = \mathbf{L}^T \mathbf{M}_B \tilde{\mathbf{A}} \mathbf{L} \tilde{\mathbf{z}} + \mathbf{L}^T \mathbf{M}_B \tilde{\mathbf{B}} \mathbf{u} \\ \mathbf{y} = \tilde{\mathbf{C}} \mathbf{L} \tilde{\mathbf{z}} \end{cases} \quad (1.10)$$

Finally, $(\mathbf{L}^T \mathbf{M}_B \mathbf{L})^{-1}$, may be pre-multiplied to the first equation in Eq. (1.10). A new transformation matrix must however be introduced simply to reduce the excess inputs and outputs. The new matrix is denoted \mathbf{L}_u and is formed from a matrix \mathbf{E}_u as before, $\mathbf{L}_u = \text{null}(\mathbf{E}_u)$. In other words, for a system with two synthesised components the new reduction matrix is $\mathbf{E}_u = [\mathbf{I} \ \mathbf{0} \ \mathbf{0} \ \mathbf{0}]$. The implication of this transformation is that in the synthesised model, to which this new matrix is applied, the first component of the considered vector will be removed. This new matrix is introduced in the equations by the transformations $\mathbf{u} = \mathbf{L}_u \bar{\mathbf{u}}$ and $\bar{\mathbf{y}} = \mathbf{L}_u^T \mathbf{y}$ as shown in Eq. (1.12). The last step is only true for systems with an equal number of inputs and outputs but is easily generalised. The final system can be written as follows:

$$\begin{cases} \dot{\tilde{\mathbf{z}}} = \hat{\mathbf{A}}\tilde{\mathbf{z}} + \hat{\mathbf{B}}\bar{\mathbf{u}} \\ \bar{\mathbf{y}} = \hat{\mathbf{C}}\tilde{\mathbf{z}} \end{cases} \quad (1.11)$$

Where each part in the equation above is then identified as:

$$\begin{cases} \hat{\mathbf{A}} = (\mathbf{L}^T \mathbf{M}_B \mathbf{L})^{-1} (\mathbf{L}^T \mathbf{M}_B \tilde{\mathbf{A}} \mathbf{L}) \\ \hat{\mathbf{B}} = (\mathbf{L}^T \mathbf{M}_B \mathbf{L})^{-1} (\mathbf{L}^T \mathbf{M}_B \tilde{\mathbf{B}}) \mathbf{L}_u \\ \hat{\mathbf{C}} = \mathbf{L}_u^T (\tilde{\mathbf{C}} \mathbf{L}) \end{cases} \quad (1.12)$$

1.2.3.2 Second Order Form Equivalent of Synthesised First Order Form

An analytical model written on second order form can easily be rewritten on first order form by doubling the number of states [24]. The transformation from a first order form to a second order form with half the number of states is not as trivial, even when possible.

Begin the second order system shown in Eq. (1.5). Methods for rewriting such a system to the first-order form of Eq. (1.3) are well-known [24, 25]. It is assumed that the output is the entire displacement vector, such that all DOFs are considered as

outputs. A transformation matrix is introduced in Eq. (1.13) which transforms a state-space system to coupling form under the assumption that the original system is analytically derived with state vector $\mathbf{x}^T = [\mathbf{q} \ \dot{\mathbf{q}}]^T$ and displacement output such that $\mathbf{q} = \mathbf{y} = \mathbf{C}\mathbf{x}$

$$\mathbf{T}^i = \begin{bmatrix} \mathbf{C}_c^i \mathbf{A}^i \\ \mathbf{C}_c^i \\ \mathbf{C}_b^i \mathbf{A}^i \\ \mathbf{C}_b^i \end{bmatrix} \quad (1.13)$$

This transformation will produce a new state vector, $\tilde{\mathbf{x}} = [\tilde{\mathbf{y}}_c^i \ \mathbf{y}_c^i \ \dot{\mathbf{y}}_b^i \ \mathbf{y}_b^i]^T$, where the superscript i represents the subcomponent system. Again, the subscript c denotes the coupling partition of the input and output matrices, i.e. the block row and column of the \mathbf{B} and \mathbf{C} matrices, respectively. The difference between this transformation and the transformation in [14], is that the internal states are represented by physical coordinates here. In a theoretical representation this is valid, but in an experimental representation it would imply a significant constraint on the model to allow only twice as many states as there are sensors. The coupling form obtained through Eq. (1.13) is shown below

$$\left\{ \begin{array}{l} \tilde{\mathbf{A}}^i = \mathbf{T}^i \mathbf{A}^i \mathbf{T}^{i-1} = \begin{bmatrix} \mathbf{A}_{cvc}^i & \mathbf{A}_{cdc}^i & \mathbf{A}_{cvb}^i & \mathbf{A}_{cdb}^i \\ \mathbf{I} & \mathbf{0} & \mathbf{0} & \mathbf{0} \\ \mathbf{A}_{bvc}^i & \mathbf{A}_{bdc}^i & \mathbf{A}_{bvb}^i & \mathbf{A}_{bdb}^i \\ \mathbf{0} & \mathbf{0} & \mathbf{I} & \mathbf{0} \end{bmatrix} \\ \tilde{\mathbf{B}}^i = \mathbf{T}^i \mathbf{B}^i = \begin{bmatrix} \mathbf{C}_c^i \mathbf{A}^i \mathbf{B}^i \\ \mathbf{C}_c^i \mathbf{B}^i \\ \mathbf{C}_b^i \mathbf{A}^i \mathbf{B}^i \\ \mathbf{C}_b^i \mathbf{B}^i \end{bmatrix} = \begin{bmatrix} \mathbf{C}_c^i \mathbf{A}^i \mathbf{B}^i \\ \mathbf{0} \\ \mathbf{C}_b^i \mathbf{A}^i \mathbf{B}^i \\ \mathbf{0} \end{bmatrix} = \begin{bmatrix} \mathbf{B}_{c,c}^i & \mathbf{B}_{c,b}^i \\ \mathbf{0} & \mathbf{0} \\ \mathbf{B}_{b,c}^i & \mathbf{B}_{b,b}^i \\ \mathbf{0} & \mathbf{0} \end{bmatrix} \\ \tilde{\mathbf{C}}^i = \mathbf{C}^i \mathbf{T}^{i-1} = \begin{bmatrix} \mathbf{I} & \mathbf{0} & \mathbf{0} & \mathbf{0} \\ \mathbf{0} & \mathbf{0} & \mathbf{I} & \mathbf{0} \end{bmatrix} \end{array} \right. \quad (1.14)$$

It can be shown that the transformation of the input matrix \mathbf{CAB} , with the assumptions introduced above, is but the inverse of the mass matrix, thus simplifying the $\tilde{\mathbf{B}}$ matrix as follows (recall that the full system mass matrix is a block-diagonal matrix):

$$\left\{ \begin{array}{l} \mathbf{B}_{cc}^i = \mathbf{M}_{cc}^{i-1} \\ \mathbf{B}_{cb}^i = \mathbf{0} \\ \mathbf{B}_{bc}^i = \mathbf{0} \\ \mathbf{B}_{bb}^i = \mathbf{M}_{bb}^{i-1} \end{array} \right. \quad (1.15)$$

Synthesising two systems by the procedure described above yields the following model, here reorganised such that it is recognisable as the usual state-space formulation of a second order system [25]:

$$\begin{aligned} \begin{pmatrix} \dot{\tilde{\mathbf{y}}}_c \\ \dot{\mathbf{y}}_b^1 \\ \dot{\mathbf{y}}_b^2 \\ \ddot{\tilde{\mathbf{y}}}_c \\ \ddot{\mathbf{y}}_b^1 \\ \ddot{\mathbf{y}}_b^2 \end{pmatrix} &= \begin{bmatrix} \mathbf{0} & \mathbf{0} & \mathbf{0} & \mathbf{I} & \mathbf{0} & \mathbf{0} \\ \mathbf{0} & \mathbf{0} & \mathbf{0} & \mathbf{0} & \mathbf{I} & \mathbf{0} \\ \mathbf{0} & \mathbf{0} & \mathbf{0} & \mathbf{0} & \mathbf{0} & \mathbf{I} \\ \bar{\mathbf{A}}_{cdc} & \bar{\mathbf{A}}_{cdb}^1 & \bar{\mathbf{A}}_{cdb}^2 & \bar{\mathbf{A}}_{cvc} & \bar{\mathbf{A}}_{cvb}^1 & \bar{\mathbf{A}}_{cvb}^2 \\ \mathbf{A}_{bdc}^1 & \mathbf{A}_{bdb}^1 & \mathbf{0} & \mathbf{A}_{bvc}^1 & \mathbf{A}_{bvb}^1 & \mathbf{0} \\ \mathbf{A}_{bdc}^2 & \mathbf{0} & \mathbf{A}_{bdb}^2 & \mathbf{A}_{bvc}^2 & \mathbf{0} & \mathbf{A}_{bvb}^2 \end{bmatrix} \begin{pmatrix} \bar{\mathbf{y}}_c \\ \mathbf{y}_b^1 \\ \mathbf{y}_b^2 \\ \dot{\tilde{\mathbf{y}}}_c \\ \dot{\mathbf{y}}_b^1 \\ \dot{\mathbf{y}}_b^2 \end{pmatrix} + \begin{bmatrix} \mathbf{0} & \mathbf{0} & \mathbf{0} \\ \mathbf{0} & \mathbf{0} & \mathbf{0} \\ \mathbf{0} & \mathbf{0} & \mathbf{0} \\ \bar{\mathbf{B}}_{cc} & \mathbf{0} & \mathbf{0} \\ \mathbf{0} & \mathbf{B}_{bb}^1 & \mathbf{0} \\ \mathbf{0} & \mathbf{0} & \mathbf{B}_{bb}^2 \end{bmatrix} \begin{pmatrix} \bar{\mathbf{u}}_c \\ \mathbf{u}_b^1 \\ \mathbf{u}_b^2 \end{pmatrix} \\ \begin{pmatrix} \bar{\mathbf{y}}_c \\ \mathbf{y}_b^1 \\ \mathbf{y}_b^2 \end{pmatrix} &= \begin{bmatrix} \mathbf{I} & \mathbf{0} & \mathbf{0} & \mathbf{0} & \mathbf{0} & \mathbf{0} \\ \mathbf{0} & \mathbf{I} & \mathbf{0} & \mathbf{0} & \mathbf{0} & \mathbf{0} \\ \mathbf{0} & \mathbf{0} & \mathbf{I} & \mathbf{0} & \mathbf{0} & \mathbf{0} \end{bmatrix} \begin{pmatrix} \bar{\mathbf{y}}_c \\ \mathbf{y}_b^1 \\ \mathbf{y}_b^2 \\ \dot{\tilde{\mathbf{y}}}_c \\ \dot{\mathbf{y}}_b^1 \\ \dot{\mathbf{y}}_b^2 \end{pmatrix} \end{aligned} \quad (1.16)$$

The lower part can be identified as a second order system which is directly comparable to the direct coupling procedure [1]. The two second order systems can be written with an interface part (c) and a body part (b) for two components, $i = 1, 2$.

$$\begin{cases} \mathbf{M}^i = \begin{bmatrix} \mathbf{M}_{cc}^i & \mathbf{0} \\ \mathbf{0} & \mathbf{M}_{bb}^i \end{bmatrix} \\ \mathbf{K}^i = \begin{bmatrix} \mathbf{K}_{cc}^i & \mathbf{K}_{cb}^i \\ \mathbf{K}_{bc}^i & \mathbf{K}_{bb}^i \end{bmatrix} \\ \mathbf{V}^i = \begin{bmatrix} \mathbf{V}_{cc}^i & \mathbf{V}_{cb}^i \\ \mathbf{V}_{bc}^i & \mathbf{V}_{cc}^i \end{bmatrix} \end{cases} \quad (1.17)$$

The synthesised system then becomes

$$\begin{cases} \mathbf{M}_{as} = \begin{bmatrix} \mathbf{M}_{cc}^1 + \mathbf{M}_{cc}^2 & \mathbf{0} & \mathbf{0} \\ \mathbf{0} & \mathbf{M}_{bb}^1 & \mathbf{0} \\ \mathbf{0} & \mathbf{0} & \mathbf{M}_{bb}^2 \end{bmatrix} \\ \mathbf{K}_{as} = \begin{bmatrix} \mathbf{K}_{cc}^1 + \mathbf{K}_{cc}^2 & \mathbf{K}_{cb}^1 & \mathbf{K}_{cb}^2 \\ \mathbf{K}_{bc}^1 & \mathbf{K}_{bb}^1 & \mathbf{0} \\ \mathbf{K}_{bc}^2 & \mathbf{0} & \mathbf{K}_{bb}^2 \end{bmatrix} \\ \mathbf{V}_{as} = \begin{bmatrix} \mathbf{V}_{cc}^1 + \mathbf{V}_{cc}^2 & \mathbf{V}_{cb}^1 & \mathbf{V}_{cb}^2 \\ \mathbf{V}_{bc}^1 & \mathbf{V}_{bb}^1 & \mathbf{0} \\ \mathbf{V}_{bc}^2 & \mathbf{0} & \mathbf{V}_{bb}^2 \end{bmatrix} \end{cases} \quad (1.18)$$

For comparison, the second order system from Eq. (1.16) is pre-multiplied by the inverse of its input matrix, which is diagonal. The resulting matrix is split in two, one part representing the stiffness and the other the damping. The following is then obtained

$$\begin{cases} \mathbf{M}_{as} \equiv \mathbf{M}_{sss} = \begin{bmatrix} \bar{\mathbf{B}}_{cc}^{-1} & \mathbf{0} & \mathbf{0} \\ \mathbf{0} & \bar{\mathbf{B}}_{bb}^{-1} & \mathbf{0} \\ \mathbf{0} & \mathbf{0} & \bar{\mathbf{B}}_{bb}^{-2-1} \end{bmatrix} = \begin{bmatrix} \mathbf{M}_{cc}^1 + \mathbf{M}_{cc}^2 & \mathbf{0} & \mathbf{0} \\ \mathbf{0} & \mathbf{M}_{bb}^1 & \mathbf{0} \\ \mathbf{0} & \mathbf{0} & \mathbf{M}_{bb}^2 \end{bmatrix} \\ \mathbf{K}_{as} \equiv \mathbf{K}_{sss} = \begin{bmatrix} \bar{\mathbf{B}}_{cc}^{-1} \bar{\mathbf{A}}_{cdc} & \bar{\mathbf{B}}_{cc}^{-1} \bar{\mathbf{A}}_{cdb} & \bar{\mathbf{B}}_{cc}^{-1} \bar{\mathbf{A}}_{cdb} \\ \bar{\mathbf{B}}_{bb}^{-1} \bar{\mathbf{A}}_{bdc} & \bar{\mathbf{B}}_{bb}^{-1} \bar{\mathbf{A}}_{bdb} & \mathbf{0} \\ \bar{\mathbf{B}}_{bb}^{-2-1} \bar{\mathbf{A}}_{bdc}^2 & \mathbf{0} & \bar{\mathbf{B}}_{bb}^{-2-1} \bar{\mathbf{A}}_{bdb}^2 \end{bmatrix} = \begin{bmatrix} \mathbf{K}_{cc}^1 + \mathbf{K}_{cc}^2 & \mathbf{K}_{cb}^1 & \mathbf{K}_{cb}^2 \\ \mathbf{K}_{bc}^1 & \mathbf{K}_{bb}^1 & \mathbf{0} \\ \mathbf{K}_{bc}^2 & \mathbf{0} & \mathbf{K}_{bb}^2 \end{bmatrix} \\ \mathbf{V}_{as} \equiv \mathbf{V}_{sss} = \begin{bmatrix} \bar{\mathbf{B}}_{cc}^{-1} \bar{\mathbf{A}}_{cvc} & \bar{\mathbf{B}}_{cc}^{-1} \bar{\mathbf{A}}_{cvb} & \bar{\mathbf{B}}_{cc}^{-1} \bar{\mathbf{A}}_{cvb}^2 \\ \bar{\mathbf{B}}_{bb}^{-1} \bar{\mathbf{A}}_{bvc} & \bar{\mathbf{B}}_{bb}^{-1} \bar{\mathbf{A}}_{bvb} & \mathbf{0} \\ \bar{\mathbf{B}}_{bb}^{-2-1} \bar{\mathbf{A}}_{bvc}^2 & \mathbf{0} & \bar{\mathbf{B}}_{bb}^{-2-1} \bar{\mathbf{A}}_{bvb}^2 \end{bmatrix} = \begin{bmatrix} \mathbf{V}_{cc}^1 + \mathbf{V}_{cc}^2 & \mathbf{V}_{cb}^1 & \mathbf{V}_{cb}^2 \\ \mathbf{V}_{bc}^1 & \mathbf{V}_{bb}^1 & \mathbf{0} \\ \mathbf{V}_{bc}^2 & \mathbf{0} & \mathbf{V}_{bb}^2 \end{bmatrix} \end{cases} \quad (1.19)$$

It is now obvious that both methods produce exactly the same systems.

1.3 Analytical Models

The two analytical FE models that were used were created in FEMAP and solved with MD Nastran. NX Nastran was used for verification where non-reduced models were solved.

1.3.1 Blade

A version of the blade FE model described in [20] (Nastran model can be found online at [12]) was used and is visualised in Fig. 1.1. The model consisted of 20,523 nodes and 96,416 elements. The model has a solid core, for which solid elements were used and a laminate skin model, for which laminate plate elements were used. For a thorough explanation of the composite material model and how it was calibrated, see Johansson et al. [20] (Fig. 1.2).

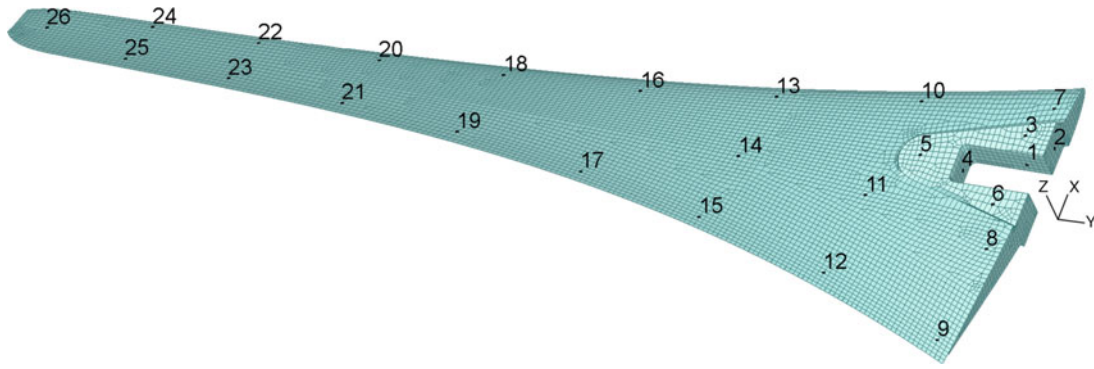
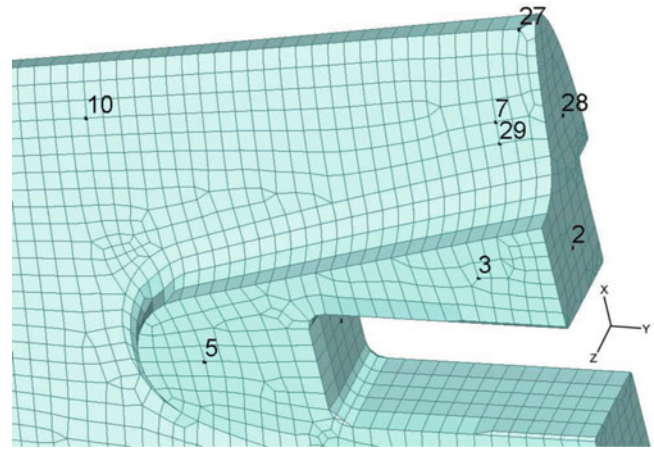


Fig. 1.1 FE model of the blade with numbering used in the FE model but also during the vibration tests

Fig. 1.2 Close-up view of the three inputs of the blade



The accelerometer positions in the vibrations test and for the FE blade model are shown in Fig. 1.1. These were chosen as close to the physical locations of the accelerometers as possible for the MAC correlations to yield correct results. Note that the numbering starts at the coupling positions.

1.3.2 Bracket

The bracket geometry was received from TU Delft. It was modelled by 24,707 solid parabolic elements and an isotropic material model with stiffness $E = 2 \cdot 10^{11} \text{ N/m}^2$ and density $\rho = 5,000 \text{ kg/m}^3$. The shaft which is inserted into the bracket was modelled as an integrated part of the bracket. Parabolic elements were used so that the shaft curvature would be described better. The bracket model is shown in Fig. 1.3. The numbers 1, 2 and 3 are the coupling positions coupled to the blade at positions 3, 4 and 5, thus matching DOFs were used at each of the components coupling locations.

1.3.3 FE Coupling

The coupling between the blade and the bracket can be seen in Fig. 1.4a, b, where the area around the holes on the blade have been constrained with rigid links. All the DOFs on the bracket in contact with the blade when mounted were constrained with rigid links to a six DOFs node located at the centre of the three holes. The bracket coupling type was constrained at the holes, see Fig. 1.4b. The same configurations were used in the experimental-analytical coupling. All three configurations were used in coupling of the analytical models. It should be noted that the blade bracket constraints configuration are on the same side of the blade which creates asymmetric modeshapes.

The assembled blade bracket structure along with the measurement points can be seen in Fig. 1.5.

Fig. 1.3 FE model of the blade with numbering used in the FE model and during the vibration tests

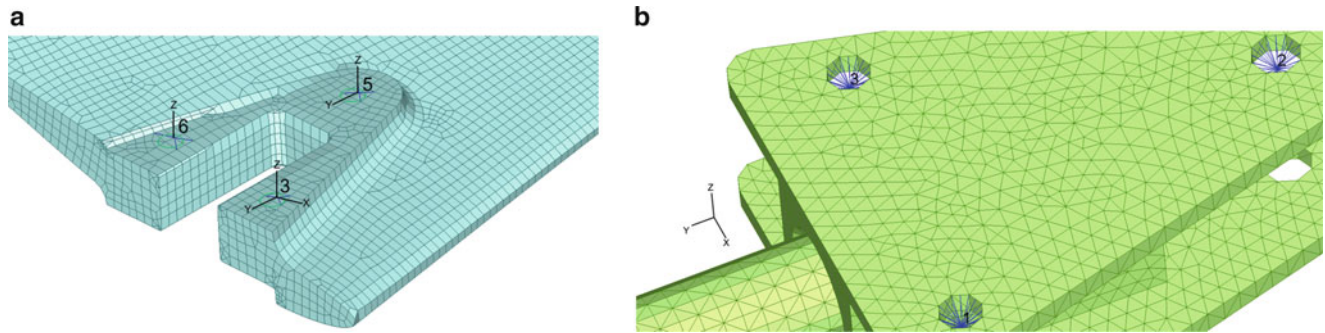
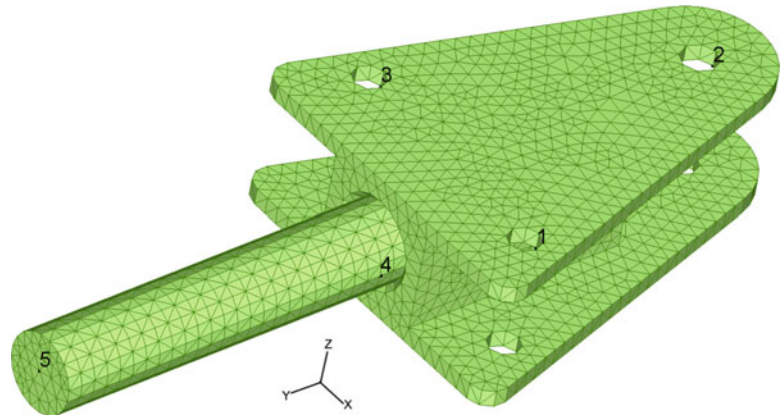


Fig. 1.4 The coupling configurations for the blade and the bracket using rigid links attached to a six DOFs coupling node. (a) Blade coupling configuration. (b) Bracket coupling configuration

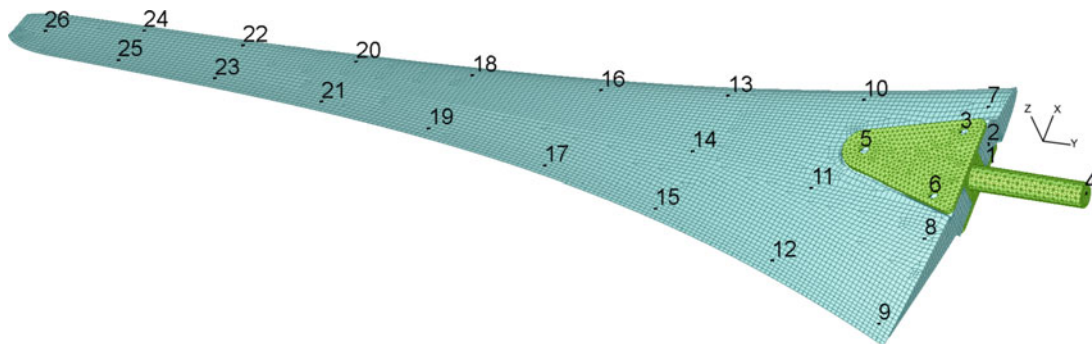


Fig. 1.5 The FE model of the blade mounted to the FE model of the bracket with measurement locations

1.4 Experiments

Three different blades from the same Ampair 600 wind turbine were considered. Each blade had a unique mounting brackets so that each blade was mounted to its own bracket. The three experimental blades will henceforth be denoted by their serial number; 841, 722 and 819 and the brackets will be numbered, 01, 02 and 03. Coupling between the blade and their corresponding bracket was blade 841 and bracket 01, blade 722 and bracket 02 and blade 819 and bracket 03. The bracket numbers will usually be omitted when the blade bracket configuration is discussed but occasionally they will be abbreviated as blade/bracket, e.g. 841/01 would represent a blade 841 which in turn is mounted to bracket 01.

The experiments were performed at Chalmers Vibration and Smart Structures Lab. The measurements were performed with a stepped sine input with 0.25 Hz step size from 20 to 800 Hz for the blade and blade bracket measurements. For the fully assembled system the measurements were performed from 10 to 300 Hz with a step size of 0.1 and 0.01 Hz at some particular frequency intervals. A total of three measurements for the blade and blade bracket models were made. The configurations

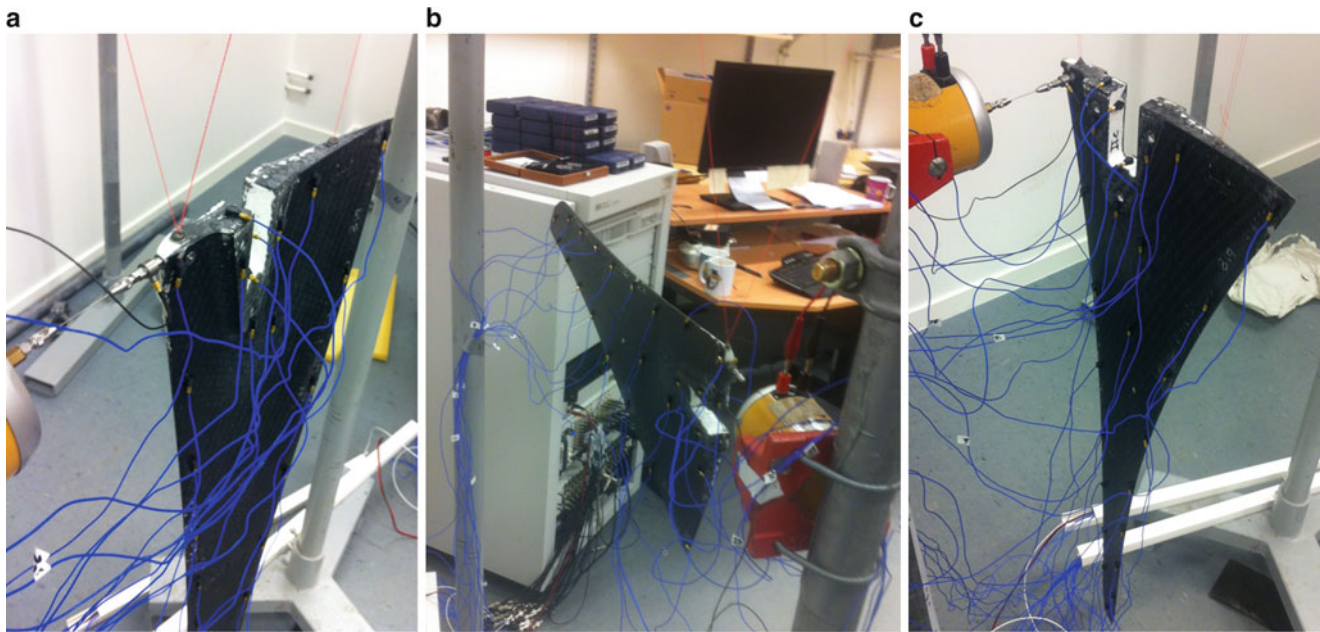


Fig. 1.6 The input directions and test setup for the blades. (a) Input in the x direction. (b) Input in the y direction. (c) Input in the z direction

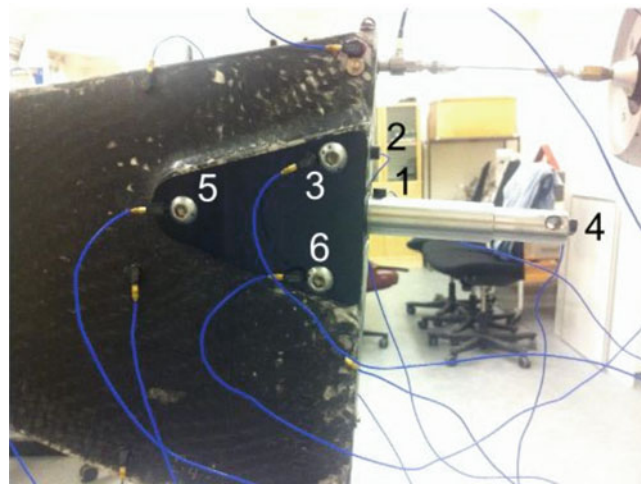


Fig. 1.7 A detailed view of the blade bracket assembly is shown with the accelerometer placements

considered were: the three blades alone and the three blades with brackets mounted. Note that measurements made in a specific direction (x, y or z) means that the input was aligned with that axis. See Fig. 1.1 for an orientation of a generic blade and Fig. 1.2 for the different input locations.

1.4.1 Test Setup

The three different input directions are shown in Fig. 1.6. This coordinate system is consistent with the FE analysis coordinate system. The test setup shown in Fig. 1.4 is also general for all measurements. It was exactly the same, both for the measurement of blades alone and for the blade measurements with a bracket attached. It can be seen, from Fig. 1.6, that the measured blades (and bracket mounted blades) were hung at three locations when measured in the x and y directions, which made it easier to position the components relative to the load cell. Measurements in the z direction for the blade and blade with attached bracket were only hung at two positions. Further, it should be noted that the components were hung in fasteners which were glued to the components, the same fastener was used for the load cell attachment and can be seen in Fig. 1.7. All the fasteners were mounted on the blades during all measurements for consistency.

The interface locations of the blade are shown in Fig. 1.2 but with the interface accelerometer from position 6 located under the stinger and used as a direct acceleration for a comparison with the accelerometer at position 1.

For a view of a bracket and blade assembled see Fig. 1.7. A detailed view of the interface accelerometers can also be seen. Different input directions to the bracket coupled with a blade had the same accelerometer locations and the same input locations were used as shown in Fig. 1.6.

1.5 Experimental Models

To obtain experimental models, system identification was performed on the obtained frequency response data (FRD). The system identification of the substructures, see Sect. 1.4.1, was conducted using an automated method for order selection and identification developed by Yaghoubi and Abrahamsson, see [29, 32]. This method is based on obtaining a number of realisations of the same dataset, using MATLAB's `n4sid` method, which is a state-space subspace method, see McKelvey et al. [28]. The realisations is then statistically evaluated, using the MOC, to discard non-physical modes. The only input required by the user is a high model order from start. In general, the method worked very well for the experimental data of the blade. Only occasionally did it give non-physical modes that could be removed manually. The synthesised models correlate well with measured data and the spread in response between the different blades can be seen in Fig. 1.8.

1.6 Results

In this section correlation between the eigenvalues of the blade models and the blade bracket coupled models are presented. Then, analytical coupling between the components is presented together with the experimental-analytical coupling results. Comparisons between the state-space and the frequency-based methods compared to analytical coupling and finally results based on measurements compared to experimental-analytical coupling.

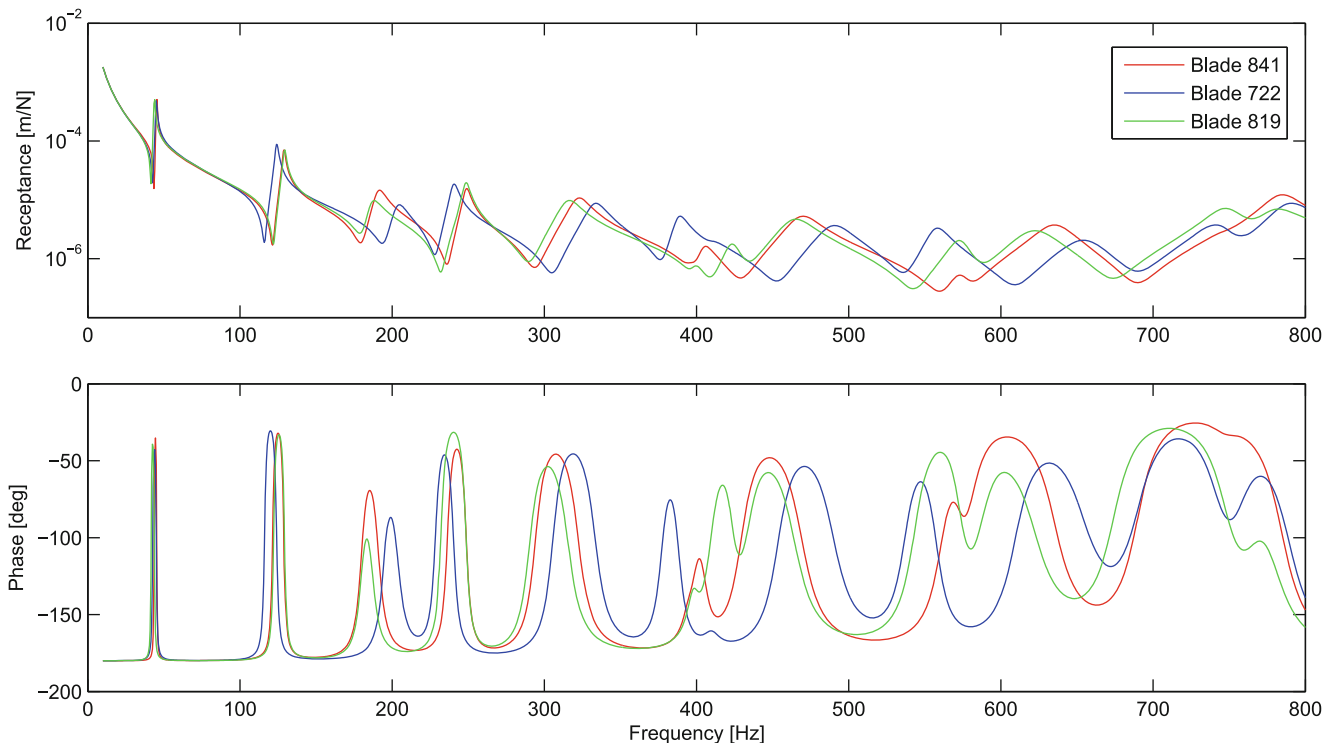


Fig. 1.8 Spread between the synthesised FRFs of the blades with input in z and output from channel 7

Table 1.1 Eigenfrequencies (Hz) and mass (g) for all the blades along with mean (μ , Hz and g), standard deviation (σ , Hz and g) and coefficient of variation (COV, %) of all the experimental blades

| Component | Blades | | | | Statistics | | | |
|-----------|--------|--------|--------|--------|------------|----------|----------|-------|
| | 841 | 722 | 819 | FEA | μ | σ | COV | Error |
| Mode 1 | 45.37 | 45.00 | 43.72 | 45.82 | 44.70 | 0.86 | 1.93 | 2.51 |
| Mode 2 | 128.76 | 124.08 | 129.24 | 130.67 | 127.36 | 2.85 | 2.24 | 2.60 |
| Mode 3 | 190.79 | 203.49 | 186.66 | 197.65 | 193.65 | 8.77 | 4.53 | 2.06 |
| Mode 4 | 248.64 | 240.32 | 248.44 | 254.21 | 245.80 | 4.75 | 1.93 | 3.42 |
| Mode 5 | 322.12 | 333.15 | 315.29 | 339.93 | 323.52 | 9.01 | 2.79 | 5.07 |
| Mode 6 | 395.36 | 388.16 | 398.94 | 412.58 | 394.16 | 5.49 | 1.39 | 4.67 |
| Mode 7 | 404.56 | 410.33 | 423.24 | 453.22 | 412.71 | 9.56 | 2.32 | 9.82 |
| Mode 8 | 468.74 | 489.54 | 463.86 | 495.47 | 474.05 | 13.64 | 2.88 | 4.52 |
| Mode 9 | 572.88 | 557.26 | 573.00 | 598.12 | 567.71 | 9.05 | 1.59 | 5.36 |
| Mode 10 | 635.25 | 654.52 | 621.72 | 660.11 | 637.16 | 16.49 | 2.59 | 3.60 |
| Mode 11 | 746.52 | 742.21 | 747.93 | 758.33 | 745.55 | 2.98 | 0.40 | 1.71 |
| Mass | 830.50 | 829.70 | 830.10 | 797.11 | 830.10 | 0.40 | 4.89e-04 | -3.97 |

The FE model eigenfrequencies (Hz) and mass (g) are also shown along with the relative error (%) between the measured mean and the FE element blade

Table 1.2 Eigenfrequencies (Hz) for all the bracket mounted blades along with the error (%) between the measured mean and the experimental-analytical synthesised components with the state-space method

| Set Component | Blades/brackets | | | | Error | | |
|------------------|-----------------|------------|------------|------------|---------|---------|---------|
| | μ | SS 841/FEA | SS 722/FEA | SS 819/FEA | Error 1 | Error 2 | Error 3 |
| Mode 1 | 40.19 | 43.01 | 41.92 | 41.08 | 5.39 | 4.24 | 3.89 |
| Mode 2 | 115.73 | 119.52 | 114.17 | 120.55 | 2.04 | 2.04 | 2.03 |
| Mode 3 | 193.79 | 187.35 | 201.35 | 184.91 | -1.11 | -1.3 | -1.59 |
| Mode 4 | 222.7 | 229.24 | 220.29 | 229.33 | 1.54 | 0.64 | 2.63 |
| Mode 5 | 321.03 | 308.69 | 322.83 | 304.88 | -3.21 | -2.92 | -2.15 |
| Mode 6 | 365.02 | 391.92 | 355.8 | 391.27 | 6.51 | -0.34 | 5.72 |
| Mode 7 | 383.58 | 410.04 | 405.19 | 408.84 | 9.37 | 4.46 | 5.38 |
| Mode 8 | 486.16 | 437.3 | 466.13 | 442.78 | -7.93 | -8.24 | -6.89 |
| Mode 9 | 536.26 | 548.52 | 518.58 | 537.05 | 0.51 | -1.9 | 0.49 |
| Mode 10 | 653.62 | 584.9 | 606.98 | 582.37 | -7.75 | -13.3 | -7.09 |
| Mode 11 | 726.88 | 634.01 | 645.84 | 617.42 | -14.68 | -11.58 | -12.68 |

Error 1 stand for the relative error between SS 841/FEA and measured mean, Error 2 between SS 722/FEA and measured mean and Error 3 between SS 819/FEA and measured mean

1.6.1 Analytical and Synthesised Blade Models

The 11 first eigenfrequencies for the three experimental blade models and the FE blade are shown in Table 1.1 along with the mean (μ , Hz), the standard deviation (σ , Hz) and the coefficient of variance (COV, %) for the three experimental blades. Also, the relative error (%) between the measured mean relative to the FE blade is given. It can be seen that the spread between the blades is considerable and that the errors for modes 8 and 10 are considerably larger compared to the other modes. The mass (gramme) is also given in the table for the three blades and the FE blade along with the mean (gramme) of the three blades, the standard deviation (gramme), the coefficient of variance and the relative error with respect to the FE model. It should also be noted that the spread of the mass is very small.

1.6.2 Blade Bracket

From Table 1.2 it can be seen that a relatively large spread is obtained for mode 7, 8, 10 and 11.

In Fig. 1.9 the FRFs for the difference between the coupled models are shown for models coupled using frequency based and state space coupling. It can be seen that the two coupling procedures produces identical results.

In Fig. 1.10 the difference between the individual measured FRFs of the blade bracket assemblies as well as the state space coupled systems becomes eminent.

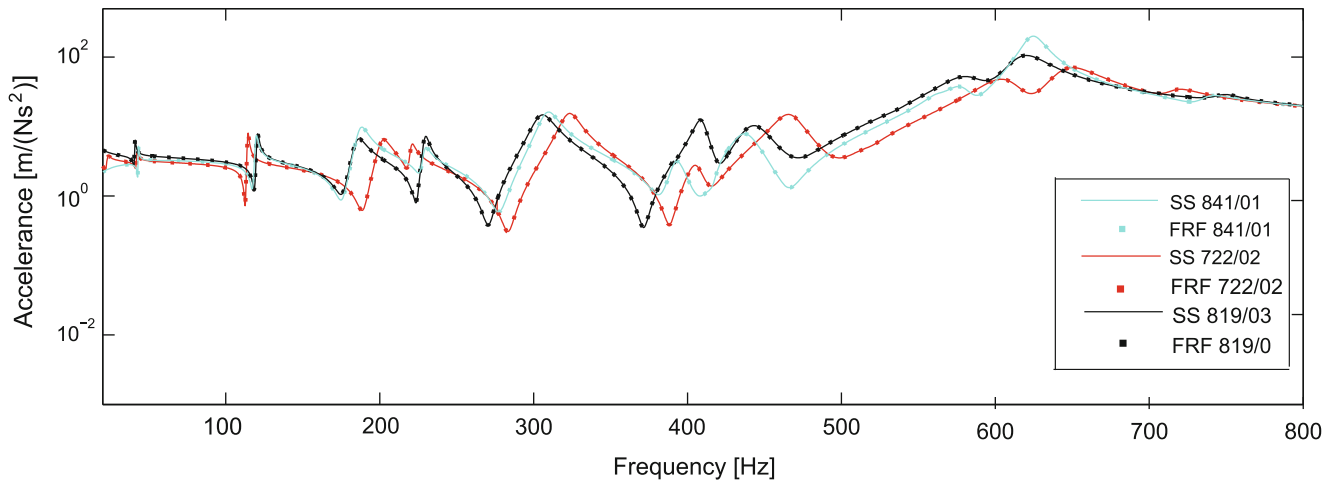


Fig. 1.9 Difference between frequency based and state-space based substructuring methods when $\mathbf{CB} = \mathbf{0}$, for experimental-analytical coupling of the blade bracket system

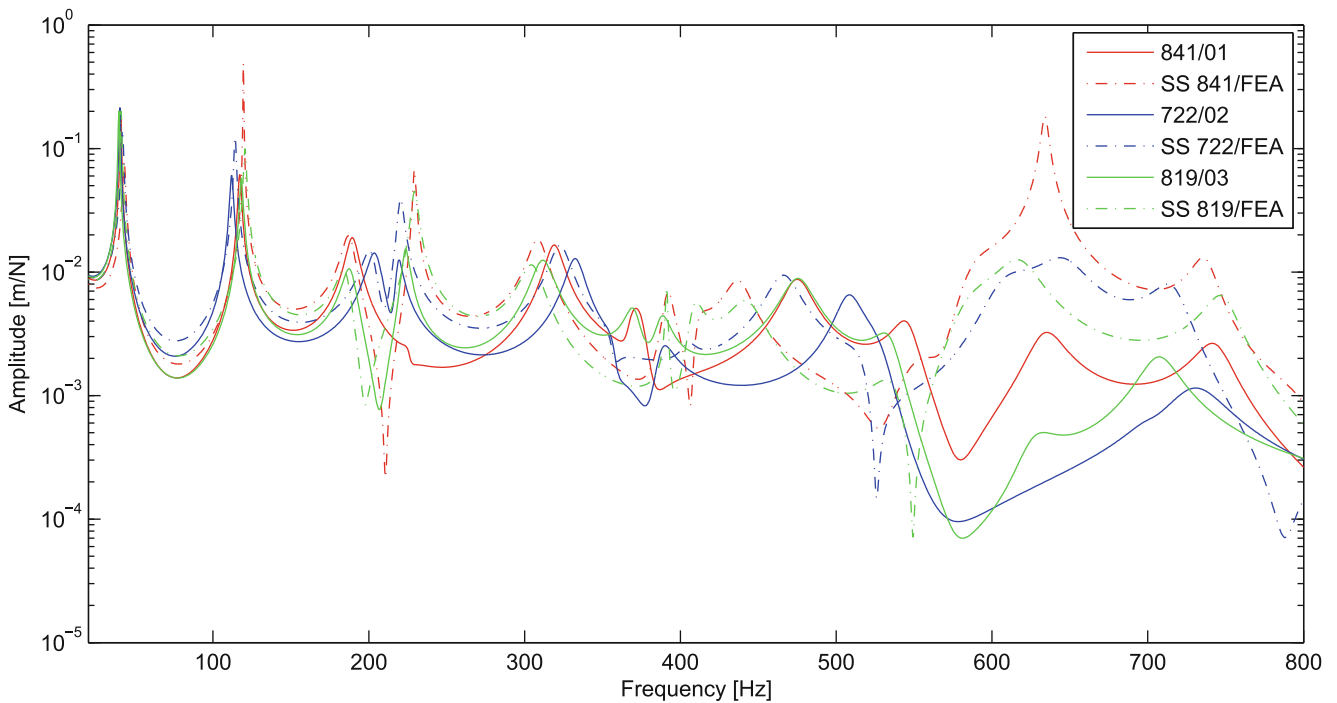


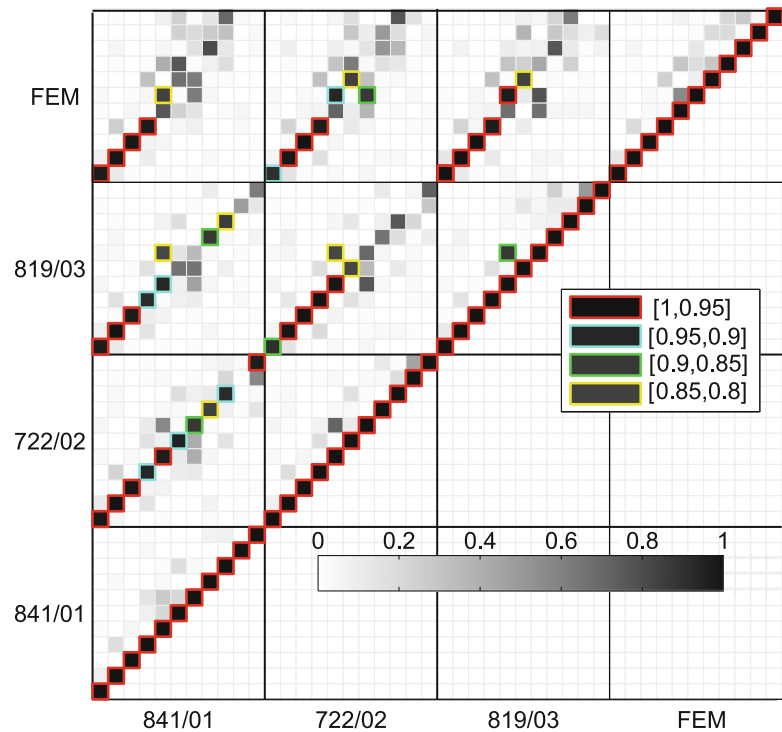
Fig. 1.10 FRF comparison between the coupled state space blade bracket models and the measured models

In Fig. 1.11, the three considered configurations of the analytical couplings are compared to the measured components. The analytical model correlated well with the four first modes. After that the analytical model did not correlate very well with any of the blades.

1.7 Conclusions and Further work

In this paper, an experimental-analytical synthesis of components for the SEM Substructuring focus group test bed, the Ampair 600W wind turbine, has been presented using a state-space method for the coupling. Experimental models of the blades of the turbine were identified through system identification techniques and coupled to analytical models of the brackets

Fig. 1.11 MAC matrix for the 11 first modes between the experimental (measured) models and the three different coupling configurations of the analytical bracket mounted blade. Four colour codes are given where *red* marks a correlation between 0.95 and 1, *cyan* a correlation between 0.9 and 0.95, *green* a correlation between 0.85 and 0.9 and *yellow* a correlation between 0.8 and 0.85 (Color figure online)



normally used to fix them to the hub. The results were compared to those of a frequency-based method and the results were equivalent.

A comparison with results obtained from coupling a finite element blade model to the same bracket model as the experimental models has been performed. When using the same coupling configuration, the experimental-analytical coupling version outperforms the analytical-analytical one. Owing to the greater flexibility in adapting the interface between the two analytical models however, the analytical-analytical model can be tuned to show slightly better results than the experimental ones, see further the full MSc report by Gibanica [5]. This motivates investigation of interfacing techniques such as the transmission simulator method in the context of state-space substructuring.

A theoretical comparison to a second order system coupling technique was performed for the state-space synthesis. It shows that, under certain conditions, the system produced by the method is equal to that obtained by component mode synthesis/direct coupling techniques. The state-space method is also translated into the general framework of de Klerk et al. [1].

An ad-hoc solution for enforcing passivity to systems identified through system identification has been utilized in this paper. In the future, further theoretical development of this technique is needed.

Also, the next step will be to couple the blades together through the hub.

References

1. de Klerk D, Rixen DJ, Voormeeren SN (2008) General framework for dynamic substructuring: history, review and classification of techniques. *AIAA J* 46(5):1169–1181
2. Bishop RED, Johnson DC (1960) *The mechanics of vibration*. Cambridge University Press, Cambridge
3. Jetmundsen B, Bielawa RL, Flannely WG (1988) Generalized frequency domain substructure synthesis. *J Am Helicopter Soc* 33(1):55–54
4. Craig RR Jr, Bampton MCC (1968) Coupling of substructures for dynamic analyses. *AIAA J* 6:1313–1319
5. Gibanica M (2013) *Experimental-analytical dynamic substructuring: a state-space approach*. Master's thesis, Chalmers University of Technology
6. Mayes RL (2012) An introduction to the sem substructures focus group test bed - the ampair 600 wind turbine. In: Conference proceedings of the Society for Experimental Mechanics series. 30th IMAC, a conference on structural dynamics, pp 61–71
7. Mayes RL (2012) Tutorial on experimental dynamic substructuring using the transmission simulator method. In: Conference proceedings of the Society for Experimental Mechanics series. 30th IMAC, a conference on structural dynamics, pp 1–9
8. Rohe DP, Mayes RL (2013) Coupling of a bladed hub to the tower of the ampair 600 wind turbine using the transmission simulator method. In: Conference proceedings of the Society for Experimental Mechanics series. 31th IMAC, a conference on structural dynamics

9. Nurbhai M, Macknelly D (2013) Dynamic substructuring wind turbine blade finite element model update and correlation with test. In: Conference proceedings of the Society for Experimental Mechanics series. 31th IMAC, a conference on structural dynamics
10. Rahimi S, de Klerk D, Rixen DJ (2013) The ampair 600 wind turbine benchmark: results from the frequency based substructuring applied to the rotor assembly. In: Conference proceedings of the Society for Experimental Mechanics series. 31th IMAC, a conference on structural dynamics
11. Brunetti J, Culla A, D'Ambrogio W, Fregolent A (2013) Selection of interface dofs in hub-blade(s) coupling of ampair wind turbine test bed. In: Conference proceedings of the Society for Experimental Mechanics series. 31th IMAC, a conference on structural dynamics
12. SEM Substructuring Focus Group (2013) SEM Substructuring Wiki. <http://substructure.engr.wisc.edu/substwiki/>. October 2013
13. Steinepreis D, Reuss P, Schempp F, Gaul L (2013) Interface damping of the ampair wind turbine test bed (presentation only). In: Conference proceedings of the Society for Experimental Mechanics series. 31th IMAC, a conference on structural dynamics
14. Sjövall P, Abrahamsson T (2007) Component system identification and state-space model synthesis. *Mech Syst Signal Process* 21(7): 2697–2714
15. Su T-J, Juang J-N (1994) Substructure system identification and synthesis. *J Guid Control Dyn* 17(5):1087–1095
16. Harvie J, Avitabile P (2012) Comparison of some wind turbine blade tests in various configurations. In: Conference proceedings of the Society for Experimental Mechanics series. 30th IMAC, a conference on structural dynamics, pp 73–79
17. Nurbhai M, Macknelly D (2012) Modal assessment of wind turbine blade in preparation of experimental substructuring. In: Conference proceedings of the Society for Experimental Mechanics series. 30th IMAC, a conference on structural dynamics, pp 71–72
18. Macknelly D, Nurbhai M, Monk N (2013) Additional modal testing of turbine blades and the application of transmission simulator substructuring methodology for coupling. In: Conference proceedings of the Society for Experimental Mechanics series. 31th IMAC, a conference on structural dynamics
19. Gibanica M, Johansson AT, Rahrovani S, Khorsand M, Abrahamsson T (2013) Spread in modal data obtained from wind turbine blade testing. In: Conference proceedings of the Society for Experimental Mechanics series. 31th IMAC, a conference on structural dynamics
20. Johansson AT, Lindholm C-J, Khorsand M, Abrahamsson T (2013) Modeling and calibration of small-scale wind turbine blade. In: Conference proceedings of the Society for Experimental Mechanics series. 31th IMAC, a conference on structural dynamics
21. Linderholt A (2013) Model calibration of an a600 wind turbine blade. In: Conference proceedings of the Society for Experimental Mechanics series. 31th IMAC, a conference on structural dynamics
22. Antoulas AC (2005) Approximation of large-scale dynamical systems. *Advances in design and control*. Society for Industrial and Applied Mathematics, Philadelphia
23. Kailath T (1980) *Linear systems*. Prentice-Hall, Englewood Cliffs
24. Craig RR, Kurdila AJ (2006) *Fundamentals of structural dynamics*, 2nd edn. Wiley, New York
25. Abrahamsson T (2000) *Linear system theory in vibration engineering*. Applied Mechanics, Anders Johansson, Chalmers
26. Ewins DJ (2000) *Modal testing: theory and practice*, 2nd edn. Research Studies Press, Letchworth
27. Ljung L (1999) *System identification: theory for the user*, 2nd edn. Prentice Hall, Upper Saddle River
28. McKelvey T, AkCay H, Ljung L (1996) Subspace-based multivariable system identification from frequency response data. *IEEE Trans Automat Control* 41(7):960–979
29. Yaghoubi V, Abrahamsson T (2012) Automated modal analysis based on frequency response function estimates. In: Conference proceedings of the Society for Experimental Mechanics series. 30th IMAC, a conference on structural dynamics, pp 9–18
30. McKelvey T, Moheimani SOR (2005) Estimation of phase constrained mimo transfer functions with application to flexible structures with mixed collocated and non-collocated actuators and sensors. In: Proceedings of the 16th IFAC world congress
31. Sjövall P (2004) Component synthesis and identification in structural dynamics. Licentiate thesis, Chalmers University of Technology
32. Yaghoubi V, Abrahamsson T (2013) The modal observability correlation as a modal correlation metric. In: Conference proceedings of the Society for Experimental Mechanics series. 31th IMAC, a conference on structural dynamics

Chapter 2

Experimental Dynamic Substructuring of the Ampair Wind Turbine Test Bed

Jacopo Brunetti, Antonio Culla, Walter D'Ambrogio, and Annalisa Fregolent

Abstract In a recent paper, the authors discussed the selection of a reduced set of interface DoFs in order to describe the coupling between the blades and the hub of the Ampair test bed wind turbine rotor. The study was conducted using simulated FRFs obtained from Finite Element model of the blades and the hub, but in view of using experimental FRFs. In this paper, test data measured on the turbine by the UW-Madison participants in the IMAC Focus Group on Experimental Dynamic Substructuring, and posted on the Wiki page of the group, are used for dynamic substructuring of the wind turbine test bed.

Keywords Experimental dynamic substructuring • Wind turbine • Modal identification • Frequency response function synthesis • Frequency based substructuring

2.1 Introduction

Experimental Dynamic Substructuring is a very powerful tool in the analysis of dynamic behavior of complex mechanical systems and responds to actual industrial needs. Two main problem can be defined that allow to perform the addition (coupling) and the subtractions (decoupling) of substructures.

In experimental contexts, coupling techniques allow to estimate the dynamic response of a complex structure that cannot be tested in one piece while the model of the component systems can be derived from experimental tests. On the contrary, decoupling techniques can be useful in complete structures where some components cannot be accessed easily or when some components cannot be removed and tested separately.

Addition of substructures (coupling) can be seen as a structural modification problem [1]. Similarly, the decoupling problem can be seen as a structural modification problem with negative modification. Due to modal truncation problems, in experimental dynamic substructuring, the use of FRFs (Frequency Based Substructuring) can be preferred with respect to the use of modal parameters. The main algorithm for frequency based substructuring is the improved impedance coupling [2] that involves just one matrix inversion with respect to the classical impedance coupling technique that requires three inversions. A general framework for dynamic substructuring is provided in [3,4]: in this context, the so called dual domain decomposition is very useful for experimental application, since it allows to retain the full set of global DoFs by ensuring equilibrium at the interface between substructures. A similar formulation for the decoupling problem is developed and discussed in [5–7].

J. Brunetti

Dipartimento di Ingegneria Industriale e dell'Informazione e di Economia, Università dell'Aquila, Via G. Gronchi, 18
I-67100 L'Aquila (AQ), Italy

LaMCos, Contacts and Structural Mechanics Laboratory, Université de Lyon, CNRS, INSA-Lyon, UMR 5259, rue des Sciences, 69621
Villeurbanne, France

A. Culla • A. Fregolent

Dipartimento di Ingegneria Meccanica e Aerospaziale, Università di Roma La Sapienza, Via Eudossiana 18, I 00184 Rome, Italy

W. D'Ambrogio (✉)

Dipartimento di Ingegneria Industriale e dell'Informazione e di Economia, Università dell'Aquila, Via G. Gronchi, 18
I-67100 L'Aquila (AQ), Italy
e-mail: walter.dambrogio@univaq.it

In this paper, dynamic substructuring is applied to the Ampair 600 wind turbine. This system has been proposed as a test bed by the Society of Experimental Mechanics focus group on experimental dynamic substructuring, to enable advancements in experimental dynamic substructuring technology and theory. Several specimens of the turbine have been bought by some participants in the focus group. A description of the turbine with modifications made to the system to make it more linear is presented in [8] together with results from a rudimentary modal test on the whole turbine. In a recent paper [9], the authors discussed the selection of a reduced set of interface DoFs in order to describe the coupling between the blades and the hub of the Ampair test bed wind turbine rotor. The study was conducted using simulated FRFs obtained from Finite Element model of the blades and the hub, but in view of using experimental FRFs.

The experimental FRFs used in this paper are measured by UW-Madison on the full turbine, on the two-bladed turbine and on a mass-loaded bladed, and are posted on the Wiki page of the IMAC Experimental Dynamics Substructuring Focus Group. Curve fitting of raw measured FRFs is performed after a reciprocity analysis aimed to select the more convenient reference DoFs, using a poly-reference Least Square Frequency Domain technique. Since some unmeasured FRFs are required to apply the coupling procedure, they are synthesized using the identified modal parameters. Finally, the results of substructuring are presented and discussed.

2.2 Coupling and Decoupling in the Frequency Domain

The coupled structural system is assumed to be made by two (or more) subsystems joined through a number of couplings (see Fig. 2.1). The degrees of freedom (DoFs) of the coupled system can be partitioned into internal DoFs (not belonging to the couplings) and coupling DoFs.

2.2.1 Addition of Subsystems

If addition of subsystems (coupling problem) is considered, all subsystems are assumed to be known whilst the FRF of the coupled system is unknown. In the frequency domain, the equation of motion of a linear time-invariant subsystem r may be written as:

$$[Z^{(r)}(\omega)] \{u^{(r)}(\omega)\} = \{f^{(r)}(\omega)\} + \{g^{(r)}(\omega)\} \quad (2.1)$$

where:

- $[Z^{(r)}]$ is the dynamic stiffness matrix of subsystem r ;
- $\{u^{(r)}\}$ is the vector of degrees of freedom of subsystem r ;
- $\{f^{(r)}\}$ is the external force vector;
- $\{g^{(r)}\}$ is the vector of connecting forces with other subsystems (constraint forces arising from compatibility conditions).

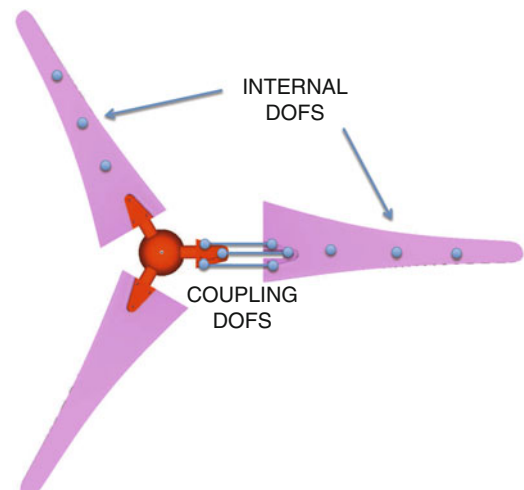


Fig. 2.1 Scheme of the substructuring problem

For the sake of simplicity, the explicit frequency dependence will be omitted. Furthermore, the procedure will be developed with reference to two subsystems, bearing in mind that it can be easily extended to more subsystems.

The equation of motion of the subsystems to be coupled can be written in a block diagonal format as:

$$[Z] \{u\} = \{f\} + \{g\} \quad \text{i.e.} \quad \begin{bmatrix} [Z^{(1)}] & [0] \\ [0] & [Z^{(2)}] \end{bmatrix} \begin{Bmatrix} \{u^{(1)}\} \\ \{u^{(2)}\} \end{Bmatrix} = \begin{Bmatrix} \{f^{(1)}\} \\ \{f^{(2)}\} \end{Bmatrix} + \begin{Bmatrix} \{g^{(1)}\} \\ \{g^{(2)}\} \end{Bmatrix} \quad (2.2)$$

The compatibility condition at the interface DoFs implies that any pair of matching DoFs $u_l^{(1)}$ and $u_m^{(2)}$, i.e. DoF l on subsystem 1 and DoF m on subsystem 2 must have the same displacement, that is $u_l^{(1)} - u_m^{(2)} = 0$.

This condition can be generally expressed as:

$$[B] \{u\} = \{0\} \quad \text{i.e.} \quad \begin{bmatrix} [B^{(1)}] & [B^{(2)}] \end{bmatrix} \begin{Bmatrix} \{u^{(1)}\} \\ \{u^{(2)}\} \end{Bmatrix} = 0 \quad (2.3)$$

where each row of $[B]$ corresponds to a pair of matching DoFs. Note that $[B]$ is, in most cases, a signed Boolean matrix and it can be written by distinguishing the contribution of the different subsystems.

The equilibrium condition for constraint forces associated with the compatibility conditions implies that, when the connecting forces are added for a pair of matching DoFs, their sum must be zero, i.e. $g_l^{(1)} + g_m^{(2)} = 0$: this holds for any pair of matching DoFs. Furthermore, if DoF k on subsystem 1 (or 2) is not a connecting DoF, it must be $g_k^{(1)} = 0$: this holds for any non-interface DoF.

Overall, the above conditions can be expressed as:

$$[L]^T \{g\} = \{0\} \quad (2.4)$$

where the matrix $[L]$ is a Boolean localisation matrix. Note that the number of rows of $[L]^T$ is equal to the number of non-interface DoFs plus the number of pairs of interface DoFs.

Equations (2.2)–(2.4) can be put together to obtain the so called 3-field formulation [3]:

$$\begin{cases} [Z] \{u\} = \{f\} + \{g\} \\ [B] \{u\} = \{0\} \\ [L]^T \{g\} = \{0\} \end{cases} \quad (2.5)$$

2.2.1.1 Dual Formulation in the Frequency Domain [3]

In the dual formulation, the total set of DoFs is retained, i.e. each interface DoF is present as many times as there are substructures connected through that DoF. The equilibrium condition $g_l^{(1)} + g_m^{(2)} = 0$ at a pair of interface DoFs is ensured by choosing, for instance, $g_l^{(1)} = -\lambda$ and $g_m^{(2)} = \lambda$. Due to the construction of $[B]$, the overall interface equilibrium can be ensured by writing the connecting forces in the form:

$$\{g\} = -[B]^T \{\lambda\} \quad (2.6)$$

where $\{\lambda\}$ are Lagrange multipliers corresponding to connecting force intensities. Since there is a unique set of connecting force intensities λ , the interface equilibrium condition Eq. (2.4) is satisfied automatically for any λ , i.e.

$$[L]^T \{g\} = -[L]^T [B]^T \{\lambda\} = \{0\} \quad (2.7)$$

Then $[B]^T$ is the nullspace of $[L]^T$, so Eq. (2.7) is always satisfied and the system of Eq. (2.5) becomes:

$$\begin{cases} [Z] \{u\} + [B]^T \{\lambda\} = \{f\} \\ [B] \{u\} = \{0\} \end{cases} \quad (2.8)$$

In matrix notation:

$$\begin{bmatrix} [Z] & [B]^T \\ [B] & [0] \end{bmatrix} \begin{Bmatrix} \{u\} \\ \{\lambda\} \end{Bmatrix} = \begin{Bmatrix} \{f\} \\ \{0\} \end{Bmatrix} \quad (2.9)$$

that is:

$$\begin{bmatrix} [Z^{(1)}] & [0] & [B^{(1)}]^T \\ [0] & [Z^{(2)}] & [B^{(2)}]^T \\ [B^{(1)}] & [B^{(2)}] & [0] \end{bmatrix} \begin{Bmatrix} \{u^{(1)}\} \\ \{u^{(2)}\} \\ \{\lambda\} \end{Bmatrix} = \begin{Bmatrix} \{f^{(1)}\} \\ \{f^{(2)}\} \\ \{0\} \end{Bmatrix} \quad (2.10)$$

Note that $[B^{(1)}]$ and $[B^{(2)}]$ extract the coupling DoFs among the full set of DoFs.

By eliminating $\{\lambda\}$, it is possible to obtain a relation in the form $\{u\} = [H] \{f\}$, which provides the FRF of the coupled system [6]:

$$\{u\} = \left([Z]^{-1} - [Z]^{-1} [B]^T \left([B] [Z]^{-1} [B]^T \right)^{-1} [B] [Z]^{-1} \right) \{f\} \quad (2.11)$$

In expanded notation:

$$\begin{aligned} \begin{Bmatrix} \{u^{(1)}\} \\ \{u^{(2)}\} \end{Bmatrix} &= \left(\begin{bmatrix} [Z^{(1)}] & [0] \\ [0] & [Z^{(2)}] \end{bmatrix}^{-1} - \begin{bmatrix} [Z^{(1)}] & [0] \\ [0] & [Z^{(2)}] \end{bmatrix}^{-1} \begin{bmatrix} [B^{(1)}]^T \\ [B^{(2)}]^T \end{bmatrix} \right. \\ &\quad \times \left. \begin{bmatrix} [B^{(1)}] & [B^{(2)}] \end{bmatrix} \begin{bmatrix} [Z^{(1)}] & [0] \\ [0] & [Z^{(2)}] \end{bmatrix}^{-1} \begin{bmatrix} [B^{(1)}]^T \\ [B^{(2)}]^T \end{bmatrix} \right)^{-1} \\ &\quad \times \begin{bmatrix} [B^{(1)}] & [B^{(2)}] \end{bmatrix} \begin{bmatrix} [Z^{(1)}] & [0] \\ [0] & [Z^{(2)}] \end{bmatrix}^{-1} \begin{Bmatrix} \{f^{(1)}\} \\ \{f^{(2)}\} \end{Bmatrix} \end{aligned} \quad (2.12)$$

i.e., by introducing the FRFs $[H^{(1)}]$ and $[H^{(2)}]$ at the full set of DoFs instead of $[[Z^{(1)}]]^{-1}$ and $[[Z^{(2)}]]^{-1}$:

$$\begin{aligned} [H^{RU}] &= \begin{bmatrix} [H^{(1)}] & [0] \\ [0] & [H^{(2)}] \end{bmatrix} - \begin{bmatrix} [H^{(1)}] & [0] \\ [0] & [H^{(2)}] \end{bmatrix} \begin{bmatrix} [B^{(1)}]^T \\ [B^{(2)}]^T \end{bmatrix} \\ &\quad \times \left(\begin{bmatrix} [B^{(1)}] & [B^{(2)}] \end{bmatrix} \begin{bmatrix} [H^{(1)}] & [0] \\ [0] & [H^{(2)}] \end{bmatrix} \begin{bmatrix} [B^{(1)}]^T \\ [B^{(2)}]^T \end{bmatrix} \right)^{-1} \begin{bmatrix} [B^{(1)}] & [B^{(2)}] \end{bmatrix} \begin{bmatrix} [H^{(1)}] & [0] \\ [0] & [H^{(2)}] \end{bmatrix} \end{aligned} \quad (2.13)$$

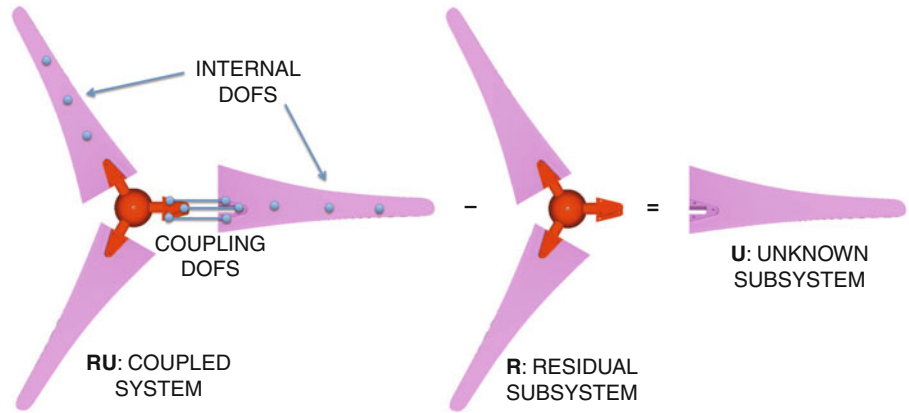
With the dual formulation, the rows and columns corresponding to the coupling DoFs appear twice in $[H^{RU}]$. Obviously, only independent entries are retained.

2.2.2 Subtraction of Subsystems Using the Dual Domain Decomposition [6]

If subtraction of subsystems (decoupling problem) is considered, the coupled structural system RU and a residual subsystem R are assumed to be known whilst the FRF of subsystem U is unknown. The unknown subsystem U and the residual subsystem R are joined through a number of couplings (see Fig. 2.2). The degrees of freedom (DoFs) of the coupled system can be partitioned into internal DoFs (u) of subsystem U (not belonging to the couplings), internal DoFs (r) of subsystem R , and coupling DoFs (c).

It is required to find the FRF of the unknown substructure U starting from the FRF of the coupled system RU . The subsystem U can be extracted from the coupled system RU by canceling the dynamic effect of the residual subsystem R . This can be accomplished by adding to the coupled system RU a fictitious subsystem with a dynamic stiffness opposite to that of the residual subsystem R and satisfying compatibility and equilibrium conditions. According to this point of view, the interface between the coupled system RU and the fictitious subsystem should not only include the coupling DoFs between

Fig. 2.2 Scheme of the decoupling problem



subsystems U and R , but should as well include the internal DoFs of subsystem R . However, it can be shown that the problem can be solved by considering a number of interface DoFs at least equal to the number of coupling DoFs n_c . Therefore, three options for interface DoFs can be considered:

- standard interface, including only the coupling DoFs (c) between subsystems U and R ;
- extended interface, including also some internal DoFs ($i \subseteq r$) of the residual substructure;
- mixed interface, including some coupling DoFs ($d \subseteq c$) and/or some internal DoFs ($i \subseteq r$) of the residual substructure.

In the framework of the dual formulation in the frequency domain (see Sect. 2.2.1.1), the union between the coupled system RU and the fictitious subsystem can be written (see Eq. (2.10)) as:

$$\begin{bmatrix} [Z^{RU}] & [0] & [B_E^{RU}]^T \\ [0] & -[Z^R] & [B_E^R]^T \\ [B_C^{RU}] & [B_C^R] & [0] \end{bmatrix} \begin{Bmatrix} \{u^{RU}\} \\ \{u^R\} \\ \{\lambda\} \end{Bmatrix} = \begin{Bmatrix} \{f^{RU}\} \\ \{f^R\} \\ \{0\} \end{Bmatrix} \quad (2.14)$$

Following the same procedure used in Sect. 2.2.1.1, it is possible to obtain the FRF of the unknown subsystem U .

$$\begin{aligned} [H^U] &= \begin{bmatrix} [H^{RU}] & [0] \\ [0] & -[H^R] \end{bmatrix} - \begin{bmatrix} [H^{RU}] & [0] \\ [0] & -[H^R] \end{bmatrix} \begin{bmatrix} [B_E^{RU}]^T \\ [B_E^R]^T \end{bmatrix} \\ &\times \left(\begin{bmatrix} [B_C^{RU}] & [B_C^R] \end{bmatrix} \begin{bmatrix} [H^{RU}] & [0] \\ [0] & -[H^R] \end{bmatrix} \begin{bmatrix} [B_E^{RU}]^T \\ [B_E^R]^T \end{bmatrix} \right)^{-1} \begin{bmatrix} [B_C^{RU}] & [B_C^R] \end{bmatrix} \begin{bmatrix} [H^{RU}] & [0] \\ [0] & -[H^R] \end{bmatrix} \end{aligned} \quad (2.15)$$

Note that $[H^{RU}]$ and $[H^R]$ are the FRFs at the full set of DoFs of the coupled system and the residual subsystem.

2.3 Test Structure

In this paper the dynamic behavior of the Ampair 600 wind turbine is analyzed. The rotor is composed by three blades clamped to the hub by three bolt and two aluminum plates that sandwich each blade. The rotor is positioned at the top of an aluminum pole fixed on a heavy basement. The whole structure is supported on an elastic trampoline during experimental tests.

Blades are made of glass reinforced polyester and they are coated with a white epoxy. Internal components of the rotor are eliminated and replaced by a dummy mass. The cavity of the hub is filled by a potting material to fix all the components and block the pitch mechanism of the blades.

Non-linearities of composite materials are very hard to model numerically and experimental characterization is the best way to obtain a reliable representation of the dynamic behavior of the blade.

In this paper two substructures are considered to solve the coupling problem. The first subsystem is the blade and the other substructure is the turbine without a blade. Experimental data of the two subsystems are provided by the University of Wisconsin—Madison and can be coupled by means of frequency based substructuring to find the behavior of the whole system.

2.4 Experimental Dynamic Substructuring

In this section the results of experimental dynamic substructuring performed on the Ampair Wind turbine are reported. The dynamic behavior of the whole system is predicted by coupling the mass loaded blade and the two bladed turbine subsystems by means of the Frequency Based Substructuring technique. The predicted FRFs are compared with those measured on the assembled system.

2.4.1 Experimental Data Description

The experimental data used for this substructuring are the data shared by the University of Wisconsin—Madison on the Wiki of the substructuring focus group, acquired on the mass loaded blade and on the two bladed turbine.

Data provided for the mass loaded blade are acceleration FRFs (inertances) measured over three response DoFs by accelerometers placed at two different points (on the tip and on the root of the blade) and for 59 different excitation DoFs, roving the instrumented hammer over 27 points along different directions (Fig. 2.3a). Three nodes are located in correspondence with the three bolts used to fix the blade to the rest of the structure (nodes 16, 17, 18) and excitations are applied on the three spatial directions for each of the three nodes.

A mass-load is applied on the mounting interface of the blade to simulate how the blade is held by the wind turbine. This mass is composed by a block of steel sandwiched between two aluminum plates. This mass results to be rigid in the frequency range of interest. Starting from the pictures published on the wiki internet site, a solid model of the mass is built and inertial characteristics (mass and moments of inertia) are calculated.

The experimental data used to characterize the two-bladed turbine subsystem are measured on three points with bi-axial accelerometers. Excitations are applied by an instrumented hammer over 94 DoFs placed on 51 different points. Also in this case, three nodes are placed in correspondence with the coupling interface and excitations are applied on the nine translational DoFs (Fig. 2.3b).

The dynamic response of the whole turbine is obtained coupling the two subsystems and canceling the load mass effect from the coupled structure.

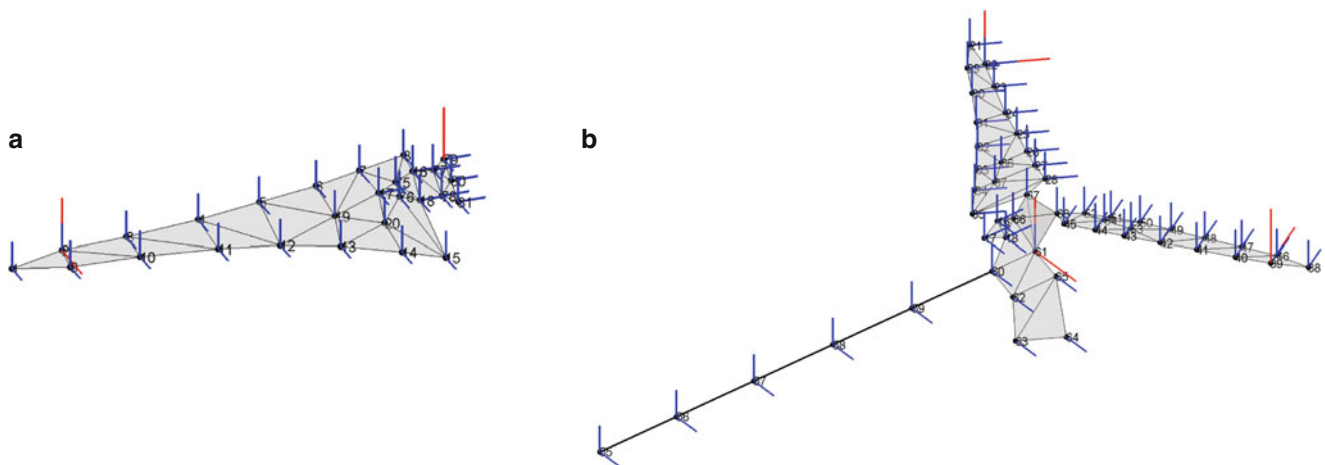


Fig. 2.3 Nodes and directions of the measured data. — excitation DoFs; — response DoFs. (a) Measured inertances on the mass loaded blade subsystem. (b) Measured inertances on the 2 bladed turbine subsystem (Color figure online)

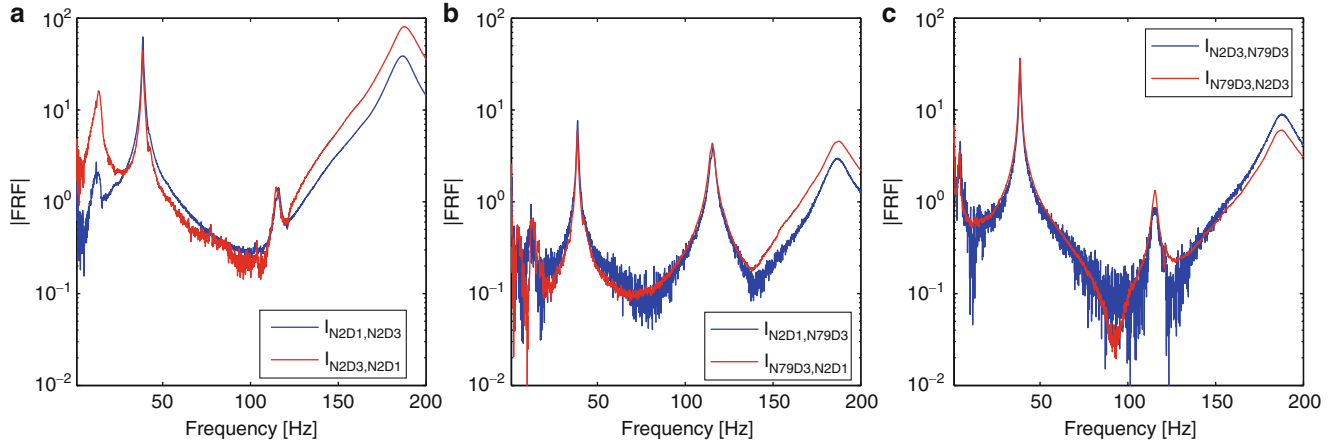


Fig. 2.4 Reciprocal terms of the measured Inertance Matrix for the blade subsystem. (a) FRFs between 2x-2z. (b) FRFs between 2x-79z. (c) FRFs between 2z-79z (Color figure online)

2.4.2 Response Selection and Curve Fitting

From a preliminary observation of the experimental data (Figs. 2.4 and 2.5), it appears that there is a lack of coherence between some of the reciprocal terms of the inertance matrix that are expected to be equal. Two series of results have been considered to perform the modal identification of the blade. Data selected for modal identification are data measured on the node 2 and 79 in the third local direction (Fig. 2.4c).

The same problem is encountered on the two bladed turbine subsystem (Fig. 2.5c, e, f) and a reduced set of the measured FRFs is selected to guarantee that reciprocal terms of the inertance matrix are almost equal. The subset selected for modal identification is composed by response data on nodes 22, 39 and 61 in the local x direction (Fig. 2.5a, b, d).

Modal identification is performed by means of Poly-Reference Least Square Complex Frequency Domain (Poly-LSCF) optimized to guarantee the symmetry of the residue matrix [10].

FRFs are defined for several excitation DoFs and a few response DoFs. The experimental inertance matrix is a rectangular matrix of size $n \times m$ where n is the number of response DoFs and $m > n$ is the number of excited DoFs. For the use of Poly-LSCF method the transposed matrix is considered where n is the number of references and m is the number of outputs of the poly-reference method.

Figure 2.6a shows the stabilization plot for the mass loaded blade in the frequency range 0–150 Hz for a model order in the range 20–50. Modes below 20 Hz correspond to the suspension system of the blade adopted for experimental tests but they are considered in the curve fitting in order to account for the effects of rigid body modes in the synthesis of unmeasured FRFs (see Sect. 2.4.3). Figure 2.6b shows the result of modal identification for the selected model order 34 highlighting a good quality of curve fitting of the experimental data both in amplitude and in phase for the blade subsystem. The modal identification shows two main modes of the mass loaded blade at 38 and 115 Hz. Other modes are found that are not physical modes of the blade but are necessary to fit the experimental responses.

Figure 2.7a shows the stabilization plot for the two bladed turbine subsystem in the frequency range 1–150 Hz for a model order in the range 40–80. The two bladed turbine subsystem presents a very complex dynamic behavior in the considered range. Figure 2.7b shows the curve fitting results for the selected model order 77 highlighting also in this case a good agreement between experimental and fitted data.

2.4.3 Synthesis of the Unmeasured FRF Elements

Substructuring techniques in the frequency domain need the knowledge of the complete (square) Frequency Response matrix of the two substructures to couple at least in the coupling DoFs (Eq. (2.13)).

Experimental data fitted by means of Poly-LSCF method provide in this case a rectangular FRF matrix (having the same size of the transposed experimental inertance matrix). The identification of modal parameters provides for each mode r the eigenvector $\{\psi\}_r$ having the same length m of output DoFs, the modal participation factors $\{\tilde{L}\}_r$ having the same length n of reference DoFs and the eigenvalue λ_r . In experimental data $n < m$ and the vector of modal participation is incomplete.

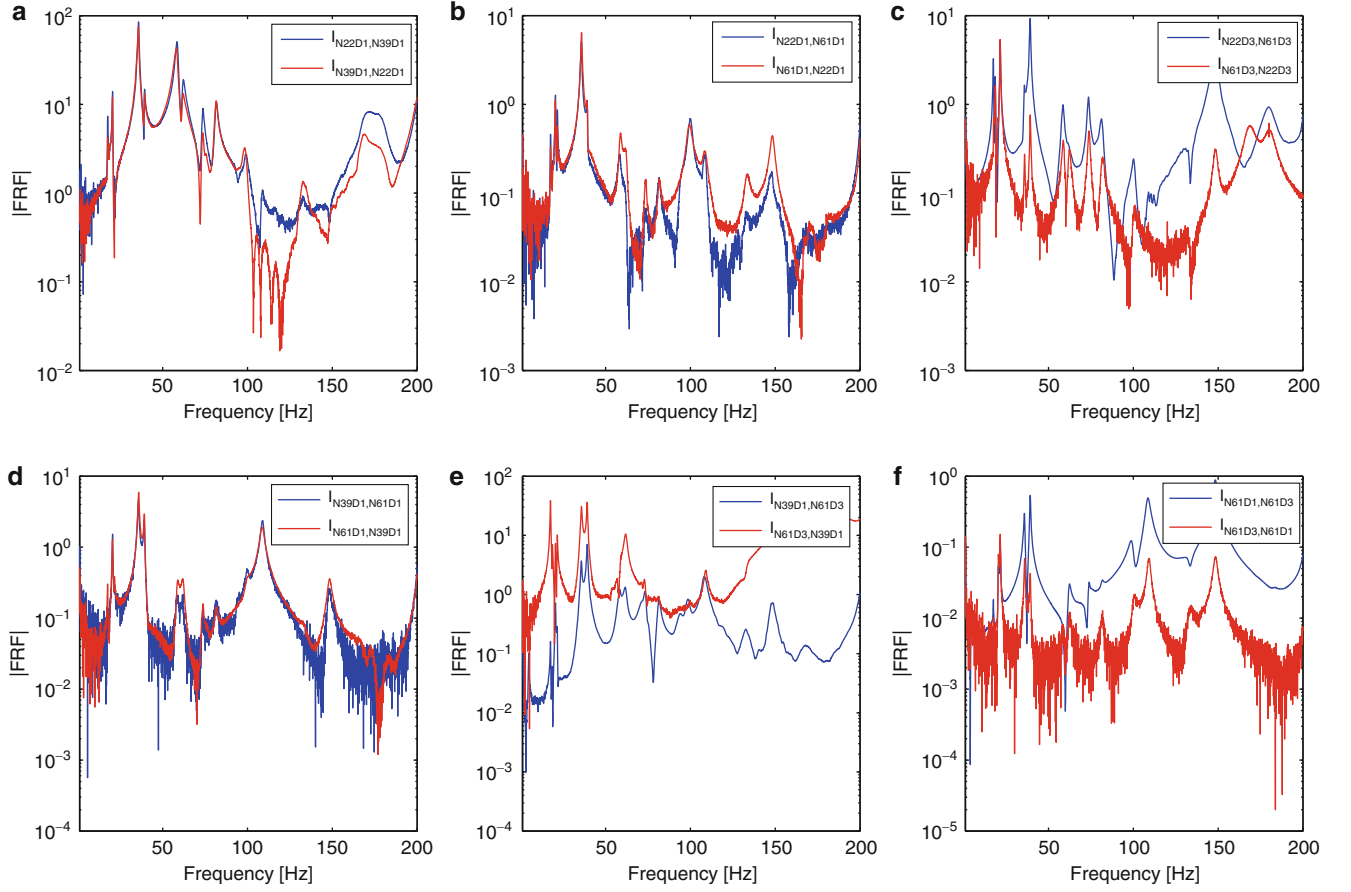


Fig. 2.5 Reciprocal terms of the measured inertance matrix for the two bladed turbine subsystem. (a) FRFs between 22x-39x. (b) FRFs between 22x-61x. (c) FRFs between 22z-61z. (d) FRFs between 39x-61x. (e) FRFs between 39x-61z. (f) FRFs between 61x-61z (Color figure online)

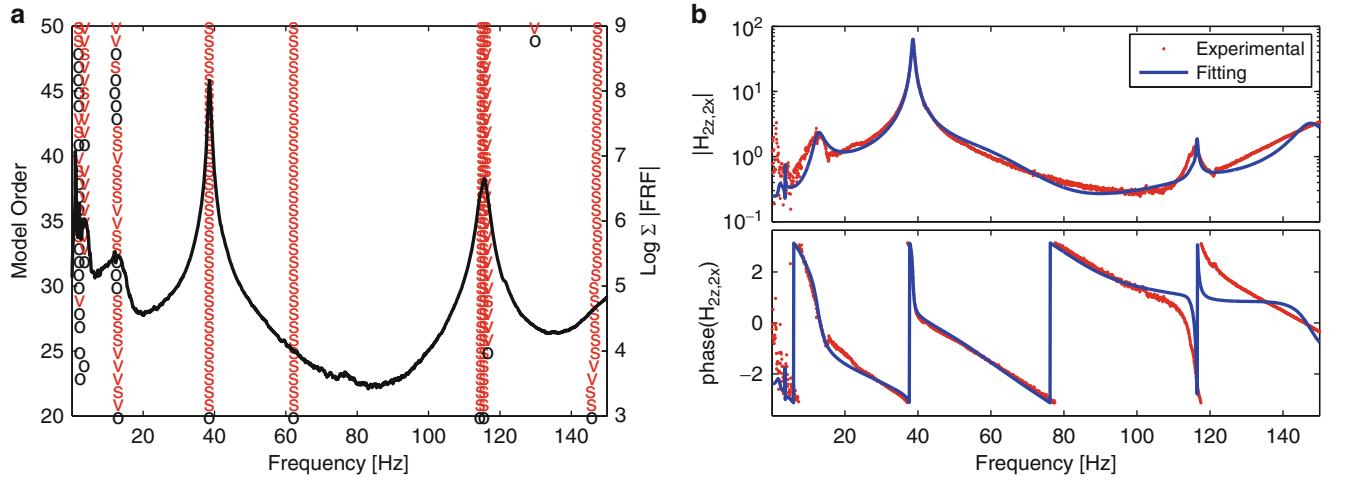


Fig. 2.6 Modal identification of the mass loaded blade subsystem. (a) Stabilization plot of the Ploy-LSCF. (b) Identification results

From the theory, the complete vector of modal participation factors $\{L\}_r$ is proportional to the corresponding eigenvector $\{\psi\}_r$. For each reference DoF n , a complex proportionality constant c_n can be defined as:

$$c_n = \frac{\tilde{L}_{n,r}}{\psi_{n,r}} \quad (2.16)$$

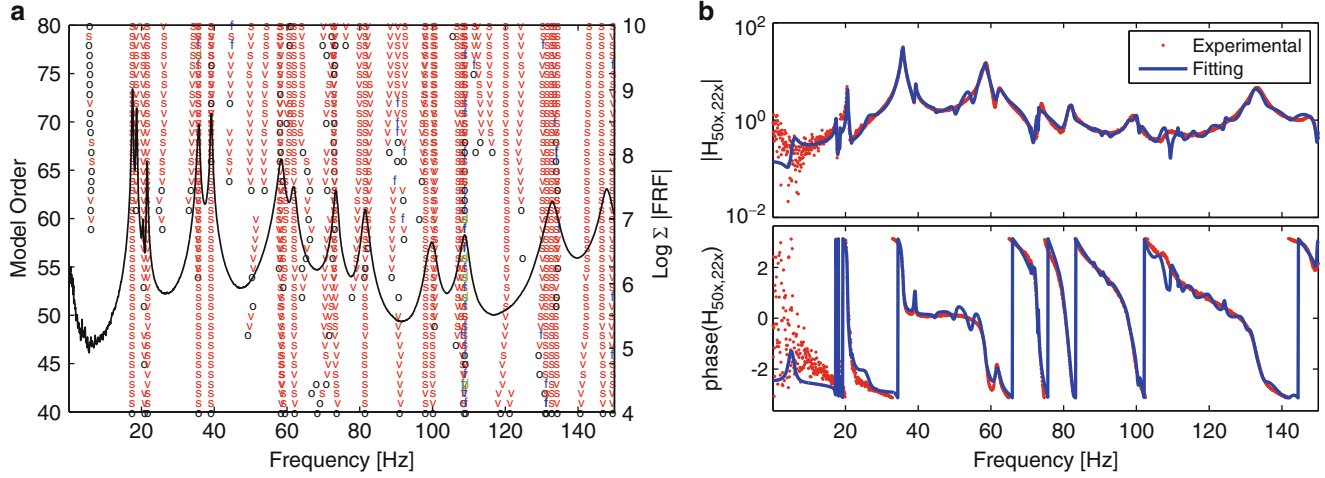


Fig. 2.7 Modal identification of the two bladed turbine subsystem. (a) Stabilization plot of the Poly-LSCF. (b) Identification results

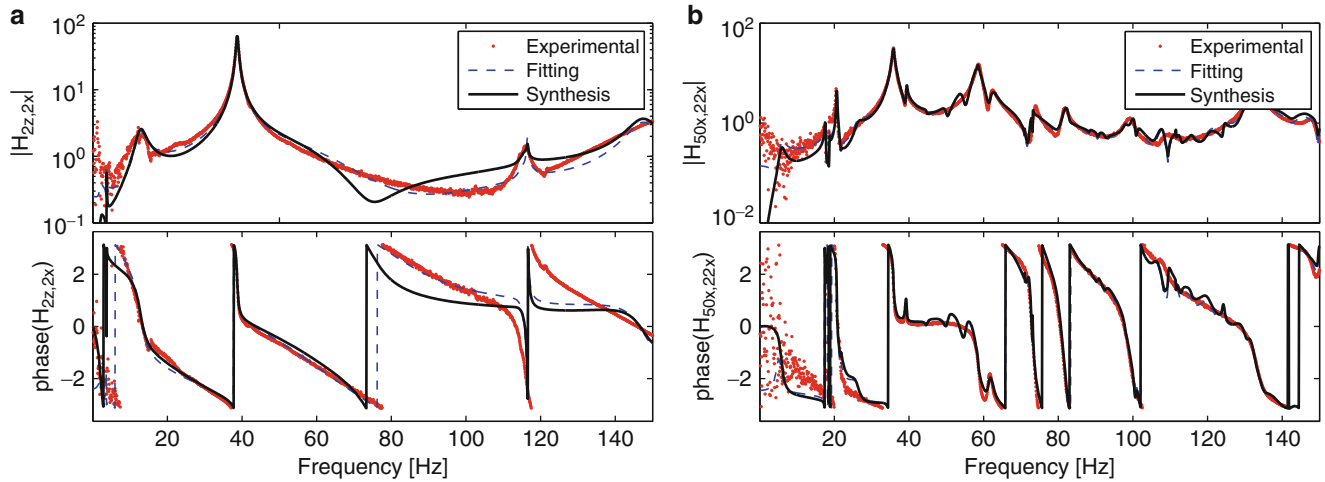


Fig. 2.8 Comparison between experimental, fitted and synthesized FRFs. (a) Mass loaded blade subsystem. (b) Two bladed turbine subsystem

and an average value c can be used to find the r -th modal participation vector as:

$$\{L\}_r = c \{\psi\}_r \quad (2.17)$$

Finally, the full matrix of FRFs (inertances) defined also on unmeasured DoFs can be expressed as:

$$[H(i\omega)] = -\omega^2 \sum_{r=1}^n \left(\frac{\{\psi\}_r \{L\}_r^T}{i\omega - \lambda_r} + \frac{\{\psi\}_r^* \{L\}_r^{T*}}{i\omega - \lambda_r^*} \right) \quad (2.18)$$

In this case, due to the complexity, to the high nonlinearity of the dynamic behavior of the system and to the lack of coherence between different measurement, it can be more convenient to select a single proportionality constant rather than to average the different proportionality constants on all the reference DoFs.

For the mass loaded blade subsystem, the proportionality constant used to compute the participation vectors is the one corresponding to the reference DoF on Node 2 in x local direction. For the two bladed turbine the selected DoF used to compute the proportionality constant is the one corresponding to node 22 on the x local direction.

The response synthesized according to Eq. (2.18) are reported in Fig. 2.8. Below 15 Hz, the absence of low frequency residuals, that are taken into account in the curve fitting but cannot be considered in the synthesized FRFs, produces a relevant error. Synthesized FRFs are quite reliable for frequency higher than 15 Hz.

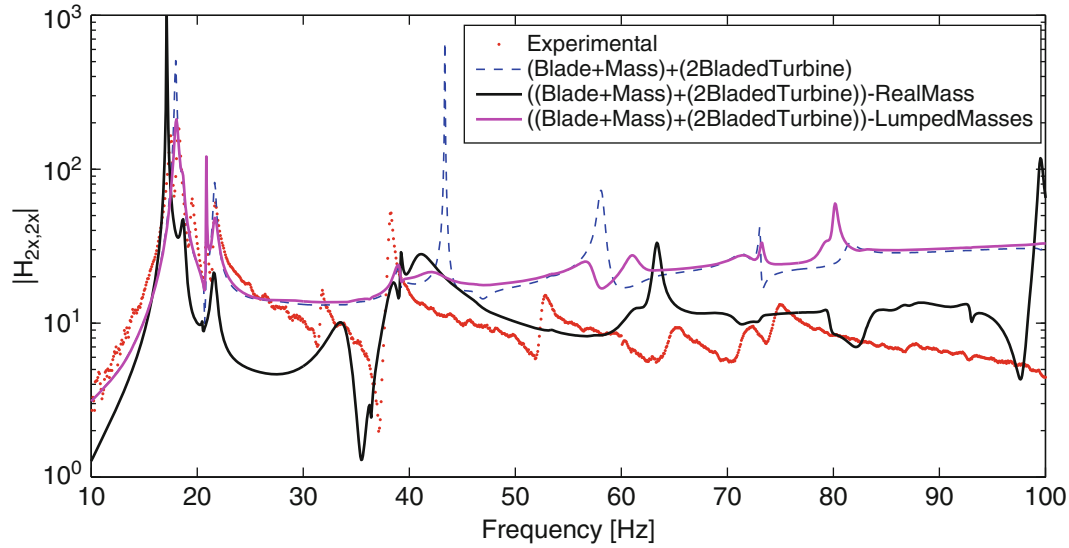


Fig. 2.9 Experimental (***) vs. predicted FRF of the coupled structure: without cancellation of the added mass (- - -); with cancellation of the added mass modeled by 3 lumped masses (—) or by a rigid body (—) (Color figure online)

2.4.4 Coupling of the Blade with the Two Bladed Turbine and Mass Cancellation

The subsystems identified in the previous section are here used to perform the coupling operation in the frequency domain. To find the dynamic response of the whole system the mass loaded blade is first coupled with the two bladed turbine and then the mass is subtracted from the whole structure by a decoupling operation.

Coupling DoFs are those on nodes 16, 17, 18 along the three spatial directions. The corresponding FRFs are synthesized according to Eq. (2.18). The equilibrium and compatibility conditions are defined for all nine coupling DoFs. The effect of the mass added to the blade can be subsequently canceled by a decoupling operation. The loading mass was initially modeled by three lumped masses placed at the coupling nodes. In this case, the inertance matrix can be expressed as a diagonal matrix with the element on the main diagonal equal to $3/m$ where m is the total added mass. The added mass is also modeled as a continuous rigid body, using a consistent mass matrix that takes into account static and inertia moments of the body.

Figure 2.9 shows the FRF of the assembled system, resulting from preliminarily coupling the two substructures and subsequently decoupling the loading mass, compared with the experimental FRF, both referred to node 2 in x local direction. The predicted FRF computed by decoupling the added mass, modeled using a consistent mass matrix, reproduces the experimental response globally better than the FRF computed by decoupling the model with three lumped masses. However, the decoupling of the lumped masses shows a more faithful reproduction of the experimental behavior for frequencies lower than 30 Hz.

To discuss this difference, we can analyze the FRFs predicted at points that are far from the coupling interface, after coupling the two substructures. It can be noticed that the coupling operation doesn't substantially modify the FRFs: Figure 2.10 shows the FRFs of the substructures before and after the coupling procedure for an internal DoF (node 9 in z local direction) of the mass loaded blade (Fig. 2.10a) and for an internal DoF (node 36 in z local direction) of the two bladed turbine substructure (Fig. 2.10b). Below 60 Hz, the FRFs before and after coupling are similar in both cases, whilst a substantial variation of the response amplitude can be noticed for the mass loaded blade at frequencies higher than 60 Hz. It can be concluded that in the low frequency range the two substructures have an almost independent dynamic behavior. Therefore, it is preferable to obtain a low error above 40 Hz as provided by the consistent mass model (Fig. 2.9).

2.5 Conclusions

In this paper, the dynamic response of a complex structure, the Ampair 600 test bed wind turbine, is predicted by a Frequency Based Substructuring technique. The dynamic behavior of the assembled Ampair turbine is obtained by coupling the mass-loaded blade with the two-bladed turbine, and subsequently canceling the contribution of the added mass. The experimental

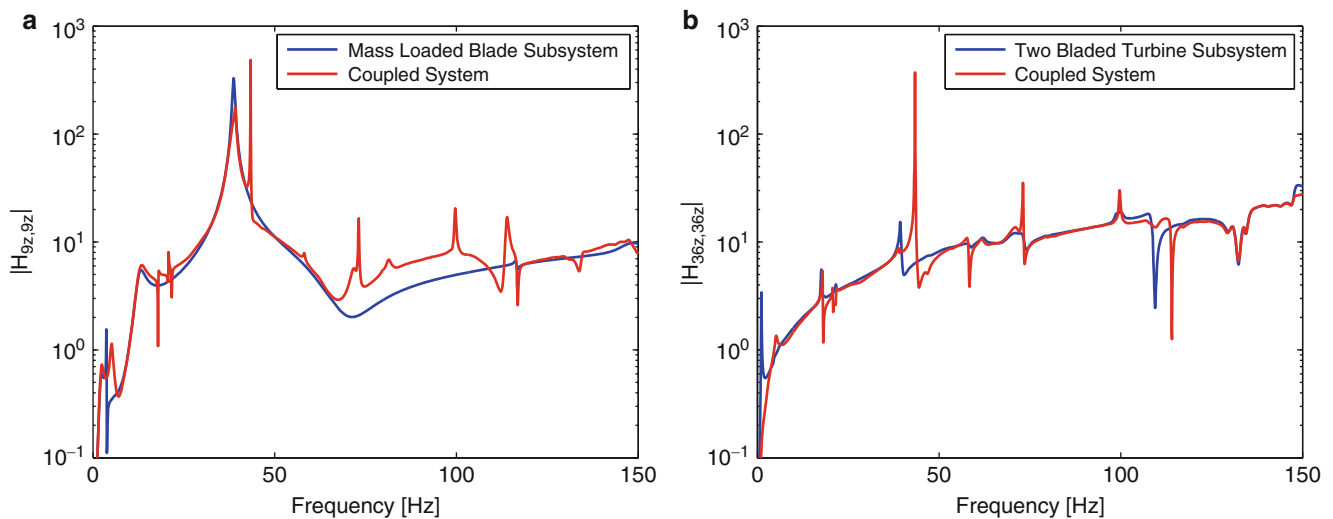


Fig. 2.10 Predicted FRF of the coupled system (—) vs. synthesized FRF of the component substructures (—) at two internal DoFs of the component substructures. (a) Effect of coupling on the mass loaded blade. (b) Effect of coupling on the two bladed turbine (Color figure online)

data used for substructuring are the inertances measured over a set of excitation and response DoFs. These data are shared by the University of Wisconsin-Madison.

Due to the lack of coherence between some reciprocal terms of the inertance matrix, Poly-LSCF modal identification is applied using a reduced set of reference DoFs. The comparison between the measured and the fitted FRFs shows a good agreement in the frequency range up to 150 Hz.

Substructuring techniques in the frequency domain need the complete FRFs matrix at the coupling DoFs. Since the available measurements do not include all the required FRFs, a consistent FRF matrix is synthesized using the identified modal parameters. Synthesized FRFs are quite reliable for frequencies higher than 15 Hz. Below 15 Hz, the lack of low frequency residuals, that are considered in the curve fitting but can not be included in the synthesizing procedure, produces some error.

The predicted FRF of the assembled structure, obtained by coupling the mass-loaded blade with the two-bladed turbine, and subsequently decoupling the added mass, modeled as a continuous rigid body, shows an acceptable agreement with the tests. Of course, the complexity of the structure must be considered together with the challenging task of synthesizing good FRFs from measurements. At frequencies below 30 Hz, the predicted FRF is not very satisfactory, but at higher frequencies it follows better the experimental result. On the contrary, the results obtained by decoupling the added mass, modeled as three lumped masses, show a better agreement with the experimental FRFs at low frequencies. However, at low frequencies the two substructures have an almost independent dynamic behavior and at such frequencies the effect of coupling is not very interesting. Therefore, the better prediction above 40 Hz provided by the consistent mass model is preferred.

Acknowledgements This research is supported by University of Rome La Sapienza and University of L'Aquila. The authors acknowledge the dynamic substructuring group of UW-Madison for sharing the results of experimental tests conducted on the Ampair wind turbine test bed on the Wiki site of the Experimental Dynamic Substructuring Focus Group.

References

1. D'Ambrogio W, Sestieri A (2004) A unified approach to substructuring and structural modification problems. *Shock Vib* 11(3–4):295–310
2. Jetmundsen B, Bielawa R, Flannelly W (1988) Generalised frequency domain substructure synthesis. *J Am Helicopter Soc* 33(1):55–64
3. de Klerk D, Rixen DJ, Voormeeren S (2008) General framework for dynamic substructuring: history, review, and classification of techniques. *AIAA J* 46(5):1169–1181
4. de Klerk D (2009) Dynamic response characterization of complex systems through operational identification and dynamic substructuring. Ph.D. thesis, TU Delft
5. D'Ambrogio W, Fregolent A (2009). In: Decoupling procedures in the general framework of frequency based substructuring. Proceedings of 27th IMAC, Orlando, February 2009
6. D'Ambrogio W, Fregolent A (2010) The role of interface DoFs in decoupling of substructures based on the dual domain decomposition. *Mech Syst Signal Process* 24(7):2035–2048. doi:10.1016/j.ymssp.2010.05.007, also in Proceedings of ISMA 2010, Leuven, Belgium, pp 1863–1880

7. Voormeeren SN, Rixen DJ (2012) A family of substructure decoupling techniques based on a dual assembly approach. *Mech Syst Signal Process* 27:379–396. doi:10.1016/j.ymssp.2011.07.028
8. Mayes RL (2012) An introduction to the SEM substructures focus group test bed - the Ampair 600 wind turbine. In: Mayes R, Rixen D, Griffith D, De Klerk D, Chauhan S, Voormeeren S, Allen M, Proulx T (eds) *Topics in experimental dynamics substructuring and wind turbine dynamics*, vol 2. Conference proceedings of the Society for Experimental Mechanics series, vol 27. Springer, New York, pp 61–70. doi:10.1007/978-1-4614-2422-2_7
9. Brunetti J, Culla A, D'Ambrogio W, Fregolent A (2014) Selection of interface DoFs in hub-blade(s) coupling of Ampair wind turbine test bed. In: Mayes R, Rixen D, Allen M (eds) *Topics in experimental dynamic substructuring*, vol 2. Conference proceedings of the Society for Experimental Mechanics series. Springer, New York, pp 167–178
10. Culla A, D'Ambrogio W, Fregolent A (2012) Getting a symmetric residue matrix from the poly-reference least square complex frequency domain technique. In: Sas P (ed) *Proceedings of ISMA 2012 - international conference on noise and vibration engineering*, Leuven, Belgium, Sept 2012, pp 2755–2764

Chapter 3

Are Rotational DoFs Essential in Substructure Decoupling?

Walter D'Ambrogio and Annalisa Fregolent

Abstract Substructure decoupling consists in the identification of the dynamic behavior of a structural subsystem, starting from the known dynamic behavior of both the coupled system and the remaining part of the structural system (residual subsystem). The degrees of freedom (DoFs) of the coupled system can be partitioned into internal DoFs (not belonging to the couplings) and coupling DoFs. In direct decoupling, a fictitious subsystem that is the negative of the residual subsystem is added to the coupled system, and appropriate compatibility and equilibrium conditions are enforced at interface DoFs. Compatibility and equilibrium can be required either at coupling DoFs only (standard interface), or at additional internal DoFs of the residual subsystem (extended interface), or at some coupling DoFs and/or some internal DoFs of the residual subsystem (mixed interface). Using a mixed interface, rotational coupling DoFs could be eliminated and substituted by internal translational DoFs. This would avoid difficult measurements of rotational FRFs. This possibility is verified in this paper using simulated experimental data.

Keywords Substructure decoupling • Rotational DoFs • Mixed interface • Experimental dynamic substructuring • Frequency based substructuring

3.1 Introduction

The identification of the dynamic behaviour of a structural subsystem, starting from the known dynamic behaviour of both the coupled system and the remaining part of the structural system (residual subsystem), is also known as decoupling problem, subsystem subtraction or inverse dynamic substructuring. Decoupling is a relevant issue for subsystems that cannot be tested separately, but only when coupled to their neighboring substructure(s) (e.g. a fixture needed for testing or subsystems in operational conditions).

Decoupling is a special case of experimental dynamic substructuring, where experimental means that the model of at least one subsystem derives from tests. In Frequency Based Substructuring, Frequency Response Functions (FRFs) are used instead of modal parameters. A general framework for dynamic substructuring is provided in [1], where the primal assembly and the dual assembly are introduced.

Decoupling is a very critical problem even in apparently trivial applications. It has been highlighted that subsystem identification problems are affected by ill-conditioning around a discrete number of frequencies, that depends on the choice of the measured DoFs [2, 3]. Additional problems arise that are strictly connected with the use of measured FRFs: among others, systematic errors and inconsistencies.

Furthermore, a well known issue in experimental dynamic substructuring is related to rotational DoFs. In substructure coupling, whenever coupling DoFs include rotational DoFs, the related rotational FRFs must be obtained experimentally.

W. D'Ambrogio (✉)

Dipartimento di Ingegneria Industriale e dell'Informazione e di Economia, Università dell'Aquila, Via G. Gronchi, 18
I-67100, L'Aquila (AQ), Italy
e-mail: walter.dambrogio@univaq.it

A. Fregolent

Dipartimento di Ingegneria Meccanica e Aerospaziale, Università di Roma La Sapienza, Via Eudossiana 18, I 00184 Rome, Italy
e-mail: annalisa.fregolent@uniroma1.it

This becomes a quite complicated task when measuring only translational FRFs, as shown in [4]. Several techniques for measuring rotational responses have been devised since then, see e.g. [5,6]. However, when such rotational FRFs are used for substructure coupling, results are still unsatisfactory.

For some time, it was believed that issues related to rotational DoFs also applied to substructure decoupling. However, in this case the effect of rotational DoFs is already embedded in each measured FRF of the assembled system, whose dynamics depends on how subsystems are connected together. In practice, the use of a mixed interface [7] may allow to substitute some unwanted connecting DoFs with internal DoFs of the residual substructure: unwanted connecting DoFs include rotational DoFs and DoFs that should for instance be measured at bolted joints.

In this paper, it is attempted to answer a question on how essential are rotational DoFs in substructure decoupling. To this aim, simulated test data on a fixed–fixed beam made by two cantilever beams joined together, are used.

3.2 Direct Decoupling Techniques

The coupled structural system RU (N_{RU} DoFs) is assumed to be made by an unknown subsystem U (N_U DoFs) and a residual subsystem R (N_R DoFs) joined through a number of couplings (see Fig. 3.1). The degrees of freedom (DoFs) of the coupled system can be partitioned into internal DoFs (not belonging to the couplings) of subsystem U (u), internal DoFs of subsystem R (r), and coupling DoFs (c).

It is required to find the FRF of the unknown substructure U starting from the FRFs of the coupled system RU and of the residual subsystem R . The subsystem U can be extracted from the coupled system RU by cancelling the dynamic effect of the residual subsystem R . This can be accomplished by adding to the coupled system RU a “negative” subsystem with a dynamic stiffness opposite to that of the residual subsystem R . The dynamic equilibrium of the coupled system RU and of the negative subsystem is expressed in block diagonal format as:

$$\begin{bmatrix} \mathbf{Z}^{RU} & \mathbf{0} \\ \mathbf{0} & -\mathbf{Z}^R \end{bmatrix} \begin{Bmatrix} \mathbf{u}^{RU} \\ \mathbf{u}^R \end{Bmatrix} = \begin{Bmatrix} \mathbf{f}^{RU} \\ \mathbf{f}^R \end{Bmatrix} + \begin{Bmatrix} \mathbf{g}^{RU} \\ \mathbf{g}^R \end{Bmatrix} \quad (3.1)$$

where:

- \mathbf{Z}^{RU} , \mathbf{Z}^R are the dynamic stiffness matrices of the coupled system RU and of the residual subsystem R ;
- \mathbf{u}^{RU} , \mathbf{u}^R are the vectors of degrees of freedom of the coupled system RU and of the residual subsystem R ;
- \mathbf{f}^{RU} , \mathbf{f}^R are the external force vectors on the coupled system RU and on the fictitious subsystem;
- \mathbf{g}^{RU} , \mathbf{g}^R are the vectors of connecting forces between the coupled system and the fictitious subsystem, and viceversa (constraint forces associated with compatibility conditions).

According to this point of view, the interface between the coupled system RU and the fictitious subsystem should not only include all the coupling DoFs between subsystems U and R , but should as well include all the internal DoFs of subsystem R . However, it can be shown that the problem can be solved by considering a number of interface DoFs at least equal to the number of coupling DoFs n_c . Therefore, three options for interface DoFs can be considered:

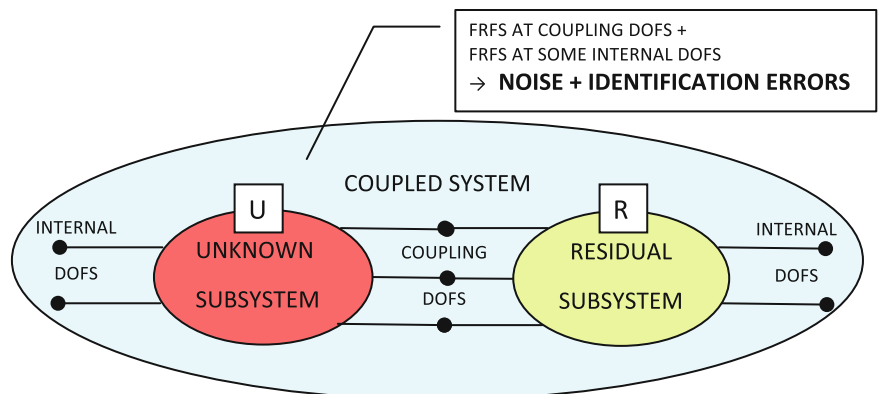


Fig. 3.1 Scheme of the decoupling problem

- standard interface, including only the coupling DoFs (c) between subsystems U and R ;
- extended interface, including the coupling DoFs and a subset of internal DoFs ($i \subseteq r$) subsystem R ;
- mixed interface, including subsets of coupling DoFs ($d \subseteq c$) and/or internal DoFs ($i \subseteq r$) of subsystem R .

The use of a mixed interface may allow to substitute rotational coupling DoFs with translational internal DoFs.

The compatibility condition at the (standard, extended, mixed) interface DoFs implies that any pair of matching DoFs u_l^{RU} and u_m^R , i.e. DoF l on the coupled system RU and DoF m on subsystem R must have the same displacement, that is $u_l^{RU} - u_m^R = 0$. Let the number of interface DoFs on which compatibility is enforced be denoted as N_C .

The compatibility condition can be generally expressed as:

$$\begin{bmatrix} \mathbf{B}_C^{RU} & \mathbf{B}_C^R \end{bmatrix} \begin{Bmatrix} \mathbf{u}^{RU} \\ \mathbf{u}^R \end{Bmatrix} = \mathbf{0} \quad (3.2)$$

where each row of $\mathbf{B}_C = \begin{bmatrix} \mathbf{B}_C^{RU} & \mathbf{B}_C^R \end{bmatrix}$ corresponds to a pair of matching DoFs. Note that \mathbf{B}_C has size $N_C \times (N_{RU} + N_R)$ and is, in most cases, a signed Boolean matrix.

It should be noted that the interface DoFs involved in the equilibrium condition need not to be the same as DoFs used to enforce compatibility. In this case, the approach is called non-located [7], whereas the traditional approach, in which compatibility and equilibrium DoFs are the same, is called collocated.

Let N_E denote the number of interface DoFs on which equilibrium is enforced. The equilibrium of constraint forces implies that their sum must be zero for any pair of matching DoFs, i.e. $g_r^{RU} + g_s^R = 0$. Furthermore, for any DoF k not involved in the equilibrium condition, it must be $g_k^{RU} = 0$ and $g_k^R = 0$.

Overall, the above conditions can be expressed as:

$$\begin{bmatrix} \mathbf{L}_E^{RU} \\ \mathbf{L}_E^R \end{bmatrix}^T \begin{Bmatrix} \mathbf{g}^{RU} \\ \mathbf{g}^R \end{Bmatrix} = \mathbf{0} \quad (3.3)$$

where the matrix $\mathbf{L}_E = \begin{bmatrix} \mathbf{L}_E^{RU} & \mathbf{L}_E^R \end{bmatrix}$ is a Boolean localisation matrix. Note that the number of columns of \mathbf{L}_E is equal to the number N_E of equilibrium interface DoFs plus the number N_{NE} of DoFs not belonging to the equilibrium interface. Note that $N_{NE} = N_{RU} + N_R - 2N_E$: in fact, the number of DoFs belonging to the equilibrium interface must be subtracted once from N_{RU} and once from N_R . Therefore, the size of \mathbf{L}_E is $(N_{RU} + N_R) \times (N_{RU} + N_R - N_E)$.

Equations (3.1)–(3.3) can be gathered to obtain the so-called three-field formulation. Starting from the three-field formulation, several assembly techniques can be devised:

- dual assembly [1, 3] where equilibrium is satisfied exactly by defining a unique set of connecting force intensities;
- primal assembly [1, 8] where compatibility is satisfied exactly by defining a unique set of interface DoFs;
- hybrid assembly [9] where both compatibility and equilibrium are satisfied exactly.

In the sequel, only the dual assembly is recalled. It can be shown [9] that whenever $N_C = N_E$, i.e. the number of compatibility DoFs is the same as the number of equilibrium DoFs, all assembly techniques provide the same result.

3.2.1 Dual Assembly

In the dual assembly, the equilibrium condition $g_r^{RU} + g_s^R = 0$ at a pair of equilibrium interface DoFs is ensured by choosing $g_r^{RU} = -\lambda$ and $g_s^R = \lambda$. If a Boolean matrix \mathbf{B}_E related to interface equilibrium DoFs is defined similarly to \mathbf{B}_C , the overall interface equilibrium can be ensured by writing the connecting forces in the form:

$$\begin{Bmatrix} \mathbf{g}^{RU} \\ \mathbf{g}^R \end{Bmatrix} = - \begin{bmatrix} \mathbf{B}_E^{RU T} \\ \mathbf{B}_E^R T \end{bmatrix} \boldsymbol{\lambda} \quad (3.4)$$

where $\boldsymbol{\lambda}$ are Lagrange multipliers corresponding to connecting force intensities and \mathbf{B}_E is a $N_E \times (N_{RU} + N_R)$ matrix. Since there is a unique set of connecting force intensities $\boldsymbol{\lambda}$, the interface equilibrium condition is satisfied automatically for any $\boldsymbol{\lambda}$, i.e.

$$\begin{bmatrix} \mathbf{L}_E^{\text{RU}} \\ \mathbf{L}_E^{\text{R}} \end{bmatrix}^T \begin{Bmatrix} \mathbf{g}^{\text{RU}} \\ \mathbf{g}^{\text{R}} \end{Bmatrix} = - \begin{bmatrix} \mathbf{L}_E^{\text{RU}} \\ \mathbf{L}_E^{\text{R}} \end{bmatrix}^T \begin{bmatrix} \mathbf{B}_E^{\text{RU}T} \\ \mathbf{B}_E^{\text{R}T} \end{bmatrix} \boldsymbol{\lambda} = \mathbf{0} \quad (3.5)$$

In the dual assembly, the total set of DoFs is retained, i.e. each interface DoF appears twice. Since Eq. (3.5) is always satisfied, the three-field formulation reduces to:

$$\begin{cases} \begin{bmatrix} \mathbf{Z}^{\text{RU}} & \mathbf{0} \\ \mathbf{0} & -\mathbf{Z}^{\text{R}} \end{bmatrix} \begin{Bmatrix} \mathbf{u}^{\text{RU}} \\ \mathbf{u}^{\text{R}} \end{Bmatrix} + \begin{bmatrix} \mathbf{B}_E^{\text{RU}T} \\ \mathbf{B}_E^{\text{R}T} \end{bmatrix} \boldsymbol{\lambda} = \begin{Bmatrix} \mathbf{f}^{\text{RU}} \\ \mathbf{f}^{\text{R}} \end{Bmatrix} \\ \begin{bmatrix} \mathbf{B}_C^{\text{RU}} & \mathbf{B}_C^{\text{R}} \end{bmatrix} \begin{Bmatrix} \mathbf{u}^{\text{RU}} \\ \mathbf{u}^{\text{R}} \end{Bmatrix} = \mathbf{0} \end{cases} \quad (3.1^*)$$

$$\begin{cases} \begin{bmatrix} \mathbf{Z}^{\text{RU}} & \mathbf{0} \\ \mathbf{0} & -\mathbf{Z}^{\text{R}} \end{bmatrix} \begin{Bmatrix} \mathbf{u}^{\text{RU}} \\ \mathbf{u}^{\text{R}} \end{Bmatrix} + \begin{bmatrix} \mathbf{B}_E^{\text{RU}T} \\ \mathbf{B}_E^{\text{R}T} \end{bmatrix} \boldsymbol{\lambda} = \begin{Bmatrix} \mathbf{f}^{\text{RU}} \\ \mathbf{f}^{\text{R}} \end{Bmatrix} \\ \begin{bmatrix} \mathbf{B}_C^{\text{RU}} & \mathbf{B}_C^{\text{R}} \end{bmatrix} \begin{Bmatrix} \mathbf{u}^{\text{RU}} \\ \mathbf{u}^{\text{R}} \end{Bmatrix} = \mathbf{0} \end{cases} \quad (3.2)$$

or in more compact form:

$$\begin{cases} \mathbf{Z}\mathbf{u} + \mathbf{B}_E^T \boldsymbol{\lambda} = \mathbf{f} \\ \mathbf{B}_C \mathbf{u} = \mathbf{0} \end{cases} \quad (3.1^*)$$

$$\begin{cases} \mathbf{Z}\mathbf{u} + \mathbf{B}_E^T \boldsymbol{\lambda} = \mathbf{f} \\ \mathbf{B}_C \mathbf{u} = \mathbf{0} \end{cases} \quad (3.2)$$

To eliminate $\boldsymbol{\lambda}$, Eq. (3.1^{*}) can be written:

$$\mathbf{u} = -\mathbf{Z}^{-1} \mathbf{B}_E^T \boldsymbol{\lambda} + \mathbf{Z}^{-1} \mathbf{f} \quad (3.1^*)$$

which substituted in Eq. (3.2) gives:

$$\mathbf{B}_C \mathbf{Z}^{-1} \mathbf{B}_E^T \boldsymbol{\lambda} = \mathbf{B}_C \mathbf{Z}^{-1} \mathbf{f} \quad (3.6)$$

from which $\boldsymbol{\lambda}$, to be back-substituted in Eq. (3.1^{*}), is found as:

$$\boldsymbol{\lambda} = (\mathbf{B}_C \mathbf{Z}^{-1} \mathbf{B}_E^T)^+ \mathbf{B}_C \mathbf{Z}^{-1} \mathbf{f} \quad (3.7)$$

To obtain a determined or overdetermined matrix for the generalized inversion operation, the number of rows of \mathbf{B}_C must be greater or equal than the number of rows of \mathbf{B}_E , i.e.

$$N_C \geq N_E \geq n_c \quad (3.8)$$

Note that, if $N_C > N_E$, Eq. (3.6) is not satisfied exactly by vector $\boldsymbol{\lambda}$ given by Eq. (3.7), but only in the minimum square sense. This implies that also Eq. (3.2) is not satisfied exactly, i.e. compatibility conditions at interface are approximately satisfied. On the contrary, equilibrium is satisfied exactly due to the introduction of the connecting force intensities $\boldsymbol{\lambda}$ as in Eq. (3.4).

By substituting $\boldsymbol{\lambda}$ in Eq. (3.1^{*}), it is obtained:

$$\mathbf{Z}\mathbf{u} + \mathbf{B}_E^T (\mathbf{B}_C \mathbf{Z}^{-1} \mathbf{B}_E^T)^+ \mathbf{B}_C \mathbf{Z}^{-1} \mathbf{f} = \mathbf{f} \quad (3.9)$$

Finally, \mathbf{u} can be written as $\mathbf{u} = \mathbf{H}\mathbf{f}$, which provides the FRF of the unknown subsystem U :

$$\mathbf{u} = \left(\mathbf{Z}^{-1} - \mathbf{Z}^{-1} \mathbf{B}_E^T (\mathbf{B}_C \mathbf{Z}^{-1} \mathbf{B}_E^T)^+ \mathbf{B}_C \mathbf{Z}^{-1} \right) \mathbf{f} \quad (3.10)$$

i.e., by noting that the inverse of the block diagonal dynamic stiffness matrix can be expressed as:

$$\begin{bmatrix} \mathbf{Z}^{\text{RU}} & \mathbf{0} \\ \mathbf{0} & -\mathbf{Z}^{\text{R}} \end{bmatrix} = \mathbf{Z}^{-1} = \mathbf{H} = \begin{bmatrix} \mathbf{H}^{\text{RU}} & \mathbf{0} \\ \mathbf{0} & -\mathbf{H}^{\text{R}} \end{bmatrix} \quad (3.11)$$

where \mathbf{H}^{RU} and \mathbf{H}^{R} are the FRFs of the assembled structure and of the residual substructure, it is:

$$\mathbf{H}^U = \mathbf{H} - \mathbf{H}\mathbf{B}_E^T (\mathbf{B}_C\mathbf{H}\mathbf{B}_E^T)^+ \mathbf{B}_C\mathbf{H} \quad (3.12)$$

With the dual assembly, the rows and the columns of \mathbf{H}^U corresponding to compatibility and equilibrium DoFs appear twice. Furthermore, when using an extended or mixed interface, \mathbf{H}^U contains some meaningless rows and columns: those corresponding to the internal DoFs of the residual substructure R . Obviously, only meaningful and independent entries are retained.

3.3 Test Structure

The proposed decoupling technique is tested on an aluminium beam (Fig. 3.2). The residual substructure R (left) consists of a long uniform cantilever beam (1). The unknown substructure U (right) is a short uniform cantilever beam (2). The two substructures are assumed to be rigidly connected at the free ends, involving both translational and rotational DoFs.

The mechanical properties of the structures are: $E = 7.0 \cdot 10^{10}$ N/m², $\rho = 2,700$ kg/m³, modal damping $\zeta = 0.005$. The geometrical properties of the items are shown in Table 3.1.

To verify the limits and the reliability of the decoupling technique, an analysis is performed using simulated data, eventually polluted by random noise. An FE model of both substructures is built using beam elements. The FE model of the assembled structure is obtained by assembling the FE models of the two substructures. Inertance FRFs are obtained from the FE models at DoFs shown in Fig. 3.2: among them, DoFs $9y$ and $9\vartheta_z$ are the coupling DoFs, DoFs $1y$ – $8y$ are internal DoFs of the residual substructure R , and DoFs $10y$ – $13y$ are internal DoF of the unknown substructure U . Table 3.2 shows the natural frequencies of the two substructures and of the assembled structure, obtained from FE models.

To simulate the effect of noise on the FRFs of the assembled structure and of the residual substructure, a complex random perturbation is added to FRFs \hat{H}_{rs} computed from the FE model:

$$H_{rs}(\omega_k) = \hat{H}_{rs}(\omega_k) + m_{rs,k} + i n_{rs,k} \quad (3.13)$$

where $m_{rs,k}$ and $n_{rs,k}$ are independent random variables with gaussian distribution, zero mean and a standard deviation proportional to the average value of the FRF modulus.

3.4 Decoupling

The FRFs of subsystem U can be determined by using the procedure described previously and summarized in Eq. (3.12), where compatibility and equilibrium DoFs are defined case by case.

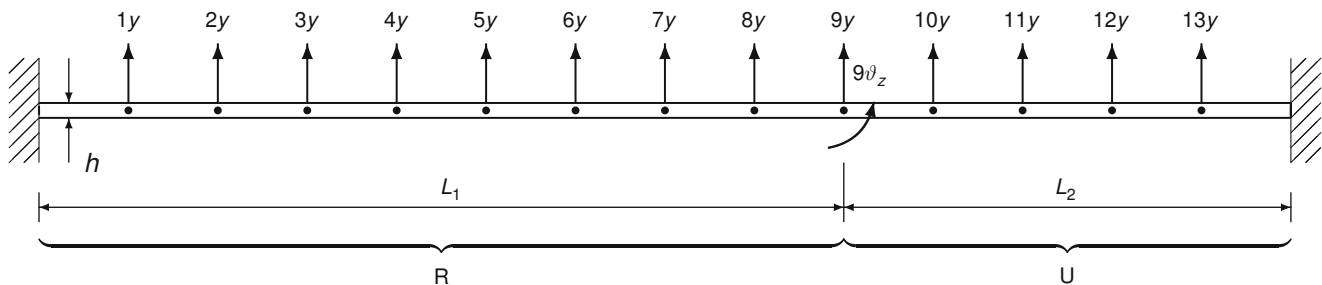


Fig. 3.2 Sketch of the test structure

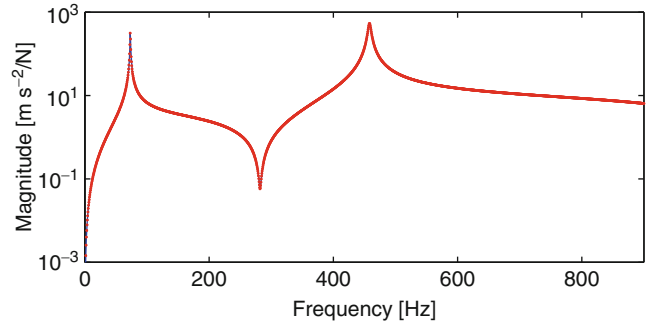
Table 3.1 Geometrical dimensions

| Item | Length (mm) | Width (mm) | Height (mm) |
|---------------|-------------|------------|-------------|
| 1. Long beam | 540 | 40 | 8 |
| 2. Short beam | 300 | 40 | 8 |

Table 3.2 Natural frequencies

| Mode | 1 | 2 | 3 | 4 | 5 |
|---------------------------|-------|--------|--------|--------|--------|
| Assembled structure RU | 59.34 | 163.58 | 320.68 | 530.09 | 791.87 |
| Residual substructure R | 22.57 | 141.42 | 395.97 | 775.95 | – |
| Unknown substructure U | 73.11 | 458.19 | – | – | – |

Fig. 3.3 $H_{11y,11y}^U$: true (—), computed using either standard interface with coupling DoFs $9y$, $9\vartheta_z$ (***) , or mixed interface with internal DoFs $1y$, $5y$, $8y$ (***) (Color figure online)



3.4.1 Results Without Added Noise

First of all, the case of standard interface (FRFs known only at the coupling DoFs $9y$ and $9\vartheta_z$) is considered. The internal DoF $11y$ of the unknown substructure U is used as a reference DoF to compare results obtained even when no coupling DoF is included among interface DoFs. In this case, $N_C = 2$, $N_E = 2$, $N_O = 1$ and

$$\mathbf{B}_C = \mathbf{B}_E = \begin{bmatrix} u_{9y}^{RU} & u_{9\vartheta_z}^{RU} & u_{11y}^{RU} & u_{9y}^R & u_{9\vartheta_z}^R \\ \mathbf{1} & \mathbf{0} & \mathbf{0} & -\mathbf{1} & \mathbf{0} \\ \mathbf{0} & \mathbf{1} & \mathbf{0} & \mathbf{0} & -\mathbf{1} \end{bmatrix} \quad (3.14)$$

\mathbf{B}_C^{RU} \mathbf{B}_C^R

As expected, the FRF of the unknown subsystem is predicted without errors (Fig. 3.3).

Since the coupling DoFs can be difficult to measure, especially when, as in the present case, they include rotational DoFs, a mixed interface is considered that uses only internal DoFs $1y$, $5y$, $8y$. Again, the internal DoF $11y$ of the unknown substructure U is used as a reference DoF. Therefore $N_C = 3$, $N_E = 3$, $N_O = 1$ and

$$\mathbf{B}_C = \mathbf{B}_E = \begin{bmatrix} u_{1y}^{RU} & u_{5y}^{RU} & u_{8y}^{RU} & u_{11y}^{RU} & u_{1y}^R & u_{5y}^R & u_{8y}^R \\ \mathbf{1} & \mathbf{0} & \mathbf{0} & \mathbf{0} & -\mathbf{1} & \mathbf{0} & \mathbf{0} \\ \mathbf{0} & \mathbf{1} & \mathbf{0} & \mathbf{0} & \mathbf{0} & -\mathbf{1} & \mathbf{0} \\ \mathbf{0} & \mathbf{0} & \mathbf{1} & \mathbf{0} & \mathbf{0} & \mathbf{0} & -\mathbf{1} \end{bmatrix} \quad (3.15)$$

\mathbf{B}_C^{RU} \mathbf{B}_C^R

Also in this case, the FRF of the unknown substructure U is predicted without errors: in Fig. 3.3 the predicted FRF is hidden by the FRF obtained using the standard interface. Although this result could be expected from theory, nevertheless it seems quite surprising that the FRF of the unknown substructure can be obtained without considering the FRFs at the coupling DoFs.

3.4.2 Results Using Raw FRFs with Added Noise of 0.05 %

This step is aimed to highlight ill-conditioning problems and other possible troubles that might arise due to the choice of interface DoFs. A very small amount of noise, i.e. 0.05 % of the average value of each FRF, is enough to trigger such effects. Furthermore, the use of raw FRFs avoids fitting error and its influence.

Fig. 3.4 $H_{11y,11y}^U$: true (—), computed using standard interface with coupling DoFs $9y$, $9\vartheta_z$ (***) (Color figure online)

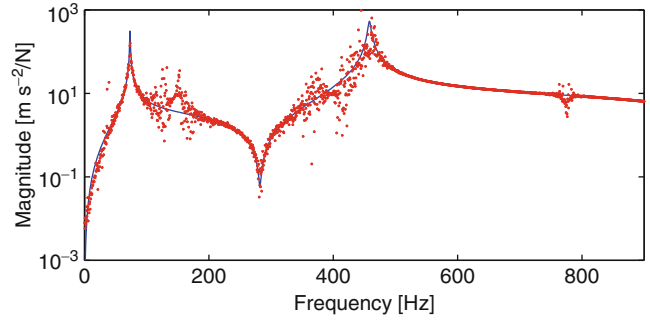
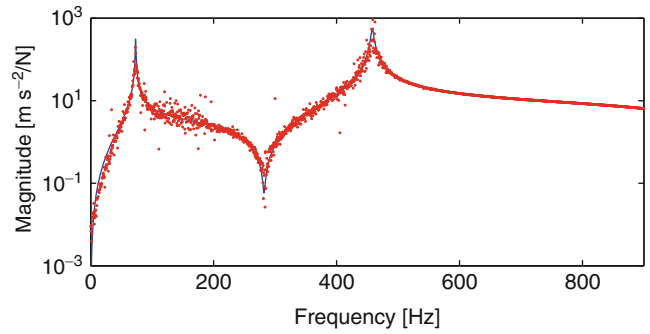


Table 3.3 Natural frequencies of subsystem R with interface DoFs locked, below 900 Hz

| Interface DoFs | Ill-conditioned frequencies | | |
|------------------------|-----------------------------|-------|-------|
| $9y, 9\vartheta_z$ | 143.6 | 395.8 | 776.0 |
| $9y, 9\vartheta_z, 1y$ | 172.2 | 476.9 | — |
| $1y, 5y, 8y$ | 474.5 | 683.0 | — |

Fig. 3.5 $H_{11y,11y}^U$: true (—), computed using extended interface with coupling DoFs $9y$, $9\vartheta_z$ and additional internal DoF 1 (1, 0.00, 0.00***) (Color figure online)



The case of standard interface (FRFs known only at the coupling DoFs $9y$, $9\vartheta_z$ and at the internal DoF $11y$ of the unknown substructure U) is considered first. The matrix $\mathbf{B}_C = \mathbf{B}_E$ is still given by Eq. (3.14). The predicted FRF of the unknown substructure U is shown in Fig. 3.4: it can be noticed that the peak around the second natural frequency presents some scatter, and some spurious peaks due to ill conditioning appear at frequencies 143.6, 395.8 and 776 Hz as reported in the first row of Table 3.3. As shown in [3], such frequencies are the natural frequencies of the residual subsystem with interface DoFs locked.

Normally, results are improved by using an extended interface that involves, together with coupling DoFs, some additional internal DoFs of the residual substructure. Therefore, besides the coupling DoFs $9y$, $9\vartheta_z$, the additional internal DoF $1y$ is used. Again, the internal DoF $11y$ of the unknown substructure U is used as a reference DoF. Therefore $N_C = 3$, $N_E = 3$, $N_O = 1$ and

$$\mathbf{B}_C = \mathbf{B}_E = \left[\begin{array}{cccc|ccc} u_{9y}^{RU} & u_{9\vartheta_z}^{RU} & u_{1y}^{RU} & u_{11y}^{RU} & u_{9y}^R & u_{9\vartheta_z}^R & u_{1y}^R \\ 1 & 0 & 0 & 0 & -1 & 0 & 0 \\ 0 & 1 & 0 & 0 & 0 & -1 & 0 \\ 0 & 0 & 1 & 0 & 0 & 0 & -1 \end{array} \right] \quad (3.16)$$

\mathbf{B}_C^{RU}

\mathbf{B}_C^R

The predicted FRF of the unknown substructure U is shown in Fig. 3.5: the peak around the second natural frequency is better defined, and some scatter appears around the ill conditioned frequency of 172 Hz (see second row of Table 3.3). As expected, there is some definite improvement with respect to the standard interface. Also, it can be noticed that the effect of the ill conditioned frequency around 477 Hz can be masked by the resonance at the close frequency of 458 Hz.

To avoid using coupling DoFs, a mixed interface is again considered, including only internal DoFs $1y$, $5y$, $8y$, and the internal DoF $11y$ of the unknown substructure U . The matrix $\mathbf{B}_C = \mathbf{B}_E$ is still given by Eq. (3.15). The predicted FRF of the unknown substructure U is shown in Fig. 3.6: some scatter appears around the antiresonance and the second natural frequency, and, quite surprisingly, the overall FRF is improved with respect to the one obtained using standard interface. Both the ill conditioned frequencies (see third row of Table 3.3) seem to have no effect.

Fig. 3.6 $H_{11y,11y}^U$: true (—), computed using mixed interface with internal DoFs $1y, 5y, 8y$ (***) (Color figure online)

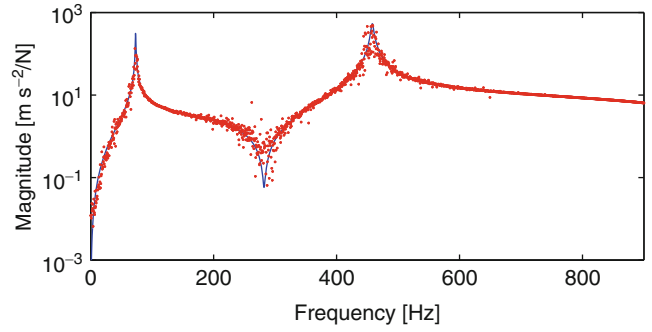
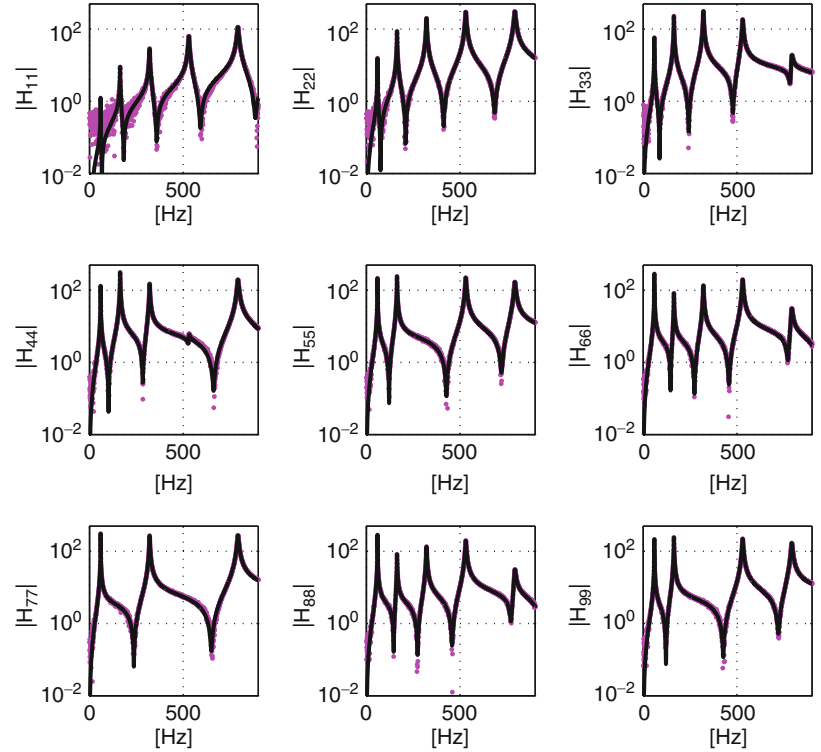


Fig. 3.7 Noise polluted (***) and fitted (—) drive point FRFs of the coupled structure (Color figure online)



3.4.3 Results Using Fitted FRFs with Added Noise of 1%

A more realistic noise level of 1% of the average value of each FRF in the frequency range 0–2,000 Hz is used. In this case, raw FRFs are unable to provide any result. Therefore, the FRFs are curve fitted using a polyreference least square complex frequency domain technique having assumed that only translational FRFs are available. Figure 3.7 shows the raw (noise polluted) and fitted drive point FRFs of the coupled structure RU . Similar results are obtained for the residual substructure R .

In this case, the rotational coupling DoF $9\theta_z$ is not available. Therefore, the use of standard and extended interfaces is not permitted.

First, the largest possible mixed interface is used, including the translational coupling DoFs $9y$ and all the internal DoFs $1y$ – $8y$, so that $N_C = 9$, $N_E = 9$, $N_O = 1$ and the matrix expressing the compatibility condition is built accordingly. The predicted FRF of the unknown substructure U is shown in Fig. 3.8: although the predicted FRFs is quite clean, some shifts of the natural frequencies and of the antiresonance appear. Moreover, the dynamic range is significantly reduced.

In practice, it can be complicated to measure such a large number of internal DoFs. Therefore, some attempts are performed using a limited number of internal DoFs. One of the best result is obtained using a mixed interface with coupling DoF $9y$ and internal DoFs $1y, 3y, 5y$. In this case, $N_C = 4$, $N_E = 4$, $N_O = 1$ and the matrix expressing the compatibility condition is built accordingly. The predicted FRF of the unknown substructure U is shown in Fig. 3.9: the predicted FRFs is quite clean, as usual when using fitted FRFs. However, larger shifts of the natural frequencies and of the antiresonance appear together with a significant reduction of the dynamic range.

Fig. 3.8 $H_{11,11}^U$: true (—), computed from fitted FRFs using mixed interface with coupling DoF $9y$ and internal DoFs $1y$ – $8y$ (***) (Color figure online)

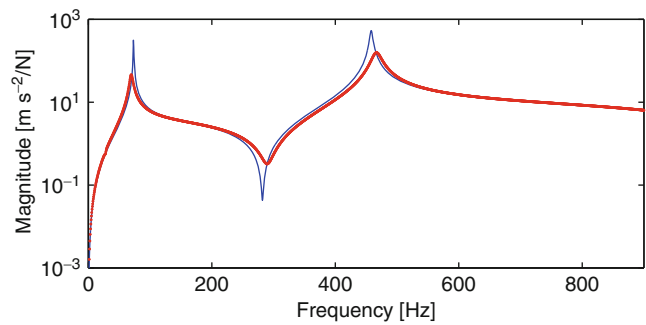
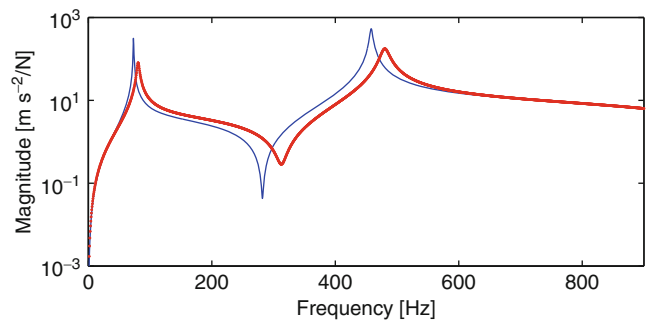


Fig. 3.9 $H_{11,11}^U$: true (—), computed from fitted FRFs using mixed interface with coupling DoF $9y$ and internal DoFs $1y$, $3y$, $5y$ (***) (Color figure online)



In both the reported cases, and to a larger extent when different sets of internal DoFs are used, it seems that the systematic error due to the curve fitting procedure significantly affects the precision of the predicted FRFs and especially the location of resonances and antiresonances, and the sharpness of the related peaks and dips.

3.5 Summary and Discussion

In this paper, it is tried to establish if rotational DoFs, possibly included among the connecting DoFs, are essential in substructure decoupling. In fact, the experimental estimation of rotational FRFs is a quite complicated task.

Differently from the coupling problem, where rotational DoFs can not be neglected, in the decoupling case this is possible because the actions exchanged through the connecting DoFs, and specifically through rotational DoFs, are already embedded in each FRF of the assembled system. In the decoupling case, a mixed interface can in fact be considered that allows to substitute undesired coupling DoFs with internal DoFs of the residual subsystem.

To check the procedure, simulated test data on a fixed–fixed beam made by two cantilever beams joined together, are used. Using FRFs without added noise, the FRFs of the unknown substructure are correctly predicted, both using a standard interface including only coupling DoFs and using a mixed interface without coupling DoFs. By considering raw FRFs with added noise, the results obtained using a mixed interface without coupling DoFs are much less scattered than those obtained using a standard interface and not worse than the results obtained using an extended interface. By considering FRFs fitted after adding noise, the results using a mixed interface without the rotational DoF show some resonance and antiresonance shifts, and a significant reduction of the dynamic range. Both effects could be ascribed to systematic errors on FRFs due to the curve fitting procedure.

According to the obtained results, it can be stated that, as predicted by the theory, rotational DoFs are not essential in the decoupling problem. They can be substituted by internal translational DoFs without altering the results.

Acknowledgements This research is supported by grants from University of Rome La Sapienza and University of L'Aquila.

References

1. de Klerk D, Rixen DJ, Voormeeren S (2008) General framework for dynamic substructuring: history, review, and classification of techniques. *AIAA J* 46(5):1169–1181
2. Sjövall P, Abrahamsson T (2008) Substructure system identification from coupled system test data. *Mech Syst Signal Process* 22(1):15–33

3. D'Ambrogio W, Fregolent A (2010) The role of interface DoFs in decoupling of substructures based on the dual domain decomposition. *Mech Syst Signal Process* 24(7):2035–2048. doi:10.1016/j.ymsp.2010.05.007. Also in *Proceedings of ISMA 2010*, Leuven, Belgium, pp 1863–1880
4. Sestieri A, Salvini P, D'Ambrogio W (1991) Reducing scatter from derived rotational data to determine the frequency response function of connected structures. *Mech Syst Signal Process* 5(1):25–44
5. Stanbridge A, Ewins D (1996) Measurement of translational and angular vibration using a scanning laser Doppler vibrometer. *Shock Vib* 3:141–152
6. Bello M, Sestieri A, D'Ambrogio W, La Gala F (2003) Development of PZT's as rotational transducers. *Mech Syst Signal Process* 17(5):1069–1081
7. Voormeeren SN, Rixen DJ (2012) A family of substructure decoupling techniques based on a dual assembly approach. *Mech Syst Signal Process* 27:379–396. doi:10.1016/j.ymsp.2011.07.028
8. D'Ambrogio W, Fregolent A (2011) Direct decoupling of substructures using primal and dual formulation. In: *Conference proceedings of the Society of Experimental Mechanics series*, vol 4. *Linking models and experiments*, vol 2, pp 47–76, Jacksonville, FL, 31 January–3 February, 2011. Springer, Berlin
9. D'Ambrogio W, Fregolent A (2012) Direct hybrid formulation for substructure decoupling. In: *Conference proceedings of the Society for Experimental Mechanics series*, vol 27. *Topics in experimental dynamics substructuring and wind turbine dynamics*, vol 2, pp 89–107, Jacksonville, FL, 30 January–2 February 2012

Chapter 4

Validation of Blocked-Force Transfer Path Analysis with Compensation for Test Bench Dynamics

D.D. van den Bosch, M.V. van der Seijs, and D. de Klerk

Abstract This paper presents a validation of the Blocked-Force Transfer Path Analysis (BF-TPA) method that was proposed earlier in 2009 as the Gear Noise Propagation (GNP) method. The method allows to simulate the propagation of noise and vibrations generated by a system component to responses elsewhere in the system. The total systems FRFs are needed in combination with a measurement of the system's component on a rigid test bench. Although the method is physically correct, a rigid test bench is hard to design up to higher frequencies. Therefore a compensation method for the test bench dynamics was derived.

This paper validates the BF-TPA for a vehicle steering gear with and without compensation for its test bench dynamics. In order to be successful, a technique is introduced to obtain the required Rotational DoFs and Moments on both the component test bench measurement and total system FRFs.

Keywords Transfer path analysis • Blocked force • Frequency based substructuring • Experimental substructuring • NVH

4.1 Introduction

In many engineering applications product optimization is achieved by matching the active components excitation levels with the dynamic behaviour of the total system. In for instance the automotive industry, the active components may be the combustion engine and (electro-mechanic) mechatronics that cause NVH¹ responses in the interior of the vehicle. In order to investigate the transmission of those vibrations, a Transfer Path Analysis (TPA) is often performed that attempts to characterise the perceived vibrations in terms of the excitations induced by a *source* and the corresponding *transfer paths* to the *receiver*. In a breakdown of subsystems, the first is part of the *active component* (e.g. the engine) whereas the latter is related to the connected *passive component* (e.g. the vehicle bodywork and interior). Such a decomposition into subsystems can be established by applying Dynamic Substructuring (DS) as presented by for instance [4].

Literature shows various ways of nomenclature, often case specific. Within the family of TPA, we propose to make a distinction between *classical TPA* and *component TPA* methods. The first family identifies the interface forces between the active and passive component and thereafter applies these forces to the passive component. The latter family characterises the interface forces of the isolated active component after which these forces are applied at the interface between the active and passive component. These forces are referred to as blocked forces and are applied as external forces to the assembled system. Especially for the first family various practical implementations exist, often involving inverse procedures to determine the forces indirectly. Examples of classical TPA are numerous and can be found in for instance [1, 6, 11].

¹Short for *Noise, Vibration and Harshness*, a common designation for structural/acoustic vibration problems.

D.D. van den Bosch (✉) • M.V. van der Seijs • D. de Klerk
Faculty of Mechanical, Maritime and Materials Engineering, Department of Precision and Microsystems Engineering, Section Engineering Dynamics, Delft University of Technology, Mekelweg 2, 2628CD Delft, The Netherlands
e-mail: ddvandenbosch@gmail.com; m.v.vanderseijs@tudelft.nl

The component methods are less established compared to the classical methods. If one is to optimise the passive component for optimal NVH performance, the family of component based TPA methods is better suited though. Depending on the case and dimensions of the components, one may characterise the effects of the operational load by either measuring the interface forces between the active component and a rigid test bench, or the motion of the active component when the interfaces are left free. Historically, the concept of replacing an active component by an equivalent load is related to the Thévenin equivalent source in electronic network theory; derived implementations for structural vibrations and analogies were first reported in for instance [7, 10, 12]. For the test case as presented here, the blocked interface force variant is adopted.

4.1.1 Paper Outline

The focus of this paper is to validate the Blocked-Force Transfer Path Analysis (BF-TPA) method for an experimental test case and discuss some practical challenges.² Conceptually, the blocked force approach is as straightforward as its classical counterparts. In practice however it appears difficult to realise a fully blocked interface, such that the forces measured at the test bench interface are generally lower than the theoretically needed blocked forces. Section 4.2 therefore derives the blocked forces in a general sense that is valid regardless of the rigidity of the test bench.³ The derivation provides means to judge whether or not the test bench dynamics need to be taken into account, based on the receptance of the active component and the test bench.

Section 4.3 discusses the Virtual Point Transformation [14] and a procedure to complement the measured interface forces and moments using information of the test bench dynamics. These methods are vital for a successful BF-TPA validation as measuring rotational DoF information is challenging in practice.

The combined methodology is applied to a test case in the automotive industry in Sect. 4.4. The study focuses on the prediction of interior sound caused by the vibrations transmitted by the electric power steering system. To perform a blocked force measurement, a test bench was constructed in collaboration with the BMW Group.

Finally, conclusions and recommendations are discussed in Sect. 4.5.

4.2 Theory

This section derives the Blocked-Force TPA method. The method yields a dynamic response at the passive (/receiving) component based on the active (/source) components excitation. This response is obtained using the blocked interface forces applied at the interface between the active and passive component. It will be shown that, by measuring the interface forces and displacements of the active component mounted to a test bench, the response in a different setup involving this active component can be predicted.

The reader is guided to the final result of the derivation in three steps. First the response of the passive component to an excitation on the active component is derived in Sect. 4.2.1. Section 4.2.2 then shows what forces should be applied to the interface of the same assembly in order to obtain the same result. Finally, it is shown how these calculated forces relate to measured interface forces on a test bench in Sect. 4.2.3. These steps combined thus show how to predict the coupled response of the active and passive component using measurements involving a test bench.

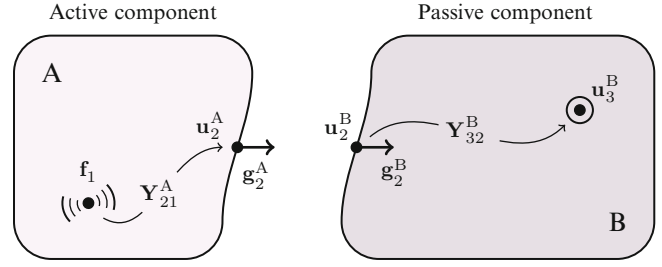
4.2.1 Substructured Response

Consider two substructures as shown in Fig. 4.1. Substructure A denotes the active component which is excited by the vector of unknown internal forces \mathbf{f}_1 on internal DoF vector \mathbf{u}_1^A . Next, substructure B denotes the passive component, which will be coupled to the active substructure on DoFs \mathbf{u}_2 . The responses to be predicted on the passive substructure are denoted with

²The BF-TPA method was previously proposed as the Component TPA [2] or Gear Noise Propagation (GNP) method [3].

³The compensation for test bench dynamics was already proposed in the original publication [3] using an impedance notation.

Fig. 4.1 Two substructures: the active component A with the unknown excitation at point 1 and passive component B with receiver at point 3



set \mathbf{u}_3^B . On the interfaces, both substructures are subjected to interface forces \mathbf{g}_2 . The system of equations of this coupled assembly can be written in block diagonal form as:

$$\begin{bmatrix} \mathbf{u}_1^A \\ \mathbf{u}_2^A \\ \mathbf{u}_2^B \\ \mathbf{u}_3^B \end{bmatrix} = \begin{bmatrix} \mathbf{Y}_{11}^A & \mathbf{Y}_{12}^A & \mathbf{0} \\ \mathbf{Y}_{21}^A & \mathbf{Y}_{22}^A & \mathbf{0} \\ \mathbf{0} & \mathbf{0} & \mathbf{Y}_{22}^B & \mathbf{Y}_{23}^B \\ \mathbf{0} & \mathbf{0} & \mathbf{Y}_{32}^B & \mathbf{Y}_{33}^B \end{bmatrix} \begin{bmatrix} \mathbf{f}_1 \\ \mathbf{g}_2^A \\ \mathbf{g}_2^B \\ \mathbf{0} \end{bmatrix} \quad (4.1)$$

Here the upper part contains all Frequency Response Functions⁴ (FRFs) of the active component, whereas the lower part contains all FRFs of the passive component. In order to couple both substructures, the interface is subjected to a compatibility condition and an equilibrium condition, written respectively as:

$$\text{Compatibility : } \mathbf{B} \mathbf{u} = \begin{bmatrix} \mathbf{0} & -\mathbf{I} & \mathbf{I} & \mathbf{0} \end{bmatrix} \begin{bmatrix} \mathbf{u}_1^A \\ \mathbf{u}_2^A \\ \mathbf{u}_2^B \\ \mathbf{u}_3^B \end{bmatrix} = \mathbf{0} \quad (4.2a)$$

$$\text{Equilibrium : } \mathbf{g} = -\mathbf{B}^T \boldsymbol{\lambda} \quad (4.2b)$$

Here \mathbf{B} represents a signed boolean matrix.⁵ To determine the coupled response of \mathbf{u}_3^B due to excitation \mathbf{f}_1 , first the equilibrium equation (4.2b) is substituted into (4.1):

$$\begin{bmatrix} \mathbf{u}_1^A \\ \mathbf{u}_2^A \\ \mathbf{u}_2^B \\ \mathbf{u}_3^B \end{bmatrix} = \begin{bmatrix} \mathbf{Y}_{11}^A & \mathbf{Y}_{12}^A & \mathbf{0} \\ \mathbf{Y}_{21}^A & \mathbf{Y}_{22}^A & \mathbf{0} \\ \mathbf{0} & \mathbf{0} & \mathbf{Y}_{22}^B & \mathbf{Y}_{23}^B \\ \mathbf{0} & \mathbf{0} & \mathbf{Y}_{32}^B & \mathbf{Y}_{33}^B \end{bmatrix} \begin{bmatrix} \mathbf{f}_1 \\ \boldsymbol{\lambda} \\ -\boldsymbol{\lambda} \\ \mathbf{0} \end{bmatrix} \quad (4.3)$$

Next the interface forces $\boldsymbol{\lambda}$ are determined by substituting (4.3) into (4.2a):

$$\boldsymbol{\lambda} = -(\mathbf{Y}_{22}^A + \mathbf{Y}_{22}^B)^{-1} \mathbf{Y}_{21}^A \mathbf{f}_1 \quad (4.4)$$

Finally, the response of interest is found by substituting (4.4) into the last line of (4.3)⁶:

$$\mathbf{u}_3^B = -\mathbf{Y}_{32}^B \boldsymbol{\lambda} = \mathbf{Y}_{32}^B (\mathbf{Y}_{22}^A + \mathbf{Y}_{22}^B)^{-1} \mathbf{Y}_{21}^A \mathbf{f}_1 \quad (4.5)$$

Note that (4.5) can also be expressed in the assembled system's receptance, using

$$\mathbf{Y}_{31}^{AB} = \mathbf{Y}_{32}^B (\mathbf{Y}_{22}^A + \mathbf{Y}_{22}^B)^{-1} \mathbf{Y}_{21}^A \quad (4.6)$$

Where superscript AB, denotes the receptance pertains to coupled structure. This approach is consistent with LM-FBS method.⁷

In summary this section derived the response of the passive component caused by the excitation of the active component, e.g. $\mathbf{u}_3^B = \mathbf{Y}_{31}^{AB} \mathbf{f}_1$, based on the FRFs of the subsystems.

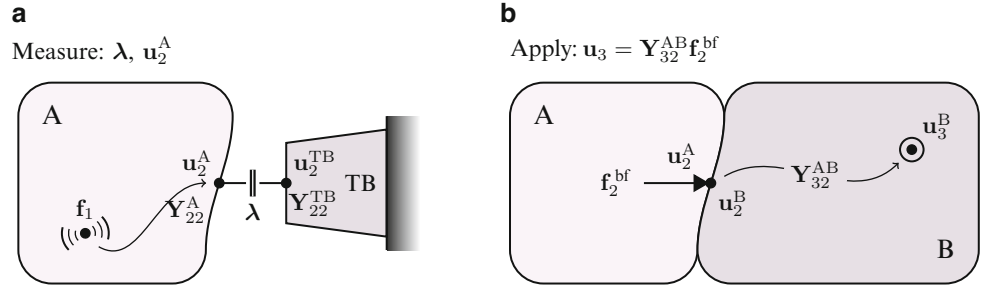
⁴The FRFs in \mathbf{Y}^A and \mathbf{Y}^B are measured on the separate components.

⁵For more information on the expression of the compatibility condition using signed boolean matrices, the reader is referred to [4].

⁶Note that additional excitations on the passive side can formally be included as well by defining \mathbf{f}_3 and including it in the force vector in (4.3).

⁷It can be verified that (4.6) can also be obtained by development of the LM-FBS notation $\mathbf{Y}^{AB} = \mathbf{Y} - \mathbf{YB}^T (\mathbf{BYB}^T)^{-1} \mathbf{BY}$.

Fig. 4.2 Blocked-Force TPA workflow. **(a)** Measurement of operational interface forces at the test bench. **(b)** Application of blocked forces to the assembled system



4.2.2 Blocked-Force Response

As explained introducing this section, it is chosen to present the following theory top-down, i.e. starting with the derivation of the responses of interest \mathbf{u}_3^B as a result of some equivalent interface forces \mathbf{f}_2^{bf} applied to the assembled receptance. From this point onwards, these equivalent forces will be referred to as blocked forces. It will shown later that these forces actually correspond to the interface forces when the interface would have been fully blocked. Section 4.2.3 therefore describes how these blocked interface forces are obtained from a measurement under operation. In practice, the workflow is the other way around, as visualised in Fig. 4.2.

It is desired to obtain an expression for the blocked forces \mathbf{f}_2^{bf} that can be applied to the coupled structure at the interface, such that the same response \mathbf{u}_3^B is obtained as when \mathbf{f}_1 was active, as discussed in Sect. 4.2.1:

$$\mathbf{u}_3^B = \mathbf{Y}_{32}^{AB} \mathbf{f}_2^{bf} \quad (4.7)$$

This corresponds to setting \mathbf{f}_1 in (4.3) to $\mathbf{0}$ and applying \mathbf{f}_2^{bf} to the interface nodes, as illustrated in Fig. 4.2b. In other words, the operational excitation is removed and replaced by the blocked forces at the interface, representing the operational excitation. This requires the coupled receptance of the interface DoFs to the response of interest \mathbf{u}_3^B , which can be determined in a manner analogue to (4.6):

$$\mathbf{Y}_{32}^{AB} = \mathbf{Y}_{32}^B (\mathbf{Y}_{22}^A + \mathbf{Y}_{22}^B)^{-1} \mathbf{Y}_{22}^A \quad (4.8)$$

Next, by requiring that the blocked forces \mathbf{f}_2^{bf} yield the same response as found in (4.5)

$$\mathbf{u}_3^B = \mathbf{Y}_{32}^B (\mathbf{Y}_{22}^A + \mathbf{Y}_{22}^B)^{-1} \mathbf{Y}_{22}^A \mathbf{f}_2^{bf} = \mathbf{Y}_{32}^B (\mathbf{Y}_{22}^A + \mathbf{Y}_{22}^B)^{-1} \mathbf{Y}_{21}^A \mathbf{f}_1 \quad (4.9)$$

one finds for the required blocked forces:

$$\mathbf{f}_2^{bf} = (\mathbf{Y}_{22}^A)^{-1} \mathbf{Y}_{21}^A \mathbf{f}_1 \quad (4.10)$$

Now a description of the blocked forces \mathbf{f}_2^{bf} is known. Since \mathbf{f}_1 are internal forces and thus unmeasurable, the next section elaborates on how to obtain the blocked forces \mathbf{f}_2^{bf} from measurable data.

4.2.3 Operational Response on Test Bench

To obtain \mathbf{f}_2^{bf} , a setup is considered with subsystem A connected to a test bench, denoted by TB, as illustrated by Fig. 4.2a. Again, the substructures are coupled on the interface DoFs \mathbf{u}_2 . The new system of equations, similar to (4.3), reads:

$$\begin{bmatrix} \mathbf{u}_1^A \\ \mathbf{u}_2^A \\ \mathbf{u}_2^{TB} \end{bmatrix} = \begin{bmatrix} \mathbf{Y}_{11}^A & \mathbf{Y}_{12}^A & \mathbf{0} \\ \mathbf{Y}_{21}^A & \mathbf{Y}_{22}^A & \mathbf{0} \\ \mathbf{0} & \mathbf{0} & \mathbf{Y}_{22}^{TB} \end{bmatrix} \begin{bmatrix} \mathbf{f}_1 \\ \boldsymbol{\lambda} \\ -\boldsymbol{\lambda} \end{bmatrix} \quad (4.11)$$

Note that the displacements and interface forces in this equation are unequal to the ones previously obtained in Sect. 4.2.1. Rewriting the second line of (4.11) yields the measurable interface forces as a function of the unknown excitation \mathbf{f}_1 and interface displacements \mathbf{u}_2^A

$$\boldsymbol{\lambda} = (\mathbf{Y}_{22}^A)^{-1} (\mathbf{u}_2^A - \mathbf{Y}_{21}^A \mathbf{f}_1) \quad (4.12)$$

Note that (4.12) is essential since it describes the relation between the unknown internal excitation \mathbf{f}_1 and the measured interface forces $\boldsymbol{\lambda}$ and displacements \mathbf{u}_2^A due to the test bench flexibility. This allows us to set up the following expression for \mathbf{f}_2^{bf} :

$$\mathbf{f}_2^{\text{bf}} = -(\boldsymbol{\lambda} + \mathbf{f}^{\text{comp}}) \quad \text{with} \quad \mathbf{f}^{\text{comp}} \triangleq -(\mathbf{Y}_{22}^A)^{-1} \mathbf{u}_2^A \quad (4.13)$$

It can be seen that \mathbf{f}^{comp} compensates for the underestimation of the measured test bench forces $\boldsymbol{\lambda}$ due to the interface motion \mathbf{u}_2^A . Now, in order to gain more insight in the influence of the ratio between $\|\mathbf{Y}_{22}^A\|$ and $\|\mathbf{Y}_{22}^{\text{TB}}\|$, independent expressions for both $\boldsymbol{\lambda}$ and \mathbf{u}_2^A can be established. An expression for $\boldsymbol{\lambda}$ is found, in a manner analogue to (4.4), by solving the compatibility condition $\mathbf{u}_2^A = \mathbf{u}_2^{\text{TB}}$. The independent expression for \mathbf{u}_2^A is then found by substituting the obtained expression (4.14a) for $\boldsymbol{\lambda}$ in the second line of (4.11)

$$\mathbf{f}_2^{\text{bf}} = -(\boldsymbol{\lambda} - (\mathbf{Y}_{22}^A)^{-1} \mathbf{u}_2^A) \quad \text{using} \quad \begin{cases} \boldsymbol{\lambda} = -(\mathbf{Y}_{22}^A + \mathbf{Y}_{22}^{\text{TB}})^{-1} \mathbf{Y}_{21}^A \mathbf{f}_1 & (4.14a) \\ \mathbf{u}_2^A = [\mathbf{I} - \mathbf{Y}_{22}^A (\mathbf{Y}_{22}^A + \mathbf{Y}_{22}^{\text{TB}})^{-1}] \mathbf{Y}_{21}^A \mathbf{f}_1 & (4.14b) \end{cases}$$

From a general point of view, (4.14a) and (4.14b) apply regardless of the test bench properties. Besides that, they depict the influence of increasing or decreasing test bench flexibility on the interface forces $\boldsymbol{\lambda}$, the interface motion \mathbf{u}_2^A and therefore also the compensation forces for the interface motion \mathbf{f}^{comp} . Two extremes can be discussed:

- It can be seen that, for the scenario $\|\mathbf{Y}_{22}^{\text{TB}}\| \ll \|\mathbf{Y}_{22}^A\|$, i.e. the test bench is significantly stiffer than the active component, the interface displacements \mathbf{u}_2^A go to $\mathbf{0}$ and thereby the compensation forces \mathbf{f}^{comp} reduce to $\mathbf{0}$. This can be interpreted as if the interfaces were fully blocked and \mathbf{f}_2^{bf} is determined solely by the measured interface forces $\boldsymbol{\lambda}$.
- For the other extreme case that $\|\mathbf{Y}_{22}^{\text{TB}}\| \gg \|\mathbf{Y}_{22}^A\|$, i.e. the test bench stiffness is negligible, it can be seen that the interface forces $\boldsymbol{\lambda}$ go to $\mathbf{0}$ and \mathbf{f}_2^{bf} is determined by only the forces compensating for the interface motion \mathbf{f}^{comp} . This can be interpreted as free interface motion.

The above theory gives a physical interpretation to the blocked force concept that can be historically related to a Thévenin or Norton equivalent system; see for instance [7, 8, 12]. Now it is clear that the blocked forces indeed corresponds to the interface forces that would have been measured if the interface was fully blocked. Hence, the name blocked force.

4.2.4 Equivalent Forces from Inverse BF-TPA

For reference purposes, an additional method is considered to find the blocked interface forces. Applying the BF-TPA inversely, the blocked forces \mathbf{f}_2^{bf} can be approximated from measured displacements \mathbf{u}^{TB} at the test bench, where the test bench itself is now considered as the passive component. Provided that the set of displacements \mathbf{u}^{TB} is large enough to observe the complete set of interface forces, \mathbf{f}_2^{bf} follows from the inverse application of the BF-TPA procedure. This method was earlier proposed by [10]. The inverse TPA method will be used in Sect. 4.4 as a reference. The method is briefly summarised here.

Section 4.2.2 demonstrated the relation between the blocked forces \mathbf{f}_2^{bf} and the responses of interest \mathbf{u}_3^{B} . Recall from (4.7):

$$\mathbf{u}_3^{\text{B}} = \mathbf{Y}_{32}^{\text{AB}} \mathbf{f}_2^{\text{bf}}$$

Let us now consider a situation where the active subsystem (A) is mounted to the test bench (TB). In a manner analogue to (4.7), the following can be written:

$$\begin{bmatrix} \mathbf{u}_2^{\text{TB}} \\ \mathbf{u}_4^{\text{TB}} \end{bmatrix} = \begin{bmatrix} \mathbf{Y}_{22}^{(\text{A}|\text{TB})} \\ \mathbf{Y}_{42}^{(\text{A}|\text{TB})} \end{bmatrix} \mathbf{f}_2^{\text{bf}} \quad (4.15)$$

Here superscript (A|TB) for receptance \mathbf{Y} denotes the coupled receptance of the active subsystem mounted to the test bench, measured at its interface \mathbf{u}_2^{TB} and additional points \mathbf{u}_4^{TB} elsewhere on the test bench. Now, the blocked forces are found by inversion of Eq. (4.15):

$$\mathbf{f}_2^{\text{bf}} = \begin{bmatrix} \mathbf{Y}_{22}^{(\text{A|TB})} \\ \mathbf{Y}_{42}^{(\text{A|TB})} \end{bmatrix}^+ \begin{bmatrix} \mathbf{u}_2^{\text{TB}} \\ \mathbf{u}_4^{\text{TB}} \end{bmatrix} \quad (4.16)$$

Indeed, (4.16) is found from a pseudo-inverse of the measured receptance of the coupled system, which requires the set of measured displacements to be larger than or equal to the set of blocked forces. To improve the approximation, additional internal responses \mathbf{u}_4^{TB} may therefore be included.

4.3 Practice

The quality of a TPA depends on the completeness of the description of the transmission paths, which can be directly observed from (4.7). It is often seen that for low frequencies the translational transfer functions of the receiving structure are dominant, such that the majority of the operational excitation is transmitted through translational vibrations at the interface. However for higher frequencies (typically in a multi-kHz range) the rotational vibrations will start to contribute significantly [9, 13]. It is therefore needed to determine the blocked forces as well as the blocked moments at the interface with high accuracy. This gives rise to a number of challenges in practice.

The first challenge to be discussed is the description of rotations and moments. It was shown in the previous section that the motion due to test bench flexibility at the interface can be used to augment the determination of the blocked forces. When 6-DoF coupling is desired, this implies that rotations also need to be determined per interface point. The proposed solution relies on the Virtual Point Transformation [14] that allows to determine rotational information using translational data at multiple measurement points near the virtual interface points.

Another challenge that may arise is measuring the interface moments during the operational blocked force measurement. Again, when the subsystems are coupled in 6 DoFs, interface moments have to be measured in order to perform a complete BF-TPA. However, force sensors that measure both translational and rotational loads are not commonly available. A solution is proposed to determine the complete set of interface loads by a least-squares error minimisation using information of the test bench receptance at hand.

4.3.1 Description of Collocated 6-DoF Motion and Loads

In order to obtain a complete 6-DoF description for the motion and loads⁸ at the interface, the Virtual Point Transformation is used in this work [14]. The method is shortly summarised here for the purpose of 6-DoF receptance determination, but can be straightforwardly applied to measure operational motion and loads at the test bench interfaces. A key benefit of the method is that the resulting generalised motion and loads are collocated in a single point, the so-called *virtual point*. As such compatibility is automatically ensured with FE models, which can be beneficial for structural optimisation purposes.⁹ Additionally the method suppresses uncorrelated measurement noise due to the least-square nature of the transformation. For more details background on the method, the reader is referred to [5, 13, 14].

Let us consider an interface point surrounded by N translational DoFs \mathbf{u} . This set of measured DoFs can be reduced to M generalised DoFs \mathbf{q} by means of a mapping matrix \mathbf{R}_u . Since the number of generalised DoFs is smaller than the amount of measured DoFs ($M < N$), a vector of residual displacements $\boldsymbol{\mu}$ is added:

$$\mathbf{u} = \mathbf{R}_u \mathbf{q} + \boldsymbol{\mu} \quad (4.17)$$

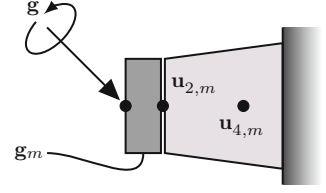
When one chooses \mathbf{q} to describe three translations and three rotations for each virtual point, the columns of \mathbf{R}_u represent the so-called rigid Interface Displacement Modes (IDMs). It can be shown that \mathbf{q} can be written as a function of \mathbf{u} by making a least-squares approximation:

$$\mathbf{q} = \mathbf{T}_u \mathbf{u} \quad \text{with} \quad \mathbf{T}_u \triangleq (\mathbf{R}_u^T \mathbf{R}_u)^{-1} \mathbf{R}_u^T \quad (4.18a)$$

⁸The terms motion and loads are used when referred to the 6-DoF set of respectively displacements/rotations and forces/moments.

⁹This only applies to FE models containing 6-DoF nodes. A major part of the finite elements consist of 3-DoF nodes.

Fig. 4.3 Interface loads and measured quantities on test bench



To determine virtual point loads, the same technique applies. By choosing \mathbf{R}_f for mapping applied forces \mathbf{f} to virtual point loads \mathbf{p} , one can write:

$$\mathbf{f} = \mathbf{T}_f^T \mathbf{p} \quad \text{with} \quad \mathbf{T}_f \triangleq (\mathbf{R}_f^T \mathbf{R}_f)^{-1} \mathbf{R}_f^T \quad (4.18b)$$

Using the above expressions the receptance of measured excitations to displacements can be rewritten to the virtual point description by substitution of (4.18a) and (4.18b) into $\mathbf{u} = \mathbf{Y}\mathbf{f}$:

$$\mathbf{q} = \mathbf{T}_u \mathbf{Y} \mathbf{T}_f^T \mathbf{p} = \mathbf{H} \mathbf{p} \quad (4.19)$$

where $\mathbf{H} \triangleq \mathbf{T}_u \mathbf{Y} \mathbf{T}_f^T$ denotes the collocated virtual point receptance. \mathbf{H} can be used for substructuring with other components, either derived from experimental or from numerical models, provided that the description of the virtual points is chosen such that it corresponds to the six degrees of freedom of a node.

4.3.2 Determination of Non-measurable Interface Loads

Having obtained the assembled receptance for 6-DoF per coupling point, one now needs to measure the operational interface forces and moments for the same set of DoFs. Due to geometrical restrictions or absence of a suitable 6-DoF load sensor, some of the loads may be difficult or impossible to measure in practice. Using the available measurement data and known receptance of the test bench, a (weighted) least-square estimate can be made.

In general, two relationships can be established concerning the complete set of interface loads \mathbf{g} . One can consider the interface loads as an applied load to the test bench interface only. Hence, the test bench motion due to this load is solely determined by the test bench receptance, as visualised by Fig. 4.3. Therefore one relation can be established between the measured displacements \mathbf{u}_m and the interface loads \mathbf{g} analogue to (4.1), namely (4.20a). Since the measured displacements exhibit a certain measurement error, a data residual term $\boldsymbol{\varepsilon}_u$ is added. In a similar sense, the relation between the measured interface forces \mathbf{g}_m and the actual interface forces \mathbf{g} can be established, with the residual term $\boldsymbol{\varepsilon}_g$ in (4.20b). Note that for convenience of notation the superscripts TB and subscripts 2 have been omitted

$$\left\{ \begin{array}{l} \mathbf{u}_m = \mathbf{Y} \mathbf{g} + \boldsymbol{\varepsilon}_u \\ \mathbf{g}_m = \mathbf{g} + \boldsymbol{\varepsilon}_g \end{array} \right. \quad (4.20a) \quad (4.20b)$$

The measured displacements \mathbf{u}_m do not all necessarily pertain to the interface. Additional points on the structure can be taken into account as long as the transfer paths (receptance \mathbf{Y}) to these points are known. Note that \mathbf{Y} can be measured at the test bench before mounting the active component. Alternatively, the test bench construction may be modelled

In order to find \mathbf{g} from the overdetermined problem of (4.20), the residual terms can be minimised using a weighted cost function $J(\mathbf{g})$. The minimum of $J(\mathbf{g})$ will provide the weighted least-squares solution for the interface loads \mathbf{g}

$$\begin{aligned} J(\mathbf{g}) &= \boldsymbol{\varepsilon}_u^H \mathbf{W}_u \boldsymbol{\varepsilon}_u + \boldsymbol{\varepsilon}_g^H \mathbf{W}_g \boldsymbol{\varepsilon}_g \\ &= (\mathbf{u}_m^H - \mathbf{g}^H \mathbf{Y}^H) \mathbf{W}_u (\mathbf{u}_m - \mathbf{Y} \mathbf{g}) + (\mathbf{g}_m^H - \mathbf{g}^H) \mathbf{W}_g (\mathbf{g}_m - \mathbf{g}) \end{aligned} \quad (4.21)$$

Note that both weighting matrices \mathbf{W} have to compensate for the difference in dimension between $\boldsymbol{\varepsilon}_u$ and $\boldsymbol{\varepsilon}_g$. One can choose the weighting matrices to be diagonal, giving a single weight to every measured DoF. Alternatively one can adopt \mathbf{W}_u and \mathbf{W}_g as respectively a (dynamic) stiffness and admittance matrix, such that local residual energy is minimised. Since a minimal

$J(\mathbf{g})$ is desired, the derivative of $J(\mathbf{g})$ is taken with respect to \mathbf{g}^H and equated to $\mathbf{0}$. Due to the quadratic nature of the cost function, this yields the global minimum for $J(\mathbf{g})$ with respect to the choices for \mathbf{W}_u and \mathbf{W}_g

$$\frac{\partial J(\mathbf{g})}{\partial \mathbf{g}^H} = 2 (\mathbf{Y}^H \mathbf{W}_u \mathbf{Y} \mathbf{g} - \mathbf{Y}^H \mathbf{W}_u \mathbf{u}_m) + 2 \mathbf{W}_g \mathbf{g} - 2 \mathbf{W}_g \mathbf{g}_m = \mathbf{0} \quad (4.22)$$

Finally, using (4.22), the following weighted least-squares approximation for \mathbf{g} is obtained:

$$\mathbf{g} = (\mathbf{Y}^H \mathbf{W}_u \mathbf{Y} + \mathbf{W}_g)^{-1} (\mathbf{Y}^H \mathbf{W}_u \mathbf{u}_m + \mathbf{W}_g \mathbf{g}_m) \quad (4.23)$$

Remarks

- Note that choosing diagonal weighting matrices \mathbf{W}_u and \mathbf{W}_g results in the inverse part of (4.23) to be symmetric positive definite and is therefore expected to be well-conditioned.
- In the inconvenient case of all loads being unmeasurable, their weighting \mathbf{W}_g reduces to $\mathbf{0}$. The solution for \mathbf{g} then reduces to the pseudo-inverse problem $\mathbf{g} = \mathbf{Y}^+ \mathbf{u}_m$, meaning that the loads are solely “model-based”, i.e. depending on \mathbf{Y} and some weighting choices in \mathbf{W}_u .

4.3.3 Application: Determination of Interface Moments

The proposed method of Sect. 4.3.2 was applied for the test case to determine the full set of operational interface loads, while only translational interface forces are measured. In this case a distinction is made between the translational forces and rotational forces, i.e. $\mathbf{g} \triangleq \text{col}(\mathbf{g}_T; \mathbf{g}_R)$. Concerning the displacements, the set consists of the translational and rotational interface DoFs, plus some additional displacements elsewhere on the test bench: $\mathbf{u} \triangleq \text{col}(\mathbf{u}_{2T}; \mathbf{u}_{2R}; \mathbf{u}_4)$.¹⁰ The measured quantities are depicted in Fig. 4.3. Using (4.20), the system reads:

$$\begin{bmatrix} \mathbf{u}_{2T} \\ \mathbf{u}_{2R} \\ \mathbf{u}_4 \end{bmatrix}_m = \begin{bmatrix} \mathbf{Y}_{2T2T} & \mathbf{Y}_{2T2R} \\ \mathbf{Y}_{2R2T} & \mathbf{Y}_{2R2R} \\ \mathbf{Y}_{42T} & \mathbf{Y}_{42R} \end{bmatrix} \begin{bmatrix} \mathbf{g}_T \\ \mathbf{g}_R \end{bmatrix} + \boldsymbol{\varepsilon}_u \quad (4.24a)$$

$$\begin{bmatrix} \mathbf{g}_T \\ \mathbf{g}_R \end{bmatrix}_m = \begin{bmatrix} \mathbf{g}_T \\ \mathbf{g}_R \end{bmatrix} + \boldsymbol{\varepsilon}_g \quad (4.24b)$$

Now taking into account that the interface moments $\mathbf{g}_{R,m}$ were not measured, the weighting matrix \mathbf{W}_g can be chosen as follows:

$$\mathbf{W}_g = \begin{bmatrix} \mathbf{W}_T & \mathbf{0} \\ \mathbf{0} & \mathbf{W}_R \end{bmatrix}_g = \begin{bmatrix} \mathbf{W}_{TT} & \mathbf{0} \\ \mathbf{0} & \mathbf{0} \end{bmatrix}_g \quad (4.25a)$$

such that the non-measured moments do not contribute to the cost function. Concerning the weighting of residual terms on the displacements, \mathbf{W}_u will take the form:

$$\mathbf{W}_u = \begin{bmatrix} \mathbf{W}_{2T} & \mathbf{0} & \mathbf{0} \\ \mathbf{0} & \mathbf{W}_{2R} & \mathbf{0} \\ \mathbf{0} & \mathbf{0} & \mathbf{W}_4 \end{bmatrix}_u \quad (4.25b)$$

Both (4.25a) and (4.25b) can now be substituted into (4.23) to solve the interface loads \mathbf{g} .

¹⁰Do note that the displacement vector does not necessarily have to contain virtual point transformed DoFs. As mentioned, the approximation in this section benefits from larger displacement sets and therefore the original sensor displacements are preferred here. However, this also requires the transfer path information (receptance \mathbf{Y}) to the original sensor locations. When both the receptance and BF-TPA measurement are performed with the same set of mounted sensors, this gives no problems. In this particular case, the used receptance \mathbf{Y} will only be virtual point transformed at the right side associated with the generalised forces/moments.

4.4 Test Case

To validate the proposed methodology, a test case has been conducted at the research facility of the BMW Group in Munich. The test case involved an active and passive subsystem and a test bench. The active component used for the test was the electric power steering (EPS) system. The EPS has four connections (interfaces) to the bodywork of the vehicle, which is considered as the passive subsystem.

For the purpose of the operational blocked force measurement, a test bench has been constructed as shown in Fig. 4.4a. The test bench has four supports rigidly connected to a test table. The steering gear is bolted onto the supports with 3D force sensors in between, as shown in Fig. 4.4b. To simulate true steering operation, additional parts such as wheels and suspension parts are mounted. The construction is uncoupled from the steering gear to make sure that the blocked force measurement is not affected. A variable weight is applied to the front axle carrier, such that the lateral forces between the wheels and the EPS system can be matched to operational values. This has been validated. The measurement data discussed below is obtained by performing a typical parallel parking steering manoeuvre.

Note that when applying the theory from Sect. 4.2, it is assumed that virtual point transformations, as discussed in Sect. 4.3.1, are applied on measured displacements sets, force sets and receptances. However, one exception is to be made. As discussed in Sect. 4.3.3, the approximation of the interface loads does not benefit from a virtual point transformation.

4.4.1 Determination of the Interface Loads

As discussed in Sects. 4.3.2 and 4.3.3, an approximation for the complete set of interface loads was made, based on the measured 3D interface forces and measured accelerations at various locations around the interfaces. The forces shown in Fig. 4.5 correspond to the load case of a single impact on the EPS system.

Figure 4.5a demonstrates the application of the weighted least-squares method applied to the interface force of the first EPS support in X -direction (driving direction). By altering the weighting, the LS-approximated interface force shifts between the measured interface force \mathbf{g}_m and the model-based interface force, approximated by $\mathbf{g} = \mathbf{Y}^{-1} \mathbf{u}_m$. For this particular case, an FE model has been used for the test bench receptance \mathbf{Y} . However, an experimentally determined model should be preferred over an FE model.

Figure 4.5b shows the estimated interface moment around the X -axis. The figure shows that the estimated moment is similar to the model based interface moment, subject to $\mathbf{g} = \mathbf{Y}^{-1} \mathbf{u}_m$. Although the estimation does not rely on the moments in \mathbf{g}_m , the estimation is slightly influenced by additional parameters, as seen in (4.23), explaining the small difference. It was verified that this can be controlled by changing the parameters of the weighting matrices.

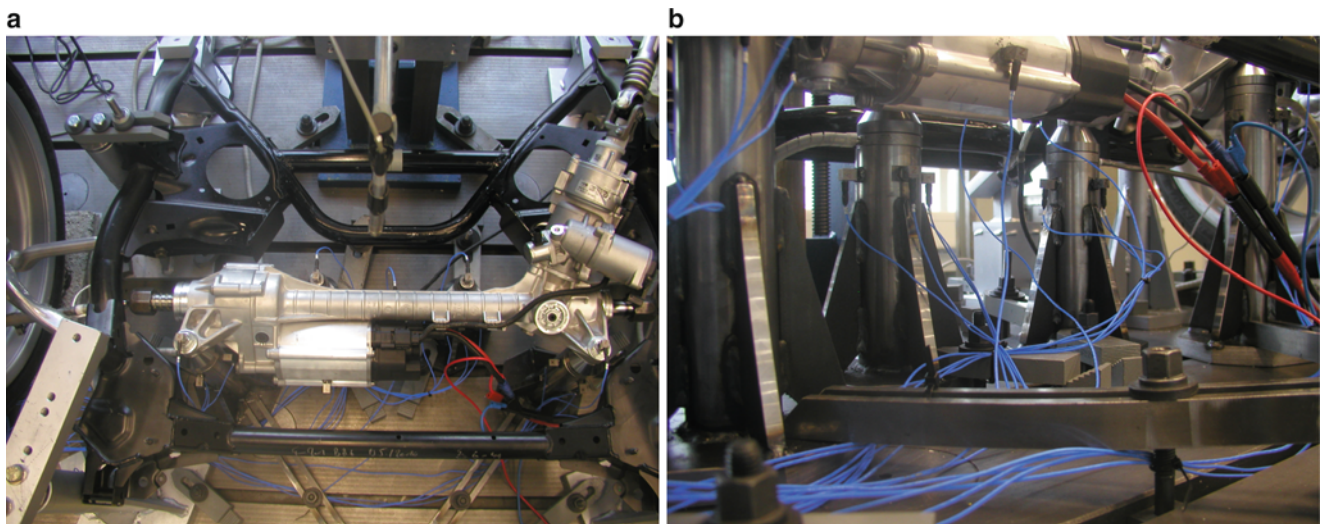


Fig. 4.4 The test bench. (a) Overview of the test bench. (b) Test bench supports

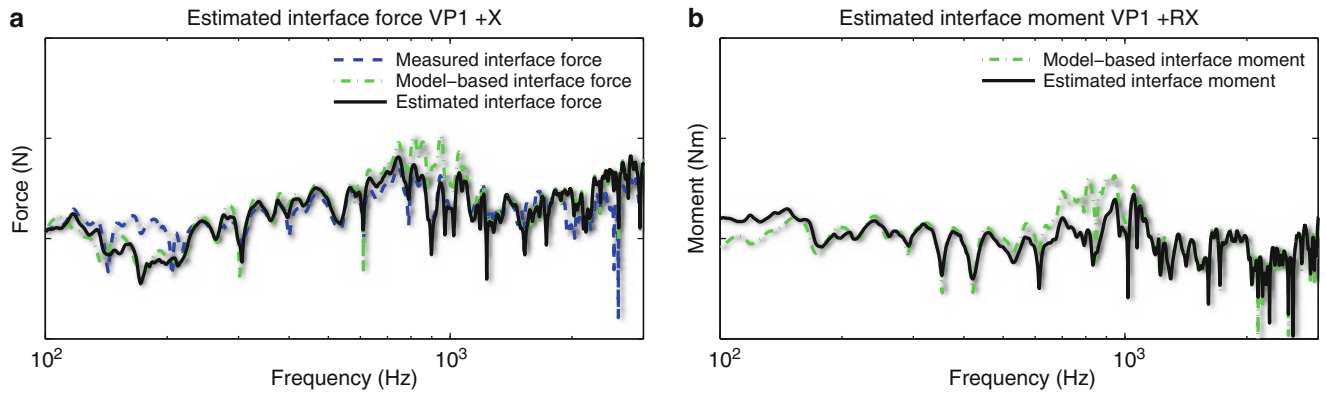


Fig. 4.5 Estimated interface loads. (a) Estimated interface force (*black*) for the first support in the *X*-direction, averaged between the measurement (*green*) and the model (*blue*). (b) Estimated interface moment (*black*) for the first support around the *X*-axis. Due to the lack of measured moments, it is only based on the model (*blue*) (Color figure online)

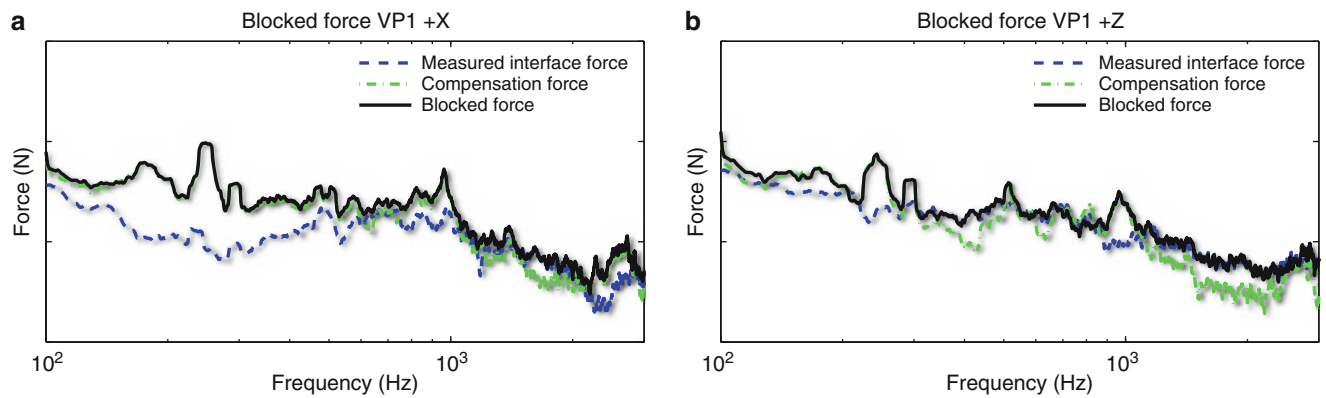


Fig. 4.6 Composition of blocked forces \mathbf{f}_2^{bf} for the first support. The blocked force consist of a measured interface force part λ and a compensation force part \mathbf{f}^{comp} . (a) *X*-direction; (b) *Z*-direction

4.4.2 Composition of the Blocked Force

To gain more insight in the influence of the test bench dynamics on the BF-TPA, the composition of \mathbf{f}_2^{bf} , as earlier shown in (4.13), can be further investigated. Figure 4.6 shows the ratio between the measured test bench force λ and the compensation force for the test bench dynamics \mathbf{f}^{comp} .

The blocked force \mathbf{f}_2^{bf} for the first support in the *X*-direction is shown in Fig. 4.6a. First it can be noticed that the measured interface force λ and the compensation force \mathbf{f}^{comp} maintain roughly the same order of magnitude, such that neither one of the components is negligible. The figure clearly shows that the compensation force \mathbf{f}^{comp} dominates for the majority of the frequency range, especially in the lower frequencies.

Figure 4.6b shows the blocked force \mathbf{f}_2^{bf} for the first support in *Z*-direction. Due to the construction of supports, the test bench is significantly stiffer in the *Z*-direction than in the *X*-direction. The figure also indicates that the measured interface force λ has in general a higher contribution to the blocked force \mathbf{f}_2^{bf} than for the *X*-direction. Some parts of the shown frequency range are dominated by the measured interface force λ , while others are dominated by the compensation force \mathbf{f}^{comp} .

4.4.2.1 Blocked Force Using Inverse BF-TPA

Section 4.2.4 discussed an alternative method to derive the blocked forces \mathbf{f}_2^{bf} ; an inverse BF-TPA derivation. Although in theory both methods should yield the same result, practice proves different. Figure 4.7 compares the blocked forces, as discussed above and the inverse BF-TPA forces. Figure 4.7a compares both forces for the *X*-direction of the first support, whereas Fig. 4.7b compares both for the *Z*-direction for the first support.

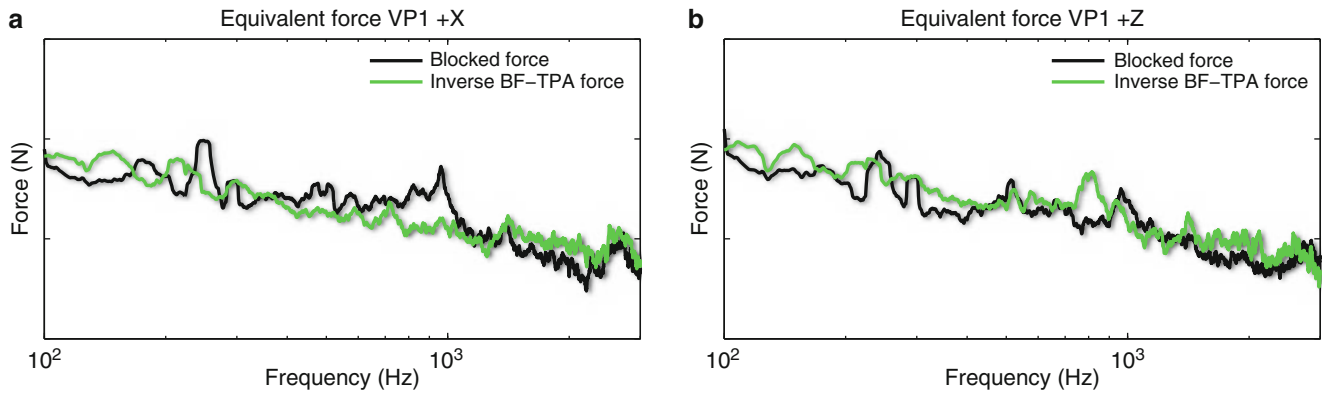
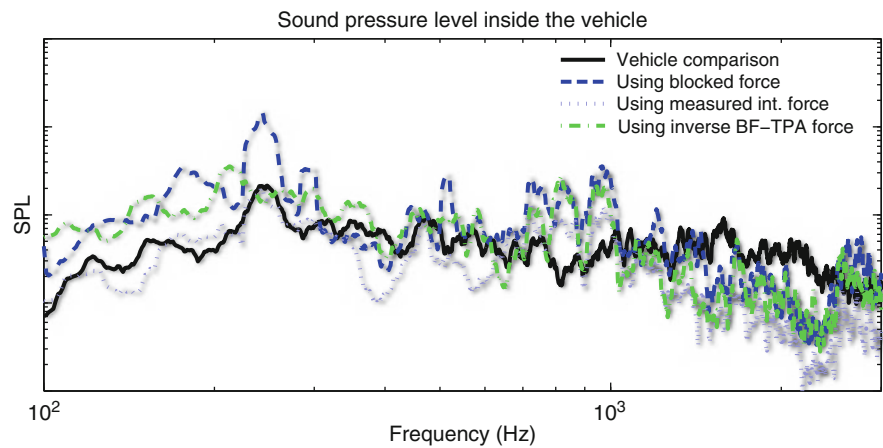


Fig. 4.7 Comparison of the blocked force \mathbf{f}_2^{bf} (black) for the first support with the inverse BF-TPA force (green). (a) X-direction; (b) Z-direction (Color figure online)

Fig. 4.8 Sound pressure level in the car determined by measurement (black), BF-TPA using the blocked forces (blue), BF-TPA using only the measured interface forces (gray) and BF-TPA using the inverse BF-TPA forces (green) (Color figure online)



In both figures, the blocked force and the inverse BF-TPA force are roughly in the same order of magnitude, although some differences are significant. These differences might be explained by the fact that an FE model was used for the test bench receptance \mathbf{Y}^{TB} , influencing the coupled receptance $\mathbf{Y}^{(\text{A}|\text{TB})}$ used for determining the inverse BF-TPA forces. Besides that, differences can also be caused by discrepancies in the measured forces, displacements and receptances.

4.4.3 BF-TPA Results

In an attempt to validate the BF-TPA method, various estimations for the sound pressure level in the vehicle are shown in Fig. 4.8:

- BF-TPA using the calculated blocked forces (blue);
- BF-TPA using the measured interface forces only (gray);
- BF-TPA using the inverse BF-TPA forces (green);
- A comparison measurement in the vehicle (black).

The reference measurement consists of the coupled subsystems A and B, i.e. the EPS mounted in the vehicle, in operation.

It can be seen that neither the BF-TPA using the blocked forces, nor the BF-TPA using the inverse BF-TPA forces shows a decent estimate of the sound pressure level as measured in the vehicle. However for the lower frequencies, the estimate using the directly measured interface forces shows a good agreement.

Remarks

- One could argue whether the transfer path from the EPS system through the wheel suspension to the bodywork of the car should also be taken into account. However, these interfaces cannot be blocked since the EPS would no longer be able to steer. Fortunately, it has been verified that the contribution of this transfer path is negligible compared to the direct transfer paths and has therefore been left out.
- The definition in (4.13) shows that the compensation forces \mathbf{f}^{comp} are determined from the interface displacements \mathbf{u}_2^A and the inverted interface receptance of the active component \mathbf{Y}_{22}^A . It is known that rotational information determined using virtual transformations is highly sensitive to measurement errors. Since the computation of the compensation forces comprises two virtual point transformations and a matrix inversion, errors on rotations are easily amplified. To minimise the amplification of errors in the compensation forces \mathbf{f}^{comp} , only the translational DoFs are considered for the compensation.

4.5 Conclusions

This paper has proposed a methodology for the Blocked-Force Transfer Path Analysis. Based on the results, some conclusions can be drawn.

Regarding the estimation of the interface loads, it was shown that the proposed method in Sect. 4.3.2 provides a successful estimation for the interface loads by shifting between the measured loads and the model based loads. However the choice of the weighting matrices, determining the dominance of components, is still open for discussion.

Section 4.2.2 has provided insight in the composition of the blocked forces. It was shown that the compensation forces for the test bench motion are dominant over the measured interface loads in this particular test case. This is not to be expected, since the test bench is designed to be more rigid than the active component.

The BF-TPA results depicted in Sect. 4.4.3 have shown that both the estimates involving the blocked forces and the inverse BF-TPA forces fail to approximate the reference measurement. The BF-TPA without compensation for the test bench dynamics did however show a reasonable agreement for the lower frequencies. In addition, it was observed in Sect. 4.4.2 that the compensation forces are dominant in this frequency range. It is therefore possible that the compensation forces for the test bench dynamics are overestimated. To draw conclusions regarding test bench dynamics, the used receptances for both the active component and the test bench should be reconsidered.

Acknowledgements This study was performed in close collaboration with the BMW Group, whom we greatly acknowledge for their support and organisation.

References

1. de Klerk D, Ossipov, A (2010) Operational transfer path analysis: theory, guidelines and tire noise application. *Mech Syst Signal Process* 24(7):1950–1962. doi:<http://dx.doi.org/10.1016/j.ymssp.2010.05.009>. <http://www.sciencedirect.com/science/article/pii/S0888327010001524>. Special Issue: ISMA 2010 [ISSN 0888-3270]
2. de Klerk D, Rixen D (2010) Component transfer path analysis method with compensation for test bench dynamics. *Mech Syst Signal Process* 24(6):1693–1710. doi:10.1016/j.ymssp.2010.01.006. <http://www.sciencedirect.com/science/article/pii/S0888327010000397> [ISSN 0888-3270]
3. de Klerk D, Rixen DJ, Valentin C (2007) An experimental gear noise propagation method for a gearbox on a test bench. In: Proceedings of the XXV international modal analysis conference, Orlando. Society for Experimental Mechanics, Bethel
4. de Klerk D, Rixen D, Voormeeren S (2008) A general framework for dynamic substructuring. History, review and classification of techniques. *AIAA J* 46(8):1169–1181
5. de Klerk D, Rixen D, Voormeeren S, Pasteuning F (2008) Solving the RDOF problem in experimental dynamic substructuring. In: Proceedings of the XXVI international modal analysis conference, Orlando. Society for Experimental Mechanics, Bethel
6. de Klerk D, Lohrmann M, Quickert M, Foken W (2009) Application of operational transfer path analysis on a classic car. In: DAGA, Rotterdam
7. Gardonio P, Brennan M (2002) On the origins and development of mobility and impedance methods in structural dynamics. *J Sound Vib* 249(3):557–573. doi:<http://dx.doi.org/10.1006/jsvi.2001.3879>. <http://www.sciencedirect.com/science/article/pii/S0022460X01938799> [ISSN 0022-460X]
8. Hixson EL (1961) Mechanical impedance and mobility, Chap 10. In: Harris C, Crede C (eds) *Shock and vibration handbook*, 1st edn. McGraw-Hill, New York, pp 1–59
9. Liu W, Ewins D (1999) The importance assessment of RDOF in FRF coupling analysis. In: Proceedings of the XVII international modal analysis conference, Orlando. Society for Experimental Mechanics, Bethel, pp 1481–1487

10. Moorhouse A, Elliott A, Evans T (2009) In situ measurement of the blocked force of structure-borne sound sources. *J Sound Vib* 325 (4–5):679–685. doi:<http://dx.doi.org/10.1016/j.jsv.2009.04.035>. <http://www.sciencedirect.com/science/article/pii/S0022460X09003794> [ISSN 0022-460X]
11. Plunt J (2005) Finding and fixing vehicle nvh problems with transfer path analysis. *Sound Vib* 39(11):12–17
12. Rixen DJ, Boogaard A, van der Seijs MV, van Schothorst G, van der Poel T (2013) Source description in vibration transmission between substructures: blocked forces and free velocities. *J Sound Vib* (submitted) <http://www.lmsfrance.fr/download.asp?id=A5AF1B71-301F-4DB2-992F-D8A213AE37F2>
13. van der Seijs M, de Klerk D, Rixen D, Rahimi S (2013) Validation of current state frequency based substructuring technology for the characterisation of steering gear – vehicle interaction. In: Proceedings of the XXXI international modal analysis conference, Los Angeles. Society for Experimental Mechanics, Bethel
14. van der Seijs M, van den Bosch D, Rixen D, de Klerk D (2013) An improved methodology for the virtual point transformation of measured frequency response functions in dynamic substructuring. In: Papadrakakis M, Papadopoulos V, Plevris V (eds) COMPDYN 2013 4th, ECCOMAS thematic conference on computational methods in structural dynamics and earthquake engineering, Kos Island, Greece, 12–14 June 2013

Chapter 5

Prediction of Forced Response on Ancillary Subsystem Components Attached to Reduced Linear Systems

Sergio E. Obando and Peter Avitabile

Abstract Multi-component structural systems are commonly used in the modeling of dynamic systems. In order to simplify such complex mathematical models, peripheral/ancillary components are often times grouped as larger substructures of the total assembly. The dynamic response of the structural system will have the embedded characteristics of the appended ancillary components but the fidelity of the model will be highly dependent on the quality and resolution of the model. In particular, sufficient substructure information is needed for an accurate prediction of the response of the appendage and/or its coupling structure. This implies that proper characterization of the structure may require measurements at the subcomponent level or in the absence of sufficient data, a large and detailed finite element model.

In this work, analytical models of a multi-component beam system were created to investigate the prediction of the dynamic response of ancillary subcomponents. The ancillary structure will be assumed to be dynamically active but inaccessible/immeasurable. The models will be created first at full space as a reference and then reduction techniques will be used to determine the necessary information in order to accurately predict the force or displacement imparted to the appendages. The dynamic characteristics of the ancillary component will be extracted using the subcomponent information available from the system.

Keywords Forced linear response • Reduced order modeling

Nomenclature

Symbols

| | |
|-----------|---------------------------------|
| $\{X_n\}$ | Full set displacement vector |
| $\{X_a\}$ | Reduced set displacement vector |
| $\{X_d\}$ | Deleted set displacement vector |
| $[M_a]$ | Reduced mass matrix |
| $[M_n]$ | Expanded mass matrix |
| $[K_a]$ | Reduced stiffness matrix |
| $[K_n]$ | Expanded stiffness matrix |
| $[U_a]$ | Reduced set shape matrix |
| $[U_n]$ | Full set shape matrix |
| $[U_a]^g$ | Generalized inverse |
| $[T]$ | Transformation matrix |
| $[T_U]$ | SEREP transformation matrix |
| $\{p\}$ | Modal displacement vector |
| $[M]$ | Physical mass matrix |

S.E. Obando (✉) • P. Avitabile

Structural Dynamics and Acoustic Systems Laboratory, University of Massachusetts Lowell, One University Avenue, Lowell, MA 01854, USA
e-mail: sergio.e.obando@gmail.com; peter_avitabile@uml.edu

| | |
|--------------------|-----------------------------------|
| [C] | Physical damping matrix |
| [K] | Physical stiffness matrix |
| {F} | Physical force vector |
| { \ddot{x} } | Physical acceleration vector |
| { \dot{x} } | Physical velocity vector |
| {x} | Physical displacement vector |
| α | Parameter for Newmark integration |
| β | Parameter for Newmark integration |
| Δt | Time step |
| [U ₁₂] | Mode contribution matrix |

Acronyms

| | |
|-------|---|
| ADOF | Reduced degrees of freedom |
| DOF | Degrees of freedom |
| ERMT | Equivalent reduced model technique |
| FEM | Finite element model |
| MAC | Modal assurance criterion |
| NDOF | Full space degrees of freedom |
| SEREP | System equivalent reduction expansion process |
| TRAC | Time response assurance criterion |

5.1 Introduction

During the analysis of complex structural models, these may be decomposed into simpler systems/components (or assemblies) that in turn can be further broken down to the subcomponent (or subsystem) level depending on the desired degree of resolution of the model. These subcomponents can be considered simple appendages or ancillary subcomponents of the assemblies. While the contribution to the dynamic characteristics of the system from the subsystem ancillary components can seem small, the accuracy of the prediction of the system level response may be compromised if a sufficiently detailed model is not used. In particular, the fidelity of the model can be drastically affected if these subcomponents are dynamically active and if the interaction with the coupling structure is nonlinear in nature. Therefore, there is significant motivation in developing a methodology for determining necessary model information for the accurate calculation of subsystem component response.

Recent developments in the computation of reduced order model response have allowed for the accurate calculation of system's time response while retaining all the highly refined and complex characteristics of full finite element models. Work by Thibault [1] and Marinone [2] showed that system level response can be accurately and efficiently calculated for highly reduced system models. Moreover, Pingle and Avitabile [3, 4, 5] demonstrated that the expansion of such systems can be used for the prediction of full field results such as stress and strain. The advantages of using reduced order models can be seen from a substantial reduction in computation time even when such systems involve nonlinear effects. Using these new efficient methodologies, this work aims to extend the application of reduced linear system modeling to the case in which the goal is not only the prediction of the dynamics of the full system but also the characterization of subsystem ancillary components.

In this paper, the common case of multi-component structural systems is addressed in the context of retaining embedded structural information of ancillary subcomponents for the calculation of reduced order model time response. A full space finite element model consisting of two systems, one of which contains a dynamically active ancillary subcomponent, will be reduced to a smaller set of degrees freedom and used for the prediction of the forced time response of the system. The reduced order model (with embedded ancillary subcomponent information) will then be used to expand back to the full space finite element model and to extract the predicted forced response of the ancillary subcomponent. This study will show advantages and drawbacks of common reduction/expansion methodologies (such as SEREP and Guyan reduction) in the characterization of the subsystem component from available reduced system information. Moreover, the selection of degrees of freedom during the reduction process will explore whether it is necessary to include the connecting degrees of

freedom of the ancillary component and the larger coupling structure or if these can be omitted as long as the preserved modes of the reduced system span the space of all modes of interest of the system. This is of particular importance in real life experimentation, as often times, measurements cannot be made exactly at the connecting degrees of freedom of multi-component structures or highly detailed finite element models are necessary to approximate the behavior of the system at those locations.

5.2 Theory

The fundamentals of the study of the forced response of reduced linear systems spans a variety of theoretical topics briefly presented here. The summary starts with a description of linear multiple degree of freedom systems and continues with an overview of structural dynamic modification, analytical model reduction and expansion, model updating and forced time response computations. Further information can be found in the respective references.

5.2.1 Equations of Motion for Multiple Degree of Freedom System

The general equation of motion for a multiple degree of freedom system written in matrix form is

$$[M_1] \{\ddot{x}\} + [C_1] \{\dot{x}\} + [K_1] \{x\} = \{F(t)\} \quad (5.1)$$

Assuming proportional damping, the eigensolution is obtained from

$$[[K_1] - \lambda [M_1]] \{x\} = \{0\} \quad (5.2)$$

The eigensolution yields the eigenvalues (natural frequencies) and eigenvectors (mode shapes) of the system. The eigenvectors are arranged in column fashion to form the modal matrix $[U_1]$. Often times, only a subset of modes is included in the modal matrix to save on computation time. Exclusion of modes results in truncation error which can be serious if key modes are excluded. Truncation error will be discussed in further detail in the structural dynamic modification section.

The physical system can be transformed to modal space using the modal matrix as

$$[U_1]^T [M_1] [U_1] \{\ddot{p}_1\} + [U_1]^T [K_1] [U_1] \{p_1\} = [U_1]^T \{F(t)\} \quad (5.3)$$

Scaling to unit modal mass yields

$$[I_1] \{\ddot{p}_1\} + [\Omega_1^2] \{p_1\} = [U_1^n]^T \{F(t)\} \quad (5.4)$$

where $[I_1]$ is the identity matrix and $[\Omega_1^2]$ is the diagonal natural frequency matrix. More detailed information on the equation development is contained in *Twenty Years of Structural Dynamic Modification – A Review* [6].

5.2.2 Structural Dynamic Modification

Structural Dynamic Modification (SDM) is a technique that uses the original mode shapes and natural frequencies of a system to estimate the dynamic characteristics due to changes in the mass and/or stiffness of the system. First, the change of mass and stiffness are transformed to modal space as shown

$$[\Delta \bar{M}_{12}] = [U_1]^T [\Delta M_{12}] [U_1] \quad (5.5)$$

$$[\Delta \bar{K}_{12}] = [U_1]^T [\Delta K_{12}] [U_1] \quad (5.6)$$

The modal space mass and stiffness changes are added to the original modal space equations to obtain

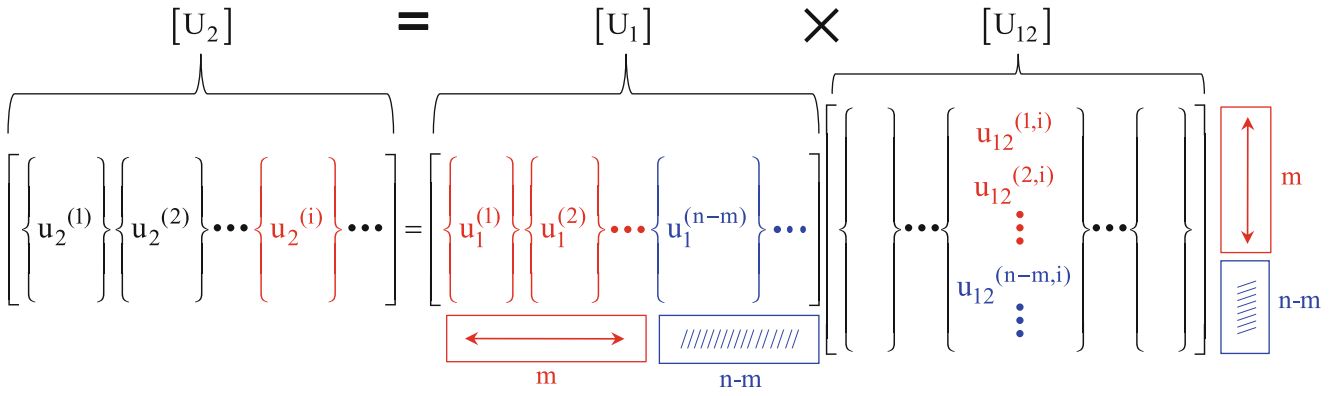


Fig. 5.1 Structural dynamic modification, mode contribution identified using U_{12} [7]

$$\left[\begin{bmatrix} \ddots & & \\ & \bar{M}_1 & \\ & & \ddots \end{bmatrix} + [\Delta \bar{M}_{12}] \right] \{\ddot{p}_1\} + \left[\begin{bmatrix} \ddots & & \\ & \bar{K}_1 & \\ & & \ddots \end{bmatrix} + [\Delta \bar{K}_{12}] \right] \{p_1\} = [0] \quad (5.7)$$

The eigensolution of the modified modal space model is computed and the resulting eigenvalues are the new frequencies of the system. The resulting eigenvector matrix is the $[U_{12}]$ matrix, which is used to transform the original modes to the new modes as indicated by

$$[U_2] = [U_1] [U_{12}] \quad (5.8)$$

The new mode shapes are $[U_2]$. The new mode shapes are formed from linear combinations of the original mode shapes. The $[U_{12}]$ matrix shows how much each of the $[U_1]$ modes contributes to forming the new modes. Figure 5.1 shows the formation of the new mode shapes as seen on Eq. (5.8). See [6] for additional information on SDM.

5.2.3 General Reduction/Expansion Methodology and Model Updating

Model reduction is a tool used to reduce the number of degrees of freedom (DOF) in order to diminish the required computation time of an analytical model, while attempting to preserve the full DOF dynamic characteristics. The relationship between the full space and reduced space model can be written as

$$\{x_n\} = \begin{Bmatrix} x_a \\ x_d \end{Bmatrix} = [T] \{x_a\} \quad (5.9)$$

where subscript 'N' signifies the full set of DOF (NDOF), 'a' signifies the reduced set of DOF (ADOF) and 'd' is the deleted DOF (those DOF not used during the reduced computation process). The transformation matrix $[T]$ relates the full set of NDOF to the reduced set of ADOF. The transformation matrix is used to reduce the mass and stiffness matrices as

$$[M_a] = [T]^T [M_n] [T] \quad \text{and} \quad [K_a] = [T]^T [K_n] [T] \quad (5.10)$$

The eigensolution of these 'a' set mass and stiffness matrices are the modes of the reduced model. These modes can be expanded back to full space using the transformation matrix

$$[U_n] = [T] [U_a] \quad (5.11)$$

If an optimal 'a' set is not selected when using methods such as Guyan Condensation [8] or Improved Reduced System Technique [9], the reduced model may not perfectly preserve the dynamics of the full space model. If System Equivalent Reduction Expansion Process (SEREP) [10] is used, the dynamics of selected modes will be perfectly preserved regardless of the 'a' set selected.

5.2.3.1 Expansion of System Modes from Uncoupled Component Modes

Expansion is generally used for providing full N-space mode shape information extracted from limited a-space information. The expansion to full space in this paper is based on recent work by Nonis [11] showing that full N-space mode shape information for an assembled system model can be obtained using the expansion matrices from the uncoupled, unconnected, original component modes of each component. Figure 5.2 shows the entire expansion process schematically to further describe the overall procedure. Reference [11] further details the expansion process and considerations for modes included.

5.2.3.2 System Equivalent Reduction Expansion Process (SEREP)

The SEREP modal transformation relies on the partitioning of the modal equations representing the system DOFs relative to the modal DOFs [10]. The SEREP technique utilizes the mode shapes from a full finite element solution to map to the limited set of master DOF. SEREP is not performed to achieve efficiency in the solution but rather is intended to perform an accurate mapping matrix for the transformation. The SEREP transformation matrix is formed using a subset of modes at full space and reduced space as

$$[T_U] = [U_n] [U_a]^g \quad (5.12)$$

where $[U_a]^g$ is the generalized inverse and $[T_U]$ is the SEREP transformation matrix. When the SEREP transformation matrix is used for model reduction/expansion as outlined in the previous section, the reduced model perfectly preserves the full space dynamics of the modes in $[U_n]$ [10].

5.2.3.3 KM_AMI Reduction

A more recent technique has been developed that utilizes Guyan Reduction along with direct updating of the reduced system matrices with the full space modal vectors as targets for the updating process [12]. This reduction technique also overcomes some of the rank problems associated with SEREP and provides a reduced set of ADOF that retain all the eigenvalues and eigenvectors of the full system matrices. The Guyan reduced mass and stiffness matrices are updated using

$$[M_I] = [M_S] + [V]^T [[I] - [\overline{M}_S]] [V] \quad (5.13)$$

and

$$[K_I] = [K_S] + [V]^T [[\Omega_{REF}^2] + [\overline{K}_S]] [V] - [[K_S] [U_{REF}] [V]] - [[K_S] [U_{REF}] [V]]^T \quad (5.14)$$

with

$$[V] = [\overline{M}_S]^{-1} [U_{REF}]^T [M_S] \quad (5.15)$$

5.2.4 System Forced Response Analysis

The computation of the time response developed in this paper is based on the Equivalent Reduced Model Technique (ERMT), a technique developed by Avitabile and Thibault [1, 7]. This technique uses an exact reduced model representation for the calculation of the system response. Newmark integration technique [13] is used to perform the direct integration of the equations of motion for the ERMT solution process. From the known initial conditions for displacement and velocity, the initial acceleration vector is computed using the equation of motion and the applied forces as

$$\ddot{\vec{x}}_0 = [M]^{-1} \left(\vec{F}_0 - [C] \dot{\vec{x}}_0 - [K] \vec{x}_0 \right) \quad (5.16)$$

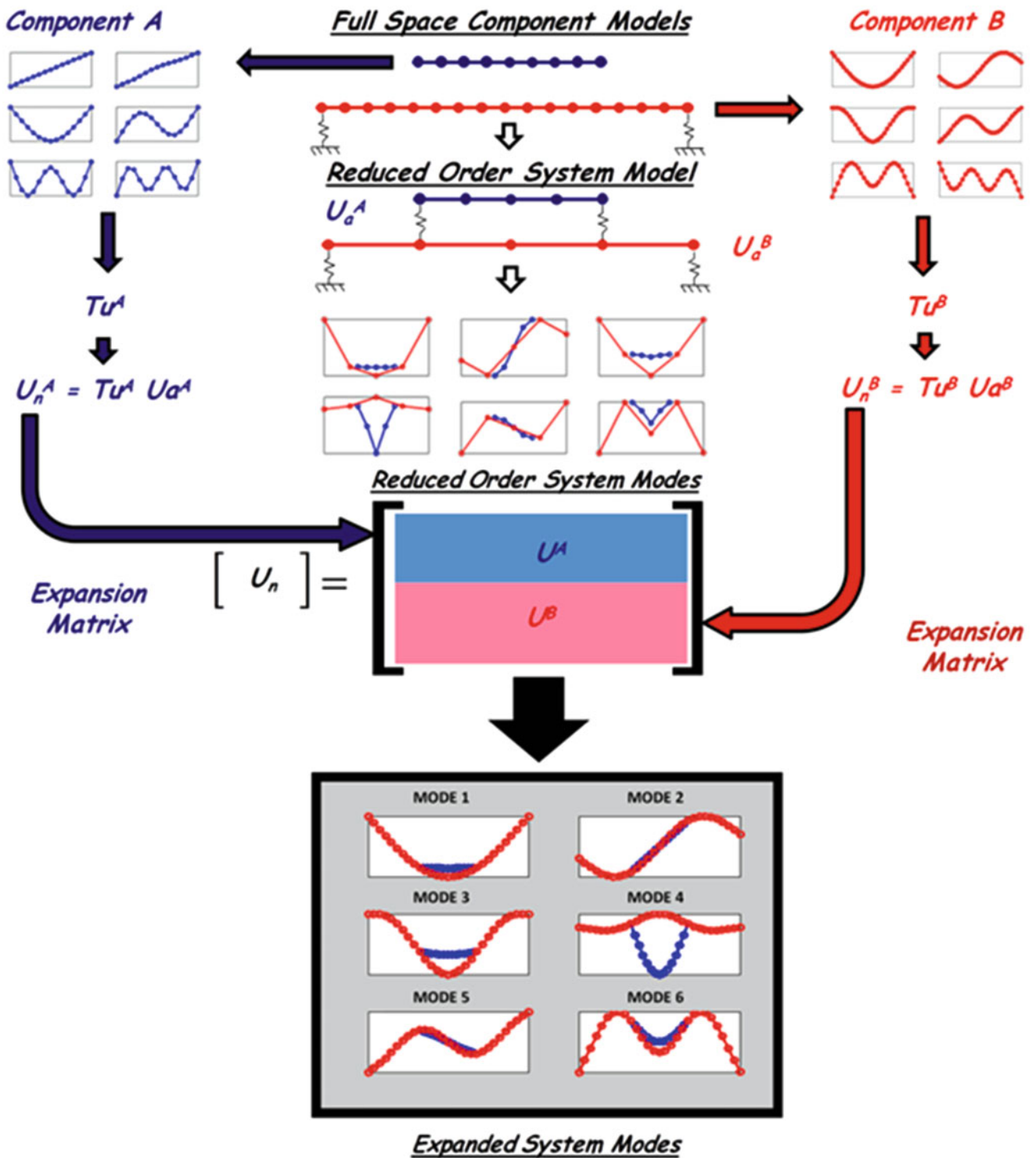


Fig. 5.2 Overall expansion process schematic using the transformation matrices from unconnected system components [11]

where

- $\ddot{\vec{x}}_0 =$ Initial Acceleration Vector
- $\dot{\vec{x}}_0 =$ Initial Velocity Vector
- $\vec{x}_0 =$ Initial Displacement Vector
- $\vec{F}_0 =$ Initial Force Vector

Choosing an appropriate Δt , α , and β , the displacement vector is

$$\begin{aligned} \vec{x}_{i+1} = & \left[\frac{1}{\alpha(\Delta t)^2} [M] + \frac{\beta}{\alpha(\Delta t)} [C] + [K] \right]^{-1} \left\{ \vec{F}_{i+1} + [M] \left(\left(\frac{1}{\alpha(\Delta t)^2} \right) \vec{x}_i + \left(\frac{1}{\alpha(\Delta t)} \right) \dot{\vec{x}}_i + \left(\frac{1}{2\alpha} - 1 \right) \ddot{\vec{x}}_i \right) \right. \\ & \left. + [C] \left(\left(\frac{\beta}{\alpha(\Delta t)} \right) \vec{x}_i + \left(\frac{\beta}{\alpha} - 1 \right) \dot{\vec{x}}_i + \left(\frac{\beta}{\alpha} - 2 \right) \frac{\Delta t}{2} \ddot{\vec{x}}_i \right) \right\} \end{aligned} \quad (5.17)$$

The values chosen for α and β were $\frac{1}{4}$ and $\frac{1}{2}$, respectively. This assumes constant acceleration and the integration process is unconditionally stable, where a reasonable solution will always be reached regardless of the time step used. However, the time step should be chosen such that the highest frequency involved in the system response can be characterized properly to avoid numerical damping in the solution.

Following the displacement vector calculation, the acceleration and velocity vectors are computed for the next time step using

$$\dot{\vec{x}}_{i+1} = \dot{\vec{x}}_i + (1 - \beta) \Delta t \ddot{\vec{x}}_i + \beta \Delta t \ddot{\vec{x}}_{i+1} \quad (5.18)$$

$$\ddot{\vec{x}}_{i+1} = \frac{1}{\alpha(\Delta t)^2} (\vec{x}_{i+1} - \vec{x}_i) - \frac{1}{\alpha \Delta t} \dot{\vec{x}}_i - \left(\frac{1}{2\alpha} - 1 \right) \ddot{\vec{x}}_i \quad (5.19)$$

This process is repeated at each time step for the duration of the time response solution desired.

5.2.5 Time Response Correlation Tools

In order to quantitatively compare two different time solutions, two correlation tools were employed: The Modal Assurance Criterion (MAC) and the Time Response Assurance Criterion (TRAC).

5.2.5.1 Modal Assurance Criterion (MAC)

The Modal Assurance Criterion (MAC) [14] is widely used as a vector correlation tool. In this work, the MAC was used to correlate all DOF at a single instance in time. The MAC is written as

$$MAC_{ij} = \frac{\left[\{X1_i\}^T \{X2_j\} \right]^2}{\left[\{X1_i\}^T \{X1_i\} \right] \left[\{X2_j\}^T \{X2_j\} \right]} \quad (5.20)$$

where $X1$ and $X2$ are displacement vectors. MAC values close to 1.0 indicate strong similarity between vectors, where values close to 0.0 indicate minimal or no similarity.

5.2.5.2 Time Response Assurance Criterion (TRAC)

The Time Response Assurance Criterion (TRAC) [15] quantifies the similarity between a single DOF across all instances in time. The TRAC is written as

$$TRAC_{ji} = \frac{\left[\{X1_j\}^T \{X2_i\} \right]^2}{\left[\{X1_j\}^T \{X1_j\} \right] \left[\{X2_i\}^T \{X2_i\} \right]} \quad (5.21)$$

where $X1$ and $X2$ are displacement vectors. TRAC values close to 1.0 indicate strong similarity between vectors, where values close to 0.0 indicate minimal or no similarity.

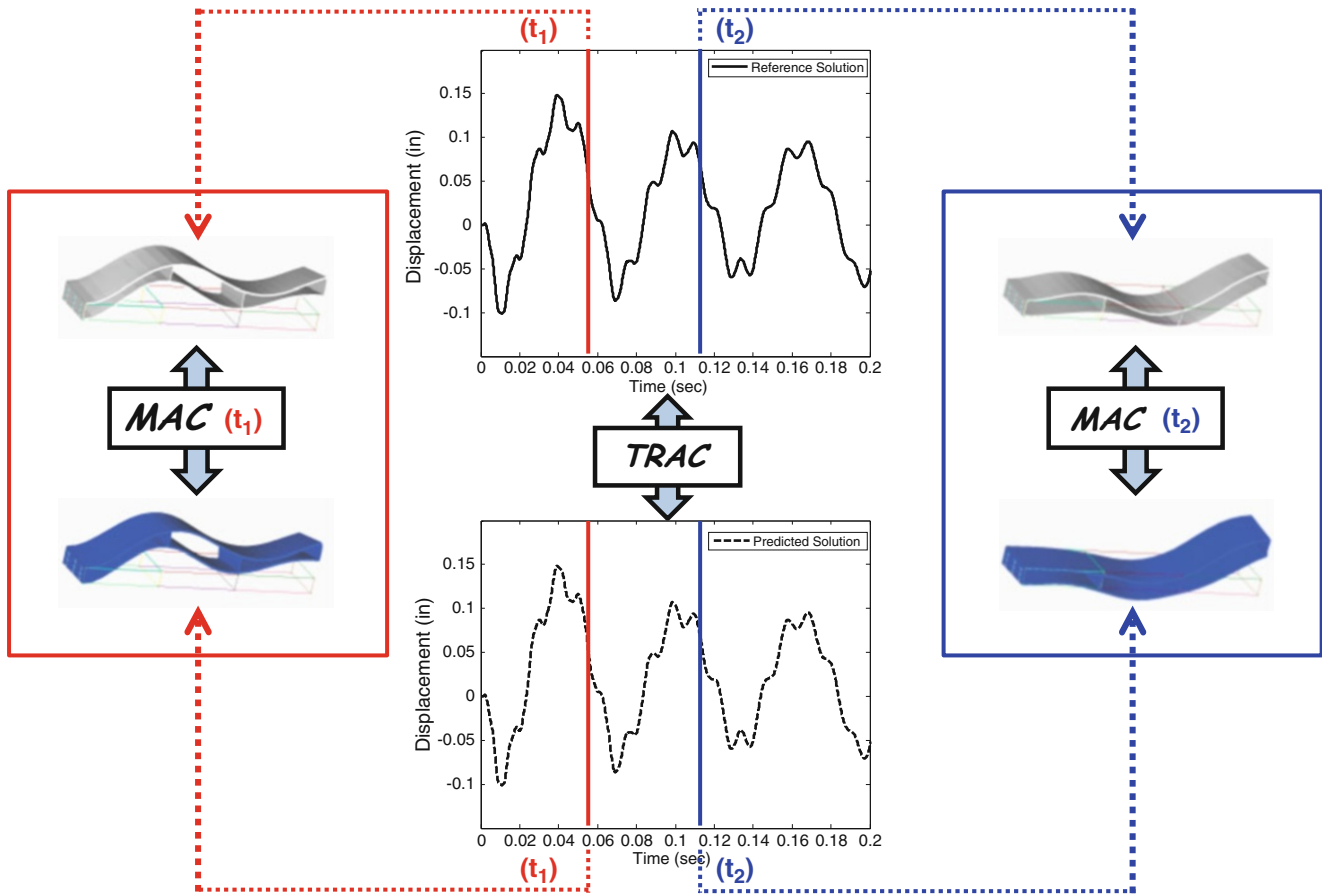


Fig. 5.3 Physical interpretation of MAC and TRAC

In this work, the MAC is calculated between the shapes of the full space reference solution and estimated solution obtained from the reduced order model at each time step. Similarly the TRAC is used to compare the time response from the reduced order model to the time response from the full space finite element solution at each degree of freedom. A diagram detailing the two comparison techniques is shown in Fig. 5.3.

5.3 Model Description

Analytical models of a multi-component beam system were created to investigate the prediction of the dynamic response of the system including subcomponents and ancillary attachments. The models consisted of three beams, as illustrated in Fig. 5.4, attached asymmetrically by linear springs and such that all components are dynamically active.

Planar element beam models of the three beams were generated using MAT_SAP [16], which is a finite element modeling (FEM) program developed for MATLAB [17] and forced response calculations were performed in MATLAB using Newmark integration scripts based on code originally written by Thibault [1]. The beam models were set to have dimensions and characteristics as described in Figs. 5.5 and 5.6.

The 3 beam system was subjected to a double sided force pulse at the left end of the support beam (see Fig. 5.4) and this input force was set as to only excite the modes in the frequency band of approximately 1,000 Hz of the system as shown in Fig. 5.7.

With all 100 elements of the system (i.e. 206 DOF) the full N-space reference solution to the system was calculated and served as a point of comparison for all subsequent reduced order model calculations. The frequencies of the individual components and of the full assembled system with or without the ancillary subcomponent are shown in Table 5.1.

Fig. 5.4 Schematic of 3 beam analytical model and input force location (not to scale)

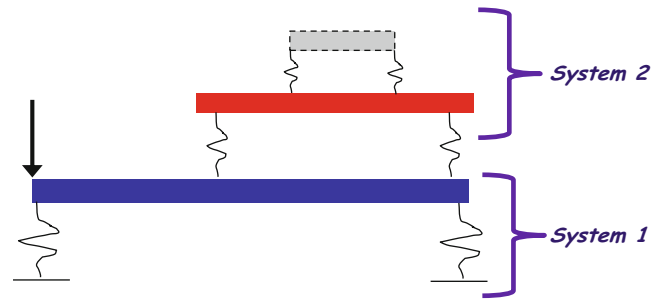


Fig. 5.5 Dimensions of top (red) and support/base (blue) beams of the analytical beam system

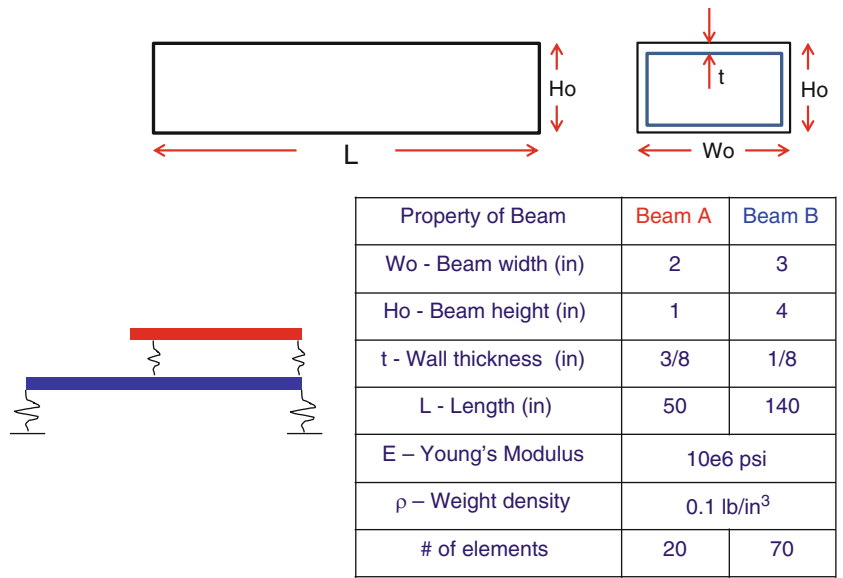
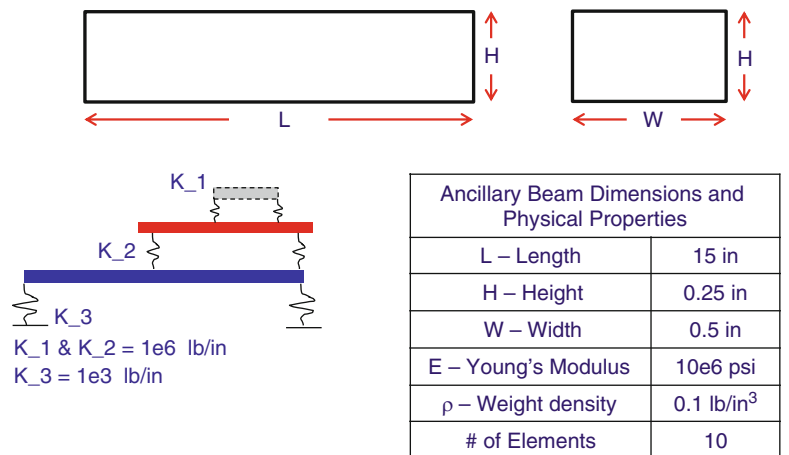


Fig. 5.6 Dimensions and characteristics of ancillary subcomponent (grey) of 3 beam system



5.4 Cases Studied

The forced response of the full space reference model with 206 DOF was first calculated. Structural Dynamic Modification was used to calculate the U_{12} matrix and determine the necessary modes of the system to preserve the first five modes of the 3 beam system. Subsequently, reduction techniques were used to reduce the active DOF of the system to an 'a' set not including DOF on the ancillary beam. The forced response of the reduced ADOF linear system was calculated. The dynamic characteristics of the ancillary subcomponent were then extracted using the system information available from the reduction process. This is equivalent to assuming the subcomponent of the system (ancillary beam) is inaccessible/immeasurable and

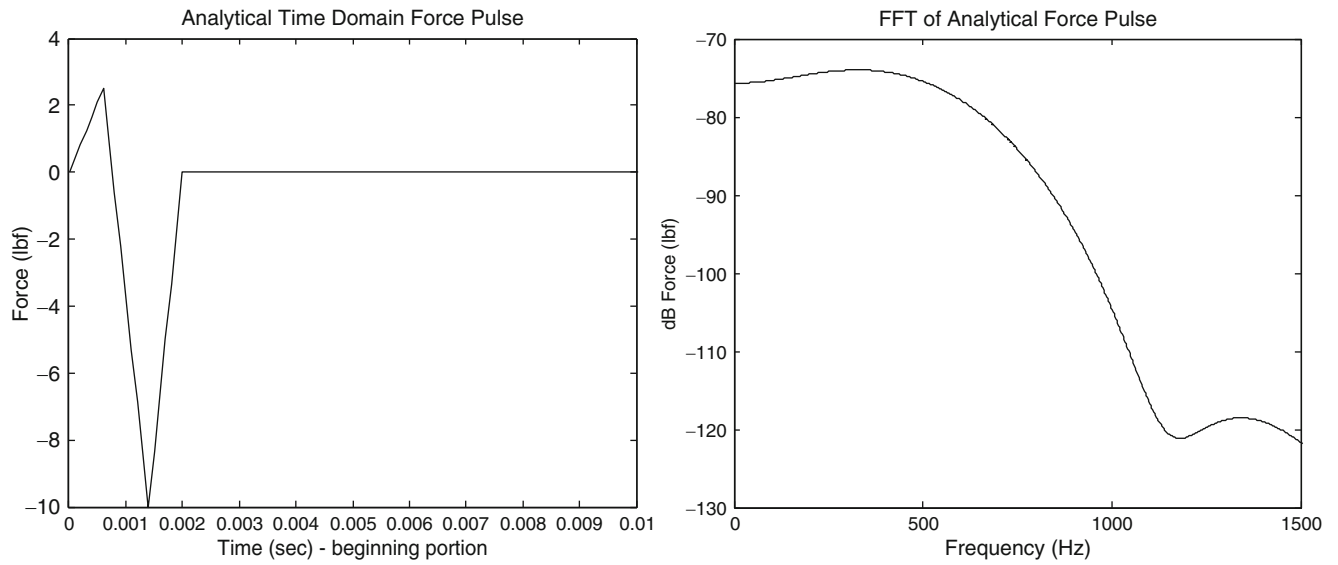
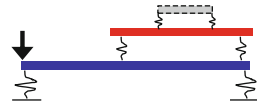


Fig. 5.7 Time (left) and frequency (right) domain plots of input analytical force pulse

Table 5.1 Frequencies of the first 15 modes of the 3 beam system and its components



| Mode | Frequency (Hz) | | | | |
|------|----------------|--------|---------------|-----------------|--------|
| | Beam A | Beam B | Sub-Component | System w/o A.C. | System |
| 1 | 0.0015 | 18.9 | 0.010 | 16.8 | 16.8 |
| 2 | 0.0024 | 45.9 | 0.014 | 37.6 | 37.5 |
| 3 | 87.6 | 80.9 | 224.5 | 68.2 | 68.1 |
| 4 | 241.4 | 161.4 | 619.0 | 86.9 | 84.6 |
| 5 | 473.2 | 299.7 | 1214.3 | 129.1 | 102.1 |
| 6 | 782.3 | 489.4 | 2010.4 | 210.5 | 129.1 |
| 7 | 1168.8 | 728.2 | 3011.1 | 282.8 | 210.0 |
| 8 | 1633.1 | 1015.5 | 4223.0 | 343.1 | 282.0 |
| 9 | 2175.4 | 1351.0 | 5653.7 | 477.1 | 343.0 |
| 10 | 2796.3 | 1734.7 | 7302.3 | 645.5 | 396.2 |
| 11 | 3496.7 | 2166.4 | 9071.4 | 716.4 | 477.3 |
| 12 | 4277.7 | 2646.2 | 12046.9 | 959.5 | 645.3 |
| 13 | 5140.7 | 3174.1 | 14493.9 | 1118.7 | 716.3 |
| 14 | 6087.4 | 3750.0 | 17502.7 | 1311.7 | 889.0 |
| 15 | 7120.0 | 4373.9 | 21038.3 | 1617.3 | 960.6 |

Yellow cells highlight similar frequencies after addition of ancillary subcomponent (AC) to the system

therefore predicting its response from the information of the other two components (the red and blue beam). The test cases presented here are intended to show the results when a proper set of modes are selected such that no information is lost in the reduction process and an inappropriate reduced model where the modes do not span the space of the system.

The cases presented here are summarized as:

Case 1—Reference Model

206 DOF Total; System 1/Beam B 142 DOF; System 2—Beam A 42 DOF and Ancillary 22 DOF

Case 2—Guyan Reduced Order Model

12 DOF Total; Beam B—ADOF 65, 117, 169, 199, and 205; Beam A—ADOF 23, 31, 33, 41, 43, 55 and 63

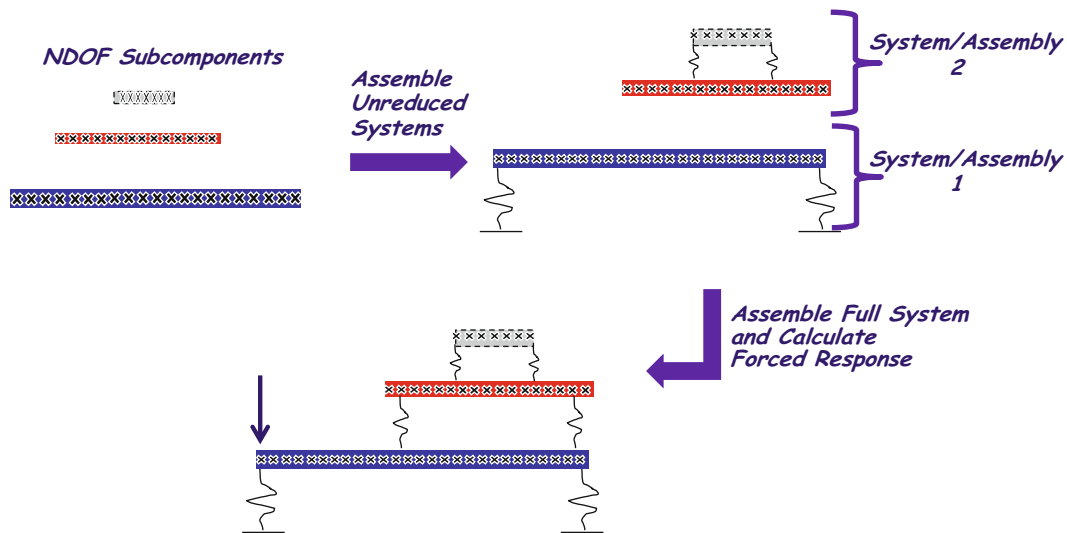


Fig. 5.8 Sequence for the development of assembled reference model

Case 3—SEREP Reduced Order Model

12 DOF Total; Beam B—ADOF 65, 117, 169, 199, and 205; Beam A—ADOF 23, 31, 33, 41, 43, 55 and 63

Case 4—KM_AMI Model Improvement from Guyan Reduced Order Model

12 DOF Total; Beam B—ADOF 65, 117, 169, 199, and 205; Beam A—ADOF 23, 31, 33, 41, 43, 55 and 63

Case 5—Considerations for Additional Modes in the Model Reduction

Case 6—Considerations for DOF Selection in the Model Reduction

5.4.1 Case 1: Reference Model

The NDOF unreduced subcomponents were tied together to form two systems, the support (System 1) and the top assembly (System 2). The frequencies and mode shapes of both untied and tied subcomponents were calculated for reference. The assembled 3 beam system consisting of the tied System 1 and System 2 was then tied together at full N-space and the linear forced response calculated using the analytical input force of Fig. 5.7. The forced response of this NDOF (206 DOF) served as the reference solution for the reduced cases. Figure 5.8 shows the sequence of the assembly of the system subcomponents used to create the assembled system reference solution.

The frequencies of the system and subcomponents are shown in Table 5.1 and the mode shapes of the 3 beam system can be seen in Fig. 5.9. The ancillary (grey) subcomponent can be observed to be dynamically active on the first 15 modes of the system and therefore sufficient component information needs to be preserved in the reduction process in order to not only accurately predict the force response of the ancillary subcomponent (during expansion) but also to properly capture the dynamics of the coupling red beam.

5.4.1.1 Component Mode Contribution— U_{12}

Calculation of the U_{12} matrix for the system response is of utmost importance to understand and mitigate the effects of truncation error in the reduction process. The modes from Systems 1 and System 2 required to preserve the first five modes of the assembled full 3 beam system were chosen using the resulting U_{12} shown in Fig. 5.10. As seen on the U_{12} contribution matrix, a total of 12 modes of the system components are required to preserve five modes of the assembled 3 beam system. System 1 (the blue support beam) contributes five modes to the reduced model while System 2 (the top red beam and its attached ancillary subcomponent) provides seven modes. The larger contribution from system 2 is already an indication of the strong influence of the dynamic ancillary subcomponent and emphasizes that a larger amount of information from this component (system 2) is needed to fully characterize the system level response of the 3 beam structure.

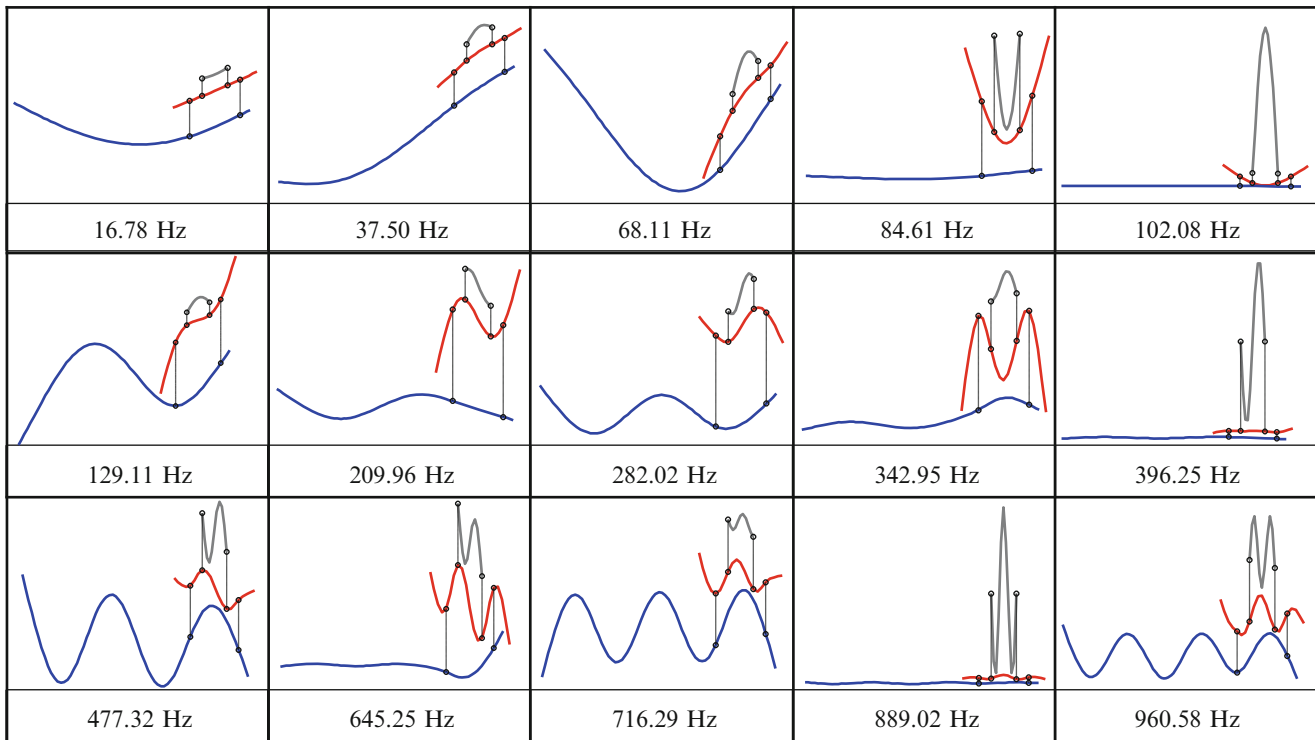


Fig. 5.9 Mode shapes of full 206 N-space 3 beam system used as reference solution

5.4.2 Overview of Reduced Models

Full N-space subcomponents were assembled into two systems (System 1 and System 2) as in the reference case. The two systems were reduced separately and then tied together. For System 2, containing the ancillary subcomponent, the reduction was made as to omit any active DOF in the ancillary beam. The idea is that the reduction process, if carried out successfully, should embed the necessary component information onto the reduced assembled system. Figure 5.11 shows the assembly sequence performed to reduce the system components and the extraction of the subcomponent response from the calculated reduced model forced response.

Three reduction methods were used to highlight particular advantages of each procedure. Guyan reduction, as explained in the theory section, does not fully preserve the dynamics of the system if an optimal ADOF set is not selected. On the other hand, SEREP will accurately preserve the selected modes of the system but issues may arise regarding full rank of the reduced mass and stiffness matrices of the system. Lastly, a model improvement technique, KM_AMI, is used to update the mass and stiffness matrices of the Guyan reduced model by seeding target frequencies and mode shapes and therefore preserving the exact model information while preserving the full rank advantages of a Guyan reduced model. These issues will be covered in the three cases described below.

5.4.3 Case 2: Guyan Reduced Model

As with the other reduced models covered in this study, the selected DOF for the reduction did not include DOFs of the ancillary subcomponent. As indicated by the U_{12} matrix in Figs. 5.10 and 5.12, there are 12 modes of the system's components necessary to accurately span the space of the first five modes of the assembled 3 beam system. Figure 5.13 shows the layout of connection DOF of the 3 beam system. Figure 5.14 shows the reduced order model frequencies compared to the reference N-space solution.

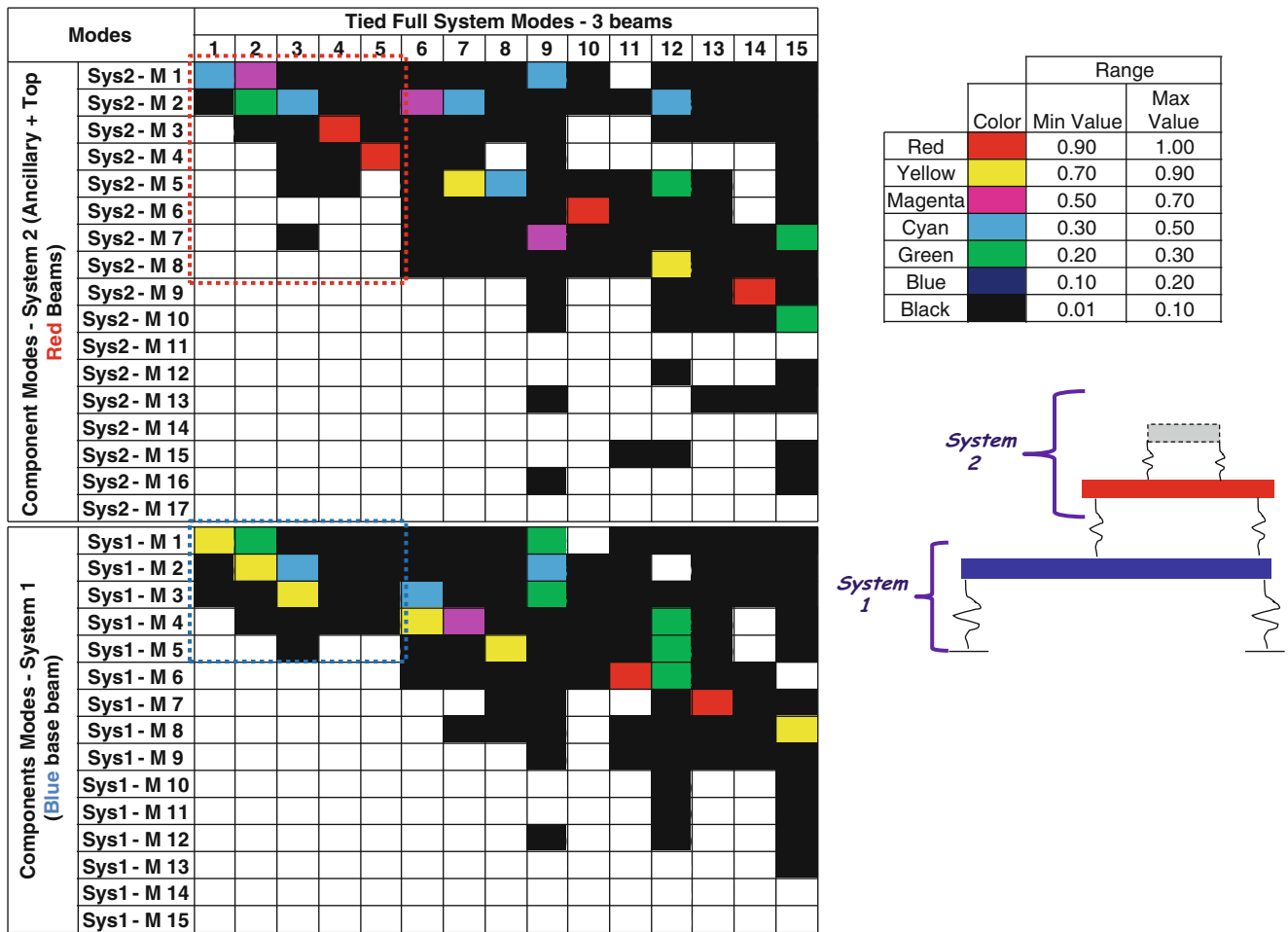


Fig. 5.10 U_{12} mode contribution matrix from system components to full 3 beam system

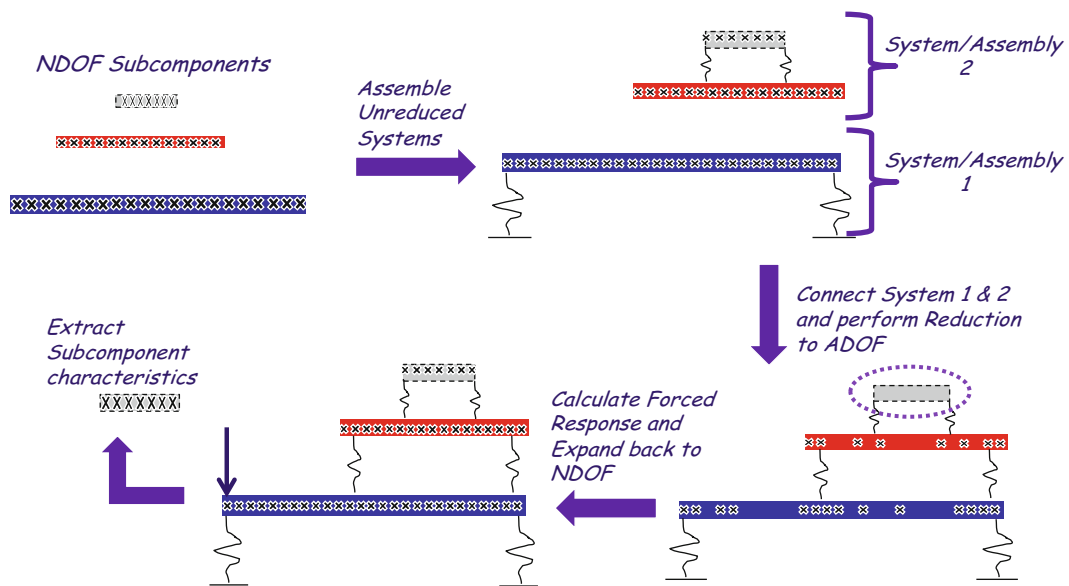


Fig. 5.11 Sequence for the development of reduced system response models

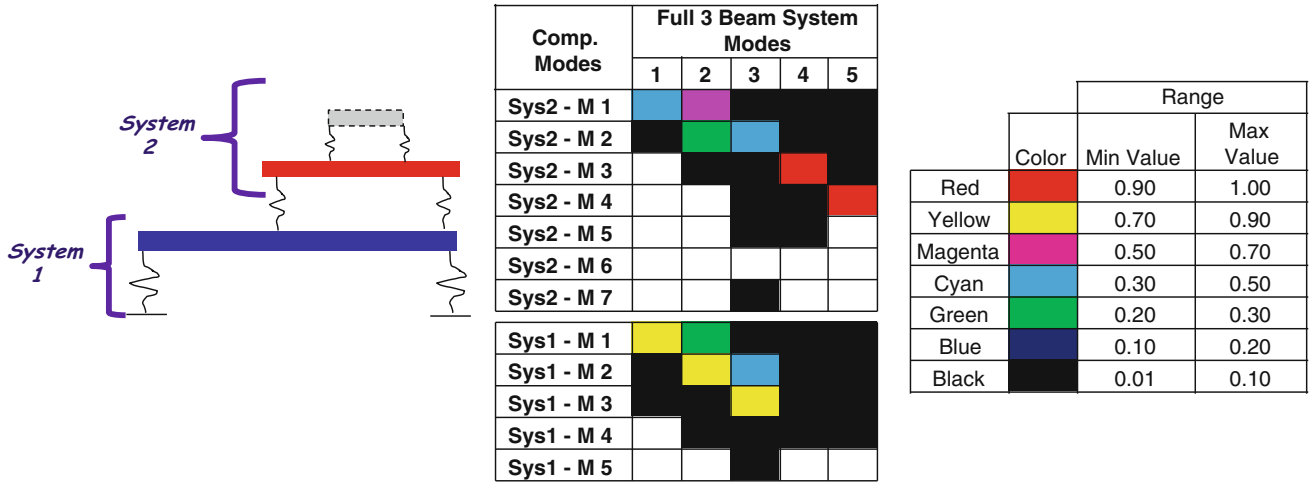


Fig. 5.12 Selected portion of U_{12} mode contribution matrix from system components to first five modes of full 3 beam system

Fig. 5.13 Summary of numbering of 3 beam system NDOF (206) and connecting DOF

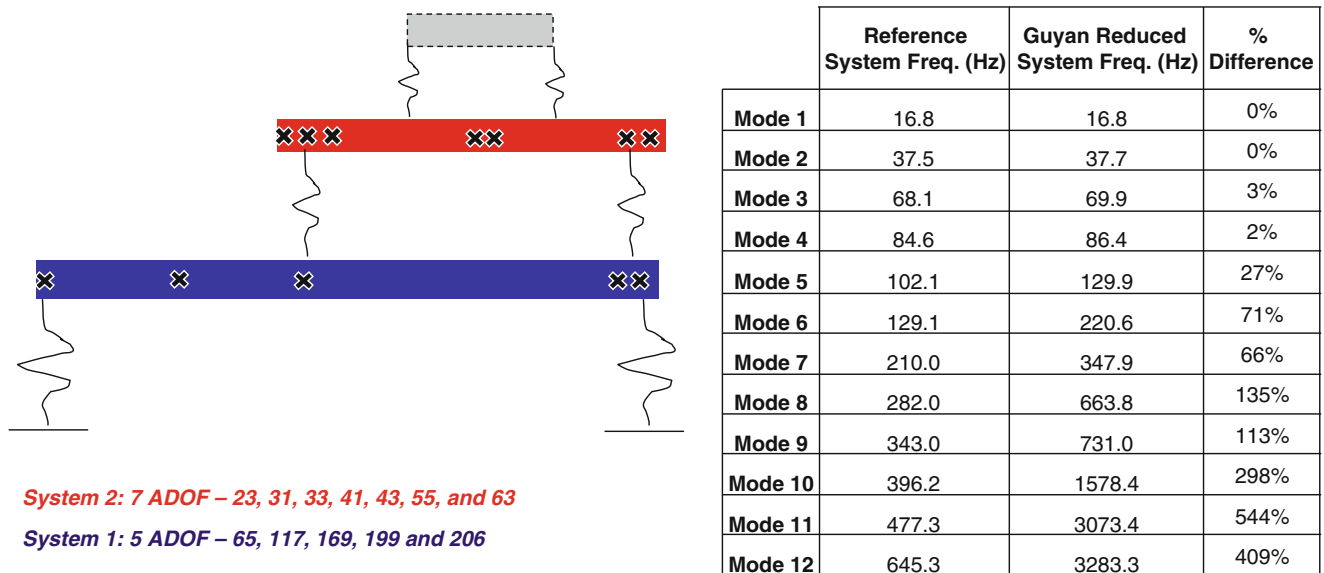
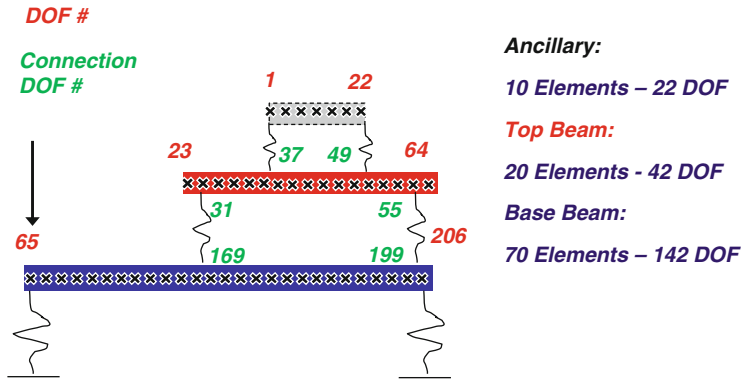


Fig. 5.14 Comparison of Guyan reduced order model (12 DOF) frequencies with respect to (206 DOF) reference solution

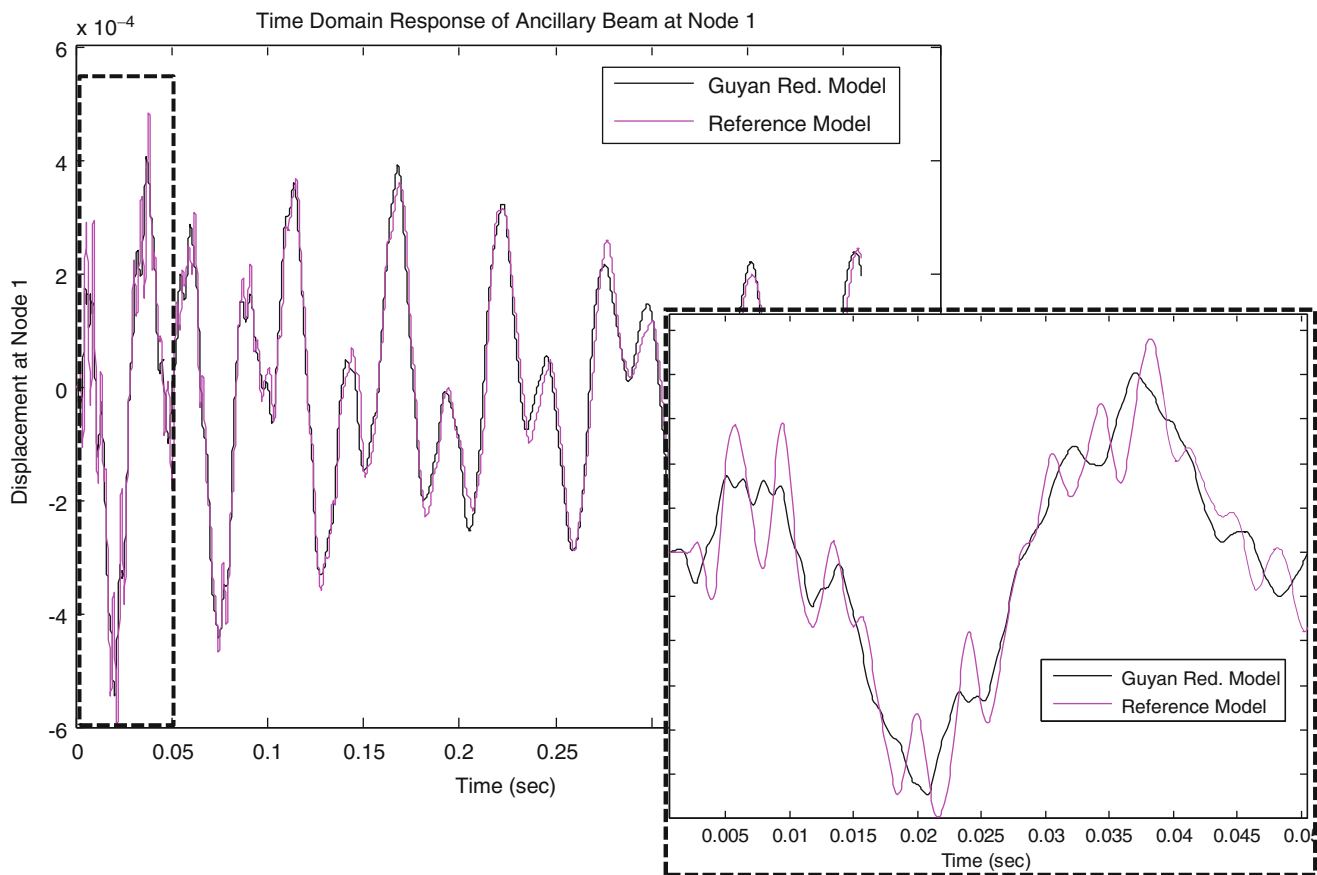


Fig. 5.15 Comparison of time response at node 1 of the ancillary subcomponent from the expansion of a 12 DOF Guyan reduced model versus the 206 DOF full space reference solution. Zoomed in region shows the response for the first 0.05 s

Note that there are no DOF from 1 to 22 since these are the ancillary subcomponent DOFs and moreover, DOF 37 and 49 connecting the top red beam to the ancillary beam were omitted as well. As discussed in the theory section, even with sufficient modes selected in the reduction process (according to the U_{12} contribution matrix) and a well placed selection of ADOF, Guyan reduced did not preserve the five modes of interest as seen in the table of Fig. 5.14. The error can be observed to increase quickly for modes higher than 3 and the predicted system response is not expected to yield accurate results. The forced response of the Guyan reduced order model was calculated and using the transformation matrix $[T]$, the results were expanded back to full N -space (206 DOF). The ancillary subcomponent response was found from the expanded forced response of the system. Figure 5.15 shows a comparison of the displacement at the first node of the ancillary subcomponent with respect to the full space reference solution. The average MAC and TRAC were found to be 0.6 and 0.53 respectively. Figure 5.16 shows the MAC and TRAC for the expanded Guyan reduced model.

From Fig. 5.16 and from the calculation of time response correlation tools, the response of the expanded Guyan reduced model showed low correlation to the reference solution. Clearly mode truncation does not allowed for the accurate characterization of the reduced system, let alone the characterization of the ancillary subcomponent from embedded system information. While addition of extra DOF may diminish the effects of mode truncation, there is always an intrinsic risk of error in the Guyan reduction process and ADOF selection.

5.4.4 Case 3: SEREP Reduced Model

The goal of preserving the first five modes of the full 3 beam system requires the selection of five modes of System 1 and seven modes of System 2. The same ADOF selection from Case 2 was used during the SEREP reduction process. Figure 5.17 shows the resulting frequencies of the reduced system.

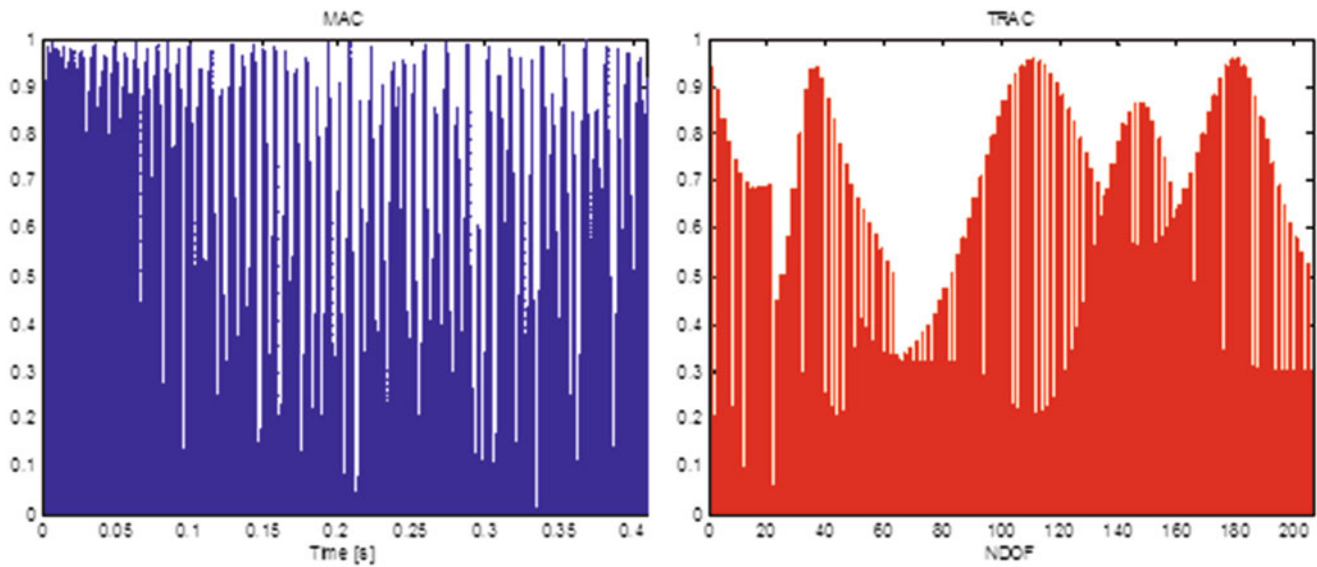


Fig. 5.16 MAC and TRAC bar plots showing the correlation of the expanded Guyan reduced model to the reference model

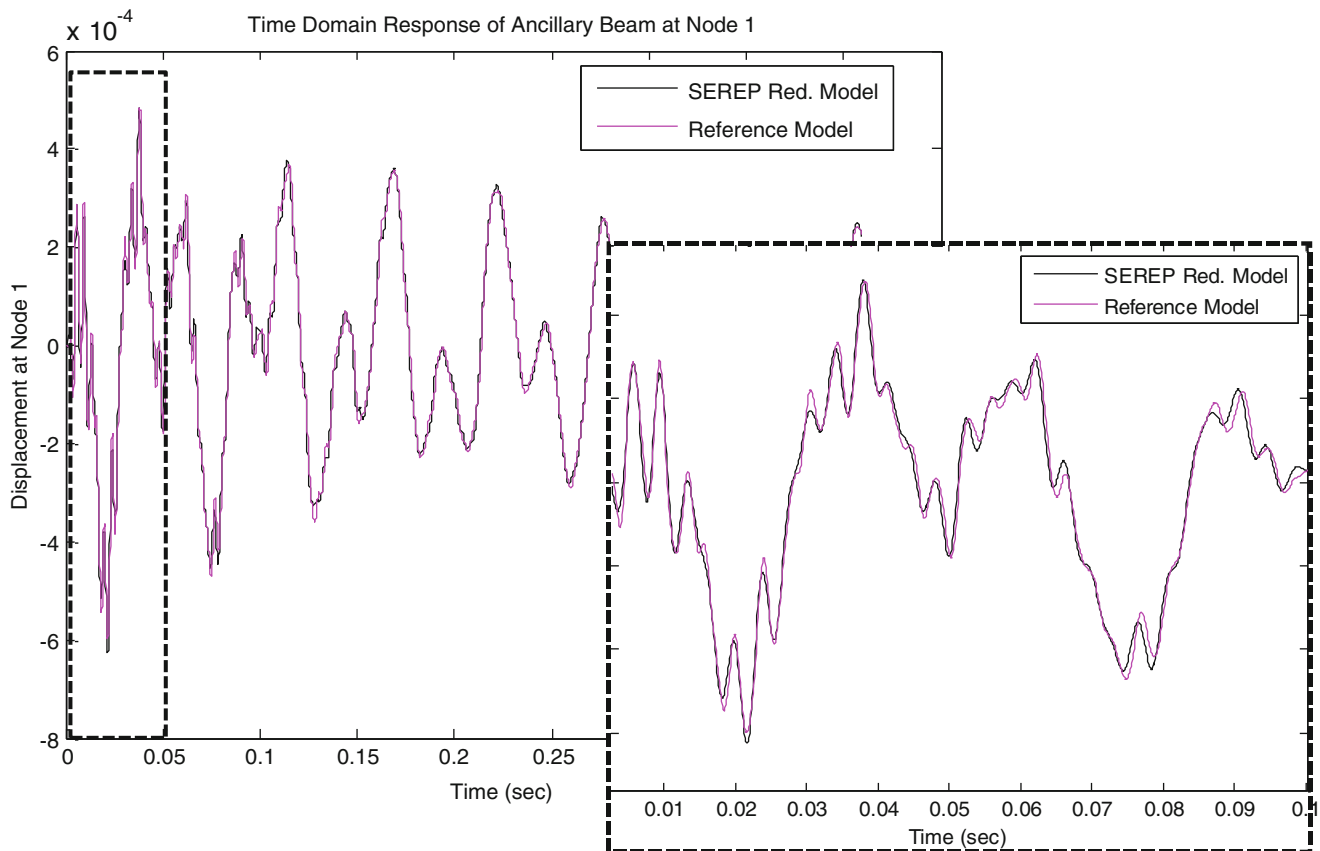


Fig. 5.17 Comparison of time response at node 1 of the ancillary subcomponent from the expansion of a 12 DOF SEREP reduced model versus the 206 DOF full space reference solution. *Zoomed in* region shows the response for the first 0.1 s

From Fig. 5.18 and upon comparison to Fig. 5.14 showed that the SEREP reduced order model preserved the five modes of interest and resulted on a smaller error for some of the remaining seven modes. Calculation of the time response was then performed for the ADOF reduced model. The resulting time response was then expanded to all 206 DOF using the $[T_U]$ SEREP transformation matrix. The response of the ancillary subcomponent was extracted from the expanded response of the

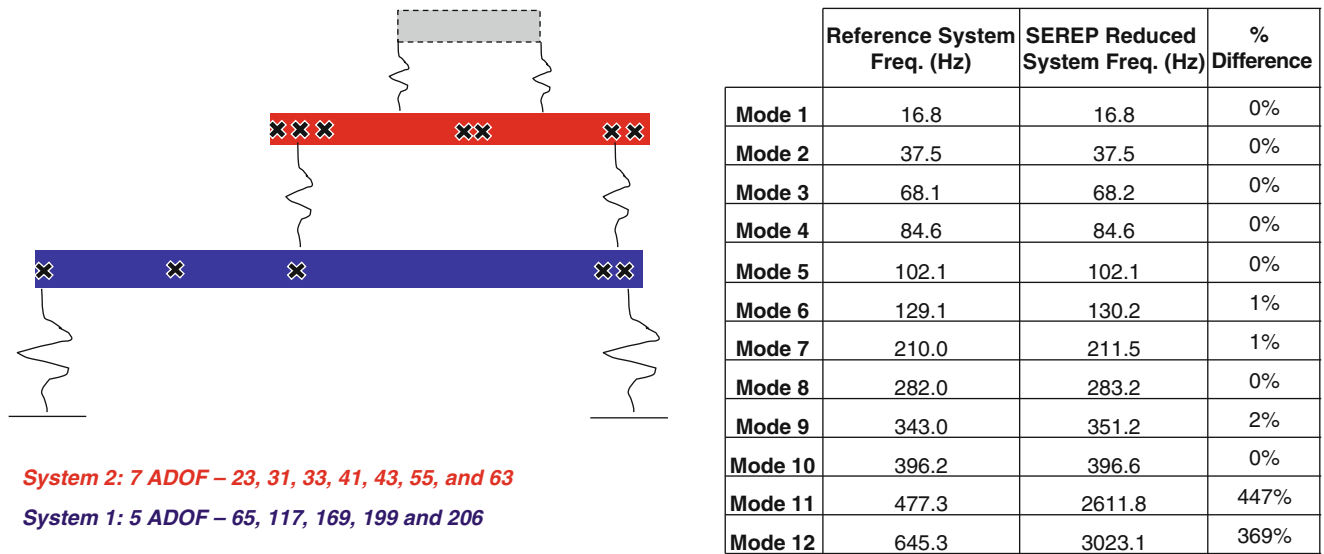


Fig. 5.18 Comparison of SEREP reduced order model (12 DOF) frequencies with respect to (206 DOF) reference solution

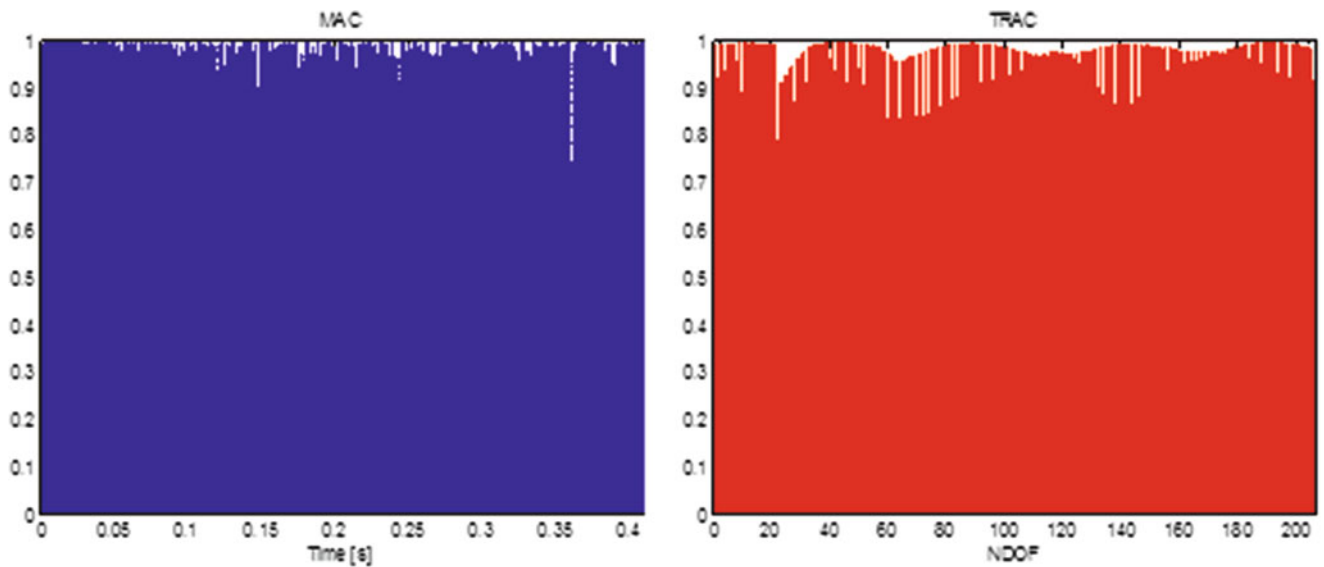


Fig. 5.19 MAC and TRAC bar plots showing the correlation of the expanded SEREP reduced model to the reference model

system. Figure 5.17 shows a comparison of time response at the first node of the ancillary beam (from the expanded SEREP reduced model) with respect to the reference solution; while only one node is shown for brevity, all of the nodes on the ancillary component had similar agreement. The average MAC and TRAC were found to be 0.97 and 0.95 respectively. Figure 5.19 shows the MAC and TRAC bar graphs correlating the expanded SEREP reduced model to the reference solution.

The SEREP reduction and expansion process resulted in high correlation using the same amount of DOF as the Guyan reduced model. Furthermore, the omission of the connecting DOF for the ancillary subcomponent did not yield additional error as will be shown in Case 6. Moreover, issues can only arise if the selected DOF do not yield full rank reduced mass and stiffness matrices but this issue was not encountered in the analytical models studied. Nevertheless, Case 4 discusses the KM_AMI Model Improvement which can alleviate any issues arising from the rank deficiency in the reduction process while preserving the accuracy of the SEREP reduction methodology.

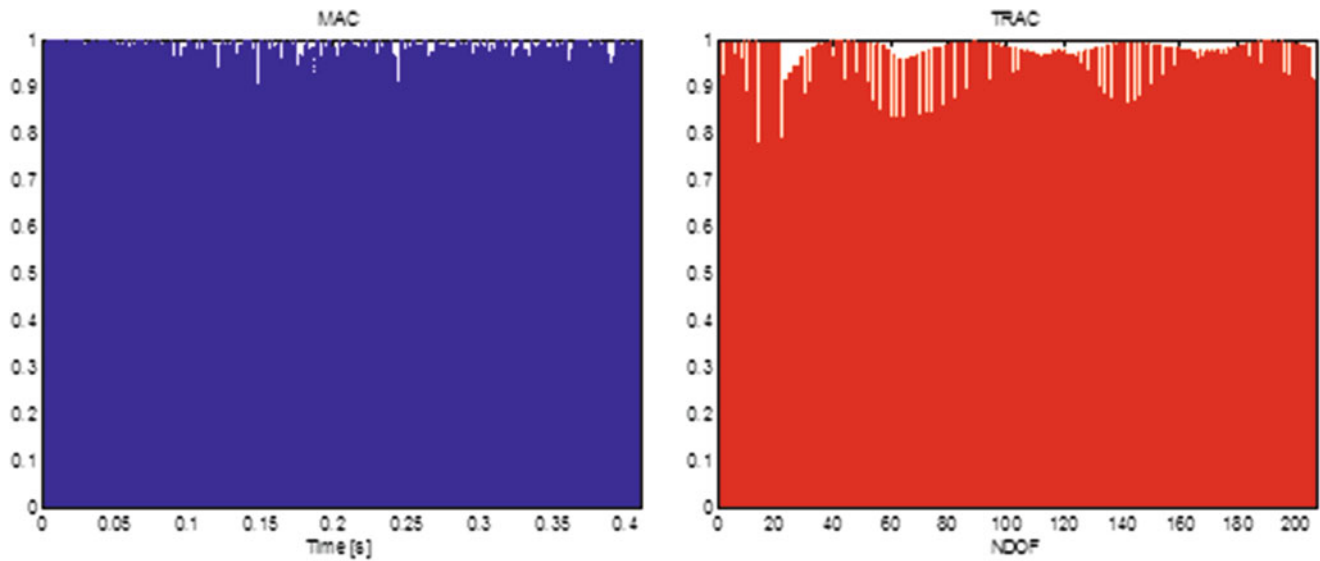


Fig. 5.20 MAC and TRAC bar plots showing the correlation of the expanded Guyan improved model to the reference model

5.4.5 Case 4: KM_AMI Model Improvement from Guyan Reduced Model

The Guyan reduced model of Case 2 was shown to be drastically affected by the selection of ADOF as well as the number of modes in the reduction. The need to use Guyan reduction may arise from limitations of currently available finite element software or from the need to have a fully ranked reduced mass and stiffness matrices. For such situations, this case explores using the exact frequencies and mode shapes of the system to update the reduced order model using the KM_AMI approach. The target frequencies and mode shapes (e.g. the first five modes of the fully assembled 3 beam system) are directly seeded to the Guyan reduced model of Case 2. The MAC and TRAC of the expanded KM-AMI updated Guyan model resulted in an average of 0.97 and 0.95 respectively just as the SEREP reduction model of Case 3. Figure 5.20 shows the MAC and TRAC bar plots for the improved Guyan reduced model using KM-AMI updating.

The improved reduced model using the KM_AMI approach showed significant gain in accuracy compared to the original Guyan reduced model. Not only where the five frequencies and mode shapes of the assembled model preserved exactly (as these were directly seeded to the reduced model) but also an accurate ancillary subcomponent response was extracted from the expanded reduced order model.

The cases discussed thus far have shown that the Guyan reduced model (Case 2) does not accurately preserve the embedded characteristics of the ancillary subcomponent during the reduction process while the SEREP and KM_AMI (Cases 3 and 4 respectively) model reductions produce remarkable accuracy in the prediction of the response of both components and the embedded ancillary subcomponent. Now, Cases 5 and 6 will discuss some considerations regarding the accuracy of the reduced model when either additional modes (modes beyond the ones specified by the U_{12} contribution matrix requirements) or DOF are used in the reduced order models.

5.4.6 Case 5: Considerations for Additional Modes in the Model Reduction

Addition of modes beyond the 12 modes indicated in the U_{12} matrix in the SEREP reduced model showed large improvement from the resulting expanded model response. Additional 5 modes were included, 2 from System 1 and 3 from System 2 for a total of 17 modes. The ADOF selected once again did not include the connecting DOF (37 and 49) of the ancillary subcomponent. The ADOF set selected was DOF 65, 100, 117, 169, 183, 199, and 205 from System 1/Beam B and ADOF 23, 27, 31, 33, 39, 41, 43, 51, 55 and 63 from Beam A of System 2. The expanded SEREP reduced model response resulted in an average MAC and TRAC of 0.998 and 0.997 respectively. Figure 5.21 shows the MAC and TRAC bar plots for this newly reduced 17 DOF model (Note the change in the y-axis of the MAC).

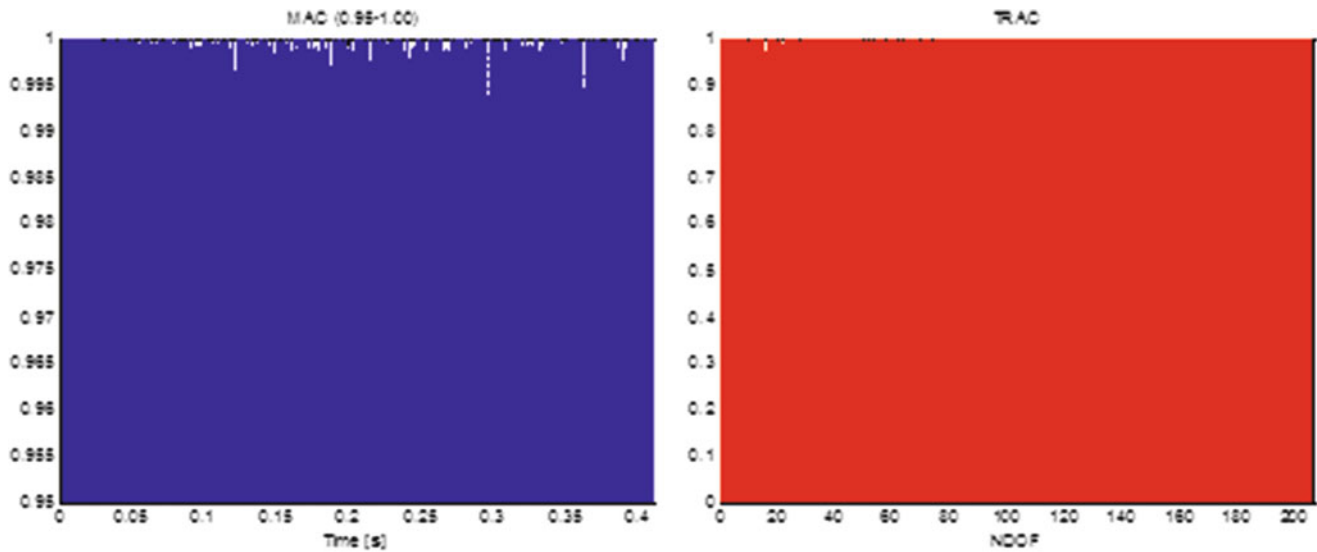


Fig. 5.21 MAC and TRAC bar plots showing correlation of the expanded 17 DOF SEREP reduced model to reference model. MAC y-axis is showing values from 0.95 to 1.0

When the reduction process is successful (as it was with the SEREP and KM_AMI models), the modes selected span the space of the system response. Modes beyond the 12 indicated by the U_{12} smooth the approximation of the system response and further addition of modes results in better results until the reduced ‘a’ space model approaches the full ‘N’ space solution and hence spans the whole space of the full assembled system response.

Up to this point, the selection of ADOF was almost arbitrary other than purposely avoiding the inclusion of the connection DOF in the reduction process. As explained in the theory section, Guyan reduced models are highly affected by DOF selection while this has no effect on the SEREP and KM_AMI methodologies. This independence from DOF selection is in fact a central point on why the connection DOFs can be omitted and how the subcomponent information is preserved during the SEREP reduction. Case 6 investigates the addition of the connection DOF in the model reduction.

5.4.7 Case 6: Considerations for DOF Selection in the Model Reduction

A reduced model using 12 DOF (as in Case 2, 3 and 4) was created using the connection DOF 37 and 49 from the ancillary subcomponent. The ADOF set selected was DOF 65, 117, 169, 199, and 205 from System 1/Beam B and ADOF 23, 31, 33, 37, 49, 55 and 63 from Beam A of System 2. Figure 5.22 shows a comparison of the SEREP reduction models carried out with and without use of the connection DOF of the ancillary subcomponent.

The 12 DOF reduced model utilizing the connecting DOF to the ancillary beam did not yield a higher average MAC or TRAC and no significant gain was observed from the selection of these DOF. This phenomenon is not surprising because SEREP reduction, as it has already been mentioned, is not dependent on the location of the selected DOF as long as the reduced set of modes span the space of the system. To further illustrates that omitted DOF are sufficiently recovered from the available system information, Fig. 5.23 shows a comparison of the time response at the connecting DOF of both the ancillary beam and the top red beam of System 2.

The connecting DOF of the subcomponents of System 2 are expected, and in fact, show the same time response. Therefore, the number of modes, as shown in Case 5, has a more significant contribution to the accuracy of the predicted response than the selection of ADOF in the reduced model.

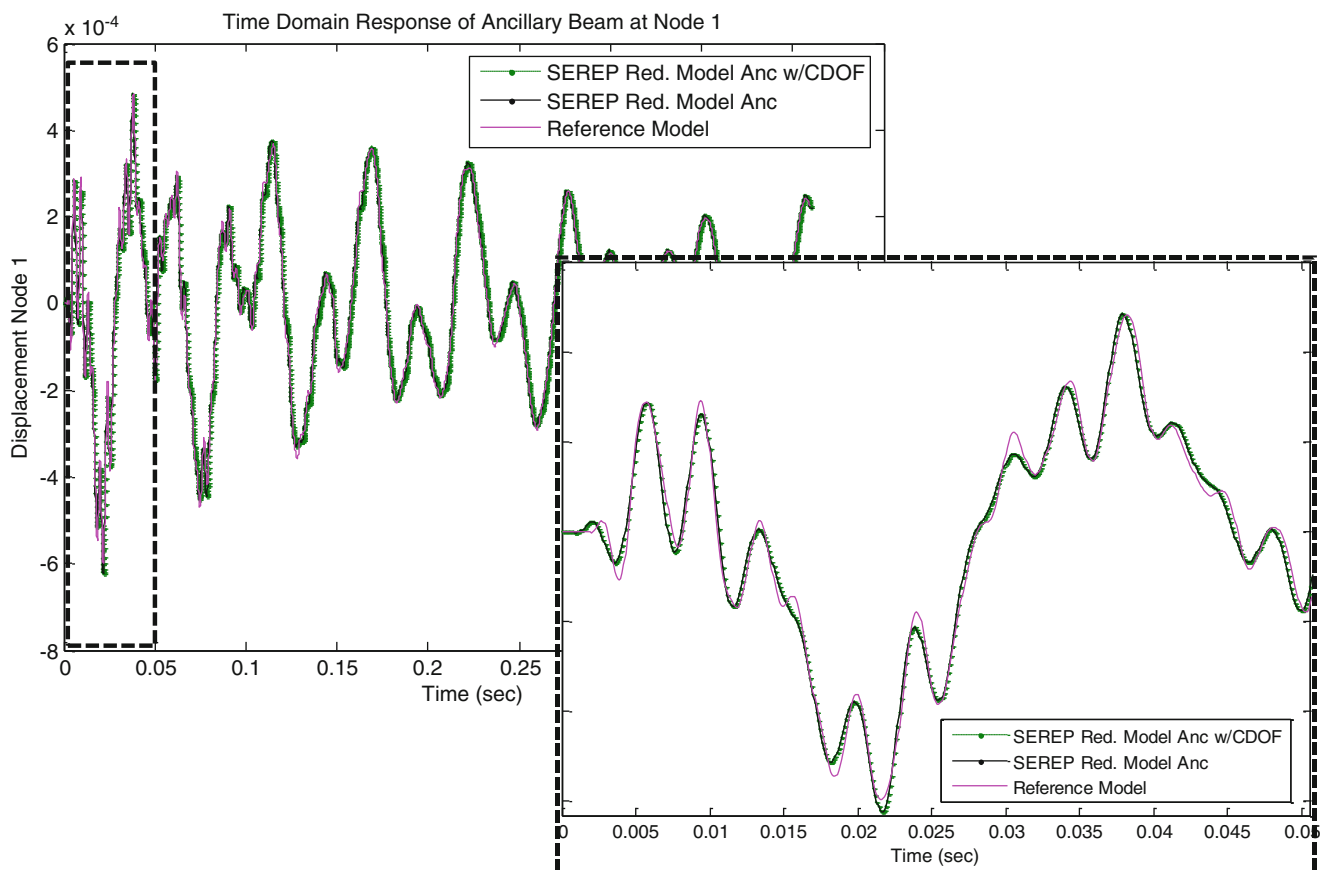


Fig. 5.22 Comparison of time response at node 1 of ancillary subcomponent from two expanded SEREP reduced models (Model in *green* uses the connecting DOF of the ancillary beam while the model in *black* uses the previously selected ADOF set)

5.4.8 Observations

The expanded SEREP reduced model of Case 3 and the KM_AMI model of Case 4 were shown to accurately preserve embedded structural component information. While there are slight differences in the time traces of the system response, these are not necessarily an artifact of the reduction process but more a result of the effect of higher order modes at the beginning of the response as well as the approximation of the damping in the system (damping was assumed to be 1 % for all modes of the system). Increasing the duration of the time pulse could reduce the number of higher modes excited and in turn yield a better representation without the need for more modes in the reduction process.

From Cases 5 and 6, selection of DOF was shown to be not as significant as the number of modes in the reduced model. Increasing the number of modes in the ‘a’ space resulted in a set of modes that better spans the space of the fully assembled reference model. Furthermore, when the ‘a’ space modes span the space of the system the selection of the connection DOF of the ancillary subcomponent brought no additional gain in accuracy in the predicted response of the system.

5.5 Conclusion

An efficient reduced order modeling technique for system forced response calculation (ERMT) was used to calculate the time response of multi-component structure. The reduced model was made of components with embedded subcomponent information. The transformation matrices from the reduction process were used to expand the time response from a selected ADOF set back to the full NDOF space. The selected ADOFs omitted the connecting DOF of the ancillary subcomponent and the expansion process was shown to correctly predict the response of the embedded component as long as the modes of the reduced system spanned the space of all the modes of interest.

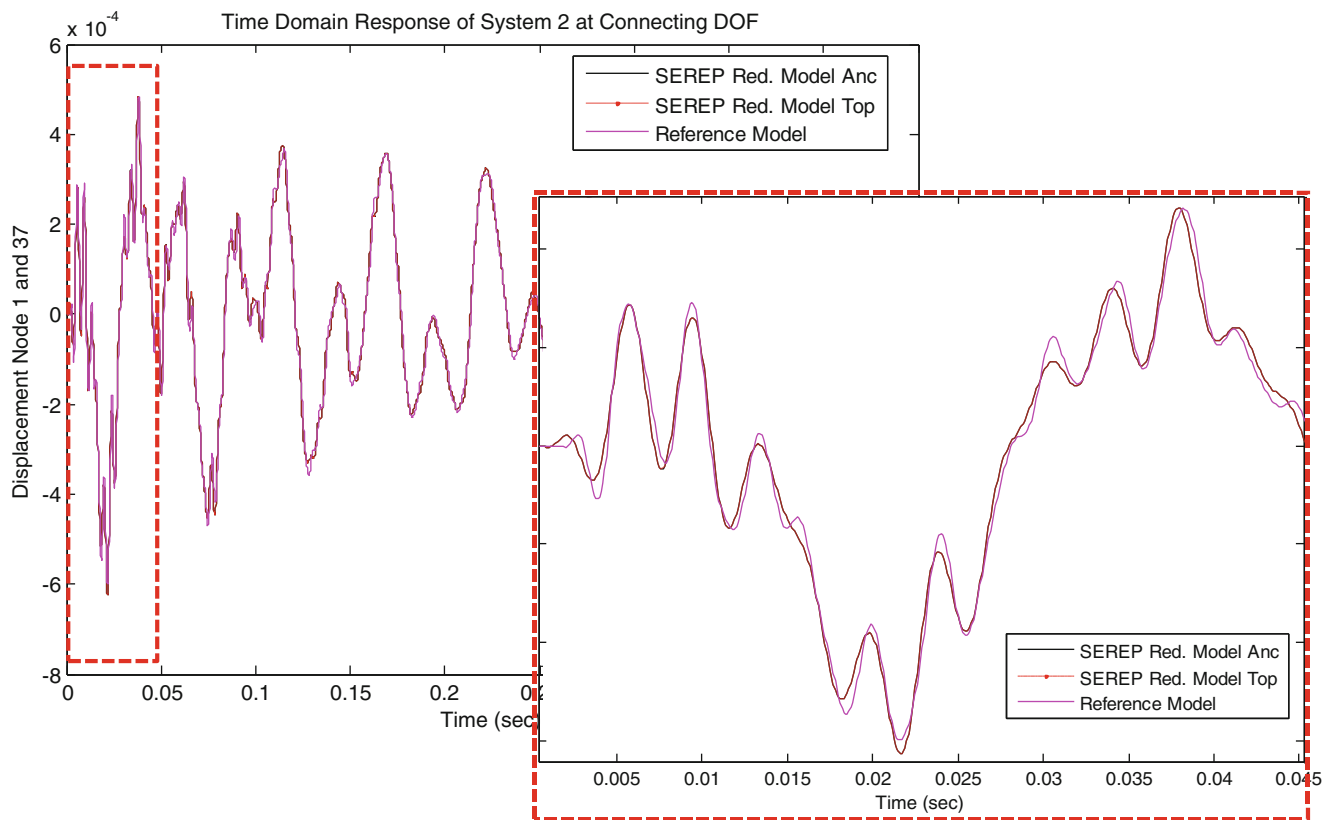


Fig. 5.23 Comparison of connecting DOF time response for both ancillary subcomponent and *top red beam* of System 2

Guyan and SEREP reduction were used to obtain the reduced order models but mode truncation in the Guyan reduced system resulted in poor correlation of the response of the system. SEREP reduced models and the expanded models were shown to accurately preserve the dynamics of the system as well as the dynamics of the embedded ancillary subcomponent; the reduced model did not contain any DOF associated with the ancillary connection to the subcomponent. No additional gain was found from the addition of the connecting DOF of the subcomponents as long as the modes selected were sufficient in accordance to the U_{12} contribution matrix.

KM-AMI updating of the Guyan reduced mass and stiffness matrices with target frequencies and mode shapes showed to mitigate the inherent errors in Guyan reduction process and ADOF selection. Addition of modes to the SEREP and KM-AMI models was shown to give significant gains in the correlation of the system to the full space reference solution.

Acknowledgements Some of the work presented herein was partially funded by Air Force Research Laboratory Award No. FA8651-10-1-0009 “Development of Dynamic Response Modeling Techniques for Linear Modal Components”. Any opinions, findings, and conclusions or recommendations expressed in this material are those of the authors and do not necessarily reflect the views of the particular funding agency. The authors are grateful for the support obtained.

References

1. Thibault L (2012) Development of equivalent reduced model technique for linear modal components interconnected with nonlinear connection elements. Master’s Thesis, University of Massachusetts Lowell
2. Marinone T (2012) Efficient computational nonlinear dynamic analysis using modal modification response technique. Master’s Thesis, University of Massachusetts Lowell
3. Marinone T, Thibault L, Avitabile P (2013) Expansion of nonlinear system response using linear transformation matrices from reduced component model representations. Proceedings of the thirty-first international modal analysis conference, Garden Grove, CA, Feb 2013
4. Pingle P, Niezrecki C, Avitabile P (2011) Full field numerical stress-strain from dynamic experimental measured data. EURO DYN 2011, Leuven, Belgium, July 2011

5. Avitabile P, Harvie J (2013) Reduced order system model nonlinear response and expansion for full field results. Eleventh international conference on recent advances in structural dynamics, Pisa, Italy, July 2013
6. Avitabile P (2003) Twenty years of structural dynamic modification – a review. *Sound and Vibration Magazine*, pp 14–27
7. Thibault L, Avitabile P, Foley J, Wolfson J (2012) Equivalent reduced model technique development for nonlinear system dynamic response. Proceedings of the thirtieth international modal analysis conference, Jacksonville, FL, Feb 2012
8. Guyan RJ (1965) Reduction of stiffness and mass matrices. *AIAA J* 3(2):380
9. O’Callahan JC (1989) A procedure for an improved reduced system (IRS) model. Proceedings of the seventh international modal analysis conference, Las Vegas, NV, Feb 1989
10. O’Callahan JC, Avitabile P, Riemer R (1989) System equivalent reduction expansion process. Proceedings of the seventh international modal analysis conference, Las Vegas, NV, Feb 1989
11. Nonis C, Avitabile P (2013) System model modes developed from expansion of uncoupled component dynamic data. Eleventh international conference on recent advances in structural dynamics, Pisa, Italy, July 2013
12. Marinone T, Butland A, Avitabile P (2012) A reduced model approximation approach using model updating methodologies. Conference proceedings of the society for experimental mechanics series 2012, Topics in modal analysis II, vol 6, pp 625–636
13. Newmark NM (1959) A method of computation for structural dynamics. *J Eng Mech Div ASCE* 85(3):67–94
14. Allemang RJ, Brown DL (2007) A correlation coefficient for modal vector analysis. Proceedings of the first international modal analysis conference, Orlando, FL, Feb 2007
15. Van Zandt T (2006) Development of efficient reduced models for multi-body dynamics simulations of helicopter wing missile configurations. Master’s Thesis, University of Massachusetts Lowell
16. MAT_SAP/MATRIX (1986) A general linear algebra operation program for matrix analysis. Dr. John O’Callahan, University of Massachusetts Lowell
17. MATLAB R2010a. The MathWorks, Natick, MA 2010

Chapter 6

Towards Dynamic Substructuring Using Measured Impulse Response Functions

M.V. van der Seijs, P.L.C. van der Valk, T. van der Horst, and D.J. Rixen

Abstract The Impulse Based Substructuring (IBS) method has been proposed lately as an alternative approach to evaluate the dynamic response of a system, using the experimentally determined Impulse Response Functions (IRFs) of its components. In previous research a first experimental IBS analysis was performed using measurements on two interface points of a POM bar. It was observed that the IRFs obtained from the imperfect impulses (by means of impact hammer testing) result in stability issues in the substructuring analysis.

To obtain IRFs associated with a “true” Dirac impulse, several approaches are discussed. It is known that frequency domain averaging leads to small phase errors and thereby non-causality in the IRF obtained through inverse Fourier transformation. Alternatively a time-domain approach is presented which allows for averaging of multiple impacts while avoiding Fourier transformations. By writing the convolution product of the dynamic system using a Toeplitz matrix, the IRF can be found from solving a least-square linear system. To improve efficiency, the system can be formulated as an inverse filter operation. The time-domain procedure is illustrated by application to the one-dimensional POM bar.

Keywords Impulse based substructuring • Experimental substructuring • Toeplitz matrix • FIR • Impact testing

6.1 Introduction

In dynamic substructuring (DS) one tries to find the dynamic behavior of large and complex structures by dividing it into several substructures. Although is this already a quite well known and often applied for numerical simulations, where ones employs the Component Mode Synthesis methods, such as Guyan reduction [7] and/or the Craig-Bampton method [2], the field of experimental dynamic substructuring is less known and still an active field of research. Experimental substructuring poses a set of extra challenges in comparison to the numerical substructuring methods, as one has to deal with noise, experimental errors, difficulties measuring rotational degrees of freedom, limited number of measurement locations, points that can not be measured or excited and so on. Still, a huge leap forward has been made in the field, since the first methods were proposed in the 1980s by Crowley et al. [3] and Jetmundsen et al. [8]. These methods are all based on the assembly of frequency response functions (FRFs) using different methods, where some are more successful than others. An historical overview of the field can be found in [5].

Recently, a new idea in the field of dynamic substructuring was proposed [10]. In this method, *Impulse Based Substructuring* (IBS), impulse response functions (IRFs) are assembled using Lagrange multipliers that enforce compatibility between the different substructures. As impulse response functions are, essentially, the time-domain counterparts of frequency response functions, the IBS method can be interpreted as a convolution of the LM-FBS method [4], that operates in the frequency domain. As these impulse response functions can be measured, they can be used directly in the IBS method

M.V. van der Seijs • P.L.C. van der Valk (✉) • T. van der Horst
Faculty of Mechanical, Maritime and Materials Engineering, Department of Precision and Microsystems Engineering, Section Engineering Dynamics, Delft University of Technology, Mekelweg 2, 2628CD, Delft, The Netherlands
e-mail: m.v.vanderseijs@tudelft.nl; p.l.c.vandervalk@tudelft.nl

D.J. Rixen
Faculty of Mechanical Engineering, Institute of Applied Mechanics, Technische Universität München, Boltzmannstr. 15, 85748, Garching, Germany

and assembled to other measured or simulated IRFs, as was already demonstrated for a relatively simple 1D bar problem [9]. From the paper by Rixen it followed that one of the biggest issues is in fact the imperfection of the impulse.

In this paper some of the solutions proposed for handling this imperfect impulse are discussed in more detail. Section 6.2 gives a summary of the IRF-based dynamic simulations and the procedures to couple substructures in the time-domain. Also the representation of displacement, velocity and acceleration IRFs is discussed. In Sect. 6.3 the time-domain IRF determination is presented and illustrated for a 1D POM bar problem. Thereafter some observations and practical challenges are discussed in Sect. 6.4.

6.2 Recap of Impulse Based Substructuring

This section will give of brief recap of the theory of using impulse response functions for solving dynamic substructuring problems. First, the theory of using impulse response functions for determining dynamic structural responses is recalled. In addition, this idea is expanded in order to handle partitioned systems by applying Lagrange multipliers for enforcing compatibility between the different substructures. As one can choose to measure accelerations, velocities and or displacements, we will show for all cases how the method is to be implemented and which of those IRFs is used in this work.

6.2.1 Using Impulse Response Functions for Time Integration

Let us call $\mathbf{Y}(t)$ the matrix of the displacement responses due to a unit impulse at $t = 0$ for a linear system that is initially at rest. In other words a coefficient $[\mathbf{Y}(t)]_{ij}$ of the impulse response matrix represents the response of degree of freedom (DoF) i to a unit impulse on DoF j at time t . The response of the linear system, initially at rest, to an applied force $\mathbf{f}(t)$ can then be evaluated by the convolution product (Duhamel's integral) between the impulse response function matrix and the applied forces:

$$\mathbf{u}(t) = \mathbf{Y}(t) * \mathbf{f}(t) = \int_0^t \mathbf{Y}(t - \tau) \mathbf{f}(\tau) d\tau \quad (6.1a)$$

This is a classical result of time analysis of linear systems, usually obtained using Laplace transforms (see for instance [6]). Similarly, we can define this as well for the velocities and accelerations of the system. By calling $\dot{\mathbf{Y}}(t)$ and $\ddot{\mathbf{Y}}(t)$, respectively the matrices of the velocity and acceleration responses due to a unit impulse at $t = 0$ for a linear system initially at rest, such that:

$$\dot{\mathbf{u}}(t) = \int_0^t \dot{\mathbf{Y}}(t - \tau) \mathbf{f}(\tau) d\tau \quad (6.1b)$$

$$\ddot{\mathbf{u}}(t) = \int_0^t \ddot{\mathbf{Y}}(t - \tau) \mathbf{f}(\tau) d\tau \quad (6.1c)$$

These convolution products can be interpreted as follows: the response at time t is an infinite sum of the responses to the infinitesimal impulses $\mathbf{f}(\tau) d\tau$ before time t (see Fig. 6.1). Each impulse at time τ gives a contribution through the impulse response from τ to t , that is $\mathbf{Y}(t - \tau)$.

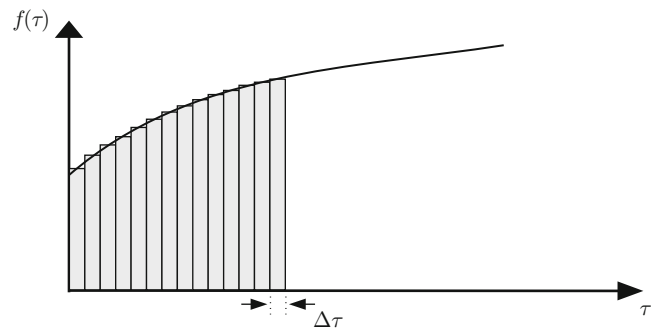


Fig. 6.1 Forcing function as a series of impulses [10]

The impulse responses can be obtained either numerically, by time integrating the equations of motion or by means of solving these analytically [10], or experimentally, which is the focus of the current paper.

6.2.2 Coupling of Impulse Response Functions by Means of Lagrange Multipliers

Let us now assume that the problem has been decomposed into N_s substructures. The velocity response of each substructure can be obtained using the convolution product for velocities (6.1b), but for the solutions to be the responses of the substructures as part of a full system the coupling forces on the interface between the substructures must be included in the forcing function. The interface forces are unknown beforehand, but we know that those interface forces coupling the interface DoFs must be such that the interface is compatible in the assembled problem.

Calling $\mathbf{B}^{(s)}$ the signed Boolean matrices localizing the interface DoFs (see for instance [5]), the compatibility condition on the interface, namely the condition stating that the DoFs on each side of the interface are equal, can be written as

$$\sum_{s=1}^{N_s} \mathbf{B}^{(s)} \dot{\mathbf{u}}^{(s)} = \mathbf{0} \quad (6.2)$$

Hence the extension of Duhamel's integral (6.1a) to a partitioned problem writes

$$\left\{ \begin{array}{l} \dot{\mathbf{u}}^{(s)}(t) = \int_0^t \dot{\mathbf{Y}}^{(s)}(t-\tau) \left(\mathbf{f}^{(s)}(\tau) - \mathbf{B}^{(s)T} \boldsymbol{\lambda}(\tau) \right) d\tau \\ \sum_{s=1}^{N_s} \mathbf{B}^{(s)} \dot{\mathbf{u}}^{(s)}(t) = \mathbf{0} \end{array} \right. \quad (6.3a)$$

$$\left\{ \begin{array}{l} \sum_{s=1}^{N_s} \mathbf{B}^{(s)} \dot{\mathbf{u}}^{(s)}(t) = \mathbf{0} \end{array} \right. \quad (6.3b)$$

where $-\mathbf{B}^{(s)T} \boldsymbol{\lambda}$ represent the interface forces, namely the reactions associated to interface compatibility constraint, $\boldsymbol{\lambda}$ being the Lagrange multipliers.

However, in reality one can never obtain the true continuous IRFs, as one takes samples during measurements and thus obtains a discrete version of the IRFs. By taking this into account, the integral over time is replaced by a discrete summation over time and results in:

$$\left\{ \begin{array}{l} \dot{\mathbf{u}}_n^{(s)} = \Delta t \sum_{i=0}^n \dot{\mathbf{Y}}_{n-i}^{(s)} \left(\mathbf{f}_i^{(s)} - \mathbf{B}^{(s)T} \boldsymbol{\lambda}_i \right) \end{array} \right. \quad (6.4a)$$

$$\left\{ \begin{array}{l} \sum_{s=1}^{N_s} \mathbf{B}^{(s)} \dot{\mathbf{u}}_n^{(s)} = \mathbf{0} \end{array} \right. \quad (6.4b)$$

where, Δt is the sampling time step. By substituting the first line of Eq. (6.4) into the second line, an expression for the Lagrange multipliers, or in other words for the interface forces, is found,

$$\boldsymbol{\lambda}_n = \left(\Delta t \sum_{s=1}^{N_s} \mathbf{B}^{(s)} \dot{\mathbf{Y}}_0^{(s)} \mathbf{B}^{(s)T} \right)^{-1} \sum_{s=1}^{N_s} \mathbf{B}^{(s)} \dot{\mathbf{u}}_n^{(s)}, \quad (6.5)$$

where,

$$\dot{\mathbf{u}}_n^{(s)} = \Delta t \sum_{i=0}^{n-1} \dot{\mathbf{Y}}_{n-i}^{(s)} \left(\mathbf{f}_i^{(s)} - \mathbf{B}^{(s)T} \boldsymbol{\lambda}_i \right) + \Delta t \mathbf{Y}_0^{(s)} \mathbf{f}_n^{(s)}. \quad (6.6)$$

Hence, to give some physical understanding regarding Eqs. (6.5) and (6.6), one can regard Eq. (6.6) as a sort of *predictor* step, where the responses of all subsystems are computed without taking into account the compatibility condition. The result of this predictor can, potentially, lead to a violation of the compatibility condition, therefore the Lagrange multipliers needed to enforce the compatibility condition are computed using Eq. (6.5).

6.2.3 Which IRFs to Use: Displacement, Velocity or Acceleration IRFs?

In Sect. 6.2.2, the IBS method was shown for coupling velocity IRFs. Note that this choice is not arbitrarily, as we will show in this subsection. For a simple undamped 1-DoF, initially at rest, one can use the Laplace transform to find the impulse response functions in terms of accelerations, velocities and displacements:

$$\ddot{u}(t) + \omega_n^2 u(t) = \frac{1}{m} \delta(t) \quad \left\{ \begin{array}{l} y(t) = \frac{1}{m\omega_n} \sin(\omega_n t) \quad \text{for } t > 0 \\ \dot{y}(t) = \frac{1}{m} \cos(\omega_n t) \quad \text{for } t > 0 \\ \ddot{y}(t) = -\frac{\omega_n}{m} \sin(\omega_n t) \quad \text{for } t > 0 \end{array} \right. \quad \begin{array}{l} (6.7a) \\ (6.7b) \\ (6.7c) \end{array}$$

where, m is the mass of the system and ω_n is its natural frequency. As a true Dirac function is a unit impulse and is infinitely short, the response of the system is a sudden increase of velocity and is given as:

$$m\dot{u}(t_+) - m\dot{u}(t_-) = \int_{\tau=t_-}^{t_+} \delta(\tau) d\tau = 1 \quad (6.8)$$

where $\delta(t)$ is the Dirac function. Obviously, this leads to a discontinuity for the accelerations, therefore the expressions in Eq. (6.7) can be considered to start from time t_+ , which results in a smooth expression for the accelerations as well. But as information about the actual impact is lacking from $\ddot{y}(t)$, it cannot be used in the IBS scheme. Hence, one is left with the option of using either the velocity or displacement IRFs. As can be seen from Eq. (6.7a), at t_0 the displacements are equal to zero and one will have to compute the associated interface problem (Eq. (6.6)) at $t = \Delta t$. If the sample frequency is high, $y(\Delta t)$ could be very small, which can lead to numerical errors in solving the interface problem. In addition to this, the actual value of $y(\Delta t)$ is dependent on the size of the sample time step chosen, which is considered to be not ideal. A better choice would therefore be to use the velocities ($\dot{y}(t)$), as these have their maximum value at t_0 and, in addition, $\dot{y}(0)$ is not dependent on the sample time step chosen. Therefore, it was chosen to use measured velocity impulse response functions in this work.

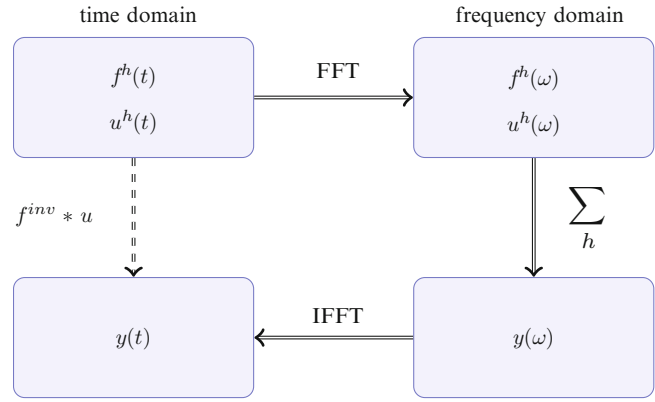
6.3 Obtaining Impulse Response Functions from Experiments

This section will elaborate on various methods to obtain Impulse Response Function (IRF) data from experiments. It is chosen to follow the same measurement procedures as when applying standard Experimental Modal Analysis (EMA) procedures to obtain Frequency Response Function (FRF) data. In particular, the workflow of impact measurements is adopted meaning that measured velocity data $\dot{u}^h(t)$ for various hammer impacts $f^h(t)$ is used. To obtain response functions that objectively characterise the system dynamics, the following operations should typically be performed, regardless of the choice for time or frequency domain:

1. Scaling of spectral amplitude, such that the response corresponds to a unity impulse loading of 1 Ns with a flat input spectrum. Typically the spectrum of the impact force $f(\omega)$ has its highest value at 0 Hz and drops several orders of magnitude for increasing frequencies. The response $u(\omega)$ should be compensated for this spectral envelope, meaning that the amplitudes corresponding to higher frequencies need to be amplified.
2. Shifting in time, such that the response is synchronised to an impulse at $t = 0$ and is causal throughout the response, i.e. no energy is added to the system after the initial impulse. For the frequency domain this implies that the phase of $f(\omega)$ is subtracted from the phase of $u(\omega)$.
3. Averaging for various impacts h , such that measurement noise is attenuated and differences in response due to errors on the position of the impact are averaged out. Concerning measurement noise, it may depend on the measurement setup (e.g. signal-to-noise ratio, completeness of impact spectrum) whether or not averaging is indeed necessary. Concerning the impact location, it is known that the anti-resonances are particularly sensitive to position differences.

In the following sections, first the conventional frequency domain method will be summarised, after which a direct time-domain method is proposed.

Fig. 6.2 Workflow of IRF determination; through the frequency domain or directly in the time domain



6.3.1 Frequency-Domain Approach

In the frequency domain the first two tasks can be performed in a single step, typically by dividing the complex FFT spectra of the response and force signal. The relation for a single impact measurement h is then found to be:

$$y^h(\omega) = \frac{u^h(\omega)}{f^h(\omega)} \quad (6.9)$$

In addition, the averaging step for N_h impacts is implemented by considering the averaged auto-power spectra (APS) and cross-power spectra (CPS) of the input and output signals, normally computed using the Fast Fourier Transform (FFT):

$$y(\omega) = \frac{G_{fu}(\omega)}{G_{ff}(\omega)} \quad \text{with} \quad \begin{cases} G_{fu}(\omega) \triangleq \frac{1}{N_h} \sum_h f^h(\omega)^* \cdot u^h(\omega) \\ G_{ff}(\omega) \triangleq \frac{1}{N_h} \sum_h f^h(\omega)^* \cdot f^h(\omega) \end{cases} \quad (6.10)$$

It can be shown that Eq. (6.10) performs least-squares averaging on the input spectra f^h and provides the so-called H1 estimator for the FRF [1]. To obtain now the time-domain IRF, one simply computes the inverse Fourier transform of the averaged FRF using an IFFT. The whole procedure is depicted in Fig. 6.2.

Although the frequency-domain approach as summarised is easily implemented, it has certain shortcomings:

- The phase of the estimated FRF is fully determined by the phase of the averaged CPS $G_{fu}(\omega)$. This does however not guarantee that the resulting IRF is causal. Instead it is often experienced that the computed IRF shows a rapidly growing oscillation near the end of the time response.
- FRF determination uses FFTs of the measurement blocks. If the response has not died out completely within the length of the measurement block, windowing should be applied to prevent spectral leakage. This is cumbersome as windowing adds artificial damping to the response.

As we are seeking for a method to perform the abovementioned steps in order to obtain the IRF $y(t)$ rather than the FRF $y(\omega)$, it seems natural to seek for a solution in the time-domain as well. However this is not trivial; it can be understood from the division in Eq. (6.9) that the time-domain counterpart involves a deconvolution of $u(t)$ with $f(t)$, as was already reported in [9]. Direct deconvolution is known to be a delicate procedure, highly prone to measurement noise. It is there suggested to follow an alternative route, which is presented next.

6.3.2 Time-Domain Approach

Let us recall Eq. (6.1a) and write the time-discretised convolution product for a one-dimensional case¹ in a similar way as Eq. (6.4a). The indexing of the equations is adjusted such that y_1 holds the response to the unit impulse at $t_1 = 0$.

¹For now, displacements IRFs are considered in the derivation.

$$\begin{aligned}
u_n &= \sum_{i=1}^{n-1} y_{n-i+1} f_i \Delta t \\
&= \sum_{i=1}^{n-1} f_{n-i+1} y_i \Delta t
\end{aligned} \tag{6.11}$$

Eq. (6.11) is known as the *Cauchy product* and is commutative for the order of y and f . Let us write out the product for u_n in a matrix format for the full length of $n = 1$ until $n = N$:

$$\underbrace{\begin{bmatrix} u_1 \\ u_2 \\ \vdots \\ u_N \end{bmatrix}}_{N \times 1} = \underbrace{\begin{bmatrix} f_1 & 0 & \cdots & 0 \\ f_2 & f_1 & \ddots & \vdots \\ \vdots & f_2 & \ddots & 0 \\ f_M & \vdots & \ddots & f_1 \\ 0 & f_M & \vdots & f_2 \\ \vdots & \ddots & \ddots & \vdots \\ 0 & \cdots & 0 & f_M \end{bmatrix}}_{N \times Q} \underbrace{\begin{bmatrix} y_1 \\ y_2 \\ \vdots \\ y_Q \end{bmatrix}}_{Q \times 1} \Delta t = \mathbf{F} \mathbf{y} \Delta t \tag{6.12}$$

Matrix \mathbf{F} is referred to as a *Toeplitz* matrix; it represents the forcing vector \mathbf{f} along a tapped-delay line such that the convolution product of Eq. (6.11) is obtained. It has dimension $N \times Q$ with $Q < N$, which implies that it is overdetermined by construction and should be solved in a least-square sense.² Let us now have a closer look at the dimensions of the vectors:

- N The length of the displacement vector \mathbf{u} . This is normally equal to the block size of the (impact) measurement.
- M The length of the forcing vector \mathbf{f} that needs to be smaller than \mathbf{u} : $M \ll N$. For impact measurements this is a natural choice.
- Q The length of the IRF vector \mathbf{y} : $Q = N - M + 1$. We furthermore require Q to be an odd number (this will prove to be beneficial later).

By construction, the system of equations of Eq. (6.12) is overdetermined. One solution for \mathbf{y} can therefore be found by writing the pseudo-inverse:

$$\mathbf{y} = \frac{1}{\Delta t} (\mathbf{F}^T \mathbf{F})^{-1} \mathbf{F}^T \mathbf{u} \tag{6.13}$$

or by defining the inverse matrix operator:

$$\mathbf{y} = \frac{1}{\Delta t} \mathbf{F}^{inv} \mathbf{u} \quad \text{with} \quad \begin{cases} \mathbf{F}^{inv} \triangleq \mathbf{R}^{-1} \mathbf{F}^T & \text{the inverse force matrix} \\ \mathbf{R} \triangleq \mathbf{F}^T \mathbf{F} & \text{the auto-correlation matrix} \end{cases} \tag{6.14}$$

Eq. (6.14) is sufficient to estimate \mathbf{y} from measured \mathbf{u} and \mathbf{f} but unfortunately not very efficient: the size of the problem is prescribed by N : the length of the measured response. This means that in the field of experimental dynamics this matrix deconvolution procedure is computationally expensive and therefore not very practical.

²Note that if $Q = N$, \mathbf{F} would be a lower triangular square matrix and the solution loses its least-square property. In that case, it follows from forward substitution that the first element y_1 is fully determined by f_1 , which is normally very small. This results in a highly unstable determination of \mathbf{y} . This problem was already reported in [9].

6.3.3 Inverse Filter Approach

It is suggested to find an *inverse force filter* \mathbf{f}^{inv} that is the filter counterpart of the matrix operator \mathbf{F}^{inv} . If a force filter can be found that obeys $\mathbf{f}^{inv}(t) * \mathbf{f}(t) = \delta(t)$, then the IRF \mathbf{y} can be found from convolution of the inverse force filter with \mathbf{u} , which is the filter equivalent of Eq. (6.14):

$$\mathbf{y} = \frac{1}{\Delta t} \mathbf{f}^{inv} * \mathbf{u} \quad (6.15)$$

Formally, the inverse filter of a finite impulse response (FIR) must be an infinite impulse response (IIR) and is generally non-causal. Still it is possible to approximate a finite inverse force filter that is shorter than N , resulting in a more efficient IRF determination. Without presenting a full proof, the procedure of computing the inverse force filter is discussed next.

Let us start by writing the convolution of the force signal with the inverse force filter that has to be determined. By definition, the discrete convolution of a signal with its inverse results in the discrete unit function:

$$\mathbf{f} * \mathbf{f}^{inv} = \delta \quad (6.16)$$

δ should have one element equal to 1 (the rest being zero) depending on the length and indexing of \mathbf{f}^{inv} . Using the notation of Eq. (6.12), we can write Eq. (6.16) as a matrix multiplication with \mathbf{F} . The width of the matrix, again denoted by Q , is now directly linked to the size of the inverse filter, which is again chosen to be odd-numbered. The computation is proceeded as follows:

$$\begin{aligned} \mathbf{F} \mathbf{f}^{inv} &= \delta \\ \mathbf{F}^T \mathbf{F} \mathbf{f}^{inv} &= \mathbf{F}^T \delta \\ \mathbf{R} \mathbf{f}^{inv} &= \mathbf{f}^{rv} \end{aligned} \quad (6.17)$$

Matrix \mathbf{R} is again the auto-correlation matrix of \mathbf{f} . Vector \mathbf{f}^{rv} represents the reversed force vector, padded with $Q - M$ zeros. The unit function effectively picks one column out of the transpose of \mathbf{F} resulting in a reversed order of the elements; the location of the unit in δ is denoted by c and determines the distribution of the padded zeros over both sides of \mathbf{f}^{rv} . This has a direct consequence for the alignment of the non-causal inverse force filter in the vector \mathbf{f}^{inv} . In other words: c determines where the instance $t = 0$ in the inverse force filter is expected. It can be verified from the matrix in Eq. (6.12) that $M \leq c \leq (Q - M)$ to ensure that a complete vector \mathbf{f} is obtained. It is here chosen to put the unit in the centre of δ , i.e. $c = \frac{1}{2}(Q - M)$, such that the vector \mathbf{f}^{inv} stores as much negative as positive time of the infinite filter.

Let us now have a look at matrix \mathbf{R} . It is easily verified that the coefficients read:

$$\mathbf{R} = \begin{bmatrix} r_1 & r_2 & \cdots & r_M & 0 & 0 \\ r_2 & r_1 & r_2 & \cdots & r_M & 0 \\ \vdots & r_2 & r_1 & \ddots & \ddots & r_M \\ r_M & \vdots & \ddots & \ddots & \ddots & \vdots \\ 0 & r_M & \ddots & \ddots & \ddots & r_2 \\ 0 & 0 & r_M & \cdots & r_2 & r_1 \end{bmatrix} \quad \text{with} \quad \begin{cases} r_1 = f_1 f_1 + f_2 f_2 + f_3 f_3 + \cdots + f_M f_M \\ r_2 = f_2 f_1 + f_3 f_2 + \cdots + f_M f_{M-1} \\ \vdots \\ r_M = f_M f_1 \end{cases} \quad (6.18)$$

Indeed, \mathbf{R} is the $Q \times Q$ auto-correlation matrix for \mathbf{f} and is sparse with a bandwidth of $2M - 1$. Besides that, it contains a lot of redundant data. Hence an equivalent auto-correlation vector \mathbf{r} can be written comprising all the auto-correlation coefficients, padded with some zeros if $Q > 2M - 1$:

$$\mathbf{r} = \mathbf{f} \star \mathbf{f} = [\cdots 0 r_M \cdots r_2 r_1 r_2 \cdots r_M 0 \cdots] \quad (6.19)$$

which appears exactly in the centre row/column of the auto-correlation matrix if Q is odd-numbered. Hence the auto-correlation matrix \mathbf{R} can be constructed efficiently by creating a Toeplitz matrix from the complete vector \mathbf{r} and truncating such that r_1 ends up at the diagonal.

As matrix \mathbf{R} is invertible, the inverse force filter can be found by inversion of Eq. (6.17):

$$\mathbf{f}^{inv} = \mathbf{R}^{-1} \mathbf{f}^{rv} \quad (6.20)$$

And it can be verified that $\mathbf{f} * \mathbf{f}^{inv}$ indeed results in a unit on element c . The IRF \mathbf{y} is then approximated by applying Eq. (6.15).

6.3.4 Multiple Impact Averaging

The system of equations of Eq. (6.12) can be extended to allow for averaging of multiple impacts $h = 1, \dots, H$. The number of equations grows with the number of impacts ($H * N$) while the number of IRF elements to determine remains constant (Q). Hence the over-determination grows with factor H , which is beneficial for the accuracy of the estimation. The system of equations for two impacts is shown in Eq. (6.21).

$$\begin{bmatrix} \mathbf{u}^1 \\ \mathbf{u}^2 \end{bmatrix} = \begin{bmatrix} u_1^1 \\ \vdots \\ u_N^1 \\ u_1^2 \\ \vdots \\ u_N^2 \end{bmatrix} = \begin{bmatrix} c & & & \\ f_1^1 c & \cdots & 0 & \\ \vdots & \ddots & & \\ f_M^1 c & \cdots & f_1^1 & \\ \vdots & \ddots & & \\ 0 & c & \cdots & f_M^1 \\ f_1^2 c & \cdots & 0 & \\ \vdots & \ddots & & \\ f_M^2 c & \cdots & f_1^2 & \\ \vdots & \ddots & & \\ 0 & c & \cdots & f_M^2 \end{bmatrix} \begin{bmatrix} y_1 \\ y_2 \\ \vdots \\ y_Q \end{bmatrix} \Delta t = \begin{bmatrix} \mathbf{F}^1 \\ \mathbf{F}^2 \end{bmatrix} \mathbf{y} \Delta t \quad (6.21)$$

One could interpret Eq. (6.21) as a longer recording of repeating impacts that are all convolved with the same IRF \mathbf{y} . This indicates that the method can be used for a more general load case, e.g. white noise bursts, as long as an appropriate spectral range is covered.

The procedure as presented above can be straightforwardly applied to find the averaged auto-correlation matrix \mathbf{R}_{avg} . This can be used to compute the inverse force filters for the individual measurements (the denotation h is put as a subscript here):

$$\mathbf{f}_h^{inv} = \mathbf{R}_{avg}^{-1} \mathbf{f}_h^{rv} \quad (6.22)$$

The IRF reconstruction of multiple replicate measurements is estimated by the summation of the inverse force filters convolved with the corresponding output responses \mathbf{u}_h :

$$\mathbf{y}_{avg} = \frac{1}{\Delta t} \sum_{h=1}^H \mathbf{y}_h^{inv} * \mathbf{u}_h \quad (6.23)$$

Comparing with the frequency-domain estimation of H1 by Eq. (6.10), a certain similarity can be observed. The averaged auto-correlation matrix \mathbf{R}_{avg} calculated by Eq. (6.22) can be related to the averaged APS G_{ff} . The remaining operation is $\mathbf{F}^T \mathbf{u}$ which is analogue to the averaged CPS $\mathbf{G}_{fu}(\omega)$. It can thus be concluded that the estimation is inherently analogue to the H1 estimation of the FRF:

$$y(\omega) = \frac{G_{fu}(\omega)}{G_{ff}(\omega)} \iff \mathbf{h}(t) = \mathbf{R}^{-1}(t) \mathbf{F}^T(t) \mathbf{u}(t) \quad (6.24)$$

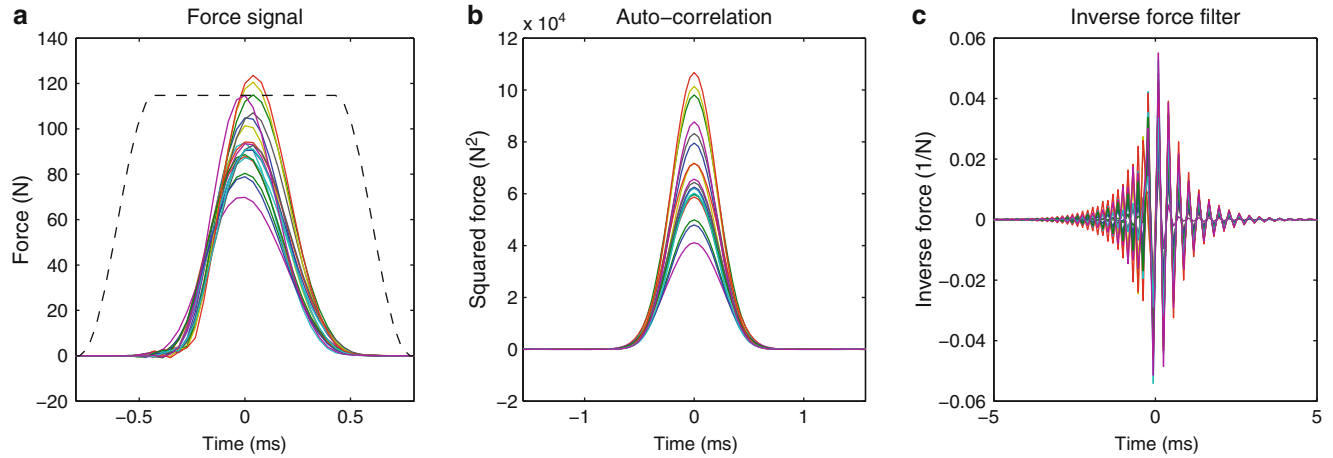


Fig. 6.3 Procedure of time-domain IRF estimation. Multiple impacts are shown. (a) Impacts. (b) Auto-correlations. (c) Inverse force filters

To summarise, the time-domain estimation of the IRF can be performed as follows:

1. Windowing and truncation of the force impacts \mathbf{f}_h ;
2. Calculation of the individual auto-correlation vectors \mathbf{r}_h by Eq. (6.19);
3. Construction of the averaged auto-correlation matrix \mathbf{R}_{avg} from the averaged auto-correlation vector \mathbf{r}_{avg} according to Eq. (6.18);
4. Calculation of the individual inverse force filters by Eq. (6.22);
5. Reconstruction of the IRF by Eq. (6.23).

6.3.5 Application to a POM Bar

The procedure is illustrated for the velocity IRF of a POM bar (similar as in [9]). Figure 6.3a shows 20 impact loads, centred and windowed. The corresponding auto-correlations are shown in Fig. 6.3b. Note that the impacts with higher amplitude have a larger contribution to the calculation of the IRF. It can however be chosen to normalise the impacts and associated responses to a unit impulse, such that every measurement has an equal contribution.

The centre parts of the inverse force filters are shown Fig. 6.3c. It appears that the inverse filter is indeed finite. By padding the auto-correlation vector with zeros, the inverse filter will get longer and the resulting “deconvolution” will be more accurate. The accuracy of the inverse filter can be examined by checking if $\mathbf{f} * \mathbf{f}^{inv}$ indeed results in a unit pulse.

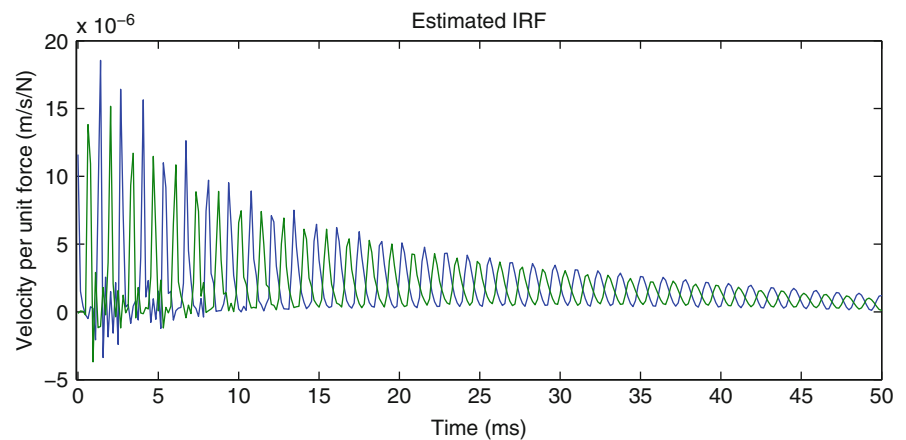
The IRFs constructed from the 20 measurements are shown in Fig. 6.4 for both the driving point IRF (blue) and the cross-point IRF (green) to the other end of the bar. The velocities indeed represent a travelling wave through the bar. The driving point IRF shows its first response at $t = 0$, while the cross-point at the end of the bar starts half a period later. It was furthermore verified that the complete IRF decays to zero, suggesting that the method results in a better causality than the frequency domain approach.

6.4 Observations and Outlook

The filter approach as presented proves to be a robust method to estimate IRFs in the time-domain. At this stage however, no results can be reported yet on the IBS coupling. Let us therefore conclude with some observations:

- When coupling two substructures using their IRF description, the interface problem is solved using the receptance of the first element of the driving point IRF, as stated by Eq. (6.5). To ensure stability, it was observed that this first response needs to be larger than the remaining part of the IRF. In addition it was found that any cross-point must always have a smaller amplitude than the driving point. For the case of the POM bar, the first element of the IRF appears to be estimated

Fig. 6.4 IRF constructed from 20 measurements. The *blue line* corresponds to the driving point of the measurement; the *green line* corresponds to the other end of the POM bar (Color figure online)



too low, resulting in unstable coupling results. Increasing the value indeed renders the simulation stable but result in partial coupling: when the travelling wave arrives at the interface, part of it reflects back.

- It appears that the condition number of \mathbf{R} can be directly related to the APS of the force input. Generally, the APS of an hammer impact has its highest value at 0 Hz and reduces for higher frequencies. If the APS drops into the noise range beyond a certain frequency, this will result in a high condition number of the \mathbf{R} and an amplification of measurement noise. To prevent noisy frequency content to contaminate the IRF, one can apply a Tikhonov regularisation. This can be done by computing an singular value decomposition of \mathbf{R} and setting the eigenvalues below a certain threshold to zero. An incomplete inverse can then be computed which results in a low-passed IRF.
- Unlike the FRF estimation, the time-domain method does not need the complete length of the decayed response \mathbf{u} to reconstruct the IRF. If one is interested in applying a least-square complex exponential fit to obtain modal parameters of a very weakly damped structure, it suffices to analyse only the initial response.

References

1. Bendat J, Piersol A (1980) Engineering applications of correlation and spectral analysis. Wiley, New York
2. Craig R, Bampton M (1968) Coupling of substructures for dynamic analysis. AIAA J 6(7):1313–1319
3. Crowley J, Klosterman A, Rocklin G, Vold H (1984) Direct structural modification using frequency response functions. In: Proceedings of the second international modal analysis conference, Orlando, FL, p 58–65, Bethel, CT, February 1984. Society for Experimental Mechanics
4. de Klerk D, Rixen D, de Jong J (2006) The frequency based substructuring (FBS) method reformulated according to the dual domain decomposition method. In: Proceedings of the twenty fourth international modal analysis conference, St. Louis, MO, Bethel, CT, February 2006. Society for Experimental Mechanics
5. de Klerk D, Rixen D, Voormeeren S (2008) General framework for dynamic substructuring: history, review and classification of techniques. AIAA J 46(5):1169–1181
6. Géradin M, Rixen D (1997) Mechanical vibrations – theory and application to structural dynamics. Wiley, Chichester
7. Guyan R (1965) Reduction of stiffness and mass matrices. AIAA J 3:380
8. Jetmundsen B, Bielawa R, Flannelly W (1988) Generalized frequency domain substructure synthesis. J Am Helicopter Soc 33:55–65
9. Rixen D (2010) A substructuring technique based on measured and computed impulse response functions of components. In: Proceedings of the international conference on noise and vibration engineering (ISMA 2010), Leuven, Belgium, 20–22 September 2010
10. Rixen DJ, van der Valk PLC (2013) An impulse based substructuring approach for impact analysis and load case simulations. J Sound Vib 332(26):7174–7190 2013. doi: 10.1016/j.jsv.2013.08.004. URL <http://www.sciencedirect.com/science/article/pii/S0022460X13006615>

Chapter 7

Hybrid Modeling of Floating Raft System by FRF-Based Substructuring Method with Elastic Coupling

Huang Xiuchang, Zhang Zhenguo, Hua Hongxing, and Xu Shiyin

Abstract The FRF-based substructuring method with elastic coupling by using hybrid experimental and numerical FRFs and impedance is investigated for predicting vibration transmission in floating raft system. The floating raft system composed of one machine, upper and lower isolators, raft and base under symmetric and unsymmetrical excitation conditions is studied experimentally to show the influence of rotational Degrees of Freedom (DOFs). The results demonstrate that if the system is exposed to unsymmetrical excitation, the isolators will undergo bending deformation and it should consider the vibration transmission by rotational DOFs. For hybrid modeling, since measurement of FRFs is limited to some translational DOFs, FRFs of other DOFs are calculated by numerical methods. Three possible ways are proposed to improve the modeling accuracy. The identification method for mobility of isolators in rotational DOFs under static load is suggested. Filters constructed by piecewise linear interpolation method is used to condition the numerical FRFs with the measured FRFs. The truncated Singular Value Decomposition (SVD) approach is used to improve the quality of measured FRFs in the presence of measurement errors. Careful application of the proposed measures may result in better prediction.

Keywords Floating raft system • FRF-based substructuring method • Hybrid modeling • Elastic coupling • Rotational DOFs

7.1 Introduction

Dynamic substructuring (DS) is a useful tool in modeling of complex built-up systems. Generally, two types of DS can be identified: numerical DS and experimental DS. The numerical DS, in which only numerical substructures are coupled, is already well developed. The experimental DS, in which substructures obtained through measurements are involved, can be done in either the modal domain using component mode synthesis (CMS) methods or in the frequency domain using frequency response function (FRF) coupling methods. The latter is found to be more convenient and attractive for being able to incorporate experimental FRFs directly into its spectral formulation without modal decomposition. Ochsner and Bernhard [1] used this modeling technique to analyze the structure-borne noise transmission from the tyre spindle through the suspension into the passenger compartment of an automobile. The FRFs of each component used in their calculations were measured directly from component set-ups and the bushing connectors were modeled as simple spring damper elements. Lim and Steyer [2] applied this method to analyze some automotive noise and vibration problems by using experimental FRFs of a moderately high-modal density body component and obtained reasonably good results. The development of DS leads to hybrid modeling [3–5], in which the substructures with high-modal density is represented by the experimental results while the substructures with low-modal density can be determined numerically. Or part of the FRF matrices of one substructure is obtained from experiment and the rest is calculated by numerical model.

For a numerical component, calculation of coupling information follows directly from the model and does not pose any problems. For an experimental component, some of the translational FRFs can usually be easily measured, while the rotational FRFs are hard to obtain due to lack of measurement equipment that can apply pure torque excitation and sensors

H. Xiuchang (✉) • Z. Zhenguo • H. Hongxing • X. Shiyin

State Key Laboratory of Mechanical System and Vibration, Shanghai Jiao Tong University, No. 800 Dongchuan Road, Min Hang District, Shanghai, P.R. China 200240

e-mail: xchhuang@sjtu.edu.cn; zzgtx@sjtu.edu.cn; hxx@sjtu.edu.cn; xushiyin0628@sjtu.edu.cn

that measure rotation, making assembling rotational DOFs a major challenge. For rigid coupling, the importance of including rotational DOFs is well addressed and a lot of measures were proposed [6, 7]. While for elastic coupling, the research on the influence and the solution of the rotational DOFs is still lacking.

Another factor that affects the accuracy of FRF based DS is measurement noise. Sanliturk and Cakar [8] presented a method based on singular value decomposition (SVD) for the elimination of noise from measured FRFs so as to improve the quality of the measured data. Gaul and Moll [9] suggested a method to remove phase errors in complex eigenvectors from experimental data by normalizing the complex eigenvectors, with the aim to perform coupled analysis by using an experimentally determined modal database. Carne and Dohrmann [10] developed a conditioning filter to remove the hidden anomalies (negative imaginary part in the driving-point FRFs) in the measurement-based FRF matrices.

In this study, the floating raft system, a complex system composed of multiple flexible substructures connected by elastic isolators, is taken as an example to show the influence of rotational DOFs. For the substructures are connected by several isolators, usually only the FRFs at these connection points are measured. It is impossible to extract the modal parameters to reconstruct the FRFs. How to eliminate the measurement noise and obtain FRFs of other DOFs is a tough problem.

7.2 Influence of Rotational DOFs—A Simple Experiment

The influence of rotational DOFs on the DS modeling is investigated through a comparative experiment. The experimental set-up of the floating raft system is shown in Fig. 7.1, including one mass, upper and lower isolators, raft, and base under symmetric (excitation at point A, which is the center of the system) and unsymmetrical excitation (excitation at point B, which is 225 mm away from point A) by an exciter. The substructures are connected by bolts. White noise is employed to drive the exciter. The system is placed on a platform supported by four air springs to simulate free-boundary conditions. An averaging of 100 times is performed to obtain the FRFs.

The adopted modeling technique is FRF-based substructuring method [11]. The FRFs of all the substructures and the impedance of the isolators are obtained by using the measured FRFs. Measurement of the FRFs of the mass is shown in Fig. 7.1 (Under unsymmetrical excitation, the FRFs at the corresponding connection points are measured and adopted). Measurement of the impedance of isolators is based on the theory in [12]. In the modeling process, only the FRFs of the vertical DOFs are adopted to perform the synthesis. Modeling results under two excitation conditions are shown in Figs. 7.2 and 7.3, respectively. It can be seen that, under both excitations, the results are reasonable to some extent and the errors are a little larger for the unsymmetrical excitation. The errors mainly come from the following aspects, firstly, the responses on

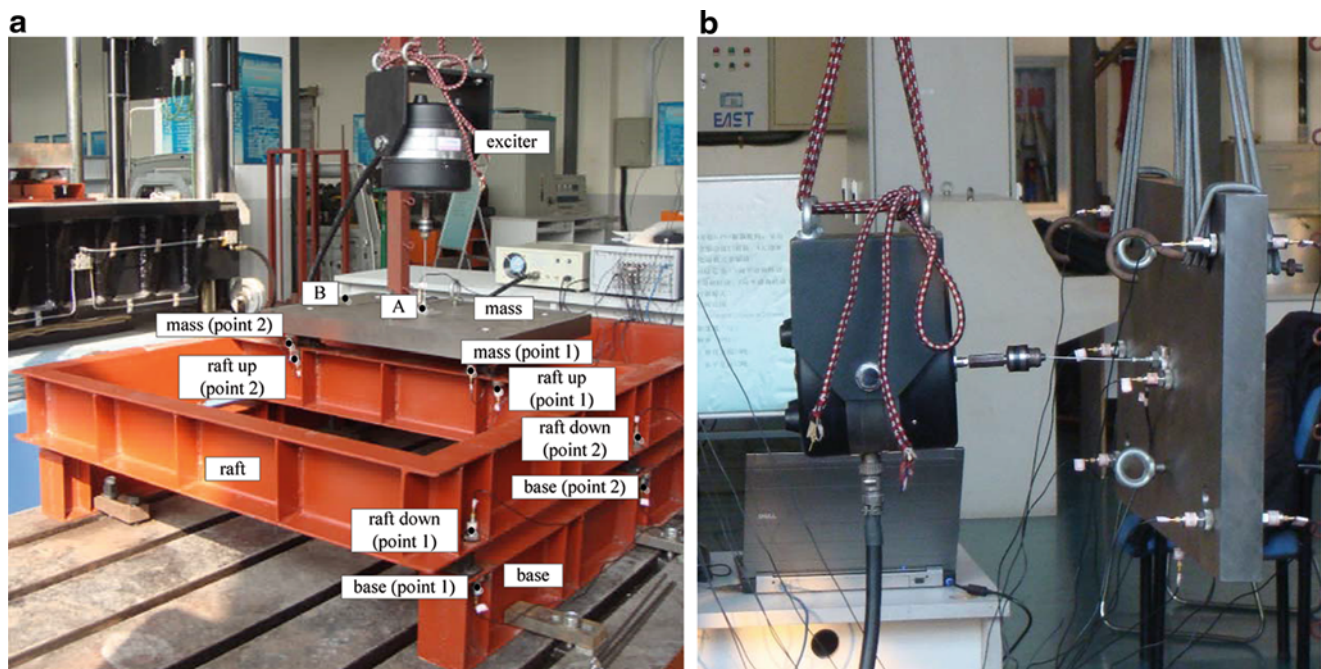


Fig. 7.1 The experimental set-up of measuring a floating raft system (a) and the mass (b)

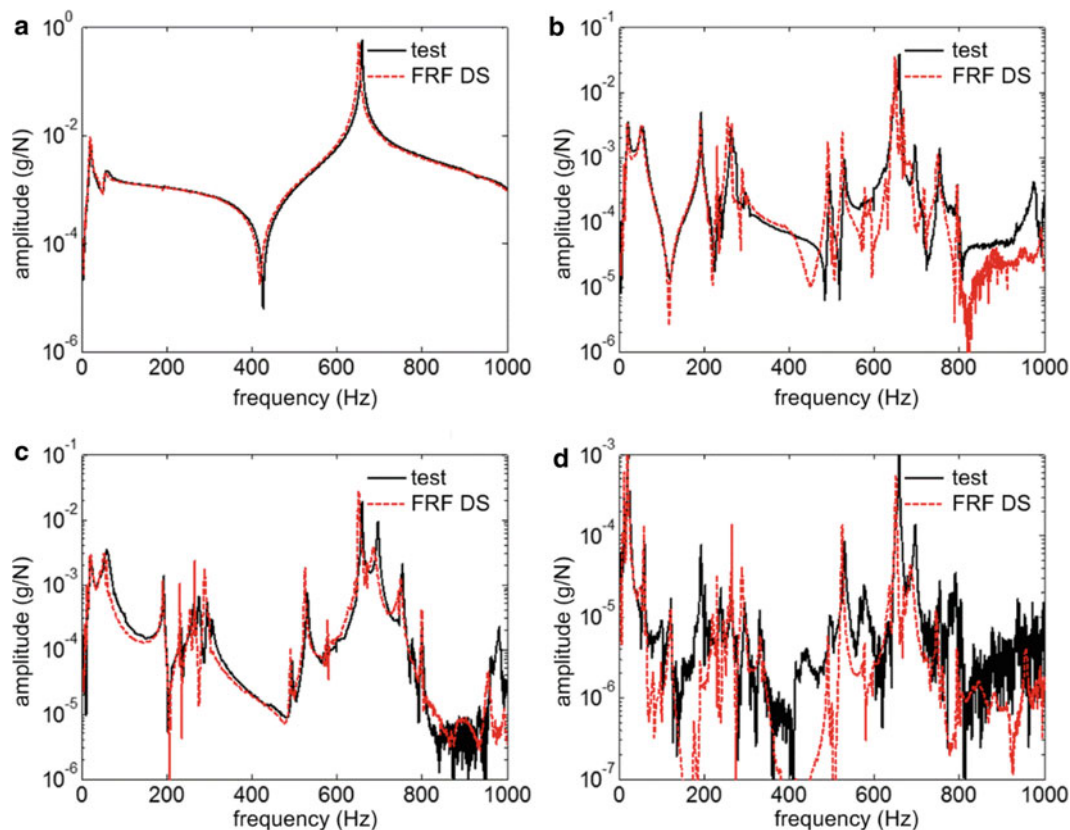


Fig. 7.2 The comparison of tested FRFs and the synthesis results for floating raft system under symmetric excitation. (a) driving-point FRF; (b) FRF between the driving point and the point 1 on up raft; (c) FRF between the driving point and the point 2 on down raft; (d) FRF between the driving point and the point 1 on base

the base is mixed with glitches due to the poor signal-to-noise ratio as a result of the two-stage vibration isolation; secondly, the bias between the excitation point on substructures when testing FRFs of substructures and the real connection points will introduce some errors; thirdly, the errors induced by the excitation system due to the coupling between the exciter and the system. One point worth attention is that, although the synthesis method is the same, unsymmetrical excitation introduces larger errors including some unpredicted new peaks. This is attributed to the fact that under unsymmetrical excitation, the isolator will undergo bending deformation due to the moment exerted on it, as shown in Fig. 7.4. Therefore the modes corresponding to the rotational DOFs are excited. If the rotational DOF does not accounted for, the peaks will not be reflected in the modeling results.

In a word, if the excitation is symmetric about the system, the DOFs in the vertical direction are enough to describe the vibration transmission in the system; while if the excitation is not symmetric about the system, the vibration transmission will also contain the contribution of bending deformation due to the moment. The influence is mainly concentrated on several discrete frequency points. Therefore, the rotational DOFs also play a very important role in the DS modeling of the system connected by elastic isolators.

7.3 Possible Ways to Improve the Accuracy of DS Modeling

To improve the accuracy of the DS modeling, it is necessary to include rotational DOFs of the substructures and improve the quality of the tested FRFs. For isolators, an experimental set-up is developed to identify the mobility of rotational DOFs; for substructures, the numerical models are employed to calculate the rotational FRFs and a conditioning method is advised to improve the credibility of the numerical FRFs. The truncated SVD is used to eliminate the measurement noise.

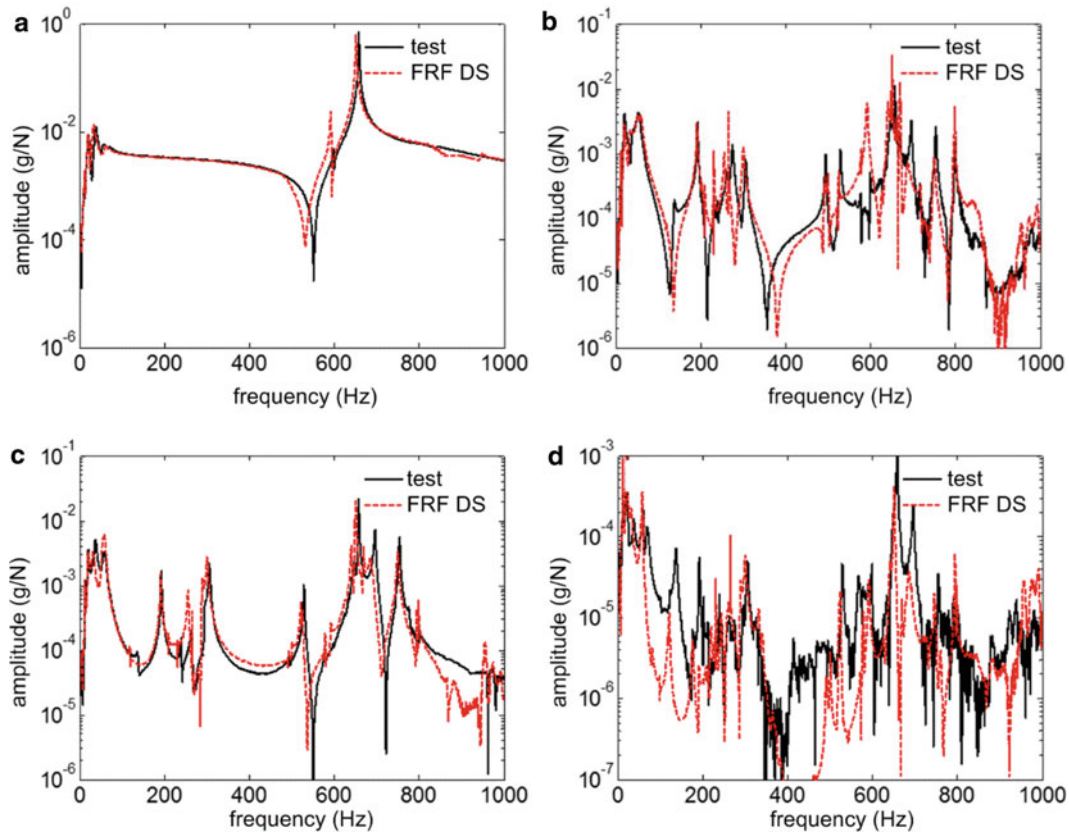
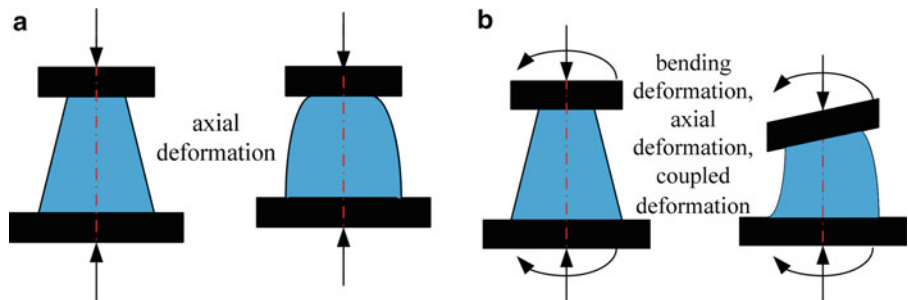


Fig. 7.3 The comparison of tested FRFs and the synthesis results for floating raft system under unsymmetrical excitation. (a)–(d) Same as in Fig. 7.2

Fig. 7.4 The axial deformation (a) and the coupled axial/bending deformation (b) of the isolator



7.3.1 Experimental Set-Up to Identify the Rotational Mobility of Isolators

The impedance of isolators has been studied extensively. While most effort is focused on translational DOFs. Literatures concerning the impedance of rotational DOFs are rare. The characterization method proposed by Kim and Singh can be applied to identify the rotational stiffness [13]. While there are two short backs, one is the characterization cannot take into account the static loading; the other is that the method cannot identify the impedance of the DOF corresponding to the torsional deformation of the isolator. Forrest [14] presented a method to measure the dynamics of isolators in free-free conditions and calculate the four-pole parameters. The natural frequencies, mode shapes and associated modal damping are applied to construct the FRFs in all DOFs, including coupling between different DOFs. For the same reason, the static load cannot be considered. As seen from the results in [15], the static load can influence the vibration transmission for troughs at higher frequencies. In what follows, an improved measurement set-up based on Lim and Singh that can consider the static load is proposed. The difference is the loading parts composed of several air springs, which support the system in a very low frequency simulating the free-free condition and provide static forces for the system by varying pressure in the air bags. The whole system is hung by the elastic cord. When exciting at point 1, the axial mobility can be identified; when exciting at point 2, the transverse mobility and the bending mobility can be identified (Fig. 7.5).

Fig. 7.5 The experimental set-up for characterization of isolators under static load

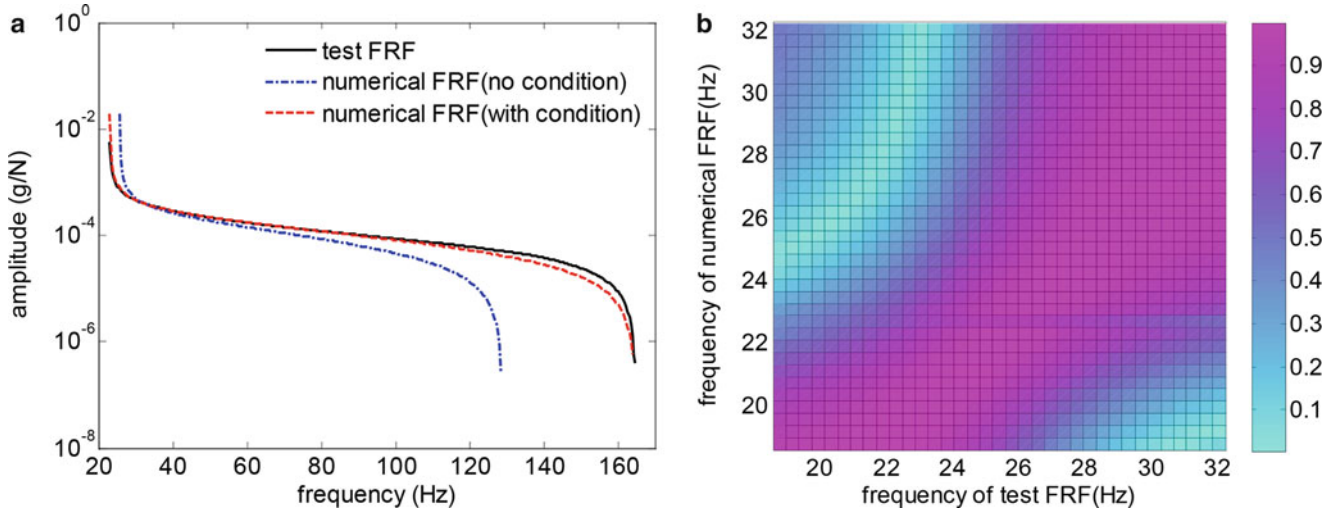
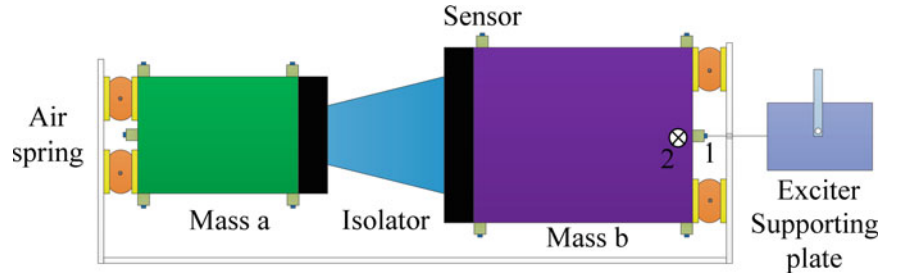


Fig. 7.6 Conditioning of FRFs of raft through piecewise linear interpolation (a) and the distribution of FDAC (b)

7.3.2 Filters to Condition the Numerical FRFs with the Measured FRFs

In a hybrid DS modeling, if some part of the FRF matrix for one substructure is from the measurement and the others are calculated from the numerical model. It is necessary to verify the credibility of the two FRFs, since they may have different resonances. One way is to update the numerical model, making the numerical FRFs coincide with the tested FRFs. This is a big challenge for a middle scale problem. Another method is proposed here. Suppose the tested FRFs are ‘exact’ and the FRFs of all DOFs have the same resonances (this may not hold for some situations), an algorithm is constructed to make both FRFs have the same resonances. Firstly, the two FRFs are analyzed to show their similarity at different frequencies. The Frequency Domain Assurance Criterion (FDAC) is defined to evaluate the level of similarity between the test and the numerical FRFs

$$FDAC(\omega_n, \omega_t, j) = \frac{\left(\{H_n(\omega_n)\}_j^T \{H_t(\omega_t)\}_j \right)}{\left| \{H_n(\omega_n)\}_j \right| \left| \{H_t(\omega_t)\}_j \right|} \quad (7.1)$$

where the subscript ‘ n ’ denotes numerical and ‘ t ’ denotes test; j represents the j th column of the FRF matrices. The value of FDAC is in $[-1, 1]$ with $FDAC > 0$ meaning the two FRFs are in phase. The closer the FDAC is to 1, the larger the level of similarity. A map between the resonances of the two FRFs are identified by FDAC. Then the whole FRF spectrum is divided into several segments by the resonances and a piecewise linear interpolation algorithm is performed to make the resonances coincide.

The analysis is performed on the FRFs of the same connection point, the result is shown in Fig. 7.6 and the FDAC is also shown. It can be seen that the deeper the color, the more relevant of the FRF at this frequency. The reconstructed FRF is compared with the tested FRF and the two FRFs almost coincide with each other after interpolation. However, if there are only tested FRFs for vertical DOF and the FRFs of other DOFs are to be filtered, it is more difficult since the anti-resonances are not the same for different FRFs. Another difficulty is determining the amplitude at the resonances or anti-resonances for the numerical FRFs. Thus there is still a long way to go.

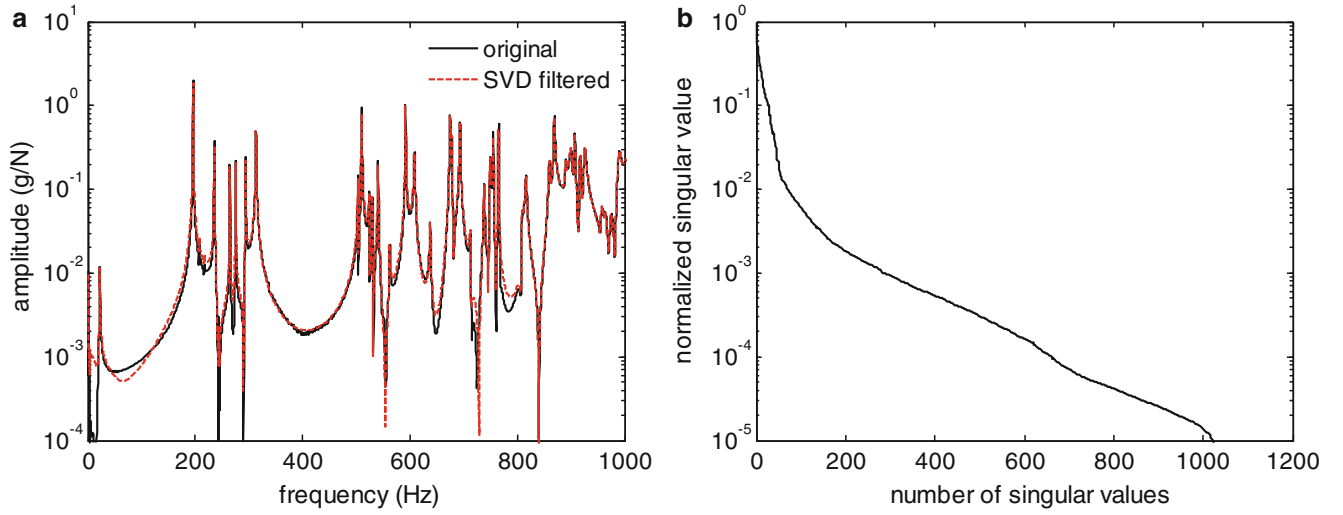


Fig. 7.7 Original and filtered FRFs of raft (a) and the normalized singular values (b)

7.3.3 Truncated SVD to Eliminate Measurement Noise

Although a lot of techniques such as averaging, filtering during the measurement and different FRF estimators for system identification (such as H_1 and H_2) have been used, it is impossible to perform noise-free measurements. If one wants to use the measured FRFs directly, the level of noise in the measured data determines the success of the analysis. Minimizing the noise content in FRFs after measurement is necessary to improve the quality of the measured data. The truncated SVD scheme is used to eliminate the measurement error. For a given FRF $\mathbf{H}_{ij}(\omega)$, which is composed of N discrete frequency points, $\mathbf{H}_{ij}(\omega) = [H_1, H_2 \dots H_N]^T$, the corresponding Impulse Response Function (IRF) can be obtained through FFT. Suppose the IRF is $\mathbf{h}_{ij}(t) = [h_1, h_2 \dots h_N]^T$, the Hackle matrix is formulated as

$$\mathbf{A}_{m \times n} = \begin{bmatrix} h_1 & h_2 & \dots & h_n \\ h_2 & h_3 & \dots & h_{n+1} \\ \dots & \dots & \dots & \dots \\ h_m & h_{m+1} & \dots & h_s \end{bmatrix} \quad (7.2)$$

where $m + n - 1 = s$, $\mathbf{A}_{ij} = h_{i+j-1}$. The SVD is performed $\mathbf{A} = \mathbf{U}\mathbf{D}\mathbf{V}$, where \mathbf{U} and \mathbf{V} are unitary matrices and \mathbf{D} contains the singular values. By retaining the first r singular values with threshold d_0 , i.e., $\mathbf{D}(r,r) > d_0\mathbf{D}(1,1)$ and $\mathbf{D}(r+1, r+1) < d_0\mathbf{D}(1,1)$, the filtered Hackle matrix is constructed by the reduced unitary matrix $\bar{\mathbf{A}} = \mathbf{U}_r\mathbf{D}_r\mathbf{V}_r$. The i th element of the filtered IRF is

$$\bar{h}_i = \frac{1}{k-l+1} \sum_{j=l}^k \bar{\mathbf{A}}_{i-j+1,j} \quad (l = \max(1, i-m+1), k = \min(n, i)) \quad (7.3)$$

where the length of \bar{h} is s , the filtered FRF $\bar{\mathbf{H}}(\omega)$ is obtained by IFFT.

The algorithm is carried out for one FRF of the raft. The threshold d_0 is chosen as 0.001. i.e., all the singular values which are larger than 0.1 % of the largest singular value are taken into account for each frequency line. The result is shown in Fig. 7.7. Generally speaking, it can be claimed that the noise has been smoothed out and FRF based on applying truncated SVD is significantly improved and of physical meaning. This is because the influence of measurement noise is reduced to some extent since the truncated SVD scheme can inherently deal with random errors.

7.4 Conclusion

This article describes a process for combining test-based and numerical-based models to perform DS modeling for a floating raft system containing multiple elastic connections. Difficulties concerning the modeling are pointed out. Three ways are proposed to improve the accuracy of the modeling. Careful application of the proposed measures may result in better prediction.

References

1. Ochsner SD, Bernhard RJ (1995) Application of a component mobility modeling technique to automotive suspension systems. *Noise Control Eng J* 43(3):73–82
2. Lim TC, Steyer GC (1992) Hybrid experimental-analytical simulation of structure-borne noise and vibration problems in automotive systems. *Journal of Passenger Cars* 101:585–591
3. Huizinga A, Van Campen D, De Kraker A (1997) Application of hybrid frequency domain substructuring for modelling an automotive engine suspension. *J Vib Acoust* 119(3):304–310
4. Mayes RL, Hunter PS, Simmermacher TW et al (2008) Combining experimental and analytical substructures with multiple connections. *Proceedings of the 26th international modal analysis conference, Orlando, FL*
5. Allen MS, Mayes RL (2007) Comparison of FRF and modal methods for combining experimental and analytical substructures. *Proceedings of the 25th international modal analysis conference, Orlando, FL (Bethel, CT)*
6. Duarte MLM (1996) Experimentally-derived structural models for use in further dynamic analysis. *University of London, London*
7. De Klerk D, Rixen D, Voormeeren S (2008) General framework for dynamic substructuring: history, review, and classification of techniques. *AIAA J* 46(5):1169–1181
8. Sanliturk K, Cakar O (2005) Noise elimination from measured frequency response functions. *Mech Syst Signal Process* 19(3):615–631
9. Gaul L, Moll W (2002) Substructuring using experimental modal data. *Proceeding of the 20th international modal analysis conference, Los Angeles, CA*
10. Carne TG, Dohrmann CR (2006) Improving experimental frequency response function matrices for admittance modeling. *Proceeding of the 24th international modal analysis conference, St. Louis, MO*
11. Huang XCh, Hua HX, Chen F, Xu ShY (2013) Uncertainty propagation in floating raft system by FRF-based substructuring method for elastic coupling. *Proceeding of the 31st international modal analysis conference, Garden Grove, CA*
12. Dickens J, Norwood C (2001) Universal method to measure dynamic performance of vibration isolators under static load. *J Sound Vib* 244(4):685–696
13. Kim S, Singh R (2001) Multi-dimensional characterization of vibration isolators over a wide range of frequencies. *J Sound Vib* 245(5):877–913
14. Forrest J (2006) Experimental modal analysis of three small-scale vibration isolator models. *J Sound Vib* 289(1–2):382–412
15. Norwood C, Dickens J (1998) The effect of vibration isolator properties and structural stiffness on isolator performance. *J Vib Control* 4(3):253–275

Chapter 8

Experimental Based Substructuring Using a Craig-Bampton Transmission Simulator Model

Mathew S. Allen, Daniel C. Kammer, and Randy L. Mayes

Abstract Recently, a new experimental based substructure formulation was introduced which reduces ill-conditioning due to experimental measurement noise by imposing the connection constraints on substructure modal coordinates instead of the physical interface coordinates. The experimental substructure is tested in a free-free configuration, and the interface is exercised by attaching a flexible transmission simulator. An analytical representation of the fixture is then used to subtract its effects from the experimental substructure. The resulting experimental component is entirely modal based, and can be attached in an indirect manner to other substructures by constraining the modal degrees of freedom of the transmission simulator to those substructures. This work explores a different alternative in which the transmission simulator is modeled with a Craig-Bampton model, a model that may be more appropriate when the interfaces are connected rigidly. The new method is compared to the authors' previous approaches to evaluate the errors due to modal truncation using finite element models of several beam systems including one in which the transmission simulator is connected to the component of interest at two points, potentially producing an ill-conditioned inverse problem.

Keywords Experimental substructures • Substructuring • Craig-Bampton

8.1 Introduction

Experimental-analytical substructuring is attractive in many applications where there is motivation to replace one subcomponent with an experimental model. For example, a component may be difficult to model if it contains materials with unknown properties, intricate geometry that would require many elements to approximate or joints or interfaces with unknown stiffness and damping properties. In other cases the component may be produced by an external supplier, in which case it may be inefficient to expend effort modeling a component that one cannot change. In any case, it will be necessary to test the component at some point in order to validate the computational model. In these scenarios, one can perform a careful dynamic test and extract an experimental-based model for the subcomponent(s) of interest. This model can then be coupled to finite element (or other) models for the rest of the structure to predict the response.

Substructuring can be used to couple physical or modal models of each subcomponent to create a model (e.g. a set of ordinary differential equations) for the assembly, or, for linear systems, one can also operate on the frequency responses directly to predict those of the assembled system. The latter approach is called frequency based substructuring or impedance coupling and an excellent review is provided in [1]. This work focuses on the former, which is commonly referred to as

Sandia National Laboratories is a multi-program laboratory managed and operated by Sandia Corporation, a wholly owned subsidiary of Lockheed Martin Corporation, for the U.S. Department of Energy National Nuclear Security Administration under Contract DE-AC04-94AL85000.

M.S. Allen (✉) • D.C. Kammer
Department of Engineering Physics, University of Wisconsin, Madison, WI 53706, USA
e-mail: msallen@engr.wisc.edu; kammer@engr.wisc.edu

R.L. Mayes
Structural Dynamics, Sandia National Laboratories, Albuquerque, NM, USA
e-mail: rlmayes@sandia.gov

modal substructuring, although the authors have found that frequency based substructuring and modal substructuring give similar results when the data sets used are identical [2, 3].

In [4] Allen, Mayes & Bergman presented a specific substructuring strategy, now known as the Transmission Simulator (TS) method, in which the component of interest is tested with a fixture known as the transmission simulator attached in order to improve the experimental model for the component. The transmission simulator allows one to capture the compliance and damping of the bolted joints at the interface, provides a means for dealing with continuous, compliant interfaces where one cannot easily reduce the interface to a few connection points, and improves the modal basis of the experimental component by exercising the interface. The disadvantage to this approach is that the transmission simulator must be modeled very accurately and its model must be subtracted from the experimental model, potentially introducing negative mass or stiffness [5, 6].

In the authors' previous works, the transmission simulator has always been modeled with a free interface. More specifically, the modal model for the TS was described by up to six rigid body modes and a collection of elastic modes where all of the connection points were free. This basis may not be ideal in some applications, especially when the TS is rigidly connected to a stiff structure of interest. This work explores a new alternative where a Craig-Bampton model of the TS is created and subtracted from the experimental measurements. Hence, the modal basis is described by the fixed-interface modes of the TS rather than its free modes, and this has been found to improve the results in a few test cases.

The following section reviews the theory underlying the transmission simulator method and how the transmission simulator model is replaced with a Craig-Bampton model. The method is evaluated on a T-shaped beam structure in Sect. 8.3 and conclusions are presented in Sect. 8.4.

8.2 Theoretical Development

8.2.1 Free-Free Modal Transmission Simulator (FF-TS)

The transmission simulator method is explained in detail in [4, 7, 8] so only a cursory review will be presented here. One is presumed to have a finite element model of the transmission simulator, denoted substructure A, and this can be used to compute its mode shapes, Φ^A , natural frequencies, ω_r^A , $r = 1 \dots n_A$ and its modal damping ratios, ζ_r^A are also presumed to be known (e.g. they are typically taken to be half of the loss modulus of the material). In the traditional approach, these are computed with the interface degrees of freedom free, and hence the first few modes are rigid body modes. An actual physical transmission simulator is also constructed and attached to the substructure of interest, denoted B, and the assembly, denoted C, is tested to identify its modal parameters. The equations of motion of C and (-A) can then be concatenated as follows

$$\begin{bmatrix} \mathbf{I}^C & \mathbf{0} \\ \mathbf{0} & -\mathbf{I}^A \end{bmatrix} \begin{Bmatrix} \ddot{\mathbf{q}}^C \\ \ddot{\mathbf{q}}^A \end{Bmatrix} + \begin{bmatrix} [2\zeta_r \omega_r] & \mathbf{0} \\ \mathbf{0} & -[2\zeta_r \omega_r] \end{bmatrix} \begin{Bmatrix} \dot{\mathbf{q}}^C \\ \dot{\mathbf{q}}^A \end{Bmatrix} + \begin{bmatrix} [\omega_r^2] & \mathbf{0} \\ \mathbf{0} & -[\omega_r^2] \end{bmatrix} \begin{Bmatrix} \mathbf{q}^C \\ \mathbf{q}^A \end{Bmatrix} = \begin{Bmatrix} (\Phi^C)^T \mathbf{F}^C \\ (\Phi^A)^T \mathbf{F}^A \end{Bmatrix} \quad (8.1)$$

$$\begin{Bmatrix} \mathbf{u}^C \\ \mathbf{u}^A \end{Bmatrix} = \begin{bmatrix} \Phi^C & \mathbf{0} \\ \mathbf{0} & \Phi^A \end{bmatrix} \begin{Bmatrix} \mathbf{q}^C \\ \mathbf{q}^A \end{Bmatrix}$$

where the DOF, \mathbf{q} , are the generalized modal coordinates of each substructure. Let the set of degrees of freedom where the TS joins the substructure be denoted as the c-set (or connection point set). Then one would ideally enforce equal motion between substructure C and the TS at these points.

$$\mathbf{u}_c^C = \mathbf{u}_c^A \quad (8.2)$$

However, this leads to several difficulties and hence Allen, Mayes & Bergman, instead defined a set of measurement points that completely characterize the transmission simulator (e.g. so that Φ_m^A is full rank). Then the following constraints are enforced, which constrain all of the modes of the transmission simulator to their projection onto the motion of C,

$$\begin{bmatrix} (\Phi_m^A)^\dagger \Phi_m^C & -\mathbf{I}^A \end{bmatrix} \begin{Bmatrix} \mathbf{q}^C \\ \mathbf{q}^A \end{Bmatrix} = \mathbf{0} \quad (8.3)$$

where, $()^\dagger$, denotes the pseudo-inverse of the matrix $()$. These constraints are enforced using the transformation $[\mathbf{q}_C^T \quad \mathbf{q}_A^T]^T = \mathbf{B}\mathbf{q}_C$ where $\mathbf{B} = \left[(\mathbf{I}^C)^T \quad \left((\Phi_m^A)^\dagger \Phi_m^C \right)^T \right]^T$ is in the null space of the constraint matrix, the matrix on the left in Eq. (8.3).

This method will only succeed in proportion to how well the modes of the transmission simulator, Φ_m^A , span the space of the motions observed on C, or Φ_m^C . While the free-interface modes have worked well in the cases studied so far, the authors have noted cases where these modes did not adequately span the space of the observed motions (see, e.g. [5]), leading to less accurate results or negative mass in the assembled system. Furthermore, it would be preferable to obtain a Craig-Bampton model for the subcomponent, with its constraint modes that capture the interface stiffness and allow it to accurately capture the motion of the subcomponent when it is connected to a variety of structures.

8.2.2 Craig-Bampton Transmission Simulator

In order to create a Craig-Bampton (CB) model of the transmission simulator, the physical displacement vector for substructure A is partitioned into two sets, the c-set, corresponding to the connection degrees of freedom, and the o-set, corresponding to the interior degrees of freedom (DOF). The resulting partitioned mass and stiffness matrices can be written as

$$\mathbf{M}^A = \begin{bmatrix} \mathbf{M}_{oo}^A & \mathbf{M}_{oc}^A \\ \mathbf{M}_{co}^A & \mathbf{M}_{cc}^A \end{bmatrix} \quad \mathbf{K}^A = \begin{bmatrix} \mathbf{K}_{oo}^A & \mathbf{K}_{oc}^A \\ \mathbf{K}_{co}^A & \mathbf{K}_{cc}^A \end{bmatrix} \quad (8.4)$$

The displacement vector for component A can be transformed into CB [9] coordinates using the relation

$$\mathbf{u}^A = \begin{Bmatrix} \mathbf{u}_o^A \\ \mathbf{u}_c^A \end{Bmatrix} = \begin{bmatrix} \widehat{\Phi}^A & \Psi^A \\ \mathbf{0} & \mathbf{I}_c \end{bmatrix} \begin{Bmatrix} \widehat{\mathbf{q}}^A \\ \mathbf{u}_c^A \end{Bmatrix} = \mathbf{T}_{CB}^A \mathbf{u}_{CB}^A \quad (8.5)$$

where $\widehat{\Phi}^A$ is a matrix of n_A fixed-interface modes, $\Psi^A = -(\mathbf{K}_{oo}^A)^{-1}\mathbf{K}_{oc}^A$, \mathbf{I}_c is an identity matrix of order equal to the number of interface DOF, $\widehat{\mathbf{q}}^A$ is the vector of displacements of the fixed-interface modes, and \mathbf{u}_c^A represents the physical displacement of the interface. The CB representation describes the deformation of the transmission simulator in terms of dynamic fixed-interface modes, and static shapes, called constraint modes $\Psi^A = \left[(\Psi^A)^T \quad \mathbf{I}_c \right]^T$, in which each column gives the static response of component A due to a unit deflection of one of the interface DOF holding the others fixed. The corresponding CB mass and stiffness matrices are then given by

$$\mathbf{M}_{CB}^A = (\mathbf{T}_{CB}^A)^T \mathbf{M}^A \mathbf{T}_{CB}^A = \begin{bmatrix} \mathbf{I}^A & \mathbf{M}_{qc}^A \\ \mathbf{M}_{cq}^A & \mathbf{M}_S^A \end{bmatrix} \quad (8.6)$$

$$\mathbf{K}_{CB}^A = (\mathbf{T}_{CB}^A)^T \mathbf{K}^A \mathbf{T}_{CB}^A = \begin{bmatrix} \left[\widehat{\omega}_{r_i}^2 \right]^A & 0 \\ 0 & \mathbf{K}_S^A \end{bmatrix} \quad (8.7)$$

where it has been assumed that the fixed-interface modes have been mass normalized, $\left[\widehat{\omega}_{r_i}^2 \right]^A$ is a diagonal matrix of fixed-interface modal frequencies, and \mathbf{M}_S^A and \mathbf{K}_S^A are the component A mass and stiffness matrices statically reduced to the interface DOF, respectively. As mentioned previously, the advantage of this transmission simulator representation over a free-free modal representation is that the fixed-interface modes do a better job of representing the shape of the simulator in the coupled system being tested, and the physical interface DOF are directly retained for connection to other substructures.

The CB representation of component A must now be subtracted from the experimental modal representation of the combined system C. The authors have explored two methods for doing this, which will be outlined in the following two subsections.

8.2.2.1 Method 1: Free Modes of Craig Bampton Model (CB-TS)

The CB representation of substructure A has the following equation of motion (omitting the damping terms for simplicity)

$$\mathbf{M}_{CB}^A \ddot{\mathbf{u}}_{CB}^A + \mathbf{K}_{CB}^A \mathbf{u}_{CB}^A = (\mathbf{T}_{CB}^A)^T \mathbf{F}^A \quad (8.8)$$

This model can then replace the model for A in Eq. (8.1), so the concatenated equations become,

$$\begin{aligned} \begin{bmatrix} \mathbf{I}^C & 0 \\ 0 & -\mathbf{M}_{CB}^A \end{bmatrix} \begin{Bmatrix} \ddot{\mathbf{q}}^C \\ \ddot{\mathbf{u}}_{CB}^A \end{Bmatrix} + \begin{bmatrix} [\backslash \omega_r^2 \backslash]^C & \mathbf{0} \\ \mathbf{0} & -\mathbf{K}_{CB}^A \end{bmatrix} \begin{Bmatrix} \mathbf{q}^C \\ \mathbf{u}_{CB}^A \end{Bmatrix} &= \begin{Bmatrix} (\Phi^C)^T \mathbf{F}^C \\ (\mathbf{T}_{CB}^A)^T \mathbf{F}^A \end{Bmatrix} \\ \begin{Bmatrix} \mathbf{u}^C \\ \mathbf{u}^A \end{Bmatrix} &= \begin{bmatrix} \Phi^C & \mathbf{0} \\ \mathbf{0} & \mathbf{T}_{CB}^A \end{bmatrix} \begin{Bmatrix} \mathbf{q}^C \\ \mathbf{u}_{CB}^A \end{Bmatrix} \end{aligned} \quad (8.9)$$

In keeping with the modal constraint philosophy, all of the modes of the transmission simulator will be coupled to their projection on C, using the following constraints, where once again the measurement set, m , includes enough sensors to fully characterize the motion of the transmission simulator.

$$\begin{bmatrix} (\mathbf{T}_{CB,m}^A)^\dagger \Phi_m^C & -\mathbf{I}^A \end{bmatrix} \begin{Bmatrix} \mathbf{q}^C \\ \mathbf{u}_{CB}^A \end{Bmatrix} = 0 \quad (8.10)$$

Since the model for substructure A is known, after assembling the system one can recover the response at any point on A (including the connection point \mathbf{u}_c^A , both displacement and rotation!) using Eq. (8.5). Hence, one can estimate the fixed-interface modes of the B system by applying the constraints $\mathbf{u}_c^A = 0$ by defining an appropriate transformation matrix, \mathbf{B} , and then using the procedure outlined above. It is also interesting to note that one could obtain the same result by using the CB model to estimate the free-interface modes of the TS and then using those in Eq. (8.1) together with the usual transmission simulator approach. The free-interface modes thus estimated would not be the true free-interface modes but simply another basis for the CB model, and hence this would produce the exact same result as the procedure outlined in Eqs. (8.9) and (8.10). In fact, this approach was used in this computations described in Sect. 8.3.

8.2.2.2 Method 2: Motion Relative to the Interface (CB-IP)

The method presented in the previous section is clearly very different from the way in which Craig Bampton models have been employed in the analytical domain over the past several decades. Specifically, no effort was made to retain the structure of the CB model nor the partition of interface degrees of freedom as unique coordinates. Hence, an alternative is presented here, which will be denoted CB-IP for ‘‘Interface Preserving.’’

Once again, following the modal constraint approach [4], coupling will be accomplished by enforcing physical displacement compatibility between the two components at the measured locations

$$\mathbf{u}_m^A - \mathbf{u}_m^C = 0 \quad (8.11)$$

where it is assumed that none of the connection DOF are in the set of measured locations. Transforming to CB coordinates for component A and modal coordinates for experimental component C, Eq. (8.11) becomes

$$\widehat{\Phi}_m^A \widehat{\mathbf{q}}^A + \psi_m^A \mathbf{u}_c^A - \Phi_m^C \mathbf{q}^C = 0 \quad (8.12)$$

in which the subscript m indicates a row partition corresponding to the measured DOF. Equation (8.12) can be solved for the transmission simulator fixed-interface modal response

$$\widehat{\mathbf{q}}^A = \widehat{\Phi}_m^{A\dagger} [\Phi_m^C \mathbf{q}^C - \psi_m^A \mathbf{u}_c^A] \quad (8.13)$$

where $\widehat{\Phi}_m^{A\dagger} = \left[\widehat{\Phi}_m^{AT} \widehat{\Phi}_m^A \right]^{-1} \widehat{\Phi}_m^{AT}$ is the generalized inverse of the fixed-interface modes row partitioned to the measurement locations. The existence of this inverse requires that matrix $\widehat{\Phi}_m^A$ is full column rank, implying that $n_m \geq n_A$. Notice that the constraints here can be viewed as projecting the motion of C relative to the interface onto the fixed-interface modes of A.

The modal constraint can be applied by defining the coordinate transformation

$$\mathbf{u}_G = \begin{Bmatrix} \mathbf{q}^C \\ \widehat{\mathbf{q}}^A \\ \mathbf{u}_c^A \end{Bmatrix} = \mathbf{T} \mathbf{u}_r = \begin{bmatrix} \mathbf{I} & 0 \\ \widehat{\Phi}_m^{A\dagger} \Phi_m^C & -\widehat{\Phi}_m^{A\dagger} \psi_m^A \\ 0 & \mathbf{I} \end{bmatrix} \begin{Bmatrix} \mathbf{q}^C \\ \mathbf{u}_c^A \end{Bmatrix} \quad (8.14)$$

Applying the constraint to the uncoupled system in Eq. (8.9) gives the approximation of the equation of motion for the experimental based substructure B

$$\tilde{\mathbf{M}}^B \ddot{\mathbf{u}}^B + \tilde{\mathbf{K}}^B \mathbf{u}^B = \mathbf{T}^T \begin{Bmatrix} (\Phi^C)^T \mathbf{F}^C \\ (\mathbf{T}_{CB}^A)^T \mathbf{F}^A \end{Bmatrix} \quad (8.15)$$

in which the reduced displacement vector \mathbf{u}_r in Eq. (8.14) has been renamed \mathbf{u}^B where

$$\mathbf{u}^B = \begin{Bmatrix} \widehat{\mathbf{q}}^B \\ \mathbf{u}_c^B \end{Bmatrix} \quad (8.16)$$

and

$$\tilde{\mathbf{M}}^B = \mathbf{T}^T \begin{bmatrix} \mathbf{I}^C & 0 \\ 0 & -\mathbf{M}_{CB}^A \end{bmatrix} \mathbf{T} = \begin{bmatrix} \mathbf{I}^C - \tau^T \tau & \tau^T \psi - \tau^T \mathbf{M}_{qc}^A \\ \psi^T \tau - \mathbf{M}_{cq}^A \tau & \mathbf{M}_{cq}^A \psi + \psi^T \mathbf{M}_{qc}^A - \psi^T \psi - \mathbf{M}_S^A \end{bmatrix} \quad (8.17)$$

$$\tilde{\mathbf{K}}^B = \mathbf{T}^T \begin{bmatrix} \left[\backslash \widehat{\omega}_{r\backslash}^2 \right]^C & 0 \\ 0 & -\mathbf{K}_{CB}^A \end{bmatrix} \mathbf{T} = \begin{bmatrix} \left[\backslash \widehat{\omega}_{r\backslash}^2 \right]^C - \tau^T \left[\backslash \widehat{\omega}_{r\backslash}^2 \right]^A \tau & \tau^T \left[\backslash \widehat{\omega}_{r\backslash}^2 \right]^A \psi \\ \psi^T \left[\backslash \widehat{\omega}_{r\backslash}^2 \right]^A \tau & -\psi^T \left[\backslash \widehat{\omega}_{r\backslash}^2 \right]^A \psi - \mathbf{K}_S^A \end{bmatrix} \quad (8.18)$$

with $\tau = \widehat{\Phi}_m^{A\dagger} \Phi_m^C$ and $\psi = \widehat{\Phi}_m^{A\dagger} \psi_m^A$. The substructure representation for component B, given by Eqs. (8.17) and (8.18), is not precisely a CB representation because the stiffness matrix is not block diagonal. However, it is CB-like in that the displacement vector \mathbf{u}^B contains modal degrees of freedom $\widehat{\mathbf{q}}^B$, and the physical degrees of freedom \mathbf{u}_c^B at the points where component B will connect to other substructures. The experimental based representation for component B can then be easily connected to other FEM based substructures using traditional assembly methods. However, unlike the CB representation, the modal degrees of freedom cannot be truncated based on frequency due to the stiffness coupling between the modal and interface DOF in Eq. (8.18).

An advantage of the proposed component B substructure representation is that the fixed-interface modes and frequencies can be determined directly by just crossing out the block row and column associated with the interface DOF. The resulting constrained interface mass and stiffness matrices, $\tilde{\mathbf{M}}_c^B$ and $\tilde{\mathbf{K}}_c^B$, just correspond to the expressions in the upper-left quadrants of the matrices in Eqs. (8.17) and (8.18). Therefore, the fixed-interface modes and frequencies of component B can be derived from a free-free vibration test of the composite system C including the transmission simulator. If the proper number of free-free experimental modes for component C and fixed-interface modes from the transmission simulator are retained in the analysis, the matrices $\tilde{\mathbf{M}}_c^B$ and $\tilde{\mathbf{K}}_c^B$ should both be positive definite. Further details regarding this approach can be found in [10].

8.3 Numerical Examples

This new approach was explored by applying it to two systems, one of which was studied in a previous work [10]. The second system contains two connection points (statically indeterminate interface) and was developed specifically for this work.

Fig. 8.1 Schematic of the T-beam substructuring problem. The goal is to experimentally derive a model of component B, the horizontal (cyan) beam, from measurements of the assembly C

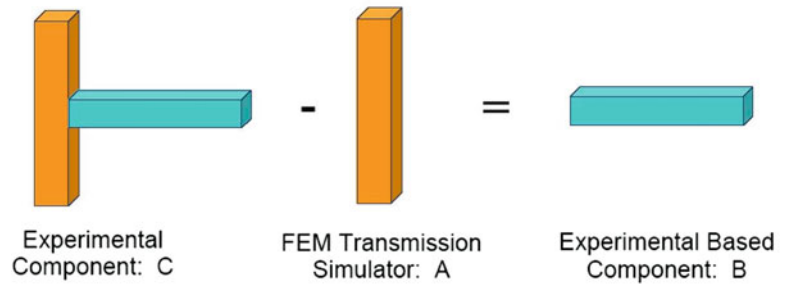


Table 8.1 Free-interface modes of component B estimated by each substructuring approach

| N | Actual | CB-IP (Craig Bampton) | | FF-TS (Free-Interface) | | | CB-TS (Craig Bampton) | | |
|----|---------|-----------------------|---------|------------------------|-----------|---------|-----------------------|-----------|---------|
| | FEA | Freq (Hz) | % Error | N | Freq (Hz) | % Error | N | Freq (Hz) | % Error |
| 4 | 45.4 | 45.4 | 0.01 | 4 | 45.4 | 0.00 | 4 | 45.4 | 0.00 |
| 5 | 125.1 | 125.1 | 0.00 | 5 | 125.1 | 0.00 | 5 | 125.1 | 0.00 |
| 6 | 245.3 | 245.4 | 0.02 | 6 | 245.3 | 0.00 | 6 | 245.3 | 0.00 |
| 7 | 405.5 | 405.7 | 0.05 | 7 | 405.5 | 0.00 | 7 | 405.6 | 0.01 |
| 8 | 605.8 | 606.5 | 0.12 | 8 | 605.8 | 0.01 | 8 | 606.0 | 0.03 |
| 9 | 846.1 | 848.1 | 0.23 | 9 | 846.2 | 0.01 | 9 | 846.6 | 0.05 |
| 10 | 1,126.5 | 1,131.2 | 0.42 | 10 | 1,126.8 | 0.02 | 10 | 1,127.5 | 0.09 |
| 11 | 1,447.0 | 1,457.5 | 0.72 | 11 | 1,447.5 | 0.04 | 11 | 1,449.0 | 0.14 |
| 12 | 1,807.6 | 1,829.6 | 1.22 | 13 ^a | 1,808.6 | 0.05 | 12 | 1,811.3 | 0.20 |
| 13 | 2,118.7 | 2,118.4 | -0.01 | 14 | 2,118.8 | 0.00 | 13 | 2,128.9 | 0.48 |
| 14 | 2,208.3 | 2,253.5 | 2.05 | 15 | 2,210.1 | 0.08 | 14 | 2,214.8 | 0.30 |
| 15 | 2,649.2 | 2,741.3 | 3.48 | 16 | 2,652.3 | 0.12 | 15 | 2,660.3 | 0.42 |
| 16 | 3,130.3 | | | 18 ^a | 3,135.4 | 0.16 | 17 ^a | 3,148.8 | 0.59 |
| 17 | 3,651.7 | | | 19 | 3,659.8 | 0.22 | 18 | 3,682.1 | 0.83 |
| 18 | 4,213.6 | | | 20 | 4,226.1 | 0.30 | 19 | 4,265.3 | 1.23 |
| 19 | 4,237.3 | | | 21 | 4,237.4 | 0.00 | 20 | 4,480.4 | 5.74 |
| 20 | 4,816.0 | | | 22 | 4,836.4 | 0.42 | 21 | 4,929.8 | 2.36 |

^aSpurious modes were omitted from the table

8.3.1 T-Beam System from [10]

The first system studied is the T-beam system shown in Fig. 8.1, which was used in [10] to demonstrate the method that will be denoted the CB-IP method here. The transmission simulator is a 24-in. long steel beam with 0.5 by 0.5-in. cross section while the structure of interest, component B, is a 36-in. long steel beam with 0.35 by 0.5-in. cross section. Note that this system's TS is significantly more flexible than that used in [4–6], so it is more difficult to subtract from the assembly. Further details regarding the setup are provided in [10]. As in the cited works, finite element models for these beams will be used to simulate substructuring by truncating the modal basis.

As in [10], the frequency range of interest is 0–2,500 Hz, so 24 modes of C are retained with natural frequencies ranging from 0 Hz (three rigid body modes) to 4,780 Hz, or over about twice the frequency range of interest. In [10], 13 fixed-interface modes were used to describe substructure A, with the highest mode at 15.9 kHz, and after applying 13 constraints a model for B was obtained. As a first step in evaluating the success of the substructuring calculations, the free modes of component B were calculated, and they are compared to those of the FEA truth model in Table 8.1 in the column labeled CB-IP.

The same process was repeated using the traditional transmission simulator method with free-interfaces modes, the FF-TS method, and the result of that calculation is compared with the proposed method which uses a Craig-Bampton model to describe the transmission simulator, the CB-TS method, and those results are also shown in Table 8.1. Both of these models used 10 modes to describe the transmission simulator, 3 rigid body modes plus 7 free-interface elastic modes for the FF-TS method and 3 constraint modes plus 7 fixed-interface modes for the CB-TS method. These modes spanned a frequency range of 0–13.7 kHz for the FF-TS method and 0–8.4 kHz for the CB-TS method. Note that because the interface (connection point) is at the center of the transmission simulator, its fixed interface modes came in pairs in which either the top or bottom vibrated as a cantilever while other side remained stationary. As a result, a larger number of modes would be required to span the same frequency range.

Table 8.2 Fixed-interface modes of component B estimated by each substructuring approach

| N | Actual | CB-IP (Craig Bampton) | | | FF-TS (Free-Interface) | | | CB-TS (Craig Bampton) | | |
|----|---------|-----------------------|-----------|---------|------------------------|-----------|---------|-----------------------|-----------|---------|
| | FEA | N | Freq (Hz) | % Error | N | Freq (Hz) | % Error | N | Freq (Hz) | % Error |
| 1 | 7.127 | 1 | 7.14 | 0.18 | 1 | 7.07 | -0.80 | 1 | 7.127 | 0.00 |
| 2 | 44.707 | 2 | 44.71 | 0.01 | 2 | 44.36 | -0.78 | 2 | 44.707 | 0.00 |
| 3 | 125.19 | 3 | 125.2 | 0.00 | 3 | 124.2 | -0.77 | 3 | 125.18 | 0.00 |
| 4 | 245.32 | 4 | 245.3 | 0.00 | 4 | 243.45 | -0.76 | 4 | 245.30 | -0.01 |
| 5 | 405.53 | 5 | 405.5 | 0.00 | 5 | 402.48 | -0.75 | 5 | 405.49 | -0.01 |
| 6 | 605.80 | 6 | 605.8 | 0.00 | 6 | 601.30 | -0.74 | 6 | 605.71 | -0.01 |
| 7 | 846.12 | 7 | 846.2 | 0.01 | 7 | 839.91 | -0.74 | 7 | 845.95 | -0.02 |
| 8 | 1,059.3 | 8 | 1,059.3 | 0.00 | 8 | 808.03 | -23.72 | 8 | 1,059.3 | 0.00 |
| 9 | 1,126.5 | 9 | 1,126.6 | 0.01 | 9 | 1,118.3 | -0.73 | 9 | 1,126.2 | -0.03 |
| 10 | 1,447.0 | 10 | 1,447.1 | 0.01 | 10 | 1,436.5 | -0.72 | 10 | 1,446.5 | -0.04 |
| 11 | 1,807.6 | 11 | 1,807.8 | 0.01 | 11 | 1,794.6 | -0.72 | 11 | 1,806.8 | -0.04 |
| 12 | 2,208.3 | 12 | 2,208.6 | 0.01 | 13 ^a | 2,192.6 | -0.71 | 12 | 2,207.1 | -0.06 |
| 13 | 2,649.2 | 13 | 2,649.5 | 0.01 | 14 | 2,630.4 | -0.71 | 13 | 2,647.4 | -0.07 |
| 14 | 3,130.3 | 16 ^a | 3,130.7 | 0.01 | 16 ^a | 3,108.3 | -0.70 | 15 ^a | 3,127.8 | -0.08 |
| 15 | 3,178.0 | 17 | 3,178.0 | 0.00 | 17 | 3,672.1 | 15.55 | 16 | 3,178.1 | 0.00 |
| 16 | 3,651.7 | 18 | 3,652.3 | 0.01 | 18 | 3,626.2 | -0.70 | 17 | 3,648.2 | -0.10 |
| 17 | 4,213.6 | 19 | 4,214.2 | 0.01 | 19 | 4,184.3 | -0.70 | 18 | 4,208.6 | -0.12 |
| 18 | 4,816.0 | 20 | 4,815.5 | -0.01 | 20 | 4,782.5 | -0.69 | 19 | 4,809.4 | -0.14 |
| 19 | 5,296.6 | 21 | 5,327.3 | 0.58 | — | — | — | 20 | 6,289.3 | 18.74 |
| 20 | 5,459.2 | 22 | 5,498.4 | 0.72 | — | — | — | — | — | — |
| 21 | 6,143.3 | — | — | — | 21 | 6,915.0 | 26.67 | — | — | — |

^aSpurious modes were omitted from the table

The results show that, while any of the methods produces good estimate of the B system's free-free natural frequencies in the frequency range of interest, the traditional FF-TS method is somewhat more accurate than the others. This is, perhaps, to be expected since our goal is to obtain a Craig-Bampton-like model for system B, and while a Craig-Bampton model would be excellent at describing B in an assembly, it might not produce the best results when the interface is free or lightly coupled. In those cases another subcomponent model, such as a Craig-Chang model [11], would probably be preferred and the FF-TS method produces a model that is more along those lines. On the other hand, the table also shows the mode number of each mode that is being compared in the column labeled "N." The modes were matched using a MAC and so only modes that were similar are compared in the table. The FF-TS and CB-TS methods both show gaps in the mode number. The modes that are not shown had purely imaginary natural frequencies and hence were not included. The one exception was mode 12 in the FF-TS method which appeared to be reasonable. The gaps reveal that the first spurious mode occurred above 1,400 Hz (after the 11th mode) for the FF-TS method and not until above 2,660 Hz (after the 15th mode) for the CB-TS method. This could suggest that the CB-TS method captures the deformation of the transmission simulator more effectively.

When the component of interest will be connected to a fairly rigid substructure, it may be more important for the substructure model to accurately predict the component's fixed-interface modes rather than its free modes. The fixed-interface modes of each of the substructure models were derived by constraining the three interface DOF as mentioned in Sects. 8.2.2.1 and 8.2.2.2. Then the fixed-interface natural frequencies were found and are compared in Table 8.2.

The results in Table 8.2 show that the methods that use a Craig Bampton basis to describe the transmission simulator produced considerably more accurate predictions of the fixed-interface modes. Indeed, both the CB-IP and CB-TS methods estimated all of the natural frequencies below 5 kHz (twice the bandwidth of interest) with less than 0.2 % error. The errors for the CB-IP method are somewhat lower, although any of these modal truncation errors would probably be negligible relative to measurement errors when the methods are applied in practice. In contrast, while the natural frequencies predicted by the FF-TS method are quite reasonable for most of the modes (typically below 1 %), the errors in modes 8 and 17 were quite large and the model contains a larger number of spurious modes. To diagnose this, the number of modes used to describe the TS in the FF-TS method was varied between 3 and 11. In all cases the FF-TS method predicted a reasonable number of free-interface modes correctly (e.g. with errors in the natural frequencies below 1 %). It also gave reasonable estimates for the lower fixed-interface modes, with about 2 % maximum error over the first eight modes for $n_A = 3$ decreasing to less than 9 % maximum error (1.5 % average error) for the first 15 modes for $n_A = 8$. As more modes were added to the TS modes 8 and 17 began to degrade as seen above while the other natural frequencies became even more accurate. In contrast, the CB-TS method gave excellent predictions for the fixed-interface modes for $n_A > 5$, with all of the lower natural frequencies having less than 1 % errors.

These results are somewhat surprising. While one would expect that, if one could create a Craig Bampton model for subcomponent B, that it would do an excellent job of predicting the fixed interface modes (actually the result would be perfect since the CB model contains the fixed-interface modes). However, here we have used a relatively small number of the free modes of the assembly C and a CB model for A to derive an approximate CB model for B by computing $B = (C-A)$, and the result is excellent!

As has been mentioned in the authors' previous works [5, 6], when one substructure is subtracted from another it is possible for the mass matrix to become indefinite (contain negative eigenvalues), and these in turn tend to produce additional spurious modes in the substructuring predictions. The authors presented two algorithms in [6] to address this issue. The Craig-Bampton method presented in this work is essentially interchangeable with the FF-TS method in the authors previous works, so the same algorithms can be used to force positive mass when substructuring. This was explored here by using the "Added Mass" method in [6] to add mass to the substructure model for B until its mass matrix became positive definite. This algorithm was used to correct the models for B for the case presented in Tables 8.1 and 8.2 by adding the minimum amount of mass which caused the mass matrix to become positive definite. For the FF-TS method the mass added was 0.65 % of the total mass of substructure B, while for the CB-TS method only 0.00015 % mass had to be added. The added mass didn't change the CB-TS results appreciably. On the other hand, for the FF-TS method it was surprising to see that the added mass dramatically improved the predictions of 8th and 17th fixed interface modes, reducing the errors in those natural frequencies just a few percent. All of these results suggest that a Craig-Bampton model is a more accurate basis for the transmission simulator in this application.

In the authors previous works [4–6], they have also studied a T-beam system which is similar to that described here (and in [10]) although it had a stiffer transmission simulator. The CB-TS method was also applied to that system and the results obtained showed similar trends to those presented above, so for brevity those results will not be included here.

8.3.2 Two-Dimensional Structure with Indeterminate Interface

In this next case study, a system is considered which could lead to an ill-conditioned substructuring problem. The system of interest is the C-shaped assembly highlighted with a dash-dot (blue) box in Fig. 8.2. In the assembly of interest (on the left in Fig. 8.2), system B is connected to another C-shaped beam creating a box structure with an additional appendage that is 305 mm long. As shown in Fig. 8.2, the beams that complete the box in the assembly of interest are thicker than those in B, having a height of 25 mm where the beams comprising B have a height of 19 mm. The box in both C and in the assembly of interest is 457 mm square and all of the beams had a width of 25 mm. A transmission simulator was designed to replicate the C-shaped beam in the assembly of interest, although the cross section of the transmission simulator was 19 mm high by 25 mm thick, so it is less stiff than the system in the assembly of interest. All of the other dimensions were identical to those in the assembly of interest. The interface between the TS and system B consists of two separate arms and hence is reminiscent of the system studied by P. Ind in his PhD thesis [12]. Ind's work showed that a system such as this can exhibit dramatic sensitivity to noise because the measurements are likely to contain very little relative motion of the arms and yet that motion provides the only available information about how the structure will move once the transmission simulator is removed. However, in this case the problem should not be as poorly conditioned as the system studied by Ind because the transmission simulator does allow some motion of the interface DOF in its lower modes of vibration.

One dimensional FEA models were created for each beam, with 25 mm long elements, and the resulting nodes are shown in Fig. 8.3. Duplicate nodes were merged when assembling the system. Then, to simulate a modal test the modes of the FEA model for assembly C were computed out to 3 kHz, resulting in a 16 mode model for C that included three rigid body modes. A Craig Bampton model was then created of the transmission simulator, with six constraint modes and two elastic (fixed-interface) modes. Those two elastic modes were the only fixed-interface modes below 1 kHz.

Figure 8.4 shows 12 of the 13 elastic modes of Assembly C. (The first elastic mode, which is not shown, was a first ovaling mode along the diagonal of the frame.) The higher modes show considerable bending of the frame suggesting that a modal model based on these modes should be able to capture relatively complicated motion of component B. The fixed interface and constraint modes of the transmission simulator are shown in Figs. 8.5 and 8.6 respectively. This truncated model for the TS was evaluated by computing its free-interface modes and comparing their natural frequencies with the true free-interface natural frequencies. This revealed that the Craig-Bampton model for the TS accurately predicted the first three modes of the free-free transmission simulator (up to 650 Hz) to within 1.2 %, while the next few modes (beginning at 1.2 kHz) were not predicted accurately, although their shapes were vaguely similar.

These "measured" modes for C were combined with the CB model for the transmission simulator and Eq. (8.9) was used with the constraint in Eq. (8.10) to compute a model for subcomponent B. In practice the model for B would then be

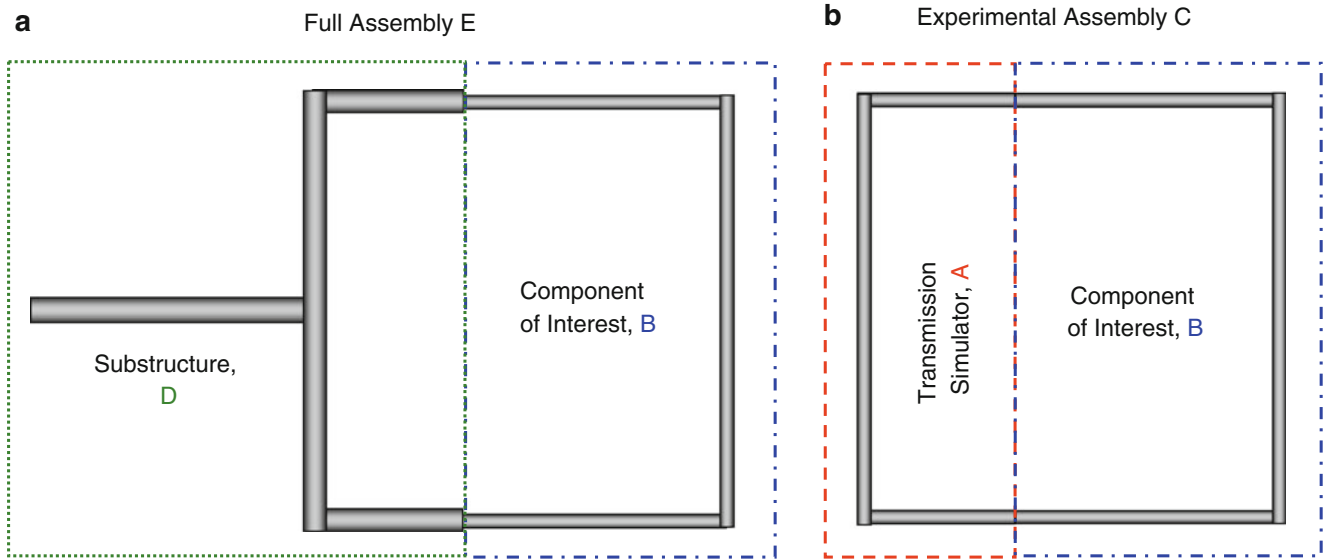
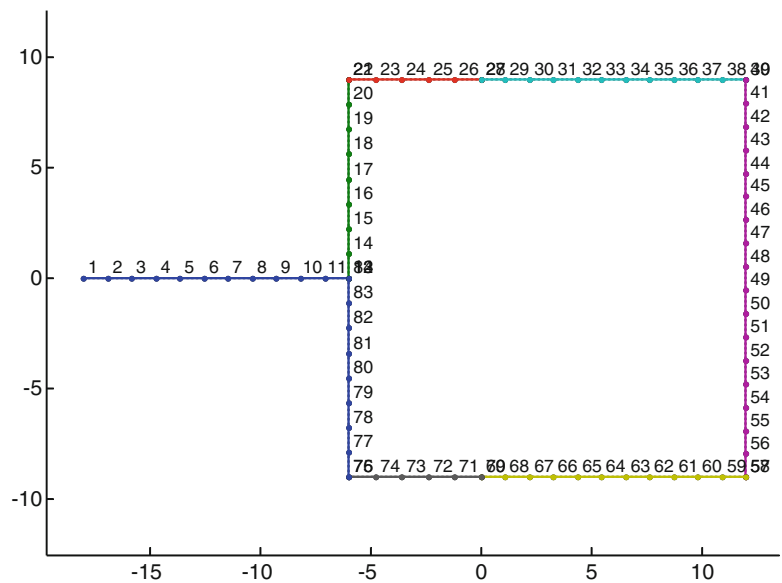


Fig. 8.2 Schematic of two-dimensional structure with a statically indeterminate interface. (a) Full Assembly $E = B + D$. (b) Assembly C. We desire to predict the motion of the assembly on the *left* but wish to avoid creating an FEA model for B. A transmission simulator, A, is created and attached to B and the modes of the assembly are found and used to derive the model for B

Fig. 8.3 Finite element mesh of the assembly of interest



used to predict the response of the assembly of interest, or of various design iterations of that assembly. In this work, the true assembly is already known (via the full finite element model), and so its modes will be compared with those predicted by substructuring to evaluate the CB procedure. Before doing this, two other intermediate cases were considered to seek to explain what information is captured in the “experimentally” derived model for B. First, both of the legs of B were constrained to ground at the connection points. In this case the model for B accurately predicted the first three natural frequencies, with errors of 5 % or less, and the next few modes were also quite reasonable with about 10 % error. Next, only one leg of B was constrained to ground leaving the other leg free. In this case the model produced qualitatively accurate estimates of the first three modes although their natural frequencies were about 30 % too high. This reveals that, while the CB procedure does produce a Craig-Bampton-like model for substructure B, it will not necessarily have the same resolution as a real analytical Craig-Bampton model with the same number of modes. The authors have previously suggested that the best practice is to use a transmission simulator that mimics the interface in the assembly of interest, and the TS used here clearly does this so one would hope that the model for B will be accurate in that assembly.

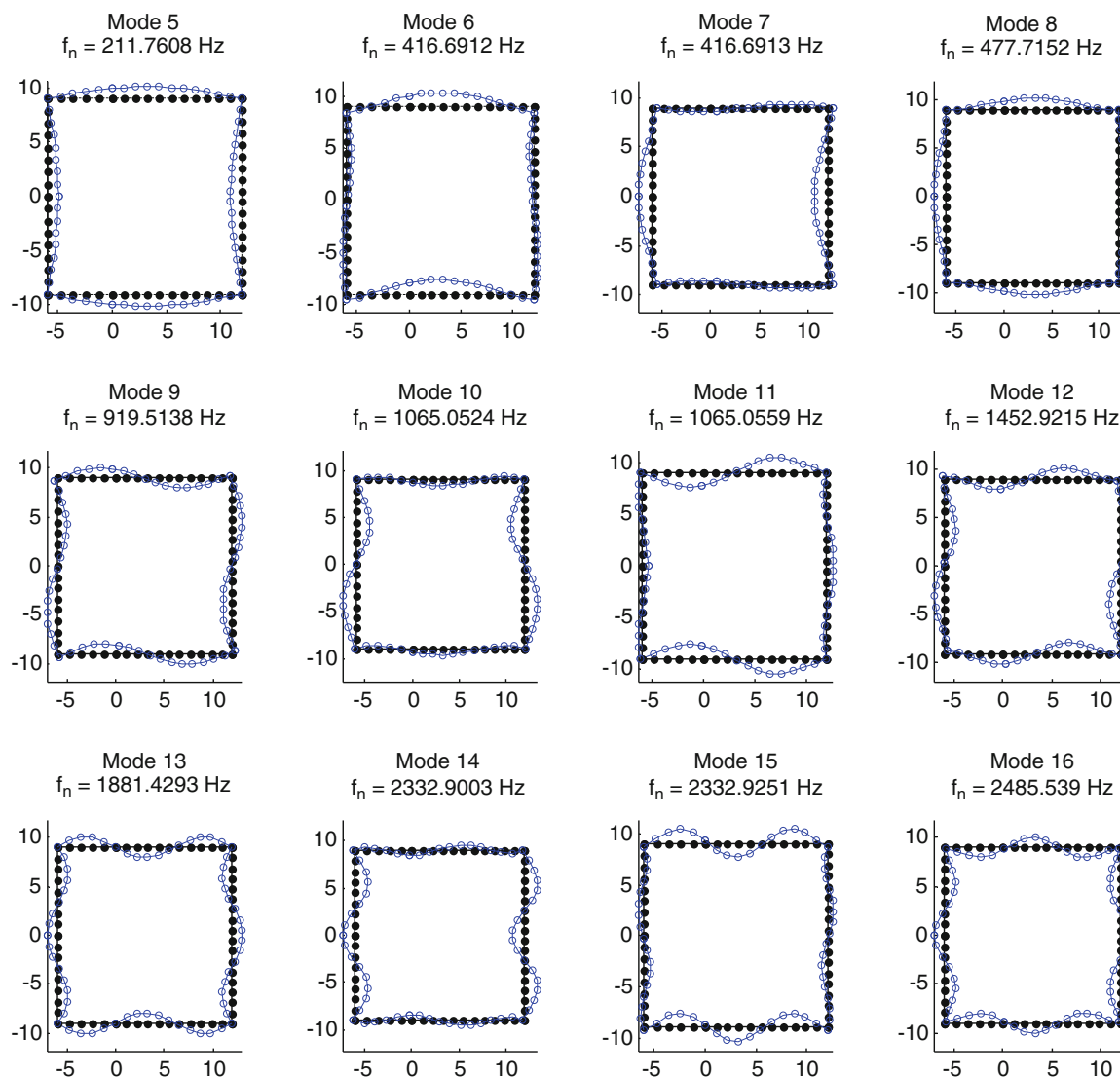


Fig. 8.4 Elastic modes of Assembly C in the frequency range of interest

8.3.2.1 Results for Assembly of Interest

The true modes of the system in the application of interest are shown in Fig. 8.7. Each of the modes estimated by the substructuring procedure was matched to the system modes using the MAC matrix shown in Fig. 8.8. Then, the natural frequencies for the modes that corresponded were compared in Table 8.3. The substructuring procedure was repeated using the CB-TS method as well as the original FF-TS method from [4]. Both methods used eight modes to model the transmission simulator. In the case of the FF-TS method, the highest mode was at 2.2 kHz, considerably higher than the highest free-interface mode that the CB-TS model predicted accurately.

The results in Table 8.3 show that the CB-TS method produced considerably more accurate estimates for this assembly in the application of interest, at least in the lower frequency range. For the modes below 1 kHz (or one third of the frequency range over which the C assembly was tested), the CB method accurately estimated all of the modes with less than 0.5 % error in any natural frequency and almost all of the MAC values above 0.999. On the other hand, the FF-TS method also provides reasonable predictions although the frequencies were less accurate, sometimes in error by as much as 16 %, and the mode shapes were also somewhat less accurate as shown by the MAC. On the other hand, the FF-TS method provided reasonable estimates of all of the modes below 2 kHz while the CB-TS method predicted several spurious modes beginning at 1.2 kHz.

These models were found to contain some negative mass, so, as was done in Sect. 8.3.1, the “Added Mass” method from [6] was used to add mass to the substructure model for B until its mass matrix became positive definite. Figure 8.9 and

Fig. 8.5 Fixed-interface modes of the transmission simulator

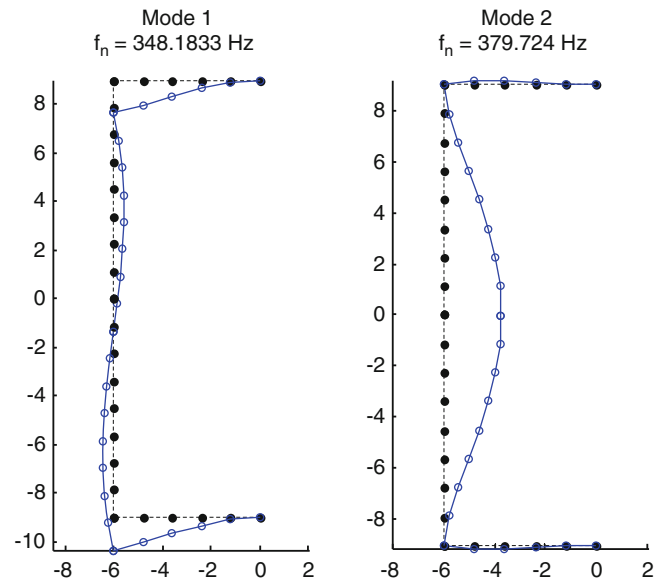


Fig. 8.6 Constraint modes of the transmission simulator

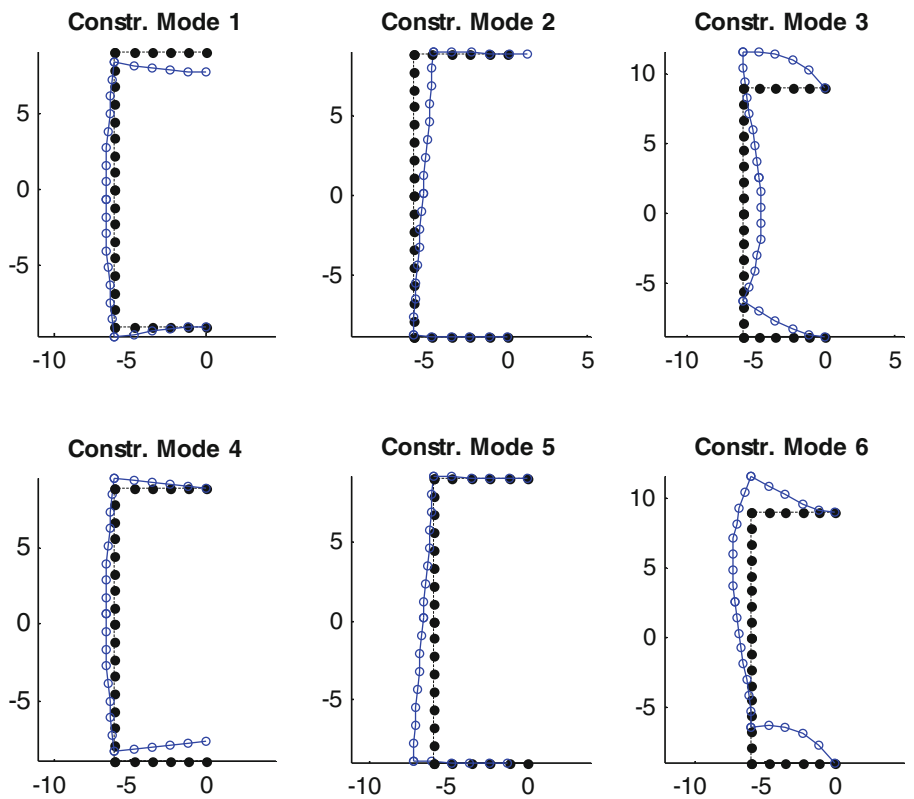


Table 8.4 show the results when positive mass is forced onto the substructuring results. The ratio of the norm of the mass added to that of the mass matrix in each case was 0.0766 and 0.0226 for the CB-TS and FF-TS methods respectively. While the CB-TS method required three times as much mass to obtain a positive mass matrix, this simple addition of mass improved the results remarkably. With added mass the CB-TS method produced only one spurious mode and predicted all of the modes below 2 kHz quite accurately. On the other hand, the model predicted by the FF-TS method did not improve significantly, except perhaps in its estimates of the rigid body modes.

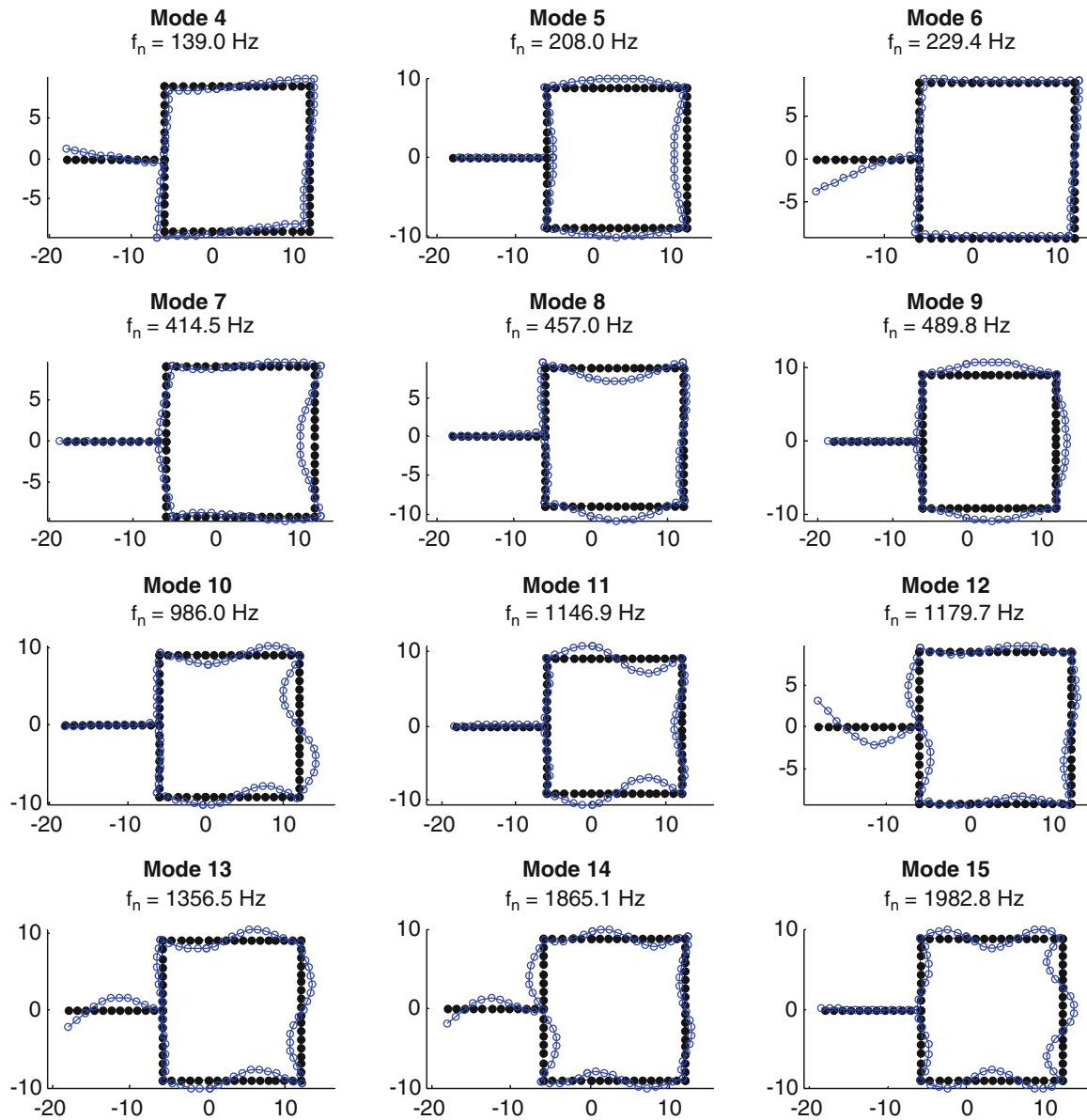


Fig. 8.7 Mode shapes of the truth model for the application of interest

Table 8.3 Natural frequencies (Hz) of the assembly of interest estimated by substructuring

| Mode | Truth | N | CB-TS | CB Error | MAC | N | FF-TS | FF-Error | MAC |
|------|---------|----|---------|----------|--------|----|---------|----------|--------|
| 4 | 139.0 | 4 | 138.8 | -0.2 % | 1.0000 | 4 | 128.0 | -7.9 % | 0.9962 |
| 5 | 208.0 | 5 | 208.4 | 0.2 % | 0.9999 | 5 | 200.2 | -3.7 % | 0.9950 |
| 6 | 229.4 | 6 | 229.5 | 0.0 % | 0.9999 | 6 | 228.0 | -0.6 % | 0.9979 |
| 7 | 414.5 | 7 | 416.6 | 0.5 % | 0.9993 | 7 | 396.7 | -4.3 % | 0.9858 |
| 8 | 457.0 | 8 | 457.1 | 0.0 % | 0.9996 | 8 | 452.9 | -0.9 % | 0.9977 |
| 9 | 489.8 | 9 | 490.0 | 0.0 % | 0.9999 | 9 | 488.2 | -0.3 % | 0.9977 |
| 10 | 986.0 | 10 | 990.6 | 0.5 % | 0.9695 | 10 | 887.2 | -10.0 % | 0.8290 |
| 11 | 1,146.9 | 11 | 1,238.0 | n/a | n/a | 11 | 962.4 | -16.1 % | 0.9038 |
| 12 | 1,179.7 | 12 | 1,172.0 | 2.2 % | 0.8392 | 12 | 1,134.0 | -3.9 % | 0.7124 |
| 13 | 1,356.5 | 14 | 1,314.3 | -3.1 % | 0.7867 | 13 | 1,263.4 | -6.9 % | 0.7421 |
| 14 | 1,865.1 | | | | | 14 | 1,802.1 | -3.4 % | 0.7132 |
| 15 | 1,982.8 | | | | | 15 | 1,854.4 | -6.5 % | 0.9923 |

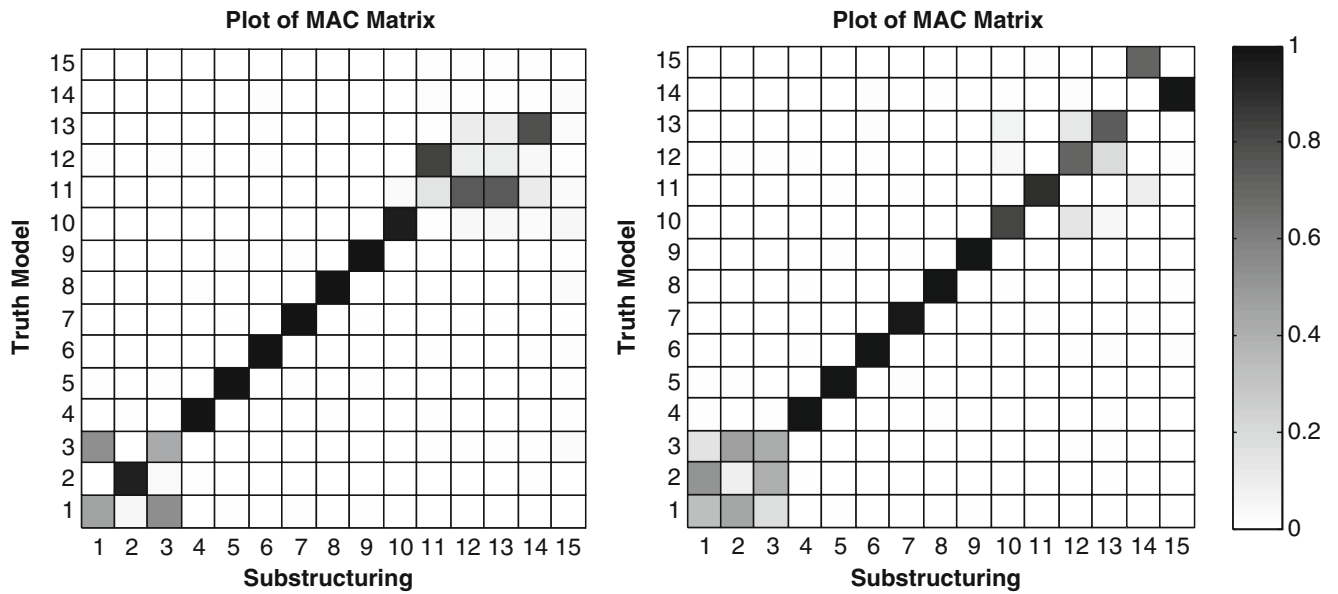


Fig. 8.8 MAC between the modes of the truth model and those predicted by substructuring using the (left) CB-TS and (right) FF-TS methods

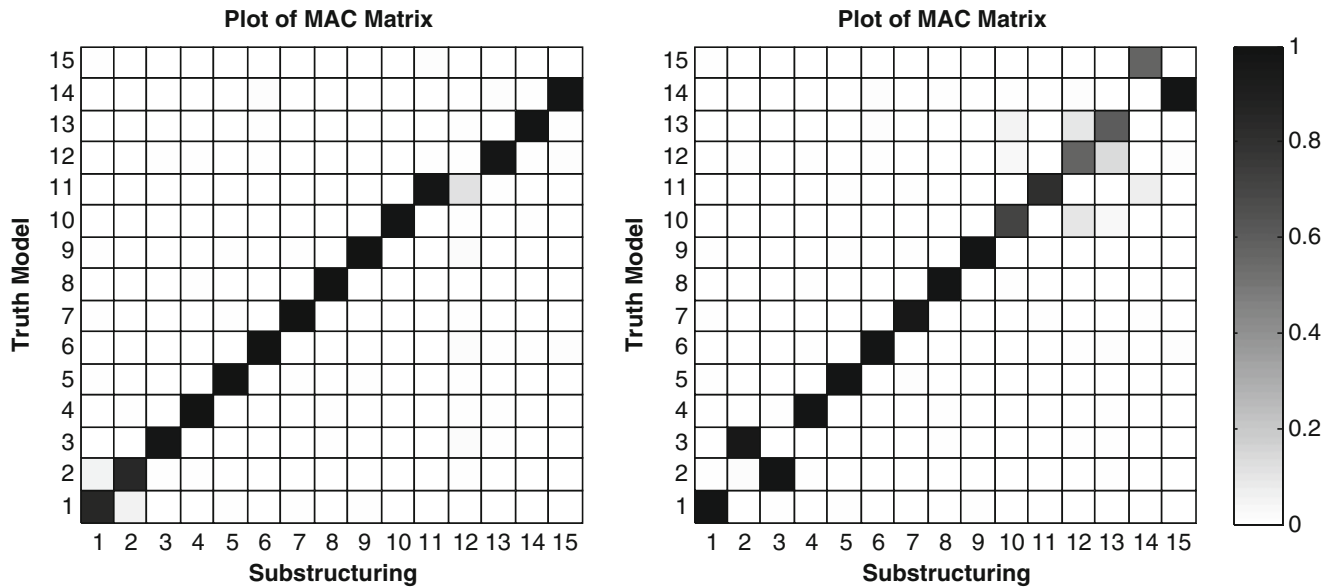


Fig. 8.9 MAC matrices for the cases mentioned in Fig. 8.8, when positive mass is enforced for each method: (left) CB-TS and (right) FF-TS

8.4 Conclusion

This work has presented an alternative to the Transmission Simulator method in which the TS is modeled with a Craig-Bampton model. This is expected to produce a more accurate model of the TS in applications where the TS is rigidly connected to the subcomponents of interest. The method was validated by applying it to a few simple beam structures and the results showed that this new method did indeed give more accurate estimates of the assembly’s natural frequencies. However, if one’s goal was to estimate the free modes of the structure of interest (e.g. if it will not be assembled to a rigid component after removing the transmission simulator) then the CB method was somewhat less accurate than the authors’ previous approach, which used free-interface modes to model the TS.

The last application presented here explored a potentially ill-conditioned problem of removing a TS that connects to the subcomponent of interest at two points. In this case, one already requires six modes for the constraint modes of the CB model; if the interface was modeled with more points then it would almost certainly be necessary to reduce the interface in

Table 8.4 Natural frequencies (Hz) of the assembly of interest estimated while enforcing positive mass

| Mode | Truth | N | CB-TS | CB Error | MAC | N | FF-TS | FF-Error | MAC |
|------|---------|----|---------|----------|--------|----|---------|----------|--------|
| 4 | 139.0 | 4 | 138.3 | −0.6 % | 1.0000 | 4 | 128.0 | −7.9 % | 0.9962 |
| 5 | 208.0 | 5 | 208.4 | 0.2 % | 0.9999 | 5 | 200.2 | −3.7 % | 0.9949 |
| 6 | 229.4 | 6 | 229.3 | −0.1 % | 0.9999 | 6 | 228.0 | −0.6 % | 0.9979 |
| 7 | 414.5 | 7 | 415.8 | 0.3 % | 0.9997 | 7 | 396.7 | −4.3 % | 0.9855 |
| 8 | 457.0 | 8 | 456.3 | −0.1 % | 1.0000 | 8 | 452.9 | −0.9 % | 0.9977 |
| 9 | 489.8 | 9 | 489.7 | 0.0 % | 0.9999 | 9 | 488.2 | −0.3 % | 0.9974 |
| 10 | 986.0 | 10 | 978.8 | −0.7 % | 0.9981 | 10 | 887.2 | −10.0 % | 0.8295 |
| 11 | 1,146.9 | 11 | 1,135.3 | −1.0 % | 0.9919 | 11 | 962.4 | −16.1 % | 0.9040 |
| 12 | 1,179.7 | 13 | 1,178.3 | −0.1 % | 0.9929 | 12 | 1,134.0 | −3.9 % | 0.7121 |
| 13 | 1,356.5 | 14 | 1,344.3 | −0.9 % | 0.9967 | 13 | 1,263.4 | −6.9 % | 0.7416 |
| 14 | 1,865.1 | 15 | 1,866.8 | 0.1 % | 0.9981 | 14 | 1,802.1 | −3.4 % | 0.7152 |
| 15 | 1,982.8 | | | | | 15 | 1,854.4 | −6.5 % | 0.9949 |

some way or there might be more TS modes than there are in system C making this subtraction impossible. In this regard, the traditional FF-TS method is convenient as it simply uses the free modes of the transmission simulator to approximate the interface so this does not become an issue unless the system is such that too many free modes are required to adequately model the TS.

Acknowledgements This work was supported by Sandia National Laboratories. Notice: This manuscript has been authored by Sandia Corporation under Contract No. DE-AC04-94AL85000 with the U.S. Department of Energy. The United States Government retains and the publisher, by accepting the article for publication, acknowledges that the United States Government retains a non-exclusive, paid-up, irrevocable, world-wide license to publish or reproduce the published form of this manuscript, or allow others to do so, for United States Government purposes.

References

- de Klerk D, Rixen DJ, Voormeeren SN (2008) General framework for dynamic substructuring: history, review, and classification of techniques. *AIAA J* 46:1169–1181
- Allen MS, Mayes RL (2007) Comparison of FRF and modal methods for combining experimental and analytical substructures. Presented at the 25th international modal analysis conference (IMAC XXV), Orlando, FL
- Mayes RL, Stasiunas EC (2007) Lightly damped experimental substructures for combining with analytical substructures. Presented at the 25th international modal analysis conference (IMAC XXV), Orlando, FL
- Allen MS, Mayes RL, Bergman EJ (2010) Experimental modal substructuring to couple and uncouple substructures with flexible fixtures and multi-point connections. *J Sound Vib* 329:4891–4906
- Allen MS, Kammer DC, Mayes RL (2012) Metrics for diagnosing negative mass and stiffness when uncoupling experimental and analytical substructures. *J Sound Vib* 331:5435–5448
- Mayes RL, Allen MS, Kammer DC (2013) Correcting indefinite mass matrices due to substructure uncoupling. *J Sound Vib* 332:5856–5866
- Mayes RL, Arviso M (2010) Design studies for the transmission simulator method of experimental dynamic substructuring. Presented at the international seminar on modal analysis (ISMA2010), Lueven, Belgium
- Mayes RL, Ross MR (2012) Advancements in hybrid dynamic models combining experimental and finite element substructures. *Mech Syst Signal Process* 31:56–66
- Craig RR, Bampton MCC (1968) Coupling of substructures for dynamic analysis. *AIAA J* 6:1313–1319
- Kammer DC, Allen MS, Mayes RL (2013) Formulation of a Craig-Bampton experimental substructure using a transmission simulator. Presented at the 31st international modal analysis conference (IMAC XXXI), Garden Grove, CA
- Craig RRJ (1981) *Structural dynamics*. Wiley, New York, NY
- Ind P (2004) The non-intrusive modal testing of delicate and critical structures. Ph.D., Imperial College of Science, Technology & Medicine, University of London, London

Chapter 9

Consideration of Interface Damping in Shrouded Mistuned Turbine Blades

F. Schreyer, J. Gross, P. Reuss, M. Junge, and H. Schoenenborn

Abstract Running turbines are exposed to high mechanical load. Due to gas excitations the structure can vibrate with high oscillation amplitudes which can damage the turbine blades. Mistuning can additionally lead to high local stresses which must be taken into account in the turbine design process. Introducing damping due to friction in the interface of shrouded turbines can be used to decrease this oscillation amplitudes. The computation of full turbine finite-element models with nonlinear coupling forces causes high computational costs. As a consequence, Component Mode Synthesis methods are used to reduce the number of DOFs of each blade substructure. Mistuning of the blades can now be applied in modal space. Coupling of the mistuned substructures is done by nonlinear interface forces which have to be included in the substructuring formulation. The resulting reduced and mistuned system with nonlinear coupling forces is solved with a Harmonic Balance Method such that the effect of mistuning and interface damping can be studied very efficiently.

Keywords Turbine • Mistuning • Interface damping • Component Mode Synthesis • Harmonic Balance Method

9.1 Introduction

Calculating the steady state response of turbine blades is an important task during the design process of turbines. To analyze the oscillation of randomly mistuned turbine blades stochastic analysis must be done. In general, this requires many calculations and therefore a very fast numeric routine is desirable. If nonlinear contacts are considered, the calculation is very time expensive. In this contribution a fast approximation for the nonlinear contact on shrouded blades is presented using the Harmonic Balance Method (HBM). Additionally, a Component Mode Synthesis (CMS) to reduce the linear substructures is used to decrease the calculation time to a minimum.

A small benchmark model is considered in order to show the approach and illustrate numeric results. In Fig. 9.1 the components as well as the assembly of the used FE-model are shown.

This paper is organized as follows. In Sect. 9.2 the reduction and adjacent assembly of the substructures are described in detail. Section 9.3 is addressed to the used mistuning formulation. The coupling method applied to the shroud interfaces is demonstrated in Sect. 9.4. Subsequently, the Harmonic Balance Method is shortly reviewed in Sect. 9.5 and Sect. 9.6 is dedicated to the obtained results. The paper closes with a brief conclusion.

F. Schreyer (✉) • J. Gross • P. Reuss
Institute of Applied and Experimental Mechanics, University of Stuttgart, Pfaffenwaldring 9, 70550 Stuttgart, Germany
e-mail: schreyer@iam.uni-stuttgart.de; gross@iam.uni-stuttgart.de; reuss@iam.uni-stuttgart.de

M. Junge • H. Schoenenborn
MTU Aero Engines, Muenchen, Germany

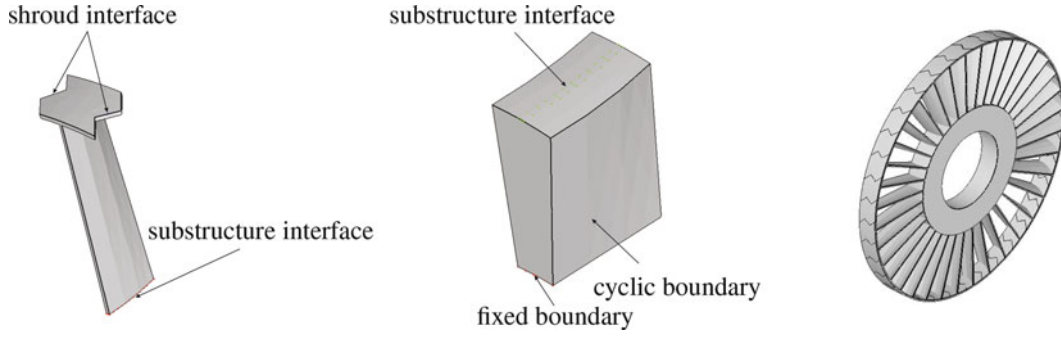


Fig. 9.1 Blade-, disk-components and assembly of the finite-element model

9.2 Component Mode Synthesis of the Turbine

Finite-element models of turbine blades have a large number of degrees of freedom (DOFs). By using a model reduction method the order of the system can be reduced to save computational costs. Following the approach presented in [1–3], a CMS is used to reduce the disk and blade segments separately, and assemble to the full system hereafter.

9.2.1 Reduction of the Blade

The DOFs of the blade are reduced using the Craig-Bampton method. Interface DOFs are kept in the physical domain, while free DOFs are replaced by a combination of fixed interface modes and constraint modes. Therefore, the mass and stiffness matrix, \mathbf{M}^b and \mathbf{K}^b must be partitioned into free (f) and interface (i) DOFs. The upper index denotes the blade (b). Note, that here the interface (i) consists of the shroud interface (i_{shr}) and the segment interface of the disk (i_d)

$$\underbrace{\begin{bmatrix} \mathbf{M}_{ff}^b & \mathbf{M}_{fi}^b \\ \mathbf{M}_{if}^b & \mathbf{M}_{ii}^b \end{bmatrix}}_{\mathbf{M}^b} \begin{bmatrix} \ddot{\mathbf{x}}_f^b \\ \ddot{\mathbf{x}}_i^b \end{bmatrix} + \underbrace{\begin{bmatrix} \mathbf{K}_{ff}^b & \mathbf{K}_{fi}^b \\ \mathbf{K}_{if}^b & \mathbf{K}_{ii}^b \end{bmatrix}}_{\mathbf{K}^b} \begin{bmatrix} \mathbf{x}_f^b \\ \mathbf{x}_i^b \end{bmatrix} = \begin{bmatrix} \mathbf{0} \\ \mathbf{f}_i^b \end{bmatrix}, \quad \text{with } \mathbf{x}_i^b = \begin{bmatrix} \mathbf{x}_{id}^b \\ \mathbf{x}_{ishr}^b \end{bmatrix}. \quad (9.1)$$

Consequently, to determine the fixed interface modes, the eigenvalue problem

$$\left(\mathbf{K}_{ff}^b - \omega_j^2 \mathbf{M}_{ff}^b \right) \boldsymbol{\phi}_j^b = \mathbf{0} \quad (9.2)$$

must be solved. The dynamics of the reduced system is defined by the first n eigenvectors $\boldsymbol{\phi}^b = [\boldsymbol{\phi}_1^b, \dots, \boldsymbol{\phi}_n^b]$. The number of required eigenvectors to achieve accurate solutions depends on the analyzed frequency range. Additionally, the reduction base $\boldsymbol{\Theta}$ is enriched by the constraint modes so that it can be written as

$$\begin{bmatrix} \mathbf{x}_f^b \\ \mathbf{x}_i^b \end{bmatrix} = \begin{bmatrix} \boldsymbol{\phi}^b & -\mathbf{K}_{ff}^{b-1} \mathbf{K}_{fi}^b \\ \mathbf{0} & \mathbf{I} \end{bmatrix} \begin{bmatrix} \mathbf{p}^b \\ \mathbf{x}_i^b \end{bmatrix} = \boldsymbol{\Theta} \begin{bmatrix} \mathbf{p}^b \\ \mathbf{x}_i^b \end{bmatrix}. \quad (9.3)$$

The reduced matrices are obtained by multiplying the reduction base to the system matrices

$$\mathbf{M}_{\text{red}}^b = \boldsymbol{\Theta}^T \mathbf{M}^b \boldsymbol{\Theta}, \quad \mathbf{K}_{\text{red}}^b = \boldsymbol{\Theta}^T \mathbf{K}^b \boldsymbol{\Theta}. \quad (9.4)$$

In order to expand the blade to a complete system of N_s segments, the single blade matrices, Eq. (9.4) can be arranged in a block diagonal form. If the system matrices are represented in the Cartesian system the coordinates of n -th blade must be transformed by a rotation matrix \mathbf{T}_n , containing a multiple of the sector angle,

$$\bar{\mathbf{M}}_{\text{red}}^b = \text{blkdiag}(\mathbf{T}_n^T \mathbf{M}_{\text{red},n}^b \mathbf{T}_n)_{n=1(1)N_s} \quad \bar{\mathbf{K}}_{\text{red}}^b = \text{blkdiag}(\mathbf{T}_n^T \mathbf{K}_{\text{red},n}^b \mathbf{T}_n)_{n=1(1)N_s}. \quad (9.5)$$

The bar symbol constitutes global coordinates of all n blades.

9.2.2 Reduction and Cyclic Transformation of the Disk

For the reduction of the disk cyclic symmetry can be used. The cyclic symmetric boundary condition can be applied by the matrix transformation

$$\begin{bmatrix} \mathbf{x}_f \\ \mathbf{x}_{i_{cyc,r}} \\ \mathbf{x}_{i_{cyc,l}} \end{bmatrix} = \begin{bmatrix} \mathbf{I} & \mathbf{0} \\ \mathbf{0} & \mathbf{I} \\ \mathbf{0} & \mathbf{T} e^{-i\alpha h} \end{bmatrix} \begin{bmatrix} \mathbf{x}_f \\ \mathbf{x}_{i_{cyc,r}} \end{bmatrix}, \quad (9.6)$$

which forces the left boundary $\mathbf{x}_{i_{cyc,l}}$ to oscillate phase shifted with respect to the right one $\mathbf{x}_{i_{cyc,r}}$. This phase shift is defined by the harmonic index h , the sector angle α . The matrix \mathbf{T} describes the geometrical rotation from the left to the right boundary. To capture the global disk dynamics, all indices $h = 0(1)N_s - 1$ must be taken into account. The dynamic behavior of the disk can, thus, be expressed in a block diagonal form

$$\tilde{\mathbf{M}}^d = \text{blkdiag}_{h=0(1)N_s-1}(\tilde{\mathbf{M}}_h^d), \quad \tilde{\mathbf{K}}^d = \text{blkdiag}_{h=0(1)N_s-1}(\tilde{\mathbf{K}}_h^d), \quad (9.7)$$

where each submatrix represents one harmonic index. The harmonic indices are decoupled by definition [1], and therefore the Craig-Bampton reduction can be performed for each harmonic index separately. Consequently, after the reduction the disk is described by modal and cyclic coordinates which results to a much smaller number of DOFs,

$$\tilde{\mathbf{M}}_{\text{red}}^d = \text{blkdiag}_{n=0(1)N_s-1}(\boldsymbol{\Theta}_h^T \tilde{\mathbf{M}}_h^d \boldsymbol{\Theta}_h), \quad \tilde{\mathbf{K}}_{\text{red}}^d = \text{blkdiag}_{n=0(1)N_s-1}(\boldsymbol{\Theta}_h^T \tilde{\mathbf{K}}_h^d \boldsymbol{\Theta}_h). \quad (9.8)$$

9.2.3 Assembly and Interface Reduction

After the modal reduction of the single segment components and their adjacent expansion to full systems of N_s sectors, the coupling of the substructure interface can be performed. The interface DOFs of the blades are still in physical domain, while the interface DOFs of the disk are expressed in cyclic coordinates. Therefore, to couple the interface DOFs of the blades are transformed using the Fourier matrix $\tilde{\mathbf{F}}$

$$\tilde{\mathbf{x}}_{id}^b = \begin{bmatrix} \mathbf{x}_{id1}^b & \cdots & \mathbf{x}_{idN_s}^b \end{bmatrix}^T = \tilde{\mathbf{F}} \tilde{\mathbf{x}}^d \quad (9.9)$$

which is defined as

$$\tilde{\mathbf{F}} = \mathbf{I} \otimes \mathbf{F} \quad \text{with} \quad \mathbf{F}(kk, ll) = \frac{1}{N_s} e^{i(kk-1)(ll-1)\alpha}. \quad (9.10)$$

The blades and disk can now be assembled by the assembly matrix \mathbf{T}_{cms} , which transforms and couples the substructure interface DOFs,

$$\begin{bmatrix} \tilde{\mathbf{p}}_f^d \\ \tilde{\mathbf{x}}_i^d \\ \tilde{\mathbf{p}}_f^b \\ \tilde{\mathbf{x}}_i^b \\ \tilde{\mathbf{x}}_r^b \end{bmatrix} = \underbrace{\begin{bmatrix} \mathbf{I} & \mathbf{0} & \mathbf{0} & \mathbf{0} \\ \mathbf{0} & \mathbf{I} & \mathbf{0} & \mathbf{0} \\ \mathbf{0} & \mathbf{0} & \mathbf{I} & \mathbf{0} \\ \mathbf{0} & \tilde{\mathbf{F}} & \mathbf{0} & \mathbf{0} \\ \mathbf{0} & \mathbf{0} & \mathbf{0} & \mathbf{I} \end{bmatrix}}_{\mathbf{T}_{\text{cms}}} \begin{bmatrix} \tilde{\mathbf{p}}_f^d \\ \tilde{\mathbf{x}}_i^d \\ \tilde{\mathbf{p}}_f^b \\ \tilde{\mathbf{x}}_r^b \end{bmatrix}. \quad (9.11)$$

Note, that in this case only conforming meshes of the substructure interfaces are considered [9]. The mass matrix \mathbf{M}_{cms} of the assembly, can be written as

$$\mathbf{M}_{\text{cms}} = \mathbf{T}_{\text{cms}}^T \begin{bmatrix} \tilde{\mathbf{M}}_{\text{red}}^d & \mathbf{0} \\ \mathbf{0} & \tilde{\mathbf{M}}_{\text{red}}^b \end{bmatrix} \mathbf{T}_{\text{cms}} = \begin{bmatrix} \tilde{\mathbf{M}}_{\text{red,ff}}^d & \tilde{\mathbf{M}}_{\text{red,fi}}^d & \mathbf{0} & \mathbf{0} \\ \tilde{\mathbf{M}}_{\text{red,if}}^d & \tilde{\mathbf{M}}_{\text{red,ii}}^d & \tilde{\mathbf{M}}_{\text{red,if}}^b \tilde{\mathbf{F}} & \tilde{\mathbf{M}}_{\text{red,ir}}^b \tilde{\mathbf{F}} \\ \mathbf{0} & \tilde{\mathbf{F}}^T \tilde{\mathbf{M}}_{\text{red,fi}}^b & \tilde{\mathbf{M}}_{\text{red,ff}}^b & \tilde{\mathbf{M}}_{\text{red,fr}}^b \\ \mathbf{0} & \tilde{\mathbf{F}}^T \tilde{\mathbf{M}}_{\text{red,ri}}^b & \tilde{\mathbf{M}}_{\text{red,rf}}^b & \tilde{\mathbf{M}}_{\text{red,rr}}^b \end{bmatrix}. \quad (9.12)$$

The assembly stiffness matrix \mathbf{K}_{cms} is defined accordingly. The size of the system is still dominated by the large number of cyclic interface DOFs, which can be further reduced by an interface reduction. The modal reduction basis of the interface is obtained by solving the eigenvalue problem of the interface partitions from Eq. (9.12)

$$\left(\tilde{\mathbf{K}}_{\text{red,ii}} - \omega_{\text{ii}}^2 \tilde{\mathbf{M}}_{\text{red,ii}} \right) \tilde{\boldsymbol{\phi}}_{\text{ii}} = \mathbf{0} \quad (9.13)$$

The eigenvectors of the interface $\tilde{\boldsymbol{\phi}}_{\text{ii}}$ span the same subspace as the constraint modes of the global interface between disk and blades, which can be truncated by keeping only the eigenvectors associated with the lowest k eigenfrequencies $\omega_{k,\text{ii}}$. The transformation for the new set coordinates can be formulated as

$$\begin{bmatrix} \tilde{\boldsymbol{p}}_f^d \\ \tilde{\boldsymbol{x}}_i \\ \tilde{\boldsymbol{p}}_f^b \\ \tilde{\boldsymbol{x}}_r^b \end{bmatrix} = \underbrace{\begin{bmatrix} \mathbf{I} & \mathbf{0} & \mathbf{0} & \mathbf{0} \\ \mathbf{0} & \tilde{\boldsymbol{\phi}}_{k,\text{ii}} & \mathbf{0} & \mathbf{0} \\ \mathbf{0} & \mathbf{0} & \mathbf{I} & \mathbf{0} \\ \mathbf{0} & \mathbf{0} & \mathbf{0} & \mathbf{I} \end{bmatrix}}_{\boldsymbol{\Theta}_i} \begin{bmatrix} \tilde{\boldsymbol{p}}_f^d \\ \tilde{\boldsymbol{p}}_i \\ \tilde{\boldsymbol{p}}_f^b \\ \tilde{\boldsymbol{x}}_r^b \end{bmatrix}, \quad (9.14)$$

and the assembled system matrices can be rewritten as

$$\mathbf{M}_{\text{cms,red}} = \boldsymbol{\Theta}_i^T \mathbf{M}_{\text{cms}} \boldsymbol{\Theta}_i, \quad \mathbf{K}_{\text{cms,red}} = \boldsymbol{\Theta}_i^T \mathbf{K}_{\text{cms}} \boldsymbol{\Theta}_i, \quad (9.15)$$

where $\boldsymbol{\Theta}_i$ represents the interface reduction matrix. The assembled system can be further reduced by a final Craig-Bampton reduction of the system matrices, substituting the individual blade and disk modes by a set of global modes. The shroud-coupling DOFs are kept in the physical domain.

9.3 Mistuning

The perfect cyclic symmetry of a bladed disk is destroyed, when mistuning is present. Especially blades are highly affected by variations of the manufacturing process as well as operational wear which leads to significant disturbance in the spread of vibrational energy in the system. Assuming only a variance of the Young's modulus, a nondimensional mistuning parameter can be defined as

$$\delta_n = \frac{\omega_{n,\text{mist}}^2 - \omega_{\text{nom}}^2}{\omega_{\text{nom}}^2}. \quad (9.16)$$

The nominal eigenfrequency of the tuned blade is denoted by ω_{nom}^2 , and $\omega_{n,\text{mist}}^2$ describes the mistuned eigenfrequency of the n -th blade. Furthermore, proportional mistuning is assumed, that means the percentage deviation of natural frequencies is the same for all modes, [4]. The mistuning deviations are small compared to nominal properties in the modal domain, i.e., $|\delta| \ll 1$, and it is hypothesized that the mode shapes are the same for a mistuned blade as for the tuned one.

Note, that for a validation the mistuning parameters are preferably obtained from measured cantilevered modes. However, when sliding condition is applied, the shroud constraint modes also need to be mistuned to describe the motion of the blade more accurately, [4]. Therefore, the mistuning projection requires two sets of modes. On the one hand $\mathbf{U}_{\text{shr}}^b$, including the fixed interface modes $\boldsymbol{\phi}^b$ in combination with the shroud constraint modes, which were already obtained in Eq. (9.3). On the other hand the fixed-interface normal modes $\boldsymbol{\phi}_{\text{cnt}}^b$, which in contrast to $\boldsymbol{\phi}^b$ are obtained by neglecting the shroud coupling. The $\boldsymbol{\phi}_{\text{cnt}}^b$ are associated with the mistuning parameters δ_n and therefore are used to transfer the mistuned stiffness matrix into physical domain. The modal stiffness deviation matrix $\Delta \mathbf{K}_{n,\text{mist}}^b$ is obtained by adjacent projecting on $\mathbf{U}_{\text{shr}}^b$, which leads to

$$\Delta \mathbf{K}_{\text{mist},n}^b = \mathbf{U}_{\text{shr}}^b{}^T \mathbf{M}^b \boldsymbol{\phi}_{\text{cnt}}^b \delta_n \boldsymbol{\phi}_{\text{cnt}}^b{}^T \mathbf{K}_{\text{red},n}^b \mathbf{U}_{\text{shr}}^b, \quad (9.17)$$

with

$$\mathbf{U}_{\text{shr}}^b = \begin{bmatrix} \boldsymbol{\phi}^b & -\mathbf{K}_{\text{ff}}^b \mathbf{K}_{\text{fi,shr}}^b \\ \mathbf{0} & \mathbf{I} \end{bmatrix}, \quad \boldsymbol{\phi}_{\text{cnt}}^b = \begin{bmatrix} \boldsymbol{\phi}_{\text{cnt}} \\ \mathbf{0} \end{bmatrix}. \quad (9.18)$$

Note, that here mistuning is applied to the partitions of the free DOFs as well as the shroud DOFs. The modal mistuned stiffness matrix of each blade is then given by

$$\mathbf{K}_{\text{mist},n}^b = \Delta \mathbf{K}_{\text{mist},n}^b + \mathbf{K}_{\text{red},n}^b. \quad (9.19)$$

9.4 Coupling of the Shrouds

Due to the reduction method described above the interface DOFs of the shroud remain in physical coordinates. Node-to-node contact model can be applied there directly. In order to achieve fast calculations a simple Jenkins model with the assumption of a constant normal force is used [5]. Therefore, the normal directions of the contact faces are rigidly connected to each other and the tangential relative displacements are used to calculate the friction forces [6]. It should be noted that any kind of contact could be considered here. For reasons of clarity the procedure is explained by taking a general mechanical system representation. For the results presented in Sect. 9.6 the described procedure is applied on the reduced matrices derived in the previous sections. The set of assembled system equations can be written as

$$\mathbf{M}\ddot{\mathbf{x}} + \mathbf{D}\dot{\mathbf{x}} + \mathbf{K}\mathbf{x} = \mathbf{f} + \mathbf{g} \quad (9.20)$$

where \mathbf{f} is the vector of external forces and \mathbf{g} the vector of contact forces between the substructures. Due to the matching meshes of the shroud interfaces the relative displacement vector \mathbf{u} of the contact nodes can be expressed with a signed boolean matrix \mathbf{B} . In order to apply different types of coupling to the normal and tangential direction, \mathbf{B} can be partitioned into \mathbf{B}_p for the “perfect” coupling in normal and \mathbf{B}_f for the tangential “flexible” coupling [7]

$$\begin{bmatrix} \mathbf{u}_N \\ \mathbf{u}_T \end{bmatrix} = \begin{bmatrix} \mathbf{B}_p \\ \mathbf{B}_f \end{bmatrix} \mathbf{x}. \quad (9.21)$$

Note that in general a coordinate transformation is needed to obtain the normal and tangential directions of the interfaces.

Considering the rigid coupling, the forces are eliminated as unknowns using the interface equilibrium. According to Eq. (9.21) the compatibility condition can be expressed by

$$\mathbf{B}_p \mathbf{x} = \mathbf{0} \quad (9.22)$$

and the force equilibrium condition is given by

$$\mathbf{L}_p^T \mathbf{g} = \mathbf{0}. \quad (9.23)$$

The matrix \mathbf{L}_p locates the unique set of DOFs \mathbf{q} in the whole DOFs vector. Due to the fact that the compatibility condition must be fulfilled for all \mathbf{q} it can be shown that \mathbf{L}_p must be the null space of \mathbf{B}_p and vice versa,

$$\mathbf{B}_p \mathbf{x} = \mathbf{B}_p \mathbf{L}_p \mathbf{q} = \mathbf{0} \quad \forall \mathbf{q} \quad \implies \quad \mathbf{L}_p = \text{null}(\mathbf{B}_p). \quad (9.24)$$

Consequently, a rigid coupling between the normal displacements of the shroud interfaces can be achieved by transforming the equation of motion with the matrix \mathbf{L}_p . When nonlinear coupling forces in tangential direction are present, the compatibility condition no longer equals zero. Following [7] the tangential interface forces can be defined using Lagrange multipliers

$$\mathbf{g} = -\mathbf{B}_f^T \boldsymbol{\lambda}, \quad (9.25)$$

where $\boldsymbol{\lambda}$ denotes the force intensities. Due to the characteristic of the Boolean matrix \mathbf{B}_f the equilibrium condition always is satisfied. Additionally, the Boolean matrix defines the relative displacements as

$$\mathbf{u}_T = \mathbf{B}_f \mathbf{x}. \quad (9.26)$$

These relative displacements are then used to calculate the nonlinear force vector $\boldsymbol{\lambda}$ by considering the Jenkins model properties [6]. With Eqs. (9.20) and (9.25) all nonlinear forces can be built into the FE-system.

The described method can be used to couple the shrouds and different interface conditions can be applied:

- free shrouds: no coupling is applied
- fixed shrouds: all DOFs are fixed
- linear sliding contact: only normal directions of nodes are rigidly coupled, all the others are free.
- nonlinear friction contact: normal direction is rigidly coupled and nonlinear forces are present in tangential plane

The final equation of the reduced and coupled system, which is to be solved can now be expressed as

$$\mathbb{M}\ddot{\mathbf{q}} + \mathbb{D}\dot{\mathbf{q}} + \mathbb{K}\mathbf{q} + \mathbf{F}_{nl}(\dot{\mathbf{q}}, \mathbf{q}) = \mathbf{f}_{exc}, \quad (9.27)$$

where

$$\mathbb{M} = \mathbf{L}_p^T \mathbf{M} \mathbf{L}_p, \quad \mathbb{D} = \mathbf{L}_p^T \mathbf{D} \mathbf{L}_p, \quad \mathbb{K} = \mathbf{L}_p^T \mathbf{K} \mathbf{L}_p, \quad (9.28)$$

$$\mathbf{F}_{nl} = \mathbf{L}_p^T \mathbf{B}_f^T \begin{bmatrix} \mathbf{F}_{nl,1,x} \\ \mathbf{F}_{nl,1,y} \\ \vdots \\ \mathbf{F}_{nl,N_s,x} \\ \mathbf{F}_{nl,N_s,y} \end{bmatrix} \quad \text{and} \quad \mathbf{f}_{exc} = \mathbf{L}_p^T \mathbf{f}.$$

9.5 Harmonic Balance Method

To reach higher accuracy, the solution of the nonlinear Eq. (9.28) can also be approximated by the Higher Harmonic Balance method. The mandatory transformation of the system equations into the frequency domain may introduce complex valued amplitudes in the displacement and force vectors [6], which are denoted by the hat symbol. The mathematical representation of the system equations in frequency domain is given by

$$\begin{bmatrix} \mathbb{H}_{lin,0} & \mathbf{0} & \cdots & \mathbf{0} \\ \mathbf{0} & \mathbb{H}_{lin,1} & \mathbf{0} & \vdots \\ \vdots & \mathbf{0} & \ddots & \mathbf{0} \\ \mathbf{0} & \cdots & \mathbf{0} & \mathbb{H}_{lin,m_h} \end{bmatrix} \begin{bmatrix} \hat{\mathbf{q}}_0 \\ \hat{\mathbf{q}}_1 \\ \vdots \\ \hat{\mathbf{q}}_{m_h} \end{bmatrix} = \begin{bmatrix} \hat{\mathbf{f}}_{exc,0} \\ \hat{\mathbf{f}}_{exc,1} \\ \vdots \\ \hat{\mathbf{f}}_{exc,m_h} \end{bmatrix} - \begin{bmatrix} \hat{\mathbf{F}}_{nl,0}(\hat{\mathbf{q}}_0, \dots, \hat{\mathbf{q}}_{m_h}) \\ \hat{\mathbf{F}}_{nl,1}(\hat{\mathbf{q}}_0, \dots, \hat{\mathbf{q}}_{m_h}) \\ \vdots \\ \hat{\mathbf{F}}_{nl,m_h}(\hat{\mathbf{q}}_0, \dots, \hat{\mathbf{q}}_{m_h}) \end{bmatrix}, \quad (9.29)$$

where $\mathbb{H}_{lin,m} = \mathbb{K} + i(m\omega)\mathbb{D} - (m\omega)^2\mathbb{M}$ is the dynamic stiffness matrix, and the considered higher harmonics are indexed by $m = 0(1)m_h$. Each row of Eq. (9.29) represents an independent set of equations for an individual harmonic. However, the equations become coupled because of the nonlinear forces, which are dependent on all harmonics.

Naturally, if only the first harmonic ($m = 1$) is considered, Eq. (9.29) reduces to the conventional Harmonic Balance method formulation.

9.6 Results

The performance of the reduction code is investigated with respect to the described shroud conditions as well as different mistuning cases. Note, that all figures are normalized by the respective eigenfrequency and amplitude of the linear and tuned setup.

The full FE-model features 59,508 DOFs. Linear frequency response functions (FRF) plot using rigid shroud coupling and 300 considered modal DOFs is shown in Fig. 9.2 on the left. The mistuning pattern, given by the frequency deviation factors of the blades with respect to the tuned blade, is presented on the right. Referring to the tuned peak at 1, which is excited by the engine order 9 [8], strong mistuning effects in the considered frequency range can be observed. Due to the mistuning other nodal diameters are excited as well and frequency splitting occurs.

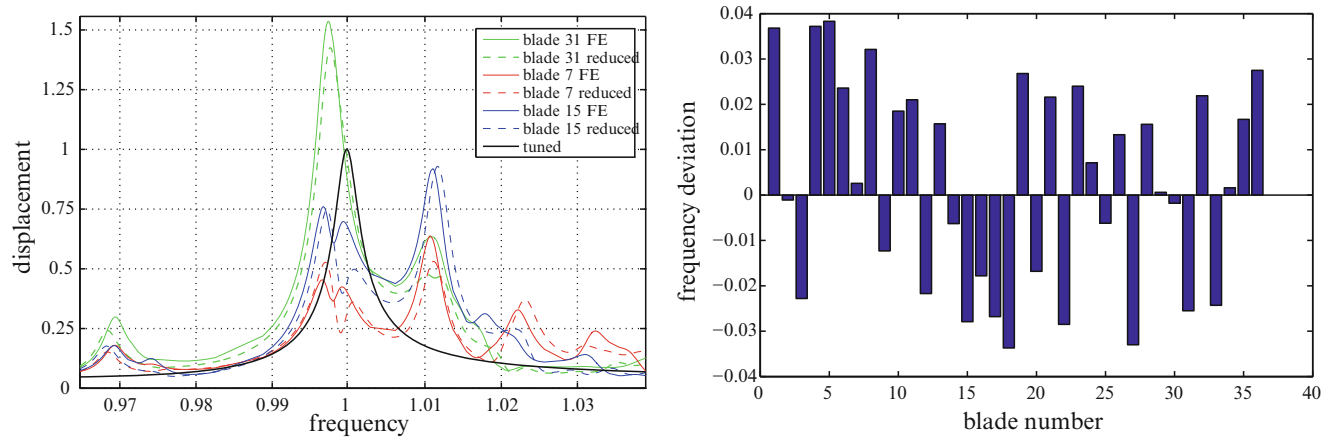


Fig. 9.2 Linear FRF of mistuned turbine with engine order 9 (*left*) and the used mistuning pattern (*right*)

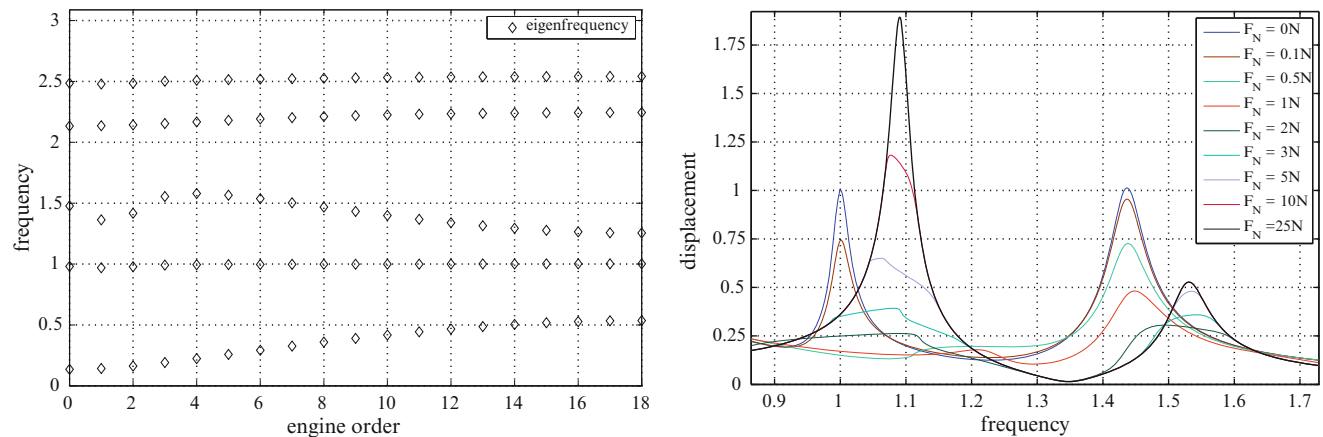


Fig. 9.3 Nodal diameter plot of system with sliding condition (*left*), nonlinear FRF of tuned turbine with engine order 9 and different normal forces (*right*)

The nonlinear analysis is usually preceded by the determination of a frequency range of interest. For this purpose a linear calculation, using the linear sliding condition, is performed to obtain a nodal diameter diagram (Fig. 9.3 (left)). Different normal forces are used to calculate FRFs using the HBM. It can be observed in Fig. 9.3 (right) that for small normal forces the nonlinear response remains very similar to the response using linear sliding. However, the behavior drastically changes, when normal forces increase. Generally, a frequency shift of the FRFs, caused by the stiffening effects in the system, can be observed. A decline of the amplitudes is apparent for $F_N \leq 5N$, because relative motion of the shrouds is still present and friction occurs. For higher normal forces ($F_N > 5N$) the amplitudes increase again, because stick becomes dominant and less energy can be dissipated by friction. Figure 9.4 (left) gives a detailed representation of the nonlinear FRFs with the normal force of $F_N = 3N$. Nonlinear damping effects as well as mistuning effects can be seen. Compared to the linear case, in this particular setup both peak amplitudes in the considered frequency range are reduced by a factor of 0.4. However, compared to the tuned case, the amplitude amplification due to mistuning effects reaches a factor of 1.2 at the second peak. The global mistuned displacements at the first eigenfrequency are visualized on the right.

9.7 Conclusion

In this work, a procedure to calculate nonlinear frequency response functions of mistuned turbine blades is presented. Considering constant normal forces, an approximation of the nonlinear frequency response function can be calculated very fast using the Harmonic Balance Method. Higher harmonics can be taken into account. With the presented Component Mode Synthesis the size of the system can be significantly reduced without considerable loss of accuracy.

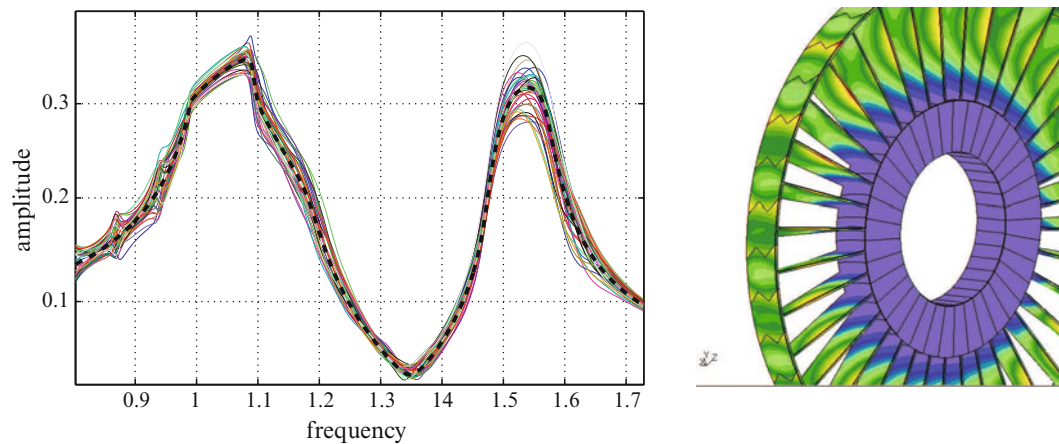


Fig. 9.4 Nonlinear FRF of mistuned turbine with engine order 9 and a normal force $F_N = 2\text{ N}$ (left) amplitude of the displacement at 880 Hz (right)

In order to extend the contact formulation, e.g. including the possibility of varying normal forces, further friction models are to be investigated in the future.

References

1. Panning L (2009) Systematische Verstimmung und mehrfach gekoppelte Schaufelkränze von Turbomaschinen. FVV-Abschlussbericht Nr. 898, University of Hannover
2. Hohl A, Siewert C, Panning L, Wallaschek J (2009) A substructure based reduced order model for mistuned bladed disks. FVV-Abschlussbericht Nr. 898, University of Hannover
3. Becker J, Gaul L (2008) CMS-methods for efficient damping prediction for structures with friction. In: Proceedings of the IMAC-XXVI, Orlando, FL, USA
4. Lim S, Bladh R, Castanier MP, Pierre C (2007) Compact, generalized component mode mistuning representation for modeling bladed disk vibration. AIAA J 45(9), 2285–2298
5. Bograd S, Reuss P, Schmidt A, Gaul L, Mayer M (2011) Modeling the dynamics of mechanical joints. Mech Syst Signal Process 25(8): 2801–2826
6. Reuss P, Zeumer B, Herrmann J, Gaul L (2012) Consideration of interface damping in dynamic substructuring. In: Proceedings of the IMAC-XXX, Jacksonville, FL, USA
7. De Klerk D, Rixen D, Voormeeren S (2008) General framework for dynamic substructuring: history, review and classification of techniques. AIAA J 46(5):1169–1181. doi:10.2514/1.33274
8. Panning L (2005) Auslegung von Reibelementen zur Schwingungsdämpfung von Turbinenschaufeln. Ph.D. thesis, University of Hannover
9. Voormeeren S, van der Valk P, Rixen D (2010) Practical aspects of dynamic substructuring in wind turbine engineering. In: Proceedings of the IMAC-XXVIII, Jacksonville, FL, USA

Chapter 10

Coupling Elements for Substructure Modelling of Lightweight Multi-storey Buildings

Ola Flodén, Kent Persson, and Göran Sandberg

Abstract Accurately modelling the dynamic behaviour of multi-storey buildings in wood requires the geometry involved to be represented in great detail, resulting in systems having many millions of degrees of freedom. Consequently, there is a need for model order reduction and the methodology of substructure modelling is employed here to create reduced models for analysis of low-frequency vibrations. The full finite element model of a building is divided into substructures which are reduced in size before being assembled to form the global model. The efficiency of the reduced models is strongly dependent on the number of degrees of freedom at the interface surfaces of the substructures, why it may be necessary to perform interface reduction of some sort. Multi-storey buildings in wood are often constructed with elastomer layers separating the structural components, these offering a natural choice of dividing the buildings into substructures. In this paper, the methodology of introducing a condensation node is adopted for employing interface reduction at the interfaces between the elastomer layers and the structural components in wood. Different methods of coupling the condensation node to the interface surfaces were compared in a test model consisting of a floor–ceiling structure in wood, where the floor and the ceiling are separated by elastomer blocks. It was concluded that a rigid coupling is the most appropriate choice for the interface surfaces of the elastomer blocks, while a distributed coupling provides the most accurate results for the interface surfaces of the floor and the ceiling.

Keywords Multi-storey buildings • Vibrations • Finite element method • Substructure modelling • Interface reduction

10.1 Introduction

In 1994, a century-old ban on the construction of wooden buildings more than two storeys in height in Sweden was lifted, leading to the reintroduction of such buildings. The use of wood as a construction material in fact has many advantages. The lightweight properties of wood, for example, lower the material transportation costs involved and reduce the size of the foundations needed [1]. In addition, the energy consumption which occurs during the construction and the lifecycle of wooden buildings is lower than that of concrete buildings of comparable size [2]. At the same time, however, it is more difficult to build lightweight structures of wood in such a way that noise and disturbing vibrations in the different storeys and rooms is avoided, especially at low frequencies. The vibrations can be caused by, for example, footsteps, airborne sound, vibrating machines and external sources such as railway and road traffic.

To produce buildings of high performance regarding vibrations and structure-borne sound, it is desirable to have tools for predicting the effects of structural modifications prior to construction. Testing prototypes and performing experiments is both time-consuming and expensive. The long-term aim is therefore to develop prediction tools making use of finite element (FE) models that are valid for general load-cases. Accurately assessing the dynamic behaviour of lightweight multi-storey buildings requires use of FE models representing the geometry in considerable detail, resulting in very large models, the number of degrees of freedom (dofs) of which easily exceeds the limits of computer capacity. The question arises then of how such FE models can be reduced in size while at the same time being able to represent the dynamic characteristics of

O. Flodén (✉) • K. Persson • G. Sandberg

Department of Construction Sciences, Faculty of Engineering, Lund University, John Ericssons väg 1, SE-223 63 Lund, Sweden
e-mail: ola.floden@construction.lth.se

the building or buildings in question with sufficient accuracy. In the study, multi-storey buildings in wood are modelled by adopting a substructuring approach, in which the FE model of the full geometry is divided into substructures, these being reduced in size by employing some model order reduction method and coupled to form a reduced global model.

The methodology of substructuring originates from the component mode synthesis (CMS) by Craig and Bampton, presented in [3]. It is a suitable methodology for constructing reduced order models of structures which are divided into components in a natural way, such as engines and turbines, when the flexibility of each component has to be accounted for. A set of interface nodes, required for coupling of the substructures, are identified for the FE model of each substructure. The dofs at the interface nodes are retained when employing model order reduction, the other dofs being eliminated. Model order reduction is a Ritz procedure [4], selecting a number of basis vectors to approximate the deflection of the full model. Usually, the reduced models include deflection patterns caused by static loads acting on each interface dof, resulting in exact responses for static load cases. The dynamics of the eliminated dofs are approximated by including a set of additional Ritz basis vectors, in CMS by Craig and Bampton selected to be the eigenmodes of the substructure having the interface dofs constrained. Other model order reduction methods, offering alternative methods for selecting the Ritz basis vectors have been proposed and the efficiency of different reduction methods has been evaluated for various types of structures in Flodén (Reduction methods for the dynamic analysis of substructures of lightweight building structures, unpublished results) [5–8]. In general, the reduced system matrices have large bandwidths, making substructures with more than a few thousand dofs infeasible to analyse. It can therefore be necessary to restrict the number of interface dofs of each substructure, which can be rather large in case the substructure is in contact with the surroundings at surfaces with dense node distribution.

In a methodology commonly adopted for interface reduction, an additional node, referred to as a condensation node, is introduced to act as the interface to other substructures. The condensation node has both translational and rotational dofs, resulting in six dofs in a three-dimensional analysis, and is coupled to the nodes of the interface surface by some constraints. The coupling between a condensation node and the interface surface can be realised in different ways, a rigid body constraint for the interface surface being the most common option. Alternatively, the forces and moments acting on the condensation node can be distributed to the nodes of the interface surface by certain weight factors, resulting in the motion of the condensation node being a weighted average of the motion of the interface dofs. The two different types of coupling will be referred to here as rigid coupling and distributed coupling. These types of couplings are investigated in [9] and their respective advantages and drawbacks discussed. Rigid coupling will introduce additional stiffness in the model while distributed coupling is likely to underestimate the stiffness since it allows for sliding and penetration of the contact surfaces.

It should be noted that interface reduction is independent of the model order reduction of a substructure. The interface reduction will on the other hand affect the efficiency of the model order reduction since the Ritz basis vectors generated by a certain model order reduction method will be affected by the constraints imposed in the interface reduction. A number of studies have been presented in which the methodology of a condensation node is employed, for example, using rigid coupling in [10–12], distributed coupling in [13–15] and a combination of both types of couplings in [16]. There is, however, a lack of publications comparing the efficiency of different types of couplings for interface reduction. Moreover, the efficiency of different couplings are likely to vary to a great extent for different problems.

10.1.1 Timber Volume Elements

The lightweight properties of wood simplifies the use of prefabrication in the construction process compared to conventional concrete buildings. A type of prefabricated multi-storey building in wood, increasing in popularity in Sweden, is timber volume element (TVE) buildings. A TVE is a prefabricated module consisting of floor-, roof- and wall elements completed with electrical installations, flooring, cabinets, wardrobes, finishing etc. Each TVE typically constitutes a small apartment, one room or part of a larger room. The TVEs are transported to the construction site where they are stacked to form a complete building. In Fig. 10.1, the conceptual layout of a TVE building is illustrated, and in Fig. 10.2, drawings of junctions between a floor–ceiling structure and an apartment separating wall (to the left) and a façade wall (to the right) are shown. An advantage regarding vibrations and acoustic performance is that a floor is structurally separated from the ceiling of the storey below; the upper volume contains the floor whereas the lower volume comprises the ceiling. In between volumes, elastomer blocks are placed on the flanks to reduce the vibration transmission through the junctions. The elastomers are frequency dependent visco-elastic materials, the properties of such a material being determined in Negreira et al. (Characterization of an elastomer for noise and vibration isolation in lightweight timber buildings – Part I: obtaining material properties from laboratory testing, material modelling, and finite element simulations, unpublished results). The major structural connection between adjacent volumes is by means of the elastomers, the only additional connection being through a few tie plates used to fixate the TVEs.

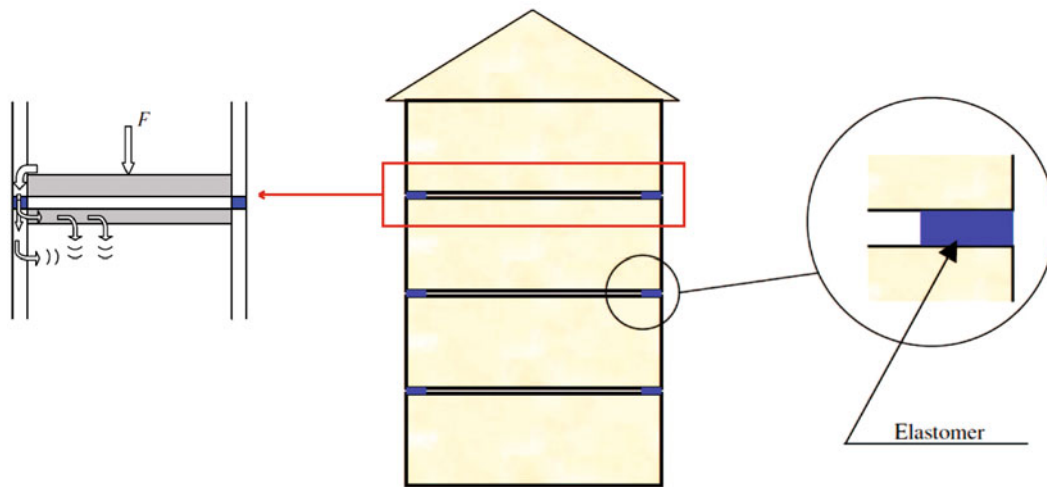


Fig. 10.1 Sketch of a TVE building [17]. The path of structural vibrations between storeys is illustrated in the figure to the *left* and an elastomer block is illustrated in the figure to the *right*

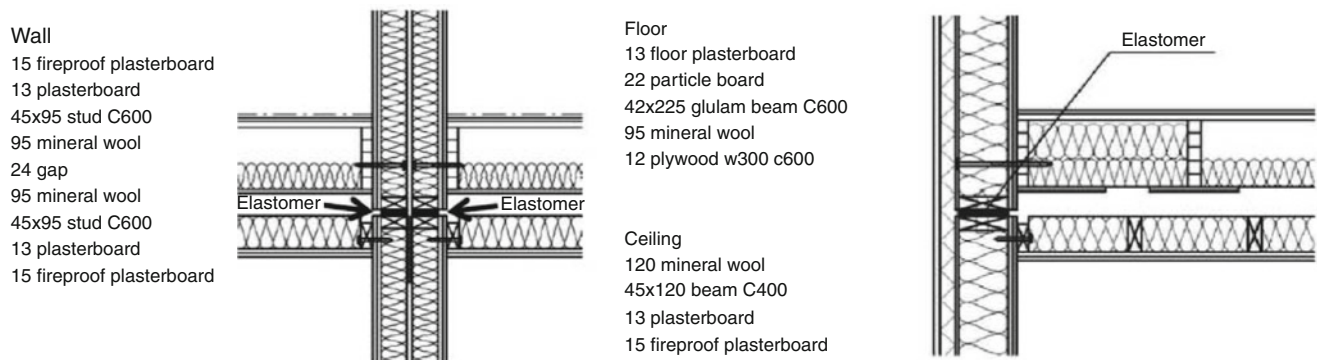


Fig. 10.2 Drawings of the TVE building system, showing sections of a floor–ceiling structure and junctions with an apartment separating wall (*left*) and a façade wall (*right*)

10.1.2 Objective

The studies presented in the paper provide important input to a project aiming at enabling the modelling of an assembly of TVEs. A FE model of a single TVE, meshed to behave accurately up to 200 Hz, contains millions of dofs. Hence, model order reduction is required to analyse a complete assembly of modules, even when powerful computational resources available. The TVE buildings, consisting of stacked volume elements coupled by small elastomer blocks, is suitable for substructure modelling, considering each module as a substructure. Since the material properties of the elastomers are frequency-dependent, the blocks cannot be included in conventional substructures, which are described by constant, frequency-independent, system matrices. Consequently, elastomer blocks will act as coupling elements, connecting the TVEs in the assembly of substructures.

Although a TVE is in contact with elastomer blocks only at small part of its surface, there is still a need for interface reduction since the TVEs can be connected to more than a hundred elastomer blocks, resulting in the total number of interface nodes being large. The methodology of using a condensation node is therefore employed to obtain efficient coupling of the substructures. Condensation nodes will be created both for the interface surfaces of the elastomer blocks and the TVEs. The displacement field of the elastomer blocks is not of interest, why the models of the elastomers can be modelled as some sort of coupling elements, describing the transfer function between the condensation nodes on each side of the blocks. Such an approach is described in Sect. 10.3. Section 10.4 presents a test model which was used for investigating how different methods for interface reduction affect the vibrations transmitted from a floor structure to the ceiling below, having a geometry of the type found in TVE buildings. The models were created and analysed in the commercial FE software *Abaqus*.

10.2 Governing Theory

When a model has been divided into substructures, two main issues has to be considered: selecting a reduced basis for each substructure and defining efficient coupling of the substructures. This section describes the general theory of model order reduction and, in specific, the method of CMS by Craig and Bampton, commonly employed in substructure modelling. Moreover, a mathematical description is presented for the constraints involved in the interface reduction methods employed in the studies presented in this paper.

10.2.1 Model Order Reduction

Assuming linear deformations, the dynamics of each substructure can be described by a FE system of equations of the following form [18]:

$$\mathbf{M}\ddot{\mathbf{u}} + \mathbf{C}\dot{\mathbf{u}} + \mathbf{K}\mathbf{u} = \mathbf{F}, \quad (10.1)$$

where $\mathbf{M}, \mathbf{C}, \mathbf{K} \in \mathbb{R}^{n \times n}$ are the mass, damping and stiffness matrices respectively, $\mathbf{F} = \mathbf{F}(t) \in \mathbb{R}^{n \times 1}$ is the load vector and $\mathbf{u} = \mathbf{u}(t) \in \mathbb{R}^{n \times 1}$ is the state vector. A dot denotes differentiation with respect to time, t . The objective of model reduction is to find a system of m dofs in which $m \ll n$, one which preserves the dynamic characteristics of the full model. The general approach is to approximate the state vector by use of the transformation $\mathbf{u} = \mathbf{T}\mathbf{u}_R$, where $\mathbf{T} \in \mathbb{R}^{n \times m}$ is a transformation matrix and $\mathbf{u}_R \in \mathbb{R}^{m \times 1}$ is a reduced state vector. Applying the transformation in question to Eq. (10.1) results in

$$\mathbf{M}_R \ddot{\mathbf{u}}_R + \mathbf{C}_R \dot{\mathbf{u}}_R + \mathbf{K}_R \mathbf{u}_R = \mathbf{F}_R, \quad (10.2)$$

$$\mathbf{M}_R = \mathbf{T}^T \mathbf{M} \mathbf{T}, \quad \mathbf{K}_R = \mathbf{T}^T \mathbf{K} \mathbf{T}, \quad \mathbf{C}_R = \mathbf{T}^T \mathbf{C} \mathbf{T}, \quad \mathbf{F}_R = \mathbf{T}^T \mathbf{F}, \quad (10.3)$$

where $\mathbf{M}_R, \mathbf{K}_R, \mathbf{C}_R \in \mathbb{R}^{m \times m}$ are the reduced mass, damping and stiffness matrices respectively and $\mathbf{F}_R \in \mathbb{R}^{m \times 1}$ is the reduced load vector. The dofs in the reduced state vector can be divided into two categories: physical dofs and generalised coordinates. Physical dofs are the dofs of the full system that are retained in the reduction process, whereas the generalised coordinates represent the amplitudes of various Ritz basis vectors that describe deflection shapes of the full model that are allowed in the reduced model.

In recent decades, many different model order reduction methods, involving procedures of varying types for establishing the transformation matrix and the reduced state vector involved, have been proposed in the literature. Guyan (static) reduction [19], Improved reduction system (IRS) [20] and CMS by Craig and Bampton [3] and by Craig and Chang [21] are examples of methods with physical interpretation, specifically developed for problems in structural dynamics, while methods based on Krylov subspace iterations [22] and balanced truncation [23], originating from control theory, can be employed for structural dynamics as well.

10.2.1.1 Component Mode Synthesis by Craig and Bampton

The first step in obtaining a system reduced according to CMS by Craig and Bampton is to perform a static reduction, retaining only the interface dofs. In the derivations below, the interface dofs are referred to as master dofs (m) and the remaining dofs referred to as slave dofs (s). Partitioning the state vector in terms of the master and slave categories enables the system matrices in Eq. (10.1) to be partitioned into sub-blocks as follows:

$$\begin{bmatrix} \mathbf{M}_{mm} & \mathbf{M}_{ms} \\ \mathbf{M}_{sm} & \mathbf{M}_{ss} \end{bmatrix} \begin{bmatrix} \ddot{\mathbf{u}}_m \\ \ddot{\mathbf{u}}_s \end{bmatrix} + \begin{bmatrix} \mathbf{K}_{mm} & \mathbf{K}_{ms} \\ \mathbf{K}_{sm} & \mathbf{K}_{ss} \end{bmatrix} \begin{bmatrix} \mathbf{u}_m \\ \mathbf{u}_s \end{bmatrix} = \begin{bmatrix} \mathbf{F}_m \\ \mathbf{F}_s \end{bmatrix}. \quad (10.4)$$

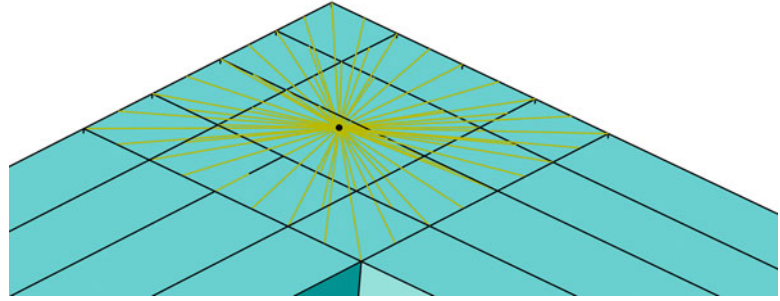
Solving the equation in the second row in Eq. (10.4) for \mathbf{u}_s results in

$$\mathbf{u}_s = -\mathbf{K}_{ss}^{-1} (\mathbf{M}_{sm} \ddot{\mathbf{u}}_m + \mathbf{M}_{ss} \ddot{\mathbf{u}}_s + \mathbf{K}_{sm} \mathbf{u}_m), \quad (10.5)$$

where it has been assumed that there are no loads acting on the slave dofs, so that $\mathbf{F}_s = 0$. The inertia terms in Eq. (10.5) are neglected, resulting in the following transformation of the state vector for Guyan reduction:

$$\begin{bmatrix} \mathbf{u}_m \\ \mathbf{u}_s \end{bmatrix} = \begin{bmatrix} \mathbf{I} \\ -\mathbf{K}_{ss}^{-1} \mathbf{K}_{sm} \end{bmatrix} \mathbf{u}_m = \mathbf{T}_{\text{Guyan}} \mathbf{u}_m. \quad (10.6)$$

Fig. 10.3 Illustration of a condensation node (black dot) coupled to the nodes of an interface surface, the constraints being illustrated by the yellow lines (Color figure online)



The inertia terms neglected in the condensation are compensated for by including a set of generalised coordinates ξ . These generalised coordinates represent the amplitudes of a set of eigenmodes for the slave structure, calculated with the master dofs being fixed. Setting $\mathbf{u}_m = 0$ and $\mathbf{F}_s = 0$ in Eq. (10.4) and assuming a harmonic solution results in the following eigenvalue problem:

$$\mathbf{K}_{ss}\Phi = \lambda\mathbf{M}_{ss}\Phi, \quad (10.7)$$

which can be solved for the eigenmodes Φ and the eigenvalues λ . A number of eigenmodes obtained from Eq. (10.7), referred to as retained eigenmodes, are selected as additional basis vectors to the approximation of the slave dofs in Eq. (10.6), resulting in

$$\mathbf{u}_s = -\mathbf{K}_{ss}^{-1}\mathbf{K}_{sm}\mathbf{u}_m + \sum \Phi_i \xi_i = \Psi\mathbf{u}_m + \Phi\xi, \quad (10.8)$$

which gives the transformation of the state vector for CMS by Craig and Bampton:

$$\begin{bmatrix} \mathbf{u}_m \\ \mathbf{u}_s \end{bmatrix} = \begin{bmatrix} \mathbf{I} & \mathbf{0} \\ \Psi & \Phi \end{bmatrix} \begin{bmatrix} \mathbf{u}_m \\ \xi \end{bmatrix} = \mathbf{T}_{\text{CMS}} \begin{bmatrix} \mathbf{u}_m \\ \xi \end{bmatrix}. \quad (10.9)$$

The accuracy of the reduced model depends upon the selection of retained eigenmodes, certain eigenmodes having a larger influence than others on the solution of a specific problem. To obtain a reduced model with as great an accuracy for general load distributions as possible, however, all the eigenmodes up to some chosen limit should be included, all eigenmodes below twice the highest frequency of interest being a rule of thumb. Substructures described by systems of the form in Eq. (10.9) can be coupled at the interface dofs, \mathbf{u}_m , either by a direct assembling procedure or by use of Lagrange multipliers [18].

10.2.2 Interface Reduction

Without the use of interface reduction, the vector \mathbf{u}_m in Eq. (10.4) will contain all dofs of the interface surfaces for a certain substructure, making the model order reduction inefficient in case the number of interface nodes is large. The efficiency can be improved by coupling the dofs of each interface surface to a condensation node, as illustrated in Fig. 10.3, resulting in \mathbf{u}_m containing only the dofs of the condensation nodes. In the simplest approach, a rigid coupling between an interface surface and its condensation node is assumed, such that the displacements \mathbf{u}_i in node i of the interface surface is described by

$$\mathbf{u}_i = \mathbf{u}_c + \Theta_c \times \mathbf{r}_{ci}, \quad (10.10)$$

assuming small deformations. \mathbf{u}_c and Θ_c are the displacements and rotations of the condensation node respectively and \mathbf{r}_{ci} is the vector from the condensation node to node i of the interface surface. In case two connecting substructures have very different stiffness properties, a rigid coupling is likely to provide acceptable results for the softer surface. If the additional stiffness introduced by the rigid coupling, however, results in large errors, a distributed coupling can be a more suitable alternative. In a distributed coupling, the forces and moments acting on the condensation node are distributed over the nodes of the interface surface according to

$$\mathbf{F}_i = \hat{\omega}_i (\mathbf{F}_c + (\mathbf{T}^{-1} (\mathbf{M}_c + \mathbf{r}_c \times \mathbf{F}_c)) \times \mathbf{r}_i), \quad (10.11)$$

$$\mathbf{T} = \sum_i \hat{\omega}_i ((\mathbf{r}_i \cdot \mathbf{r}_i) \mathbf{I} - (\mathbf{r}_i \mathbf{r}_i)), \quad (10.12)$$

$$\mathbf{r}_i = \mathbf{x}_i - \bar{\mathbf{x}}, \quad \mathbf{r}_c = \mathbf{x}_c - \bar{\mathbf{x}}, \quad (10.13)$$

$$\bar{\mathbf{x}} = \sum_i \hat{\omega}_i \mathbf{x}_i, \quad \hat{\omega}_i = \frac{\omega_i}{\sum_i \omega_i}, \quad (10.14)$$

where \mathbf{F}_i is the force acting on node i of the interface surface, \mathbf{F}_c and \mathbf{M}_c are the force and moment acting on the condensation node, \mathbf{x}_i and \mathbf{x}_c are the coordinates of node i and the condensation node respectively and ω_i is the weight factor for node i . The method of distributing the forces and moments leads to the motion of the condensation node being a weighted average of the displacements in the interface surface nodes,

$$\mathbf{u}_c = \sum_i \hat{\omega}_i \mathbf{u}_i, \quad (10.15)$$

$$\Theta_c = \sum_i \hat{\omega}_i \frac{\mathbf{r}_{ci}}{|\mathbf{r}_{ci}|^2} \times \mathbf{u}_i. \quad (10.16)$$

The weight factors are arbitrary, meaning that an infinite number of distributed coupling methods can be defined. Four methods for determining the weight factors, all implemented in *Abaqus*, are presented below. The most straightforward method is uniform weighting, distributing equal load to all nodes of the interface surface. The three remaining methods employ decreasing weight at farther distance from the condensation node, using polynomials of different degrees.

Uniform weighting

$$\omega_i = 1. \quad (10.17)$$

Linearly decreasing weighting

$$\omega_i = 1 - \left| \frac{\mathbf{r}_{ci}}{\mathbf{r}_{c0}} \right|, \quad (10.18)$$

where \mathbf{r}_{c0} is the vector from the condensation node to the furthest node at the interface surface.

Quadratically decreasing weighting

$$\omega_i = 1 - \left| \frac{\mathbf{r}_{ci}}{\mathbf{r}_{c0}} \right|^2. \quad (10.19)$$

Cubically decreasing weighting

$$\omega_i = \left| \frac{\mathbf{r}_{ci}}{\mathbf{r}_{c0}} \right|^2 + 2 \left| \frac{\mathbf{r}_{ci}}{\mathbf{r}_{c0}} \right|^3. \quad (10.20)$$

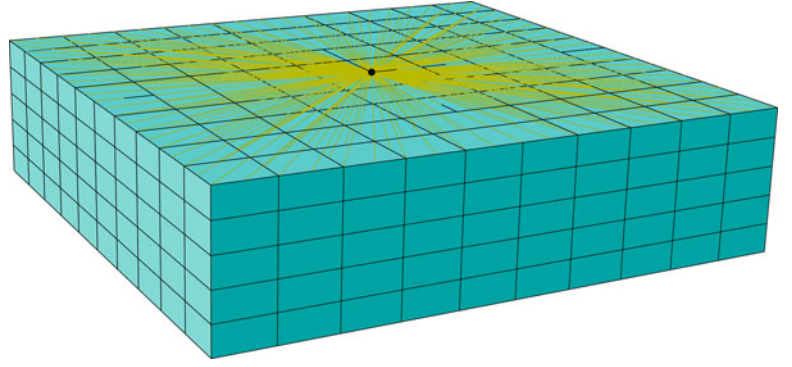
10.3 Elastomer Blocks as Coupling Elements

The elastomer layers were, in the numerical studies presented here, modelled as blocks of Sylodyn[®], a closed-cell polyurethane material manufactured by Getzner Werkstoffe G.m.b.H. A Sylodyn elastomer block of size $100 \times 95 \times 25 \text{ mm}^3$, used in real TVE buildings, was studied, the FE mesh being shown in Fig. 10.4. In Negreira et al. (Characterization of an elastomer for noise and vibration isolation in lightweight timber buildings – Part I: obtaining material properties from laboratory testing, material modelling, and finite element simulations, unpublished results), frequency-dependent visco-elastic material parameters were evaluated for a type of Sylodyn, these parameters being employed here.

Having frequency-dependent substructures is possible in steady-state analyses but results in inefficient models since different system matrices are required for each frequency step in the analyses. It is therefore preferable to exclude the elastomer blocks from the substructures because of their frequency-dependent material properties. This results in the substructures being described by constant, frequency-independent, system matrices.

In substructure models of TVE buildings, the elastomer blocks can be regarded as coupling elements connecting the substructures of TVE modules. The interface surfaces are the top and bottom surfaces of the elastomer blocks, these being reduced by introducing condensation nodes as illustrated in Fig. 10.4, resulting in a total of twelve interface dofs per

Fig. 10.4 The FE mesh for the model of an elastomer block. The *black dot* illustrates a condensation node and the *yellow lines* the constraints between the condensation node and the interface surface (Color figure online)



elastomer block. The elastomers are in general much softer than the wood components they are connected to. Consequently, the interface surfaces of the elastomer blocks are exposed to relatively small strains compared to the rest of the blocks, implying rigid coupling to be a good approximation in the interface reduction.

The displacement field in the elastomer blocks are in general not of interest, why the full model of a block may be replaced by some sort of simplified coupling element connecting the condensation nodes on each side. It is assumed here that the elastomer block can be represented by six frequency-dependent spring-damper systems connecting each of the six dofs, three translations and three rotations, of the two condensation nodes. The motion of a parallel spring-damper system connecting two nodes with displacements u_1 and u_2 is described by

$$k \begin{bmatrix} 1 & -1 \\ -1 & 1 \end{bmatrix} \begin{bmatrix} u_1 \\ u_2 \end{bmatrix} + c \begin{bmatrix} 1 & -1 \\ -1 & 1 \end{bmatrix} \begin{bmatrix} \dot{u}_1 \\ \dot{u}_2 \end{bmatrix} = \begin{bmatrix} f_1 \\ f_2 \end{bmatrix}, \quad (10.21)$$

where k is the stiffness coefficient, c the damping coefficient and f_1 and f_2 the forces acting on the two nodes. By assuming $u_1 = 0$ and a harmonic load and response for the system,

$$f_2 = F_2 \exp(i\omega t), \quad u_2 = U_2 \exp(i\omega t), \quad (10.22)$$

where F_2 and U_2 are the complex force and load amplitudes and ω the angular frequency), Eq. (10.21) is reduced to

$$k(\omega)U_2 + i\omega c(\omega)U_2 = F_2, \quad (10.23)$$

where the frequency dependence of $k(\omega)$ and $c(\omega)$ is introduced. Applying a unit load, $F_2 = 1$, results in

$$k(\omega) + i\omega c(\omega) = \frac{1}{U_2}, \quad (10.24)$$

which is used to identify $k(\omega)$ and $c(\omega)$ as

$$k(\omega) = \operatorname{Re} \left(\frac{1}{U_2} \right), \quad c(\omega) = \frac{1}{\omega} \operatorname{Im} \left(\frac{1}{U_2} \right). \quad (10.25)$$

The two condensation nodes of the elastomer block shown in Fig. 10.4 have the translational dofs $u_{1,2,3}^1$ and $u_{1,2,3}^2$ respectively and the rotational dofs $\Theta_{1,2,3}^1$ and $\Theta_{1,2,3}^2$ respectively, where the superscripts denote the condensation node and the subscripts denotes the direction of the dof. The forces acting on the two condensation nodes are denoted $f_{1,2,3}^1$ and $f_{1,2,3}^2$ and the momentums denoted $m_{1,2,3}^1$ and $m_{1,2,3}^2$. Replacing the elastomer block with six frequency-dependent spring-damper systems of the form in Eq. (10.21) results in the following equation system describing the block:

$$\mathbf{K}\mathbf{u} + \mathbf{C}\dot{\mathbf{u}} = \mathbf{F}, \quad (10.26)$$

$$\mathbf{K}(\omega) = \begin{bmatrix} \mathbf{K}_1^u(\omega) & \mathbf{0} & \cdots & \cdots & \mathbf{0} \\ \mathbf{0} & \mathbf{K}_2^u(\omega) & & & \\ \vdots & & \mathbf{K}_3^u(\omega) & & \\ & & & \mathbf{K}_1^\Theta(\omega) & \vdots \\ \vdots & & & & \mathbf{K}_2^\Theta(\omega) & \mathbf{0} \\ \mathbf{0} & \cdots & \cdots & \mathbf{0} & \mathbf{0} & \mathbf{K}_3^\Theta(\omega) \end{bmatrix},$$

$$\mathbf{C}(\omega) = \begin{bmatrix} \mathbf{C}_1^u(\omega) & \mathbf{0} & \cdots & \cdots & \mathbf{0} \\ \mathbf{0} & \mathbf{C}_2^u(\omega) & & & \\ \vdots & & \mathbf{C}_3^u(\omega) & & \\ & & & \mathbf{C}_1^\Theta(\omega) & \vdots \\ \vdots & & & & \mathbf{C}_2^\Theta(\omega) & \mathbf{0} \\ \mathbf{0} & \cdots & \cdots & \mathbf{0} & \mathbf{0} & \mathbf{C}_3^\Theta(\omega) \end{bmatrix},$$

$$\mathbf{u}^T = [u_1^1 \quad u_1^2 \quad u_2^1 \quad u_2^2 \quad u_3^1 \quad u_3^2 \quad \Theta_1^1 \quad \Theta_1^2 \quad \Theta_2^1 \quad \Theta_2^2 \quad \Theta_3^1 \quad \Theta_3^2],$$

$$\mathbf{F}^T = [f_1^1 \quad f_1^2 \quad f_2^1 \quad f_2^2 \quad f_3^1 \quad f_3^2 \quad m_1^1 \quad m_1^2 \quad m_2^1 \quad m_2^2 \quad m_3^1 \quad m_3^2],$$

where $\mathbf{K}_{1,2,3}^{u,\Theta}, \mathbf{C}_{1,2,3}^{u,\Theta} \in \mathbb{R}^{2 \times 2}$ are the stiffness and damping matrices as defined in Eq. (10.21) for each of the six spring-damper systems. Equation (10.25) can be used to identify all the matrices $\mathbf{K}_{1,2,3}^{u,\Theta}$ and $\mathbf{C}_{1,2,3}^{u,\Theta}$ by studying one of the six spring-damper systems at a time, locking eleven of the twelve interface dofs and applying a unit force/momentum at the free dof. This approach neglects any coupling between the dofs acting in different directions, as seen by the zero terms in the system matrices in Eq. (10.26). The full matrices can be determined by applying a unit displacement at one dof at a time, where the corresponding column of the stiffness and damping matrices are determined from the real and imaginary parts of the reaction forces/momentums, respectively. Involving the full matrices would require user implemented elements to be employed in commercial FE software. The spring-damper systems can, however, be employed directly in such software, a practical advantage when dealing with models involving many different coupling elements. The validity of employing the spring-damper approach for modelling the elastomer blocks was checked in the test model presented in the following section.

10.4 Test Model

A model of a floor–ceiling structure in wood, the FE mesh being shown in Fig. 10.5, was investigated in order to compare the accuracy of different methods for interface reduction. The structure is $3,690 \times 3,045 \times 510 \text{ mm}^3$ large, with the floor and ceiling consisting of five load-bearing wooden beams each, the floor having a particle board surface and the ceiling having a plaster board surface. Both the floor and the ceiling have beams placed at the ends of the load-bearing beams, perpendicular to these, creating box-like structures. The orthotropic material properties in Table 10.1 was employed for the wood beams and the isotropic properties in Table 10.2 was employed for the particle board and the plaster board. The floor and ceiling structures are connected through elastomer blocks with dimensions $95 \times 100 \times 25 \text{ mm}^3$, having the frequency-dependent

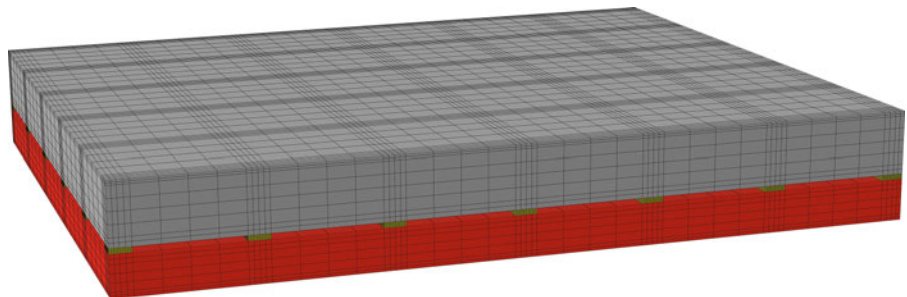


Fig. 10.5 The FE mesh for the model of the floor–ceiling structure. The floor is shown in grey, the ceiling in red and the elastomer blocks in yellow (Color figure online)

Table 10.1 The material parameters used for the wooden beams, the stiffness parameters being given in terms of MPa and the density in kg/m³

| E_1 | E_2 | E_3 | G_{12} | G_{13} | G_{23} | ν_{12} | ν_{13} | ν_{23} | ρ |
|-------|-------|-------|----------|----------|----------|------------|------------|------------|--------|
| 8,500 | 350 | 350 | 700 | 700 | 50 | 0.2 | 0.2 | 0.3 | 432 |

Table 10.2 The material parameters used for the particle board and the plaster board, the modulus of elasticity being given in terms of MPa and the density in kg/m³

| | E | ν | ρ |
|----------------|-------|-------|--------|
| Particle board | 3,000 | 0.3 | 767 |
| Plaster board | 2,000 | 0.2 | 692 |

visco-elastic material properties determined in Negreira et al. (Characterization of an elastomer for noise and vibration isolation in lightweight timber buildings – Part I: obtaining material properties from laboratory testing, material modelling, and finite element simulations, unpublished results). The blocks were placed at a centre-to-centre distance of 600 mm around the flanks and provide the only connection between the floor and the ceiling.

The floor–ceiling structure was analysed by steady-state analyses for frequencies up to 200 Hz, applying a vertical unit load at the middle of the floor surface and having the displacements at the four corners of the ceiling surface locked. In order to investigate the vibration transmission from the floor to the ceiling when employing different methods for reducing the interface surfaces to the elastomer blocks, the vibration amplitudes in the nodes at the ceiling surface was evaluated by a root-mean-square (RMS) value of the complex magnitudes of the displacements. Due to symmetry, the displacements were evaluated in a fourth of the ceiling surface. For each frequency step in the steady-state analyses, the RMS value was calculated as

$$u_{RMS}(f) = \sqrt{\frac{1}{n} \sum_{i=1}^n U_i(f)^2}, \quad (10.27)$$

where U_i is the magnitude of the three complex displacement magnitudes in node i , n is the number of nodes in a fourth of the ceiling surface and f is frequency. The model employing interface reduction was compared to the full model by calculating a relative error in RMS-values according to

$$u_{RMS}^{error}(f) = \frac{|u_{RMS}^{red}(f) - u_{RMS}^{full}(f)|}{u_{RMS}^{full}(f)} \cdot 100, \quad (10.28)$$

where u_{RMS}^{red} is the RMS value of a model employing interface reduction and u_{RMS}^{full} is the RMS value of the full model. The quotient is multiplied by 100 to obtain the relative error in percent. In the result figures presented here, green, blue and red dashed lines are included to indicate the 0.1, 1 and 10 % error levels.

First, the validity of employing the spring-damper approach for modelling the elastomer blocks was checked. This was carried out by modelling the interface surfaces between elastomer blocks and wood components as rigid in the full model. A model employing the spring-damper systems for the elastomer blocks, with the interface surfaces of the wood components being modelled as rigid, was compared to the full model with rigid interface surfaces. In case the spring-damper systems would represent the full model of an elastomer block exactly, the two models would yield precisely the same results since the properties of the spring-damper systems were evaluated assuming rigid interface surfaces. The relative error of the model employing the spring-damper systems, compared to the full model with rigid interface surfaces, is shown in Fig. 10.6. It can be observed that the error is lower than 1 % for most frequencies, the exception being frequencies between 30 and 100 Hz where the error reaches a maximum of 4 %. Consequently, the spring-damper systems offers a fairly good representation of the full model of an elastomer block. In the results presented below, where different interface reduction methods are compared, the spring-damper systems were employed in the models (the full model of course involving the full elastomer block models, without assuming rigid interface surfaces).

Fig. 10.6 Relative error in RMS values when employing the spring-damper representation of an elastomer block, compared to a full model with rigid interface surfaces

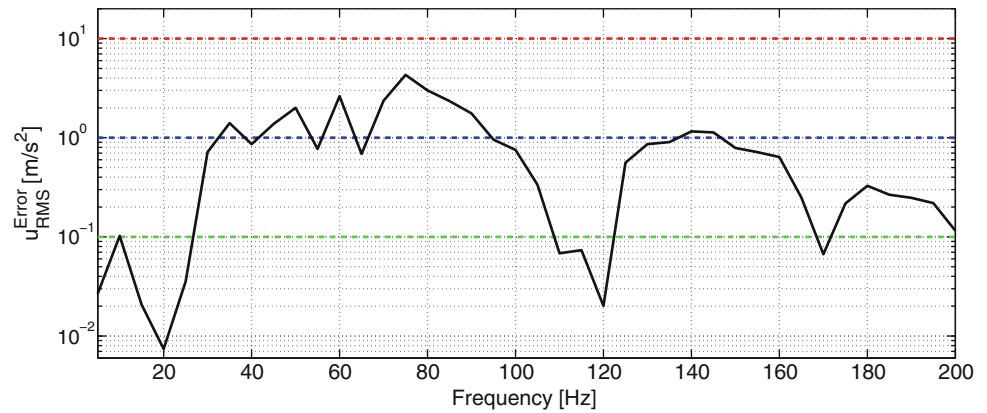


Fig. 10.7 Relative error in RMS values when employing the five different methods for interface reduction

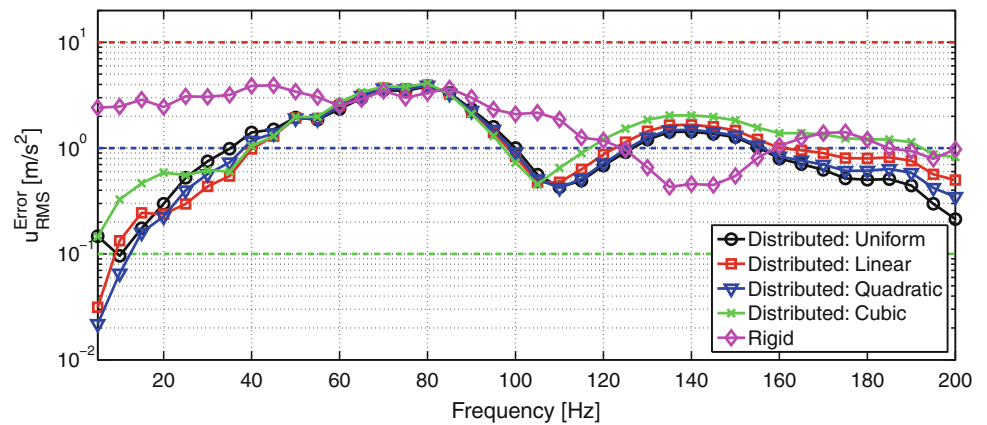


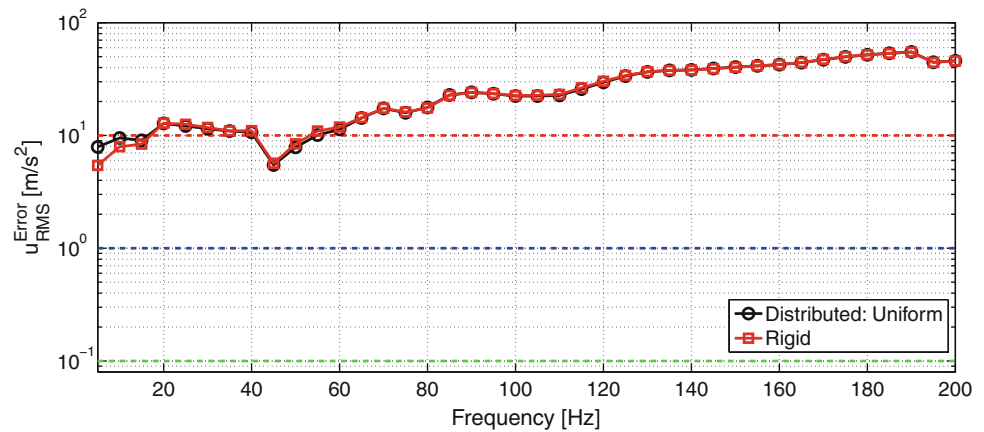
Table 10.3 Maximum and average values of the relative errors in RMS values when employing the five different methods for interface reduction

| | Distributed uniform | Distributed linear | Distributed quadratic | Distributed cubic | Rigid |
|-------------------|---------------------|--------------------|-----------------------|-------------------|-------|
| Maximum error (%) | 4.47 | 4.51 | 4.52 | 4.56 | 5.86 |
| Average error (%) | 1.00 | 1.06 | 1.01 | 1.25 | 1.66 |

The five different methods for interface reduction (rigid coupling and four variants of distributed coupling) were employed at the interface surfaces of the floor and the ceiling. In Fig. 10.7, the spectra of relative errors obtained when employing the five methods, compared to the full model, is shown and in Table 10.3, the maximum and average values of the error spectra are presented. It can be observed that a rigid coupling for the interface surfaces is the least accurate method, especially at lower frequencies (<60 Hz). The different variants of distributed coupling provide similar results, a lower degree of the weighting polynomial in general resulting in lower errors, with uniform weighting providing the best accuracy regarding both maximum and average errors. Rigid coupling can, however, be the most suitable method in certain situations, depending on the frequencies of interest. It can be observed in Fig. 10.7 that the errors obtained when employing rigid coupling is significantly lower than that of the distributed coupling methods for frequencies between 130 and 150 Hz.

Finally, it was investigated how employing distributed coupling for the interface surfaces of the elastomer blocks affects the accuracy. The properties of the spring-damper systems replacing the full models of the elastomer blocks were, consequently, evaluated when employing distributed coupling. The relative errors obtained when employing distributed coupling with uniform weighting for the elastomer blocks are shown in Fig. 10.8, using both rigid coupling and distributed coupling, also with uniform weighting, for the interface surfaces of the floor and the ceiling. It can be observed how the error levels are very high in comparison to the results shown in Fig. 10.7, where rigid coupling was employed for the interface surfaces of the elastomer blocks. As discussed in Sect. 10.3, where rigid coupling was assumed to be suitable for interface reduction of the elastomer blocks, this can be explained by the large difference in stiffness between the wood components and the elastomer blocks, resulting in relatively small strains at the interface surfaces compared to the strains in the rest of the elastomer blocks.

Fig. 10.8 Relative error in RMS values when employing distributed coupling with uniform weighting for the interface surfaces of the elastomer blocks. The two plots show the errors when employing rigid coupling and distributed coupling with uniform weighting for the interface surfaces of the floor and the ceiling



10.5 Conclusions

The results presented in the paper provide important information in the process of establishing efficient substructure models of multi-storey buildings in wood. It was investigated, by numerical studies on a test model, how the interface surfaces should be treated when employing the methodology of condensation nodes for interface reduction.

The frequency-dependent spring-damper systems, employed as simplified coupling elements representing the elastomer blocks, proved to model the coupling between the two condensation nodes of the elastomer blocks fairly good. Depending on the required level of accuracy, it may, however, be necessary to include the full matrices coupling all dofs of the two condensation nodes and not only the corresponding dofs of each node, as is the case when employing the spring-damper systems. The reasons for not including the full coupling matrices are purely practical, simplifying the modelling process when working with commercial FE software.

For the elastomer blocks, rigid coupling at the interface surfaces was superior to distributed coupling, the latter resulting in very large errors. For the interface surfaces of the wood components (the floor and the ceiling in the test model) distributed couplings was the most accurate method, a lower degree of the weighting polynomial in general resulting in lower errors. Depending on the frequencies of interest, however, a rigid coupling can be the most suitable alternative in certain cases.

Acknowledgements The financial support for this work provided by the Silent Spaces project, a part of the EU program Interreg IV A, is gratefully acknowledged.

References

1. Stehn L, Rask LO, Nygren I, Östman B (2008) Byggandet av flervåningshus i trä – Erfarenheter efter tre års observation av träbyggandets utveckling. Technical Report, Luleå University of Technology, Sweden
2. Gustavsson L, Pingoud K, Sathre R (2006) Carbon dioxide balance of wood substitution: comparing concrete- and wood-framed buildings. *Mitig Adapt Strateg Glob Change* 11:667–691
3. Craig RR, Bampton M (1968) Coupling of substructures in dynamic analysis. *AIAA J* 6:1313–1319
4. Arnold RR, Citerley RL (1985) Application of Ritz vectors for dynamic analysis of large structures. *Comput Struct* 21(5):901–907
5. Fehr J, Eberhard P (2011) Simulation process of flexible multibody systems with non-modal model order reduction techniques. *Multibody Syst Dyn* 25(3):313–334
6. Nowakowski C, Kürschner P, Eberhard P, Benner P (2013) Model reduction of an elastic crankshaft for elastic multibody simulations. *J Appl Math Mech* 93(4):198–216
7. Koutsovasilis P, Beitelschmidt M (2008) Comparison of model reduction techniques for large mechanical systems. *Multibody Syst Dyn* 20(2):111–128
8. Witteveen W (2012) On the modal and non-modal model reduction of metallic structures with variable boundary conditions. *World J Mech* 2(6):311–324
9. Heirman GHK, Desmet W (2010) Interface reduction of flexible bodies for efficient modeling of body flexibility in multibody dynamics. *Multibody Syst Dyn* 24(2):219–234
10. Albers A, Emmrich D, Haeussler P (2002) Automated structural optimization of flexible components using MSC.Adams/Flex and MSC.Nastran Sol200. In: 1th Europ MSC.ADAMS users conference, London
11. Albers A, Otnad J, Weiler H, Haeussler P (2007) Methods for lightweight design of mechanical components in humanoid robots. In: IEEE-RAS 7th international conference on humanoid robots, Pittsburg, pp 609–615

12. Peeters J (2006) Simulation of dynamic drive train loads in a wind turbine. Ph.D. dissertation, Katholieke Universiteit Leuven, Belgium
13. Helsen J, Heirman G, Vandepitte D, Desmet W (2008) The influence of flexibility within multibody modeling of multi-megawatt wind turbine gearboxes. In: Proceedings of the ISMA 2008 international conference on noise and vibration engineering
14. Helsen J, Vandepitte D, Desmet W, Peeters J, Goris S, Vanhollenbeke F, Marrant B, Meeusen W (2009) From torsional towards flexible 6 dofs models for dynamic analysis of wind turbine gearboxes. In: Proceedings of the European wind energy conference and exhibition, Marseille, France
15. Kuratani F, Okuyama M, Yamauchi T, Washio S (2010) Finite element modeling of spot welds for vibration analysis. In: 5th Asian conference on multibody dynamics, vol 1, pp 981–988
16. Ricci S (2013) Model reduction techniques in flexible multibody dynamics with application to engine cranktrain simulation. Ph.D. dissertation, University of Bologna, Italy
17. Ljunggren F, Ågren A (2011) Potential solutions to improved sound performance of volume based lightweight multi-storey timber buildings. *Appl Acoust* 72(4):231–240
18. Bathe KJ (1996) Finite element procedures. Prentice Hall, New York
19. Guyan RJ (1965) Reduction of stiffness and mass matrices. *AIAA J* 3:380
20. O'Callahan J (1989) A procedure for an improved reduced system (IRS) model. In: Proceedings of the 7th international modal analysis conference, pp 17–21
21. Craig RR, Chang CJ (1976) A review of substructure coupling methods for dynamic analysis. *Adv Eng Sci* 2:393–408
22. Lohmann B, Salimbahrami B (2003) Introduction to Krylov subspace methods in model order reduction. *Methods Appl Autom* 1–13
23. Reis T, Stykel T (2008) Balanced truncation model reduction of second-order systems. *Math Comput Model Dyn Syst* 14(5):391–406

Chapter 11

Deformation Mode Selection and Orthonormalization for an Efficient Simulation of the Rolling Contact Problem

Karim Sherif and Wolfgang Witteveen

Abstract The dynamic simulation of contact in rolling processes is very time-consuming. This is mainly based on the fine resolution of the surface domain of each roll, which, however, is essential in order to capture the effect of concentrated contact forces. Existing model order reduction techniques cannot be readily applied due to the nonlinear nature of the contact dynamics. In order to improve the speed of contact analysis, the present paper proposes a sophisticated combination of so-called characteristic static correction modes and vibration normal modes for describing the deformation of each roll. While the characteristic static correction modes are required to capture the concentrated nonlinear contact forces, the vibration normal modes describe the global deformation behavior of the rolls. For the computation of the characteristic static correction modes, first attachment modes are computed for a longitudinal sub-area of each roll. Then an eigenanalysis is performed on the component mode synthesis mass and stiffness matrices that correspond to the attachment modes. The resultant eigenvectors have been truncated and applied to the entire surface domain of the rolls. In order to obtain well-conditioned equations, all modes are finally orthonormalized. An example from the metal forming industry is used to demonstrate the results.

Keywords Rolling contact • Component mode synthesis • Craig-Bampton method • Attachment modes • Interface modes

Nomenclature

| | |
|--------------------|---|
| \mathbf{M} | Mass matrix of FE model |
| \mathbf{K} | Stiffness matrix of FE model |
| \mathbf{f} | External force vector of FE model |
| \mathbf{u} | Vector of nodal DOF of FE model |
| \mathbf{u}_b | Boundary DOF of FE model |
| \mathbf{u}_i | Inner DOF of FE model |
| \mathbf{u}_c | Potential contact DOF of FE model |
| \mathbf{u}_n | DOF of set \mathbf{u}_i minus DOF of set \mathbf{u}_c |
| Φ_n | Fixed-interface normal modes |
| Ψ_c | Constraint modes |
| Ψ_a | Attachment modes |
| $\hat{\Psi}_a$ | Characteristic attachment modes |
| \mathbf{q} | Generalized coordinates of reduced model |
| \mathbf{F}_{ESL} | Equivalent static load case matrix |

K. Sherif (✉)

Johannes Kepler University Linz, Altenbergerstr. 69, 4040 Linz, Austria
e-mail: karim.sherif@jku.at

W. Witteveen

University of applied sciences—Wels, Stelzhamerstr. 23, 4600 Wels, Austria
e-mail: wolfgang.witteveen@fh-wels.at

11.1 Introduction and Motivation

The simulation of contact problems has occupied an important place in mechanical engineering problems. In the engineering practice, contact problems are usually analyzed by the means of commercial Finite Element (FE) codes. However, for contact problems the total number of degrees of freedom (DOF) is usually very large due to the fine discretization of the contact area, which however is required for describing the dynamic behavior of the entire system sufficiently accurate. Due to the huge number of DOF an economically handling of such systems is, in general, not possible, even not with modern computers. In order to reduce the number of DOF of the entire system, and, thus, to increase computational efficiency, some form of component mode synthesis (CMS) is usually applied to the FE model. The underlying idea of CMS methods is to divide the entire system into substructures or components, and to represent the deflection of each component by a linear combination of preselected modes on the expense of restricting accuracy of the solution to a smaller frequency domain. Usually, the set of preselected modes consists of normal modes and Ritz-vectors, whereby the Ritz-vectors are derived from static deformation shapes. The latter Ritz-vectors are often also called static correction modes. Clearly, after dividing the entire system into components, the components have to be combined at the interfaces again, which are in case of contact problems the contact areas.

Most applications of CMS take advantage of one of the two methods, the fixed-interface or the free-interface method. The fixed-interface CMS technique presented by Hurty [1, 2] and modified by Craig and Bampton [3] is widely used, since the reduction procedure is straightforward and typically produces highly accurate models with relatively few component modes [4]. A detailed discussion and a comprehensive review on the different CMS methods are given in [5, 6] and [7]. In the present paper the focus is only on the widely adopted fixed-interface Craig-Bampton method due to its superior accuracy and its ease in implementation. The Craig-Bampton method uses fixed-interface normal modes and so-called constraint modes. The constraint modes are static correction modes.

The Craig-Bampton CMS method can be effectively and consistently used for the time integration of large linear elastic structures, but it is not applicable for structures with nonlinear local effects in terms of contact problems. This is based on the fact that the latter reduction method does preserve the nodal DOF at interfaces and each interface DOF leads to an additional mode in the mode base. For an accurate application of contact law and (or) friction law in the contact region (nonlinear effects) all nodal DOF of a contact area need to be considered as interface DOF and this leads to an unacceptable number of modes.

The latter problem of a huge number of modes due to a fine discretization in the contact area could be solved by applying a form of interface reduction method. The idea of interface reduction was first suggested by Craig and Chang in a report to NASA [8]. Several papers can be found in the literature where interface modes are suggested for the fixed-interface CMS method, see e.g. [9–11]. In these methods, the static correction modes are replaced by so-called interface modes. The latter modes are the first few modes after performing an eigenanalysis on the component mode synthesis mass and stiffness matrices that correspond to the static correction modes. The interface reduction method, so to say, replaces the static correction modes by a few generalized coordinates associated with the interface modes. Alternative interface reduction methods were proposed in [8, 9, 12, 13].

Although it is possible to reduce the number of static correction modes by applying an interface reduction method, the latter method is not directly applicable to a component of a rolling contact problem. This is the case because the entire surface of each component of the rolling contact system has to be considered as potential contact area, which leads, even after applying an interface reduction method, to a mode basis with a very huge number of DOF. This is mainly based on the fact that the actual contact surface is very small compared to the potential contact area and, therefore, for accurately representing local deformation effects a very huge number of interface modes would be required. The accurate representation of local deformation effects is, however, of great importance in case of contact problems, because contact forces depend strongly on local deflections. The extension of the Craig-Bampton CMS method with interface modes is for many problems a targeted problem solution. However, in case of rolling contact problems this sub-structuring methodology is inefficient, since a huge number of DOF in the reduced basis is needed to approximate the solution to a given accuracy. Therefore, the main goal of the present paper is to define an efficient sub-structuring methodology for rolling contact problems by choosing a novel way for computing those modes, which are needed to represent the local deformation effects.

Our paper is outlined as follows. Firstly, a short review on the fixed-interface Craig-Bampton CMS method will be given. Then, a methodology for generating a tailored concept for computing a mode basis for rolling contact problems will be presented. This methodology consists, in a first step, in computing interface modes (also called characteristic attachment modes (CAM) in the present paper) for a longitudinal sub-area of each roll of the rolling contact problem. In the second step of the methodology presented, an eigenanalysis is performed on the component mode synthesis mass and stiffness matrices that correspond to the attachment modes of the latter sub-area. In a third step, the resultant eigenvectors were truncated and applied to the entire surface domain of the rolls. Finally, a numerical example from the metal forming industry is presented in order to demonstrate the proposed algorithm, and some conclusions are drawn to close the paper.

11.2 Craig-Bampton CMS Method

In this section the Craig-Bampton CMS method is shortly summarized. More details on this method can be found in [3].

The equation of motion of an unreduced component of the system can be formally written as

$$\mathbf{M}\ddot{\mathbf{u}} + \mathbf{K}\mathbf{u} = \mathbf{f} \quad (11.1)$$

where \mathbf{M} and \mathbf{K} are the assembled symmetric mass and stiffness matrices of the component, \mathbf{f} represents the time-varying and in case of contact problems state-dependent force vector, and the vector \mathbf{u} contains the set of FE DOF (usually nodal displacements) of the component model. The vector $\ddot{\mathbf{u}}$ is the second derivative of \mathbf{u} with respect to time. The following partitioned form of Eq. (11.1) will be useful in the derivation of the fixed-interface normal modes and the interface constraint modes, where the boundary coordinates are assembled in the set \mathbf{u}_b and the free (interior) coordinates in the set \mathbf{u}_i :

$$\begin{bmatrix} \mathbf{M}_{bb} & \mathbf{M}_{bi} \\ \mathbf{M}_{ib} & \mathbf{M}_{ii} \end{bmatrix} \begin{bmatrix} \ddot{\mathbf{u}}_b \\ \ddot{\mathbf{u}}_i \end{bmatrix} + \begin{bmatrix} \mathbf{K}_{bb} & \mathbf{K}_{bi} \\ \mathbf{K}_{ib} & \mathbf{K}_{ii} \end{bmatrix} \begin{bmatrix} \mathbf{u}_b \\ \mathbf{u}_i \end{bmatrix} = \begin{bmatrix} \mathbf{f}_b \\ \mathbf{0} \end{bmatrix} \quad (11.2)$$

Restraining all boundary DOF and solving the eigenvalue problem

$$\left(\mathbf{K}_{ii} - \omega_p^2 \mathbf{M}_{ii} \right) \Phi_p = \mathbf{0} \quad (11.3)$$

one obtains the fixed-interface normal modes. According to the partitioning of Eq. (11.2) the fixed-interface modal matrix Φ_n for the entire coordinates takes the form

$$\Phi_n = \begin{bmatrix} \mathbf{0}_{bn} \\ \Phi_p \end{bmatrix} \quad (11.4)$$

Typically, only those m_k normal modes are retained with an eigenfrequency below the maximum frequency of interest.

The interface constraint modes are the static deformation of the interior coordinates by imposing a unit displacement at one physical coordinate of the set \mathbf{u}_b , while the remaining DOF of the same set are restrained. This procedure is applied consecutively to all coordinates of the set \mathbf{u}_b . That is,

$$\begin{bmatrix} \mathbf{K}_{bb} & \mathbf{K}_{bi} \\ \mathbf{K}_{ib} & \mathbf{K}_{ii} \end{bmatrix} \begin{bmatrix} \mathbf{I}_{bb} \\ \Psi_{ib} \end{bmatrix} = \begin{bmatrix} \mathbf{R}_{bb} \\ \mathbf{0}_{ib} \end{bmatrix} \quad (11.5)$$

where \mathbf{R}_{bb} is the corresponding external force matrix and \mathbf{I}_{bb} is the $(b \times b)$ identity matrix. Consequently, the constraint-mode matrix Ψ_c is given by

$$\Psi_c = \begin{bmatrix} \mathbf{I}_{bb} \\ \Psi_{ib} \end{bmatrix} = \begin{bmatrix} \mathbf{I}_{bb} \\ -[\mathbf{K}_{ii}^{-1} \mathbf{K}_{ib}] \end{bmatrix} \quad (11.6)$$

The Craig-Bampton CMS method is a displacement-based CMS method and consists in expressing the displacements of the substructure as a linear combination of the Ritz-vectors in a projection base Φ

$$\mathbf{u} = \Phi \mathbf{q} \quad (11.7)$$

where the vector \mathbf{q} represents the vector of generalized coordinates. The matrix Φ is called the projection base, Ritz-vector base, dynamic component mode superset, or simply transformation matrix and consists, in case of the Craig-Bampton method, of the retained m_k fixed-interface normal modes of Eq. (11.4) and the interface constrained modes, such that

$$\Phi = [\Psi_c \Phi_n] \quad (11.8)$$

It is worth noting that by using the Craig-Bampton transformation matrix all physical coordinates of the set \mathbf{u}_b are retained in the reduced subsystem. In case of contact problems, the FE mesh has to be very fine, which leads to a very large number of constraint modes. In order to reduce this number of static modes, all nodes of the potential contact area are compressed in the set \mathbf{u}_i and will be treated in a different form. The next chapter is devoted to this issue.

11.3 Extension of the Craig-Bampton Reduction Base with Characteristic Attachment Modes for Rolling Contact Problems

11.3.1 Attachment Modes

In order to capture the effect of concentrated contact forces, the Craig-Bampton transformation matrix of Eq. (11.8) is supplemented by so-called attachment modes. An attachment mode is defined as the static displacement resulting from applying a unit force at one coordinate of the set \mathbf{u}_i (or a unit pressure at a predefined sub-area).

As previously mentioned, all coordinates of the potential contact area are compressed in the set \mathbf{u}_i . Further, for the computation of the attachment modes let the set \mathbf{u}_i be divided into a set \mathbf{u}_c , which contains all nodes of the potential contact area, and its complement \mathbf{u}_n , which contains all nodes that are not externally loaded during the dynamic simulation. For the computation of the attachment modes, which supplement the Craig-Bampton transformation matrix, one has to restrain all nodes of the set \mathbf{u}_b and apply a unit force to one coordinate of the set \mathbf{u}_c and zero forces on both the remainder of the set \mathbf{u}_c and the set \mathbf{u}_n . Thus, the matrix of attachment modes is computed as

$$\begin{bmatrix} \mathbf{K}_{bb} & \mathbf{K}_{bc} & \mathbf{K}_{bn} \\ \mathbf{K}_{cb} & \mathbf{K}_{cc} & \mathbf{K}_{cn} \\ \mathbf{K}_{nb} & \mathbf{K}_{nc} & \mathbf{K}_{nn} \end{bmatrix} \begin{bmatrix} \mathbf{0} \\ \Psi_{ca} \\ \Psi_{na} \end{bmatrix} = \begin{bmatrix} \mathbf{R}_{bc} \\ \mathbf{I}_{cc} \\ \mathbf{0} \end{bmatrix} \quad (11.9)$$

where \mathbf{I}_{cc} is the $(c \times c)$ identity matrix and the matrix \mathbf{R}_{bc} denotes the matrix of reaction forces. From the bottom two rows of Eq. (11.9), one can compute the sub-matrices Ψ_{ca} and Ψ_{na} such that the attachment mode matrix Ψ_a is then given by

$$\Psi_a = \begin{bmatrix} \mathbf{0} \\ \Psi_{ca} \\ \Psi_{na} \end{bmatrix} \quad (11.10)$$

11.3.2 Characteristic Attachment Modes

As mentioned above, in case of contact problems the number of DOF of the set \mathbf{u}_c is often very high. This entails that a huge number of attachment modes is needed for approximating the solution to a given accuracy. However, the number of attachment modes may be reduced by seeking a new set of modes that correspond to more natural physical motion of the DOF of the set \mathbf{u}_c . The new set can be obtained by solving an eigenanalysis on the component mode synthesis mass and stiffness matrices that correspond to the attachment modes, such that

$$(\mathbf{K}_A - \omega_a^2 \mathbf{M}_A) \Phi_a = \mathbf{0} \quad (11.11)$$

where \mathbf{K}_A and \mathbf{M}_A represent, respectively, the component mode synthesis stiffness and mass matrices that correspond to the attachment modes and are defined as:

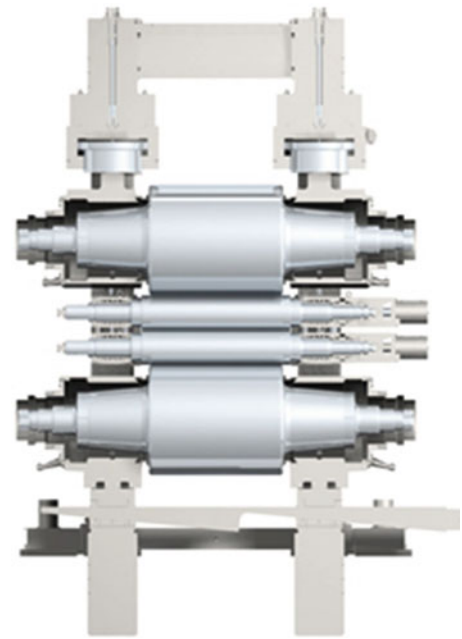
$$\mathbf{K}_A = (\Psi_a)^T \mathbf{K} \Psi_a, \quad \mathbf{M}_A = (\Psi_a)^T \mathbf{M} \Psi_a \quad (11.12)$$

The eigenvectors Φ_a are truncated and only a selected set of modes is retained. Finally, a selected eigenvector from Eq. (11.11) may be transformed from generalized coordinates in FE coordinates by the following linear combination of attachment modes

$$\hat{\Psi}_a = \Psi_a \Phi_a \quad (11.13)$$

The modes of Eq. (11.13) provide, at least in an approximated sense, the principle modes of deformation in the potential contact area. For contact problems where the potential contact area does not vary with respect to time (e.g. bolted connections, welded or screwed parts) the required number of modes for accurately representing local deformations in the contact area is acceptable and the selection of the modes is easy. Thus, by using CAM one can dramatically reduce the size of the system. However, in case of rolling contact problems the potential contact area changes with respect to the rotation angle

Fig. 11.1 Complete model of the working and the back-up roll



and, therefore, the classical computation of CAM leads to a very inefficient reduced order model (very huge number of modes). This is mainly based on two facts. On the one hand side, at any moment in time the contact area is localized with respect to the entire surface and only a few nodal DOF are loaded. On the other hand side, the CAM are computed as a linear combination of all attachment modes of the entire surface and apart from low-frequency modes a very huge number of high-frequency CAM are required for accurately representing displacements of the localized contact area. Thus, the truncation of the existing CAM is not practical.

In the next subsection an approach for developing a novel way of computing CAM for rolling contact problems is presented. For the computation of the CAM, first attachment modes are computed for a longitudinal sub-area of each roll. Then an eigenanalysis is performed on the CMS mass and stiffness matrices that correspond to the attachment modes. The resultant eigenvectors were truncated and applied to the entire surface domain of the rolls.

11.3.3 Characteristic Attachment Modes for Rolling Contact Problems

Although rolling is the most extensively used metal forming process, the realistic simulation of a rolling contact process is still a weak point and leads to very long computer runs. An example from the metal forming industry is used in order to demonstrate the different steps of the novel computational approach.

A complete model of the working and the back-up roll as they occur in the cold rolling mill can be seen in Fig. 11.1. Due to the very short contact length in the rolling process between back-up roll and working roll, a very fine spatial discretization of the rolls on the surface is essential. The FE model of the working roll has 401402 nodes whereby 52520 are surface nodes and hence potential application points of contact forces. Clearly, at any moment in time, the contact forces are localized and only a few nodal DOF will be loaded by state-dependent contact forces. However, due to the rotation of the rolls the application points of the contact forces will vary with respect to time. In order to reduce the very huge number of nodal DOF, a modal representation of each roll is indispensable. The Craig-Bampton transformation will be applied together with specialized CAM. Apart from the 12 existing constraint modes, only the first 20 fixed-interface normal modes will be considered in the final mode base. In Fig. 11.2 one can see two of the 20 fixed-interface normal modes. As mentioned above, using the classical CAM, as presented in Sect. 11.4.2, would lead for accurately representing localized displacements during simulation to a very huge number of modes.

In order to avoid such an inefficient mode base, the remainder of this chapter is devoted to the development of a tailored concept for computing CAM for rolling contact problems.

The computational algorithm for the novel CAM is identical for both rolls. Therefore, only the working roll will be used for demonstration purposes of the computational algorithm. Without loss of generality, we assume that the FE mesh of the

Fig. 11.2 Two of the 20 fixed-interfaced modes

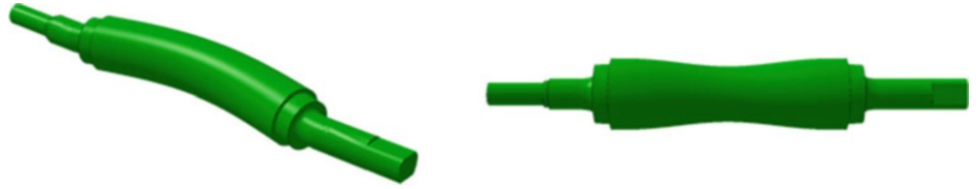


Fig. 11.3 One of the 520 sub-areas of the working roll

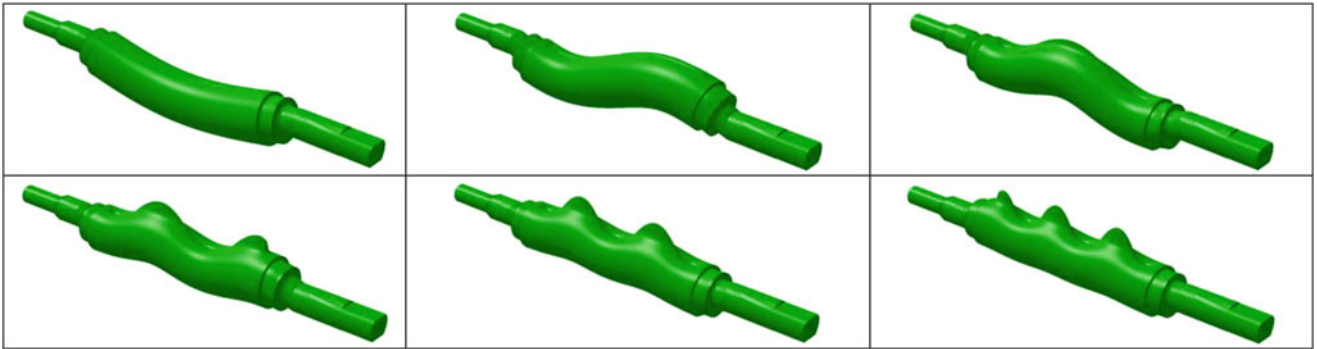
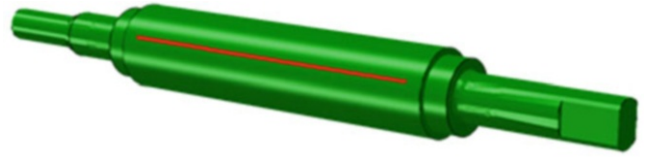


Fig. 11.4 The first six characteristic attachment modes

roll is rotationally symmetric. In a first step, the roll is divided into longitudinal equal sub-areas. In order to consider local deflection effects it is of great importance to choose the longitudinal sub-areas sufficiently small. One sub-area consists of at least one longitudinal FE nodal DOF row, see Fig. 11.3.

In the present example, the working roll is divided into 520 longitudinal sub-areas, whereby each sub-area consists of one nodal FE DOF row with 101 nodes. Each FE node has three DOF. Then, in a second step, attachment modes are computed according to Eqs. (11.9) and (11.10) by applying a unit force in radial direction at one of the nodal DOF of the longitudinal sub-area and zero forces on all other nodal FE DOF of this sub-area. This procedure is applied consecutively to all nodal DOF of the sub-area. The resulting 101 attachment modes are used for the computation of a new set of CAM. Therefore, one has to compute the CMS mass and stiffness matrices that correspond to the attachment modes and solve Eq. (11.11) of Sect. 11.4.2. The first six CAM are shown in Fig. 11.4.

Note the latter CAM are an eigenvector-based linear combination of the attachment modes. In case of rolling contact problems the rolls are pressed together and the contact area between the rolls is very small with respect to the circumferential direction and changes with respect to the rotational angle about the axis of rotation. However, due to the great force which presses the rolls together (otherwise no rolling contact would be possible), the contact is almost always ensured over the axial direction, such that only the first few CAM have to be considered for accurately representing local displacement effects inside the sub-area in the modal subspace. The truncation of the CAM dramatically reduces the number of DOF without loss of result quality, see [14]. In the present example only the first four CAM have been selected for describing the principal way in which the sub-area deforms in axial direction. That is, the number of modes has been reduced from 101 to only 4. In a further step, it is now suggested to consecutively apply the selected (in the present example the first four) CAM over the entire surface of the roll. This can be achieved by repeating the steps described above for the remaining 519 sub-areas of the roll. An alternative way in case of a rotational symmetric mesh of the FE model is to compute the static equivalent load case for each of the selected CAM and apply these load cases consecutively to all sub-areas of the roll. The static equivalent load cases that correspond to the selected characteristic attachment modes can be computed as

$$\mathbf{F}_{ESL} = \mathbf{K}\hat{\Psi}_a = \mathbf{K}\Psi_a\Phi_a = \mathbf{F}\Phi_a \quad (11.14)$$

Each static equivalent load case represents, so to say, a linear combination of those single static load cases, which have been applied in radial direction for the computation of the attachment modes, see Eq. (11.9). After computing the static

equivalent load cases for one specific sub-area, one can compute the characteristic attachment mode of all other sub-areas by simply transforming these load cases and solving the following equation

$$\mathbf{K}(\hat{\Psi}_a)_i = (\mathbf{F}_{\text{ESL}})_i \quad (11.15)$$

where $(\mathbf{F}_{\text{ESL}})_i$ represents the static equivalent load cases matrix of the i th sub-area and the matrix $(\hat{\Psi}_a)_i$ contains the CAM corresponding to the static equivalent load cases of the matrix $(\mathbf{F}_{\text{ESL}})_i$. The transformation of the static equivalent load cases from one sub-area to another one must satisfy both the transformation of the forces from the nodal DOF from one sub-area to the nodal DOF of the other one and the rotation of the forces such that they always act in radial direction.

Subsequently, a flowchart of the proposed computational algorithm is given:

Step 1: Divide the entire surface of a roll into longitudinal sub-areas.

Step 2: Define a sub-area and compute attachment modes according to Eqs. (11.9) and (11.10) by applying a single force in radial direction on one of the nodal DOF of the sub-area and zero forces to all other nodal DOF of this sub-area. This procedure is applied consecutively to all nodal DOF of the sub-area.

Step 3: Based on the modes of Step 2, compute CAM by solving Eq. (11.11).

Step 4: Truncate the CAM as in traditional modal analysis.

Step 5: Repeat Step 1–4 for all sub-areas of the surface.

As mentioned above, Step 5 can be alternatively computed by using both the static equivalent load cases of the CAM of Step 4 and Eq. (11.15).

For the rolling contact problem, it is of advantage to consider radial forces as well as tangential effects. For this case, one has to apply in Step 2 apart from the radial forces although tangential forces and then compute the CAM by performing Step 2–5. However, it is suggested to compute the truncated set of CAM (Step 2–4) for the “tangential” and “radial” attachment modes, separately. This separate treatment allows the usage of a different number of CAM for both directions. For the working roll only one characteristic attachment mode per sub-area resulting from tangential forces has been considered in the final mode base.

Thus, the final mode base consists of the modes of the Craig-Bampton transformation matrix, the 2080 CAM resulting from radial attachment modes (4 for each sub-area), and 520 (1 for each sub-area) CAM resulting from tangential attachment modes.

In the present subsection a methodology has been presented for computing a well-suited mode base of a component of a rolling contact problem. The partition of the potential contact area (entire surface of the roll) into longitudinal sub-areas enables an easy selection of those relevant CAM, which are needed for describing local displacement effects sufficiently accurate. In comparison, the truncation of CAM is not really practicable, if the CAM are computed for the entire surface without partitioning, as it is the case in the classical computation.

11.4 Run-Up Simulation of Coupled System Between Working and Back-Up Roll

A run-up simulation of the system of Fig. 11.5 is performed. The rolls were pressed together by a constant space-fixed line force of 3kN/m. Moreover, a constant torque is applied on the right hand side of the working roll. A contact search algorithm has been applied and the Quasi-Coulomb model for frictional contact interfaces of [15] has been implemented. For both rolls the CAM are computed according to Sect. 11.4.3. For the working roll the mode base presented in Sect. 11.4.3 will be used, where apart from 12 constraint modes and 20 fixed-interface modes, 2600 CAM form the final mode base. For the back-up roll as well 12 constraint modes and the first 20 fixed-interface modes have been chosen to form the Craig-Bampton mode base. However, due to memory reasons, only the first two CAM in radial and no modes in tangential direction have been taken into account. In order to perform the run-up simulation, both reduced FE models have to be integrated in a multibody-system formulation. We used the floating frame of reference formulation [16], which is based on separating the overall motion of a deformable body into a large rigid body motion (rotation and translation) and superimposed small deformations. Since the constraint modes of the Craig-Bampton transformation implicitly contain rigid body modes, and in the floating frame of reference motion the rigid body motion is already described by generalized rotational and translational coordinates, the mode base of each roll has to be orthogonalized with respect to the assembled FE mass and stiffness matrix, as described in [17]. This orthogonalization procedure removes the rigid body mode content from the mode base. After this orthogonalization one can separate the modes based on their frequency into low- and high-frequency modes, see [18]. In Fig. 11.6 one can see

Fig. 11.5 Model of the working and back-up roll

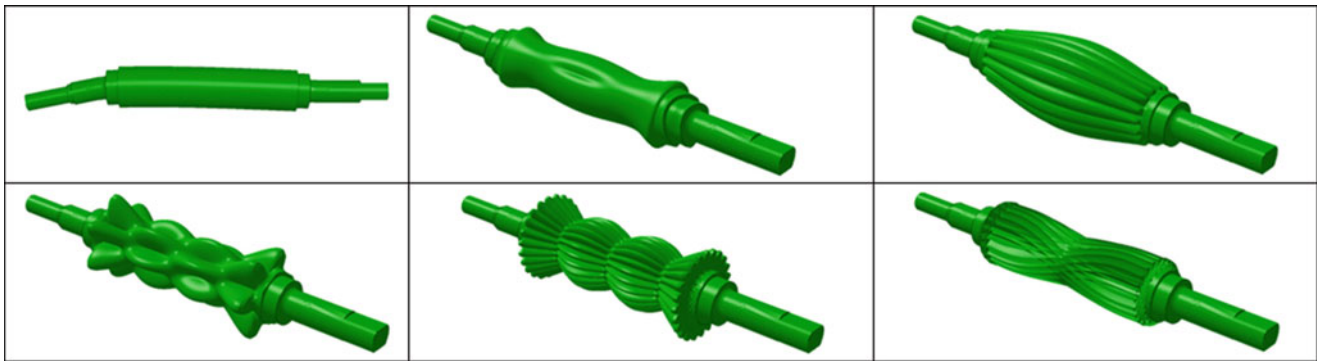
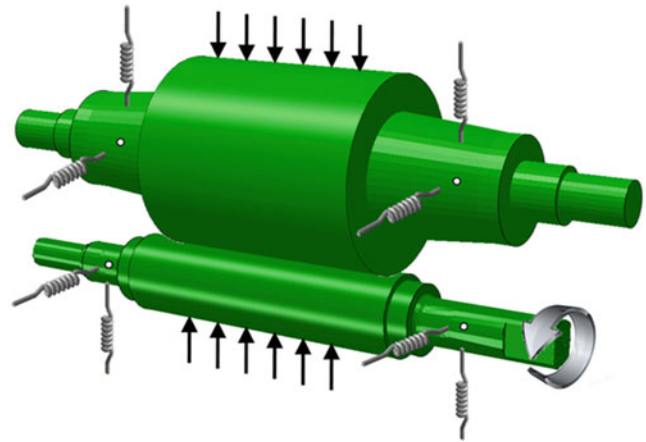
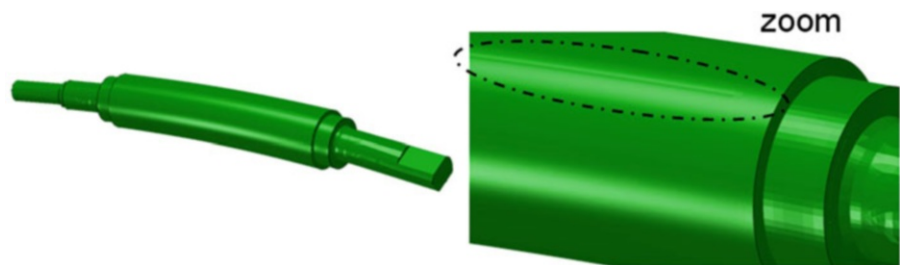


Fig. 11.6 Two low-frequency and four high-frequency modes

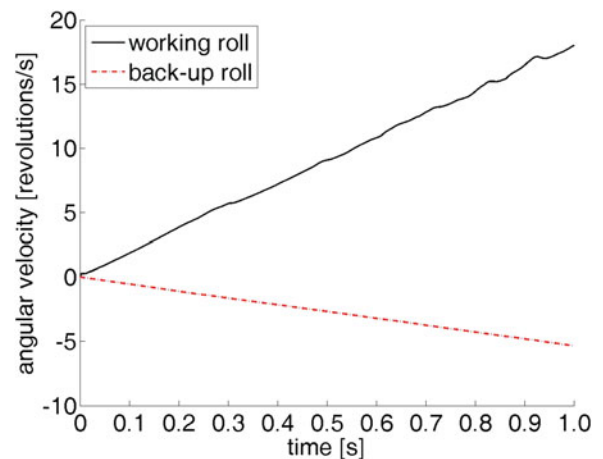
Fig. 11.7 Deformation of the working roll for a selected time-step



exemplarily two low-frequency modes and four high-frequency modes of the final mode base of the working roll after the orthogonalization procedure. The number of high-frequency modes preliminary results from the selected CAM in the mode base and, therefore, is very high (2,580 for the working roll). In contrast, the number of low-frequency modes is small. The low-frequency modes mainly reflect the modal space of the Craig-Bampton mode base. As has been shown in [18, 19], the high-frequency modes can be considered quasi-statically. This quasi-static consideration of the high-frequency modes results in a dramatically reduction of computational time. The simulation of the present example needed approximately **42 min** of CPU time on a standard PC.

In Fig. 11.7 the deformation of the working roll is depicted for a selected time step. Apart from the global deformation of the roll, one can also see local deformations, which result from considering the CAM of Sect. 11.4.3 in the mode base. Figure 11.8 shows the angular velocity of both rolls during the run-up simulation. The deviations from a linear course are caused by bending effects of the rolls, which result in partially slipping of the rolls. This effect can be seen more clearly in an animation. Unfortunately for this large scale problem, there are no comparative results. This is based on the fact that the classical computation of CAM leads to a mode base with such a huge number of modes that the time integration of the system is due to both computational time and memory reasons not possible. However, in [14], it has been demonstrated for small generic examples that the proposed methodology leads to sufficiently accurate results.

Fig. 11.8 Angular velocity of both the working and back-up roll



11.5 Conclusion

The dynamic simulation of contact in rolling processes is very time-consuming. This is mainly based on the fine resolution of the surface domain of each roll, which however is essential in order to capture the effect of concentrated contact forces. Existing model order reduction techniques cannot be readily applied due to the nonlinear nature of the contact dynamics. In order to improve the speed of contact analysis, the present paper proposes a sophisticated combination of so-called characteristic attachment modes and vibration normal modes for describing the deformation of each roll. While the characteristic attachment modes are required to capture the concentrated nonlinear contact forces, the vibration normal modes describe the global deformation behavior of the rolls. For the computation of the characteristic static correction modes, first attachment modes are computed for a longitudinal sub-area of each roll. Then an eigenanalysis is performed on the component mode synthesis mass and stiffness matrices that correspond to the attachment modes. The resultant eigenvectors were truncated and applied to the entire surface domain of the rolls. In order to obtain well-conditioned equations, all modes are finally orthonormalized and then separated into low- and high-frequency modes. The high-frequency modes were considered quasi-statically during the time integration of the equations of motion. An example from the metal forming industry has been presented in order to demonstrate the results.

Acknowledgement Support of this work in the framework of the K2-Austrian Center of Competence in Mechatronics (ACCM) and the Siemens VAI Metals Technologies GmbH is gratefully acknowledged.

References

1. Hurty WC (1960) Vibration of structural systems by component mode synthesis. *Proc Am Soc Civ Eng* 85(4):51–69
2. Hurty WC (1965) Dynamic analysis of structural systems using component modes. *AIAA J* 3(4):678–685
3. Craig RR, Bampton MCC (1968) Coupling of substructures for dynamic analyses. *AIAA J* 6(7):1313–1319
4. Craig RR (1995) Substructure methods in vibration. *J Mech Des* 117:207–213
5. Craig RR (1987) A review of time-domain and frequency-domain component mode synthesis methods. *Int J Anal Exp Modal Anal* 2(2):59–72
6. Craig RR (2000) Coupling of substructures for dynamic analysis: an overview. In: *AIAA paper no 2000-1573*, Atlanta
7. Craig RR, Kurdila AJ (2006) *Fundamentals of structural dynamics*. John Wiley & Sons Inc., New Jersey
8. Craig RR, Chang CJ (1977) *Substructure coupling for dynamic analysis and testing*, NASA CR-2781. National Aeronautics and space Administration, Washington, DC
9. Aoyama Y, Yagawa G (2001) Component mode synthesis for large-scale structural eigenanalysis. *Comput Struct* 79(6):605–615
10. Bourquin F (1992) Component mode synthesis and eigenvalues of second order operators: discretization and algorithm. *Modél Math et Anal Numér* 26(3):385–423
11. Bourquin F, D’Hennezel F (1992) Intrinsic component mode synthesis and plate vibrations. *Comput Struct* 44(1–2):315–324
12. Bouhaddi N, Lombard JP (2000) Improved free-interface substructures representation method. *Comput Struct* 77(3):269–283
13. Hassis H (2000) Proposition of a new approach for the substructure method. *J Sound Vib* 232:659–668
14. Sherif K (2013) Novel computationally efficient formulations for the equations of motion of a modally reduced flexible member undergoing large rigid body motion. Dissertation, Johannes Kepler University, Linz
15. Garino GC, Ponthot JP (2008) A Quasi-Coulomb model for frictional contact interfaces. Application to metal forming simulations. *Latin Am Appl Res* 38:95–104

16. Shabana A (2005) Dynamics of multibody systems, 3rd edn. Cambridge University Press, New York
17. Friberg O (1991) A method for selecting deformation modes in flexible multibody dynamics. *Int J Numer Methods Eng* 32(8):1637–1655
18. Sherif K, Witteveen W, Mayrhofer K (2012) Quasi-static consideration of high-frequency modes for more efficient flexible multibody simulations. *Acta Mech* 223:1285–1305
19. Sherif K, Witteveen W, Irschik H, Holl H, Mayrhofer K (2011) On the extension of global vibration modes with Ritz-vectors needed for local effects. In: Proulx T (ed) Linking models and experiments, vol 2. Proceedings of the 29th IMAC, a conference on structural dynamics 2011, vol 4. Society of Experimental Mechanics Inc., Springer, New York, pp 37–46

Chapter 12

Towards a Parallel Time Integration Method for Nonlinear Systems

Paul L.C. van der Valk and Daniel J. Rixen

Abstract Obtaining the forced dynamic response of large nonlinear structural models is in practice computationally expensive. As time integration involves solving a static-like nonlinear problem at each time steps, these simulations could take up to several days to solve. In a lot of cases however, the global nonlinearity of the model could be relatively mild or parts of the model can be assumed to behave linearly and the strong nonlinearities, that require many iterations to solve, are localized in a small number of regions of the model. Normal approaches to solve this more efficiently require one to reduce the linear and/or mildly nonlinear parts of the system. In this paper however, a different approach is taken. Here we decompose the total time integration by separating the iterations required, into iterations on the global (linearized) interface problem and iterations on the (local) substructure level. It will be shown that this approach leads to a method that can be efficiently implemented in a parallel computing environment.

Keywords Nonlinear models • Newmark time integration • Dual assembly • Simulations • Parallel computations

12.1 Introduction

Large nonlinear models are in practice extremely expensive to solve. This especially becomes an issue if one wants to obtain the forced dynamic response of the structure for multiple load cases. As time integration involves solving a static-like nonlinear problem at each time steps, these simulations could take up to several days to solve. In a lot of cases however, the global nonlinearity of the model could be relatively mild or parts of the model can be assumed to behave linearly and the strong nonlinearities, that require many iterations to solve, are localized in a small number of regions of the model. Examples of this could be interfaces with friction, locations where impacts can occur or multi-physical phenomena.

Traditional methods for efficiently solving these kinds of problems, often include reduction of the linear parts of the structure using Component Mode Synthesis techniques [1]. By reducing the linear parts, one can significantly limit the size of the total problem that needs to be solved. If large parts of the system can not be linearized, due to for instance large deformations, this is not an option however. Nonetheless, several advances have been made in reducing certain types of nonlinearities [7, 10, 11], such that one is still able to follow this approach.

In this paper however, a different approach is taken. Here we decompose the total time integration by separating the iterations required into iterations on the global (linearized) interface problem and iterations on the (local) substructure level. It will be shown that this approach leads to a method that can be efficiently implemented in a parallel computing environment. By splitting the strong nonlinearities from the mild nonlinearities it is shown that a large number of local iterations can be performed on the substructures with strong nonlinearities, while reducing the number of iterations required for the subsystems with mild nonlinearities. The idea is based on similar work that was presented for static problems in [2, 4, 6].

P.L.C. van der Valk (✉)

Faculty of 3ME, Section Engineering Dynamics, Delft University of Technology, Mekelweg 2, 2628CD, Delft, The Netherlands
e-mail: p.l.c.vandervalk@tudelft.nl

D.J. Rixen

Faculty of Mechanical Engineering, Institute of Applied Mechanics, Technische Universität München,
Boltzmannstr. 15, 85748 Garching, Germany

The paper is organized such that, in Sect. 12.2, the basic equations and concepts that are used throughout the paper are introduced. In Sect. 12.3 the method is presented and some of its benefits are discussed. A demonstration on a simple academic example is shown in Sect. 12.4, where we also investigate some of the aspects of the approach. Finally, in Sect. 12.5 some conclusions are drawn and some ideas for applying the approach in practice are given.

12.2 Dynamic Simulations for Coupled Mechanical Systems

This section will introduce the basic equations and concepts used throughout this paper. As a start, the equations of motion and concepts of *primal* and *dual assembly* are briefly summarized in Sect. 12.2.1, after which a short introduction to the Newmark time integration method is given in Sect. 12.2.2.

12.2.1 Coupling of the Equations of Motion

The equations of motion of a general nonlinear structural model, consisting of multiple substructure models, are given in Eq. (12.1). For simplicity it is assumed that the system consist of only two substructures (A and B).

$$\begin{cases} \mathbf{M}\ddot{\mathbf{u}} + \mathbf{p}(\dot{\mathbf{u}}, \mathbf{u}) = \mathbf{f} + \mathbf{g} \\ \mathbf{L}^T \mathbf{g} = 0 \\ \mathbf{B}\mathbf{u} = 0 \end{cases} \quad (12.1)$$

where \mathbf{M} denotes the mass matrix, \mathbf{p} , \mathbf{f} and \mathbf{g} are the array of internal elastic and damping forces, the array of external forces and the array of substructure coupling forces respectively, which are all arranged such that

$$\mathbf{M} = \begin{bmatrix} \mathbf{M}^{(A)} & 0 \\ 0 & \mathbf{M}^{(B)} \end{bmatrix}, \quad \mathbf{p} = \begin{bmatrix} \mathbf{p}^{(A)}(\dot{\mathbf{u}}^{(A)}, \mathbf{u}^{(A)}) \\ \mathbf{p}^{(B)}(\dot{\mathbf{u}}^{(B)}, \mathbf{u}^{(B)}) \end{bmatrix}, \quad \mathbf{u} = \begin{bmatrix} \mathbf{u}^{(A)} \\ \mathbf{u}^{(B)} \end{bmatrix},$$

$$\mathbf{f} = \begin{bmatrix} \mathbf{f}^{(A)} \\ \mathbf{f}^{(B)} \end{bmatrix}, \quad \mathbf{g} = \begin{bmatrix} \mathbf{g}^{(A)} \\ \mathbf{g}^{(B)} \end{bmatrix}, \quad \mathbf{L} = \begin{bmatrix} \mathbf{L}^{(A)} \\ \mathbf{L}^{(B)} \end{bmatrix}, \quad \mathbf{B} = [\mathbf{B}^{(A)} \quad \mathbf{B}^{(B)}].$$

It should be noted that the nonlinearity of these models is only in the elastic and damping forces, but that the method presented in this work is not limited to only these types of nonlinearities. Matrix \mathbf{B} in Eq. (12.1), is a signed Boolean, that operates on the *interface* (or boundary/coupling) DoFs, such that *compatibility* between the co-located DoFs on both sides of the interface is enforced:

$$\mathbf{u}_{[b]}^{(A)} - \mathbf{u}_{[b]}^{(B)} = \mathbf{B}^{(A)}\mathbf{u}^{(A)} + \mathbf{B}^{(B)}\mathbf{u}^{(B)} = \mathbf{B}\mathbf{u} = 0, \quad (12.2)$$

where the subscript $[b]$ denotes the interface (or boundary) DoFs and subscript $[i]$ is used to denote the internal DoFs. Similarly, matrix \mathbf{L} is a Boolean operator that locates the total set of DoFs from a unique set of DoFs, such that:

$$\mathbf{u} = \begin{bmatrix} \mathbf{u}_{[i]}^{(A)} \\ \mathbf{u}_{[b]}^{(A)} \\ \mathbf{u}_{[i]}^{(B)} \\ \mathbf{u}_{[b]}^{(B)} \end{bmatrix} = \mathbf{L} \begin{bmatrix} \mathbf{u}_{[i]}^{(A)} \\ \mathbf{u}_{[b]} \\ \mathbf{u}_{[i]}^{(B)} \end{bmatrix} = \mathbf{L}\bar{\mathbf{u}}, \quad (12.3)$$

where $\bar{\mathbf{u}}$ denotes the assembled array of DoFs. Hence, this operator is used to enforce *equilibrium* between the different substructures in Eq. (12.1), such that:

$$\mathbf{L}^T \mathbf{g} = \mathbf{g}_{[b]}^{(A)} + \mathbf{g}_{[b]}^{(B)} = 0. \quad (12.4)$$

An important property of the two Boolean operators introduced is that they are in each other null-space [3];

$$\mathbf{B}\mathbf{L} = 0 \quad (12.5)$$

Note that the set of equations given in (12.1) is still quite extensive and there are several methods for rewriting these to smaller, easier to solve equations of motion. Of these methods we will briefly introduce the two most common here, the first being the *primal assembly* method and the second is the *dual assembly* method. For more details about the different options for assembling substructure equations of motion and the Boolean operators used, the reader is referred to [9].

12.2.1.1 Primal Assembly

The first approach, often referred to as primal assembly, consists of replacing the full set of DoFs by a unique set of DoFs, as is done in Eq. (12.3). As on both sides of the interface the interface DoFs are described by the same set of interface DoFs, the *compatibility* condition is satisfied a priori. By substituting the relation given in Eq. (12.3) into the original set of coupled equations of motion and pre-multiplying those by \mathbf{L}^T , we find that:

$$\begin{cases} \mathbf{L}^T \mathbf{M} \mathbf{L} \ddot{\mathbf{u}} + \mathbf{L}^T \mathbf{p}(\mathbf{L} \dot{\mathbf{u}}, \mathbf{L} \mathbf{u}) = \mathbf{L}^T \mathbf{f} + \mathbf{L}^T \mathbf{g} \\ \mathbf{L}^T \mathbf{g} = 0 \\ \mathbf{B} \mathbf{L} \mathbf{u} = 0 \end{cases} \quad (12.6)$$

Hence, by taking into account the relation given in Eq. (12.5), we see that the expression in Eq. (12.6) can easily be simplified to:

$$\bar{\mathbf{M}} \ddot{\mathbf{u}} + \bar{\mathbf{p}}(\dot{\mathbf{u}}, \mathbf{u}) = \bar{\mathbf{f}} \quad (12.7)$$

Here, the assembled mass matrix and arrays with forces are denoted by $\bar{\star}$ and thus form the equations of motion of the assembled structure. As can be seen from the second and third line in Eq. (12.6), the primal assembly technique satisfies both the compatibility and equilibrium conditions a priori.

12.2.1.2 Dual Assembly

The second approach shown here, is the dual assembly method. Here, we will satisfy the *equilibrium* condition a priori, by enforcing that the interface forces on both sides of the interface are described by a unique set of Lagrange multipliers.

$$\begin{bmatrix} \mathbf{g}^{(A)} \\ \mathbf{g}^{(B)} \end{bmatrix} = - \begin{bmatrix} \mathbf{B}^{(A)T} \\ \mathbf{B}^{(B)T} \end{bmatrix} \boldsymbol{\lambda}, \quad (12.8)$$

Hence, by substituting Eq. (12.8) into Eq. (12.1), the dually assembled system is obtained.

$$\begin{cases} \mathbf{M} \ddot{\mathbf{u}} + \mathbf{p}(\dot{\mathbf{u}}, \mathbf{u}) + \mathbf{B}^T \boldsymbol{\lambda} = \mathbf{f} \\ \mathbf{B} \mathbf{u} = 0 \end{cases} \quad (12.9)$$

Whereas primal assembly directly results in satisfying both the compatibility and equilibrium condition, the dual assembled system needs to have the compatibility condition explicitly enforced, as can be seen from Eq. (12.9). Nonetheless, we would like to emphasize that regardless of the assembly method, Eqs. (12.7) and (12.9) describe the exact same set of coupled equations of motion.

12.2.2 Time Integrating the Equations of Motion Using Newmark's Method

In order to obtain the response in time of a system of equations, we can try and solve the second order differential equations analytically, or one can apply time integration methods. In this paper the latter of the two options is chosen and the time integration method used is briefly introduced here.

As the Newmark family of time integration methods [5] is one of the more common methods for computing the time response of a (nonlinear) finite element model, it will also be applied for the current method. In the Newmark scheme a Taylor expansion is used to deduce the velocities and displacements of the next discrete time station ($t = t_n$), according to:

$$\begin{aligned}\dot{\mathbf{u}}_n &= \dot{\mathbf{u}}_{n-1} + (1 - \gamma)h\ddot{\mathbf{u}}_{n-1} + \gamma h\ddot{\mathbf{u}}_n = \hat{\dot{\mathbf{u}}}_n + \gamma h\ddot{\mathbf{u}}_n \\ \mathbf{u}_n &= \mathbf{u}_{n-1} + h\dot{\mathbf{u}}_{n-1} + h^2\left(\frac{1}{2} - \beta\right)\ddot{\mathbf{u}}_{n-1} + h^2\beta\ddot{\mathbf{u}}_n = \hat{\mathbf{u}}_n + h^2\beta\ddot{\mathbf{u}}_n,\end{aligned}\quad (12.10)$$

where β and γ are the Newmark integration parameters and $\hat{\dot{\mathbf{u}}}_n$ and $\hat{\mathbf{u}}_n$ are referred to as the *predictors* and are dependent on the displacements, velocities and accelerations of the previous time step. By inverting the original Newmark relations (12.10) we obtain

$$\begin{aligned}\ddot{\mathbf{u}}_n &= \frac{1}{h^2\beta} (\mathbf{u}_n - \hat{\mathbf{u}}_n) \\ \dot{\mathbf{u}}_n &= \hat{\dot{\mathbf{u}}}_n + \frac{\gamma}{h\beta} (\mathbf{u}_n - \hat{\mathbf{u}}_n),\end{aligned}\quad (12.11)$$

where both the accelerations and velocities are written as a function of the displacements only. Hence, the time discretized equations of motion of a non-decomposed model at time $t = t_n$ simply write:

$$\mathbf{M}\ddot{\mathbf{u}}_n + \mathbf{p}_n = \mathbf{f}_n \quad (12.12)$$

where, $\mathbf{p}_n = \mathbf{p}(\mathbf{u}_n, \dot{\mathbf{u}}_n)$. Note that in the time discretized equations of motion given here, $\ddot{\mathbf{u}}_n$, $\dot{\mathbf{u}}_n$, \mathbf{u}_n are related to each other through the time discretization assumed in the Newmark scheme, given in Eq. (12.10). As the equations of motion are nonlinear, they cannot be solved directly and are solved iteratively. By writing Eq. (12.12) in a residual form, we can obtain a force measure of the error (\mathbf{r}_n). As we require the system to be in dynamic equilibrium, the residual should be made equal to zero.

$$\mathbf{r}_n = \mathbf{M}\ddot{\mathbf{u}}_n + \mathbf{p}_n - \mathbf{f}_n \quad (12.13)$$

Hence at each new time step, the predictors given in Eq. (12.10) are substituted in Eq. (12.13) and the residual is determined. Using a Newton-Raphson scheme, one now uses the residual to compute its Jacobian (\mathbf{S}),

$$\mathbf{S} = \frac{\partial \mathbf{r}_n}{\partial \mathbf{u}} = \mathbf{M} \frac{\partial \ddot{\mathbf{u}}}{\partial \mathbf{u}} + \frac{\partial \mathbf{p}_n}{\partial \dot{\mathbf{u}}} \frac{\partial \dot{\mathbf{u}}}{\partial \mathbf{u}} + \frac{\partial \mathbf{p}_n}{\partial \mathbf{u}} = \frac{1}{h^2\beta} \mathbf{M} + \frac{\gamma}{h\beta} \mathbf{C}_t + \mathbf{K}_t \quad (12.14)$$

which also referred to as the *effective stiffness matrix* of the system. Using the Jacobian matrix and the residual, one is able to compute an update on the displacements.

$$\mathbf{S}\Delta \mathbf{u} = -\mathbf{r}_n \quad (12.15)$$

The update on the displacements can now be used to update the velocities and accelerations as well, by using the relation found in Eq. (12.11).

$$\begin{aligned}\mathbf{u}_n &= \mathbf{u}_n + \Delta \mathbf{u} \\ \dot{\mathbf{u}}_n &= \dot{\mathbf{u}}_n + \frac{\gamma}{h\beta} \Delta \mathbf{u} \\ \ddot{\mathbf{u}}_n &= \ddot{\mathbf{u}}_n + \frac{1}{h^2\beta} \Delta \mathbf{u}\end{aligned}\quad (12.16)$$

After substituting the updated displacements, velocities and accelerations in Eq. (12.13), an update on the residual is found. This iterative process is repeated until the residual is equal to zero. Note that, as in practice it is not possible to get the residual exactly equal to zero, usually a certain tolerance is used at which the Newton-Raphson is said to be converged.

12.3 Decomposed Time Integrations

In this section it will be shown how to decompose the time integration of a dually assembled structure into a linear problem on the global interface level and several nonlinear problems on the substructure level, which is the goal of this work. Afterwards some benefits of the method are presented and an impression is given on how one could implement the method efficiently in a parallel computing environment.

12.3.1 Decomposition into Global and Local Iterations

Recalling the dual assembled system of equations (Eq. (12.9)) in the residual form, we obtain,

$$\begin{cases} \mathbf{r}_n = \mathbf{M}\ddot{\mathbf{u}}_n + \mathbf{p}_n(\dot{\mathbf{u}}, \mathbf{u}_n) + \mathbf{B}^T \boldsymbol{\lambda}_n - \mathbf{f}_n, \\ \mathbf{B}\mathbf{u} = 0 \end{cases}, \quad (12.17)$$

from which we need to solve for the Lagrange multipliers $\boldsymbol{\lambda}_n$ and the set of displacements over time \mathbf{u}_n (as the velocities and accelerations follow from Eq. (12.10)). Instead of applying the “normal” approach, where we would try to solve for both sets of unknowns in a single Newton-Raphson process, as is given in Eq. (12.9),

$$\begin{bmatrix} \mathbf{S} & \mathbf{B}^T \\ \mathbf{B} & \mathbf{0} \end{bmatrix} \begin{bmatrix} \Delta \mathbf{u} \\ \Delta \boldsymbol{\lambda} \end{bmatrix} = \begin{bmatrix} -\mathbf{r}_n \\ 0 \end{bmatrix}, \quad (12.18)$$

one can also choose to solve the unknowns in two steps. The first step for determining the interface forces ($\Delta \boldsymbol{\lambda}$) and in the second step the displacements of the different substructures ($\Delta \mathbf{u}$). Hence, in the first step we’re solving the *global interface problem*, where the compatibility condition is used to compute the interface forces required to keep the adjacent substructure boundaries attached to each other. In order to do so, the dual assembled global linearized problem, given in Eq. (12.18), is condensed on the interface.

$$\begin{aligned} \mathbf{B}\mathbf{S}^{-1}\mathbf{B}^T \Delta \boldsymbol{\lambda} &= -\mathbf{B}\mathbf{S}^{-1}\mathbf{r}_n \\ \boldsymbol{\lambda}_n &= \boldsymbol{\lambda}_n + \Delta \boldsymbol{\lambda} \end{aligned} \quad (12.19)$$

The term on the right hand side in Eq. (12.19) can be interpreted as the incompatible substructure response on the interface one would obtain if the Lagrange multipliers in Eq. (12.18) were to be neglected. By substituting the resulting interface forces ($\Delta \boldsymbol{\lambda}$) into the first line of Eq. (12.17), we obtain

$$\mathbf{S}\Delta \mathbf{u} = -\mathbf{r}_n - \mathbf{B}^T \Delta \boldsymbol{\lambda}, \quad (12.20)$$

which allows us to solve for the update on the displacements and to compute the updated set of displacements, velocities and accelerations, using Eq. (12.16). By substituting these updated sets of DoF and interface forces into (12.17), an update on the residual is found as well. Note that the result found from these steps is exactly equal to solving Eq. (12.18) in one step.

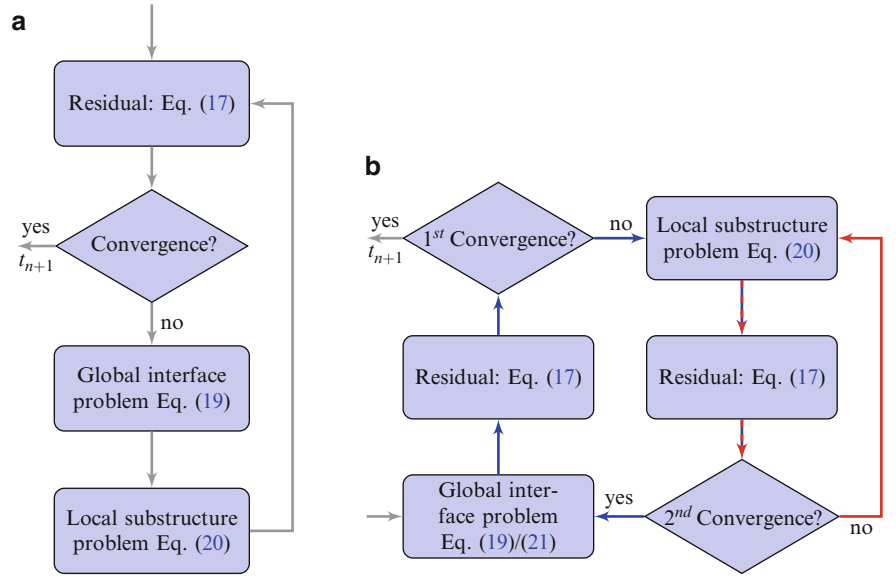
In order to proceed with the Newton-Raphson process we now have two options:

- Either start again with a step to compute the update on the interface forces, as is done in Eq. (12.19), and from there use Eq. (12.20) to find the update on the displacements. The resulting solutions scheme is visualized in Fig. 12.1a.
- Or one now assumes the $\boldsymbol{\lambda}_n$ is known in Eq. (12.17), and solves for \mathbf{u}_n using the first line in Eq. (12.17) only. As the equations of motion of the different substructures are only coupled through the Lagrange multipliers, which are now fixed, the problem becomes block-diagonal. Hence, the iterations are performed on a *per* substructure basis until all substructures have converged (Eq. (12.21)).

$$\|\mathbf{r}_n^{(s)}\| < LoTol \times \|\mathbf{p}_n^{(s)} + \mathbf{B}^{(s)T} \boldsymbol{\lambda}_n - \mathbf{f}_n^{(s)}\| \quad (12.21)$$

Here, *LoTol* is the tolerance setting for the local iterations. Obviously, by doing so the compatibility condition (second line in Eq. (12.17)) is violated. Hence, an update on the Lagrange multipliers is required in order to enforce compatibility.

Fig. 12.1 (a) Time integration with a single iteration loop; (b) Modified time integration scheme that has an outer loop (blue arrows) for solving the global interface problem and an inner loop (red arrows) that operates on the level of the substructures



These are obtained by substituting the last obtained linear substructure operators (the inverses of the substructure Jacobians; \mathbf{S}^{-1}) and the displacements obtained from the local iterations (\mathbf{u}_n) into Eq. (12.22).

$$\begin{aligned} \mathbf{B}\mathbf{S}^{-1}\mathbf{B}^T \Delta\lambda &= \mathbf{B}\mathbf{u}_n \\ \lambda_n &= \lambda_n + \Delta\lambda \end{aligned} \quad (12.22)$$

Note that the physical interpretation of Eq. (12.22) is similar to the one given for Eq. (12.19). As the Lagrange multipliers are now updated again, the substructure residuals will also have to be updated,

$$\mathbf{r}_n = \mathbf{r}_n + \mathbf{B}^T \Delta\lambda, \quad (12.23)$$

which could lead to a violation of the global convergence criteria,

$$\sum_{r=1}^{N_s} \|\mathbf{r}_n^{(r)}\| < GloTol \times \sum_{r=1}^{N_s} \|\mathbf{p}_n^{(r)} + \mathbf{B}^{(r)T} \lambda_n - \mathbf{f}_n^{(r)}\|, \quad (12.24)$$

where *GloTol* is the tolerance setting for the global iterations, and would require one to start new iterations on the substructure level. This process is repeated until the global convergence criterion is met (Eq. (12.24)). This approach would lead to the scheme given in Fig. 12.1b. In this method one would get an outer loop for the global iterations (blue arrows) and an inner loop (red arrows) for the local iterations at substructure level.

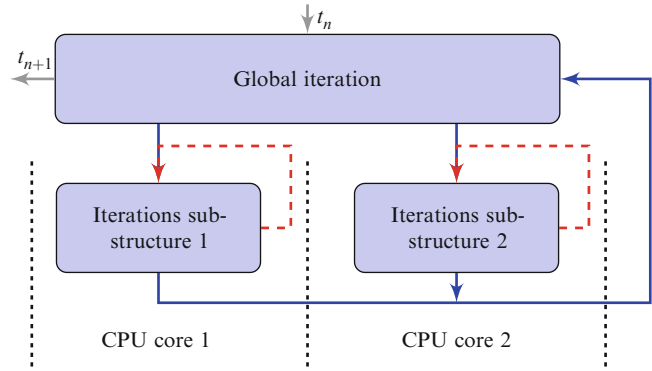
The method thus leads to a global step, where compatibility is enforced, and a local step on the level of the substructures. Hence, all the nonlinear iterations are contained within the local (substructure) level and at the global level one only needs to solve the simple linear problem in Eq. (12.22). Here it should be noted that the most expensive part to compute in Eq. (12.22); \mathbf{S}^{-1} , has already been computed during the iterations on the substructure level, therefore the global step is relatively cheap.

Also, by introducing iterations at two levels (on the global and local level) we have also introduced two convergence criteria; one on the global (Eq. (12.24)) and one on the local (Eq. (12.21)) level. As we will see later on, the correct setting of the tolerances is crucial in order to maximize the efficiency of the proposed time integration scheme.

12.3.2 Benefits of Separating the Global and Local Iterations

The method proposed in Sect. 12.3.1 has a number of benefits. Firstly, by correctly setting the global and local convergence criteria, one can ensure that the grunt of the computational work is performed on the substructure level. This way each substructure only has to perform the number of iterations that are mainly due to its own level of nonlinearity. One can

Fig. 12.2 Impression of how the substructure iterations can be divided among the various cores of the CPU



imagine that if there are two substructures, one highly nonlinear and one linear, that the linear substructure will only have to perform one local iteration to reach convergence, whereas the nonlinear one will have to do a large number of iterations. If one would chose to solve the problem monolithically (as is done in Sect. 12.2.2) or using the method shown in Fig. 12.1a, one would force the linear substructure to perform the same number of iterations as are required for the nonlinear part.

An idea is also to use the proposed approach to couple different (commercial) modeling and simulation packages [8]. This can be achieved by allowing the different programs to run as one of the substructures on the local level and developing a dedicated piece of driver-software that handles the global interface problem. Hence, the second benefit follows directly from the first, because of the fact that most of the computational work is performed on a substructure level, only a limited number of global iterations are required. This will be a big benefit if one couples different software packages as described above.

Finally, because of these distinct benefits, the method is well suited to run on computers with parallel computing capabilities. The iterations on the local level can be divided, such that the different substructures can be divided among the available CPU cores, such that these are used as optimal as possible, as is illustrated in Fig. 12.2. Note that in the linear case, only a single global and local iteration is needed and the local complexity is directly related to the number of DoFs of each substructure. So balancing the load of the CPUs is relatively easy. In the non-linear case, the complexity of each local problem (i.e. the computational costs it involves) is also dependent on the level of non-linearity (if highly non-linear, it would need a lot of local Newton-Raphson iterations). Therefore, load balancing of the CPUs will be less straightforward in the latter case.

12.4 Demonstration on a Simple Academic Model

In this section a simple academic example is used to demonstrate the accuracy and efficiency of the proposed approach. Firstly, the model and its default parameters are introduced. After this, the methods performance in terms of accuracy and computational effort is investigated.

12.4.1 The Simple Academic Model

All the test cases are based on the same model (Fig. 12.3 and Table 12.1), where the default configuration for the system is given. Subsystem A is a 7 DoF mass-spring system and subsystem B is a 4 DoF system that is also modeled using spring and mass elements. In both models damping is modeled using Rayleigh damping. The total system consists of 9 DoF, as u_{A6} is rigidly connected to u_{B1} and u_{A7} is rigidly connected to u_{B2} . A number of nonlinear elements are added to both subsystems; a nonlinear spring (with spring constant k_{A0}) and damper (with damping constant c_{A0}) in subsystem A and a nonlinear spring and damper in subsystem B (with spring constant k_{B42} and damping constant c_{B4}). As all nonlinearities are taken as being cubic, the nonlinear forces working on the systems are obtained from:

$$\begin{aligned} f_{nl}^{(A)} &= k_{A0}u_{A1}^3 + c_{A0}\dot{u}_{A1}^3 \\ f_{nl}^{(B)} &= k_{B42}u_{B4}^3 + c_{B4}\dot{u}_{B4}^3. \end{aligned} \quad (12.25)$$

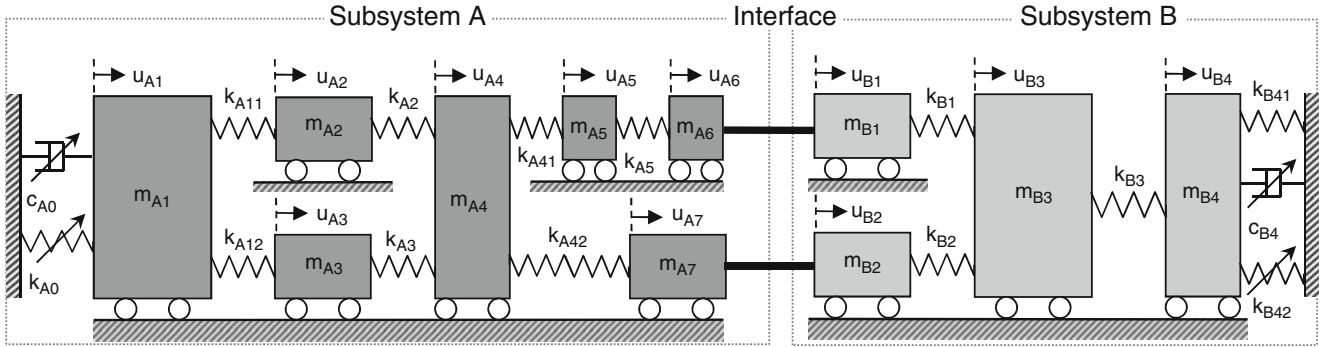
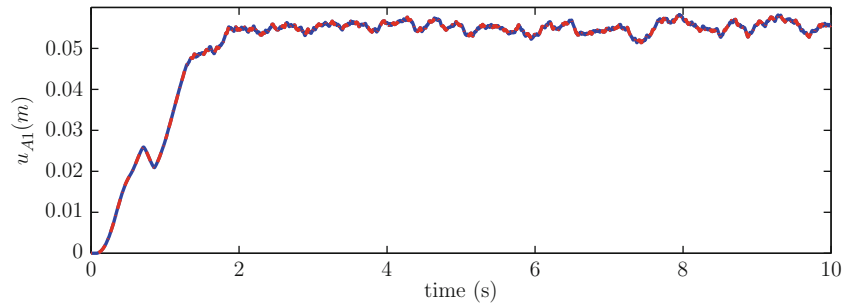


Fig. 12.3 Simple academic system used for case study

Table 12.1 Parameters of mass-spring systems

| System parameters of the default system | Subsystem A | | Subsystem B | |
|---|---------------|----------------------------|--------------------------|--------------------------|
| | Mass (kg) | Stiffness (N/m) | Mass (kg) | Stiffness (N/m) |
| General | $m_{A1} = 10$ | $k_{A11} = 2 \cdot 10^3$ | $m_{B1} = 2$ | $k_{B1} = 1 \cdot 10^3$ |
| | $m_{A2} = 3$ | $k_{A12} = 2 \cdot 10^3$ | $m_{B2} = 4$ | $k_{B2} = 1 \cdot 10^3$ |
| | $m_{A3} = 3$ | $k_{A2} = 1 \cdot 10^3$ | $m_{A3} = 8$ | $k_{B3} = 2 \cdot 10^3$ |
| | $m_{A4} = 6$ | $k_{A3} = 1 \cdot 10^3$ | $m_{B4} = 5$ | $k_{B41} = 2 \cdot 10^2$ |
| | $m_{A5} = 2$ | $k_{A41} = 0.5 \cdot 10^3$ | | |
| | $m_{A6} = 2$ | $k_{A42} = 1 \cdot 10^3$ | | |
| | $m_{A7} = 4$ | $k_{A5} = 1 \cdot 10^3$ | | |
| Non-linear components | | $k_{A0} = 2 \cdot 10^7$ | $k_{B42} = 1 \cdot 10^5$ | |
| | | $c_{A0} = 1 \cdot 10^7$ | $c_{B4} = 0$ | |

Fig. 12.4 Response of mass m_{A1} ; showing the reference solution (—); and the one obtained with the decomposed time integration (· -) (Color figure online)



In order to demonstrate the method, the system is excited by a random force on m_{B3} from $t = dt$ onwards and a second random force is applied at m_{A1} from $t = 2s$ onwards. The responses obtained using the global/local method introduced in this paper are compared to a reference solution, which is obtained by performing a Newmark time integration on the total (primally assembled) system. In addition to this, the computational effort in terms of iterations will be shown for all the different cases.

12.4.2 Accuracy of the Proposed Method

Firstly, in order to demonstrate the accuracy of the method, the responses of the force loaded DoFs are shown in Figs. 12.4 and 12.5. These response are obtained with the same global tolerance settings (GloTol) in both simulations (10^{-8}), the local tolerance (LoTol) for the decomposed time integration has been set to (10^{-6}) in this example. The tolerances are used such that the norm of the residual has to be smaller than the tolerance multiplied by a force norm,

$$|\mathbf{r}_n| < tol \times |\mathbf{p}_n + \mathbf{B}^T \boldsymbol{\lambda}_n - \mathbf{f}_n|, \quad (12.26)$$

Fig. 12.5 Response of mass m_{B3} ; showing the reference solution (—); and the one obtained with the decomposed time integration (· -)

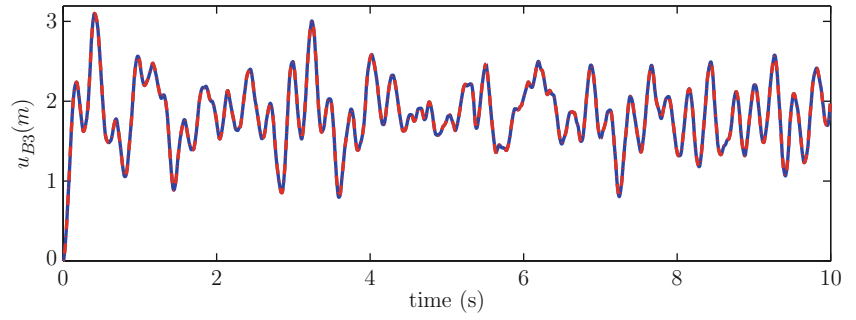
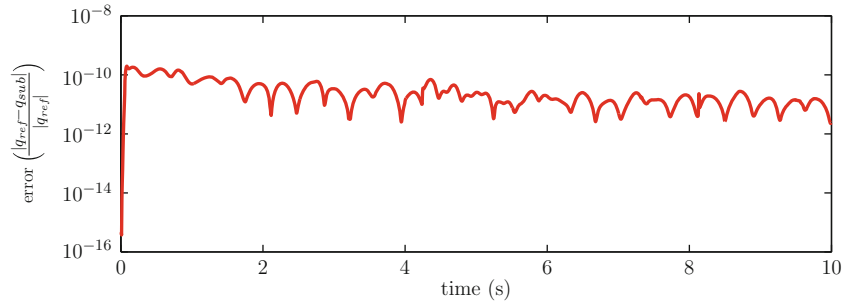


Fig. 12.6 Global error of the decomposed time integration, as given in Eq. (12.27)



where tol denotes the tolerance setting. Visually, no difference between the responses can be seen, but in order to show that the responses of both simulations are exactly identical, a global error measure has been determined,

$$\epsilon_n = \frac{|\mathbf{u}_n^{(ref)} - \mathbf{u}_n^{(sub)}|}{|\mathbf{u}_n^{(ref)}|}, \quad (12.27)$$

which is shown in Fig. 12.6. Here, one can clearly see that the decomposed time integration yields the exact same response.

12.4.3 Effect of Setting the Local and Global Tolerances

In order to show the effect of the global and local tolerance settings on the number of iterations and computational time, we've defined a ratio between the two,

$$ratio = \frac{LoTol}{GloTol}. \quad (12.28)$$

By fixing the global tolerance to (10^{-8}) and varying the ratio given in Eq. (12.28) between 1 and 10^{10} , one could get an idea of the optimal ratio between the local and global tolerances. The result of this analysis is shown in Fig. 12.7. Note that we cannot draw any conclusions for the general case about this, as this setting could very well be problem dependent as well. Nonetheless, some interesting effects are shown here.

Firstly, for low ratios the problem is dominated by the local iterations, as a too small ratio will require more local iterations than strictly required. Also note that the number of global iterations are at its minimum here. One can also clearly identify the subsystem with the strongest nonlinearities, as subsystem A requires about 3 times the number of iterations that subsystem B requires. By increasing the ratio between the tolerances, the number of local iterations decrease for both substructures, while keeping the global iterations at a constant level. At a certain moment, the iterations of subsystem B and the global iterations start to “couple”, meaning that subsystem B only requires (approximately) one iteration per global iteration. In addition to this, it appears that Subsystem A also starts to converge towards its “iteration asymptote”. As can be seen from the lower graph, this point also denotes the minimum in terms of CPU time.

By further increasing the ratio, the number of global iterations (and hence of subsystem B) start to increase, without any substantial decrease in the number of iterations for subsystem A, thereby also increasing the CPU time required. Finally, at extremely large ratios the method will degrade into the method shown in Fig. 12.1a and will require the same amount of iterations for subsystem A, B and the global interface problem, which are also equal to the number of iterations required for the reference solution.

Fig. 12.7 Number of iterations (*upper graph*) and computational time (*lower graph*) as a function of the ratio between the local and global tolerances. In the upper graph, the different lines denote the different iterations; reference solution iterations (—); Subsystem A iterations (· -); Subsystem B iterations (- -); Global iterations (···)

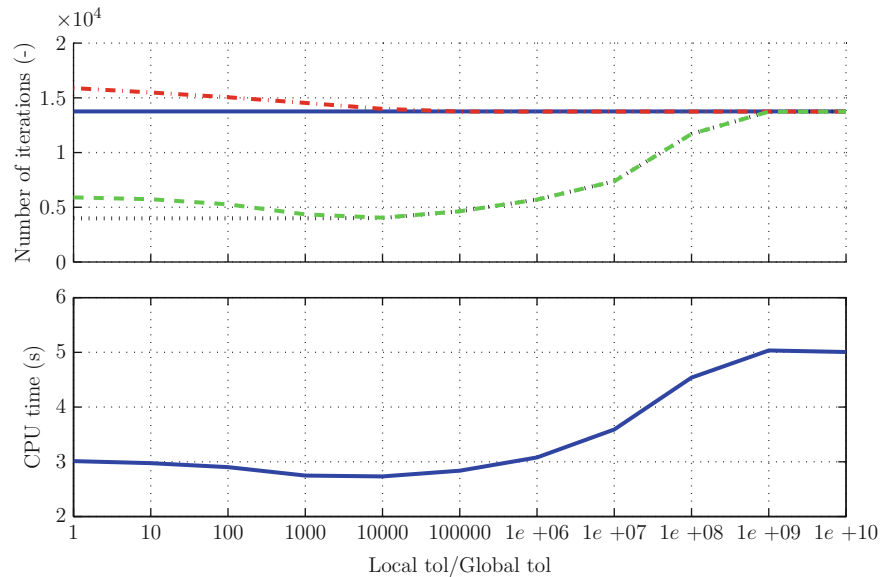
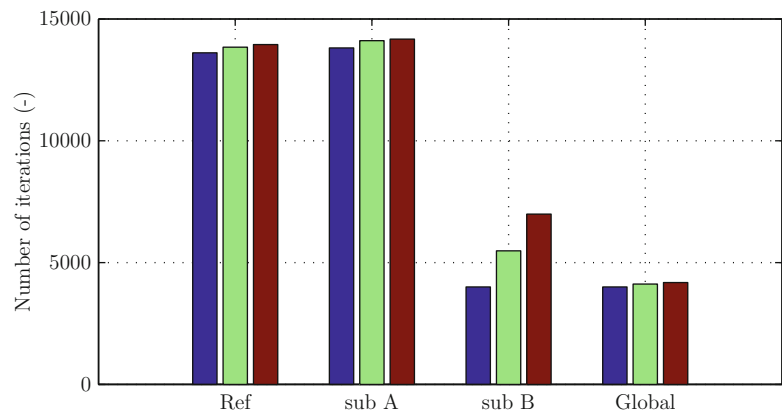


Fig. 12.8 Number of iterations required for different levels of nonlinearity in subsystem B; Subsystem B linear (■); Subsystem B mildly nonlinear (■); Subsystem B strongly nonlinear (■)



12.4.4 Effect of the Level of Nonlinearity in the Subsystems

The last effect that we'll briefly investigate is the impact of the nonlinearities on the performance of the method. In subsystem B, there is only a relatively mild cubic spring that links m_{B4} to the fixed wall. In this section it will be investigated what the effects on the amount of iterations are if we would increase the nonlinearity currently present in subsystem B ($k_{B42} = 1 \cdot 10^7$, $c_{B4} = 5 \cdot 10^7$), or if we would remove the nonlinearity from subsystem B ($k_{B42} = 0$, $c_{B4} = 0$). For this analysis it was chosen to use the "optimal" ratio between the local and global tolerances the we found from Fig. 12.7, therefore GloTol is taken as 10^{-8} and LoTol is set to 10^{-4} . The results of the investigation are shown in Fig. 12.8, here the colors of the bars indicate the different models as is indicated in the caption. The bars denoted by *Ref* are the number of iterations performed for the reference solution, the bars denoted *A* and *B* denote the number of iterations on the local level and the bar denoted *Global* is the associated number of global iterations performed. Firstly it can be seen that a higher level of nonlinearity in the system leads to more iterations in general. What is important to notice here is that the number of iterations for substructure A and the global problem only slightly increase, whereas the iterations for substructure B significantly increase. This was already expected in Sect. 12.3.2, where we stated that the decomposed method puts its computational effort there where it is needed. By increasing the nonlinearities in subsystem B, the iterations for this substructure will be mostly affected, whereas the change in the number of iterations for the other substructures and on the global level is only slightly affected. Also, what should be noted here is that in the limit case of a linear substructure B, the number of local iterations on *B* are equal to the number of global iterations, as was also expected.

12.5 Conclusions and Recommendations

In this paper a method was presented for decomposing the time integration of a nonlinear structure into a global problem, coupled with several local problems. A simple demonstration was performed in which several aspects of the method were investigated and from which we can conclude:

- The method yields the same accuracy as the associated monolithic approach.
- The ratio between the global and the local tolerance settings determine for a large part the efficiency of the method.
- The number of local and global iterations are, for this example, at the lower range of this ratio ($1 \leq \text{ratio} \leq 10,000$) inversely related to each other; A minimum of global iteration, results in a maximum of local iterations.
- By splitting the local and global (interface) level of the total structure, one is able to put the grunt of the computations there where it is needed, while reducing this work for the other substructures with milder nonlinearities.

Finally we'd like to note that the method is very suited to be efficiently implemented in a parallel computing environment.

For the future it would be interesting to investigate whether the method presented can be used to couple different (commercial) modeling and simulation packages. This can be achieved by allowing these to run as one of the substructures on the local level and developing a dedicated piece of driver-software that handles the global interface problem. Thereby allowing one to combine the best tools available for the different substructures and their specific needs, into a single "super-simulation" package.

References

1. Craig RR (2000) Coupling of substructures for dynamic analyses – an overview. In: Proceedings of AIAA/ASME/ASCE/AHS/ASC structures, structural dynamics, and materials conference and exhibit, p 1573–1584, April 2000
2. Cresta P, Allix O, Rey C, Guinard S (2007) Nonlinear localization strategies for domain decomposition methods: Application to post-buckling analyses. *Comput Meth Appl Mech Eng* 196(8):1436–1446. <ce:title>Domain Decomposition Methods: recent advances and new challenges in engineering</ce:title>
3. de Klerk D, Rixen DJ, Voormeeren SN (2008) General framework for dynamic substructuring: history, review and classification of techniques. *AIAA J* 46(5):1169–1181
4. Gendre L, Allix O, Gosselet P, Comte F (2009) Non-intrusive and exact global/local techniques for structural problems with local plasticity. *Comput Mech* 44(2):233–245
5. Newmark NM (1959) A method of computation for structural dynamics. *Proc Am Soc Civil Eng J Eng Mech Div* 85(EM3):67–94
6. Pebrel J, Rey C, Gosselet P (2008) A nonlinear dual-domain decomposition method: Application to structural problems with damage. *Int J Multiscale Comput Eng* 6(3):251–262
7. Tiso P, Rixen DJ (2013) Discrete empirical interpolation method for finite element structural dynamics. *Nonlinear Dynam Int J Nonlinear Dynam Chaos Eng Syst* 35(1):203–212
8. van der Valk PLC, Rixen DJ (2013) A co-simulation method for coupling complex foundation models and wind turbine models in aero-elastic simulations. In: Dimitrovov' a Z, Rocha de Almeida J, Gonçalves R (eds) Proceedings of the 11th international conference on vibration problems, Lisbon, Portugal, 9–12 September 2013
9. Voormeeren SN, van der Valk PLC, Rixen DJ (2011) Generalized methodology for assembly and reduction of component models for dynamic substructuring. *AIAA J* 49(5):1010–1020
10. Wasfy TM, Noor AK (2003) Computational strategies for flexible multibody systems. *Appl Mech Rev* 56(6):553–614
11. Wenneker F, Tiso P (2013) Nonlinear component mode synthesis using modal derivatives. In: Proceedings of the 11th international conference RASD 2013, 2013

Chapter 13

Efficient Model Order Reduction for the Nonlinear Dynamics of Jointed Structures by the Use of Trial Vector Derivatives

Wolfgang Witteveen and Florian Pichler

Abstract The dynamic response of a structure, which consists of jointed substructures, may be influenced by the nonlinear contact and friction forces inside the joints, even if the deformations are small. In case of joints with a large spatial distribution, like in car bodies or leaf springs, these nonlinearities dominate the overall system behavior. The use of the direct finite element method or a standard model order reduction technique leads to either huge computational costs or inaccurate results. So called ‘Joint Interface Modes’ (JIMs) overcome that problem. They represent a problem oriented extension of classical trial vectors for structures with bolted joints, spot welded seams and similar joints. The result quality is comparable to that one of a direct finite element analysis without losing the efficiency of model order reduction. In this paper a new approach for the computation of such JIMs is presented. The approach is based on so called trial vector derivatives which will be outlined in the theory part of the paper. At the end of the paper, the theory is applied to a static and dynamic example in order to underline the methods accuracy and efficiency.

Keywords Model reduction • Jointed structures • Lap joints • Interface reduction

Nomenclature

| | |
|----------------------------------|--|
| \mathbf{x} | State vector (displacements) |
| \mathbf{x}_L | Time invariant portion of state vector |
| $\Delta \mathbf{x}$ | Time varying portion of state vector |
| $\tilde{\mathbf{x}}$ | Approximation of state vector |
| $\underline{\mathbf{M}}$ | Time invariant mass matrix |
| $\underline{\mathbf{K}}$ | State depended stiffness matrix |
| $\underline{\mathbf{K}}^{(x)}$ | Constant portion of stiffness matrix |
| $\underline{\mathbf{K}}^L$ | Non constant portion of stiffness matrix |
| $\underline{\mathbf{K}}^{NL(x)}$ | |
| φ | Trial vector |
| $\varphi_{i,j}$ | Trial vector derivative of trial vector number i with respect to trial vector number j |
| $\underline{\Phi}$ | Matrix with trial vectors in its rows |
| $\underline{\Phi}$ | Matrix with trial vectors based on vibration modes |
| $\underline{\Phi}^V$ | Matrix with trial vectors based on static deflection shapes |
| $\underline{\Phi}^S$ | Matrix of joint interface modes. |
| $\underline{\Phi}^T$ | |
| \mathbf{q} | Generalized coordinates |
| Ω_i | i -th eigenfrequency |
| λ_i | Hankel singular value |

W. Witteveen (✉) • F. Pichler
 University of Applied Sciences Upper Austria, Wels Campus, Stelzhammerstr. 69, 4600 Wels, Austria
 e-mail: wolfgang.witteveen@fh-wels.at

| | |
|------|---|
| w(t) | Portion of regarded strain energy |
| n | Dimension of unreduced system |
| v | Number of trial vectors in $\underline{\Phi}^v$ |
| s | Number of trial vectors in $\underline{\Phi}^s$ |
| t | Number of trial vectors in $\underline{\Phi}^T$ |
| g | Number of considered proper orthogonal modes |
| r | Total number of trial vectors |
| p | Total number of trial vector derivatives |
| a | Number of FE node pairs which are involved in the joint contact |

13.1 Introduction

The global stiffness and damping properties of a metallic structure, which consists of jointed substructures, is strongly influenced by the local characteristics of the joints. The global stiffness and damping depend non-linearly on the joint pressure distribution, and the latter depends non-linearly on the system state. For the constitutive modeling of the mechanical behavior of joints some representative literature can be found in [1–4].

In engineering practice, jointed structural systems will be analyzed by means of commercial FE (Finite Element) codes. The strength of these FE codes usually is the static solution of FE structures with a considerable number of DOF's (up to several millions). Due to this huge number of DOF's, the time integration of such structures is economically not possible without severe restrictions. Common restrictions are the size of the FE model (the number of DOF's), the number of time integration points and the consideration of inertia effects (quasi-static instead of full dynamic simulation).

For the time integration of linear structures model reduction based on trial vectors is used. Elastic structures can be effectively and consistently represented by a linear combination of time invariant trial vectors (= deformation shapes), commonly called 'modes'. This approach reduces the number of DOF's of complex FE structures to max. 200–300 without significant loss of accuracy (within a well-defined frequency band). Different modal reduction methods have been presented during the last decades, see [5–7].

Time invariant modes are suitable for an efficient dynamic analysis of linear structures. Jointed structures with substructures connected e.g. by bolts bring into the play local non-linearities. Classical reduction bases do not take bolted joints into special account. Therefore, a lot of modes are necessary in order to represent the joints deformation accurately enough. This involves the loss of the model reduction efficiency. A problem-oriented extension to existing and well proven mode bases will be derived in this paper. It will turn out that they represent a suitable extension in order to do full long-term dynamic analysis of complex structures with bolted joints. This additional trial vectors will be named as 'joint interface modes' (JIMs) or 'joint trial vectors' and their computation is based on so called trial vector derivatives.

The present paper is organized as follows: In the next section the theory of the trial vector derivatives is shortly recalled and an energy based criterion is introduced in order to determine the important directions, out of all available trial vector derivatives. In the final section, a numerical example is given, in order to underline the methods accuracy and efficiency.

13.2 Theory

In case of a penalty formulation for both, the contact [8] and the friction [9] phenomenon, the FEM leads to a coupled and nonlinear differential equation of the form

$$\underline{\mathbf{M}}\ddot{\mathbf{x}} + \underline{\mathbf{K}}_{(x)}\mathbf{x} = \mathbf{f}_{(t)}. \quad (13.1)$$

We assume, that the structure undergoes "small vibrations" so that the state vector \mathbf{x} can be decomposed into a time invariant portion \mathbf{x}_L and a time varying portion $\Delta\mathbf{x}$.

$$\mathbf{x} = \mathbf{x}_L + \Delta\mathbf{x} \quad (13.2)$$

In the very common case that a structure vibrates around its undeformed state, the vector \mathbf{x}_L is simply the zero vector. As a consequence, the stiffness matrix can be decomposed into a time invariant part $\underline{\mathbf{K}}_L$ and a time varying portion $\underline{\mathbf{K}}_{NL(\mathbf{x})}$.

$$\underline{\mathbf{K}}_{(\mathbf{x})} = \underline{\mathbf{K}}_L + \underline{\mathbf{K}}_{NL(\mathbf{x})} \quad (13.3)$$

The constant part $\underline{\mathbf{K}}_L$ holds the linearized stiffness matrix at state \mathbf{x}_L . Inserting (13.3) into (13.1) gives

$$\underline{\mathbf{M}}\ddot{\mathbf{x}} + \underline{\mathbf{K}}_L \mathbf{x} = \mathbf{f} - \underline{\mathbf{K}}_{NL(\mathbf{x})} \mathbf{x} \quad (13.4)$$

which can be interpreted as a linear system which is loaded by external and fictive forces due to the nonlinearities. This is a well-known approach in the literature and the fictive forces are sometimes called ‘‘pseudo forces’’, see exemplarily [10] and [11].

13.2.1 Trial Vector Derivatives

In order to decrease the number of DOF's, the possible deformation state is restricted to a weighted superposition of r trial vectors in the form of

$$\mathbf{x} \approx \tilde{\mathbf{x}} = \underline{\Phi} \mathbf{q}. \quad (13.5)$$

When (13.5) is inserted into equation (13.4) a reduced model

$$\tilde{\underline{\mathbf{M}}}\ddot{\mathbf{q}} + \tilde{\underline{\mathbf{K}}}\mathbf{q} = \underline{\Phi}^T \mathbf{f} - \underline{\Phi}^T \underline{\mathbf{K}}_{NL(\tilde{\mathbf{x}})} \underline{\Phi} \mathbf{q} \quad (13.6)$$

is obtained. The $(r \times r)$ matrices $\tilde{\underline{\mathbf{M}}} = \underline{\Phi}^T \underline{\mathbf{M}} \underline{\Phi}$ and $\tilde{\underline{\mathbf{K}}} = \underline{\Phi}^T \underline{\mathbf{K}}_L \underline{\Phi}$ are the reduced mass and stiffness matrices. The reduction base $\underline{\Phi}$ should provide an approximated state $\tilde{\mathbf{x}}$ so that a proper norm of $\mathbf{x} - \tilde{\mathbf{x}}$ is somehow small. For the problem under consideration a reduction base in the form of

$$\underline{\Phi} = \left[\begin{array}{c|c|c} \underline{\Phi}_V & \underline{\Phi}_S & \underline{\Phi}_T \end{array} \right] \quad (13.7)$$

is suggested. The $(n \times v)$ matrix $\underline{\Phi}_V$ contains v vibration mode shapes and the $(n \times s)$ matrix $\underline{\Phi}_S$ contains s trial vectors which are basically deformation shapes due to static loads. The latter two matrices are provided by standard reduction methods, like the one of Craig and Bampton [12]. The key point of this publication is to extend conventional reduction bases with problem oriented ‘joint trial vectors’ which are collected in the $(n \times t)$ matrix $\underline{\Phi}_T$. The trial vectors of $\underline{\Phi}_T$ are computed based on trial vector derivatives, see [13] for detailed comments on that issue. Trial vector derivatives characterize the change of trial vector number i due to a deformation of trial vector number j . This change is zero in case of linear models but non-zero in case of state depended system matrices. For the vibration modes in the matrix $\underline{\Phi}_V$ this change can be computed with

$$\frac{\partial}{\partial q_j} \left[\left(\underline{\mathbf{K}} - \Omega_i^2 \underline{\mathbf{M}} \right) \varphi_i \right] = \mathbf{0} \quad (13.8)$$

where the deformation of mode number j is determined by its scaling factor q_j . Assuming a constant mass matrix and neglecting all inertia terms leads to

$$\varphi_{i,j} = \underline{\mathbf{K}}^{-1} \frac{\partial \underline{\mathbf{K}}}{\partial q_j} \varphi_i \quad (13.9)$$

where $\varphi_{i,j}$ is the trial vector derivative of mode number i due to mode number j . The trial vector derivatives of the static deflection shapes in $\underline{\Phi}_s$ can be given as

$$\frac{\partial}{\partial q_j} \left(\underline{\mathbf{K}} \varphi_i \right) = \frac{\partial}{\partial q_j} \mathbf{f}_i \quad (13.10)$$

which leads to

$$\varphi_{i,j} = \underline{\mathbf{K}}^{-1} \frac{\partial \underline{\mathbf{K}}}{\partial q_j} \varphi_i. \quad (13.11)$$

It can be observed, that the trial vector derivatives of vibration modes and static deflection shapes can be computed along the same equation as long as the mass effects are neglected.

13.2.2 Proper Orthogonal Decomposition (POD) for the Computation of an Optimal Set of JIMs

Using the trial vector derivatives outlined in the chapter before provides p ($= (v + s)^2$) potential trial vectors for the model reduction. This is by far too much for efficient model reduction and it is known from the literature that the space spanned by all these vectors contains a lot of redundant information, see [14] and [15]. Based on weighted POD, see [16], the important directions of the space spanned by all trial vector derivatives will be computed and the obtained trial vectors will form the final transformation matrix $\underline{\Phi}_T$. The application of weighted POD to the problem under consideration gives out of all available trial vector derivatives $\varphi_{\text{TVD},1} \dots \varphi_{\text{TVD},p}$ a set of vectors $\varphi_{T,1} \dots \varphi_{T,t}$ which minimize the cost function (13.12).

$$J(\varphi_{T,1} \dots \varphi_{T,t}) = \sum_{j=1}^p \left\| \varphi_{\text{TVD},j} - \sum_{i=1}^t \left(\varphi_{\text{TVD},j}^T \underline{\mathbf{K}}_L \varphi_{T,i} \right) \varphi_{T,i} \right\|_{A,2} \rightarrow \min \quad (13.12)$$

The vectors $\varphi_{T,1} \dots \varphi_{T,t}$ can be interpreted as those t vectors which optimally approximate the strain energy available in the space spanned by $\varphi_{\text{TVD},1} \dots \varphi_{\text{TVD},p}$. The final matrix $\underline{\Phi}_T$ contains in its columns the vectors $\varphi_{T,1} \dots \varphi_{T,t}$. As shown in [16] the practical computation of those vectors can be done with an eigenvalue problem in the form

$$\overline{\underline{\Phi}}_{\text{TVD}}^T \underline{\mathbf{K}}_L \overline{\underline{\Phi}}_{\text{TVD}} \widehat{\varphi}_{T,i} = \lambda_i \widehat{\varphi}_{T,i} \quad \text{for } i = 1..t \quad (13.13)$$

$$\varphi_{T,i} = \frac{1}{\sqrt{\lambda_i}} \overline{\underline{\Phi}}_{\text{TVD}} \widehat{\varphi}_{T,i} \quad \text{for } i = 1..t \quad (13.14)$$

where the $(n \times p)$ matrix $\overline{\underline{\Phi}}_{\text{TVD}}$ contains all available trial vector derivatives in its columns. The eigenvalue λ_i is of special interest because it is related to the importance of the vector $\varphi_{T,i}$ for the minimization of (13.12). Large eigenvalues indicate an important vector $\varphi_{T,i}$. Therefore, a ratio $w(t)$ is defined which can be used as an a-priori criterion to determine the number of t .

$$w(t) = \frac{\lambda_1 + \dots + \lambda_t}{\lambda_1 + \dots + \lambda_t + \dots + \lambda_p} \quad (13.15)$$

Note that $w(0) = 0$ and $w(p) = 1$. The value $w(t)$ gives a guide value of how much of the available strain energy is already covered by $\varphi_{T,1} \dots \varphi_{T,t}$.

13.3 Numerical Example

In this section a cantilever beam examples will be presented. The focus is on the convergence of the result with respect to the number of considered ‘joint trial vectors’ in Φ^T . A FE model of the structure under consideration is depicted in Fig. 13.1. Two metallic sheets of the dimension $125 \text{ mm} \times 25 \text{ mm} \times 0.5 \text{ mm}$ are connected via two beams. The extension of the joint is $85 \text{ mm} \times 25 \text{ mm}$. The length of the overlapping area (= the joint) is indicated in Fig. 13.1 with a thick black dashed line. The two sheets and the two beams, which can be interpreted as two weld spots, are modeled out of steel. On the left hand side, the structure is fixed mounted. On the free end, all nodal DOF are attached to a rigid bar. The free node of the rigid bar is in the middle of the sheet. This is indicated in Fig. 13.1 by a solid dark grey line and a dot. The load for the static and dynamic investigations consists of a force in y direction (F_y) and a torque around the x axis (M_x). The entire model has 906 DOF and 648 DOF are involved in the joint contact.

The matrices Φ^v and Φ^s have been computed along the widely known Craig/Bampton method [12] with respect to the undeformed reference state using zero stiffness between the contacting surfaces. For both examples the stiffness and mass matrix of the FE model have been computed by MSC.NASTRAN [17]. The matrices have been imported into Scilab [18] and all subsequent computations have been done directly in Scilab or in its toolbox Xcos [19]. The contact forces have been computed following a simple penalty model and the friction forces, if necessary, have been computed as given in [20].

13.3.1 “Joint Interface Modes” Based on Trial Vector Derivatives

As mentioned before, the reduction base for the linear system has been computed along the Craig/Bampton method [12]. The six DOF of the free end have been defined as so-called “boundary DOF”. This leads to six static deflection shapes for the matrix Φ^s . The two most relevant “Constraint Modes” (deflection along y and rotation around x) are visualized in Fig. 13.2.

For the matrix Φ^v the first ten “Fixed Boundary Normal Modes” have been considered. The eigenfrequency of the 10th mode is 1,337 Hz. Figure 13.3 contains a visualization of the first three modes (= columns) of Φ^v . It can be seen, that the first two columns represent bending modes and the third column represents a torsion mode around the x axis.

In a next step all 512 (= p) trial vector derivatives (TVD) according to the theory outlined in the chapter before have been computed. In order to get a suitable small number of ‘joint trial vectors’ weighted POD has been applied to all p TVD. Figure 13.4 contains visualizations of the first four columns of the matrix Φ^T .

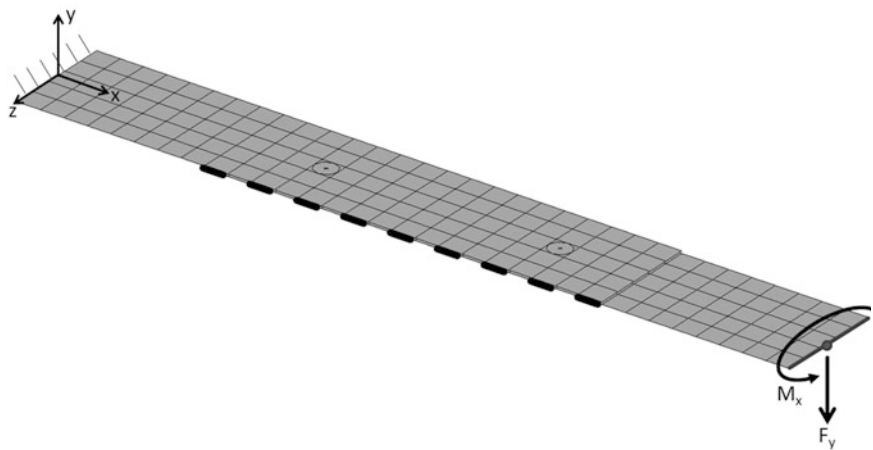


Fig. 13.1 FE model of friction bar

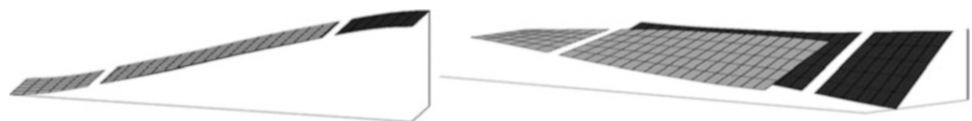


Fig. 13.2 Constraint modes along y and around x of friction bar

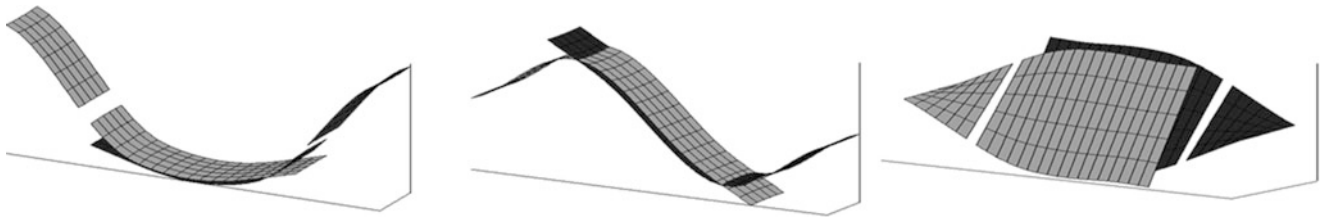


Fig. 13.3 First three columns of matrix Φ_v

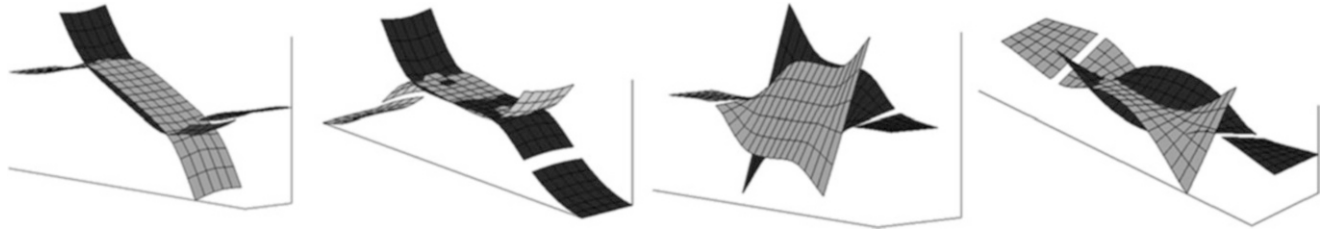


Fig. 13.4 Visualization of the first columns of Φ_T

Fig. 13.5 Convergence analysis for a static computation

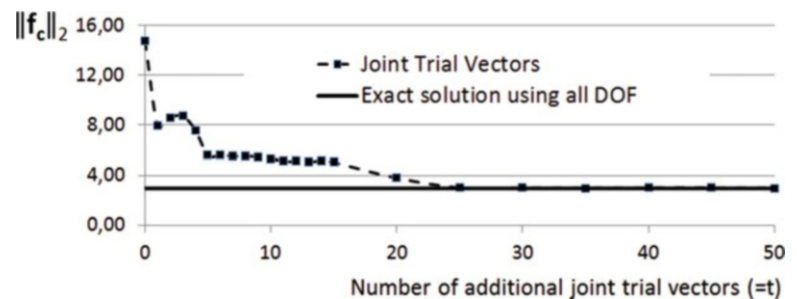
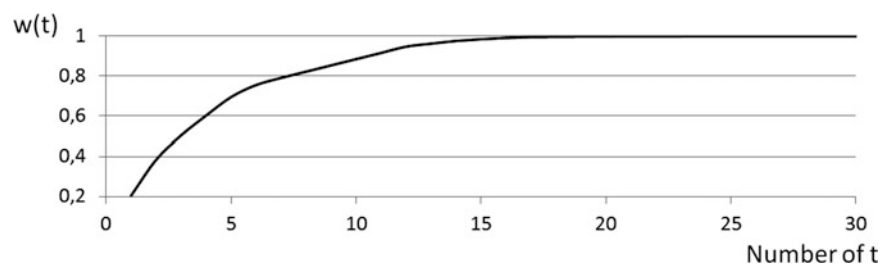


Fig. 13.6 Evaluation of the function $w(t)$



13.3.2 Static Response Computation

The static response has been computed for $F_y = -0.7$ N and $M_x = -20$ Nmm. For this computation, no friction has been considered. For the convergence analysis, a $(1 \times a)$ vector f_c is constructed. The vector contains a entries, namely $f_{c,1}$ to $f_{c,a}$, and $f_{c,i}$ ($1 \leq i \leq a$) holds the contact force at FE node pair i . As convergence criteria the Euclidean norm of the vector f_c is evaluated. Figure 13.5 contains a convergence analysis with respect to the number of considered joint trial vectors ($=t$) in the matrix Φ_T . For the reference solution the contact forces are computed based on a full nonlinear FE analysis using all nodal DOF.

It can be seen in Fig. 13.5 that 20 additional joint modes lead already to a good representation of the contact force. Figure 13.6 contains the function $w(t)$ and it seems, that this value can be used as an a-priori estimator for the number of required 'joint trial vectors'.

Fig. 13.7 Time evolution of the Euclidian norm of the contact force vector

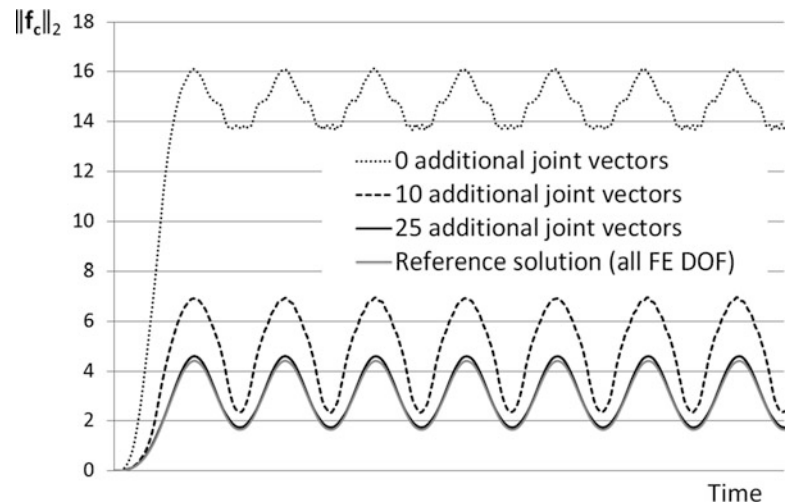
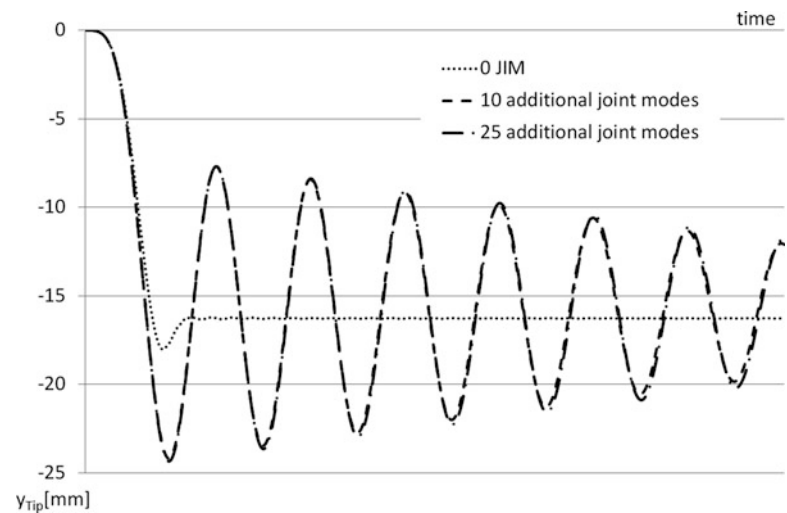


Fig. 13.8 Tip deflection in y direction



13.3.3 Dynamic Response Computation Without Friction

For the dynamic response analysis the former loads have been applied as step function to the structure. The step function was implemented as a half wave cosine with a frequency of 10 Hz. Figure 13.7 contains the evolution of the norm of the contact force vector \mathbf{f}_c with respect to the time. It can be seen, that 25 additional joint trial vectors deliver excellent results which corresponds with the convergence analysis of the static computation.

13.3.4 Dynamic Response Computation with Friction

In case of a metallic structure the dry friction inside a joint is typically the dominating source of damping, see [1–4]. In the cited literature it can be read, that a Coulomb-like dry friction model which is applied between all FE node pairs, catches already most of the relevant effects.

As mentioned before, the friction model is implemented along [20]. For the friction coefficient μ a value of 0.5 has been used. This is not realistic for a metallic structure with dry surfaces but it leads to a significant decrease of the vibration amplitude within few vibration cycles. Figure 13.8 contains the time evolution of the tip deflection in y direction. It can be seen that the consideration of no additional joint modes is not an option. The explanation can be found in Fig. 13.9 where the Euclidian norm of the $(2a \times 1)$ friction force vector \mathbf{f}_R is evaluated with respect to time. The vector \mathbf{f}_R contains friction forces in x and z direction of all a FE node pairs being involved in the joint contact.

Fig. 13.9 Time evolution of the Euclidean norm of the friction forces

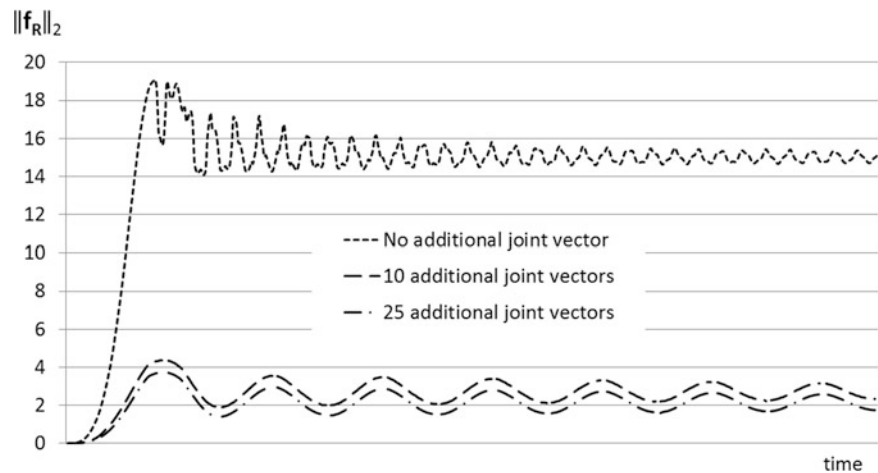


Figure 13.9 indicates that an accurate in plane joint flexibility is essential for the result quality when friction is regarded. When no additional joint vectors are regarded, the damping due to friction is extremely overestimated. The difference between 10 and 25 additional joint modes is already small and a converging behavior very similar to the example without friction can be observed. In case of friction it was not possible to compute a reference solution using all FE nodal DOF.

13.3.5 Computational Efficiency

All simulations have been performed with basically the same XCos [19] block diagram. The difference between the simulations was the particular use of the stiffness and mass matrix and the number of DOF. While the reduced models require a reduced stiffness and mass matrix the full FE model needs the matrices obtained by the FE software. For the dynamic example without friction it can be reported that the time integration with 0, 10 and 25 additional ‘joint trial vectors’ needs 0.07 %, 0.12 % and 0.25 % CPU time in comparison to the full FE model. In other words, the use of 25 additional joint modes delivers an accuracy which is comparable to that one of a full non-linear FE simulation without losing the advantages of model reduction.

13.4 Conclusion

In this paper a new reduction base for an accurate and efficient model reduction of jointed structures has been presented. Based on an initial reduction base of a linearized structure so called trial vector derivatives have been computed. In order to get an accurate and small reduction base, Proper Orthogonal Decomposition with inner weighting has been applied to the trial vector derivatives. Convergence analyses indicate that just a few of these ‘joint trial vectors’ significantly improve the system response because the joint non-linearities in terms of contact and friction can accurately be considered.

The save of trial vectors and therefore degrees of freedom has significant impact on the CPU time needed for the time integration. Even the result quality is comparable to that one of a non-linear FE computation the save of CPU time is more than a factor of hundred for the presented example.

Acknowledgement This project was supported by the program “Regionale Wettbewerbsfähigkeit OÖ 2010–2013”, which is financed by the European Regional Development Fund and the Government of Upper Austria.

References

1. Gaul L, Nitsche R (2001) The role of friction in mechanical joints. *Appl Mech Rev* 54(2):93–105
2. Song Y, McFarland DM, Berman LA, Vakakis AF (2005) Effect of pressure distribution on energy dissipation in a mechanical lap joint. *AIAA J* 43(2):420–425

3. Ren YS, Yang JM, Zhao ZL, Wang YH (1994) Nonlinear vibration analysis of beams with dry friction joint. In: Proceedings of the 12 IMAC. Honolulu, pp 1720–1727
4. Nitsche R (2001) Semi-active control of friction damped systems. VDI Fortschrittsbericht, vol 8, no 907, VDI Verlag
5. Craig RR (1985) A review of time-domain and frequency-domain component mode synthesis methods. In: Martinez D, Miller K (eds) Combined experimental/analytical modeling of dynamic structural systems, vol 67. The American Society of Mechanical Engineers, AMD, New York, pp 1–30
6. Noor AK (1994) Recent advances and applications of reduction methods. *Appl Mech Rev* 47(5):125–146
7. Zu QQ (2004) Model order reduction techniques. Springer, London. ISBN: 1852338075
8. Laursen TA (2002) Computational contact and impact mechanics. Springer, Berlin. ISBN: 3-540-42906-9 (Chapter 3.3.2)
9. Laursen TA (2002) Computational contact and impact mechanics. Springer, Berlin. ISBN: 3-540-42906-9 (Chapter 3.4.3.1)
10. Stricklin JA, Haisler WE (1977) Formulations and solution procedures for nonlinear structural analysis. *Comput Struct* 7:125–136
11. Villaverde R, Hanna MM (1992) Efficient mode superposition algorithm for seismic analysis of non-linear structures. *Earthq Eng Struct Dyn* 21:849–858
12. Craig RR, Bampton MCC (1968) Coupling of substructures for dynamic analysis. *AIAA J* 6(7):1313–1319
13. Slaats PMA, Jong J, Sauren AAHJ (1993) Model reduction tools for nonlinear structural dynamics. *Comput Struct* 54:1155–1171
14. Tiso P, Jansen E, Abdalle M (2011) Reduction method for finite element nonlinear dynamic analysis of shells. *AIAA J* 49:2295–2304
15. Tiso P (2011) Optimal second order reduction basis selection for nonlinear transient analysis. Modal analysis topics, vol 3. In: Conference proceedings of the society for experimental mechanics series. Springer, New York, pp 27–39. ISBN: 978-1-4419-9298-7
16. Volkwein S (2013) Model reduction using proper orthogonal decomposition. <http://www.uni-graz.at/imawww/volkwein/POD.pdf>, cited 16.07.2013
17. MSC.NASTRAN, Version 2011.1.0. <http://simcompanion.mssoftware.com>
18. Scilab, Version 5.4.0. <http://www.scilab.org/>
19. Scilab, Version 5.4.0. <http://www.scilab.org/scilab/features/xcos>
20. Garcia GC, Ponthot J-P (2008) A quasi-coulomb model for frictional contact interfaces Application to metal forming simulations. *Latin Am Appl Res* 38(2):95–104

Chapter 14

A Substructuring Method for Geometrically Nonlinear Structures

Frits Wenneker and Paolo Tiso

Abstract We present an extension of the well established Craig–Bampton and Rubin methods for component mode synthesis for the case of geometric nonlinearities. The internal modal basis of a substructure is enriched with modal derivatives to capture the nonlinear behavior. We show that the Rubin method outperforms the Craig–Bampton method in cases characterized by large rigid motions of the substructures.

Keywords Geometric nonlinearity • Substructuring • Component mode synthesis • Modal derivatives • Finite elements

14.1 Introduction

Geometrical nonlinear effects are becoming a key aspect to consider in the design and analysis of many structural applications. In several cases, large deflections are caused by stringent weight requirements that make the structures slender and therefore, very flexible. Examples are helicopter blades, large wind turbines, deployable solar panels and antennas for space applications, flexible robot arms. In other cases, the geometrically nonlinear behavior is exploited for a desired function: an interesting application is found in the MEMS domain, where it is possible to realize mechanical frequency dividers by chaining components working in the geometrical nonlinear regime [10].

The Finite Element (FE) models associated to the analysis of such complex systems are typically very large and the time integration of the nonlinear equations resulting from the FE discretization is a computationally demanding task. It is therefore convenient to resort to model order reduction techniques, that seek an approximate solution within a subspace of much smaller size as compared to the size of the full problem. A well established technique in linear structural analysis is the *Component Mode Synthesis* (CMS): the model is divided into subcomponents, whose response is approximated independently by a suitable reduction basis, and then assembled by prescribing equilibrium and compatibility on the common interface. Among the different techniques, the Craig–Bampton (CB) method [3] and the Rubin method [8] are widely used in linear structural analysis. In general, these methods approximate the dynamics of the components by vibration modes, and the communication with the other substructures is deemed to interface modes.

Few contributions addressed the extension of CMS to geometrically nonlinear problems. In particular, the linear internal basis of vibration modes for the CB method was augmented with nonlinear modes [1] to capture the large deflection behavior. Earlier, an efficient time integration scheme has been proposed when a large linear region of the structure can be condensed onto the nonlinear degrees of freedom [2].

We present in this work the extension of the CB and Rubin method for geometrically nonlinear analysis. The extension is based on the enrichment to the internal modal basis with *modal derivatives* [11], which capture the nonlinear deflections by an asymptotic expansion of the displacement in the direction of the retained linear modes. We show that the Rubin method offers superior performances in cases where large rigid body motion is contained in the solution.

This paper is organized as follows. The nonlinear FE discretized dynamic equations on motion are introduced in Sect. 14.2, together with the substructuring framework. Then, the CB and Rubin methods are briefly summarized. The concept of modal

F. Wenneker • P. Tiso (✉)

Faculty of Mechanical, Maritime and Materials Engineering, Department of Precision and Microsystems Engineering,
Delft University of Technology, Mekelweg 2, 2628CD Delft, The Netherlands
e-mail: p.tiso@tudelft.nl

derivatives is discussed in Sect. 14.3, and the extension for the reduction basis for the CB and Rubin is introduced. Preliminary numerical results are discussed in Sect. 14.5, and finally conclusions and future directions are given in Sect. 14.6.

14.2 Problem Formulation

We consider here the discretized FE nonlinear dynamic equations of motion of a general tridimensional structure. For this study, we do not consider damping. The governing FE system of equations, together with the boundary conditions, writes:

$$\begin{cases} \mathbf{M}\ddot{\mathbf{u}} + \mathbf{f}(\mathbf{u}) = \mathbf{p} \\ \mathbf{u}(0) = \mathbf{u}_0 \\ \dot{\mathbf{u}}(0) = \dot{\mathbf{u}}_0 \end{cases}, \quad (14.1)$$

where $\mathbf{u}(t) \in \mathbb{R}^n$ is the generalized displacement vector, $\mathbf{M} \in \mathbb{R}^{n \times n}$ is the mass matrix, $\mathbf{f}(\mathbf{u}) : \mathbb{R}^n \mapsto \mathbb{R}^n$ is the nonlinear force vector and $\mathbf{p} \in \mathbb{R}^n$ is the time dependent applied load vector. The initial conditions for the displacement and the velocity vector are indicated with \mathbf{u}_0 and $\dot{\mathbf{u}}_0$, respectively. We further assume that the nonlinearity of $\mathbf{f}(\mathbf{u})$ is caused by geometrical effects only, i.e. when the displacements are so large that a linear kinematic model does not hold. This is typically the case of thin-walled structures, which can undergo large displacements while staying in the elastic range of the material. In the case of thin-walled structures, large displacements cause coupling between the bending and in-plane stretching deformations.

14.2.1 Substructuring

Consider now a model that is divided into s non-overlapping substructures S_k , $k = 1, \dots, s$ that are to be coupled. In the absence of damping, the system of governing equations (14.1) can be divided into s subsystems that can be written in block-diagonal form as:

$$\begin{bmatrix} \mathbf{M}^{(1)} & \dots & \mathbf{0} \\ \vdots & \ddots & \vdots \\ \mathbf{0} & \dots & \mathbf{M}^{(s)} \end{bmatrix} \begin{bmatrix} \ddot{\mathbf{u}}^{(1)} \\ \vdots \\ \ddot{\mathbf{u}}^{(s)} \end{bmatrix} + \begin{bmatrix} \mathbf{f}^{(1)}(\mathbf{u}^{(1)}) \\ \vdots \\ \mathbf{f}^{(s)}(\mathbf{u}^{(s)}) \end{bmatrix} = \begin{bmatrix} \mathbf{p}^{(1)}(t) \\ \vdots \\ \mathbf{p}^{(s)}(t) \end{bmatrix} + \begin{bmatrix} \mathbf{g}^{(1)}(t) \\ \vdots \\ \mathbf{g}^{(s)}(t) \end{bmatrix} \quad (14.2)$$

where the superscript^(k) indicates quantities belonging to the substructure S_k . In addition to the terms of the governing equations (14.1), the interface connection forces $\mathbf{g}^{(k)}$ are added. For each subsystem, we have that $\mathbf{u}^{(k)} \in \mathbb{R}^{n_k \times 1}$ and the external force is assumed to be time dependent only. The assembled system equations need to satisfy compatibility and equilibrium conditions: interface displacements of connecting degrees of freedom (DOFs) need to be identical and connection forces need to be equal in magnitude and opposite in direction. These conditions can be expressed as [5]:

$$\begin{cases} \mathbf{B}\bar{\mathbf{u}} = \mathbf{0} \\ \mathbf{L}^T \bar{\mathbf{g}} = \mathbf{0} \end{cases} \quad (14.3)$$

where \mathbf{B} and \mathbf{L} are boolean matrices selecting corresponding DOFs, $\bar{\mathbf{u}} = [\mathbf{u}^{(1)T} \dots \mathbf{u}^{(s)T}]^T$ and $\bar{\mathbf{g}} = [\mathbf{g}^{(1)T} \dots \mathbf{g}^{(s)T}]^T$. The conditions in Eq. (14.3) are referred as *primal assembly*, and are here considered.

14.2.2 Component Mode Synthesis

The dynamic system of Eq. (14.2) is generally is very large, and its solution is computationally expensive. In Component Mode Synthesis (CMS), the structure is divided into independent components in which displacement is approximated by a combination of chosen mode shapes via generalized modal coordinates. The number of the generalized coordinates are much less than the original number of physical DOF, in the component. The FE discretisation of each component is therefore

followed by a second discretisation step, where the number of n_s equations in each row in of the system (14.2) is reduced to $m \ll n_s$. The physical coordinates $\mathbf{u}^{(s)}$ in terms of generalised coordinates $\mathbf{q}^{(s)}$ by the transformation:

$$\mathbf{u}^{(s)} = \begin{bmatrix} \mathbf{u}_b^{(s)} \\ \mathbf{u}_i^{(s)} \end{bmatrix} \approx \mathbf{R}^{(s)} \begin{bmatrix} \mathbf{u}_b^{(s)} \\ \boldsymbol{\eta}^{(s)} \end{bmatrix} = \mathbf{R}^{(s)} \mathbf{q}^{(s)} \quad (14.4)$$

where the columns in $\mathbf{R}^{(s)} \in \mathbb{R}^{n_s \times m}$ are linearly independent mode shapes; either static or dynamic component modes. The introduced subscripts denote whether the partitioned modes act on boundary (b) or internal (i) DOFs. Only the internal DOFs are reduced, and their contribution is split into a static and dynamic part:

$$\mathbf{u}_i = \mathbf{u}_{i,stat} + \mathbf{u}_{i,dyn} \quad (14.5)$$

By substituting Eq. (14.4) into Eq. (14.2), an error is introduced as $\mathbf{q}^{(s)} \neq \mathbf{u}^{(s)}$. This error represents the portion of the displacements that cannot be described by $\mathbf{q}^{(s)}$ and therefore it is orthogonal to the space of $\mathbf{R}^{(s)}$. Premultiplying the resulting equations of motion by $\mathbf{R}^{(s)T}$ yields the reduced equations of motion:

$$\mathbf{R}^{(s)T} \mathbf{M}^{(s)} \mathbf{R}^{(s)} \ddot{\mathbf{q}}^{(s)} + \mathbf{R}^{(s)T} \mathbf{f}^{(s)}(\mathbf{R}^{(s)} \mathbf{q}^{(s)}) = \mathbf{R}^{(s)T} \mathbf{p}^{(s)}(t) + \mathbf{R}^{(s)T} \mathbf{g}^{(s)}(t) \quad (14.6)$$

or, equivalently

$$\tilde{\mathbf{M}}^{(s)} \ddot{\tilde{\mathbf{q}}}^{(s)} + \tilde{\mathbf{f}}^{(s)}(\mathbf{R}^{(s)} \mathbf{q}^{(s)}) = \tilde{\mathbf{p}}^{(s)}(t) + \tilde{\mathbf{g}}^{(s)}(t) \quad (14.7)$$

In linear dynamic analysis, CMS techniques are widely used and have proven to be accurate. In the next section, the well-established CB and Rubin methods for CMS are briefly reminded. The substructure labels will be discarded in the rest of the paper unless needed to avoid confusion, e.g. $\mathbf{M}^{(s)} = \mathbf{M}$. Also, the reduced matrices as in Eq. (14.7) will be denoted without a tilde to minimise notational clutter.

14.2.3 Craig–Bampton Method

In the CB method for linear dynamic analysis [3], the reduction basis in Eq. (14.4) is formed a set of static *constraint modes* $\boldsymbol{\Psi}_c$ and internal vibration modes (VMs) $\boldsymbol{\Phi}$. The first set of modes accounts for the interaction with neighbouring substructures, while the latter for the dynamic behaviour of the substructure itself, as clamped at the interface dofs. The interface modes are obtained by imposing a unit displacement to each interface dofs while clamping all the other interface dofs. The CB reduction basis can be written as:

$$\begin{bmatrix} \mathbf{u}_b \\ \mathbf{u}_i \end{bmatrix} \approx {}^{CB} \mathbf{R} \mathbf{q} = \begin{bmatrix} \mathbf{I} & \mathbf{0} \\ \boldsymbol{\Psi}_c & \boldsymbol{\Phi} \end{bmatrix} \begin{bmatrix} \mathbf{u}_b \\ \boldsymbol{\eta} \end{bmatrix} \quad (14.8)$$

For linear dynamics, this reduction basis has proven to be accurate, provided the eigenfrequencies associated to the retained internal VMs are higher than the frequency range of interest for the assembled structure.

14.2.4 Rubin Method

In contrast to the CB reduction procedure, where internal VMs are used (i.e. when the substructure is clamped at the interface), the Rubin method [8] includes VMs of the free floating component. In the Rubin method, the physical displacements are approximated by means of *residual attachment modes* (RAMs) $\boldsymbol{\Psi}_r$, *rigid body modes* (RBMs) $\boldsymbol{\Phi}_r$ and free VMs $\bar{\boldsymbol{\Phi}}$. The first set statically determines the structure, similar to the constraint modes in Eq. (14.8). The second and third set account for the dynamics of the substructure. A reduction basis of the following form can be constructed:

$$\mathbf{u} \approx [\boldsymbol{\Psi}_r \ \boldsymbol{\Phi}_r \ \bar{\boldsymbol{\Phi}}] \begin{bmatrix} \mathbf{g}_b \\ \boldsymbol{\eta}_r \\ \bar{\boldsymbol{\eta}} \end{bmatrix} = \mathbf{R} \mathbf{q} \quad (14.9)$$

Note that the rigid body modes are simply the free VMs associated to zero eigenfrequency. Residual attachment modes represent the deformation of the substructure when a unit force is applied to one boundary DOF. The reduction proposed in Eq. (14.9) therefore leads to a *dual* system of equations, i.e. displacement and force DOFs combined in \mathbf{q} . In contrast to the CB method, the component modes act on the full set of DOFs rather than on the internal DOFs only. In our framework, we require a *primal* system (displacement DOFs only), where the boundary DOFs are not reduced. Therefore, the expression in Eq. (14.9) needs to be manipulated. Let us first partition the system of equations as:

$$\begin{bmatrix} \mathbf{u}_b \\ \mathbf{u}_i \end{bmatrix} \approx \begin{bmatrix} \Psi_{r,b} & \Phi_{r,b} & \bar{\Phi}_b \\ \Psi_{r,i} & \Phi_{r,i} & \bar{\Phi}_i \end{bmatrix} \begin{bmatrix} \mathbf{g}_b \\ \eta_r \\ \bar{\eta} \end{bmatrix} \quad (14.10)$$

Solving the first row in this expression for the boundary connection forces \mathbf{g}_b gives:

$$\mathbf{g}_b \approx \Psi_{r,b}^{-1} (\mathbf{u}_b - \Phi_{r,b} \eta_r - \bar{\Phi}_b \bar{\eta}) \quad (14.11)$$

From this expression a second coordinate transformation can be defined as:

$$\begin{bmatrix} \mathbf{g}_b \\ \eta_r \\ \bar{\eta} \end{bmatrix} \approx \begin{bmatrix} \Psi_{r,b}^{-1} & -\Psi_{r,b}^{-1} \Phi_{r,b} & -\Psi_{r,b}^{-1} \bar{\Phi}_b \\ \mathbf{0} & \mathbf{I} & \mathbf{0} \\ \mathbf{0} & \mathbf{0} & \mathbf{I} \end{bmatrix} \begin{bmatrix} \mathbf{u}_b \\ \eta_r \\ \bar{\eta} \end{bmatrix} = \mathbf{R}_2 \mathbf{q}_2 \quad (14.12)$$

The total coordinate transformation that is done to obtain an approximation of the displacement field \mathbf{u} , while retaining the boundary DOFs is now found by multiplying Eqs. (14.9) and (14.12):

$$\begin{bmatrix} \mathbf{u}_b \\ \mathbf{u}_i \end{bmatrix} \approx \mathbf{R} \mathbf{R}_2 \mathbf{q}_2 = {}^R \mathbf{R} \mathbf{q}_2 = \begin{bmatrix} \mathbf{I} & \mathbf{0} & \mathbf{0} \\ \Psi_{r,i} \Psi_{r,b}^{-1} & \Phi_{r,i} - \Psi_{r,i} \Psi_{r,b}^{-1} \Phi_{r,b} & \bar{\Phi}_i - \Psi_{r,i} \Psi_{r,b}^{-1} \bar{\Phi}_b \end{bmatrix} \begin{bmatrix} \mathbf{u}_b \\ \eta_r \\ \bar{\eta} \end{bmatrix} \quad (14.13)$$

14.3 Modal Derivatives

Internal and free VMs in the CB and Rubin reduction bases describe linear dynamic behaviour only. The equations of motion in Eq. (14.2) are linearised around position \mathbf{u}_{eq} . In the following we will consider the dynamic contribution to the response, i.e. $\mathbf{u}_{i,dyn}$ in Eq. (14.5). If we assume that the motion $\Delta \mathbf{u}$ around this position is small, i.e. $\mathbf{u} = \mathbf{u}_{eq} + \Delta \mathbf{u}$, the linearised reduced dynamic response can be written as:

$$\Delta \mathbf{u} \approx \sum_{i=1}^m \phi_i(\mathbf{u}_{eq}) \eta_i \quad (14.14)$$

where the free or internal VMs ϕ_i are computed by solving the eigenvalue problem associated with the linearised equations of motion; free VMs if the free floating structure is considered and internal VMs if the structure is fixed on its boundary nodes. In geometrically nonlinear systems, the VMs are configuration dependent. Therefore, the basis needs to be updated during the response analysis to account for the nonlinearities. If this needs to be done too frequently, the advantage of the reduction step might be surpassed by the computational effort necessary to extract the new modal basis.

To overcome this difficulty, the *modal derivatives* (MDs) of the VMs can be included in the basis [11]. When the displacements can no longer be considered small, the dynamic response of Eq. (14.14) should be expressed as:

$$\Delta \mathbf{u} \approx \sum_{i=1}^m \phi_i(\mathbf{u}_{eq} + \Delta \mathbf{u}) \eta_i \quad (14.15)$$

where it is highlighted that the VMs are displacement dependent. Equation (14.15) can be expanded in Taylor series around \mathbf{u}_{eq} :

$$\Delta \mathbf{u} \approx \sum_{i=1}^m \phi_i(\mathbf{u}) \eta_i \approx \sum_{i=1}^m \left. \frac{\partial \phi_i}{\partial \eta_i} \right|_{\Delta \mathbf{u}=\mathbf{0}} \eta_i + \sum_{i=1}^m \sum_{j=1}^m \left. \frac{1}{2} \frac{\partial^2 \phi_i}{\partial \eta_i^2} \right|_{\Delta \mathbf{u}=\mathbf{0}} \eta_i \eta_j \quad (14.16)$$

where the derivatives in this expansion follow from Eq. (14.15):

$$\frac{\partial \mathbf{u}}{\partial \eta_i} = \boldsymbol{\phi}_i + \sum_{j=1}^m \frac{\partial \boldsymbol{\phi}_j}{\partial \eta_i} \eta_j \quad (14.17)$$

$$\frac{\partial^2 \mathbf{u}}{\partial \eta_i^2} \eta_j = \frac{\partial \boldsymbol{\phi}_j}{\partial \eta_i} + \frac{\partial \boldsymbol{\phi}_i}{\partial \eta_j} + \sum_{j=1}^m \sum_{k=1}^m \frac{\partial^2 \boldsymbol{\phi}_k}{\partial \eta_i^2} \eta_j \eta_k \quad (14.18)$$

Evaluating these expressions at $\mathbf{u} = \mathbf{u}_{eq}$ gives:

$$\left. \frac{\partial \mathbf{u}}{\partial \eta_i} \right|_{\Delta \mathbf{u}=\mathbf{0}} = \boldsymbol{\phi}_i(\mathbf{u}_{eq}) \quad (14.19)$$

$$\left. \frac{\partial^2 \mathbf{u}}{\partial \eta_i^2} \eta_j \right|_{\Delta \mathbf{u}=\mathbf{0}} = \frac{\partial \boldsymbol{\phi}_j(\mathbf{u}_{eq})}{\partial \eta_i} + \frac{\partial \boldsymbol{\phi}_i(\mathbf{u}_{eq})}{\partial \eta_j} \quad (14.20)$$

Equation (14.19) represents the VM, whereas the term in Eq. (14.20) represent the MD $\boldsymbol{\theta}_{ij}$. The MD $\boldsymbol{\theta}_{ij}$ represents how $\boldsymbol{\phi}_i$ changes if the structure is perturbed by the displacement field $\boldsymbol{\phi}_j$.

Modal derivatives can be computed analytically by differentiating the eigenvalue problem associated with the linearised system with respect to the modal amplitudes:

$$\left(\frac{\partial \mathbf{K}_{eq}}{\partial \eta_j} - \frac{\partial \omega_i^2}{\partial \eta_j} \mathbf{M} \right) \boldsymbol{\phi}_i + (\mathbf{K}_{eq} - \omega_i^2 \mathbf{M}) \boldsymbol{\theta}_{ij} = \mathbf{0} \quad (14.21)$$

It has been shown that the inertia terms in Eq. (14.21) can be ignored [6, 7, 9]. Equation (14.21) may thus be simplified to:

$$\mathbf{K}_{eq} \boldsymbol{\theta}_{ij} = -\frac{\partial \mathbf{K}_{eq}}{\partial \eta_j} \boldsymbol{\phi}_i \quad (14.22)$$

The right-hand side of this equation represents a pseudo-load that is induced by the displacement field $\boldsymbol{\theta}_{ij}$. Note that taking the derivative of the static problem ($\mathbf{K}\boldsymbol{\phi}_i = \mathbf{0}$) with respect to the modal coordinate results in the same expression. For a constrained problem, the stiffness matrix is invertible, such that the definition of a MD may be written as

$$\boldsymbol{\theta}_{ij} = -\mathbf{K}_{eq}^{-1} \frac{\partial \mathbf{K}_{eq}}{\partial \eta_j} \boldsymbol{\phi}_i \quad (14.23)$$

For a CB linear reduction basis with m selected VMs, $r = m(m+1)/2$ MDs exist due to the mentioned symmetry. An illustration of internal VMs and their corresponding MDs is given in Fig. 14.1.

The Rubin reduction basis in Eq. (14.13) also includes RBMs. While translational RBMs results in a null right hand side of Eq. (14.22), rotational RBMs produce derivatives. In analogy to MDs corresponding to VMs, rigid body derivatives (RBDs) can be computed, i.e. MDs corresponding to rotational RBMs. A Rubin basis including M free VMs also includes three rotational RBMs. Hence, with a linear Rubin basis of order $m+3$, a maximum of $r = (m^2 + 7m + 12)/2$ unique MDs can be computed. This is an additional $3m+6$ MDs with respect to the CB method. An illustration of a rotational RBM, a free VMs and their corresponding RBDs and MDs is given in Fig. 14.2.

14.4 Augmented Reduction Bases

In order to be able to capture the geometrical nonlinearities, the MDs need to be added to the linear reduction bases of CB and Rubin in Eqs. (14.8) and (14.13), respectively. For the CB technique the internal DOFs are separated in a static and a dynamic contribution. The first is approximated using constraint modes. In a nonlinear setting, the dynamic contribution is approximated by both internal VMs and MDs:

$$\mathbf{u}_i \approx \boldsymbol{\Psi}_c \mathbf{u}_b + \boldsymbol{\Phi} \boldsymbol{\eta} + \boldsymbol{\Theta} \boldsymbol{\xi} \quad (14.24)$$

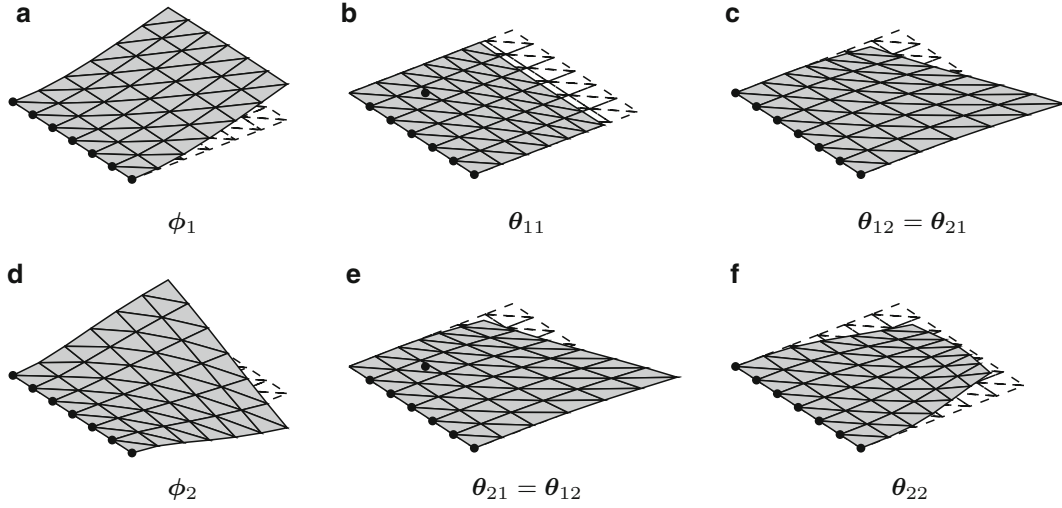


Fig. 14.1 Dynamic component modes in a Craig–Bampton reduction basis for a square plate model with left edge boundary nodes (*black dots*). (a, d) First two internal vibration modes; (b, c, e, f) modal derivatives corresponding to the internal VMs (all in-plane)

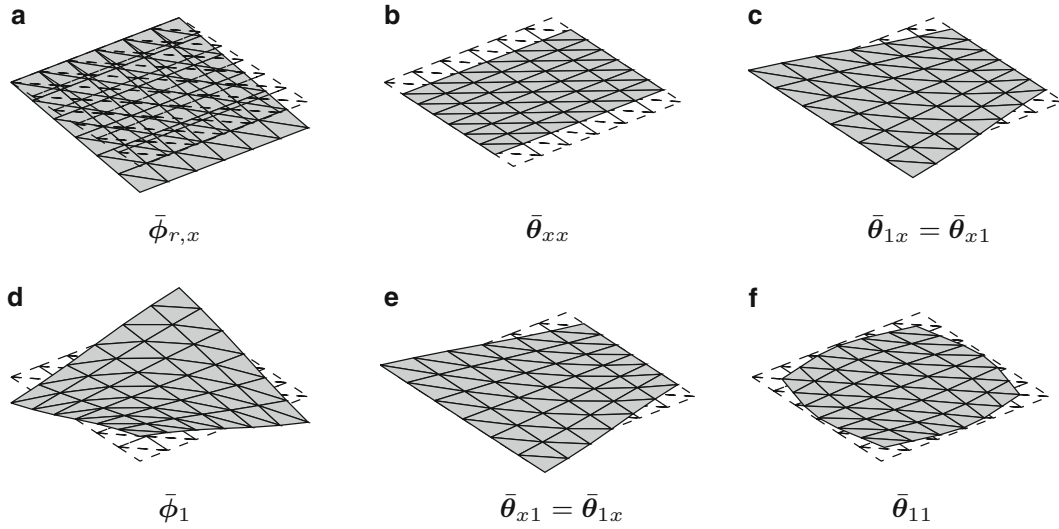


Fig. 14.2 Dynamic component modes in a Rubin reduction basis for a square plate model clamped. (a) Rotational rigid body mode about the longitudinal x axis; (d) first free vibration mode; (b, c, e, f) modal derivatives corresponding to the RBM and free VM (all in-plane)

where the columns in Θ contain the MDs and the corresponding modal amplitudes η_i, η_j are represented by the entries in ξ . As follows from Eq. (14.23), MDs computed from internal VMs only act on the internal DOFs. Hence, the CB reduction basis may be enriched in a straightforward manner:

$$\begin{bmatrix} \mathbf{u}_b \\ \mathbf{u}_i \end{bmatrix} \approx {}^{CB} \mathbf{R} \mathbf{q} = \begin{bmatrix} \mathbf{I} & \mathbf{0} & \mathbf{0} \\ \Psi_c & \Phi & \Theta \end{bmatrix} \begin{bmatrix} \mathbf{u}_b \\ \eta \\ \xi \end{bmatrix} \quad (14.25)$$

The MDs in the Rubin basis are computed from free VMs, rotational RBMs and their interaction. The system's physical response is approximated as follows:

$$\mathbf{u} \approx \Psi_r \mathbf{g}_b + \Phi_r \eta_r + \bar{\Phi} \bar{\eta} + \bar{\Theta} \bar{\xi} \quad (14.26)$$

Hence, the MDs in this expression act not only on \mathbf{u}_i , but on \mathbf{u}_b as well. Similar to the Rubin method for linear dynamics in Sect. 14.2.4, the approximation in Eq. (14.26) needs a second coordinate transformation in order to be put in the correct

CMS format (i.e. where only internal DOFs are generalised). This is analogous to the coordinate transformation Eq. (14.12), resulting in the following augmented Rubin reduction basis:

$$\begin{bmatrix} \mathbf{u}_b \\ \mathbf{u}_i \end{bmatrix} \approx {}^R \mathbf{R} \mathbf{q}_2 = \begin{bmatrix} \mathbf{I} & \mathbf{0} & \mathbf{0} & \mathbf{0} \\ \Psi_{r,i} \Psi_{r,b}^{-1} \Phi_{r,i} - \Psi_{r,i} \Psi_{r,b}^{-1} \Phi_{r,b} \bar{\Phi}_i - \Psi_{r,i} \Psi_{r,b}^{-1} \bar{\Phi}_b \bar{\Theta}_i - \Psi_{r,i} \Psi_{r,b}^{-1} \bar{\Theta}_b \end{bmatrix} \begin{bmatrix} \mathbf{u}_b \\ \eta_r \\ \bar{\eta} \\ \bar{\xi} \end{bmatrix} \quad (14.27)$$

14.5 Results

The presented nonlinear CMS techniques are tested on models of cantilevered plates modelled with shell elements. We adopt here the Von-Karman kinematic model, which is valid for moderate rotation and small strains [4]. The model, depicted in Fig. 14.3, is divided in two substructures S_i , $i = 1, 2$. A step load in z -direction with amplitude λ is applied to the indicated tip node. The model consists of 546 DOFs; 84 boundary DOFs and 462 internal DOFs.

The first model considered has a thick substructure S_1 with thickness $h_1 = 3$ mm and a relatively thin substructure S_2 with $h_2 = 0.8$ mm. With this geometry and a load amplitude of $\lambda = 70$ N, applied at the beginning of the simulation and held constant, S_1 will deform in the linear elastic regime and only S_2 needs to be considered nonlinear. A substructuring time-integration scheme proposed by Bathe [2] is used, where the linear DOFs are condensed prior to the nonlinear equilibrium iterations for optimal computational efficiency. It was found that a reduction basis with $m_1 = m_2 = 8$ VMs for both substructures accurately reproduces the full linear solution. The number of MDs that can be computed with m VMs is $r_2 = 36$ for CB and $r_2 = 66$ for Rubin (MDs are only added for S_2 as S_1 can be considered linear). The latter includes more MDs because rotational RBMs are accounted for as well. The nonlinear responses for this model are shown in Fig. 14.4a, from which it can be seen that both CMS methods accurately describe the full model response. Using the augmented CB method, the model order is reduced from 546 DOFs to 136 DOFs. The computation time needed for a nonlinear time-integration on the full order model is 82.0 s and on the CB reduced order model 25.6 s (speed-up factor of 3.2). The nonlinear Rubin method resulted in a 178 DOF system and the nonlinear response was captured in 27.8 s (speed-up factor of 2.95). It is stressed here that the computational savings are not only obtained by the model order reduction step, but also due to earlier mentioned time-integration scheme where the linear DOFs of S_1 are condensed prior to the equilibrium iterations.

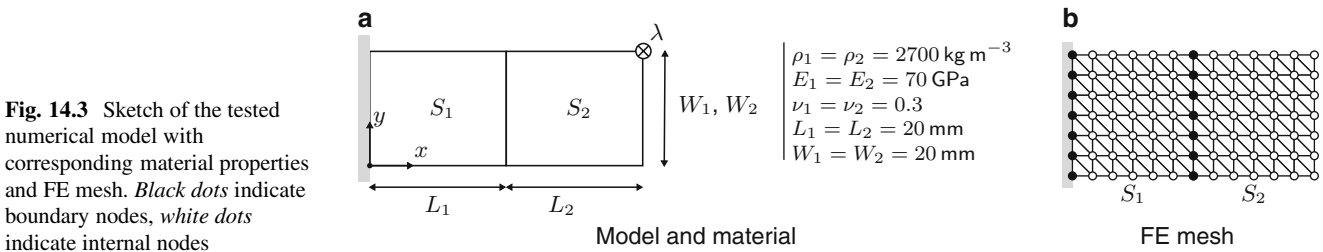
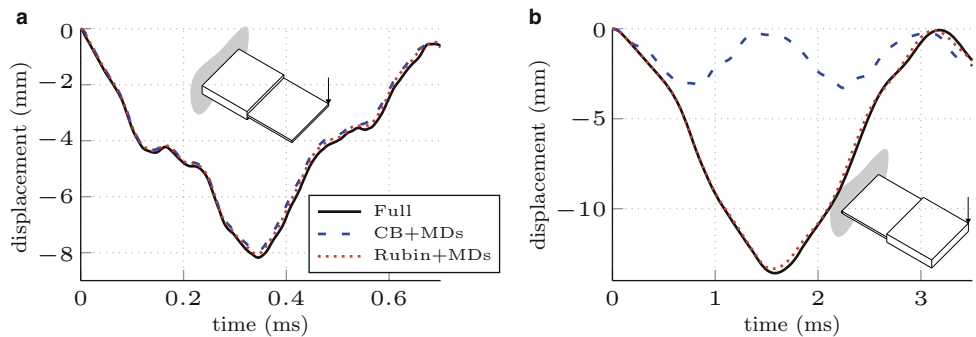


Fig. 14.3 Sketch of the tested numerical model with corresponding material properties and FE mesh. *Black dots* indicate boundary nodes, *white dots* indicate internal nodes

Fig. 14.4 Nonlinear dynamic responses to a step load on the presented models, obtained with nonlinear CB and Rubin reduced models. The plots show the response captured at the loaded tip node, in direction u_z



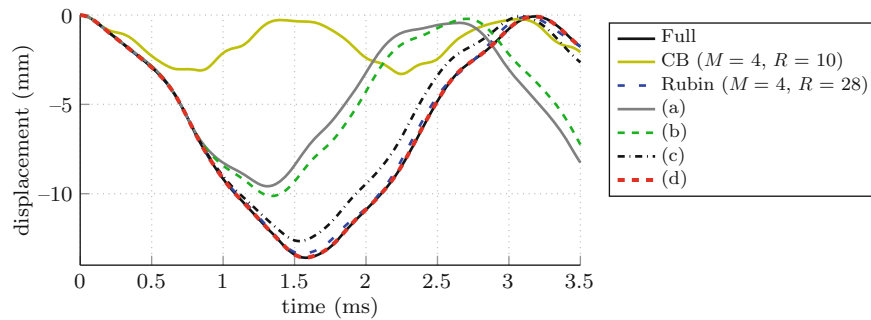


Fig. 14.5 Nonlinear dynamic responses for the thin–thick plate. The u_z component of the loaded node is shown. **(a)** CB basis augmented with rigid body derivatives only; **(b)** CB basis augmented with rigid body derivatives and 20 constraint modal derivatives; **(c)** CB basis augmented with rigid body derivatives and 100 constraint modal derivatives; **(d)** CB basis augmented with rigid body derivatives and 150 constraint modal derivatives

The second model consists of two nonlinear substructures. A thin substructure S_1 with $h_1 = 1$ mm is located near the clamped base and a thick substructure S_2 with $h_2 = 4$ mm is at the end. The second substructure S_2 hardly deforms under the specified step load with amplitude $\lambda = 50$ N, but it will still undergo large rotations which require a nonlinear description. In a linear dynamic response analysis it was found that $m_1 = m_2 = 4$ VMs per substructure were needed to accurately describe the full linear response. The Craig–Bampton reduction basis includes $r_1 = r_2 = 10$ MDs and for Rubin this is $r_1 = r_2 = 28$. The resulting vertical displacement of the loaded tip node, found with a nonlinear response analysis, is shown in Fig. 14.4b. The response approximation obtained with the nonlinear CB reduced model is unacceptably poor. The MDs computed from internal VMs do not contain any description on the nonlinear deformations of the boundaries (see Fig. 14.1). Boundary deformations are described by the static CMs in the linear CB basis. RBMs are also included, as they can be obtained as a combination of these modes. Hence, large rotations and nonlinear deformation of the boundaries are not described by the presented nonlinear CB method and therefore the method does not work in all cases. The first considered model did not feature nonlinearly behaving boundaries, nor largely rotating substructures. The augmented Rubin method reduced the model order from 546 DOFs to 160 DOFs and reduced the time needed to for a nonlinear time-integration from 140.7 to 77.4 s (speed-up factor 1.81). Unlike the previously discussed model, the computational savings on this model are purely a consequence of the CMS method, since both the substructures are considered nonlinear.

A possible remedy of the poor performance of the extended CB method is to inject the derivatives of the rigid body modes directly in the augmented reduction basis. Note that the rigid body motion of the substructure can be represented by a combination of the static interface modes. Also, MDs of the interface modes can be introduced. Preliminary results are shown in Fig. 14.5. Very slow convergence is obtained when these measures are taken.

14.6 Conclusions and Future Directions

We presented two CMS techniques for geometrically nonlinear structural analysis. Additional MDs were used to augment the linear reduction bases of CB and Rubin. It was found that the nonlinear Rubin method performs well for both the considered test cases, while the nonlinear CB method yielded accurate results only when none of the substructures undergo large rotations or nonlinear boundary deformations (Fig. 14.4a, b). The dynamic component modes in a linear Rubin reduction basis are intrinsically more flexible than those in a CB basis, as the free floating structure is used when computing the modes. Since the boundary flexibility and rigid body motion is also described by the linear modes, the corresponding MDs describe geometrically nonlinear behaviour of the boundary and the RBMs describe large rotations of the substructure.

A possible remedy of the poor performance of the extended CB method is to directly include the derivatives of the rigid body modes in the augmented reduction basis. Also, MDs of the interface modes can be introduced. Preliminary results showed a very slow convergence, that suggests a poor applicability of the extended CB method for such cases. Further work is required.

References

1. Apiwattanalungarn P, Shaw SW, Pierre C (2005) Component mode synthesis using nonlinear normal modes. *Nonlinear Dyn* 41(1–3):17–46
2. Bathe KJ, Gracewski S (1981) On nonlinear dynamic analysis using substructuring and mode superposition. *Comput Struct* 13(5–6):699–707. <http://www.sciencedirect.com/science/article/pii/0045794981900328>
3. Craig RR, Bampton MCC (1968) Coupling of substructures for dynamic analysis. *AIAA J* 6(7):1313–1319
4. Crisfield M (1991) *Non-linear finite element analysis of solids and structures*. Wiley, New York
5. de Klerk D, Rixen DJ, Voormeeren SN (2008) General framework for dynamic substructuring: history, review and classification of techniques. *AIAA J* 46(5):1169–1181
6. Idelsohn SR, Cardona A (1985) A load-dependent basis for reduced nonlinear structural dynamics. *Comput Struct* 20(1–3):203–210. doi:[http://dx.doi.org/10.1016/0045-7949\(85\)90069-0](http://dx.doi.org/10.1016/0045-7949(85)90069-0). <http://www.sciencedirect.com/science/article/pii/0045794985900690>
7. Idelsohn SR, Cardona A (1985) A reduction method for nonlinear structural dynamic analysis. *Comput Methods Appl Mech Eng* 49(3): 253–279. doi:[http://dx.doi.org/10.1016/0045-7825\(85\)90125-2](http://dx.doi.org/10.1016/0045-7825(85)90125-2). <http://www.sciencedirect.com/science/article/pii/0045782585901252>
8. Rubin S (1975) Improved Component-mode representation for structural dynamic analysis. *AIAA J* 13(8):995–1006.
9. Slaats PMA, de Jongh J, Sauren AAHJ (1995) Model reduction tools for nonlinear structural dynamics. *Comput Struct* 54(6):1155–1171. doi:[http://dx.doi.org/10.1016/0045-7949\(94\)00389-K](http://dx.doi.org/10.1016/0045-7949(94)00389-K). <http://www.sciencedirect.com/science/article/pii/004579499400389K>
10. Strachan BS, Shaw SW, Kogan O (2013) Subharmonic resonance cascades in a class of coupled resonators. *J Comput Nonlinear Dyn* 8(4):041015-1–041015-7.
11. Tiso P (2011) Optimal second order reduction basis selection for nonlinear transient analysis. In: *Modal analysis topics*, vol 3. Springer, Berlin, pp 27–39

Chapter 15

Craig-Bampton Substructuring for Geometrically Nonlinear Subcomponents

Robert J. Kuether and Matthew S. Allen

Abstract The efficiency of a modal substructuring method depends on the component modes used to reduce the subcomponent models. Methods such as Craig-Bampton (CB) and Craig-Chang have been used extensively to reduce linear finite element models with thousands or even millions of degrees-of-freedom down to a few tens or hundreds. The greatest advantage to these approaches is that they can obtain acceptable accuracy with a small number of component modes. Currently, these modal substructuring methods only apply to linear substructures. A new reduction method is proposed for geometrically nonlinear finite element models using the fixed-interface and constraint modes (collectively termed CB modes) of the linearized system. The reduced model for this system is written in terms of cubic and quadratic polynomials of the modal coordinates, and the coefficients of the polynomials are determined using a series of static loads/responses. This reduction is a nonlinear extension to the Craig-Bampton model for linear systems, and is readily applied to systems built directly in a commercial FEA package. The nonlinear, reduced modal equations for each subcomponent are then coupled by satisfying compatibility and force equilibrium. The efficiency of this new substructuring approach is demonstrated on an example problem that couples two geometrically nonlinear beams at a shared rotational degree-of-freedom. The nonlinear normal modes of the assembled models are compared with those of a truth model to validate the accuracy of the approach.

Keywords Substructuring • Reduced order modeling • Geometric nonlinearity • Component mode synthesis • Internal resonance

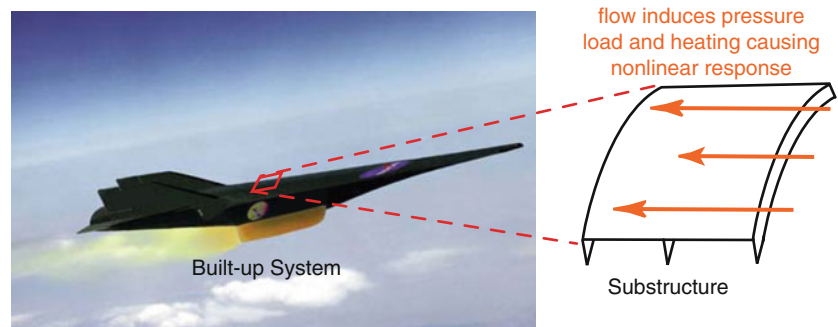
15.1 Introduction

Component mode synthesis (CMS) is used to create a structural dynamic model of an assembly of reduced order subcomponent models. These low order subcomponents are represented by a small set of component modes, significantly reducing the number of coordinates in the equations of motion. In finite element analysis (FEA), CMS is widely used as a method to assemble large scale models that are far too computationally expensive to model in their entirety, for example when the model has millions of degrees-of-freedom (DOF). One of the most popular CMS methods is the Craig-Bampton (CB) approach [1], where the linear equations of motion of a FEA model are reduced using a truncated set of fixed-interface modes, and constraint modes. This method has proven to be effective at significantly reducing the size of the subcomponent models while still producing a very accurate model of the assembly. However, the existing method has only been exploited for linear systems or for linear substructures with nonlinear connections. An extension of the CB method is proposed in this paper for finite element models with geometric nonlinearity by generating a low order set of nonlinear modal equations using the system's linearized fixed-interface and constraint modes.

Engineering structures are typically designed to operate within their linear regime so they can be more easily modeled, but some particular systems may need to operate within their nonlinear range. For instance, concept hypersonic aircraft [2, 3] experience extreme load environments due the high temperatures and pressures associated with high speed flight. The external skin panels of these aircraft are exposed to high pressure loads due to air flow and engine acoustic noise [4], causing the response to have large deformations within the elastic limits of the material. Also, the fluid-structural

R.J. Kuether (✉) • M.S. Allen
Department of Engineering Physics, University of Wisconsin-Madison, WI 53706, USA
e-mail: rkuether@wisc.edu; msallen@engr.wisc.edu

Fig. 15.1 Artists rendition of a concept hypersonic vehicle highlighting a single structural panel



interaction can produce thermal loads that can potentially cause the panels to vibrate nonlinearly about a buckled equilibrium state [5, 6]. In order to accurately predict the response of these load-bearing structures, the physical models must account for such phenomena.

Consider the schematic of the air vehicle shown in Fig. 15.1. The response of a single panel can be computed with an FEA model that accounts for geometric nonlinearity, which are typically on the order of 100,000's of DOF (or higher). However, a model of only a single panel may be insufficient to predict failure since these panels are connected to other adjacent structures (e.g. panels or structural frames) which are not infinitely stiff. A more global model must be analyzed to account for interactions between the panels, which can dramatically change the overall structure's response, but modeling the entire vehicle directly would require millions of physical DOF and when the structure exhibits nonlinearity this is far too computationally expensive for practical analysis. This paper proposes an alternative approach in which a reduced order model (ROM) of each geometrically nonlinear subcomponent is constructed and then the subcomponents are assembled to build a mathematical model of the global structure. This method is unique in that it is specifically designed for systems where the nonlinearities are geometric and hence distributed throughout all of the elements of the FEA model.

A number of methods exist to build a reduced order model of a geometrically nonlinear finite element model, as highlighted in [7, 8]. The class of techniques that are of interest here, referred to as *indirect methods*, do not require that the equations of motion be known in closed form, meaning that a ROM can be generated for a nonlinear system built directly within a commercial FEA package. Using the linear (or linearized) modes of the component, a low order set of nonlinear equations can be formulated in terms of the modal coordinates. These modal equations have a diagonal form for the linear modal mass and stiffness matrices, and are augmented with a set of nonlinear coupling terms to account for the geometric nonlinearity. These nonlinear coupling terms are assumed to be well approximated as quadratic and cubic polynomial functions of the generalized coordinates. The polynomial coefficients, which describe the nonlinear stiffness of the structure, are determined by applying a series of static load cases to the structure, computing the nonlinear static response and then using least squares to determine the coefficients that best capture the response. Because these nonlinear reduced order models (NLROMs) typically only require tens of degrees of freedom, they can be used to predict the free or forced response of the system at a dramatically lower cost compared to the direct integration of the full order model.

Most prior applications of NLROMs have been for the response prediction of a geometrically nonlinear component to various inputs (see, e.g. [4, 9, 10]). These works have all use the linearized modes of the system to define the kinematics of the nonlinear equations of motion. While these modes provide an excellent basis to capture the response of a single nonlinear component, they do not provide an optimal basis for substructuring. When this approach is used to derive a ROM for a subcomponent, the result is a substructure model in terms of free-interface modes. However, for linear systems, ROMs with the free-interface modes have long been known to provide a poor basis for a substructure when it will be rigidly attached to another subcomponent; in contrast, the Craig-Bampton method has proven to be very effective at modeling assemblies of linear subcomponents which are joined through stiff connections. This paper extends the CB method to nonlinear subcomponents by formulating a NLROM using the fixed-interface and constraint modes as generalized coordinates. Several of these NLROMs can then be assembled by satisfying the compatibility and force equilibrium conditions at the interface, as described in [11, 12]. Recently, the authors developed a substructuring approach using NLROMs generated with only free-interface modes [13] (reminiscent of the work in [14]). In the authors' previous work [13], the indirect Implicit Condensation and Expansion [15] method was used to generate the ROM equations of motion from a model built directly in a commercial FEA package. The results showed that many free-interface modes were required in each nonlinear subcomponent to obtain reasonable modal convergence of the assembly. This paper shows that better accuracy can be obtained when using the fixed-interface and constraint modes to build the NLROM.

The paper is outlined as follows. Section 15.2 introduces the theory behind Craig-Bampton nonlinear reduced order models (CB-NLROMs), and the procedure to couple two or more subcomponents. In Sect. 15.3, a case study demonstrates

the approach on the coupling of two simply supported beams with geometric nonlinearities. Each subcomponent is reduced to a low order set of equations using the fixed-interface and constraint modes. These models are then coupled, forming a low order set of equations describing the dynamics of the assembly, and the nonlinear normal modes are computed in order to observe the modal convergence of the nonlinear substructuring method. The conclusions are presented in Sect. 15.4.

15.2 Theoretical Development

Starting with the equations of motion for a conservative, N-DOF system discretized by the finite element method,

$$\mathbf{M}\ddot{\mathbf{x}} + \mathbf{K}\mathbf{x} + \mathbf{f}_{NL}(\mathbf{x}) = \mathbf{f}(t) \quad (15.1)$$

the geometric nonlinearity is defined within the $N \times 1$ nonlinear restoring force vector, $\mathbf{f}_{NL}(\mathbf{x})$, and depends on the strain model used in the large deformation analysis [16, 17]. The $N \times N$ linear mass and stiffness matrices, \mathbf{M} and \mathbf{K} , respectively, are generated using linear finite element analysis, and the external loads are defined by the $N \times 1$ vector $\mathbf{f}(t)$.

15.2.1 Craig-Bampton Nonlinear Reduced Order Model

The physical coordinates, \mathbf{x} , capture the displacements and rotations of each node defining the structural model. In order to generate the CB-NLRM of a subcomponent, each coordinate is first partitioned into a set of boundary coordinates, \mathbf{x}_b , and interior coordinates, \mathbf{x}_i . The boundary coordinates are the DOF that are either shared with an adjacent structure, or have an externally applied load to that location. The interior DOF are the other remaining coordinates that do not experience any loads. The nonlinear equations of motion in Eq. (15.1) are rearranged as

$$\begin{bmatrix} \mathbf{M}_{ii} & \mathbf{M}_{ib} \\ \mathbf{M}_{bi} & \mathbf{M}_{bb} \end{bmatrix} \begin{Bmatrix} \ddot{\mathbf{x}}_i \\ \ddot{\mathbf{x}}_b \end{Bmatrix} + \begin{bmatrix} \mathbf{K}_{ii} & \mathbf{K}_{ib} \\ \mathbf{K}_{bi} & \mathbf{K}_{bb} \end{bmatrix} \begin{Bmatrix} \mathbf{x}_i \\ \mathbf{x}_b \end{Bmatrix} + \begin{Bmatrix} \mathbf{f}_{NL,i}(\mathbf{x}) \\ \mathbf{f}_{NL,b}(\mathbf{x}) \end{Bmatrix} = \begin{Bmatrix} \mathbf{0} \\ \mathbf{f}(t) \end{Bmatrix} \quad (15.2)$$

The Craig-Bampton transformation matrix uses two sets of component modes to reduce this partitioned system of equations; namely, the fixed-interface modes and constraint modes [11]. The transformation with these basis vectors is given as,

$$\mathbf{x} = \begin{Bmatrix} \mathbf{x}_i \\ \mathbf{x}_b \end{Bmatrix} = \begin{bmatrix} \Phi_{ik} & \hat{\Psi}_{ib} \\ \mathbf{0} & \mathbf{I}_{bb} \end{bmatrix} \begin{Bmatrix} \mathbf{q}_k \\ \mathbf{x}_b \end{Bmatrix} = \mathbf{T}_{CB} \mathbf{q} \quad (15.3)$$

where Φ_{ik} is the $N_i \times N_k$ matrix of mass normalized, fixed-interface modes, $\hat{\Psi}_{ib}$ is the $N_i \times N_b$ matrix of constraint modes, and \mathbf{I} is the identity matrix. The total number of generalized coordinates in the vector \mathbf{q} is denoted as $m = N_k + N_b$, or the number of fixed-interface modes that have been retained plus the number of boundary coordinates.

The fixed-interface modes are calculated from the linear mass and stiffness matrices for the interior DOF as

$$\left[\mathbf{K}_{ii} - \omega_j^2 \mathbf{M}_{ii} \right] \phi_j = \mathbf{0} \quad j = 1, 2, \dots, N_k \quad (15.4)$$

and typically only a small number, N_k , of modes must be computed to obtain an adequate model. These fixed-interface modes have zero displacement/rotation at the boundary DOF, and must be augmented with a set of constraint modes to account for deformation at the boundary. The constraint modes are the static deflections that result due to a unit displacement at each boundary coordinate, and are computed from the linear stiffness matrix of the system as

$$\hat{\Psi} = \begin{bmatrix} \hat{\Psi}_{ib} \\ \mathbf{I}_{bb} \end{bmatrix} = \begin{bmatrix} -\mathbf{K}_{ii}^{-1} \mathbf{K}_{ib} \\ \mathbf{I}_{bb} \end{bmatrix} \quad (15.5)$$

There exist N_b constraint modes, one for each boundary DOF of the subcomponent. The full order model in Eq. (15.2) is reduced by substituting the CB transformation matrix in Eq. (15.3), then premultiplying the resulting equation by \mathbf{T}_{CB}^T . Then,

the CB-NLROM of a single subcomponent is defined by the low order set of equations,

$$\widehat{\mathbf{M}}_{CB}\ddot{\mathbf{q}} + \widehat{\mathbf{K}}_{CB}\mathbf{q} + \mathbf{T}_{CB}^T \begin{Bmatrix} \mathbf{f}_{NL,i}(\mathbf{q}) \\ \mathbf{f}_{NL,b}(\mathbf{q}) \end{Bmatrix} = \mathbf{T}_{CB}^T \begin{Bmatrix} \mathbf{0} \\ \mathbf{f}(t) \end{Bmatrix} \quad (15.6)$$

The linear portion is exactly the CB model for a linear subsystem [1, 11]. When the physical model contains geometric nonlinearity, however, additional nonlinear stiffness terms are introduced by $\mathbf{f}_{NL}(\mathbf{q})$. A functional form of the nonlinearity is not readily extracted from models defined directly in commercial FEA packages, so it is difficult to determine this function analytically. Instead, the functional form of the nonlinearity is approximated as

$$\mathbf{T}_{CB}^T \begin{Bmatrix} \mathbf{f}_{NL,i}(\mathbf{q}) \\ \mathbf{f}_{NL,b}(\mathbf{q}) \end{Bmatrix} = \boldsymbol{\theta}(\mathbf{q}) \quad (15.7)$$

Prior works assume a polynomial function to model the geometric nonlinearity in terms of the free-interface modal coordinates [7, 8], and the same approach is used again here with the CB-NLROM. Hence, the nonlinear function $\boldsymbol{\theta}(\mathbf{q})$ in Eq. (15.7) is approximated as follows for the r^{th} mode

$$\theta_r(\mathbf{q}) = \sum_{i=1}^m \sum_{j=i}^m B_r(i, j) q_i q_j + \sum_{i=1}^m \sum_{j=i}^m \sum_{k=j}^m A_r(i, j, k) q_i q_j q_k \quad (15.8)$$

The nonlinear stiffness coefficients A_r and B_r are then determined using a series of static forces applied to the full order, geometrically nonlinear structure. This is the approach used by the Implicit Condensation and Expansion method in [15] to fit the nonlinear portion of the equations. A static load is applied to the system in Eq. (15.1), in which the load is in a series of shapes proportional to a combination of the fixed-interface and constraint modes. The multi-modal force is a permutation of the sums and differences of either one, two or three CB modes in the basis set, and is defined as

$$\mathbf{F}_c = \mathbf{M} \{ \mathbf{T}_{CB,1} f_1 + \mathbf{T}_{CB,2} f_2 + \cdots + \mathbf{T}_{CB,m} f_m \} \quad (15.9)$$

The $N \times 1$ load vector \mathbf{F}_c is a combination of shapes that each have a load scale factor, f_r , for the r^{th} basis vector. The selection of each load factor dictates the level of nonlinearity in each of the characteristic shapes. Typically, each f_r is selected such that the force of a single shape applied to the linear model results in a maximum displacement on the order of the thickness of the structure for low frequency modes, but higher order modes typically require lower displacements [4]. The resulting coefficients tend to be sensitive to the selection of the scaling factor, so in practice a trial and error approach determines which load factors work the best.

Each static load is then applied to the full order model, then the resulting deformation is extracted and the amplitude of each generalized coordinate is computed using the pseudo-inverse of the CB transformation matrix. Using the resulting applied modal forces and displacements, the nonlinear terms A_r and B_r are fit to the reduced static equation,

$$\widehat{\mathbf{K}}_{CB}\mathbf{q} + \boldsymbol{\theta}(\mathbf{q}) = \mathbf{T}_{CB}^T \mathbf{F}_c \quad (15.10)$$

The fitting procedure is thoroughly discussed in [4]. After determining the nonlinear static coefficients, the CB-NLROM equations are cast into a matrix form prior to coupling, as done in [18]. First, the quadratic and cubic terms in Eq. (15.8) are separated into two nonlinear restoring force vectors, $\boldsymbol{\beta}$ and $\boldsymbol{\alpha}$, respectively, as

$$\boldsymbol{\beta} = [\beta_1 \ \beta_2 \ \dots \ \beta_m]^T \quad \text{where} \quad \beta_r = \sum_{i=1}^m \sum_{j=i}^m B_r(i, j) q_i q_j \quad (15.11)$$

$$\boldsymbol{\alpha} = [\alpha_1 \ \alpha_2 \ \dots \ \alpha_m]^T \quad \text{where} \quad \alpha_r = \sum_{i=1}^m \sum_{j=i}^m \sum_{k=j}^m A_r(i, j, k) q_i q_j q_k \quad (15.12)$$

These vectors are then differentiated with respect to each generalized coordinate in order to produce the quadratic and cubic stiffness matrices as,

$$\mathbf{N}_1(q) = \frac{\partial \boldsymbol{\beta}}{\partial \mathbf{q}} = \begin{bmatrix} \frac{\partial \boldsymbol{\beta}}{\partial q_1} & \frac{\partial \boldsymbol{\beta}}{\partial q_2} & \cdots & \frac{\partial \boldsymbol{\beta}}{\partial q_m} \end{bmatrix} \quad (15.13)$$

$$\mathbf{N}_2(q) = \frac{\partial \boldsymbol{\alpha}}{\partial \mathbf{q}} = \begin{bmatrix} \frac{\partial \boldsymbol{\alpha}}{\partial q_1} & \frac{\partial \boldsymbol{\alpha}}{\partial q_2} & \cdots & \frac{\partial \boldsymbol{\alpha}}{\partial q_m} \end{bmatrix} \quad (15.14)$$

The CB-NLROM in Eq. (15.6) is then rewritten in matrix form with the nonlinear stiffness matrices in Eqs. (15.13) and (15.14) as,

$$\widehat{\mathbf{M}}_{CB} \ddot{\mathbf{q}} + \widehat{\mathbf{K}}_{CB} \mathbf{q} + \frac{1}{2} \mathbf{N}_1(\mathbf{q}) \mathbf{q} + \frac{1}{3} \mathbf{N}_2(\mathbf{q}) \mathbf{q} = \mathbf{T}_{CB}^T \begin{Bmatrix} \mathbf{0} \\ \mathbf{f}(t) \end{Bmatrix} \quad (15.15)$$

A low order CB-NLROM is generated for each subcomponent, and is assembled to adjacent structures using the same approach in [11] for the coupling of linear CB models. The coupling procedure is reviewed for completeness in the following section.

15.2.2 Coupling with Craig-Bampton Method

Once the CB-NLROMs are generated and in matrix form, the equations are coupled by satisfying both compatibility and force equilibrium at the interface DOF. Consider the assembly of two subcomponents, A and B, whose unconstrained equations of motion are written as

$$\begin{aligned} & \begin{bmatrix} \widehat{\mathbf{M}}_{CB}^A & \mathbf{0} \\ \mathbf{0} & \widehat{\mathbf{M}}_{CB}^B \end{bmatrix} \begin{Bmatrix} \ddot{\mathbf{q}}^A \\ \ddot{\mathbf{q}}^B \end{Bmatrix} + \begin{bmatrix} \widehat{\mathbf{K}}_{CB}^A & \mathbf{0} \\ \mathbf{0} & \widehat{\mathbf{K}}_{CB}^B \end{bmatrix} \begin{Bmatrix} \mathbf{q}^A \\ \mathbf{q}^B \end{Bmatrix} + \frac{1}{2} \begin{bmatrix} \mathbf{N}_1^A(\mathbf{q}^A) & \mathbf{0} \\ \mathbf{0} & \mathbf{N}_1^B(\mathbf{q}^B) \end{bmatrix} \begin{Bmatrix} \mathbf{q}^A \\ \mathbf{q}^B \end{Bmatrix} \\ & + \frac{1}{3} \begin{bmatrix} \mathbf{N}_2^A(\mathbf{q}^A) & \mathbf{0} \\ \mathbf{0} & \mathbf{N}_2^B(\mathbf{q}^B) \end{bmatrix} \begin{Bmatrix} \mathbf{q}^A \\ \mathbf{q}^B \end{Bmatrix} = \begin{Bmatrix} \mathbf{T}_{CB}^A{}^T \\ \mathbf{T}_{CB}^B{}^T \end{Bmatrix} \begin{Bmatrix} \mathbf{0} \\ \mathbf{f}^A(t) + \mathbf{r}^A(t) \\ \mathbf{0} \\ \mathbf{f}^B(t) + \mathbf{r}^B(t) \end{Bmatrix} \end{aligned} \quad (15.16)$$

where $\mathbf{r}(t)$ is the (unknown) reaction force vector applied at each connecting DOF. Compatibility requires that the displacements of the two subcomponents must be equal at the interface, and this leads to a set of constraint equations that can be written as,

$$\mathbf{B} \begin{Bmatrix} \mathbf{x}^A \\ \mathbf{x}^B \end{Bmatrix} = \mathbf{B}_m \begin{Bmatrix} \mathbf{q}_k^A \\ \mathbf{x}_b^A \\ \mathbf{q}_k^B \\ \mathbf{x}_b^B \end{Bmatrix} = \mathbf{0} \quad (15.17)$$

Equations (15.16) and (15.17) are algebraic-differential equations that represent the assembly of two geometrically nonlinear subcomponents. These equations are difficult to solve both analytically and numerically, since any solution to Eq. (15.16) is constrained by Eq. (15.17). With the CB models, there is a redundant set of coordinates when two subcomponents are coupled by Eq. (15.16), since $\mathbf{x}_b^A = \mathbf{x}_b^B$. In order to remove this redundancy from the constrained coordinates, a new set of unconstrained coordinates, \mathbf{q}_u , are defined in order to eliminate the need to simultaneously satisfy Eq. (15.17). The coordinate transformation is defined as,

$$\begin{Bmatrix} \mathbf{q}_k^A \\ \mathbf{x}_b^A \\ \mathbf{q}_k^B \\ \mathbf{x}_b^B \end{Bmatrix} = \begin{bmatrix} \mathbf{I} & \mathbf{0} & \mathbf{0} \\ \mathbf{0} & \mathbf{0} & \mathbf{I} \\ \mathbf{0} & \mathbf{I} & \mathbf{0} \\ \mathbf{0} & \mathbf{0} & \mathbf{I} \end{bmatrix} \begin{Bmatrix} \mathbf{q}_k^A \\ \mathbf{q}_k^B \\ \mathbf{x}_b \end{Bmatrix} = \mathbf{L} \mathbf{q}_u \quad (15.18)$$

It can be shown that the connectivity matrix, \mathbf{L} , lies in the nullspace of the compatibility matrix \mathbf{B}_m in Eq. (15.17). Therefore, the unconstrained coordinates in Eq. (15.18) always satisfy the compatibility condition in Eq. (15.17). This transformation is substituted into Eq. (15.16), and the resulting equation is premultiplied by \mathbf{L}^T . The constrained equation of motion of the assembly becomes

$$\begin{aligned} \mathbf{L}^T \begin{bmatrix} \widehat{\mathbf{M}}_{CB}^A & \mathbf{0} \\ \mathbf{0} & \widehat{\mathbf{M}}_{CB}^B \end{bmatrix} \mathbf{L} \ddot{\mathbf{q}}_u + \mathbf{L}^T \begin{bmatrix} \widehat{\mathbf{K}}_{CB}^A & \mathbf{0} \\ \mathbf{0} & \widehat{\mathbf{K}}_{CB}^B \end{bmatrix} \mathbf{L} \mathbf{q}_u + \frac{1}{2} \mathbf{L}^T \begin{bmatrix} \mathbf{N}_1^A(\mathbf{q}^A) & \mathbf{0} \\ \mathbf{0} & \mathbf{N}_1^B(\mathbf{q}^B) \end{bmatrix} \mathbf{L} \mathbf{q}_u \\ + \frac{1}{3} \mathbf{L}^T \begin{bmatrix} \mathbf{N}_2^A(\mathbf{q}^A) & \mathbf{0} \\ \mathbf{0} & \mathbf{N}_2^B(\mathbf{q}^B) \end{bmatrix} \mathbf{L} \mathbf{q}_u = \mathbf{L}^T \begin{Bmatrix} \mathbf{T}_{CB}^A{}^T \begin{Bmatrix} \mathbf{0} \\ \mathbf{f}^A(t) \end{Bmatrix} \\ \mathbf{T}_{CB}^B{}^T \begin{Bmatrix} \mathbf{0} \\ \mathbf{f}^B(t) \end{Bmatrix} \end{Bmatrix} \end{aligned} \quad (15.19)$$

The differential equations in Eq. (15.19) completely describe the dynamics of the assembly of subcomponents A and B in terms of the subcomponent CB-NLROMs and the connectivity matrix \mathbf{L} . These equations can be integrated to predict the free or forced response of the assembled system of geometrically nonlinear subcomponents. Notice the reaction forces in Eq. (15.19) are no longer required as they vanish after premultiplying by \mathbf{L}^T , as explained in [12, 19]. The modal convergence of the CB-NLROM method will be evaluated in the next section, and compared to the free-interface NLROM substructuring approach developed in [13].

15.3 Numerical Results

The CB-NLROM nonlinear substructuring approach was explored by coupling two beam models with geometric nonlinearities, using the example presented in [13]. A schematic of this problem is shown in Fig. 15.2, where the two subcomponent beams were coupled at the appropriate rotational DOF. Each substructure was modeled in Abaqus[®] using B31 beam elements; the 9-in. beam had a total of 119 DOF, and the 6-in. beam had 89 DOF. The full model of assembly (C) was also constructed in Abaqus[®] in order to validate the results of the nonlinear substructuring approaches. The subcomponents have the material properties of structural steel with a Young's modulus of 29,700 ksi, shear modulus of 11,600 ksi, and a mass density of 7.36×10^{-4} lb-s²/in.⁴. Both beams had a cross sectional dimension of 0.031 in. thick by 0.5 in. wide.

The interface between each subcomponent had only one DOF, therefore each subcomponent required only a single constraint mode, and a truncated set of fixed-interface modes for the CB-NLROM. In the following, the modal convergence of this approach is compared to the method in [13], where the free-interface modes were used to model each subcomponent. The approach in [13] is termed the NLROM substructuring approach.

15.3.1 Linear Substructuring Results

First, the linear portion of the 9-in. and 6-in. beam models was used to predict the linear modes of assembly (C) using the free-interface modes approach, and the Craig-Bampton approach, in order to compare their modal convergence for the linear case. To interpret the results, one typically considers the bandwidth of the modes included in each subcomponent model. To facilitate this, the linear natural frequencies for the first eight modes (all bending) of each subcomponent are given in

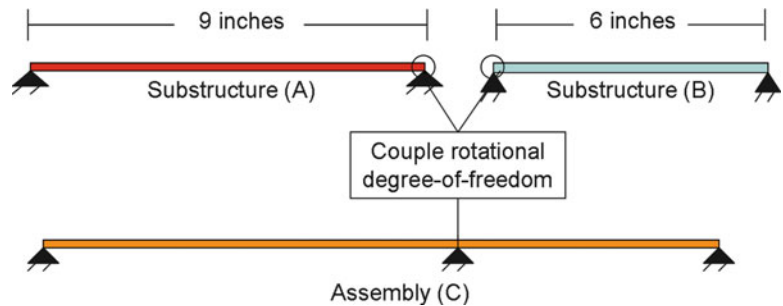


Fig. 15.2 Schematic of coupling of two geometrically nonlinear beams with simply supported boundary conditions

Table 15.1 Exact linear natural frequencies of finite element models in Fig. 15.2

| Mode number | Simply support beam A: 9 in. | | Simply support beam B: 6 in. | | Assembly (C) |
|-------------|------------------------------|----------------------|------------------------------|----------------------|---------------------|
| | Free-interface (Hz) | Fixed-interface (Hz) | Free-interface (Hz) | Fixed-interface (Hz) | Free-interface (Hz) |
| 1 | 34.85 | 54.44 | 78.41 | 122.5 | 42.50 |
| 2 | 139.4 | 176.5 | 313.8 | 397.3 | 97.73 |
| 3 | 313.8 | 368.4 | 706.4 | 829.5 | 162.7 |
| 4 | 558.2 | 630.4 | 1,257 | 1,420 | 313.8 |
| 5 | 872.7 | 962.8 | 1,966 | 2,170 | 382.1 |
| 6 | 1,258 | 1,366 | 2,835 | 3,080 | 588.0 |
| 7 | 1,714 | 1,840 | 3,866 | 4,153 | 762.5 |
| 8 | 2,241 | 2,385 | 5,059 | 5,389 | 930.0 |

Table 15.2 Percent error of predicted linear frequencies of assembly (C) using modes up to 1,000 Hz

| Assembly (C) mode number | % Error of linear substructuring | |
|--------------------------|----------------------------------|----------------------|
| | Free-interface modes | CB modes |
| 1 | 3.2 | 5.5×10^{-4} |
| 2 | 5.5 | 1.6×10^{-4} |
| 3 | 9.3 | 1.9×10^{-3} |
| 4 ^a | 2.8×10^{-6} | 2.5×10^{-2} |
| 5 | 15 | 3.4×10^{-3} |

^aInterestingly, because the lengths of the two beams have a ratio 1.5:1, the 4th mode of the assembly is perfectly described by combining one free-interface mode of each, so its natural frequency is estimated very precisely using this basis

Table 15.1, along with the exact natural frequencies of the full finite element model of assembly (C) in Fig. 15.2. The first five modes of the assembly are taken to be the modes of interest covering a frequency range from 0 to 500 Hz.

A rule of thumb for substructuring with linear subcomponents is to include modes up to 1.5–2.0 times the maximum frequency of interest. To be conservative with the target range of 500 Hz, each subcomponent includes modes (either free-interface or fixed-interface) with frequencies up to 1,000 Hz. Then that set of modes was used to predict the modes of the assembly and the errors in each of the predicted natural frequencies are given in Table 15.2. (The exact frequencies of the FEA assembly are given in the last column of Table 15.1.) It happens that this frequency range includes the same number of modes, 5 for A and 3 for B, whether fixed-interface or free-interface modes were used.

Using the free-interface substructuring approach, the maximum frequency error of 15 % occurs with the 5th assembly mode. As expected, this modal basis is not well suited for substructuring since the kinematics of the subcomponent do not account for deformation at the interface [11], and one would need far more free-interface modes before the basis could begin to properly describe this motion. In fact, in order to get the frequency error of the free-interface approach below 1 % for the first 5 modes of the assembly, each beam needed a total of 72 modes. The CB approach achieves the same performance with each beam having three fixed-interface modes, and one constraint mode. The CB approach clearly produces a more efficient substructure model because of the kinematics supplied by the constraint modes.

15.3.2 Validate Nonlinear Reduced Order Models

Next, the NLROMs and CB-NLROMs were generated for each geometrically nonlinear beam in Fig. 15.2. In the linear case, the CB method needed five and three modes, respectively, for the 9-in. beam and 6-in. beam in order to predict the assembly modes out to 500 Hz. However, due to the geometric nonlinearity in the models, higher frequency modes can be coupled to lower frequency modes, meaning that more modes are needed in each subcomponent to represent the higher frequency modes of the assembly. Because of this, each subcomponent used a total of 10 modes in the basis.

The NLROMs of each beam included the first 10 linear free-interface modes (all bending) using the ICE approach in [15]. The load scale factors in Eq. (15.9) were determined such that the amplitude of each force deformed the *linear* structure to a maximum displacement of 0.25 times the beam thickness (or 7.75×10^{-3} in.). The CB-NLROMs were generated in a similar manner, but instead included the first 10 fixed-interface modes and 1 constraint mode. The load scale factors were chosen such that each force, when applied to the linear structure with no constraints at the interface, produced a maximum displacement of 1.0 times the beam thickness (or 0.031 in.). Both the CB-NLROM and NLROMs were fit using the constrained approach

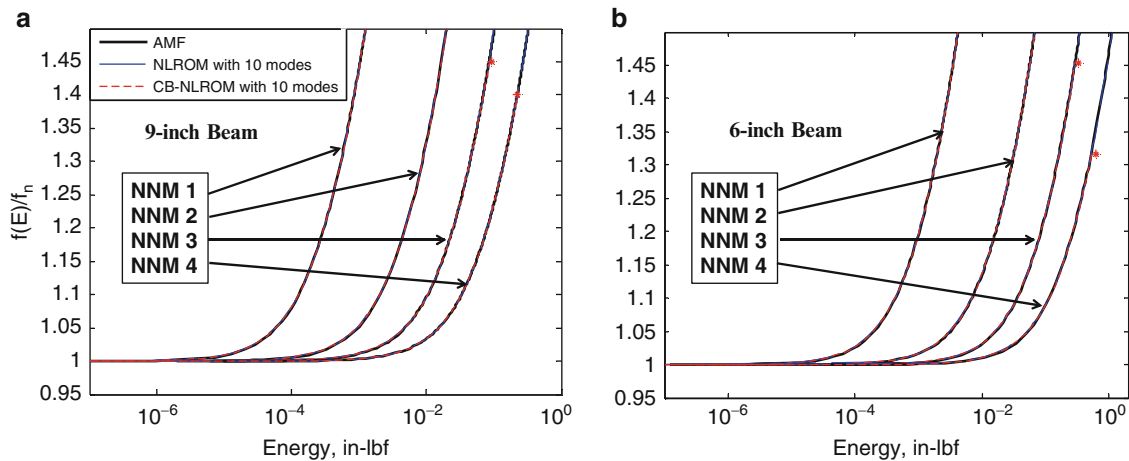


Fig. 15.3 Comparison of the first four NNMs of the (a) 9-in. beam and (b) 6-in. beam using (black) the AMF method on the full FEA model, (blue dashed) a NLROM with 10 free-interface modes, and (red short dashed) a CB-NLROM with 10 fixed-interface modes and 1 constraint mode (color figure appear online)

described in [4], in order to preserve the symmetry of the nonlinear stiffness matrices. Both ROMs included the quadratic and cubic polynomials to approximate the nonlinearity, and used static loads that were generated using the reduction factor method (e.g. combinations of forces in the shape of 2 or 3 modes reduced the load factor of each force by a factor of 2 or 3, respectively).

Each subcomponent ROM was validated by computing the first four nonlinear normal modes (NNMs) of the each beam using the pseudo-arclength continuation algorithm in [20]. As discussed in [21], it was suggested that if the NNMs of a ROM converge to the NNMs of the full model, then the ROM will accurately predict the free and forced response of the system. Also, this computation delivered insight into the load scale factors to use when generating the reduced order models. The undamped NNM used in this work is defined as a not-necessarily synchronous periodic response to the conservative, nonlinear equations of motion. A review of NNM theory can be found in [22, 23]. As a reference solution, each NNM of the full order model of the 9-in. and 6-in. beams was computed using the Applied Modal Force (AMF) algorithm described in [24]. The NNMs are plotted in Fig. 15.3a, b for the 9-in. and 6-in. beams, respectively, on the frequency versus energy plane. To facilitate this comparison, each NNM frequency was divided by its linearized modal frequency, such that at low energy the branch converges to a frequency value of 1 (or the linear frequency). The energy along the horizontal axis is the total conserved energy of the periodic response.

These results show that the NLROM with 10 modes very accurately captured the frequency-energy dependence of the fundamental NNMs of each subcomponent, up to at least a 50 % shift in each natural frequency. It is noted that all the NNMs computed with AMF algorithm only required iteration on a single linear (free-interface) bending mode to set the initial condition. This means that no other mode shapes had a significant dynamic contribution to the NNM motion within the range of energy considered for each mode. Since the NLROMs explicitly included modes 1–4 in the basis set, they were also able to accurately compute the frequency-energy dependence of the NNMs.

The CB-NLROMs accurately predicted NNMs 1 and 2 out to a 50 % frequency shift for both nonlinear beams, but both models appear to diverge with the third and fourth NNMs. At the solutions marked with an asterisk (*) in Fig. 15.3, the continuation algorithm began to reduce the step size, and continue along an internal resonance. For example, the third NNM of the 9-in. beam with a CB-NLROM captured a 1:3 internal resonance with the 6th mode of the beam. No internal resonance was computed with the full order model using AMF, suggesting that this was an error introduced by the reduction. However, this was not of primary concern since it was designed to perform well for substructuring, and not representing the free-interface modes of a single component. The CB-NLROMs predict the NNMs of the subcomponents reasonably well, suggesting that the load scale factors were appropriately chosen and the ROM does not have any degenerate behavior.

15.3.3 Nonlinear Substructuring Results

The nonlinear substructuring methods are now demonstrated on the coupling example in Fig. 15.2. Once the ROMs were assembled using Eq. (15.19), the NNMs were computed using the pseudo-arclength continuation algorithm [20]. In Figs. 15.4

Fig. 15.4 First and second NNMs of the beam assembly using (black) AMF on the full FEA model of the assembly, (blue dashed) two NLROMs with 10 free-interface modes, and (red short dashed) two CB-NLROMs with 10 fixed-interface modes and 1 constraint mode. Time histories and deflection shapes of solutions (a–d) are plotted in Fig. 15.6 (color figure appear online)

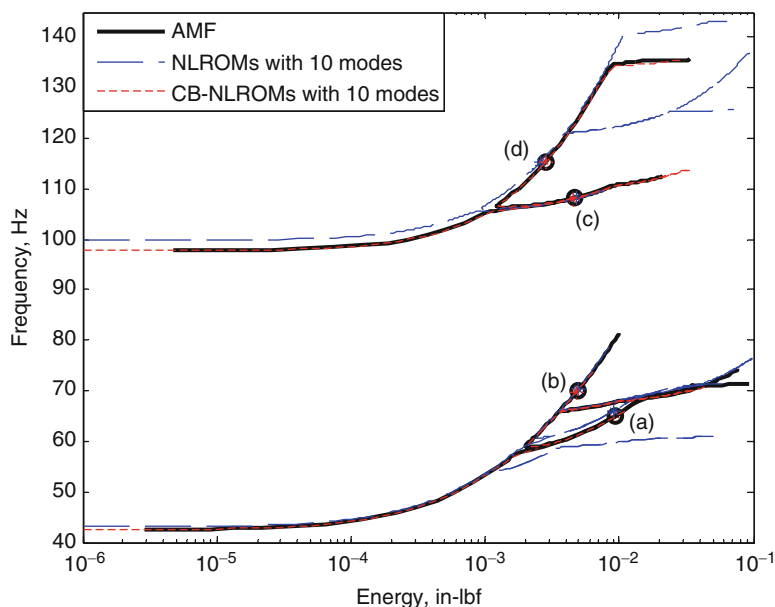
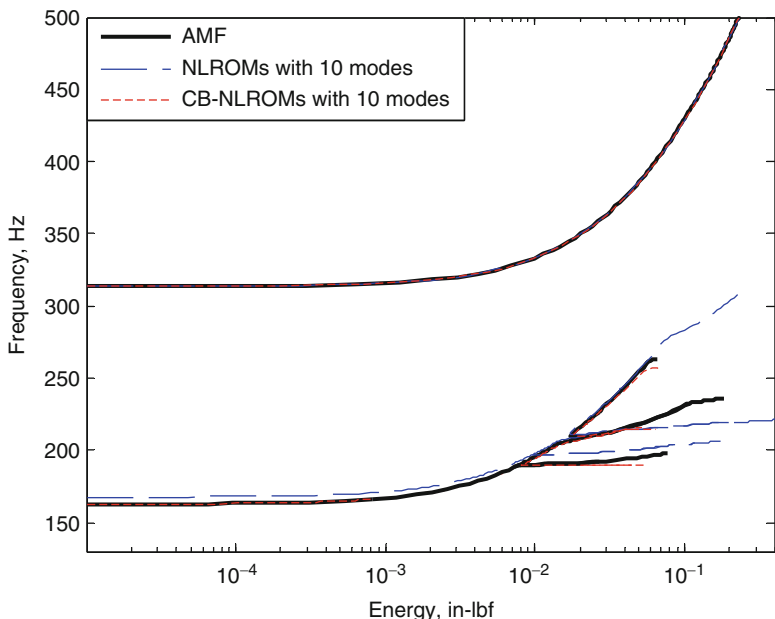


Fig. 15.5 Third and fourth NNMs of the beam assembly using (black) AMF on the full FEA model of the assembly, (blue dashed) two NLROMs with 10 free-interface modes, and (red short dashed) two CB-NLROMs with 10 fixed-interface modes and 1 constraint mode (color figure appear online)



and 15.5, the first four NNMs of the CB-NLROM and NLROM substructuring approaches are plotted, and compared with those computed by the AMF algorithm on the full order model of the assembly.

Each NNM branch initiates at a linear mode at low energy, and continues out to higher response amplitudes as energy increases. At higher energy levels, the geometric nonlinearity was exercised as indicated by the increase in the fundamental frequency. This hardening was caused by the coupling between bending and membrane deformations of the flat structure. As the frequency increased in the NNMs in Figs. 15.4 and 15.5, two features were observed in the frequency-energy curves: the backbone and the internal resonances. The backbone traces the solution at the lowest possible energy for a given frequency, and the internal resonances are the tongues that emanate from the backbone. Each internal resonance represents a modal interaction between two or more modes of the structure, with an integer ratio of oscillating frequencies.

The low energy solutions for NNMs 1 and 2 in Fig. 15.4 show nearly exact agreement between the CB-NLROM approach and the reference solution from AMF, but the NLROM substructuring has some frequency error in this linear range. This error was exactly as predicted by the linear substructuring approach, since the NNMs converge to the linear modes at low energy. As energy increased into the nonlinear region, both the CB-NLROM and NLROM approaches appeared to accurately follow the backbone of the first two NNMs. It should be noted that along the backbone, the NLROM result was always stiffer

than the CB-NLROM results, likely due to the fact that more modes would be needed to allow the structure to deform into the correct deflection shape of the coupled system.

The CB-NLROM approach accurately captured the frequencies and energies of the internal resonances observed along NNMs 1 and 2. However, NLROM substructuring predicted only two of these tongues, and introduced new internal resonances. For example, the first tongue along NNM 1 was a 1:3 interaction with NNM 3. The CB-NLROM approach matched the frequencies and energies of this tongue with the AMF results, which initiated around 57 Hz. However, the internal resonance predicted with the NLROM was shifted to a slightly higher frequency, and initiated around 59 Hz. In Fig. 15.5 one can see that NNM 3 as predicted by the NLROM approach has a frequency error of about 5 Hz at low energy. Since the location of the 1:3 internal resonance with NNM 3 depends on the accuracy of both NNM 1 and NNM 3, the NLROM predicts the wrong frequency for the internal resonance between these modes. The differences in the features in NNMs 3 and 4, shown in Fig. 15.5, can be explained in a similar manner. As noted previously, because the beam lengths had a 1.5:1 ratio, the fourth linear mode could be estimated perfectly using two linear modes. Here one also observes that the 4th NNM is also estimated very precisely using the NLROM method. The Craig-Bampton approach also predicts this mode very well, and it does not happen to exhibit internal resonance with any other modes.

The solutions at the points marked (a-d) on NNMs 1 and 2 in Fig. 15.4 are shown in Fig. 15.6. The plots in the left column show the maximum deformation (e.g. when all DOF have zero velocity) shape during the periodic response. The time histories in the right column track the transverse displacement of the beam at a location of 4.5 in. from the left end of assembly (C). The deformation shapes computed with the CB-NLROM approach appear to be in very good agreement with the NNMs computed with AMF, except for the solution on the first internal resonance of NNM 1 (Fig. 15.6a). The deformation shapes computed with the NLROM approach also agree quite well, capturing the shape of the structure with less than 10 % error at each point along the two beams. It is interesting to note that these seemingly small errors in capturing the deformation of the structure led to extra internal resonances and completely erroneous branches of NNMs in Figs. 15.4 and 15.5. The time histories of the periodic responses are also in good agreement between all three methods and once again the CB-NLROM method was noticeably more accurate. Of course, one could have selected regions in the frequency energy plane where the curves would hardly even seem reminiscent. For example, near the spurious 120 Hz internal resonance on the NLROM prediction of NNM 2.

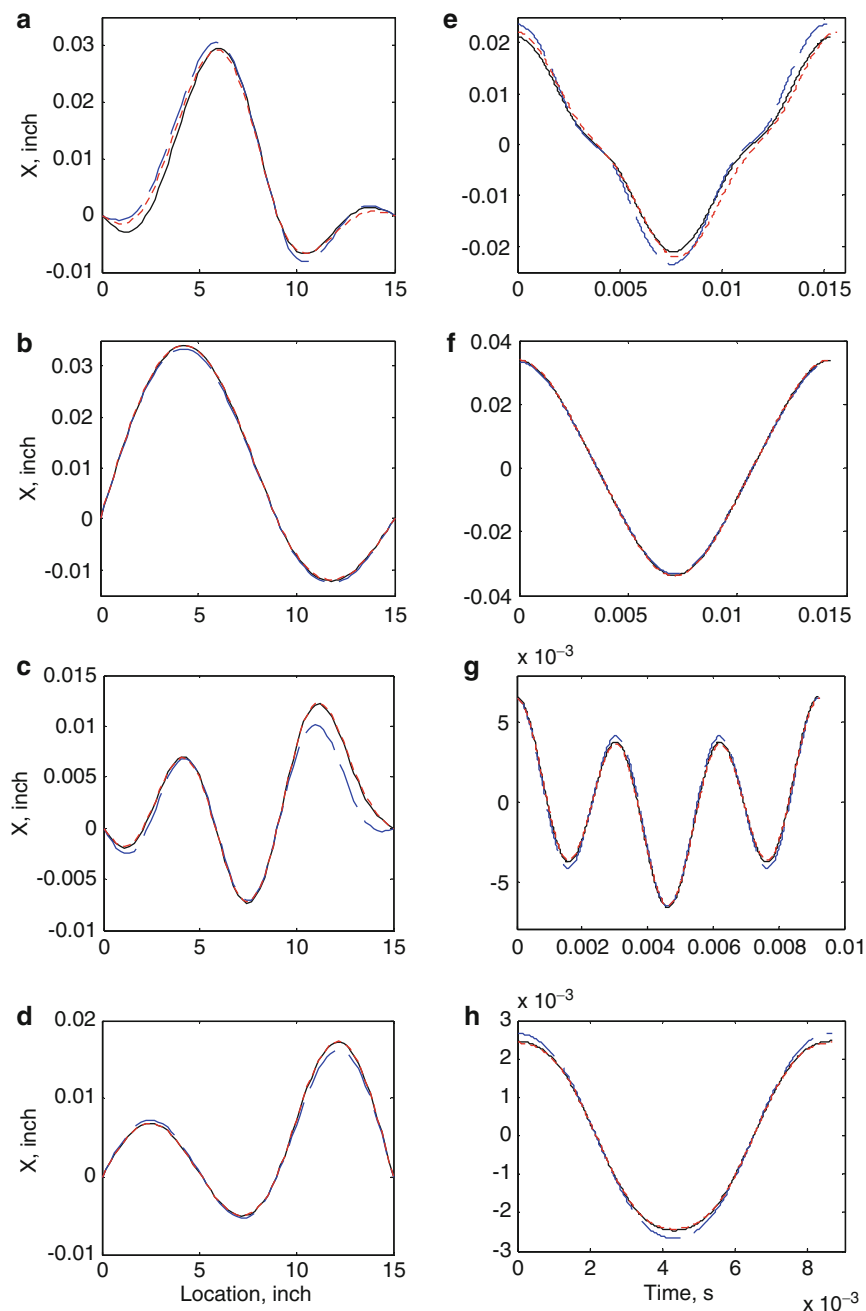
These results show that the CB-NLROM method is capable of producing highly accurate predictions of the NNMs of this assembly, including the internal resonances, so long as enough modes are used to model each subcomponent. Here the CB-NLROM for each subcomponent had a total of 11 basis vectors so after enforcing one constraint the assembly had 21 degrees of freedom. In contrast, the full FEA model, which was used to compute the AMF results, had 207 DOF. On the other hand, the linear substructuring results in Table 15.2 showed that with only five and three modes, respectively, of subcomponents A and B, the CB method could predict the first five linear natural frequencies with errors of much less than 1 %. The CB-NLROM approach was also used with a smaller number of fixed-interface modes, but in those cases the models seemed to predict spurious internal resonances which made it challenging to compute a large portion of the backbone curve with the continuation algorithm. Hence, those results were not presented here, but this issue will be explored further in subsequent works. On the other hand, perhaps this is to be expected, as nonlinearity couples higher frequency motions to lower ones, so perhaps a reduced order model must be accurate for a much larger frequency band to accurately obtain the first several NNMs.

15.4 Conclusion

This paper presented a nonlinear modal substructuring approach for geometrically nonlinear finite element models using the Craig-Bampton approach to derive a reduction basis. The fixed-interface modes and constraint modes were generated from the linearized equations of motion and used to estimate a low order set of modal equations to describe the system. The nonlinearity in the modal equations was modeled using quadratic and cubic polynomials and a series of static forces was applied to the full order model to determine the nonlinear stiffness coefficients. The methodology is readily implemented in a commercial finite element package. Once the CB-NLROMs were identified for each subcomponent, the low order equations were coupled at the interface to obtain a mathematical model of the assembly.

The NNMs of the assembled structure showed that CB-NLROM substructuring offered better accuracy than substructuring using free-interface modes, even capturing the true internal resonances of the assembly using only 10 modes of each subcomponent. On the other hand, in the linear case only five and three modes, respectively, of components A and B were needed to capture the first five modes of the assembly with high accuracy. It is, perhaps, not surprising that quite a few additional modes were needed to accurately model the nonlinear assembly, as nonlinearity can couple low frequency

Fig. 15.6 Plots (a–d) are the maximum deformation of the beam assembly corresponding to solutions (a–d) in Fig. 15.4, respectively, where (black) is AMF, (blue dashed) NLROM substructuring, and (red short dashed) CB-NLROM substructuring. Plots (e–f) show the time history over one period of the transverse displacement of the beam at $x = 4.5$ in. (color figure appear online)



motions to higher frequency motions. The CB-NLROM substructuring presented in this paper used the CB modes as a basis to generate the low order equations of motion, but this approach could be applied to any desired set of basis vectors (for example, free-interface modes with attachment modes as in the Craig-Chang method).

One foreseeable pitfall to the method presented, and indeed to the Craig-Bampton method in general, is the fact that it could require a very large number of constraint modes to capture the kinematics of a continuous interface with many interface DOF. Since one constraint mode is required for each boundary DOF, this could result in a large number of modes in the basis of the NLROM, and several works have shown that the Craig-Bampton basis becomes ineffective when there are many closely spaced boundary nodes (see, e.g. [25]). Furthermore, the computational cost of the NLROM approach grows in proportion to the number of modes in the basis, because many more nonlinear stiffness coefficients must be determined and hence many more static load cases are required [26]. To circumvent this potentially crippling cost, it may be possible to use characteristic constraint modes [27] to reduce the number of constraint modes needed to model a continuous interface.

Acknowledgements The authors gratefully acknowledge the support of the Air Force Office of Scientific Research under grant number FA9550-11-1-0035, administered by the Dr. David Stargel of the Multi-Scale Structural Mechanics and Prognosis Program.

References

1. Craig RRJ, Bampton MCC (1968) Coupling of substructures for dynamic analysis. *AIAA J* 6:1313–1319
2. Zuchowski B (2012) Predictive capability for hypersonic structural response and life prediction: phase II – detailed design of hypersonic cruise vehicle hot-structure. Air Force Research Laboratory (AFRL), Wright-Patterson Air Force Base, OH AFRL-RQ-WP-TR-2012-0280
3. Liguore SL, Pitt DM, Thomas MJ, Gurtowski N (2011) Nonlinear, low-order/reduced-order modeling applications and demonstration. Air Force Research Laboratory (AFRL), Wright-Patterson Air Force Base, OH AFRL-RB-WP-TR-2011-3102
4. Gordon RW, Hollkamp JJ (2011) Reduced-order models for acoustic response prediction. Air Force Research Laboratory (AFRL), Wright-Patterson Air Force Base, OH AFRL-RB-WP-TR-2011-3040
5. Culler AJ, McNamara JJ (2010) Studies on fluid-thermal-structural coupling for aerothermoelasticity in hypersonic flow. *AIAA J* 48:1721–1738
6. Culler AJ, McNamara JJ (2011) Impact of fluid-thermal-structural coupling on response prediction of hypersonic skin panels. *AIAA J* 49:2393–2406
7. Hollkamp JJ, Gordon RW, Spottswood SM (2005) Nonlinear modal models for sonic fatigue response prediction: a comparison of methods. *J Sound Vib* 284:1145–1163
8. Mignolet MP, Przekop A, Rizzi SA, Spottswood SM (2013) A review of indirect/non-intrusive reduced order modeling of nonlinear geometric structures. *J Sound Vib* 332:2437–2460
9. Muravyov AA, Rizzi SA (2003) Determination of nonlinear stiffness with application to random vibration of geometrically nonlinear structures. *Comput Struct* 81:1513–1523
10. Perez R, Wang X, Mignolet MP (2011) Nonlinear reduced-order models for thermoelastodynamic response of isotropic and functionally graded panels. *AIAA J* 49:630–641
11. Craig RRJ (1981) *Structural dynamics*. Wiley, New York, NY
12. Ginsberg JH (2001) *Mechanical and structural vibrations*, 1st edn. Wiley, New York, NY
13. Kuether RJ, Allen MS (2013) Nonlinear modal substructuring of systems with geometric nonlinearities. 54th AIAA/ASME/ASCE/AHS/ASC structures, structural dynamics, and materials conference, Boston, MA
14. Kawamura S, Naito T, Zahid HM, Minamoto H (2008) Analysis of nonlinear steady state vibration of a multi-degree-of-freedom system using component mode synthesis method. *Appl Acoust* 69:624–633
15. Hollkamp JJ, Gordon RW (2008) Reduced-order models for nonlinear response prediction: implicit condensation and expansion. *J Sound Vib* 318:1139–1153
16. Crisfield MA (1991) *Nonlinear finite element analysis of solids and structures*, vol 1, Essentials. Wiley, Chichester
17. Crisfield MA (1991) *Nonlinear finite element analysis of solids and structures*, vol 2, Advanced topics. Wiley, Chichester
18. Nash M (1977) *Nonlinear structural dynamics by finite element modal synthesis*. Ph.D., Department of Aeronautics, Imperial College
19. de Klerk D, Rixen DJ, Voormeeren SN (2008) General framework for dynamic substructuring: history, review, and classification of techniques. *AIAA J* 46:1169–1181
20. Peeters M, Viguié R, Sérandour G, Kerschen G, Golinval JC (2009) Nonlinear normal modes, Part II: Toward a practical computation using numerical continuation techniques. *Mech Syst Signal Process* 23:195–216
21. Kuether RJ, Brake MR, Allen MS (2014) Evaluating convergence of reduced order models using nonlinear normal modes. Presented at the 32nd international modal analysis conference (IMAC XXXII), Orlando, FL
22. Vakakis AF (1997) Non-linear normal modes (NNMs) and their applications in vibration theory: an overview. *Mech Syst Signal Process* 11:3–22
23. Kerschen G, Peeters M, Golinval JC, Vakakis AF (2009) Nonlinear normal modes. Part I. A useful framework for the structural dynamicist. *Mech Syst Signal Process* 23:170–194
24. Kuether RJ, Allen MS (2013) A numerical approach to directly compute nonlinear normal modes of geometrically nonlinear finite element models. *Mech Syst Signal Process* (accepted for publication)
25. Belloch P, Vold H (2005) Orthogonality and large models – what’s the problem? Presented at the 23rd international modal analysis conference (IMAC XXIII), Orlando, FL
26. Perez R, Wang XQ, Matney A, Mignolet MP (2012) Reduced order model for the geometric nonlinear response of complex structures. Presented at the ASME 2012 international design engineering technical conferences IDETC/CIE, Chicago, IL
27. Castanier MP, Tan Y, Pierre C (2001) Characteristic constraint modes for component mode synthesis. *AIAA J* 39:1182–1187

Chapter 16

Parameterized Reduced Order Models Constructed Using Hyper Dual Numbers

M.R. Brake, J.A. Fike, S.D. Topping, R. Schultz, R.V. Field, N.M. McPeck-Bechtold, and R. Dingreville

Abstract In order to assess the predicted performance of a manufactured system, analysts must typically consider random variations (both geometric and material) in the development of a finite element model, instead of a single deterministic model of an idealized geometry. The incorporation of random variations, however, could potentially require the development of thousands of nearly identical solid geometries that must be meshed and separately analyzed, which would require an impractical number of man-hours to complete. This paper proposes a new approach to uncertainty quantification by developing parameterized reduced order models. These parameterizations are based upon Taylor series expansions of the system's matrices about the ideal geometry, and a component mode synthesis representation for each linear substructure is used to form an efficient basis with which to study the system. The numerical derivatives required for the Taylor series expansions are obtained efficiently using hyper dual numbers, which enable the derivatives to be calculated precisely to within machine precision. The theory is applied to a stepped beam system in order to demonstrate proof of concept. The accuracy and efficiency of the method, as well as the level at which the parameterization is introduced, are discussed. Hyper dual numbers can be used to construct parameterized models both efficiently and accurately and constitute an appropriate methodology to account for perturbations in a structural system.

Keywords Model reduction theory • Parameterization • Uncertainty • Parameterized reduced order models • Hyper dual numbers

Sandia National Laboratories is a multi-program laboratory managed and operated by Sandia Corporation, a wholly owned subsidiary of Lockheed Martin Corporation, for the U.S. Department of Energy's National Nuclear Security Administration under contract DE-AC04-94AL85000.

M.R. Brake (✉) • R. Schultz • R.V. Field • R. Dingreville
Sandia National Laboratories, Albuquerque, NM 87185, USA
e-mail: mrbrake@sandia.gov

J.A. Fike
Stanford University, Stanford, CA 94305, USA
Sandia National Laboratories, Albuquerque, NM 87185, USA

S.D. Topping
University of Arizona, Tucson, AZ 85721, USA
Sandia National Laboratories, Albuquerque, NM 87185, USA

N.M. McPeck-Bechtold
University of California, Berkeley, CA, USA
Sandia National Laboratories, Albuquerque, NM 87185, USA

16.1 Introduction

Modern engineering analysis must take into account the effects of aleatoric (parametric) uncertainty in the analysis of a system. As a real system is manufactured, part-to-part variations are introduced that can have significant ramifications on the functionality of the system. Thus, in order to account for these variations at the design stage, a methodology is needed to assess the performance of many (often thousands) of permutations of a design to qualify the performance of a manufactured system.

One method to simulate the performance of a system is via high fidelity modeling, such as using the finite element (FE) method. High fidelity computational simulations can often provide very accurate predictions; however, they have a very high computational cost. In order to develop simulations that are both efficient and accurate enough, reduced order models (ROMs) often are used as surrogates for a full order model in order to decrease the computational expense of analysis.

To model the perturbations that are found in manufactured systems without a systematic, efficient reduced order approach would be prohibitively difficult. For example, consider a scenario where it takes several weeks to develop a high quality mesh for one relatively simple component. To quantify the aleatoric uncertainty associated with manufacturing, thousands of perturbations of the ideal geometry are necessary, and each likely requires a new mesh. Even with factoring in time saved from some automation of the process, the number of man hours required to construct these meshes is on the order of 20 years. In addition, the computational time to analyze all of these models is on the order of several years assuming that an entire super computer can be dedicated to the analysis. Clearly, decades of time are infeasible constraints to be incorporated into a design cycle. One method of accounting for these perturbations is to create a parameterized reduced order model (PROM) of the system [1–4]. This allows the behavior of the system to be inexpensively predicted over a range of perturbations based on a few simulations distributed about the nominal design.

A standard approach to constructing ROMs for structural dynamics is Craig-Bampton (C-B) Component Mode Synthesis (CMS) [5]. Figure 16.1 shows two approaches that can be taken to analyze a system composed of several components. The left branch of the diagram shows the traditional approach of forming a full order FE model for the system, which often is prohibitively expensive for assessing aleatoric uncertainty. The right branch shows the steps when C-B CMS is used. To account for aleatoric uncertainty, PROMs can be utilized. Simple PROMs can be constructed from a finite Taylor series expansion; for instance, in computing some scalar quantity of interest, $f(x)$, as a function of some perturbation to the nominal design, Δx , $f(x)$ can be approximated as $\bar{f}(x)$, which is based on a Taylor series expansion. For the FE and CMS cases outlined in Fig. 16.1, $f(x)$ could be elements of the mass and stiffness matrices or it could be the result of the system analysis, such as displacements or eigenvalues. The perturbations to the nominal design, Δx , could be changes in material properties or geometric variations. A parameterized model can then be created as

$$\bar{f}(x + \Delta x) = f(x) + (\Delta x)f'(x) + \frac{(\Delta x)^2}{2}f''(x) + \frac{(\Delta x)^3}{6}f'''(x) + \dots \tag{16.1}$$

In practice, this infinite sum is truncated to be finite valued. In what follows, a second order and a third order expansion are considered.

The use of these parameterized models with FE analysis requires the calculation of derivatives at the nominal design. These derivatives can be computed in many ways, such as using finite difference approximations; however, finite difference approximations can require multiple meshes for each dimension of a perturbation, which can result in an impractically large amount of man-hours. For instance, a fourth order accurate cubic finite difference expansion for just two variables could require 49 separate meshes, three variables could require 343 meshes, and N variables could require as many as 7^N . The approach proposed here is to compute the derivatives using hyper dual numbers [6]. Hyper dual numbers produce

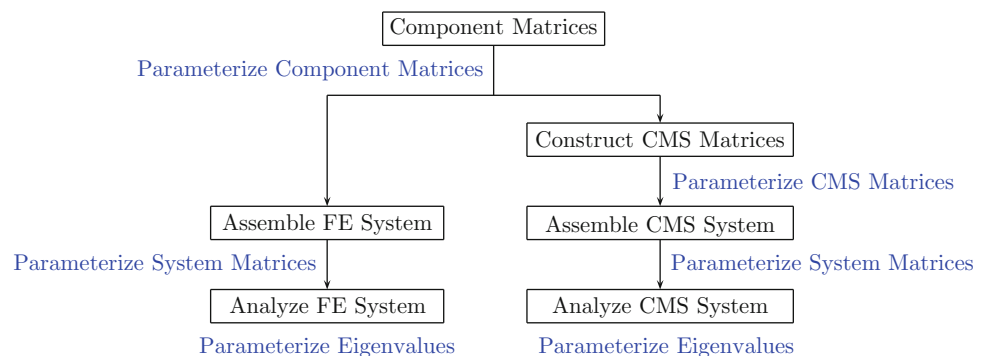


Fig. 16.1 Two possible approaches for analyzing a system composed of several components, and the levels at which parameterized models can be constructed

exact values of the derivatives, and only require a single evaluation at the nominal design, in contrast to finite difference approximations. The use of hyper dual numbers only requires the nominal mesh, but the information on how the mesh would change due to the perturbations needs to be known or calculated. In practice, this can require the introduction of hyper dual numbers into the meshing procedure.

Parameterized models can be created at several levels in the analysis procedure outlined in Fig. 16.1. One possibility is to construct parameterized models for the component mass and stiffness matrices. Another possibility is to parameterize the output of the system analysis, i.e. displacements or eigenvalues. When using CMS it is also possible to parameterize the reduced order mass and stiffness matrices. One goal of this research is to assess the efficacy of developing PROMs at each level identified in Fig. 16.1.

This paper presents a brief overview of C-B CMS in Sect. 16.2, and then in Sect. 16.3 introduces hyper dual numbers and discusses the development of PROMs, where the required derivatives are computed using hyper dual numbers [6]. Next, Sect. 16.4 assesses the efficacy of each potential level of developing a PROM, as indicated in Fig. 16.1, and conclusions are presented in Sect. 16.5.

16.2 Craig-Bampton Component Mode Synthesis

The equation of motion for an unforced and undamped structure with mass matrix $[M]$, stiffness matrix $[K]$, and displacement $\{u\}$ is

$$[M]\{\ddot{u}\} + [K]\{u\} = \{0\}. \quad (16.2)$$

The C-B CMS [5] method is based on a substructuring of the component's degrees of freedom (DOFs) into boundary (u_b) DOFs and internal (u_i) DOFs as $\{u\} = \{u_b, u_i\}^T$. Boundary DOFs typically are defined as DOFs where excitations are applied or where output quantities are desired (such as the displacement of a particular flange), whereas internal DOFs are all non-boundary DOFs, which generally are inside of the component and thus have no applied loads. This substructuring is used to recast Eq. (16.2) as

$$\begin{bmatrix} M_{bb} & M_{bi} \\ M_{ib} & M_{ii} \end{bmatrix} \begin{Bmatrix} \ddot{u}_b \\ \ddot{u}_i \end{Bmatrix} + \begin{bmatrix} K_{bb} & K_{bi} \\ K_{ib} & K_{ii} \end{bmatrix} \begin{Bmatrix} u_b \\ u_i \end{Bmatrix} = \{0\}. \quad (16.3)$$

Modal analysis is performed on the internal degrees of freedom,

$$(K_{ii} - \lambda_\ell M_{ii}) \phi_\ell = 0, \quad (16.4)$$

where λ_ℓ are individual eigenvalues and ϕ_ℓ are the corresponding eigenvectors of the fixed interface normal modes. Constraint modes, ϕ_C , are a static deflection shape and are computed by imposing a unit displacement at each individual boundary DOF while holding the other boundary DOFs fixed at zero displacement. The constraint modes can therefore be computed as

$$\phi_C = -K_{ii}^{-1} K_{ib}. \quad (16.5)$$

Subsequently, the physical DOFs (u_b and u_i) are related to the hybrid set of physical and modal DOFs (u_b and q_m) by

$$\begin{Bmatrix} u_b \\ u_i \end{Bmatrix} = \begin{bmatrix} I & 0 \\ \phi_C & \phi_N \end{bmatrix} \begin{Bmatrix} u_b \\ q_m \end{Bmatrix}, \quad (16.6)$$

where I is the identity matrix and ϕ_N is a matrix of the eigenvectors ϕ_ℓ . This allows the equation of motion for each component to be written as

$$\begin{bmatrix} M_{CC} & M_{CN} \\ M_{NC} & I \end{bmatrix} \begin{Bmatrix} \ddot{u}_b \\ \ddot{q}_m \end{Bmatrix} + \begin{bmatrix} K_{CC} & 0 \\ 0 & \Lambda^2 \end{bmatrix} \begin{Bmatrix} u_b \\ q_m \end{Bmatrix} = \{0\}, \quad (16.7)$$

assuming the eigenvectors are normalized with respect to the mass matrix M_{ii} , and with

$$M_{CC} = M_{bb} + M_{bi}\phi_C + \phi_C^T + \phi_C^T M_{ii} \phi_C, \quad (16.8)$$

$$M_{CN} = M_{NC}^T = (M_{bi} + \phi_C^T M_{ii}) \phi_N, \quad (16.9)$$

$$K_{CC} = K_{bb} + M_{bi} \phi_C, \quad (16.10)$$

where Λ is a diagonal matrix of the eigenvalues λ_ℓ .

The number of degrees of freedom can be reduced by retaining only enough fixed interface normal modes to capture the behavior of interest. In general, keeping more modes results in a more accurate approximation of the true behavior at the expense of an increased computational cost. The reduced mass and stiffness matrices for each component can be combined to form a ROM for the system. This ROM is less expensive to analyze and provides accurate results given that enough modes are kept to capture the behavior of interest.

16.3 Parameterization Using Hyper Dual Numbers

The PROM method proposed in the present work is derived using hyper dual numbers because hyper dual numbers allow for exact calculations of derivatives without needing multiple points at which the derivatives are evaluated. This is achievable due to the definition of a dual number. A dual number is defined as a class of generalized complex numbers where the non-real part is defined by the non-zero root of the number zero, as described in [6]. A hyper dual number is a dual number defined in more than one dimension. For example, two dimensional hyper dual numbers are defined to consist of one real part and three non-real parts, where the three non-real units ϵ_1 , ϵ_2 , and $\epsilon_1\epsilon_2$ have the properties that $\epsilon_1^2 = \epsilon_2^2 = (\epsilon_1\epsilon_2)^2 = 0$ but $\epsilon_1 \neq \epsilon_2 \neq \epsilon_1\epsilon_2 \neq 0$. Higher dimensional hyper dual numbers can also be considered, such as described later in the text. The Taylor series for a real-valued function subjected to a hyper dual perturbation truncates exactly at the second derivative term

$$f(x + h_1\epsilon_1 + h_2\epsilon_2 + 0\epsilon_1\epsilon_2) = f(x) + h_1f'(x)\epsilon_1 + h_2f'(x)\epsilon_2 + h_1h_2f''(x)\epsilon_1\epsilon_2 \quad (16.11)$$

for arbitrary perturbations h_1 and h_2 . There is no truncation error because all the higher order terms contain ϵ_1^2 or ϵ_2^2 or higher powers and are zero by definition. The first and second derivatives are the leading terms of the non-real parts, and these terms can be found by taking the individual non-real parts and dividing by the step size. There is no required difference operation, as in finite difference approximations, which would lead to subtractive cancelation error. The first and second derivatives can thus be computed exactly, regardless of the step size.

For the present research, third order parameterizations are needed since many geometry variables enter into the stiffness matrix as cubic terms. A hyper dual implementation that produces exact third derivatives is created by including ϵ_3 terms. This yields a Taylor series that truncates exactly at the third derivative term (with an arbitrary perturbation h_3)

$$\begin{aligned} f(x + h_1\epsilon_1 + h_2\epsilon_2 + h_3\epsilon_3 + 0\epsilon_1\epsilon_2 + 0\epsilon_1\epsilon_3 + 0\epsilon_2\epsilon_3 + 0\epsilon_1\epsilon_2\epsilon_3) \\ = f(x) + h_1f'(x)\epsilon_1 + h_2f'(x)\epsilon_2 + h_3f'(x)\epsilon_3 + h_1h_2f''(x)\epsilon_1\epsilon_2 \\ + h_1h_3f''(x)\epsilon_1\epsilon_3 + h_2h_3f''(x)\epsilon_2\epsilon_3 + h_1h_2h_3f'''(x)\epsilon_1\epsilon_2\epsilon_3. \end{aligned} \quad (16.12)$$

The use of hyper dual numbers requires overloading all of the functions in the analysis code to operate on hyper dual numbers instead of on real numbers (that is, creating a new method for a function that operates on hyper dual numbers instead of the originally intended data structure). However, there are often cases where functions are used for which the code is not available and therefore cannot be modified. In these situations it may still be possible to use hyper dual numbers, if the effect of computing the derivatives can be achieved. One example of this is the solution of a linear system, $\mathbf{A}\mathbf{y} = \mathbf{b}$, where derivatives can be computed by several calls to the real-valued routine [7]. First derivatives of the solution of a linear system, $\mathbf{A}\mathbf{y} = \mathbf{b}$, can be computed by solving

$$\mathbf{A} \frac{\partial \mathbf{y}}{\partial x_i} = \frac{\partial \mathbf{b}}{\partial x_i} - \frac{\partial \mathbf{A}}{\partial x_i} \mathbf{y}. \quad (16.13)$$

Second derivatives can then be found by solving

$$\mathbf{A} \frac{\partial^2 \mathbf{y}}{\partial x_i \partial x_j} = \frac{\partial^2 \mathbf{b}}{\partial x_i \partial x_j} - \frac{\partial^2 \mathbf{A}}{\partial x_i \partial x_j} \mathbf{y} - \frac{\partial \mathbf{A}}{\partial x_i} \frac{\partial \mathbf{y}}{\partial x_j} - \frac{\partial \mathbf{A}}{\partial x_j} \frac{\partial \mathbf{y}}{\partial x_i}, \quad (16.14)$$

and third derivatives by solving

$$\mathbf{A} \frac{\partial^3 \mathbf{y}}{\partial x_i \partial x_j \partial x_k} = \frac{\partial^3 \mathbf{b}}{\partial x_i \partial x_j \partial x_k} - \frac{\partial^3 \mathbf{A}}{\partial x_i \partial x_j \partial x_k} \mathbf{y} - \frac{\partial^2 \mathbf{A}}{\partial x_i \partial x_j} \frac{\partial \mathbf{y}}{\partial x_k} - \frac{\partial^2 \mathbf{A}}{\partial x_i \partial x_k} \frac{\partial \mathbf{y}}{\partial x_j} - \frac{\partial^2 \mathbf{A}}{\partial x_j \partial x_k} \frac{\partial \mathbf{y}}{\partial x_i} - \frac{\partial \mathbf{A}}{\partial x_i} \frac{\partial^2 \mathbf{y}}{\partial x_j \partial x_k} - \frac{\partial \mathbf{A}}{\partial x_j} \frac{\partial^2 \mathbf{y}}{\partial x_i \partial x_k} - \frac{\partial \mathbf{A}}{\partial x_k} \frac{\partial^2 \mathbf{y}}{\partial x_i \partial x_j}. \quad (16.15)$$

Using hyper dual numbers to compute derivatives for the parameterization of eigenvalues or CMS matrices requires a hyper dual version of the eigenvalue calculation routine. As with the solution of a linear system, the effect of using hyper dual numbers can be recreated without modifying the real-valued eigenvalue solver.

16.3.1 Derivatives of Eigenvalues and Eigenvectors

Eigenvalues and eigenvectors are solutions of

$$(K - \lambda_\ell M) \phi_\ell = F_\ell \phi_\ell = 0, \quad (16.16)$$

with $F_\ell = (K - \lambda_\ell M)$. This equation can be differentiated to give

$$\frac{\partial F_\ell}{\partial x_i} \phi_\ell + F_\ell \frac{\partial \phi_\ell}{\partial x_i} = 0. \quad (16.17)$$

Pre-multiplying this equation by the transpose of the eigenvector, and making use of the fact that $F_\ell \phi_\ell = 0$, yields

$$\phi_\ell^T \frac{\partial F_\ell}{\partial x_i} \phi_\ell = \phi_\ell^T \left(\frac{\partial K}{\partial x_i} - \lambda_\ell \frac{\partial M}{\partial x_i} - \frac{\partial \lambda_\ell}{\partial x_i} M \right) \phi_\ell. \quad (16.18)$$

The eigenvectors are orthonormal with respect to M , so $\phi_\ell^T M \phi_\ell = 1$, and Eq. (16.18) can be rearranged to give the first derivative of the eigenvalue

$$\frac{\partial \lambda_\ell}{\partial x_i} = \phi_\ell^T \left(\frac{\partial K}{\partial x_i} - \lambda_\ell \frac{\partial M}{\partial x_i} \right) \phi_\ell. \quad (16.19)$$

There are several methods for computing the first derivatives of eigenvectors, as summarized by Alvin [8]. The method of Nelson [9] is exact but can be computationally expensive since it involves solving a linear system for each derivative. The modal superposition method [10] represents the derivative of an eigenvector as a superposition of the other eigenvectors and is less computationally intensive than Nelson's method.

Figure 16.2 shows the first derivative of the second eigenvector with respect to the cross-sectional height computed using finite differences, Nelson's method, and modal superposition. Nelson's method and the finite difference calculation are in good agreement. The first derivative of the eigenvector has sharp corners where the individual components join together. Modal superposition requires the use of all eigenvectors in order to be exact. Using a smaller subset results in an approximation. Figure 16.2 shows the result of modal superposition with 20 modes. The modal superposition method does not capture the sharp corners, and exhibits Gibb's phenomena, as would be expected of a method relying on a finite summation of modes. When the application is CMS, only a few eigenvectors are kept, so the computational cost of Nelson's method is not expected to be an issue and is preferred over modal superposition.

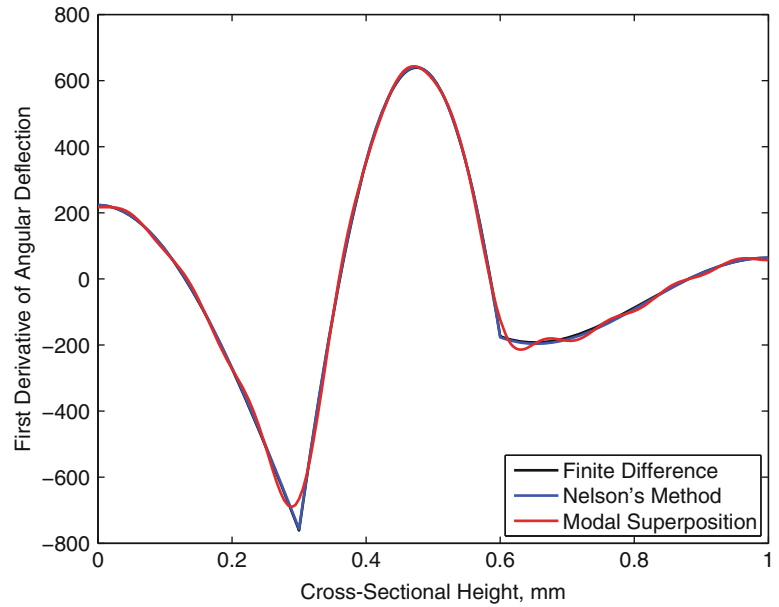
Nelson's method for computing the first derivative of an eigenvector is to represent it as a sum of two terms

$$\frac{\partial \phi_\ell}{\partial x_i} = z_i + c_i \phi_\ell. \quad (16.20)$$

The quantity z_i is found by solving Eq. (16.17) with $\frac{\partial \phi_\ell}{\partial x_i}$ replaced by z_i ,

$$F_\ell z_i = -\frac{\partial F_\ell}{\partial x_i} \phi_\ell. \quad (16.21)$$

Fig. 16.2 A comparison of three methods for computing derivatives of eigenvectors (the system and its parameters are described in Sect. 16.4)



The contribution of ϕ_ℓ is added back in by multiplying by c_i , where c_i is found by differentiating the orthonormalization equation

$$\phi_j^T M \phi_i = \delta_{ij}, \quad (16.22)$$

where δ_{ij} is the Kronecker delta function. The first derivative of the orthonormalization equation is

$$\phi^T \frac{\partial M}{\partial x_i} \phi + 2\phi^T M \frac{\partial \phi_\ell}{\partial x_i} = 0. \quad (16.23)$$

Substituting Eq. (16.20) into this equation produces

$$\phi^T \frac{\partial M}{\partial x_i} \phi + 2\phi^T M (z_i + c_i \phi_\ell) = 0, \quad (16.24)$$

and c_i can then be computed as

$$c_i = -\frac{1}{2} \phi_\ell^T \frac{\partial M}{\partial x_i} \phi_\ell - \phi_\ell^T M z_i. \quad (16.25)$$

Expressions for second and third derivatives can be derived following a similar procedure. The second derivative of an eigenvalue can be computed as

$$\begin{aligned} \frac{\partial^2 \lambda_\ell}{\partial x_i \partial x_j} &= \phi_\ell^T \left(\frac{\partial^2 K}{\partial x_i \partial x_j} - \frac{\partial \lambda_\ell}{\partial x_i} \frac{\partial M}{\partial x_j} - \frac{\partial \lambda_\ell}{\partial x_j} \frac{\partial M}{\partial x_i} - \lambda \frac{\partial^2 M}{\partial x_i \partial x_j} \right) \phi_\ell \\ &+ \phi_\ell^T \frac{\partial F_\ell}{\partial x_i} \frac{\partial \phi_\ell}{\partial x_j} + \phi_\ell^T \frac{\partial F_\ell}{\partial x_j} \frac{\partial \phi_\ell}{\partial x_i}, \end{aligned} \quad (16.26)$$

and the second derivative of the corresponding eigenvector can then be computed as

$$\frac{\partial^2 \phi_\ell}{\partial x_i \partial x_j} = z_{ij} + c_{ij} \phi_\ell, \quad (16.27)$$

where

$$c_{ij} = -\frac{1}{2} \phi_\ell^T \frac{\partial^2 M}{\partial x_i \partial x_j} \phi_\ell - \phi_\ell^T \frac{\partial M}{\partial x_i} \frac{\partial \phi_\ell}{\partial x_j} - \phi_\ell^T \frac{\partial M}{\partial x_j} \frac{\partial \phi_\ell}{\partial x_i} - \frac{\partial \phi_\ell^T}{\partial x_j} M \frac{\partial \phi_\ell}{\partial x_i} - \phi_\ell^T M z_{ij}. \quad (16.28)$$

The term z_{ij} is found by solving

$$F_{\ell} z_{ij} = -\frac{\partial^2 F_{\ell}}{\partial x_i \partial x_j} \phi_{\ell} - \frac{\partial F_{\ell}}{\partial x_i} \frac{\partial \phi_{\ell}}{\partial x_j} - \frac{\partial F_{\ell}}{\partial x_j} \frac{\partial \phi_{\ell}}{\partial x_i}. \quad (16.29)$$

The expression for the third derivative of an eigenvalue is

$$\begin{aligned} \frac{\partial^3 \lambda_{\ell}}{\partial x_i \partial x_j \partial x_k} = & \phi_{\ell}^T \left(\frac{\partial^3 K}{\partial x_i \partial x_j \partial x_k} - \frac{\partial^2 \lambda_{\ell}}{\partial x_j \partial x_k} \frac{\partial M}{\partial x_i} - \frac{\partial^2 \lambda_{\ell}}{\partial x_i \partial x_k} \frac{\partial M}{\partial x_j} - \frac{\partial^2 \lambda_{\ell}}{\partial x_i \partial x_j} \frac{\partial M}{\partial x_k} - \frac{\partial \lambda_{\ell}}{\partial x_i} \frac{\partial^2 M}{\partial x_j \partial x_k} \right. \\ & \left. - \frac{\partial \lambda_{\ell}}{\partial x_j} \frac{\partial^2 M}{\partial x_i \partial x_k} - \frac{\partial \lambda_{\ell}}{\partial x_k} \frac{\partial^2 M}{\partial x_i \partial x_j} - \lambda \frac{\partial^3 M}{\partial x_i \partial x_j \partial x_k} \right) \phi_{\ell} + \phi_{\ell}^T \frac{\partial^2 F_{\ell}}{\partial x_j \partial x_k} \frac{\partial \phi_{\ell}}{\partial x_i} + \phi_{\ell}^T \frac{\partial^2 F_{\ell}}{\partial x_i \partial x_k} \frac{\partial \phi_{\ell}}{\partial x_j} \\ & + \phi_{\ell}^T \frac{\partial^2 F_{\ell}}{\partial x_i \partial x_j} \frac{\partial \phi_{\ell}}{\partial x_k} + \phi_{\ell}^T \frac{\partial F_{\ell}}{\partial x_i} \frac{\partial^2 \phi_{\ell}}{\partial x_j \partial x_k} + \phi_{\ell}^T \frac{\partial F_{\ell}}{\partial x_j} \frac{\partial^2 \phi_{\ell}}{\partial x_i \partial x_k} + \phi_{\ell}^T \frac{\partial F_{\ell}}{\partial x_k} \frac{\partial^2 \phi_{\ell}}{\partial x_i \partial x_j}. \end{aligned} \quad (16.30)$$

The third derivative of the corresponding eigenvector can then be computed as

$$\frac{\partial^3 \phi_{\ell}}{\partial x_i \partial x_j \partial x_k} = z_{ijk} + c_{ijk} \phi_{\ell}, \quad (16.31)$$

where

$$\begin{aligned} c_{ijk} = & -\frac{1}{2} \phi_{\ell}^T \frac{\partial^3 M}{\partial x_i \partial x_j \partial x_k} \phi_{\ell} - \phi_{\ell}^T \frac{\partial^2 M}{\partial x_i \partial x_j} \frac{\partial \phi_{\ell}}{\partial x_k} - \phi_{\ell}^T \frac{\partial^2 M}{\partial x_i \partial x_k} \frac{\partial \phi_{\ell}}{\partial x_j} - \phi_{\ell}^T \frac{\partial^2 M}{\partial x_j \partial x_k} \frac{\partial \phi_{\ell}}{\partial x_i} - \frac{\partial \phi_{\ell}^T}{\partial x_k} \frac{\partial M}{\partial x_i} \frac{\partial \phi_{\ell}}{\partial x_j} \\ & - \frac{\partial \phi_{\ell}^T}{\partial x_k} \frac{\partial M}{\partial x_j} \frac{\partial \phi_{\ell}}{\partial x_i} - \frac{\partial \phi_{\ell}^T}{\partial x_k} M \frac{\partial^2 \phi_{\ell}}{\partial x_i \partial x_j} - \frac{\partial \phi_{\ell}^T}{\partial x_j} \frac{\partial M}{\partial x_k} \frac{\partial \phi_{\ell}}{\partial x_i} - \frac{\partial^2 \phi_{\ell}^T}{\partial x_j \partial x_k} M \frac{\partial \phi_{\ell}}{\partial x_i} - \frac{\partial \phi_{\ell}^T}{\partial x_j} M \frac{\partial^2 \phi_{\ell}}{\partial x_i \partial x_k} \\ & - \phi_{\ell}^T \frac{\partial M}{\partial x_i} \frac{\partial^2 \phi_{\ell}}{\partial x_j \partial x_k} - \phi_{\ell}^T \frac{\partial M}{\partial x_j} \frac{\partial^2 \phi_{\ell}}{\partial x_i \partial x_k} - \phi_{\ell}^T \frac{\partial M}{\partial x_k} \frac{\partial^2 \phi_{\ell}}{\partial x_i \partial x_j} - \phi_{\ell}^T M z_{ijk}, \end{aligned} \quad (16.32)$$

and z_{ijk} is found by solving

$$\begin{aligned} F_{\ell} z_{ijk} = & -\frac{\partial^3 F_{\ell}}{\partial x_i \partial x_j \partial x_k} \phi_{\ell} - \frac{\partial^2 F_{\ell}}{\partial x_j \partial x_k} \frac{\partial \phi_{\ell}}{\partial x_i} - \frac{\partial^2 F_{\ell}}{\partial x_i \partial x_k} \frac{\partial \phi_{\ell}}{\partial x_j} - \frac{\partial^2 F_{\ell}}{\partial x_i \partial x_j} \frac{\partial \phi_{\ell}}{\partial x_k} \\ & - \frac{\partial F_{\ell}}{\partial x_i} \frac{\partial^2 \phi_{\ell}}{\partial x_j \partial x_k} - \frac{\partial F_{\ell}}{\partial x_j} \frac{\partial^2 \phi_{\ell}}{\partial x_i \partial x_k} - \frac{\partial F_{\ell}}{\partial x_k} \frac{\partial^2 \phi_{\ell}}{\partial x_i \partial x_j}. \end{aligned} \quad (16.33)$$

16.4 Application to a Stepped Beam

The example problem being considered is a simply supported beam composed of three components, as shown in Fig. 16.3. The beam has elastic modulus E , density ρ , width B , cross-sectional height H , location of the center of the defect ℓ , and length of the defect W , with nominal values given in Table 16.1. The material properties and geometry of the center section are allowed to be perturbed from their nominal values.

Two types of parameterizations are considered: quadratic and cubic. These parameterizations are applied at all the levels shown in Fig. 16.1, although only results from the CMS branch are presented here. A parameter sweep was run for each case to determine the true behavior in order to assess the accuracy of the parameterized models. The CMS calculations are performed by keeping only three modes per component. This seems to produce accurate results although more testing is needed on the effect of varying the number of modes kept. Parameter variations are considered for each of the variables in Table 16.1, except for L .

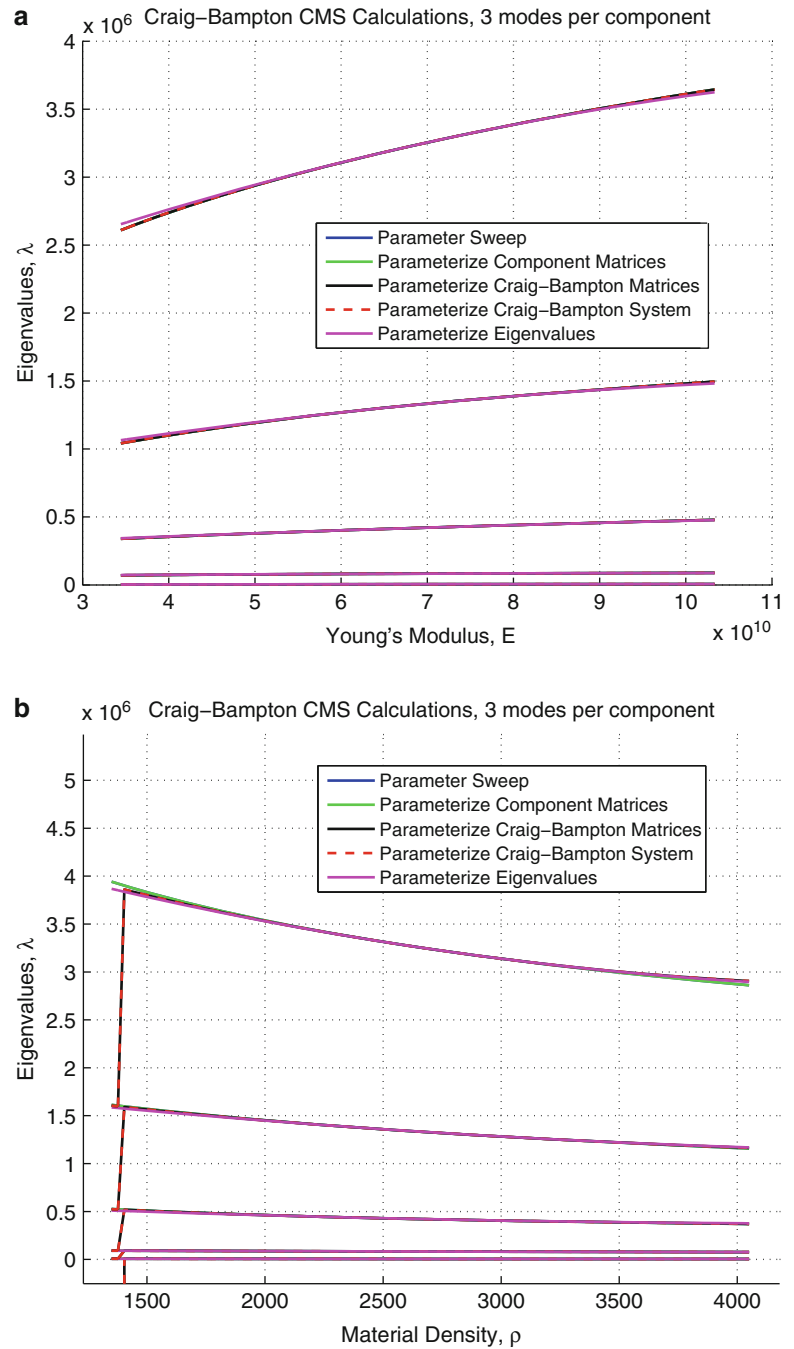


Fig. 16.3 A simply supported beam composed of three components

Table 16.1 Material and geometric properties for the beam

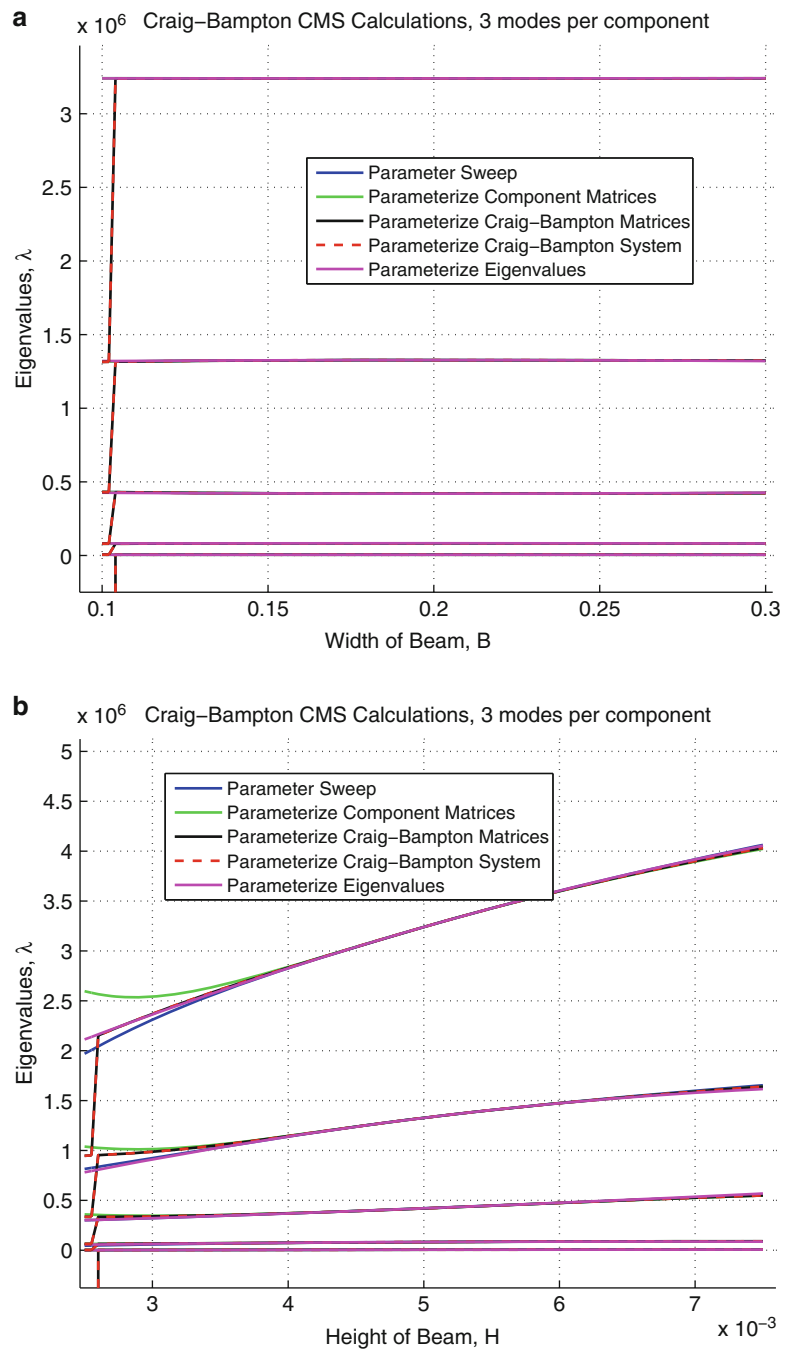
| Property | Value |
|-------------------------------------|-------------------------|
| Density, ρ | 2,700 kg/m ³ |
| Elastic modulus, E | 68.9 GPa |
| Cross-sectional width, B | 20 cm |
| Cross-sectional height, H | 5 mm |
| Location of defect's center, ℓ | 45 cm |
| Length of the defect, W | 30 cm |
| Length of the beam, L | 1 m |

Fig. 16.4 The effects on the first five eigenvalues of quadratic parameterizations for E and ρ . (a) Variations in Young's modulus. (b) Variations in material density



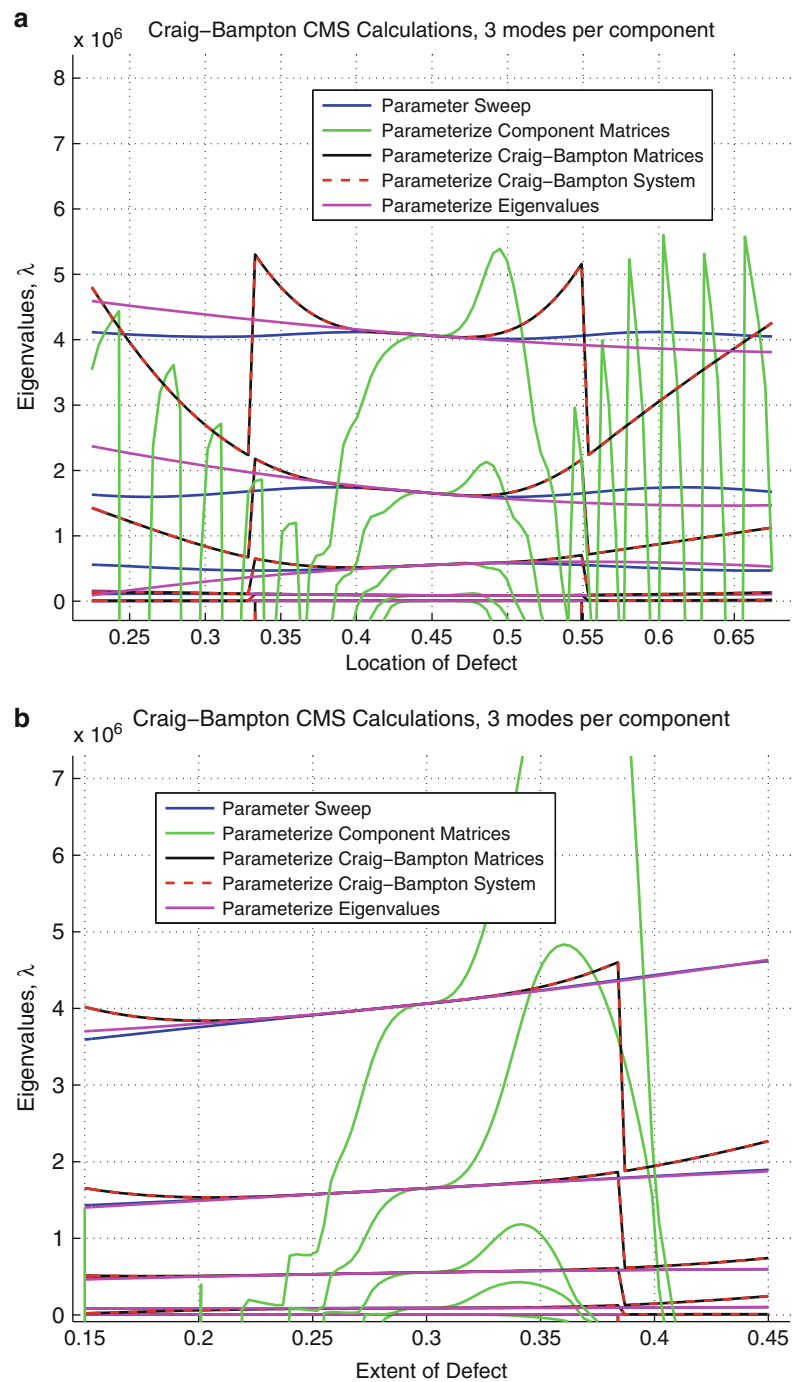
A quadratic parameterization (the first three terms of Eq. (16.1)) is used to produce the comparisons shown in Figs. 16.4, 16.5, and 16.6. Quadratic parameterization produces fairly accurate results for variations in Young's modulus, material density and cross-sectional width and height. There are some issues with the CMS parameterizations at the extremes

Fig. 16.5 The effects on the first five eigenvalues of quadratic parameterizations for B and H . (a) Variations in cross-sectional width. (b) Variations in cross-sectional height



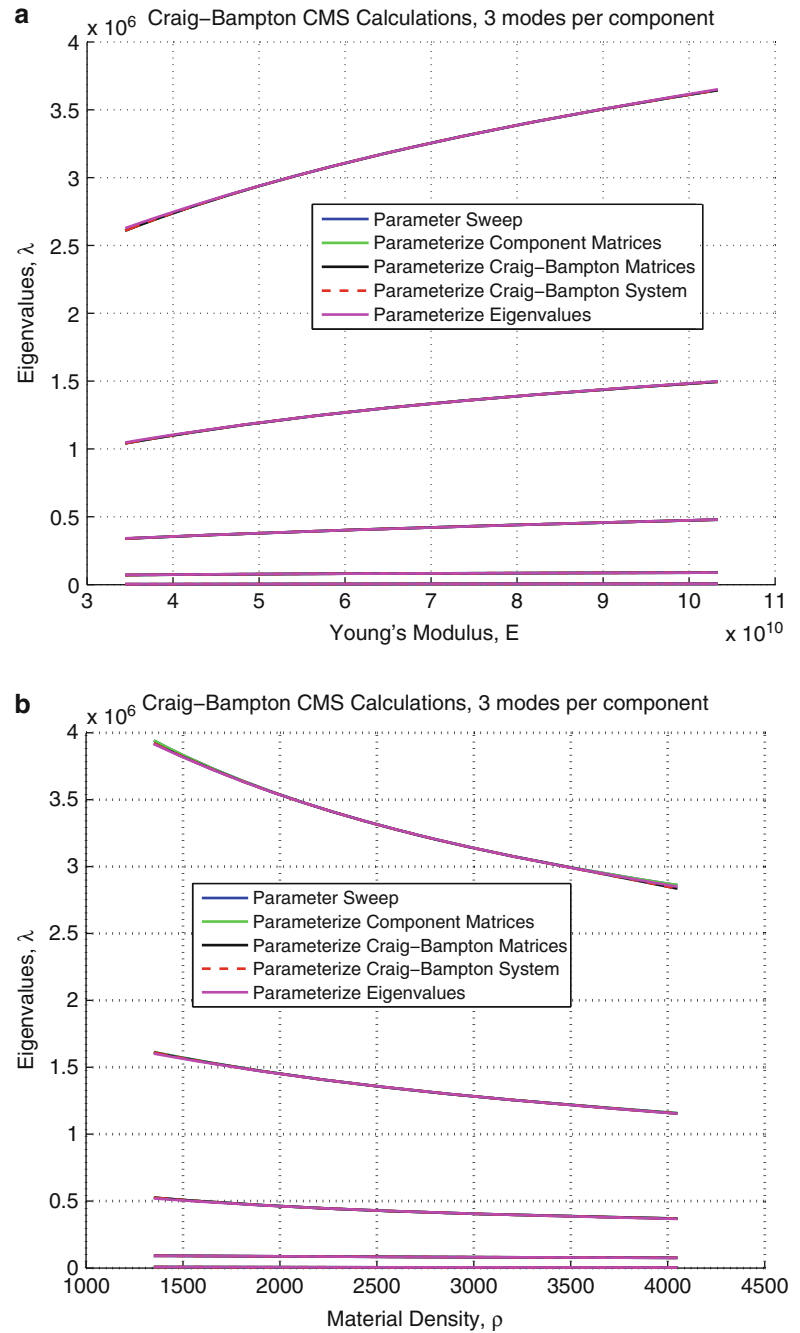
of the parameter space. For the quadratic parameterization, variations in Young's modulus, material density and cross-sectional width are exactly represented to machine precision by parameterizing the component matrices. Parameterizing the CMS matrices produces slightly less accurate results, and parameterizing the eigenvalues produces fairly accurate results. Quadratic parameterization of the full system matrices and CMS matrices is not able to accurately capture the effects of variations in cross-sectional height. Here, the system matrices are composed to represent bending stiffness (as opposed to the cross-sectional height). Bending stiffness relates to the cube of cross-sectional height, whereas the other parameters factor into the system matrices in a linear manner. For variations in location and length of the center component the parameterizations are only accurate in a small region around the nominal design. For these variations, parameterizing the eigenvalues is the most accurate, followed by parameterizing the CMS matrices, with parameterizing the component matrices the least accurate.

Fig. 16.6 The effects on the first five eigenvalues of quadratic parameterizations for ℓ and W . **(a)** Variations in location of center section. **(b)** Variations in length of center section



Cubic parameterizations, as given in Eq. (16.1), produce similar trends but are in general more accurate. The accuracy of the cubic parameterization is shown in Figs. 16.7, 16.8, and 16.9. The cubic parameterization applied to the component matrices is able to accurately represent the effect of varying the cross-sectional height, and also improves the accuracy of parameterization of the CMS matrices. The geometric variations, location and length of the center component, are accurate only in a small region around the nominal design but the accuracy is better than the quadratic parameterization. For the geometric variations, parameterizing the eigenvalues is most accurate, followed by parameterizing the CMS matrices. Parameterizing the component matrices is the least accurate approach for the geometric variations. These trends are consistent with those for using real-valued finite difference methods to construct the parameterizations instead of hyper dual numbers.

Fig. 16.7 The effects on the first five eigenvalues of cubic parameterizations for E and ρ . (a) Variations in Young's modulus. (b) Variations in material density

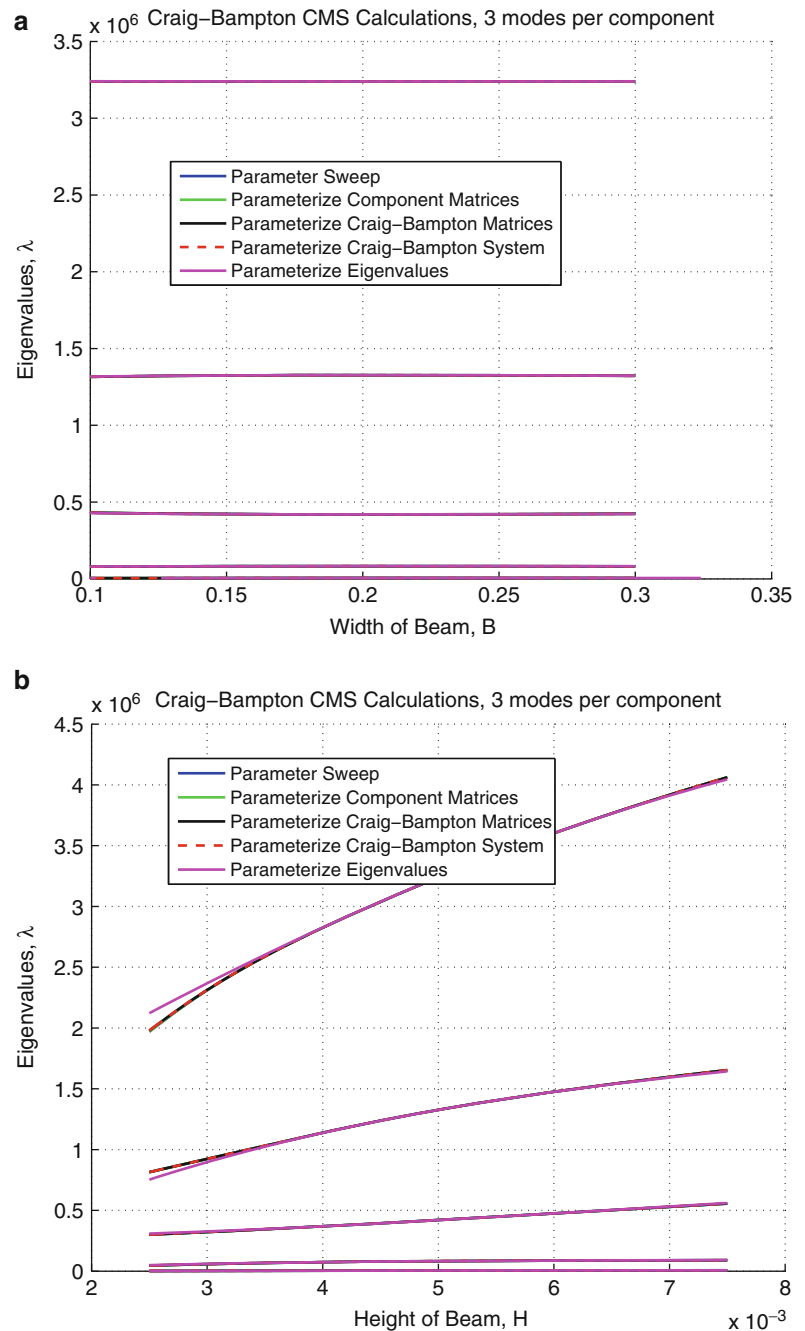


Parameters related to the geometric changes of the system, specifically ℓ and W , are expected to be more difficult to model due to their nonlinear effects on the stiffness matrix as they are varied. Other parameters, that affect the system in only a bulk sense such as B or H , or that are material properties such as E or ρ , are expected to be easier to parameterize as varying them linearly varies the system matrices linearly as well.

16.5 Conclusions and Future Work

This work demonstrates that hyper dual numbers can be used to construct parameterized reduced order models (PROMs) both efficiently (since only one mesh is needed) and accurately. With these PROMs, the task of assessing the response of a real system with aleatoric uncertainty due to manufacturing or other sources should now be feasible. Without these PROMs, the

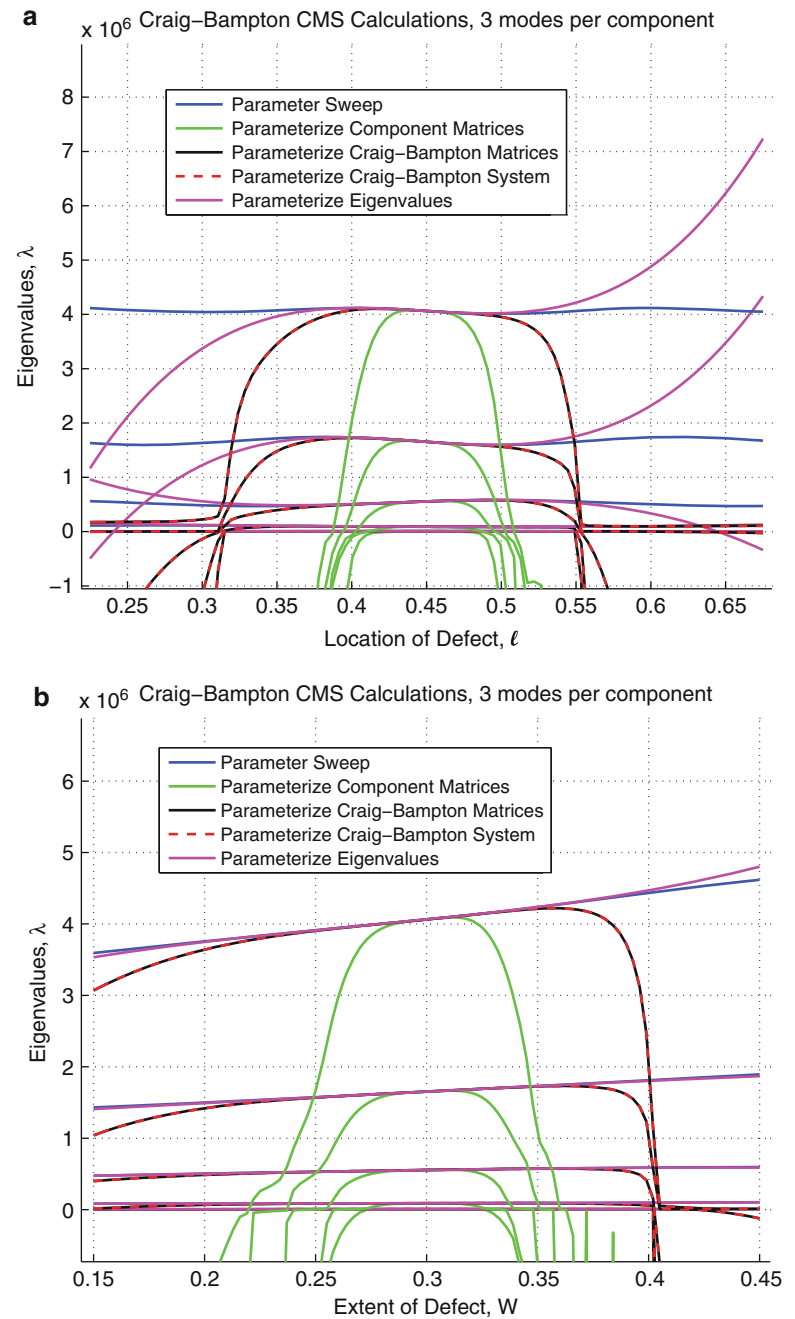
Fig. 16.8 The effects on the first five eigenvalues of cubic parameterizations for B and H . (a) Variations in cross-sectional width. (b) Variations in cross-sectional height



effort required to analyze or model aleatoric uncertainty in a real system would be prohibitively expensive. The derivatives necessary for constructing the PROMs are computed using only the nominal design, eliminating the need to construct more than one mesh as would be required by finite differencing. However, in order for this approach to be applied it is necessary to know how the mesh would change as the parameters of the design are varied. One approach would be to incorporate hyper dual numbers into the mesh generation routine.

This research also sought to determine the appropriate levels to develop PROMs. Results show that parameterization of the eigenvalues and eigenvectors is the most accurate way to reproduce a perturbation in a linear system. As well, parameterization at the component matrix level and at the system level for a CMS model produced nearly identical results. In all three cases, significant savings in both computational time and man-hours are achieved by using PROMs. Future work, though, must seek to improve the accuracy of the PROMs: currently, they are well suited to studying small perturbations in system parameters (up to 5%).

Fig. 16.9 The effects on the first five eigenvalues of cubic parameterizations for ℓ and W . **(a)** Variations in location of center section. **(b)** Variations in length of center section



In order for this approach to be useful for optimizations, the accuracy of the method must be extended to significantly larger variations. Higher order parameterizations should better capture the behavior for the geometric variations. This would require hyper dual numbers capable of producing exact fourth (or higher) derivatives. It is fairly straightforward to extend the existing hyper dual number formulation to higher derivatives, as evidenced by the extension to third derivatives. A more general approach, though, in which dual numbers are defined recursively would allow for easier extensions to arbitrary derivatives. This approach would define a hyper dual number as a dual number with dual number components. Third derivatives would then be produced by going one level further.

References

1. Hong S-K, Epureanu BI, Castanier MP (2012) Joining of components of complex structures for improved dynamic response. *J Sound Vib* 331(19):4285–4298
2. Hong S-K, Epureanu BI, Castanier MP (2013) Next-generation parametric reduced-order models. *Mech Syst Signal Process* 37(1–2):403–421
3. Kammer DC, Nimityongskul S (2011) Propagation of uncertainty in test-analysis correlation of substructured spacecraft. *J Sound Vib* 330:1211–1224
4. Kammer DC, Krattiger D (2013) Propagation of uncertainty in substructured spacecraft using frequency response. *AIAA J* 51(2):353–361
5. Craig RR, Bampton MCC (1968) Coupling of substructures for dynamic analyses. *AIAA J* 6(7):1313–1319
6. Fike JA, Alonso JJ (2011) The development of hyper-dual numbers for exact second-derivative calculations. In: AIAA paper 2011-886, 49th AIAA aerospace sciences meeting
7. Fike JA, Jongsma S, Alonso JJ, van der Weide E (2011) Optimization with gradient and Hessian information calculated using hyper-dual numbers. In: AIAA paper 2011-3807, 29th AIAA applied aerodynamics conference
8. Alvin KF (1997) Efficient computation of eigenvector sensitivities for structural dynamics. *AIAA J* 35(11):1760–1766
9. Nelson RB (1976) Simplified calculation of eigenvector derivatives. *AIAA J* 14(9):1201–1205
10. Fox RL, Kapoor MP (1968) Rates of change of eigenvalues and eigenvectors. *AIAA J* 6(12):2426–2429

Chapter 17

Efficient Stochastic Finite Element Modeling Using Parameterized Reduced Order Models

R. Schultz, M.R. Brake, S.D. Topping, N.M. McPeck-Bechtold, J.A. Fike, R.V. Field, and R. Dingreville

Abstract Finite element analysis of complex geometries is limited by several factors, including the time required to develop solid geometries and meshes, and the computational time required to perform the simulation of a system with, potentially, millions of degrees of freedom. As a result, the analysis of complex systems is often relegated to deterministic approaches in which geometries other than the idealized geometry rarely are considered. In order to robustly design a system, though, and to quantify the margins of uncertainty that a manufactured realization might yield, a stochastic sampling of the permissible geometries is needed. For complex geometries, a stochastic sampling can involve dozens, if not hundreds, of dimensions that can vary. Exploring a large sample space on even a modestly large model quickly becomes prohibitively expensive—and nearly impossible when a mesh change is required for each sample point. This paper presents a new methodology for utilizing reduced order models in which the number of necessary full degree of freedom models (and corresponding meshes) is minimized. The benefits of parameterizing the high fidelity model at an elemental level, the reduced order model at a system level, and the eigen-space representation are discussed. An application of the method on a model with a non-trivial number of degrees of freedom is presented.

Keywords Model reduction theory • Parameterization • Uncertainty • Parameterized reduced order models • Stochastic modeling

17.1 Introduction

Exploring the effects of parametric uncertainty is desirable for the analysis of many systems. For example, quantifying the effects of manufacturing variations on final system performance increases confidence in system suitability for a given application. However, thoroughly exploring uncertainty with traditional finite element (FE) methods can be prohibitively

Sandia National Laboratories is a multi-program laboratory managed and operated by Sandia Corporation, a wholly owned subsidiary of Lockheed Martin Corporation, for the U.S. Department of Energy's National Nuclear Security Administration under contract DE-AC04-94AL85000.

R. Schultz • M.R. Brake (✉) • R.V. Field • R. Dingreville
Sandia National Laboratories, Albuquerque, NM 87185, USA
e-mail: rschult@sandia.gov; mrbrake@sandia.gov

S.D. Topping
University of Arizona, Tucson, AZ 85721, USA

Sandia National Laboratories, Albuquerque, NM 87185, USA

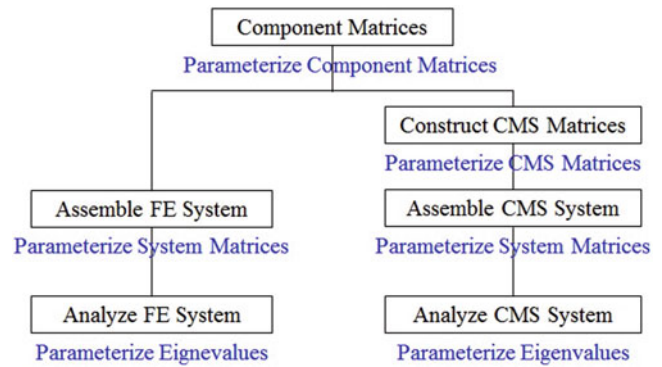
N.M. McPeck-Bechtold
University of California, Berkeley, CA, USA

Sandia National Laboratories, Albuquerque, NM 87185, USA

J.A. Fike
Stanford University, Stanford, CA 94305, USA

Sandia National Laboratories, Albuquerque, NM 87185, USA

Fig. 17.1 Two possible approaches for analyzing a system composed of several components, and the levels at which parameterized models can be constructed



expensive—dozens or hundreds of meshes must be generated and then computationally expensive finite element solutions run. The cost of man hours required for generation of several meshes and the computational cost to run several solutions often puts thorough exploration of uncertainty out of reach. One way to reduce the costs of such a study is to develop an efficient parameterized reduced order model (PROM) of the system [1–4].

Reducing the size of the model can be done by using the Craig–Bampton (C–B) Component Mode Synthesis (CMS) method [5]. This method reduces the FE model from its full degree of freedom (DOF) size to a smaller size based on the number of interface DOF between components in the system and number of retained fixed interface normal modes required to sufficiently describe the component and system dynamics of interest. While CMS still requires a full DOF FE solution to determine the component fixed interface normal modes, once this is done the cost of subsequent analyses using this reduced component can be significantly reduced.

Parameterization can be applied at several levels of the model development. Say a model is comprised of multiple components. Figure 17.1 shows the various stages at which a model can be parameterized. This work deals with parameterization of the system matrices, parameterization of the CMS system matrices and parameterization of the eigenvalues of the full DOF system. The parameterization can be accomplished using a finite Taylor series approximation of the component matrices (in full or reduced form) or eigenvalues and vectors. Once the component matrices at some perturbed value of a variable are approximated, the analysis proceeds as usual: assemble the system matrices using the component matrices, solve the eigenvalue problem. The results can then be used to explore the system’s modes or get some frequency or time dependent response to input loading. By parameterizing the reduced order CMS matrices, the computational cost of performing the system eigen solution is drastically reduced.

This paper presents methods for parameterizing component matrices and eigenvalues using a finite Taylor approximation. Then, the methods are applied to a finite element model of a two-component beam. Next, a comparison of the parameterization methods for perturbations in several different model variables is presented. Finally, conclusions are presented.

17.2 Parameterization Methods

As described previously, the parameterization can be performed at several stages of the analysis:

- Parameterization of the full DOF component matrices
- Parameterization of the reduced order CMS component matrices
- Parameterization of the eigenvalues and vectors output from a full DOF solution

This list is in order of decreasing computational cost. Parameterization using a finite Taylor approximation requires derivatives of the component matrices. Approximating these derivatives requires the analysis of the system at a few points in the parameter space. However, once the system is analyzed at these few points the system can be approximated at any other point in the parameter space using the Taylor approximation of the matrices.

An n -th order Taylor series approximation of some function, $f(x)$, about a nominal point, a , is written [6]

$$\begin{aligned}
 f(a+h) = & f(a) + f'(a)(x-a) + \frac{f''(a)}{2!}(x-a)^2 + \frac{f'''(a)}{3!}(x-a)^3 \\
 & + \dots + \frac{f^{(n)}(a)}{n!}(x-a)^n.
 \end{aligned} \tag{17.1}$$

It can be seen that truncating this to a lower order, say fourth, would require computing the fourth derivative of $f(x)$. A higher order series provides a better approximation to the function but higher order derivatives are required. The required derivatives can be approximated using the Finite Difference (FD) method. A central FD to approximate the first derivative of $f(x)$ to second order accuracy is written as [7]:

$$f'(x) \approx \frac{f(x+h) - f(x-h)}{2h}. \quad (17.2)$$

Higher-order derivatives and higher order accuracy can be obtained by using more points. The points used in the calculation of derivatives will be referred to as the “calibration” point and span a range above and below the nominal parameter value that will be referred to as the “calibration range”. Note, in the case of approximating derivatives of component matrices, each “point is a component matrix and so additional accuracy obtained by using a higher-order approximation comes at the expense of requiring the generation of additional component matrices (and therefore additional meshes, simulation runs, etc.). In this work a fourth order Taylor approximation is used, requiring fourth derivatives. Even at the lowest accuracy (second order), the fourth derivative FD approximation requires five points:

$$f^{(n)}(x) \approx \frac{f(x-2h) - 4f(x-h) + 6f(x) - 4f(x+h) + f(x+2h)}{h^4}, \quad (17.3)$$

where the five full DOF simulations are made at the perturbation points of the nominal, $x = x_n$, and two points above and below the nominal, $x_n - 2h$, $x_n - h$, $x_n + h$, $x_n + 2h$, where h is the perturbation step size. In the case of parameterization of the eigenvalues or vectors, the “point required for the approximation of derivatives are eigenvalues and vectors of a system at five perturbation values. It is perhaps obvious that each of the five mesh points used to estimate the derivatives must be similar—that is—they must have the same number of DOFs in the same order for the calculation to make sense. When the parameterized variable is geometric, it can be difficult to generate several meshes of different size or topology and guarantee they are similar. However, in order to be used for the computation of derivatives the meshes for several different lengths have to be similar. If the component matrices are different sizes, there is no way to compute the derivatives. Similarly, if the meshes do not have DOFs in the same order in each perturbation mesh, then the derivatives, while possible to calculate, would be nonsensical.

17.2.1 Analysis Process

The process of parameterizing using a fourth order Taylor approximation using the three methods is described as follows.

17.2.1.1 Parameterizing Full-DOF Component Matrices

- Generate meshes and full DOF component matrices at five parameter values (nominal and two above and below).
- Compute derivatives (first through fourth order) for the component matrices.
- For each parameterized variable value of interest, estimate the component matrices using a Taylor approximation using the calculated derivative approximations.
- Assemble the system using the component matrices for further analysis (e.g. eigen solution).

17.2.1.2 Parameterizing C–B CMS Component Matrices

- Generate C–B CMS matrices of the full DOF component matrices at five parameter values.
- Compute derivatives for these reduced order component matrices.
- For each parameterized variable value of interest, estimate the CMS component matrices using a Taylor approximation using the derivatives of the CMS matrices.
- Assemble the system using the component matrices for further analysis.

17.2.1.3 Parameterizing the Eigenvalues and Eigenvectors

- Generate full DOF component matrices at five parameter values.
- Compute the eigenvalues and vectors for each of these five models.
- Compute derivatives of these eigenvalues and vectors.
- For each parameterized variable of interest, estimate the eigenvalues and vectors using a Taylor approximation using the derivatives of the eigenvalues and vectors.
- Use the estimated eigenvalues and vectors either directly (modal) or in a subsequent analysis (e.g. modal transient).

17.3 Application of Parameterization Methods to an Example Finite Element Model

To demonstrate the parameterization methods described above and explore the accuracy when parameterizing on different types of variables a finite element model was developed. The system model is composed of two identical steel beams (Beam 1 and Beam 2) connected through a lap joint and connected with three bolts. The beam system is analyzed in a free-free condition. Figure 17.2 is a diagram of the beam system and Fig. 17.3 shows the mesh. Matrices of each of the two component beams are parameterized in full DOF and reduced order CMS form. While this model is of simple form, it is meshed such that the DOF count was non-trivial; the system matrices are 18576 by 18576 (6,192 nodes with 3 DOF each). A modest model size was chosen to show that these methods can be applied to “real” models.

To study the effects of parameterized variable type on the quality of the resulting approximated system, several variables of the beam components are parameterized: length, thickness, density, and Young’s modulus. Note that parameterizing the density and modulus do not require a change of mesh while parameterizing the length and thickness do require a new mesh for each of the five points used in the derivatives calculation. The parameterization range was chosen to be quite high: plus or minus 25 % of the nominal value for each variable except the length which uses a range of plus or minus 20 %. The calibration range, the range parameter values used for the computation of derivatives, is chosen as something smaller than the full range: plus or minus 15 %. This allows for insight into how the method works to extrapolate component matrices. This range is perhaps much larger than would normally be explored in the context of manufacturing uncertainty, but is chosen to explore the method over a very wide perturbation range, as would be necessary for design optimization. Predicted eigenvalues from each method are compared with the eigenvalue results from a solution of a full DOF model at each perturbation value.

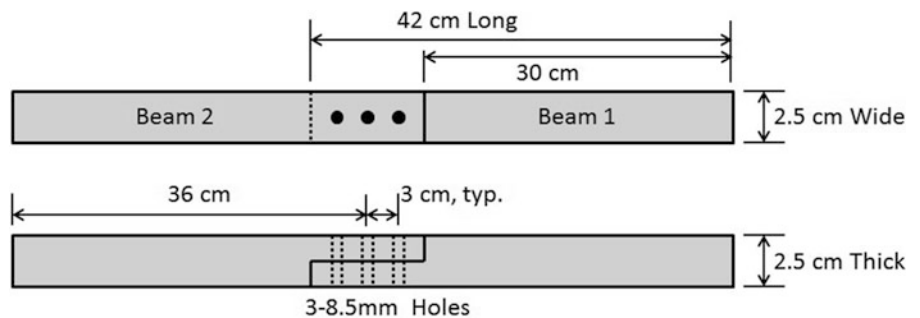


Fig. 17.2 Beam system composed of two components (Beam 1 and Beam 2) joined with three bolts

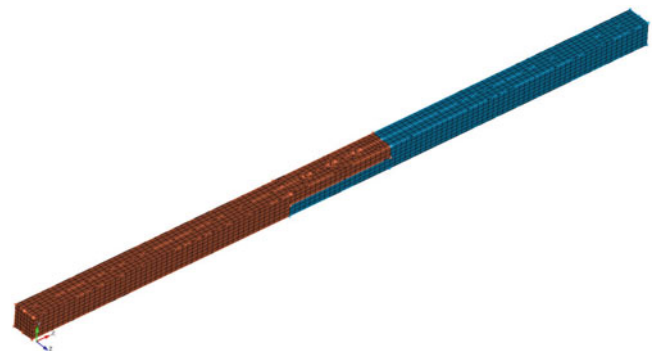


Fig. 17.3 Beam system Hex mesh

17.4 Discussion of Results

The various methods are compared by parameterizing the model in four variables: length, thickness, density and Young’s modulus and comparing the predicted eigenvalues of similar modes. With changes to parameters, the order of modes can change—mode 1 of the nominal model could shift to mode 2 of a perturbed model. To account for this, an algorithm was developed to identify modes similar to those of the nominal model using a modal assurance criteria (MAC) calculation [8,9]. The mode shapes of the nominal parameter value, full DOF FE solution are compared against the mode shapes of all the other perturbed models. The algorithm simply grabs the mode in the perturbed model that has the highest MAC value for a given mode in the nominal model. Then, the eigenvalues and vectors of the perturbed model are re-ordered to be in same order as the nominal model.

Figure 17.4 shows the comparison of the eigenvalue predictions of the three parameterization methods for the first four flexible modes. The other two curves, labeled “sweep” are the eigenvalue predictions using a full DOF and CMS solution at each perturbation value across the entire range. The full DOF “sweep” curve is considered the “truth” model to which the other methods are compared. Figure 17.5 shows the comparison more clearly by looking at the predicted frequencies of the first mode and the percent error relative to the “truth” model. It appears that the all of the parameterization methods work

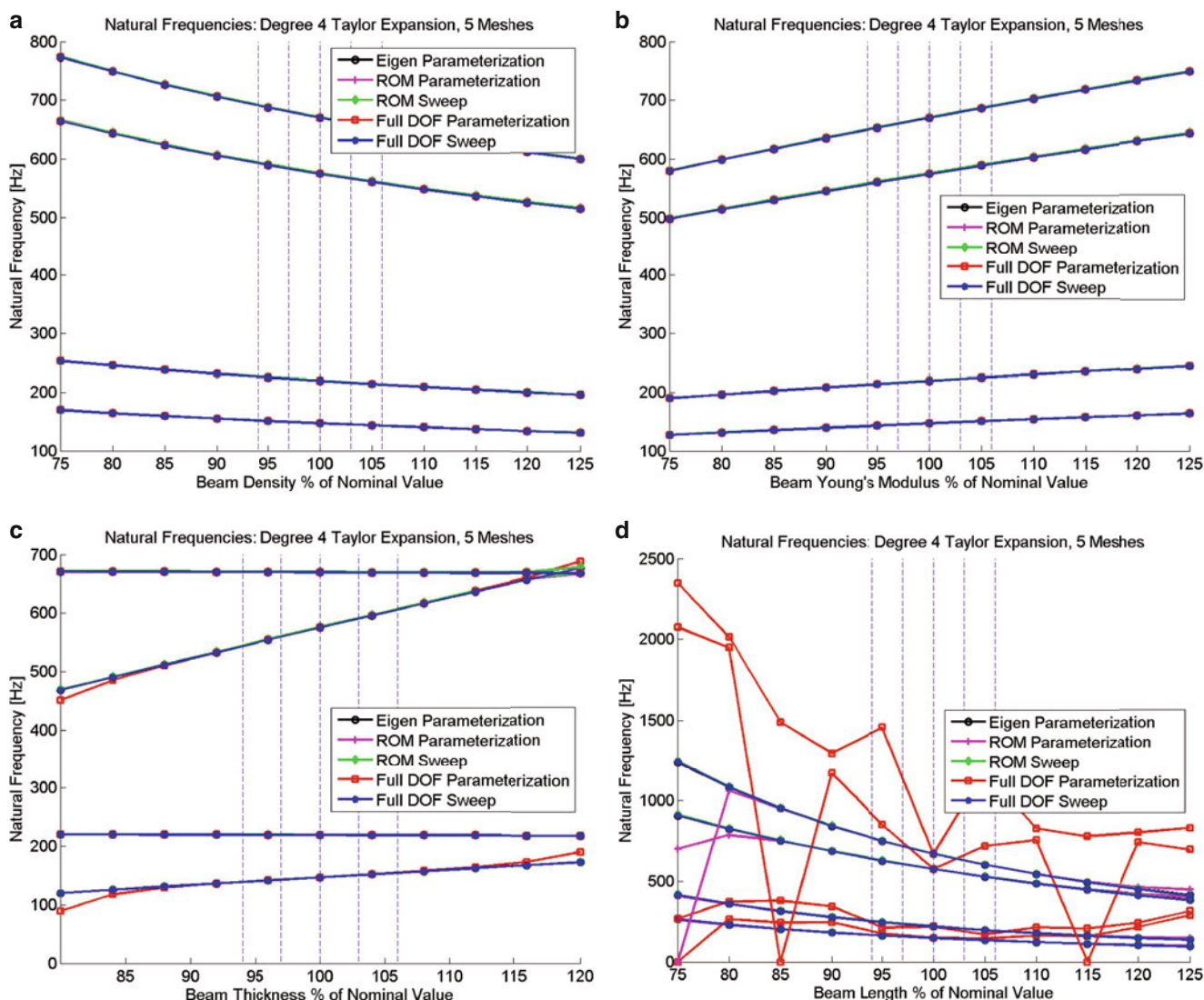


Fig. 17.4 The effects on the first four eigenvalues of the different parameterization methods for several different types of variables. *Vertical dashed lines* indicate the five parameter values used for computing derivatives. (a) Variations in density; (b) variations in Young’s modulus; (c) variations in thickness; (d) variations in length

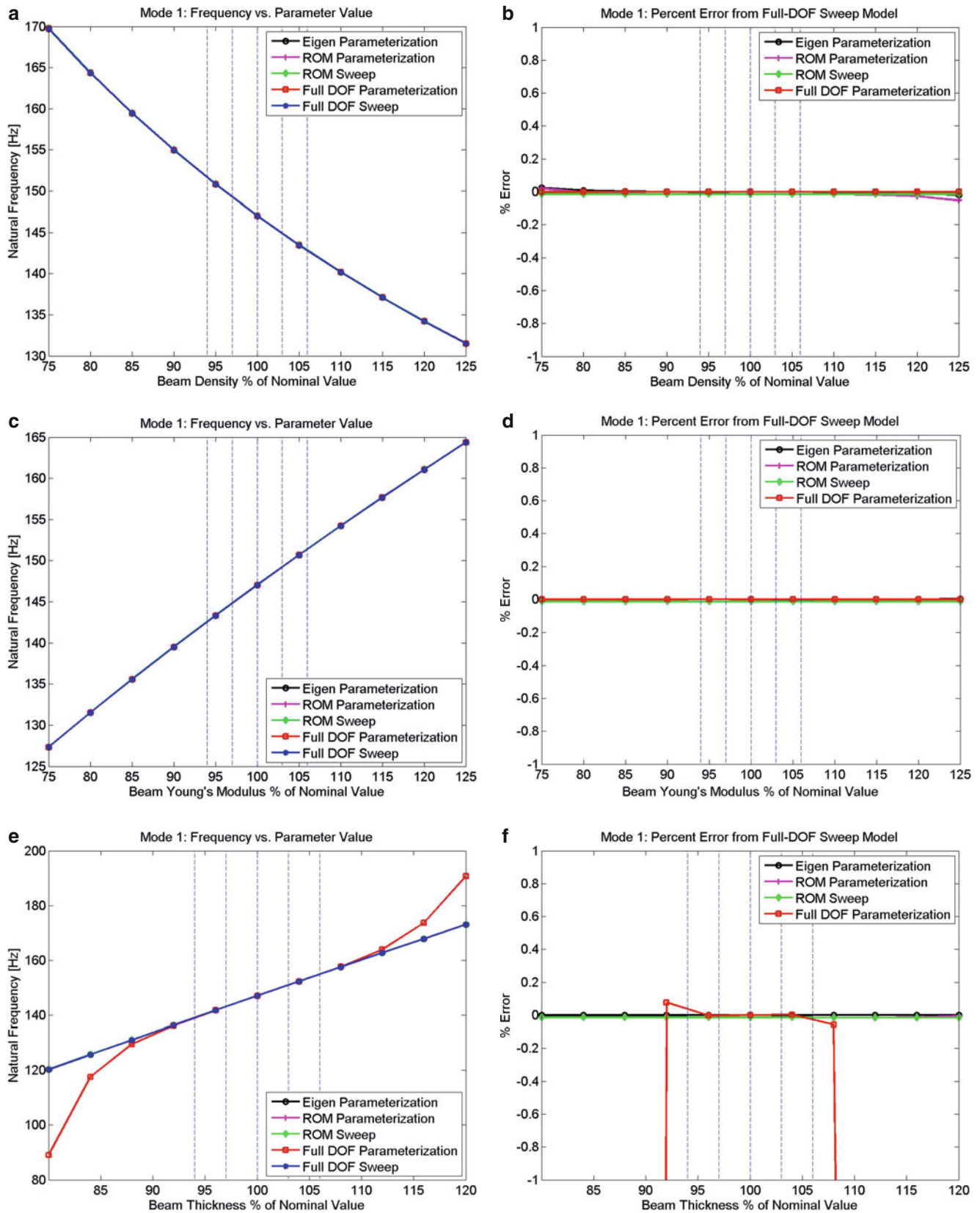


Fig. 17.5 Effect of parameter perturbations on the first mode along with percent error from the full DOF, truth solution. *Vertical dashed lines* indicate the five parameter values used for computing derivatives. (a) Mode 1 frequency: variations in density. (b) % error: variations in density. (c) Mode 1 frequency: variations in modulus. (d) % error: variations in modulus. (e) Mode 1 frequency: variations in thickness. (f) % error: variations in thickness

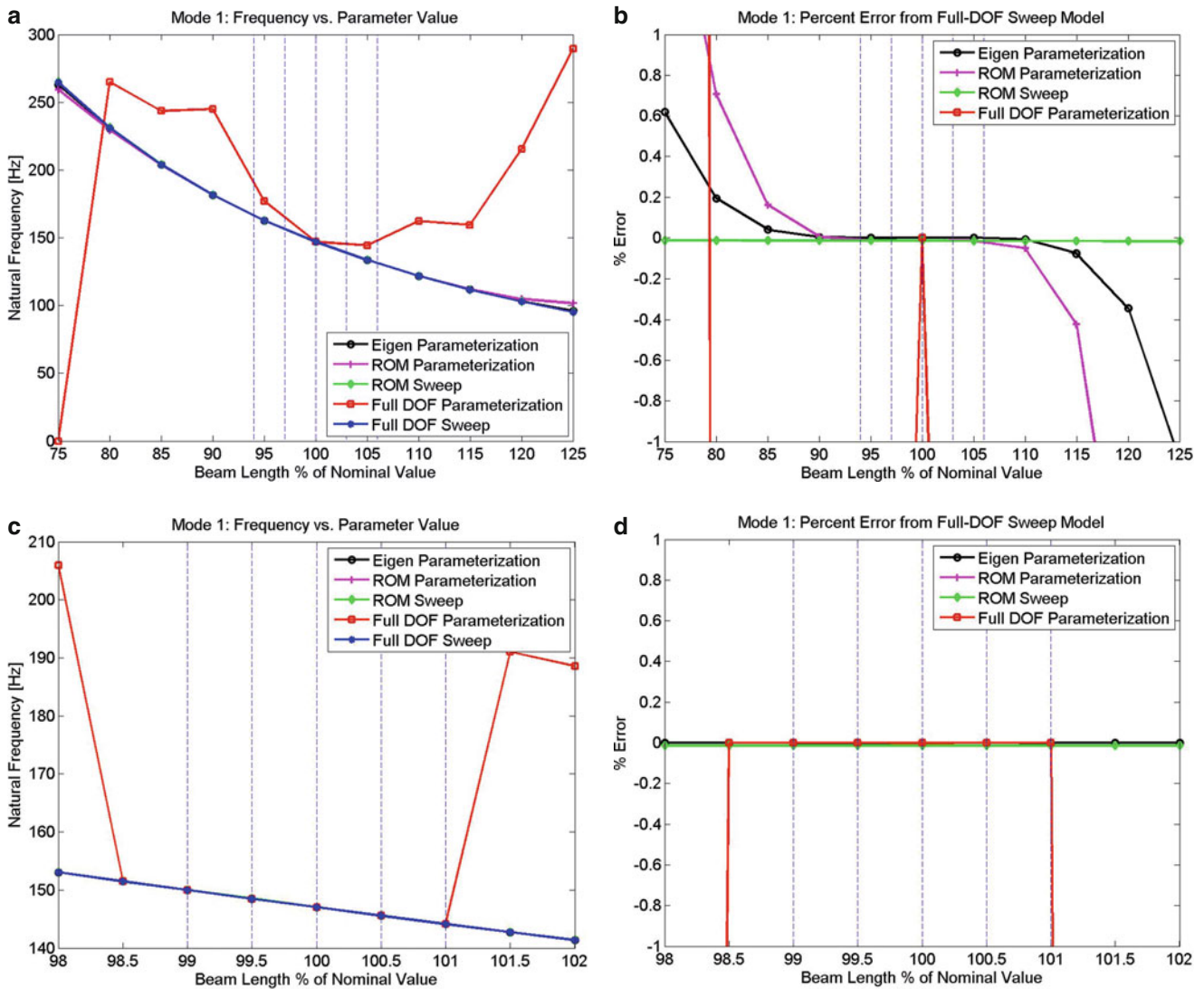


Fig. 17.6 Effect of change of length on the first mode along with percent error from the full DOF, non-parameterized solution for a wide (a) and (b) and narrow (c) and (d) parameter range. Vertical dashed lines indicate the five parameter values used for computing derivatives. (a) Mode 1, wide range: variations in length. (b) % error, wide range: variations in length. (c) Mode 1, narrow range: variations in length. (d) % error, narrow range: variations in length

quite well when modifying the density or Young’s modulus, even over a very wide perturbation range and even where the parameter value is far outside the calibration range. This makes sense as the modulus and density affect the mass and stiffness matrices uniformly and linearly. Variations on the thickness appear quite good near the calibration range. Variations in the length, however, produced eigenvalue predictions far from the truth model—even within the calibration range. This is an odd result that may have to do with the difficulty in guarantying a similar mesh at each of the five calibration points and will be the subject of further study. To explore this further, a much smaller perturbation and calibration range of $\pm 2\%$ and $\pm 1\%$, respectively is used for the length parameterization. Results of this narrower range are then compared with the original, wide range, Fig. 17.6. With the narrower ranges, length changes that occur within the calibration range are much closer to the truth model and even match well just outside the calibration range.

In terms of savings in computation, the CMS component matrices were reduced to just 64 by 64, down from 18576 by 18576. Table 17.1 compares the computational cost of three methods: the “traditional” method of a full DOF simulation each perturbation point of interest versus two of the proposed methods: parameterizing the CMS matrices and parameterizing

Table 17.1 Time required to solve for eigenvalues starting with full DOF system matrices and the full DOF sweep versus the parameterized methods for different numbers of perturbations

| Solution times (s) | | | | | |
|---------------------|---------|----------|------------|--------------|---------------|
| # Perturbations | 1 value | 5 values | 100 values | 1,000 values | 10,000 values |
| Full DOF sweep | 2.2 | 11.0 | 220.0 | 2,200.3 | 22,003.3 |
| Parameterized CMS | 11.0 | 11.2 | 14.3 | 44.3 | 344.1 |
| Parameterized eigen | 10.7 | 10.7 | 11.4 | 18.1 | 84.3 |

the eigenvalues directly. Here, it is assumed the component or system matrices have already been generated and the computational time required is only that to load matrices, compute eigen solutions, and perform the parameterization. Additional time would be required—for each mesh—to generate the system or component matrices in the case of the full DOF sweep. When only looking at a few perturbation points, there is some additional cost of parameterizing the CMS matrices or eigenvalues; it takes some additional time to compute the matrix derivatives, solve the reduced order eigenvalue problem, etc. However, once the parameter space gets larger than around six points, it becomes advantageous to use one of the parameterization methods. When the number of perturbation points is large the savings are tremendous. Computation time for predicting eigenvalues for additional perturbation points using the CMS or eigen parameterization methods becomes trivial while maintaining all the system dynamics of interest.

17.5 Conclusions and Future Work

Reducing the costs of performing a many finite element simulations of variations of a nominal model will allow for more thorough exploration of the effects of uncertainty. The goal of this work is to demonstrate a method by which uncertainty in system variables could be implemented in an efficient manner via parameterization of different forms of the system matrices or eigenvalues. The three different methods of parameterizing component matrices predict similar eigenvalues as a full DOF simulation at perturbation values far from the nominal value for changes in density and Young's modulus. Parameterizing on the two variables that require a change of mesh, thickness and length, produce good agreement inside the calibration range but degrade outside that range. Parameterizing length over a wide range produces good results for the eigen and CMS methods but poor for the full DOF method. Generally, parameterizing the eigenvalues and the CMS reduced order component matrices works well, even over a wide range. Parameterizing variables requiring a change in mesh presents some challenges in the context of these parameterization methods as the DOFs must remain similar from mesh to mesh. Parameterizing the CMS matrices gives good eigenvalue prediction while also reducing the computational cost substantially—in this case the size of the matrices dropped by more than 99%. The reduced size of these matrices also reduces the computational time for predicting eigenvalues at all points in the sampled perturbation space. Computing eigenvalue predictions using a traditional, full DOF solution at 10,000 points would take an estimated 366.7 min. Doing the same study by parameterizing the CMS matrices saves 361 min or 98.4%. Parameterizing the eigenvalues directly is even faster—saving 365 min or 99.6%. Both these methods are very fast but also provide accurate eigenvalue predictions. It should be noted that time savings in purely terms of computational time savings. Additional savings in man hours come from the fact that additional meshes for those 10,000 points do not need to be generated, everything is based off only those initial five meshes of the calibration points. Further study will focus on more efficient and accurate methods to compute derivatives of the system matrices as well as further exploration into the relationship between prediction accuracy and the perturbation/calibration range ratio. Extending this method to predict responses of a real system with aleatoric uncertainty is natural and would require only specific selection of the calibration and perturbation points.

- Parameterizing the CMS component matrices and eigenvalues proves to be much faster than computing a full DOF solution at every perturbation point. Time savings become very large even for modest sample sizes.
- Using the proposed methods, man hours required for an analysis are drastically reduced because only a small subset of the samples need unique meshes.
- The methods of parameterizing the CMS component matrices and the eigenvalues provided similar eigenvalue results to the truth model over a very wide perturbation range.

References

1. Hong S-K, Epureanu BI, Castanier MP (2012) Joining of components of complex structures for improved dynamic response. *J Sound Vib* 331(19):4285–4298
2. Hong S-K, Epureanu BI, Castanier MP (2013) Next-generation parametric reduced-order models. *Mech Syst Signal Process* 37(1–2):403–421
3. Kammer DC, Nimityongskul S (2011) Propagation of uncertainty in test-analysis correlation of substructured spacecraft. *J Sound Vib* 330: 1211–1224
4. Kammer DC, Krattiger D (2013) Propagation of uncertainty in substructured spacecraft using frequency response. *AIAA J* 51(2):353–361
5. Craig RR, Kurdila AJ (2006) *Fundamentals of structural dynamics*, 2nd edn. Wiley, New York
6. Kreyszig E (2006) *Advanced engineering mathematics*, 9th edn. Wiley, New York
7. Wolfram mathworld: finite difference (2013). <http://mathworld.wolfram.com/FiniteDifference.html>. Accessed 23 Oct 2013
8. Allemang RJ (2003) The modal assurance criterion - twenty years of use and abuse. *Sound and Vibration Magazine*, 14–21. <http://www.sandv.com/aug03.shtml>
9. Pastor M, Binda M, Harcarik T (2012) Modal assurance criterion. In: *Procedia engineering, MMaMS*, pp 543–548

Chapter 18

Application of a Novel Method to Identify Multi-axis Joint Properties

Scott Noll, Jason Dreyer, and Rajendra Singh

Abstract This article is motivated by the widespread use of shaped elastomeric body mounts that undergo broadband, multi-axis loading; whereas often in application, the principal direction mount properties are measured separately at single frequencies. An inverse method is applied to a new experiment that is constructed with an elastic metal beam end-supported by two elastomeric mounts. Due to a judiciously selected attachment location relative to the neutral axis of the beam as well as the shape of the mount, the in-plane transverse and longitudinal beam motions are found to be coupled. This method utilizes the sensitivity of the beam modal parameters, including natural frequency, mode shapes, and damping ratio, to support properties at each end to identify the multi-axis mount properties. The dynamic stiffness and loss factors of the elastomeric mounts are directly measured in a commercial elastomer test machine and agreement is found between the inverse and direct methods at small displacements. Further, this article helps provide insight into multi-axis properties with new benchmark experiments on off-the-shelf mounts that permit comparison between inverse system and direct component identification methods of the dynamic multi-axis elastomeric mount properties.

Keywords Joint identification • Experimental dynamics • Stiffness coupling • Elastomer properties • Beam structures

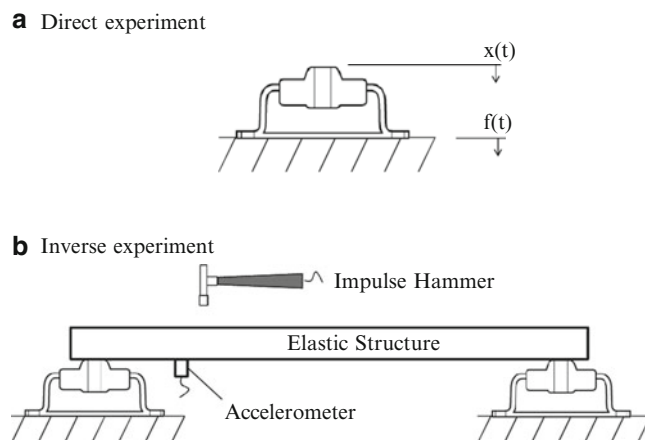
18.1 Introduction

Elastomeric joints are widely used in vehicle isolation systems and their geometries are shaped to provide favorable properties in certain directions based on the diagonal terms [1,2]. Nonetheless, non-diagonal (coupling) terms are often unknown though they are intrinsic to the design of complex automotive assemblies [3,4]. Elastomeric joints present many challenges in modeling such as amplitude and frequency dependent properties. Direct measurement of the multidimensional dynamic properties of practical elastomeric joints is not possible, and these properties are further complicated when an elastomeric component is integrated into a sub-system assembly. Typically, the dynamic properties of assemblies may differ from those of components due to preload and boundary condition effects; therefore, there is a need to develop improved experimental methods to examine these issues [4]. Identification methods that utilize computational and experimental modal analyses may be integrated into some applications as long as the structures behave in a linear manner [5,6]. For instance, Kim et al. [7] used a modal-based technique to characterize the dynamic stiffness of beam supports, each modeled by a lumped transverse spring. This prior method [7] has recently been extended by Noll et al. [8] to include the identification of multidimensional matrices. The method uses the physical system matrices developed from a discretized model (lumped parameter or finite element) without joints, and then measured natural frequencies, modal loss factors, and mode shapes are utilized to extract the joint parameters. This article provides an overview of an inverse identification method proposed recently by the same authors [8] and compares the results with the dynamic stiffness properties measured using a conventional direct test method.

S. Noll (✉) • J. Dreyer • R. Singh
The Ohio State University, 219 W. 19th Avenue, Columbus, OH 43210, USA
e-mail: noll.34@osu.edu

Fig. 18.1 Schematic of the direct and inverse experiments:

(a) elastomeric mount loaded in compression and excited by a displacement input; (b) elastic beam is end supported by two mounts, where each is bolted to the beam; it is excited by an impulse hammer



18.2 Problem Formulation

The scope of the inverse test is limited to an elastic beam structure connected to ground through two elastomeric joints, where each joint is comprised of two “off-the-shelf” mounts. The assembled system is assumed to be linear time invariant and self-adjoint; the damping of the elastomeric joints is structural, and the beam is assumed to be proportionally viscously damped. Further, the joint mass is known *a priori*, and the dynamic properties of a joint can be represented at a point by structural damping \mathbf{h} and stiffness \mathbf{k} matrices. The specific objectives of this article are as follows. 1. Design a tractable inverse beam experiment that allows a comparison with the direct measurement of the elastomeric component. 2. Use a recently extended inverse formulation of the authors [8] to identify fully populated joint dynamic matrices given limited modal measurements on the beam mount system. 3. Compare the dynamic joint properties identified with inverse and direct test methods.

The experiments are illustrated in Fig. 18.1; elastomeric mounts (Fig. 18.1a) are characterized in a single direction in a direct test method; An elastic beam system is supported by the same elastomeric mounts at each end offset from the neutral axis of the beam allowing for multi-axis loading. The offset attachment of the mounts introduces kinematic coupling to the structure which couples the slope $\theta(x,t)$ and longitudinal $u(x,t)$ motions of the beam. The modal parameters of the unconstrained (free-free) beam are selected so that the first elastic flexural mode is representative of the first elastic mode of real-world automotive subframe structures, say between 100 and 200 Hz. Further, the first three rigid body and three elastic modes (up to 1,024 Hz) are examined, as both rigid and elastic modes are of concern in practical assemblies. Elastomeric mounts are intentionally selected even though they exhibit excitation amplitude and frequency dependent properties, as well as sample to sample variations (say about 10–15 %).

18.3 Direct Joint Identification

The direct test employs a uniaxial hydraulically actuated, close loop servo-controlled elastomer test machine. A sinusoidal displacement, $x(t)$, is applied to the top side of the specimen, and the transmitted force, $f(t)$, at the bottom of the specimen is measured at the same frequency. The dynamic stiffness under a specified mean load is defined as $\tilde{k}_d(\omega) = \frac{f}{x} e^{i\delta} = |\tilde{k}_d| \angle \delta = k + ih = k(1 + i\gamma)$, where δ is the loss angle and $\gamma = \tan \delta$ is the loss factor. The elastomeric mount is characterized in a single direction as depicted in Fig. 18.1a at an initial preset of 0.5 mm from 5 to 200 Hz at 5 Hz increments. The peak-to-peak amplitude is specified at 0.1, 0.05, or 0.01 mm.

18.4 Inverse Joint Identification

The multidimensional properties of the mounts are inversely identified from the experiment depicted in Fig. 18.1b including both stiffness and structural damping. The methodology combines experimental and modeling information in order to extract the joint properties. The flow-chart of the method is depicted in Fig. 18.2 that conceptually displays the procedure from an applications viewpoint. Rigorous mathematical details given in the article by Noll et al. [8]. The parameters of the inverse

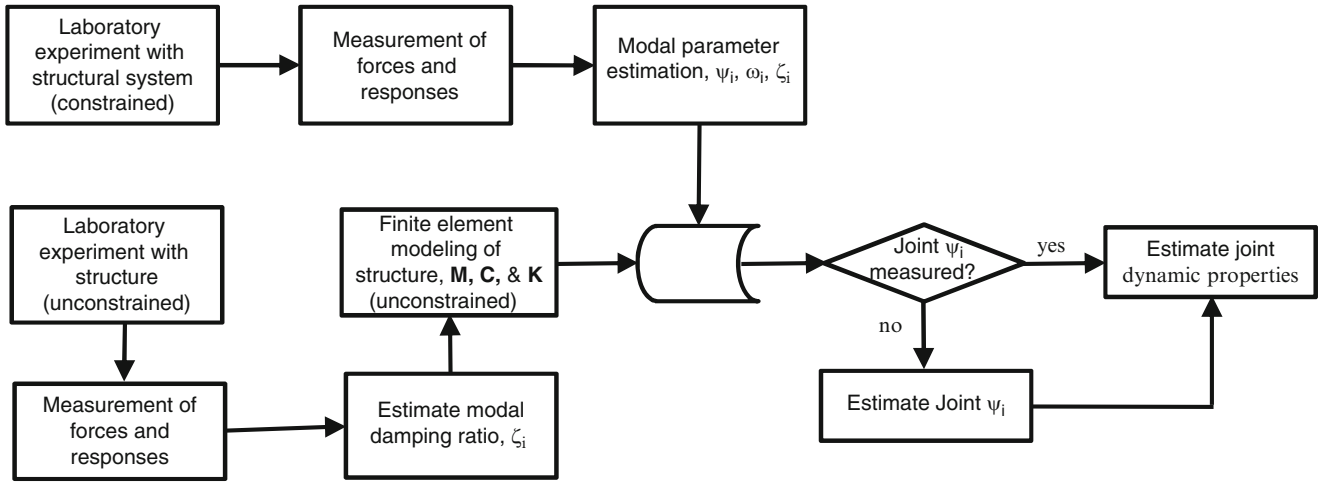


Fig. 18.2 Flow-chart of the inverse joint identification method. Refer to Noll, et al. [8] for mathematical details

beam experiment are chosen in the context of automotive structural applications. The elastomeric mounts are selected to have similar stiffness properties to automotive bushings as well as the ratio of joint to structure stiffness. To maintain the lumped joint stiffness assumption, the ratio of the contact surface dimension to beam length is kept below 0.05. With these guidelines, a steel beam (with Young's modulus, $E = 207$ GPa, Poisson's ratio, $\nu = 0.3$, and mass density, $\rho = 7,850$ kg m⁻³) is selected. The beam is 914 mm in length (L) with a rectangular cross-section of 25.4×50.8 mm where the thickness is 25.4 mm in the y direction for the desired flexural stiffness in the experiment. The beam is supported near each end by elastomeric mounts. The elastic center of the mount is intentionally offset from the neutral axis of the beam to ensure participation of multi-axis loading of the mount.

The modal experiment is conducted for the inverse beam as depicted in Fig. 18.1 with the accelerometer positioned below point 3 (corresponds to node 3 of Fig. 18.3) and the roving impulse hammer technique is employed, with force inputs at points 1, 3–9, and 11 in the transverse direction and at points 1 and 11 in the longitudinal (x) direction. Ten impacts at each location are averaged to minimize random error in the accelerance $\tilde{A}_{ij}(\omega)$ measurements. For this work, a polyreference least-squares complex frequency-domain method is utilized where this implementation estimates the natural frequencies, damping parameters, and mode shapes in a global sense [6]. Although this measurement set results in mode shape estimates at each location, only the results near the joint locations are utilized in the identification procedure, e.g. at joint I, the mode shape components at points 1 and 3 are used. The mode shape components are averaged in the longitudinal (x) direction in both magnitude and phase.

18.5 Computational Model

The computational model is comprised of 10 beam finite elements with lumped dynamic stiffness matrices at nodes 2 and 10 as depicted in Fig. 18.3. A two-node Timoshenko beam element is superposed with a longitudinal rod element to generate a two-node six degree of freedom element. This formulation assumes that elastic longitudinal and beam bending are uncoupled. The work of Friedman and Kosmatka [9] contains a complete derivation of the finite element stiffness and mass matrices for a Timoshenko beam. Each mount in the inverse experiment has a transverse eccentricity ε from the neutral axis of the beam from the beam's nodal coordinate system as shown in Fig. 18.3a. The eccentricity introduces a form of kinematic coupling that must be considered such that a suitable transformation can be made from the local coordinate system of the cylinder to the beam's nodal coordinate system. A mount exhibits a diagonal stiffness matrix at the component's elastic center as $\mathbf{k}_{mount} = \text{diag} [k_t \ k_l \ k_\theta] (1 + i\gamma)$, where k_t is the transverse stiffness, k_l is the longitudinal stiffness, and k_θ is the rotational stiffness. Assuming that the point stiffness at the elastic center follows a rigid connection to the beam neutral axis, the effective stiffness matrix of the mount in the beam nodal coordinate system can be computed via the following transformation as

$$\mathbf{k}_{eff} = \mathbf{T}_\varepsilon \mathbf{k}_{mount} \mathbf{T}_\varepsilon^{-1} = \begin{bmatrix} k_t & 0 & \varepsilon k_l \\ 0 & k_l & 0 \\ \varepsilon k_l & 0 & k_\theta + \varepsilon^2 k_l \end{bmatrix} (1 + i\gamma); \quad \mathbf{T}_\varepsilon = \begin{bmatrix} 1 & 0 & 0 \\ 0 & 1 & 0 \\ -\varepsilon & 0 & 1 \end{bmatrix}. \quad (18.1)$$

Fig. 18.3 Computational beam model with 10 elements and 11 nodes. Lumped stiffness elements are attached at nodes 2 and 10

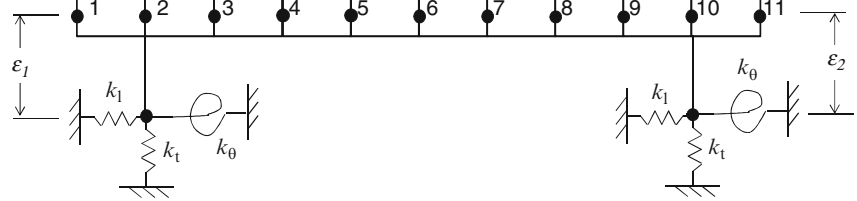
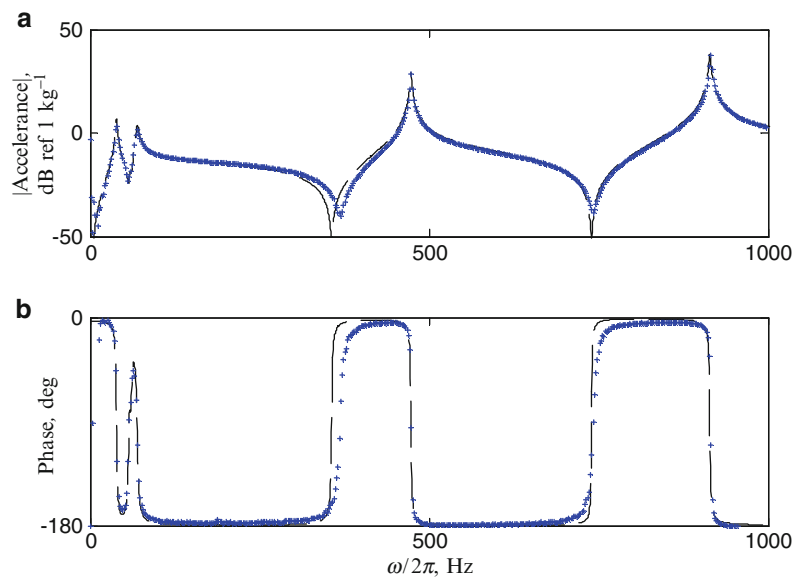


Table 18.1 Comparison of natural frequencies between the experiment and theory

| Mode index, r | Experiment, $\omega_r/2\pi$ (Hz) | Theory, $\omega_r/2\pi$ (Hz) | Percent difference |
|---------------|----------------------------------|------------------------------|--------------------|
| 1 | 39.1 | 39.0 | 0.3 |
| 2 | 59.2 | 59.3 | -0.2 |
| 3 | 69.4 | 69.1 | 0.4 |
| 4 | 187 | 188 | -0.5 |
| 5 | 474 | 472 | 0.4 |
| 6 | 916 | 914 | 0.2 |

Fig. 18.4 Driving point acceleration for the resonant beam experiment in the transverse direction at point 3 as displayed in Fig. 18.3: (a) magnitude; (b) phase. Key: (—) predicted using Eq. (18.2); (+) measured



18.6 Experimental Validation

After identification, the joint dynamic stiffness matrices are employed with the beam model to forward predict the natural frequencies and frequency response functions of the experiment. Table 18.1 lists the natural frequencies and the forward predictions which agree within 1 % of the experimental results for six modes of vibration captured within the frequency range of 0–1,024 Hz, including three rigid body and three elastic modes. Forward predictions of the accelerance spectra $\tilde{\mathbf{A}}(\omega)$ are computed by a direct inversion of the assembled dynamic stiffness matrices:

$$\tilde{\mathbf{A}}(\omega) = -\omega^2(\mathbf{Z}(\omega) + \mathbf{z})^{-1}\mathbf{f}(\omega). \tag{18.2}$$

The driving point comparison in Fig. 18.4 exhibits good agreement, though some regions show discrepancies most notably at the anti-resonance near 400 Hz. The direct identification of the dynamic stiffness of the elastomeric mount exhibits considerable amplitude and frequency dependence as shown in Fig. 18.5. The highest sensitivity to frequency dependence is observed below 50 Hz. The loss factor (Fig. 18.5b) is nearly constant with respect to frequency above 50 Hz; however, it decreases by one-third when the peak-to-peak amplitude of the excitation is reduced from 0.1 to 0.01 mm. A statistical analysis of the observations, curve-fitted values, and residuals is performed to establish a confidence interval for the identified stiffness matrix assuming a normal distribution and a confidence level of 95 %. A comparison of the direct and inverse dynamic stiffness is shown in Fig. 18.5. Generally, there is good agreement between the inverse tests and the 0.01 mm peak-to-peak excitation amplitude.

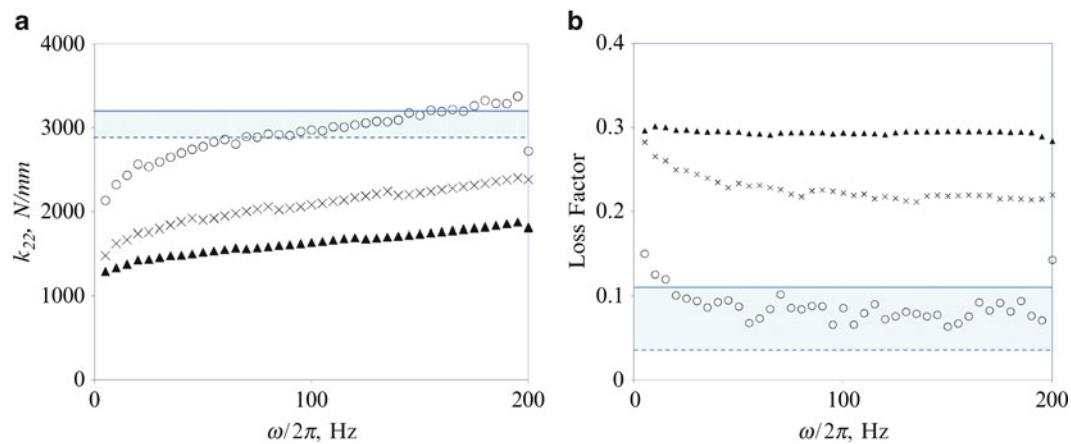


Fig. 18.5 Comparison of stiffness and loss factor identified through inverse and direct tests. (a) Stiffness (b) Loss factor Key: direct test with pk-pk amplitude of ○ 0.01 mm × 0.05 mm, and ▲ 0.1 mm; ----- inverse method with 95 % confidence interval

Table 18.2 Transverse eccentricity, ε

| Method | ε , mm |
|--------------------------|--------------------|
| Inverse, Eq. 6, Joint I | 34 |
| Inverse, Eq. 6, Joint II | 20 |
| Finite element model | 26.7 |

18.7 Estimation of the Mount Elastic Center

The elastic center of the of each mount can be estimated from the inverse beam experiment by rearranging the k_{13} element of equation 1 and solving for ε as $\varepsilon = k_{13}/k_l$, where k_{13} and k_l are previously identified from the inverse experiment. For a comparison, a finite element model of the elastomeric mount is created. The purpose of this model is to locate the elastic center considering the unique geometry of the elastomeric mount and as such a number of simplifying assumptions are made. First, the elastomeric material is assumed to have no residual stress or strain. Second, at small displacements, the material can be represented as a linear elastic material with a Poisson's ratio of 0.49 which approximates the nearly incompressible behavior of elastomers. Also, the housing of the mount is rigid in comparison to the elastomer and is modeled as a fixed boundary at the housing / elastomer interface. Finally, the vertical preload due to supporting the beam is not considered. The elastic center is then systematically investigated by applying a point force in the x -direction at varying offsets in the y -direction until no gross component rotational displacement, θ , is observed. Therefore, the computed ε is the sum of one-half the thickness of the beam in addition to the offset location found in the finite element study. Reasonable agreement is found between the identified and computed location of the elastic center and is illustrated in Table 18.2.

18.8 Conclusion

This article has contributed to the state of the art by designing new experiments and methods that permit a direct comparison of inverse and direct methods including non-diagonal terms in the stiffness matrices of joints. The proposed methodology is employed to identify the dynamic stiffness properties of joints with dimension 3 in the inverse experiment consisting of an elastic beam with two elastomeric supporting elements. A forward model successfully predicts the measured modal parameters and accelerance spectra. Good agreement is found for dynamic stiffness and loss factors between the inverse and direct methods. The methods in this article are not limited to metal beam and elastomeric joint systems, but rather are applicable to a more general class of jointed assemblies. The inverse test in this article is limited to an examination of the linearized joint properties; however, the design lends itself well to incorporate different excitation levels to examine the amplitude-dependent properties of elastomers. Further, with two opposing joints, preload or displacement can be easily added without altering the system. Finally, the work has been limited to a single structure connected to ground, whereas many

real-world assemblies contain two or more substructures. Despite these limitations, this article provides valuable insights for interpreting direct component test data with modal system data even when the selected elastomer exhibits strong amplitude dependent properties.

Acknowledgments We acknowledge the member organizations such as Transportation Research Center Inc., Honda R&D Americas, Inc., and F.tech of the Smart Vehicle Concepts Center (www.SmartVehicleCenter.org) and the National Science Foundation Industry/University Cooperative Research Centers program (www.nsf.gov/eng/iip/iucrc) for supporting this work.

References

1. Lewitzke C, Lee P (2001) Application of elastomeric components for noise and vibration isolation in the automotive industry. SAE Technical Paper 2001-01-1447
2. Oh HY, Kim KJ (2009) Design of shape for visco-elastic isolation element by topological and shape optimization methods. SAE Technical Paper 2009-01-2127
3. Kim HJ, Kim KJ (2010) Effects of rotational stiffness of bushings on natural frequency estimation for vehicles by substructure coupling based on frequency response functions. *Int J Vehicle Noise Vib* 6:215–229
4. Kim S, Singh R (2001) Multi-dimensional characterization of vibration isolators over a wide range of frequencies. *J Sound Vib* 245:877–913
5. Cook RD, Malkus DS, Plesha ME (1989) Concepts and applications of finite element analysis, 3rd edn. Wiley, New York, NY
6. Peeters B, Van der Auweraer H, Guillaume P, Leuridan J (2004) The PolyMAX frequency-domain method: a new standard for modal parameter estimation? *Shock Vib* 11:395–409
7. Kim TR, Ehmann KF, Wu SM (1991) Identification of joint structural parameters between substructures. *J Eng Ind* 113:419–424
8. Noll S, Dreyer J, Singh R (2013) Identification of dynamic stiffness matrices of elastomeric joints using direct and inverse methods. *Mech Syst Signal Process* 39(2013):227–244, <http://dx.doi.org/10.1016/j.ymssp.2013.02.003i>
9. Friedman Z, Kosmatka J (1993) An improved two-node Timoshenko beam finite element. *Comput Struct* 47:473–481

Chapter 19

Experimental Identification and Simulation of Rotor Damping

Lothar Gaul and André Schmidt

Abstract The paper at hand shows how structural damping and stiffness parameters in shrunk joints can be determined by a generic joint experiment. With thin-layer elements these parameters from the joint experiment are coupled to the structures finite element model. Equivalent modal damping factors can be determined by performing a complex numerical modal analysis, by which the stability of the rotor can be tested. The two-disc rotor is examined as an application sample. This rotor consists of a shaft with two shrunk-on discs. With the above mentioned approach, and by considering structural damping added to material damping, the modal damping of the first torsional eigenfrequency is calculated and then compared to the results of an experimental modal analysis. The paper shows that the presented approach leads to a reliable approximation of the examined structure's dissipation properties. It serves as a prediction tool for the response behavior of a turbo-generator.

Keywords Finite element method • Damping • Modal analysis • Generic joint experiment • Model of constant hysteresis

19.1 Introduction

For many applications damping is the major factor when stable operating states of a rotating machine are to be identified. In order to reliably predict if the operation state of a system is stable, dissipation properties have to be considered [1, 5]. Predictive conclusions regarding stability therefore are only possible if the damping properties of a structure under consideration can be determined and then included into a numerical model as e.g. the FEM. Besides material damping, which can easily be determined from experiments or from literature, dissipation of a standardized joint is of particular importance. In metallic structures damping of joints usually outweighs material damping by one to two decades.

In order to quantitatively determine damping of joints, experimental testing needs to be developed by which properties of joints can be identified. Besides its dissipation properties also the tangential stiffness of the joint is relevant, since the structure is weakened by the joint which reduces eigenfrequencies compared to a solid connection. However, normal stiffness of joints only has minor influence on eigenfrequencies and -modes. Therefore it can simply be estimated or taken from experience. Alternatively the normal stiffness can also be determined by numerical contact analysis.

19.2 The Two-Disc Rotor as a Test Structure

The examined structure consists of a shaft with two shrunk discs (see Fig. 19.1) which will perform torsional vibrations. All pieces are made of steel. Measures such as material allowance in the contact area, surface roughness and press fit are common parameters used for turbine construction.

A FE-analysis of the contact pressure with a press fit of 0.05 % contact overlap is shown in Fig. 19.2. This results in an average contact pressure of 100 MPa; locally the pressure is as high as 150 MPa. This contact pressure corresponds to

L. Gaul (✉) • A. Schmidt

Institute of Applied and Experimental Mechanics, University of Stuttgart, Pfaffenwaldring 9, 70550 Stuttgart, Germany
e-mail: gaul@iam.uni-stuttgart.de; schmidt@iam.uni-stuttgart.de

Fig. 19.1 3-D view of the two-disc rotor

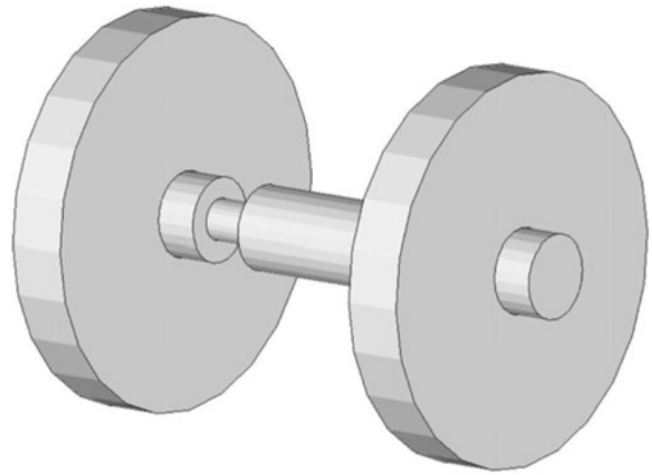
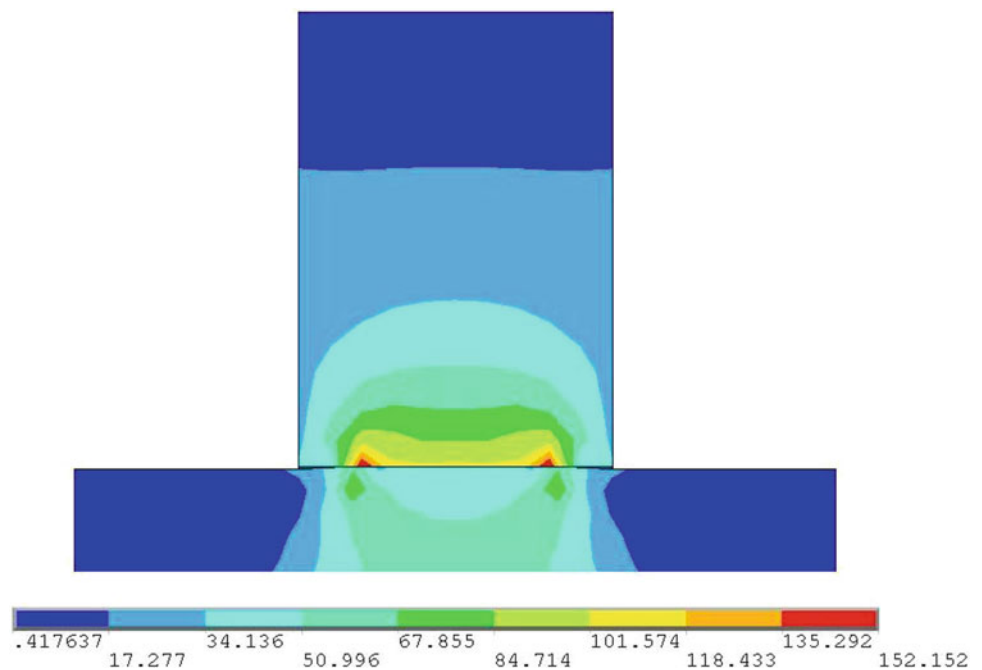


Fig. 19.2 Calculated contact pressure distribution between rotor and shrunk-on disc

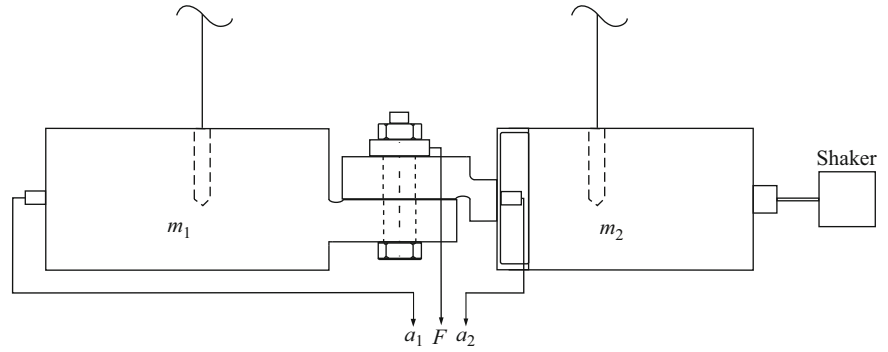


common values for rotating turbines. However, the two-disc rotor structure is examined without rotation and therefore shows the above mentioned contact pressure in a stationary state. A numerical modal analysis of the FE-model of the test structure shows that the torsional eigenfrequency is approximately 165 Hz.

19.3 Layout of the Generic Joint Experiment

Since the contact parameters between rotor and discs are known in terms of surface roughness, contact pressure and frequency, a generic experiment can be conducted in order to determine the corresponding isolated joint's parameters. Figure 19.3 shows the measurement set-up. It consists of two small contact interfaces which are pressed against each other. The normal force in the joint is controlled by a bolt and measured by a force measurement ring. An excitation of the joint in the axial direction is realized by two masses on both sides of the joint where one mass is attached to a shaker. The mass shown on the right is connected to a leaf spring, such that the set-up is a two-mass resonator. When the resonance frequency is transmitted the axial force is increased considerably. On both sides of the joint two 3-dimensional accelerometers are placed. Their signals are used for the calculation of the relative displacement and therefore also for the stiffness of the joint and its dissipation behavior (see Sect. 19.4).

Fig. 19.3 Layout of the measurement set-up for determination of isolated joint's parameters



The boundary conditions for this generic experiment are known from the examination of the two-disc rotor: the experiment should be conducted with normal pressure of about 100 MPa and an excitation frequency nearby 165 Hz. The surface roughness also corresponds to the two-disc rotor.

The size of the contact interfaces measures 30 mm × 40 mm with a 14 mm diameter drilled hole in the middle. This results in a contact area of $A = 1,046 \text{ mm}^2$, for which a bolt force of 104.6 kN is needed. The amplitude of the axial force is defined by the input signal of the shaker.

19.4 Determination of Isolated Joint's Parameters

In order to determine stiffness and damping of the joint, the resonator is suspended by two thin wires attached to the masses at their centers of gravity. The excitation frequency of the shaker is 165 Hz. The relative displacement Δx is calculated by integrating the acceleration signals twice with respect to time

$$\Delta x(t) = \iint a_1(t) dt dt - \iint a_2(t) dt dt. \quad (19.1)$$

The tangential force F_T transmitted by the joint is obtained from the product of the free suspended mass m_1 and its acceleration a_1

$$F_T(t) = m_1 a_1(t). \quad (19.2)$$

Using the results from these two time-dependent parameters, a hysteresis curve is determined (see Fig. 19.4). The area of the hysteresis curve equals the energy W_d dissipated in one period. The ratio of the energy dissipated W_d divided by 2π times the maximum potential energy U_{\max} gives the loss factor

$$\chi = \frac{W_d}{2\pi U_{\max}} \quad (19.3)$$

representing the damping in the examined joint. The slope of the hysteresis curve represents the tangential stiffness c of the joint

$$c = \frac{F_T}{\Delta x}. \quad (19.4)$$

Figure 19.5 shows several measured hysteresis curves recorded at different excitation amplitudes. The received signals are filtered in order to smoothen the curves. It can be seen that the joint's stiffness is nearly constant and the energy dissipation is small. This is due to the fact that with the chosen contact pressure and the excitation amplitudes only microslip occurs.

Fig. 19.4 Example of a hysteresis curve

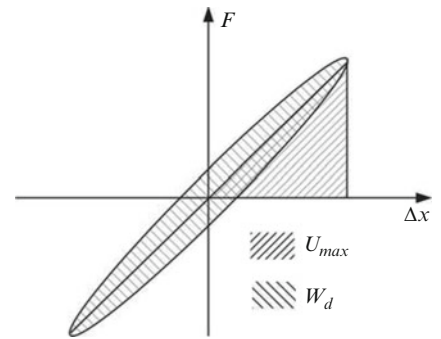


Fig. 19.5 Measured hysteresis curves

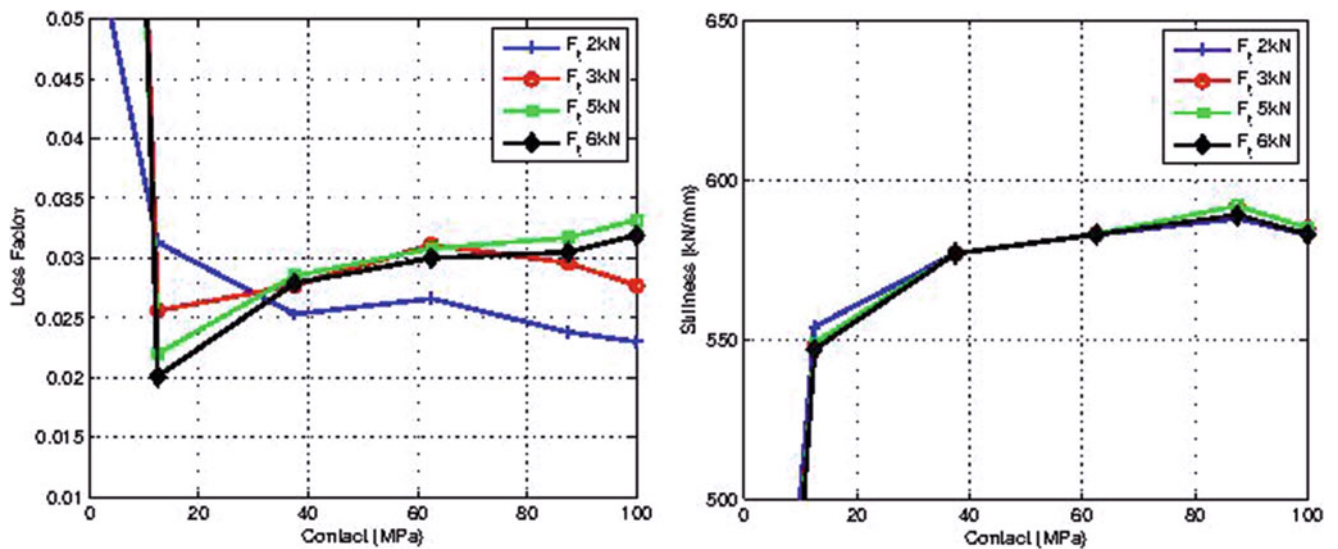
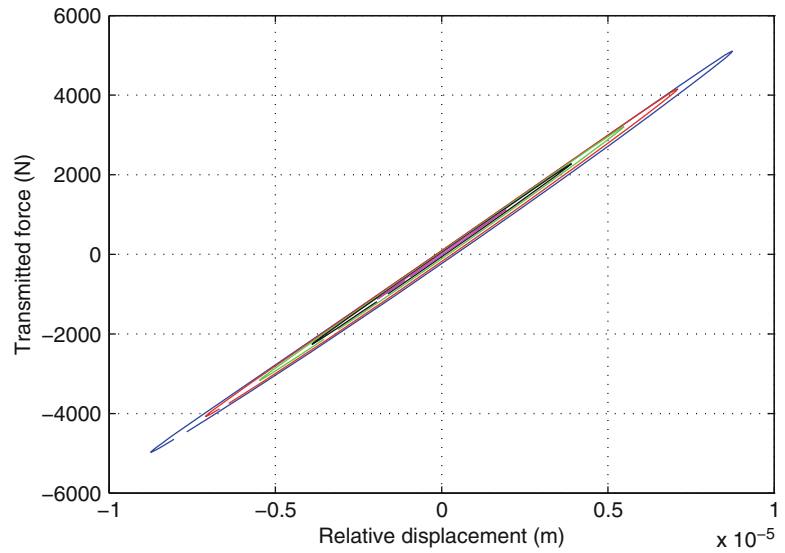


Fig. 19.6 Influence of contact pressure on loss factor and tangential stiffness

The experiment is carried out with different parameters in order to determine their influence on the parameters of the joint. In Fig. 19.6 the influence of the contact pressure on the loss factor and the tangential stiffness are shown. The excited tangential force is between 2 and 6 kN. It can be seen that above a contact pressure of 20 MPa the parameters of the joint nearly stay the same. If the contact pressure is small only macro slip occurs and the measured loss factor increases significantly, while the contact stiffness collapses.

Fig. 19.7 Influence of tangential force on loss factor

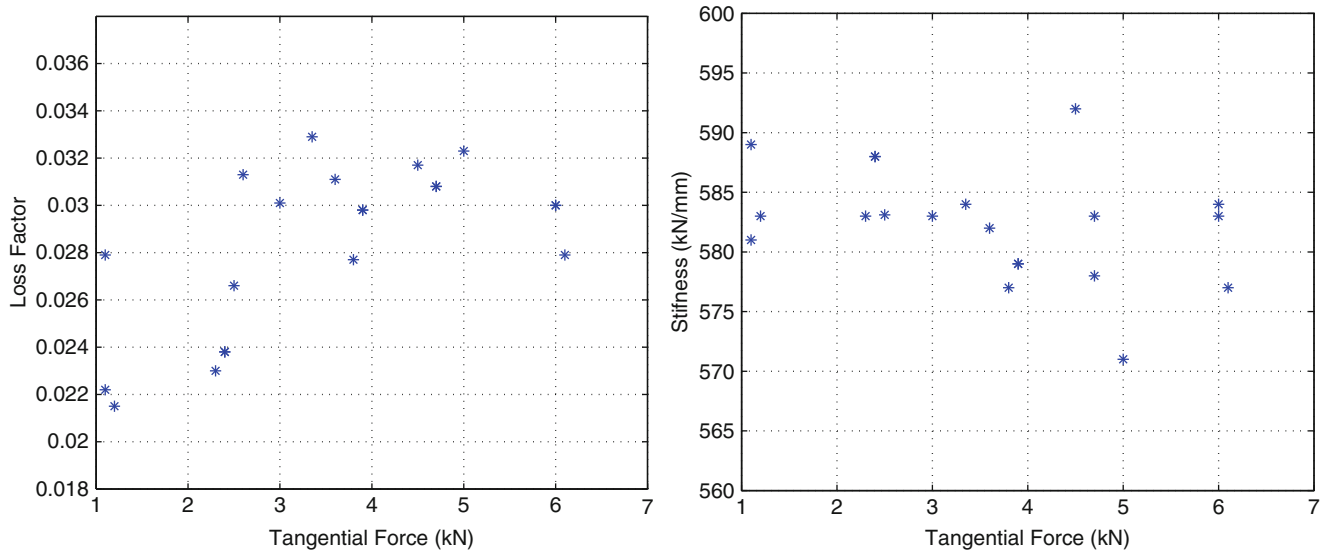
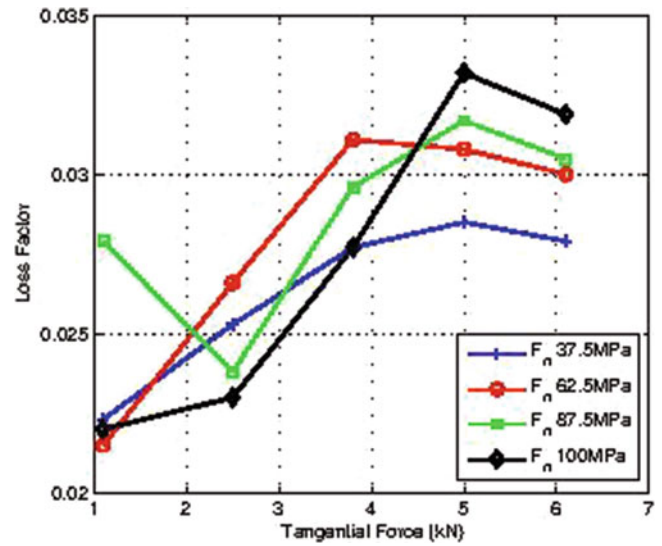


Fig. 19.8 Variation of loss factor (*left*) and tangential stiffness (*right*) measurements plotted versus different excitation levels

As shown in Fig. 19.7 an increase of the excitation force results in a moderate change of the loss factor. However, it has to be taken into account that identifying the loss factor is related to some uncertainty. An influence of the excitation force on the tangential stiffness cannot be found (see Fig. 19.5).

The influence of the surface finish is studied by changing its roughness R_z 16 to R_z 2. However, a change of the joint's parameters cannot be found.

In order to quantify the uncertainties of the measurements, the experiments are repeated a number of times with multiple reassemblies of the joint. Figure 19.8 shows exemplarily all measured results with variation of the excitation force. The result shows that the stiffness of the joint can be measured with high accuracy while the damping measurements contain a relatively high degree of uncertainty ($\pm 30\%$). The problem of precisely determining the energy dissipation in joints is also known in literature [12, 13].

The average data determined by the joint measurements are:

$$\chi \approx 0.028 \quad c \approx 580 \text{ kN/mm.} \tag{19.5}$$

19.5 Two-Disc Rotor Measurements

The experimental test set-up for measurements on the two-disc rotor is shown in Fig. 19.9. The rotor is held by two cone-shaped supports in a lathe. This set-up minimizes the losses on the boundaries at the same time allowing torsional vibration of the rotor. A small cut-out at one disc allows for torsional excitation. Modal analysis with two accelerometers and impact excitation is performed. Later, additional measurements at the driving point are made.

The FRF is shown in Fig. 19.10. It can be seen that the torsional mode at 162 Hz is excited. The measurements are done with a block size of 28.800 points and a limit frequency of $f_{\max} = 1,125$ Hz. The measurement time per sample is 26 s. During the measurement time the acceleration signal decayed to noise level.

The amplitude decay measurement is shown in Fig. 19.11. Three parameter identification methods are used to obtain damping and frequency of the torsional mode. At first, Me'Scope software is used to extract the damping from all measured data. Then, the measurements are transferred to MatLab and the damping is estimated by half-power method. Finally, an exponential function is curve-fitted to the amplitude decay measurements (Fig. 19.11). The extracted modal damping factors ξ range from 0.024 to 0.029 % of critical damping, with amplitude decay measurements showing a better consistency and a value of $\xi = 0.025$ % [3].

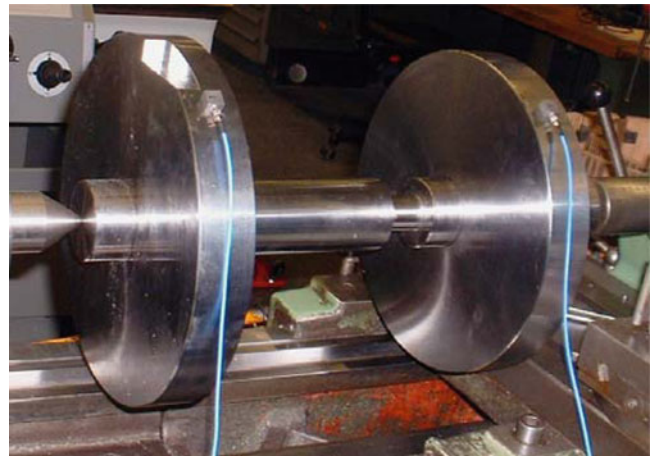


Fig. 19.9 Examined two-disc rotor with bearings and accelerometers

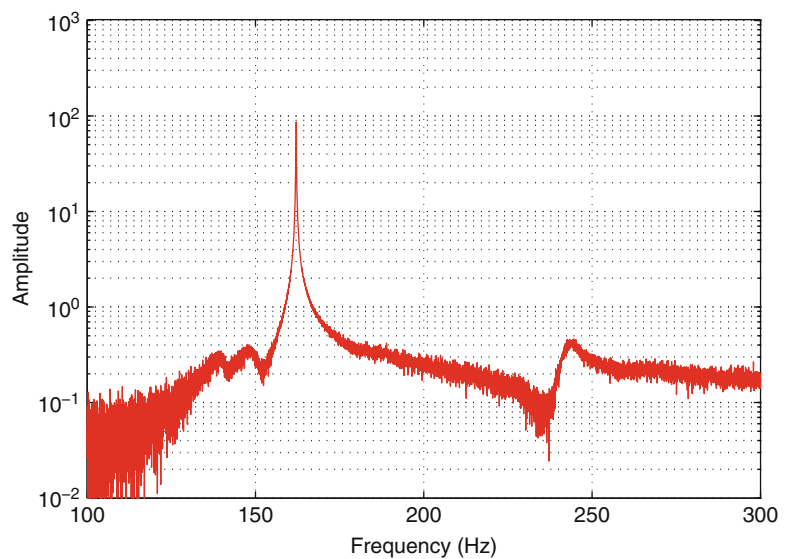
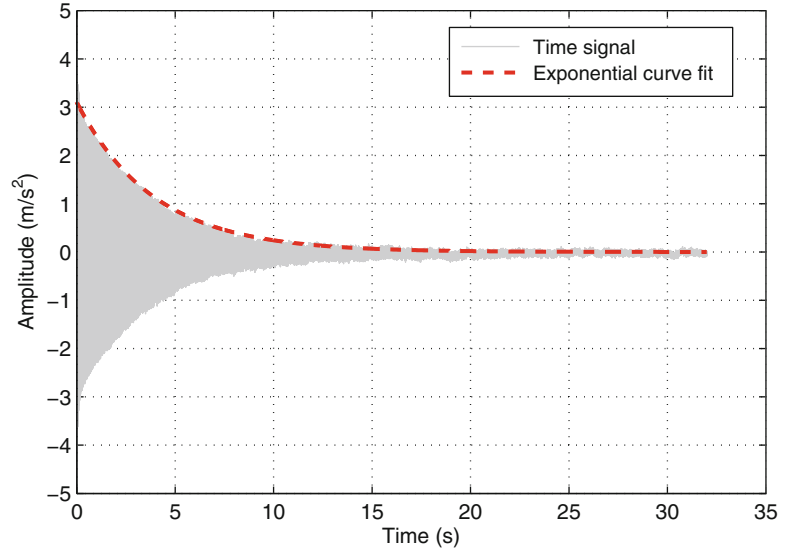


Fig. 19.10 Frequency Response Function (FRF) of the two-disk rotor

Fig. 19.11 Determining the damping factor by amplitude decay measurement



19.6 FE-Modeling

It has been shown by experimental investigations that joint damping in metal structures is nearly frequency independent. Similar results have been shown for material damping in metals. Thus, for FE approach the model of constant hysteresis will be used. Such model makes sense only in frequency domain, while in time domain it might lead to non-causal material behavior [7]. The model of constant hysteresis of structural damping implies that damping is frequency independent.

Derivation of the FE equation of motion begins with an undamped system

$$\underline{M} \ddot{\underline{x}} + \underline{K} \underline{x} = \underline{0} \quad (19.6)$$

where \underline{M} is a mass matrix, \underline{K} is a real valued stiffness matrix, and \underline{x} is the displacement vector. Eigenvalues and eigenmodes can be determined from a numerical modal analysis. Using the model of constant hysteresis, the damping in frequency domain will be incorporated by complex stiffness matrix \underline{K}^* [1, 3, 6, 7, 10, 14] with experimentally determined dissipation multipliers α_i and β_i for the material and the joint damping [4, 9, 11], respectively, and the associated elements stiffness matrices

$$\underline{K}^* = \underline{K} + j \sum_{i=1}^n \alpha_i \underline{K}_i^{(\text{material})} + j \sum_{i=1}^m \beta_i \underline{K}_i^{(\text{joint})}, \quad (19.7)$$

where n, m are the number of different materials and joints with different properties used in the model, respectively. The damping is low, implying $\alpha_i, \beta_i \ll 1$. The modified equation of motion (19.6), (19.7) can be solved for complex eigenvalues and eigenmodes with some commercial FE packages offering a complex solver, and in this case was performed with MSC.Nastran. The modal damping factors of the structure are read out from the solution file.

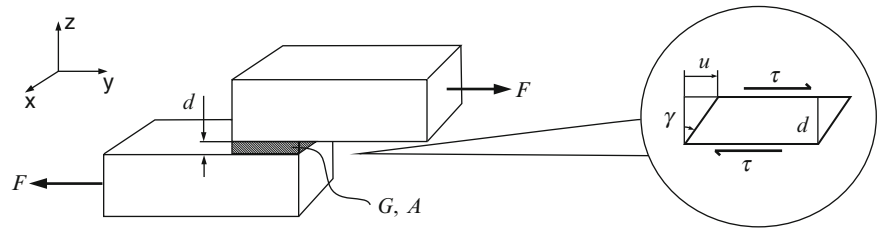
Thin-layer elements are used for the simulation of joints in the FE model [2]. The experimentally determined contact stiffness and dissipation parameters are used for constructing the stiffness matrices.

Thin-layer elements are normal hexahedral or pentahedral elements in which length or width to thickness ratio can be up to 1,000: 1 without causing numerical problems during the calculation.

The stiffness of the generic joint (19.5) must be transferred into the FE model as a parameter of the thin-layer elements. A schematic of an arbitrary joint modeled by a thin layer is depicted in Fig. 19.12. The force F , acting on both sides of the joint produces a shear stress τ in the layer. This stress can be expressed as

$$\tau = G\gamma \approx G \frac{u}{d}, \quad (19.8)$$

Fig. 19.12 Schematic of a joint with a thin-layer element



where G is the shear modulus and γ is the shear angle. The shear stress can also be calculated from the ratio of the applied tangential force F and the area of contact A

$$\tau = \frac{F}{A}. \quad (19.9)$$

By combining both equations the force can be calculated as

$$F \approx \frac{GA}{d}u = c u. \quad (19.10)$$

The stiffness c in the equation is obtained from the generic joint experiment.

A basis for further examinations is that the joint shows orthotropic behavior, thus the thin-layer elements are modeled with respective material characteristics. Consequently the contact stiffness in normal and tangented direction may differ significantly. From Eq. (19.10) the shear modulus can be approximated as

$$G = \frac{c d}{A}, \quad (19.11)$$

which depends linearly on the thickness d of the thin-layer elements [8].

Normal stiffness is not determined experimentally, but can be estimated from contact analysis. Physically sound limiting values for the selection of the normal stiffness are Youngs modulus of the surrounding material for the upper limit; for the lower limit isotropic joint behavior with disappearing transversal contraction $E = 2G$ can be used. The orthotropic matrix is defined as follows

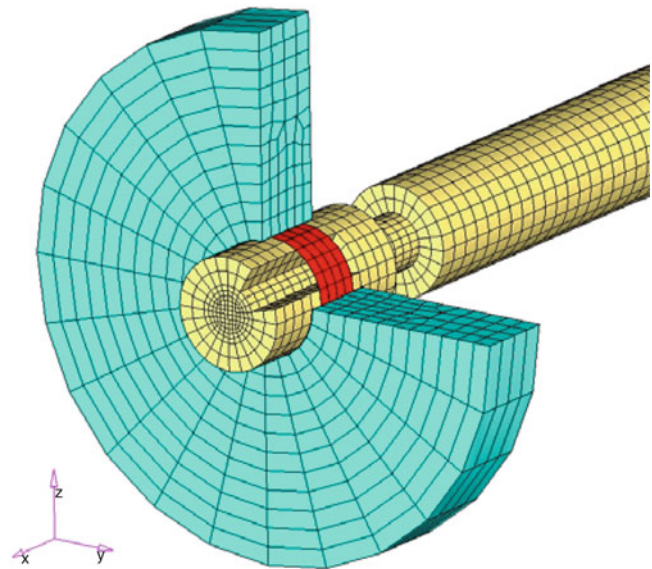
$$\begin{bmatrix} \sigma_{xx} \\ \sigma_{yy} \\ \sigma_{zz} \\ \sigma_{xy} \\ \sigma_{yz} \\ \sigma_{zx} \end{bmatrix} = \begin{bmatrix} E_{11} & E_{12} & E_{13} & 0 & 0 & 0 \\ & E_{22} & E_{23} & 0 & 0 & 0 \\ & & E_{33} & 0 & 0 & 0 \\ & & & E_{44} & 0 & 0 \\ & & & & E_{55} & 0 \\ & & & & & E_{66} \end{bmatrix} \begin{bmatrix} \varepsilon_{xx} \\ \varepsilon_{yy} \\ \varepsilon_{zz} \\ \varepsilon_{xy} \\ \varepsilon_{yz} \\ \varepsilon_{zx} \end{bmatrix}. \quad (19.12)$$

The off-diagonal terms are zero for physical reasons (there is no transversal contraction generated by the contact interface). Also, since the interface has no stiffness in x and y direction (parallel to the joints surface), the terms E_{11} and E_{22} disappear. E_{33} represents the normal stiffness, whereas $E_{55} = E_{66} = G$ define the tangential stiffness of the joint. Since the joint exhibits no stiffness for in-plane shearing, E_{44} is also zero.

19.7 FE Simulation

The FE-model of the simulated two-disc rotor can be seen in Fig. 19.13. It is modeled exclusively with isotropic hexahedral elements where the thin-layer elements have $d = 0.1$ mm thickness. In MSC.Nastran hysteretic damping can be defined by a material property card. In the FE calculation material damping is applied to all elements belonging to one of the three components of the structure, and joint damping is realized by application of damping to thin-layer elements. The parameters for the thin-layer elements are acquired from the generic joint experiment, while material damping was found in literature

Fig. 19.13 FE-model of the examined two-disc rotor



with a value of $\chi = 0.0001$ [12]. For normal stiffness a value of $E_{33} = 80$ GPa is assumed, the result for the tangential direction is $E_{55} = E_{66} = 52$ MPa. Young's modulus of steel is presumed with $E = 212$ GPa and Poisson's ratio $\nu = 0.3$.

With these values the torsional eigenfrequency is 160 Hz and the corresponding damping coefficient is $\chi = 0,00038$, converted to a modal damping factor $\xi = 0.019$ %.

A comparison of these values with the measured data (see Sect. 19.5) shows very good agreement. The difference in the eigenfrequency is only about 1 %, the modal damping factor can be well estimated under the given uncertainties. The deviation is less than 25 %.

19.8 Summary

In this article a generic joint experiment is presented which enables an engineer to extract both, the tangential stiffness and the damping properties of a bolted joint connection. It turns out that the determination of damping properties of weakly damped structures, such as joints which only show microslip, goes along with substantial uncertainties. However, it succeeds to properly determine the dimension of damping. With this procedure at hand, a design engineer is enabled to make general statements about a structure's dynamic behavior before a prototype is being built and investigated.

As an example a two-disc rotor was investigated. The above mentioned approach was used to model the dynamic behavior of the structure with the FEM. The results of a numerical modal analysis were compared with the outcome of an experimental investigation by means of the first torsional eigenmode. It shows that the eigenfrequency can be calculated accurately, while the deviation of damping properties is in the range of 25 %. Due to the difficulties of measuring small damping values the results are quite satisfactory.

References

1. Crandall S (1970) The role of damping in vibration theory. *J Sound Vib* 11(Nr. 1):3–18
2. Desai CS, Zaman NM, Lightner JG, Siriwardane HJ (1984) Thin-layer element for interfaces and joints. *Int J Num Analyt Meth Geomech* 8:19–43
3. Ewins D (2000) *Modal testing: theory practice and application*, 2nd edn. Research Studies, Baldock
4. Garibaldi L, Onah HN (1996) *Viscoelastic material damping technology*. BeccisOsiride, Torino
5. Gasch R, Nordmann R, Pfützner H (2002) *Rotordynamik*, 2.Aufl. Springer, Berlin
6. Gaul L, Nitsche R (2001) The role of friction in mechanical joints. *Appl Mech Rev* 54(Nr. 2):93–106
7. Gaul L, Bohlen S, Kempfle S (1985) Transient and forced oscillations of systems with constant hysteretic damping. *Mech Res Commun* 12(4):187–201

8. Gaul L, Schmidt A, Bograd S (2008) Experimentelle Ermittlung von Kennwerten zur Werkstoff- und Fügestellendämpfung sowie deren Berücksichtigung in Finite-Elemente-Berechnungen, Forschungsvereinigung Verbrennungskraftmaschinen (FVV), Heft 859, Frankfurt
9. Henwood DJ (2002) Approximating the hysteretic damping matrix by a viscous matrix for modeling in the time domain. *J Sound Vib* 254 (Nr. 3):575–593
10. Inaudi JA, Makris N (1996) Time-domain analysis of linear hysteretic damping. *Earthquake Eng Struct Dynam* 25:529–545
11. Lakes RS (1999) *Viscoelastic solids*. CRC, Boca Raton
12. Nashif AD, Jones DIG, Henderson JP (1985) *Vibration damping*. Wiley, New York
13. Ottl D (1981) *Schwingungen mechanischer Systeme mit Strukturdämpfung*. VDI Verlag, Düsseldorf (VDI-Forschungsheft Nr. 603)
14. Schmidt A, Gaul L (2006) On the numerical evaluation of fractional derivatives in multi-degree-of-freedom systems, *Signal Processing* 86, Nr. 10, pp 2592–2601

Chapter 20

An Approach to Identification and Simulation of the Nonlinear Dynamics of Anti-Vibration Mounts

A. Carrella, S. Manzato, and L. Gielen

Abstract This paper addresses the characterization of the amplitude-dependent stiffness of common vibration mounts. Anti-Vibration Mounts (AVMs) are very common passive vibration isolation devices used in a variety of engineering applications. These are, in most cases, off-the-shelf items which engineers select on the basis of the manufacturer's specifications (in particular their natural frequency). This value is then used for modelling and prediction purposes during the design stage. However, in many cases the nominal value is (very) different from the stiffness value in operational conditions. It is a standard practice to perform dynamic tests on the mounts in order to extract an experimental value for the stiffness. It is well known that the stiffness of rubber AVMs is dependent on a number of factors, amongst which the most important are amplitude and frequency of excitation, as well as temperature. In particular, this work considers only the amplitude-dependency of the stiffness. The approach proposed here is to identify the nonlinear stiffness from a dynamic test and use the extracted stiffness function for nonlinear prediction using a commercial-off-the-shelf (COTS) solution. It is shown that by input the nonlinear stiffness function (identified with experiments) into the numerical model of the installation, it is possible to predict the effect of different excitation amplitudes with good accuracy. This method allows engineers taking a first step towards a more complex and refined model. However, it falls short of including frequency and temperature effects, which are objects of future work.

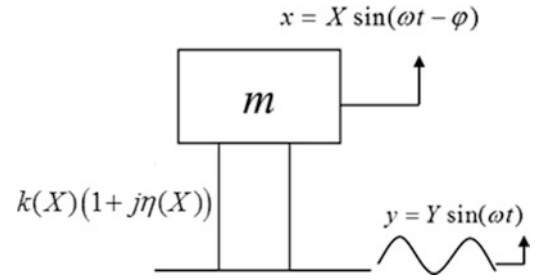
Keywords Nonlinear identification • Transmissibility • Measurement • Amplitude-dependent stiffness • Anti-vibration mounts

20.1 Introduction

In many engineering applications, numerical analysis based on mathematical models is becoming a major feature of the design stage. The main purpose of the model, most commonly a Finite Element (FE) model, is to enable the designers to predict a system's dynamic response under different structural and loading conditions. It can be argued that in order to increase the accuracy and prediction capability of the numerical models, nonlinear effects cannot be neglected. The validation process aims at ameliorating the quality of the model by comparing the numerical analysis results with experimental data and applying the necessary changes to the model in order to minimise the difference between simulations and experiments. For a more reliable and accurate model, there is thus a need for being able to extract nonlinear parameters from measured data. The modal parameters (natural frequencies, modal damping and mode shapes) extracted using standard—and nowadays very advanced—techniques, are in many cases accurate enough for structural dynamic design purposes. However, there are instances in which the nonlinear effects cannot be ignored. A nonlinear behaviour can result in drastic changes of natural frequency or damping. Furthermore, these modal quantities can be dependent on several variables, i.e. where the nature of the nonlinearities is due, for example, to amplitude of vibration, frequency of excitation, temperature, etc. There is a need for a structured procedure, or Non Linear Modal Testing (NLMT), which allow engineers and dynamicists to identify and quantify the structural nonlinearities in a standard testing environment.

A. Carrella (✉) • S. Manzato • L. Gielen
LMS International, Interleuvenlaan 68, B-3001 Leuven, Belgium
e-mail: alex.carrella@lmsintl.com

Fig. 20.1 Schematic representation of a SDOF system of a mass suspended on a nonlinear mount with complex stiffness and under base excitation



The reference textbook, and arguably the only book on the subject, on identification and quantification of nonlinearities in structural dynamics was published in 2001 by Worden and Tomlinson [1]. Some years later, Kerschen et al. [2] have contributed to the subject by publishing a review paper in which 446 references were cited. As these authors stated, their review has inevitably missed some works on the subject. Probably for reasons of commercial interest, there is a scarcity of works published on NLMT that refers to industrial research and/or practice. Some methods that the authors of this report deem of practical applicability are: the *Restoring Force Surface (RFS)* [3], the *Inverse Method* [4] and the *Linearity Plots* [5]. Link et al. [6] have also presented a practical method for nonlinear identification, and the paper is of particular interest for two main reasons: (1) because it focuses on a real, complex structure and (2) the modal parameters are extracted from the transmissibility function, as opposed to the standard Frequency Response Function (FRF).

A method for the identification and quantification of nonlinearities, based on the analysis of measured FRF data was discussed in [7]. Subsequently, the methodology was applied also to measured transmissibility function. Albeit the method presents some shortfalls which need to be addressed in the future, it is a first concrete step towards advanced identification and validation techniques which account for amplitude-dependent nonlinearities.

The aim of this study is to use the proposed identification method to reconstruct, at least to a first degree of approximation, the nonlinear stiffness function of an off-the-shelf Anti Vibration Mount (AVM) and then use the extracted stiffness function to update a numerical (Finite Element or Multibody) model. The results show that the response predicted with the Virtual.Lab Motion simulation package match the (nonlinear) behaviour observed in the lab.

20.1.1 Nonlinear Identification Method Using Transmissibility Data

The nonlinear identification method has already been presented in the past [7] and thus only a brief summary is given here.

The proposed single-degree-of-freedom identification technique is based on the assumption that the dynamics of the nonlinear system shown in Fig. 20.1 can be described by the equation of motion:

$$\{-\omega^2 \cdot m + k(X) \cdot [1 + j \cdot \eta(X)]\} X = \{k(X) \cdot [1 + j \cdot \eta(X)]\} Y \quad (20.1)$$

or

$$\{-\omega^2 \cdot m + k(X) \cdot [1 + j \cdot \eta(X)]\} Z = m \cdot \omega^2 \cdot Y \quad (20.2)$$

where $z = x - y$ is the relative displacement (and Z its amplitude) between the mass and the base, that is the deformation of the mount, ω the excitation frequency and $k(X)$ and $\eta(X)$ are the amplitude-dependent stiffness and damping loss factor respectively. The absolute transmissibility is then defined as the non-dimensional ratio that at each frequency quantifies how much disturbance has passed from the source to the receiver through the transmission path. Being $\omega_0(X)$ and $\eta(X)$ the natural frequencies and the modal loss factor at given amplitude, the absolute transmissibility for the system in Fig. 20.1 can be expressed as:

$$|T| = \left| \frac{X}{Y} \right| = \left| \frac{\omega_0^2 + j \cdot \eta \cdot \omega_0^2}{\omega_0^2 - \omega^2 + j \cdot \eta \cdot \omega_0^2} \right| = |R + j \cdot I| \quad (20.3)$$

It must be stressed however that Eq. (20.3) is the result of linearization and is only valid for a given value of the amplitude of displacement response.

By measuring the base and response accelerations and deriving their absolute transmissibility function, the functions ω_0 and η can be extracted from the real and imaginary part as:

$$\omega_0 = \frac{(R_2 - R_1) \cdot (R_2 \cdot \omega_2^2 - R_1 \cdot \omega_1^2) + (I_2 - I_1) \cdot (I_2 \cdot \omega_2^2 - I_1 \cdot \omega_1^2)}{(R_2 - R_1)^2 + (I_2 - I_1)^2}$$

$$\eta = \left| \frac{(I_2 - I_1) \cdot (R_2 \cdot \omega_2^2 - R_1 \cdot \omega_1^2) + (R_2 - R_1) \cdot (I_2 \cdot \omega_2^2 - I_1 \cdot \omega_1^2)}{\omega_0^2 \cdot [(R_2 - R_1)^2 + (I_2 - I_1)^2]} \right| \quad (20.4)$$

where R_1 and R_2 (I_1 and I_2) are the real (imaginary) parts of the transmissibility at the amplitude X , which have been measured at the frequencies ω_1 and ω_2 (before and after the resonance peak)

20.2 Application to Anti Vibration Mounts: Measurements and Results

One of these practical examples of nonlinear dynamics is the characterisation of Anti Vibration Mounts (AVMs). These are devices which are inserted between the source of vibrations and the receiver. The mounts used are standard commercially-available rubber mounts. The experimental results published in the following section have already been discussed in [8]. In this paper only the main results will be discussed and the nonlinear stiffness extracted will be used for the simulation section.

The test was performed using a shaking table LDV mod.V8, B&K triaxial accelerometers (Bruel&Kjaer 4506 B 003500 mV/g sensitivity) and the software LMS Test.Lab 10b for data acquisition and analysis. A picture of the experimental set-up is shown in Fig. 20.2. Four accelerometers were placed on the mass near the mounts. The results of the measurements are independent of the position of the sensor, thus all the data shown are relative to one point only.

Moreover, the original test was performed using different mass values for the same set of mounts in order to study the mounts behaviour under different static loads. In this analysis, only one case is considered: soft mounts (serial number: SC13435-01) supporting 31.5 kg (resulting in 7.87 kg/mount).

20.2.1 Stepped-Sine Excitation

In order to investigate the nonlinear dynamic behaviour of the AVMs, stepped sine tests were carried out using three different levels of base excitation. Stepped-sine tests are considered to be the best way to carry out experiments aimed at nonlinear identification. The main reasons behind this statement are:

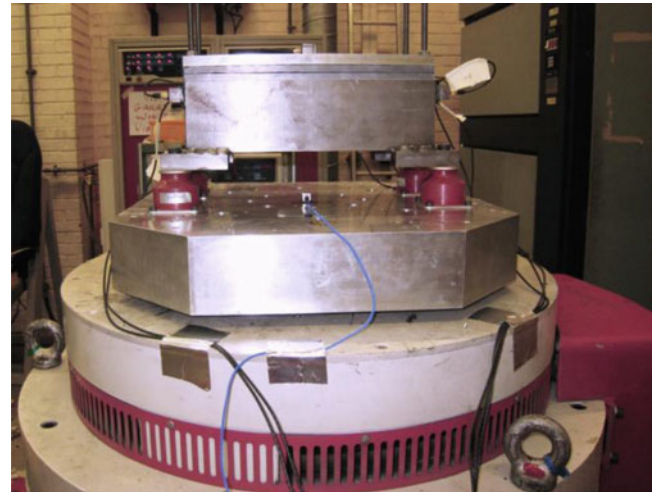


Fig. 20.2 Experimental rig: four triaxial accelerometers were placed on the mass and one on the moving base acting as reference/control. One accelerometer was also placed in the centre of the mass to monitor its vibrations

Fig. 20.3 Stepped-sine measurement: constant base excitation

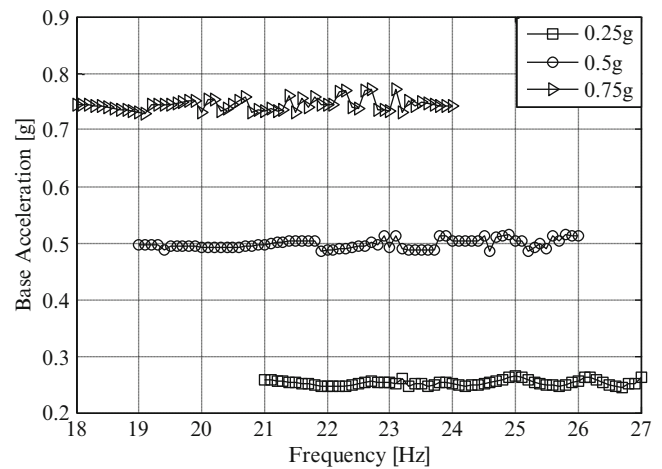


Fig. 20.4 Stepped-sine measurement: absolute transmissibilities ($|X/Y|$)

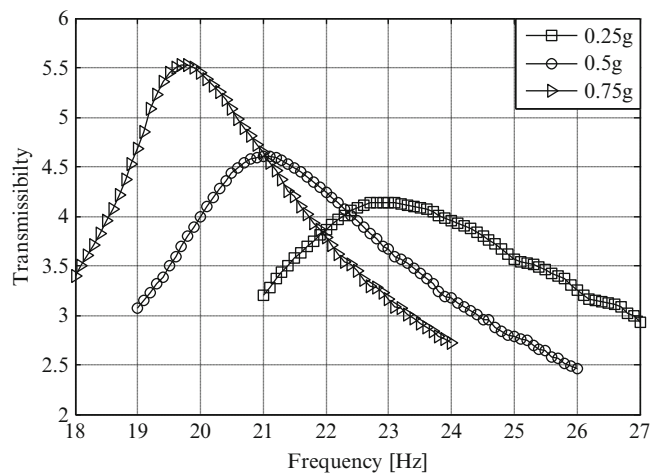


Table 20.1 List of results obtained from stepped sine test on the analyzed configuration

| Mass (kg) | Mass/Mount (kg) | Peak Acc. (g) | $ T _{\max}$ | Nat. Freq. (Hz) | Damping (%) | Dynamic stiffness (N/mm) |
|-----------|-----------------|---------------|--------------|-----------------|-------------|--------------------------|
| 31.5 | 7.9 | 0.25 | 4.14 | 22.9 | 12.1 | 163 |
| 31.5 | 7.9 | 0.5 | 4.61 | 21 | 10.8 | 137 |
| 31.5 | 7.9 | 0.75 | 5.53 | 19.7 | 9.0 | 121 |

- the signal processing does not require any averaging nor does it contain any inherent linearisation;
- sine signals input more energy into the system which, in turn, subject the test specimen to higher displacements and generally exacerbate nonlinear characteristics.

Three levels of acceleration (0.25, 0.5 and 0.75 g) have been used for exciting the structure with the stepped-sine signal. The excitation signal was selected with a 0.1 Hz increment. At each excited frequency, the transmissibility was estimated using the ratio between the steady state response to the input. In Figs. 20.3 and 20.4 an example of the acquired data is shown. After performing some broadband measurement to find the natural frequencies of the system, the stepped sine excitation was performed focusing on a narrow-band around the sprung-mass resonance to fully characterize the nonlinear behaviour of the mounts.

Figure 20.3 depicts the base acceleration levels, kept constant using the amplitude control implemented in the LMS Test.Lab software. Figure 20.4 shows the transmissibilities for the three levels of excitation applied. A marked softening effect at increasing excitation amplitude can be observed: the natural frequency decreases by 14 % as the excitation increases from 0.25 to 0.75 g. The identified frequency and damping for the analysed configuration are reported in Table 20.1, while the complete list of results can be found in [8]. The frequency, damping and dynamic stiffness results all show the softening behaviour of the mounts under increasing loads, resulting in poorer isolation properties.

Fig. 20.5 Natural frequency vs. relative displacement obtained with CONCERTO. The natural frequency obtained with Burst-random and Rap excitations are also reported for comparison

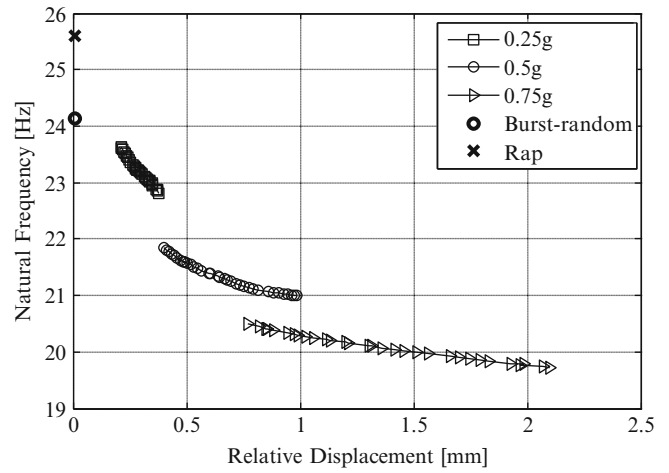
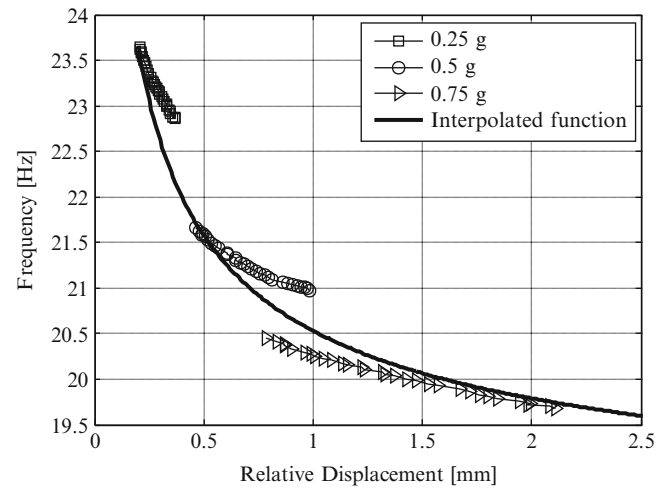


Fig. 20.6 Interpolated natural frequency function on CONCERTO results



20.2.2 Nonlinear Identification

The transmissibilities measured with stepped sine excitation have been then analyzed the identification method described in [7], also known and referred in the following as CONCERTO. This method was applied after verifying that the responses at the four measurement locations were equivalent so that considering the structure as a single-degree-of-freedom system was a valid assumption. The result of the method is then the natural frequency as a function of relative displacement in the mounts, which is shown in Fig. 20.5. The results show a marked dependency of the natural frequency on the amplitude of the mount’s deformation. A variation of natural frequency of almost 20 % is found to correspond to a ten times increase in the mount’s displacement. The results of more common excitation techniques (Burst random and hammer testing) are also shown. Even though the results of the three methods are consistent, only the applied identification method has enabled extraction of an analytical relationship between natural frequency and relative displacement, which is shown in Fig. 20.6.

The solid line in Fig. 20.6 represent the function:

$$f_n(Z) = 18 + \frac{0.08}{\sqrt{Z}} \tag{20.5}$$

where Z is the relative displacement between the moving mass and the base (effective deformation of the mounts), which interpolates the extracted natural frequencies. At this point, the analytical function in Eq. (20.5) can be used to derive the system’s stiffness as:

$$k(z) = [2 \cdot \pi \cdot f_n(z)]^2 m \tag{20.6}$$

where m is the known mass of the system. The resulting mount stiffness as a function of the relative displacement is shown in. Note that Eq. (20.6) represents the stiffness identified from the experimental data. This can now be used to create a theoretical model for numerical simulations as will be discussed in the next section. The numerical results will be then compared with the experimental one to validate the proposed procedure.

20.3 Numerical Simulations

Multibody simulations are nowadays commonly and broadly used to model the dynamic behavior of interconnected rigid or flexible bodies, each of which may undergo large translational and rotational displacement, thus allowing computing the non-linear response [9]. These tools are particularly used in robotics and vehicle dynamics. In the latter case, non-linear vibration isolators are widely used to connect suspensions, engine, transmission etc. to the chassis. Correctly identifying the dynamic characteristics (in terms of frequency and damping) is of critical importance to properly simulate not only the dynamic response under specific maneuvers but also to estimate the loads which are transmitted to the chassis and that can be used in the early development phases for its design. In this section the process implemented to virtually simulate the test activities described in Sect. 20.2 and validate the prediction capabilities of the numerical model are presented.

20.3.1 Multibody Simulation

The multibody model of the mass suspended on the AVMs and connected to the shaker table was built using the CAE environment LMS Virtual.Lab Motion. Since the analysis focuses only on the vertical motion of the mass and on the associated suspension mode, all other degrees of freedom were locked. Two rigid bodies (one for the table and one for the suspended mass) were generated. Between the two bodies, a translational joint allowing only relative vertical motion and four spring-damper elements simulating the AVMs were defined. Finally, on the shaker table body, a displacement driver was defined.

The properties of the spring-damper elements simulating the AVMs were derived from the experimental results, using Eq. (20.6) and Table 20.1. The non-linear spring characteristic in the ± 3 mm relative displacement range is shown in Fig. 20.7 the stiffness is defined up to 10 mm displacement, but the identified nonlinear behavior is significant only at much lower displacements, as can be observed from Fig. 20.6. For the damping, in this study a fixed values was selected, depending only on the excitation level. Under the assumption of single-degree-of-freedom system, the damping value is estimated from the results of Table 20.1 as:

$$c = 2 \cdot \xi \cdot m \cdot (2 \cdot \pi \cdot f_n) \quad (20.7)$$

where f_n and ξ are the natural frequency and damping of the suspension mode for a given excitation amplitude.

Since in the simulation code it is not possible to replicate exactly the test condition (stepped sine with amplitude estimation and control) an alternative procedure to excite the structure needed to be defined. On one side, a pure sine wave of given frequency can be defined to excite the structure. The response amplitude is estimated once the system reaches steady state conditions. However, this procedure requires launching a new simulation and analyzing the results at each frequency line. The methodology proposed here is to define a single excitation profile exciting all desired frequency and then post-process the results to compute the transmissibility functions. At each frequency, a sine wave of 50 cycles is defined to allow the system reaching its steady state condition. After the 50 cycles, the frequency of the sine is changed to the new one and

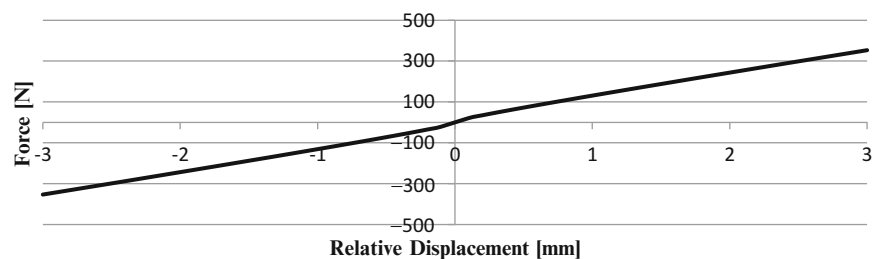


Fig. 20.7 Non-linear stiffness for the mount model

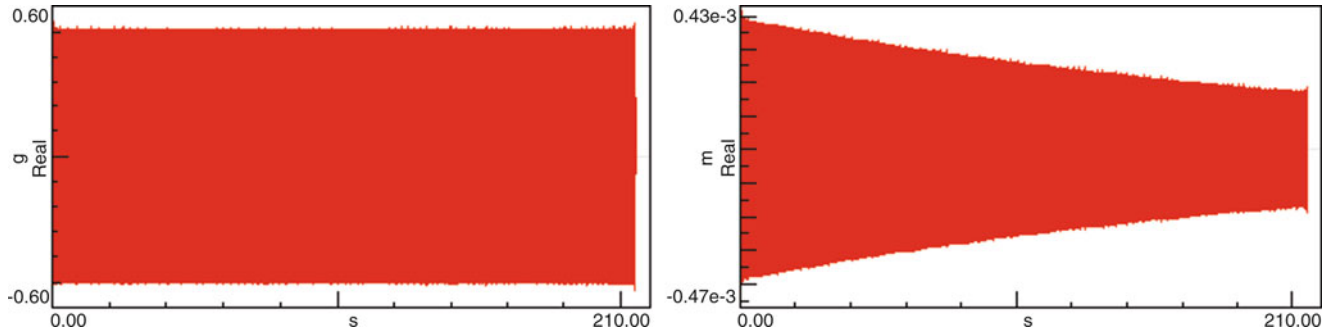
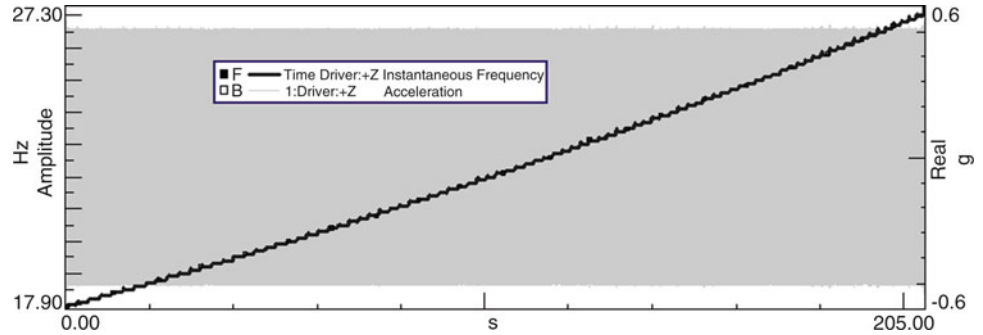


Fig. 20.8 Input excitation: (left) reference acceleration, (right) equivalent displacement

Fig. 20.9 Driver acceleration and the estimated instantaneous frequency content



the complete profile is then generated. For this study, excitation signals between 18 and 27 Hz with step of 0.1 Hz and amplitude of 0.25, 0.5 and 0.75 g are generated. Since the model is excited by a displacement driver to make the simulation more stable, the generated accelerated profile need to be transformed in an equivalent displacement one. The amplitude of the base excitation Y needs to change for each excitation frequency to ensure that the numerical simulation reproduces the constant-acceleration target profile. In general, this can be ensured by scaling, at each frequency, the displacement amplitude as $Y = A/\omega^2$. However, to generalize the proposed approach as much as possible, the Time Waveform Replication (TWR) plug-in available in LMS Virtual.Lab Motion is used. By estimating the FRF matrix model a , the TWR will generated the displacement profile to be applied directly on the driver to obtain the desired constant-amplitude acceleration at the shaker table. The target acceleration signal and the resulting displacement for the 0.5 g excitation amplitude are shown in Fig. 20.8

Once the displacement profile is computed for each amplitude profile, the acceleration at the two side of the AVMs are virtually acquired. As already mentioned, however, while during the physical test the transmissibilities can be directly estimated, during the simulation they need to be estimated from the computed acceleration a-posteriori.

20.3.2 Transmissibility Computation and Method Validation

Two techniques are available to estimate the transmissibilities from the data. The first method is the one most commonly used and is based on the H1 estimator [10]. Even if applicable, this method will estimate the transmissibility in a frequency range defined by the sampling frequency, which is way broader than the 18–27 Hz range defined for the excitation. Another alternative, which is based on the same method applied online during the test, is to estimate the excitation frequency as a function of time and then use this information to estimate amplitude and phase of the transmissibility at each frequency line. The data were processed using the Offline Sine Data Reduction tool available in the LMS Test.Lab software and the estimated instantaneous frequency together with the driver acceleration profile are shown in Fig. 20.9.

Using the instantaneous frequency signal, the response amplitude at each frequency is computed and the transmissibility can be computed using the harmonic estimator, which, compared to other estimators, allows also to estimate phase information. The output signal is modeled as a combination of sine and cosine waves as:

$$a(t) = a_c \cos(\omega_1 \cdot t) + a_s \sin(\omega_1 \cdot t) = a_c \cos(2 \cdot \pi \cdot f_1 \cdot t) + a_s \sin(2 \cdot \pi \cdot f_1 \cdot t) \quad (20.8)$$

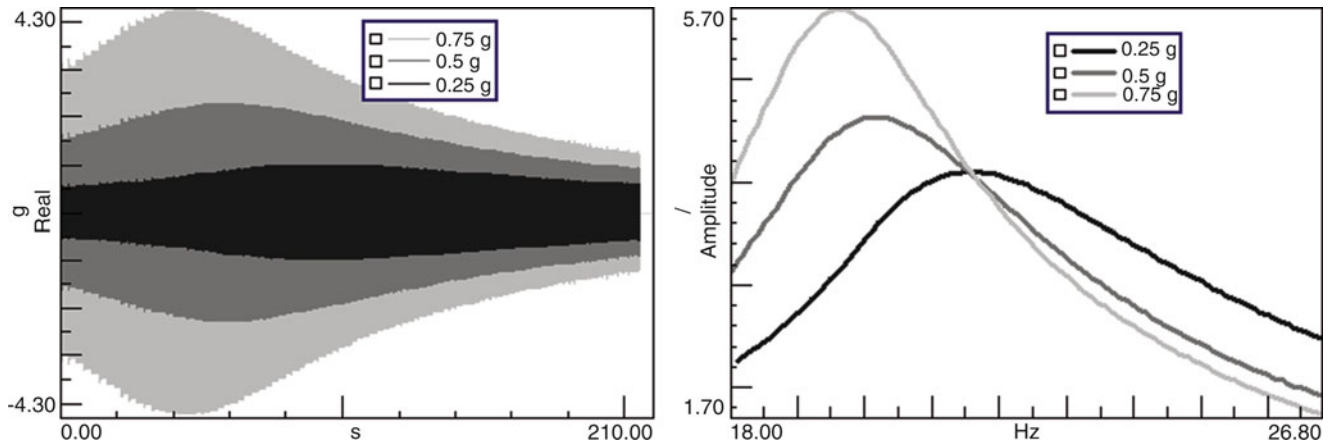
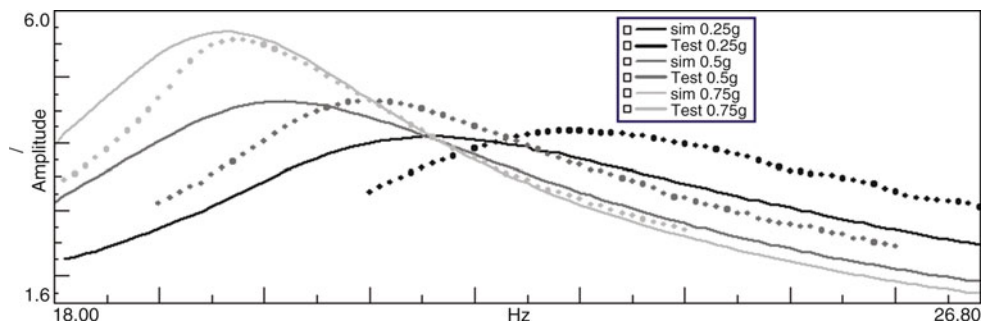


Fig. 20.10 Simulated response acceleration (*left*) and estimated transmissibilities (*right*)

Fig. 20.11 Measured (*dot*) vs. simulated (*line*) transmissibilities for the different excitation levels



where the amplitude is estimated as:

$$A(\omega_1) = \sqrt{a_c^2 + a_s^2} \tag{20.9}$$

Since the estimation is applied to sampled data and, during the analysis, the excitation frequency is changing, the amplitude is estimated by solving the following system of equations in a least square sense to obtain the best estimates for a_c and a_s from which A_{ω_l} is computed using Eq. (20.9).

$$\begin{bmatrix} a(\Delta t) \\ \vdots \\ a(i\Delta t) \\ \vdots \\ a(N\Delta t) \end{bmatrix} = \begin{bmatrix} \cos(\omega_1 \Delta t) & \sin(\omega_1 \Delta t) & \cdots & \cos(\omega_n \Delta t) & \sin(\omega_n \Delta t) \\ \vdots & \vdots & & \vdots & \vdots \\ \cos(i\omega_1 \Delta t) & \sin(i\omega_1 \Delta t) & \cdots & \cos(i\omega_n \Delta t) & \sin(i\omega_n \Delta t) \\ \vdots & \vdots & & \vdots & \vdots \\ \cos(N\omega_1 \Delta t) & \sin(N\omega_1 \Delta t) & \cdots & \cos(N\omega_n \Delta t) & \sin(N\omega_n \Delta t) \end{bmatrix} \cdot \begin{bmatrix} a_{c1} \\ a_{s1} \\ \vdots \\ a_{cn} \\ a_{sn} \end{bmatrix} \tag{20.10}$$

The estimated transmissibilities together with the acceleration from which they are estimated are shown in Fig. 20.10.

The curves in Fig. 20.10 show clearly that the simulation capability has captured the nonlinear behaviour of the system: the peak of the simulated transmissibilities (shown on the right) shift to the left following the softening behavior identified from the measured data. Figure 20.11 shows, additionally, that the natural frequencies of the simulated test are very close to those measured in the lab (given in Table 20.1). In general, the simulated transmissibilities tend to overestimate the resonance frequency, in particular for the lower excitation levels. This can be explained by rather primitive curve-fitting stage to the identified nonlinear stiffness (shown in Fig. 20.6). On the other end, the shapes of the transmissibilities are very similar and the maximum amplitudes of the resonance peaks match almost perfectly. The shift in frequencies might be related to the constant damping implemented in the model and defined in Eq. (20.7). A function similar to the one defined for the stiffness that takes into account the dependency to the excitation amplitude should be implemented. Moreover, it must be remembered that neither frequency nor temperature dependency are here considered.

20.4 Conclusions

The identification of nonlinearities from measured vibration data is a crucial step towards the realisation of more advanced and reliable models which will ensure a superior modelling capability in structural dynamics.

In this paper, an existing nonlinear identification method based on measured FRF or Transmissibilities has been applied to identify the stiffness and damping characteristic of commercial Anti Vibration Mounts (AVMs). The AVMs have been tested using a base excitation with controlled amplitude and at different levels using stepped sine excitations. Using the measured transmissibilities, the natural frequency as function of the mount displacement was derived. Subsequently, the corresponding nonlinear stiffness (function of the amplitude of displacement of the mount) was also determined.

In addition to the previous work on the identification, this paper presents a method to exploit this new available information using Virtual.Lab, a widely used off-the-shelf simulation software. A multibody model replicating the test conditions was then built and the identified function was used as a spline to define the stiffness of the mounts. From the simulated data the transmissibilities were identified and a good agreement with the measured one was found.

This work shows that it is now possible to identify nonlinear dynamic properties and use this information to obtain advanced simulation models. However, there still work to do in order to reach standard algorithms and methods as for the case of linear dynamics. For example, even in this relatively simple real case, one interesting feature of the curves in Fig. 20.5 is the overlap between the results at different excitation level. The cause of this phenomenon has not been fully understood and its investigation goes beyond the scope of this work. It can be speculated that this is a temperature effect. In fact, the tests at different levels of base excitation were performed consecutively to one other and the mount's temperature increased with time, especially as the level of vibration increased. It is a known characteristic that the stiffness of some elastomeric materials depends on the frequency of vibration, the static load, the temperature and the amplitude of deformation. Further development of the algorithm might focus on the inclusion of different type of theoretical model of the stiffness and damping (e.g. temperature dependent).

References

1. Worden K, Tomlison GR (2001) Nonlinearity in structural dynamics: detection, identification, and modelling. Institute of Physics, Bristol
2. Kerschen G et al (2006) Past, present and future of nonlinear system identification in structural dynamics. *Mech Syst Signal Process* 20(3): 505–592
3. Masri SF, Caughey TK (1979) A nonparametric identification technique for non-linear dynamic problems. *J Appl Mech* 46(2):433–447
4. He J, Ewins DJ (1987) A simple method of interpretation for the modal analysis of nonlinear structures. In: *Proceedings of IMAC V, London*
5. Goge D et al (2005) Detection and description of non-linear phenomena in experimental modal analysis via linearity plots. *Int J Nonlinear Mech* 40(1):27–48
6. Link M et al (2010) An approach to non-linear experimental modal analysis. In: *Proceedings of IMAC XXVIII, Jacksonville*
7. Carrella A, Ewins DJ (2011) Identifying and quantifying structural nonlinearities in engineering applications from measured frequency response functions. *Mech Syst Signal Process* 25(3):1011–1027
8. Carrella A (2012) Nonlinear identification using transmissibility: dynamic characterization of Anti Vibration mounts (AVMs) with standard approach and nonlinear analysis. *Int J Mech Sci* 63:74–85
9. Shabana AA (2005) *Dynamics of multibody systems*. Cambridge University Press, Cambridge
10. Heylen W, Lammens S, Sas P (1997) *Modal analysis theory and testing*. Department Werktuigkunde, Katholieke Universiteit Leuven, Leuven

Chapter 21

Test Method Development for Nonlinear Damping Extraction of Dovetail Joints

C.W. Schwingshackl, C. Joannin, L. Pesaresi, J.S. Green, and N. Hoffmann

Abstract The traditional measurement techniques to acquire the linear dynamic response of a single component are well established and have been in use for many decades to provide reliable input data for model updating. The measurement of assembled structures normally follows a very similar approach, although the presence of joints can introduce a nonlinear dynamic behaviour, which impacts the measurement results. Applying traditional linear test methods to a highly nonlinear structure, such as a dovetail joint in an aircraft engine blade-disk connection, does not necessarily take the special features of the nonlinear response into account and may lead to unreliable data. This is particularly true, if modal information such as damping are required. The influence of the measurement setup and the test procedures must be well understood for an accurate measurement. In this paper the influence of the different measurement components on a simple clamped beam and a compressor blade dove tail test rig will be investigated. A particular focus will be on the support of the test rig, the location and control of the excitation and the influence of the accelerometer on the response. Based on the findings an approach will be recommended that allows a reliable measurement of the dynamic behaviour of this heavily nonlinear structure.

Keywords Linear damping • Nonlinear damping • Nonlinear test setup • Blade vibration • Clamping

21.1 Introduction

The assembly of engineering structures introduces a range of joints that can lead to a nonlinear dynamic behaviour of the structure at high excitation levels. For example in an aircraft engine environment a wide range of joints is present where under platform dampers [1–3], blade roots [4, 5], and shrouds [6, 7] are actively designed to provide good damping behaviour and lower the amplitude response of the system. Bolted flange joints are a necessary requirement for many assemblies, but they can also add nonlinear damping [8, 9] to the structure and influence the overall dynamic response of the system. The analysis of the dynamic behaviour of contact interfaces can be quite complicated and an accurate model validation is required to ensure the reliability of the models. The measurement of the linear and especially nonlinear damping behaviour of a structure can require very high amplitude excitation of the system to introduce operational level conditions and activate the nonlinearities that often arise from various friction contact interfaces [10]. The high amplitude levels introduce new challenges to the experimental setup of the system, since the setup itself should not affect the damping of the structure, regardless of the excitation level. Past experience on a turbine blade test rig [11] has shown that this is not always easily achievable and a study on two test configurations was carried out and will be presented to provide a better understanding of the influence of different components in the test setup on the extracted damping behaviour of the system.

C.W. Schwingshackl (✉) • C. Joannin • L. Pesaresi • J.S. Green • N. Hoffmann
Mechanical Engineering, Imperial College London, Exhibition Road, SW7 2AZ London, UK
e-mail: c.schwingshackl@imperial.ac.uk

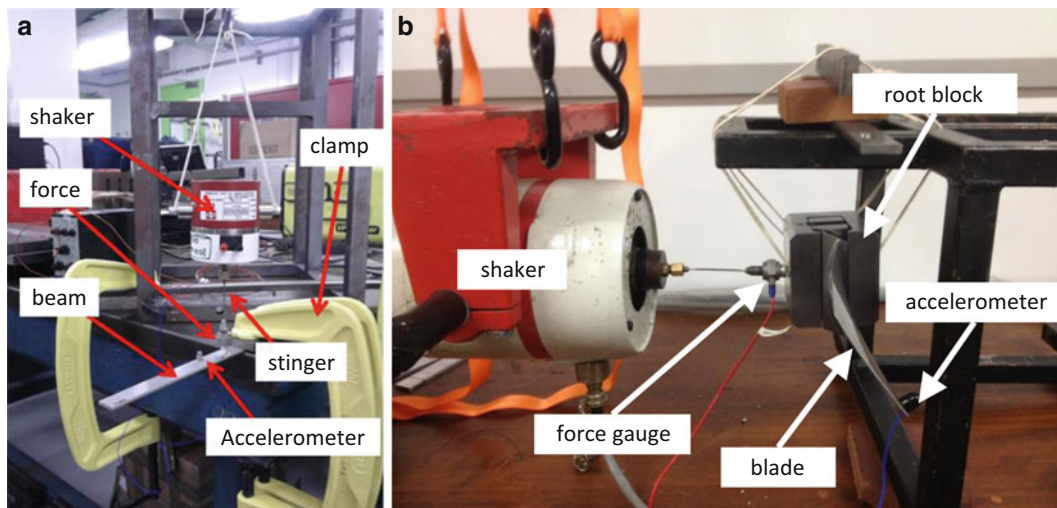


Fig. 21.1 The (a) clamped beam and (b) compressor blade test rig

21.2 The Test Rigs

Two different test rig setups will be used for this investigation. The initial one was a simple clamped aluminium beam ($320 \times 20 \times 3.5$ mm) from Fig. 21.1a. The beam was clamped to a large steel table, and excited with a shaker at very high amplitudes to extract the damping behaviour. Several different setup configurations were investigated, changing the clamping method, adjusting the excitation system, and varying the methods to extract the damping, to minimise the influence of the test rig and focus on the damping behaviour.

The second test setup in Fig. 21.1b was a small compressor blade test rig for the extraction of the nonlinear dynamic response due to slip at the root of the blade. It consisted of a rigid root block, a clamping mechanism to apply a simulated centrifugal load to the blade, and the compressor blade itself [11]. The main aim of this test rig is the measurement of the root damping for model validation and therefore an investigation was conducted to minimise the influence of the support, sensor location, excitation system, and excitation control on the extracted damping values.

21.3 Test Rig Support and Clamping

A major concern for a high amplitudes test rig is the support of the test specimen, since an inadequate support can become a major source of nonlinearity. To evaluate this influence the aluminium beam of the clamped beam test setup was suspended in a free-free configuration with a fishing wire (see Fig. 21.2a), excited with an impact hammer, and the response was measured with an accelerometer. After the free-free test the beam was clamped to a large steel table with two heavy duty C-clamps (see Fig. 21.2b) and the impact hammer test was repeated. The response was measured in the middle of the beam with an accelerometer. The modal analysis tool ICATS was used to post-process the frequency response data of the impact test and extract the loss factor with a linear line-fit method [12]. A very low loss factor of 0.075 % was observed at the first bending mode of the free-free configuration, which became 0.188 % for the first bending mode of the cantilever configuration. These low level impact tests were used as reference damping for the assessment of the rig behaviour at high amplitudes.

To reach high amplitudes a shaker was used to excite the 1st mode of the clamped beam. Several different clamping methods were investigated to minimise the effect of nonlinearities in the clamps. Heavy duty C-clamps were used to fix the beam to a 1,000 kg steel table. Initially two clamps were used with no control on the tightening moment and the clamp position (see Fig. 21.2b). The damping results in Fig. 21.3 for the un-optimised clamping configuration show a relatively high and nonlinear damping behaviour due to slip in the clamp. In a second configuration superglue was added between the clamp and the beam to minimise the slip in the contact, but the resulting damping in Fig. 21.3 was even higher, most likely due to viscous effects of the superglue, also slightly less nonlinearity was observed. Next a double hinge configuration (see Fig. 21.3a) was investigated where the beam was clamped between four round profiles to minimise the contact surface and

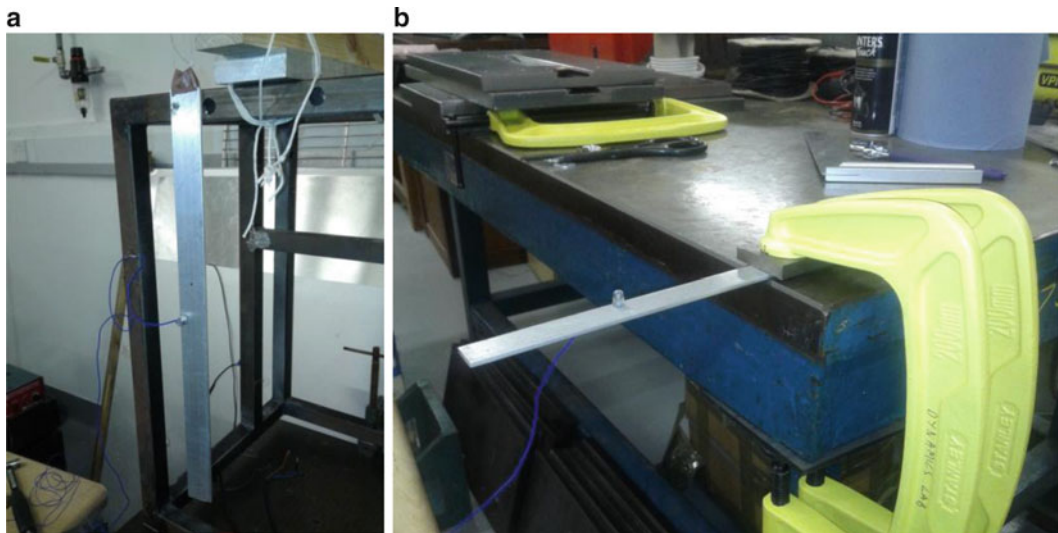
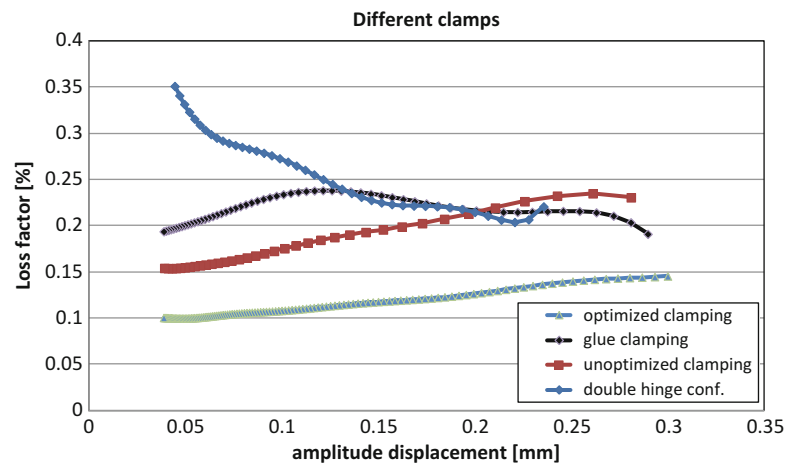


Fig. 21.2 Clamped beam rig: The (a) free-free beam and (b) the cantilever beam configuration

Fig. 21.3 Clamped beam rig: damping behaviour for different clamping configurations



concentrate the contact pressure in order to reduce the slip. The results in Fig. 21.3 showed a strongly non-linear behaviour, which indicated rolling of the hinge. The setup proved to be very sensitive to the clamping force, so that it was not suitable for the damping tests. The final optimised system in Fig. 21.4b consisted of three strong C-clamps with a load capacity of approximately 10 kN each, tightened always to the same torque value within a 10 % tolerance and positioned very accurately at the same point every time. A slight nonlinearity was still present in the results in Fig. 21.3, which was attributed to remaining microslip in the clamping setup that could not be eliminated, but the final damping values for the optimised clamping setup were between 0.1 and 0.15 % which was close to the loss factors obtained for the free-free test configuration (0.075 %) and below the impact results for the un optimised clamped beam. This last configuration was chosen as the best clamping setup for the cantilever beam test rig.

In the case of the compressor blade test rig the clamping mechanism between the blade and the root block could not be modified, but the best way how to support the full test rig needed to be addressed. Initially the root block was placed on a soft foam, but a harder foam and chipboard were also used to investigate the difference in the extracted damping. A free-free support from Fig. 21.1b was also considered to minimise the impact of the support on the system. The shaker was connected to the root block, and the frequency response function was measured at the tip of the blade. The resulting FRFs in Fig. 21.5 shows not surprisingly a strong influence of the support on the resulting response, with the hard foam adding a significant amount of damping, and the free-free support leading to the least amount of damping in the structure. The soft foam also introduced low damping, even if the relatively heavy test rig led to a strong compression of the foam. Based on the results the free-free configuration was chosen as a final configuration for the following investigations.

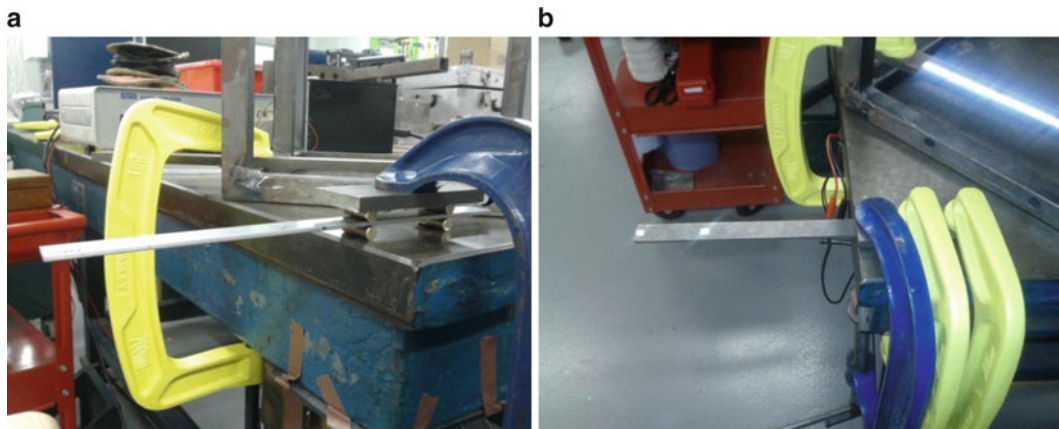
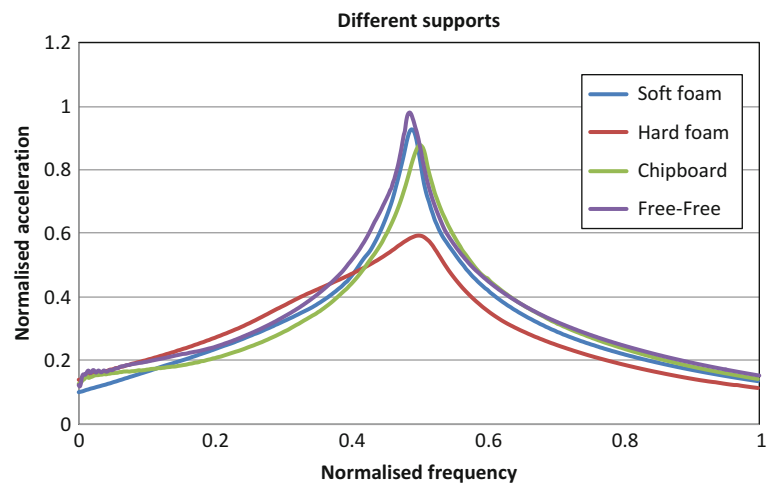


Fig. 21.4 Clamped beam rig: the (a) double hinge configuration and the (b) optimised final clamping setup

Fig. 21.5 Compressor blade test rig: influence of different supports



21.4 Excitation System

To reach the high amplitudes that are required for operational level tests and to activate possible nonlinearities in the system a shaker must be used on the clamped beam test rig. A stepped sine sweep was performed to extract the frequency response function of the cantilever beam for its first bending mode. The shaker was suspended in a free-free configuration over the cantilever beam, and it was permanently connected to the beam via a stinger (see Fig. 21.1a). A force transducer was used to measure the excitation force of the system and the response was measured with a light weight accelerometer one third along the beam from the clamp. An amplitude controlled FRF measurement was used to achieve a constant activation of the nonlinearity throughout the frequency range, leading to a linearised frequency response for a given amplitude level. This allowed the use of the linear modal analysis tool ICATS to extract the damping behaviour for each amplitude level.

Five different levels of acceleration have been tested from 10 to 70 m/s^2 (0.025–0.35 mm displacement). The FRFs in Fig. 21.6a shows some softening effects with a frequency drop of 1 % at higher response levels and a strong change in amplitude. Especially at lower amplitudes the loss factor in Fig. 21.6b shows a strong nonlinearity while at higher amplitudes the behaviour seems flatter. The extracted damping values were an order of magnitude larger than the free-free impact test values, and four times as high as the original cantilever beam impact data (0.188 %), indicating an influence of not only the clamp, but also of the shaker attachment on the damping behaviour of the overall system. Several attempts with different shaker positions and different stinger settings did not yield a satisfying improvement of the data.

The FRF measurements with the permanently attached shaker showed a strong influence of the rig setup on the extracted damping values and an improved system was needed to reduce this influence. A single frequency free-decay test was successfully used in the past to extract the nonlinear damping parameters of a blade root test rig [11], and this approach was followed to eliminate the influence of the excitation system on the damping measurements. To reach the required high excitation levels, the structure was excited by a shaker, and then the excitation source was instantly disconnected from the

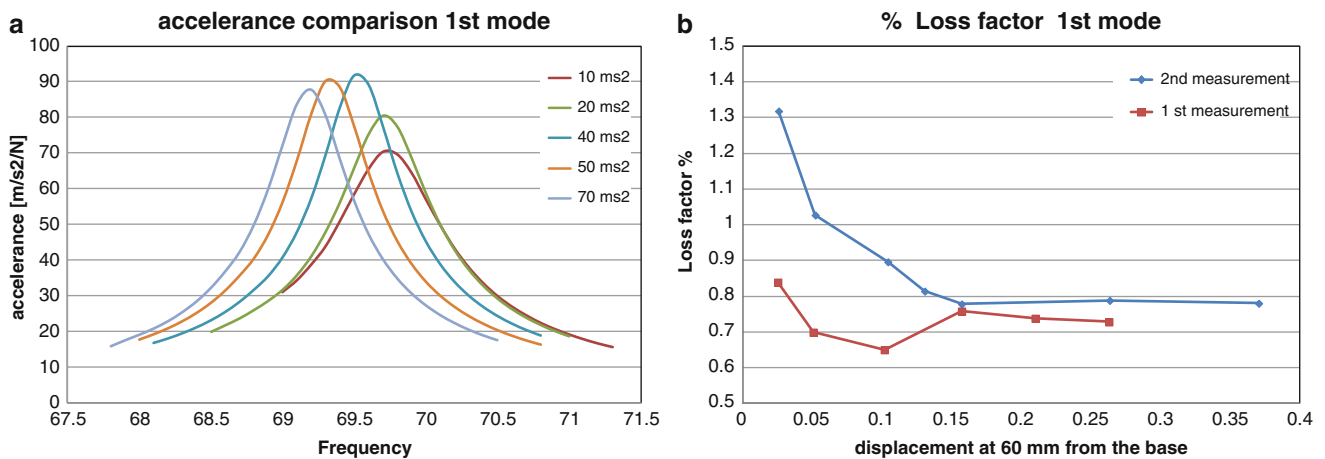


Fig. 21.6 Clamped beam rig: stinger excitation (a) the FRF measurements and (b) damping behaviour of the 1st mode

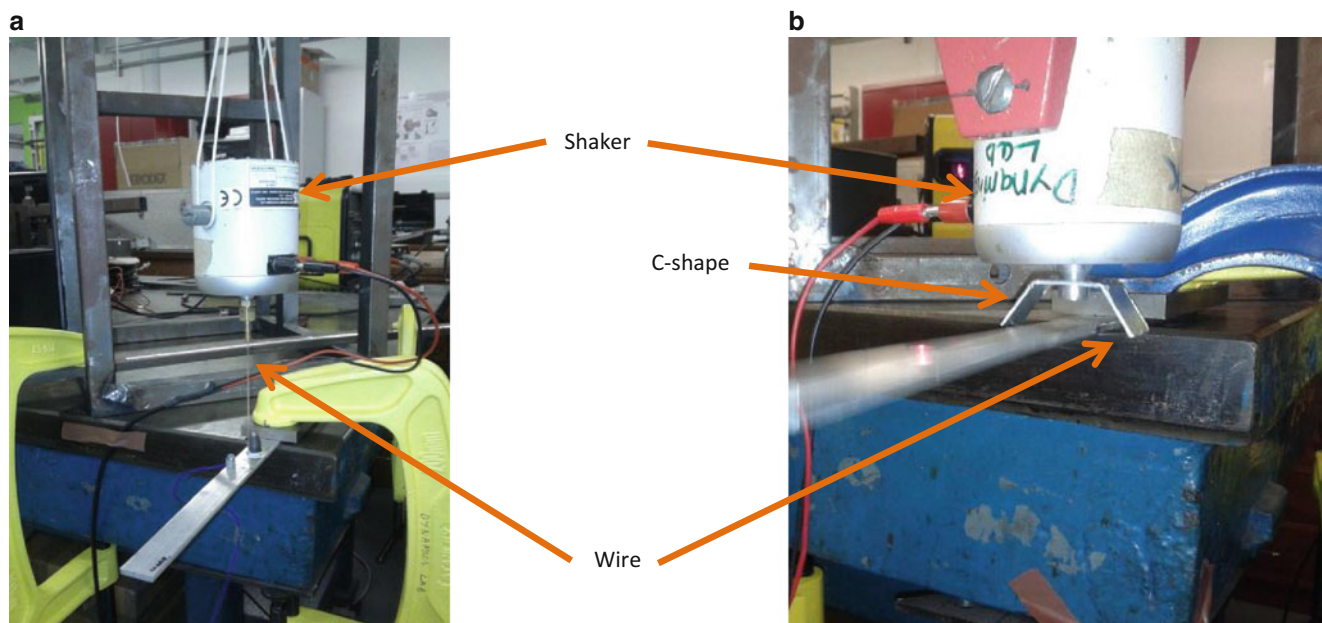


Fig. 21.7 Clamped beam rig: the (a) initial fishing wire setup and (b) the final c-shaped fishing wire excitation method

structure. The resulting free decay response of the system was recorded and the loss factor was extracted with the logarithmic decrement technique from the time domain. This approach allows the extraction of the damping-over-amplitude curve in a single measurement, and is a very efficient method to evaluate the damping behaviour of the beam. Once the excitation source is disconnected from the beam, there is no contact of the rig with the beam apart from its clamp, minimising the effect of the setup.

The instantaneous removal of the excitation system from the beam presents quite a technical challenge since on the one hand enough energy must be transmitted for the high amplitude tests, on the other hand a gentle release into free decay is required. Initially a thin fishing wire was used as a connection element between the shaker and the beam (Fig. 21.7a). Once the target amplitude was reached, the wire was burned through to release the beam into a free decay vibration. Good excitation levels could be reached with this setup, but due to the high required pretension in the fishing wire, a transient was introduced during the release (pinging) which made a reliable use of the free decay method for damping extraction relatively inaccurate. To minimise this problem a second setup in Fig. 21.7b used a C-shaped aluminium frame that placed the tensioned wire underneath the beam, orthogonal to the main excitation direction. A similar approach had been used successfully in the past [13], and it allows large excitation levels coupled with a very gentle release of the beam into a single

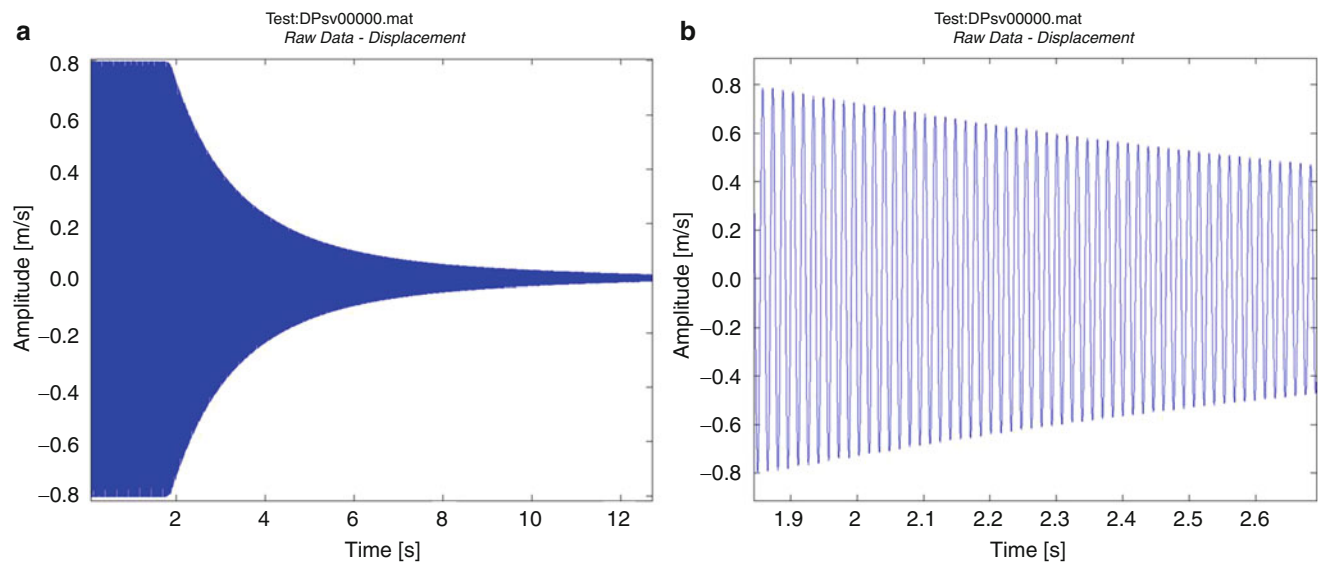


Fig. 21.8 Clamped beam rig: the (a) free decay response of the beam and (b) a detail of the measured data

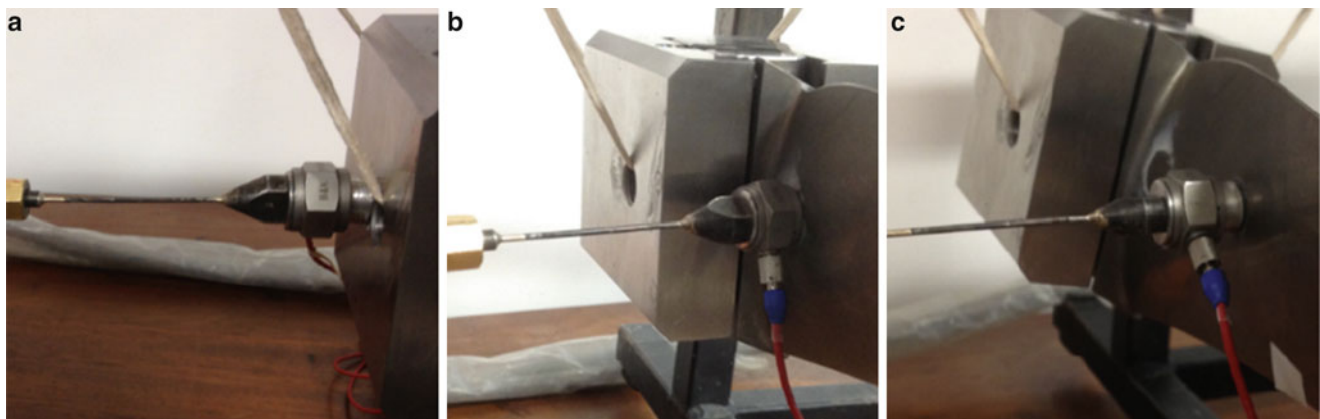


Fig. 21.9 Compressor blade test rig: shaker attachment points at (a) root block, (b) blade root, and (c) mid span

frequency free decay (see time domain data in Fig. 21.8). With this excitation and the logarithmic decay damping extraction approach the observed damping values became similar to the impact hammer tests (see results in Fig. 21.3 for optimised clamping), confirming the suitability of the proposed excitation method.

Based on the experience with the clamped beam test rig the use of a wire excitation system for the compressor blade rig was considered, but due to the required high excitation levels and the large amount of damping in the root this proved to be unfeasible. A shaker had to be attached permanently to the test rig, and after several broken thin and flexible stingers a very rigid pushrod had to be used for the experiments to transmit the required excitation force.

In order to find the best excitation point of the system, the shaker location was varied along the blade (see Fig. 21.9), to ensure that the effect of the stiff stinger could be kept to a minimum. For each location, a set of several amplitude-controlled FRFs were acquired. The behaviour of the loss factor in Fig. 21.10 appears to be significantly different when the shaker is fixed on the blade instead of the clamp, and this influence grows as the shaker is attached closer to the tip of the blade, where the acceleration is recorded. At low amplitudes a bias in the damping is introduced, but for higher amplitudes the behaviour changes and the shaker impacts the dynamics of the blade. The results suggest that due to the necessary use of the strong stinger for higher amplitudes, the shaker was not properly decoupled from the test specimen, leading to an interaction between the two. Attaching the shaker to the least flexible part of the rig with the smallest amount of motion at the clamping block led to the lowest damping values, and can be suggested for this type of experimental setup.

During the investigation two different shakers have been used for the compressor blade rig. The initial setup, used a small LDS V201 shaker which was replaced by a more powerful and larger LDS V406 shaker, which was mounted in the exact same location. Figure 21.11 shows the loss factor behaviour obtained with the two shakers over the same range of amplitudes,

Fig. 21.10 Compressor blade test rig: damping behaviour for different excitation locations

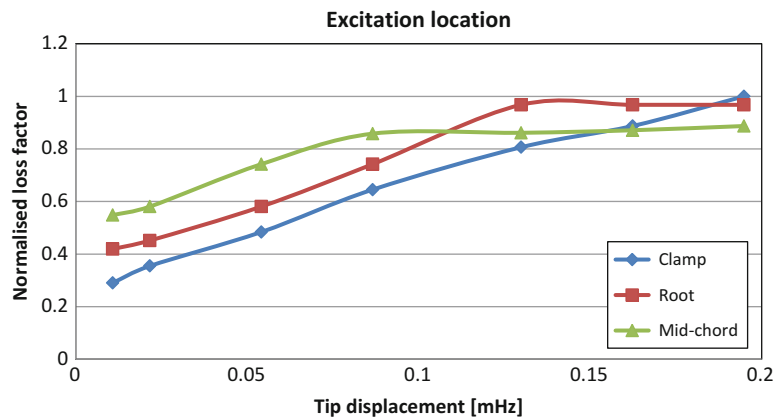
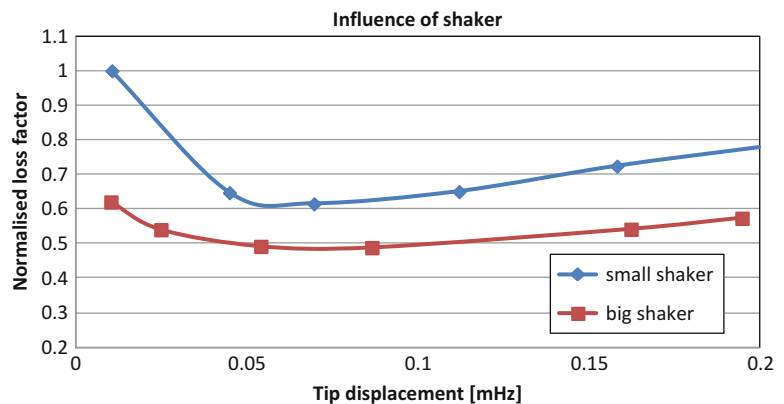


Fig. 21.11 Compressor blade test rig: influence of different shaker sizes on the damping behaviour



and highlighting the effect from the internal energy dissipation occurring in the shaker. The difference between the values given by the two rigs is nearly constant throughout the amplitude range, but the smaller and older shaker leads to more damping, indicating a stronger coupling via the ridged pushrod. Selecting the correct shaker for the experiment is therefore an important part of the setup procedure.

An additional interesting observation with regard to the test setup can be made when comparing the damping behaviour from Figs. 21.10 and 21.11. The values themselves are still similar, but the damping behaviour at lower amplitudes has changed between the two test setups. Since the setup itself was the same, this was attributed to the different times at which the measurements were taken. The results in Fig. 21.10 were taken during a hot day, whereas the results in Fig. 21.11 were obtained at a much cooler day. The change in ambient temperature may have led to a slight thermal expansion of the material resulting in a greater axial load applied at the root of the blade for one configuration, whereas the clamping torque applied to the bolts at the bottom of the clamp was not modified. This highlights the importance to ensure constant test conditions while performing the experiments, especially if they are concerned with nonlinear damping, since small changes to the contact conditions can affect the damping response significantly.

21.5 Influence of Amplitude Control

When measuring the frequency response function of a nonlinear system great care is required as to what type of excitation control is implemented during the tests, since the nonlinearity is normally activated by the level of amplitude, and as such a change of amplitude during a resonance frequency pass can lead to the measurement of different systems. Three different approaches can be chosen to carry out the measurements: (1) no control where the output voltage of the signal generation is simply kept constant, (2) force control, where the input force is monitored during the measurement and the output voltage adjusted for each frequency step to ensure a constant excitation force, or (3) amplitude control, where the response amplitude is kept constant and the output voltage to the amplifier adjusted accordingly.

The linear line fitting method [11] is being used to extract the damping parameters from the un-, force-, and amplitude-controlled FRFs. It must be noted that if the amplitude is not controlled it is not correct to refer to the value given by the

Fig. 21.12 Compressor blade test rig: (a) amplitude controlled test rig: signal (Displacement) and (b) corresponding excitation force

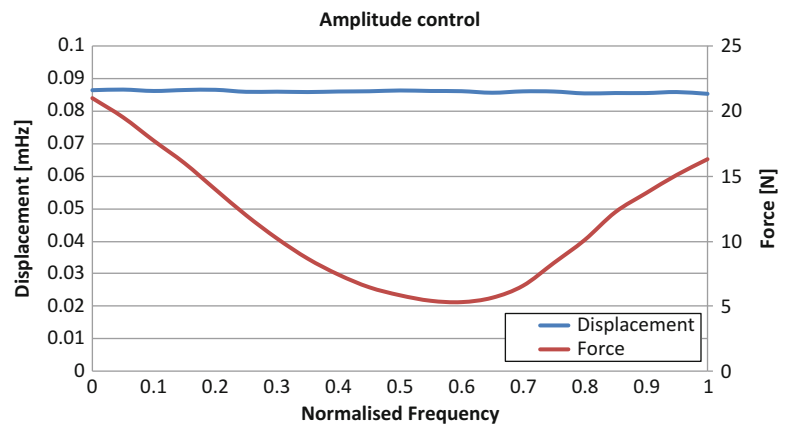
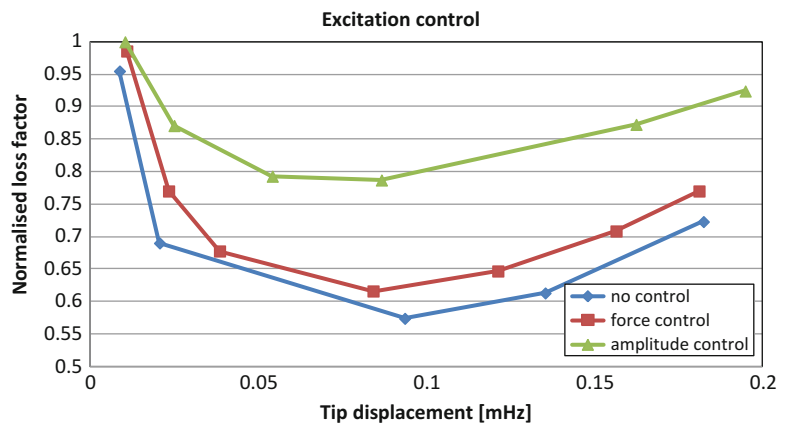


Fig. 21.13 Compressor blade test rig: difference in the damping behaviour due to different control algorithms



line-fit method as the real loss factor associated to the resonance. Due to a varying activation of the nonlinearity in the system, the damping varies through the frequency range but the line-fit method assumes a constant damping in the frequency range. The value can then only be referred to as an approximation of the loss factor over the frequency range, but not as an accurate damping parameter. A constant amplitude throughout the frequency range (see Fig. 21.12) leads to a linearisation of the system around the resonance which allows the application of traditional linear modal analysis methods to extract the damping. To investigate the influence of the different control methods on the compressor blade test rig all three methods have been implemented and the frequency response functions have been measured.

The overall damping behaviour of all three investigated control methods in Fig. 21.13 looks relatively similar, but the absolute values vary strongly from each other. All three tests lead to similar damping values at low amplitudes where the nonlinearity is not really activated, but once slip is taking place in the root the uncontrolled and force controlled damping values are much lower than the amplitude controlled values. In the free and force controlled test the maximum damping is only reached at resonance and lower damping is present the rest of the time, leading to on average lower values, whereas in the amplitude test the maximum damping is present throughout the frequency range. For a reliable extraction of the damping values of a nonlinear system an amplitude controlled test must therefore be used.

21.6 Discussion

Measuring the damping behaviour of a linear or nonlinear structure requires a careful planning of the test setup to minimise the influence of the test rig.

When clamping a test specimen to a solid foundation and exciting it a large amplitudes, great care is required that the applied clamping load is evenly distributed over the clamping surface, and that an accurate control over the clamping load is maintained to ensure minimal slip in the clamping and repeatability of the tests. Two flat clamping surfaces and a very densely packed load introduction gave the best clamping results for the clamped beam test rig. When it comes to choosing the best foundation for a test rig, then either a soft foam bed, or better a free-free support should be used, since any other support shows a strong effect on the damping behaviour.

The investigation into the best excitation method highlighted the influence of the shaker on the test results for both test rigs. Also, in theory, the stinger between the shaker and the test specimen is supposed to fully decouple the shaker from the test specimen, in practice this seems to be difficult to achieve, since a relatively stiff stinger is required to reach the large amplitudes and activate the nonlinearities. Two different approaches can be suggested to reduce the influence of the shaker on the response, either by attaching the shaker to a location of low flexibility and motion, or by replacing the permanently attached stinger with a detachable system that allows the measurement of the damping behaviour during single frequency free decay. The latter approach seems to be particularly interesting, since it yields the pure system response, but it does restrict the total amount of transmitted energy and may not always be practical.

When the extraction of the nonlinear damping behaviour from an FRF measurement is of main concern, than an amplitude controlled test is the best way to proceed, since it activates the nonlinearity at the same level over the entire frequency range linearising the system and allowing the use of standard modal analysis techniques for the damping extraction. The damping properties extracted for an amplitude-controlled test are only valid for that particular amplitude, and should not be used at other levels. No control or a force control lead to significant differences in damping behaviour, and should be avoided for this type of experiment.

21.7 Conclusion

The measurement of the linear or nonlinear damping characteristic of a structure requires significant consideration since the measured quantities are either very small, or the required amplitudes very large. To minimise the influence of the test rig the following should be implemented: (1) the correct clamping mechanism with a well distributed clamping load over a flat surface, and a good foundation for the test rig with either soft foam or a free-free suspension especially if the entire rig is vibrating; (2) the correct excitation mechanism and location, either by attaching the shaker in a relatively rigid location and using the thinnest possible stinger, or better setting the system up in a way that the excitation can be removed and a free decay measurements can be conducted; (3) the correct excitation control, since only an amplitude controlled frequency response measurement allows the reliable use of linear damping extraction methods.

Acknowledgements The authors are grateful to Rolls-Royce Plc. for providing financial support for this work and for giving permission to publish this work.

References

1. Firrone CM, Zucca S, Gola M (2009) Effect of static/dynamic coupling on the forced response of turbine bladed disks with underplatform dampers. In: Proceedings of ASME turbo expo, Orlando, GT2009-59905, 8–12 June 2009
2. Cigeroglu E, An N, Menq CH (2007) Wedge damper modeling and forced response prediction of frictionally constrained blades. In: Proceedings of ASME turbo expo, Montreal, GT2007-27963, 14–17 May 2007
3. Petrov EP (2008) Explicit finite element models of friction dampers in forced response analysis of bladed disks. *J Eng Gas Turbines Power* 130(2):022502
4. Charleux D, Gibert C, Thouverez F, Dupeux J (2006) Numerical and experimental study of friction damping in blade attachments of rotating bladed disks. *Int J Rotat Mach* Article ID 71302:1–13
5. Petrov EP, Ewins DJ (2006) Effects of damping and varying contact area at blade-disc joints in forced response analysis of bladed disc assemblies. *ASME J Turbomach* 128:403–410
6. Chen JJ, Menq CH (2001) Prediction of periodic response of blades having 3D nonlinear shroud constraints. *ASME J Eng Gas Turbines Power* 123(2001):901–909
7. Petrov EP (2004) A method for use of cyclic symmetry properties in analysis of nonlinear multiharmonic vibrations of bladed discs. *Trans ASME J Turbomach* 126:175–183
8. Schwingshackl CW, Petrov EP (2012) Modelling of flange joints for the nonlinear dynamic analysis of gas turbine engine casings. *J Eng Gas Turbines Power* 134(12):122504
9. Ruffini V, Schwingshackl CW, Green JS (2013) LDV measurement of local nonlinear contact conditions of flange joint. In: Proceedings of the international modal analysis conference XXXI, Los Angeles, CA, Jan 2013
10. Di Maio D, Bennett P, Schwingshackl CW, Ewins DJ, (2013) Experimental non-linear modal testing of an aircraft engine casing assembly. In: Proceedings of the international modal analysis conference XXXI, Los Angeles, CA, Jan 2013
11. Miyakozawa T, Peng C, Brace M, Turner S, Andrews S (2012) Pre-laboratory rig test friction damping simulations of stators and rotors of an axial compressor. In: Proceedings of ISUAT 2012, University of Tokyo, Tokyo
12. Ewins DJ (2000) *Modal testing: theory, practice and application*, 2nd edn. Research Studies Press LTD, Baldock
13. Schwingshackl CW, Zolfi F, Ewins DJ, Coro A, Alonso R (2009) Nonlinear friction damping measurements over a wide range of amplitudes. In: Proceedings of the international modal analysis conference XXVII, Orlando

Chapter 22

Microslip Joint Damping Prediction Using Thin-Layer Elements

Christian Ehrlich, André Schmidt, and Lothar Gaul

Abstract In this work, an efficient FE-modeling technique for assembled metallic structures is presented. Linear thin-layer elements containing damping and stiffness parameters are placed on the interfaces of bolted joints. The interface parameters are identified experimentally on an isolated lap joint and then used as an input for the FE-simulation. Since the presented modeling technique is linear, it delivers acceptable results only for small relative displacements in the joint interface, i.e. microslip. Therefore investigations on the transition from micro- to macroslip are conducted. A promising approach to detect macroslip is based on the significant increase of higher harmonic frequency generation. The application of this criterion results in a linear relation between the normal force and the maximum tolerable tangential force.

Keywords Joints • Damping • Thin-layer elements • Nonlinear effects • Finite element method

22.1 Introduction

Eigenfrequencies and mode shapes, even those of complex structures, can be predicted accurately with the Finite Element Method. However, correct decisions in the design phase as to whether the vibrational and acoustic properties of a certain design are satisfactory, cannot be made without knowledge of the amplitude of the vibration. Estimating modal amplitudes is only possible with an accurate damping model. Since there is no recognized, simple and accurate method for predicting the dissipative properties of complex structures, the industry either ignores damping or uses a rule of thumb. This paper presents an approach for the prediction of damping of a structure in the design phase. This method is only applicable if no nonlinearities introduced by macroslip are present. Therefore a method to distinguish between micro- and macroslip based on the nonlinearity is developed.

In a structure assembled solely with bolted joints there are two major contributors to energy dissipation (ignoring acoustic radiation and gas pumping): material damping and joint damping. Material damping is caused by inner friction within a material [8]. Therefore its effect appears throughout the entire structure and influences all modes equally. Joint damping is the paramount influence factor to modal damping of an assembled structure. Generally it is about 10–100 times higher than material damping and only occurs locally at the interface of two members. Therefore it has varying influence on different modes, depending on the participation of the interface in the particular mode.

Experimental investigations have shown that material damping and joint damping are both weakly dependent on frequency [4]. Therefore the model of constant hysteretic damping, which assumes the dissipated energy per cycle to be independent of the frequency, is applied.

In order to depict the local influence of the joint damping, thin-layer elements (TLEs) are placed on all interfaces of the assembled structure [3]. Those elements contain the stiffness and the loss factor of the joint and preserve the localization of the interface damping. Material damping is modeled using a global loss factor.

The material properties for the TLEs are determined experimentally on an isolated lap joint.

C. Ehrlich (✉) • A. Schmidt • L. Gaul

Institute of Applied and Experimental Mechanics, University of Stuttgart, Pfaffenwaldring 9, 70550 Stuttgart, Germany
e-mail: ehrllich@iam.uni-stuttgart.de

Fig. 22.1 Experimental setup for joint parameter extraction

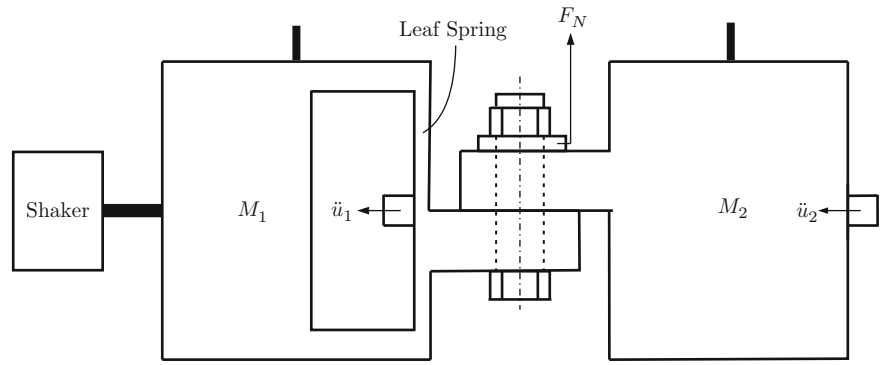
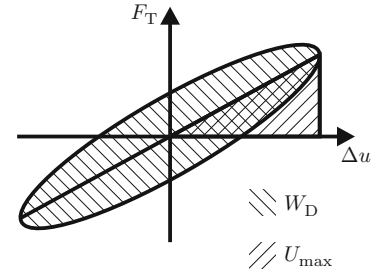


Fig. 22.2 Schematic hysteresis curve



22.2 Experimental Joint Parameter Extraction

In order to determine the parameters needed to predict the damping behavior of a complex structure, measurements on an isolated, representative joint are conducted. The experimental setup is depicted in Fig. 22.1. It consists of two masses M_1 and M_2 , each supported by thin wires at their respective center of gravity and connected with a steel lap joint. It is important to assure that the joint in the experiment reflects the joint in the assembled structure as accurately as possible. Therefore key characteristics like the materials, surface finish, and normal pressure have to be equal. M_1 features a leaf spring which improves the system response drastically. The structure is excited with a shaker and when the system is in steady state, the accelerations \ddot{u}_1 and \ddot{u}_2 are recorded with accelerometers. Additionally, the normal force in the joint F_N is monitored with a force measuring ring.

The transmitted force F_T can be calculated as product of \ddot{u}_2 and M_2 . The relative displacement Δu in the joint can be computed as the difference of the displacements u_1 and u_2 of the Masses M_1 and M_2 . The displacements are obtained by integrating \ddot{u}_1 and \ddot{u}_2 twice. Plotting the transmitted force over the relative displacement yields the hysteresis curve. The stiffness is given as the slope of the hysteresis curve. The loss factor η is defined as the dissipated energy per cycle W_D divided by 2π times the maximum stored energy U_{\max}

$$\eta = \frac{W_D}{2\pi U_{\max}}. \quad (22.1)$$

The graphical representation of W_D and U_{\max} is depicted in Fig. 22.2.

Once the joint parameters are extracted, they serve as an input to the FE simulation. The influence of different normal and tangential forces on the joint parameters and the applicability of the modeling technique will be discussed Sect. 22.4. Previous work shows no significant influence of the frequency on loss factor and stiffness [1].

22.3 FE Simulation

Due to the weak dependency of both, material damping and joint damping, on frequency, the model of constant hysteretic damping is applied [7]. This approach is only valid in the frequency domain since it is not causal in the time domain [5]. Previous work shows good correlation with experimentally determined parameters [1].

Starting point for the simulation is the equation of motion for a free undamped system

$$\underline{M} \ddot{\underline{u}} + \underline{K} \underline{u} = \underline{0}, \quad (22.2)$$

where \underline{M} is the mass matrix, \underline{K} is the real-valued stiffness matrix and \underline{u} is the displacement vector.

Using the model of constant hysteretic damping, the undamped model can be modified to include damping. For that purpose, the frequency independent damping will be incorporated into the stiffness matrix by adding the complex-valued product of the dissipation multipliers (α_i for the material and β_i for the joints) and the associated elements stiffness matrices $\underline{K}^{(\text{Material})}$ and $\underline{K}^{(\text{Joint})}$

$$\underline{K}^* = \underline{K} + j \sum_{i=1}^n \alpha_i \underline{K}_i^{(\text{Material})} + j \sum_{i=1}^m \beta_i \underline{K}_i^{(\text{Joint})}. \quad (22.3)$$

Complex modal analysis can be performed on the modified equation of motion, yielding complex eigenvectors and eigenvalues. From the complex eigenvalues, modal damping factors can be extracted, which are the central goal of this analysis.

Before this is possible, the elasticity matrix of the TLEs has to be determined. For that purpose, a TLE under shear deformation is considered. For a linear material the shear stress τ is given by

$$\tau = G\gamma \approx G \frac{\Delta u}{d}, \quad (22.4)$$

where G is the shear modulus, γ is the shear angle, Δu the relative tangential displacement and d the thickness of the TLE. Furthermore, the shear stress can be approximated by the ratio of the tangential force F_T and the area of the contact patch A

$$\tau = \frac{F_T}{A}. \quad (22.5)$$

Combining Eqs. (22.4) and (22.5) yields

$$F_T = \frac{GA}{d} u = cu, \quad (22.6)$$

where c is the experimentally extracted stiffness. Measuring c and A , the shear modulus for the TLEs can be calculated as

$$G = \frac{cd}{A}. \quad (22.7)$$

It is important to note that G depends on d , which means it must be adapted when the thickness of the TLEs is modified.

At this point, one must consider the orthotropic characteristic of bolted joints with decisively different behavior in normal and tangential direction. The tangential parameters have major influence on the overall behavior of the structure, whereas the normal parameters have little influence [10]. This leads to two conclusions. First, the TLEs should be modeled with orthotropic behavior. Second, experimental determination of the tangential parameters is sufficient. Normal parameters can be estimated. Orthotropic behavior leads to the following constitutive equation for the TLEs

$$\begin{bmatrix} \sigma_{xx} \\ \sigma_{yy} \\ \sigma_{zz} \\ \sigma_{xy} \\ \sigma_{yz} \\ \sigma_{zx} \end{bmatrix} = \begin{bmatrix} E_{11} & E_{12} & E_{13} & 0 & 0 & 0 \\ & E_{22} & E_{23} & 0 & 0 & 0 \\ & & E_{33} & 0 & 0 & 0 \\ & & & E_{44} & 0 & 0 \\ & & & & E_{55} & 0 \\ & & & & & E_{66} \end{bmatrix} \begin{bmatrix} \epsilon_{xx} \\ \epsilon_{yy} \\ \epsilon_{zz} \\ \epsilon_{xy} \\ \epsilon_{yz} \\ \epsilon_{zx} \end{bmatrix}. \quad (22.8)$$

Since there is no transversal contraction in the interface, the off-diagonal terms are zeros. Accordingly E_{11} , E_{22} , and E_{44} vanish because the interface has no stiffness parallel to the interface or for in-plane shearing. E_{33} represents the normal stiffness and $E_{55} = E_{66} = G$ define the tangential stiffness.

The validity of this modeling approach is demonstrated in [1]. There, numerical and experimental modal analysis are performed for a simple U-shaped structure. For the simulation, joint parameters are extracted from a generic experiment.

The first 10 modes of the structure are analyzed. For 8 of those modes, the predicted damping is within 25 % of the experimental value. The other two modes differ by 58 and 89 %. Considering the sensitivity of damping and the simplicity of the modeling approach, these are good results.

22.4 Differentiation Between Micro- and Macroslip

The presented modeling technique is linear which requires careful definition of the limits of its applicability.

A very important distinction in this context is between microslip and macroslip. Microslip occurs under high normal and/or low tangential forces. Small areas of the contact area slip, while a large part of the contact is still sticking. If the normal forces are decreased and/or the tangential forces increased, the components start to globally move relative to each other. This is called macroslip. While macroslip always introduces significant nonlinearity, in its absence, joint damping can still be linearized with acceptable accuracy [2]. Therefore a reliable parameter to indicate the presence of macroslip is needed.

In order to investigate the transition from micro- to macroslip experiments with the basic setup of Fig. 22.1 are conducted. For different normal force levels, the tangential load is increased until macroslip is prevalent.

Examining the hysteresis curves for different tangential loads gives a good first insight into the process. Instead of plotting F_T over Δu , \ddot{u}_2 over \ddot{u}_1 is used. Those curves show the same basic behavior but the influence of higher harmonic frequencies, e.g. non-linearities, is more apparent.

Figure 22.3 illustrates the transition from micro- to macroslip. Data for measurements at a normal force of 1,500 N and increasing tangential forces of 80, 110, and 250 N, are depicted. In the case of pure microslip, as in Fig. 22.3a, the hysteresis is typically very thin, indicating a low loss factor. Only rotating and rescaling reveals the shape which is close to an ellipse. A linear system with constant hysteretic damping shows a perfectly elliptic hysteresis loop. In the macroslip regime (Fig. 22.3c), the hysteresis curve opens significantly, showing the increase in dissipated energy. Also, the shape changes to a lancet with clearly visible sliding at the tips.

In the case of harmonic excitation, it is obvious, that the transition from micro- to macroslip must be a gradual process. As the excitation amplitude is increased, larger and larger portions of the transmitted force will exceed the maximum transferable force, therefore resulting in more and more macroslip. Therefore finding a crisp barrier between the two regimes is unlikely.

Even though evaluating the shape of the hysteresis curve provides very direct information about the occurrence of slip, it does not serve well as a sole decision criterion. It is slow, subjective, and unquantifiable. It is also not precise because a significant amount of macroslip and nonlinearity have to be present for the hysteresis curve to be visibly deformed. Other parameters to indicate the presence of macroslip are based on the progression of the loss factor and the dissipated energy [9]. However, they lack the precision needed in this case.

Yet, the observation of the hysteresis curve can be the basis to a better decision strategy. First, one has to examine the curves more closely, in order to be able to detect the first occurrence of macroslip more accurately. For that purpose one can rotate and rescale them. Figure 22.4 shows the curves of Fig. 22.3a, b. While Fig. 22.4a shows good correlation to an ellipse, Fig. 22.4b clearly deviates from that shape. Now that more precise information about the transition is available, it can be linked to the original cause for the deformation: higher harmonic frequency components. As a nonlinearity parameter, the ratio of the third harmonic amplitude A_3 and the base amplitude A_1 of the acceleration is defined

$$\kappa = \frac{A_3}{A_1}. \quad (22.9)$$

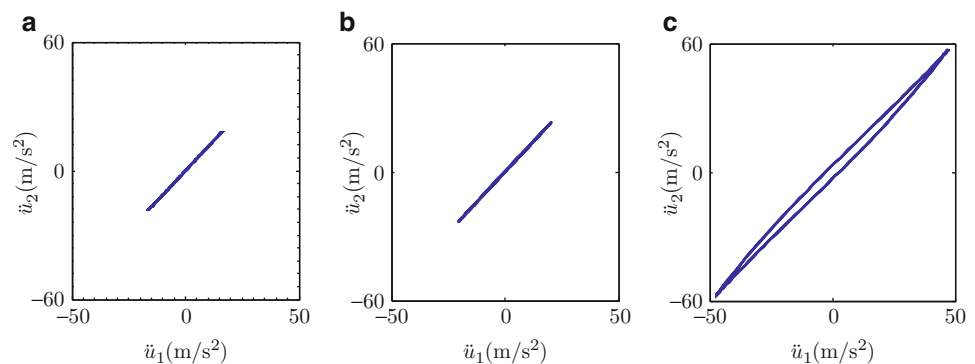


Fig. 22.3 Typical hysteresis curves for microslip (a), transition (b) and macroslip (c)

Fig. 22.4 Rotated and scaled hysteresis curves without (a) and with (b) significant deformation due to macroslip

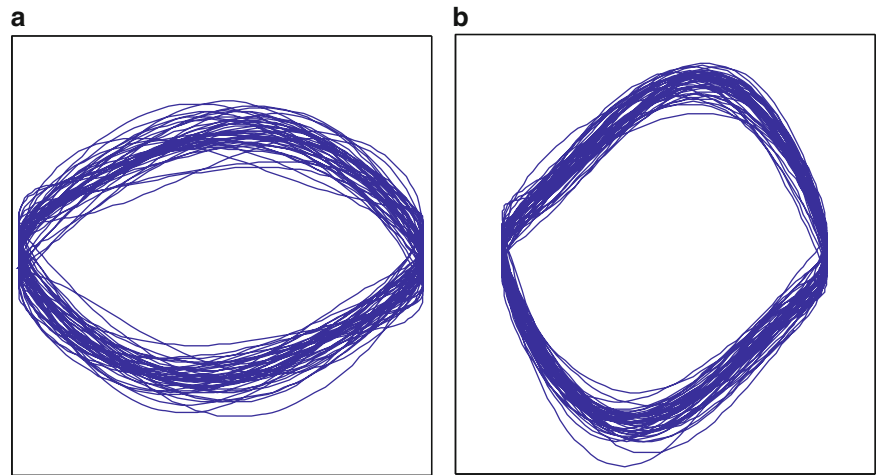
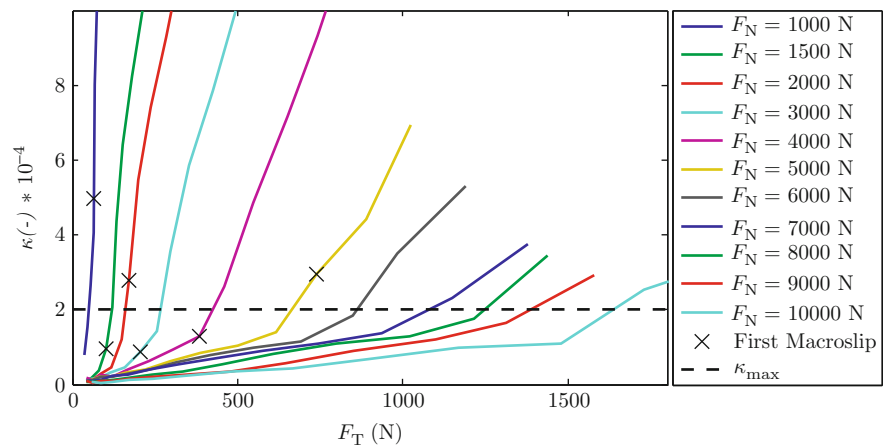


Fig. 22.5 Nonlinearity parameter for different normal and tangential forces



Since the third harmonic amplitude is the largest among the higher harmonic frequency components, it is chosen as the indicator for nonlinearity. For normal forces from 1,000 to 5,000 N, the appearance of macroslip can always be linked to a nonlinearity $0.9 \times 10^{-4} < \kappa < 5.0 \times 10^{-4}$. For higher normal forces, the hysteresis curve becomes so narrow that rescaling does not work reliably. Therefore the transition cannot be monitored as accurately. Still, a transition within the specified nonlinearity range is expected. Figure 22.5 shows the nonlinearity parameter for different normal forces and tangential forces. Additionally, the first measurement with clearly visible macroslip is marked.

Defining a barrier between micro- and macroslip is now a matter of finding a reasonable κ value. In this case $\kappa_{\max} = 2 \times 10^{-4}$ is chosen. Even though this allows for macroslip in some cases, the nonlinearity overall is still very low. Obviously there is significant uncertainty in defining a value for κ_{\max} . This stems from the gradual nature of the transition and measurement inaccuracy. The uncertainty can be dealt with mathematically by applying Fuzzy arithmetic [6], which is not within the scope of this paper.

Applying κ_{\max} to the presented measurements leads to a set of maximum tolerable tangential forces as a function of the normal force. As can be seen in Fig. 22.6, a straight line can be fitted well to the data. Thus, the limit of applicability of the presented modeling technique can be expressed by a single parameter. For the steel joint under investigation in this work, a slope of $\mu = 0.15$ is determined. Choosing $\kappa_{\max} = 0.9 \times 10^{-4}$, the lowest nonlinearity for which macroslip can be observed, results in $\mu = 0.09$.

Figure 22.7 shows the loss factor and the dissipated energy for different excitation forces and a constant normal force of 1,500 N. Additionally the maximum tolerable tangential force is marked with “x”. It can be seen, that both parameters stay almost constant below the defined transition. Therefore the uncertainty of the input parameters is restricted.

Having extracted μ , one can now check the application at hand. If the applied tangential load is lower than the tolerable force considering the applied normal force, macroslip will be avoided and the presented modeling approach is applicable.

Fig. 22.6 Maximum tolerable tangential force as function of the normal force

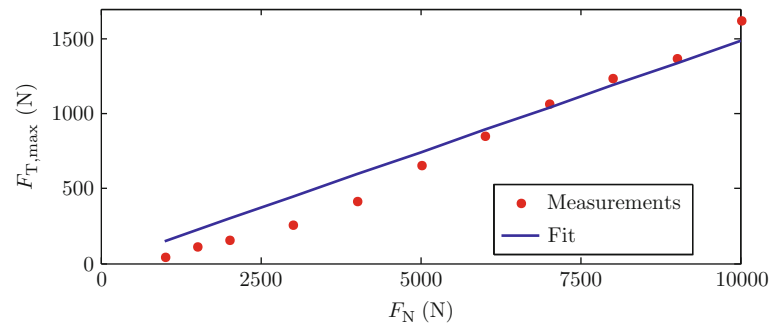
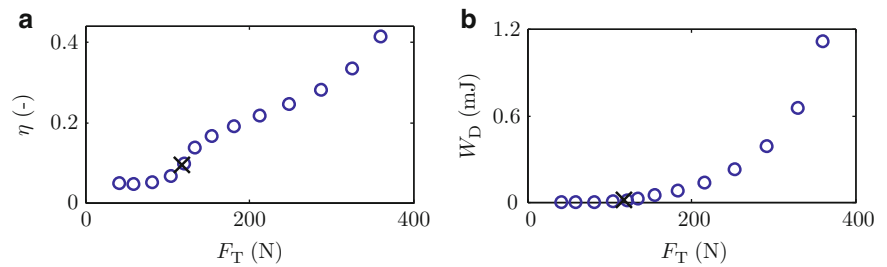


Fig. 22.7 (a) Loss factor and (b) dissipated energy for different excitation forces



22.5 Conclusion

A simple modeling technique to predict damping characteristics of assembled structures is presented. Thin-layer elements are employed to preserve the localization of joint damping. The parameters for the simulation are acquired experimentally on an isolated lap joint.

Since the presented method is linear, it only delivers acceptable results when no macroslip occurs. Experimental investigation on the transition from micro- to macroslip show that higher harmonic amplitudes serve well as an indicator for the presence of macroslip. A nonlinearity parameter based on the third harmonic amplitude is used to define the limit of applicability of the presented modeling approach. This leads to a linear relation between the maximum tolerable tangential force and the normal force. A given assembled structure may be simulated with the presented technique if the applied tangential load is less than the maximum tolerable tangential force, given the normal force.

References

1. Bograd S, Schmidt A, Gaul L (2008) Joint damping prediction by thin layer elements. In: Proceedings of IMAC XXVI: a conference and exposition on structural dynamics, Orlando, 2008
2. Bograd S, Reuss P, Schmidt A, Gaul L, Mayer M (2011) Modeling the dynamics of mechanical joints. *Mech Syst Signal Process* 25(8): 2801–2826
3. Desai CS, Zaman MM, Lightner JG, Siriwardane HJ (1984) Thin-layer element for interfaces and joints. *Int J Numer Anal Method Geomech* 8(1):19–43. ISSN 1096-9853. doi:10.1002/nag.1610080103. <http://dx.doi.org/10.1002/nag.1610080103>
4. Ewins DJ (2000) *Modal testing: theory, practice and application*, vol 2. Research Studies Press, Baldock
5. Gaul L, Klein P, Kemple S (1991) Damping description involving fractional operators. *Mech Syst Signal Process* 5(2):81–88
6. Hanss M (2002) The transformation method for the simulation and analysis of systems with uncertain parameters. *Fuzzy Set Syst* 130(3): 277–289
7. Lakes RS (1999) *Viscoelastic solids*, vol 9. CRC Press, Boca Raton
8. Lazan BJ (1968) *Damping of materials and members in structural mechanics*, vol 214. Pergamon Press, Oxford
9. Lenz J (1997) *Strukturdynamik unter dem Einfluss von Mikro- und Makroschlupf in Fügestellen*. Ph.D. thesis, Inst. A für Mechanik
10. VDI Richtlinie 3830: Damping of Materials and Members, 2005

Chapter 23

Variability and Repeatability of Jointed Structures with Frictional Interfaces

Matthew R. Brake, Pascal Reuss, Daniel J. Segalman, and Lothar Gaul

Abstract Bolted joints are found in almost every assembled system. Damping due to the friction in the interface of the bolted joints dominates the overall damping in these systems. Therefore, in order to accurately model assembled systems, the correct amount of damping as well as the nonlinear characteristics of the bolted joint must be appropriately accounted for. The level of damping, however, is sensitive to many factors, such as the interface condition and the residual stresses. The formulation of the equations of motion hereby has to involve the local properties of the interfacial damping. In this contribution, two different approaches are applied to a two-beam structure coupled by three bolted joint connections: the discontinuous basis function method and a frequency based substructuring formulation. Measurements of three related systems are used to assess the two different modeling approaches: a monolithic beam, a monolithic beam with three interfaces, and a jointed beam with three bolted joints. The FRFs of the three systems are measured in order to quantify the effect of the bolted interfaces, and future work will investigate the ability of the models to predict the FRFs.

Keywords Joints • Interfacial Mechanics • Structural Dynamics • Model Reduction • Dissipation Measurements

23.1 Introduction

With the increases in computational power and numerical methods, computer aided design has allowed engineers to study very large scale problems, including built-up structures. Inherent in these problems are nonlinearities, such as frictional interfaces found in joints. Despite advances in computational ability, these nonlinearities are often neglected or linearized in analyses due to the significant computational cost and lack of numerical stability associated with modelling them in high fidelity. One approach to incorporate these nonlinearities into assembled models efficiently and accurately is to develop reduced order models of linear substructures and then connect them at the location of the nonlinearities using accurate constitutive models of the nonlinear phenomena.

In this paper two reduced order modelling approaches, frequency-based substructuring and augmentation by discontinuous basis functions, are investigated and contrasted with a high fidelity modelling approach, and all three approaches are compared against measurements of the system. In both reduction methods, the first step of the analysis is to develop a reduced order model of the linear substructures. This is achieved via a component mode synthesis model reduction technique [1]. Frequency-based substructuring [2] develops reduced order models in the frequency domain, then couples the linear

Sandia National Laboratories is a multi-program laboratory managed and operated by Sandia Corporation, a wholly owned subsidiary of Lockheed Martin Company, for the U.S. Department of Energy's National Nuclear Security Administration under Contract DE-AC04-94AL85000.

M.R. Brake (✉)

Component Science and Mechanics, Sandia National Laboratories, PO Box 5800, Albuquerque, NM 87185-1070, USA
e-mail: mrbrake@sandia.gov

P. Reuss • L. Gaul

Institute of Applied and Experimental Mechanics, University of Stuttgart, Pfaffenwaldring 9, 70569 Stuttgart, Germany

D.J. Segalman

Multi-Physics Modeling and Simulation, Sandia National Laboratories, PO Box 969, Livermore, CA 94551-9042, USA

substructures via the nonlinear constitutive relationships using Lagrange multipliers. The harmonic balance method is then used to solve for the frequency response of the system. Augmentation by discontinuous basis functions [3, 4], by comparison, first finds the component mode synthesis representation of a related linear system, then supplements them with a set of discontinuous basis functions that are used to account for the nonlinear constitutive forces developed by the nonlinear constraints acting on the system. The response of the system using the discontinuous basis function method is then calculated via direct numerical time integration techniques.

Commonly used methods for modeling bolted interfaces in dynamics models often requires regularization of the interface. Even with calibration, accurately predicting the response of a system with frictional interfaces in a regime outside that used for calibration can be prohibitively difficult [5]. Thus, modeling is faced with two challenges: preserving the salient physics of each substructure, and accurately accounting for the interfacial physics. The two phenomenologically different approaches to model reduction of nonlinear structures presented in this paper are compared to each other and to a high fidelity analysis of the same system. Results indicate that, without sacrificing accuracy, the computational times associated with the model reduction methods are approximately three orders of magnitude faster than the high fidelity model when the same time step is used. The reduced order methods are demonstrated to be stable for a coarser time step than the high fidelity model, allowing for additional computational savings. Comparison of the modeling methods to the measurements is an on-going endeavor.

23.2 Frequency Based Substructuring

Inclusion of nonlinearities, such as interface damping [2, 6], in reduced order models is both of great interest for the computation of large finite element models and also a significant challenge due to the complexity introduced by the nonlinearity. The Craig-Bampton method of component mode synthesis [1] introduces a substructuring concept into the development of reduced order models. As the high fidelity system is recast as a reduced order model, the degrees of freedom in the reduced order model are ordered into two groups: boundary degrees of freedom and internal degrees of freedom. The internal degrees of freedom are not necessarily related to physical quantities, but rather are derived such that the reduced order model and the high fidelity model have similar eigenvectors and eigenvalues up to a specified frequency of interest.

Coupling between each linear substructure is introduced via Lagrange multipliers. The use of the Lagrange multipliers introduces a new set of constraint equations into the system, which can be expressed in terms of the stiffness and damping quantities of the coupled degrees of freedom. The Lagrange multiplier is then set equal to the nonlinear constitutive force representing the coupling between the two degrees of freedom. This results in an equation that is solved iteratively in the frequency domain using the harmonic balance method [7].

A variation on this approach is to represent the system dynamics in a reduced order model using frequency response functions instead of the eigenvalues and eigenvectors that constitute a traditional component mode synthesis representation of a system. Once the system is substructured via the methodology of component mode synthesis, the frequency response functions of the reduced subsystems are used to create a reduced stiffness matrix to describe the frequency-based reduced order model. The nonlinear constitutive models representative of the constraints in the system are then expressed in terms of Lagrange multipliers, and the resulting equations are solved in frequency space [8]. This frequency-based substructuring approach is what is used in the following comparisons.

23.3 Augmentation by Discontinuous Basis Functions

To accommodate the nonlinear interfaces ubiquitous in real structures, the method of discontinuous basis functions is used to calculate time histories of the response of large, numerical models with nonlinear connections. The first step of the method of discontinuous basis functions is to develop a component mode synthesis representation for each monolithic (linear) subcomponent of the system [1]. Those reduced order models, along with linear approximations to the interfaces, are then used to derive basis functions for the overall deformation of the structure. These basis functions consist of linear eigen modes and other functions having discontinuities at the locations of nonlinearity. These functions are devised so that the discontinuities are placed at the locations of localized nonlinearities. This set of basis functions is then used in a Galerkin formulation for the full nonlinear system.

The discontinuous basis functions referenced above are used to augment the set of linear eigen modes that represent the system without nonlinearities. The discontinuous mode shapes are derived by first inserting a linear spring at the location of the nonlinearity in the reduced order models. The eigen modes of the resulting linear structure are then computed. These eigen modes are next differentiated with respect to the spring stiffness of the inserted spring resulting in a set of discontinuous

basis functions that are sometimes referred to as joint modes [4, 9]. This process of differentiation is used in order to remove dependency on the spring stiffness from the resulting mode shapes. In practice, for numerical models, only one discontinuous basis function is needed per nonlinearity. Thus, the full nonlinear system can be modelled using as few modes as necessary for convergence in each linear subsystem, with only one additional discontinuous basis function necessary to represent each of the nonlinearities in the system. This reduced number of basis functions is possible due to the linear basis functions completely spanning the result space of the system: only one discontinuous basis function is needed since it is augmenting a set of functions that already spans the solution space. Without the discontinuous basis function, though, there is no mechanism to adequately resolve the nonlinear constitutive model that is used to couple the linear substructures.

In comparing the method of discontinuous basis functions to the predictions of high fidelity numerical simulations using the finite element method, the method of discontinuous basis functions is found to be as accurate while requiring significantly less computational time [10]. As applied to a system with 1803 degrees of freedom in the full order model, the reduced order model developed contained 18 linear modes and 2 discontinuous basis functions. The transient results for the two methods differed by 0.05 % in predictions of kinetic energy, and 0.7 % in the joint forces. At the same time, the full order model required 5,703 times more computational time than the reduced order model.

This hierarchy of model reduction steps yields very low order models for the nonlinear dynamics. Further, this reduced order system is constructed in such a way that high frequency response is suppressed (due to modal truncation in the component mode synthesis representation) and large time steps are admissible (subject to the nature of the nonlinearity). The computational time is demonstrated to be reduced by over three orders of magnitude while the fidelity at frequencies of interest is retained [4]. Monte Carlo simulations exploring statistical distributions of the nonlinear parameters become tractable, while such is not the case for the full nonlinear systems.

23.4 Experimental System

Three geometries are considered in the following measurements, as shown in Fig. 23.1: a monolithic beam, a monolithic beam with three bolts located near the center of the beam, and two jointed beams held together by three bolts. In all three cases, the system is 72 cm long with a 2.5 cm square cross-section. For both the monolithic beam with three bolts and the jointed beam, the bolt holes are 0.85 cm in diameter, and located approximately along the beam's center line. All of the beams are fabricated from ASTM A283 steel, with 5 cm long M8 bolts. Between the bolt head and the beam, and between the nut and the beam on the other side of the bolt, are 0.3 cm thick washers with a 2.1 cm outer diameter and 0.8 cm inner diameter. Natural frequencies for the three systems are reported in Table 23.1.

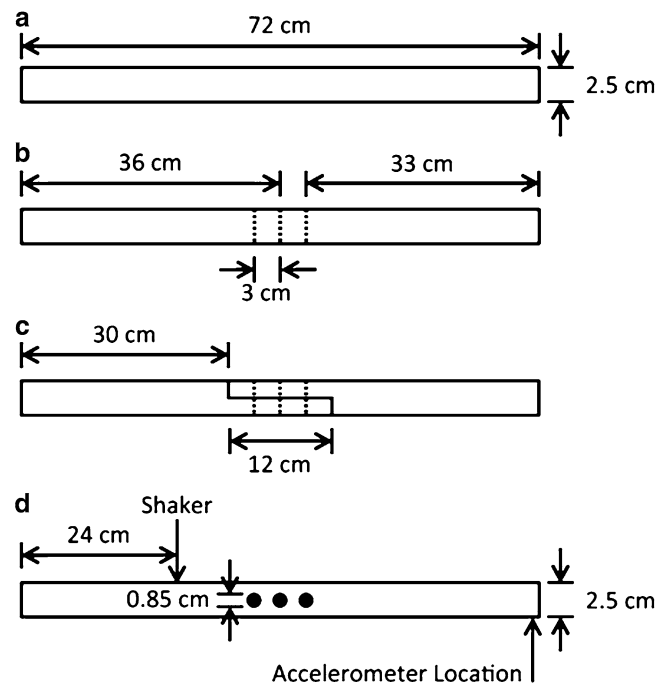
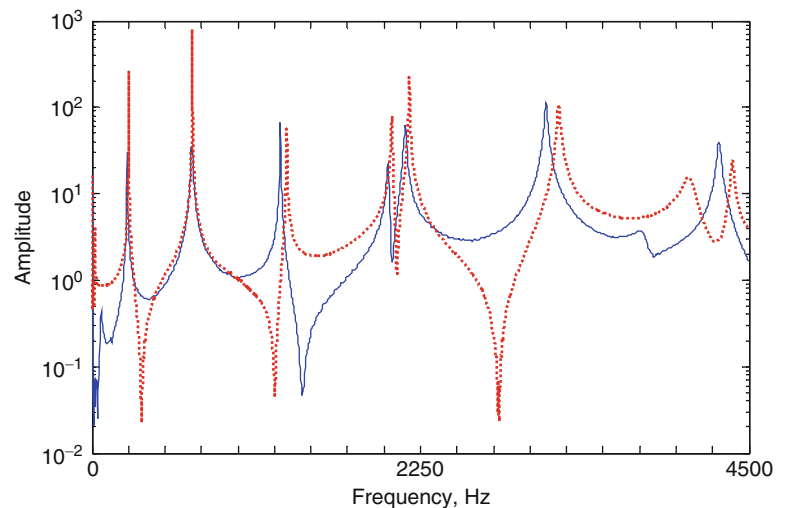


Fig. 23.1 The geometry of the (a) monolithic system, (b) monolithic system with bolt holes, (c) jointed system, and (d) top view of the monolithic system with bolt holes. For both the monolithic system with bolt holes and the jointed system, the size and position of the bolt holes and shaker/stinger attachment point are the same

Table 23.1 Natural frequencies and damping ratios for the three systems

| Mode | Monolithic | | Monolithic with bolts tightened to 10 Nm | | Jointed with bolts tightened to 4 Nm | |
|-------------|------------------------|-------------------|--|-------------------|--------------------------------------|-------------------|
| | Natural frequency (Hz) | Damping ratio (%) | Natural frequency (Hz) | Damping ratio (%) | Natural frequency (Hz) | Damping ratio (%) |
| Bending 1 | 251.4 | 0.0594 | 242.7 | 0.0991 | 240.6 | 0.0933 |
| Bending 2 | 687.4 | 0.0358 | 685.4 | 0.0505 | 684.1 | 0.1098 |
| Bending 3 | 1,333.1 | 0.1199 | 1,290.9 | 0.1840 | 1,284.0 | 0.2658 |
| Bending 4 | 2,172.1 | 0.1216 | 2,146.3 | 0.3198 | 2,115.6 | 0.2692 |
| Bending 5 | 3,196.4 | 0.2848 | 3,118.2 | 0.3560 | 3,105.0 | 0.2026 |
| Bending 6 | 4,385.4 | 0.2374 | 4,307.3 | 0.2958 | 4,281.5 | 0.2147 |
| Torsional 1 | 2,053.1 | 0.1672 | 2,027.9 | 0.2313 | 2,018.7 | 0.3854 |
| Torsional 2 | 4,093.0 | 1.1047 | 3,778.5 | 0.6863 | 3,799.1 | 1.0207 |

Fig. 23.2 FRF for the monolithic beam (*continuous line*) and the monolithic beam with bolts tightened to 10 Nm (*dashed line*)

For the monolithic beam, the natural frequencies and damping ratios are independent of load level. For the jointed system, the natural frequencies and damping ratios both varied with bolt preload, order in which the bolts were tightened, and excitation level as discussed in what follows. The response of all three systems is measured with an accelerometer located at the corner of the beam farthest from the stinger/shaker attachment point. For the monolithic beam, transfer functions are calculated between the response point and 52 excitation points on the beam in order to identify and visualize the mode shapes for the system. Excitation points on the monolithic beam are defined to be at the top and bottom of the face shown in Fig. 23.1, evenly distributed along the beam (with a distance of 3 cm between each response point along the long axis of the beam). An impact hammer is used to excite vibration in the monolithic beam. For consistency, a shaker attached to the beams via a stinger is used to excite both the monolithic beam with bolts and the jointed system. The use of a shaker instead of an impact hammer allows for a consistent application of force that would not be achievable with an impact hammer. The location of the shaker/stinger attachment to the beams is shown in Fig. 23.1 and was determined based off of the modal points observed during the modal analysis of the monolithic beam: a location where a nodal point did not exist for the first 13 modes is chosen, approximately 24 cm from the tip of the beam.

The FRF for both the monolithic beam and the monolithic beam with bolts is shown in Fig. 23.2. The presence of the bolts is shown to decrease the natural frequencies slightly (between 1 and 3.5 %) for the bending modes and first torsional mode. The shift in natural frequency is more pronounced for the second torsional mode, located near 4 kHz. This trend persists at higher frequencies as well: the bending modes change in frequency by less than 2 %, and the torsional modes differ by increasingly larger percentages.

The monolithic beam with bolts does not exhibit any strong nonlinear behaviour. Figure 23.3 presents the FRFs of the monolithic beam with bolts at four different excitation levels (0.1 N, 0.5 N, 1 N, and 2 N). Aside from the small deviation near 1 kHz, which could be an artefact of the shaker/stinger attachment, the response is effectively the same at all excitation levels. By contrast, for a nonlinear system, the response would be expected to change with the excitation level.

The jointed system shows a high degree of variability, as is evident in Fig. 23.4, which is indicative of a strong nonlinearity. Figure 23.4 presents the FRF of the system for a preload of 20 Nm on each bolt across multiple assemblies and three different

Fig. 23.3 FRF for the monolithic beam with bolts at four different excitation levels and bolts preloaded to 10 Nm

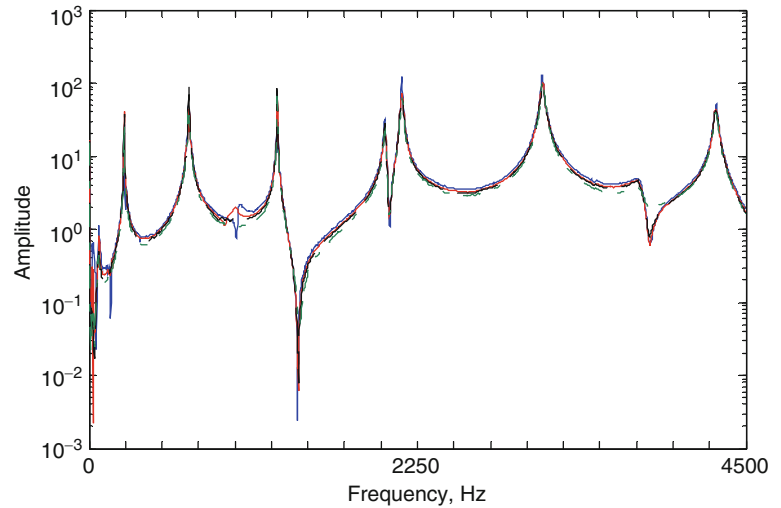
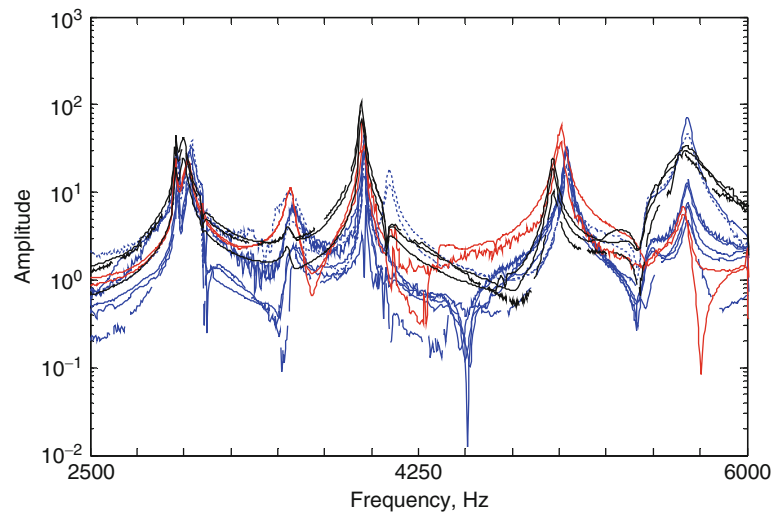


Fig. 23.4 FRF for the jointed beam with bolts tightened to a preload of 20 Nm. The different *color lines* (color figure appear online) correspond to different orders in which the bolts were tightened, and the *continuous* and *dashed lines* correspond to different assemblies of the system under the same conditions



orders of the bolts being tightened. The bolts are tightened only once per assembly as preliminary measurements indicated that there is no loss of preload during a test. There is high test-to-test variability, but the natural frequencies and damping ratios for the bending modes are relatively consistent (such as near 3, 4, and 5 kHz). The torsional modes (near 3.5, 4.2, and 5.7 kHz), however, change in frequency and damping ratio each time the system is reassembled (whether the bolts are tightened in the same order or not). This result indicates that the torsional modes are more sensitive to the interface conditions (such as alignment, roughness, etc.), and the bending modes are more sensitive to the order in which the bolts are tightened (particularly for the bending mode near 5 kHz). The order in which the bolts are tightened is posited to be directly related to differences in residual stresses between each assembly.

At lower preloads, a similar trend is observed: the bending modes (at 1.2 and 1.7 kHz in Fig. 23.5) have consistent natural frequencies across different assemblies and orders of bolt tightening, whereas the torsional mode (near 1.5 kHz in Fig. 23.5) is observed to vary significantly in frequency and slightly in terms of damping ratio. As the system is disassembled and reassembled using the same order of bolt tightening (and thus having a similar residual stress field), the natural frequencies and damping ratios of the bending modes remain consistent, though the amplitude of the response is observed to change.

As the preload of the bolts is increased to 40 Nm, shown in Fig. 23.6, the natural frequencies and damping ratios are observed to remain approximately constant across reassembly for both the torsional mode (now at 1.75 kHz) and the bending modes. This implies that the preload is sufficiently high enough, relative to the excitation level at least, for the system to behave linearly. The magnitude of the response away from the natural frequencies is still observed to be affected by reassembly, implying that the interface conditions still have an effect on the response.

Fig. 23.5 FRF for the jointed beam with bolts tightened to a preload of 5 Nm. The different *color lines* (color figure appear online) correspond to different orders in which the bolts were tightened, and the *continuous* and *dashed lines* correspond to different assemblies of the system under the same conditions

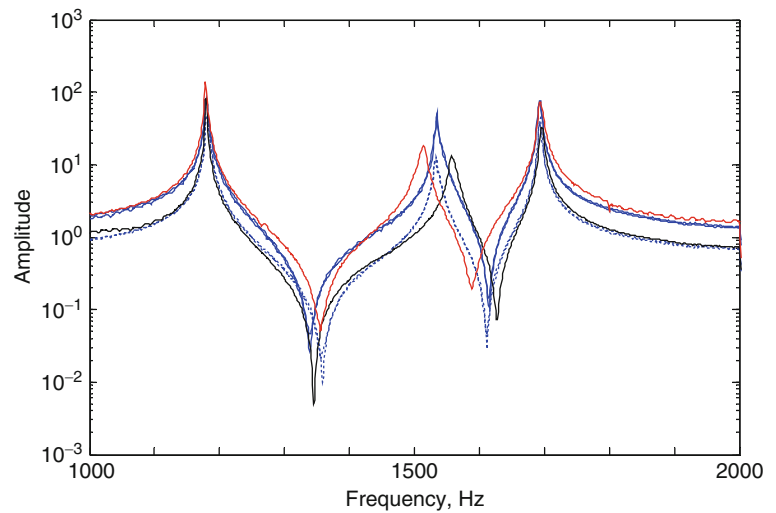


Fig. 23.6 FRF for the jointed beam with bolts tightened to a preload of 40 Nm. The different *color lines* (color figure appear online) correspond to different assemblies of the system under the same conditions

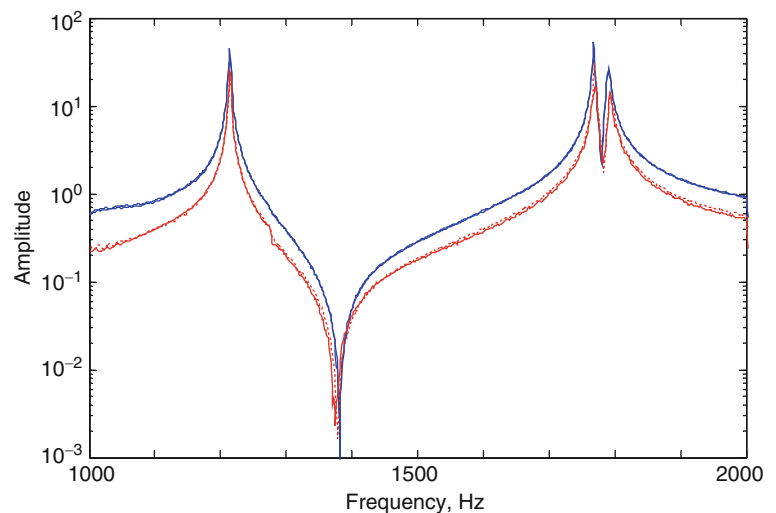


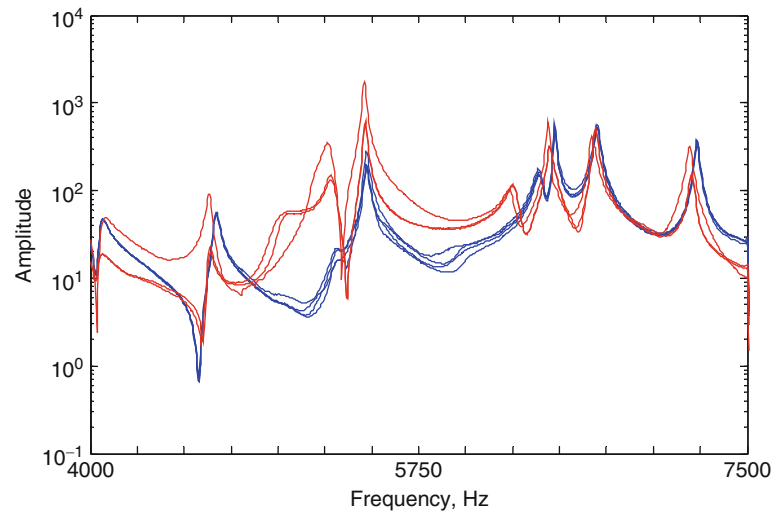
Figure 23.7 presents the FRF of the system for a preload of 4 Nm across several assemblies of the system in the same configuration. The test-to-test variability is observed to be high in this frequency range, as previously noted; however, the natural frequencies of the bending modes are approximately constant across reassembly. The torsional modes (near 5.4 and 6.3 kHz) are very sensitive to reassembly. This reinforces the observation from the previous tests:

- One class of modes (the bending modes for this system) are sensitive to the residual stresses in the system (as correlated to the order in which the bolts are tightened)
- A second class of modes (the torsional modes for this system) are so sensitive to the interfacial conditions that the effect due to the residual stresses is not distinguishable from other effects.

23.5 Model Comparison

The systems of Fig. 23.1 are modelled in an FEA program (SIERRA [11]) and reduced using the two approaches detailed in Sects. 23.2 and 23.3. The bolted joints are modelled via Iwan elements [12] for the discontinuous basis function method, and Jenkins friction elements for the frequency based substructuring method (due to the limitations of the harmonic balance approach). The Iwan element is a four-parameter model used to represent frictional joint interfaces. The four parameters in the Iwan model are used to describe the macro-slip and micro-slip properties of a joint. Similarly, the Jenkins friction element is developed as a friction slider with a coefficient of friction μ and a tangential stiffness K_T .

Fig. 23.7 FRF for the jointed beam with bolts tightened to a preload of 4 Nm. The different *color lines* (color figure appear online) correspond to different assemblies of the system under the same conditions



The comparisons between the frequency-based substructuring method and the method of discontinuous basis functions described in this paper are an on-going endeavor, and will be presented at the 2014 IMAC Conference. The computational efficiency of the two methods has been previously assessed in [13]. The two methods are demonstrated to produce a reduction in computational time of approximately 6,000-fold over a full order finite element model. When the time step for the methods is increased to the largest possible time step that allows for convergence, the methods exhibit a 24,000-fold reduction in computational time compared to a full order finite element model.

23.6 Conclusions

In the engineering analysis of complex mechanical systems, interfaces are a major and ubiquitous source of nonlinearity and variability. Predictive simulation must take into consideration these nonlinearities and address them in a statistical manner. Even with modestly reduced order models, such as with component mode synthesis for the linear substructures, direct numerical simulations are prohibitively expensive for even a few simulations, let alone the entire analysis. The many simulations that are necessitated by the statistical issues can be done only by using some radical level of model reduction, such as is demonstrated here.

In this paper, two distinct model reduction methods are summarized: frequency-based substructuring of structures with nonlinear connections, and the method of discontinuous basis functions. Both methods show promise for tremendous computational savings, with computational times that are multiple orders of magnitude less than for a high fidelity model. These computational savings enable the use of Monte Carlo modelling methods for analysis of hundreds of realizations of nominally identical systems without loss of accuracy as compared to the high fidelity model.

In studying the jointed structures, several conclusions regarding the effect of residual stress on the variability and repeatability of measurements of natural frequency and energy dissipation may be made:

1. At low preloads, the variation due to the order of the bolts being tightened (i.e. the residual stresses) is equivalent to the variation seen from disassembling and reassembling the system, implying that the non-repeatability is due to changing the interface conditions themselves, not the residual stresses.
2. At moderate preloads, torsional modes exhibit a high degree of variability (non-repeatability). These modes are very sensitive to the interface conditions (including alignment). As the preload is increased to very high levels, the variability goes away.
3. At moderate preloads, the bending modes exhibit high repeatability across assembling and disassembling. However, the bending modes are still sensitive to the order in which the bolts are tightened, implying that the residual stresses do have an effect. This repeatability goes away as the preload is decreased.

Thus, while the residual stresses are observed to have an effect on the repeatability and variability of measurements for structures with jointed interfaces, the effect is a higher order effect compared to the effects of the interface conditions (such as surface roughness, alignment, etc.). How these phenomena would evolve under the wearing in effect discussed in [14] is a topic for future work.

References

1. Craig RR Jr, Bampton MCC (1968) Coupling of substructures for dynamic analysis. *AIAA J* 6:1313–1319
2. Reuss P, Zeumer Z, Herrmann J, Gaul L (2012) Consideration of interface damping in dynamic substructuring. *Topics in Experimental Dynamics Substructuring and Wind Turbine Dynamics*, 2:81–88 http://link.springer.com/chapter/10.1007/978-1-4614-2422-2_10
3. Segalman DJ (2007) Model reduction of systems with localized nonlinearities. *ASME J Comput Nonlin Dyn* 2:249–266
4. Brake MR, Segalman DJ (2013) Modeling Localized Nonlinearities in Continuous Systems via the Method of Augmentation by Non-Smooth Basis Functions, *the Proceedings of the Royal Society A-Mathematical Physical and Engineering Sciences*, 469(2158):1–20
5. Segalman DJ, Gregory DL, Starr MJ, Resor BR, Jew MD, Lauffer JP, Ames NM (2009) Handbook on dynamics of jointed structures. Technical Report SAND2009-4164, Sandia National Laboratories
6. Bograd S, Reuss P, Schmidt A, Gaul L, Mayer M (2011) Modeling the dynamics of mechanical joints. *Mech Syst Signal Process* 25:2801–2826
7. Popp K, Maagnus K (2002) *Schwingungen*. Teubner, Wiesbaden
8. de Klerk D, Rixen DJ, Voormeeren SN (2008) General framework for dynamic substructuring: history, review, and classification of techniques. *AIAA J* 46:1169–1181
9. Milman MH, Chu C-C (1994) Optimization methods for passive damper placement and tuning. *J Guid Contr Dynam* 17:848–856
10. Griffith DT, Segalman DJ (2006) Finite element calculations illustrating a method of model reduction for the dynamics of structures with localized nonlinearities. Technical Report SAND2006-5843, Sandia National Laboratories
11. Edwards HC (2002) SIERRA framework version 3: core services theory and design. Technical Report SAND2002-3616, Sandia National Laboratories
12. Segalman DJ (2005) A four-parameter Iwan model for lap-type joints. *ASME J Appl Mech* 72:752–760
13. Brake MR, Reuss P, Gaul L, Segalman DJ (2013) Reduced order modeling of nonlinear structures with frictional interfaces. 5th world tribology conference, Torino, Italy, September 2013
14. Gregory DL, Smallwood DO, Coleman RG (1999) Experimental studies to investigate damping in frictional shear joints. 70th shock and vibration symposium, Albuquerque, NM, November 1999

Chapter 24

Evaluation of North American Vibration Standards for Mass-Timber Floors

Joshua A. Schultz and Benton Johnson

Abstract Mass-timber is an emerging building technology created by using structural adhesives to laminate layers of dimensional lumber together to create large ‘timber’ panels. These panels can be used as structural building elements in floors and walls. However, due to relatively large stiffness-to-mass ratios and low inherent damping, optimized timber floors can be vibration controlled even at spans of 3 m. There are several current North American vibration standards that can be applied to timber floors. The goal of this research is twofold: (1) investigate floor performance under various North American vibration criteria for various boundary conditions and (2) address general methods of optimizing floor performance. The impact of support compliance for CLT floors is presented in span-to-depth and span-to-frequency charts intended to assist practitioners with preliminary floor design. The results indicate that existing evaluation methods provide wide-ranging and sometimes conflicting results. However, for all criteria surveyed, it is shown that increasing rotational restraint results in up to 35% thinner floor panels.

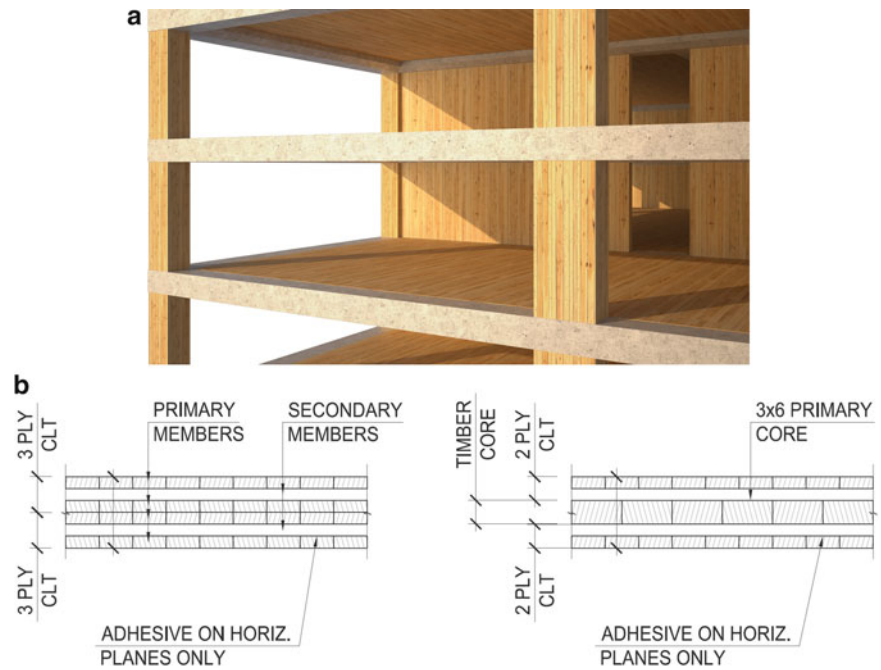
Keywords Floor vibration • Design criteria • Timber floors • CLT • Support stiffness

24.1 Introduction

Mass-timber panels such as cross-laminated timber (CLT) were developed in Europe and have recently become available in the North American market. Several projects (actual and conceptual) using product have recently been completed [1–3]. CLT is an engineered laminate comprised of solid dimensional lumber which can be manufactured in standard sizes as large as 12 m × 3 m × 300 mm. The panels are comprised of alternating, longitudinally orthogonal layers (similar to plywood construction) as shown in Fig. 24.1. The result of this composite structure is a dimensionally stable structural floor panel which can achieve spans equal to reinforced concrete slabs. However, CLT panels are lightweight and have low inherent material damping [4] which makes walking induced vibrations a design concern. Moreover, some research has been completed on the strength and deflection design of composite CLT (i.e., structural concrete topping), but little attention has been paid to the vibrational response of plain CLT floors [5]. Existing North American standards which could be used to predict vibrations of mass-timber floors include the American Institute of Steel Construction (AISC) Design Guide 11 (DG11) Chaps. 4 and 6, as well as US CLT Design Handbook (CLT DH), Chap. 7 [6, 7]. However, Chaps. 4 and 6 of AISC DG11 specify limited applicability over various ranges of mass and frequency common to CLT floor construction. As a result, these standards may have limited applicability to dynamic response of CLT floors [7]. The recently released criteria for CLT floors, CLT DH, attempts to address some of these issues, but still relies on an approach similar to AISC DG11. This paper applies these methods to design mass-timber floor panel thicknesses for a range of spans and boundary conditions in a residential building and examine the results.

J.A. Schultz (✉) • B. Johnson
Skidmore Owings and Merrill, Chicago, IL 60604, USA
e-mail: joshua.schultz@outlook.com

Fig. 24.1 (a) Rendered image of CLT construction
(b) Cross-section examples of CLT panel lay-up



24.2 Vibration Standards

In general, walking produces an excitation that has frequency content in multiples of the step frequency. These dynamic load factors for walking are described by Pernica [8]. However, high modes of vibration do not significantly participate in the vibration response, so the effort shall be focused on the fundamental mode of vibration. Furthermore, lower frequency vibration modes tend to dominate the dynamic response of the floor system [9], and current design guides focus on the fundamental natural frequency of the floor.

Current design guides rely on the relationships between mass, stiffness and natural frequency to establish guidelines for perceptibility as follows.

24.2.1 AISC DG11, Chap. 4: Design for Walking Excitation

This method is used to predict the peak floor acceleration due to walking excitation and provides limits for various occupancies. Over the frequency range of 4–8 Hz the acceleration limits are kept to a minimum due to potential resonance with human body [10]. Note that the recommended applicability of this method is limited to floor systems with frequencies <10 Hz. For those floors with greater fundamental frequencies, it is recommended to apply the additional stiffness criterion of 1 kN/mm. The AISC DG11 Chap. 4 method uses the following equations to determine design limits:

$$\frac{a_p}{g} = \frac{P_0 e^{(-0.35f_n)}}{\beta W}, \quad (24.1)$$

where

$P_0 = 289 \text{ N (65 lb)}$ excitation represented as a constant force

f_n = fundamental natural frequency of a panel area under consideration

$\beta = 5 \%$ modal damping ratio for residences with full height partitions

$W \equiv wBL$ = effective weight supported by panel under consideration.

The supported weight per unit area is w , the member span is L , and the effective width is given by

$$B_j = C_j (D_s/D_j)^{0.25} L_j. \quad (24.2)$$

For this study of a panel of uniform thickness in both directions, the parameters are taken as $C = 2$ and $D_s/D_j = 0.67$ due to the alternating direction of layers and concomitant loss of stiffness in the secondary (i.e., non-spanning) direction.

According to the limit presented in Eq. (24.1), the engineer can meet the acceleration limits by adjusting the design of the floor as realized in the parameters W and f_n . The effective panel weight, W , consists of the structural dead loads and estimated in-service, non-structural loads. The non-structural load for this study is 1.9 kPa and includes a 50 mm lightweight gypsum concrete topping, partitions, services, and expected occupancy loads. Additional structural load consists of the panel self-weight which is in the range of 0.4–1.4 kPa for standard CLT panel thicknesses. Note that for the case of CLT floor panels, the majority of the effective panel weight is due to the non-structural loads. As a result, the mass of the floor structure is less significant compared to imposed loads, i.e., increases in thickness with increase stiffness while having minimal impact on the mass. As a result, it is typically more effective to control floor vibrations when using this method by increasing the natural frequency of the system by increasing the floor stiffness.

24.2.2 AISC DG11, Chap. 6: Design for Sensitive Equipment

The method outlined in Chap. 6 of AISC DG11 is used to predict the peak floor velocity due to walking excitation. According to AISC DG11, “Stating these criteria in terms of velocity is most convenient in general, because the criterion for a given class of equipment corresponds to a constant value of velocity over most of the frequency range of interest”. The velocity criteria can also be used to evaluate human comfort as reported in Sound & Vibration Design Guidelines for Hospital and Healthcare Facilities [10].

The AISC DG11 Chap. 6 method uses the following equation to determine limits on the velocity:

$$V = \frac{U_v \Delta_p}{f_n}. \quad (24.3)$$

The value for V is the criterion and is based on the type of occupancy and is taken from Fig. 6.2 in AISC DG11 Chap. 6. For this study $V = 200 \mu\text{m/s}$. The constant U_v is used to approximate the force due to a given magnitude and velocity of an imposed harmonic walking load is defined as

$$U_v = \pi F_m f_0^2, \quad (24.4)$$

where the values for F_m and f_0 are obtained from Table 6.2 in AISC DG11. For the purposes of this study, the value for slow walking pace limits is taken as 6.8 kN-Hz².

Using Eqs. (24.3) and (24.4), the engineer is able to meet design criteria by adjusting the parameters: Δ_p and f_n . Each of these parameters is improved by increasing the stiffness of the floor panels. Note that in this method, increasing the floor mass is detrimental to vibration response as it decreases the natural frequency of the system. The effect of mass in this method is opposite to the impact of mass in the method of Chap. 4 where increasing the effective panel weight reduces floor vibrations.

24.2.3 CLT DH, Chap. 7: Vibration

This method was published in 2013 and is conceptually derivative to the vibration method presented in AISC DG11 Chap. 6. However, because the CLT mass and fundamental frequencies are potentially outside of the scope of AISC DG11, the CLT DH uses adjustments to the vibration criteria to account for differences in the material performance of laminated wood panels [4, 8]. The CLT DH Chap. 7 uses the following equation to limit vibrations.

$$\frac{f_n}{d} \geq 13.0. \quad (24.5)$$

Note that this method is similar to the AISC DG11 Chap. 6 method for limiting floor velocity. As a result, the design engineer can adjust the design via two parameters in this method, d and f_n ; similar to the AISC DG11 Chap. 6 method.

24.3 Floor Stiffness

For each of the three vibration standards discussed, the most effective way to improve the vibration response of a floor system is to increase the stiffness. The stiffness of mass-timber floor panels can be increased in one of three ways: (1) by using a higher/select grade of wood with a higher modulus of elasticity, (2) increasing the panel thickness, or (3) improving the boundary conditions. Since the use of higher (i.e., “select”) grades of wood is atypical in industry (due to cost premiums and availability), this study focuses on optimizing vibrations by controlling panel thicknesses and boundary conditions. The panel thicknesses are designed for each span length according to each design criteria.

The boundary conditions are investigated for three common scenarios: (1) pinned-pinned (i.e., simply supported), (2) fixed-fixed and (3) support rotation stiffness, k , obtained by constraining the mid-span and end moments to equivalent values, $6 EI/L$ (i.e., stiffness resulting in balanced moments).

24.4 Scope of Study

One-way spanning CLT panels are investigated for the range of spans: 3.05 m, 6.10 m, 9.15 m, and 12.20 m. Panels are assumed to be well supported at the edges. The effect of the boundary conditions listed above was investigated for each span length. The required panel thickness to satisfy the vibration standards was then determined for each combination of span and boundary condition. For the numerical modeling, resulting floor thicknesses are in the range of 50–200 mm. The timber is defined as Spruce-Pine-Fir (SPF) No. 1/2 with an average density of 4.7 kN/m^3 (30 pcf). The material is modeled as pseudo-isotropic material with 2/3 strength in the direction perpendicular to the span. FEA analysis was used to determine natural frequencies and system stiffness due to reference point loads.

24.5 Results

Figure 24.2a, b shows the trends in span-to-thickness for CLT floors having been designed to meet AISC DG11 criteria found in Chaps. 4 and 6, respectively.

Figure 24.3a, b shows the trends in span-to-frequency for CLT floors having been designed to meet AISC DG11 criteria found in Chaps. 4 and 6, respectively.

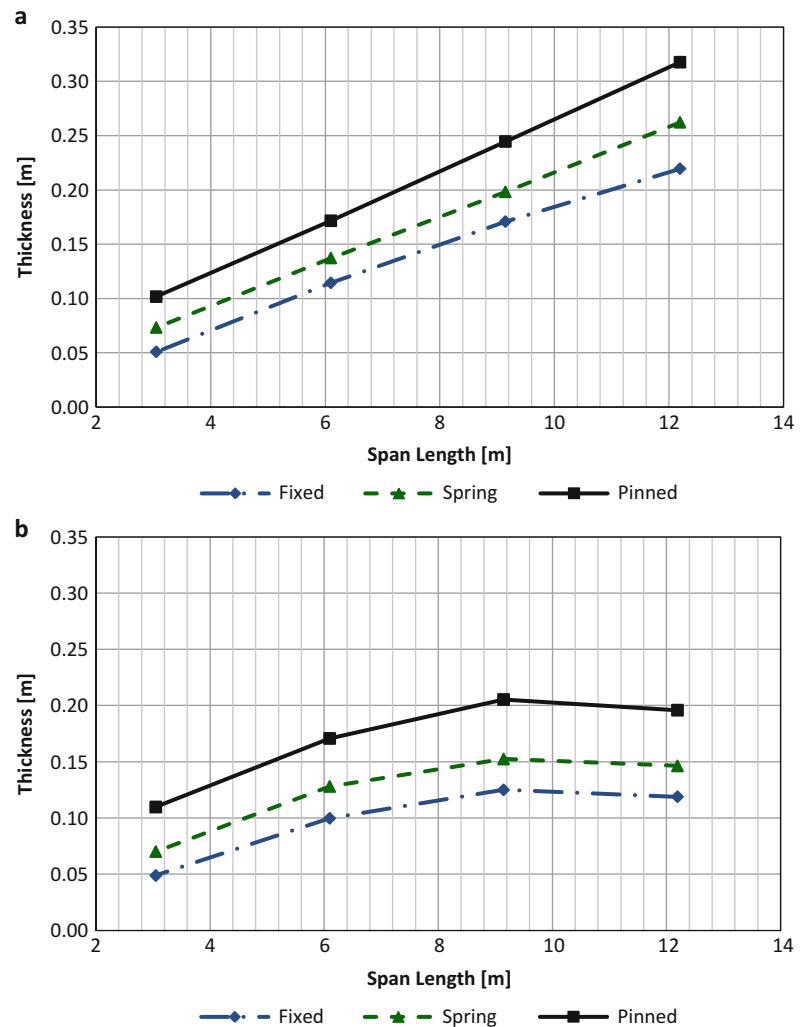
Figure 24.4a, b shows the trends in span-to-frequency for CLT floors having been designed to meet CLT DH criteria.

The following trends are observed from the results in Figs. 24.2, 24.3, and 24.4.

24.5.1 AISC DG11, Chap. 4: Design for Walking Excitation

- The span-to-depth ratio required to satisfy the criteria exhibits a non-constant variation.
- The effective panel weight dominates the vibration estimation over floor system frequency for long spans. The applicability of this method is evident once frequencies drop below 3 Hz as shown by a decreased panel thickness required for the 12.2 m span.
- The required panel thickness is decreased with rotational end restraint due to increased panel stiffness and resulting higher natural frequency.
- The natural frequency was similar for the different boundary conditions studied for a given span.

Fig. 24.2 Plots of span length and slab thickness for
 (a) Velocity-based criteria from AISC DG11 Chap. 6
 (b) Acceleration-based criteria from AISC DG11 Chap. 4



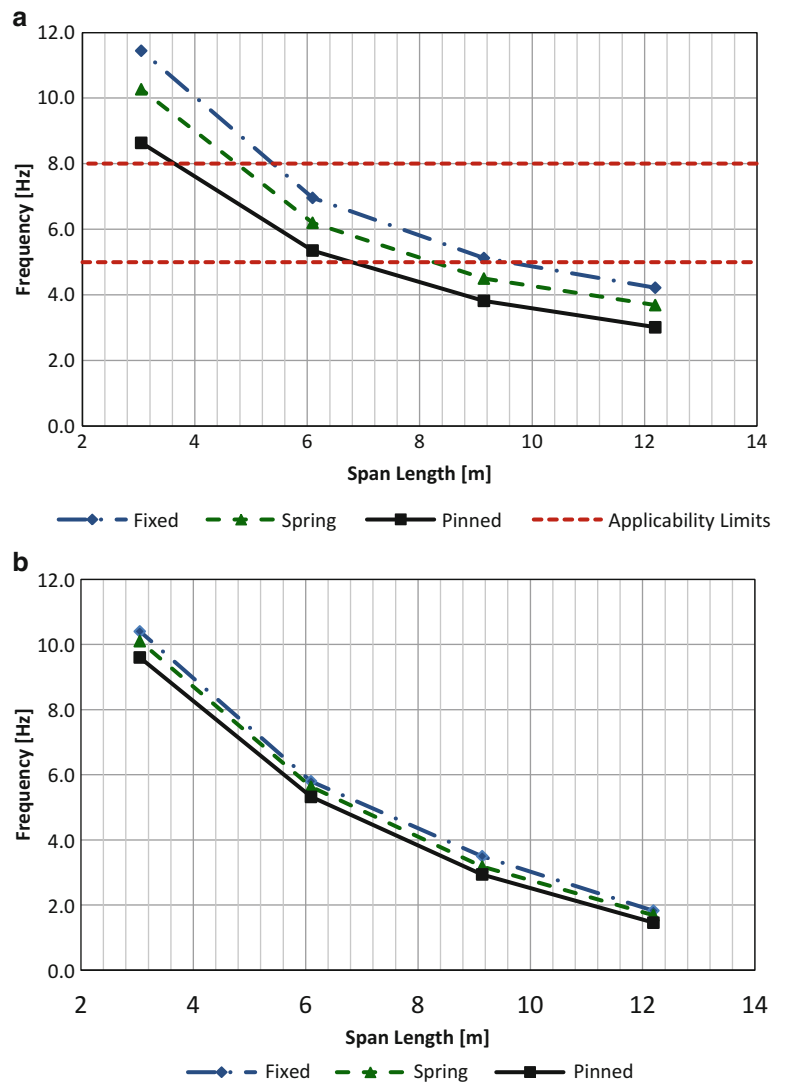
24.5.2 AISC DG11, Chap. 6: Design for Sensitive Equipment

- The span-to-depth ratio required to satisfy the criteria is approximately constant.
- The required panel thickness was similar to the AISC DG Chap. 4 method for spans less than 6.1 m. The required panel thickness was greater than the AISC DG Chap. 4 method for spans greater than 6.1 m.
- The required panel thickness decreased with increased end rotational restraint.
- The natural frequency was higher for the end rotation restrained boundary condition for a given span.

24.5.3 CLT DH, Chap. 7: Vibration

- The span-to-depth ratio required to satisfy the criteria exhibits a non-constant variation.
- The required thicknesses to satisfy the criteria are greater than those required by the AISC methods. This result may be due to natural frequencies which were lower than 9 Hz which is the limit of applicability for this method.
- The results of the AISC DG11 Chap. 6 and CLT DH Chap. 7 are in agreement regarding panel thickness savings with end rotation restraint.

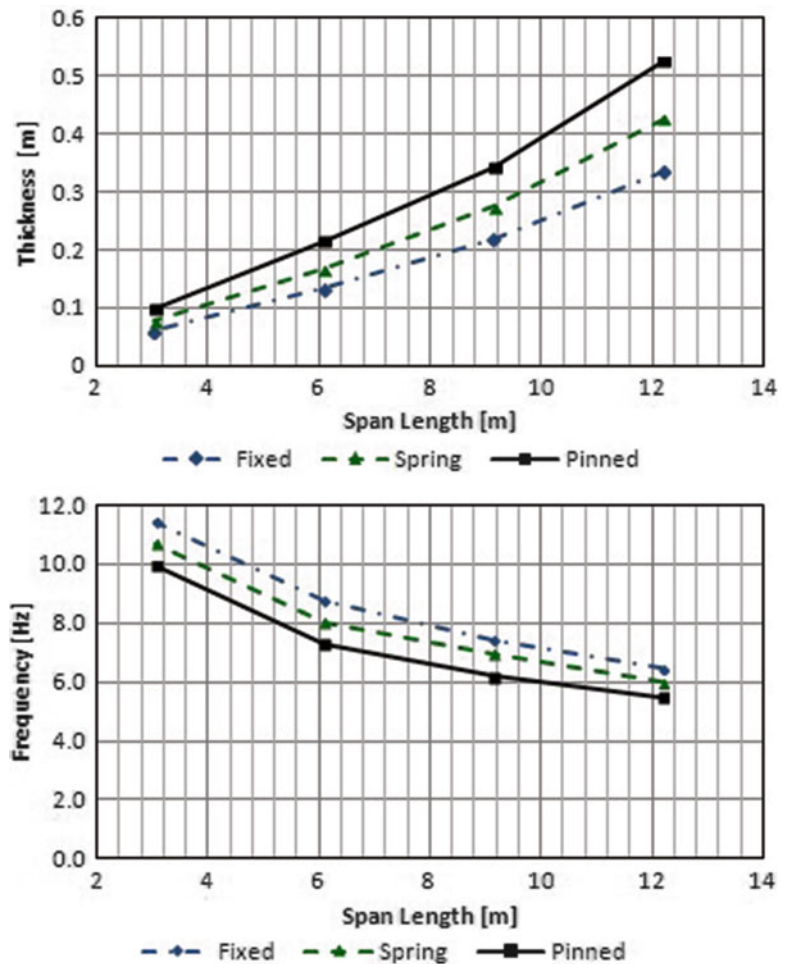
Fig. 24.3 Plots of span length and fundamental frequency for (a) Velocity-based criteria from AISC DG11 Chap. 6 (b) Acceleration-based criteria from AISC DG11 Chap. 4



24.6 Conclusions

Mass-timber floor panels are lightweight structures with low inherent damping that may be prone to vibration excitation due to human activities. Existing North American standards give conflicting results and more detailed methods to evaluate these structures should be considered. Designs that restrain rotation at the ends of the floor panels will likely result in thinner floor panels when vibrations govern the design.

Fig. 24.4 Plots of span length to
 (a) Thickness and
 (b) Fundamental frequency
 for criteria from CLT DH



References

- Green M (2012) Tall wood: the case for tall wood buildings. Canadian Wood Council, Wood Enterprise Coalition, and Forestry Innovation Investment, 22 Feb 2012. <http://wecbc.smallboxcms.com/database/rte/files/Tall%20Wood.pdf>. Accessed 17 Aug 2012
- CREE (2012) The natural change in urban architecture: LifeCycle Tower, 10 Oct 2012. http://www.creebyrhomborg.com/lct1/index_en.php
- Skidmore, Owings and Merrill, LLP (2013) Timber tower research project. Softwood Lumber Board, Chicago, 5 Mar 2013. <https://www.som.com/publication/timber-tower-research-project>
- Sturzenbecher R, Hofstetter K, Eberhardsteiner J (2010) Structural design of Cross Laminated Timber (CLT) by advanced plate theories. *Compos Sci Technol* 70:1368–1379
- Gerber C, Crews K, Foscoliano M, Agus F (2010) Development of timber concrete composite flooring in Australia and New Zealand. In: *Proceedings of the world conference on timber engineering*, Trentino, pp 1–8
- Murray TM, Allen DE, Ungar EE (1997) Floor vibrations due to human activity. In: *AISC steel design guide #11*, American Institute of Steel Construction, Chicago, IL
- Karacabeyli E, Douglas B (2013) Vibration performance of cross-laminated timber floors, chapter 7. In: *Cross laminated timber handbook*. U.S. Department of Agriculture, Forest Products Laboratory, Binational Softwood Lumber Council, Surrey, BC
- Pernica G (1990) Dynamic load factors for pedestrian movements and rhythmic exercises. *Can Acoust* 18(2):3–18
- Smith I, Chui YH (1988) Design of lightweight wooden floors to avoid human discomfort. *Can J Civ Eng* 15(2):254–262
- Sykes D, Tocci G, Cavanaugh W (2013) *Sound & vibration 2.0: design guidelines for health care facilities*. Springer, New York

Chapter 25

Improving Model Predictions Through Partitioned Analysis: A Combined Experimental and Numerical Analysis

Garrison Stevens, Sez Atamturktur, and Joshua Hegenderfer

Abstract Numerical modeling of civil infrastructure often involves assumptions about boundary conditions between adjacent structural components. For steel frame structures, such connections tend to be semi-rigid and often exhibit nonlinear mechanical behavior, making it difficult to determine the rotational stiffness when the connection is evaluated in an isolated manner. This article adapts a partitioned analysis approach using the Block Gauss-Seidel coupling technique to account for the semi-rigid, nonlinear nature of connections in steel frame structures. A case study of a steel frame with bolted connections is presented in which a constituent model is developed for the steel frame with rotational springs to represent the connections. Next, high fidelity, three-dimensional constituent models are developed for three different connection types present in the frame. At the cut-off points of the connection models the internal forces and displacements, calculated by the frame model under a predefined external load, are transferred to the constituent connection models as boundary conditions. Subsequently with the connection models, the rotational stiffness is calculated and transferred back to the frame model through the Block Gauss-Seidel iterations. Coupling iterations are repeated until the connection stiffness calculated by two successive iterations converges, at which point load applied to the frame is increased to develop a full moment-rotation curve. Comparison of the coupled model predictions against experiments show that coupled treatment of the constituent frame and connection models significantly increase the predictive capability of the overall model.

Keywords Partitioned analysis • Joint modeling • Strong coupling • Test analysis correlation • Experimental modal analysis • Mode shape • Natural frequency

25.1 Introduction

True systems in nature rarely act independently; rather, one physical phenomenon has effects on other physical phenomena. More accurate solutions for many complex engineering problems can be made possible by considering all relevant interactions and dependencies between physical phenomena through the development of coupled models. Such coupled models may be developed in two different manners: (i) a monolithic approach or (ii) partitioned approach. The monolithic approach involves developing a single model anew that accounts for the coupled physics relationships inherently, while the partitioned approach involves coupling constituent models developed as discrete entities through coupling algorithms [1]. Partitioned analysis has distinct advantages over the monolithic approach, mainly the ability to utilize mature codes, eliminating the need for costs and time to be spent developing a new model [2]. Additionally, partitioned analysis may be used to couple independent models with different domains [3] and discretization schemes [4, 5].

Hence, partitioned approach enables numerical simulations developed in an isolated manner to interact and affect each other's input and output [6] (Fig. 25.1), eliminating the need for strong and occasionally unwarranted assumptions regarding the boundaries of multiple phenomena [7] and results in more accurate representations of reality [8]. This allows for prediction of the behavior of a system, which is more complex than the individual constituents alone.

G. Stevens • S. Atamturktur (✉)
Glenn Department of Civil Engineering, Clemson University, Clemson, SC 29634, USA
e-mail: sez@clemson.edu

J. Hegenderfer
URS Corporation, Fort Mill, SC 29707, USA

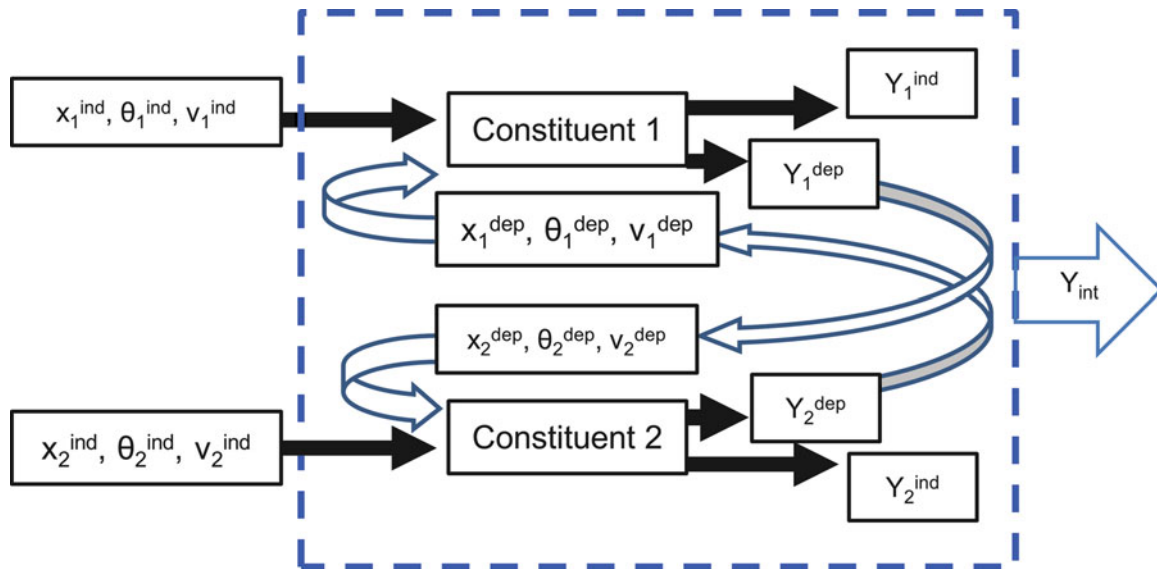
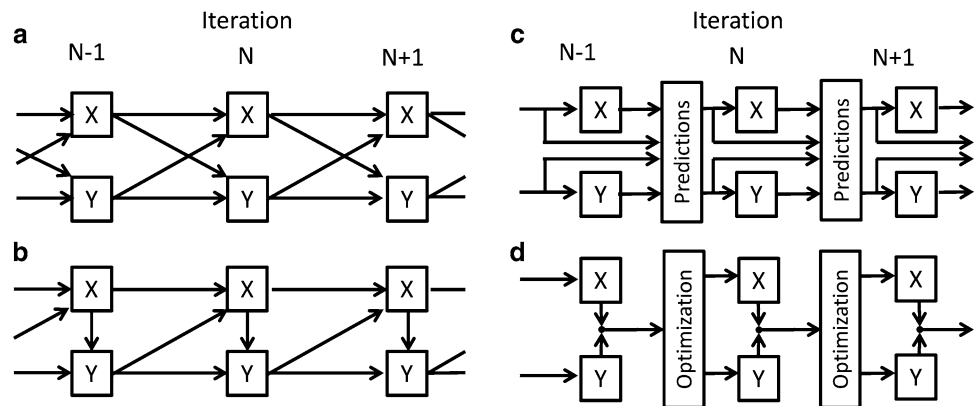


Fig. 25.1 Strongly coupled system with independent and dependent parameters

Fig. 25.2 Coupling algorithms: (a) Block-Jacobi, (b) Block Gauss-Seidel, (c) Block Newton, and (d) optimization based Coupling



Coupling in partitioned approach can be either weak (also referred to as explicit coupling) or strong (also referred to as implicit coupling), depending on the manner in which parameters are shared between models. Weak coupling occurs when interaction of constituent model's inputs and outputs is not mutual [9, 10]. Strong coupling occurs when the input to both constituent models is dependent upon the output of the other constituent [11, 12] (Fig. 25.1). For strong coupling, typically, partitioned analysis procedures require iterative techniques to be implemented for the coupling algorithms [13–15], where input parameters for strong coupling problems are distinguished as dependent or independent. Dependent parameters rely on the output of another constituent model and therefore, become the critical components of the coupling algorithm. The central question in strongly coupled problems involves determining the values for these dependent parameters for which several algorithms have been proposed (Fig. 25.2a–d): the Block-Jacobi method [6, 16], the Block Gauss-Siedel method [5, 6], gradient-based Newton-like methods [11, 16–18], and optimization-based methods [8].

Implementing Block Gauss-Siedel coupling algorithm, this article demonstrates the improvements one can gain in the predictive ability through strong coupling of constituent models. The concept is demonstrated using a finite element (FE) model for a two-story steel frame with semi-rigid connections, where the need for assumptions about joint behavior are eliminated through the coupling of high-fidelity FE models of connections. Each constituent model is individually validated against their corresponding separate-effect experiments. The predictive ability of the coupled system is then determined using integral-effect experiments, which involve both experimental static and modal analysis tests completed on a laboratory specimen.

This paper is organized as follows. Section 25.2 introduces the case study application of a steel frame as well as the static and dynamic experiments completed on this frame. Section 25.3 details the development of an initial baseline model

neglecting semi-rigid behavior by assuming either rigid or a free connections, a common, widespread assumption in practice. Section 25.4 presents the development of constituent models for each connection and the implemented of the Block Gauss-Seidel procedure for coupling these connection models. The connection models are coupled with the baseline frame model incrementally allowing an evaluation of the relative improvement with each additional constituent. The initial FE model and the coupled model are compared in Sect. 25.5 along with a discussion on the correlation of the coupled model to experimental data. Finally, in Sect. 25.6, concluding remarks summarize the findings and discuss the limitations of this study.

25.2 Case Study

25.2.1 Structure

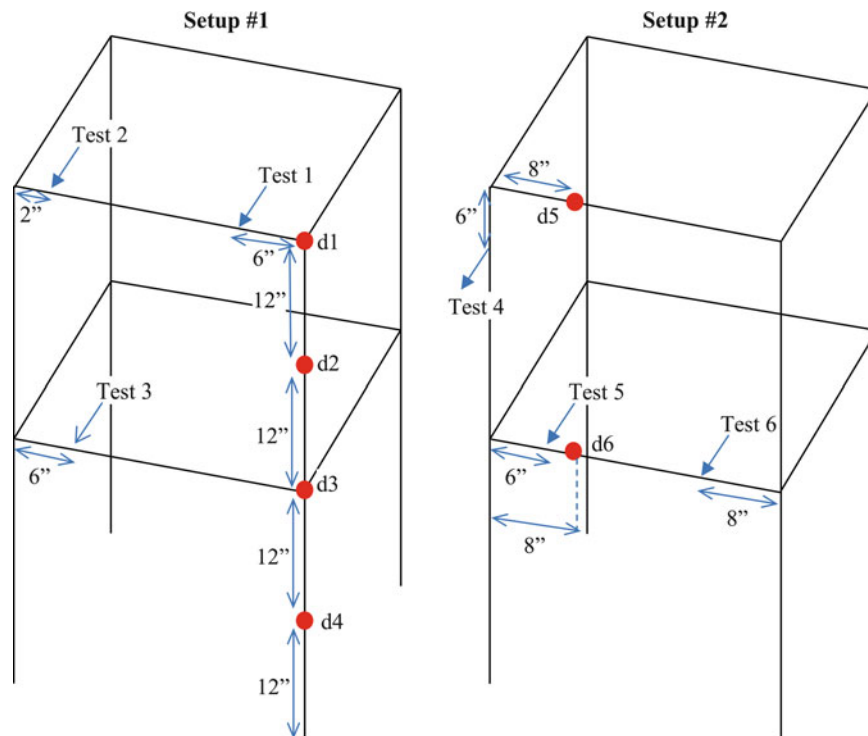
The structure studied herein is a two story, single bay steel frame with bolted connections (Fig. 25.3). Each connection is secured with two bolts, torqued to 9.0 Nm, spaced 2.54 cm (1 in.) apart. Grade 5 bolts with a diameter of 0.66 cm are used. Dimensions of the structural components are shown in Table 25.1.



Fig. 25.3 Steel frame with bolted connections

Table 25.1 Structural component dimensions

| Member | Cross-section | | |
|--------------------|---------------|--------------------|-------------|
| | Type | Dimensions (cm) | Length (cm) |
| Columns | Angle | 5.08 × 5.08 × 0.32 | 63.5 |
| Beams | Flat | 5.08 × 0.32 | 124.46 |
| Base connectors | Angle | 5.08 × 5.08 × 0.32 | 5.08 |
| Column base plates | Flat | 15.24 × 15.24 | 1.27 |
| Frame base plate | Flat | 121.92 × 243.84 | 1.27 |

Fig. 25.4 Experimental setup for static testing

25.2.2 Experimental Campaign

25.2.2.1 Static Testing

Deflection of the steel frame under varying static loads was measured in the laboratory. Lateral point loads were applied in six different tests with varying combinations of loading and measuring points. For Tests 1–3, the frame was set up with four deflection indicators placed along a column (d1–d4) and for Tests 4–6, the deflection indicators were moved to beam locations (d5–d6) as shown in Fig. 25.4. Federal C8IS Dial Deflection indicators were used to measure deflection and a cable and pulley system was used to apply the static load (Fig. 25.5).

25.2.2.2 Modal Testing

Dynamic response of the structure was studied through modal testing. Model 4507B Brüel & Kjær (B&K) unidirectional accelerometers were placed at 88 locations on the steel beams and columns, each spaced 15.24 cm (6 in.) apart and the structure was excited using an impact force from a Model 8107 B&K modal sledge hammer. Natural frequencies and mode shapes are extracted from the collected data through Frequency Domain Decomposition algorithm. To reduce error resulting from noise, each hammer strike was repeated five times and the data was averaged. General stability diagrams for model selection were developed using the rational fraction polynomial technique. The first three global modes are shown in Fig. 25.6.

Fig. 25.5 Static test comparison between two alternative FE models (pinned connections and fixed connections) and experimental data measured at point d6 [19]

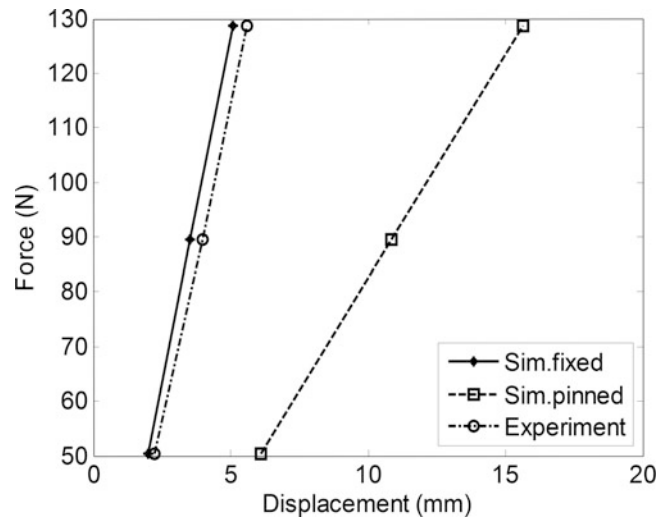


Fig. 25.6 Mode shapes from experimental modal testing

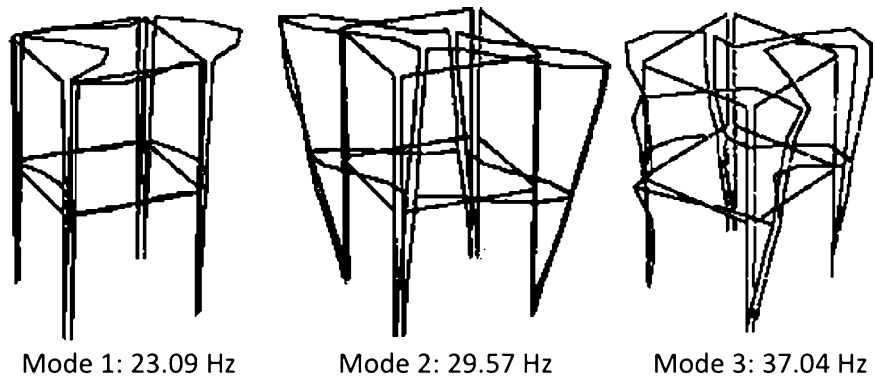


Table 25.2 Comparison of deflection results of experimental static testing and baseline model predictions

| Baseline model | Test | | | | | | Mean |
|--------------------|------|-------|------|------|-------|-------|------|
| | 1 | 2 | 3 | 4 | 5 | 6 | |
| Rigid connections | 44.4 | 84.8 | 55.6 | 46.8 | 24.3 | 18.9 | 45.8 |
| Pinned connections | 32.8 | 196.5 | 76.7 | 18.8 | 100.5 | 126.3 | 91.9 |

25.3 Model A: Linear Finite Element Model with Rigid Connections

In the literature, factors such as the number of bolts and bolt pattern were used in combination with expert judgment to approximate a steel connection as either rigid or pinned [20, 21]. Following this principle, an initial, simplified FE model (henceforth referred to as *baseline model*) is developed implementing a binary representation for connections (rigid or pinned).

The baseline model is developed using ANSYS v. 13.0 with two-noded, six-degree-of-freedom linear BEAM188 elements [22]. An isotropic linear elastic material model is implemented to impose the standard characteristics for mild structural steel, including a Young’s modulus of 29,000 ksi and Poisson’s ratio of 0.20. Beam-to-column connections are modeled to the centroid considering geometric offsets, similar to the approach discussed in Zapico et al. [23].

Tables 25.2 and 25.3 compare the predictions of two alternative baseline models developed with pinned and rigid connections to both static and dynamic measurements and demonstrate that both modeling options exhibit large errors in reproducing the measurements. As expected, the model with rigid connections underestimates deformations and overestimates natural frequencies while the model with pinned connections overestimates deformations and underestimates natural frequencies. Though neither model predicts static or dynamic responses with sufficient accuracy, the model with rigid connections yields a 46.1 % lower average error than the model with pinned connections. Furthermore, unlike the model with pinned connections, the model with rigid connections predicts modes in the correct order.

Therefore, the baseline model, representative of models built for practical applications, is developed assuming rigid connections. Note that this baseline model still contains an approximate error of 45 % for static response predictions and

Table 25.3 Global modes from experimental testing and initial numerical models

| Mode | Experimental | Option A: rigid connections | | Option B: pinned connections | |
|------|----------------|-----------------------------|-----------|------------------------------|-----------|
| | Frequency (Hz) | Frequency (Hz) | Error (%) | Frequency (Hz) | Error (%) |
| 1 | 23.09 | 27.97 | 21.13 | 16.30 | 29.41 |
| 2 | 29.58 | 33.21 | 12.27 | 14.01 | 52.64 |
| 3 | 37.04 | 47.56 | 28.40 | 25.96 | 29.91 |

an average error of 20 % for dynamic response predictions. These results demonstrate that assuming either rigid or pinned connections, rather than incorporating semi-rigid behaviors, may result in significant errors. This observation has been acknowledged earlier by many other investigations in both static [20], dynamic [21, 24, 25], and failure analysis [20, 26]. The accuracy of the predictions of this baseline model can be improved by accounting for semi-rigid connections, as it will be discussed in the following section.

25.4 Linear Finite Element Model with Semi-Rigid Connections (Coupled Models)

The case-study structure (described earlier in Sect. 25.2.1) is composed of two key components: (i) the structural frame (steel beams and columns) and (ii) the bolted connections. Semi-rigid behavior of bolted connections between beams and columns and columns to the base is highly uncertain, yet extremely important in both design and analysis of steel structures. Methods for approximation of semi-rigid connection behavior have been established [20, 27], however, these methods rely on restricting assumptions, such as small deformations in connections, negligible deformation of structural members and negligible slip deformations. To fully account for semi-rigid, nonlinear behavior of steel connections, rather than making broad assumptions, individually developed, high fidelity connection models are incorporated into the baseline model.

In doing so, first three linear, rotational springs are introduced to the frame model at each connection to control the rotation of connections in each direction. Linear COMBIN14 (spring-damper) elements [22] are used for the modeling of the springs. Low spring constants, tending to zero essentially act as pinned connections while high spring constants, tending to infinity, act as rigid connections. The ability to vary these spring constants allows semi-rigid behavior. However, the real difficulty lies in determining the sufficiently accurate values of the spring constants needed to represent connection behavior. This model with rotational springs representing the connections is used to complete a sensitivity analysis, as discussed in Sect. 25.4.1. To determine the spring constant values as well as their dependency on the applied force, nonlinear FE models (i.e. constituents) are developed for each of the three connections accounting for factors such as friction and pretensioning of bolts (see Sect. 25.4.2). These models are individually calibrated against experimental modal data collected in small-scale connection samples in the laboratory (see Sect. 25.4.3).

Finally, Sect. 25.4.4 discusses the coupling of the three connection models with the frame model one at a time through Block Gauss-Siedel iterations. Coupling sequence is determined according to the sensitivity analysis. As a result, three new models are obtained with increasing number of connection models coupled with the frame model. The improvement in predictive ability achieved by coupling is quantified in terms of the reduction in discrepancy considering both static and modal experiments.

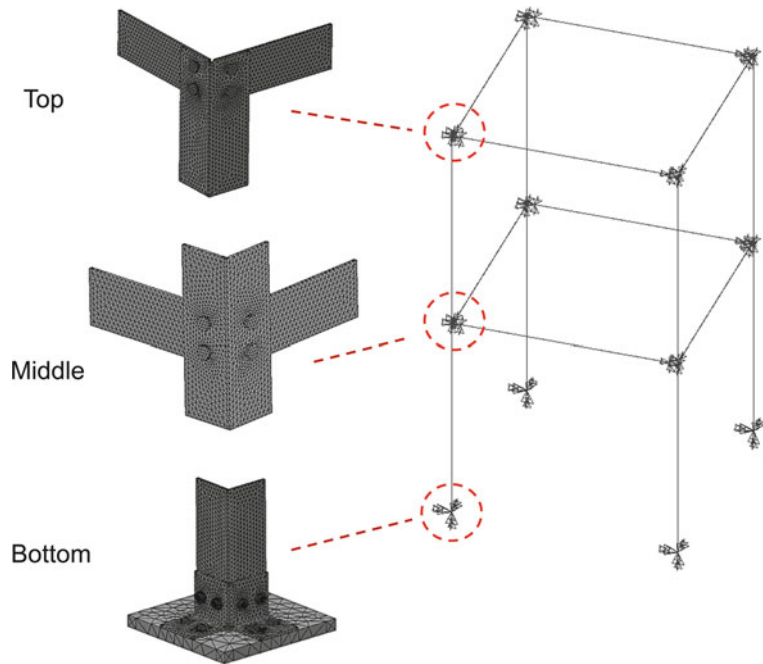
25.4.1 Sensitivity Analysis

A global effect sensitivity analysis known as an analysis of variance is utilized to evaluate the relative importance of each spring stiffness in the frame model. The range for each spring is determined by varying the spring constant from free to an approximately rigid condition one spring at a time keeping rest of the springs remain at nominal values. As one spring constant is varied, the natural frequencies vary between an upper bound (corresponding to a rigid connection) and a lower bound (corresponding to a pinned connection) in an asymptotic manner. Appropriate ranges for each spring constant are then selected to ensure a semi-rigid behavior.

Furthermore, the analytically computed modes are observed to switch their order when the stiffness constant is varied. Hence, an automated mode-pairing algorithm which operates on the spatial properties of modes to detect swapped modes and adjust accordingly based on a predefined mode sequence, need to be devised such that analysis of variance may operate properly using natural frequencies.

Table 25.4 Sensitivity analysis with normalized R^2 (%) values for each parameter

| Parameter number and stiffness component | Natural frequency | | | Max horizontal displacement | | | | Σ | Total |
|--|-------------------|--------|--------|-----------------------------|------------------------|----------------|-------|----------|-------|
| | Mode 1 | Mode 2 | Mode 3 | Δ Beam (top) | Δ Beam (middle) | Δ Coln. | | | |
| Base 1 Rotational (strong axis) | 47.7 | 36.9 | 65.3 | 18.1 | 7.3 | 37.2 | 212.3 | 212.3 | |
| 2 Torsional | 0.00 | 0.00 | 0.00 | 0.00 | 0.00 | 0.00 | 0.01 | | |
| Middle 3 Rotational (strong axis) | 33.2 | 51.8 | 23.1 | 17.1 | 5.9 | 35.2 | 166.3 | 251.6 | |
| 4 Rotational (weak axis) | 2.2 | 0.02 | 0.17 | 0.08 | 82.8 | 0.00 | 85.3 | | |
| 5 Torsional | 0.00 | 0.00 | 0.00 | 0.00 | 0.00 | 0.00 | 0.00 | | |
| Top 6 Rotational (strong axis) | 12.0 | 11.1 | 11.2 | 13.4 | 4.0 | 27.6 | 79.2 | 136.1 | |
| 7 Rotational (weak axis) | 4.9 | 0.30 | 0.32 | 51.3 | 0.02 | 0.00 | 56.9 | | |
| 8 Torsional | 0.00 | 0.00 | 0.00 | 0.00 | 0.00 | 0.00 | 0.00 | | |

Fig. 25.7 Finite element joint models

Analysis of variance is then used to evaluate the sensitivity of lateral displacements and natural frequencies to the spring constants. Table 25.4 lists the relative contribution of the stiffness constants to the overall variability in the predicted features, where the normalized sensitivities are summed for each connection level. As seen in Table 25.4, the sensitivity analysis indicates model output is most sensitive to middle, base, and top connections, respectively. The torsional stiffness constants are found to be insensitive for all connections and thus, are left at rigid values and not included in further discussion.

25.4.2 Connection Model Development

Three three-dimensional non-linear FE connection models are developed also using ANSYS v. 13.0; for top, middle, and base connections (Fig. 25.7). Following the suggestions of Kim et al. [28], Bursi and Jaspart [29–31] and Selamet and Garlock [32], portions of the steel members as well as the individual bolts are included in the connection models. Solid 187 elements (ten-noded tetrahedral element with quadratic displacement interpolation) are used to model the steel member and bolts. The material behavior for the steel members is modeled using a multilinear isotropic hardening model using the von Mises yield criterion and the typical stress–strain relationship [33]. Similarly, the bolts are modeled with a bilinear material model with the stress–strain relationship shown in Fig. 25.8 [34]. Frictional effects are modeled at all interfaces (including: member to member, bolt to member, and bolt shank to bolt hole) using contact and target elements CONTA174 and TARGET170, respectively. The coefficient of friction is set to 0.35 in accordance with AISC [35]. A mesh refinement study is completed for all elements to ensure discretization is sufficient for capturing both deformation and stress concentrations in critical regions (not reported herein due to space limitations).

Fig. 25.8 Bi-linear material models for bolts and steel frame members

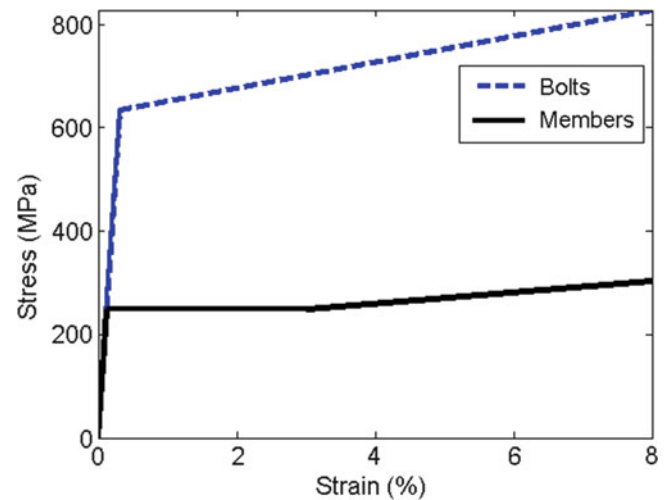
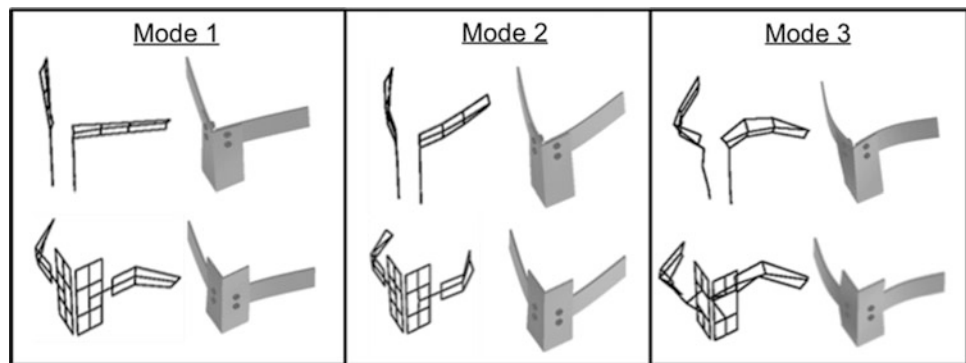


Fig. 25.9 Experimental (*left*) and predicted (*right*) mode shapes of top (*top*) and middle (*bottom*) connections



Pretensioning of the bolts is considered in the model [28, 36–38] by directly applying a pretensioning force to the bolt volumes (as opposed to using the commonly applied temperature of initial displacement method). This is achieved through the use of pretension elements, PRETS179, in ANSYS v. 13.0. The torque applied to each bolt is converted to an equivalent pretensioning force using the equation [34]:

$$F_{PT} = T / Kd \quad (25.1)$$

where T is the applied torque, F_{PT} is the pretensioning force, K is the dimensionless nut factor, and d is the nominal bolt diameter. A K value of 0.17–0.22, as recommended for zinc-plated fasteners [34].

25.4.3 Test Analysis Correlation of Connection Models

Coupling connection models with the frame model can only be effective if the connection models themselves are first validated against experiments. To ensure the fidelity of connection model predictions, test analysis correlation with experimental measurements is completed. Scaled laboratory models of each connection supported with rigid boundaries were used in dynamic modal analysis to determine the natural frequency of the first few modes of each connection. Experimental and simulated global model shapes are presented in Figs. 25.9 and 25.10 and Table 25.5 summarizes error the numerical results.

As shown in Table 25.5, the base connection model has the highest average error of 13.3 % and the top connection model has the lowest average error of less than 1.0 %. Higher errors in the middle connection are attributed to difficulty in creating a rigid boundary condition for the experimental set up and errors in the base connection are attributed to higher relative noise during data collection due to low amplitude response levels. With the average error overall being less than 8 %, the connection models are determined to be sufficiently accurate for coupling to improve estimates of connection stiffness.

Fig. 25.10 Experimental (*left*) and predicted (*right*) mode shapes of base connection

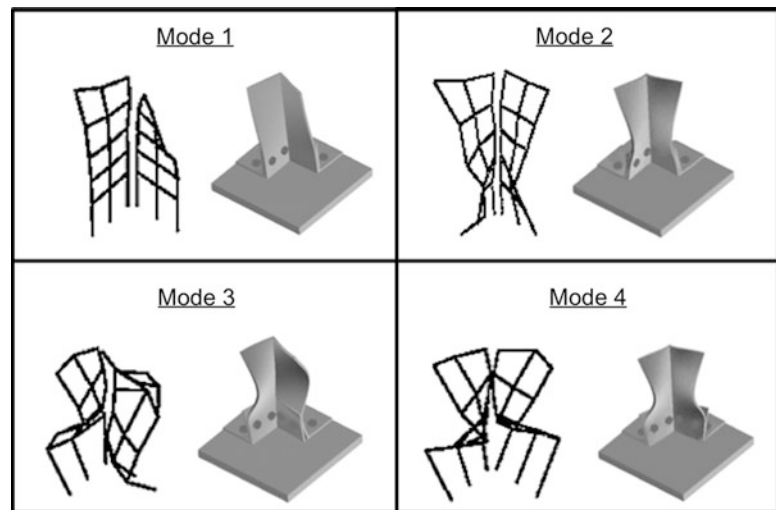


Table 25.5 Connection test-analysis correlation for connection models

| Connection | Mode | Frequency (Hz) | | % Error |
|------------|------|----------------|-----------|---------|
| | | Experimental | Predicted | |
| Base | 1 | 472.1 | 561.04 | 17.22 |
| | 2 | 2,048.0 | 2,016.82 | 9.11 |
| | 3 | 2,642.0 | 3,107.61 | 12.09 |
| | 4 | 3,005.0 | 3,644.65 | 14.95 |
| Middle | 1 | 144.3 | 125.60 | 12.96 |
| | 2 | 158.3 | 166.97 | 5.48 |
| | 3 | 688.3 | 650.46 | 5.50 |
| Top | 1 | 79.9 | 79.11 | 0.99 |
| | 2 | 143.2 | 142.27 | 0.65 |
| | 3 | 459.4 | 460.16 | 0.17 |

25.4.4 Coupling of Frame and Connection Models

Figure 25.11 illustrates the iterative process used to develop the moment-rotation curves. Initially, a global loading condition is induced on the frame model, applying a load at the midpoint of the beam for top and middle connection and 1/8th of the length from the bottom of the column for the base connection. The load, F_g , is applied in the direction that critically affects the stiffness of each specific connection. The rotational stiffness constants are initiated as rigid values, P_0 . Next, displacements and rotations at the points where the connection models are cut-off, BC_g , and the moment at the connection, M_g , are calculated by the frame model and passed to the coupling interface. The displacements and rotations at the cut-off points of the beams and columns are then entered as inputs for the connection model, which in turn is executed to calculate the corresponding rotation at the connection, θ_g . Similar to approaches by Bursi and Jaspart [29] and Pirmoz et al. [37], the rotation of the connection is computed by taking the relative difference between the rotation of the column and the rotation of the beam. Next, this calculated rotation is then passed to the interface. The stiffness constant, P_g^h , at iteration h for load F_g is computed from the ratio of the computed moment to rotation and then compared to the stiffness constant computed in the previous iteration, $h-1$. The algorithm is terminated if the change in the computed stiffness constant between the last two iterations is less than a set threshold value. Otherwise, the new stiffness constant is passed back to the frame baseline model and the process is iterated until convergence is achieved. Upon achieving convergence for a given load, the load, F_g is then increased and the process is repeated several times until the full moment-rotation curve has been developed (Fig. 25.12) for each of the rotational springs. Note that points of small rotations (less than 0.00017 radians) are likely to have large numerical errors, and these points have been disregarded from further analysis.

Fig. 25.11 Coupled process: (left) schematic representation, and (right) numerical algorithm

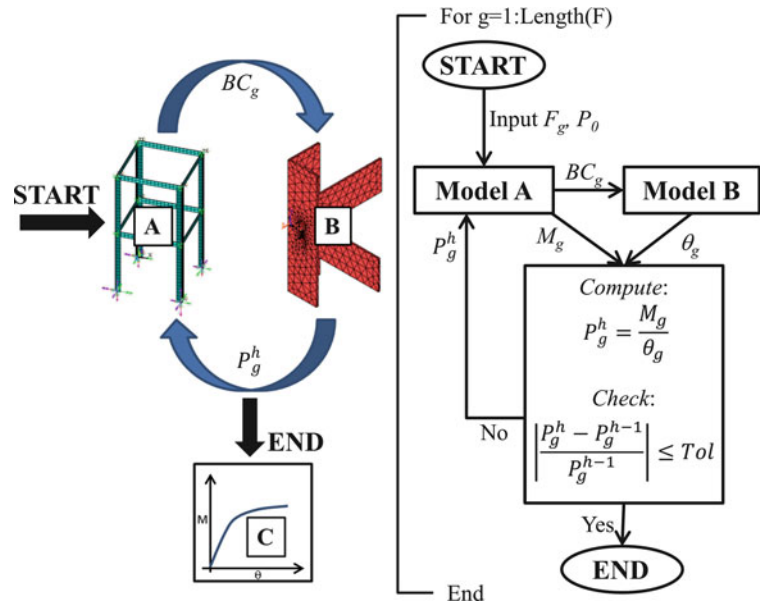


Fig. 25.12 Moment-rotation curves [19]

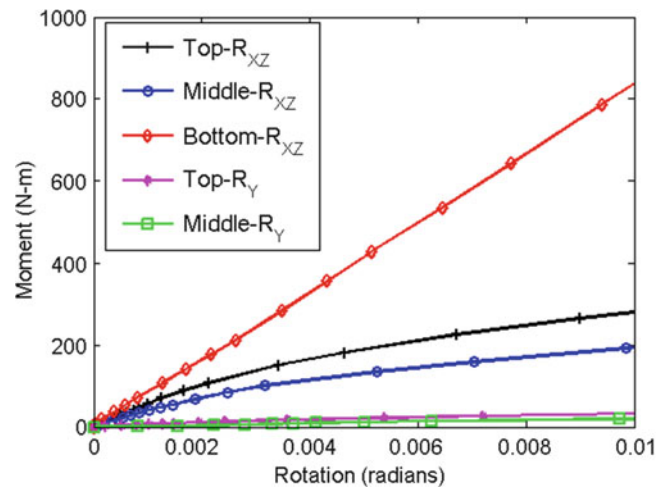


Table 25.6 Comparison experiments to predictions for static analysis

| Test | Mean disagreement (%) | | | |
|------|-----------------------|----------------|----------------|---------------------|
| | Baseline model | Semi-coupled 1 | Semi-coupled 2 | Fully coupled model |
| 1 | 44.42 | 33.12 | 18.91 | 11.08 |
| 2 | 84.83 | 89.00 | 79.68 | 73.73 |
| 3 | 55.60 | 52.57 | 48.74 | 46.29 |
| 4 | 46.75 | 37.35 | 25.37 | 18.05 |
| 5 | 24.26 | 19.39 | 17.42 | 16.43 |
| 6 | 18.93 | 13.98 | 12.75 | 11.96 |

25.5 Results and Discussion

The four models (ranging from baseline to fully coupled) are compared with static and dynamic experimental data collected in Sect. 25.2. The average discrepancy, or disagreement, between experiments and model predictions for static analysis is presented in Table 25.6. Similarly, discrepancy in the frequency prediction of the first four global modes of the frame is shown in Table 25.7. These results clearly indicate an increase in prediction accuracy from the baseline model to the fully coupled model as more connection models are added. This trend is consistent for nearly all predicted features, with the exception of Mode 2, which results in an underestimation by the fully coupled model nearly equivalent to the overestimation by the baseline model.

Table 25.7 Comparison of experimental natural frequencies to model predictions for dynamic analysis

| Mode | Experimental | Baseline model | | Semi-coupled 1 | | Semi-coupled 2 | | Fully coupled model | |
|------|--------------|----------------|------------|----------------|------------|----------------|------------|---------------------|------------|
| | Freq. (Hz) | Freq. (Hz) | Discr. (%) | Freq. (Hz) | Discr. (%) | Freq. (Hz) | Discr. (%) | Freq. (Hz) | Discr. (%) |
| 1 | 23.09 | 27.97 | 21.13 | 26.50 | 14.78 | 26.26 | 13.73 | 25.30 | 9.56 |
| 2 | 29.58 | 33.21 | 12.27 | 28.55 | 3.48 | 28.38 | 4.06 | 27.11 | 8.35 |
| 3 | 37.04 | 47.56 | 28.40 | 42.70 | 15.29 | 41.65 | 12.45 | 38.47 | 3.86 |

25.6 Conclusion

Complex physical phenomena contain many interdependencies and relationships that if neglected in numerical models may result in significant errors. These physical phenomena are often amenable to decomposition in various forms depending upon the specific analysis or design objectives. Decomposition into constituents presents an ideal application for coupled modeling using partitioned analysis. Though all numerical models contain inaccuracies, eliminating assumptions through integration of constituent models along with rigorous verification, validation and uncertainty quantification presents an opportunity to reduce biases and uncertainties.

While we acknowledge the inherent inaccuracy of the numerical models used for simulations of complex coupled systems, the biases and uncertainties in model predictions can be reduced through further improvement of the simulation models, and rigorous verification, validation and uncertainty quantification activities. Modeling of semi-rigid connections, as presented in this case study, is an ideal application for improving model predictions through partitioned analysis. Constituent models of each connection remove invalid assumptions regarding connection behavior and produce improved model predictions, when compared to experiments, for both static and dynamic tests.

In regard to the stiffness of the semi-rigid connections presented in this study, time and resource constraints limited the experimental campaign to the linear region. A suggested area for continued and future work remains by taking the static testing campaign into the nonlinear regime such that the nonlinear moment-rotation curves can be further validated.

References

- Rugonyi S, Bathe KJ (2001) On finite element analysis of fluid flows fully coupled with structural interactions. *Comput Model Eng Sci* 2:195–212
- Ibrahimbegovic A, Knopf-Lenoir C, Kučerová A, Villon P (2004) Optimal design and optimal control of elastic structures undergoing finite rotations and deformations. *Int J Numer Meth Eng* 61:2428–2460
- Leiva JS, Blanco PJ, Buscaglia GC (2010) Iterative strong coupling of dimensionally heterogeneous models. *Int J Numer Meth Eng* 81:1558–1580
- Kassiotis C, Ibrahimbegovic A, Niekamp R, Matthies H (2011) Partitioned solution to nonlinear fluid–structure interaction problems. Part I: Implicit coupling algorithms and stability proof. *Comput Mech* 47:305–323
- Joosten MM, Dettmer WG, Peric D (2009) Analysis of the block gauss–seidel solution procedure for a strongly coupled model problem with reference to fluid–structure interaction. *Int J Numer Meth Eng* 78:757–778
- Matthies HG, Niekamp R, Steindorf J (2006) Algorithms for strong coupling procedures. *Comput Meth Appl Mech Eng* 195:2028–2049
- Lieber M, Wolke R (2008) Optimizing the coupling in parallel air quality model systems. *Environ Model Software* 23(2):235–243
- Farajpour I, Atamturktur S (2012) Optimization-based strong coupling of multiple single-solver models. *J Comput Civ Eng* 26(5):648–660
- Matthies HG, Steindorf J (2002) Fully coupled fluid–structure interaction using weak coupling. *Proc Appl Math Mech* 1(1):37–38
- Wang JG, Nogami T, Dasari GR, Lin PZ (2004) A weak coupling algorithm for seabed–wave interaction analysis. *Comput Meth Appl Mech Eng* 193:3935–3956
- Matthies HG, Steindorf J (2003) Partitioned strong coupling algorithms for fluid–structure interaction. *Comput Struct* 81:805–812
- Zhang Q, Hisada T (2004) Studies of the strong coupling and weak coupling methods in FSI analysis. *Int J Numer Meth Eng* 60:2013–2029
- Felippa CA, Park KC, Farhat C (2001) Partitioned analysis of coupled mechanical systems. *Comput Meth Appl Mech Eng* 190:3247–3270
- Larson J, Jacob R, Ong E (2005) The model coupling toolkit: a new fortran90 toolkit for building multi-physics parallel coupled models. *Int J High Perform Comput Appl* 19(3):277–292
- Larson JW (2009) Ten organising principles for coupling in multiphysics and multiscale models. *ANZIAM J* 48:C1090–C1111
- Fernandez MA, Moubachir M (2005) A Newton method using exact Jacobians for solving fluid–structure coupling. *Comput Struct* 83:127–142
- Heil M (2004) An efficient solver for the fully coupled solution of large-displacement fluid–structure interaction problems. *Comput Meth Appl Mech Eng* 193:1–23
- Matthies HG, Steindorf J (2002) Partitioned but strongly coupled iteration schemes for nonlinear fluid–structure interaction. *Comput Struct* 80:1991–1999
- Hegenderfer J, Atamturktur S (2013) Prioritization of code development efforts in partitioned analysis. *Comput Aided Civ Infrastruct Eng* 28(4):289–306

20. Lee SS, Moon T-S (2002) Moment-rotation model of semi-rigid connections with angles. *Eng Struct* 24:227–237
21. Galvao AS, Silva ARD, Silveira RAM, Goncalves PB (2010) Nonlinear dynamic behavior and instability of slender frames with semi-rigid connections. *Int J Mech Sci* 52:1547–1562
22. ANSYS (2010) User's manual, release 13.0. ANSYS, Inc.
23. Zapico JL, Gonzalez-Buegla A, Gonzalez MP, Alonso R (2008) Finite element model updating of a small steel frame using neural networks. *Smart Mater Struct* 17(045016):1–11
24. da Silva JGS, de Lima LRO, da Vellasco PCG, de Andrade SAL, de Castro RA (2008) Nonlinear dynamic analysis of steel portal frames with semi-rigid connections. *Eng Struct* 30:2566–2579
25. Turker T, Kartal ME, Bayraktar A, Muvafik M (2009) Assessment of semi-rigid connections in steel structures by model testing. *J Construct Steel Res* 65:1538–1547
26. Liu Y, Xu L, Grierson DE (2010) Influence of semi-rigid connections and local joint damage on progressive collapse of steel frameworks. *Comput Aided Civ Infrastruct Eng* 25:184–204
27. European Committee for Standardisation (1993) Eurocode 3 ENV-1993-1-1. Revised Annex J. Design of steel structures. Doc. CEN/TC250/SC3-N419E
28. Kim J, Yoon J-C, Kang B-S (2007) Finite element analysis and modeling of structure with bolted joints. *Appl Math Model* 31:895–911
29. Bursi OS, Jaspart JP (1998) Benchmark for finite element modeling of bolted steel connection. *J Construct Steel Res* 43(1–3):17–42
30. Bursi OS, Jaspart JP (1997) Calibration of a finite element model for isolated bolted end-plate steel connections. *Construct Steel Res* 44(3):225–262
31. Bursi OS, Jaspart JP (1998) Basic issues in the finite element simulation of extended end plate connections. *Comput Struct* 69:361–382
32. Selamat S, Garlock M (2010) Guidelines for modeling three dimensional structural connection models using finite element methods. International symposium: steel structures: culture and sustainability 2010, Istanbul, Turkey, Paper No. 14
33. Hibbeler RC (2008) *Mechanics of materials*, 7th edn. Pearson Prentice Hall, Upper Saddle River, NJ, p 90
34. Fastenal (2005) Technical reference guide, s7028, rev. 9
35. American Institute of Steel Construction (AISC) (2008) *Steel construction manual*, 13th edn. AISC, Chicago, 16.1-349
36. Citipitioglu AM, Haj-Ali RM, White DW (2002) Refined 3D finite element modeling of partially-restrained connections including slip. *J Construct Steel Res* 58:995–1013
37. Pirmoz A, Daryan AS, Mazaheri A, Darbandi HE (2008) Behavior of bolted angle connections subjected to combined shear force and moment. *J Construct Steel Res* 64:436–446
38. Pirmoz A, Ahmadi MM, Valadi E, Farajkhah V, Balanoji SR (2010) Performance of the PR connections under combined Axial-tension and moment loading. *Electron J Struct Eng* 10:66–73

Chapter 26

Model Reduction and Lumped Models for Jointed Structures

G. Chevallier, H. Festjens, J.-L. Dion, and N. Peyret

Abstract The jointed structures are widely spread but their behaviour is quite hard to model and to simulate. The talk deals with a decomposition in linear and non-linear substructures that allows to make the simulations easier. The authors show that the modal subspace is not optimal to reduce the order of the model. Another choice of reduction subspace is shown to be more optimal as it requires less state-variables and leads to a better correlation with Full Order Models. Finally, the authors show how it is possible to characterize experimentally the joints by loading them in the reduction subspace and to integrate an experimental model in the reduce order simulations of the structure.

Keywords Jointed structure • Model reduction • Vibration damping • Non-linear vibrations

26.1 Introduction

Assemblies structures are very common in engineering but, paradoxically, the finite element simulations of these structures are difficult to achieve due to non-linearities of contact and friction. Two behaviors are commonly referred to: the loss of stiffness and the dependence of the damping according to the vibration amplitude. A large number of studies have ever been conducted to understand and define the mechanisms of energy losses (EL) in jointed structures. Among the most famous: clamped beams with a longitudinal interface, see Goodman and Klumpp [1], sandwich beams loaded with a pure transverse force, see Metherell and Diller [2] or lap joints, see Earles [3], beam elements screwed together, see Esteban and Rogers [4]. More recently, Peyret et al. [5] and [6] proposed a new test device for measuring the behavior of flat connections. In order to predict the EL in the contact interfaces, one can compute the energy dissipation during the vibration motion, see for example [7] or [8]. The work of Caignot et al. [9] shows that it is possible to predict the damping thanks to a Finite Element simulation with contact and friction non-linearity. For few years, several studies have focused on model reduction of structures including the joints behaviors, see Segalman [10], Qu [11], Witteveen and Irschik [12] or Becker and Gaul [13]. Reduced Order Models (ROM) are generally built in order to make simulation processes faster. These methods are very useful as part of an optimization process using a high fidelity Finite Element (FE) model parametrized by design variables or as part of the acceleration process for simulations with a high number of Degrees of Freedoms (DoFs). For an optimization, it is interesting to build a reduced parametric model of a small size, while for an acceleration process, design parameters are useless but accuracy is the main goal. We focus on the framework of optimization even if this paper refers to the modelling step only. Some of the methods detailed in [10–13] are based on a modal decomposition. More recently Festjens et al. [14] have shown that it is more efficient to focus on a “Principal Joint Strains Basis”. This talk deals with the different steps to reduce a model by this way.

G. Chevallier (✉) • H. Festjens • J.-L. Dion • N. Peyret
ISMEP LISMMA, 3 rue Fernand Hainaut, 93407 Saint-Ouen Cedex, France
e-mail: gael.chevallier@supmeca.fr

26.2 Technical Aspects

This section deals with the different ways to obtain a Reduced Order Model from a Full Order Model obtained thanks to the Finite Element Method:

$$\mathbf{M}\ddot{\mathbf{u}} + \mathbf{K}\mathbf{u} + \mathbf{F}(\mathbf{u}, r) = f_e \quad (26.1)$$

where \mathbf{M} and \mathbf{K} respectively denote the mass and stiffness matrices; \mathbf{u} is the vector of nodal displacements, f_e the excitation forces and \mathbf{F} denotes the nodal contact and friction non-linear forces, which depend on the nodal displacements \mathbf{u} and may also depend on internal variables r that allow to take other physics such as plasticity, thermal behavior, etc. into account.

26.2.1 “Modal” Approaches

In the following, a displacement-based basis is sought in a Rayleigh-Ritz sense, in order to approximate solutions in a reduced subspace, spanned by the basis

$$\mathbf{u} = \Phi q \quad (26.2)$$

where the vector \mathbf{u} contains the N unknown physical displacements and rotations and the vector q the $m \ll N$ reduced model variables. The matrix Φ is called the reduction basis or Ritz basis. As vibration-modes are generally used for building the reduction basis, it is often called modal basis. Nevertheless, this basis can be calculated using eigenvectors, Krylov enhancement or Craig-Bampton basis according to the aim of the reduction. With such approaches, the reduced order model becomes:

$${}^T \Phi \mathbf{M} \Phi \ddot{q} + {}^T \Phi \mathbf{K} \Phi q + {}^T \Phi \mathbf{F}(\Phi q, r) = {}^T \Phi f_e \quad (26.3)$$

Linear terms are easy to compute thanks to a Finite Element Model. This leads to the classical modal equations. Unfortunately, the non-linear force \mathbf{F} is numerically evaluated every time-step of the solver-algorithm. Thus, there is no analytical expression of the reduced order non-linear force. So, one has to choose a macro model to govern its behavior. The models of Dahl [15], Iwan [16], Lugre [17] are able to govern the joint behavior. But in a modal subspace, it is very difficult to identify the non-linear forces as they are very coupled. This means that one must identify the non-linear reduced order force including the coupling between all the directions

$$f = {}^T \Phi \mathbf{F}(\Phi q, r) = \begin{bmatrix} f_1(q_1 \cdots q_m, r_1 \cdots r_m) \\ f_2(q_1 \cdots q_m, r_1 \cdots r_m) \\ \vdots \\ f_m(q_1 \cdots q_m, r_1 \cdots r_m) \end{bmatrix} \quad (26.4)$$

Moreover, the eigenvectors or the vibration vectors does not span the smallest subspace in order to compute the more accurate results.

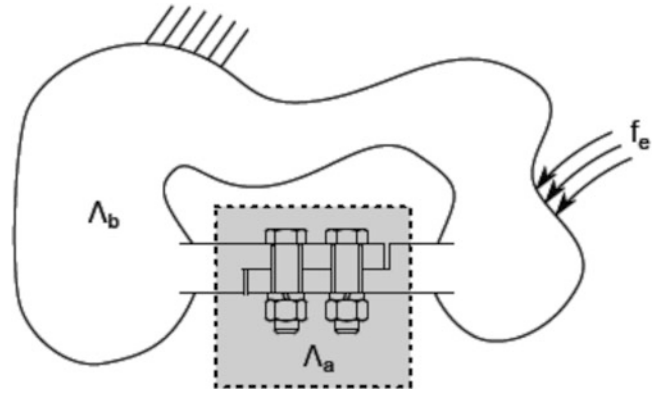
26.2.2 Principal Joint Strains Basis

To address the shortcomings of modal approaches, our purposes are: to find a subspace in which the non-linear forces can be considered as uncoupled, to find a subspace in which, we will be able to compute an accurate result and to find a subspace in which the reduced non-linear forces f can be identified from simulations or identified from experiments.

Let us consider a structure splitted into a linear substructure Λ_a and a non-linear substructure Λ_b (Fig. 26.1):

$$\mathbf{M} \begin{bmatrix} \ddot{\mathbf{u}}_a \\ \ddot{\mathbf{u}}_b \end{bmatrix} + \mathbf{K} \begin{bmatrix} \mathbf{u}_a \\ \mathbf{u}_b \end{bmatrix} + \begin{bmatrix} \mathbf{F}(\mathbf{u}_a, r) \\ \mathbf{0} \end{bmatrix} = f_e \quad (26.5)$$

Fig. 26.1 Sub-structuring: the interfaces are not the interfaces of the joints. Λ_a includes the joint. Moreover the domain is not limited to the non-linear DoFs, but extended to the region around the joint. Λ_b is assumed to behave linearly



We define the Principal Joint Strain Basis as a small size basis \mathbf{V} in which we can decompose the local displacements \mathbf{u}_a .

$$\mathbf{u}_a = \mathbf{V}p \quad (26.6)$$

Of course \mathbf{u}_b can be decomposed on a modal basis. This leads to:

$$\begin{bmatrix} \mathbf{u}_a \\ \mathbf{u}_b \end{bmatrix} = \begin{bmatrix} \mathbf{V} & \mathbf{0} \\ \mathbf{0} & \Phi_{bb} \end{bmatrix} \begin{bmatrix} p \\ q \end{bmatrix} \quad (26.7)$$

We assume that if two macro-models of the same joint are associated with deformations vectors which are *LOCALLY* orthogonal, then these two models are *UNCOUPLED*. Unfortunately, the modal vectors are *GLOBALY* orthogonal but their restrictions to some DoF are not. Let us decompose the modal basis:

$$\begin{bmatrix} \mathbf{u}_a \\ \mathbf{u}_b \end{bmatrix} = \begin{bmatrix} \Phi_{aa} & \Phi_{ab} \\ \Phi_{ba} & \Phi_{bb} \end{bmatrix} \begin{bmatrix} q_a \\ q_b \end{bmatrix} \quad (26.8)$$

Our purpose is to compute a SVD-basis from the rectangular matrix Φ_{aa} such as:

$$\Phi_{aa} = \mathbf{V}\mathbf{S}^T\mathbf{W} \quad (26.9)$$

The matrix \mathbf{V} is constituted with orthogonal vectors that span the subspace of modal deformations of the joint. The number of “important” vectors in this basis is less or equal to the number of modes in the modal basis. In this basis, as the vectors are orthogonal, we assume that non-linear forces are uncoupled, so that:

$$f = {}^T\mathbf{V}\mathbf{F}(\mathbf{V}p, r) = \begin{bmatrix} f_1(p_1, r_1) \\ f_2(p_2, r_2) \\ \vdots \\ f_m(p_m, r_m) \end{bmatrix} \quad (26.10)$$

26.2.3 How to Build the Macro-models Associated with the PJSB

The PJSB can be used as a load case in a numerical study assuming quasi-static conditions to compute the reduced order non-linear force, see Festjens et al. [18] or Caignot et al. [9]. The PJSB can also be used to design an experimental setup that allow to obtain the behavior of the joint under a load that corresponds to one of the vectors of the PJSB.

26.3 Examples

The talk will be illustrated with two examples. The first one aims to show that it is possible to reduce FE models of any realistic geometry on a small PJSB. The second one aims to show the lack of accuracy of the modal-based reductions.

26.3.1 Size of the PJSB Methods

The following example aims to show that it is possible to find a small basis that span the subspace of the joint-deformations. Let us consider a 3D-Finite Element model, see Fig. 26.2. Its five first modes are shown to be bending modes in xy-plane and in xz-plane and a torsion mode. Their restriction to the region of the joint have been computed. Then thanks to the SVD computation, the PJSB has been extracted. Figure 26.3 show both basis and the Modal Assurance Criterium (MAC) between both. This result is important because it shows that the PJSB is not necessarily collinear to the modal-basis. Moreover the PJSB span the same subspace than the modal basis with less vectors. This leads to less variables in the reduced order model.

26.3.2 Accuracy of the PJSB Methods

The PJSB method is investigated on a simple example. The considered whole structure, depicted in Fig. 26.4, is a clamped-free steel beam assembled with a bolted-joint at its middle, see Festjens et al. [14] for more information. The flexural behavior of this structure is investigated. The linear part of its FEM is composed of 10 hermitian 2D beam elements governed by

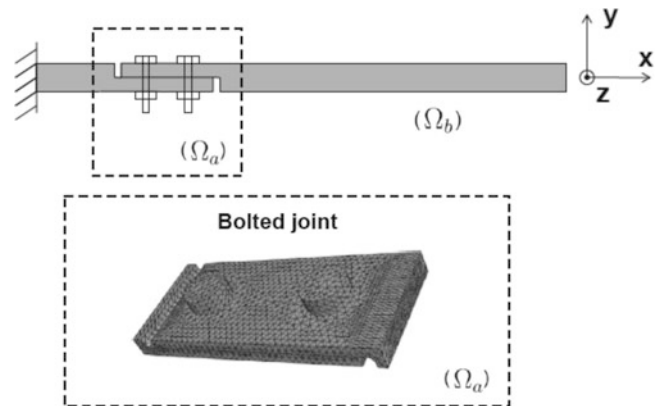


Fig. 26.2 3D Finite Element Model of a jointed structure, see [18]

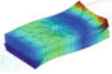
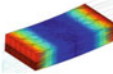
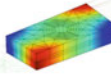

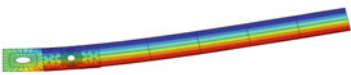



| |  |  |  |
|---|--|---|---|
|  | >80% | <10% | <10% |
|  | <10% | >80% | <10% |
|  | >80% | <10% | <10% |
|  | >80% | <10% | <10% |
|  | <10% | >30% | >60% |

Fig. 26.3 Decomposition of the 5 first modes on the PJSB. Modal Assurance criterium between modal vector and PJSB vectors

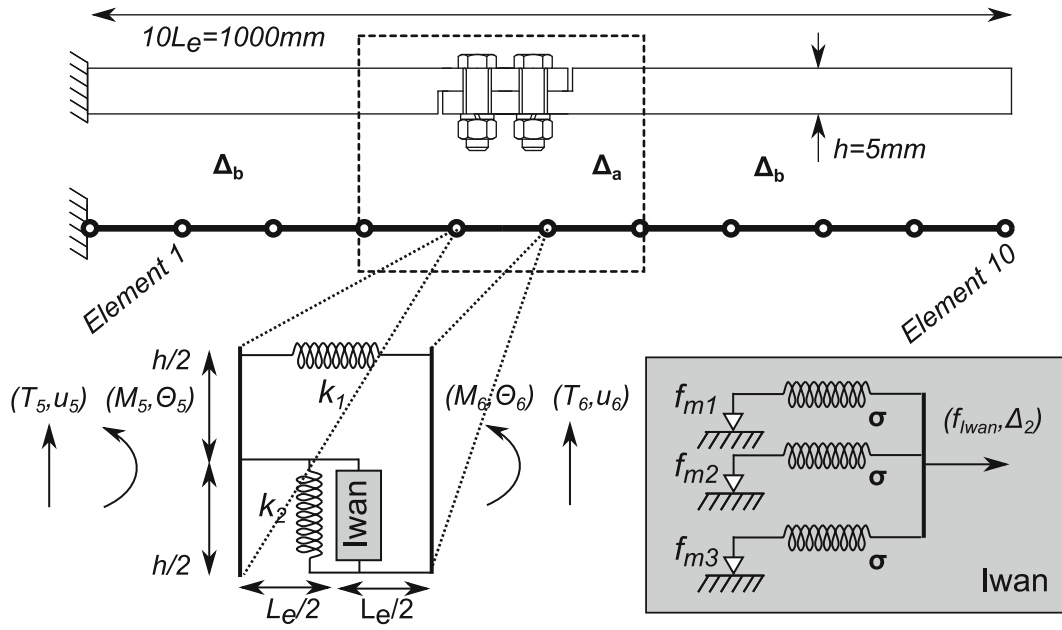


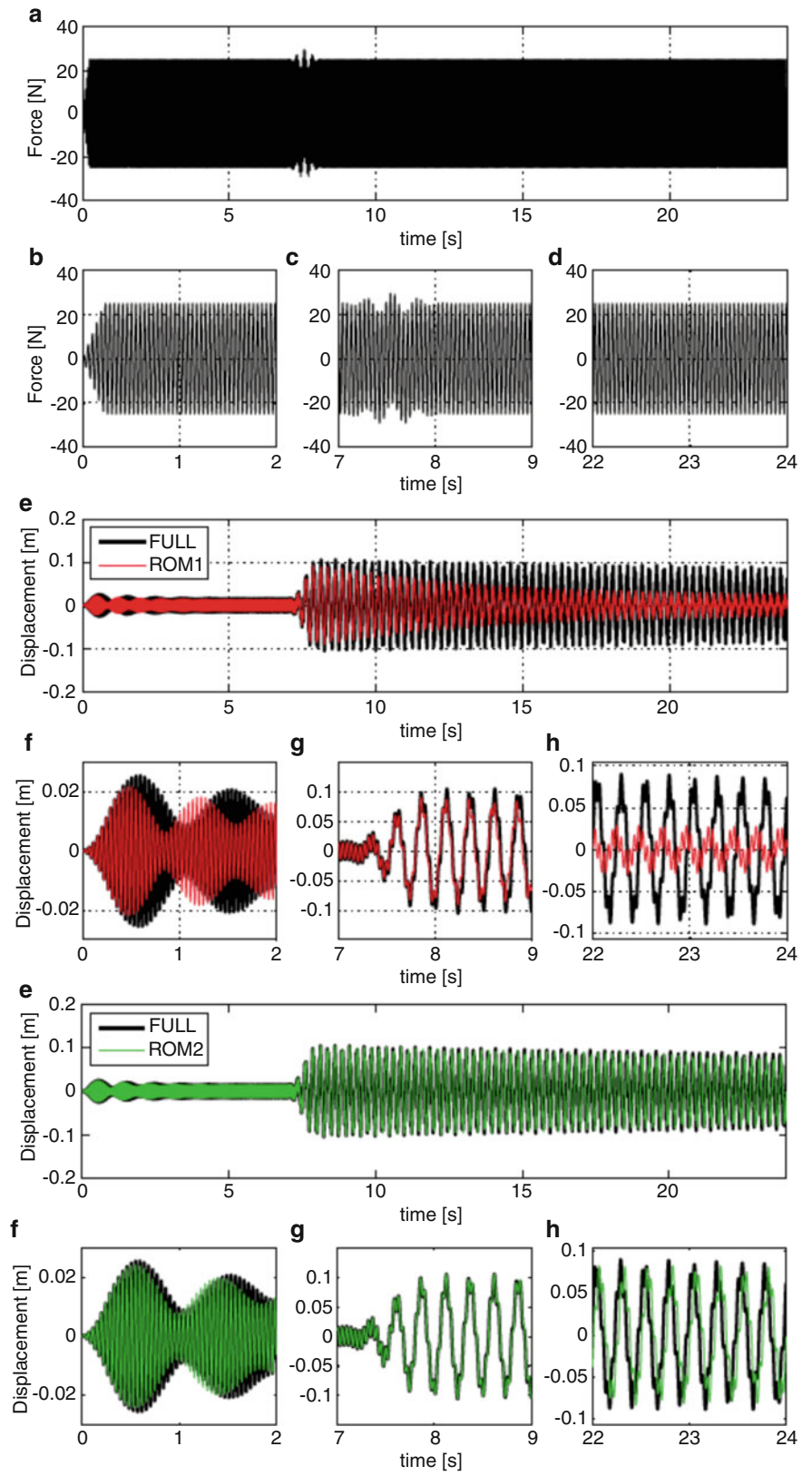
Fig. 26.4 1D Finite Element Model of a jointed structure, see [14]

Bernoulli formulation. The j^{th} element has two transverse displacement DoFs denoted u_j and u_{j+1} and two rotational DoFs denoted θ_j and θ_{j+1} . Non-linearities in real joints have a local extent and thus contains both non-linear as well as linear elements. The fifth element of the whole structure is fitted with a nonlinear hysteretic model. This model, referred to as an Adjusted Iwan Beam Element (AIBE), see [10], rely on the reduction of the 2D linear elastic beam element to rigid bars and linear springs. The adjusted Iwan beam element is obtained by replacing these two springs with one-dimensional hysteretic models. The model is first reduced using a modal basis. The obtained ROM is called ROM1. The model is secondly reduced using the PJSB. The obtained ROM is called ROM2. To evaluate the accuracy of both model reduction methods, the following load case is studied on the 1D-model. A sinusoidal force of frequency close to the one of the second mode is applied until the steady state regime is reached; Then a wavelet excitation is applied to excite the first mode and the unstationary response is observed. The response of the structure is multi-modal. This load case highlights the coupling effects that may occur in jointed structures. On the one hand, the global amplitude of ROM1 decreases faster than the Full Order Model. This ROM1 stands for the situation where no coupling effect is considered and is not able to take into account the coupling effect due to non-linear damping predicted by the full order model. On the contrary, ROM2 is able to take into account this effect. ROM1 may strongly underestimate the actual amplitude of vibration. In a conception process, this situation can lead to an underdimensioning of the structure. The presented load case may correspond to excessively severe conditions, but in general, the actual dissipation generated by joint depends on the real amplitude. As a the projection on a global Ritz basis is not suitable contrary to the use of a local basis (Fig. 26.5).

26.4 Conclusions

This paper provides a pragmatic and accurate way for reducing the models of jointed structures. The method is founded on the intuition that the modes of a “local” basis are adequate to generate the principal movements that the joints may carry out under low frequency dynamic excitations. The proposed formulation couples together the modes of the whole structure. It also keeps a geometrical meaning and thus the reduced order model is able to take into account the local damping as well as the softening effect induced by the joints. Finally the joints macro-models are directly updated from experimental data. As a result, the obtained models are very light but nevertheless accurate.

Fig. 26.5 Comparison between the results obtained from classical modal reduction and PJSB reduction



References

1. Goodman L, Klumpp J (1956) Analysis of slip damping with reference to turbine-blade vibration. *ASME J Appl Mech* 23(3):421–429
2. Metherell A, Diller S (1968) Instantaneous energy dissipation rate in a lap joint-uniform clamping pressure. *ASME J Appl Mech* 35:123–128
3. Earles SWE (1966) Theoretical estimation of the frictional energy dissipation in a simple lap joint. *J Mech Eng Sci* 8:207–214
4. Esteban J, Rogers CA (2000) On the damping effect due to bolted junctions in space structures subjected to pyro-shock. *Comput Struct* 75:347–359
5. Dion J-L, Chevallier G, Peyret N (2013) Improvement of measurement techniques for damping induced by micro-sliding. *Mech Syst Signal Process* 34(1–2):106–115
6. Peyret N, Dion J-L, Chevallier G, Argoul P (2010) Micro-slip induced damping in planar contact under constant and uniform normal stress. *Int J Appl Mech* 02:281. doi:10.1142/S1758825110000597
7. Festjens H, Chevallier G, Dion J-L (2012) A numerical quasi-static method for the identification of frictional dissipation in bolted joints. In: *ASME IDETC*, Chicago, 2012
8. Chen W, Deng X (2005) Structural damping caused by micro-slip along frictional interfaces. *Int J Mech Sci* 47:1191–1211
9. Caignot A, Ladeveze P, Neron D, Gallo VL, Romeuf T (2007) Prediction by virtual testing of damping in the spatial structures. In: *Proc. Colloque national en calcul de structures*, 2007
10. Segalman DJ (2007) Model reduction of systems with localized nonlinearities. *J Comput Nonlinear Dyn* 2(3):249
11. Qu Z-Q (2002) Model reduction for dynamical systems with local nonlinearities. *AIAA J* 40(2):327–333
12. Witteveen W, Irschik H (2007) Efficient modal formulation for vibration analysis of solid structures with bolted joints. In: *Proceedings of IMAC 25th*, Society of Experimental Mechanics Inc., Paper (385)
13. Becker J, Gaul L (2008) CMS methods for efficient damping prediction for structures with friction. In: *Proceedings of the IMAC-XXVI*, Orlando
14. Festjens H, Chevallier G, Dion J-L (submitted) Nonlinear model order reduction of jointed structures for dynamic analysis. *J Sound Vib* 333(7):2100–2113
15. Dahl PR (1976) Solid friction damping of mechanical vibrations. *AIAA J* 14(12):1675–1682
16. Iwan WD (1967) On a class of models for the yielding behavior of continuous and composite systems. *J Appl Mech* 34:612
17. Canudas de Wit C, Tsiotras P (1999) Dynamic tire friction models for vehicle traction control. In: *Proceedings of the 38th IEEE conference on decision and control*, 1999, N/A, vol 4. IEEE, pp 3746–3751
18. Festjens H, Chevallier G, Dion J-L (2013) A numerical tool for the design of assembled structures under dynamic loads. *Int J Mech Sci* 75:170–177

Chapter 27

A Complex Power Approach to Characterise Joints in Experimental Dynamic Substructuring

E. Barten, M.V. van der Seijs, and D. de Klerk

Abstract The dynamic response of coupled structures is influenced by the joints connecting the individual substructures. The friction induced by the interfaces causes non-linear and damping-like effects, which need to be taken into account when applying Experimental Dynamic Substructuring techniques. This paper proposes a compliant interface model in the framework of substructuring, in order to account for the influence of jointed connections. Rather than modelling damping as a separate phenomenon, the proposed compliant interface model characterises (non-linear) damping as a function of the interface force and motion directly. As such the model fits into the Lagrange-Multiplier FBS method. In addition, the concept of complex power is adopted to characterise the effect of damping and isolate the contribution of the interface from the overall dissipation. The theory is illustrated with a test-case on a dedicated test structure. A successful attempt was made to identify damping parameters based on power dissipation of the structure.

Keywords Frequency Based Substructuring • Experimental Dynamic Substructuring • Compliant interface • Complex power • Damping

Nomenclature

| | |
|--|---|
| $\mathbf{u}, \mathbf{f}, \mathbf{g}$ | Vector of displacements, external forces, internal forces |
| $\Delta \mathbf{u}_c, \lambda$ | Vector of relative displacement at the interface, interface force intensity |
| $\mathbf{M}, \mathbf{C}, \mathbf{K}$ | Mass-, damping- and stiffness matrix of unassembled structure |
| $\mathbf{M}_c, \mathbf{C}_c, \mathbf{K}_c$ | Mass-, damping- and stiffness matrix of the compliant interface |
| \mathbf{B}, \mathbf{L} | Signed Boolean matrix, Boolean Localisation matrix |
| \mathbf{Z}, \mathbf{Y} | Dynamic stiffness, receptance |
| $\mathbf{Z}_c, \mathbf{Y}_c$ | Dynamic stiffness, receptance of compliant interface |
| $\mathcal{P}_e, \mathcal{P}_i$ | Excitation power, interface power |
| $\mathcal{P}_d, \mathcal{P}_k$ | Dissipative power, exchange power |
| DS | Dynamic Substructuring |
| LM-FBS | Lagrange Multiplier Frequency Based Substructuring |
| FRF | Frequency Response Function |
| DoF | Degree of freedom |
| FEM | Finite Element Method |

E. Barten (✉) • M.V. van der Seijs • D. de Klerk
Department of Precision and Microsystem Engineering, Section Engineering Dynamics, Faculty of Mechanical, Maritime and Materials Engineering, Delft University of Technology, Mekelweg 2, 2628CD Delft, The Netherlands
e-mail: emielbarten@gmail.com; m.v.vanderseijs@tudelft.nl

27.1 Introduction

It is known that joints used for assembly of substructures have a significant influence on the dynamic response of coupled structures [11]. At the interface between two individual substructures, non-linear and damping-like effects are a result of friction which in turn highly influences the energy dissipation of the entire structure. Different strategies to implement the effects of mechanical joints have been proposed in literature. One approach tries to implement the effects from a physical understanding of friction, such as the Iwan model which uses four parameters to characterise the behaviour of a jointed interface [9]. With this same purpose, Bograd et al. [3] proposed a so called non-linear Jenkins model from which equivalent linear stiffness and damping coefficients can be derived. Alternatively, methods have been proposed to characterise the influence of the interface experimentally by means of Dynamic Substructuring (DS) coupling and decoupling techniques (see for instance [6, 16]). In [2] and [13] procedures are proposed that employ substitute parts to keep the interfaces connected during measurement, such that the interface effects are indeed present. The added dynamics associated with these substitutes is then either removed or interchanged in a later stage.

The interface model as proposed in this work can be positioned in between both approaches. Essentially, the substructures are coupled following the procedures of DS, but without the strict requirement of rigid compatibility at the interface. Instead, a certain compliance can be implemented based upon physical (damping and stiffness) parameters, possibly derived from abovementioned physical models. In [17] a method was already described to implement a compliant interface in the DS framework. This description is however limited to the time domain. This paper proposes an extension of this method to make it also applicable for Lagrange-Multiplier Frequency Based Substructuring (LM-FBS) [5].

A useful tool to analyse a structure is to consider the flow of power when subjected to a harmonic excitation [8, 18]. This complex valued quantity allows for identification of dissipative power which is associated with damping present in a structure. The compliant interface as discussed before allows to distinguish between the power dissipated due to intrinsic damping and the power dissipated at the interface.

This paper starts in Sect. 27.2 with theory of DS and how a compliant interface fits in its framework. The concept of complex power is explained in Sect. 27.3 and how it can be used to obtain the dissipation due to a compliant interface. Section 27.4 continues with an academic example which illustrates the use of complex power to identify the compliance of an interface. The paper is concluded in Sects. 27.5 and 27.6 which includes an outlook for future research.

27.2 Interface Coupling in the Framework of DS

The key concept of Dynamic Substructuring is to divide rather complex structures into smaller, less complex structures [6]. When the dynamic responses of the individual substructures are known, the dynamic behaviour of the full structure can be constructed by numerically coupling its subcomponents at the interfaces. Let us write the equation of motion for n unassembled subsystems in the physical domain:

$$\mathbf{M}\ddot{\mathbf{u}} + \mathbf{C}\dot{\mathbf{u}} + \mathbf{K}\mathbf{u} = \mathbf{f} + \mathbf{g} \quad (27.1)$$

with system matrices (mass, damping and stiffness)

$$\begin{aligned} \mathbf{M} &\triangleq \text{diag}(\mathbf{M}^{(1)}, \dots, \mathbf{M}^{(n)}), & \mathbf{C} &\triangleq \text{diag}(\mathbf{C}^{(1)}, \dots, \mathbf{C}^{(n)}), \\ \mathbf{K} &\triangleq \text{diag}(\mathbf{K}^{(1)}, \dots, \mathbf{K}^{(n)}) \end{aligned}$$

and sets of displacements, external forces and interface forces¹

$$\mathbf{u} \triangleq \begin{bmatrix} \mathbf{u}^{(1)} \\ \vdots \\ \mathbf{u}^{(n)} \end{bmatrix}, \quad \mathbf{f} \triangleq \begin{bmatrix} \mathbf{f}^{(1)} \\ \vdots \\ \mathbf{f}^{(n)} \end{bmatrix}, \quad \mathbf{g} \triangleq \begin{bmatrix} \mathbf{g}^{(1)} \\ \vdots \\ \mathbf{g}^{(n)} \end{bmatrix}$$

For the definitions the reader is referred to Fig. 27.1a.

¹The explicit time dependencies are omitted for simplicity.

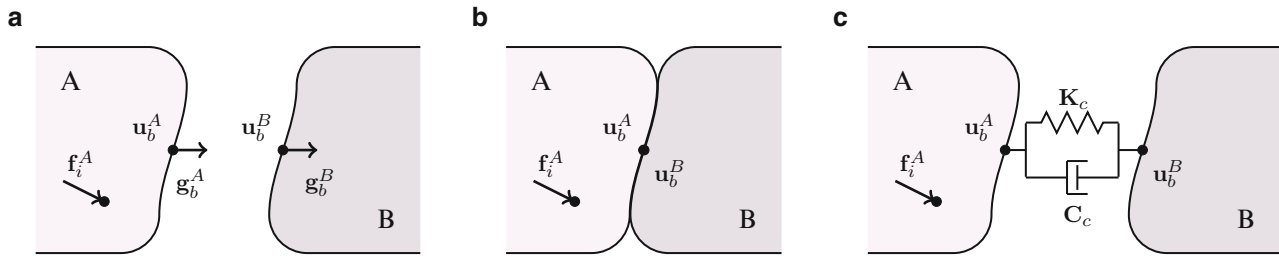


Fig. 27.1 Assembly of two substructures A and B using one node at each interface. (a) Assembly of two substructures A and B. \mathbf{u} are displacements, \mathbf{g} internal forces and \mathbf{f} applied forces. (b) Assembly using a rigid connection, i.e. no relative displacement at the interface. (c) Assembly using a compliant connection, i.e. relative displacement at the interface. The interfaces are connected by a linear spring and dashpot in parallel

Starting with a recap of the DS framework, a rigid connection is considered first, i.e. no relative displacement between substructures at the interface is allowed. This is followed by the introduction of the compliant interface model. In both cases, an expression in terms of system matrices as well as the system's receptance is considered.

27.2.1 Rigid Connection

Traditional substructuring techniques couple substructures as if they are rigidly connected, i.e. no relative displacement of the interface nodes between the substructures is allowed, see Fig. 27.1b. This results in two conditions that need to be satisfied when coupling substructures:

1. *Compatibility*: this condition states that the Degrees of Freedom (DoFs) associated with coinciding interface nodes of the respective substructures are equal. The compatibility condition can be expressed by

$$\mathbf{B}\mathbf{u} = \mathbf{0} \quad (27.2)$$

where as \mathbf{B} is a signed boolean matrix operating on the interface DoFs. This expression states that any pair of matching interface DoFs \mathbf{u}_b^A and \mathbf{u}_b^B have the same displacement, i.e. $\mathbf{u}_b^A - \mathbf{u}_b^B = 0$.

2. *Equilibrium*: this condition requires force equilibrium between the interface DoFs. The equilibrium condition can be expressed by

$$\mathbf{L}^T \mathbf{g} = \mathbf{0} \quad (27.3)$$

where \mathbf{L} is a boolean matrix localising the interface DoFs from the global set (for more details on constructing \mathbf{B} and \mathbf{L} , the reader is referred to [6]). This expression states that the sum of a matching pair of interface DoFs \mathbf{g}_b^A and \mathbf{g}_b^B should be equal to zero, i.e. $\mathbf{g}_b^A + \mathbf{g}_b^B = 0$.

The coupled system can be obtained by using either a primal or a dual formulation approach, as discussed in [6]. When the primal formulation is used, a unique set of interface DoFs is defined while the interface forces are eliminated as unknowns. In the dual formulation however, the full set of DoFs is retained. Additionally, the dual assembled system is obtained by satisfying the interface equilibrium a priori. For an interface model which allows for relative displacement between the two substructures, the dual formulation is therefore the only feasible formulation. Consequently, the equilibrium condition is implemented by defining

$$\mathbf{g} = -\mathbf{B}^T \boldsymbol{\lambda} \quad (27.4)$$

with $\boldsymbol{\lambda}$ being a Lagrange Multiplier representing the interface force intensity. It can be verified that Eq. (27.4) automatically satisfies the equilibrium condition [6].

In Terms of System Matrices

Substituting this relation in Eq. (27.1), and moving λ to the left-hand side together with the unknown degrees of freedom, the dual formulation is found:

$$\begin{cases} \mathbf{M}\ddot{\mathbf{u}} + \mathbf{C}\dot{\mathbf{u}} + \mathbf{K}\mathbf{u} + \mathbf{B}^T\lambda = \mathbf{f} & (27.5a) \\ \mathbf{B}\mathbf{u} = \mathbf{0} & (27.5b) \end{cases}$$

In the frequency domain one can conveniently write the dynamic stiffness for $\mathbf{u}(\omega)$ as $\mathbf{Z}(\omega) = -\omega^2\mathbf{M} + j\omega\mathbf{C} + \mathbf{K}$. The dually assembled system in the frequency domain reads:

$$\begin{cases} \mathbf{Z}\mathbf{u} + \mathbf{B}^T\lambda = \mathbf{f} & (27.6a) \\ \mathbf{B}\mathbf{u} = \mathbf{0} & (27.6b) \end{cases}$$

In Terms of Receptance

Typically, the dynamics of a system is characterised by measuring a limited number of input and output points. Therefore, no explicit mass, damping and stiffness matrix is obtained experimentally. Instead a receptance matrix $\mathbf{Y}(\omega)$ is measured, comprising the Frequency Response Functions (FRFs) of the tested structure. It can be shown that the receptance matrix is the inverse of the dynamic stiffness $\mathbf{Z}(\omega)$ of the system constrained at the measurement points, such that displacements and forces are related by $\mathbf{u} = \mathbf{Y}\mathbf{f}$. Similarly, the mobility matrix relates the excitation with velocities, i.e. $\dot{\mathbf{u}} = j\omega\mathbf{u} = j\omega\mathbf{Y}\mathbf{f}$.

To be able to do the assembly, Eq. (27.6a) can be rewritten by eliminating the interface force intensity λ . This formulation is suitable for receptance matrices obtained by experiment. This method is called the Lagrange Multiplier Frequency Based Substructuring (LM-FBS) and has been well established in the experimental substructuring community [4, 5, 10].

$$\mathbf{u} = \mathbf{Y}\mathbf{f} - \mathbf{Y}\mathbf{B}^T(\mathbf{B}\mathbf{Y}\mathbf{B}^T)^{-1}\mathbf{B}\mathbf{Y}\mathbf{f} \quad (27.7)$$

The separate terms can be distinguished to give a mechanical interpretation:

$$\mathbf{u} = \mathbf{Y}\mathbf{f} - \mathbf{Y}\mathbf{B}^T\lambda \quad (27.8)$$

$$\lambda = \mathbf{Z}_{int}\Delta\mathbf{u}_{int} \quad (27.9)$$

$$\Delta\mathbf{u}_{int} = \mathbf{B}\mathbf{Y}\mathbf{f}, \quad \mathbf{Z}_{int} = (\mathbf{B}\mathbf{Y}\mathbf{B}^T)^{-1} \quad (27.10)$$

The response of the individual, unassembled, substructures, resulting from a force input, is given by $\mathbf{u} = \mathbf{Y}\mathbf{f}$. This force input results in a $\Delta\mathbf{u}_{int}$ which represents the distance between the substructures at the interface in the uncoupled situation. In order to close this distance, an interface force λ is applied. Finally, \mathbf{Z}_{int} gives the dynamic stiffness of the substructures condensed at the interface, which relates the force needed to obtain a unit gap at the interface. When this term is multiplied with the initial gap $\Delta\mathbf{u}_{int}$, the intensity of the force required to close the gap is obtained.

27.2.2 Compliant Interface

As previously discussed, regular substructuring techniques require compatibility and equilibrium conditions to be satisfied at all time. Indeed, a rigid connection is assumed where no relative displacement between the substructures is allowed. However in reality, due to some interface *compliance*, relative displacement between two subcomponents can occur. In other words, the compatibility conditions no longer hold. What will follow is a description of a method by which this compliance can be accounted for, based on [17], see Fig. 27.1c. Again, a description is given in terms of system matrices as well as the system's receptance.

In Terms of System Matrices

Friction at the interface will be modelled by a stiffness and damping term only. Mass corresponding to for instance a bolt can either be added as a separate substructure or by a distributed contribution to the diagonal of the mass matrices. Since the interface is modelled without an interface mass, i.e. the equilibrium is not affected by internal dynamics, the force equilibrium condition still holds. On the contrary, the compatibility condition can be reformulated when relative displacement between the structures is allowed:

$$\begin{cases} \mathbf{M}\ddot{\mathbf{u}} + \mathbf{C}\dot{\mathbf{u}} + \mathbf{K}\mathbf{u} + \mathbf{B}^T \boldsymbol{\lambda} = \mathbf{f} \\ \mathbf{B}\mathbf{u} = \Delta \mathbf{u}_c \end{cases} \quad (27.11a)$$

$$(27.11b)$$

where the subscript c indicates a correspondence with the incompatibility at the interface. Please note the difference between $\Delta \mathbf{u}_{int}$ and $\Delta \mathbf{u}_c$ in Eq. (27.8); $\Delta \mathbf{u}_{int}$ represents the distance between the uncoupled substructures, whereas $\Delta \mathbf{u}_c$ represents the “play” at the interface between the coupled structures in case of a compliant interface.

Now instead of leaving the set of interface intensities $\boldsymbol{\lambda}$ as unknowns, they can be written in terms of the relative displacement and relative velocity between the substructures interfaces. By assuming a linear dependency, a stiffness and damping term can be distinguished

$$\boldsymbol{\lambda} = \mathbf{C}_c \Delta \dot{\mathbf{u}}_c + \mathbf{K}_c \Delta \mathbf{u}_c \quad (27.12)$$

This is equivalent with modelling a linear spring and viscous damper between the coupling DoFs of the substructures. Note that \mathbf{C}_c and \mathbf{K}_c reside in the space of the interface problem, which is dimensionally different than the physical domain of the system matrices. More discussion of \mathbf{C}_c and \mathbf{K}_c is found at the end of this section.

Substituting Eq. (27.11b) in Eq. (27.12) results in the following expression for the interface force intensities

$$\boldsymbol{\lambda} = \mathbf{C}_c \mathbf{B}\dot{\mathbf{u}} + \mathbf{K}_c \mathbf{B}\mathbf{u} \quad (27.13)$$

When finally Eq. (27.5a) is combined with Eq. (27.13), the interface model can be included in the equation of motion

$$\mathbf{M}\ddot{\mathbf{u}} + (\mathbf{C} + \mathbf{B}^T \mathbf{C}_c \mathbf{B})\dot{\mathbf{u}} + (\mathbf{K} + \mathbf{B}^T \mathbf{K}_c \mathbf{B})\mathbf{u} = \mathbf{f} \quad (27.14)$$

In Terms of Receptance

In order to implement the compliant interface in the frequency domain, one starts with the dual assembled matrix notation of the equation of motion as given in Eq. (27.6a). Recall that the compatibility condition is reformulated as $\mathbf{B}\mathbf{u} = \Delta \mathbf{u}_c$.

$$\begin{cases} \mathbf{Z}\mathbf{u} + \mathbf{B}^T \boldsymbol{\lambda} = \mathbf{f} \\ \mathbf{B}\mathbf{u} = \Delta \mathbf{u}_c \end{cases} \quad (27.15a)$$

$$(27.15b)$$

Rewriting the first equation in Eq. (27.15a) yields \mathbf{u} explicitly and after subsequently pre-multiplying with \mathbf{B} one obtains²:

$$\mathbf{B}\mathbf{u} = \mathbf{B}\mathbf{Y}\mathbf{f} - \mathbf{B}\mathbf{Y}\mathbf{B}^T \boldsymbol{\lambda} \quad (27.16)$$

Recall the compliant interface model of Eq. (27.12) and write it as frequency dependent compliance:

$$\boldsymbol{\lambda} = \mathbf{Z}_c \mathbf{B}\mathbf{u} \quad (27.17)$$

$$\text{with } \mathbf{Z}_c \triangleq j\omega \mathbf{C}_c + \mathbf{K}_c \quad (27.18)$$

²Note that the inverse of the dynamic stiffness equals the receptance, i.e. $\mathbf{Y} \triangleq \mathbf{Z}^{-1}$.

\mathbf{Z}_c represents the *dynamic interface stiffness*. Inverting Eq. (27.18) to obtain the *dynamic interface receptance* \mathbf{Y}_c , one can write for the interface incompatibility of Eq. (27.17):

$$\mathbf{Z}_c^{-1} \boldsymbol{\lambda} = \mathbf{Y}_c \boldsymbol{\lambda} = \mathbf{B} \mathbf{u} \quad (27.19)$$

Substituting this result in Eq. (27.16), one now finds for the interface force intensity of the compliant connection:

$$\boldsymbol{\lambda} = (\mathbf{B} \mathbf{Y} \mathbf{B}^T + \mathbf{Y}_c)^{-1} \mathbf{B} \mathbf{Y} \mathbf{f} \quad (27.20)$$

Finally substitution of this expression in Eq. (27.15a) results in an extension of the LM-FBS method where a compliant interface is accounted for

$$\mathbf{u} = \mathbf{Y} \mathbf{f} - \mathbf{Y} \mathbf{B}^T (\mathbf{B} \mathbf{Y} \mathbf{B}^T + \mathbf{Y}_c)^{-1} \mathbf{B} \mathbf{Y} \mathbf{f} \quad (27.21)$$

This allows for a clear mechanical interpretation. The result is similar to the rigid connection expression, except for the dynamic stiffness of the interface

$$\mathbf{Z}_{int} = (\mathbf{B} \mathbf{Y} \mathbf{B}^T + \mathbf{Y}_c)^{-1} \quad (27.22)$$

The total dynamic interface stiffness is extended by the \mathbf{Y}_c corresponding to the compliance of the interface. Clearly, when no compliance is present, the expression is the same as in Eq. (27.7), i.e. the connection is considered rigid. The more compliant the interface, the bigger the contribution to the dynamic interface stiffness.

The following remarks on the construction of the compliant interface model are noteworthy:

- \mathbf{C}_c and \mathbf{K}_c can by default be constructed as diagonal matrices. As a result \mathbf{Z}_c and \mathbf{Y}_c are also diagonal. It is possible however to introduce coupling between certain degrees of freedom by introducing off-diagonal terms.
- Besides viscous damping, it is possible to have hysteretic damping at the interface by writing $\mathbf{K}_c = \mathbf{K}_c^r + j \mathbf{K}_c^i$.
- The proposed linear compliant interface model fits well in the DS framework. On top of that it is possible to implement non-linear models such as the Jenkins model [3] or Iwan model [9]. For instance in [3], an approach is proposed that results in equivalent interface stiffness and damping values that are possibly frequency dependent.

27.3 Complex Power

A useful tool to analyse a system is to consider the complex power flow of a structure. The strength of complex power is the possibility to distinguish between the real and the imaginary component, both having a clear physical interpretation. It will be shown later that the real part of the power is associated with *dissipative power*, later referred to as \mathcal{P}_d . The imaginary part is associated with *exchange power*, later referred to as \mathcal{P}_k . The latter one can be interpreted as power being exchanged between the inertia and elastic forces.

Two types of complex power are defined. The first one is the so called *excitation power*, later referred to as \mathcal{P}_e . Excitation power gives information about the power flow in the structure as a result of a forced excitation. It gives for instance insight in how much of the input power is dissipated. However, since it is a global measure it does not give any information about the source of the power dissipation. If one is interested in the power flow over the interface, one can examine the so called *interface power*, later referred to as \mathcal{P}_i . This helps to identify the amount of power dissipated over the interface due to its compliance. Both terms will be discussed in this section separately.

To be able to demonstrate phase differences in the complex power, we assume a forced harmonic vibration $\mathbf{u}(\omega) = \hat{\mathbf{u}} e^{j\omega t}$, where the amplitude shape $\hat{\mathbf{u}}$ can be complex-valued.

27.3.1 Excitation Power

As mentioned earlier, excitation power gives information about the power in the system as a whole. It can be used to examine by which extend power is dissipated in the structure as a result of the input power. What will follow is the derivation of the excitation power, both in terms of the system matrices and in terms of the receptance matrix.

In Terms of System Matrices

The excitation power can be defined as the projection of the applied force \mathbf{f} onto the corresponding structure's velocities $\dot{\mathbf{u}}$ in the complex plane. Information about a possible phase difference between force and velocity is given by the complex valued amplitude shapes

$$\mathcal{P}_e = \dot{\mathbf{u}}^H \mathbf{f} = \dot{\mathbf{u}}^H (\mathbf{M}\ddot{\mathbf{u}} + \mathbf{C}\dot{\mathbf{u}} + \mathbf{K}\mathbf{u}) \quad (27.23)$$

When oscillatory excitation and motion is assumed, it follows that

$$\begin{aligned} \mathcal{P}_e(\omega) &= -j\omega e^{-j\omega t} \hat{\mathbf{u}}^H (-\omega^2 \mathbf{M} + j\omega \mathbf{C} + \mathbf{K}) \hat{\mathbf{u}} e^{j\omega t} \\ &= -j\omega (\hat{\mathbf{u}}^H (-\omega^2 \mathbf{M} + \mathbf{K}) \hat{\mathbf{u}} + \hat{\mathbf{u}}^H (j\omega \mathbf{C}) \hat{\mathbf{u}}) \\ &= j\mathcal{P}_k + \mathcal{P}_d \end{aligned} \quad (27.24)$$

In Eq. (27.24) the total power is decomposed in its real and its imaginary part. The imaginary part of the complex power of a structure corresponds to the *exchanged* power (\mathcal{P}_k). The remaining part is *dissipated* (\mathcal{P}_d), which is the real part of the complex power. This term exists only due to the presence of damping

$$\begin{aligned} \mathcal{P}_k(\omega) &= \text{Im} \{ \mathcal{P}_e(\omega) \} = -\omega (\hat{\mathbf{u}}^H (-\omega^2 \mathbf{M} + \mathbf{K}) \hat{\mathbf{u}}) \\ \mathcal{P}_d(\omega) &= \text{Re} \{ \mathcal{P}_e(\omega) \} = -\omega (\hat{\mathbf{u}}^H (\omega \mathbf{C}) \hat{\mathbf{u}}) \end{aligned} \quad (27.25)$$

In Terms of Receptance

When the dynamics of a system are represented by its FRFs, one might want to write the power of the system in terms of its receptance \mathbf{Y} or its mobility $j\omega \mathbf{Y}$. Recall that the excitation power of the system is the complex projection of the velocity $\dot{\mathbf{u}}$ onto the excitation force \mathbf{f} .

$$\begin{aligned} \mathcal{P}_e(\omega) &= \dot{\mathbf{u}}^H \mathbf{f} \\ &= (j\omega \mathbf{Y} \hat{\mathbf{f}} e^{j\omega t})^H \hat{\mathbf{f}} e^{j\omega t} \\ &= -j\omega \hat{\mathbf{f}}^H \mathbf{Y}^H \hat{\mathbf{f}} \end{aligned} \quad (27.26)$$

Observe that if the excitation is given at a single degree of freedom l , the excitation power is simply determined by an element of the conjugated mobility matrix:

$$\mathcal{P}_e(\omega) = -j\omega Y_{ll}^* f_l^2$$

To give an example, Fig. 27.2a shows the power for a limited frequency range, being illustrative for an entire frequency range. Clearly, dissipative power dominates at resonances as well as anti-resonances. The drop of exchange power at the resonance frequency is a result of the elastic and inertia forces being in equilibrium. At the anti-resonance frequencies, due to the very nature of the anti-resonance, the system is not receptive for motion. Hence, exchange power will not be present meaning that all power is directly dissipated.

Figure 27.2b shows the ratio of the dissipative power over the excitation power, giving a measure for the relative power dissipated compared to the power input. Clearly, maxima can be observed at both anti-resonance and resonance frequencies.

27.3.2 Interface Power

Consider a compliant interface as described in Sect. 27.2.2. Damping-like behaviour can be present due to local friction behaviour at the interface. Therefore, it can be interesting to examine the influence of a compliant interface onto the power in a structure. To that extend consider the complex projection of the relative velocity between two interface DoFs $\Delta \dot{\mathbf{u}}_c$ onto

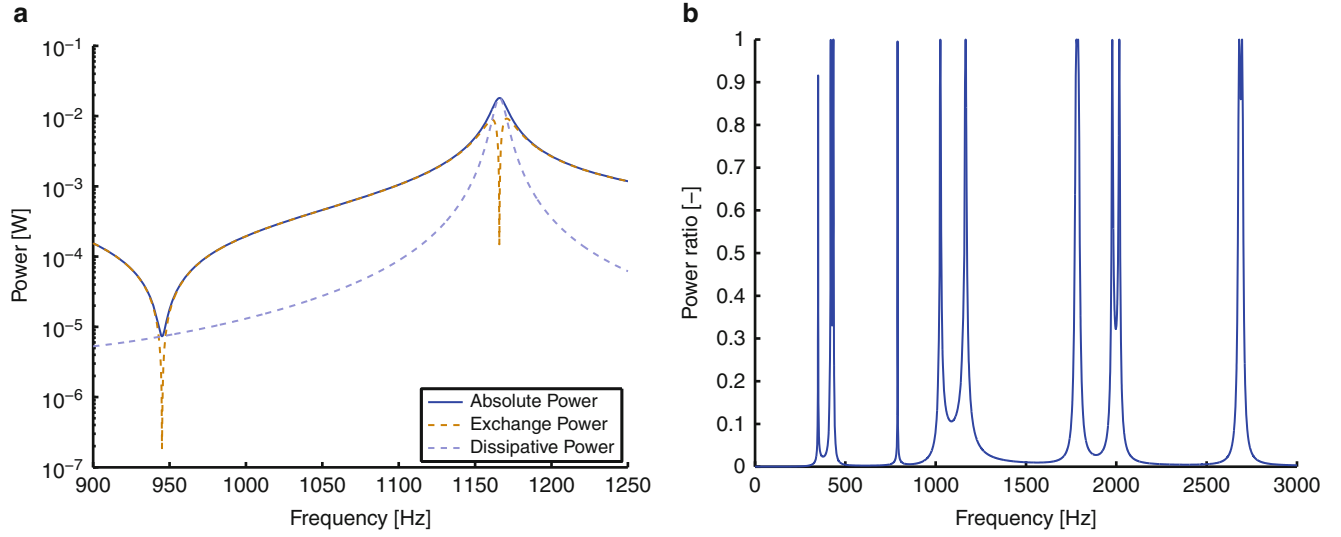


Fig. 27.2 Example of complex power plots to illustrate its characteristics. (a) Zoom of excitation power being typical for the full frequency range. (b) Ratio of dissipative power over total power

the interface force intensity λ in order to obtain the power over the interface

$$P_i = \Delta \dot{\mathbf{u}}_c^H \boldsymbol{\lambda} \quad (27.27)$$

Assume again oscillatory excitation and response, both with a possibly complex amplitude. Recall the following expressions for the relative displacement and velocity at the interface

$$\Delta \mathbf{u}_c = \mathbf{B} \mathbf{u} = \mathbf{B} \hat{\mathbf{Y}} \hat{\mathbf{f}} e^{j\omega t} \quad \Delta \dot{\mathbf{u}}_c = \mathbf{B} \dot{\mathbf{u}} = j\omega \mathbf{B} \hat{\mathbf{Y}} \hat{\mathbf{f}} e^{j\omega t} \quad (27.28)$$

In Sect. 27.2.2 it was proposed to decompose the interface force $\boldsymbol{\lambda}$ into a linear stiffness and damping term

$$\begin{aligned} \boldsymbol{\lambda} &= \mathbf{C}_c \Delta \dot{\mathbf{u}}_c + \mathbf{K}_c \Delta \mathbf{u}_c \\ &= \mathbf{C}_c \mathbf{B} \dot{\mathbf{u}} + \mathbf{K}_c \mathbf{B} \mathbf{u} \\ &= j\omega \mathbf{C}_c \mathbf{B} \hat{\mathbf{Y}} \hat{\mathbf{f}} e^{j\omega t} + \mathbf{K}_c \mathbf{B} \hat{\mathbf{Y}} \hat{\mathbf{f}} e^{j\omega t} \end{aligned} \quad (27.29)$$

Substituting Eqs. (27.28) and (27.29) into Eq. (27.27) leads to the following expression for the power over the interface

$$\begin{aligned} P_e &= \Delta \dot{\mathbf{u}}_c^H \boldsymbol{\lambda} \\ &= (j\omega \mathbf{B} \hat{\mathbf{Y}} \hat{\mathbf{f}} e^{j\omega t})^H \left(j\omega \mathbf{C}_c \mathbf{B} \hat{\mathbf{Y}} \hat{\mathbf{f}} e^{j\omega t} + \mathbf{K}_c \mathbf{B} \hat{\mathbf{Y}} \hat{\mathbf{f}} e^{j\omega t} \right) \\ &= -j\omega \hat{\mathbf{f}}^H \mathbf{Y}^H \mathbf{B}^T e^{-j\omega t} (j\omega \mathbf{C}_c \mathbf{B} \hat{\mathbf{Y}} + \mathbf{K}_c \mathbf{B} \hat{\mathbf{Y}}) \hat{\mathbf{f}} e^{j\omega t} \\ &= \underbrace{\omega^2 \hat{\mathbf{f}}^H \mathbf{Y}^H \mathbf{B}^T \mathbf{C}_c \mathbf{B} \hat{\mathbf{Y}} \hat{\mathbf{f}}}_{\text{real, dissipative power}} + \underbrace{-j\omega \hat{\mathbf{f}}^H \mathbf{Y}^H \mathbf{B}^T \mathbf{K}_c \mathbf{B} \hat{\mathbf{Y}} \hat{\mathbf{f}}}_{\text{imaginary, exchange power}} \end{aligned} \quad (27.30)$$

Notice the two different terms in Eq. (27.30) denoting power corresponding to interface damping and interface stiffness, both coefficients being real valued. Since damping can be the only source of dissipation, real power is considered to be dissipative. On the contrary, the power associated to the stiffness is imaginary and therefore represents the exchange power over the interface.

Note that both \mathbf{K} and \mathbf{K}_c can be complex valued in case of hysteretic damping, i.e. $\mathbf{K} = \mathbf{K}^r + j\mathbf{K}^i$, resulting in the dissipation term in the equations from Eq. (27.24) to be extended by the imaginary component of the stiffness.

27.4 Test Case

This section addresses an application of the compliant coupling of two substructures, based on the theory discussed in Sect. 27.2. The complex power method of Sect. 27.3 is used to estimate proper compliant interface parameters.

Figure 27.3 shows the considered assembled structures being a U-shaped beam and a straight beam. The substructures are attached at two locations, which is realised by two M10 bolts. The simplicity in geometry of the structures makes it easy to numerically model. Although having two interface connections, the high level of symmetry of the structure allows for good interpretation of the contribution of a single connection. Moreover, the structures are made out of a single piece of aluminium which ensures homogeneous material properties, unaffected by welds or any other form of connection. Finally, the physical attachment is realised by a bolted connection typically used in industry.

The dynamics of the two unassembled structures and the assembled structure is experimentally obtained by combining the following experiments: (1) The eigenmodes are obtained by hammer impact and acceleration measurement. Unfortunately, the wire of the acceleration sensor used for the impact measurement contributed significantly to the damping. (2) A second measurement was therefore done where the response was obtained acoustically using a microphone. This resulted in a much more accurate estimation of the eigenfrequencies and damping values. For the interested reader, the methods used for the damping estimation is discussed in Appendix.

To avoid the use of measured response data which might be contaminated with measurement noise, the assembly is realised based on the FEM modes (obtained by ANSYS) of both substructures. A comparison of the FEM modes with the measured modes based on the Modal Assurance Criteria (MAC) [1] results in values between 0.9 and 1 in the considered frequency range of 3 kHz. Moreover, the FEM eigenfrequencies are within 1 % agreement with respect to the experimentally obtained eigenfrequencies. Even beyond the considered bandwidth up to 6 kHz, still a 1.5 % agreement is obtained. Both results proof good resemblance between the FEM model and the experimentally obtained modal data.

In the substructuring results that follow, the contribution of the bolts and sensor is accounted for by means of adding lumped masses with accompanying inertia to the assembled structure.

A good comparison with experimental data is realised by re-synthesis of the measured response, rather than using the measured response directly. The re-synthesis is based on the measured eigenfrequencies and modal damping values.

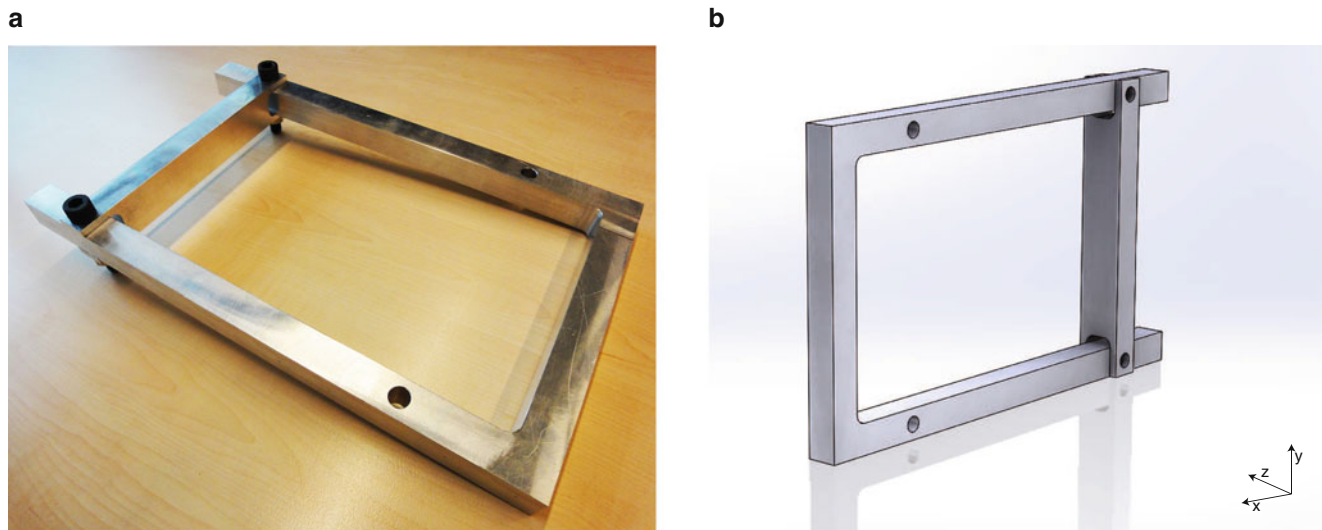


Fig. 27.3 A picture and a CAD model of the considered assembly. The in-plane coordinates are x and y . The out of plane coordinate is z . (a) Picture of the considered assembled structure ($20 \times 200 \times 300$ mm). The structure is made out of a single piece of aluminium. (b) CAD model of the considered assembled structure. The contribution of the bolts is added in a later stage

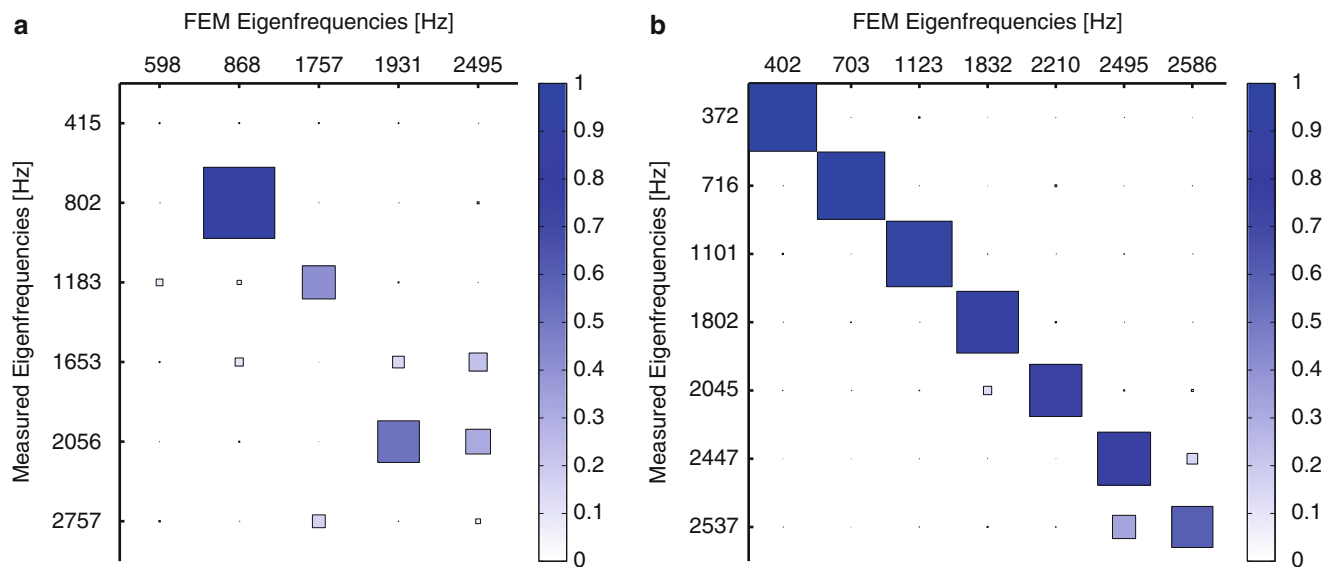


Fig. 27.4 MAC table of the measured eigenmodes and substructured eigenmodes with a rigid interface connection. Resonance at 2,495 Hz showed both in-plane and out-of-plane displacements. (a) In-plane eigenmodes. (b) Out-of-plane eigenmodes

27.4.1 Classical Rigid Interface Connection Results

First, a comparison is made using different sets of coupling DoFs based on a rigid connection, i.e. where no relative displacement is allowed between the coupling degrees of freedom. Distinction is made between the following sets of coupling DoFs.

1. Direct node coupling considering only translation information. A selection of six DoFs is taken from three nodes spanning a plane, being three translations in node 1, two translations in node 2 and one translation in node 3.
2. A Virtual Point Transformation [14] using the 6-DoF translational and rotational rigid Interface Deformation Modes (IDMs), i.e. no flexible IDMs are considered. The nodes closest to the virtual point are used for the transformation.
3. A rigidified interface condensed in one point having both translational and rotational information. All nodes at the interface are connected by rigid links to a single point which is used for assembly. This results in a truly rigid interface.

Direct node coupling did not give satisfactory results. Neither eigenmodes nor eigenfrequencies did match the measurement. The other two options on the other hand showed better similarity with the experimentally obtained eigenmodes. The eigenfrequencies however were significantly higher than the measured eigenfrequencies. Clearly, the considered connection is stiffer than reality, which shows its largest influence for the in-plane response.

Moreover, the rigidified eigenfrequencies were slightly higher than the virtual point eigenfrequencies. This is due to the fact that, for the virtual point transformation, compatibility is enforced only for the rigid part of the interface behaviour while the elastic part remains uncoupled. For a rigidified interface on the other hand, the interface is fully rigid and assembled as such. So it is expected that the virtual point connection underestimates the stiffness of the interface, whereas the rigidified interface yields an overestimation. The true interface stiffness is therefore most likely somewhere in between.

Based on these results and the fact that a rigidified interface showed better out-of-plane results when compliantly connected, compared to the same connection with a virtual point, it is chosen to continue this test case with the rigidified interface. Recall that only the inertial contribution of the bolt was accounted for. The rigidified interface therefore accounts for the added stiffness of the bolt, making it the best possible option for this test case.

For the considered frequency band the observed modes are, due to the geometry of the structures, either purely in-plane or out-of-plane. Therefore, the response of the structure is considered accordingly. Figures 27.4 and 27.5 show the results of a rigid connection by means of a MAC table and FRFs. The figures show that the out-of-plane result is already quite promising in contrast with the in-plane result, which indicates that the interface has its largest influence on the in-plane dynamics.

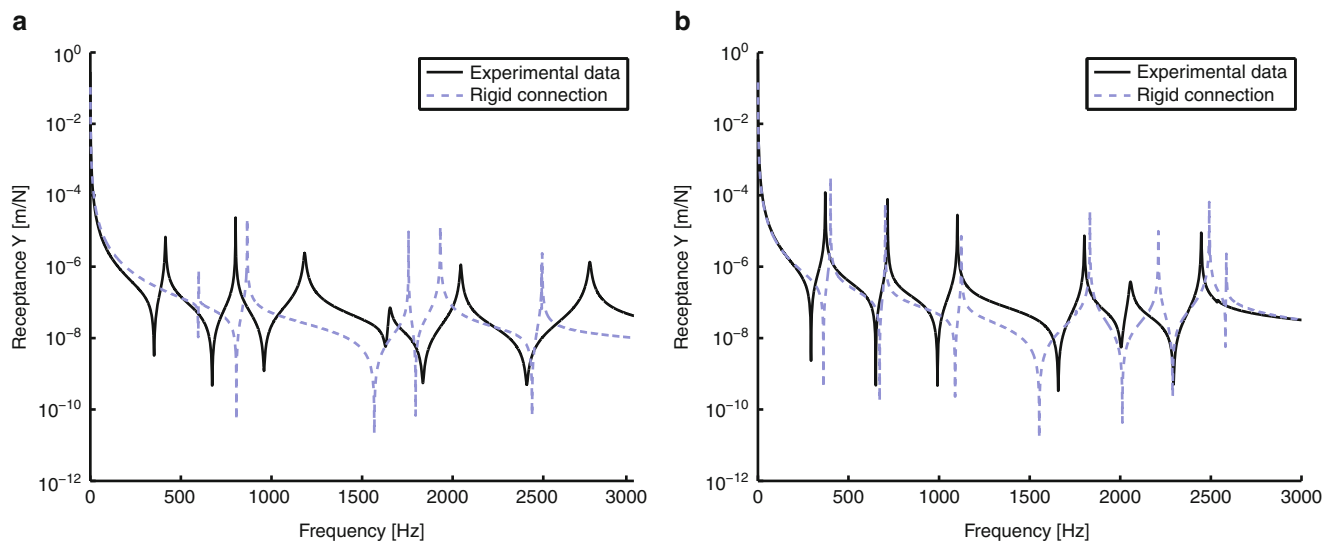


Fig. 27.5 (a) In-plane and (b) out-of-plane response of the assembled structure, using (1) rigid connection, (2) compliant connection case 1. The compliant connection (1) only affects the in-plane dynamics

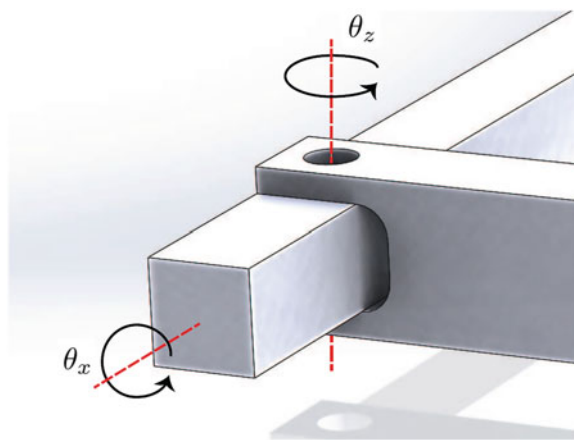


Fig. 27.6 CAD model showing the compliant directions of the interface connection

27.4.2 Compliant Interface Connection Results

The aim is to improve the results by implementing a compliant interface for both connections. Consider the following three cases.

1. Solely the in-plane rotation, i.e. the rotations around the bolts, are compliantly connected. Only flexibility is added, no damping (k_{θ_z}).
2. Both in-plane and out-of-plane rotation is compliant in stiffness ($k_{\theta_x}, k_{\theta_z}$).
3. Both in-plane and out-of-plane rotation is compliant in stiffness ($k_{\theta_x}^r, k_{\theta_z}^r$) and damping ($k_{\theta_x}^i, k_{\theta_z}^i, c_{\theta_x}, c_{\theta_z}$).

It holds for all cases that the remaining DoFs are rigidly connected and that the compliance is symmetrically applied, i.e. both sides of the structure have the same compliance. Each subsequent case uses the same compliant stiffness values as used in its preceding case (Fig. 27.6).

In Fig. 27.7 the measured (resynthesised) response is compared with both a rigid connection as well as compliant connection case 1. The in-plane response shows the influence of adding compliance in a single DoF. Clearly, due to the compliance in θ_z , only the in-plane resonances have shifted in frequency. The out-of-plane response given in Fig. 27.7b is not affected by the in-plane compliance. This allows for independent shifting of eigenfrequencies for either in-plane or out-of-plane vibration modes.

The results are improved (both eigenfrequency and eigenmode) when the compliance of the interface connection is extended by a compliance for the out-of-plane motion (case 2), not shown in the figure.

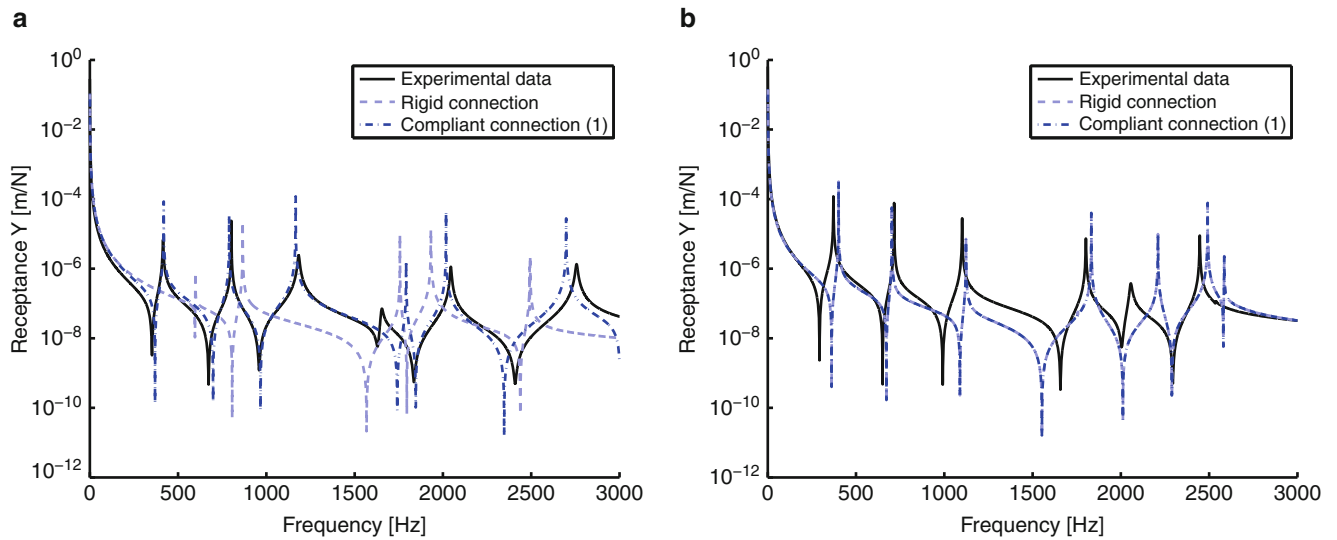


Fig. 27.7 (a) In-plane and (b) out-of-plane response of the assembled structure, using (1) rigid connection, (2) compliant connection case 1. The compliant connection (1) only affects the in-plane dynamics

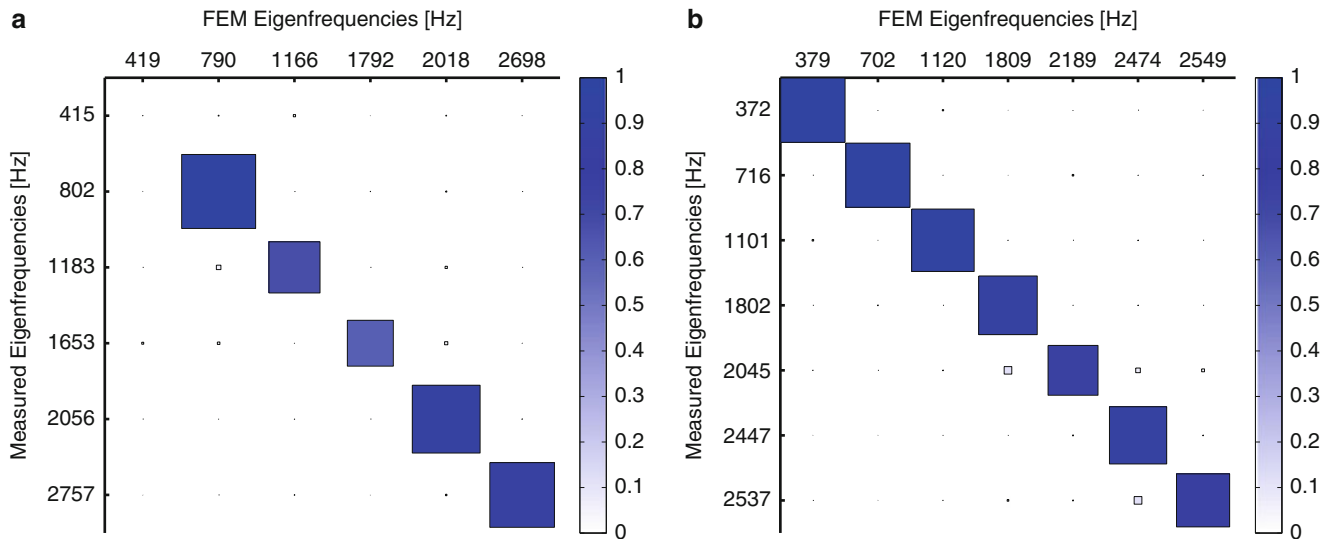


Fig. 27.8 MAC table of the measured eigenmodes and substructured eigenmodes with compliant interface case 2. (a) In-plane eigenmodes. (b) Out-of-plane eigenmodes

Next, a MAC comparison is made between the measured modeshapes and the substructured modeshapes of case 2, see Fig. 27.8. The majority of both in-plane and the out-of-plane eigenmodes have MAC values close to one, proving a good resemblance with the measured data. Note that a MAC value for the first in-plane mode is missing; this mode was not identified correctly.

Estimation of Interface Damping Based on Complex Power

The excitation power for the assembled structure is computed from the resynthesised receptance using Eq. (27.26). Focussing on the dissipative part of the power helps one to identify the dissipative phenomena on the interface and make an estimate of the involved interface damping. Figure 27.9 gives the dissipative power of the resynthesised measurement and the compliant interface cases 2 and 3. The essential difference between the two compliant interfaces is the presence of interface damping in case 3.

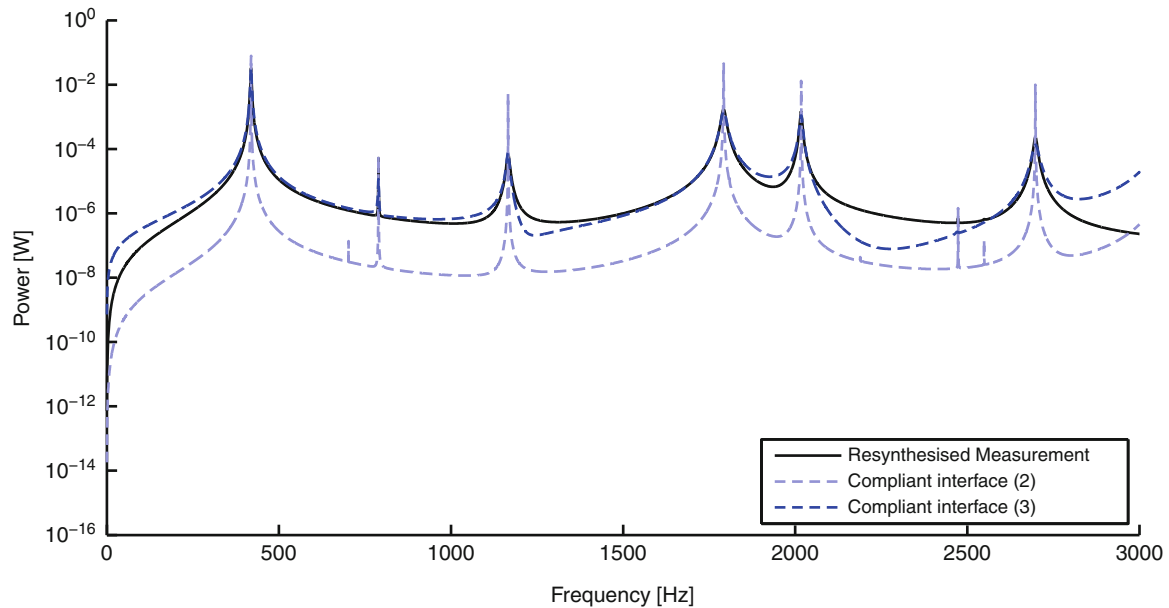


Fig. 27.9 Dissipative part of the excitation power of the resynthesised measurement, compliant interface case 2 and case 3

When no interface damping is present, obviously the only damping of the system is due to the contribution of the damping present in the individual structures. The corresponding dissipation level is clearly underestimated. It is therefore not sufficient to describe the interface connection solely with stiffness terms. Adding damping, both in viscous and hysteretic form, improves the result significantly. By tuning the damping values, the overall dissipation level increases and the dissipation close to resonance frequencies approximate the measurement much better.

Unfortunately, due to measurement limitations it is not possible to directly obtain the interface power. Also, the way the measured response is resynthesised results in a global level of the interface damping, hence no information about the interface dissipation can be obtained. Nonetheless the effect of the interface for the overall damping can indeed be indicated by comparing the total amount of dissipation of the assembled structure with the dissipation of the substructures being rigidly coupled.

We have already shown that the substructured eigenfrequencies and eigenmodes show good resemblance with the measurement. On top of that we now have a good estimate of the interface damping since the dissipation levels match. Now finally the substructured response based on compliant interface case 3 can be compared with the resynthesised measurement, see Fig. 27.10. For the majority of eigenmodes, both the in-plane as well as the out-of-plane substructured response approximate the measured response very well.

27.5 Conclusions

This paper introduces a method to implement interface compliance in the context of Experimental Dynamic Substructuring. The method is validated by means of a test case in which it is shown that one can approximate the eigenfrequencies by choosing the proper compliance of the interface in a certain degree of freedom.

Complex power was used to judge the damping of the interface compliance. By looking at the dissipation level, one can tune the interface damping such that it approaches the measured dissipation. It was shown that by adding both hysteretic and viscous damping for a small set of interface degrees of freedom, the power level showed good resemblance with the resynthesised power dissipation.

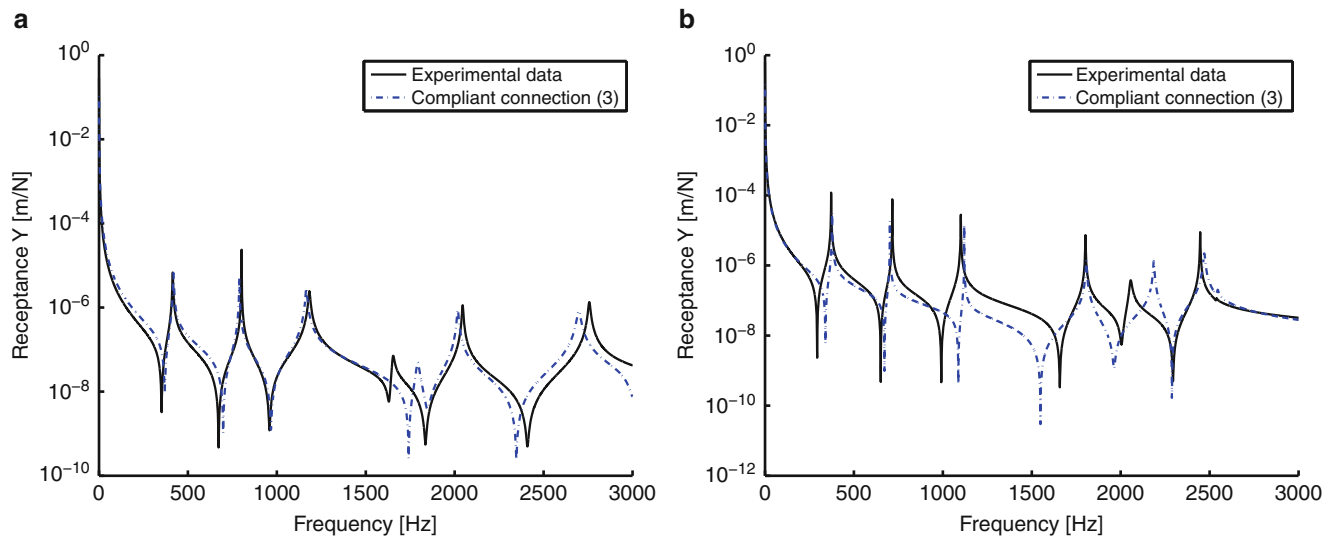


Fig. 27.10 Response of assembled structure. The resynthesised measurement is compared with compliant interface case 3. (a) The in-plane response. (b) The out-of-plane response

27.6 Outlook

As for now, the excitation power is used to tune the damping values of the compliant interface. For future work, however, it can be interesting to examine the possibilities to use interface power to estimate the compliant interface parameters.

Yet to be done is to categorise stiffness and damping parameters of typical joints in order to implement jointed connections directly from the shelf into the compliant interface model.

Appendix: Damping Estimation

Two methods are adopted to determine modal damping: a frequency domain approach and a time domain approach. The Circle Fit [7] method is a well known frequency domain approach and relies on the fact that a response in the vicinity of a resonance follows a circular shape when plotted in the complex plane. Using a circle to fit the response data, one can determine the damping as a function of the sweep rate of the response over the circle, see Fig. 27.11a.

The time domain approach relies on the assumption that any signal in time can be modelled as a superposition of periodic components with its specific frequency and amplitude (the deterministic part) plus uncorrelated noise (the stochastic part). When an eigenfrequency is considered, the amplitude of the corresponding wave has the analytical expression of $x(t) = Ae^{-\zeta_r \omega_r t}$. When plotted on a logarithmic scale, a straight line can be fitted up to a certain noise level, see Fig. 27.11b. The damping associated to that eigenfrequency is a function of the slope of this line.³

For both methods it is assumed that damping in the structure described in the test case of Sect. 27.4 is well described by modal damping. The order of magnitude of the damping ratio ranging from 10^{-3} to 10^{-5} justifies this assumption. For eigenfrequencies for which both methods were successful, the obtained damping values are within 10 % agreement.

³Rather than using a conventional Least-Squares Complex Exponential (LSCE) algorithm to fit modal parameters to the time data, a Vold-Kalman filter (VKF) was used, more commonly applied for non-stationary order-tracking (see for instance [15] or an implementation [12]). Unlike the LSCE, the VKF does not require the amplitude envelope to follow an exponential decay. Instead, the instantaneous complex amplitude is determined, to which an exponential damping slope can be fitted until the noise floor is reached. It therefore proves to be a robust way to identify extremely low damping values from noisy measurement data such as microphone recordings.

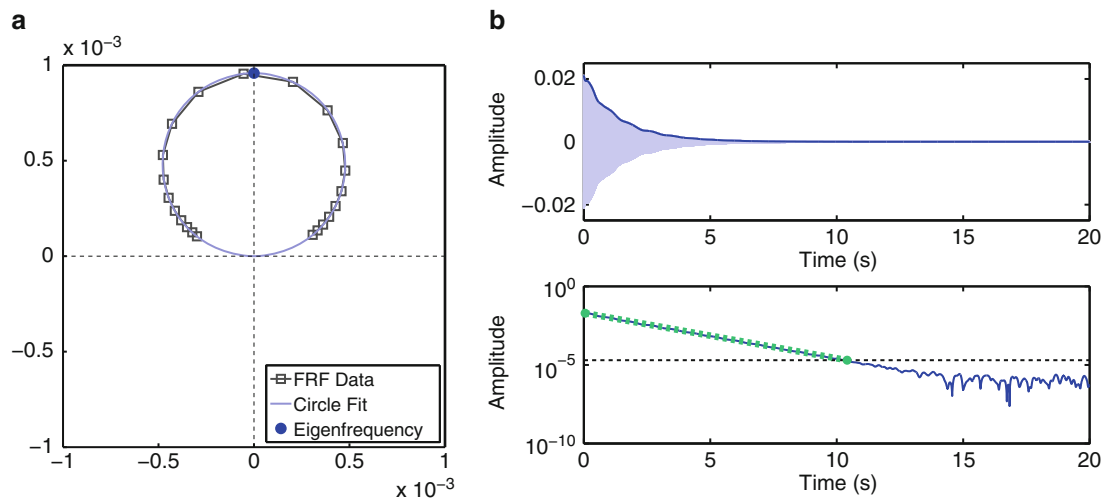


Fig. 27.11 A frequency and time domain approach to determine modal damping. **(a)** Circle fit of acceleration response data. **(b)** Response in time domain (*top*) and linear fit of response envelope on a logarithmic scale up to a certain noise level (*bottom*)

References

1. Allemang R (2003) The modal assurance criterion: twenty years of use and abuse. *Sound Vib Mag* 14–21. ISSN 1541-0161. <http://www.sandv.com/downloads/0308alle.pdf>
2. Allen M, Mayes R, Bergman E (2010) Experimental modal substructuring to couple and uncouple substructures with flexible fixtures and multi-point connections. *J Sound Vib* 329(23):4891–4906. ISSN 0022-460X. doi:10.1016/j.jsv.2010.06.007. <http://www.sciencedirect.com/science/article/pii/S0022460X10003792>
3. Bograd S, Reuss P, Schmidt A, Gaul L, Mayer M (2011) Modeling the dynamics of mechanical joints. *Mech Syst Signal Process* 25(8):2801–2826. ISSN 0888-3270. doi:http://dx.doi.org/10.1016/j.ymsp.2011.01.010. <http://www.sciencedirect.com/science/article/pii/S0888327011000203>
4. D'Ambrogio W, Fregolent A (2010) The role of interface dofs in decoupling of substructures based on the dual domain decomposition. *Mech Syst Signal Process* 24(7):2035–2048. ISSN 0888-3270. doi:http://dx.doi.org/10.1016/j.ymsp.2010.05.007. <http://www.sciencedirect.com/science/article/pii/S0888327010001500>. Special Issue: {ISMA} 2010
5. de Klerk D, Rixen D, de Jong J (2006) The frequency based substructuring method reformulated according to the dual domain decomposition method. In: Proceedings of the XXIV international modal analysis conference, Society for Experimental Mechanics, 2006
6. de Klerk D, Rixen D, Voormeeren S (2008) A general framework for dynamic substructuring—history, review and classification of techniques. *AIAA J* 46(5):1169–1181
7. Ewins D (1986) *Modal testing: theory and practice*. Engineering dynamics series. Research Studies Press for Bruel & Kjaer, Baldock. ISBN 9780863800368. <http://books.google.ca/books?id=gq5zAAAACAAJ>
8. Géradin M, Rixen D (1997) *Mechanical vibrations: theory and application to structural dynamics*. Wiley, New York. ISBN 9780471975243. <http://books.google.nl/books?id=IY9RAAAAMAAJ>
9. Iwan WD (1966) A distributed-element model for hysteresis and its steady-state dynamic response. *J Appl Mech* 33:893. doi:10.1115/1.3625199
10. Jetmundsen B, Bielawa R, Flannelly WG (1988) Generalized frequency domain substructure synthesis. *J Am Helicopter Soc* 33(1):55–64. doi:10.4050/JAHS.33.55
11. Reuss P, Zeumer B, Herrmann J, Gaul L (2012) Consideration of interface damping in dynamic substructuring. In: Topics in experimental dynamics substructuring and wind turbine dynamics, vol 2. Springer, New York, pp 81–88
12. van der Seijs M (2012) Second generation Vold-Kalman Order Filtering. The Mathworks file exchange, April 2012. <http://www.mathworks.com/matlabcentral/fileexchange/36277>
13. van der Seijs M, de Klerk D, Rixen D, Rahimi S (2013) Validation of current state frequency based substructuring technology for the characterisation of steering gear—vehicle interaction. In: Proceedings of the XXXI international modal analysis conference, Los Angeles. Society for Experimental Mechanics, Bethel
14. van der Seijs M, van den Bosch D, Rixen D, de Klerk D (2013) An improved methodology for the virtual point transformation of measured frequency response functions in dynamic substructuring. In: Papadrakakis M, Papadopoulos V, Plevis V (eds) COMPDYN 2013 4th, ECCOMAS thematic conference on computational methods in structural dynamics and earthquake engineering, Kos Island, Greece, 12–14 June 2013
15. Vold H, Herlufsen H, Mains M, Corwin-Renner D (1997) Multi axle order tracking with the Vold-Kalman tracking filter. *Sound Vib* 31(5): 30–35
16. Voormeeren S, Rixen D (2012) A family of substructure decoupling techniques based on a dual assembly approach. *Mech Syst Signal Process* 27(18):379

17. Voormeeren S, Valk P, Rixen D (2011) Practical aspects of dynamic substructuring in wind turbine engineering. In: Proulx T (ed) Structural dynamics and renewable energy, vol 1. Conference proceedings of the Society for Experimental Mechanics series. Springer, New York, pp 163–185. ISBN 978-1-4419-9715-9. doi:10.1007/978-1-4419-9716-6_16. http://dx.doi.org/10.1007/978-1-4419-9716-6_16
18. Weisser T, Gonidou L-O, Foltête E, Bouhaddi N (2011) Vibration transfer analysis of component interfaces by a power flow mode approach. *Eur J Comput Mech* 20(1–4):29–47. doi:10.3166/ejcm.20.29-47. <http://www.tandfonline.com/doi/abs/10.3166/ejcm.20.29-47>

Chapter 28

Prediction of Dynamics of Modified Machine Tool by Experimental Substructuring

Christian Brecher, Stephan Bäumlér, and Matthias Daniels

Abstract Until now the methods of experimental substructuring are rarely adopted in the machine tool sector, except for receptance coupling of tools and tool holders. In this paper, the methods are adopted to predict a general modification of a machine tool structure by coupling experimental and numerical models. This approach seems appropriate, since most design changes of machine tools affect only some part of the structure. Additionally, single components of a machine tool are easier to simulate than the complete machine tool, since they include less joints, which are usually difficult to parameterize. This contribution evaluates the proposed method, when it is applied to a single axis test bench. The slide is taken as the modified component—thus its dynamics are modeled analytically—and the remaining assembly is modeled experimentally. Particular emphasis is put on the modeling of the interfaces of the linear guides connecting the slide to the frame. Both a fixed connection between slide and frame and a linear spring-damper joint are adopted. Moreover, the dynamics of the assembly are predicted, for different positions of the slide. As a reference, the dynamics of the test bench are measured, when the slide is mounted.

Keywords Vibration • Machine tool • Frequency based substructuring • Joints • Design modification

28.1 Introduction

The dynamic behavior is an important criterion, when evaluating the performance of machine tools, [1]. The dynamic compliance at the Tool Center Point (TCP) describes the relative compliance between tool and work piece and is commonly measured or calculated as Frequency Response Functions (FRFs). These FRFs are used to compare different machine tools, but also represent the dynamic behavior of machine tools, when simulating the stability of cutting processes. In [2] the stability simulation is proposed as a decision criterion during the development of machine tools. As stressed there, the reliability of the stability prediction strongly depends on how well the dynamic behavior of the machine tool is modeled. Previous works (e.g. [2–4]) mostly update the parameters of a full machine model with respect to measurements of the corresponding physical machine. This approach is not satisfying with regard to the prediction of machine dynamics during the development since it presumes the existence of the physical machine. Moreover model updating of a complete machine tool is an elaborate task, considering that in most of the cases only rough initial estimates for the numerous joint characteristics (stiffness and damping properties) are possible, [1]. Especially the reliable choice of damping coefficient is currently a major research topic in the machine tool sector, [5].

Regarding that the majority of development tasks in the machine tool division are design variations or design adaptations [6], where only machine components, e.g. the machine table or a machine axis are modified, the combination of experimental and analytical models might allow to predict the dynamic machine tool behavior more efficiently. The unmodified part of the machine tool is then modeled experimentally while the modified part is modeled analytically. Following this approach the

C. Brecher • S. Bäumlér • M. Daniels (✉)
Laboratory for Machine Tools and Production Engineering (WZL), RWTH Aachen University,
Steinbachstraße 19, 52074 Aachen, Germany
e-mail: m.daniels@wzl.rwth-aachen.de

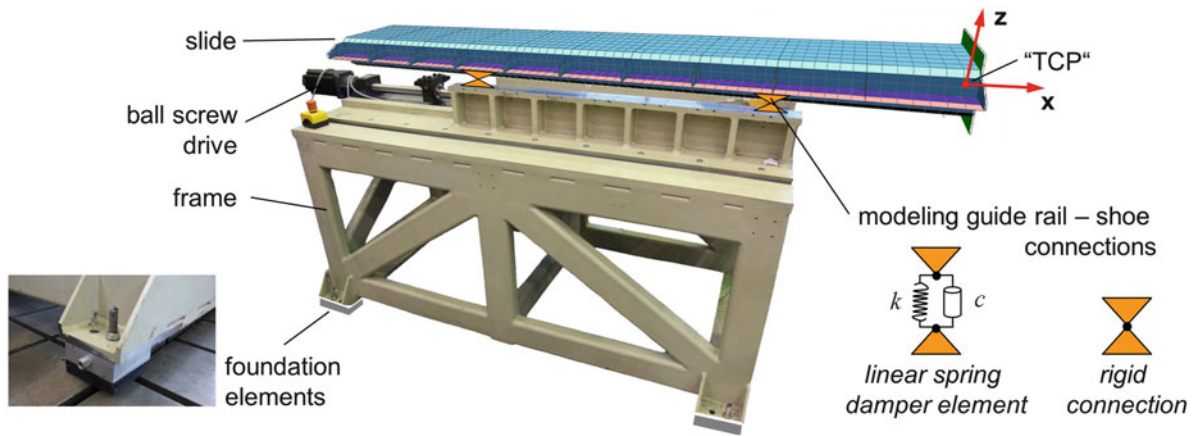


Fig. 28.1 Single axis test bench for dynamic substructuring

number of joints to be parameterized is kept minimal. Here the mentioned approach is used to predict the dynamic behavior of a single axis test bench, depicted in Fig. 28.1. The slide is guided linearly in x-direction, the guiding rails are fixed to the slide, the guiding shoes are fixed on the frame. A ball screw drive is installed to move the slide in x-direction. The frame is mounted on four bolt-through leveling wedges, each including an elastomeric insulation plate. The slide is seen as the modified component while the frame remains unchanged and is thus modeled experimentally.

While analytical dynamic substructuring methods are state of the art in the finite element (FE) and multi body simulations of machine tool dynamics, until now, experimental substructuring has primarily been used for the prediction of TCP FRFs for different milling tools, which is also known as receptance coupling (e.g. [7–9]). The goal of this paper is to predict the FRF at the TCP of the single axis test bench at different x-positions of the slide using a frequency based substructuring approach. Since this test bench includes several machine tool components, another goal is to assess the adaptability of experimental substructuring to machine tool structures. Firstly, the analytical reduced model of the slide is presented and correlated with measurements. Secondly, the experimental model of the frame is derived from measurements. In a third step, the frequency based coupling with joints leads to the desired FRF prediction. Finally the predicted FRFs are compared to measurements.

28.2 Analytical Model of Slide

The slide is a welded steel assembly (see Figs. 28.2 and 28.6) of a rectangular hollow steel section, finned side profiles holding the linear guides and a rectangular end plate. An aluminum block is screwed to the end plate and represents the TCP of the test bench. The slide is FE-modeled and the FE-matrices are exported to Matlab[®] environment. Moreover five slave nodes are added to this model and connected to the nodes of the slide (master nodes) by interpolation multi point constraints (RBE3 constraints). One of these nodes represents the place where the TCP FRF is measured, the other four nodes represent the nodes where the connection forces from the frame are transmitted into the slide. Thus the position of the latter are changed, when the x-position of the slide is changed. To speed up the assembly process, the slide model is reduced before the slave nodes are added. The reduction of the slide is done using the dual Craig-Bampton method according to [10]. Here, only the substantial equations are reflected, more detailed explanations can be found in [10–12]. The dual equations of motion of the slide are expressed by

$$\begin{bmatrix} M & 0 \\ 0 & 0 \end{bmatrix} \begin{pmatrix} \ddot{u} \\ \ddot{g}_B \end{pmatrix} + \begin{bmatrix} K & -b^T \\ -b & 0 \end{bmatrix} \begin{pmatrix} u \\ g_B \end{pmatrix} = \begin{pmatrix} f \\ 0 \end{pmatrix} + \begin{pmatrix} 0 \\ -u_B \end{pmatrix}. \quad (28.1)$$

M and K are the FE-matrices, u expresses all displacements and g_B expresses the boundary forces, f comprises all external forces while u_B comprises the displacements at the boundaries. The boundary nodes are the master nodes for the RBE3 constraints. The boolean matrix b selects the boundary DOFs out of all DOFs ($bu = u_b$). Depending on the x-position of the slide the matrix b changes and another set of boundary DOFs u_b and g_b is selected. The reduction basis R_{DCB} is built by a truncated number of free interface vibration modes Φ (25 modes are included in our application) and residual flexibility

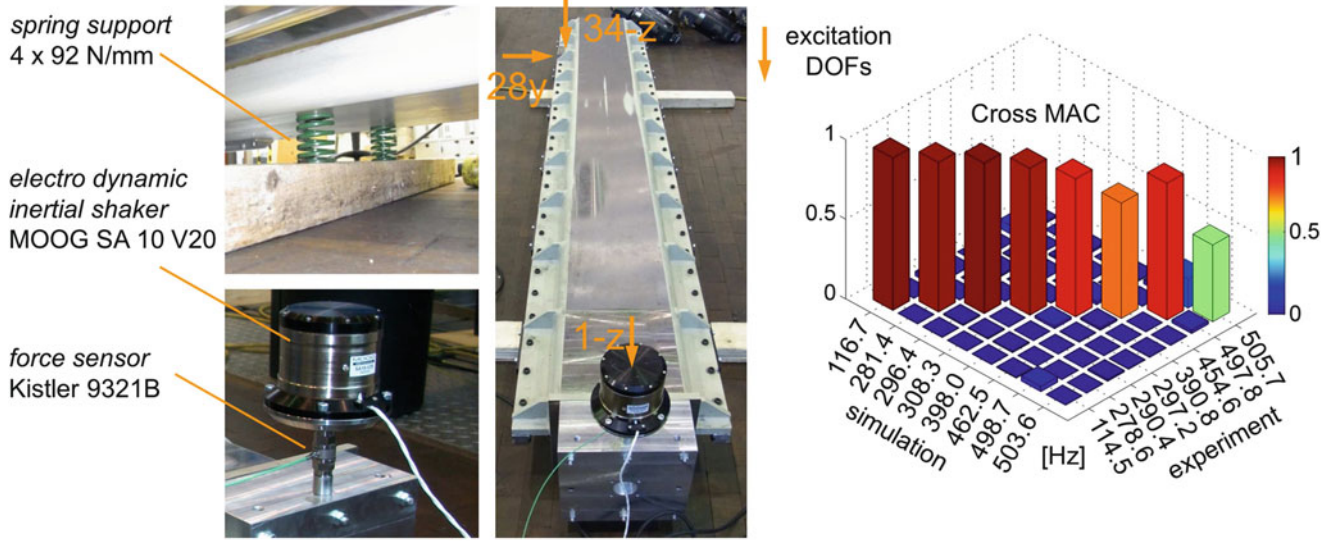


Fig. 28.2 Correlation between mode shapes obtained from finite element and experimental model

attachment modes Ψ_{ar} . With help of the reduction, the displacement DOFs are replaced by modal DOFs η , which determine the contribution of the free interface vibration modes Φ to the total displacements u .

$$R_{DCB} = \begin{bmatrix} \Phi & \Psi_{ar} \\ 0 & I \end{bmatrix}, \begin{pmatrix} u \\ g_B \end{pmatrix} = R_{DCB} \begin{pmatrix} \eta \\ g_B \end{pmatrix} \quad (28.2)$$

The residual flexibility attachment modes are mass and stiffness orthogonal to the free interface vibration modes Φ . This leads to the dual Craig-Bampton reduced Matrices \tilde{M} and \tilde{K} ,

$$\tilde{M} = R_{DCB}^T \begin{bmatrix} M & 0 \\ 0 & 0 \end{bmatrix} R_{DCB} = \begin{bmatrix} I & 0 \\ 0 & \Psi_{ar}^T M \Psi_{ar} \end{bmatrix}, \quad \tilde{K} = R_{DCB}^T \begin{bmatrix} K & -b^T \\ -b & 0 \end{bmatrix} R_{DCB} = \begin{bmatrix} \Omega^2 & -\Phi^T b^T \\ -b\Phi & -b\Phi_{ar} \end{bmatrix}. \quad (28.3)$$

As soon as the reduced slide matrices are available, the system can be assembled, for a certain position of the slide. The example in Eq. (28.4) shows the primal assembly between the reduced slide matrices and one slave node, which is connected by an RBE3 constraint. The assembled system matrices are obtained by matrix L , that reduces the force DOFs g_{B1} and g_{B2} to the unique force DOFs λ . The total DOFs u_A are thereby reduced to the unique DOFs x .

$$M_A = \text{diag} \left(\begin{bmatrix} I & 0 \\ 0 & \Psi_{ar}^T M \Psi_{ar} \end{bmatrix}_1, \begin{bmatrix} 0 & 0 \\ 0 & 0 \end{bmatrix}_2 \right), K_A = \text{diag} \left(\begin{bmatrix} \Omega^2 & -\Phi^T b^T \\ -b\Phi & -b\Phi_{ar} \end{bmatrix}_1, \begin{bmatrix} 0 & -b^T \\ -b & 0 \end{bmatrix}_2 \right),$$

$$u_A = \left((\eta \ g_B)_1^T \ (u \ g_B)_2^T \right)^T, x = (\eta_1 \ u_2 \ \lambda)^T, u = Lx, L = \begin{bmatrix} I & 0 & 0 \\ 0 & 0 & -R_S^{-1} R_M \\ 0 & I & 0 \\ 0 & 0 & -I \end{bmatrix}, \tilde{M}_A = L^T M_A L, \tilde{K}_A = L^T K_A L. \quad (28.4)$$

The second and fourth line of L express the RBE3 constraint between g_{B1} , g_{B2} and λ , whose derivation is given in [13]. The result of [13] is a relation between the slave and master displacement DOFs, u_1 and u_2 ,

$$\begin{bmatrix} I & R_S^{-1} R_M \end{bmatrix} \begin{pmatrix} u_1 \\ u_2 \end{pmatrix} = Bu = 0. \quad (28.5)$$

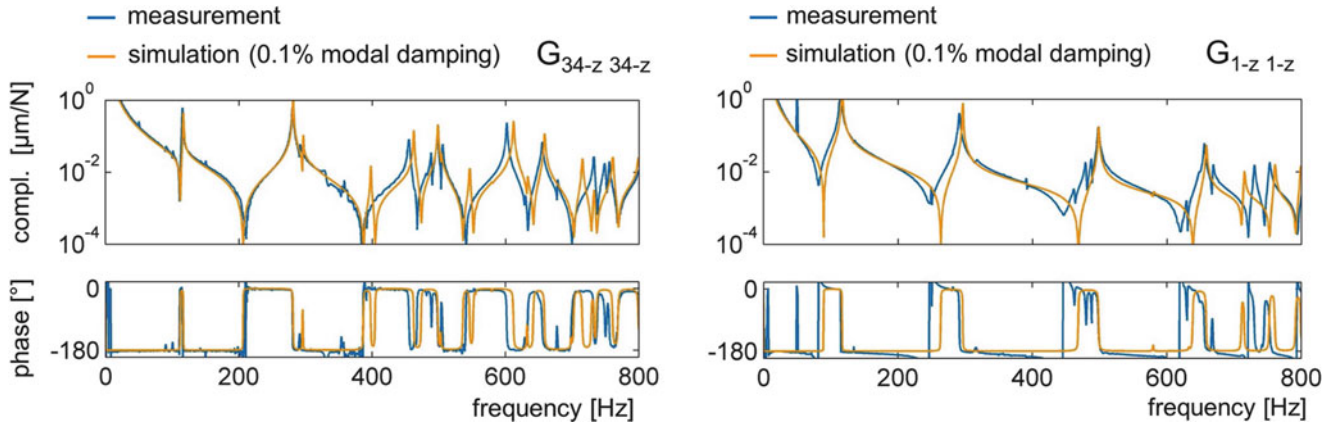


Fig. 28.3 Comparison of FRFs: simulation vs. experiment

Equation (28.5) comprises six constraint equations for the connection of one slave node (six DOFs) with several master DOFs. The matrices R_S and R_M are functions of the coordinates of the slave and master nodes. For the assembly using interface forces, the same Matrix B is used, [12], and Eq. (28.6) is used to form L .

$$\begin{pmatrix} g_1 \\ g_2 \end{pmatrix} = - \begin{bmatrix} I \\ R_S^{-1} R_M \end{bmatrix} \lambda = -B^T \lambda \quad (28.6)$$

As soon as the assembled matrices \tilde{M}_A and \tilde{K}_A are available, the FRF matrix needed for the frequency based coupling of slide and frame, can be calculated. Having solved the eigenvalue problem formed by the assembled matrices, the (mass-normalized) eigenvectors \tilde{V}_A and undamped (angular) eigenfrequencies ω_0 are available. The eigenvectors correspond to the reduced and assembled DOFs x . Hence, a backward transformation ($R_{ADCB}L$) and a DOF-selection (B_S) precedes (28.7) the calculation (28.8) of the FRF matrix, that is derived in [14]. The reduction matrix R_{ADCB} is a block diagonal matrix built from the reduction matrices of all the components. In our case it is built from the reduction matrix of the slide and zero matrices for the DOFs of the added slave nodes. As we only take into account the z-slave-DOFs, the FRF matrix H has the size five by five by n_f , with n_f as the number of considered frequency lines.

$$V = B_S R_{ADCB} L \tilde{V}_A \quad (28.7)$$

$$H(\omega) = V (diag_{k=1..n} (\omega_{0,k}^2) - \omega^2 I + diag_{k=1..n} (2\omega_{0,k} \xi_k))^{-1} V^T \quad (28.8)$$

In contrast to assemblies, which comprise several components and interconnecting joints, an ad hoc accordance of simulation and experiment is more probable when dealing with single components. Nevertheless, the correlation of calculated and measured mode shapes and resonance frequencies of the slide is determined. Figure 28.2 (left) shows the setup for the experimental modal analysis of the slide. For the test, the component is supported with flexible springs and is excited at three different positions using an inertial electro dynamic shaker. The depicted MAC matrix is calculated based on this poly reference modal analysis and indicates good correlations for the first seven mode shapes. Moreover, the frequency differences for this modes are low. It is supposed that the lower correlation at mode eight is not due to an incorrect model but rather due to the shaker, that influences the dynamics of the slide, when it is mounted at different excitation locations.

The measured drive point FRFs at the DOFs 1-z and 34-z are plotted in Fig. 28.3 together with the corresponding simulated FRF. The simulated FRFs are calculated using modal damping $\xi_k = 0.001$ in Eq. (28.8) for all considered modes k . Especially at DOF 1-z the measured FRF shows more peaks than the simulated one. It is supposed that the used inertial shaker generates considerable shear forces, and thus, more DOFs and more modes are excited than intended. Both comparisons indicate a better agreement for lower frequencies than for higher frequencies.

28.3 Experimental Model of Frame

In this study we concentrate on the z-DOFs of the guide rail—shoe connections and neglect the connection of the housing of the ball screw nut to the slide. Due to the high bending flexibility of the ball screw spindle, this connection is estimated to have minor effect on the predicted FRF. As there are four guiding shoes, the FRF matrix is of size four by four by n_f . The measurements are performed at the geometric center of each guide shoe. The guide shoes are not part of the experimental model. Respecting the (theoretical) symmetry of the FRF matrix, the number of measured FRFs is 10. As depicted in Fig. 28.4, the measurements are performed using an impact sledge hammer.

To check the symmetry of the FRF matrix, an extra FRF (G_{1z4z}) was measured. Moreover, two configurations of the frame assembly are investigated. For the first configuration, the bolts, which fix the frame to the test field and pretension the leveling wedges as well as the elastomeric insulation plates, are tightened. These bolts are untightened for the second configuration. Figure 28.1 includes a picture of such a foundation element. In Fig. 28.5 the two FRFs G_{1z4z} and G_{4z1z} and the direct FRF G_{1z1z} are plotted for the two configurations. The coherence values indicate a good quality of the FRFs in the frequency range from 25 to 300 Hz for the first configuration and from 10 to 300 Hz for the second one. Tensioning the foundation elements has considerable effect on the dynamic behavior below 250 Hz. In the case of loose bolts, the lowest remarkable resonance is found at lower frequencies, and comes along with a higher compliance. The FRFs G_{1z4z} and G_{4z1z} show a slightly better agreement in the case of loose bolts.

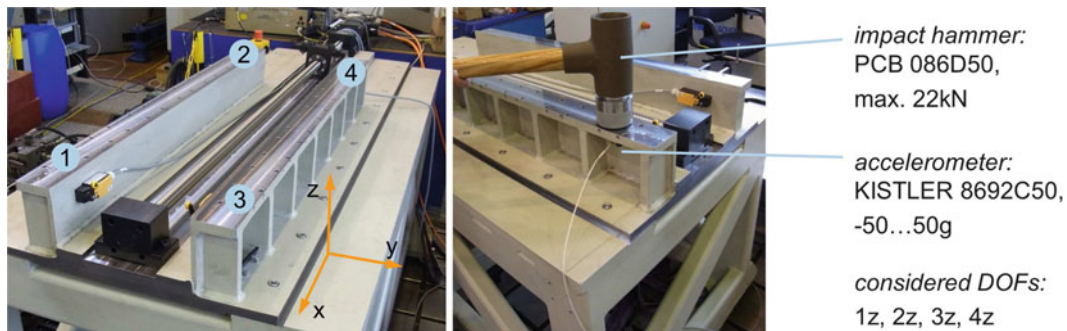


Fig. 28.4 FRF measurement at boundary DOFs

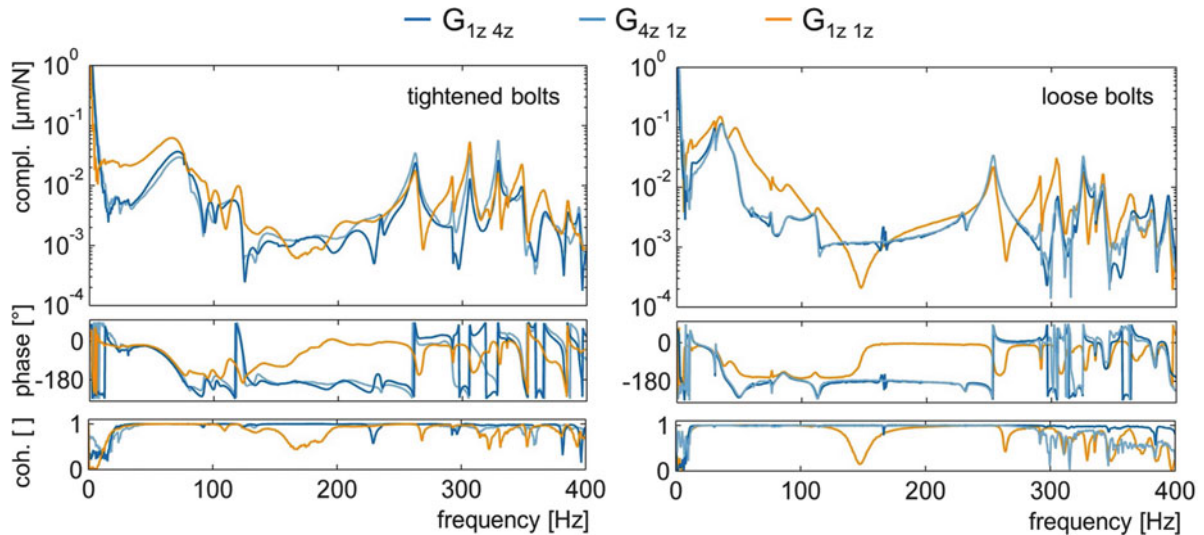


Fig. 28.5 Symmetry of FRFs and direct FRF for tightened and loose bolts of foundation elements

28.4 Frequency Based Substructuring with Joints

The assembly of the analytical slide model and the experimental frame model bases on the frequency based substructuring method presented in [15], and uses the extension of the method, presented in [16], to take into account linear stiffness and damping properties of the guide rail—shoe connections. The used basic relations are reflected here. Starting from the not assembled block diagonal system matrices M , C , K and the concatenated external and connection force vectors, f and g , as well as the concatenated DOFs x , an expression for the stiffness matrix Z and the equation of motion in frequency domain are derived.

$$\begin{aligned} M &= \text{diag}(M^{(1)}, M^{(2)}), C = \text{diag}(C^{(1)}, C^{(2)}), K = \text{diag}(K^{(1)}, K^{(2)}), f = \begin{pmatrix} f^{(1)} \\ f^{(2)} \end{pmatrix}, g = \begin{pmatrix} g^{(1)} \\ g^{(2)} \end{pmatrix}, x = \begin{pmatrix} x^{(1)} \\ x^{(2)} \end{pmatrix} \\ Zx &= f + g, Z = M(j\omega)^2 + C(j\omega) + K \end{aligned} \quad (28.9)$$

As the connection forces g can be expressed as a function of the unique interface forces λ ,

$$g = -B^T \lambda, \quad (28.10)$$

by means of a signed boolean Matrix B and the interface forces depend on the relative motion of the joint-connected interfaces,

$$\lambda = (\text{diag}(k^{(1)}, k^{(2)}, \dots, k^{(n)}) + j\omega \text{diag}(c^{(1)}, c^{(2)}, \dots, c^{(n)})) Bx = JBx, \quad (28.11)$$

where the stiffness k and damping coefficients c of the n joint DOFs are arranged in diagonal matrix form, one can rewrite the system Eq. (28.9), using the joint matrix J .

$$(Z + B^T JB)x = f. \quad (28.12)$$

The sum of matrices on the left side of Eq. (28.12) can be inverted, e.g. according to [17]. This inversion yields the flexibility matrix G of the assembled system,

$$G = (Z + B^T JB)^{-1} = Y \left(I - B^T (J^{-1} + BYB^T)^{-1} BY \right). \quad (28.13)$$

Applying this equation to the present coupling task, where only the FRF at the TCP H_{TCP} shall be calculated, Eq. (28.13) can be simplified to

$$H_{TCP\ TCP} = Y_{TCP\ TCP}^{(1)} - Y_{TCP\ B}^{(1)} (J^{-1} + Y_{BB}^{(1)} - Y_{BB}^{(2)})^{-1} Y_{B\ TCP}^{(1)}. \quad (28.14)$$

The superscripts (1) and (2) denote matrices belonging to the slide and the frame, respectively. The subscripts TCP and B denote the DOFs at the TCP and the boundary DOFs, respectively. Since four boundary DOFs are involved, the size of the joint matrix J and the matrices $Y_{BB}^{(1)}$ and $Y_{BB}^{(2)}$ is four by four by n_f . The matrix $Y_{TCP\ B}^{(1)}$ is of size one by four by n_f and its transpose matrix $Y_{B\ TCP}^{(1)}$ is of size four by one by n_f . The matrices $Y_{TCP\ TCP}^{(1)}$ and $H_{TCP\ TCP}$ represent a single FRF.

28.5 Coupling Results

Reference measurements of the TCP FRF are made in different x -positions of the slide and for both configurations of the foundation elements. Again, the inertial shaker is used to excite the structure. Figure 28.6 shows the measurement setup and the amplitudes of the measured FRFs for different x -positions and the two configurations. It becomes obvious that the configuration of the foundation elements has a great effect on the TCP FRFs. In case of the fixed bolts, the first resonance peak undergoes a greater shift in frequency and the corresponding amplitude increases remarkably, when the slide is moved in positive x -direction. In case of loose bolts, the frequency of the first resonance peak remains almost constant, when the x -position of the slide is changed. Also, the height of these resonance peaks does not change as much as in the other configuration.

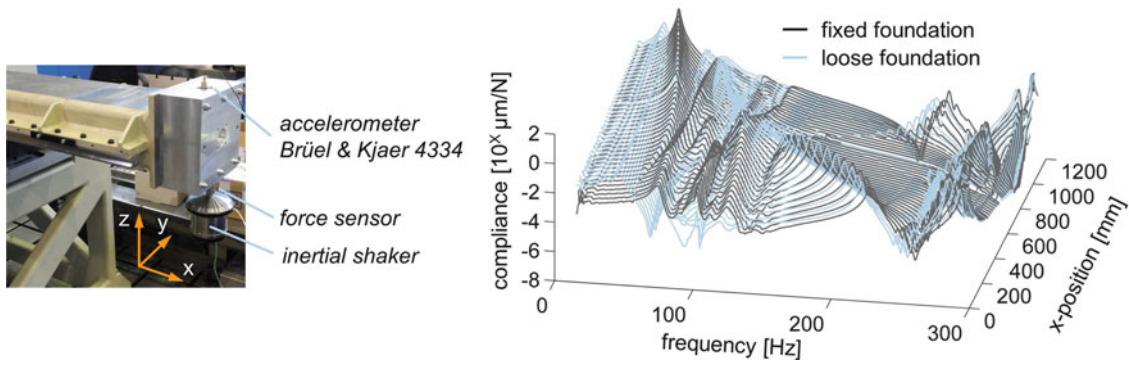


Fig. 28.6 Reference measurements in different positions of the slide

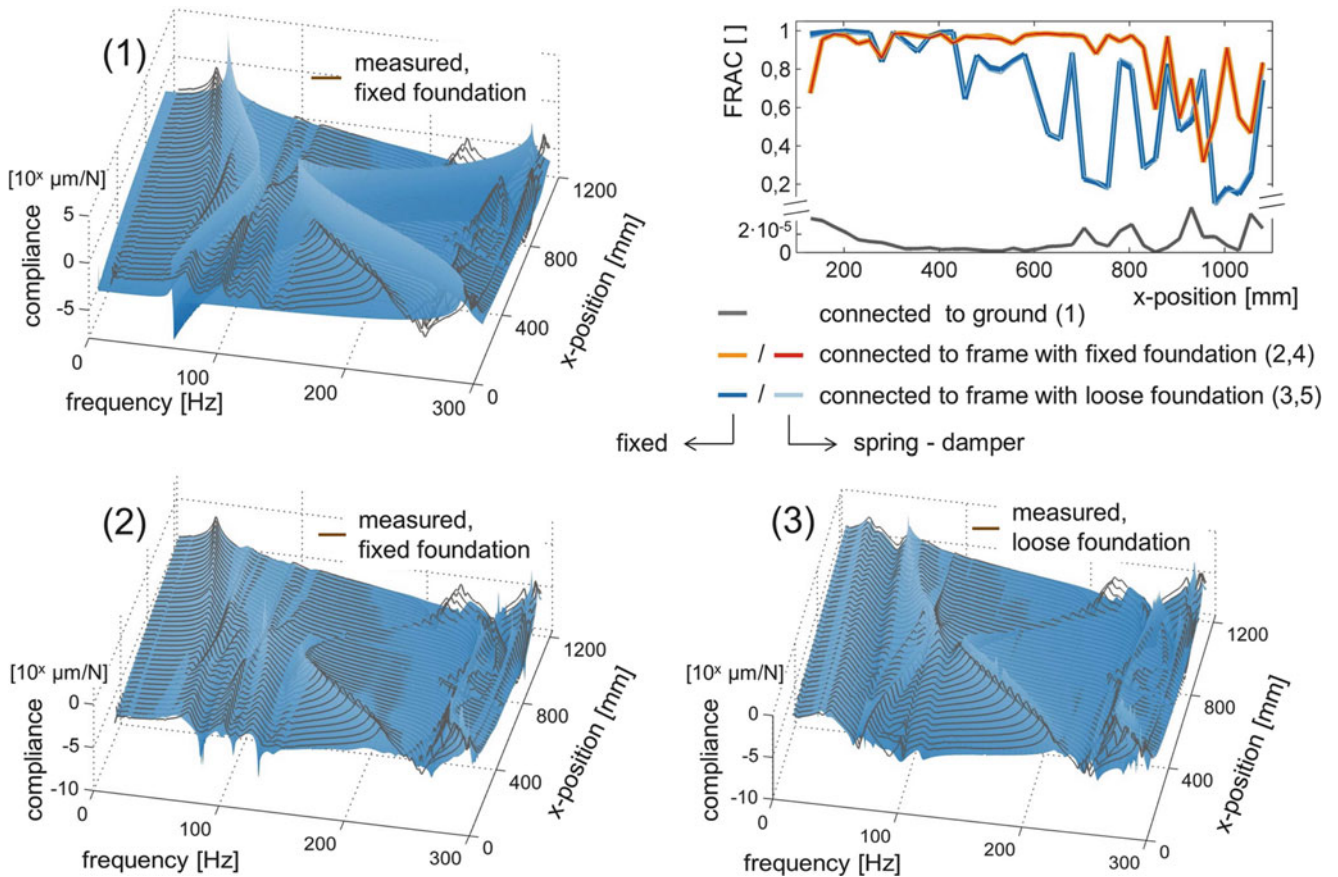


Fig. 28.7 Comparison of measured and predicted FRFs

In order to set up a good model for the test bench dynamics, different approaches are compared. The first approach is to take the analytical model of the slide and to suppress movement of the boundary DOFs. This is done by setting the flexibility matrix of the second component and the inverse of the joint matrix (Y_{BB}^2 and J^{-1} in Eq. (28.14)) to zero. This procedure is repeated for several x-positions of the slide. The amplitudes of the resulting position dependent FRFs are presented in the upper left of Fig. 28.7. The amplitudes of the measured FRFs (fixed foundation) are plotted in the same axes to serve as a reference. As can be seen, the correlation between the FRFs is low for all the positions. This observation is confirmed by low FRAC values (0–300 Hz) for all the x-positions, whose values are plotted in the upper right.

A better correlation is achieved, when the dynamics of the frame are taken into account (Y_{BB}^2 is filled with measured FRFs). In the lower half of Fig. 28.7, the position dependent FRFs resulting from the rigid connection (J^{-1} is zero) of the reduced analytical slide model and the experimental frame model are depicted for both foundation configurations, next to the

corresponding measured FRFs. According to the FRAC values, the correlation in the case of loose bolts is better than in the case of tightened bolts. In both cases, the FRAC values are lower at higher x-positions. This mismatches at higher positions can also be seen in the FRF graphs, especially at approx. 250 Hz.

While the manufacturer of the linear guides specifies a value of $1,250 \text{ N}/\mu\text{m}$ as the vertical stiffness of the guide rail—shoe assembly [18], the damping of this joint is unknown. As the mentioned stiffness value is introduced in the model (according to Eq. (28.13) or Eq. (28.14)), it can be seen that the assembly behaves almost like in the case of a fixed connection. This is confirmed by the FRAC values, which are almost equal to the case of rigid connections between slide and frame. Moreover the high stiffness value prevents the damping properties of the guide rail—shoe connections from affecting the predicted FRFs. Hence, we conclude, that in our particular application example the flexibility and damping properties of the guide rail—shoe connections are of minor effect on the dynamic behavior of the assembly.

28.6 Conclusion

As the dynamic behavior of a machine tool is an important characteristic, the machine tool development uses models to predict the dynamic machine behavior. State of research is to use finite-element or multi-body models of the complete machine tool. Often, the creation of these models is an enormous task and they lack accuracy due to uncertainties about numerous modeling parameters. Since most design tasks start from an existing machine design, the methods of experimental substructuring are a good option to improve the modeling of machine tool dynamics, especially if an experimental model of the existing assembly is connected with an analytical model of the modified components. In this paper the mentioned concept is adopted to the structure of a single axis test bench. An experimental model of the frame is connected with an analytical model of the slide using frequency based substructuring. In this particular application, it is shown, that a good quality of the predicted FRFs can already be achieved, if the guide rail—shoe connections are modeled as a rigid connection, and only their z-DOFs are taken into account. A future research task will be to investigate, whether or not the prediction can be improved if the connection of the housing of the ball screw nut to the slide is considered. Additionally, the influence of the boundary DOFs in x-direction should be determined.

The results achieved in the presented study motivate a wider research on the use of experimental substructuring techniques for modeling machine tool dynamics. Besides the prediction of the effect of design modifications of a structural component, other application fields seem possible. One of these is the assessment of factory floors and foundations, on which machine tools shall be placed. Other fields may be the dimensioning of auxiliary mass dampers or the consideration of changing work piece dynamics.

Acknowledgements This research and development project is funded by the German Federal Ministry of Education and Research (BMBF) within the Framework Concept "Research for Tomorrow's Production (funding number 02PJ1173) and managed by the Project Management Agency Karlsruhe (PTKA). The author is responsible for the contents of this publication.

References

1. Weck M, Brecher C (2006) *Werkzeugmaschinen – Messtechnische Untersuchung und Beurteilung, dynamische Stabilität*. Springer, Berlin
2. Sitte B (2013) *Prozessstabilität als Bewertungskriterium im Entwicklungsprozess von Werkzeugmaschinen*. Dissertation RWTH Aachen, Apprimus, Aachen
3. Witt ST (2007) *Integrierte Simulation von Maschine, Werkstück und spanendem Fertigungsprozess*. Dissertation RWTH Aachen, Shaker, Aachen
4. Queins M (2005) *Simulation des dynamischen Verhaltens von Werkzeugmaschinen mit Hilfe flexibler Mehrkörpermodelle*. Dissertation RWTH Aachen, Shaker
5. Brecher C, Fey M, Bäuml S (2013) Damping models for machine tool components of linear axis. *CIRP Ann Manuf Technol* 62(1):399–402
6. Romanow P (1995) *Konstruktionsbegleitende Kalkulation von Werkzeugmaschinen*. Dissertation TU München, Springer, Berlin
7. Park SS, Altintas Y, Movahhedy M (2003) Receptance coupling for end mills. *Int J Mach Tool Manufact* 43:889–896
8. Schmitz TL (2000) Predicting of high-speed machining dynamics by substructure analysis. *Ann CIRP* 49(1):303–308
9. Schmitz TL, Scott Duncan G (2005) Three-component receptance coupling substructure analysis for tool point dynamics prediction. *ASME J Manuf Sci Eng* 127(4):781–790
10. Rixen DJ (2003) The dual craig bampton method. *Proceedings of international modal analysis conference, IMAC XXI, Kissimmee, FL*
11. Voormeeren SN (2013) *Dynamic substructuring methodologies for integrated dynamic analysis of wind turbines*. Dissertation, TU Delft
12. van der Valk PLC (2010) *Model reduction & interface modeling in dynamic substructuring: application to a multi-megawatt wind turbine*. MSc Thesis, TU Delft

13. (2011) user reference manual for the MYSTRAN general purpose finite element structural analysis computer program, App. E: derivation of the RBE3 element constraint equations, pp. 267–275 <http://www.mystran.com/Executable/MYSTRAN-Users-Manual.pdf>, asat02/24/2014
14. Heylen W, Lammens L, Sas P (2007) Modal analysis theory and testing, 2nd edn. KU Leuven, Leuven (Heverlee), Belgium
15. de Klerk D, Rixen DJ, de Jong J (2006) The frequency based substructuring (FBS) method reformulated according to the dual domain decomposition method. Proceedings of international modal analysis conference, IMAC XXIV, St. Louis, MO
16. Reuss P, Bernhard Z, Hermann J, Gaul L (2012) Consideration of interface damping in dynamic substructuring. Proceedings of international modal analysis conference, IMAC XXX, Jacksonville, FL
17. Isermann R, Münchhoff M (2011) Identification of dynamic systems – an introduction with applications. Springer, Heidelberg
18. (2011) technical documentation, catalog linear guideways, HIWIN motion control & systems. Produktkatalog Profilschienenführungen, Brücklesbünd [http://www.hiwin.de/en/Products.html?co_id{\mathsurround=\opskip\\$=}4263](http://www.hiwin.de/en/Products.html?co_id{\mathsurround=\opskip$=}4263), asat02/26/2014

Chapter 29

Static Torsional Stiffness from Dynamic Measurements Using Impedance Modeling Technique

Hasan G. Pasha, Randall J. Allemang, David L. Brown, and Allyn W. Phillips

Abstract Static torsional stiffness of a structure is the measure of the resistance it offers to twisting. It is an important design parameter for structures subjected to torsion loading. Estimating the static torsional and bending stiffness values of a structure from test rigs is resource intensive. In order to obtain reasonable estimates of static torsional stiffness at a minimal cost and less time, diagnostic procedures that are efficient and accurate are needed. A method that utilizes the impedance modeling technique to extract the static stiffness from free-free modal test is discussed in this paper. The results of applying this technique on a rectangular plate structure are compared with analytical estimates for static torsional stiffness. The merits and limitations of this technique are also discussed.

Keywords Impedance modeling • Dynamic stiffness method • Compliance method • Hybrid impedance method • Static torsional stiffness

Notation

| Symbol | Description |
|--------------------|---------------------------------------|
| $[\cdot]^{-1}$ | Inverse of matrix $[\cdot]$ |
| $[\cdot]^{+1}$ | Pseudo-inverse of matrix $[\cdot]$ |
| Δ | Vertical deflection (in.) |
| θ | Angular deflection (rad) |
| ω | Frequency (rad/s) |
| F | Applied force (lb _f) |
| $[H(\omega)]$ | Free boundary FRFs ($\frac{X}{F}$) |
| $[H_{mod}]$ | Modified compliance/FRF matrix |
| $[\Delta K_{dyn}]$ | Modification dynamic stiffness matrix |
| $[K_{mod}]$ | Modified dynamic stiffness matrix |
| K_{SS} | Driving-point stiffness |
| K_T | Static torsional stiffness |
| L_f | Distance between front DOFs (in.) |
| L_r | Distance between rear DOFs (in.) |
| T | Applied Torque (lb _f in) |
| DOF | Degree of freedom |
| DOF 1 | Left front DOF, z-direction |
| DOF 2 | Right front DOF, z-direction |
| DOF 3 | Left rear DOF, z-direction |
| DOF 4 | Right rear DOF, z-direction |

H.G. Pasha (✉) • R.J. Allemang • D.L. Brown • A.W. Phillips
 University of Cincinnati – Structural Dynamics Research Lab (UC-SDRL), Cincinnati, OH, USA
 e-mail: pashahg@mail.uc.edu

29.1 Introduction

The performance of an automobile with respect to vehicle dynamics and passenger ride comfort is characterized by the auto-body's global static and dynamic stiffnesses [1, 2]. Currently, special test rigs are used to estimate static stiffnesses. A method based utilizing dynamic measurements (usually taken from a free-free modal test) together with modeling techniques to estimate the static stiffnesses has been developed. Both existing approaches take considerable resources to arrive at a reasonable estimate of the global torsion and bending stiffnesses. In order to obtain reasonable estimates of static global stiffnesses at a minimal cost and less time, diagnostic procedures that are efficient and accurate are needed. A method based on impedance modeling technique to estimate the static global stiffnesses involving dynamic testing tools is described here. Experimental validation of the method using a rectangular plate structure is presented.

29.2 Impedance Modeling Method

To solve engineering problems such as machine chatter and flutter, it is often desired to predict the effect of structural modification on the dynamics of a system. This modification may be additive or subtractive, that is two subsystems may be combined together to form a larger system, or a large system might be broken down into its component parts. Several different modeling methods have been developed to solve this problem: finite element analysis, model modeling, and impedance modeling to name a few. Unlike modal modeling, which operates on the modal vectors of a system, impedance modeling can be viewed as taking one step back and operating on the raw measured FRFs. As a result, the amount of data required to yield similar results to the modal model is much greater, as the information captured by the data has not yet been distilled down. This was a problem historically, as computing power and storage were at a premium. As a result, the impedance modeling technique has been limited to the investigation of the effect of structural modification on a subset of individual FRFs. The technique can be expanded, however, to include the full set of FRFs needed for extraction of the modal parameters using standard parameter estimation techniques.

29.2.1 Theory

This modeling technique attempts to describe the dynamic behavior of an assemblage of subsystems. All subsystems are considered have known properties from which to expand the model. In an analytical case, input-output relationships at each DOF can be calculated. In an experimental case, measurements must be taken at each DOF. Graphically stated, these systems can be represented by shown in Fig. 29.1.

The points s_1 and s_2 , at which the systems are to be connected, are considered the driving points of the system. The driving point FRFs must be known for each body in order to make modifications or connections at these points. The points r and t represent points of interest in the combined system. To accurately predict the modified FRFs after attaching the additional component to the main structure, cross FRFs must also be known for each body at these points. We may utilize one of three methods to develop an impedance model to predict the response of the altered system:

- (1) Dynamic Stiffness Method
- (2) Compliance Method
- (3) Hybrid Method

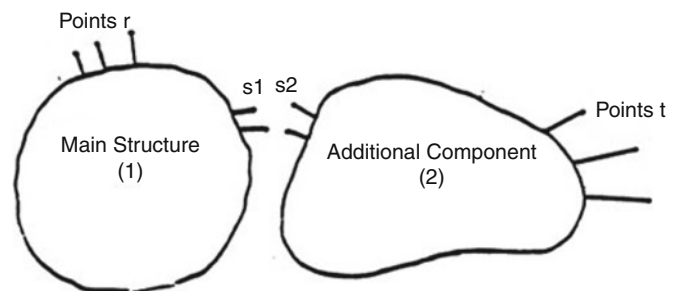


Fig. 29.1 Dynamics stiffness method: substructures

29.2.2 Dynamic Stiffness Method

The dynamic stiffness method begins with the input-output relationship of the connected systems in the form

$$\{F\} = [K]\{X\} \quad (29.1)$$

with $\{F\}$ representing the forcing vector, $\{X\}$ representing the response vector, and $[K]$ representing the dynamic stiffness matrix. The equation of motion for each component of the system is described theoretically by:

$$\{f\} = [-\omega^2[M] + [K] + j\omega[C]]\{x\} \quad (29.2)$$

or experimentally for component 1 and 2 by Eqs. (29.3) and (29.4) respectively,

$$\begin{Bmatrix} \{F_r\} \\ \{F_{s_1}\} \end{Bmatrix} = \begin{bmatrix} [K_{rr}] & [K_{rs_1}] \\ [K_{s_1r}] & [K_{s_1s_1}] \end{bmatrix} \begin{Bmatrix} \{X_r\} \\ \{X_{s_1}\} \end{Bmatrix} \quad (29.3)$$

$$\begin{Bmatrix} \{F_t\} \\ \{F_{s_2}\} \end{Bmatrix} = \begin{bmatrix} [K_{tt}] & [K_{ts_2}] \\ [K_{s_2t}] & [K_{s_2s_2}] \end{bmatrix} \begin{Bmatrix} \{X_t\} \\ \{X_{s_2}\} \end{Bmatrix} \quad (29.4)$$

Rigidly connecting the components at points s_1 and s_2 , setting the internal forces equal to zero, and assuming no external forces yields the combined expression:

$$\begin{Bmatrix} \{F_r\} \\ \{0\} \\ \{F_t\} \end{Bmatrix} = \begin{bmatrix} [K_{rr}] & [K_{rs_1}] & [0] \\ [K_{s_1r}] & [K_{s_1s_1}] + [K_{s_2s_2}] & [K_{s_2t}] \\ [0] & [K_{ts_2}] & [K_{tt}] \end{bmatrix} \begin{Bmatrix} \{X_r\} \\ \{X_{s_1}\} \\ \{X_t\} \end{Bmatrix} \quad (29.5)$$

While overlapping the matrices in this fashion models the connection as perfectly rigid, it is also possible to connect these points using springs. In the latter case, the off diagonal terms of the matrix corresponding to the connected points would hold a negative value. This should generate almost the same answer, though there will be a slight numerical difference. The stiffer the connection, the more closely they will agree. However, we must be careful when connecting components using very high stiffness values, as this may cause the solution to be numerically unstable.

To solve for the impedance FRFs, we simply loop through each frequency to build the matrix.

29.2.3 Compliance Method

This method is the most commonly used method for impedance modeling when dealing with experimental data. It is mathematically identical to the dynamic stiffness method, but FRFs are easier to generate from an arbitrary input force than it is to precisely control motions experimentally. The compliance method begins with the input-output relationship of the system in the form

$$\{X\} = [H]\{F\} \quad (29.6)$$

with $[H]$ representing the FRF matrix, which is the inverse of the dynamic stiffness matrix, $[K]$.

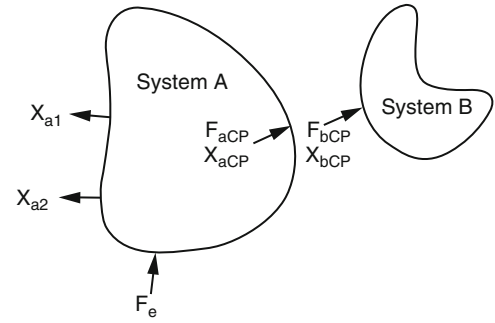
Consider systems A and B, as shown in Fig. 29.2, with X_{a1} and X_{a2} representing displacements at points of interest, F_{aCP} and F_{bCP} representing the internal forces at the connection points, and F_e representing an external force. The equations relating the inputs (F_e and F_{CP}) and outputs (X_{a1} , X_{a2} , and X_{CP}) for each of the disconnected subsystems are as shown in Eqs. (29.7) and (29.8),

$$\begin{Bmatrix} \{X_1\} \\ \{X_2\} \\ \{X_{CP}\} \end{Bmatrix}^A = \begin{bmatrix} [H_{1,CP}] & [H_{1,e}] \\ [H_{2,CP}] & [H_{2,e}] \\ [H_{CP,CP}] & [H_{CP,e}] \end{bmatrix}^A \begin{Bmatrix} \{F_{CP}\} \\ \{F_e\} \end{Bmatrix}^A \quad (29.7)$$

and

$$\{\{X_{CP}\}\}^B = [H_{CP,CP}]^B \{F_{CP}\}^B \quad (29.8)$$

Fig. 29.2 Compliance method:
substructures



with the elements of the $[H]$ matrices corresponding to either the driving-point or cross-point FRF measurements (experimental) or calculations (analytical) of the separate subsystems. When the subsystems are connected, the motion at the connection point on each object will be equal, and the forces acting on each body will be equal and opposite. This is equivalent to writing the constraint equations shown in Eqs. (29.9) and (29.10),

$$F_{CP}^A + F_{CP}^B = 0 \quad (29.9)$$

$$X_{CP}^A - X_{CP}^B = 0 \quad (29.10)$$

These constraint equations, along with the equations relating the inputs and output of the individual subsystems and the value of the added external force are then arranged into a matrix form allowing for their simultaneous solution. To simplify the calculations in the following examples, we assume here that $F_e = 1$. This arrangement isolates all of the unknowns (the force and displacement variables) into a single vector as shown in Eq. (29.11),

$$\begin{bmatrix} 1 & 0 & 0 & -H_{1,CP}^A & -H_{1,e}^A & 0 & 0 \\ 0 & 1 & 0 & -H_{2,CP}^A & -H_{2,e}^A & 0 & 0 \\ 0 & 0 & 1 & -H_{CP,CP}^A & -H_{CP,e}^A & 0 & 0 \\ 0 & 0 & 0 & 0 & 0 & 1 & -H_{CP,CP}^B \\ 0 & 0 & 1 & 0 & 0 & -1 & 0 \\ 0 & 0 & 0 & 1 & 0 & 0 & 1 \\ 0 & 0 & 0 & 0 & 1 & 0 & 0 \end{bmatrix} \begin{bmatrix} X_1^A \\ X_2^A \\ X_{CP}^A \\ F_{CP}^A \\ F_e \\ X_{CP}^B \\ F_{CP}^B \end{bmatrix} = \begin{bmatrix} 0 \\ 0 \\ 0 \\ 0 \\ 0 \\ 0 \\ 1 \end{bmatrix} \quad (29.11)$$

The left-most matrix is known, as the FRFs of each system are known, and the right hand side only contains the value of the external force applied. Solving for the vector of unknowns gives the solution to the combined system for a given external force.

By setting the external force to unity, the responses in the solution vector above will correspond to the FRF ratio between the external force input and the corresponding responses. This system can be solved several times, each time moving the location of the external force to solve for the entire FRF matrix of the combined system as a function of frequency.

29.2.4 Hybrid Impedance Modeling

The theoretical formulations for impedance modeling shown in the previous sections were the standard formulations used in the 1970s and 1980s. These formulations reduced the size of the problem by algebraically reducing the size of the solution to a minimum of measurements such that the FRF matrix could be inverted and that the problem was small enough to run in the existing computer systems. With the advent of much more powerful computers and linear algebra programming languages, such as Matlab, it became possible to formulate the problem so that a singular FRF matrix and/or a Dynamic Stiffness matrix could be estimated, which captured all of the information of interest in the modeling process.

The response of a mechanical system excited by external force can be estimated directly from its FRF matrix by the following relationship,

$$\{x_n\}_{m \times 1} = [H_n]_{m \times m} \{f_n\}_{m \times 1} \quad (29.12)$$

where $[H_n]$ is the Compliance and/or the FRF matrix for component n , it includes all the points of interest on any given component n .

The system matrix $[H_s]$ is generated simply by constructing a matrix of all the components. The component matrices are simply put into a system matrix whose size is equal to the summation of the sizes of the component matrices. The components are arranged along the diagonal of the system matrix similar to what was done in the lumped mass modeling,

$$[H_s] = \begin{bmatrix} [H_1] & 0 & 0 & \dots & 0 \\ 0 & [H_2] & 0 & \dots & 0 \\ 0 & \vdots & \vdots & \ddots & 0 \\ 0 & 0 & 0 & \dots & [H_n] \end{bmatrix} \quad (29.13)$$

The Dynamic Stiffness Matrix is the inverse of the Frequency Response Function matrix as mentioned in lumped mass modeling or,

$$[K_s]_{m \times m} = [H_s]_{m \times m}^{-1} \approx [H_s]_{m \times m}^{+1} \quad (29.14)$$

The components FRF matrix $[H_n]$ may be partially measured and as a result the inverse of the system matrix $[H_s]$ may not exist. In fact, $[H_s]$ is normally ill conditioned and, in general, a pseudo inverse solution can be used. The pseudo inverse will generate a system dynamic stiffness matrix that can be used predict the response of the modified system only at the measured points of interest. The measured FRFs require driving-point measurement at all connection points and at points where external forces might act on the system model. Cross measurement are required between the connection/external force points and response points of interest.

The primary reason for choosing this matrix formulation is that it is very simple to develop the modification matrix where the measurement DOF corresponds to the row or column space of the Dynamic Stiffness matrix. This modification matrix is also the same as the matrix used in the Lumped Modeling and Modal Modeling processes. The modification dynamic stiffness matrix $[\Delta K_{dyn}]$ in terms of $[M]$, $[C]$ and $[K]$ matrices is,

$$[\Delta K_{dyn}] = [-\omega^2[\Delta M] + j\omega[\Delta C] + [\Delta K]] \quad (29.15)$$

where ω is the frequency measured in rad/s.

The modified dynamic stiffness matrix $[K_{smod}]$ is equal to system dynamic stiffness matrix plus the modification dynamic stiffness matrix or:

$$[K_{smod}] = [\Delta K_s] + [\Delta K_{dyn}] \quad (29.16)$$

and the modified Compliance/Frequency Response Function matrix $[H_{mod}]$ is the inverse or the pseudo inverse of the Modified Dynamic Stiffness Matrix.

$$[H_{mod}] = [K_{smod}]^{-1} \approx [K_{smod}]^{+1} \quad (29.17)$$

This is important, because the modification matrix will be common between the Impedance and Modal Modeling cases, which means that it is simple to program systems with both analytical and experimentally based components.

The system matrices $[H]$ will always be square and the system matrix will be generated by placing the component matrices along the diagonal. As a result, the matrix size of the system matrix will be equal to the sum of all the component matrices sizes. This tremendously reduces the book-keeping for the keeping track of the modifications. Hence it is relatively easy using indexing to keep track of information. The same indexing can be used in the Impedance, Model Modeling and analytical modeling scripts.

This method is simple to program and on analytical datasets will estimate the modifications of the system to the numerical accuracy of the computer. For example, in Matlab simulations, the accuracy of solution is to 15 decimal places.

29.3 Experimental Validation

Impedance modeling is a valuable technique for predicting the result of a structural modification to the system. The proposed method to evaluate the static torsional stiffness involves the use of the dynamic stiffness method. The technique is demonstrated to estimate the static torsional stiffness of a rectangular steel plate structure. The addition of stiffness constraints to the measured FRF data for three perturbed mass configurations will be utilized to numerically model the fixed-free configurations utilized in the static testing test-rigs.

Table 29.1 Comparison of modal frequencies

| Mode | Mode description | Modal frequency (Hz) | | | Rel error (%) | |
|------|--------------------|----------------------|----------------------|--------------|---------------|------------------|
| | | FE | FE w/ spring support | Experimental | Vs FE | Vs FE w/ springs |
| 1 | I Torsion | 41.3 | 41.7 | 42.3 | 2.19 | 1.27 |
| 2 | I X Bending | 43.7 | 43.8 | 44.2 | 1.11 | 0.95 |
| 3 | II Torsion | 95 | 95.4 | 95.7 | 0.71 | 0.36 |
| 4 | I Y Bending | 103.1 | 103.2 | 104.7 | 1.51 | 1.44 |
| 5 | II X Bending | 118.2 | 118.2 | 119.2 | 0.81 | 0.77 |
| 6 | Antisymm X Bending | 137.4 | 137.7 | 138.1 | 0.54 | 0.32 |
| 7 | III Torsion | 175.5 | 175.9 | 176.5 | 0.53 | 0.34 |
| 8 | X and Y Bending | 202.9 | 203.4 | 204 | 0.55 | 0.27 |
| 9 | III X Bending | 244.2 | 244.8 | 245.2 | 0.4 | 0.17 |

29.3.1 Model Calibration and Validation

An FE model of the rectangular steel plate structure of dimensions 34"x22.5"x.25" was developed. A cold rolled steel rectangular plate structure was fabricated ($E = 2.05 \times 10^{11}$ Pa, $\nu = 0.29$ and $\rho = 7,850$ kg/m³), with 160 points marked on a 2"x2" grid. Each of these 160 points were impacted and FRFs were measured at 21 reference locations using uniaxial accelerometers.

The FE model was calibrated to the match measured modal frequencies and modal vectors. The FE model was validated by comparing analytical FRFs from the model with the measured FRFs. In addition, the results obtained for two perturbed mass configurations with unconstrained boundaries were compared with the predictions from the updated model to check its robustness. The predicted values were within 1.5 % relative error for modal frequencies, which satisfied the validation criteria. The comparison of modal frequencies for the no added mass case is shown in Table 29.1.

29.3.2 Estimation of Static Torsional Stiffness Analytically

The static torsional stiffness of the rectangular plate can be estimated analytically. Four points on the calibrated plate model are chosen such that they are symmetric about the centerline. Points 23 and 135 represent the front DOF and points 28 and 140 represent the rear DOFs as shown in Fig. 29.3. The distance between the front and rear DOF is 10 in. and the distance between points 23–135 and points 28–140 is $L_f, L_r = 14$ in. The rear DOFs are constrained in the vertical direction and a couple is applied at the front DOFs. The static torsional stiffness is estimated using Eq. (29.18),

$$K_T = \frac{T}{\theta} = \frac{FL_f}{\theta} \quad (29.18)$$

where K_T is the static torsional stiffness, T is the torque, F is the applied couple, L_f is the moment arm and θ is the angular deflection. $\theta = \frac{2\Delta}{L_f}$ rad, when the rotation angle meets small angle criteria, where Δ is the vertical deflection.

A static analysis was performed on the plate. The static torsional stiffness was estimated to be 3,607.15 lb_fin/deg for the no added mass configuration.

29.3.3 Stiffness Estimation from Impedance Modeling

The modal modeling technique can be applied to estimate the static torsional stiffness. However, due to modal truncation, to get reasonable estimates of the static stiffness, the frequency range for modal testing should contain all the influential modes. Typically, the first 17–30 deformation modes are required for the static stiffness estimates that are in the right range. Impedance modeling method lends well for this purpose as the measured FRF data contains the contribution of the out-of-band modes in addition to the modes in the frequency range of interest.

In order to estimate the static torsional stiffness of the plate using the dynamic stiffness method, a reduced dataset containing driving-point and cross-point measured frequency response functions corresponding to the front and rear DOFs needs to be assembled. Stiffness constraints need to be applied to the dynamic stiffness matrix (inverse of the FRF matrix)

Fig. 29.3 Rectangular plate:
front and rear DOF

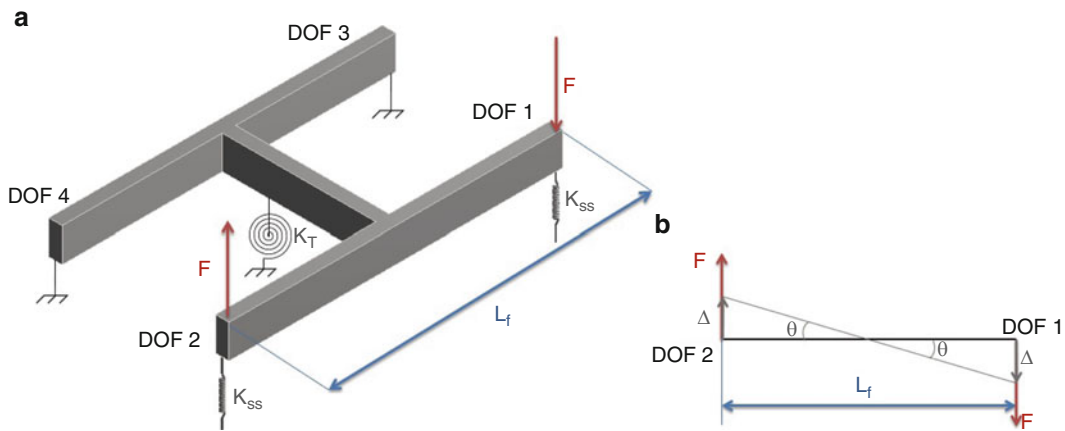
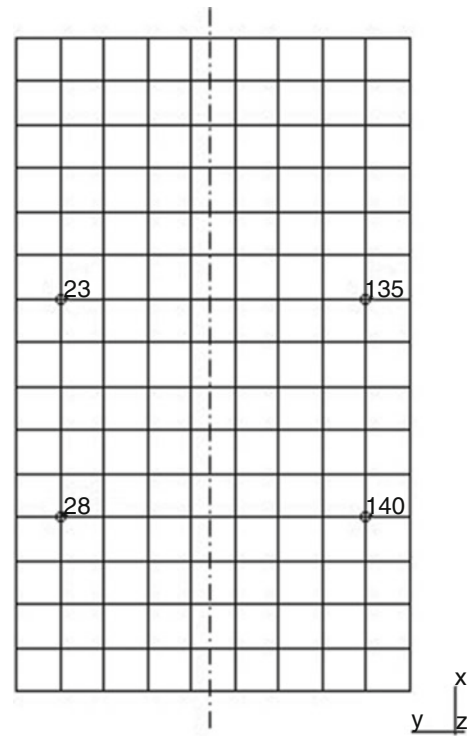


Fig. 29.4 (a) Relation between driving-point stiffness, and (b) static torsional stiffness

at locations corresponding the rear DOFs. Subsequently, the torsion loading points (front DOF driving-points) dynamic stiffness functions should be plotted and an appropriate parameter estimation method should be used to fit the stiffness in the low frequency region. This fit yields the torsion loading point stiffness K_{SS} , which in turn is related to the static torsional stiffness by Eq. (29.19). A visual illustration of this relationship for a built-up beam structure is shown in Fig. 29.4

$$K_T = \frac{K_{SS} \Delta L_f}{\theta} = \frac{K_{SS} L_f^2}{2} \tag{29.19}$$

29.3.3.1 Rigid Body Modes

Since the vertical motion was only measured using the uniaxial accelerometers, modal parameter estimation would yield three rigid body modes, namely the pitch, bounce and roll modes, fairly close to 0 Hz. By applying constraints using high stiffness at the rear DOFs, it is anticipated that the rigid body modes get eliminated and the asymptote of the first deformation

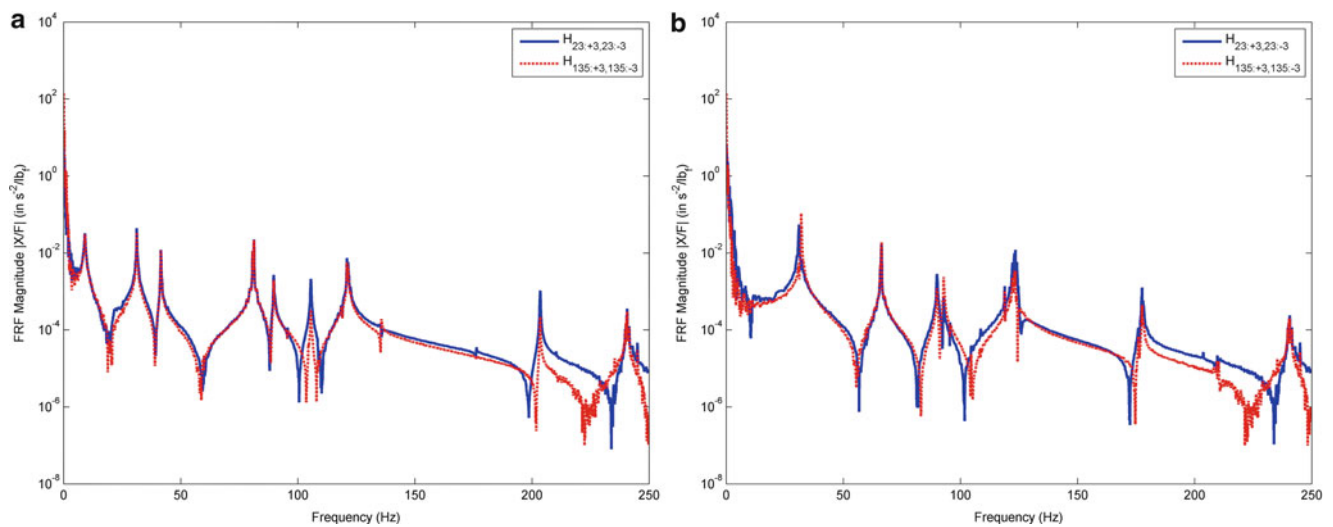


Fig. 29.5 Torsion loading point FRFs. (a) With two rear constraints. (b) With two rear constraints and one centerline constraint

mode would yield the driving-point stiffness value K_{SS} . While the bounce and roll modes were pushed high up in frequency, the pitch mode was still observable at 9.1 Hz as shown in Fig. 29.5a.

In order to estimate the static torsional stiffness, this mode has to be eliminated. The torsional modes contribute significantly to the static torsional stiffness. These modes have nodal lines along the centerline of the structure. A third constraint point could be incorporated at any point along the centerline to eliminate the 9.1 Hz pitch mode. The CMIF plot of the structure with three constraints is shown in Fig. 29.5b.

29.3.3.2 Measurement Noise Issue

Data acquisition during modal testing is subjected to measurement noise issues. Signal processing techniques can be used to reduce measurement noise, however it is difficult to eliminate noise issues completely. When the DOFs are constrained, the useful portion of the signal that corresponds to motion of the structure is discarded, but the measurement noise is not eliminated. This can limit the applicability of the impedance modeling method for estimation of static torsional stiffness in the presence of high measurement noise.

29.3.3.3 Parameter Estimation

Using a zeroth order polynomial to fit the dynamic stiffness in the low frequency range (10–20 Hz) yielded a value of 2.08×10^3 lb_f/in, which corresponds to a static torsional stiffness of 3,557.68 lb_fin/deg. A comparison of the impedance modeled data with the analytical constrained data is shown using a CMIF plot in Fig. 29.6a. The frequencies and the overall level of the modeled and analytical data are in close proximity. The dynamic stiffness of the two driving-points obtained from the constrained measurements and the driving-point stiffness fit are shown in Fig. 29.6b, c respectively.

29.4 Conclusions

A method based on impedance modeling technique to estimate the static torsional stiffness of a structure was presented. In contrast to the resource intensive methods based on static testing and modal modeling, this method is simple to implement and realize. This method requires FRF driving-point and cross-point measurements at the two front and rear locations. With the rear locations are constrained, the torsion loading point stiffness values can be utilized to estimate the static torsional

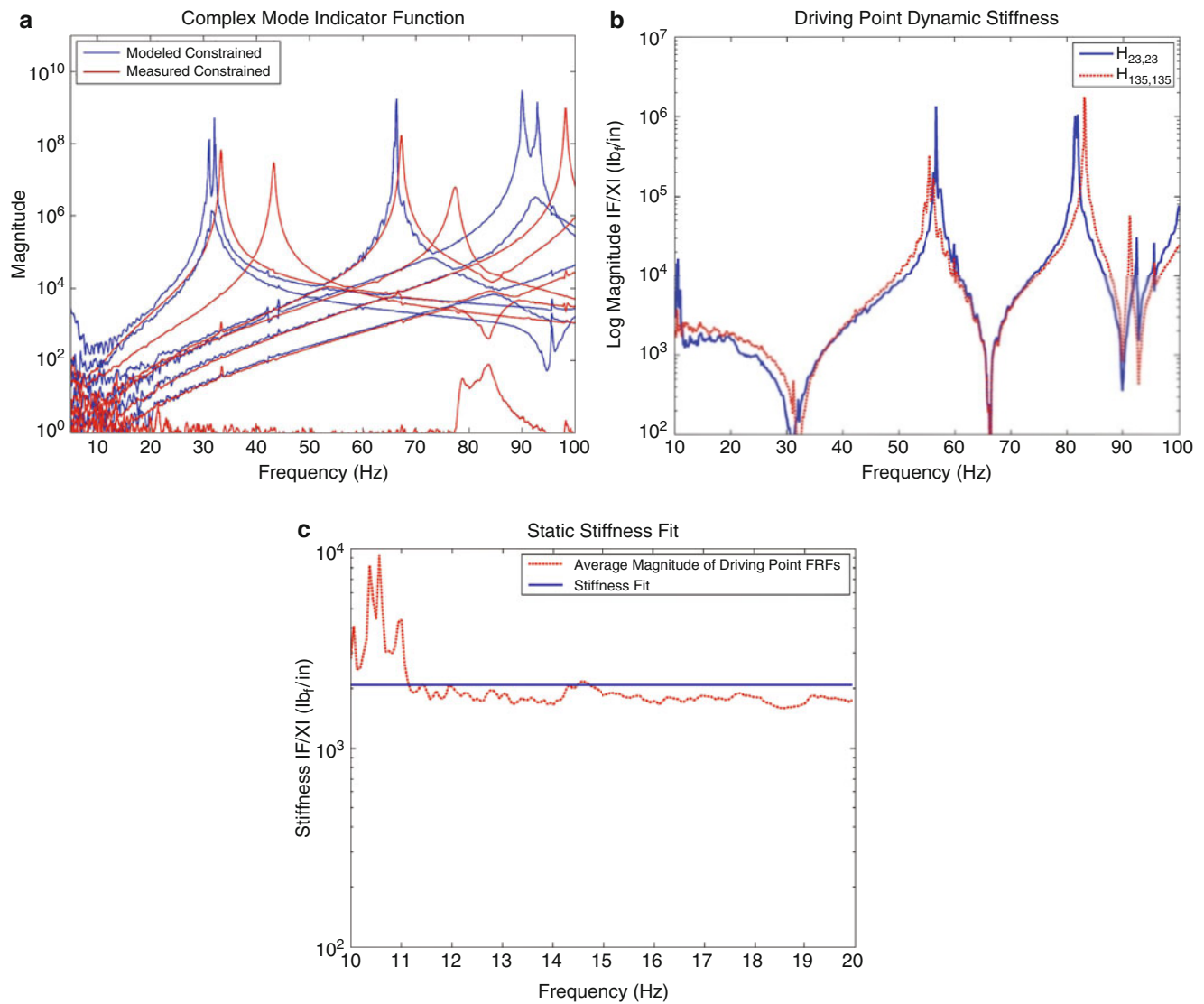


Fig. 29.6 Parameter estimation. (a) Complex mode indicator function. (b) Driving-point dynamic stiffness. (c) Stiffness fit

stiffness. When low frequency rigid body modes exist, it is necessary to constrain an additional point along the centerline (nodal line for torsion modes) to simplify the parameter estimation process. This method did not work as well as it was hoped. Currently work is being done on other methods to overcome some of the shortcomings of this method.

References

1. Griffiths D, Aubert A, Green ER, Ding J (2003) A technique for relating vehicle structural modes to stiffness as determined in static determinate tests, SAE Technical Paper Series (2003-01-1716)
2. Deleener J, Mas P, Cremers L, Poland J (2010) Extraction of static car body stiffness from dynamic measurements, SAE Technical Paper Series (2010-01-0228)
3. Catbas FN, Lenett M, Brown DL, Doebling CR, Farrar CR, Tuner A (1997) Modal analysis of multi-reference impact test data for steel stringer bridges. In: Proceedings IMAC, 1997
4. Lenett M, Catbas FN, Hunt V, Aktan AE, Helmickie A, Brown DL (1997) Issues in multi-reference impact testing of steel stringer bridges. In: Proceedings, IMAC Conference, 1997

5. Catbas FN (1997) Investigation of global condition assessment and structural damage identification of bridges with dynamic testing and modal analysis. Ph.D., Dissertation University of Cincinnati, Civil and Env. Engineering Department
6. Klosterman A (1971) On the experimental determination and use of modal representation of dynamic characteristics. Ph.D. Dissertation, University of Cincinnati, Mechanical Engineering Department
7. Brown DL, Witter MC (2010) Review of recent developments in multiple reference impact testing (MRIT). In: Proceedings, IMAC conference, 17 pp, 2010

Chapter 30

Full Field Dynamic Strain on Wind Turbine Blade Using Digital Image Correlation Techniques and Limited Sets of Measured Data from Photogrammetric Targets

Jennifer Carr, Christopher Niezrecki, and Peter Avitabile

Abstract Wind turbine blades are subjected to dynamic loadings in operation (as well as in the certification process) that result in dynamic stresses and strains that are important to understand. Generally, only a small number of strain gages are used in the certification process and even fewer, if any at all, are installed for operational measurements. Recent advances in digital image correlation (DIC) and digital photogrammetry (DP) have allowed for new opportunities for blade inspection and structural health monitoring.

This paper presents several different methods for determining the dynamic stresses and strains using (a) digital image correlation techniques, (b) dynamic photogrammetry techniques and (c) a newly developed expansion process in conjunction with the finite element model to predict stresses and strains from limited measurement locations. All three approaches are discussed and used in the evaluation of a Southwest Wind Power turbine blade subjected to static loading and dynamic loading (sine dwell, multi-sine dwell and pluck testing) typical of the certification process. The advantages of each of the techniques are described and discussed in the paper.

Keywords Model reduction • Model expansion • Dynamic strain • Digital image correlation • Dynamic photogrammetry

30.1 Introduction

With the ever increasing growth and demand for clean renewable energy, the utilization of wind turbines will continue to expand in their contribution to the total global energy profile. To increase their acceptance, lower cost of energy (COE) compared to fossil fuels is important. A major component in reducing wind turbine's COE is directly related to improved reliability and therefore these large structures need to have some type of structural health monitoring to maintain the turbine's safe operation, while helping to reduce repair costs and downtime. One major component of these wind turbines are the blades which can negatively impact operation, safety, and energy generation if failure occurs.

Recent work has shown that optical measuring systems can be used for monitoring these large bladed structures while they are rotating in normal service conditions. The ability to take full-field data on these structures has opened doors for new possibilities to better understand their inherent dynamics and structural health. Current efforts have been directed to understanding the proper procedures necessary to make meaningful measurements for these large systems. The primary advantage of these optical techniques is that the full-field displacement and strain measurements can be acquired from a set of images without the need for instrumented sensors or contact.

Although optical techniques can provide large amounts of surface data, information about the internal structural members cannot be obtained with these techniques, and often the internal structural components are the regions of the structure where detailed information for strain are needed. Some very new approaches have been developed to use surface information (in conjunction with orthogonal projection vectors available from the finite element model) to expand limited sets of measured operating/transient data resulting in full-field stress-strain estimates. This approach can be performed without specific

J. Carr • C. Niezrecki • P. Avitabile (✉)
Structural Dynamics and Acoustic Systems Laboratory, University of Massachusetts Lowell,
One University Avenue, Lowell, MA 01854, USA
e-mail: peter_avitabile@uml.edu

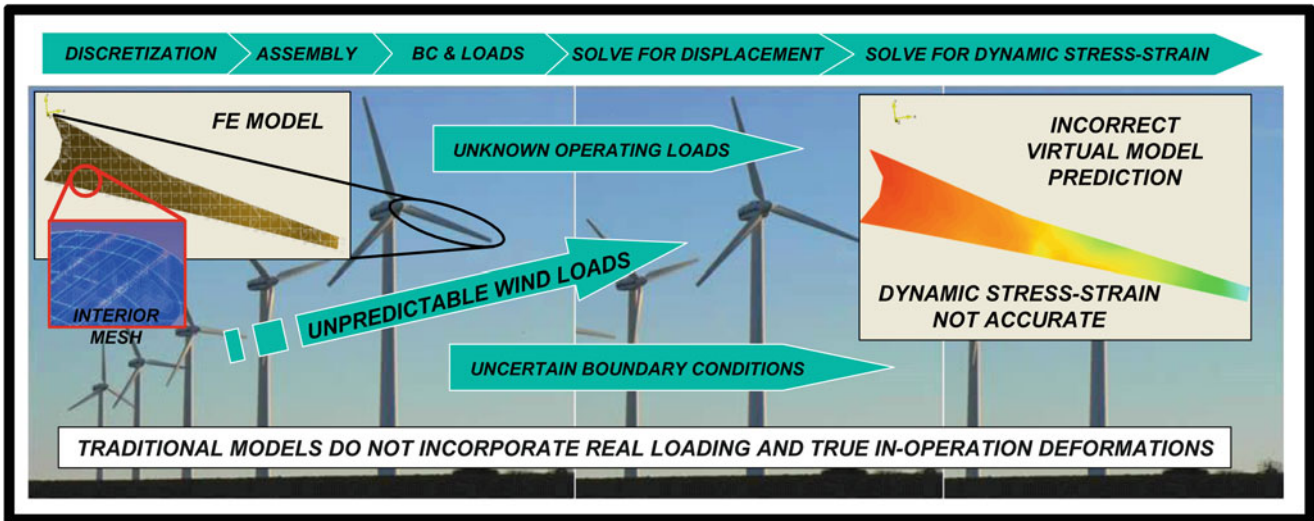


Fig. 30.1 Schematic showing traditional finite element model development

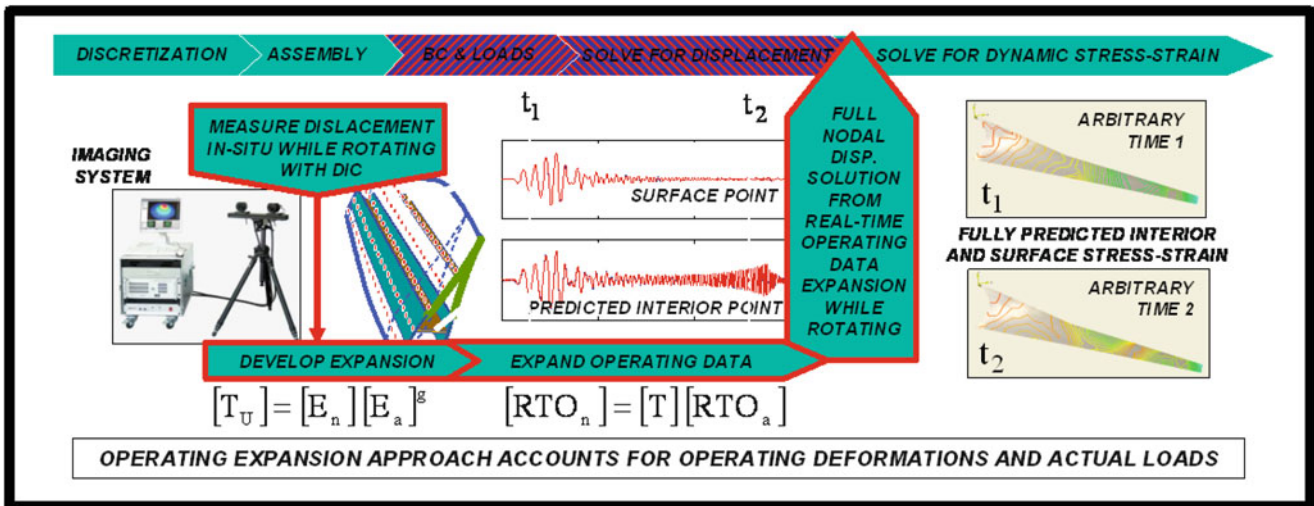


Fig. 30.2 Schematic showing alternation expansion/solution sequence

knowledge of the actual applied forces that excite the system. A byproduct of this approach is that system forces can be better estimated if needed. This methodology has been used on academic structures [1] to demonstrate proof of concept and is currently being further explored on wind turbine blade structures in a laboratory environment in preparation for utilization in the field.

The traditional modeling approach relies on the general development of a finite element model, the assembly of the system matrices, the application of loads and boundary conditions, followed by the solution of the set of equations, and the recovery of the stress–strain solution. This procedure is shown schematically in Fig. 30.1 for a wind turbine blade where significant loadings may occur during normal operation (i.e. rotating). For many situations, the actual loading is not known and the actual boundary conditions are not well understood.

For the approach considered in this work, the difference from traditional modeling is that the actual application of the loads and boundary conditions and the solution of the system set of equations are not specifically performed. Rather, the sparse set of displacements, measured from an actual operating event, is used with a set of orthogonal expansion functions to obtain the full-field displacement solution. This displacement solution is then used with the normal recovery of the stress–strain solution in the finite element modeling process. This procedure is shown schematically in Fig. 30.2, where the limited set of measurement degrees of freedom are used with expansion processes to obtain the full-field displacement for the system.

With this approach, the finite element modeling solution process is intercepted and replaced with the expansion of the limited set of measured degrees of freedom. The actual expansion process has been presented in [1]. Using these newly developed approaches, the methodology has been demonstrated on a laboratory structure subjected to transient impact excitation with very good results. Current work is directed at applying these techniques for a wind turbine blade in a laboratory setting followed by implementation in a field environment. This paper presents the results of work done in the laboratory on a wind turbine blade.

30.2 Theoretical Background

Within this work, two significant techniques are utilized, namely, Digital Image Correlation/Dynamic Photogrammetry and Model Reduction/Expansion techniques. These are described in the next two sections.

30.2.1 *Digital Image Correlation and Dynamic Photogrammetry*

Digital Image Correlation (DIC) and 3D Dynamic Point Tracking (3DPT) are measurement techniques that employ stereophotogrammetry to locate the 3D coordinates on a surface of a structure and tracking methods to determine the displacements of those points over time from a set of images. The work presented in this paper was performed using AramisTM and PontosTM dynamic 3D analysis software.

To utilize the Pontos software, which performs 3DPT, the structure of interest first must be prepared by placing black and white points (optical targets) on the surface of the structure at the desired measurement locations. Then two cameras are positioned and calibrated to determine their position in space relative to each other. An ellipse-finder algorithm is used to find, number, and determine the location of the measurement points in space. Throughout the test, the cameras take a series of images at a defined rate. For each image, the ellipse-finder identifies the points, and these points are tracked from image to image. Stereophotogrammetry is used to determine the 3D coordinates of the points using the images taken by the two cameras. The cameras identify a common point on each image. A line-of-sight can be constructed from the camera locations to the point on the object. Because the positions of the cameras are determined through the calibration process, the intersection of the line-of-sight rays can be determined through triangulation, which gives the 3D coordinates of the points. Displacement measurements can be made based on changes in coordinates between the images. An overview of the 3D Point Tracking measurement process is shown in Fig. 30.3. Through the use of the 3DPT software, the deformation and motion of a complex structure can be captured with this non-contact technique.

The optical measurement technique of Digital Image Correlation (DIC) was performed using the software Aramis, which computes the strain on the surface of the structure from a measured displacement point cloud. To use this software, the structure is first prepared by applying a speckle pattern to the measurement surface. Once again, before testing, two cameras must be positioned and calibrated to determine their position in space relative to each other. When the structure is deformed, these cameras take digital pictures of the measurement surface. Each digital image is divided into a square array of pixels, and each pixel is assigned a light intensity value corresponding to the grayscale value at that location in the image. The pixels are divided into numerous (e.g. hundreds or thousands) of groups called facets. The combinations of pixel light intensity values make each facet unique, which allows for pattern tracking. The center of each facet is determined and tracked throughout the series of images using the principles of stereophotogrammetry, similar to the 3DPT of the optical targets. The strain at each point, or facet center, is then found by calculating the deformation of an array of points that surround the measurement point. As the array deforms throughout the image series, the linear strains and shear angle are calculated. When the strain is calculated for each facet, full-field strain results on the surface of the structure is produced. An overview of the DIC process is shown in Fig. 30.4. The use of DIC allows for the measurement of dynamic strain on the surface of a complex structure.

30.2.2 *Model Reduction and Modal Expansion*

Model reduction is necessary in order to develop expansion algorithms for the modal data of the unmeasured translational DOF (degree of freedom) as well as for rotational DOF. For this work, the expansion is needed for augmenting the limited set of real-time operating data to provide a full field displacement solution. The reduction techniques are the basis of the

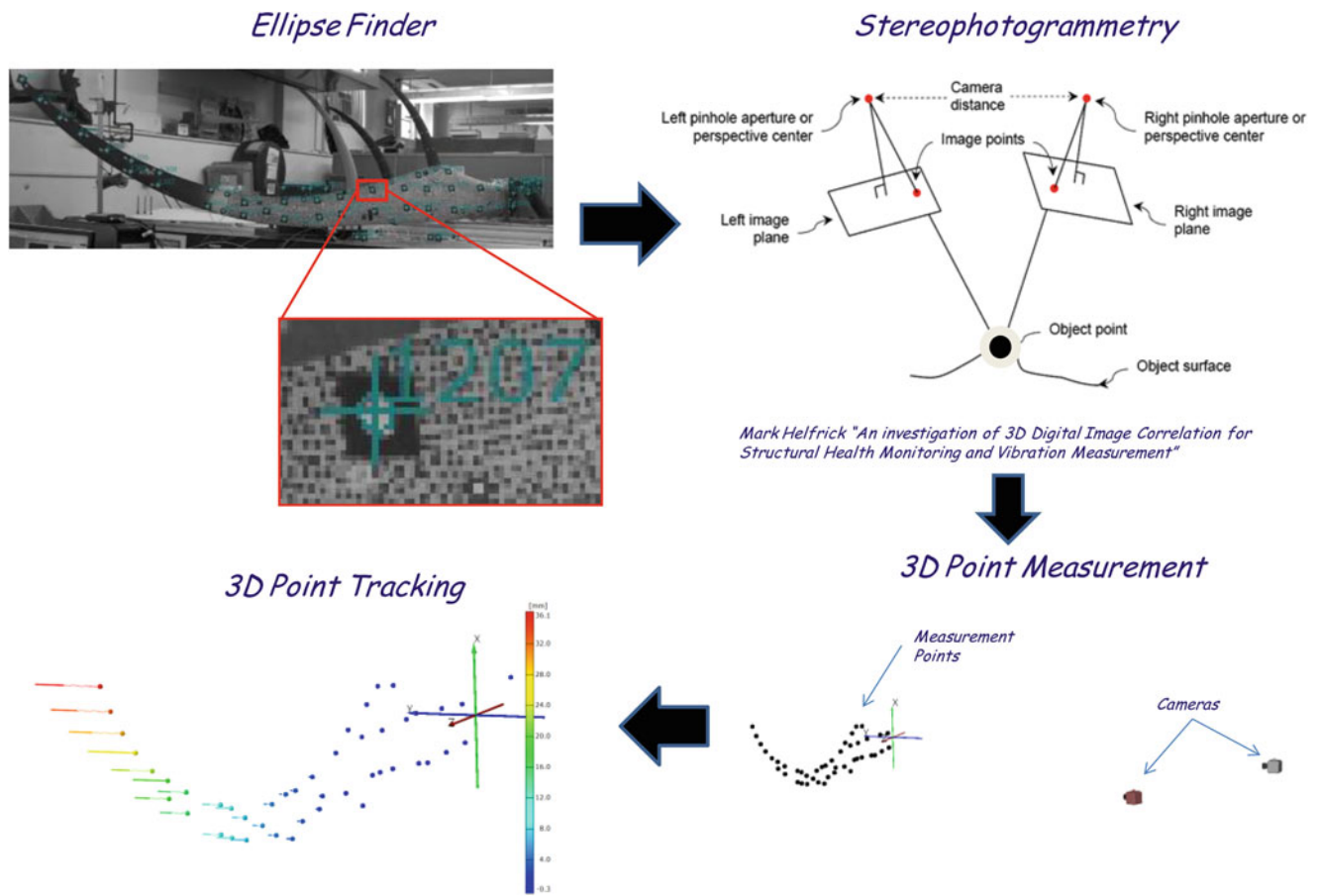


Fig. 30.3 3D dynamic point tracking measurement overview

expansion discussed in this work. These techniques have been presented in earlier works cited in the references; only summarizing equations are presented below. Several model reduction methods have commonly been used for expansion of measured data, but the SEREP (System Equivalent Reduction-Expansion Process) [2] technique is used for this work. For any reduction/expansion process, the relationship between the full set of degrees of freedom and a reduced set of degrees of freedom can be written as

$$\{X_n\} = [T] \{X_a\} \tag{30.1}$$

The transformation matrix [T] is used to project the full mass and stiffness matrices to a smaller size. The reduced matrices can be formulated as

$$[M_a] = [T]^T [M_n] [T] \tag{30.2}$$

$$[K_a] = [T]^T [K_n] [T] \tag{30.3}$$

For the specific work in this paper, the SEREP method has been used for the expansion of mode shapes. The SEREP produces reduced matrices for mass and stiffness that yield the exact frequencies and mode shapes as those obtained from the eigensolution of the full size matrix. The SEREP transformation is formed as

$$[T_U] = [U_n] [U_a]^g \tag{30.4}$$

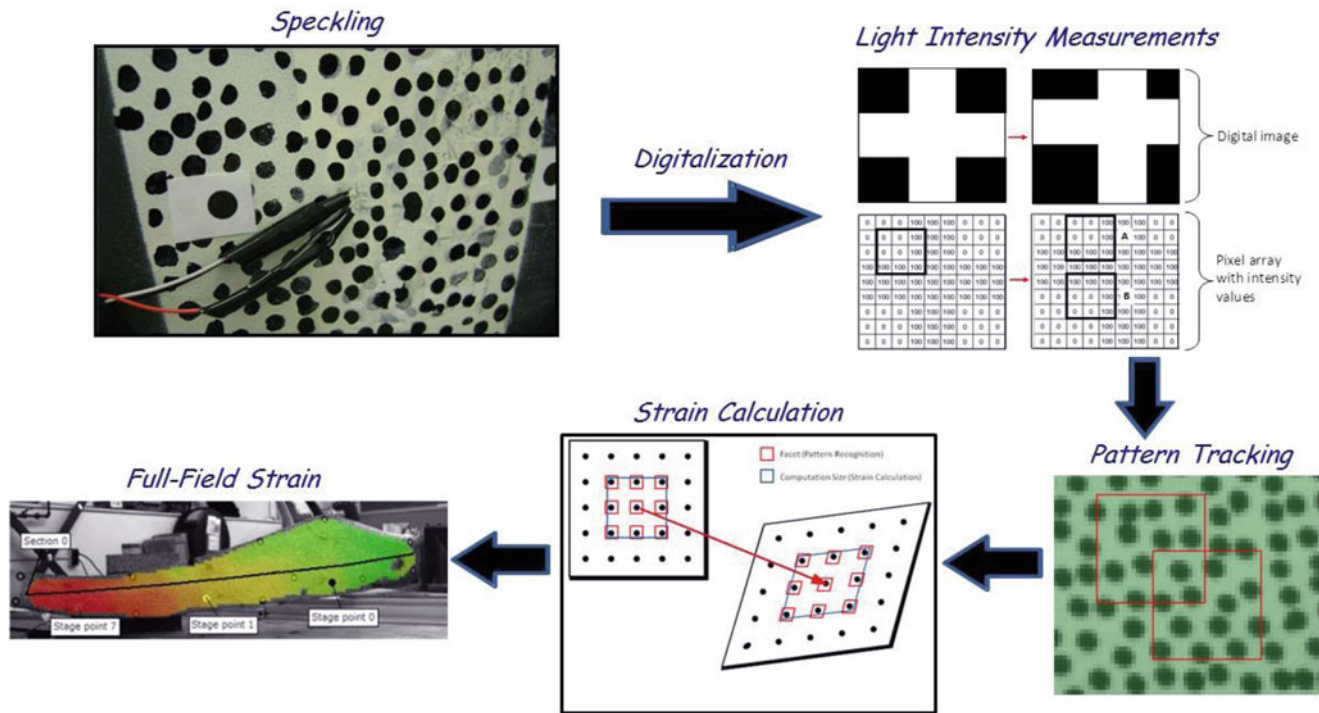


Fig. 30.4 Digital image correlation overview

The SEREP transformation is developed with analytical mode shapes for the structure (but can also be evaluated using measured modal vectors as done in Chipman's work [3] and Pingle's work [1]). Equation 30.1 is used for expansion of measured real-time operating data $[RTO_a]$ to the full space of the finite element model $[ERTO_n]$ and is written as

$$[ERTO_n] = [T] [RTO_a] \quad (30.5)$$

The transformation matrix, $[T]$, can be one of the commonly used matrices used but SEREP is utilized for all the work presented herein.

30.3 Test Structure and Measured Displacement/Strain Comparisons

The work here concentrates on the use of DIC, 3DPT, and expansion for wind turbine blade applications but can also be applied (and has been applied) to a variety of different structures.

30.3.1 Test Article Description: Model and Dynamic Characteristics

A small wind turbine blade, provided by Southwest Windpower, was tested while clamped in a fixture specifically designed for testing a wind turbine blade. It is important to note that a validation structure (a cantilevered boxed-beam), with easy to define mechanical and dynamic properties, was also subjected to similar tests and analysis to validate the results obtained for the turbine blade represented here; that work is contained in [4, 5]. Figure 30.5 shows an overview of the test setup.

A finite element model of the blade was created and validated through correlation to measured mode shapes. The model is needed to perform the modal expansion for predicting full-field displacements and ultimately strain on all surfaces of the structure. The finite element model of the wind turbine blade was created using solid elements. The process in developing this model is described in [6]; the model consisted of 56,299 nodes and 29,648 elements. Figure 30.6 shows a correlation of the finite element modes to the free-free modal testing shapes using the Modal Assurance Criterion (MAC). Only the flapwise modes were correlated, as those were the modes of interest.

Fig. 30.5 Test rig including the mounting fixture, turbine blade, Whiffle tree, and pneumatic actuator

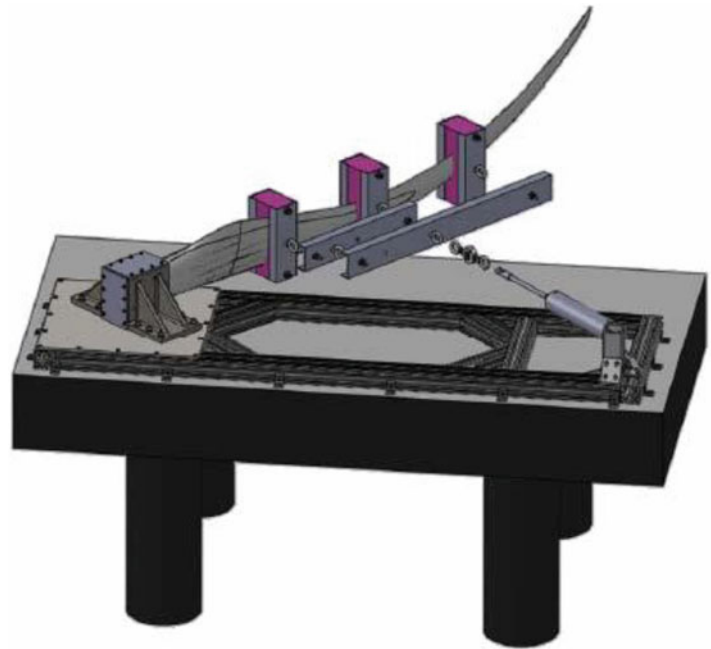
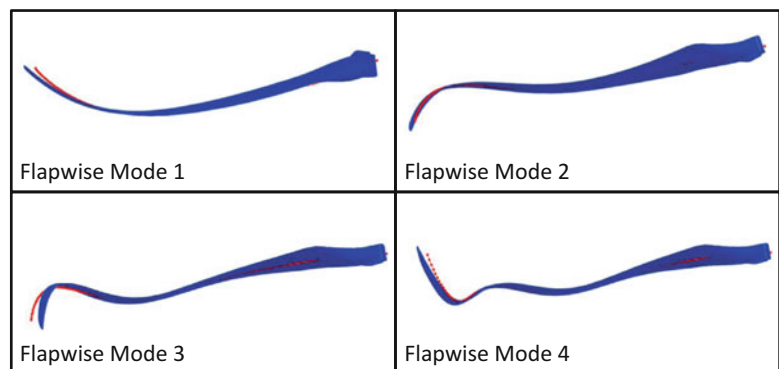


Fig. 30.6 Correlation of free-free test to blade FEA model



| Mode Pair | FEA (Hz) | EMA (Hz) | % Diff | MAC |
|-----------|----------|----------|--------|------|
| 1 | 14.56 | 14.47 | -1.66 | 96.4 |
| 2 | 27.63 | 28.80 | -4.05 | 98.8 |
| 3 | 53.04 | 54.22 | -2.17 | 99.1 |
| 4 | 88.37 | 90.11 | -1.93 | 98.9 |

30.3.2 Strain Gage Vs. DIC Strain Comparison: Static Testing

For validation and calibration of the system and finite element model, a static test was performed on the blade [7]. The load was applied using a pneumatic actuator. Incremental loads of 50 lbs were applied up to a 200 lb load, and then incremental loads of 25 lbs were applied up to a 300 lb load. At each loading stage, data was taken using strain gages and DIC cameras; strains were computed using the Aramis system and the results were compared to the strain gage results.

The DIC data can be used to generate a full-field strain plot over the surface of the blade. To compare the results of the strain gages and the DIC data, the results from one measurement point of the speckle pattern located in the center of the strain gages was compared to the strain gage data, as shown in the plot of Fig. 30.7. Overall, the results from the strain gage and DIC compare very well. The acceptable correlation of data from a static test validates the testing approach and permits dynamic testing to be performed with confidence.

Using DIC techniques to measure strain provides full-field strain results on a structure, which is a large advantage over conventional discrete strain measurement techniques. Because strain gages only measure discrete points, unexpected strain values due to defects in the structure would only be captured if a strain gage were placed at that precise location.

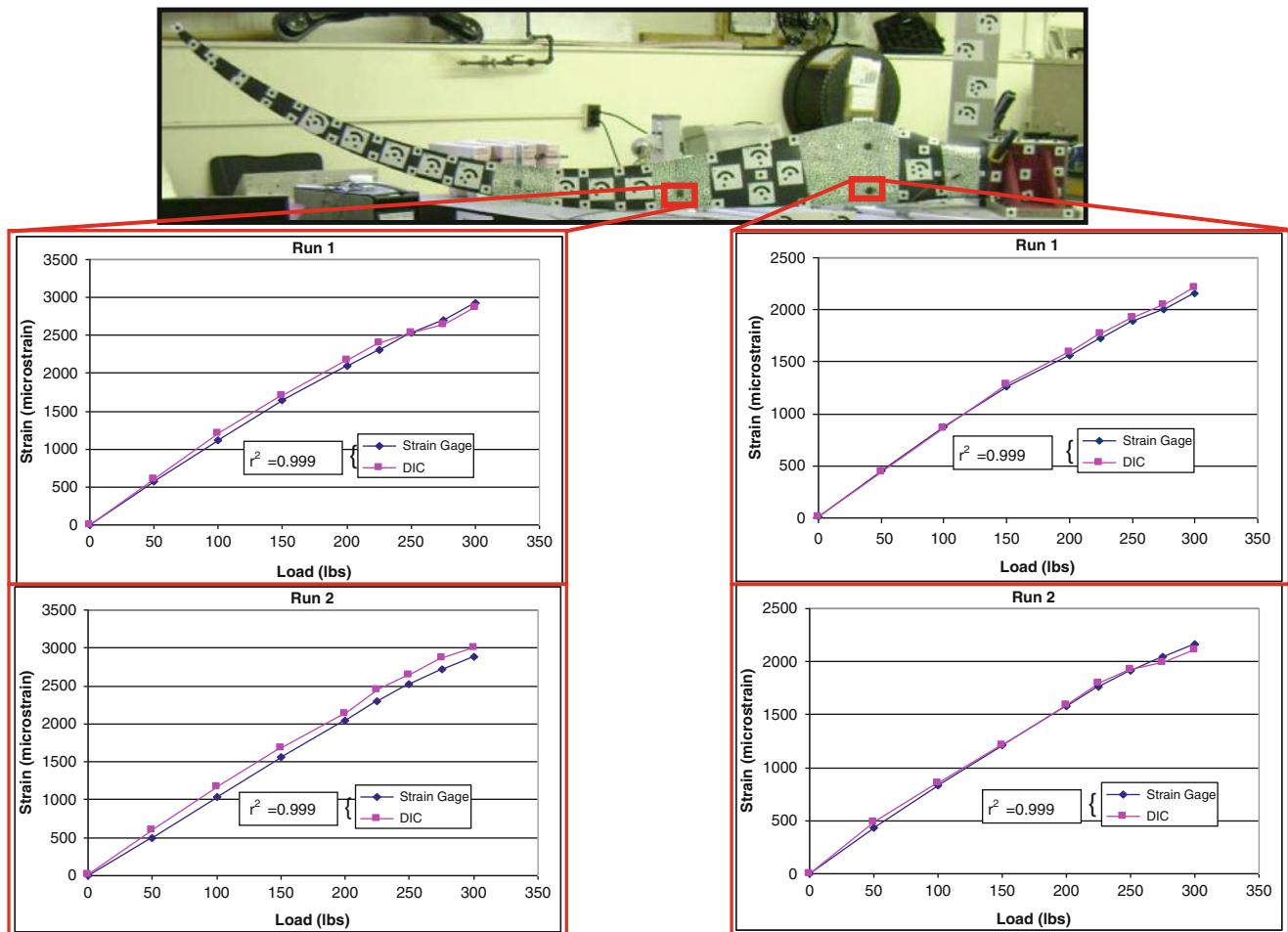


Fig. 30.7 Comparison of strain measured from strain gages and ARAMIS system on wind turbine blade

However, current studies show that measuring strain along a structure using DIC techniques allows for the detection of defects due to changes in the full-field strain results. Additionally, using DIC permits measurements to be taken without the preparation time and wiring required when using strain gages.

30.3.3 Strain Gage Vs. DIC Strain Comparison: Dynamic Testing—Pluck and Sine Test

Two different dynamic tests were performed to study the effectiveness of the image correlation techniques. The first dynamic test performed on the blade was a pluck test. For this test, the tip of the beam was displaced a certain distance. The blade was then released and allowed to oscillate. Tip displacements were measured with respect to the optical table on which the structure rests. The results of the pluck tests are shown in Fig. 30.8.

As displayed in Fig. 30.8, the DIC data contains more measurement noise compared to the strain sensor. However a 100 Hz filter was applied to the strain gage measurements during testing, and the strain gage data was smoothed. The calculation of strain from the DIC measurement involves spatial filtering of the images. For this test, the default settings were used in the Aramis™ software. Other filter settings may affect the processed data, but further studies on the effects of applying a filter to the DIC data are beyond the scope of this paper. Also, within the DIC data, there is a low frequency oscillation that is caused by the movement of the optical table. If this table oscillation were removed from the data, the peak strain results would match better. Although there is noise on the DIC data, the strain gage and DIC measurements match very well. In Fig. 30.8, the peak-to-peak values of strain are comparable between the strain gage and DIC measurements, which demonstrates that the DIC produces measurements of strain that are comparable to strain gage measurements.

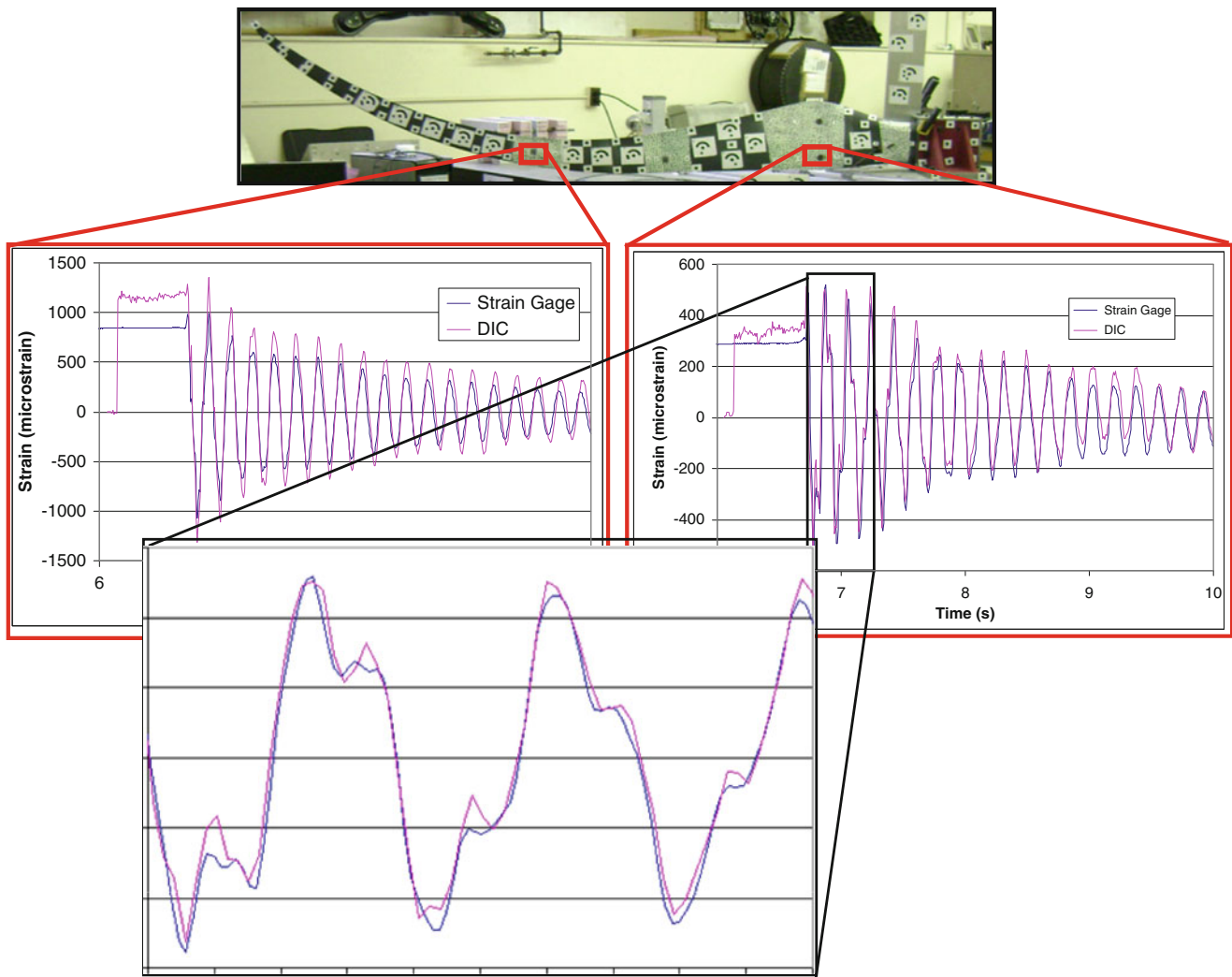


Fig. 30.8 Comparison of pluck test strain measured from strain gages and ARAMIS system on wind turbine blade

For the second dynamic test, a shaker was placed 16 in. from the base on the back side of the blade [7]. A discrete sine input at the first natural frequency (determined to be 5.6 Hz through modal testing) of the system was applied. The strain on the blade was measured using both strain gages and DIC, and the results were compared. A comparison of the results is shown in Fig. 30.9. For the discrete sine test, the peak strain measurements are again comparable and provide additional confirmation of the adequacy of the DIC results.

30.3.4 Strain Gage Vs. Full Field Expansion: Dynamic Testing

The turbine blade was tested again with a sinusoidal excitation and the dynamic displacement data was captured from the photogrammetric targets and used with the expansion process previously described to obtain full-field displacement and then full-field strain. Single frequencies were first investigated followed by multiple mixed sine waves to demonstrate the response due to multimode excitation.

The first test was the shaker test with a discrete sine input near the first system natural frequency (determined to be 5.6 Hz through modal testing). This test was performed first due to the simplicity of expanding data when primarily only one mode is excited. The strain results are shown in Fig. 30.10. The top image in the figure depicts the predicted strain field from the expanded displacements applied to the finite element model, with red indicating the areas of highest strain. From this model, the predicted strain was compared to strain gages mounted to the blade at three points. These results compare very well overall.

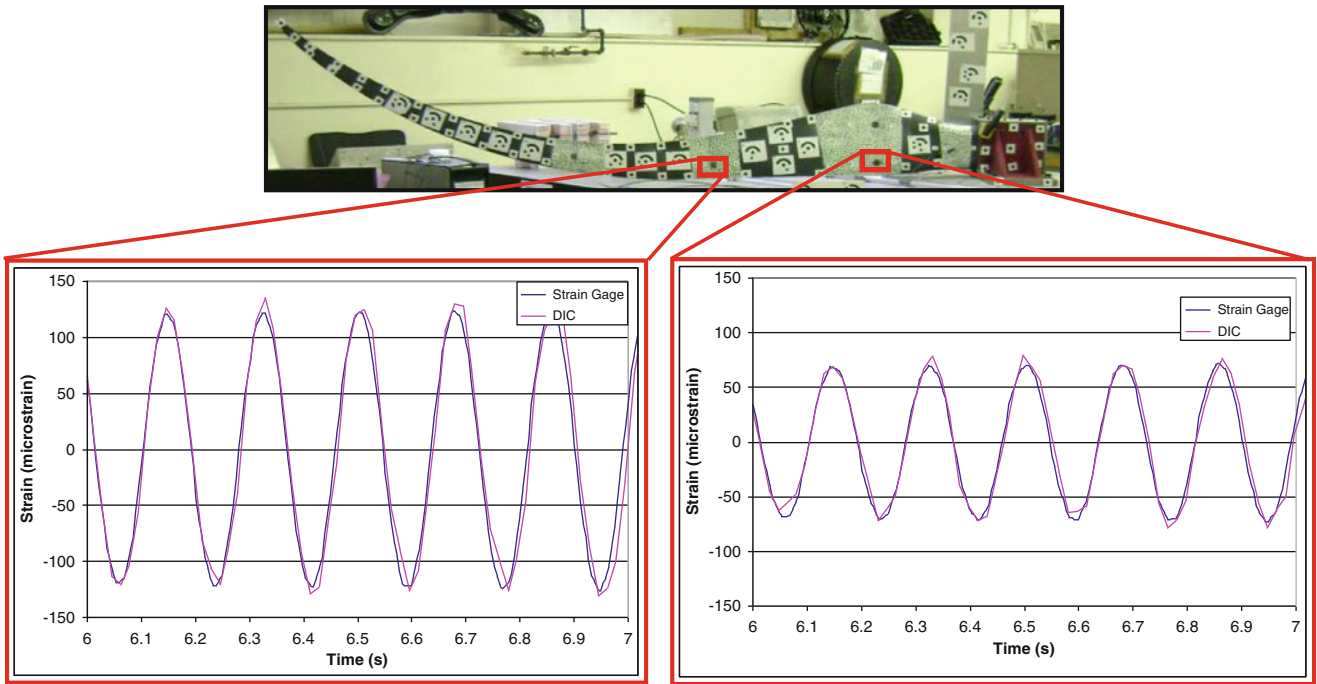


Fig. 30.9 Comparison of sine test strain measured from strain gages and ARAMIS system on wind turbine blade

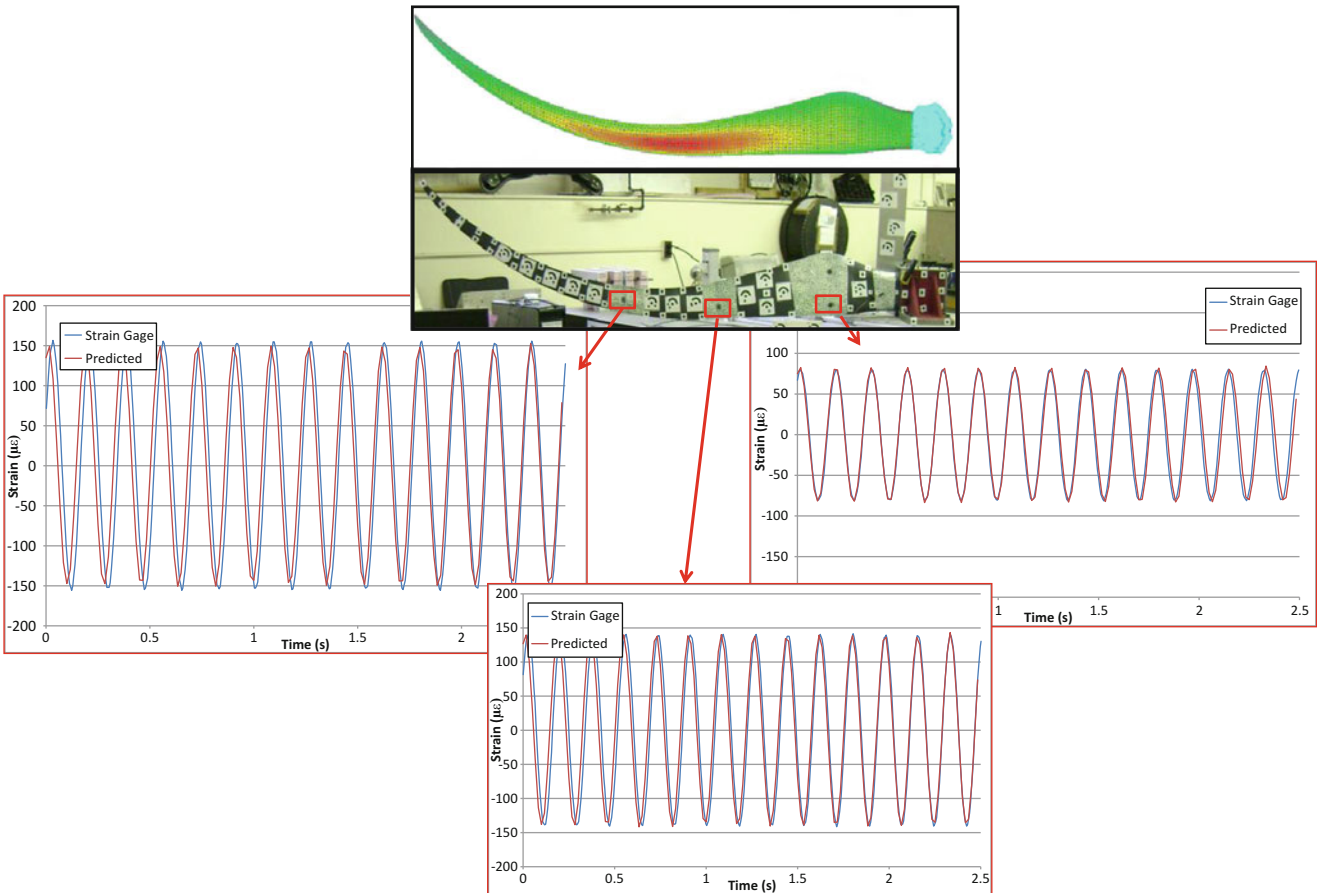


Fig. 30.10 Shaker excitation of a blade comparing experimental and modal expansion results for a single sine wave excitation

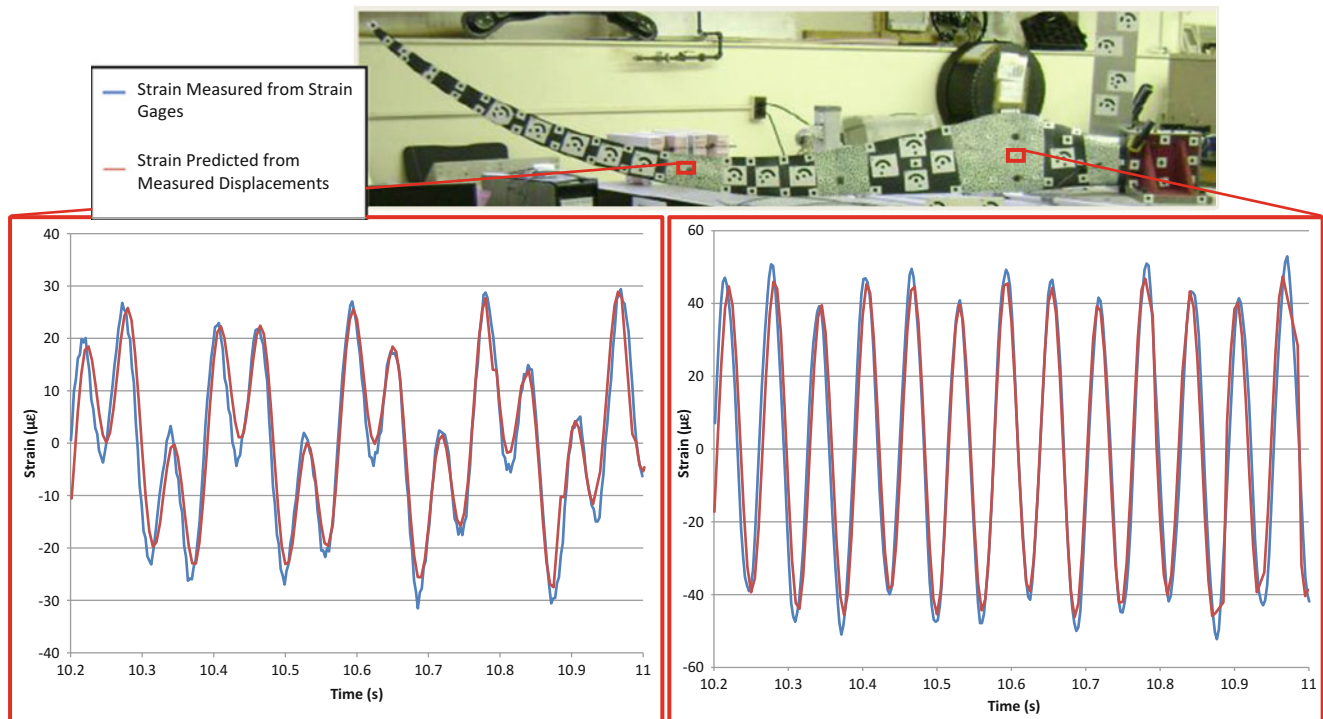


Fig. 30.11 Shaker excitation of a blade comparing experimental and modal expansion results for a multi-sine wave excitation for visible surface measurements

Following the single sine excitation, several sine waves were mixed to form a multi-mode excitation and the expansion of the measured displacement to find the full field strain. For these tests, the signal was the sum of two sine waves with frequencies of 5.6 Hz and 16.1 Hz; the amplitude of the 16.1 Hz wave was three times greater than the amplitude of the 5.6 Hz wave to ensure the multiple-mode excitation had similar amplitudes for each mode. Figure 30.11 shows the results of the multi-mode excitation where two strain gages are compared to the expanded displacement results applied to the finite element model. As seen, the results compared very well overall.

In addition to the results shown in Fig. 30.11 (where both strain gages are on the front side within the line of sight for the optical system), one additional strain gage was also placed on the non-visible side of the blade; the expansion process was used to expand the displacement results to obtain strain results on the non-visible portion of the blade (which could have been interior in the blade). Figure 30.12 shows these results which compare very well to the measured strain. This is a very important result because the expansion technique can be used to identify full field information and is not limited to the line of sight of the optical measurement system. The expansion process is very useful to augment the results of the optical line of sight measurements which cannot provide interior or non-visible surfaces and regions.

The very important result of these cases is that a very limited set of real time operating data can be collected on a structure in operation, and without any knowledge of the force applied to the system, the measured response can be expanded back to the full space of the finite element model and used in the back substitution process of the FEA to obtain full-field dynamic displacement and dynamic strain.

30.4 Conclusion

This paper presents two very important coupled approaches necessary for the prediction of dynamic stress–strain for large structures (e.g. rotating wind turbines) while in operation. These are: (a) the use of an empirical non-contacting optical imaging approach for the prediction of full-field surface displacement (or strain) and (b) the use of a newly developed expansion approach to obtain dynamic displacement followed by dynamic stress–strain using a very limited set of measurements. The optical empirical measurements provide data that are used to drive the analytical expansion approach.

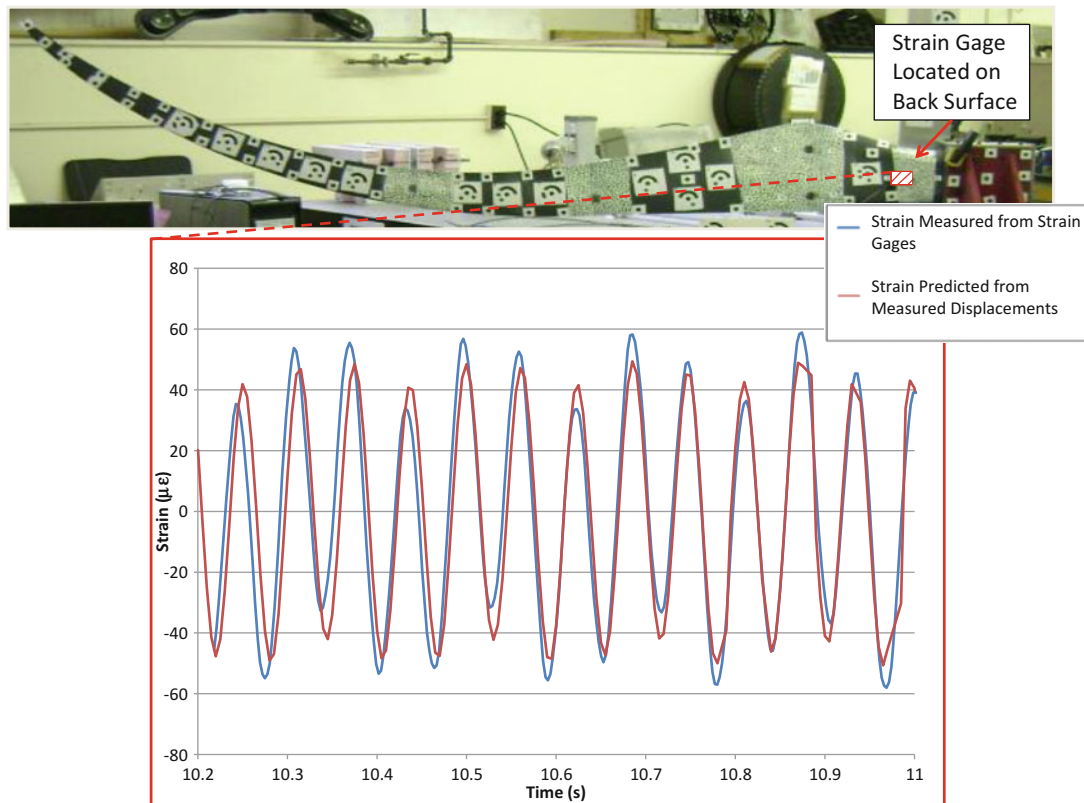


Fig. 30.12 Shaker excitation of a blade comparing experimental and modal expansion results for a multi-sine wave excitation for non-visible surface measurements

Within this work, digital image correlation (DIC) has been used on a wind turbine blade to predict full-field surface dynamic strain and is compared to conventional strain gage measurements at a few select locations. Comparisons of the DIC measured static and dynamic strain (using a pluck test and sinusoidal tests) to those of conventional strain gages were shown to be in agreement. The advantage of DIC is that full-field surface strain can be captured while the structure is in operation whereas the strain gages can only measure at a limited number of locations where gages are placed. The DIC approach provides an abundance of data to describe the entire surface dynamic strain.

The 3D point tracking has also been used to measure surface displacements for dynamic events and has been used in conjunction with the modal expansion algorithm. The use of very limited sets of dynamic measured data can be used with the new expansion process to obtain full-field dynamic stress-strain in conjunction with the finite element model. Limited measurements were expanded to the full space of the finite element model to obtain the full-field displacement solution at all time steps for a dynamic transient deformation and subsequently used with the finite element constitutive relationships to predict strain over an entire turbine blade. These results were compared to the traditional strain gage results and show very good agreement for the cases presented. Both techniques complement each other and provide a significant step forward in the assessment of the structural health of large structures such as wind turbine blades while in operation.

Acknowledgements Some of the work presented herein was partially funded by the National Science Foundation Civil, Mechanical and Manufacturing Innovation (CMMI) program (Grant No. 0900543; entitled “Dynamic Stress-strain Prediction of Vibrating Structures in Operation”). Any opinions, findings, and conclusions or recommendations expressed in this material are those of the authors and do not necessarily reflect the views of the particular funding agency. The authors are grateful for the support obtained.

The test rig used in the tests performed in this paper was a direct result of the effort of a Capstone Design Team during the Spring Semester of 2011. Jennifer Carr, Samuel Dyas, Matthew Ertos, Jack LoPiccolo, Christopher Nonis, and Joseph Romano were responsible for the design and fabrication of the test rig and development of test plans and procedures for operating the test rig. Their efforts were substantial and very much appreciated.

Southwest Windpower supplied several blades and CAD models and provided consultation related to this work. Their time and support and materials are greatly appreciated.

References

1. Pingle P (2010) Prediction of full-field dynamic stress-strain from limited sets of measured displacement data. Doctoral thesis, University of Massachusetts Lowell, Aug 2010
2. O'Callahan JC, Avitabile P, Riemer R (1989) System equivalent reduction expansion process. In: Seventh international modal analysis conference, Las Vegas, Feb 1989
3. Chipman C (2009) Expansion of real time operating data. Master's Thesis, University of Massachusetts Lowell, May 2009
4. Carr J, Baqersad J, Avitabile P, Niezrecki C (2011) Dynamic stress-strain on turbine blade using digital image correlation techniques part 1 – static load and calibration. In: Proceedings of the IMAC-XXX, Jacksonville, 30 Jan–2 Feb 2011
5. Carr J, Baqersad J, Avitabile P, Niezrecki C (2011) Dynamic stress-strain on turbine blade using digital image correlation techniques part 2 – dynamic measurements. In: Proceedings of the IMAC-XXX, Jacksonville, 30 Jan–2 Feb 2011
6. LoPiccolo J, Carr J, Niezrecki C, Avitabile P (2011) Validation of a finite element model used for dynamic stress-strain prediction. In: Proceedings of the IMAC-XXX, Jacksonville, 30 Jan–2 Feb 2011
7. Carr J, Dyas S, Ertos M, LoPiccolo J, Nonis C, Romano J (2011) Static and dynamic testing of a 7-ft wind turbine blade. Department of Mechanical Engineering, James B. Francis College of Engineering, Capstone Design, University of Massachusetts Lowell, 6 May 2011

Chapter 31

Comparison of Multiple Mass Property Estimation Techniques on SWiFT Vestas V27 Wind Turbine Nacelles and Hubs

Timothy Marinone, David Cloutier, Kevin Napolitano, and Bruce LeBlanc

Abstract Rigid body mass properties have proven to be valuable data for use in a variety of analyses; a complex structure can be simplified into a single mass element provided the mass, CG, and moments of inertia are known. Because traditional experimental methods often require significant time, effort, and resources to set up and perform, much work has been done to find ways to use data from other test setups to obtain these properties.

In this paper, multiple methods used to obtain rigid body mass properties were performed on two different test articles: a Vestas V27 wind turbine hub and a Vestas V27 wind turbine nacelle. The methods compared are use of a load cell and bifilar pendulum, use of mass-line values obtained from measured transfer functions, and use of modal parameters extracted from rigid body modes. The modal parameter method produced the most accurate results, while the mass-line approach was nearly as accurate but suffered from some experimental error.

Keywords Modal Parameter Estimation • Wind turbines • Modal testing • Analytical methods • Inertia properties

31.1 Introduction

Sandia National Laboratories (SNL) is developing the Scaled Wind Farm Technology (SWiFT) center to enable rapid, cost-efficient testing and development of transformative wind energy technology. The site is intended to study complex turbine wake interactions and focus on damage mitigation, improved power performance, and recommended future site layouts. Since this site is designed to be open source and to provide data to all interested parties, the models must be accurate enough to be used for the desired analyses while preserving Vestas' proprietary information. For this paper, the hub and nacelle of the Vestas V27 (V27) wind turbines used on site were tested to obtain the mass inertia properties, as this allows the model to accurately reflect the wind turbines installed while eliminating the need to fully model the hub and nacelle.

The traditional approach to obtaining inertia properties, commonly taught as part of an undergraduate course sequence, uses a bifilar or trifilar pendulum procedure. If the test article is unwieldy or complex, however, this approach often requires a complex fixture design to be used. In addition, large experimental errors are introduced if assumptions inherent in the procedure are not satisfied.

Two methods for obtaining inertia properties from modal data using mass-line values or using modal parameters extracted from rigid body modes were presented by Bretl and Conti [1]. In their paper, they presented the mathematical framework for both techniques and used them to obtain the rigid body mass properties of an engine assembly supported by elastomeric mounts to the ground. Values obtained by the two methods were consistent and indicated the usefulness of the techniques. These and other techniques have been used for other test articles [2–6] and have generally produced good results.

Sandia is a multiprogram laboratory operated by Sandia Corporation, a Lockheed Martin Company, for the U.S. Department of Energy under Contract DE-AC04-94AL85000.

T. Marinone (✉) • D. Cloutier • K. Napolitano
ATA Engineering, San Diego, CA 92130, USA
e-mail: tmarinon@ata-e.com

B. LeBlanc
Sandia National Laboratories, Albuquerque, NM 87185, USA

31.2 Review of Mass Inertia Matrix

The matrix form of the equation of motion for a rigid body is written as

$$\begin{Bmatrix} F_x \\ F_y \\ F_z \\ M_x \\ M_y \\ M_z \end{Bmatrix} = \begin{bmatrix} m & 0 & 0 & 0 & 0 & 0 \\ 0 & m & 0 & 0 & 0 & 0 \\ 0 & 0 & m & 0 & 0 & 0 \\ 0 & 0 & 0 & I_{xx} & -I_{xy} & -I_{xz} \\ 0 & 0 & 0 & -I_{xy} & I_{yy} & -I_{yz} \\ 0 & 0 & 0 & -I_{xz} & -I_{yz} & I_{zz} \end{bmatrix} \begin{Bmatrix} a_x \\ a_y \\ a_z \\ \alpha_x \\ \alpha_y \\ \alpha_z \end{Bmatrix}. \quad (31.1)$$

Provided that the forces F_x, F_y, F_z and moments M_x, M_y, M_z input into the test article are known, and the output linear and angular accelerations $a_x, a_y, a_z, \alpha_x, \alpha_y, \alpha_z$ are measured, the inertia measurements can easily be obtained. Although this condition can be reasonably represented by testing the structure in an approximately free-free boundary condition with soft supports, the common setup for modal testing does not involve measuring the moments imparted to the system, the linear acceleration at the CG location, or the angular acceleration experienced by the test article. As a result, the approaches used are rewritten to account for the use of multiple accelerometers measuring only linear accelerations.

For all of the following approaches, the rigid body transformation matrix R is used, which maps the six DOF of the origin to the six DOF of each test node.

31.3 Mass-Line Approach

An alternative variation using mass-line values can be formulated where the mass of the object has not been measured. The fully populated FRF matrix is transformed from physical degrees of freedom to rigid body degrees of freedom by the rigid body transformation matrix. The rigid body FRF matrix can then be evaluated over the mass-line frequency range and used to calculate the rigid body mass matrix as shown. Then the rigid body mass matrix can be rearranged to yield the familiar terms of mass, CG, and moments of inertia.

$$H_{RBM} = R^* H. \quad (31.2)$$

$$MRB = \left[(R^T R)^{-1} R^T \right] H_{RBM} \left[(R^T R)^{-1} R^T \right]. \quad (31.3)$$

31.4 Rigid Body Modal Parameter Estimation Approach

Test-measured rigid body mode shapes can also be used to estimate the rigid body mass properties. The assumption in this method is that rigid body mode shapes are, in fact, rigid and not contaminated by the flexible mode shapes. The fully populated mass matrix can be obtained from the rigid body shapes as shown. The rigid body mass matrix can then be calculated by premultiplying by the rigid body transformation matrix; then the rigid body mass matrix can be rearranged to yield the familiar terms of mass, CG, and moments of inertia.

$$M = \left[(\Phi^{*T} \Phi^*)^{-1} \Phi^{*T} \right] \left[(\Phi^T \Phi)^{-1} \Phi^T \right]. \quad (31.4)$$

$$MRB = R^{-1*} M^* R. \quad (31.5)$$

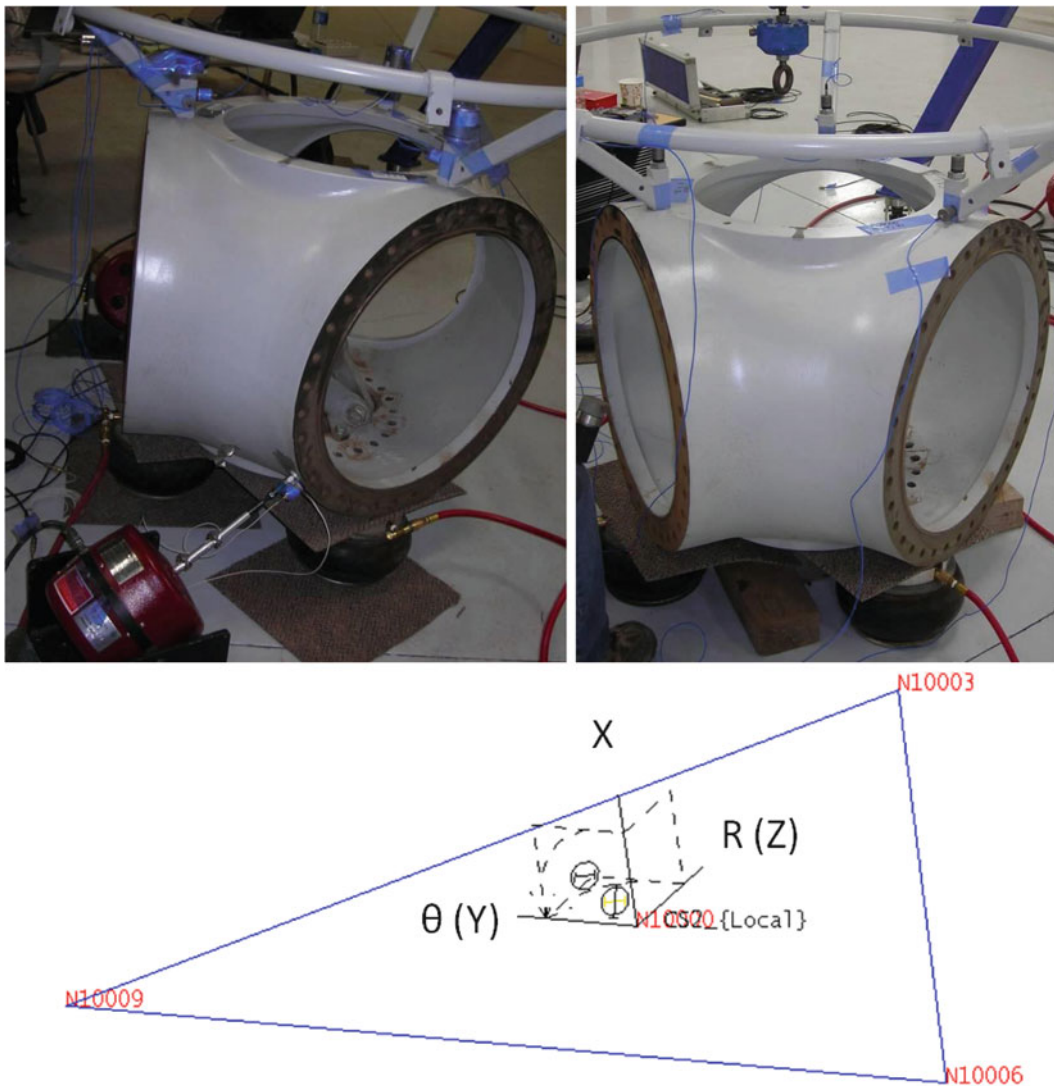


Fig. 31.1 Hub supported (*upper left*), hub excited by shakers (*upper right*), and test-display model showing node locations (*bottom*)

31.5 Test Articles

Testing was performed on the nacelle and hub of the V27 wind turbines used in SNL's SWiFT facility. The hub was suspended on air bags, and a test-display model was created, as shown in Fig. 31.1. Drive point measurements were obtained through impacts at all nine response DOF to create a fully populated transfer function matrix for use in obtaining the mass lines. Two shakers were also used to excite the hub to ensure highly accurate rigid body modes. The hub was also suspended rigidly to use the bifilar pendulum approach for comparison.

The nacelle was suspended on air bags and a test-display model was created, as shown in Fig. 31.2.

Two shakers were also used to excite the nacelle to ensure highly accurate rigid body modes.

31.6 Data Collection and Signal Processing

Seismic accelerometers (PCB 393B04) were mounted to both the hub and nacelle at the node locations in all three axes. Multi-Sine sweeps at 0.2 decades/min were run with sweeps between 1 and 50 Hz for a total of 730 s, while the data was sampled at 128 Hz. This sample rate was sufficient to capture the entire response of the structure while providing sufficient frequency resolution for the modal parameter estimation. Impacts were performed every 32 s, and data was sampled at 128 Hz.

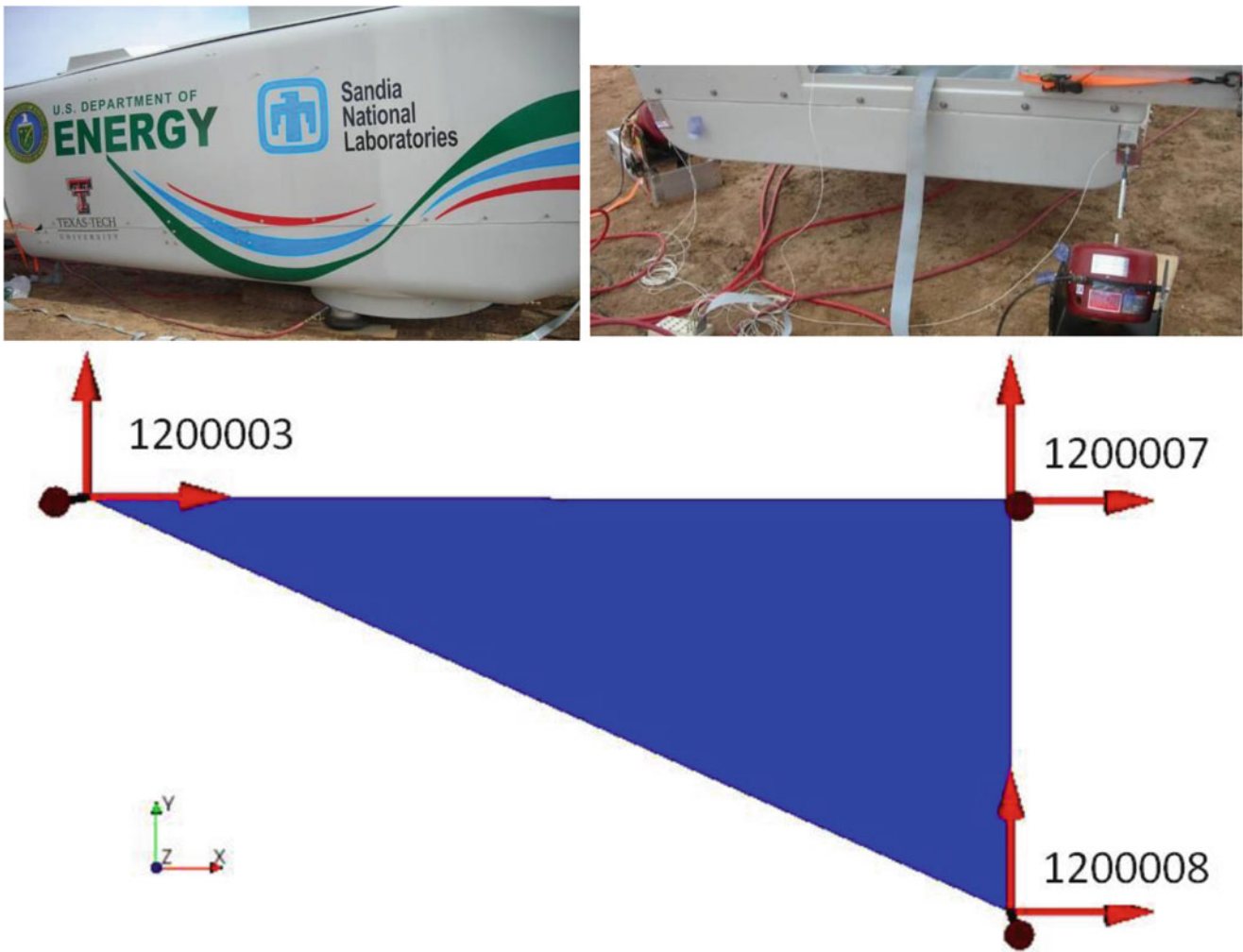


Fig. 31.2 Nacelle supported (*upper left*), nacelle excited by shakers (*upper right*), and test-display model showing node locations (*bottom*)

Signal processing for the shaker runs used a Hanning broad window with overlap averaging. The impact runs were processed with no window since the excitation and response signals were near zero at the beginning and end of each frame of data.

31.7 Test Results

This section documents the test results. The rigid body modes were estimated for the two nacelles and one hub. The mass-line approach was only applied to the hub.

Figure 31.3 shows the power spectrum mode-indicator function (PSMIF) for the nacelle with a single reference. While two shakers were used during the test, a single reference provided better fits and mass estimation than both references. The PSMIF, as the summation of all FRFs multiplied by each FRF conjugate, is an ideal function to visualize the overall response of the structure. The six rigid body modes are observed in the six peaks of the response. To evaluate the quality of the rigid body modes obtained, the PSMIF was then synthesized using only the six rigid body modes. The synthesized PSMIF shows a high level of correlation with the test data. As such, there is confidence that the extracted rigid body modes will accurately describe the inertia properties of the nacelles.

Figure 31.4 shows the complex mode-indicator function (CMIF) for testing the hub with two shakers. Again, all six rigid body modes can be seen in the peaks of the response (the CMIF is plotted for both shaker references in order to clearly distinguish modes 5 and 6). To evaluate the quality of the rigid body modes obtained, the CMIF was then synthesized using

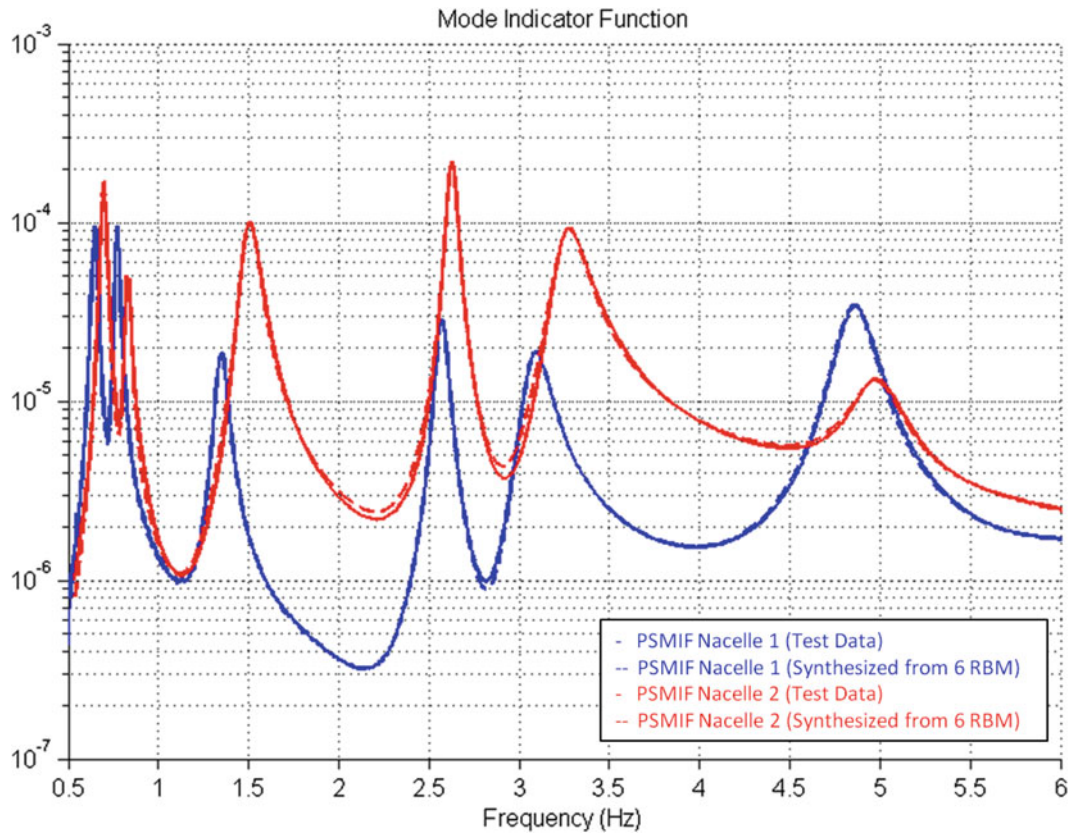


Fig. 31.3 PSMIF for both nacelles comparing test data to synthesized data from the six rigid body modes

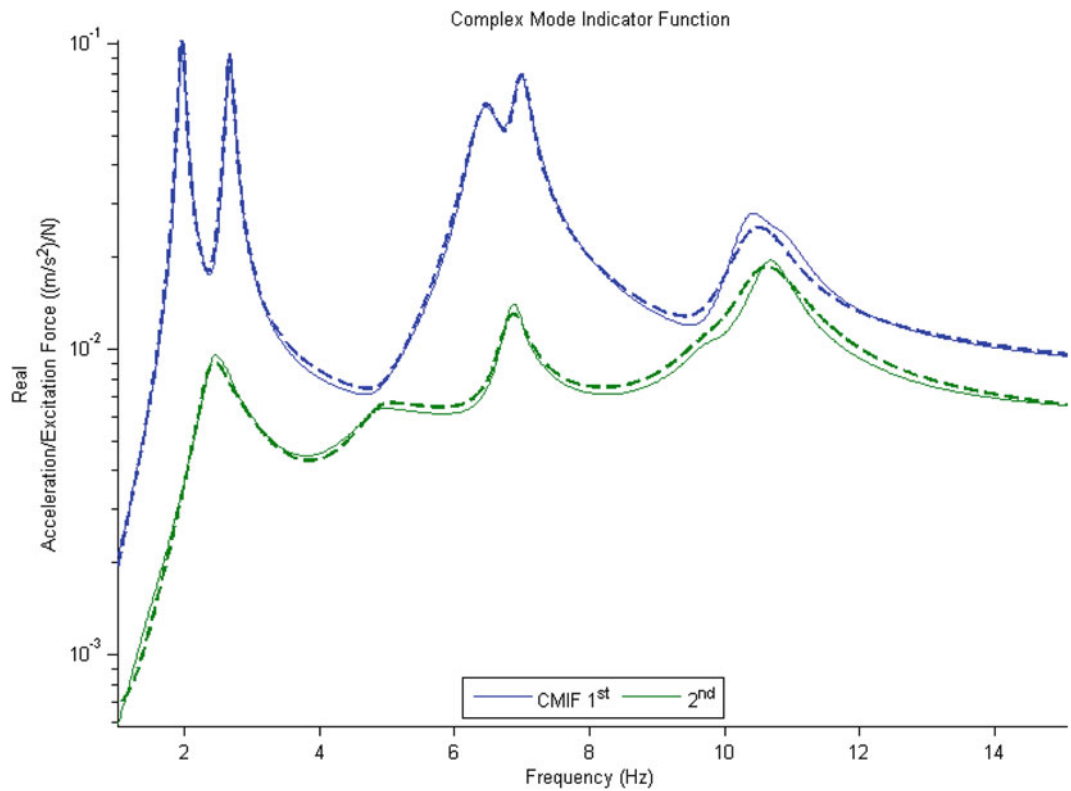


Fig. 31.4 CMIF for the hub comparing test data to synthesized data from the six rigid body modes

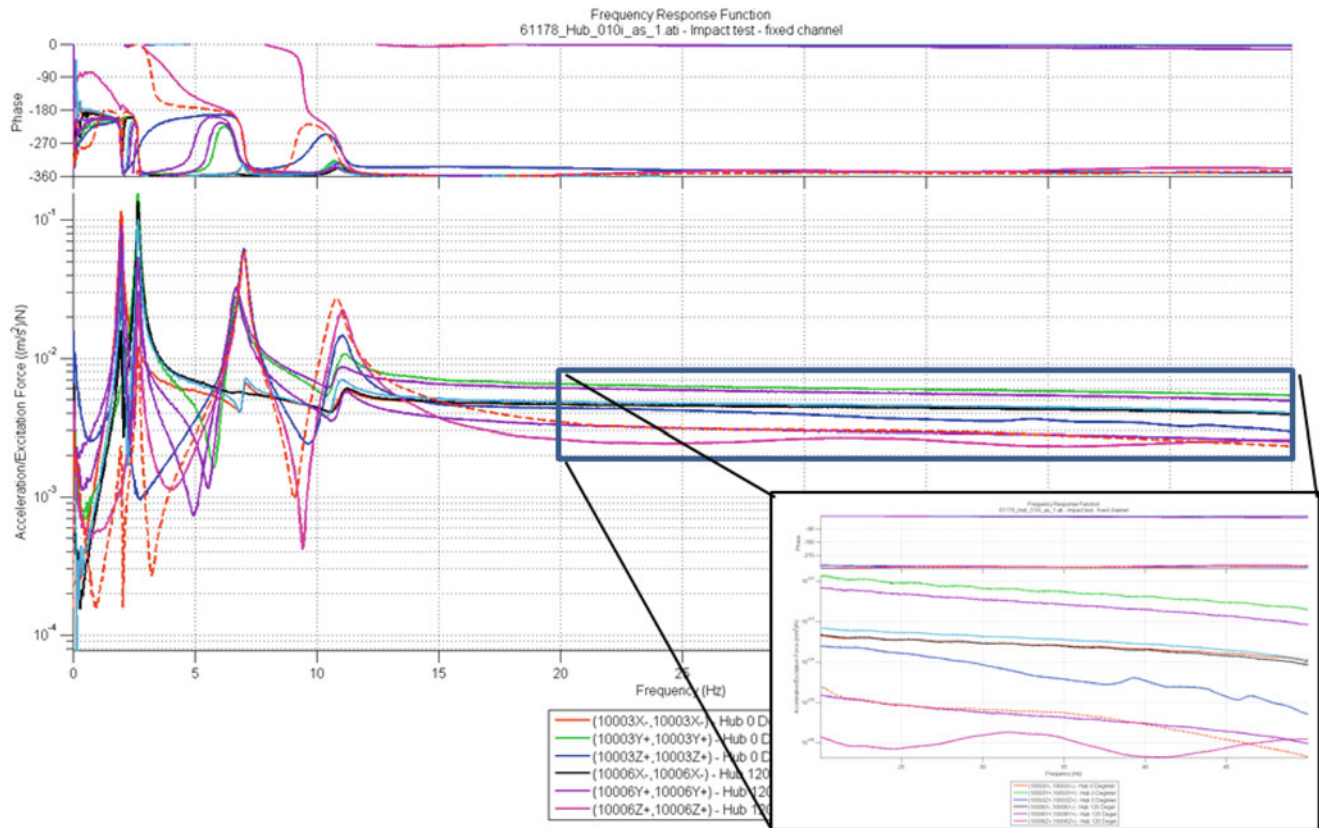


Fig. 31.5 Drive point FRFs from impact runs, showing mass lines

only the six rigid body modes. The synthesized CMIF shows a high level of correlation with the test data. As such, there is confidence that the extracted rigid body modes will accurately describe the inertia properties of the hub as well.

Figure 31.5 shows the drive point measurements for all of the DOFs where the six rigid body modes are evident in the peaks seen in the responses. There are clear mass lines from 20 to 50 Hz, showing good separation between the rigid body and flexible modes. As seen in the zoomed-in portion, however, there is a small but noticeable oscillation in some of the mass lines, which is associated with experimental error caused by double impacts at some of the less-repeatable drive points. As a result, there is expected to be some error involved in the estimation of the terms using this method.

The inertia results from modal inversion for the nacelle are shown in Table 31.1. The masses of the nacelles were also measured independently by a crane company during transportation, and these are included for completeness. The mass and CG properties of nacelle 3 were also obtained, but modal testing was not performed on that nacelle.

The two nacelles have fairly consistent properties, which were expected due to the assumed similarity in manufacture of the nacelles. The CG of the nacelles in the X direction (fore-aft) is aft of the origin; however, the CG measured in the modal inversion method is closer to the origin than that measured with load cells. The aft CG is expected, as the nacelle should be balanced when the rotor is assembled: without the rotor, the nacelle will be significantly back-heavy. The CG about the Y direction (side-side) is relatively close to the origin, although computed on the opposite side for nacelle 2 using the modal inversion method. The offset is expected to be positive due to the generator being primarily located on the positive-Y side of the nacelle.

Substantial rigging was used when the nacelles were being lifted by the crane, which accounts for some of the discrepancy in the masses obtained between the crane, load cell, and modal inversion methods. Additionally, oil and equipment were installed after the initial inertia testing, changing the mass and CG of the nacelle. The results obtained from the crane and the load cell are assumed to be more accurate than the modal inversion method, as those methods obtained the loads directly from the calibrated load cells, in contrast to estimating them from the modal mass of the rigid body shapes. The error seen using modal inversion may be due to error in measurement, curve-fitting, or accelerometer location measurement. However, the mass and CG are within 20 % of the load cell results, which indicates that the moment of inertia terms are reasonably accurate. Finally, the moment of inertia about the Y-axis is the largest, which is expected since the mass is most spread out about the Y-axis.

Table 31.1 Final list of inertia properties for V27 nacelles

| Mass and Inertia Properties of V27 Nacelles | | | | |
|---|-----------|-------|-----------|-----------------|
| Property | Nacelle # | Crane | Load Cell | Modal Inversion |
| Mass (kg) | 1 | 6804 | 7038 | 5577 |
| | 2 | 6577 | 6781 | 5551 |
| | 3 | 6668 | 7203 | |
| CGx (m) | 1 | | 0.67 | 0.25 |
| | 2 | | 0.61 | 0.16 |
| | 3 | | 0.65 | |
| CGy (m) | 1 | | 0.09 | 0.04 |
| | 2 | | 0.07 | -0.08 |
| | 3 | | 0.09 | |
| CGz (m) | 1 | | | 0.06 |
| | 2 | | | 0.12 |
| | 3 | | | |
| Ixx (kg*m ²) | 1 | | | 2569 |
| | 2 | | | 2453 |
| Iyy (kg*m ²) | 1 | | | 9937 |
| | 2 | | | 10876 |
| Izz (kg*m ²) | 1 | | | 9038 |
| | 2 | | | 10141 |

Table 31.2 Final list of inertia properties for V27

| Mass and Inertia Properties of V27 Hubs (Pitch Yaw Linkage Included) | | | | | |
|---|-------|-----------|------------------|-------------------|---------------------|
| Property | Hub # | Load Cell | Bifilar Pendulum | Modal Inversion** | Mass Line Inversion |
| Mass (kg) | 1 | 481.7 | | 508.1 | 483.7 |
| | 2 | 474.0 | | | |
| CGx (m)* | 1 | | | -0.438 | -0.754 |
| Cgy (m)* | | | | 0.015 | 0.105 |
| CGz (m)* | | | | 0.005 | -0.143 |
| Ixx (kg*m ²) | | | 26.6 | 69.1 | 110.8 |
| Iyy (kg*m ²) | | | | 76.3 | 343.6 |
| Izz (kg*m ²) | | | | 86.2 | 151.6 |
| * Origin Defined at Front Face of Hub Rotor About the Center Using Rotor Csys | | | | | |
| ** Includes the Effective Mass of the Airbags | | | | | |

The modal inversion method and the mass-line inversion method were used to calculate the rigid body mass matrix of the hub. The resulting terms were compared to the mass obtained from the load cell and the inertia term obtained from the bifilar pendulum approach. Table 31.2 lists the various terms obtained from all of the methods used.

As seen in the table, the modal inversion and mass-line inversion methods yield approximately the same mass as the load cell, to within 5 %. The CG locations are similar between both methods, but there is an observable discrepancy between the two. The inertia for the bifilar pendulum is significantly lower than either of the two methods, and the mass-line inversion is noticeably higher than the modal inversion.

All four methods used to obtain the mass and inertia properties are discussed here to explain possible sources of error and to comment on their accuracy. The load cell used to measure the mass is a calibrated transducer with accuracy down to the tenth of a kilogram, so these measurements are assumed to be accurate. Use of the bifilar pendulum assumes that the two straps are equal in length and hang perfectly vertical, but since visual inspection of the straps shows that neither of these assumptions was valid, the resulting term is likely to be inaccurate.

The modal inversion was shown to have a high fit between the test data and the synthesized response. The highest percent error on any of the modes was 2 %, also indicating a high level of correlation. The result for the mass is high due to the

influence of the airbags, as the upper airbag plate is considered part of the system and is therefore added to the weight. The results seen for the CG appear reasonable; the Y and Z terms should be close to zero, as the hub is symmetrical about those two axes. The X term should be about half a meter, as the test origin was obviously away from the expected CG of the hub. The inertia terms about Y and Z are also fairly close, which was expected due to the symmetry of the hub.

The mass-line inversion was shown to have some oscillations, which indicated that the estimated results would therefore contain error. Although the results are fairly reasonable, they are high for all of the CG and inertia terms. Due to the hub's physical structure, drive point measurements of less-than-ideal quality were obtained at some of the node locations, which adversely affected the accuracy of the results.

31.8 Summary

Two alternative methods to a traditional bifilar or trifilar pendulum test for obtaining mass inertia properties were discussed in this paper. These alternative methods were used to test a nacelle and hub of a Vestas V27 wind turbine that Sandia National Laboratories had installed. Both methods yielded fairly accurate results.

References

1. Bretl J, Conti P (1987) Rigid body mass properties from test data. Proceedings of the 5th international modal analysis conference, IMAC, London, pp 655–659
2. Okuzumi H (1991) Identification of the rigid body characteristics of a powerplant by using experimental obtained transfer functions. Central Engineering Laboratories, Nissan Motor Co., Ltd., June 1991
3. Leurs W, Gielen L, Burghmans M, Dierckx B (1997) Calculation of rigid body properties from FRF data: practical implementation and test cases. Proceedings of the 15th international modal analysis conference, Tokyo
4. Okubo N, Furukawa T (1983) Measurement of rigid body modes for dynamic design. Proceedings of the 2nd IMAC, pp 545–549
5. Bretl J, Conti P (1989) Mount stiffness and inertia properties from modal test data. *J Vib Acoust Stress Reliab* 111(2):134–138
6. Napolitano K, Schlosser M (2011) Calculation of rigid body mass properties of flexible structures. Proceedings of the 29th IMAC, Jacksonville, FL, pp 73–94

Chapter 32

Overview of the Dynamic Characterization at the DOE/SNL SWiFT Wind Facility

Bruce LeBlanc, David Cloutier, and Timothy Marinone

Abstract The Scaled Wind Farm Technology (SWiFT) facility has been developed by Sandia National Laboratories to enable rapid, cost-efficient testing and development of transformative wind energy technology. As part of this effort, ATA Engineering was contracted by SNL to perform component and system level dynamic tests to acquire data for model updating and validation. The component work included modal and mass properties testing of the blades, towers, hubs, and nacelles; while the system level tests included modal tests of each tower mounted on its foundation, and two fully erected turbines, using both impact and wind-excitation. This paper presents an overview of all modal and mass property tests performed to support this project as well as key results used in aeroelastic model development for the modified V27 wind turbines.

Keywords Wind turbines • Wind energy • Turbine-turbine interaction • Model updating • Modal characterization

32.1 Overview of Facility

In the past several years wind energy installations have increased exponentially due to a competitive levelized cost of energy (LCOE) and favorable governmental policy [1]. Modern utility scale wind turbines are very efficient in extracting the available energy within the swept rotor area, approaching near theoretically limited efficiencies for horizontal axis wind turbines. Upon recognizing this, the U.S. Department of Energy (DOE) has begun a focus to study turbine-turbine interaction in order to better quantify the effects of turbine wakes on the power production from wind plants and the life cycle fatigue of turbines. As a part of this effort the DOE has enlisted Sandia National Laboratories (SNL) to develop and operate the Scaled Wind Farm Technology (SWiFT) facility based in Lubbock, Texas shown in Fig. 32.1.

There are multiple research goals of this facility including cost-efficient testing of innovative rotor technologies, and detailed turbine-turbine interaction studies. In support of these goals, it is essential to maintain an accurate simulation capability of the tests performed at SWiFT. This encompasses the development of design level aero-elastic simulation models such as FAST [2], as well as multi-body dynamic analysis, and detailed finite element models of components. In recognizing the importance of detailed component models to overall system performance accuracy, SNL contracted ATA Engineering to characterize each main component and sub-assembly to experimentally determine mass properties and essential modal characteristics. Traditional impact modal tests and naturally excited modal tests were also performed on two fully installed wind turbines. These tests were performed throughout the construction phase of the SWiFT facility, and are described in detail in several works [3–5]. This paper gives a summary of the tests and how they were used to update the models in order to provide accurate simulation capability for future SWiFT testing.

B. LeBlanc (✉)
Sandia National Laboratories, Albuquerque, NM 87111, USA
e-mail: blebla@sandia.gov

D. Cloutier • T. Marinone
ATA Engineering, San Diego, CA 92130, USA



Fig. 32.1 Scaled wind farm technology facility concept (*left*) and completed construction (*right*)

32.2 Turbine Characterization

The main test article is a heavily modified Vestas V27 wind turbine (V27). Originally the V27 was a two-speed collective pitch machine capable of producing 225 kilo-watts (kW) of power. While this was a revolutionary design of the late 1980s, the capabilities needed to be updated to address issues related to modern larger utility scale machines. In order to accomplish this, the turbines were upgraded to fully variable speed, variable pitch machines with power capability of 300 kW. Several major components of the turbines, such as the generator and entire control system, were completely redesigned due to the conversion. The structural changes caused by a new generator modified the mass properties of the turbine. As these properties are fundamental to the system behavior they needed to be measured experimentally. The boundary condition for the entire system, the foundation, was also completely redesigned, and is again crucial to the system performance. The turbine blades were also tested for mass properties and modal characteristics in order to improve the finite element and aeroelastic models of the rotor.

The tests performed on the components, sub-assemblies, and full turbines were:

- Mass properties and modal characteristics of six wind turbine blades
- Mass properties of the rotor hub
- Mass properties of the nacelle
- Free-free modal analysis of each tower
- Modal analysis of each tower mounted to the installed foundation
- Full turbine artificially excited modal analysis of each turbine
- Naturally excited (wind) modal analysis of one turbine

Figures 32.2 and 32.3 show images of the test setups for the components and full turbine characterizations, respectively. Results of the testing are discussed in the following section.

32.3 Model Updating and Correlation

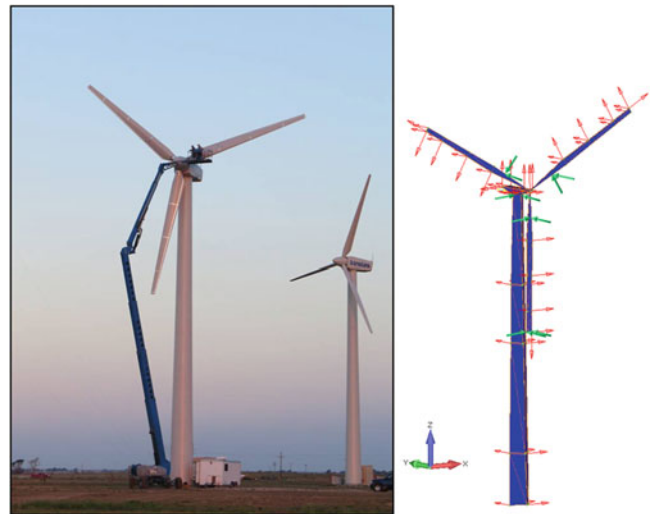
Initial models of each component were developed using available documents and design drawings when available from the manufacturer. Due to the nature of the turbine installed being an older turbine with many variations in product design manufacturing, as well as the known design changes made to the turbines, there were many uncertainties in the model which could lead to poor correlation in future experiments at the SWiFT facility.

The averaged mass properties of the nacelles and hubs were needed for inputs into the aeroelastic and multi-body dynamic analysis codes for correct turbine response and performance predictions. These were estimated by ATA Engineering [5] the results are shown in Table 32.1.



Fig. 32.2 Images of component testing at SWiFT

Fig. 32.3 Image of full turbine modal testing with test display model



Several tests were conducted throughout the measurement campaign on each 13 m turbine blade. A mass properties test and modal analysis test was conducted by ATA Engineering [4], and a static pull test on each blade was conducted by the National Renewable Energy Laboratory (NREL) as a certification criterion for receipt of the wind turbine blades from the supplier. The initial model of the turbine blades far under-predicted the mass and missed the CG location (585 kg, 4.77 m)

Table 32.1 Mass properties of V27 nacelle and hub

| | Nacelle ^a | Hub ^b |
|----------------------------|----------------------|------------------|
| Mass (kg) | 7,007 | 477 |
| CGx (m) | 0.64 | -0.08 |
| CGy (m) | 0.08 | 0.015 |
| CGz (m) | .09 | 0.005 |
| Ixx (kg × m ²) | 2,511 | 69.1 |
| Iyy (kg × m ²) | 10,406 | 76.3 |
| Izz (kg × m ²) | 9,589 | 86.2 |

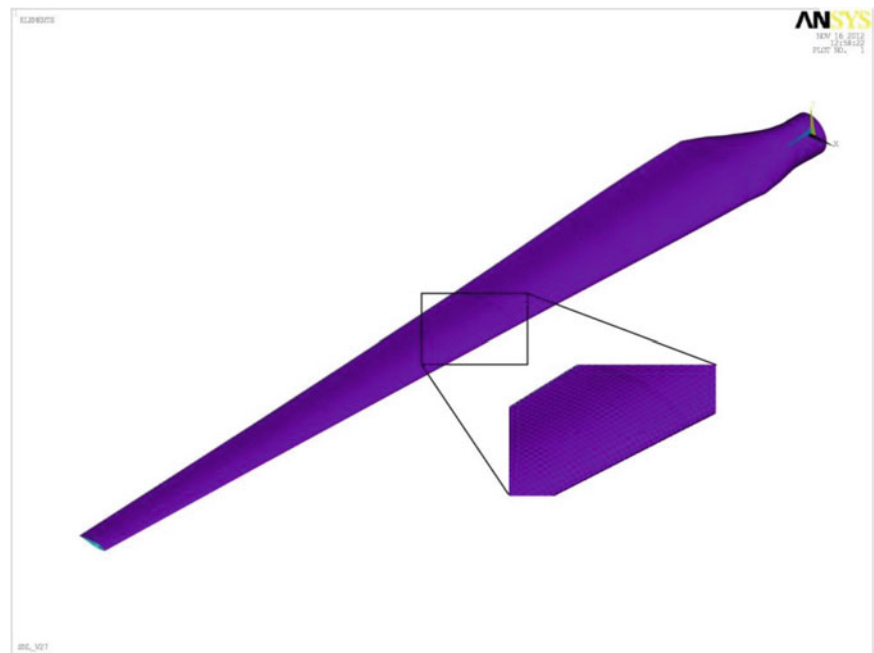
Note: Coordinate systems defined per standard as expressed in [2]

^aNacelle origin defined on center of tower axis and top of yaw bearing

^bHub origin defined at center on the rotor plane

Table 32.2 Blade testing and model results

| | Mass (kg) | CG (m) | 1st Flap (Hz) | 1st Edge (Hz) | 2nd Flap (Hz) |
|----------------------|-----------|--------|---------------|---------------|---------------|
| Model | 641.9 | 4.31 | 4.82 | 10.09 | 12.56 |
| Average experimental | 659.2 | 4.195 | 4.86 | 11.53 | 12.45 |
| Percent difference | -2.63 | 2.74 | -0.8 | -12.5 | 0.9 |

Fig. 32.4 Finite element model of V27 wind turbine blade

and was far off on the static load cases. Details which were not expressly provided by the design documentation, or which were determined to be questionable within the blades were updated, such as fabric thickness, density of infused epoxy, exact material layup etc. were scaled within realistic realms in order to provide good correlation with all collected test data. Table 32.2 displays the resulting blade model properties in comparison with the average of all blade tests. Figure 32.4 shows the finite element shell model of the V27 blade used for model updating. The properties of this updated model were used to create the aeroelastic model to predict system performance.

The turbine towers are 31 m long steel conical tubes weighing approximately 12,000 kg. Each tower was tested in a free-free configuration by resting them on specially designed stands and inflating a set of airbags, shown in Fig. 32.2. The results of the free-free test were used to update the tower properties of the 3D finite element shell model. Results of the free-free calibration are shown in Table 32.3 and the updated tower properties are shown in Table 32.4.

The foundation stiffness is an important parameter to the performance of the turbine which is difficult to measure directly. In order to quantify this stiffness, a modal test was performed with the tower installed on the foundation. A two-dimensional

Table 32.3 Free-Free tower calibration results

| | ANSYS (Hz) | Tower 1 (Hz) | Tower 2 (Hz) | Experimental avg. (Hz) | Difference |
|-------------|------------|--------------|--------------|------------------------|------------|
| 1st Bending | 10.7 | 10.66 | 10.61 | 10.635 | 0.61 % |
| 1st Bending | 10.7 | 10.88 | 10.69 | 10.785 | -0.79 % |
| 2nd Bending | 28.055 | 28.34 | 28.29 | 28.315 | -0.92 % |
| 2nd Bending | 28.055 | 29.1 | 28.8 | 28.95 | -3.09 % |

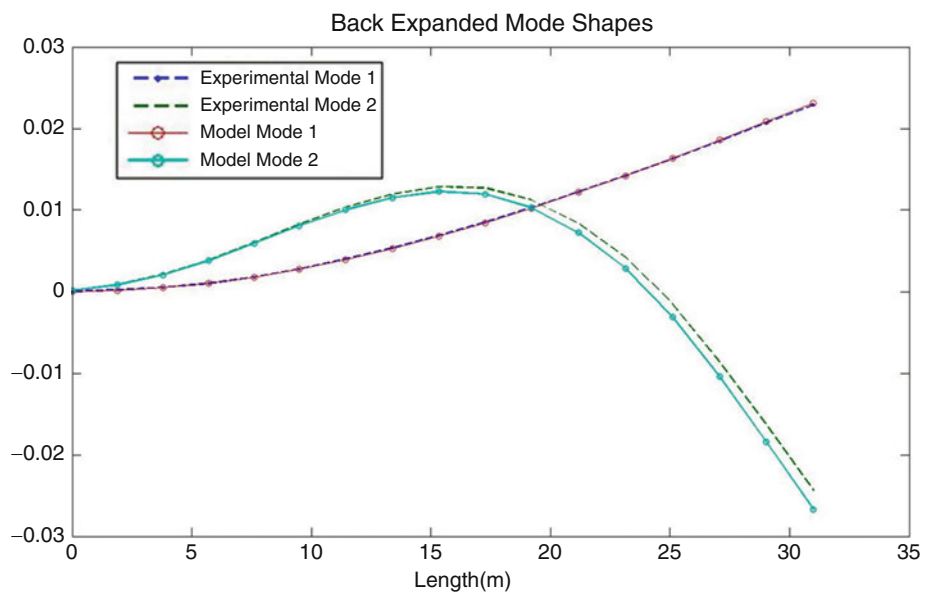
Table 32.4 Updated tower properties

| | |
|----------------------------|------------------------|
| Elastic modulus, GPa | 193.94 (200) |
| Poisson ratio | 0.3 |
| Shear modulus | $\frac{E}{2(1 + \nu)}$ |
| Density, kg/m ³ | 8,713 (7,850) |

Table 32.5 Tower on foundation experimental vs. model correlation

| Mode | Exp (Hz) | Model (Hz) | % Difference | MAC | POC |
|--------|----------|------------|--------------|------|------|
| Mode 1 | 2.68 | 2.67 | -0.3 | 0.99 | 1.0 |
| Mode 2 | 11.55 | 11.92 | 3.2 | 0.98 | 0.99 |

Fig. 32.5 Expanded mode shapes of V27 tower installed on foundation



beam model was created with the updated tower properties in order to represent the foundation as a translational and a rotational spring at the base of the tower. A translational and a rotational spring of 2 GN/m and 13 GN-m/theta, respectively, were added to the already correlated free-free tower model. The order of magnitude of the springs was initially based upon design documentation and typical foundation stiffness for similar turbines.

The experimental frequencies of the first two fore-aft and side-side bending modes were averaged in order to provide a representative 2-D solution for comparative purposes, as there is only a single first and second bending mode (fore-aft and side-side are not distinguishable). The experimental mode shapes of the tower on foundation test were scaled to unit-modal-mass and used for comparison to the tower model with approximated foundation stiffness. The full-space (34 DOF) model was reduced to 5 translational DOF that corresponded to measurement locations of the tower [4] by the System Equivalent Reduction Expansion Process (SEREP) [6], which preserves the target mode shapes and frequencies exactly during the reduction process. A Modal Assurance Criterion (MAC) and a Pseudo-Orthogonality Check (POC) [7] was performed on the experimental and reduced model DOF. The results of the correlation are shown in Table 32.5. For display purposes the experimental shapes were then expanded to full space using the SEREP method, see Fig. 32.5.

The full turbine aeroelastic model was updated to reflect each of the test-correlated finite element models and mass property analyses. The full turbine experimental and natural excitation tests have been used to determine operating frequencies for the newly designed variable-speed variable pitch controller, and will be used for many studies in the future.

32.4 Summary

The Scaled Wind Farm Technology facility has been developed by Sandia National Laboratories to enable rapid, cost efficient design and implementation of innovative rotor technologies for the U.S. Department of Energy. As part of this installation, a series of component and full system finite element and aeroelastic models have been developed to predict performance of the facility. ATA Engineering was contracted to perform characterization testing on components, sub-assemblies, and fully assembled wind turbines. Results of these tests have been used to update open-source models of each component and sub-assemblies. The open-source full turbine aeroelastic model will be used to predict turbine performance at the SWiFT facility during baseline operations, new rotor technology development / design, and turbine-turbine interaction studies.

Acknowledgements Sandia is a multi-program laboratory operated by Sandia Corporation, a Lockheed Martin Company, for the United States Department of Energy's National Nuclear Security Administration under contract DE-AC04-94AL85000.

References

1. U.S. Department of Energy (2013) 2012 Wind technologies market report. U.S. Department of Energy
2. Jonkman J, Buhl M (2005) FAST user's guide. National Renewable Energy Laboratory, Golden
3. Cloutier D, Marinone T, LeBlanc B, Anderson P, Carne T (2014) Artificial and natural excitation testing of SWiFT Vestas V27 wind turbines. Orlando
4. Marinone T, Cloutier D, LeBlanc B (2014) Modal testing and model validation issues of SWiFT turbine tests V27. Orlando
5. Marinone T, Napolitano K, Cloutier D, LeBlanc B (2014) Comparison of multiple mass property estimation techniques on SWiFT Vestas V27 wind turbine nacelles and hubs. Orlando
6. O'Callahan J, Avitabile P, Riemer R (1989) System equivalent reduction expansion process (SEREP). Las Vegas, Seventh International Modal Analysis Conference, Las Vegas, Nevada
7. Allemang R, Brown D (1982) A correlation coefficient for modal vector analysis, Proc. 1st International Modal. Analysis Conference, Orlando, FL

Chapter 33

Artificial and Natural Excitation Testing of SWiFT Vestas V27 Wind Turbines

Timothy Marinone, David Cloutier, Bruce LeBlanc, Thomas Carne, and Palle Andersen

Abstract The Scaled Wind Farm Technology facility has been developed by Sandia National Laboratories to enable rapid, cost-efficient testing and development of transformative wind energy technology. As part of this effort, ATA Engineering was contracted by Sandia to perform modal testing on multiple fully assembled wind turbines to gain a better understanding of the structures.

This paper presents the results obtained from experimental modal analysis and operational modal analysis performed on Vestas V27 wind turbines recently installed at the Scaled Wind Farm Technology facility. Experimental modal results are compared between two identical wind turbines, identifying variability in both components and boundary conditions. Additionally, operational modal analysis was used on a single parked wind turbine under natural wind excitation. The operational modal results compare well to the results obtained from a conventional impact modal survey, providing promising results for future testing on larger turbines where measured external excitation may not be feasible.

Keywords Wind turbines • Operational modal analysis • Stochastic subspace identification • Experimental modal characterization • Modal parameter estimation

33.1 Introduction

Sandia National Laboratories (SNL) is developing the Scaled Wind Farm Technology (SWiFT) facility to enable rapid, cost-efficient testing and development of transformative wind energy technology. The site is intended to study complex turbine wake interactions and focus on damage mitigation, improved power performance, and recommended future site layouts. Since this site is designed to be open source and to provide data to all interested parties, the models must be accurate enough to be used for the desired analyses while preserving Vestas' proprietary information. For this paper, two Vestas V27 (V27) wind turbines installed on site were tested to obtain modal properties for the validation of analysis models.

Sandia is a multiprogram laboratory operated by Sandia Corporation, a Lockheed Martin Company, for the U.S. Department of Energy under Contract DE-AC04-94AL85000.

T. Marinone • D. Cloutier (✉)
ATA Engineering, San Diego, CA 92130, USA
e-mail: dave.cloutier@ata-e.com

B. LeBlanc
Sandia National Laboratories, Albuquerque, NM 87185, USA

T. Carne
MannaTech Engineering, Bozeman, MT 59715, USA

P. Andersen
Structural Vibration Solutions A/S, Aalborg East, Denmark

Experimental modal analysis (EMA) was performed on several components and two fully assembled SWiFT Vestas V27 wind turbines. In addition to modal testing performed on the full turbines, operational modal analysis (OMA) was performed on a turbine with the blades parked, using the wind as a source of natural excitation. While the SWiFT V27 turbines are of a size where reasonable excitation can be imparted to the structure using a modal impact sledge, determining OMA limitations with respect to EMA provides greater insight for future testing of larger turbines. During construction and assembly of the wind farm, ATA Engineering, Inc., (ATA) was contracted to perform modal testing on the blades, hubs, nacelles, and towers in the free-free configuration and installed on the concrete foundations, as well as two fully assembled turbines. As instrumentation was already installed from the modal survey, time histories were recorded with rotors locked during periods of higher wind when modal testing could not be performed. These time histories were used in Structural Vibration Solutions' Ambient Response Testing and Modal Identification (ARTEMIS) Modal software to extract modal parameters for comparison to the experimental modal results.

The use of natural excitation to extract modal parameters has been shown to be a valid approach for many large structures. The natural excitation technique (NExT) was initially conceived in the 1980s for use on wind turbines. NExT has been successfully performed on several vertical axis wind turbines [1, 2] and shown to be a valid alternative to experimental modal analysis; both Polyreference and Eigensystem Realization algorithms were used as time-domain modal identification on auto- and cross-correlation functions computed from measured time histories.

Further development in OMA has led to additional techniques for use in civil, aerospace, and the automotive industries, where traditional modal testing may be impractical or too expensive. Frequency Domain Decomposition (FDD) [3, 4] and Stochastic Subspace Identification (SSI) are two common algorithms for extracting modal parameters. Both techniques have additional variations for improving modal extraction. In general, FDD uses a singular value decomposition of the power spectral density, in which the mode shapes are estimated as the singular vectors at each peak. SSI is a more sophisticated time-domain algorithm using a linear least-squares estimation of the model; with this approach, the full measured time histories are used. The limiting constraint with all techniques is the assumption that the test article is excited by steady-state random white noise across the frequency band of interest, which is a valid assumption in the case of a parked wind turbine.

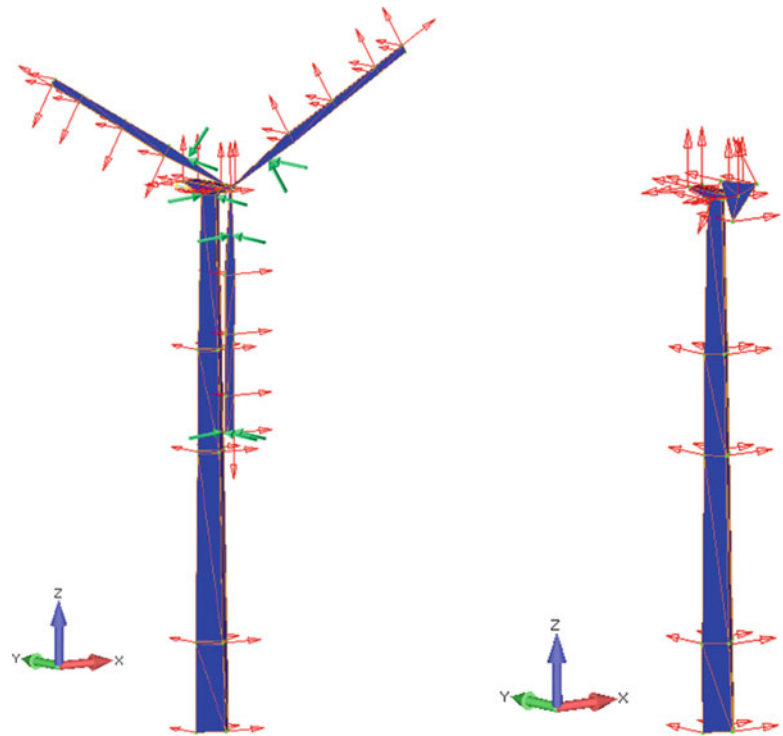
33.2 Test Article and Data Collection

Three Vestas V27 225 kW wind turbines were recently installed at the Sandia National Laboratories (SNL) Scaled Wind Farm Technology (SWiFT) facility hosted at Texas Tech University in Lubbock, Texas. The turbines are heavily instrumented and modified variable-speed, variable-pitch V27 turbines. The two turbines shown in the middle and right side of Fig. 33.1 are funded by the Department of Energy's Office of Energy Efficiency and Renewable Energy and are named SNL1 and SNL2, with SNL1 located on the right. The third turbine, shown in the left of Fig. 33.1, was installed by Vestas R&D of Houston.



Fig. 33.1 SWiFT Vestas V27 wind farm at Texas Tech University in Lubbock, Texas

Fig. 33.2 Test display models for SNL1 (*left*) and SNL2 (*right*). *Green arrows* represent excitation locations



The SNL1 turbine was fully instrumented with 80 PCB T333B modal accelerometers installed on the blades, hub, nacelle, and tower, in addition to six seismic accelerometers on the foundation. Figure 33.2 shows the test display model with instrumentation locations. All accelerometers installed on the tower, nacelle, and hub were installed internally and could be accessed by the ladder mounted to the tower. Accelerometers installed externally on the blades could only be accessed by aerial lift. Both experimental modal analysis and operational modal analysis was performed on SNL1.

Due to high winds and limited test time, on SNL2 a reduced set of instrumentation was installed and only experimental modal testing was performed. This reduced set included 41 accelerometers installed in the tower, nacelle, and hub, which matched locations on SNL1, and single biaxial accelerometers on each blade located near the maximum chord location, as shown in the right of Fig. 33.2.

The wind speed significantly increased from morning to afternoon, so modal testing was limited to the early morning to reduce the effects of unmeasured excitation. Impact modal testing was performed with a modal sledge at locations indicated by the green arrows in Fig. 33.2. Approximately 6–8 averages were acquired at each impact location, using a sampling frequency of 80 Hz and a block size of 2,056. Figure 33.3 shows a picture of the modal test being performed on SNL1.

Operational data was collected at 80 Hz for approximately 2 h, with wind speeds around 14 m/s. The rotors were yawed approximately parallel to the wind direction, with the blades pitched to zero degrees. This configuration provided adequate excitation to the blades in both the edgewise and flapwise directions, as the flapwise modes are in general more easily excited.

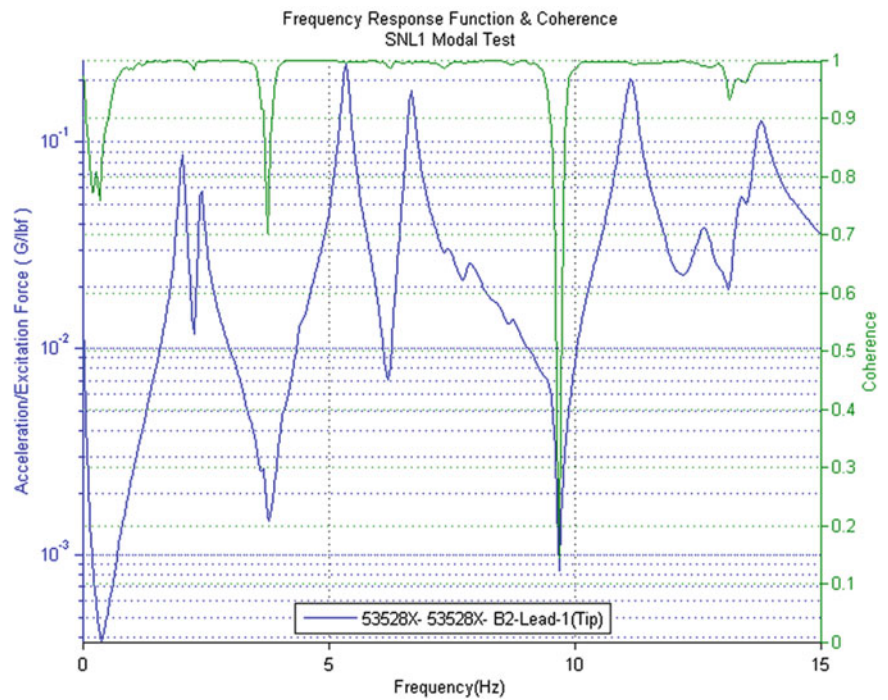
33.3 Test Results

While the modal testing was performed early in the mornings to minimize the unmeasured excitation to the structure from the wind, a noticeable amount of excitation was still present at the low wind speeds of approximately 4 m/s. However, in spite of the unmeasured excitation, the overall coherence levels were still high for the majority of rotor accelerometers. Figure 33.4 presents the drive point frequency response function (FRF) and coherence overlay for excitation at the blade tip of SNL1 (indicated in Fig. 33.2), showing good coherence across the frequency band of interest.

Fig. 33.3 Impact modal testing performed on SNL1



Fig. 33.4 Drive point FRF and coherence from impact on SNL1 blade tip



ATA Engineering’s AFPoly™ was used to extract modal parameters from the impact modal survey. Twenty modes were extracted in the 0–15 Hz frequency band. The synthesized power spectrum mode-indicator function (PSMIF) in Fig. 33.5 shows an overall good fit of the modal parameters. A test-analysis model (TAM) was made for back-expansion of the mode shapes for better visualization, providing an estimation of shape information to missing DOF; the back-expanded first three blade flapwise bending modes are shown in Fig. 33.6.

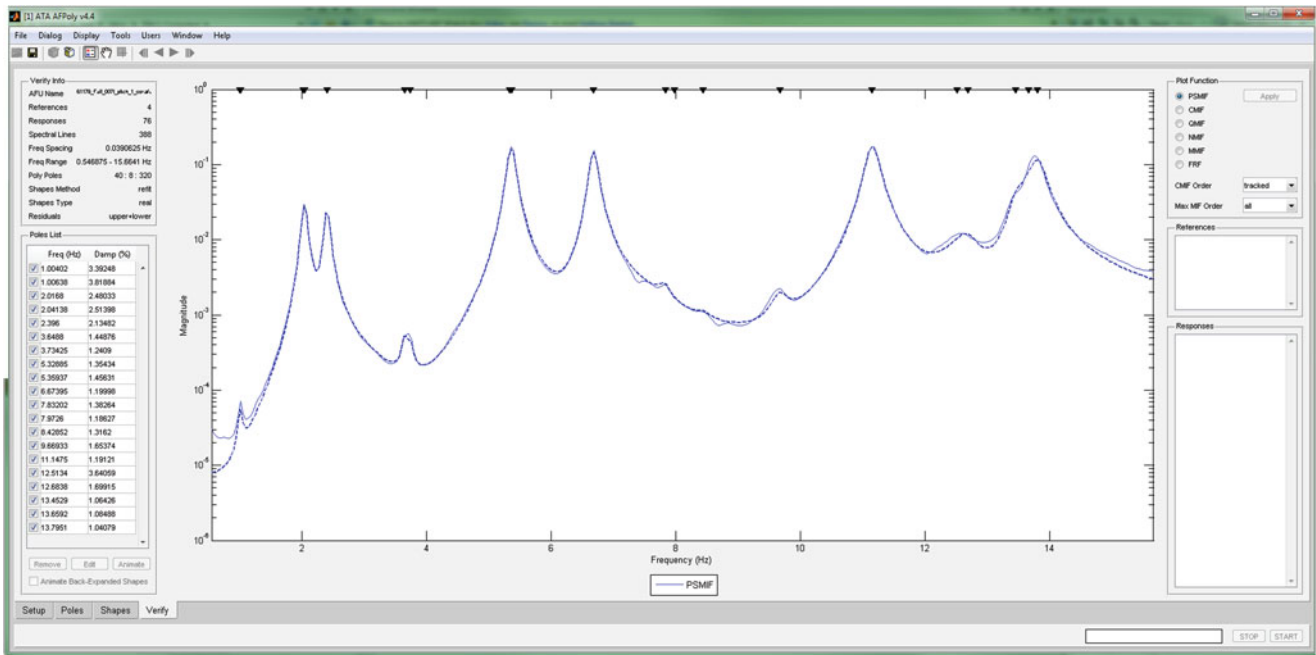


Fig. 33.5 PSMIF overlay from fitted modal parameters

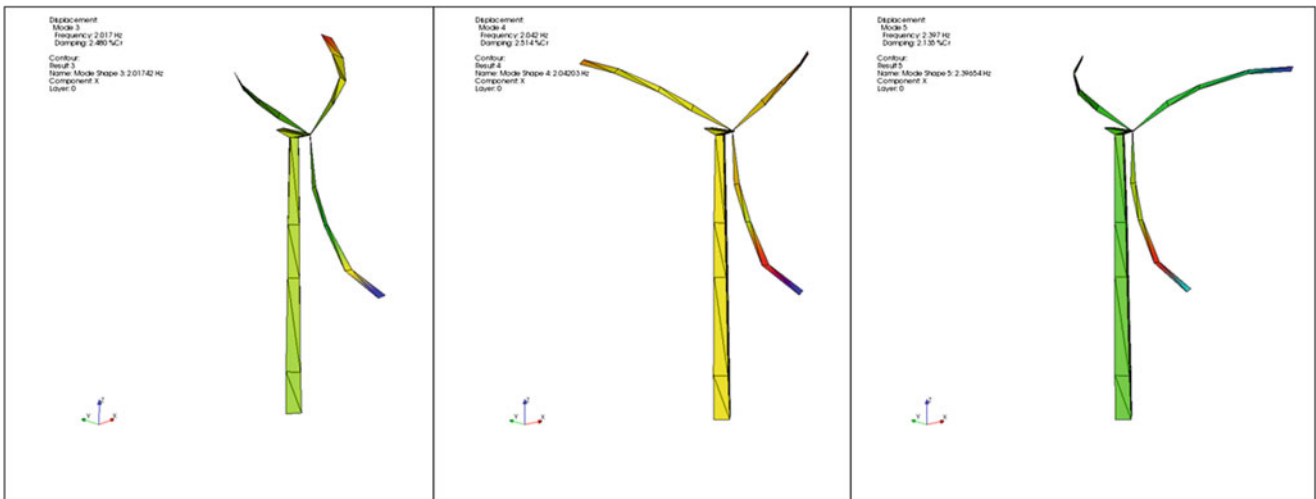


Fig. 33.6 First three flapwise bending modes

As the modal survey on SNL2 had a significantly reduced sensor set on the rotors, not all modes in the 0–15 Hz range could be easily identified. To compare modes between SNL1 and SNL2, a combination of frequency, MAC at the reduced sensor set, and comparing PSMIFs at the reduced sensor set were all used. Also, not all modes could be extracted or verified to correlate between the two turbines. The final comparison of modes between SNL1 and SNL2 is given in Table 33.1. An average of less than 2 % frequency difference exists across all matched modes.

Using wind as natural excitation to the turbine with the rotors parked, operational modal analysis was performed to extract modal parameters. The same instrumentation set used for the impact modal survey was used to collect time histories during the day, when wind speeds were at approximately 14 m/s. During this testing, the rotors were parked approximately parallel to the wind direction, which allowed for better excitation of the edgewise bending modes. Approximately 2 h of continuous data was measured for the operational modal extraction. Figure 33.7 provides some example time histories for instrumentation on the blades, showing sufficient excitation.

Table 33.1 Mode comparison between SNL1 and SNL2

| Mode | SNL1 | | SNL2 | | Diff (%) | MAC | Description |
|------|----------------|-------------------|----------------|-------------------|----------|-----|---|
| | Frequency (Hz) | Damping (% Crit.) | Frequency (Hz) | Damping (% Crit.) | | | |
| 1 | 1.00 | 3.39 | 0.97 | 2.66 | -3% | 96 | 1st Tower Bending Edgewise |
| 2 | 1.01 | 3.82 | 0.99 | 2.95 | -2% | 83 | 1st Tower Bending Flapwise |
| 3 | 2.02 | 2.48 | 1.88 | 2.87 | -7% | 68 | 1st Blade Flapwise Bending - Asym |
| 4 | 2.04 | 2.51 | 2.00 | 2.36 | -2% | 50 | 1st Blade Flapwise Bending - Asym |
| 5 | 2.40 | 2.13 | 2.37 | 1.59 | -1% | 82 | 1st Blade Flapwise Bending - Sym |
| 6 | 3.65 | 1.45 | | | | | 1st Blade Edgewise Bending - Asym |
| 7 | 3.73 | 1.24 | 3.75 | 0.01 | 0% | 32 | 1st Blade Edgewise Bending - Asym |
| 8 | 5.33 | 1.35 | 5.05 | 1.96 | -5% | 76 | 2nd Blade Flapwise Bending - Asym |
| 9 | 5.36 | 1.46 | 5.34 | 1.26 | 0% | 68 | 2nd Blade Flapwise Bending - Asym |
| 10 | 6.67 | 1.20 | 6.70 | 0.98 | 0% | 88 | 2nd Blade Flapwise Bending - Sym |
| 11 | 7.83 | 1.38 | 7.76 | 1.18 | -1% | 90 | 2nd Tower Bending Flapwise |
| 12 | 7.97 | 1.19 | 7.99 | 1.52 | 0% | 85 | 2nd Tower Bending Edgewise |
| 13 | 8.43 | 1.32 | 8.34 | 0.80 | -1% | 89 | 1st Tower Torsion, 2nd Blade Edgewise Bending |
| 14 | 9.67 | 1.65 | 9.99 | 1.64 | 3% | 73 | 2nd Blade Edgewise Bending - Sym |
| 15 | 11.15 | 1.19 | 11.12 | 1.29 | 0% | 83 | 3rd Blade Flapwise Bending - Asym |
| 16 | 12.52 | 3.64 | | | | | 3rd Blade Flapwise Bending-Asym |
| 17 | 12.69 | 1.70 | 12.17 | 2.68 | -4% | 84 | 2nd Blade Edgewise Bending - Asym / 3rd Blade Flap - Asym |
| 18 | 13.45 | 1.06 | 13.22 | 1.11 | -2% | 71 | 2nd Blade Edgewise Bending - Asym |
| 19 | 13.66 | 1.08 | 13.82 | 1.98 | 1% | 66 | 2nd Blade Edgewise Bending - Asym / 3rd Blade Flap -Sym |
| 20 | 13.80 | 1.04 | | | | | 3rd Blade Flapwise Bending-Sym |

The time histories recorded on SNL1 were then used in Structural Vibration Solutions' ARTeMIS software. ARTeMIS has several modal parameter extraction algorithms, which were all investigated with the data. The Crystal Clear Canonical Variate Analysis Stochastic Subspace Identification (SSI-CVA) and the Crystal Clear Unweighted Principal Components Stochastic Subspace Identification (SSI-UPC) were shown to extract a significantly greater number of modes than the other SSI and FDD algorithms available. In the 0–15 Hz frequency band of interest, 18 modes were extracted with the SSI-CVA and 22 modes were extracted with the SSI-UPC algorithm. The stability diagram for the Crystal Clear SSI-CVA algorithm is shown in Fig. 33.8, and the stability diagram for the Crystal Clear SSI-UPC is shown in Fig. 33.9.

A MAC was used to compare the modes extracted using OMA to the EMA-extracted modes. Out of the all the modes extracted in ARTeMIS, 18 modes correlated to the EMA modes. Table 33.2 lists the comparisons between the EMA and OMA results on SNL1 and shows that none of the 18 modes correlated had a frequency difference greater than 3 %. In addition, several of the modes correlated had damping differences of less than 20 %, indicating very high-quality modal parameters estimated with both techniques. While the SSI-CVA and SSI-UPC yielded similar results, the best set was compiled for the final comparison between EMA and OMA.

The first two tower bending modes have poor MAC values between the EMA and OMA shape. These modes were visually examined and determined to be similar, though bending in slightly different directions and accordingly yielding poor MAC values. The complete MAC table between the EMA and OMA is provided in Table 33.3.

Using OMA to obtain modal properties of large structures such as wind turbines has several advantages. Imparting large measured external excitation can be a difficult, time-consuming, and expensive task. In addition, these structures may be in an environment where unmeasured external excitation is significant, making it difficult to take high-quality measurements using traditional modal methods. With the test presented in this paper, natural wind excitation was present, and there was little time when the wind was at a minimal speed acceptable for performing an impact modal survey. The higher wind speeds during

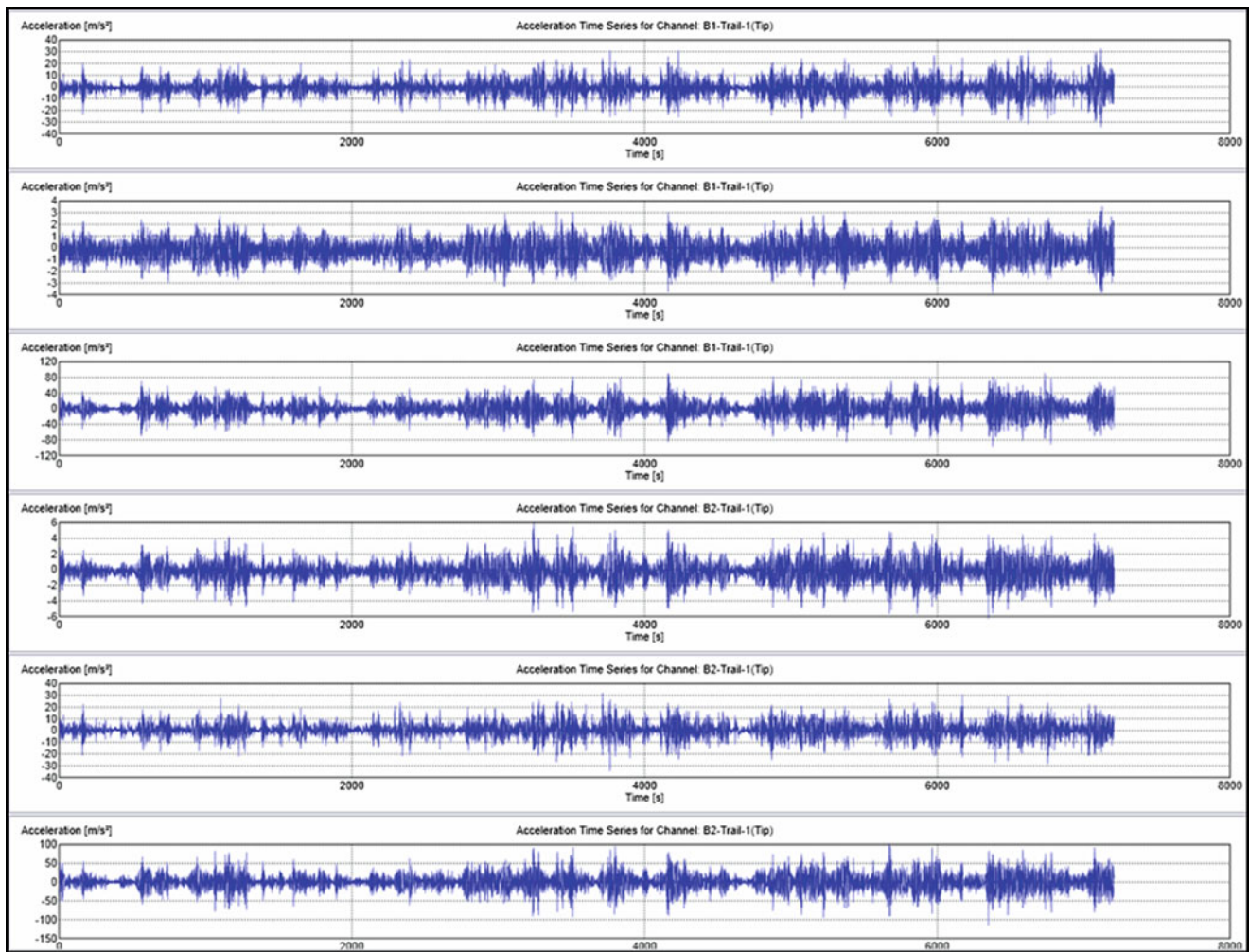


Fig. 33.7 Example time histories collected using natural wind excitation

the majority of the day made modal testing impossible not only because of the wind excitation producing more response in the structure than the modal impact sledge but also because of safety limitations of using a personnel lift at that height. With OMA, once instrumentation was installed, data collection could happen over the course of several hours to several days with minimal support.

33.4 Summary

ATA Engineering was contracted by SNL to perform modal testing on components and assemblies of two Vestas V27 wind turbines at the SWiFT facility in Lubbock, Texas. Modal testing was performed on two full turbines, and frequencies, damping, and shapes were shown to correlate, although with minor differences between the turbines. This paper also demonstrated that natural wind excitation is sufficient to excite the majority of modes of a parked V27 wind turbine up to 15 Hz. Using SVS's ARTEMIS software, 18 modes were highly correlated to the experimental modal results on the SNL turbine.

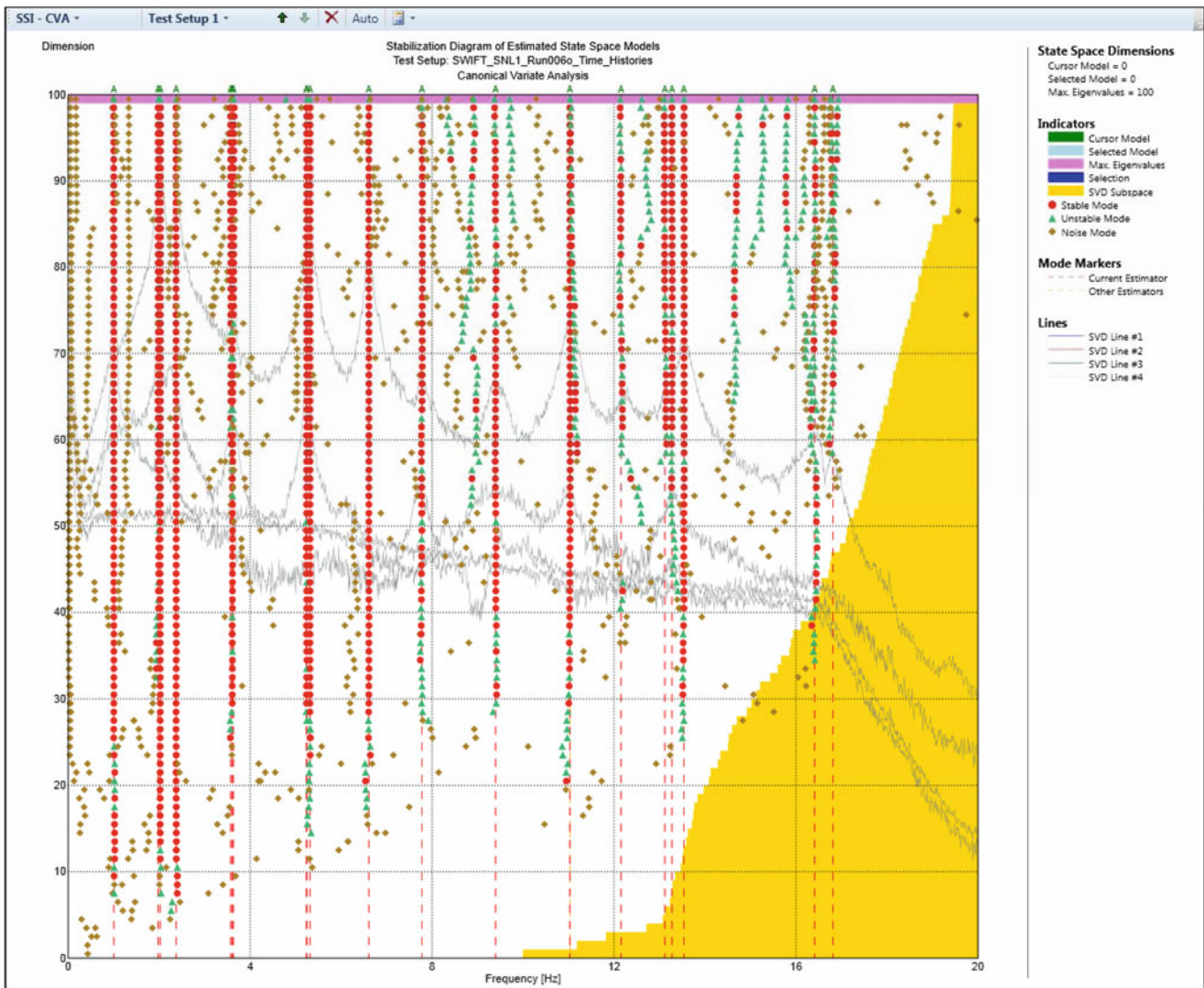


Fig. 33.8 Stability diagram in ARTeMIS for the SSI-CVA algorithm

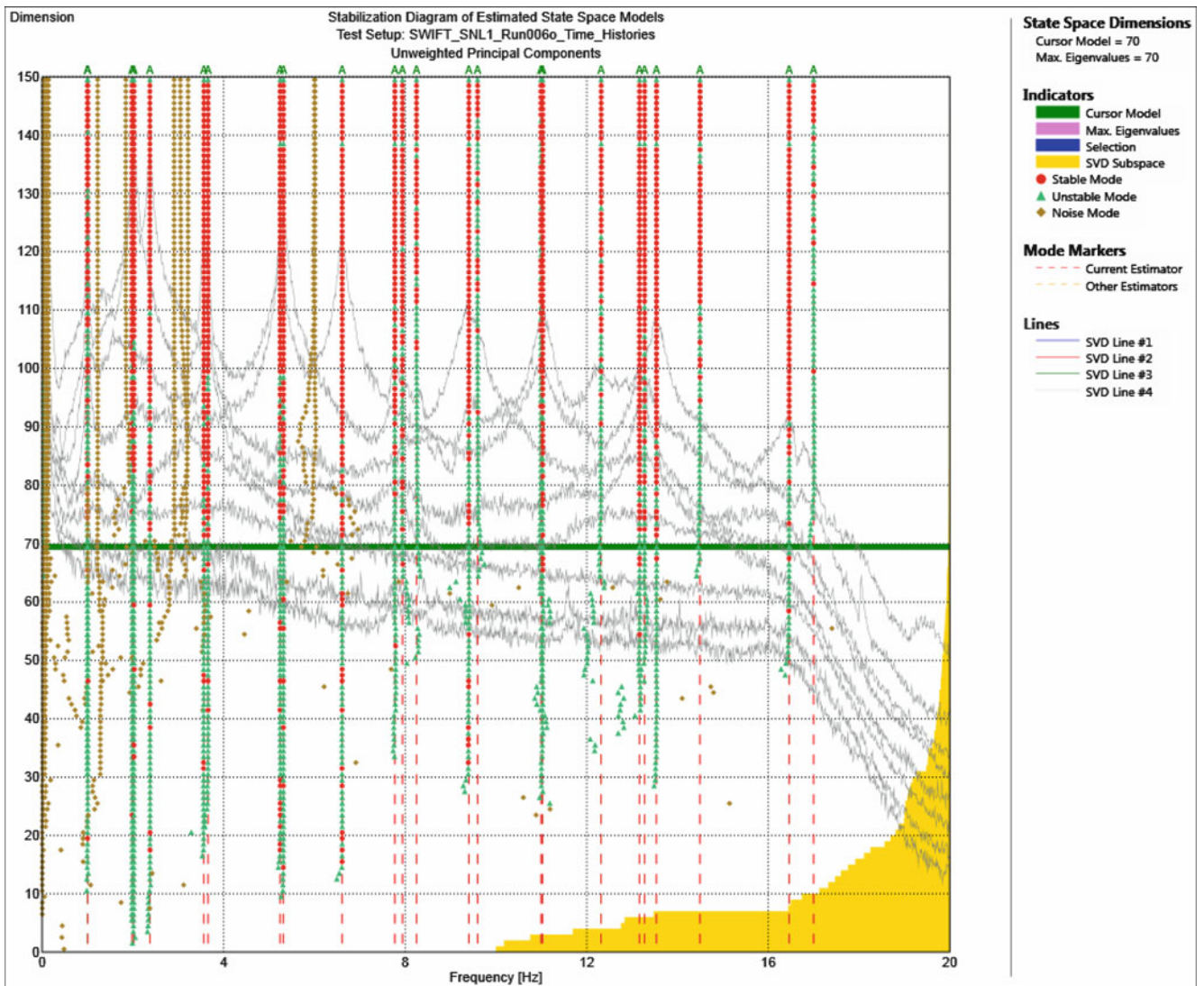


Fig. 33.9 Stability diagram in ARTeMIS for the SSI-UPC algorithm

Table 33.2 Mode comparisons between EMA and OMA of SNL1

| Mode | SNL1 - EMA | | SNL1 - OMA | | | Frequency Diff (%) | Damping Diff (%) | MAC | Description |
|------|----------------|-------------------|----------------|-------------------|---------------|--------------------|------------------|-----|---|
| | Frequency (Hz) | Damping (% Crit.) | Frequency (Hz) | Damping (% Crit.) | OMA Algorithm | | | | |
| 1 | 1.00 | 3.39 | 1.00 | 0.90 | UPC | -1% | -116% | 51 | 1st Tower Bending Edgewise |
| 2 | 1.01 | 3.82 | 1.00 | 0.14 | UPC | 0% | -186% | 64 | 1st Tower Bending Flapwise |
| 3 | 2.02 | 2.48 | 1.98 | 2.73 | CVA | -2% | 10% | 85 | 1st Blade Flapwise Bending - Asym |
| 4 | 2.04 | 2.51 | 2.02 | 2.33 | CVA | -1% | -8% | 98 | 1st Blade Flapwise Bending - Asym |
| 5 | 2.40 | 2.13 | 2.37 | 1.89 | CVA | -1% | -12% | 100 | 1st Blade Flapwise Bending - Sym |
| 6 | 3.65 | 1.45 | 3.57 | 1.02 | CVA | -2% | -35% | 96 | 1st Blade Edgewise Bending - Asym |
| 7 | 3.73 | 1.24 | 3.65 | 0.79 | UPC | -2% | -44% | 97 | 1st Blade Edgewise Bending - Asym |
| 8 | 5.33 | 1.35 | 5.24 | 1.43 | CVA | -2% | 5% | 92 | 2nd Blade Flapwise Bending - Asym |
| 9 | 5.36 | 1.46 | 5.32 | 1.27 | CVA | -1% | -14% | 94 | 2nd Blade Flapwise Bending - Asym |
| 10 | 6.67 | 1.20 | 6.61 | 1.04 | CVA | -1% | -14% | 100 | 2nd Blade Flapwise Bending - Sym |
| 11 | 7.83 | 1.38 | 7.78 | 1.27 | CVA | -1% | -8% | 99 | 2nd Tower Bending Flapwise |
| 12 | 7.97 | 1.19 | 7.94 | 1.11 | UPC | 0% | -7% | 78 | 2nd Tower Bending Edgewise |
| 13 | 8.43 | 1.32 | 8.25 | 1.95 | UPC | -2% | 39% | 95 | 1st Tower Torsion, 2nd Blade Edgewise Bending |
| 14 | 9.67 | 1.65 | 9.40 | 2.09 | CVA | -3% | 23% | 96 | 2nd Blade Edgewise Bending - Sym |
| 15 | 11.15 | 1.19 | 11.03 | 1.14 | CVA | -1% | -4% | 100 | 3rd Blade Flapwise Bending - Asym |
| 16 | 12.52 | 3.64 | | | | | | | 3rd Blade Flapwise Bending - Asym |
| 17 | 12.69 | 1.70 | 12.32 | 3.44 | UPC | -3% | 68% | 91 | 2nd Blade Edgewise Bending - Asym / 3rd Blade Flap - Asym |
| 18 | 13.45 | 1.06 | 13.12 | 1.08 | CVA | -3% | 1% | 98 | 2nd Blade Edgewise Bending - Asym |
| 19 | 13.66 | 1.08 | | | | | | | 2nd Blade Edgewise Bending - Asym / 3rd Blade Flap -Sym |
| 20 | 13.80 | 1.04 | 13.54 | 1.11 | CVA | -2% | 6% | 97 | 3rd Blade Flapwise Bending -Sym |

Table 33.3 MAC comparing modes between EMA and OMA on SNL1

| EMA/OMA Cross MAC Table | | | | | | | | | | | | | | | | | | | | | | |
|-------------------------|-----|------------|------|------|------|------|------|------|------|------|------|------|------|------|------|-------|-------|-------|-------|-------|-------|------|
| | | EMA Shapes | | | | | | | | | | | | | | | | | | | | |
| | | 1 | 2 | 3 | 4 | 5 | 6 | 7 | 8 | 9 | 10 | 11 | 12 | 13 | 14 | 15 | 16 | 17 | 18 | 19 | 20 | |
| OMA Shapes | MAC | 1.00 | 1.01 | 2.02 | 2.04 | 2.40 | 3.65 | 3.73 | 5.33 | 5.36 | 6.67 | 7.83 | 7.97 | 8.43 | 9.67 | 11.15 | 12.52 | 12.69 | 13.45 | 13.66 | 13.80 | |
| | 1 | 1.00 | 0.51 | | | | 0.26 | | | | | | | | | | | | | | | |
| | 2 | 1.00 | | 0.64 | | | 0.43 | | | | | | | | | | | | | | | |
| | 3 | 1.98 | | | 0.85 | | | | | 0.24 | | | | | 0.25 | | | 0.25 | 0.22 | | | |
| | 4 | 2.02 | | | 0.41 | 0.98 | | | | 0.22 | 0.47 | | 0.25 | | | 0.34 | | | | | | |
| | 5 | 2.37 | | 0.23 | | | 1.00 | | | | | 0.54 | | | | | | | | | 0.21 | 0.26 |
| | 6 | 3.57 | | | | | | 0.96 | | | | | | | | | | | | 0.25 | | |
| | 7 | 3.65 | | | | | | | 0.97 | | | | | | | | | | | | | |
| | 8 | 5.24 | | | | | | | | 0.92 | | 0.36 | | 0.46 | | | | | 0.41 | | | |
| | 9 | 5.32 | | | 0.32 | 0.51 | | | | 0.21 | 0.94 | 0.43 | | | | 0.55 | 0.24 | | | | | |
| | 10 | 6.61 | | | | | 0.54 | | | | | 1.00 | | | | | | | | | 0.44 | 0.54 |
| | 11 | 7.78 | | | | 0.31 | | | | 0.51 | 0.30 | 0.99 | | | | 0.64 | | | | | | |
| | 12 | 7.94 | | | | | | | | | | | 0.78 | | | | | | | | | |
| | 13 | 8.25 | | | 0.21 | | | | | 0.21 | 0.27 | | | | 0.95 | | | 0.54 | 0.32 | | | |
| | 14 | 9.40 | | | | | | | | | | | | | | 0.96 | | | | | | |
| | 15 | 11.03 | | | | 0.36 | | | | 0.31 | 0.42 | 0.61 | | | | 1.00 | | | | | | |
| | 16 | 12.32 | | | | | | | | 0.23 | | | | | 0.47 | | | 0.85 | 0.91 | | | |
| | 17 | 13.12 | | | | | | 0.26 | | | | | | | | | | | | 0.98 | | |
| | 18 | 13.54 | | | | | 0.28 | | | | | 0.58 | | | | | | | | | 0.80 | 0.97 |

References

1. James GH, Carne TG, Lauffer JP, Nord AR (1992) Modal testing using natural excitation. In: Proceedings of the 10th international modal analysis conference (IMAC), San Diego, pp 1209–1216
2. Carne TG, James GH (2010) The inception of OMA in the development of modal testing technology for wind turbines. *Mech Syst Signal Process* 24:1213–1226
3. Brinker R, Andersen P, Zhang L (2000) Modal identification from ambient responses using frequency domain decomposition. In: Proceedings of the 18th international modal analysis conference (IMAC), San Antonio, pp 625–630
4. Brinker R, Zhang L, Andersen P (2001) Modal identification of output-only systems using frequency domain decomposition. *Smart Mater Struct* 10:441–445

Chapter 34

Effects of Boundary Conditions on the Structural Dynamics of Wind Turbine Blades—Part 1: Flapwise Modes

Javad Baqersad, Christopher Niezrecki, and Peter Avitabile

Abstract Mode shapes and resonant frequencies of an individual wind turbine blade can be readily determined in either a laboratory or a blade test facility using experimental modal analysis. However, performing a modal test on a utility-scale wind turbine with several blades attached to a tower can be a challenge due to the number of sensors required, the size of these structures, the time required for testing, and cost. Therefore, understanding the influence of the coupled three-bladed turbine/tower system and identifying a correlation between the dynamic behavior of an assembled wind turbine to an individual blade or three-bladed turbine attached to a hub while disconnected from the tower is desirable. In this paper, which is the first part of a two-part paper, the influence of boundary conditions on flapwise mode shapes and resonant frequencies of wind turbine blades are numerically studied using a finite element beam analysis (a similar study was performed on edgewise modes of the turbine and is presented in the second part of this paper). In the current paper, translational and rotational springs are mounted to the hub of a three-bladed turbine and the sensitivity of dynamic characteristics (natural frequencies and mode shapes) to variations in the spring constants are investigated. Then, a model is developed of the three-bladed turbine installed on a tower and the dynamic characteristics of the assembly are compared to the three-bladed turbine with a free-free or fixed boundary condition at the hub. Furthermore, the mode contribution matrix of the assembled wind turbine is used to identify the necessary set of modal vectors of the tower and three-bladed turbine to accurately obtain the dynamic behavior of the final assembly. Many flapwise mode shapes of the assembled three-bladed wind turbine can be estimated by applying a fixed condition for a single blade (or a three-bladed turbine) instead of using a free-free boundary condition.

Keywords Blade • Wind turbine • Boundary condition • Tower • Mode contribution

34.1 Introduction

In recent years, there has been growing interest in wind power as one of the major resources of clean renewable energy. Modern horizontal axis wind turbines (HAWTs) have continually grown in size to meet increasing energy demands while reducing the cost of energy compared to fossil fuels. As the size of these machines increases, wind turbines are subjected to a combination of increased static and dynamic loading that has an impact on their performance, efficiency, and reliability. The excessive capital investment of large sized HAWTs makes health monitoring and damage prognosis of these machines important. In order to predict their performance and diagnose a healthy state of operation, it is important to have validated numerical models of these structures. Likewise, an expansion algorithm in conjunction with a finite element model can be used to augment the limited set of operating measured data at sensor locations and predict the full-field dynamic strain in rotating wind turbines. A validated model of the wind turbine assembled to a tower is an essential part of the expansion algorithm. However, performing an experimental modal test on a utility-scale wind turbine is very challenging. Therefore, the work performed in the current paper is an attempt to verify how the mode shapes of a single cantilever blade or a three-bladed wind turbine correlate with the mode shapes of the wind turbine attached to a tower.

J. Baqersad (✉) • C. Niezrecki • P. Avitabile
Structural Dynamics and Acoustic Systems Laboratory, One University Avenue, Lowell, MA 01854, USA
e-mail: javad_baqersad@student.uml.edu

Researchers have developed several methods to model the dynamic behavior of wind turbines. From a theoretical point of view, the dynamics of rotating structures such as wind turbines and helicopter rotors have been modeled using multi-body dynamics approaches [1–8], modal analyses [9, 10] and finite element analyses [11–20].

The multi-body method uses several rigid and flexible elements to replicate the dynamic behavior of structures. While masses and springs are integral parts of multi-body systems, beams, and flexible elements are used in the hybrid multi-body models. The method is capable of modeling linear as well as non-linear [1, 6, 7] dynamics of structures. Multi-body models of wind turbines are usually so complex that they require some commercial codes such as MSC.ADAMS™ and MBDyn™ to analyze the problem [1, 2, 5].

Modal analysis or the mode superposition method is typically used for reduced order models and can represent the linear dynamics of a wind turbine at a reduced set of points that are selected for the analysis [9, 10]. The FAST (Fatigue, Aerodynamic, Structures, and Turbulence) code, which uses modal superposition analysis to study the dynamic behavior of wind turbines, has been employed in several papers for validation purposes [5, 7].

FE beam elements have traditionally been used for modeling rotating blades [11, 12]. Using beam elements for dynamic analysis is so efficient that some codes such as BModes and DYMORE have recently been developed based upon this method [2, 13]. A combination of finite element and modal analysis methods has also been used in the literature [14]. Three-dimensional (3D) solid finite element models represent the full detailed dynamics of wind turbines along with their dynamic stress and strain; however, they are computationally expensive. Because solid FE models of blade assemblies have a significant number of elements (10^5 – 10^6 degrees of freedom) and are computationally intensive, these models have been typically used for studying only single blades or towers of wind turbine [17–20].

All the previously mentioned theoretical modeling approaches can represent the dynamic behavior of wind turbines; however, experimental validation remains a challenge. Experimental set-ups to perform the modal analysis of an individual blade can be readily conducted in either a laboratory or a blade test facility. Thus, numerous researchers have performed experimental modal analysis on single blades [21–26]. However, the sheer size of three-bladed wind turbines makes the modal analysis of the entire structures very challenging. Thus, having a comprehensive understanding of the dynamic characteristics of wind turbines, identifying the effects of boundary conditions on modes of a three-bladed turbine, and correlating the dynamic behavior of a three-bladed wind turbine assembly to modes of individual blades are desirable.

Yang et al. [27] showed that some modes of the wind turbine assembly occur at frequencies close to the frequencies of the cantilevered blade. Griffith et al. [28] suggested a novel mixed boundary condition for experimental modal testing of an individual blade. They proposed a test rig which was composed of a seismic mass on the top of an airbag to represent a mixture of free-free and fixed boundary conditions. Despite numerous studies on wind turbine dynamics, little information can be found in the literature about classifications of modes of three-bladed turbines and effects of support stiffness on the modes. In addition, comparisons of the mode shapes of the wind turbine to single blades have not been quantified in previous studies.

In the current study, a finite element beam model of a wind turbine blade is developed and used to study the effects of boundary conditions on the flapwise mode shapes of a three-bladed assembly. The paper aims to investigate correlations between the modes of the blades on the wind turbine assembly to the modes of the individual blades. Additionally, a classification of the flapwise modes of a wind turbine is presented. The current work, which is the first part of a two-part paper, focuses on the flapwise modes of the turbine. A companion paper (Part 2) studies the effects of boundary conditions on the edgewise modes.

34.2 Theoretical Background

34.2.1 Modal Assurance Criterion

The modal assurance criterion (MAC) [29] is a tool for quantifying the correlation between two vectors at all degrees of freedom. The MAC is given by:

$$\text{MAC}_{ij} = \frac{\left[\{u_i\}^T \{u_j\} \right]^2}{\left[\{u_i\}^T \{u_i\} \right] \left[\{u_j\}^T \{u_j\} \right]} \quad (34.1)$$

where u_i and u_j are displacement vectors of the modes i and j respectively. MAC values close to 1.0 indicate strong similarity between vectors, where values close to 0.0 indicate minimal or no similarity. The MAC values are typically presented in percent (0–100). The MAC values are typically calculated for the vectors with the same length.

In some parts of the current work, however, the correlation between a component and a component of an entire assembly is desirable. For instance, the correlation between the mode shapes of an individual blade, and a single blade in a three-bladed wind turbine assembly is desirable. The number of degrees of freedom for the mode vectors of the single blade and the three-bladed turbine are different. In these cases, only the displacements of the nodes that existed in both parts are paired up and used in the MAC calculations. Therefore, in order to compare a single blade to one of the blades in the assembly, the single blade displacement is overlaid to a blade in the assembly and only the displacements of nodes that are paired up contribute in the MAC.

34.2.2 Mode Contribution Identification

The mode contribution matrix is used to identify the contributions of component modes in the assembled system modes. Based on the structural dynamic modification theory:

$$[U_2] = \begin{bmatrix} [U_1^A] \\ [U_1^B] \end{bmatrix} [U_{12}] \quad (34.2)$$

where $[U_1^A]$ and $[U_1^B]$ are respectively the mode shapes of component A and B before assembly which are organized into a partitioned matrix, $[U_2]$ represents the mode shapes of assembled system. $[U_{12}]$ is mode contribution matrix which can be used to obtain the modes of an assembly system by using modes of unmodified components. On the other hand, the mode contribution matrix ($[U_{12}]$) indicates which modes of components are more critical to obtain the modes of the assembly.

The mode contribution matrix can be determined using the following equation [30]:

$$[U_{12}] = \begin{bmatrix} [U_1^A] \\ [U_1^B] \end{bmatrix}^T [M_2] [U_2] \quad (34.3)$$

where $[M_2]$ is the assembled system mass matrix (the subscript “2” indicates that the mass matrix of the assembly was used in the equation whereas the subscript 1 indicates that it is the mass of just one component and not of the three assembled components). The matrix can also be extracted by applying structural dynamic modification theory which essentially leads to the same results as Eq. (34.3). However, in the current paper, Eq. (34.3) is used to extract $[U_{12}]$.

34.3 Model Description and Cases Studied

In order to study effects of boundary conditions on wind turbine blades, seven cases are examined in the current work. A flowchart of the work that was completed in the paper is shown in Fig. 34.1.

In the current work, all finite element models were developed using ABAQUS [31]. However, model modifications, mode shape correlations, and matrix multiplications were performed using MATLAB [32].

34.3.1 Case 1: Modeling a 3D Wind Turbine Blade Using Beam Elements

In order to investigate the dynamic characteristics of a wind turbine, a solid element model of the Skystream 4.7™ from Southwest Windpower was initially developed in ABAQUS using the CAD model provided by the manufacturer. The solid finite element model is shown in Fig. 34.2. An extensive description of the finite element modeling and material properties of the blade along with the correlation of the solid models to the experimental measurements can be found in the references [23, 33]. A solid element model can be used to study deformations or to extract stress and strain in the blade; however, using the solid model with numerous DOFs for the study of boundary conditions would be very computationally expensive. Furthermore, in the solid model, due to complexity of the geometry, modes that are essentially flapwise may show small

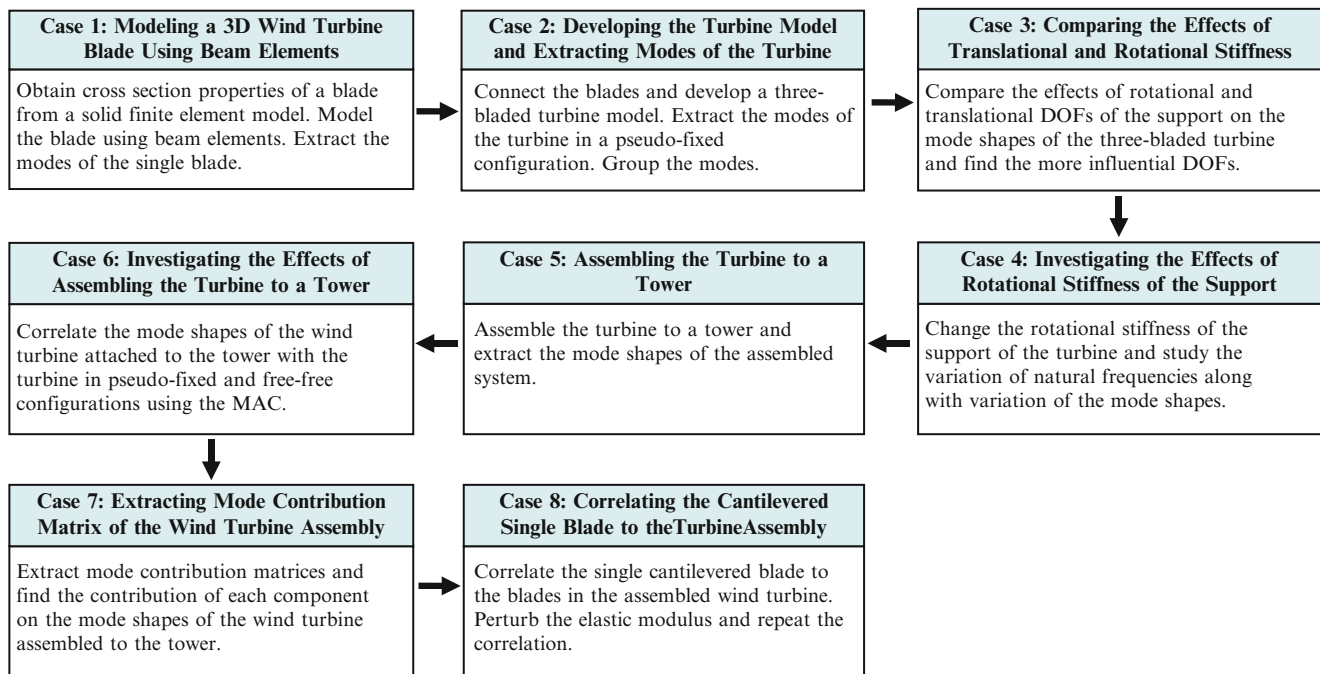


Fig. 34.1 A flowchart of the work that was performed in the current paper

Fig. 34.2 The solid element model of the Southwest Windpower Skystream 4.7™ blade



deformations in the edgewise direction. This issue may create some difficulties when one wants to interpret whether a mode of the three-bladed turbine is flapwise or edgewise; whereas in this paper, the model is used as a sample for the study and the model does not necessarily need to exactly replicate the blade. Due to the mentioned concerns, a blade model composed of 3D beam elements was used for the current study. It should be noted that based on the previous studies mentioned in the literature [11–14, 23], using beam elements to study dynamics of wind turbine blades did not degrade the results when they were compared to other theoretical and solid element models.

To develop a FE beam model, a straight beam with four different cross sections was created with the total length and weight equivalent to the original solid blade (see Fig. 34.3). While the solid model had over 100,000 DOFs, the beam model was a much simpler representation of the blade with 600 DOFs. Reducing the number of DOFs leads to significant computational savings. To accurately obtain the cross section properties of each part of the beam model, cross section properties of the blade on the corresponding length were measured from the solid model. The cross section properties of the desired length were averaged and assigned to the beam model. Therefore, a small inconsistency between the solid model and the beam model might exist that can be attributed to the averaging that was performed on cross sections. The accuracy of the beam model to represent the dynamics of the blade was verified by comparing the mode shapes of the beam model to the solid model in free-free and cantilevered configurations.

The cantilevered boundary condition is a common configuration in which the wind turbine blades are tested in laboratories and test facilities. The mode shapes of the individual blade in this configuration are correlated to the three-bladed turbine in the following sections to quantify the change of the mode shapes in the turbine model. To create the cantilevered boundary condition for the individual blade, the foremost node of the FE beam model was fixed; the same nodes of three blades were

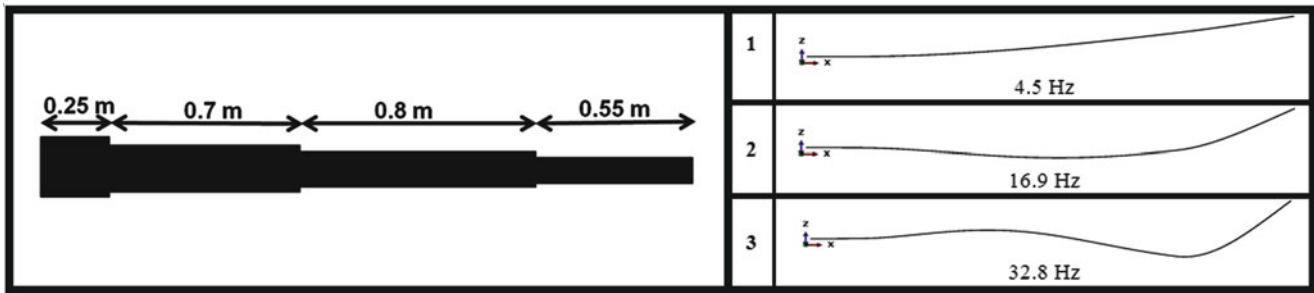


Fig. 34.3 A schematic of the beam model with four different cross sections emulating the Skstream blade and flapwise natural frequencies and mode shapes of the model in a cantilevered boundary condition (below 40 Hz)

used to develop the three-bladed turbine. An eigenvalue solution was performed on the model in a cantilevered configuration in order to extract the mode shapes of the individual cantilever blade (see Fig. 34.3). The coordinate system of the single blade is denoted by xyz with the origin at the center of rotation in which the x and y axes are located in the turbine blades' rotating plane and x -axis points toward the blade tip. Thus, z displacement of the blade shows the out-of-plane or flapwise bending and y axis represents the edgewise or in plane bending. As shown in Fig. 34.3, the cantilever blade contains three flapwise modes below 40 Hz (the modes in this frequency span were selected for the current study).

34.3.2 Case 2: Developing the Turbine Model and Extracting Modes of the Turbine in a Pseudo-Fixed Configuration

The three-bladed turbine model consists of three blades that are oriented 120° apart. Three single blade models of the blade needs to be joined together to develop the three-bladed turbine model. Comparing the material properties and thickness of the hub to the blades, the hub has a significantly higher stiffness (blades were made of plastic with elastic modulus of 15.8 GPa; hub consisted of a very thick cast aluminum part with elastic modulus of 72.4 GPa, and a steel plate with elastic modulus of 180 GPa). Accordingly, after arranging the blades in the appropriate positions to shape the three-bladed model, the translational and rotational DOFs of the root nodes of the single blades were completely tied together creating a rigid connection. The blade of the turbine which is aligned to the x -axis is called Blade 1. Blades 2 and 3 are oriented in a counterclockwise direction looking from positive z axis.

An eigensolution was performed on the turbine model in a pseudo-fixed configuration. The model was called "pseudo-fixed" because the rotation at the center of the hub was not fully constrained. If a fully fixed condition is provided for the center point, i.e. setting the rotational DOFs of the center to zero, each blade deforms like an individual cantilevered blade without any interaction to the other blades. As the modes of the three-bladed assembly with interactions among the blades were targeted, the pseudo-fixed condition rather than the fully fixed condition was used for the analysis.

All the nine flapwise mode shapes and their corresponding natural frequencies (below 40 Hz) are shown in Fig. 34.4. It can be seen that for modes 3, 6, and 9 all the three blades of the turbine have the same phase; they are called *umbrella* or *collective* type mode shapes. However, for some mode shapes, the blades do not have the same phase; they are called *differential* modes. Because higher order modes show a similar dynamic behavior to low order modes (e.g. higher order modes also are in groups of three and they can be categorized into differential and collective modes), only the first nine flapwise modes of the turbine (below 40 Hz) are shown.

Figure 34.4 also shows that each trio of modes contain repeated roots (i.e. have similar natural frequencies). By comparing the mode shapes, it can be inferred that each set of three modes of the three-bladed turbine have very similar natural frequencies. Therefore, modes of the three-bladed turbine can be categorized in groups of three.

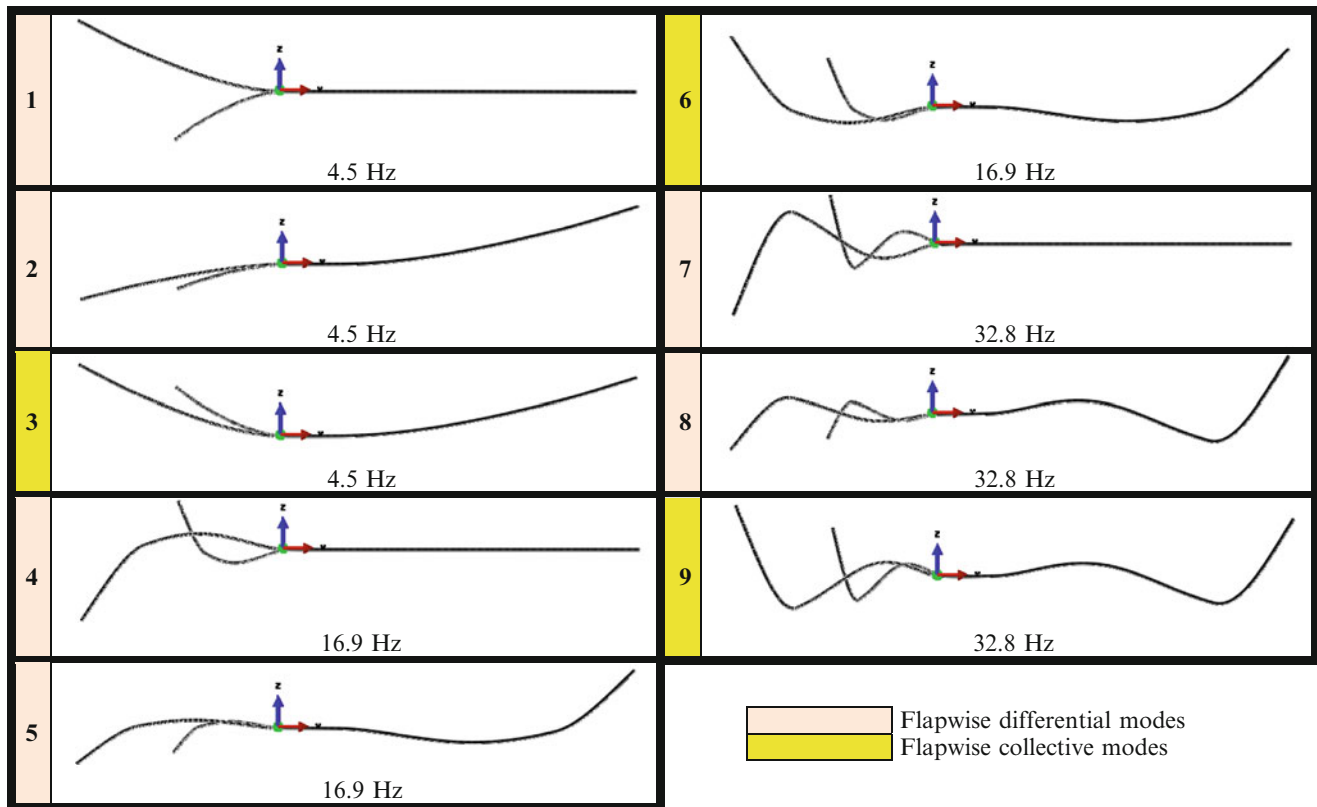


Fig. 34.4 Flapwise mode shapes and resonant frequencies of the turbine (below 40 Hz) in a pseudo-fixed configuration

34.3.3 Case 3: Comparing the Effects of Translational and Rotational Stiffness of the Support on the Modes of the Turbine

This case aims to show how the translational and rotational DOFs of the support are changing the dynamics of the three-bladed turbine. Therefore, the wind turbine is provided with three different boundary conditions. The first model which is used as a reference model is the free-free configuration. In the second configuration, the translational DOFs of the three-bladed turbine center were fixed, which is called a “hinged model”. In the third model, the hinged model was provided with three stiff rotational springs at the center creating a pseudo-fixed model. On the other hand, in the hinged model, there was no translational displacement at the center of the hub. Whereas, in the pseudo-fixed model, in addition to providing zero translational displacements at the center, the center of the blade is restricted from rotation by using very stiff springs.

The modes of the turbine in the hinged and pseudo-fixed boundary conditions are compared to the reference model that is in a free-free configuration using the MAC and the percent differences in natural frequencies (see Tables 34.1 and 34.2). As shown in Table 34.1, by providing a hinged boundary condition at the three-bladed turbine center, apart from collective modes (modes 3, 6, and 9) which experience some changes, the other modes retain their shapes. However, the pseudo-fixed configuration has made noticeable changes to the differential modes of the three-bladed turbine. The changes are considerable both in frequencies and in mode shapes.

As can be seen from Table 34.2, the rotational stiffness of the support can significantly change the differential modes (that represent approximately 2/3 of the flapwise modes) both in natural frequencies and mode shapes. However, constraining the translational DOFs of the support slightly changes the collective modes (see Table 34.1). Therefore, in the following sections of the current work, a more detailed study on the change of modes due to variation in the rotational stiffness of the support is performed.

Table 34.1 The modes of the turbine in a hinged boundary condition compared to the modes of the turbine in a free-free configuration (collective modes are shaded in yellow)

| Mode | Free-Free Wind Turbine | Hinged Wind Turbine | Correlation | |
|------|------------------------|---------------------|-------------------------|-----|
| | Frequency (Hz) | Frequency (Hz) | Frequency Deviation (%) | MAC |
| 1 | 0 | 0 | 0 | N/A |
| 2 | 0 | 0 | 0 | N/A |
| 3 | 5.4 | 4.5 | 17 | 93 |
| 4 | 10.0 | 10.0 | 0 | 100 |
| 5 | 10.0 | 10.0 | 0 | 100 |
| 6 | 19.3 | 16.9 | 12 | 93 |
| 7 | 24.3 | 24.3 | 0 | 100 |
| 8 | 24.3 | 24.3 | 0 | 100 |
| 9 | 37.4 | 32.8 | 12 | 90 |

Table 34.2 The modes of the turbine in a pseudo-fixed boundary condition compared to the modes of the turbine in a free-free configuration (collective modes are shaded in yellow)




| Mode | Free-Free Wind Turbine | Pseudo-Fixed Wind Turbine | Correlation | |
|------|------------------------|---------------------------|--------------------------|-----|
| | Frequency (Hz) | Frequency (Hz) | Frequency Difference (%) | MAC |
| 1 | 0 | 4.5 | - | 71 |
| 2 | 0 | 4.5 | - | 71 |
| 3 | 5.4 | 4.5 | 17 | 93 |
| 4 | 10.0 | 16.9 | 69 | 73 |
| 5 | 10.0 | 16.9 | 69 | 73 |
| 6 | 19.3 | 16.9 | 12 | 93 |
| 7 | 24.3 | 32.8 | 35 | 75 |
| 8 | 24.3 | 32.8 | 35 | 75 |
| 9 | 37.4 | 32.8 | 12 | 90 |

34.3.4 Case 4: Investigating the Effects of Rotational Stiffness of the Support on Flapwise Modes

In this section, a hinged wind turbine was used to examine the effects of adding rotational stiffness to the support. Two torsion springs were attached to the central node of the turbine. The springs can provide resistance to the out of plane rotation of the turbine. In this study, the stiffness of the torsion springs was increased and the variation of natural frequencies and mode shapes were studied.

Table 34.3 shows the change of natural frequencies of the three-bladed turbine due to an increase of rotational stiffness of the support. In the first model of Table 34.3 ($k_t = 0$), no rotational stiffness was considered; this model resembles a hinged boundary condition. The other columns show the variations of natural frequencies when different rotational stiffness for the support was considered. The final model (i.e. the last column of Table 34.3) shows the wind turbine in a pseudo-fixed condition. As can be seen, adding the rotational stiffness has a pronounced effect on the differential modes of the three-bladed turbine, while the collective modes remain essentially unaffected. The table shows that by adding the rotational stiffness of the support, the natural frequencies of the differential modes increase to approach their corresponding collective modes. Furthermore, as the torsion stiffness increases, the rigid body modes (mode 1 and 2) convert to differential flexible modes (i.e. 4.5 Hz).

Table 34.3 Effects of rotational stiffness of the support on the resonant frequencies of the hinged three-bladed turbine (collective modes are shaded in yellow)

| |  |  | | | | | |  |
|--------|---|---|----------------------|----------------------|----------------------|----------------------|----------------------|---|
| Mode # | $k_t=0$ | $k_t=5E2$ (N/rad) | $k_t=1E3$ (N/rad) | $k_t=5E3$ (N/rad) | $k_t=1E4$ (N/rad) | $k_t=1E5$ (N/rad) | $k_t=1E6$ (N/rad) | $k_t=1E8$ (N/rad) |
| 1 | 0 | 1.1 | 1.5 | 2.8 | 3.4 | 4.4 | 4.5 | 4.5 |
| 2 | 0 | 1.1 | 1.5 | 2.8 | 3.4 | 4.4 | 4.5 | 4.5 |
| 3 | 4.5 | 4.5 | 4.5 | 4.5 | 4.5 | 4.5 | 4.5 | 4.5 |
| 4 | 10 | 10.1 | 10.3 | 11.4 | 12.5 | 16.0 | 16.8 | 16.9 |
| 5 | 10 | 10.1 | 10.3 | 11.4 | 12.5 | 16.0 | 16.8 | 16.9 |
| 6 | 16.9 | 16.9 | 16.9 | 16.9 | 16.9 | 16.9 | 16.9 | 16.9 |
| 7 | 24.3 | 24.4 | 24.4 | 25.0 | 25.8 | 30.6 | 32.5 | 32.8 |
| 8 | 24.3 | 24.4 | 24.4 | 25.0 | 25.8 | 30.6 | 32.5 | 32.8 |
| 9 | 32.8 | 32.8 | 32.8 | 32.8 | 32.8 | 32.8 | 32.8 | 32.8 |

k_{tx} : Rotational stiffness in x-direction; k_{ty} : Rotational stiffness in y-direction; $k_{tx} = k_{ty} = k_t$

Figure 34.5 shows the change of the mode shapes as the rotation stiffness of the support changes. As can be seen, for a collective mode for a boundary condition with any rotational stiffness, each blade of the three-bladed turbine deforms similarly to the shape of a cantilevered single blade. However, the differential mode shapes change with an increase in the rotational stiffness. For the high stiffness case, the blades of the three-bladed turbine have approximately a zero slope at the blade root, similar to cantilevered beams.

34.3.5 Case 5: Assembling the Turbine to a Tower

In the previous section, the effects of support stiffness on the dynamic characteristics of the three-bladed turbine were investigated. In the current section, the effects of attaching the three-bladed turbine to a tower are studied. By mounting the three-bladed turbine to a tower, not only the stiffness of the support changes but also a set of new modes will be added to the system. In order to investigate the effects of adding a typical tower, the turbine was mounted to a 10.2-m monopole tower. The tower material properties were found from the webpage of the manufacturer [34]. The first three mode shapes of the tower in a cantilevered condition are shown in Fig. 34.6. It should be noted that in order to consider the mass effects of the equipment including a generator, nacelle, and hub, a 53 kg point mass (an estimate weight for the equipment extracted from the company webpage) was added to the tower tip. The rotational inertia of the equipment was not considered in the current study and will not change the outcomes of the trends and observations made in this work.

After attaching the three-bladed turbine to the tower, an eigensolution was performed on the model. The flapwise modes of the assembly are shown in Fig. 34.7. A point mass of 53 kg was already installed at the tip of the tower to compensate the mass of the equipment; however, adding the blades to the tower imposed the mass of the blades to the tip of the tower and decreased the natural frequencies of tower modes. Because nine flapwise modes of the three-bladed turbine (below 40 Hz) were targeted and studied in the previous sections, only the modes of the tower that are less than 40 Hz are shown.

34.3.6 Case 6: Investigating the Effects of Assembling the Turbine to a Tower

In an effort to verify how the mode shapes of the assembly correlate with the three-bladed turbine, the modal assurance criterion was used to compare mode shapes of the free-free three-bladed turbine (i.e. the reference model) to mode shapes of the turbine mounted to the tower. Figure 34.8 compares the assembled system to the multi-blade turbine in a free-free configuration. It can be seen that collective modes of the turbine (modes 3, 5, 9 of the free-free wind turbine) show a strong

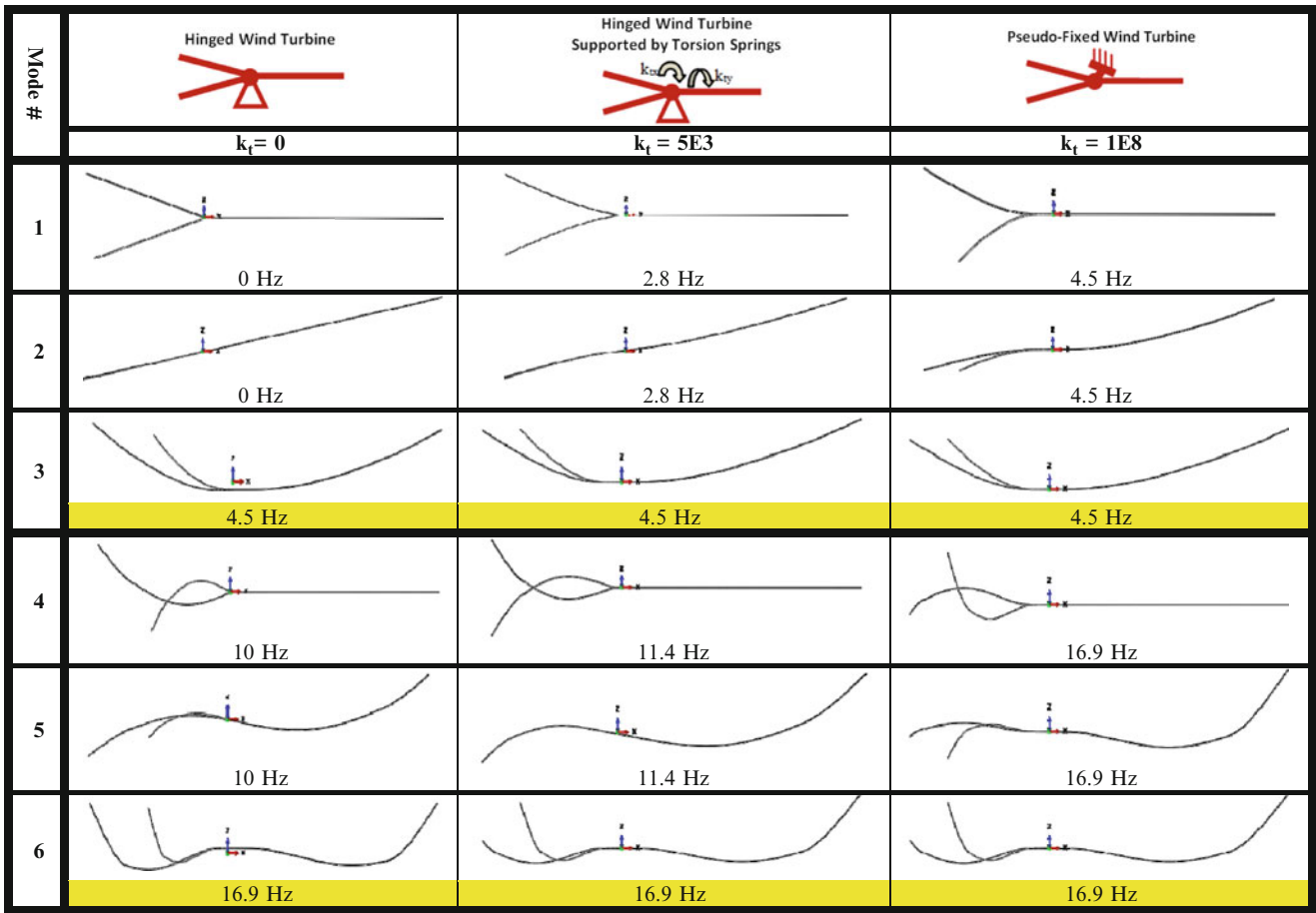
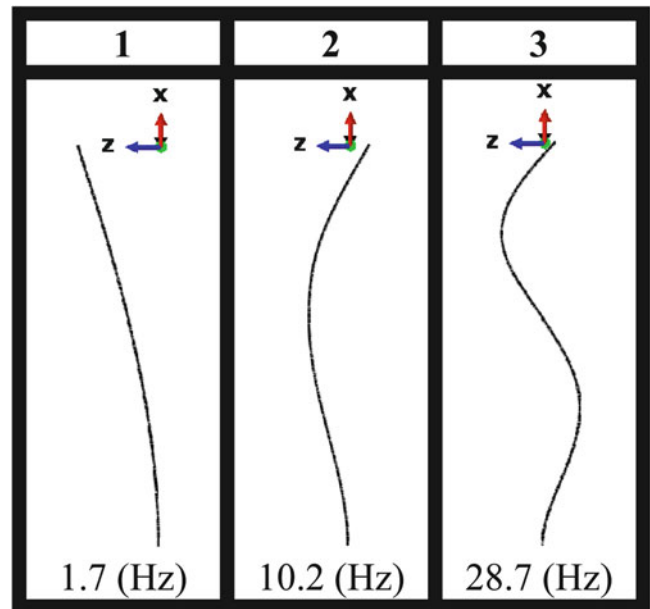


Fig. 34.5 Effects of rotational stiffness of the support on the flapwise modes of the turbine (collective modes are shaded in yellow)

Fig. 34.6 First three flapwise mode shapes and resonant frequencies of the tower with the tip mass



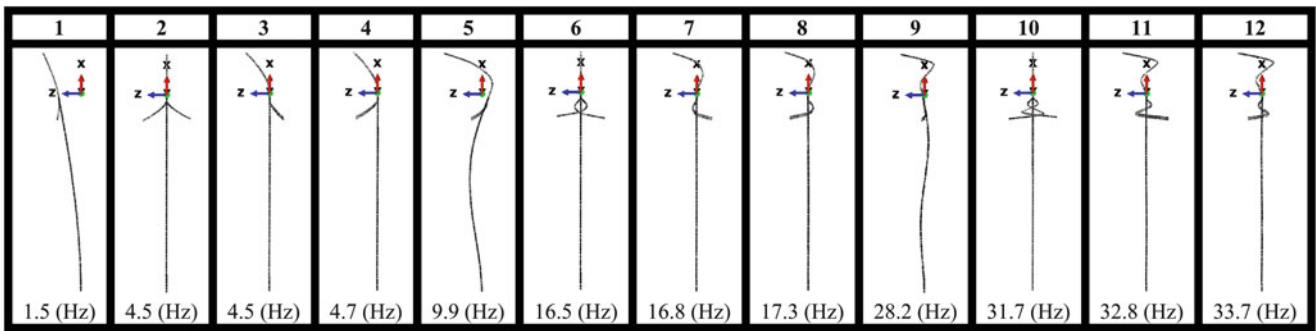


Fig. 34.7 Flapwise mode shapes and resonant frequencies of the wind turbine assembly

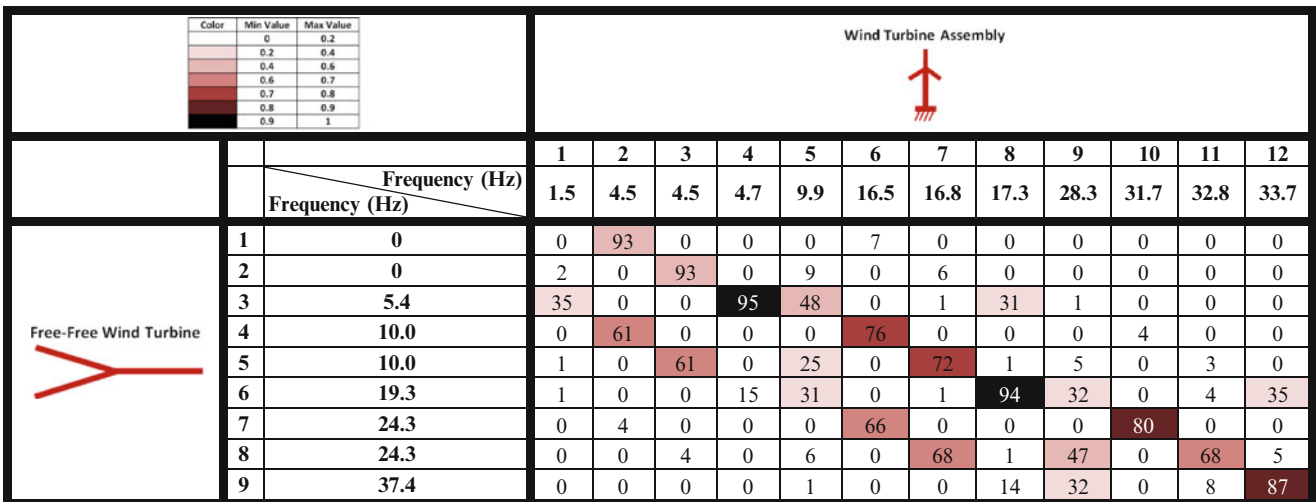


Fig. 34.8 MAC for comparing the flapwise modes of the wind turbine assembly to the flapwise modes of the turbine in a free-free condition

correlation to the modes of the assembly (modes 4, 8, and 12 of the wind turbine assembly). However, the differential modes do not show strong correlations.

In another effort to establish the correlation between the wind turbine assembly and the three-bladed turbine, the pseudo-fixed turbine was overlaid with the turbine model that was attached to the tower. The MAC comparison of the mode shapes of these models are shown in Fig. 34.9. As can be seen, apart from the modes that occur at the frequencies close to the modes of the tower, all the modes of the three-bladed turbine show a strong correlation with the three-bladed system in pseudo-fixed configurations. The modes of the assembly that show a strong correlation to the three-bladed turbine are called turbine-originated modes. Likewise, modes with low correlation with the turbine are called tower-originated modes (modes 1, 5, and 9 of the assembly).

34.3.7 Case 7: Extracting Mode Contribution Matrix of the Wind Turbine Assembly

The mode contribution matrix is used to verify the effects of each component on the dynamic characteristic of the assembly. The wind turbine assembly consists of the three-bladed turbine and the tower. In this section, the contribution of each component on the modes of the assembly is studied. As previously described, the generator and nacelle add a considerable amount of mass to the tip of the tower; therefore, in all the following cases, the tower included the mass of the generator and nacelle located at its tip. It should be noted that in order to develop the mode contribution matrix of the assembly, the modes of the turbine $[[U_1^t]$ in Eq. (34.2)] in the pseudo-fixed condition was used.

Figure 34.10 shows the mode contribution matrix of the wind turbine assembly when the modes of the assembly consist of the mode shapes of the pseudo-fixed three-bladed turbine and the tower. The dark colors in Fig. 34.10 for some modes

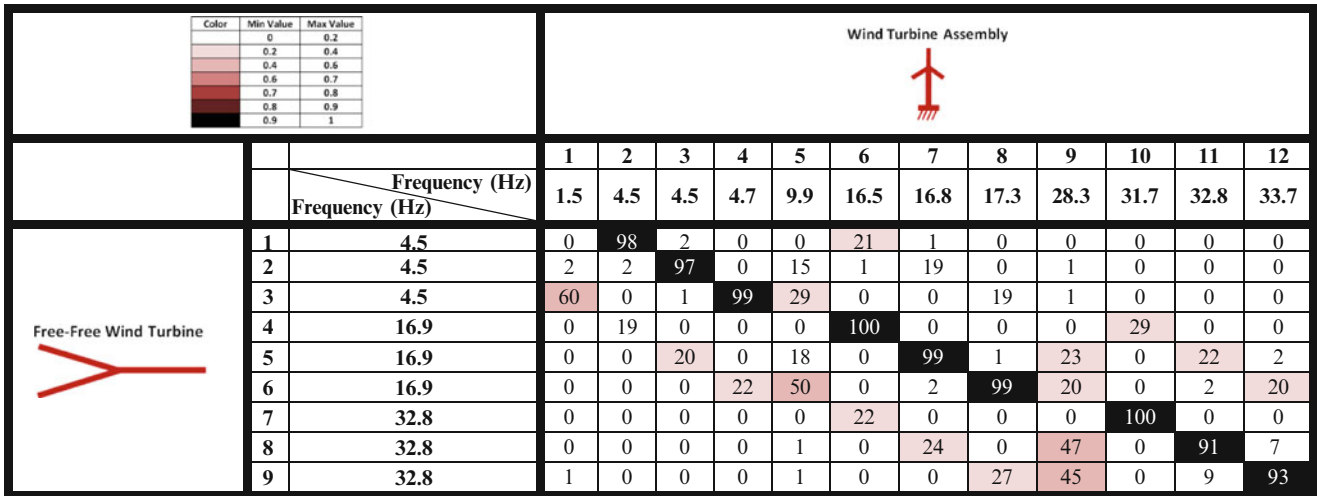


Fig. 34.9 MAC for comparing the flapwise modes of the wind turbine assembly to the flapwise modes of the turbine in the pseudo-fixed conditions

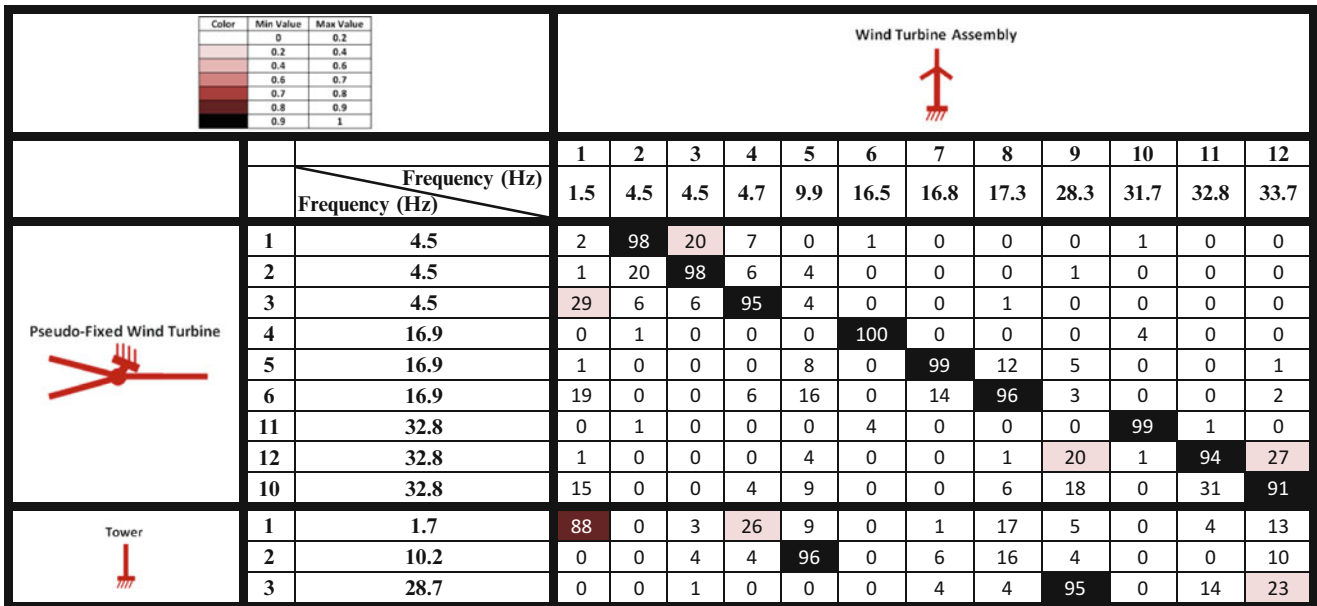


Fig. 34.10 Mode contribution matrix showing the contribution of the pseudo-fixed turbine and the tower in obtaining the flapwise modes of the wind turbine assembly

of the pseudo-fixed turbine shows that those modes are adequate to represent the modes of the wind turbine model with a high degree of accuracy. Accordingly, the modes of the wind turbine assembly that occur at frequencies close to the modes of the pseudo-fixed turbine (modes 2, 3, 4, 6, 7, 8, 10, 11, and 12 of the assembly) mainly consist of the turbine modes. Therefore, excluding the tower modes from the modal database will have a small effect on the mode shapes of the assembly for most modes. However, the tower does have a significant contribution to the response of the assembled turbine system for the tower-originate modes (modes 1, 5, and 9).

34.3.8 Case 8: Correlating the Cantilevered Single Blade to the Blades of an Assembled Wind Turbine and Perturbing the Elastic Modulus

This case shows an effort to compare the modes of the blades assembled to the tower to modes of the single cantilevered blade. The results of the correlation are shown in Fig. 34.11. As can be seen, there are strong correlations between blade


| Color | | | Wind Turbine Assembly | | | | | | | | | | | |
|---------------------------|-----------|------|---|-----|-----|-----|-----|------|------|------|------|------|------|------|
| Min Value | Max Value | |  | | | | | | | | | | | |
| 0 | 0.2 | | | | | | | | | | | | | |
| 0.2 | 0.4 | | | | | | | | | | | | | |
| 0.4 | 0.6 | | | | | | | | | | | | | |
| 0.6 | 0.7 | | | | | | | | | | | | | |
| 0.7 | 0.8 | | | | | | | | | | | | | |
| 0.8 | 0.9 | | | | | | | | | | | | | |
| 0.9 | 1 | | | | | | | | | | | | | |
| Frequency (Hz) | | | 1 | 2 | 3 | 4 | 5 | 6 | 7 | 8 | 9 | 10 | 11 | 12 |
| Frequency (Hz) | | | 1.5 | 4.5 | 4.5 | 4.7 | 9.9 | 16.5 | 16.8 | 17.3 | 28.3 | 31.7 | 32.8 | 33.7 |
| Cantilevered Single Blade | 1 | 4.5 | 69 | 100 | 99 | 99 | 50 | 22 | 20 | 17 | 2 | 1 | 0 | 0 |
| | 2 | 16.9 | 1 | 18 | 21 | 24 | 72 | 99 | 99 | 98 | 43 | 30 | 25 | 19 |
| | 3 | 32.8 | 1 | 0 | 0 | 0 | 2 | 21 | 25 | 31 | 82 | 98 | 98 | 97 |

Fig. 34.11 MAC comparison between modes of the blades of the turbine assembled to the tower and the cantilevered single blade (the cantilevered single blade is overlapped at each blade in 120° orientations and their mode shapes are compared using the MAC)

originated modes of the wind turbine assembly to the modes of the cantilevered single blade; this indicates that the blade originated modes of the wind turbine assembled to a tower can be predicted using modes of the single cantilevered blade.

Another important factor that needs to be investigated is to examine whether the mode shapes of the wind turbine assembly can be predicted when the blades of a wind turbine are not exactly similar (when there are slight changes between the natural frequencies of different blades). This dissimilarity typically exists in manufactured blades and can be attributed to the fact that the material properties and manufacturing process might be different from one blade to another. Therefore, in this part of the study, the elastic modulus of one of the blades in the turbine assembly was perturbed by 20 % and the correlation between the modes of the single cantilevered blade with original material properties and blades in the assembled wind turbine were examined. This change in elastic modulus changes the natural frequencies of some modes of the assemble system about 10 %. However, the results of the study revealed that the modes of the unmodified single cantilevered blade still show strong correlations to all of the blades of the turbine mounted to the tower (including the modified blade). The MAC values varied less than 3 % from the previous comparison between unmodified systems in Fig. 34.11; therefore, they are not shown.

34.4 Observations

The results of the study show that there are two types of flapwise modes for free-free and cantilevered three-bladed turbines. Some observations based on the studies can be made:

1. Collective flapwise modes: These modes represent approximately 1/3 of the flapwise modes and are essentially independent of the rotational boundary conditions; however, translational constraints at the center of the hub slightly change these modes. They occur at the frequencies close to the modes of the cantilevered individual blade. Furthermore, the deformation of each blade of the three-bladed turbine in those modes is similar to mode shapes of the individual cantilever blade. Therefore, these modes can be predicted with high accuracy if the natural frequencies and modes of the cantilevered blades are known.
2. Differential flapwise modes: These modes represent approximately 2/3 of the flapwise modes and are independent of the translational stiffness but dependent on the rotational stiffness of the support. The natural frequencies and mode shapes of the blades in the wind turbine for these modes approach the modes of the cantilevered blade when the stiffness of the support increases. When the turbine was attached to the typical tower, it could be seen that the tower provided a stiff support for these modes. Thus, these kinds of modes for the turbine attached to the tower can also be predicted with good accuracy if the natural frequencies and modes of the individual cantilevered blade are known.

It should be noted that the results presented in this paper are for first nine modes. For higher order modes, the effects of stiffness of the support decreases. Therefore, less change can be expected for those modes when the stiffness of the support varies.

34.5 Conclusion

In this research, a comprehensive investigation on the flapwise modes of a three-bladed system was performed. The modes of the three-bladed turbine were categorized in groups of three and the effects of boundary conditions on the mode shapes of the turbine were studied. It was shown that the boundary conditions affected some modes of the three-bladed turbine. However, some modes did not significantly change by changing rotational stiffness of the support. This fact can be used to predict the modes of a wind turbine assembly when modes of an individual blade in a cantilevered boundary condition are known. The mode contribution matrix showed the effects of the components on the modes of the wind turbine assembly. It was shown that a pseudo-fixed three-bladed turbine had a higher correlation to the assembled wind turbine than compared to a free-free three-bladed turbine. The results of this investigation showed that some modes of the wind turbine assembly can be predicted by using the modes of a single cantilevered blade, independent of the tower and the boundary condition that the tower imparts on the hub. Furthermore, the results of this study showed that for the sample wind turbine and tower that was studied in the current paper, the turbine-originated flapwise modes of the turbine can be predicted using the mode shapes of the pseudo-fixed three-bladed wind turbine. The results of the comparison between the modes of the blades of a wind turbine attached to the tower and modes of a single cantilevered blade showed that even by perturbing the elastic modulus of the blade, turbine originated modes of the assembled system show strong correlations to the cantilevered blade.

Acknowledgements This material is based upon work supported by the National Science Foundation under Grant Number 1230884 (Achieving a Sustainable Energy Pathway for Wind Turbine Blade Manufacturing). Any opinions, findings, and conclusions or recommendations expressed in this material are those of the author(s) and do not necessarily reflect the views of the National Science Foundation.

References

1. Ortiz JL, Bir GS (2006) Verification of new MSC.ADAMS linearization capability for wind turbine applications. In: 44th AIAA aerospace sciences meeting and exhibit, Reno, 13, pp 9443–9455
2. Shen J, Masarati P, Roget B, Piatak DJ, Singleton JD, Nixon MW (2008) Modeling a stiff-inplane tiltrotor using two multibody analyses: a validation study. In: 64th annual forum – AHS international, vol 3, pp 2307–2315
3. Bir G, Stol K (1999) Operating modes of a teetered-rotor wind turbine. In: Proceedings of the 17th international modal analysis conference, IMAC. Part 1 (of 2), vol 2, pp 1586–1596
4. Park JH, Park HY, Jeong SY, Lee SI, Shin YH, Park JP (2010) Linear vibration analysis of rotating wind-turbine blade. *Curr Appl Phys* 10(2 Suppl):S332–S334
5. White JR, Adams DE, Rumsey MA (2010) Theoretical analysis of acceleration measurements in a model of an operating wind turbine. *Active and passive smart structures and integrated systems. Proc SPIE* 7643:10
6. Larsen JW, Nielsen SRK (2006) Non-linear dynamics of wind turbine wings. *Int J Nonlinear Mech* 41(5):629–643
7. Wang L, Sweetman B (2012) Simulation of large-amplitude motion of floating wind turbines using conservation of momentum. *Ocean Eng* 42:155–164
8. Zhao X, Maïßer P, Wu J (2007) A new multibody modelling methodology for wind turbine structures using a cardanic joint beam element. *Renew Energy* 32(3):532–546
9. Murtagh PJ, Basu B, Broderick BM (2005) Along-wind response of a wind turbine tower with blade coupling subjected to rotationally sampled wind loading. *Eng Struct* 27(8):1209–1219
10. Murtagh PJ, Basu B, Broderick BM (2004) Mode acceleration approach for rotating wind turbine blades. *Proceedings of the institution of mechanical engineers, Part K. J Multibody Dynam* 218(3):159–166
11. Hoa SV (1979) Vibration of a rotating beam with tip mass. *J Sound Vib* 67(3):369–381
12. Peters DA, Rossow MP, Korn A, Ko T (1986) Design of helicopter rotor blades for optimum dynamic characteristics. *Comput Math Appl* 12(1 PART A):85–109
13. Bir G (2009) Blades and towers modal analysis code (BModes): verification of blade modal analysis capability. In: 47th AIAA aerospace sciences meeting including the New Horizons Forum and aerospace exposition, Orlando
14. Xiong L, Xianmin Z, Gangqiang L, Yan C, Zhiqian Y (2010) Dynamic response analysis of the rotating blade of horizontal axis wind turbine. *Wind Eng* 34(5):543–560
15. Tsai GC (2004) Rotating vibration behavior of the turbine blades with different groups of blades. *J Sound Vib* 271(3–4):547–575
16. Liu C, Jiang D, Chen J (2010) Vibration characteristics on a wind turbine rotor using modal and harmonic analysis of FEM. In: 2nd world non-grid-connected wind power and energy conference, WNWEC, Nanjing, pp 112–116
17. Cui Y, Shi L, Zhao F (2010) Modal analysis of wind turbine blade made of composite laminated plates. In: Asia-Pacific power and energy engineering conference, Chengdu
18. Bechly ME, Clausen PD (1997) Structural design of a composite wind turbine blade using finite element analysis. *Comput Struct* 63(3): 639–646
19. Alhamaydeh M, Hussain S (2011) Optimized frequency-based foundation design for wind turbine towers utilizing soilstructure interaction. *J Frankl Inst* 348(7):1470–1487

20. Li D, Ye Z, Chen Y, Nengsheng B (2003) Load spectrum and fatigue life analysis of the blade of horizontal axis wind turbine. *Wind Eng* 27(6):495–506
21. Paquette J, Laird D, Griffith DT, Rip L (2006) Modeling and testing of 9m research blades. In: 44th AIAA aerospace sciences meeting, Reno, 19, pp 14569–14581
22. Ye Z, Ma H, Bao N, Chen Y, Ding K (2001) Structure dynamic analysis of a horizontal axis wind turbine system using a modal analysis method. *Wind Eng* 25(4):237–248
23. LoPiccolo J, Carr J, Niezrecki C, Avitabile P, Slattery M (2012) Validation of a finite element model used for dynamic stress-strain prediction. In: 30th IMAC, a conference on structural dynamics, vol 2, Jacksonville, pp 205–214
24. Deines K, Marinone T, Schultz R, Farinholt K, Park G (2011) Modal analysis and SHM investigation of CX-100 wind turbine blade. In: 29th IMAC, a conference on structural dynamics, vol 5, Jacksonville, pp 413–438
25. Marinone T, LeBlanc B, Harvie J, Niezrecki C, Avitabile P (2012) Modal testing of 9 m CX-100 turbine blades. In: 30th IMAC, a conference on structural dynamics, vol 2, Jacksonville, pp 351–358
26. Harvie J, Avitabile P (2012) Comparison of some wind turbine blade tests in various configurations. In: 30th IMAC, a conference on structural dynamics, vol 2, Jacksonville, pp 73–79
27. Yang S, Allen MS (2012) Output-only modal analysis using continuous-scan laser Doppler Vibrometry and application to a 20 kW wind turbine. *Mech Syst Signal Process* 31:228–245
28. Griffith DT, Hunter PS, Kelton DW, Carne TG, Paquette JA (2009) Boundary condition considerations for validation of wind turbine blade structural models. In: SEM annual conference and exposition on experimental and applied mechanics, vol 2, Albuquerque, pp 1117–1127
29. Allemang RJ, Brown DL (1982) Correlation coefficient for modal vector analysis. In: Proceedings of the 1st international modal analysis conference & exhibit, Orlando, pp 110–116
30. Thibault L, Avitabile P, Foley JR, Wolfson J (2012) Equivalent reduced model technique development for nonlinear system dynamic response. In: 30th IMAC, a conference on structural dynamics, vol 3, pp 95–127
31. Abaqus/CAE 6.10-2. In: Dassault System, RI, USA, (2010)
32. MATLAB 7.12.0 (R2011a). In: The MathWorks, Inc., Natick MA, (2011)
33. Baqersad J, Carr J, Lundstrom T, Niezrecki C, Avitabile P, Slattery M. (2012) Dynamic characteristics of a wind turbine blade using 3D digital image correlation. *Proceedings of SPIE - The International Society for Optical Engineering*, 8348, art. no. 83482I, San Diego, CA.
34. (2012) <http://www.windenergy.com>

Chapter 35

Effects of Boundary Conditions on the Structural Dynamics of Wind Turbine Blades. Part 2: Edgewise Modes

Javad Baqersad, Christopher Niezrecki, and Peter Avitabile

Abstract Mode shapes and resonant frequencies of an individual wind turbine blade can be readily determined in either a laboratory or a blade test facility using experimental modal analysis. However, performing a modal test on a utility-scale wind turbine with several blades attached to a tower can be a challenge due to the number of sensors required, the size of these structures, and cost. Therefore, understanding the influence of the coupled three-bladed turbine/tower system and identifying a correlation between the dynamic behavior of an assembled wind turbine to an individual blade or three-bladed turbine on a hub is desirable. In the current paper, which is the second part of a two-part paper, variation in natural frequencies and mode shapes of a three-bladed turbine due to the increase in stiffness of the support is numerically studied using a finite element beam analysis (a similar study was performed on flapwise modes of a turbine and is presented in the first part of this paper). The results of the study reveals that differential edgewise modes of the turbine that represent approximately 2/3 of edgewise modes are independent of the rotational stiffness of the support; thus, these modes can be predicted when the modes of cantilevered single blade are known. However, collective edgewise modes change significantly by changing rotational stiffness of the support. The mode contribution matrix of the wind turbine attached to a tower indicates the necessary set of modal vectors of the tower and three-bladed turbine to accurately obtain the edgewise dynamics of the final assembly.

Keywords Blade • Wind turbine • Boundary condition • Tower • Mode contribution

35.1 Introduction

Recently, wind power has been emerging as one of the major resources of clean renewable energy. Modern wind turbines are manufactured significant in size to reduce the cost of energy compared to fossil fuels and to meet increasing energy demands. As the size of the wind turbines scales up, the capital investment for these machines is escalating. Therefore, periodic damage prognosis and condition based monitoring of wind turbines have become of particular interest. A validated numerical model of a wind turbine is an essential part of most of the health monitoring algorithms. Likewise, an expansion algorithm in conjunction with a finite element model can be used to augment the limited set of operating measured data at sensor locations and predict the full-field dynamic strain in rotating wind turbines. However, performing experimental modal tests on utility-scale wind turbines attached to towers to validate the finite element models is very challenging. Therefore, the work performed in the current paper is an attempt to understand how the edgewise mode shapes of a single cantilever blade or a three-bladed wind turbine correlate with the mode shapes of the wind turbine attached to a tower.

Numerous researches have tried to model the dynamic behavior of wind turbines using the finite element (FE) method. Beam elements were traditionally used for modeling rotating blades [1, 2]. Furthermore, three-dimensional (3D) solid element models require a high computation time; hence, they are typically used for modeling single blades or towers [3–6]. On the other hand, the finite element models need to be validated and/or updated using experimental measurements.

The sheer size of three-bladed wind turbines makes the modal analysis of entire structures very challenging. Thus, experimental measurements to validate numerical models are typically performed on single blades [7–12]. The number of studies found in the published literature in which modal tests were performed on a group of blades is limited [13].

J. Baqersad (✉) • C. Niezrecki • P. Avitabile
Structural Dynamics and Acoustic Systems Laboratory, One University Avenue, Lowell, MA 01854, USA
e-mail: javad_baqersad@student.uml.edu

Recent developments in digital image correlation and photogrammetry have enabled researchers to measure dynamics of rotating structures during operation [14–16]. However, extracting modes of the structure from measured data that are dominated by harmonics of the blade passage frequency remain a challenge. Thus, having a comprehensive understanding of the dynamic characteristics of wind turbines, identifying the effects of boundary conditions on modes of a multi-bladed turbine, and correlating the dynamic behavior of a three-bladed wind turbine assembly to modes of individual blades are desirable.

Yang et al. [17] showed that some modes of the wind turbine assembly occur at frequencies close to the frequencies of the cantilevered blade. Griffith et al. [18] suggested a novel mixed boundary condition for experimental modal testing of an individual blade. They proposed a test rig that was composed of a seismic mass on the top of an airbag to represent a mixture of free-free and fixed boundary conditions. Despite numerous studies on wind turbine dynamics, little attention has been paid to the classifications of modes of turbines and effects of support stiffness on the modes. In addition, comparisons of the mode shapes of the wind turbine to single blades have not been quantified in previous studies.

In the current work, the effects of boundary conditions on a wind turbine are studied using finite element beam models. The paper shows the correlation between the modes of the blades on a wind turbine assembly to the modes of individual blades. Furthermore, a classification of the edgewise modes of a wind turbine is presented. The current paper, which is the second part of a two-part paper, focuses on the edgewise modes of the turbine. A companion paper [19] studies the effects of the boundary conditions on the flapwise modes.

35.2 Model Description and Cases Studied

In the current paper, seven cases are examined to study the effects of boundary conditions on edgewise modes of a three-bladed wind turbine. A flowchart of the work that was carried out for the paper is shown in Fig. 35.1. In fact, the same procedures that were investigated for the flapwise modes in Part 1 of the paper [19] are now repeated to study the effects of boundary conditions on the edgewise modes.

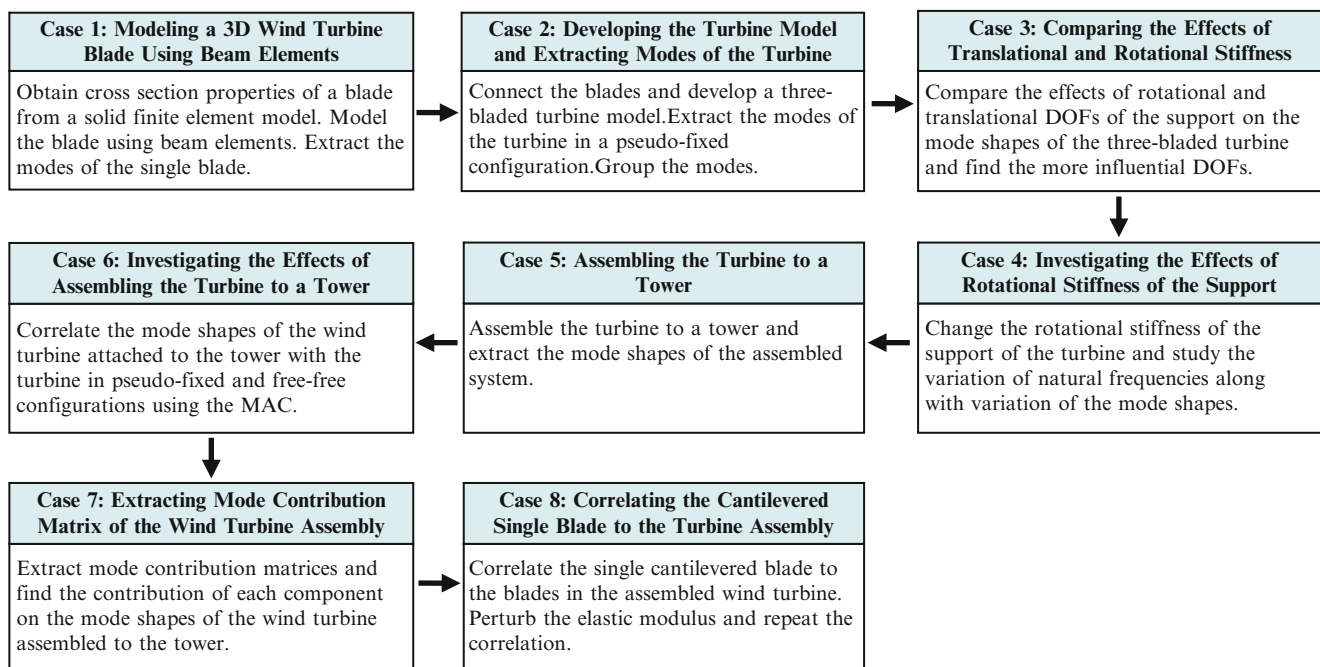


Fig. 35.1 A flowchart of the work that was performed in the current paper

Fig. 35.2 The solid element model of the Southwest Windpower Skystream 4.7™ blade

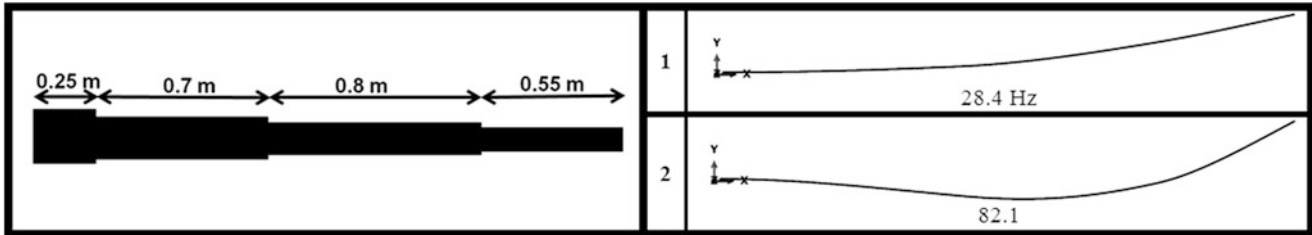


Fig. 35.3 A schematic of the beam model with four different cross sections emulating the Skystream blade (left); edgewise natural frequencies below 40 Hz and their corresponding mode shapes of the beam model in a cantilevered boundary condition (right)

35.2.1 Case 1: Modeling a 3D Wind Turbine Blade Using Beam Elements

A solid element model of a Skystream 4.7™ wind turbine from Southwest Windpower was initially developed in Abaqus™ [20] as shown in Fig. 35.2. The finite element model of the single blade showed a strong correlation to the experimental measurements [9, 21]. In order to study effects of the boundary conditions on the dynamics of the wind turbine, the solid element model was simplified using beam elements (see Fig. 35.3). This simplification reduces the computation time and leads to an easier interpretation of the results. It should be noted that using beam element to study dynamics of wind turbine does not degrade the results based on the previous studies [1, 2, 22, 23].

The beam model of the blade consisted of several beam elements with four different cross section properties. The section properties were extracted from the solid element model. The accuracy of the beam model to represent the dynamics of the blade was verified by comparing the modes of the beam model to the solid model in free-free and cantilevered configurations.

35.2.2 Case 2: Developing the Turbine Model and Extracting Modes of the Turbine in a Pseudo-Fixed Configuration

In order to develop a finite element model of the turbine, three individual beam models of the blades were rigidly connected together after arranging the blades in the appropriate positions that form the three-bladed turbine. The rigid connection replicates the performance of the hub that is significantly stiffer than the blades (blades were made of plastic with elastic modulus of 15.8 GPa; hub consisted of a very thick cast aluminum part with elastic modulus of 72.4 GPa, and a steel plate with elastic modulus of 180 GPa).

An eigensolution was performed on the three-bladed turbine model in a pseudo-fixed configuration to extract the mode shapes and natural frequencies. The fully fixed condition (i.e. setting the rotational DOFs of the center point to zero) leads each blade to have isolated dynamic behavior. As the modes of the three-bladed assembly with interactions among the blades were targeted, the pseudo-fixed condition rather than the fully fixed condition was used for the analysis. In the pseudo-fixed configuration, very stiff springs connect the center point to the ground. All the edgewise mode shapes of the three-bladed turbine below 100 Hz in a pseudo-fixed configuration are shown in Fig. 35.4 (the modes in this frequency span were selected for the current study).

The edgewise modes can be categorized as either collective or differential modes. The collective modes are the modes with the same phase on three blades such as modes 1 and 4. The other modes are called differential modes because the blades do not have the same phase.

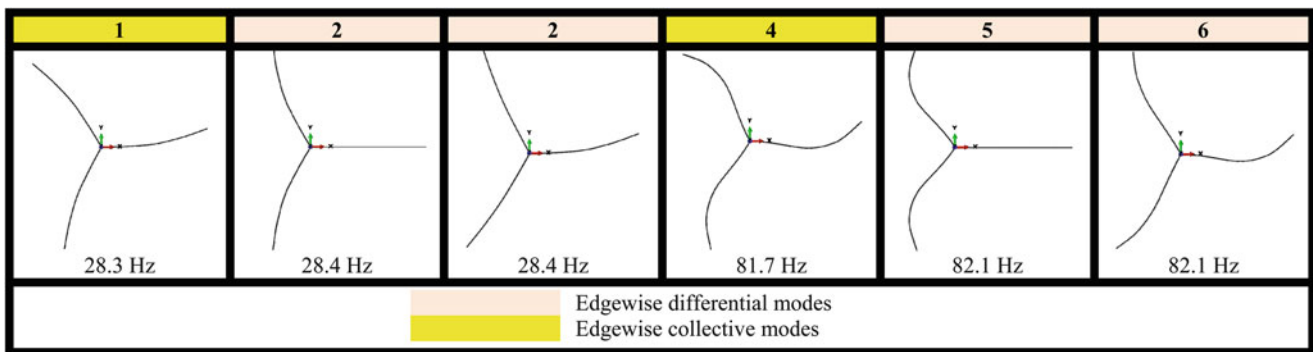


Fig. 35.4 Flexible edgewise mode shapes and resonant frequencies of the three-bladed turbine in the pseudo-fixed configuration from the front view (below 100 Hz)

Table 35.1 Mode pairing of free-free and hinged turbines comparison using the percent differences in frequencies and the MAC (collective modes are shaded in yellow)

| Mode | Free-Free Turbine | Hinged Wind Turbine | Correlation | |
|------|-------------------|---------------------|-------------------------|-----|
| | Frequency (Hz) | Frequency (Hz) | Frequency Deviation (%) | MAC |
| 1 | 0 | 0 | 0 | 100 |
| 2 | 30.5 | 28.4 | 7 | 97 |
| 3 | 30.5 | 28.4 | 7 | 97 |
| 4 | 51.3 | 51.3 | 1 | 100 |
| 5 | 91 | 82.1 | 10 | 93 |
| 6 | 91 | 82.1 | 10 | 93 |

As can be seen in Fig. 35.4, the edgewise modes of turbine below 100 Hz can be placed into groups of modes in which each group includes three modes (one collective and two differential modes). Modes in each group have approximately the same natural frequencies (i.e. repeated roots). Furthermore, the deflection of the blades for each group is similar to an edgewise mode of a single cantilevered blade. Figure 35.4 also shows that each trio of modes contain repeated roots (i.e. have very close natural frequencies). Therefore, modes of the three-bladed turbine can be categorized in groups of three. Because higher order modes show a similar dynamic behavior to low order modes (e.g. higher order modes also are in groups of three and they can be categorized into differential and collective modes), only the first 9 flapwise modes of the turbine (below 40 Hz) are shown.

35.2.3 Case 3: Comparing the Effects of Translational and Rotational Stiffness of the Support on the Modes of the Turbine

In order to compare the effects of translational and rotational DOFs of the support, the edgewise mode shapes of the turbine in a free-free condition were compared to the modes of the turbine in hinged and pseudo-fixed boundary conditions. The first model in Table 35.1 which is used as a reference model is the free-free configuration. In the second configuration, the translational DOFs of the three-bladed turbine center were fixed, which is called a “hinged model”. In the third model, the hinged model was provided with three stiff rotational springs at the center creating a pseudo-fixed model. On the other hand, in the hinged model, there was no translational displacement at the center of the hub. Whereas, in the pseudo-fixed model, in addition to providing zero translational displacements at the center, the center of the blade is restricted from rotation by using very stiff springs.

The first six edgewise modes of the turbine were used for the current study (below 100 Hz). It should be noted that for the free-free turbine, the first mode is the in-plane rigid body mode that has the highest correlation to the first mode of the pseudo-fixed turbine (in this mode, the turbine rigidly spins around the center point; the two other in-plane rigid body modes, translational modes, are not listed because they did not show strong correlations to the first mode shown in Fig. 35.4). Tables 35.1 and 35.2 show that although creating hinged boundary condition influences the differential modes of the turbine,

Table 35.2 Mode pairing of free-free and pseudo-fixed turbines comparison using the percent differences in frequencies and the MAC (collective modes are shaded in yellow)

| Mode | Free-Free Turbine | Pseudo-Fixed Turbine | Correlation | |
|------|-------------------|----------------------|-------------------------|-----|
| | Frequency (Hz) | Frequency (Hz) | Frequency Deviation (%) | MAC |
| 1 | 0 | 28.3 | N/A | 71 |
| 2 | 30.5 | 28.4 | 7 | 97 |
| 3 | 30.5 | 28.4 | 7 | 97 |
| 4 | 51.3 | 81.7 | 59 | 76 |
| 5 | 91 | 82.1 | 10 | 93 |
| 6 | 91 | 82.1 | 10 | 99 |

Table 35.3 Effects of rotational stiffness of the support on the natural frequencies of the hinged three-bladed turbine (collective modes are shaded in yellow)

| Mode # | Hinged Wind Turbine | Hinged Turbine Supported by a Torsion Spring | | | | | | | Pseudo-Fixed Turbine |
|--------|---------------------|--|-------------------|-------------------|-------------------|-------------------|-------------------|-------------------|----------------------|
| | $k_t=0$ | $k_t=5E2$ (N/rad) | $k_t=1E3$ (N/rad) | $k_t=5E3$ (N/rad) | $k_t=1E4$ (N/rad) | $k_t=1E5$ (N/rad) | $k_t=1E6$ (N/rad) | $k_t=1E7$ (N/rad) | $k_t=1E8$ (N/rad) |
| 1 | 0 | 0.8 | 1.1 | 2.4 | 3.4 | 10.3 | 22.6 | 27.7 | 28.3 |
| 2 | 28.4 | 28.4 | 28.4 | 28.4 | 28.4 | 28.4 | 28.4 | 28.4 | 28.4 |
| 3 | 28.4 | 28.4 | 28.4 | 28.4 | 28.4 | 28.4 | 28.4 | 28.4 | 28.4 |
| 4 | 51.0 | 51.0 | 51.1 | 51.1 | 51.2 | 52.7 | 63.0 | 78.2 | 81.7 |
| 5 | 82.1 | 82.1 | 82.1 | 82.1 | 82.1 | 82.1 | 82.1 | 82.1 | 82.1 |
| 6 | 82.1 | 82.1 | 82.1 | 82.1 | 82.1 | 82.1 | 82.1 | 82.1 | 82.1 |

a more significant change in collective modes (i.e. modes 1 and 4) can be observed when the pseudo-fixed condition is applied to the three-bladed turbine. Therefore, only the effects of adding a rotational spring were investigated in the current study.

35.2.4 Case 4: Investigating the Effects of Rotational Stiffness of the Support on Edgewise Modes

The hinged model of the turbine that possessed in-plane deformations was used for the study. A torsion spring was connected to the central node of the wind turbine. By changing the stiffness of the spring, the natural frequencies and mode shapes of the in-plane modes of the turbine change. Variation of natural frequencies of the three-bladed turbine due to an increase in rotational stiffness of the support is shown in Table 35.3. As can be seen, only the natural frequencies of the first and fourth modes change by increasing the rotational stiffness of the support. For the case of very stiff support, 1E8 N/rad, there are a set of three modes that have approximately same frequency. Mode shapes of the turbine for different rotational stiffness of the support are shown in Fig. 35.5. As can be seen, among all the modes of the three-bladed turbine, only collective modes (modes 1 and 4) changed by increasing the rotational stiffness of the support.

For the free-free wind turbine, two modes occur at frequencies close to the frequency of the cantilevered blade for the edgewise modes (unlike the flapwise modes such that one mode occurs at the frequency close to the natural frequency of the single cantilever blade [19]).

35.2.5 Case 5: Assembling the Turbine to a Tower

In the current section, the effects of attaching the turbine to a sample tower are studied. By mounting the free-free turbine to a tower, not only the stiffness of the support changes but also a set of new modes are added to the system.

Fig. 35.5 Effects of rotational stiffness of the support on the edgewise mode shapes and natural frequencies for the turbine (collective modes are shaded in yellow)

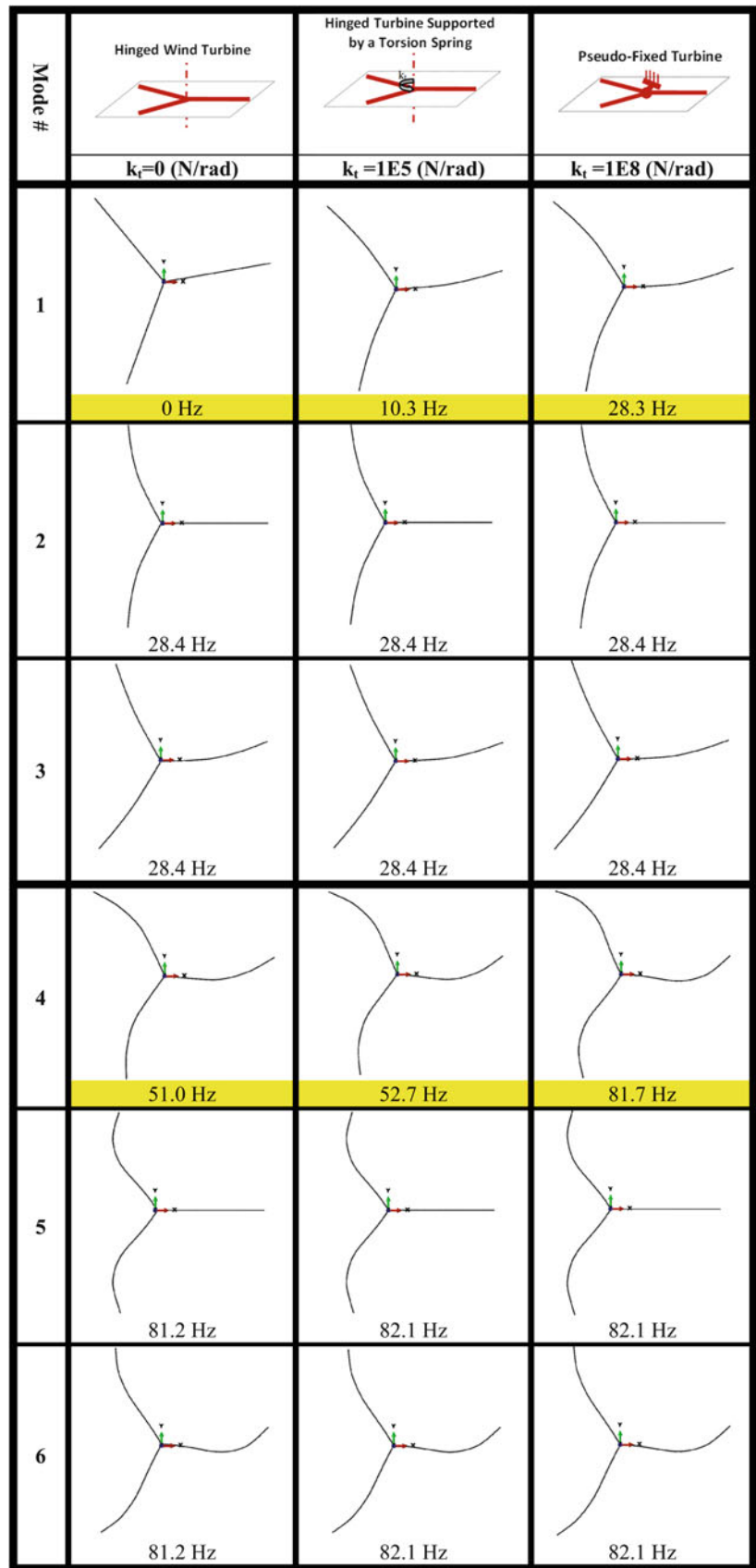


Fig. 35.6 First five edgewise mode shapes and resonant frequencies of the tower with the tip mass

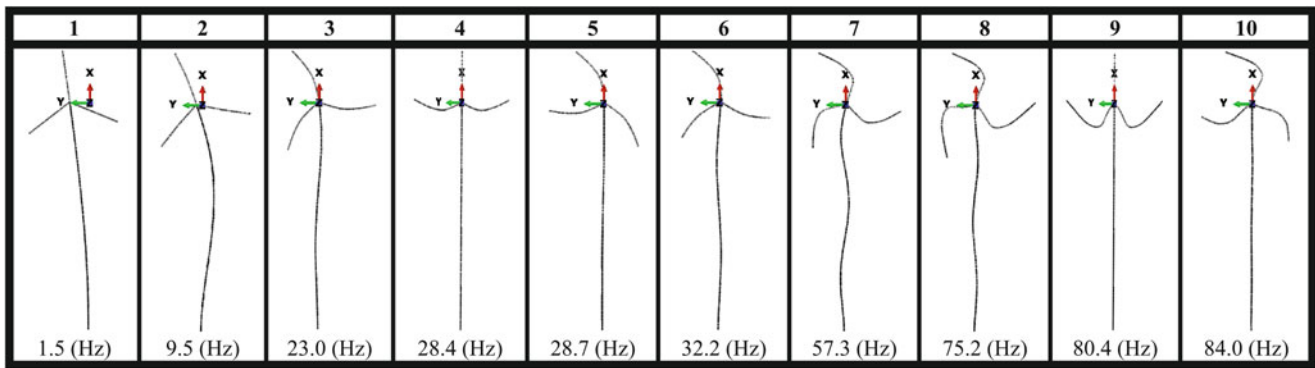
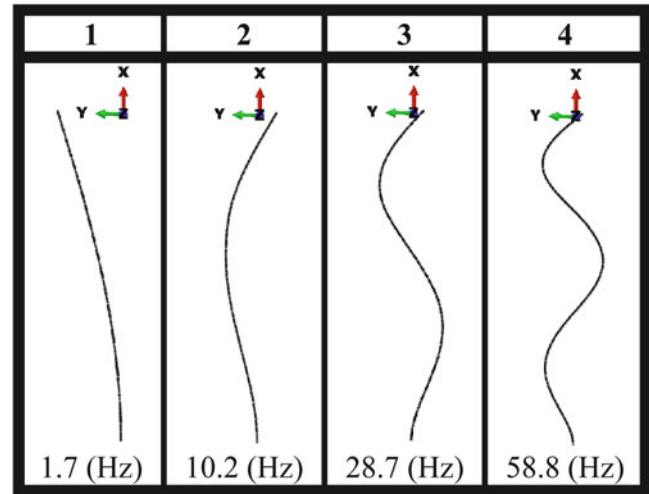


Fig. 35.7 Edgewise mode shapes and resonant frequencies of the wind turbine assembly

The turbine was mounted to a 10.2-m monopole tower with a rigid connection. The tower properties were found from the webpage of the manufacturer [24]. A 53-kg point mass was added to the tip of the tower to consider the effects of the generator and nacelle (the weight was estimated based on the information provided on the manufacturer's website; the rotational inertia of the equipment was not considered in the current study and will not change the outcomes of the trends and observations made in this work). Five natural frequencies and mode shapes of the three-bladed turbine in the bandwidth from 0 to 100 Hz (the bandwidth that was previously used for the study of the edgewise modes) are shown in Fig. 35.6.

The edgewise mode shapes and natural frequencies of the wind turbine assembly in the bandwidth of interest are shown in Fig. 35.7. The modes of the assembly that show a strong correlation to the three-bladed turbine are called turbine-originated modes (modes 3, 4, and 5 of the assembly). Likewise, modes with low correlation with the turbine are called tower-originated modes. The first two mode shapes in Fig. 35.7 are tower-originated modes of the assembly. As was shown in Table 35.3, in order for the collective edgewise modes to approach a pseudo-fixed configuration, a very high rotational stiffness ($10E8$ N/rad) is needed at the support. However, the tower could not provide enough stiffness to replicate pseudo-fixed configuration for the turbine; that is why the third mode has a lower natural frequency than the natural frequencies of modes 4 and 5.

35.2.6 Case 6: Investigating the Effects of Assembling the Turbine to a Tower

A comparison between the mode shapes of the assembly and the free-free three-bladed and pseudo-fixed turbine (which are common test configurations) was performed using Modal Assurance Criterion. As can be seen in Fig. 35.8, some of the turbine originated modes of the assembly (modes 4, 5, 7, and 10) show strong correlations to the free-free turbine.

A comparison of the mode shapes of the wind turbine to the mode shapes of the pseudo-fixed turbine is shown in Fig. 35.9. The turbine-originated modes of the assembly can be clearly distinguished with their high correlations to the modes of the

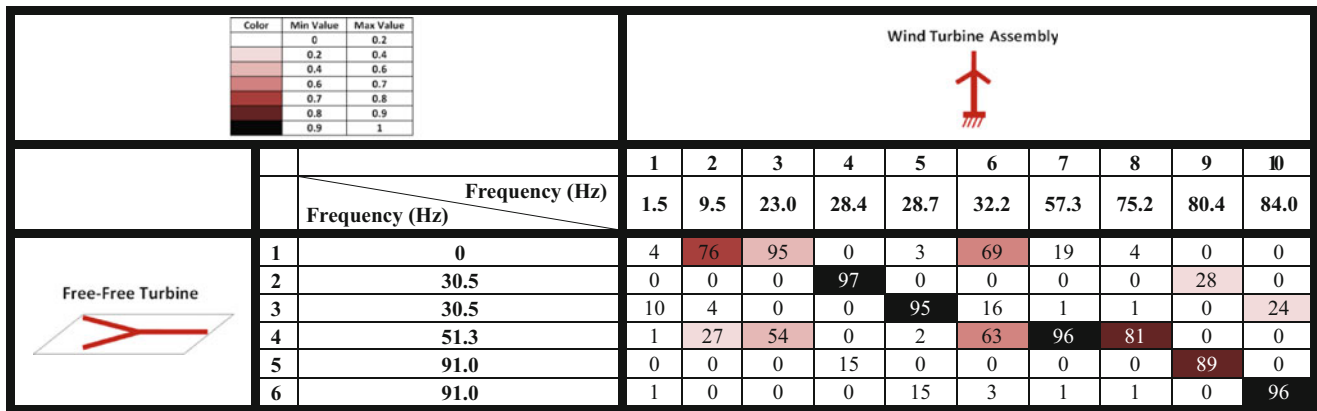


Fig. 35.8 MAC for comparing the edgewise modes of the wind turbine to the modes of the turbine in free-free condition

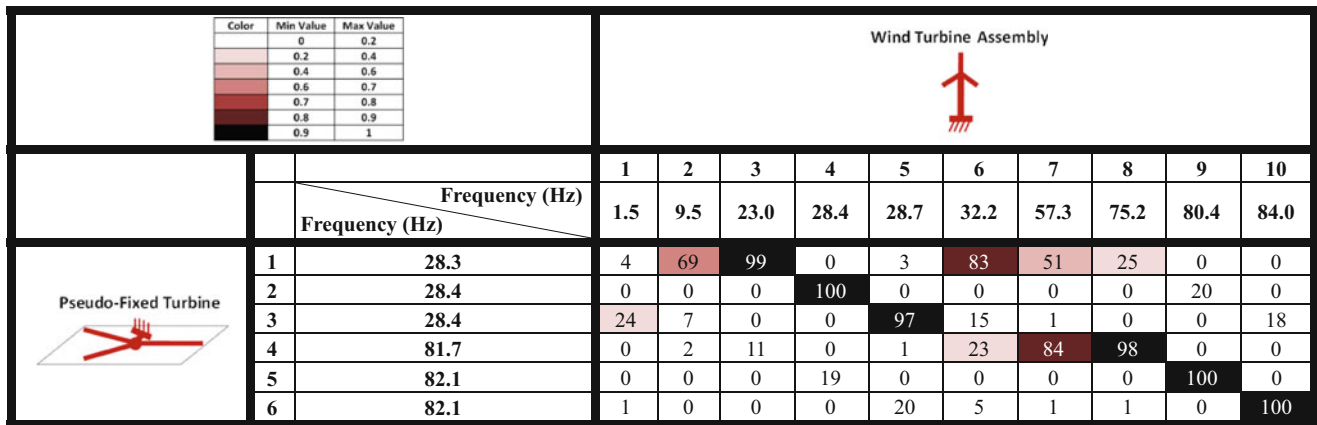


Fig. 35.9 MAC for comparing the edgewise modes of the wind turbine assembly to the modes of the pseudo-fixed turbine

three-bladed turbine. Figure 35.9 also shows that if the total rotational stiffness of the tower is used to support the turbine, the modes of pseudo-fixed turbine have a high correlation to the turbine-originated modes of the assembled model.

35.2.7 Case 7: Extracting Mode Contribution Matrix of the Wind Turbine Assembly

The mode contribution matrix can be used to obtain the modes of an assembly system by using modes of unmodified components and to verify the effects of each component on the dynamic characteristic of the assembly (the equation to extract the mode contribution matrix can be found in Part 1 of the paper [19]). The wind turbine assembly consists of the three-bladed turbine and the tower. In this section, the contribution of each component on the modes of the assembly is studied. Figure 35.10 shows the contribution of the free-free turbine and the tower in the wind turbine assembly. Among turbine-originated modes of the assembly, differential modes (modes 4, 5, 9, and 10 of the assembled turbine) can be more accurately obtained using their corresponding free-free turbine modes, whereas collective modes need a contribution of more than one mode in order to be accurately represented.

Figure 35.11 shows the mode contribution matrix ($[U_{12}]$) when the dynamic properties of the wind turbine assembly are represented by using the mode shapes of the pseudo-fixed three-bladed turbine and the tower. Some modes of the assembly essentially originate from modes of the three-bladed turbine (modes 3, 4, 5, 8, 9, and 10). Figure 35.11 also shows that all of turbine-originated modes apart from the collective modes (modes 4 and 8) can be accurately obtained by using the modes of the pseudo-fixed turbine. This occurs because the edgewise stiffness of the tower is not high enough to fully mimic pseudo-fixed condition. For instance, the third mode of the wind turbine assembly could approach a natural frequency of 28.4 if the tower could provide more rotational stiffness.


| Color | | | Wind Turbine Assembly | | | | | | | | | | | |
|-----------|-----------|--|---|-----|----------------|-------------------|----------------|------|-------------------|------|----------------|-------------------|----|--|
| Min Value | Max Value | |  | | | | | | | | | | | |
| 0 | 0.2 | | 1 | 2 | 3 | 4 | 5 | 6 | 7 | 8 | 9 | 10 | | |
| 0.2 | 0.4 | | Frequency (Hz) | | Frequency (Hz) | | Frequency (Hz) | | Frequency (Hz) | | Frequency (Hz) | | | |
| 0.4 | 0.6 | | 1.5 | 9.5 | 23.0 | 28.4 | 28.7 | 32.2 | 57.3 | 75.2 | 80.4 | 84.0 | | |
| 0.6 | 0.7 | | Free-Free Turbine | | | Free-Free Turbine | | | Free-Free Turbine | | | Free-Free Turbine | | |
| 0.7 | 0.8 | | 1 | 2 | 3 | 4 | 5 | 6 | 7 | 8 | 9 | 10 | | |
| 0.8 | 0.9 | | 0 | 39 | 19 | 1 | 19 | 26 | 6 | 5 | 8 | 23 | 25 | |
| 0.9 | 1 | | 2 | 0 | 0 | 0 | 92 | 5 | 1 | 0 | 0 | 20 | 1 | |
| | | | 3 | 0 | 1 | 1 | 5 | 91 | 24 | 3 | 4 | 1 | 13 | |
| | | | 4 | 0 | 1 | 23 | 0 | 7 | 34 | 48 | 71 | 0 | 3 | |
| | | | 5 | 0 | 0 | 0 | 2 | 0 | 0 | 0 | 0 | 84 | 2 | |
| | | | 6 | 0 | 0 | 0 | 0 | 2 | 0 | 2 | 10 | 2 | 92 | |
| | | | Tower | | | Tower | | | Tower | | | Tower | | |
| | | | 1 | 2 | 3 | 4 | 5 | 6 | 7 | 8 | 9 | 10 | | |
| | | | 1.7 | 88 | 13 | 6 | 0 | 14 | 0 | 4 | 2 | 0 | 15 | |
| | | | 10.2 | 0 | 93 | 24 | 0 | 6 | 10 | 4 | 6 | 0 | 9 | |
| | | | 28.7 | 0 | 2 | 56 | 0 | 15 | 78 | 6 | 13 | 0 | 7 | |
| | | | 59.2 | 0 | 0 | 8 | 0 | 1 | 10 | 87 | 44 | 0 | 9 | |

Fig. 35.10 Mode contribution matrix showing the contribution of the free-free turbine and the tower in obtaining the edgewise modes of the wind turbine assembly


| Color | | | Wind Turbine Assembly | | | | | | | | | | | |
|-----------|-----------|--|---|-----|----------------|-------------------|----------------|------|-------------------|------|----------------|-------------------|----|--|
| Min Value | Max Value | |  | | | | | | | | | | | |
| 0 | 0.2 | | 1 | 2 | 3 | 4 | 5 | 6 | 7 | 8 | 9 | 10 | | |
| 0.2 | 0.4 | | Frequency (Hz) | | Frequency (Hz) | | Frequency (Hz) | | Frequency (Hz) | | Frequency (Hz) | | | |
| 0.4 | 0.6 | | 1.5 | 9.5 | 23.0 | 28.4 | 28.7 | 32.2 | 57.3 | 75.2 | 80.4 | 84.0 | | |
| 0.6 | 0.7 | | Free-Free Turbine | | | Free-Free Turbine | | | Free-Free Turbine | | | Free-Free Turbine | | |
| 0.7 | 0.8 | | 1 | 2 | 3 | 4 | 5 | 6 | 7 | 8 | 9 | 10 | | |
| 0.8 | 0.9 | | 28.3 | 6 | 24 | 77 | 0 | 15 | 54 | 15 | 4 | 0 | 0 | |
| 0.9 | 1 | | 2 | 0 | 0 | 0 | 100 | 2 | 1 | 0 | 0 | 1 | 0 | |
| | | | 3 | 17 | 9 | 1 | 3 | 96 | 20 | 1 | 0 | 0 | 1 | |
| | | | 4 | 3 | 11 | 14 | 0 | 0 | 9 | 45 | 79 | 0 | 5 | |
| | | | 5 | 0 | 0 | 0 | 0 | 0 | 0 | 0 | 0 | 97 | 1 | |
| | | | 6 | 18 | 8 | 0 | 0 | 3 | 7 | 5 | 14 | 1 | 97 | |
| | | | Tower | | | Tower | | | Tower | | | Tower | | |
| | | | 1 | 2 | 3 | 4 | 5 | 6 | 7 | 8 | 9 | 10 | | |
| | | | 1.7 | 88 | 13 | 6 | 0 | 14 | 0 | 4 | 2 | 0 | 15 | |
| | | | 10.2 | 0 | 93 | 24 | 0 | 6 | 10 | 4 | 6 | 0 | 9 | |
| | | | 28.7 | 0 | 2 | 56 | 0 | 15 | 78 | 6 | 13 | 0 | 7 | |
| | | | 59.2 | 0 | 0 | 8 | 0 | 1 | 10 | 87 | 44 | 0 | 9 | |

Fig. 35.11 Mode contribution matrix showing the contribution of the pseudo-fixed turbine and the tower in obtaining the edgewise modes of the wind turbine assembly

35.2.8 Case 8: Correlating the Cantilevered Single Blade to the Blades of an Assembled Wind Turbine and Perturbing the Elastic Modulus

The modes of the blades in the wind turbine assembly can be correlated to modes of the single cantilevered blades to verify how the mode shapes changes. As shown in Fig. 35.12, there are strong correlations between the turbine-originated modes of the assembly to the modes of the cantilevered blade. Furthermore, some tower originated modes of the assembly that are close to the wind turbine modes (e.g. mode 6 of the assembly) show strong correlations to the modes of the single cantilevered blade.

Manufactured wind turbine blades may not be identical to each other. The dissimilarity between manufactured wind turbine blades can be attributed to the fact that the material properties and manufacturing process might be different from one blade to another. Therefore, in this section, the elastic modulus of one of the blades in the turbine assembly was perturbed by 20 % and the correlation between the modes of the non-modified single cantilevered blade to the all the blades in the wind turbine (including the modified blade) were examined. It was revealed that the change in material properties results in


| | | Color | | Min Value | | Max Value | | Wind Turbine Assembly | | | | | | | | | | | |
|---------------------------|---|-------|--|-----------|--|-----------|--|---|-----|------|------|------|------|------|------|------|------|--|--|
| | | 0 | | 0.2 | | 0.4 | |  | | | | | | | | | | | |
| | | 0.2 | | 0.4 | | 0.6 | | | | | | | | | | | | | |
| | | 0.4 | | 0.6 | | 0.8 | | | | | | | | | | | | | |
| | | 0.6 | | 0.7 | | 0.8 | | | | | | | | | | | | | |
| | | 0.7 | | 0.8 | | 0.9 | | | | | | | | | | | | | |
| | | 0.8 | | 0.9 | | 1 | | | | | | | | | | | | | |
| | | 0.9 | | 1 | | | | | | | | | | | | | | | |
| | | | | | | | | 1 | 2 | 3 | 4 | 5 | 6 | 7 | 8 | 9 | 10 | | |
| | | | | | | | | 1.5 | 9.5 | 23.0 | 28.4 | 28.7 | 32.2 | 57.3 | 75.2 | 80.4 | 84.0 | | |
| | | | | | | | | Frequency (Hz) | | | | | | | | | | | |
| | | | | | | | | Frequency (Hz) | | | | | | | | | | | |
| Cantilevered Single Blade | 1 | 28.4 | | | | | | 30 | 75 | 99 | 100 | 100 | 97 | 51 | 25 | 21 | 18 | | |
| | 3 | 82.1 | | | | | | 1 | 3 | 11 | 19 | 20 | 26 | 85 | 99 | 100 | 99 | | |

Fig. 35.12 MAC comparison between the edgewise modes of the blades of the turbine assembled to the tower and the cantilevered single blade (the shape of the cantilevered single blade is replicated at each 120° orientation and their mode shapes are compared using the MAC)

approximately a 5 % change in the natural frequencies of the assembled system. However, the change in MAC values is less than 3 % from the previous comparison and the MAC results are similar to Fig. 35.12.

35.3 Observations on Edgewise Modes and Comparisons of Flapwise and Edgewise Modes

The results of the study show that there are two types of edgewise modes for free-free and cantilevered three-bladed turbines. Some observations based on the studies can be made:

1. Differential edgewise modes: These modes represent approximately 2/3 of the edgewise modes and tend to be independent of the rotational stiffness of the support. They occur at the frequencies close to the natural frequencies of edgewise modes of the cantilevered blade. Therefore, they tend to be predictable.
2. Collective edgewise modes: These modes represent approximately 1/3 of edgewise modes and are dependent on the rotational stiffness of the support. The deflection of the blades in the turbine for these modes approaches the edgewise modes of a single cantilevered blade when the rotational stiffness of the support increases significantly. However, for the wind turbine assembly, the tower could not provide very high rotational stiffness for the edgewise modes. Furthermore, because the edgewise stiffness is provided to the blades through the generator, the rotational stiffness of the support may not always remain constant during wind turbine operation. Therefore, the frequencies of these modes may change during operation based on the resisting torque provided from the generator.

The results of the current paper are compared to results from Part I of the paper pertaining to flapwise modes [19] to help identify the similarities and differences between the edgewise and flapwise modes. A comparison between the results is shown in Table 35.4.

35.4 Conclusion

In the current research, a comprehensive investigation on the edgewise modes of a three-bladed system was performed. The modes of the three-bladed turbine were categorized in groups of three and the effects of boundary conditions on the mode shapes of the turbine were studied. It was shown that the translational boundary conditions slightly affects differential edgewise modes of the turbine. However, collective edgewise modes significantly change by changing rotational stiffness of the support. This fact can be used to help predict some modes of a wind turbine assembly when edgewise modes of an individual blade in a cantilevered boundary condition are known. The mode contribution matrix showed the effects of the components on the modes of the wind turbine assembly. It was shown that a pseudo-fixed three-bladed turbine had a higher correlation to the assembled wind turbine than compared to a free-free three-bladed turbine. The results of this investigation showed that some modes of the wind turbine assembly could be predicted by using the modes of a single cantilevered blade, independent of the tower and the boundary condition it places on the hub.

Acknowledgement This material is based upon work supported by the National Science Foundation under Grant Number 1230884 (Achieving a Sustainable Energy Pathway for Wind Turbine Blade Manufacturing). Any opinions, findings, and conclusions or recommendations expressed in this material are those of the author(s) and do not necessarily reflect the views of the National Science Foundation.

Table 35.4 A comparison between flapwise and edgewise modes of the turbine

| Flapwise modes (summary of part I) | Edgewise modes (summary of part II) |
|--|---|
| A collective flapwise mode of the turbine in a free-free configuration occurs at a frequency close to the frequency of a flapwise mode of the single cantilevered blade | Two differential edgewise modes of the turbine in a free-free configuration occur at a frequency close to the frequency of the edgewise mode of a single cantilevered blade |
| Differential flapwise modes are very dependent on the rotational stiffness of the support | Collective edgewise modes are very dependent on the rotational stiffness of the support |
| By comparing the results in this paper with the results from Table 35.3 in the first paper (Part I), it was found that as the rotational stiffness increased, the group of flapwise modes converged to the frequency of the collective modes more quickly than compared to the edgewise modes. For example, for the same level of frequency convergence required a smaller stiffness (1 E6 N/rad) for flapwise modes compared to edgewise modes (1 E8 N/rad). For a group of three modes, the flapwise modes will approach the frequency of the collective mode more quickly than the edgewise modes do, as the torsional stiffness is increased. Therefore, a group of edgewise modes are more likely to be separated in frequency than a group of flapwise modes | |
| Both flapwise and edewise modes can be categorized in groups of three | |
| Both flapwise and edewise modes contain collective and differential modes | |
| For both flapwise and edewise modes, if a built-in configuration is provided for the turbine, each tree modes of the turbine occur at the frequency of the cantilever blade | |

References

1. Hoa SV (1979) Vibration of a rotating beam with tip mass, *J Sound Vib* 67(3):369–381
2. Peters DA, Rossow MP, Korn A, Ko T (1986) Design of helicopter rotor blades for optimum dynamic characteristics. *Comput Math Appl* 12(1 PART A):85–109
3. Cui Y, Shi L, Zhao F (2010) Modal analysis of wind turbine blade made of composite laminated plates. In: Asia-Pacific power and energy engineering conference, APPEEC, Chengdu
4. Bechly ME, Clausen PD (1997) Structural design of a composite wind turbine blade using finite element analysis. *Comput Struct* 63(3): 639–646
5. Alhamaydeh M, Hussain S (2011) Optimized frequency-based foundation design for wind turbine towers utilizing soilstructure interaction. *J Frankl Inst* 348(7):1470–1487
6. Li D, Ye Z, Chen Y, Nengsheng B (2003) Load spectrum and fatigue life analysis of the blade of horizontal axis wind turbine. *Wind Eng* 27(6):495–506
7. Paquette J, Laird D, Griffith DT, Rip L (2006) Modeling and testing of 9 m research blades. In: 44th AIAA aerospace sciences meeting. 19, pp 14569–14581
8. Ye Z, Ma H, Bao N, Chen Y, Ding K (2001) Structure dynamic analysis of a horizontal axis wind turbine system using a modal analysis method. *Wind Eng* 25(4):237–248
9. LoPiccolo J, Carr J, Niezrecki C, Avitabile P, Slattery M (2012) Validation of a finite element model used for dynamic stress–strain prediction. In: 30th IMAC, a conference on structural dynamics, vol 2, pp 205–214
10. Deines K, Marinone T, Schultz R, Farinholt K, Park G (2011) Modal analysis and SHM investigation of CX-100 wind turbine blade. In: 29th IMAC, a conference on structural dynamics, vol 5, pp 413–438
11. Marinone T, LeBlanc B, Harvie J, Niezrecki C, Avitabile P (2012) Modal testing of 9 m CX-100 turbine blades. In: 30th IMAC, a conference on structural dynamics, vol 2, pp 351–358
12. Harvie J, Avitabile P (2012) Comparison of some wind turbine blade tests in various configurations. In: 30th IMAC, a conference on structural dynamics, vol 2, pp 73–79
13. Baqersad J, Niezrecki C, Avitabile P, Slattery M (2013) Dynamic characterization of a free-free wind turbine blade assembly. In: 31th IMAC, a conference on structural dynamics, pp 215–220
14. Ozbek M, Rixen DJ, Erne O, Sanow G (2010) Feasibility of monitoring large wind turbines using photogrammetry. *Energy* 35(12):4802–4811
15. Lundstrom T, Baqersad J, Niezrecki C, Avitabile P (2012) Using high-speed stereophotogrammetry techniques to extract shape information from wind turbine/rotor operating data. In: 30th IMAC, a conference on structural dynamics, vol 6, pp 269–275
16. Lundstrom T, Baqersad J, Niezrecki C (2013) Using high-speed stereophotogrammetry to collect operating data on a helicopter. In: 31th IMAC, a conference on structural dynamics

17. Yang S, Allen MS (2012) Output-only modal analysis using continuous-scan laser doppler vibrometry and application to a 20 kW wind turbine. *Mech Syst Signal Process* 31:228–245
18. Griffith DT, Hunter PS, Kelton DW, Carne TG, Paquette JA (2009) Boundary condition considerations for validation of wind turbine blade structural models. In: SEM annual conference and exposition on experimental and applied mechanics, vol 2, pp 1117–1127
19. Baqersad J, Niezrecki C, Avitabile P (2014) Effects of boundary conditions on the structural dynamics of wind turbine blades. Part 1: flatwise modes. In: 32th IMAC, a conference on structural dynamics
20. [Abaqus/CAE 6.10-2] Dassault System (2010)
21. Baqersad J, Carr J, Lundstrom T, Niezrecki C, Avitabile P, Slattery M (2012) Dynamic characteristics of a wind turbine blade using 3D digital image correlation. In: Health monitoring of structural and biological systems, processing of SPIE 8348
22. Xiong L, Xianmin Z, Gangqiang L, Yan C, Zhiquan Y (2010) Dynamic response analysis of the rotating blade of horizontal axis wind turbine. *Wind Eng* 34(5):543–560
23. Bir G (2009) Blades and towers modal analysis code (BModes): verification of blade modal analysis capability. In: 47th AIAA aerospace sciences meeting including the New Horizons forum and aerospace exposition
24. [<http://www.windenergy.com>] (2012)

Chapter 36

Modal Testing and Model Validation Issues of SWiFT Turbine Tests

Timothy Marinone, David Cloutier, and Bruce LeBlanc

Abstract Sandia National Laboratories is developing the Scaled Wind Farm Technology center to enable rapid, cost-efficient testing and development of transformative wind energy technology. ATA Engineering, Inc., was contracted as part of this effort to dynamically characterize a number of components and assemblies to be used at the Scaled Wind Farm Technology center.

This paper documents several of the tests that were performed and describes the approaches, results, and challenges encountered during testing. The test articles that were dynamically characterized are the Vestas V27 wind turbine blades, Vestas V27 towers in a free-free boundary condition, and Vestas V27 towers in a bolted condition.

Keywords Wind turbines • Modal testing • Model validation • Inertia properties • Correlation and updating

36.1 Introduction

Sandia National Laboratories (SNL) is developing the Scaled Wind Farm Technology (SWiFT) center to enable rapid, cost-efficient testing and development of transformative wind energy technology. The site is intended to study complex turbine wake interactions and focus on damage mitigation, improved power performance, and recommended future site layouts. Since this site is designed to be open source and to provide data to all interested parties, the models must be accurate enough to be used for the desired analyses while preserving the proprietary information from Vestas. As such, ATA Engineering, Inc., (ATA) was contracted as part of this effort to dynamically characterize a number of components and assemblies to be used at SWiFT.

The SWiFT site consists of three modified 225 kW Vestas V27 (V27) turbines that were reworked by SNL. ATA characterized all major components of the turbine in order to provide test-verified data for use in updating SNL's models. This paper focuses on the testing of three components: the V27 wind turbine blades in a free-free boundary condition, the V27 towers in a free-free boundary condition, and the V27 towers in a bolted boundary condition. Additional papers [1–3] focus on the testing of the remaining components (hub and nacelle), testing the fully assembled turbine, and summarize the overall test program. The objective of this paper is to present the results of the tests described above.

Sandia is a multiprogram laboratory operated by Sandia Corporation a Lockheed Martin Company for the U.S. Department of Energy under Contract DE-AC04-94AL85000

T. Marinone (✉) • D. Cloutier
ATA Engineering, San Diego, CA 92130, USA
e-mail: tmarinon@ata-e.com

B. LeBlanc
Sandia National Laboratories, Albuquerque, NM 87185, USA

36.2 Test Article: Wind Turbine Blades

The Vestas V27 (V27) wind turbine blades are 13 m long with a half-meter-diameter root section. These blades had been retired from the field after many years in service, and significant rework and repair were performed to make them functional again. Multiple sensors were installed into the blades to provide data at multiple points along the blades. Figure 36.1 shows an overall view of the blade, with a zoomed-in rework section and the test-display model used for mode visualization.

The mass and CG of the blades were obtained by using two calibrated load cells at known distances along the blade to rigidly suspend the blade and record the load measured at each location. The mass moment of inertia was obtained by suspending the blade from two equal-length cords equidistant from the CG and measuring the period of oscillation about the desired axis. The following equation can then be used to solve for the mass moment of inertia term where the variables needed are the weight (W), length of the rigid strap (L), distance from the CG to the strap (x), and period of oscillation (T).

$$I = \frac{Wx^2T^2}{L} \frac{1}{4\pi^2}. \quad (36.1)$$

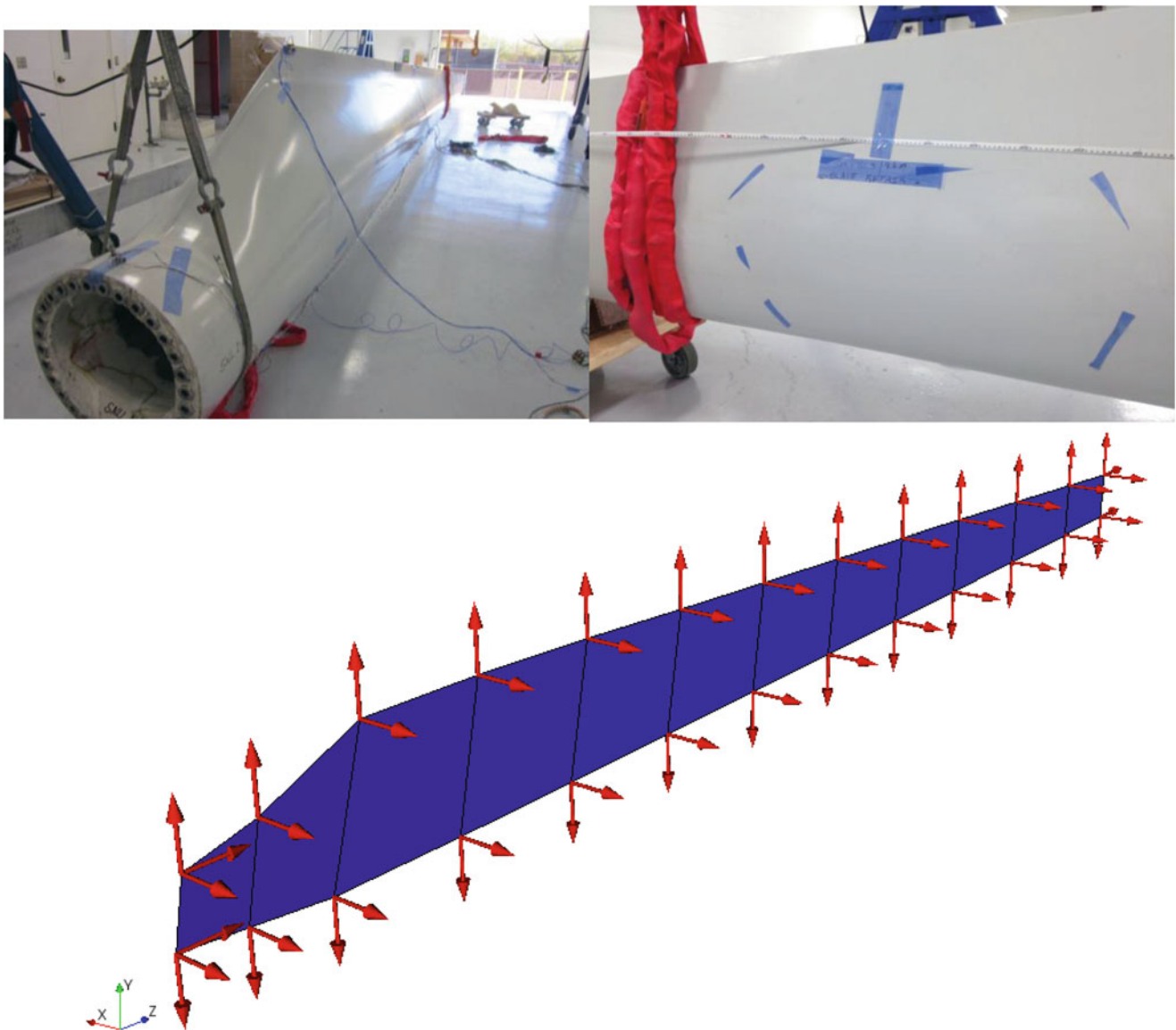


Fig. 36.1 Overall view of the blade (*upper left*), zoomed-in section showing rework (*upper right*), and test-display model showing sensor locations (*bottom*)

36.3 Test Results: Wind Turbine Blades

This section documents the wind turbine blade test results. Figure 36.2 shows the FRF for the tip drive point in the flap direction and indicates a high-quality measurement due to the near-unity coherence and distinct resonance peaks.

Table 36.1 lists the weight, CG, and moment of inertia about the y-axis for all six blades. Due to the multiple rotor sets, the manufacturing variability in older turbine blades, and the significant rework performed on several of the blades, the variation in weight and CG between blades is noticeable (8 %). Because the moment of inertia is affected by both the CG and weight, its variation between blades is more significant (19 %).

Table 36.2 lists the frequency for all six wind turbine blades. The flapwise and edgewise modes have minimal variation (5 %) between all six blades, indicating that the blades have a high degree of similarity. The torsion modes have a much higher variation (13 %), which indicates that these modes are more sensitive to the rework. Table 36.3 shows an orthogonality comparison performed between the two blades that contained a full set of instrumentation; note that there are high-orthogonality terms between the two sets of modes.

The SNL V27 wind turbine blade model was updated to better reflect the actual blades based on the test results. The thickness of layup materials as well as the density of resin was used to match the mass, CG location, static deflection, and modal parameters. The comparison of the model results to test data is listed in Table 36.4.

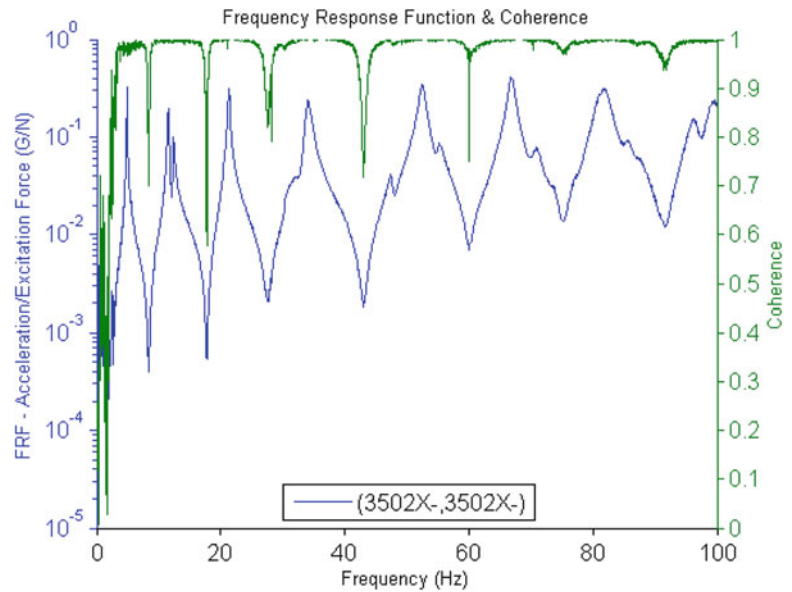


Fig. 36.2 FRF and coherence for impact hammer drive point node (3502X-)

Table 36.1 V27 wind turbine blades’ mass and inertia properties

| | SNL1_BL1 | SNL1_BL2 | SNL1_BL3 | SNL2_BL1 | SNL2_BL2 | SNL2_BL3 | Average | Max Difference (%) |
|-------------------------------|----------|----------|----------|----------|----------|----------|---------------|--------------------|
| Weight (N) | 6343 | 6357 | 6303 | 6552 | 6423 | 6787 | 6460.8 | 7.7 |
| CG - X Axis (m) | - | - | - | - | - | - | - | - |
| CG - Y Axis (m) | - | - | - | - | - | - | - | - |
| CG - Z Axis (m) | 4.18 | 4.15 | 4.19 | 4.29 | 4.16 | 4.20 | 4.20 | 3.4 |
| Ixx (kg*m²) | - | - | - | - | - | - | - | - |
| Iyy (kg*m²) | 5002.8 | 5466.0 | 5097.4 | 4967.0 | 5887.3 | 5796.4 | 5369.5 | 18.5 |
| Izz (kg*m²) | - | - | - | - | - | - | - | - |

* Coordinate System Origin Defined at Blade Root Center

Table 36.2 V27 wind turbine blades' modes sorted by test frequency

| Mode # | Description | Blade Frequency (Hz) | | | | | | Average (Hz) | Max Difference (%) |
|--------|--------------|----------------------|------------|------------|------------|------------|------------|--------------|--------------------|
| | | SNL1 - BL1 | SNL1 - BL2 | SNL1 - BL3 | SNL2 - BL1 | SNL2 - BL2 | SNL2 - BL3 | | |
| 1 | 1st Flapwise | 4.79 | 4.80 | 4.94 | 4.90 | 4.82 | 4.88 | 4.86 | 3.16 |
| 2 | 2nd Flapwise | 11.30 | 11.40 | 11.89 | 11.64 | 11.41 | 11.55 | 11.53 | 5.27 |
| 3 | 1st Edgewise | 12.35 | 12.37 | 12.67 | 12.66 | 12.29 | 12.35 | 12.45 | 3.08 |
| 4 | 3rd Flapwise | 21.49 | 21.40 | 21.97 | 21.54 | 21.69 | 21.29 | 21.56 | 3.19 |
| 5 | 2nd Edgewise | 30.10 | 29.96 | 30.86 | 31.05 | 30.59 | 30.26 | 30.47 | 3.64 |
| 6 | 1st Torsion | 34.70 | 30.58 | 31.08 | 33.11 | 32.40 | 32.43 | 32.38 | 13.47 |
| 7 | 4th Flapwise | 33.60 | 34.24 | 34.90 | 34.64 | 34.64 | 34.04 | 34.34 | 3.88 |
| 8 | 2nd Torsion | 50.46 | 47.75 | 48.66 | 50.02 | 51.69 | 52.53 | 50.19 | 10.01 |
| 9 | 3rd Edgewise | 55.36 | 55.50 | 57.74 | 56.89 | 56.10 | 55.19 | 56.13 | 4.62 |

Table 36.3 V27 final test modes (SNL2_BL1 and SNL2_BL3 at full instrumentation set): self-orthogonality

| Test Self Orthogonality Table | | | | | | | | | | | | | | | | | | | |
|-------------------------------|-----|----------|------|------|------|------|------|------|------|----------|------|------|------|------|------|------|------|------|------|
| Test Shapes | | SNL2_BL1 | | | | | | | | SNL2_BL3 | | | | | | | | | |
| | Ott | 1 | 2 | 3 | 4 | 5 | 6 | 7 | 8 | 9 | 10 | 11 | 12 | 13 | 14 | 15 | 16 | 17 | 18 |
| SNL2_BL1 | 1 | 4.9 | 1.00 | | | | | | | | 0.99 | | | | | | | | |
| | 2 | 11.6 | | 1.00 | | | | | | | | 0.99 | | | | | | | |
| | 3 | 12.7 | | | 1.00 | | | | | | | | 0.99 | | | | | | |
| | 4 | 21.5 | | | | 1.00 | | | | | | | | 0.97 | | | | | |
| | 5 | 31.1 | | | | | 1.00 | | | | | | | | 0.87 | | | | |
| | 6 | 33.1 | | | | | | 1.00 | 0.56 | | | | | | | 0.98 | 0.69 | | |
| | 7 | 34.6 | | | | | | 0.56 | 1.00 | | | | | | | | 0.98 | | |
| | 8 | 50.0 | | | | | | | | 1.00 | | | | | | | | 0.98 | 0.52 |
| | 9 | 56.9 | | | | | | | | | 1.00 | | | | | | | | 0.95 |
| | 10 | 4.9 | 0.99 | | | | | | | | | 1.00 | | | | | | | |
| SNL2_BL3 | 11 | 11.5 | | 0.99 | | | | | | | | 1.00 | | | | | | | |
| | 12 | 12.3 | | | 0.99 | | | | | | | | 1.00 | | | | | | |
| | 13 | 21.3 | | | | 0.97 | | | | | | | | 1.00 | | | | | |
| | 14 | 30.3 | | | | | 0.87 | | | | | | | | 1.00 | | | | |
| | 15 | 32.4 | | | | | | 0.98 | | | | | | | | 1.00 | 0.61 | | |
| | 16 | 34.0 | | | | | | 0.69 | 0.98 | | | | | | | 0.61 | 1.00 | | |
| | 17 | 52.5 | | | | | | | | 0.98 | | | | | | | | 1.00 | 0.51 |
| | 18 | 55.2 | | | | | | | | 0.52 | 0.95 | | | | | | | 0.51 | 1.00 |

Table 36.4 V27 wind turbine blade model correlation results

| | Mass (kg) | CG (m) | 1st Flapwise (Hz) | 2nd Flapwise (Hz) | 1st Edgewise (Hz) |
|----------------------|-----------|--------|-------------------|-------------------|-------------------|
| Model | 641.9 | 4.31 | 4.82 | 10.09 | 12.56 |
| Average Experimental | 659.2 | 4.195 | 4.86 | 11.53 | 12.45 |
| Percent Difference | -2.63% | 2.74% | -0.8% | -12.5% | 0.9% |

36.4 Test Article: Wind Turbine Towers

The Vestas V27 (V27) towers are 31 m long, made of a steel alloy, and weigh approximately 13 tons (26,000 lbs). The overall view of the tower and the test-display model used for mode visualization are shown in Fig. 36.3 in the simulated free-free configuration. The towers were supported on frames located approximately at the nodes of the first bending mode, and

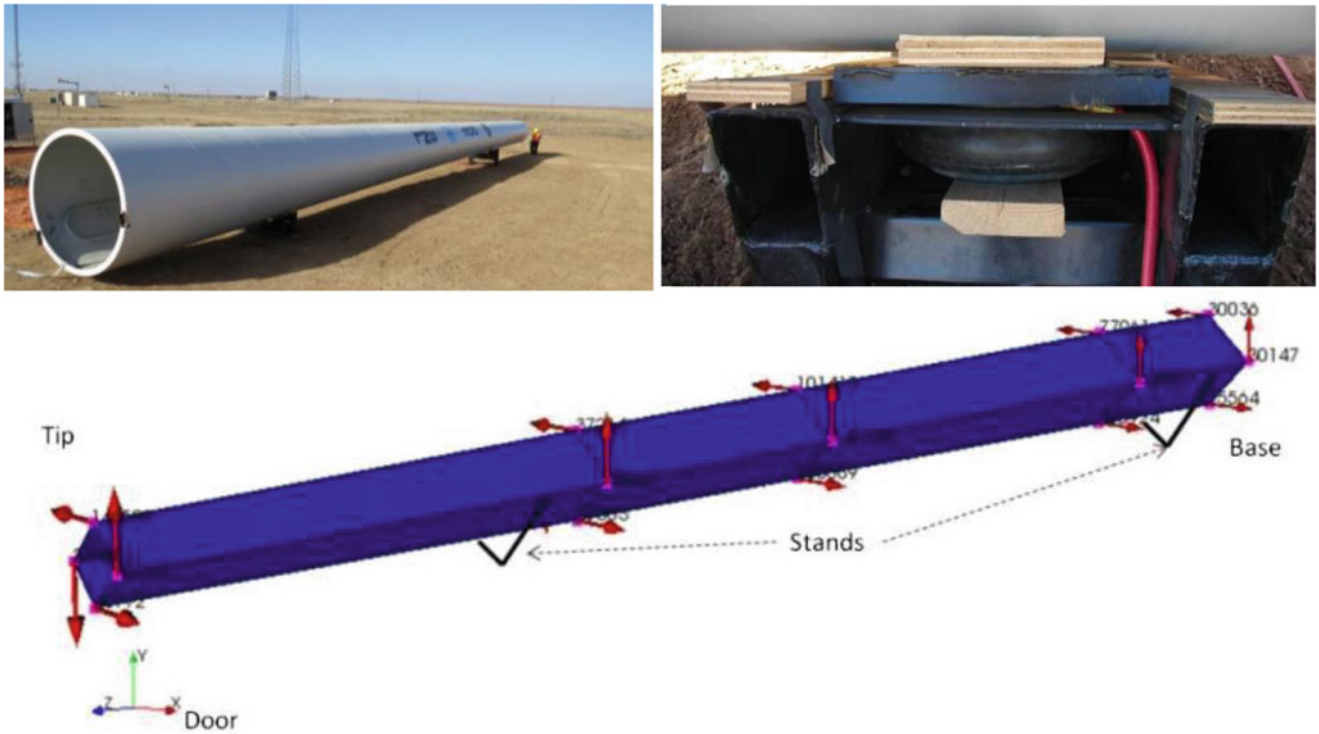
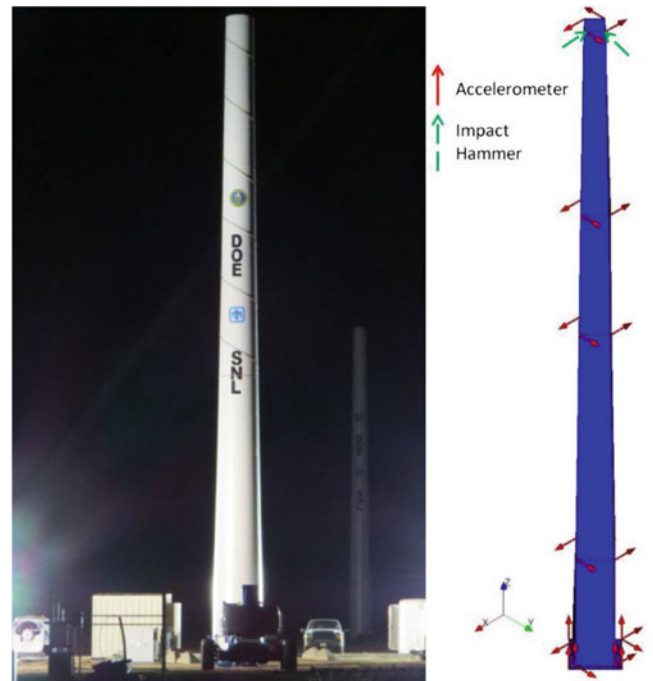


Fig. 36.3 Overall view of the tower (*left*), support stand with airbags (*right*), and test-display model (*bottom*) in the free-free configuration

Fig. 36.4 Overall view of the tower (*left*) and test-display model (*right*) in the bolted configuration



during testing, airbags were inserted into the frames and used to lift the tower at four points to simulate a free-free boundary condition. Figure 36.4 shows the overall view of the towers bolted to the foundation and the corresponding test-display model.

36.5 Test Results: Wind Turbine Towers

This section documents the wind turbine tower test results.

Figure 36.5 shows the FRF for the tip drive point and indicates a high-quality measurement due to the near-unity coherence and distinct resonance peaks.

Table 36.5 lists the frequency differences between the two towers in the free-free configuration, and Table 36.6 lists the frequency differences between the two towers in the bolted configuration. Although the frequencies and damping of the mode shapes compare well for the tower in the free-free boundary condition, the towers were oriented differently on the support stands. As a result, the orthogonal axes of bending were different, causing the corresponding mode shape vectors to be oriented at different angles. This led to poor MAC values, which are therefore not shown. When the towers were tested in a bolted configuration, however, they were oriented the same, and the mode shapes were compared and found to be very similar ($MAC > 90$) for the first bending mode.

In addition to verifying that the towers were similar, effort was focused on characterizing the foundation stiffness. Most modelers assume that the foundation is completely fixed, which introduces error. Thus, to determine the foundation stiffness, seismic accelerometers (393B04) were mounted on the concrete foundation in the vertical direction. Accelerometers were also mounted on the base of the tower to determine if there was relative motion between the tower and the foundation. A comparison of the FRFs from the two accelerometers is shown in Fig. 36.6.

The FRF comparison shows minimal difference between the two accelerometers, which indicates that there is no relative motion between the tower and foundation. There is a clear natural frequency near 12 Hz, however, indicating that the foundation cannot be assumed to be completely fixed. Based on this information and the modal results from above, the tower boundary condition was changed from fixed to translational and rotary springs. A translational spring of 2 GN/m representing the horizontal stiffness of the foundation and a rotational spring of 13 GN-m/rad to represent the rocking stiffness were applied to a representative two-dimensional beam model of the tower. The results are shown in Table 36.7.

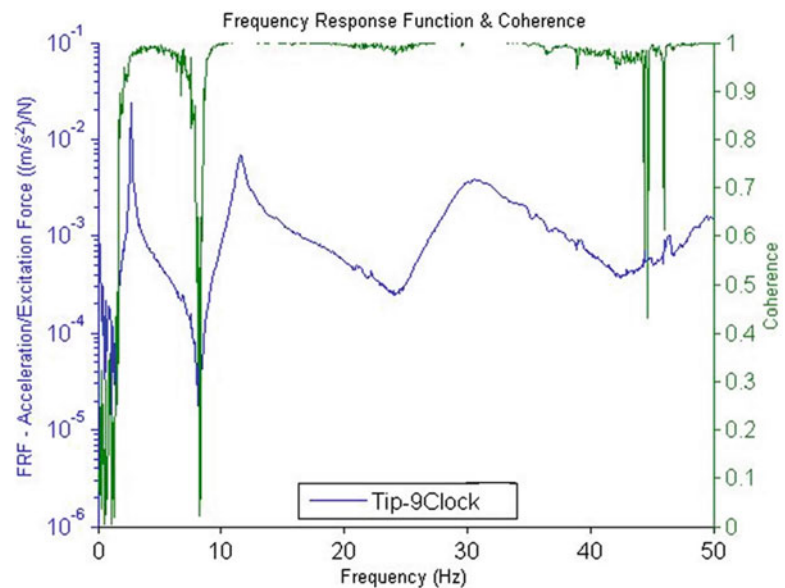


Fig. 36.5 FRF and coherence for impact hammer drive point 3502x-, run 22

Table 36.5 V27 wind turbine tower modes sorted by test frequency: free-free boundary condition

| | Tower 1 | | Tower 2 | |
|---------------------|----------------|------------------|----------------|------------------|
| | Frequency (Hz) | Damping (% Crit) | Frequency (Hz) | Damping (% Crit) |
| First Bending Mode | 10.66 | 1.47 | 10.61 | 1.10 |
| | 10.88 | 2.47 | 10.69 | 1.92 |
| Second Bending Mode | 28.34 | 3.06 | 28.29 | 0.85 |
| | 29.10 | 2.24 | 28.80 | 1.09 |
| Rigid Body Mode | 2.12 | 6.86 | 2.08 | 5.48 |

Table 36.6 V27 wind turbine tower modes sorted by test frequency: bolted boundary condition

| | Axis of Motion | Tower 1 | | Tower 2 | | MAC |
|---------------------|----------------|----------------|------------------|----------------|------------------|------|
| | | Frequency (Hz) | Damping (% Crit) | Frequency (Hz) | Damping (% Crit) | |
| First Bending Mode | Fore-Aft (X) | 2.70 | 0.56 | 2.61 | 0.82 | 0.95 |
| | Side-Side (Y) | 2.73 | 0.98 | 2.67 | 0.50 | 0.90 |
| Second Bending Mode | Fore-Aft (X) | 11.58 | 2.24 | 11.32 | 2.49 | 0.81 |
| | Side-Side (Y) | 11.71 | 1.76 | 11.58 | 1.57 | 0.84 |

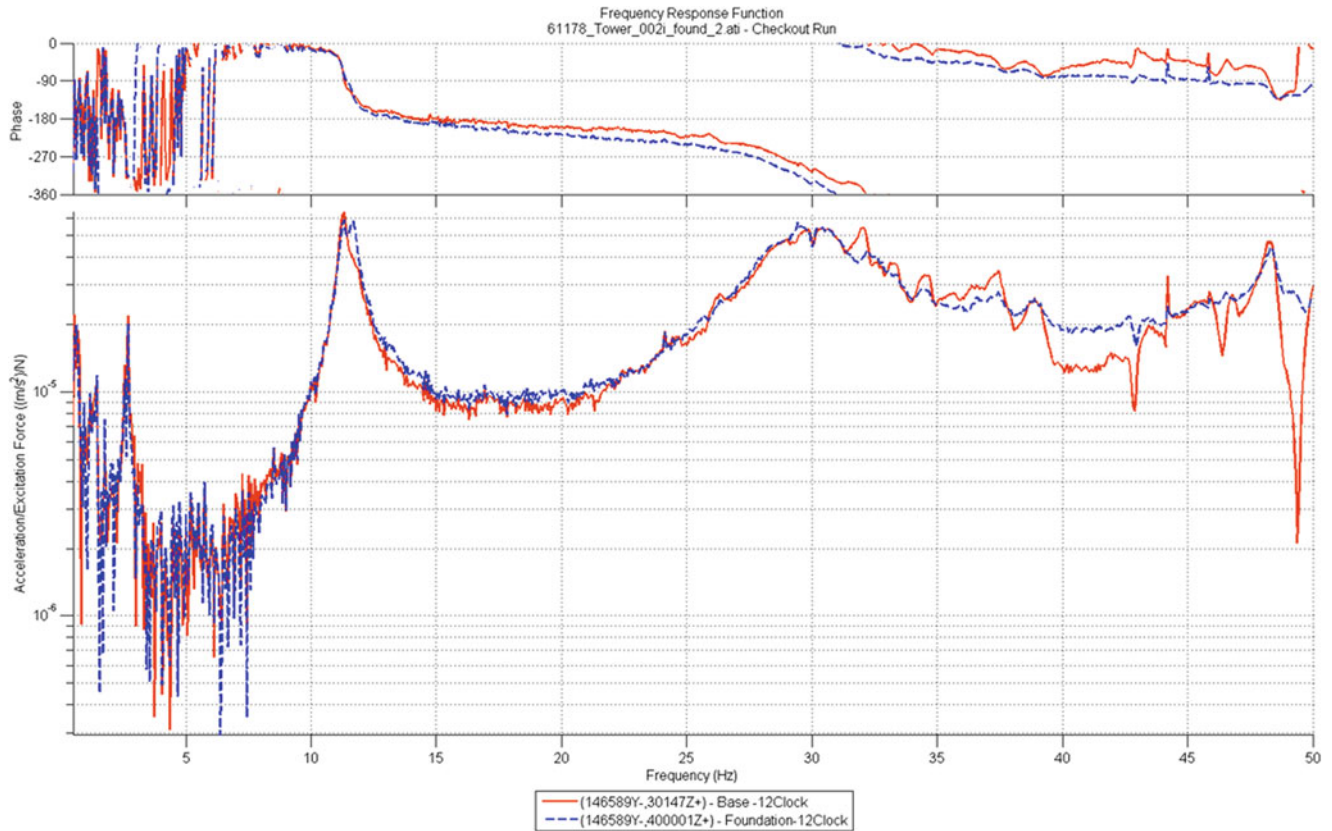


Fig. 36.6 Comparison of FRFs between vertical accelerometers on tower foundation and tower base

Table 36.7 V27 wind turbine tower model correlation results

| Mode | Experimental (Hz) | Model (Hz) | % Difference | MAC |
|------|-------------------|------------|--------------|------|
| 1 | 2.68 | 2.67 | -0.3 | 0.99 |
| 2 | 11.55 | 11.92 | 3.2 | 0.98 |

36.6 Summary

This paper presented the results obtained from testing multiple components of the SWiFT V27 wind turbine.

The first test was on the six wind turbine blades, and the mass inertia and dynamic characteristics were obtained. The blades showed noticeable variation in mass and CG due to the rework done on the blades; the effects of this rework were also clearly seen in the torsional modes.

The second test was on the two wind turbine towers in both the free-free and bolted boundary conditions. Measurements taken on the foundation showed that the foundation was not fixed, and the boundary condition was updated to reflect the motion of the foundation.

The results obtained from these tests allow Sandia’s wind turbine models to be more accurate for use in future analyses.

References

1. Marinone T, Napolitano K, Cloutier D, LeBlanc B (2014) Comparison of multiple mass property estimation techniques on SWiFT Vestas 27 wind turbine nacelles and hubs. In: Proceedings of 32nd IMAC, Orlando
2. Cloutier D, Marinone T, LeBlanc B, Anderson P, Carne T (2014) Artificial and natural excitation testing of SWiFT Vestas 27 wind turbines. In: Proceedings of 32nd IMAC, Orlando
3. LeBlanc B, Cloutier D, Marinone T (2014) Overview of the dynamic characterization at the SWiFT wind facility. In: Proceedings of 32nd IMAC, Orlando

Chapter 37

Development of Simplified Models for Wind Turbine Blades with Application to NREL 5 MW Offshore Research Wind Turbine

Majid Khorsand Vakilzadeh, Anders T. Johansson, Carl-Johan Lindholm, Johan Hedlund,
and Thomas J.S. Abrahamsson

Abstract Integration of complex models of wind turbine blades in aeroelastic simulations places an untenable demand on computational resources and, hence, means of speed-up become necessary. This paper considers the process of producing simplified rotor blade models which accurately approximate the dynamics of interest. The novelty, besides applying an efficient model updating procedure to the wind turbine blade, is to challenge the conventional beam element formulation utilized in the majority of aeroelastic codes. First, a 61.5 m blade, previously reported by the National Renewable Energy Laboratory, is selected as a case study and a verified industry-standard three dimensional shell model is developed based on its actual geometry. Next, given the reported spanwise cross sectional properties of the blade, a calibrated beam model is developed, using an efficient model updating process, that shows an excellent agreement to the low frequency dynamics of the baseline model in terms of mode shapes, resonance frequency and frequency response function. The simulation study provides evidence that a beam model cannot capture all the important features found in a large-scale 3D blade. This motivates a departure from conventional beam element formulation and suggests addressing the problem of producing simplified models in the framework of model reduction techniques. A modified modal truncation algorithm is applied to the baseline model to produce a simpler model which accurately approximates its input–output behavior in a given frequency range. It is concluded that besides the computational efficiency of the reduction algorithm, the resulting approximation error is guaranteed to be bounded and the yielded low-order model can, in turn, be served in wind turbine design codes.

Keywords Model calibration • Model reduction • Wind turbine blade • Frequency response calibration • Beam modeling

37.1 Introduction

Wind energy as one of the most promising sources of renewable energy is going to provide 7–8 % of the demanded world's electricity power by 2020. However, for wind energy to meet such an impressive rate of growth, future wind turbines must be designed for maximum energy conversion efficiency. In response to this demand, the size of wind turbine blades has dramatically increased within the last few years and it is predicted that the wind turbines installed within the next 10–15 years will have rotor diameter of 180–200 m [1]. To design for future wind turbine blades, development of models will become more and more crucial to performing entire wind turbine simulations by using aeroelastic modeling tools and with the purpose of aerodynamic load estimation, reliability analysis and so forth. While coupling high fidelity large scale three dimensional Finite Element (FE) blade models in such aeroelastic settings results in more accurate prediction of performance, it also poses overwhelming demands on computational resources making the development of simplified engineering models become more and more necessary. For this reason, the present study briefly reviews common simplified blade modeling techniques and then proposes to address the problem of simplified blade model development within the model reduction framework.

M.K. Vakilzadeh (✉) • A.T. Johansson • T.J.S. Abrahamsson
Department of Applied Mechanics, Chalmers University of Technology, SE-412 96 Göteborg, Sweden
e-mail: khorsand@chalmers.se

C.-J. Lindholm • J. Hedlund
CCG Composites Consulting Group, SE-312 22 Laholm, Sweden

Mollineaux et al. [2] developed a simplified three dimensional FE model based on an accurate description of the geometry for the CX-100 blade designed at Sandia National Laboratory. As the main simplification, the cross sectional areas of the blade are modeled using isotropic material properties instead of complex multilayer composite materials. Another simplification was to use a coarse level of mesh resolution to be able to run a modal extraction code in a specified upper limit of time. They applied a Verification and Validation (V&V) technique to show that this simplified model is validated and is capable to capture the first three flapwise bending modes as dynamic of interest. In a companion paper [3], Bayesian inference is utilized to calibrate the proposed fast-running model against experimental data. As the main drawback, the developed simplified model is only capable of predicting the first three flapwise bending modes and the resulting approximation error is not reported in the study.

The formulation of the beam modeling is widely used to model complex applications such as helicopter and wind turbine rotor blades to provide approximations of reality which can be used in fast-running calculations [4, 5]. Geometrically exact formulation, which stiffness matrices are calculated using original three-dimensional finite element model or sectional analysis method, is a common practice to model wind turbine blades. In addition to complex spanwise distribution of blade characteristics in modern blades, the manufacturing process and material uncertainties cause an influential difference between reality and the designed intention. Thus, it is crucial to use finite element model updating procedure as an additional step to provide beam models which indicate the best possible fidelity to the reality [4]. In this study, the model updating problem is formulated as a logarithmic least-square approach. Since the FE model updating problem is mathematically ill-posed, selection of the output deviation metric poses a challenging problem. Against most of the methods which use modal data, a discrete frequency response based deviation metric together with a damping equalization technique is used in this paper to make the updating problem regularized.

Model order reduction is another possible alternative for simulation speed-up which seeks to approximate large-scale models with a low order model that preserves the input–output map of the original model. Once a high fidelity reduced model of blade is obtained it can reliably be used in the aero-elastic simulation codes in coupling with other components of the wind turbines. Although techniques such as Krylov-based methods, optimal Hankel approach, balanced truncation [6], and proper orthogonal decomposition [7] have received considerable attention throughout control community, they are inappropriate for modeling of wind turbine blade since the natural frequencies of the model are not guaranteed to remain unchanged. This paper applies a modal truncation technique which projects the original system onto a smaller subspace using projection bases consists of the most dominant eigenmodes. A new frequency restricted input–output measure is used as the modal dominance criterion which is the \mathcal{H}_2 -norm of the transfer function of the error system caused by neglecting each eigensolution from the original system.

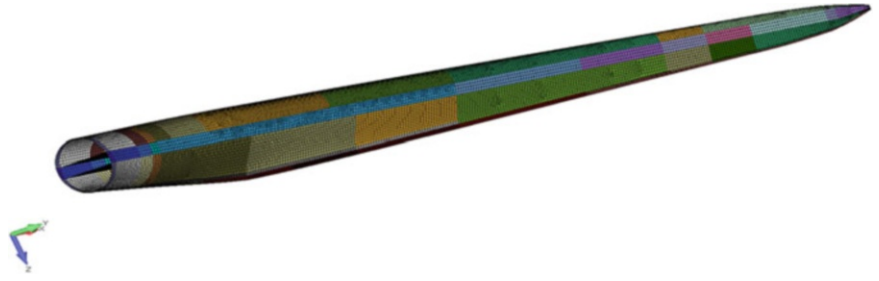
This study reviews two simplification algorithms to establish efficient simplified models for the 61.5 m research wind turbine blade developed at the National Renewable Energy Laboratory (NREL). An industry-standard beam model is developed based on the reported cross sectional properties of the reference model. The cross sectional flapwise, edgewise and torsional stiffnesses of the beam model are calibrated against the high fidelity FE model. The dynamic of interest for the calibration process is the model frequency response over the frequency ranges from 0.4 to 8 Hz. Our main goal is to show that the calibrated beam model cannot capture all the couplings found in the baseline model which in turn results in low prediction accuracy. To this end, a second simplified model is developed by applying a recent model reduction algorithm [8]. Within this algorithm, the baseline model is projected to a smaller subspace using a projection matrix that includes the most dominant eigensolutions. Credibility of the reduced baseline model, comparing to the reduced beam model, rests on its ability to accurately preserve the input–output relation of the baseline model. Two different load conditions are considered to illustrate the effectiveness of the reduction algorithm.

37.2 Development of FE Models for NREL 5 MW Wind Turbine Blade

37.2.1 Baseline Model

FE modeling of the blade was performed using Siemens pre- and post-processor FEMAP 11.0. The blade is 61.5 m long. Figure 37.1 demonstrates the high-fidelity FE model of NREL 5 MW wind turbine blade. The element mesh has been built up from a surface model where the created mesh comprises of 2D shell, 3- and 4-noded laminate elements, CQUAD4 and CTRI3 for a total of 27,309 elements containing 26,626 nodes. These elements have a special feature for composite and sandwich materials, where the laminate elements property is build up by stacking n number of plies in a certain order in which each ply is given a specific material and thickness with a specified angle in case of 2D Orthotropic materials such as

Fig. 37.1 Schematic view of the high fidelity FE model, baseline model, of the NREL 5 MW wind turbine blade



E-glass as used in this FE model. The 0° orientation for the shell elements is then set towards the tip of the blade. The skin of the model was furthermore modeled using an offset to ensure that the outer surface of the geometry is also the outer surface of the model. The skin sides consist of double biaxial E-glass fabrics, with core and reinforced Uni-Directional (UD) working as a core pending on area of the blade. On the outside of the spar cap, balsa wood is used in the first part of the blade as core material. In front of this and up to the tip a Divinycell PET foam core is used to build up the sandwich structure. At the spar cap itself, UD E-glass is used as reinforcement between the two skins. UD reinforcements are also used at the trailing edge to improve the edgewise eigenfrequencies and buckling properties. The webs are reinforced with balsa wood to build up a sandwich structure.

37.2.2 Nominal Beam Model

The nominal beam model of NREL 5 MW wind turbine blade is analyzed with the MSC Nastran software. This model is based on the spanwise distribution of the blade structural properties reported by Jonkman et al. [9]. For the sake of compatibility with the available information, the Euler Bernoulli beam formulation is utilized to develop the FE model containing 48 beam elements and 49 nodes, which results in a model of order 294. The values for the cross sectional flapwise and edgewise stiffnesses and mass moment of inertias are reported [9] in the principal axis of each section, as oriented by the structural twist angle. The insignificant values for the shear center and flapwise center of mass offset from the blade pitch axis are neglected. Isotropic material is defined within each element.

37.3 FE Model Updating of Beam Model

This section explains a FE model calibration strategy to improve the predictive capability of the simplified beam model over the frequency range of interest [10].

37.3.1 Problem Statement

The dynamical system is a damped fixed structure around the nominal configuration and is subjected to an external load. Using the FE method to discretize the boundary valued problem, results in a set of ordinary differential equation of motion as

$$\mathbf{M}\ddot{\mathbf{x}}(t) + \mathbf{V}\dot{\mathbf{x}}(t) + \mathbf{K}\mathbf{x}(t) = \mathbf{f}(t) \quad (37.1)$$

where $\mathbf{x}(t) \in \mathbb{R}^{n_x}$ is the displacement vector, $\mathbf{f}(t)$ is the external load vector which is governed by a Boolean transformation of excitation vector $\mathbf{f}(t) = \mathbf{P}_u \mathbf{u}(t)$; with $\mathbf{u}(t) \in \mathbb{R}^{n_u}$. Real positive-definite symmetric matrices $\mathbf{M}, \mathbf{V}, \mathbf{K} \in \mathbb{R}^{n_x \times n_x}$ are mass, damping and stiffness matrices, respectively. The finite element model can be parameterized using a set of identified parameter vector of $\mathbf{p} \in \mathbb{R}^{n_p}$ such that mass and stiffness matrices are denoted as $\mathbf{M}(\mathbf{p})$ and $\mathbf{K}(\mathbf{p})$. The state-space realization of the equation of motion in (37.1) can be written as

$$\dot{\mathbf{z}}(t) = \mathbf{A}\mathbf{z}(t) + \mathbf{B}\mathbf{u}(t), \quad \mathbf{y}(t) = \mathbf{C}\mathbf{z}(t) + \mathbf{D}\mathbf{u}(t) \quad (37.2)$$

where $\mathbf{A} \in \mathbb{R}^{n_x \times n_x}$, $\mathbf{B} \in \mathbb{R}^{n_x \times n_u}$, $\mathbf{C} \in \mathbb{R}^{n_y \times n_x}$, and $\mathbf{D} \in \mathbb{R}^{n_y \times n_u}$. \mathbf{A} is non-defective matrix. $\mathbf{z}(t) = [\mathbf{x}(t) \dot{\mathbf{x}}(t)]^T \in \mathbb{R}^{2n_x}$ is the state vector, and $\mathbf{y}(t) \in \mathbb{R}^{n_y}$ is the system output. We denote this system as Σ throughout. \mathbf{A} and \mathbf{B} are related to mass, damping and stiffness as follows [10]

$$\mathbf{A} = \begin{bmatrix} \mathbf{0} & \mathbf{I} \\ -\mathbf{M}^{-1}\mathbf{V} & -\mathbf{M}^{-1}\mathbf{K} \end{bmatrix}, \quad \mathbf{B} = \begin{bmatrix} \mathbf{0} \\ \mathbf{M}^{-1}\mathbf{P}_u \end{bmatrix} \quad (37.3)$$

Whenever the input vector is exponentially bounded, the Laplace transform can be used to write the transfer function of system Σ as $\mathbf{G}(s) = \mathbf{C}(s\mathbf{I} - \mathbf{A})^{-1}\mathbf{B} + \mathbf{D}$ for $s \in \mathbb{C}$. We denote the transfer function established by the FE method by \mathbf{G}^A throughout. On the experimental side of the model calibration, the measured transfer function \mathbf{G}^X can be expressed as

$$\mathbf{G}^X(\omega) = \mathbf{G}^A(\omega) + \mathbf{N}_G(\omega) \quad (37.4)$$

where $\mathbf{N}_G(\omega) \in \mathbb{C}^{n_y \times n_u}$ is the additive error due to measurement noise and unmodelled dynamics. It is assumed that \mathbf{N}_G is an independent (over frequency ω), zero-mean, and circular complex normally distributed random variable, resulting that it has independent real and imaginary parts and the higher order moments of \mathbf{N}_G are zero. The model calibration problem is to find the parameter setting \mathbf{p}^* which minimizes the deviation between $\mathbf{G}^X(\omega)$ and $\mathbf{G}^A(\omega)$.

37.3.2 Parameter Estimation

The great challenge in FE model calibration resides in the fact that it usually does not end up with a unique solution. Logarithmic least-square (LOG) optimization is a response to this challenge. In a frequency domain context, the LOG framework formulation of the FE model calibration problem is

$$\mathbf{p}^* = \underset{\mathbf{p}}{\operatorname{argmin}} (\delta^T \delta) \quad (37.5)$$

where the deviation metric $\delta(\mathbf{p})$ is

$$\delta(\mathbf{p}) = \ln \operatorname{vect}(\mathbf{G}^X) - \ln \operatorname{vect}(\mathbf{G}^A(\mathbf{p})) \quad (37.6)$$

in which $\operatorname{vect}(\cdot)$ is a vectorizing operator that collects all the $n_y \times n_u$ elements of the system transfer function at all sampling frequencies into a column vector belonging to $\mathbb{C}^{n_y n_u n_f \times 1}$, where n_f is the number of sampling frequencies. Taking the logarithm of the system transfer function restricts the range of the frequency response function which increases the likelihood of obtaining a unique solution and, thus, the well-posedness of the FE model updating problem. However, noise on the logarithm of the measured transferred function is expressed as $\mathbf{N} = \ln(\mathbf{I} + \mathbf{N}_G/\mathbf{G}^A)$ which is, in turn, a nonzero mean noise. Thus, the LOG estimator is theoretically inconsistent. Nevertheless, it can be shown [11] that if the assumed conditions are valid for \mathbf{N}_G and the frequency domain system output has a signal-to-noise ratio larger than 10 dB, the LOG estimator is “practically” consistent and the maximum magnitude of the bias term is smaller than 2×10^{-6} . Then, it may assume that the same conditions are also valid for \mathbf{N} .

Since FE model calibration is computationally demanding, a sampling strategy must be selected such that simultaneously provides enough information over the frequency range of interest while the deviation metric is as inexpensive as possible to manipulate. Such sampling strategy targets the half-band-width of a damped resonance frequency, since it contains most of the system information. Recall that for a damped resonance frequency, ω_i , the half-band-width is

$$\Delta\omega_i = 2\xi_i \omega_i \quad (37.7)$$

Where ξ_i is the relative modal damping of the i th eigenmode. To keep the number of samples constant in one half-band-width within the frequency range, the sampling frequency steps must increase linearly with frequency. This means taking constant frequency steps in the logarithmic scale, i.e.,

$$\log \omega_{i+1} - \log \omega_i = 2\xi_i + 1 \quad (37.8)$$

Note that logarithmically spaced frequency grids as the sampling strategy weight all modes equally when the relative damping of all modes is equal. Since this rarely happens for the experimentally collected eigenmodes, in this study, damping equalization technique is used to assign the same relative damping to all modes, see [10] for further information.

37.3.3 Parameterization of the Beam Model

The spanwise distribution of the cross sectional properties of the NREL 5 MW reference wind turbine blade is reported in Jonkman et al. [9] for 49 sections along the blade pitch axis to accurately represent the high gradient and jump discontinuities, due to ending of the shear webs, in the property distribution. In this study, flapwise, edgewise and torsional stiffnesses at each cross section are selected as parameters subjected to calibration. For the sake of simplicity, we assume that the mass per unit span can be scaled for the entire blade to meet the total mass of the baseline model described in Sect. 37.2. However, the direct use of such pointwise sectional properties make the FE model updating problem impractical for the following reasons. First, the number of parameters would be 147 which implies a very high dimensional parameter space which in turn implies unmanageable demands on computational resources. Second, representing the structural properties of the beam model using a large number of parameters results in poorly identifiable unknown parameters. In order to address these problems, unknown parameters are selected as multiplicative coefficients altering a given structural property over a segment of the blade. This approach couples the structural properties together over a segment and makes the effect of unknown parameters less local in comparison to the direct use of pointwise sectional properties. Let the blade span be divided into n_s segments, where the j th segment involves c_j cross sections. Then, the structural properties over the segment j can be expressed as

$$\begin{aligned} \begin{bmatrix} k_1^f & \cdots & k_{c_j}^f \end{bmatrix}^T &= \begin{bmatrix} \bar{k}_1^f & \cdots & \bar{k}_{c_j}^f \end{bmatrix}^T (1 + p_j^f), \\ \begin{bmatrix} k_1^e & \cdots & k_{c_j}^e \end{bmatrix}^T &= \begin{bmatrix} \bar{k}_1^e & \cdots & \bar{k}_{c_j}^e \end{bmatrix}^T (1 + p_j^e), \\ \begin{bmatrix} k_1^t & \cdots & k_{c_j}^t \end{bmatrix}^T &= \begin{bmatrix} \bar{k}_1^t & \cdots & \bar{k}_{c_j}^t \end{bmatrix}^T (1 + p_j^t). \end{aligned} \quad (37.9)$$

where k_i^f , k_i^e and k_i^t , for $i = 1 \dots c_j$, are the flapwise bending, edgewise bending and torsional stiffnesses, respectively, over the j th segment and \bar{k}_i^f , \bar{k}_i^e and \bar{k}_i^t , for $i = 1 \dots c_j$, are the flapwise bending, edgewise bending and torsional stiffnesses at the nominal configuration. Finally, the vector of unknown parameters for the optimization problem can be defined as

$$\mathbf{p} = \left[\dots \quad p_j^f \quad p_j^e \quad p_j^t \quad \dots \right]^T, \quad j = 1 \dots n_s \quad (37.10)$$

with $\mathbf{p} \in \mathbb{R}^{3n_s \times 1}$.

37.4 Model Reduction of Baseline Model

37.4.1 Model Reduction Problem

Given the linear dynamical system Σ in Eq. (37.2), model reduction attempts to construct the reduced system of the form

$$\begin{aligned} \dot{\mathbf{x}}_r(t) &= \mathbf{A}_r \mathbf{x}_r(t) + \mathbf{B}_r \mathbf{u}(t) \\ \mathbf{y}_r(t) &= \mathbf{C}_r \mathbf{x}_r(t) + \mathbf{D} \mathbf{u}(t) \end{aligned} \quad (37.11)$$

with transfer function $\mathbf{G}_r(s) = \mathbf{C}_r(s\mathbf{I} - \mathbf{A}_r)^{-1} \mathbf{B}_r + \mathbf{D}$. We denote the reduced system by Σ_r throughout. For structural models, including the wind turbine blade considered in this paper, $\mathbf{A}_r \in \mathbb{R}^{n_r \times n_r}$, $\mathbf{B}_r \in \mathbb{R}^{n_r \times n_u}$, $\mathbf{C}_r \in \mathbb{R}^{n_y \times n_r}$, with $n_r \ll n_x$, are determined such that the following properties are satisfied: (a) for all inputs, the input–output mapping of Σ is approximated with small error, $\mathbf{y}_r(t) \approx \mathbf{y}(t)$, (b) the reduction algorithm is computationally efficient, and (c) important features of Σ such as eigensolutions and stability are preserved. Among the different methods of order reduction, modal truncation [12] yields high

fidelity reduced models in which the modal properties of the original system remain unchanged. Thus, this method shows the most promise to govern a simplified model of wind turbine blade. The next section gives an overview of an efficient modal truncation method.

37.4.2 Modal Truncation

Assume that the dynamical system Σ is diagonalizable and let \mathbf{A} be a matrix which has the eigenvalue set of $\lambda = \{\lambda_1, \lambda_2, \dots, \lambda_{n_x}\}$ and the corresponding eigenvector matrix $\Phi = [\phi_1, \phi_2, \dots, \phi_{n_x}]$. Using the projection $z(t) = \Phi^{-1}x(t)$, the dynamical system Σ can be projected onto modal coordinates in form of

$$\begin{aligned} \dot{z}(t) &= \Lambda z(t) + \widehat{\mathbf{B}}u(t) \\ y(t) &= \widehat{\mathbf{C}}z(t) + \mathbf{D}u(t) \end{aligned} \quad (37.12)$$

where $z(t) \in \mathbb{R}^{n_x}$ is the modal coordinate vector, $\Lambda = \text{diag}(\lambda_1, \lambda_2, \dots, \lambda_{n_x}) = \Phi^{-1} \mathbf{A} \Phi$, $\widehat{\mathbf{B}} = \Phi^{-1} \mathbf{B} = [\widehat{b}_1, \widehat{b}_2, \dots, \widehat{b}_{n_x}]$ is the modally projected input matrix, and $\widehat{\mathbf{C}} = \mathbf{C} \Phi = [\widehat{c}_1, \widehat{c}_2, \dots, \widehat{c}_{n_x}]$ is the modally projected output matrix. The transformed system of (37.12) can be partitioned as

$$\begin{bmatrix} \dot{z}_1(t) \\ \dot{z}_2(t) \end{bmatrix} = \begin{bmatrix} \Lambda_1 & 0 \\ 0 & \Lambda_2 \end{bmatrix} \begin{bmatrix} z_1(t) \\ z_2(t) \end{bmatrix} + \begin{bmatrix} \widehat{\mathbf{B}}_1 \\ \widehat{\mathbf{B}}_2 \end{bmatrix} u(t), \quad y(t) = \begin{bmatrix} \widehat{\mathbf{C}}_1 & \widehat{\mathbf{C}}_2 \end{bmatrix} \begin{bmatrix} z_1(t) \\ z_2(t) \end{bmatrix} + \mathbf{D}u(t) \quad (37.13)$$

where $z_1(t)$ is the vector of n_r dominant modal coordinates and Λ_1 is a diagonal matrix which contains the n_r most dominant eigenvalues of the dynamical system. The quadruple of $\Sigma_r = (\Lambda_1, \widehat{\mathbf{B}}_1, \widehat{\mathbf{C}}_1, \mathbf{D})$ is then the reduced system.

Different combinations of eigenmodes in the projection matrix result in distinct reduced models with varied input–output properties. It is, hence, of central importance to develop an appropriate measure to include a combination of the most dominant eigenmodes in the projection basis. In this paper, the modal dominance criterion developed by Vakilzadeh et al. [8] is considered as an appropriate input–output measure.

Let $\tilde{\mathbf{G}}_i$ denotes the resulting transfer function when the i th modal coordinate has been eliminated from (37.12). The square of the \mathcal{H}_2 -norm of the error transfer function over frequency range of interest $[\omega_1, \omega_2]$ after eliminating one modal coordinate from the original system can be written as

$$\begin{aligned} \left\| \mathbf{G}(j\omega) - \tilde{\mathbf{G}}_i(j\omega) \right\|_{\mathcal{H}_2}^2 &= \frac{1}{2\pi} \int_{\omega_1}^{\omega_2} \text{trace} \left[\widehat{\mathbf{b}}_i^H \frac{1}{(j\omega - \lambda_i)} \widehat{\mathbf{c}}_i^H \widehat{\mathbf{c}}_i \frac{1}{j\omega - \lambda_i} \widehat{\mathbf{b}}_i \right] d\omega \\ &+ \frac{1}{2\pi} \int_{-\omega_2}^{\omega_1} \text{trace} \left[\widehat{\mathbf{b}}_i^H \frac{1}{(j\omega - \lambda_i)} \widehat{\mathbf{c}}_i^H \widehat{\mathbf{c}}_i \frac{1}{j\omega - \lambda_i} \widehat{\mathbf{b}}_i \right] d\omega \end{aligned} \quad (37.14)$$

Fortunately, these integrals can be expressed in explicit form [8]. Consequently, the truncation error resulted from elimination of the i th modal coordinates in the \mathcal{H}_2 sense is defined as

$$M_i = \left\| \mathbf{G}(j\omega) - \tilde{\mathbf{G}}_i(j\omega) \right\|_{\mathcal{H}_2}^2 = \frac{1}{\pi} \text{trace} \left\{ \widehat{\mathbf{b}}_i^H \widehat{\mathbf{c}}_i^H \widehat{\mathbf{c}}_i \widehat{\mathbf{b}}_i \left[\frac{1}{|\Re(\lambda_i)|} \arctan \left(\frac{\omega}{|\Im(\lambda_i)|} \right) \right]_{\omega_1 - |\Im(\lambda_i)|}^{\omega_2 - |\Im(\lambda_i)|} \right\} \quad (37.15)$$

where $\Re(\cdot)$ and $\Im(\cdot)$ denotes the real and imaginary parts of a variable, respectively. The frequency-restricted dominance definition can be expressed as

Definition 1 For a given threshold value $\varepsilon > 0$ and frequency interval $[\omega_1, \omega_2]$, let n_r be the number of eigensolutions for which $M_k > \varepsilon$, $k = 1, \dots, n_r$. then, the full model of order n_x has n_r dominant and $n_x - n_r$ non-dominant eigensolutions. \square

Vakilzadeh et al. [8] also proposed to utilize the QR factorization to functionally improve the performance of the dominance analysis method in case of equal or closely spaced eigenvalues. Toward this end, let the modally projected input matrix corresponding to the subsystem associated to a given eigenvalue λ_j of multiplicity n_m , $\widehat{\mathbf{B}}_j \in \mathbb{R}^{n_m \times n_u}$, where $n_m \geq n_u$,

be factorized into a unitary matrix $\mathbf{Q} \in \mathbb{R}^{n_m \times n_m}$ whose columns are orthonormal and an upper triangular matrix $\mathbf{R} \in \mathbb{R}^{n_m \times n_u}$ as follows

$$\widehat{\mathbf{B}}_j = \mathbf{Q}\mathbf{R} = [\mathbf{Q}_1 \quad \mathbf{Q}_2] \begin{bmatrix} \mathbf{R}_1 \\ \mathbf{0} \end{bmatrix} \quad (37.16)$$

here, \mathbf{Q}_1 is an orthonormal basis for the column space of $\widehat{\mathbf{B}}_j$ and \mathbf{Q}_2 forms a basis for its nullspace. Introducing a new coordinate transformation $z_j = \mathbf{Q}_2' z_j'$ to the corresponding subsystem, the last $n_m - \text{rank}(\widehat{\mathbf{B}}_j)$ generalized modes of the subsystem are projected to the nullspace of the modally projected input matrix and would not be excited by the system input. Thus, they are rejected by the modal dominancy criterion. It follows from the orthogonality property of \mathbf{Q} , i.e. $\mathbf{Q}^T \mathbf{Q} = \mathbf{I}$, that the state-space equations are still diagonalized after transformation. The subsystem triple associated to the j th set of eigenvalues can be defined as

$$\tilde{\Sigma}_j = (\Lambda_j, \tilde{\mathbf{B}}_j, \tilde{\mathbf{C}}_j), \Lambda_j = \text{diag}(\lambda_j, \lambda_j, \dots, \lambda_j), \tilde{\mathbf{B}}_j = \mathbf{R}, \tilde{\mathbf{C}}_j = \mathbf{C}\mathbf{Q} \quad (37.17)$$

and the corresponding eigenvectors are replaced by $\tilde{\Phi}_j = \Phi_j \mathbf{Q}$, where Φ_j is the j th block columns of the right eigenvector matrix.

37.4.3 Improved Modal Truncation Algorithm

This section presents a complete summary of the modal based model reduction technique proposed in [8] to govern an approximant which contains the dominant eigensolutions of the original system,

- (1) Given the state-space matrix \mathbf{A} , compute its eigensolution (Φ, λ) .
- (2) Project Σ to its decomposed modal form $(\Lambda, \widehat{\mathbf{B}}, \widehat{\mathbf{C}}, \mathbf{D})$ using the projection matrix of $\Phi = [\phi_1, \phi_2, \dots, \phi_{n_x}]$.
- (3) Find all multiple eigenvalues with dimension of multiplicity larger than the column rank of the modally projected input matrix $\widehat{\mathbf{B}}$. Denote number of multiple eigenvalues by n_c .
- (4) For $j = 1$ to n_c repeat
 - (a) Factorize $\widehat{\mathbf{B}}_j$ using the QR decomposition such that $\widehat{\mathbf{B}}_j = \mathbf{Q}\mathbf{R}$
 - (b) Project the corresponding subsystem to the new modal coordinate using \mathbf{Q}^T
 - (c) Set the associated new subsystem to $\tilde{\Sigma}_j = (\Lambda_j, \tilde{\mathbf{B}}_j, \tilde{\mathbf{C}}_j)$
 - (d) Replace the corresponding right eigenvectors by $\tilde{\Phi}_j$
- (5) Set the frequency range of interest $[\omega_1, \omega_2]$, using the frequency information of wind.
- (6) Compute the dominancy criterion using (37.15).
- (7) Determine the n_r dominant modes according to Definition 1.
- (8) Use the projection matrix $\mathbf{T} = [\phi_1 \quad \dots \quad \phi_{n_r}]$ to obtain the reduced dynamical system as $\Sigma_r = (\mathbf{T}^T \mathbf{A} \mathbf{T}, \mathbf{T}^T \mathbf{B}, \mathbf{C} \mathbf{T}, \mathbf{D})$.

37.5 Results

Beam models are routinely used in full-system analysis of wind turbines. A common practice is to perform calibration against experimental data to improve the predictive capability of the beam models. As mentioned, this study deviates from the common path by proposing that the fast-running blade models should be yielded by using the model reduction algorithms to keep the demanded prediction accuracy. This paper considers two parallel algorithms to govern a simplified model of the NREL 5 MW wind turbine blade, as a simulation study, with the goal of verifying the strength of reduced baseline model to predict the dynamic behavior of the original model in comparison to calibrated beam models. The comparison procedure used herein can be summarized as follows,

- (1) The edgewise, flapwise and torsional stiffnesses of the beam model are estimated on the basis of the high fidelity baseline model described in Sect. 37.2.

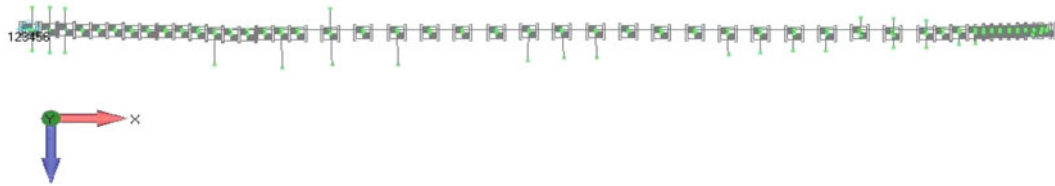
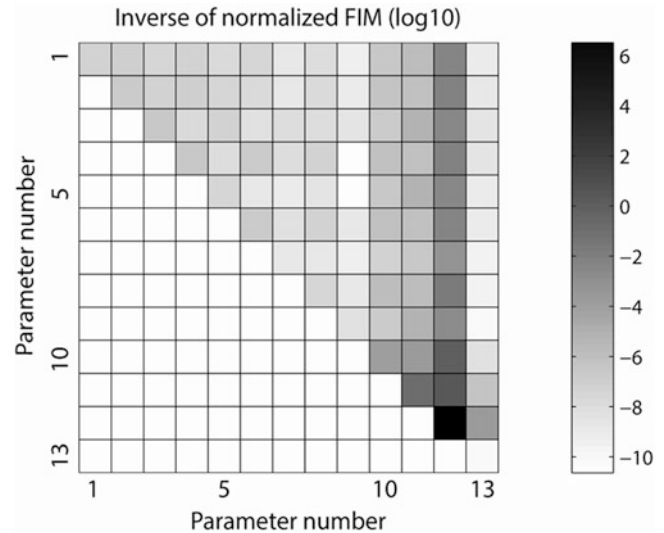


Fig. 37.2 Schematic view of the nominal beam model of the NREL 5 MW wind turbine blade. The branching elements are massless beams ending at reference nodes added for comparison with baseline model

Fig. 37.3 Graphical illustration of the inverse of the Fisher Information matrix evaluated at nominal configuration



- (2) The model reduction algorithm described in Sect. 37.3 is applied to the calibrated beam and the baseline models to yield reduced models of the same order.
- (3) The resulting low-order models are subjected to point excitations at the blade tip and the resulting approximation error is computed and then compared for different model orders of the two reduced order modeling approaches.

Numerical results obtained in at the different steps above are presented in this section.

37.5.1 Model Updating of the Beam Model

The analysis begins with updating the structural properties of the beam model against the simulation data obtained from the baseline model. To this end, the blades are clamped at the root and are subjected to three point forces; two tip forces in the flapwise and edgewise directions, and a point force in the flapwise direction at the node aimed at introducing strong torsional motion. In the baseline model, the Effective Independence [13] (EI) indices are computed to select a set of 50 output directions in which the mode shapes with natural frequency below 8 Hz are well identifiable. In the beam model, a corresponding set of output nodes is created and connected to the blade pitch axis using mass-less beam elements, shown in Fig. 37.2. The acceleration frequency responses are collected for the selected directions. The additive error due to measurement noise is neglected in this simulation study. For the sake of simplicity, in a preliminary step, the cross sectional masses are tuned such that the total mass and center of gravity of the beam model are in agreement with the baseline model. The identification parameters are selected as constant multipliers defined on six equally spaced segments for flapwise and edgewise stiffnesses. For the torsional stiffness a constant multiplier is defined over the entire blade. Consequently, the parameterized beam model consists of 13 structural parameters.

The identifiability of the parameters is tested by computing the inverse Fisher Information matrix illustrated in Fig. 37.3, the lower triangular part of the matrix is blanked due to its symmetric and the numbers are in logarithmic scale. This figure reveals that the structural parameters on the last segment (parameters 11 and 12) are poorly identifiable and can result in a large parameter covariance if the calibration is performed considering measurement noise. This fact is also reported by

Table 37.1 Comparison between the nominal and calibrated parameter values

| | Section number | Nominal value | Calibrated value |
|-----------|----------------|---------------|------------------|
| Flapwise | 1 | 0 | -0.3615 |
| | 2 | 0 | -0.4175 |
| | 3 | 0 | 0.0407 |
| | 4 | 0 | 1.9738 |
| | 5 | 0 | -0.2344 |
| | 6 | 0 | 0 |
| Edgewise | 1 | 0 | -0.5018 |
| | 2 | 0 | -0.5339 |
| | 3 | 0 | -0.0616 |
| | 4 | 0 | -0.5096 |
| | 5 | 0 | -0.8169 |
| | 6 | 0 | 0 |
| Torsional | Entire blade | 0 | -0.0705 |

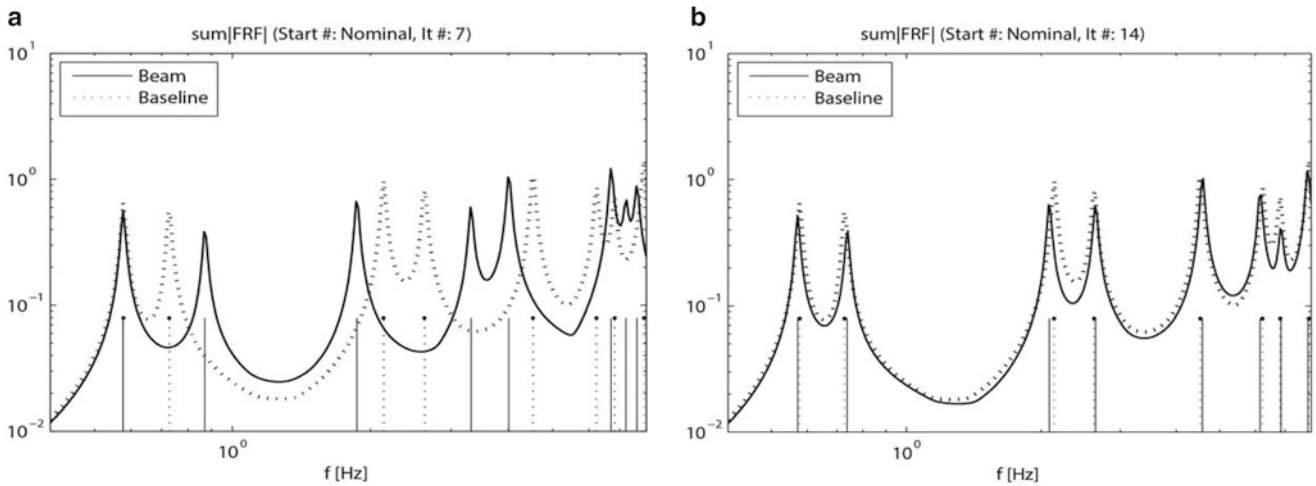


Fig. 37.4 Deviation of the nominal (a) and the calibrated beam model (b) from the baseline FE model. Curves show the sum of the magnitude of accelerances and stem bars indicate the location of eigenfrequencies

Table 37.2 Comparison between eigenfrequencies of the nominal and updated beam models and the baseline FE model in (Hz)

| | Mode 1 | Mode 2 | Mode 3 | Mode 4 | Mode 5 | Mode 6 | Mode 7 | Mode 8 |
|--------------------|--------|--------|--------|--------|--------|--------|--------|--------|
| Nominal beam model | 0.767 | 0.796 | 2.226 | 2.953 | 5.088 | 6.808 | 7.397 | 8.968 |
| Updated beam model | 0.574 | 0.732 | 2.087 | 2.633 | 4.580 | 6.179 | 6.853 | 7.873 |
| Baseline FE model | 0.577 | 0.727 | 2.136 | 2.622 | 4.526 | 6.229 | 6.822 | 7.906 |

Bottasso et al. [4] and, likewise, is attributed to the fact that the tip segment contributes the least to the rigidity of the structure. Herein, these parameters are frozen at their nominal values in the model updating procedure.

The FE model calibration procedure explained in Sect. 37.4 is used to estimate the structural parameters of the parameterized beam model. The results of the FE model updating procedure are listed in Table 37.1. Figure 37.4a demonstrates a comparison between the frequency response of the nominal beam and the baseline model summed over all the sensors in the frequency interval of 0.4–8 Hz. While this figure presents a significant difference between the prediction based on the calibrated nominal beam model and the baseline model, Fig. 37.4b shows that the updating procedure converged and the predictions based on the beam and the baseline model are well aligned in terms of natural frequencies, and frequency responses in the frequency range of interest.

Table 37.2 reports the eigenfrequencies of the baseline model as well as the eigenfrequencies of the nominal and calibrated beam model. The ability of the calibrated beam model to predict the low-frequency mode shapes of the baseline model is illustrated in Fig. 37.5. The degree of correlation between the mode shapes of the baseline model and the calibrated beam model is quantified using the Modal Assurance Criterion (MAC) defined by

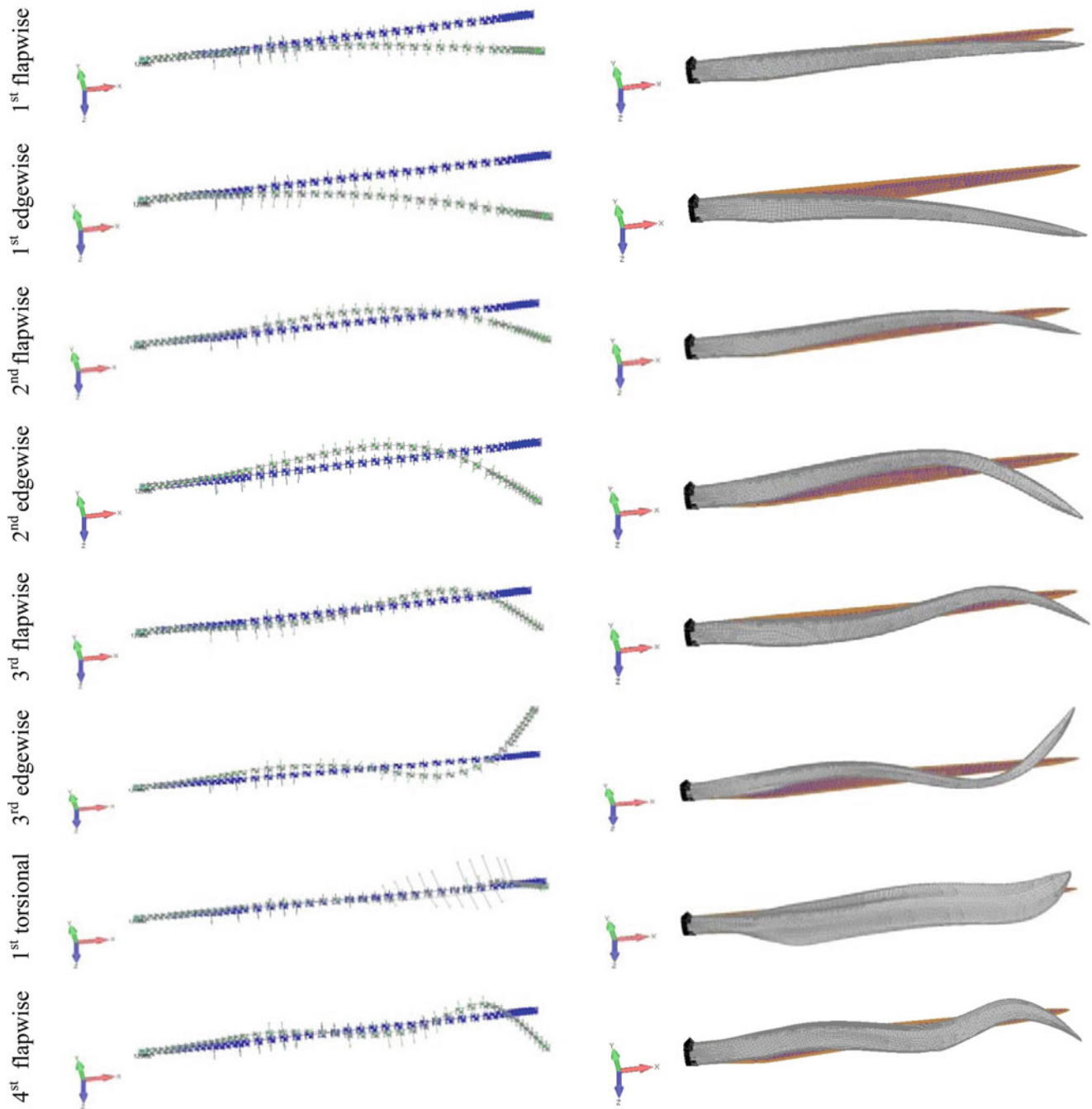


Fig. 37.5 Comparison of the first eight fixed-free mode shapes of the calibrated beam model and the baseline model

$$\text{MAC} = \frac{(\Phi_S^T \cdot \Phi_B)^2}{(\Phi_S^T \cdot \Phi_S)(\Phi_B^T \cdot \Phi_B)} \quad (37.18)$$

Where ϕ_S and ϕ_B are the mode shapes of the baseline shell and beam model respectively. The calculated MAC values corresponding to pre- and post-calibration steps are illustrated in Fig. 37.6, respectively. Generally, large MAC values represent which baseline mode shape is related to which mode shape of the beam model. An average value of 0.89 for the diagonal MAC values shows the ability of the calibrated beam model to predict the mode shapes of baseline model. The figure also indicates a decoupling between torsional, edgewise and flapwise bending modes of the beam model that was not present in the nominal beam model.

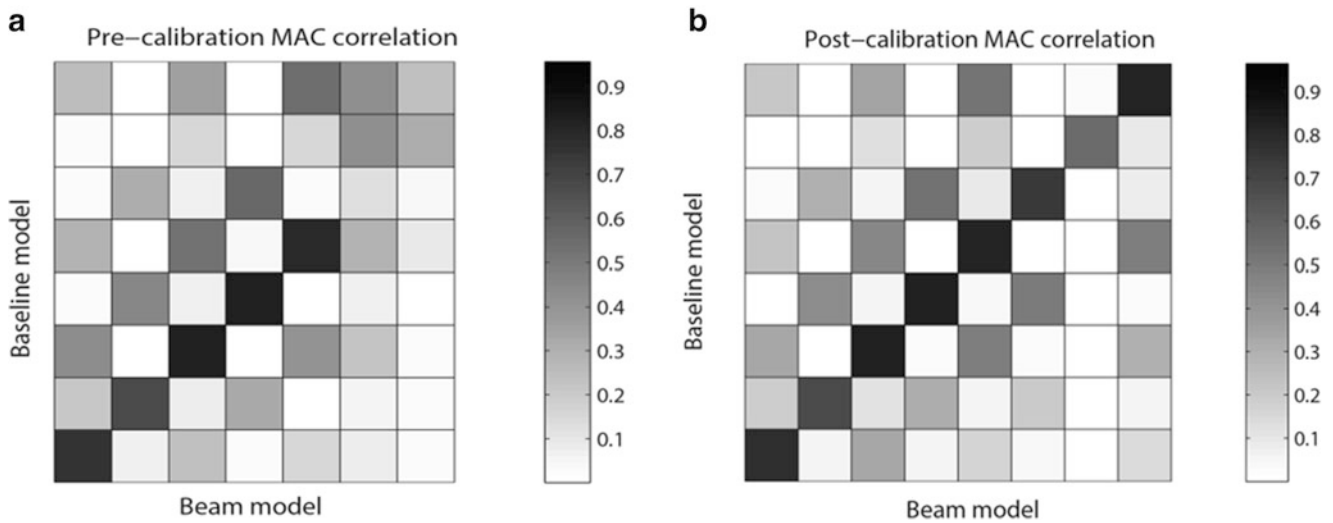


Fig. 37.6 The pre-calibration (a) and post-calibration (b) mode shape MAC values

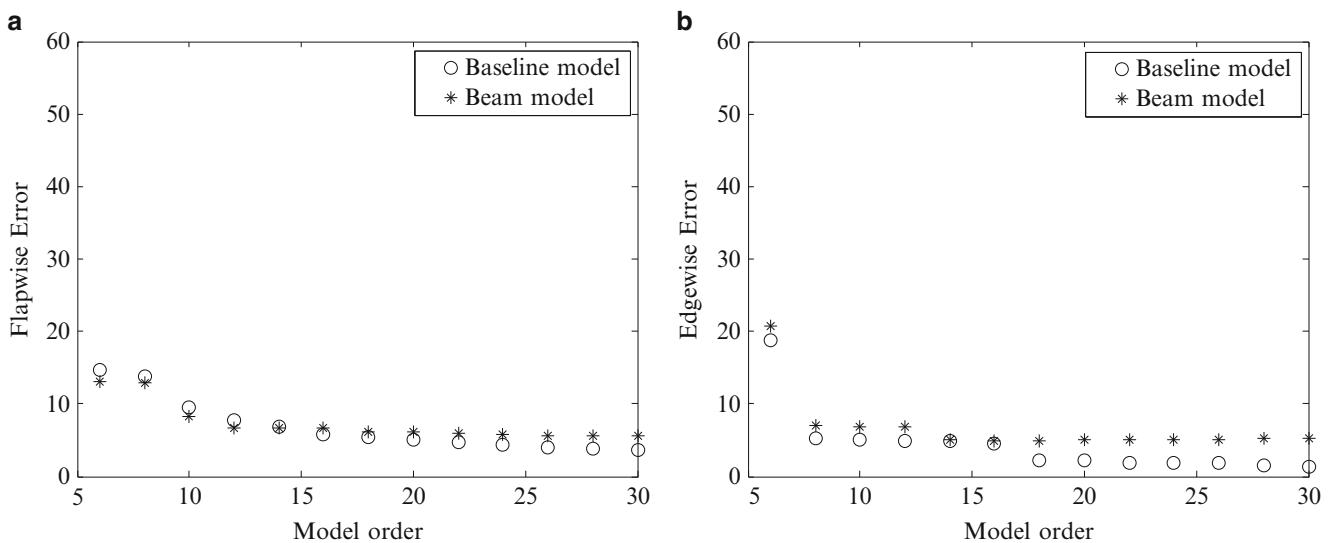


Fig. 37.7 The relative approximation error (%) of the baseline FE and beam model for different model orders. The input and output are in the same direction as; (a) flapwise and (b) edgewise. The input is a step function

37.5.2 Model Reduction of Rotor Blade Models

At this point, the beam model is calibrated against the baseline model to replicate its behavior in the frequency range from 0.4 to 8 Hz. Since common practice in wind turbine industry is to keep a few low frequency modes of the beam model in aeroelastic codes, for the purpose of entire wind turbine simulation, it remains to apply the mentioned model reduction algorithm to the calibrated beam and baseline models to yield reduced models of far smaller size. To this end, models are imported in MATLAB to assess the predictive power of the reduced updated beam model against the reduced baseline model. Models are clamped at the root and a relative modal damping of 1% is mapped to all the modes. The reduced-order models of dimension 6–30 by step of two states are computed where the modes have been ranked according to the modal dominance criterion of (37.15) considering no frequency weighting.

The performance of the reduced models is considered using two different load conditions. First, the models are subjected to step excitation inducing first the flapwise bending, and then the edgewise bending to assess the steady state approximation error. Figure 37.7a demonstrates the relative approximation error for different model orders when the blade is subjected with

a tip load in flapwise direction and the output is the displacement of the same node in the same direction. Figure 37.7b demonstrates a similar error analysis in the edgewise direction. For the baseline model, as the dimension of the reduced-order models increases, the approximation error is gradually decreasing and will approach to zero for high order models, as expected. For the beam model, as the model order of the reduced model is increased, the approximation error converges to a constant value constituting the model bias error. This behavior may indicate the fact that the beam formulation used in this study cannot capture all the coupling available in the baseline model even though the calibrated beam model shows an excellent agreement to the low frequency dynamics of the baseline model in terms of the eigenfrequencies and mode shapes, see Figs. 37.4 and 37.6. It also should be noted that the reduced models obtained based on the calibrated beam model and the baseline model indicate a similar capability to replicate the steady state behavior of the original baseline model in case of unidirectional excitation. This phenomenon motivates us to excite the reduced models with a more complicated load condition.

The second load condition belongs to the class of periodic random signals, random phase multisines. This signal is designed such that the amplitude spectrum is constant over all frequency lines range from 0.4 to 8 Hz, the same frequency interval as the calibration process. The phase spectrum is selected as a uniformly distributed noise sequence. The time domain realization of the signal is shown in Fig. 37.8a. The designed signal is simultaneously applied, as two tip point forces, in the flapwise and edgewise directions. The response is the displacement of the same node in the same directions. Figure 37.9 demonstrates the resulted relative approximation error for different model orders. Similar to the previous load condition, this figure illustrates that the approximation error resulted by reduced models based on the beam model is not converging to zero as the number of included modes in the projection bases is increasing. In comparison to the previous load condition, the approximation error resulted from the reduced beam model is substantially larger than the one obtained from the reduced baseline model. This figure also confirms that the reduced beam model cannot capture all the coupling features found in the baseline model. To investigate this fact in more details, the time domain response of models, full modes and reduced models of order 6, to the designed multisine signal is shown in the Fig. 37.8. Figure 37.8b confirms that the total approximation error resulted from reduced beam model is larger than the one resulted from the reduced baseline model. An interesting observation in Fig. 37.8c, e is that the predictive precision of the full beam model to replicate the behavior of the full baseline model differs in the flapwise and edgewise directions. The reason to this fact is twofold. First, the frequency response contains one more flapwise bending mode within the calibration frequency range which in turn results in higher predictive precision of the calibrated beam model in this direction. Second, in agreement to [4], the flapwise stiffness is more precisely identifiable than the edgewise stiffness, see Fig. 37.3. This fact can subsequently lead to more precise prediction of the resonance frequencies and mode shapes in the flapwise direction.

37.6 Conclusion

This paper discussed the development of a simplified model for the NREL 5 MW wind turbine blade. A particular effort has been made to calibrate an industry-standard beam model against a high fidelity three dimensional shell model. It was shown that in spite of the simplicity of the utilized beam formulation, an excellent agreement to the frequency response of the baseline model was achieved. A model reduction was considered as another alternative to develop a simplified blade model. The reduction of the baseline FE model was accomplished using a reduction basis consisting of dominant eigensolutions. The dominant eigenmodes were selected based on their contribution to the \mathcal{H}_2 -norm of the error transfer function. Two different load conditions were applied to the obtained simplified models. The results showed that the calibrated beam model cannot well capture the coupling features of the baseline model because of its inherent limitations. Although more accurate formulations such as the one obtained from VABS theory [14] may be employed in order to enhance the overall accuracy of beam formulation, model reduction formulation, used in this study, is a computationally efficient framework which provides simplified models that are able to mimic the input–output behavior of the original model. Based on obtained results, it is suggested to integrate the simplified blade model obtained by model reduction algorithm into aeroelastic simulations in order to keep the input–output error of the system at a low level.

Acknowledgment The present study is made possible through the financial support of the Swedish Wind Power Technology Center (SWPTC).

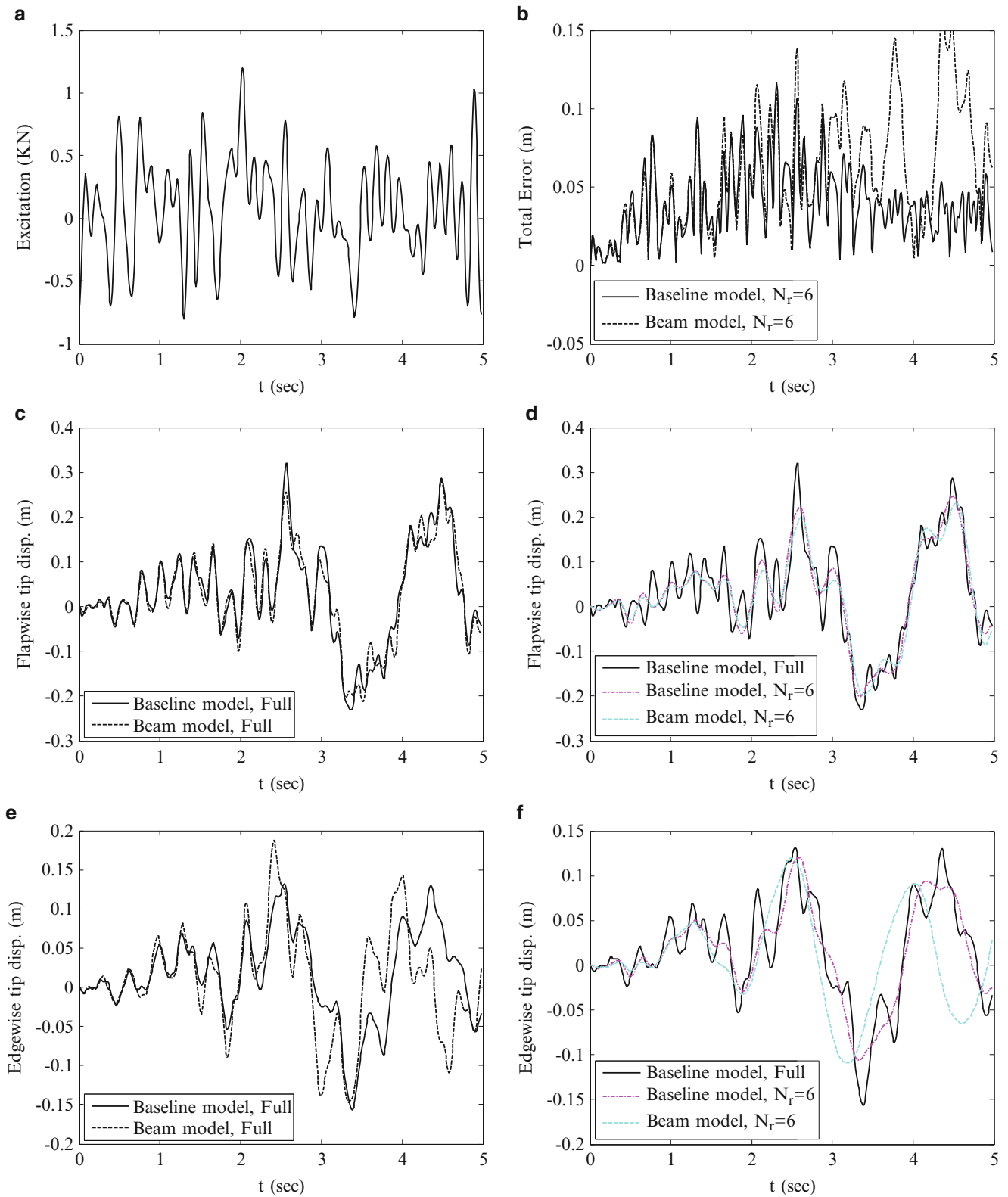


Fig. 37.8 Comparison of the performance of the full and reduced models of the baseline and beam models in response to multisine signal. (a) the designed multisine signal, (b) the total approximation errors, the flapwise (c) and edgewise (e) tip displacement of full models, the flapwise (d) and edgewise (f) tip displacements of the reduced models

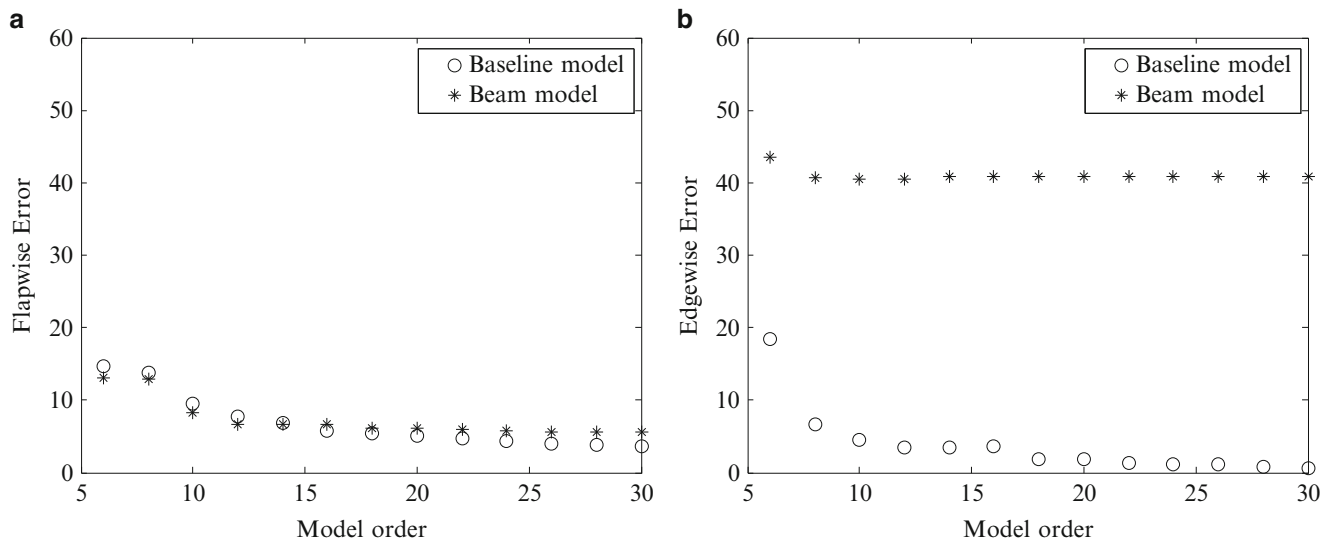


Fig. 37.9 The relative approximation error (%) of the baseline FE and beam model for different model orders. The model is simultaneously excited in both the flapwise and edgewise direction using the designed multisine signal. The output is measured in (a) flapwise and (b) edgewise directions

References

1. Yang B, Sun D (2013) Testing, inspecting and monitoring technologies for wind turbine blades: a survey. *Renewable Sustainable Energy Rev* 22:515–526
2. Mollineaux MG, Van Buren KL, Hemez FM, Atamturktur S (2013) Simulating the dynamics of wind turbine blades: part I, model development and verification. *Wind Energy* 16(5):694–710
3. Van Buren KL, Mollineaux MG, Hemez FM, Atamturktur S (2013) Simulating the dynamics of wind turbine blades: part II, model validation and uncertainty quantification. *Wind Energy* 16(5):741–758
4. Bottasso CL, Cacciola S, Croce A (2013) Estimation of blade structural properties from experimental data. *Wind Energy* 16(4):501–518
5. Cárdenas D, Escárpita AA, Elizalde H, Aguirre JJ, Ahuett H, Marzocca P, Probst O (2012) Numerical validation of a finite element thin-walled beam model of a composite wind turbine blade. *Wind Energy* 15(2):203–223
6. Antoulas AC (2005) *Approximation of large-scale dynamical systems*. Society for Industrial and Applied Mathematics, Philadelphia
7. Kerschen G, Golinval JC, Vakakis AF, Bergman LA (2005) The method of proper orthogonal decomposition for dynamical characterization and order reduction of mechanical systems: an overview. *Nonlinear Dyn* 41(1–3):147–169
8. Vakilzadeh MK, Rahrovani S, Abrahamsson T (2013) Modal reduction based on accurate input–output relation preservation, IMAC XXXI, Orange County, CA 45:333–342
9. Jonkman J, Butterfield S, Musial W, Scott G (2007) Definition of a 5-MW reference wind turbine for offshore system development, National Renewable Energy Laboratory, Golden
10. Abrahamsson TJS, Kammer DC (2014) FEM calibration with FRF damping equalization. In: IMAC XXXII, Orlando
11. Pintelon R, Schoukens J (2012) *System identification: a frequency domain approach*, 2nd edn. Wiley-IEEE Press, New Jersey
12. Friswell MI (1990) Candidate reduced order models for structural parameter estimation. *J Vib Acoust Stress Reliability Des* 112(1):93–97
13. Kammer D (1996) Optimal sensor placement for modal identification using system-realization methods, *J Guid Control Dyn* 19(3):729–731
14. Carrera E, Giunta G, Nali P, Petrolo M (2010) Refined beam elements with arbitrary cross-section geometries. *Comput Struct* 88(5–6):283–293

Chapter 38

A Wiki for Sharing Substructuring Methods, Measurements and Information

Matthew S. Allen, Jill Blecke, and Daniel Roettgen

Abstract The experimental substructures focus group recently created an online wiki to provide a central repository for data, computer code, etc. . . . to facilitate collaboration between interested researchers. The goal of the wiki is to simplify collaboration and to help those involved in substructuring research to keep informed about work that has been or will be done at other institutions. The wiki currently has a wealth of information regarding the focus group's test bed based on an Ampair wind turbine, including finite element models, test data for various components in several different configurations and other information. Contributors to the site include: Sandia National Laboratories, The University of Wisconsin-Madison, Chalmers University, the University of Massachusetts-Lowell, Delft University of Technology, University of L'Aquila and University of Stuttgart. This paper will provide an overview of the current information contained on the wiki and discuss how one can gain access to post additional measurements, publications and/or analysis results.

Keywords Experimental dynamic substructuring • Impedance coupling • Structural modification • Admittance modeling • Frequency based substructuring

38.1 Introduction

The dynamic substructuring focus group is a group of collaborating researchers with particular interest in experimental and analytical dynamic substructuring. The dynamic substructuring wiki has been created as an online collaboration tool and will act as a central location for sharing data, models, and computer code to assist interested researchers. This paper will give basic information about the dynamic substructuring wiki including some examples of items contained within the wiki.

The dynamic substructuring wiki can be accessed at the web address:

<http://substructure.engr.wisc.edu/>

This address will direct the user to the wiki main page. All of the data, models, and other information can be accessed by any visitor. To edit the wiki you must have a user account. A user may log in on any page of the wiki by typing their log-in ID and password into the box on the upper-left of the page. New users can request an account by sending an email to substructurewiki@cae.wisc.edu. The basic functions for new users are covered in Sect. 38.3. This paper serves as an overview of the functionality and current contents of the dynamic substructuring wiki.

M.S. Allen

Department of Engineering Physics, University of Wisconsin-Madison, 535 Engineering Research Building,
1500 Engineering Drive, Madison, WI 53706, USA
e-mail: msallen@engr.wisc.edu

J. Blecke (✉)

Sandia National Laboratories, Component Science Mechanics Org. 1515, Eubank Blvd SE, MS 0346, Albuquerque, NM 87123, USA
e-mail: jblecke@sandia.gov

D. Roettgen

Department of Engineering Physics, University of Wisconsin-Madison, Madison, WI 53706, USA
e-mail: droettgen@wisc.edu

Page [Discussion](#) [Read](#) [View source](#) [View history](#)

Dynamic Substructuring Wiki

(Redirected from [Main Page](#))

Welcome to the SEM/IMAC dynamic substructuring focus group's web space.
In this space we will share ideas and data. Feel free to edit this page or other pages!

Contents [\[hide\]](#)

- 1 [Main Pages](#)
- 2 [Getting started](#)
- 3 [Tutorials on Substructuring](#)
- 4 [About the Focus Group](#)

Main Pages

[Contributors](#) | Here is a list of the current contributors. Add information about what you are working on, etc.

[Experiments](#) | Here is a list of current and past experiments on the Ampair wind turbine test bed. |

[Models](#) | Here are models developed by contributors

[Test Bed Information](#) | Here is basic information on our test bed, the Ampair 600 Wind Turbine

[Bibliography](#) | Here is a list of links to papers and journals about dynamic substructuring.

Getting started

- [Usage Guidelines](#)
- [Wiki-Basics](#)
- [Guide for Uploading Files](#)
- Consult the [User's Guide](#) [☞](#) for information on using the wiki software.
- [MediaWiki FAQ](#) [☞](#)

Tutorials on Substructuring

[Tutorials](#) | See the tutorial page by clicking this link

About the Focus Group

The Dynamics Substructuring focus group is a group of collaborating researchers who meet annually at the [Society for Experimental Mechanics](#) [☞](#) International Modal Analysis Conference each year. The group is led (unofficially) by [Randall L. Mayes](#) ([Sandia National Laboratories](#) [☞](#)) and by [Matt Allen](#) ([University of Wisconsin-Madison](#) [☞](#)) and [Daniel Rixen](#) ([Technische Universität München](#) [☞](#)). This Wiki is maintained by Dr. Allen's research group.

Fig. 38.1 Wiki main page

38.1.1 Wiki Organization

Figure 38.1 shows the main page that users see when they come to the wiki. You can return to this page at any time by clicking “Main page” in the left sidebar menu. Several links have been added to the main page including links to a list of contributors, experiments, and useful papers and journal entries, but much of this information can also be found using the left sidebar menu.

It is important to note that the wiki is organized primarily as a searchable database, not as a static web page. Any content added to the wiki is tagged according to criteria listed below. Visitors to the site can then find what they are interested in by viewing lists of all information with a particular tag. Items in these categories can be found from any point within the site using the left sidebar menu, or using the links on the *Main page*, which is shown in Fig. 38.2.

- **Contributors**—see all information sorted according to who contributed it
- **Experiments**—see all experimental data, descriptions of experiments, etc. . . .
- **Models**—see all computational models contributed

University of Wisconsin--Madison

(Redirected from [Wisconsin](#))

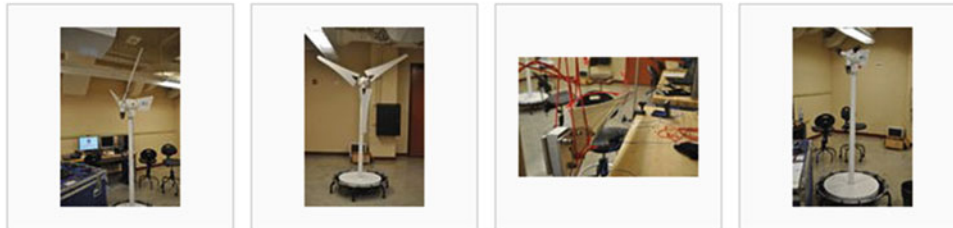
Contents [hide]

- 1 Overview
- 2 Experiments Performed
- 3 Calculations Performed
- 4 Summary of Ampair Tests
- 5 Links



Overview

The University of Wisconsin--Madison has performed multiple tests on the turbine in various stages of disassembly. Current Plans are to perform substructuring predictions with some of these models, for instance, fixing one blade to a rigid boundary condition and attaching a blade to the disassembled turbine.



Experiments Performed

- Tests Performed Fall 2011
 - 2-bladed Turbine Roving Hammer Test-UW Madison
 - Full Turbine Roving Hammer Test-UW Madison
 - Mass Loaded Blade Test-UW Madison
 - No-blade Turbine Roving Hammer Test-UW Madison
- Tests performed by Dan Rohe (UW-Madison) and Randall Mayes (Sandia)
 - Full Turbine (forthcoming)
 - Hub + 3 Blades (forthcoming)
 - Tower + Hub (forthcoming)

Calculations Performed

- Substructuring of UW-Madison Test Results (~Fall 2011)
 - UW Blade to Fixed-Base (forthcoming)
 - UW Blade to 2-bladed Turbine (forthcoming)
 - UW 3 Blades to Blade-less Turbine (forthcoming)
- Substructuring of Sandia Test Results (Summer 2012)
 - Hub+blades to Hub+Tower (forthcoming)
 - Paper Describing This: [RoheMayes_SubstAmpairWT_IMAC2013.pdf](#)

Fig. 38.2 Example University of Wisconsin-Madison contributor page

There are also a few static pages that one can navigate to from the main page.

- **Test Bed Information**—overview of Ampair test bed
- **Bibliography**—page with a list of publications relevant to substructuring
- **Tutorials**—collection of tutorials (slides, papers, etc. . . .) providing an introduction to selected topics
- **Substructuring at IMAC**—a list of substructuring publications presented at IMAC

The “Toolbox” menu on the far left contains tools that contributors may use to add to the site.

38.2 Wiki Contents

There is already wealth of information uploaded to the dynamic substructuring wiki. Users can locate information on the tests and substructuring calculations that have been performed by various contributors or on substructuring methods. Users can also find models and measurement results in various forms from experiments performed by contributors. Examples of several pages of wiki content will be displayed in this section of the paper. *While this represents a significant start, the authors hope that the wiki will be used far more extensively in the future to enhance collaborations and enable new engineers, students or researchers to learn quickly from the substructuring research that has been performed.*

38.2.1 Contributor Pages

Each contributor should have a *Contributor* page which provides an overview of all of the information that they have added to the wiki. This is a great place to let the substructuring community know what current projects your group is working on or interested in. It is also very helpful to provide an overview of research that you have previously performed as well as links to any other websites, conference or journal articles, etc. . . . where interested readers can learn more. The general format for a contributor page includes a summary of experiments/research completed along with current plans and links to any experiments, methods, or calculations available on the wiki. An example of the University of Wisconsin-Madison contributor page is shown in Fig. 38.2.

The goal of the wiki is to simplify collaboration and to help those involved in substructuring research to keep informed about work that has been or will be done at other institutions. If you are a new contributor, begin by adding a simple list of projects that your group has been involved in, publications that have resulted and your contact information. In the course of their work, most researchers will receive requests to share measurements, models or computational routines used in their work. When those requests come, post these items to the wiki (rather than attaching them to an email message or posting them on some external site). Encourage your collaborators to enhance your post by adding additional notes that were helpful to them as they used your contribution. As more of this information is captured on the wiki, it will quickly become an increasingly valuable resource.

38.2.2 Models

A few contributions have already been added to the models section of the wiki. The Atomic Weapons Establishment contributed a detailed solid model of a blade of the Ampair turbine while Walter D’Ambrogio contributed a NASTRAN model of a blade which has already been used by several researchers, as reported in several recent IMAC papers (Fig. 38.3).

38.2.3 Experiments

As shown in Fig. 38.2 a contributor page may provide links to summaries of several experiments or substructuring calculations. If desired, each experiment may have its own description page including an overview, photos, models, and experimental data, or simply post slides from a presentation that you have given regarding your experiments. Data and

Category [Discussion](#) [Read](#) [Edit](#) [View history](#)

Category:Models

Here is a list of any models we have created. To make your page appear here, tag it by adding `[[Category:Models]]` in the wiki text.

CAD Geometry for the Ampair 600 Blade: This is the blade geometry produced by AWE following scanning laser measurements averaged and surface/curve fitted using 3 Ampair 600 blades. This file ([Media:Scanned_averaged_blade_geometry.txt](#)) is actually in 'step' model format so please rename to *.stp after downloading.

Pages in category "Models"

The following 2 pages are in this category, out of 2 total.

A

- [Atomic Weapons Establishment](#)

L

- [L'Aquila](#)

Media in category "Models"

The following 2 files are in this category, out of 2 total.



| | |
|--|--|
|  |  |
| LAquila AMPAIR BLADE.rar 836,289 bytes | Scanned averaged blade... 443,371 bytes |

Fig. 38.3 Page listing all contributions that have been tagged with the “Models” category

information from these experiments can be uploaded directly to the wiki or linked via external web-sites. This will enable the substructuring community to learn from your work and to begin to validate new methods and calculations with real experimental data without the cost of running the experiments. Note that experiments can be tagged with the “Experiments” category tag (see Sect. 38.3.4 for additional information on category tags). An example experiment page created from a University of Wisconsin-Madison experiment is shown in Fig. 38.4.

38.2.4 Bibliography

The wiki bibliography can be accessed from the wiki main page. This contains links and titles of many useful papers related to dynamic substructuring. Users can add papers to this list by editing the page or sending a list of publications to the wiki

2-bladed Turbine Roving Hammer Test-UW Madison

Contents [\[hide\]](#)

- [1 Details](#)
- [2 Photos](#)
- [3 Data and Geometry](#)
- [4 Results](#)

Details

[\[edit\]](#)

This test was performed in early January 2012

Two sets of measurements were taken with varying accelerometer locations.

The hammer was roved over approximately 40 points on the structure to obtain a fairly dense pattern of points, primarily on the blade.

The span of the test was 0 to 800 Hz.

Photos

[\[edit\]](#)



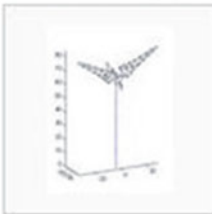
2-bladed Turbine Configuration

Data and Geometry

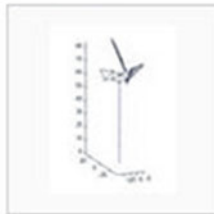
[\[edit\]](#)

All data sets are in the universal file format. Use [WinRAR](#) or similar to decompress the Dataset Files

[Geometry File](#) | [Dataset 1](#) | [Dataset 2](#)



Point Resolution, Front View



Point Resolution, Side View

Fig. 38.4 Example experiment page

administrators at substructurewiki@cae.wisc.edu. Note that an author typically retains the right to share their work in a pre-publication form (prior to reviews or formatting by the conference or journal) on a website such as this, so you may be able to upload some papers directly to the wiki site. Or, you can simply provide a link to the Digital Object Identifier (DOI) or some other external link for the papers.

User:Droettgen

Dan Roettgen - droettgen(replace with at symbol)wisc.edu

Education History

Ph.D. Student, Engineering Mechanics, [[University of Wisconsin](#)], 2013 - Present

M.S. Mechanical Engineering, [[Ohio State University](#)], April 2012

B.S. Mechanical Engineering, [[University of Kentucky](#)], June 2009

Research Interests: Dynamics, Vibrations, Dynamic Substructuring, Controls, Fuzzy Logic

Links

- [AIAA](#)
- [EAA](#)
- [SEM](#)
- [[Fuzzy Logic Control Wikipedia Entry](#)]

Category: [Wisconsin](#)

User:MSAllen

Dr. Matthew S. Allen, Associate Professor, University of Wisconsin-Madison

<http://silver.neep.wisc.edu/~msallen/>

Fig. 38.5 Examples of user pages

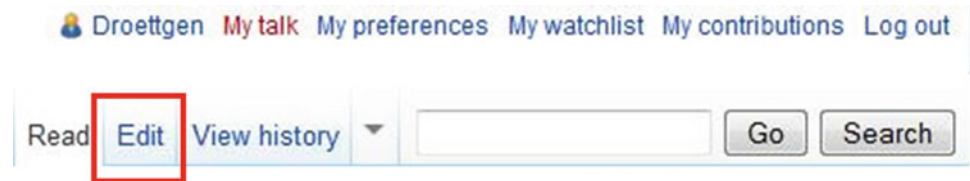
38.2.5 User Pages

Each user can also create a user page. This lets other users know more about each other, each other's research interests, and other pertinent information. An example of a user page is shown in Fig. 38.5, but included details are not limited to those shown. Note that user pages can also be tagged with categories (see Sect. 38.3.4).

38.3 User Basics

This section of the paper is intended to provide a new user with an overview of how to begin contributing to the dynamic substructuring wiki. This section of the paper will overview steps required to create an account, how to edit or contribute to the wiki, as well as some useful tools and links for uploading files and learning wiki syntax. The wiki was created using "Mediawiki," the same package used for Wikipedia and many other sites, so a wealth of additional information and samples are available on the web.

Fig. 38.6 User options menu



38.3.1 Login or New User Set-Up

In order to modify the wiki, a user must log in using the link at the top-left of any page. If you do not already have an account, the wiki administrators can create one for you by sending an e-mail the wiki e-mail address substructurewiki@cae.wisc.edu. You can also use this email to ask questions about how to use the wiki or to report any bugs or other errors that you encounter.

Once an account has been made, a new user can log in to their account. This will give the user several user options at the upper right-hand corner of the wiki, known as the user options menu (shown in Fig. 38.6). To set up a user-page, a user simply clicks on their user name. This will navigate to their user page which they may edit to add their contact information.

38.3.2 Editing an Existing Page

There are multiple ways to contribute to the dynamic substructuring wiki. In order to update a page, a user must navigate to that page then click the “Edit” tab near their user options menu (highlighted with a red box in Fig. 38.6). This will navigate the user to the editing page for the previously viewed page. All editing is done within your browser on this page. A good way to start learning the wiki-language syntax is to click “Edit” to view or copy the source code used on an existing page and see the source “wiki” code used to create it. One can do this by clicking edit on an existing page. The University of Wisconsin contributor page is a good example of how to include links, pictures, category labels, etc. . . . It can be found at:

<http://substructure.engr.wisc.edu/substwiki/index.php/Wisconsin>

38.3.3 Create a New Page

The wiki-language syntax is simple and fairly intuitive, so most users should be able to begin posting content to existing pages within a few minutes of their first login. However, it may not be quite so obvious how to create a new page. One way to do this is to first create a link from an existing page to the new one. This link will initially show up as dead on the current page. For example, notice the bullet “Full Turbine (forthcoming)” in Fig. 38.2. The Wikimedia code used to create this was simply: “** [[UW Blade to Fixed-Base]] (forthcoming)”. When the user clicks on the link the wiki will generate a new page which one can edit and add content to. If your research group does not yet have a contributor page, you can create one by creating a user page and then adding a link to a contributor page on your user page.

38.3.4 Categories

When searching through pages, it is often useful to sort wiki pages by categories. Categories are keywords used to tag a page. For example, at the bottom of each contributor page there is a Categories box with the tag “Contributor”. UW-Madison’s contributor page has the following code at the bottom: `[[Category:Contributor]] [[Category:Broken Links]] [[Category:Wisconsin]]`. Referencing the specified categories, Wikimedia generates the box shown in Fig. 38.7, which a user can use to navigate to a list of all other pages with that keyword. As this wiki grows this will be a great tool for navigating to useful data and models. In this case, the page has been tagged with the categories: contributor, broken links, and Wisconsin. The tag Wisconsin can be used to easily find and navigate to other pages containing information, experiments, and other useful data associated with the University of Wisconsin-Madison. The tag for Broken Links can be used to help edit the wiki and find links that may lead to missing files or upcoming information. As you edit the wiki, feel free to add any categories that you feel would be helpful.



Fig. 38.7 Categories box

38.3.5 *Help and Support*

Several wiki tools are available in the left sidebar menu under the tool box header. From the left sidebar menu, users can find links to the homepage and various contributor pages. Users can also find a recent changes page highlighting recent updates to the wiki. The “Upload File” application is also available in the sidebar providing users the ability to upload images, data sets, and other files to the wiki. It is worth noting that large files or certain file types may be blocked by the server that hosts this wiki. At the moment this cannot be corrected, but several alternatives are available, as described at

http://substructure.engr.wisc.edu/substwiki/index.php/Guide_for_Uploading_Files

In addition to these tools there are many support and help sites to help users learn the wiki language. From the main page, one can navigate to a wiki-basics guide as well as the media-wiki F.A.Q. If any additional assistance is needed e-mail the wiki administrators by sending an e-mail to substructurewiki@cae.wisc.edu.

38.4 Conclusion

The dynamic substructuring wiki contains a wealth of information including experiments, models, tutorials, and reference papers and this is expected to grow in the coming years. As the members of the substructuring focus group continue to collaborate, the wiki will be expanded adding more information and highlighting more research. The hope is that the focus group will find this wiki useful in educating new members while sharing the research and experimentation already being completed within the group. In the coming months and years additional content will be posted including tutorials and papers concerning dynamic substructuring as well as additional experimental data and results. Be sure to check the wiki periodically for updates and new information.

Acknowledgements This work was conducted/supported by Sandia National Laboratories. Sandia is a multi-program laboratory operated under Sandia Corporation, a Lockheed Martin Company, for the United States Department of Energy under Contract DE-AC04-94-AL85000.

Chapter 39

Novel Parametric Reduced Order Model for Aeroengine Blade Dynamics

Jie Yuan, Giuliano Allegri, Fabrizio Scarpa, and Ramesh Rajasekaran

Abstract The work proposes a reduced order modelling (ROM) technique for turbofan engine blades. The aim is to develop a simplified structural layout that allows describing the dynamic behaviour associated with the first six modes of full-scale fan blades. This is done by introducing equivalent frame models for the blade, which can be tailored to represent coupled flexural/torsional mode shapes, the relevant natural frequencies and static masses. Both 2D and 3D frame models are considered with initial configurations obtained from structural identification equations. The frame configurations are refined via an optimization process based on simulated annealing with stochastic tunnelling. The cost function comprises a linear combination of relative errors on the vibration frequencies, the individual modal assurance criteria (MAC) and the static mass. We demonstrate that an optimized 3D frame can represent the blade dynamic behaviour with a 6 % error on the MAC and a 1 % error on the associated modal frequencies. The approach proposed in this paper is considerably more accurate than ROMs based on single equivalent beams, either Euler–Bernoulli or Timoshenko, and highly computational efficient. Therefore, this technique is suitable for application to the analysis of mistuned bladed discs, particularly for determining the sensitivity to manufacturing and assembly tolerances in joints.

Keywords Beam frame • Turbofan blades • Mistuning analysis • Structure dynamics updating • Simulated annealing

Nomenclature

| | |
|----------------------------|--|
| A_i | Area of i th element |
| L_i | Length of i th element |
| M_R, K_R | Reduced mass, stiffness matrix |
| M_a, M_o | Total mass in analytical model and FE model |
| m_i^G, k_i^G | Global coordinate mass, stiffness matrix of i th element |
| \bar{m}_i^G, \bar{k}_i^G | m_i^G, k_i^G in an assembled size matrix |
| I_{xi} | Polar moment of area for i th element |
| I_{yi}, I_{zi} | Second moment of area in y, z direction for i th element |
| w_i | Weight of i th natural frequency or objective |
| Φ | Assembled mode shapes |
| ϕ_i^r | r th mode shape for i th element |
| ϕ_m, ϕ_s | Master, Slave degree of freedoms of mode shape |
| ω_i, ω_i^a | i th natural frequency from FE model i th natural frequency from analytical model |
| ν_{rs} | Kronecker delta function |

J. Yuan (✉) • G. Allegri • F. Scarpa
Advanced Composites Centre for Innovation and Science, University of Bristol, BS8 1TR Bristol, UK
e-mail: [jy0387@bristol.ac.uk](mailto: jy0387@bristol.ac.uk)

R. Rajasekaran
Mechanical Methods, Rolls-Royce plc, PO Box 31, DE24 8BJ Derby, UK

39.1 Introduction

Typically, a bladed disk consists of a set of disk-blade sectors that are designed to be identical. However, there are always small inevitable variations in structural properties of individual blades, resulting from manufacturing tolerances, material defectiveness or non-uniformity, operational wear and tear, non-uniform assembly of the blades. These variations leading to the deviation of blade's natural frequency with respect to their nominal value is called bladed mistuning. It was demonstrated that mistuning on the free response will split the natural frequency of double modes for each circumferential mode and distort its mode shapes [1–5]. Simultaneously, its mode shape would have multiple harmonic contents of nodal diameter rather than a simply pure one so that it can be excited by any engine order [6]. The worse consequence is that the present of mistuning leads to mode localization phenomenon in which vibration energy of a mode is transferred and confined to only a blade or a few blades, resulting in drastically larger amplitude magnifications than ideal tuned design [7, 8]. As thousands of cycles accumulated rapidly due to high rotation speeds of the engine, its detrimental influence on bladed disc high-cycle fatigue life leads to seriously negative impact on durability and reliability of the aero engine.

Accurate and efficient bladed disc models can not only provide an insight look at dynamic mechanism of mistuning system but also be beneficial for prediction of maximum dynamic response for security inspection and robustness designs. However, the existing of mistuning destroys the cyclic symmetry of bladed disc system and greatly changes its dynamic behavior [6]. It makes cyclic symmetry expansion analysis of using one sector is not suitable for mistuning analysis. A full scale FE model of bladed disc system has to be constructed. Although the capability of computing nowadays has been evolved to a high level, a full scale FE model with millions of degree of freedoms (dofs) still makes computers incapable to deal with. The case becomes even worse when we employ Monte Carlo simulations for statistical analysis of this mistuned system.

As a result, a numerous of FE based reduced order methods in the last two decades has been widely developed and can be mainly classified into two generations both of that are based on the modal reduction techniques. The first generation method developed from 1983 to 2000 was called component mode synthesis (CMS) [9–11]. The second generation method initiated by Yang and Griffin in [12] is called as system mode based method followed by extended Fundamental Mistuning Model [13], Component Mode Mistuning [14], Integral Mode Mistuning [1]. It is found in industry applications that prediction from these two generations models for linear system is reasonably accurate by employing enough modes. However, these methods are not suitable for non-linear behavior included system. Besides, these models are not able to directly perturb specific parameters in modal domain for mistuning analysis but generally introduce the mistuning in a form of natural frequency deviation. It obstructs their sensitivity study for robustness design. The most popular parametrical model used for mistuning analysis is still lumped parameter model. Although these models can evidence much of its rich dynamic features of bladed disk systems and are good for statistical investigation purpose, it cannot accurately predict dynamic behavior of specific bladed disc system.

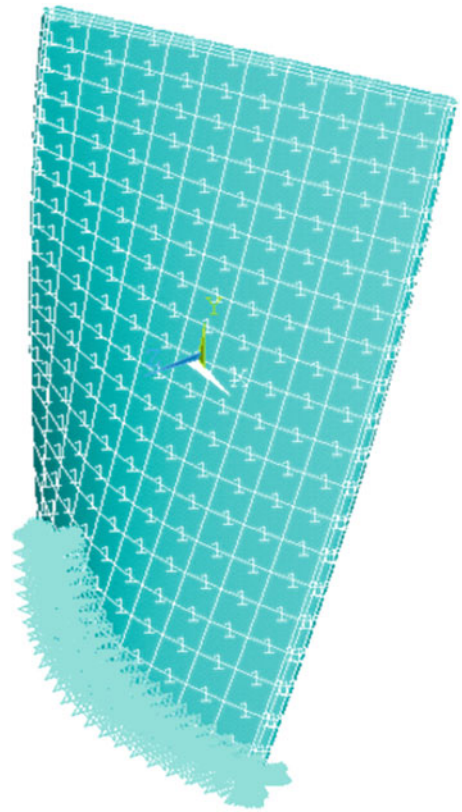
This paper proposes a reduced order modelling technique for turbofan engine blades. The approach is based on introducing a simplified structural layout that provides a dynamic behavior equivalent to that of the full-scale blade. The ROM model developed is primarily meant to be employed in sensitivity analyses where the uncertainties associated to manufacturing tolerances and assembly tolerance [15]. In the following sections, modal analysis of a specific FE aerofoil model is initially performed. Three structure concepts are then proposed and compared based on feature analysis of the first six modes. Beam framework are then selected and established with 2D and 3D beam element separately. Their initial configurations are then determined by the indications from derived structure identification equations. An optimization process of geometry parameters is finally presented aiming to minimize the NF, MAC and weight error followed by main results discussion and conclusion sectors.

39.2 Blade Reference and Modal Analysis

A FE model of aerofoil established in commercial software ANSYS 2008 is employed as reference in this research. It is constructed with solid eight-node elements and homogenous titanium material. It can be observed in Fig. 39.1 that this industry-employed blade features low aspect ratio of near 4 and increasing twist from root to tip for aerodynamic efficiency.

The modal analysis is performed with boundary condition of clamping the all dofs at the root of airfoil. The first six modes in three translation directions are shown in Fig. 39.2. The natural frequencies of the first six modes are clustered within 1,000 Hz and bending, torsion and edge-wise flap motions in out of plane direction dominate the first six modes. Both in plane bending motion and extruding modes with high in plane and spanwise stiffness have not shown up in the first six modes. Specifically, the first mode is purely out of plane flexural mode while the next four modes are all coupled with both torsion and bending in different orders. It is followed by sixth mode dominated by edge-wise flap mode. Therefore, it

Fig. 39.1 Finite element aerofoil model in ANSYS



can be seen that modal displacement in spanwise direction is ten times smaller than that in out of plane direction. Although out-of-plane deformations dominate the low order modes, significant deformations still appear along the in-plane chord-wise direction, especially close to the blade tip. This is due to the geometric twist of the structure. All six modes exhibit a high level of asymmetry along the chordwise direction.

39.3 Simplified Model Concepts

In the previous research, a straight Euler Bernoulli beam or Timoshenko beam model were traditionally employed as reduced model attempting to capture the dynamic behaviour of a blade (Fig. 39.2). Though these simplified modes might capture first few fundamental modes, it is infeasible to employ these models to capture coupled modes shown above. Three new concepts structures are thus proposed here based on feature analysis of first six modes. The first concept is made up of several uniform plane elements with certain thickness which could consider crosswise motion. The second concept is sloped Timoshenko beam elements with lumped masses. The last concept is a beam frame in which each element could have different geometrical properties. The specific comparison of these three concepts is qualitatively compared in terms of convenience of updating and accuracy of representation in the Table 39.1.

Overall, beam framework concept is employed since it combine both advantages in both plane structure to represent chordwise motion and sloped beam with lumped masses to represent asymmetrical motion. It is mainly because this concept can flexibly adjust the local geometry properties of each beam element. Beam frame concept also can be directly updated from experimental database from mode identification.

39.4 Beam Framework Construction

The number and location of selected nodes for framework is critical for accuracy of describing the mode shapes. Insufficient nodes will make MAC unreliable in demonstrating off diagonal corrections between the model and experiment due to spatial aliasing [16]. The auto MAC is thus used in this research to determine if the number and location of the chosen measurement

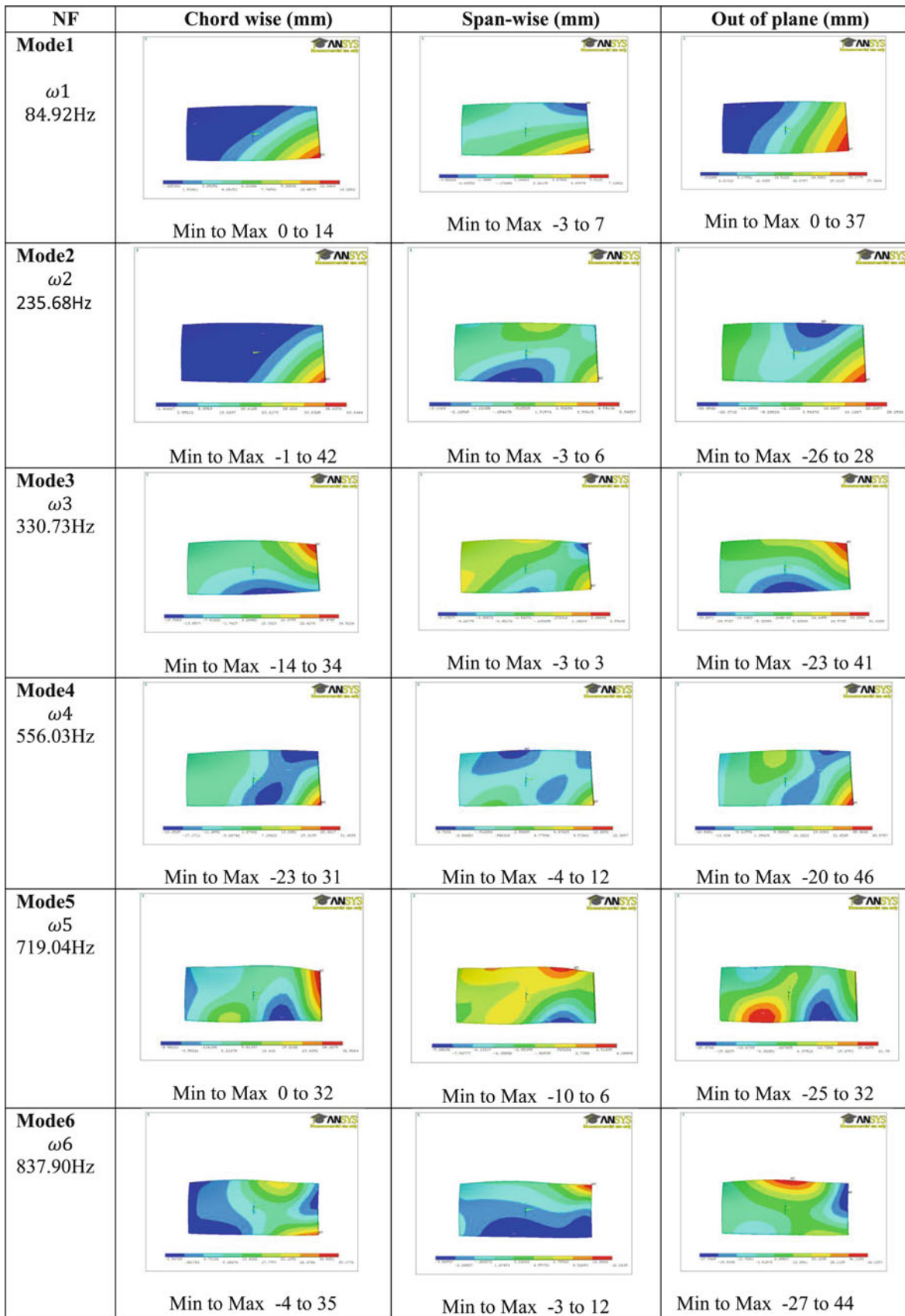


Fig. 39.2 The first six modes of the aerofoil

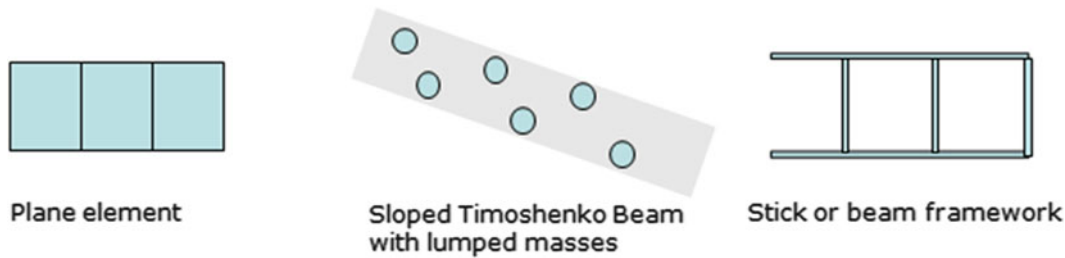


Fig. 39.3 Three structure concepts to represent blade

Table 39.1 Qualitative comparison three structure concepts

| | Plane element | Sloped beam | Beam framework |
|---------------|--|---|---|
| Advantages | <ul style="list-style-type: none"> – Easy to implement since matrix given in literature – Able to consider chordwise motion | <ul style="list-style-type: none"> – Easy to implement since matrix given – Able to consider asymmetrical bending motion – Able to present coupling effect between torsion and bending | <ul style="list-style-type: none"> – Easy to implement due to known single beam matrix – Able to consider asymmetrical chordwise motion and coupling out of plane motion since define local element property and define 3D geometry |
| Disadvantages | <ul style="list-style-type: none"> – Difficult to represent highly twist modes due to its uniform geometry – Cannot define local properties in a single element – Cannot define 3D geometry | <ul style="list-style-type: none"> – Hard to determine the location of lumped masses and their values – Not able to represent chord wise motion like edge wise flap mode | <ul style="list-style-type: none"> – Hard to determine their initial values |

dofs are sufficient to distinguish the modes from each other [16]. The selected nodes are to avoid the static nodes and try to reflect main features of first six shapes. Based on the feature analysis of first six modes in Sect. 39.2, the framework can be constructed by using nodes on the both chordwise edge sides as a certain number of these nodes are sufficient to represent first, second and third torsion and bending modes as well as edgewise flap mode. Eight nodes are then selected in FE model illustrated in Fig. 39.4 and their modal displacements of first six modes are simultaneously extracted out. The auto MAC is then plotted shown in Fig. 39.5 and it can be seen most off-diagonal corrections in the eight nodes plot approach to zero with maximum MAC value of 0.3 in a few points. Although it means some modes are not totally linear independent, the first six modes can be easily distinguished. Referring to papers [17, 18] it is thus considered eight nodes are sufficient to represent first six modes.

2D Euler Bernoulli beam is firstly used as basic element to construct the beam framework to represent the out of plane motion of the aerofoil. It can be justified by the fact that the first six modes are dominated by out of plane motions while extruding and in plane bending can be assumed negligible. Out of plane motion in blade also is of most interest in assembled bladed disc. Framework is then constructed in a plane with each node of an element three degrees of freedom (u_z , r_x , r_y) shown in Fig. 39.6a. This model has a potential to include torsion, bending and edgewise flap motion with highly computational efficiency. Nevertheless, the weakness of this model is that it cannot take 3D twisted geometry into account and fail to consider coupled displacement from chordwise direction. Therefore, 3D Euler Bernoulli beam is then proposed to construct framework considering 3D twisted geometry with six dofs in each node shown in Fig. 39.6b. All the out of plane, in plane and spanwise motions can be represented in this model. It is highly likely to further improve the extent to capture the out of plane motion compared with 2D case but compromise the computational efficiency owing to introduction of double sized matrix and much more number of variables for the optimization process. Both configurations will be attempted and compared in term of their accuracy and computational efficiency in this article.

The positions of internodes in frameworks are the same as that of measuring points in blades shown in Fig. 39.3. Out of plane coordinates for the nodes in 2D beam case are assumed to be zero while all three coordinates of points will be fully described in 3D beam framework case. The length of the each beam element can be thus calculated accordingly. The isotropic Titanium is employed for both framework configurations as same as FE model, with Young's modulus of 1.15e5 MPa, density of 4.43e−9 t/mm³ and passion ratio of 0.32. The geometry of cross section for each beam element is assumed arbitrary but

Fig. 39.4 Measuring points on the blade corresponding to the nodes on the ROMs

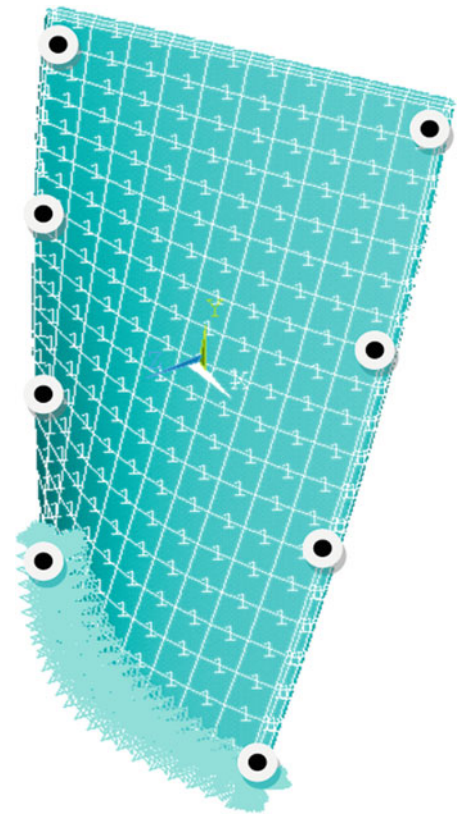
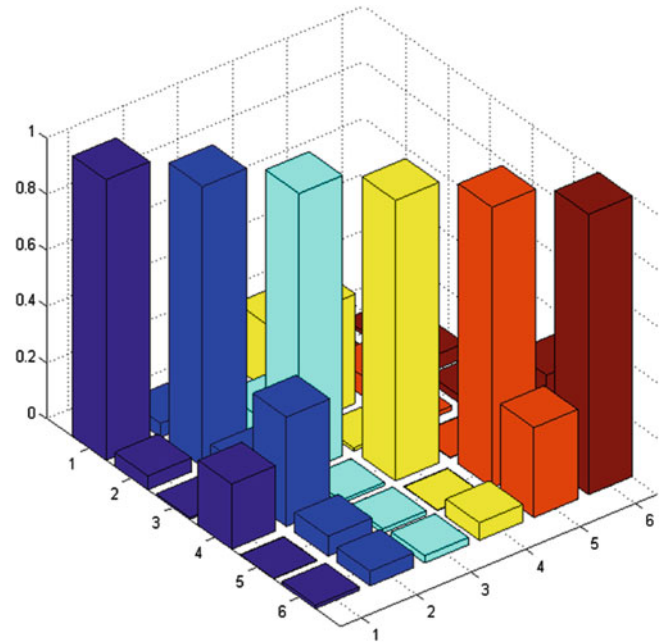


Fig. 39.5 Auto MAC plot for first six modes with eight nodes



symmetrical of x or y axis and uniform across the length. The unknown cross section properties for each element in 2D beam case are A_i, I_{xi}, I_{yi} framework and in 3D beam case are $A_i, I_{xi}, I_{yi}, I_{zi}$. The mass and stiffness matrix of single beam element and transforming matrix from local to global coordinates are available in [19] and will be directly used herein. The parametrical framework models with both 2D and 3D beam elements are then assembled and established in MATLAB software.

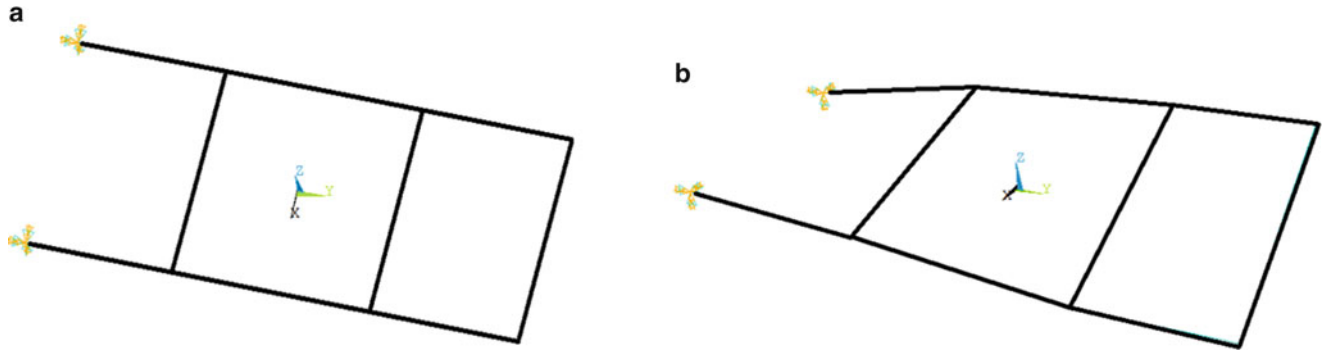


Fig. 39.6 (a) Deformed 2D frame (b) deformed 3D frame

39.5 Initial Value Determination

The initial values of variables in beam framework have to be reasonably estimated in order to improve the probability for optimizers to successfully locate globally optimal solution. However, they are hard to be directly estimated from either FE model or experimental samples. Most of previous research in equivalently dynamical model construction often employs strain and kinetic energy equivalent principle evaluated from FE model [20]. Nevertheless, this technique does not fit the purpose herein since proposed approach is required to be independent of FE model. Furthermore, initial values of these parameters are expected as exact solution but make optimizers possess a good start point. Classical modal updating techniques, either direct methods or iterative methods, are also not suitable since these techniques require a detailed and relatively accurate initial model as baseline [21]. Structure identification equations developed in [22] would be employed here. This method is independent of FE model by using only experimental modes and provides a simple mean to determine initial values of unknown parameters. Although some results might be significantly affected by ill conditioning problem due to expansion error of mode shapes, it is sufficient to provide the indications of initial guesses for optimization process. Three steps shown below are followed in this case to determine the initial values.

39.5.1 Step One: Expanding Mode Shape

Since values of rotation degrees in the measuring points are not available in experiment or in FE model with solid elements, the mode shapes have to be expanded before evaluating the initial values. Inversed Improved Reduced System (IRS) expansion based on static reduction method is employed in this case [23]. The first six modes' displacements in translational dofs with respect to measuring points are extracted from FE model denoted as master mode shape ϕ_m . The transformation matrix T_I by including the inertia terms as pseudo static force is evaluated by Eq. (39.2) where T_S, M_R, K_R denotes as static transformation, static reduced mass and stiffness matrix separately. These values and matrix S can be evaluated by a set of equations in (39.3) in which M, K are original mass and stiffness matrix sorted by master and slaver dofs shown in Eq. (39.4). It is worth noting that initial guess values of geometrical parameters have been employed to calculate original mass and stiffness matrix during the expansion. The modal displacement in slave dofs can be then expanded in Eq. (39.1).

$$\begin{Bmatrix} \phi_m \\ \phi_s \end{Bmatrix} = T_I \phi_m \quad (39.1)$$

$$T_I = T_S + S M T_S M_R^{-1} K_R \quad (39.2)$$

$$T_S = \begin{bmatrix} I & \\ -K_{ss}^{-1} K_{sm} & \end{bmatrix} \quad S = \begin{bmatrix} 0 & 0 \\ 0 & K_{ss}^{-1} \end{bmatrix} \quad M_R = T_S^T M T_S \quad K_R = T_S^T K T_S \quad (39.3)$$

$$M = \begin{bmatrix} M_{mm} & M_{ms} \\ M_{sm} & M_{ss} \end{bmatrix} \quad K = \begin{bmatrix} K_{mm} & K_{ms} \\ K_{sm} & K_{ss} \end{bmatrix} \quad (39.4)$$

39.5.2 Step Two: Deriving Structure Identification Equations

Once full scale mode shapes have been identified, mass and stiffness orthogonality of modes can be presented in Eqs. (39.5) and (39.6) where the global matrix is separately substituted by the sum of partitioned element matrixes \bar{m}_i^G, \bar{k}_i^G in global coordinate. The full mode shapes are then spread out and separately allocated to relate nodes of each element denoted as $\phi_1^r, \phi_2^r, \dots, \phi_9^r$ for r th mode shape. As a result, Eqs. (39.5) and (39.6) are further split for each element in $[I]$ and $[\cdot \cdot \omega_r^2 \cdot \cdot]$ expressing by summing up orthogonally detached elements shown in Eqs. (39.7) and (39.8). ν_{rs} is denoted as Kronecker delta which is equal to one when $r = s$ and equal to zero when $r \neq s$. The mass and stiffness matrixes of single beam element m_1^G, k_1^G are then substituted and thus a series of equations with unknown geometrical parameters are then derived for 3D beam framework shown in Eqs. (39.9) and (39.10). $\alpha^{rs}, \beta^{rs}, \gamma^{rs}, \delta^{rs}, \zeta^{rs}, \eta^{rs}$ are known parametrical coefficients of orthogonality between γ^{th} and s^{th} mode. As six modes of blade are used herein, 21 equations in a form of Eqs. (39.9) and (39.10) can be separately constructed. In addition, static mass constraint will be imposed shown in Eq. (39.7). The general derivation process can be referred to [22].

$$[\Phi^T] \sum_{i=1}^9 \bar{m}_i^G [\Phi] = [I] \quad (39.5)$$

$$[\Phi^T] \sum_{i=1}^9 \bar{k}_i^G [\Phi] = [\cdot \cdot \omega_r^2 \cdot \cdot] \quad (39.6)$$

$$\{\phi_1^r\}^T [m_1^G] \{\phi_1^s\} + \{\phi_2^r\}^T [m_2^G] \{\phi_2^s\} + \dots + \{\phi_9^r\}^T [m_9^G] \{\phi_9^s\} = \nu_{rs} \quad (39.7)$$

$$\{\phi_1^r\}^T [k_1^G] \{\phi_1^s\} + \{\phi_2^r\}^T [k_2^G] \{\phi_2^s\} + \dots + \{\phi_9^r\}^T [k_9^G] \{\phi_9^s\} = \omega_r^2 \nu_{rs} \quad (39.8)$$

$$\alpha_1^{rs} A_1 + \beta_1^{rs} I_{x1} + \alpha_2^{rs} A_2 + \beta_2^{rs} I_{x2} + \dots + \alpha_9^{rs} A_9 + \beta_9^{rs} I_{x9} = \nu_{rs} \quad (39.9)$$

$$\begin{aligned} \gamma_1^{rs} A_1 + \delta_1^{rs} I_{y1} + \zeta_1^{rs} I_{z1} + \eta_1^{rs} I_{x1} + \gamma_2^{rs} A_2 + \delta_2^{rs} I_{y2} + \zeta_2^{rs} I_{z2} + \eta_2^{rs} I_{x2} + \dots \\ + \gamma_9^{rs} A_9 + \delta_9^{rs} I_{y9} + \zeta_9^{rs} I_{z9} + \eta_9^{rs} I_{x9} = \omega_r^2 \nu_{rs} \end{aligned} \quad (39.10)$$

$$\rho A_1 L_1 + \rho A_2 L_2 + \dots + \rho A_9 L_9 = M_0 \quad (39.11)$$

39.5.3 Step Three: Sort Out Ill-Condition Problems and Solve the Equations

Ill conditioning problems can be easily introduced due to expansion error and the order of magnitude of unknown parameters while solving above equations. Therefore, it will remove parameters whose related motions contribute negligible amount to modal strain energy otherwise some parameters leads to extremely small or large value. In this case, extension motions and in plane motion can be eliminated in stiffness related equations since out of plane motion will be dominated the mode shapes. Another issue is the number of equations in most cases is much less than that of parameters. The other way to solve it is to make elements with similar geometry as a group with same properties to reduce number of variables in order to match with the number of equations. In this case, two beam elements linked to boundary condition can be regarded possessing same geometrical parameters due to the similar geometry. It is worth noting that the experimental NFs will be used in the structural identification equations shown in Eq. (39.7) and this process can be repeated several times until reasonable result appears. The initial values of all geometrical parameters can be then estimated from the iterative results.

39.6 Optimization Process

Once the initial values of beam framework have been identified, an optimization process will be performed. In order to retain the physical meaning of the model, material property (density and Young’s modulus) are remained same as reference model. Meanwhile, the locations of each measured points are fixed and thus length of beam elements kept unchanged. The only variables of both configurations are geometrical properties with respect to cross section for each element. In the case of 2D beam element framework, the variables are cross section area and second moment of area for out of plane bending. To 3D beam framework case, second moment of area for in plane bending and polar moment of area would also be added as variables. Therefore, there are 18 variables for 2D beam framework and 36 variables for 3D beam framework.

Natural frequency error, MAC error in term of out of plane motion and static mass error are taken as three objectives to be minimized in the optimization process. The reason why taking weight error as an objective rather than constraint is it will restrict the global optimizer to go through possibly narrowed and separated the design variables space. Since it is a multi-objective problem, all the objectives are normalized by using least square which is listed in Eqs. (39.12)–(39.14). It is worth noting that since first NF will obviously increase with rotation speed during the working operation known as stress stiffening effect [24, 25], higher weight thus is added on the first NF in Obj1 to lower its error in order to avoid intersections in the first few NFs in Campbell plot. The overall cost function is shown in Eq. (39.15) by sum of weighted objectives. In terms of constraints, all the variables and eigenvalue are restricted to be real and positive.

$$\text{Obj 1} = \sqrt{\sum_{i=1}^6 \left\{ (w_i (\omega_i^a - \omega_i) / \omega_i)^2 \right\}} \tag{39.12}$$

$$\text{Obj 2} = \sqrt{\sum_{i=1}^6 (1 - \text{MAC}(i))^2} \tag{39.13}$$

$$\text{Obj 3} = \left| (M_a - M_o) / M_o \right| \tag{39.14}$$

$$\text{Cost function} = \sum_{i=1}^3 w_i \text{Obj}_i \tag{39.15}$$

The surface responses in term of single NF with geometrical variables shown in Fig. 39.7 are smooth without complex eigenvalue which is suitable for optimization process. It also can be deduced response surface of cost function with more than 20 variables would be rugged with a numbers of local minimums rather than pure convex making gradient based local optimizers unsuitable in this case. As a result, great attention has been paid on stochastic global optimizers. In fact, simulated annealing and genetic algorithm are commonly employed in the optimization of engen problem in structure dynamic updating. They performed quite well to locate the global minimum and both of methods can achieve similar optimal

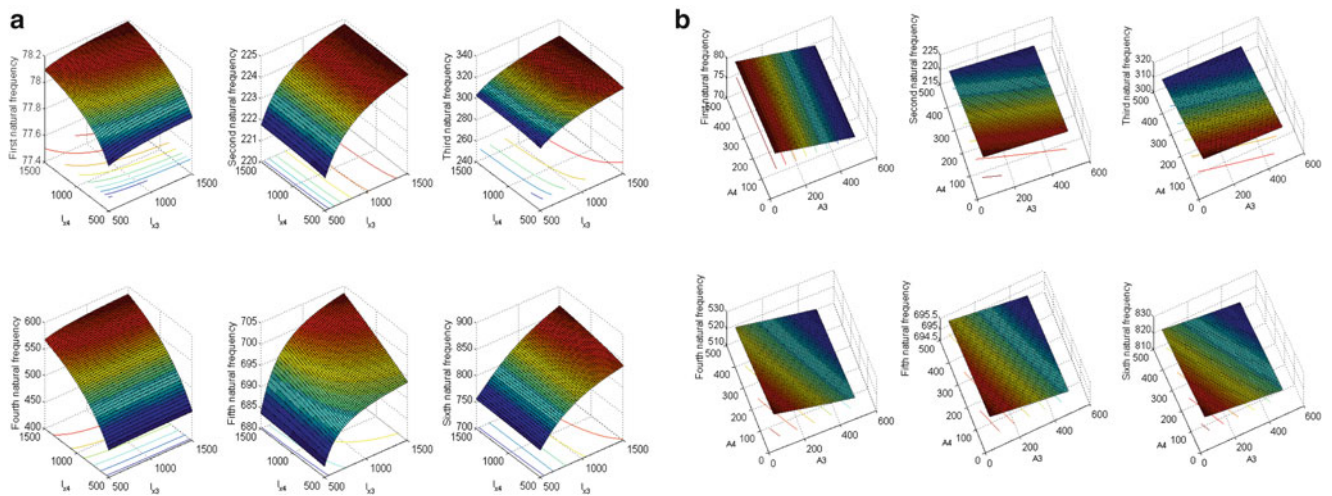


Fig. 39.7 (a) Surface responses of NFs with I_{x3} , I_{x4} (b) Surface responses of NFs with A_3 , A_4

[26]. However, traditional simulated annealing will encounter freezing problem in stochastic minimization methods arises when the energy difference between “adjacent” local minima on the potential energy surface is much smaller than the energy of intervening transition states separating them. Fortunately, stochastic tunneling method has been put forward and proved to be effectively overcome this issue. It makes large improvement of success rate to find global minimum by applying a nonlinear transformation to the potential energy surface [27]. It allows the particle to go through forbidden regions when it is judged that they are irrelevant for the low-energy properties of the problem. Therefore, simulated annealing with stochastic tunneling method will be employed as global optimizer in this research.

39.7 Main Results and Discussion

Figure 39.8a, b show the best Pareto fronts of the 2D and 3D ROMs from 40,000 feasible solutions, respectively with weight ratios of 2:2:1 and 2:7:1. The values of the static mass errors are expressed by the colormap. CPU times are also indicated. The optimal solutions cluster near the Pareto front. This shows the sensitivity to different combinations of NF and MAC errors, depending on the weight ratio imposed in the cost function. The two models provide similar performance for a total mass error below 1%. The location of the Pareto front in the 2D case is mainly within the region between 0.7 and 0.85 for Obj₂, and from 0.1 to 0.4 for Obj₁. For the 3D frame the intervals defining the Pareto front are different, with Obj₂ ranging from 0.16 to 0.18 and Obj₁ bounded between 0.003 and 0.06. These results suggest that the 3D ROM outperforms the 2D model in terms of NF and MAC errors. However, the computational time required for the 3D ROM is 3.5 times that spent for calibrating the 2D frame.

2D and 3D beam frames are then further compared by a specifically optimal solution when the weights of three objectives are equal. The each NF and MAC error of first six modes in 2D and 3D framework model are respectively plotted together against the initial errors (Fig. 39.9). It is shown the simulated annealing with stochastic tunneling method effectively reduces the initial errors in both cases. The weight error in both models has been optimized to be almost zero. The average NF errors in both cases are very low with 6% for 2D frame and 1% for 3D ROM. The 2D frame yields a MAC error (30% average) that is substantially higher than the 8% observed for the 3D ROM case. The superior performance of 3D ROM is justified by the intrinsic coupling between in-plane deformations and out-of-plane torsion existing in the ROM, which increases the accuracy of the optimization process in identifying the beam parameters. Although 2D beam framework model has four times lower CPU expense than 3D case during the optimization process, it cannot justify its much lower accuracy especially when accuracy is the dominated driver. In the 3D case, the average MAC error can be further decreased to 6% with compromise of increasing NF error to 0.75%.

The first natural frequency is able to be controlled less than 5% satisfying the requirement of intersection limit. The first six modes of 3D framework mode against the original shape are plotted in Fig. 39.10. It demonstrates good agreement with mode shape shown in Fig. 39.2.

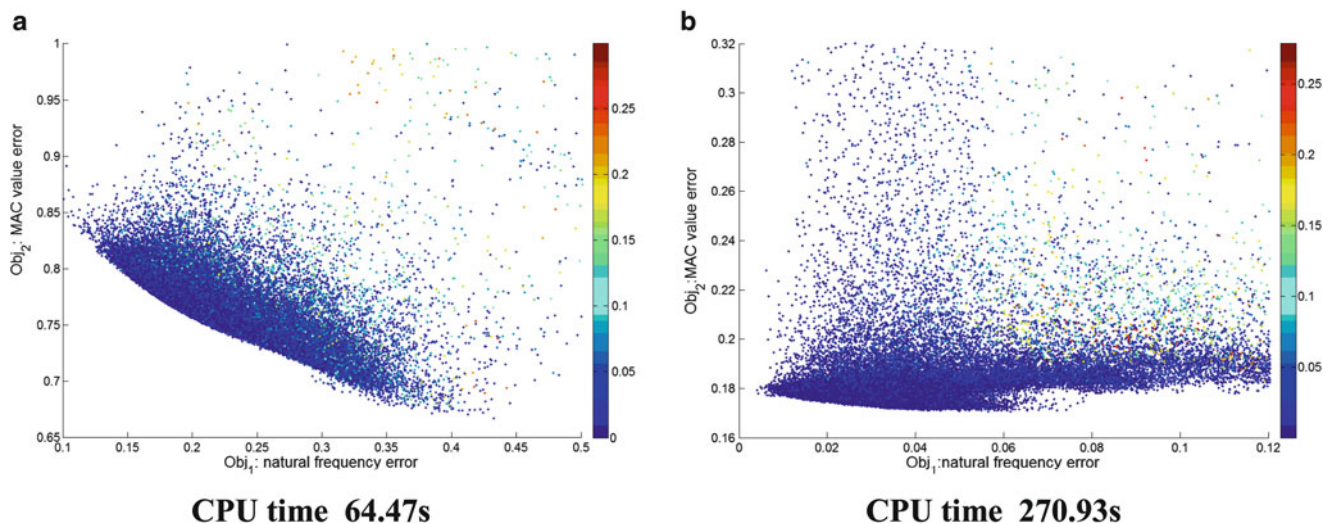


Fig. 39.8 (a) Best Pareto front plots for 2D frame (b) Best Pareto front plots for 3D frame

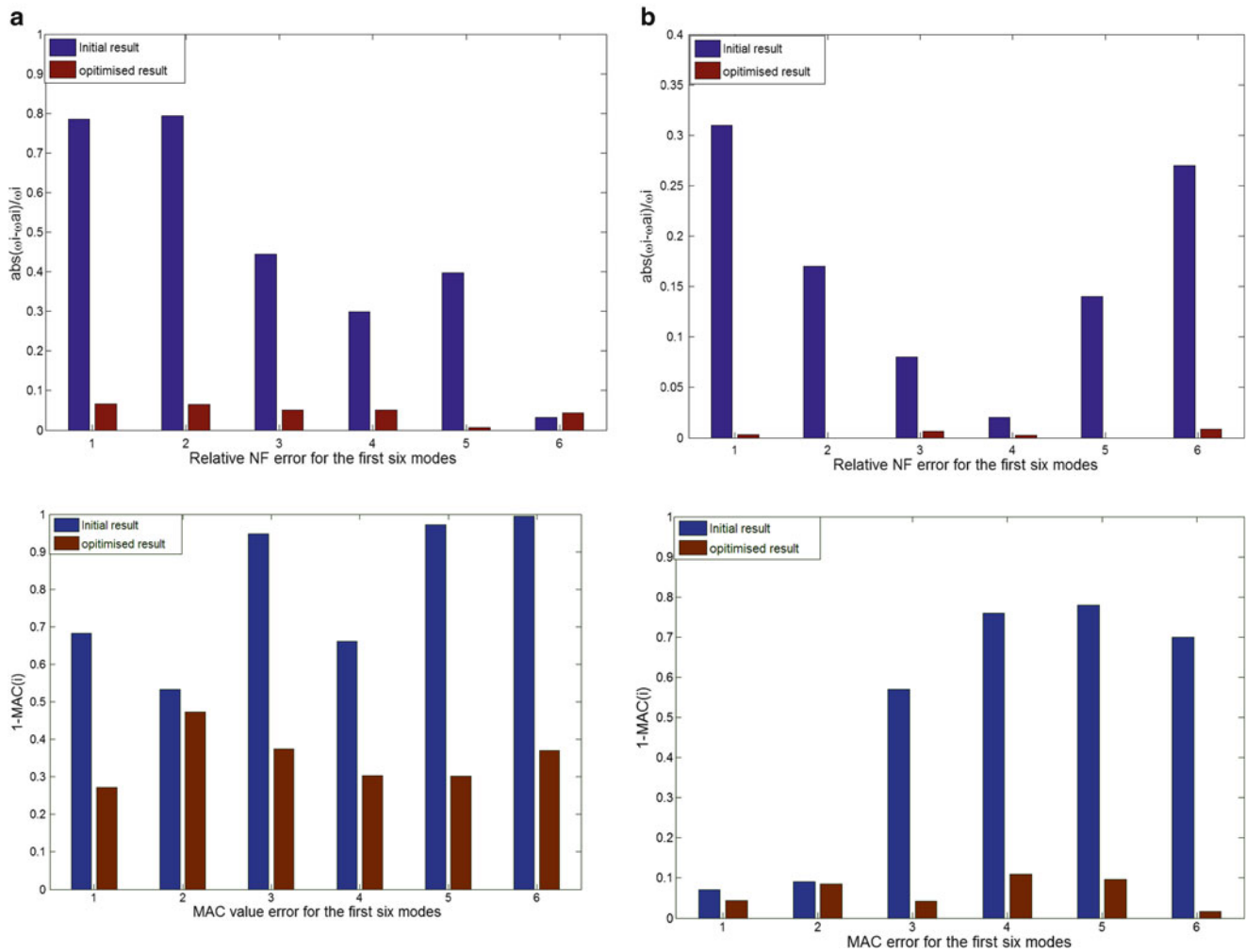


Fig. 39.9 From *top to bottom* (a) NF and MAC error for the 2D frame (b) NF and MAC error for the 3D frame

39.8 Conclusion

The main objective of this work is the development of a parametric ROM representing a typically twisted aero-engine blade. The ROM consists in a simplified structural layout that provides an equivalent dynamic behavior of the full-scale blade for the first six modes. The ROM concept makes use of 2D and 3D Euler–Bernoulli frames, whose beam elements are connected at locations that correspond to the experimental measurement points of frequency response functions on a real blade. The ROM frame concept can represent coupled flexural/torsional mode shapes, the relevant natural frequencies and static masses of the baseline reference case. A high fidelity FE model representing a real blade was employed as the aforementioned reference. The initial configurations of the ROM frames have been identified by exploiting the orthogonality properties of the modes obtained from the high-fidelity FE model. The parameters defining the frame configurations have been further calibrated via an optimization process based on simulated annealing with stochastic tunneling. The cost functions of the optimization process are expressed by linear combinations of relative errors associated to the natural frequencies, the individual MAC, and static masses.

It turns out parametrical framework model can effectively present the dynamic behavior of an aerofoil in contrast to previous pure beam model. Both models 2D and 3D model can achieve good NF correction under 6 and 1 % error separately while 3D optimized beam frame greatly outperform 2D case in mode shape correlation (8–30 %) in a same weight ratio. However, updating a 3D beam framework model would consume four times CPU than 2D case. The optimal NF error and MAC error will be changed through the adjustment of weight ratio dependent on the specific requirement in application. It has been demonstrated 3D beam frame can achieve 94 % of MAC value while maintain less than 1 % NF error for the first

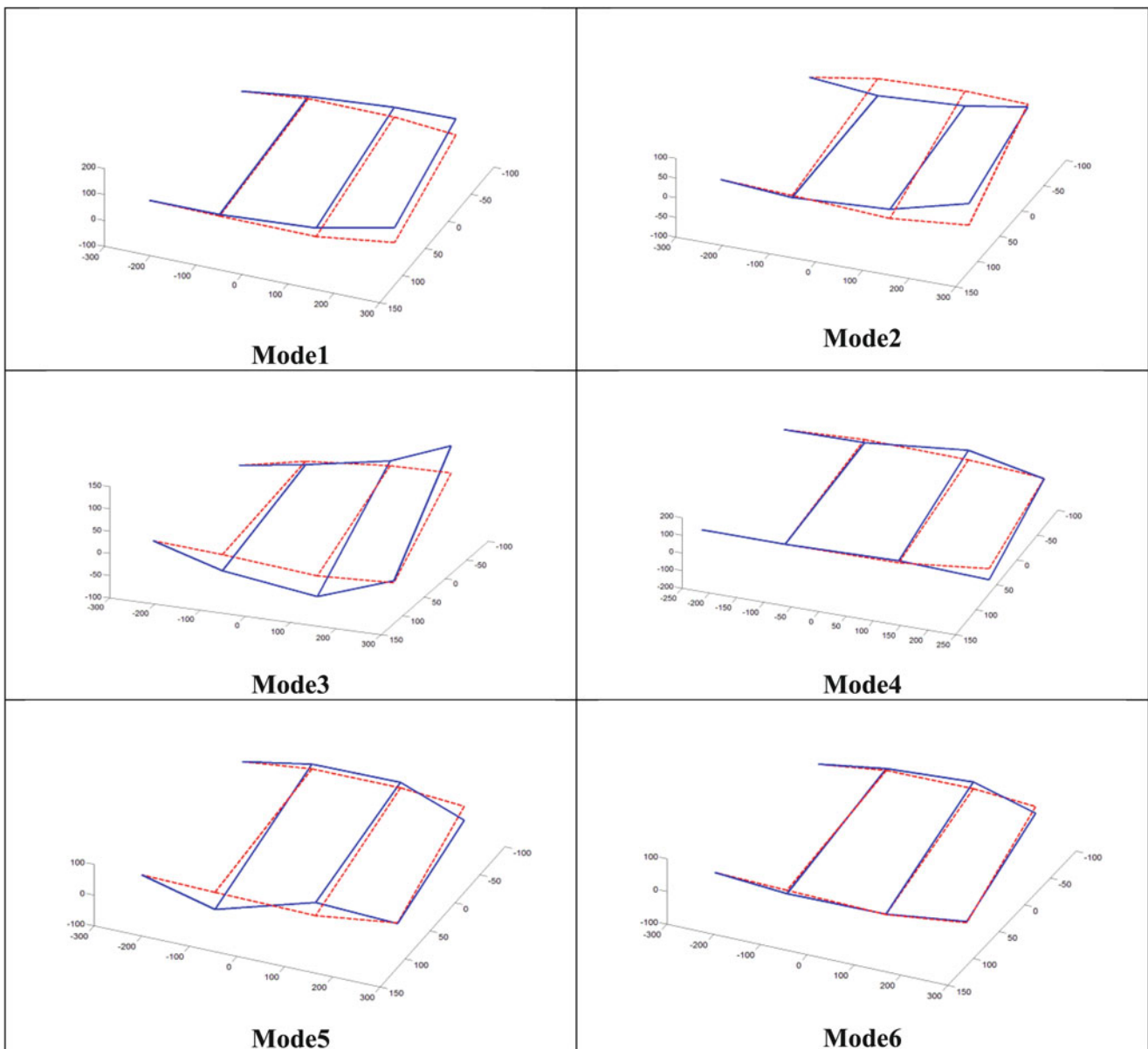


Fig. 39.10 The first six modes plot of optimized 3D beam framework. *Dash line*: original shape, *Solid line*: deformed shape (color figures online)

six modes. Overall, this parametrical and reduced order beam frame greatly improves the accuracy of representing first six modes compared with a single beam model. The ROM beam frame concept is suitable for applications related to the analysis of full-scale mistuned bladed discs with reduced computational costs.

Acknowledgements This work is funded by the Strategic Investment in Low carbon Engine Technology (SILOET) programme supported by Rolls-Royce plc & the Technology Strategy Board (TSB), and by the China Scholarship Council.

References

1. Vargiu P et al (2011) A reduced order model based on sector mistuning for the dynamic analysis of mistuned bladed disks. *Int J Mech Sci* 53(8):639–646
2. Ewins DJ (1969) The effects of detuning upon the forced vibrations of bladed disks. *J Sound Vib* 9(1):65–79
3. Hodges CH (1982) Confinement of vibration by structural irregularity. *J Sound Vib* 82(3):411–424

4. Hodges C, Woodhouse J (1983) Vibration isolation from irregularity in a nearly periodic structure: theory and measurements. *J Acoust Soc Am* 74:894
5. Pierre C (1988) Mode localization and eigenvalue loci veering phenomena in disordered structures. *J Sound Vib* 126(3):485–502
6. Castanier MP, Pierre C (2006) Modeling and analysis of mistuned bladed disk vibration: current status and emerging directions. *J Propulsion Power* 22(2):384–396
7. MacBain J, Whaley P (1984) Maximum resonant response of mistuned bladed disks. *J Vib Acous Stress Reliability Des* 106:218
8. Whitehead D (1998) The maximum factor by which forced vibration of blades can increase due to mistuning. *J Eng Gas Turbines Power* 120(1):115–119
9. Irretier H (1983) Spectral analysis of mistuned bladed disk assemblies by component mode synthesis. In: Srinivasan DJEAV (ed) *Vibrations of bladed disk assemblies*. American Society of Mechanical Engineers, New York
10. Öttarsson G (1994) Dynamic modeling and vibration analysis of mistuned bladed disks. University of Michigan, Ann Arbor
11. Yang M-T, Griffin J (1997) A reduced order approach for the vibration of mistuned bladed disk assemblies. *J Eng Gas Turbines Power* 119(1):161–167
12. Yang M-T, Griffin J (2001) A reduced-order model of mistuning using a subset of nominal system modes. *J Eng Gas Turbines Power* 123(4):893–900
13. Feiner DM, Griffin J (2002) A fundamental model of mistuning for a single family of modes. *J Turbomachinery* 124(4):597–605
14. Lim S-H et al (2007) Compact, generalized component mode mistuning representation for modeling bladed disk vibration. *AIAA J* 45(9): 2285–2298
15. Campus SK (2006) Effects of damping and varying contact area at blade-disk joints in forced response analysis of bladed disk assemblies. *J Turbomachinery* 128:403
16. Fotsch D, Ewins D (2000) Application of MAC in the frequency domain. *ROLLS ROYCE PLC-REPORT-PNR*
17. Joo W et al (1965) Dynamic analysis of structural systems using component modes. *AIAA J* 3(4):678–685
18. Friswell MI, Garvey SD, Penny JET (1995) Model reduction using dynamic and iterated IRS techniques. *J Sound Vib* 186(2):311–323
19. Przemieniecki JS (1985) *Theory of matrix structural analysis*. Dover Publications, New York
20. Lee U (1990) Dynamic continuum modeling of beamlike space structures using finite-element matrices. *AIAA J* 28(4):725–731
21. Ewins D (2000) Adjustment or updating of models. *Sadhana* 25(3):235–245
22. Karaağaçlı T, Yıldız EN, Nevzat Özgüven H (2012) A new method to determine dynamically equivalent finite element models of aircraft structures from modal test data. *Mech Syst Signal Process* 31:94–108
23. Friswell M, Mottershead JE (1995) *Finite element model updating in structural dynamics*, vol 38. Springer, Dordrecht
24. Rzadkowski R (1994) The general model of free vibrations of mistuned bladed discs, Part I: theory. *J Sound Vib* 173(3):377–393
25. Ewins DJ (2010) Control of vibration and resonance in aero engines and rotating machinery – an overview. *Int J Press Vessels Piping* 87(9): 504–510
26. Levin R, Lieven N (1998) Dynamic finite element model updating using simulated annealing and genetic algorithms. *Mech Syst Signal Process* 12(1):91–120
27. Wenzel W, Hamacher K (1999) Stochastic tunneling approach for global minimization of complex potential energy landscapes. *Phys Rev Lett* 82(15):3003–3007

Chapter 40

Practical Seismic FSSI Analysis of Multiply-Supported Secondary Tanks System

Nam-Gyu Kim, Choon-Gyo Seo, and Jong-Jae Lee

Abstract The recent explosion of nuclear power plant (NPP) in Japan was mainly due to performance malfunction in cooling system caused by an earthquake. Thus, seismic analysis has been of great importance for auxiliary feed water (AFW) tank, which is one of the cooling systems in NPP. The existing simple analysis of the water tank is based on the entire aux stick finite element model with AFW tank, which leads to a very conservative result. In this research, two types of fluid tank analysis methods, static analysis including the effect of dynamic pressure and frequency domain analysis accounting for both dynamic mass and spring, have been proposed using the substructure method for an AFW tank.

The proposed analysis method accounted for multi-physical interactions (Fluid-structure-Soil interaction, FSSI), soil-structure, fluid-structure, and structure-structure interactions and needed only finite element model of the AFW tank for effective substructure method. The fluid forces subjected to the tank wall were displaced to the fluid pressures or the hydrodynamic model in the existing Code & Standard. The control motion was the floor responses at the Auxiliary Building (AB) 100 ft, and it was computed by SASSI analysis. The effective stiffness was taken as the constants identifying the structure-structure interaction of the AB-Fluid tank. Compared to existing conventional analysis packages, the results of the proposed analysis methods showed an effective solution for seismic analysis of fluid storage tanks in nuclear power plant.

40.1 Introduction

Cooling system of Nuclear Power Plant (NPP) related to Fukushima NPP explosion caused by an earthquake belongs to seismic category I. Since then, the seismic design and analysis of AFW tanks associated with refrigerating NPP has been of great attention to researchers. In the existing analysis methods of the AFW tanks, finite element model has the entire aux stick model with AFW tank, and ground is displaced to fixed conditions. Fluid forces subjected to the tank wall were displaced to the fluid added mass, and then the response spectrum analysis was performed. Since input motion, boundary condition, and fluid effect are different from those of the real structure, existing analysis method cannot reflect the actual behavior of NPP structures. Furthermore, the analysis method requires an entire FE model resulting in a very conservative value.

The development of an effective seismic analysis method that could account for all the multi-physical interactions, that is, soil-structure, fluid-structure, and structure-structure interactions, is highly required. In this research, two types of fluid tanks analysis methods, static analysis considering the dynamic pressure and frequency domain analysis method considering dynamic mass and spring have been proposed based on the substructure method for an AFW tank. In order to evaluate the applicability of the proposed analysis methods, the result of the proposed methods were compared with those of the existing analysis method.

N.-G. Kim • J.-J. Lee (✉)
Department of Civil and Environmental Engineering, Sejong University, Seoul, Korea
e-mail: jongjae@sejong.ac.kr

C.-G. Seo
KEPCO Engineering and Construction Company, Seongnam, Korea

40.2 Theoretical Background

40.2.1 Dynamic Pressure for Fluid Tanks

When a rectangular tank is subjected to the simultaneous action of three components of seismic motion, the tank wall may experience hydrodynamic pressures and inertia force in addition to the hydrostatic pressure. The hydrodynamic pressures on tank walls and base slab corresponding to the impulsive, convective and vertical response modes are defined according to the codes, TID-7024 and ACI 350.3. The mechanical FSI model can be illustrated as below. The hydrodynamic and hydrostatic pressures are calculated on the walls for each direction. In this research, a rectangular tank of cross-sectional dimensions of $2L_1$ and $2L_2$, height H and liquid level z is considered, as shown in Figs. 40.1 and 40.2.

The TID-7024 and ACI 350.3 provide the impulsive pressure of the rectangular tank as following.

$$P_i(z) = 0.132S_a(T_i)\gamma_f(L/H)^2 \tanh(1.732L/H) [4H - 6h_i - (6H - 12h_i)(z/H)] \tag{40.1}$$

$$T_i = 2\pi \sqrt{(W_i + W_w)/(gk)} \tag{40.2}$$

$$W_i = W_t \frac{\tanh\left(\sqrt{3}\frac{L}{H}\right)}{\sqrt{3}\frac{L}{H}} \tag{40.3}$$

$$h_i = L(0.5 - 0.1875(L/H)) \text{ (if } L/H \geq 1.333) \tag{40.4}$$

where P_i is the impulsive pressure at level z ; S_a is the value of the floor response spectral acceleration with SSI effect corresponding to the fundamental impulsive period T_i ; h_i is the height of impulsive lateral force; γ_f is the unit weight of fluid; W_i is the effective impulsive weight, W_w is the weight of the wall and W_t is total weight of the fluid; k is the flexible stiffness of the wall; and g is the gravity acceleration ($=32.17 \text{ ft/s}^2$).

Fig. 40.1 Description of tank dimensions and mechanical model

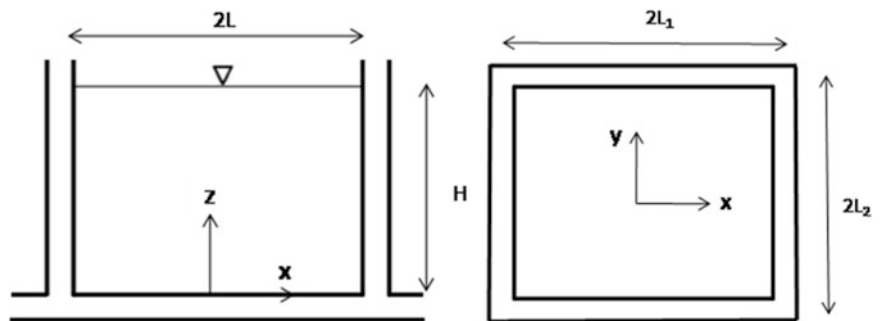
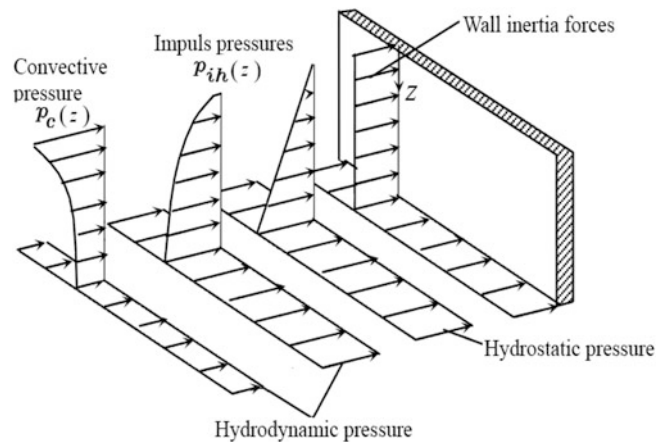


Fig. 40.2 Impulsive and convective pressure for fluid tanks



The TID-7024 and ACI 350.3 also provide the convective pressure of the tank as following.

$$P_c(z) = 0.132S_a(T_c)\gamma_f(L/H)^2 \tanh(1.732L/H) [4H - 6h_c - (6H - 12h_c)(z/H)] \quad (40.5)$$

$$T_c = \frac{2\pi}{w_c} = \frac{2\pi}{\sqrt{\frac{1.58g}{L} \tanh\left(1.58\frac{H}{L}\right)}} \quad (40.6)$$

$$W_c = 0.264W_t \left(\frac{L}{H}\right) \tanh\left(3.16\frac{L}{H}\right) \quad (40.7)$$

$$h_c = H \left(1 - \frac{\cosh\left[1.58\left(\frac{H}{L}\right)\right] - 1}{1.58\left(\frac{H}{L}\right) \sinh\left(1.58\frac{H}{L}\right)}\right) \quad (40.8)$$

where P_c is the convective pressure at level z ; T_c is the fundamental convective period; and h_c is the height of convective lateral force.

40.2.2 Frequency Domain Analysis Method

Frequency domain analysis can be carried out by transforming the equation of motion on time domain to frequency domain and then calculating the solution, for the equation of motion [1]. In general, the equation of motion can be formally transformed into the frequency domain using the Fourier or Laplace transform. In addition, this method can calculate the solution more effectively than the time domain method.

Fourier transform is more common than Laplace transform in the frequency domain analysis field. Specifically, the integral transformation of the discrete data can be processed easily by using fast Fourier transform technique. The inverse Fourier transform for the dynamic response is shown below.

$$U(\omega) = \mathfrak{F}\{u(t)\} = \int_{-\infty}^{\infty} u(t)e^{-i\omega t} dt$$

$$u(t) = \mathfrak{F}^{-1}\{U(\omega)\} = \frac{1}{2\pi} \int_{-\infty}^{\infty} U(\omega)e^{i\omega t} d\omega \quad (40.9)$$

In the above formula, the frequency response function $U(\omega)$ can be found by multiplying the simple both transfer function $H(\omega)$ and input load $F(\omega)$. In particular, transfer function in single degree of freedom system represents the inverse of dynamic stiffness $S(\omega)$.

$$U(\omega) = H(\omega)F(\omega) \leftarrow H(\omega) = S^{-1}(\omega) = \frac{1}{-\omega^2m + i\omega c + k} \quad (40.10)$$

Frequency domain analysis follows the hysteretic behavior damping. This damping does not change the damping characteristics depending on the frequency. The hysteretic behavior damping considers the modulus of elasticity by changing the complex elasticity modulus such as $E^* = E(1 + i2\beta)$.

In the formula, $i = \sqrt{-1}$ and E is the modulus of elasticity. β is hysteretic behavior damping ratio. Frequency domain analysis method is less commonly used than the time domain analysis method for seismic analysis. However, if the frequency dependent characteristics such as soil-structure interaction are apparent, frequency domain analysis method is more efficient than time domain analysis method.

40.3 Earthquake Analysis for Fluid Tanks in Nuclear Power Plant

40.3.1 Simple Analysis Method

Simple analysis method for AFW tanks in NPP is the response spectrum analysis method for the Auxiliary building. The Finite element model and sequence of existing analysis method is shown in Figs. 40.3 and 40.4.

In the analysis methods for AFW tanks, finite element model has the entire stick model with AFW tank on the fixed base. This method defines that all fluid mass would be considered as the added mass on the tank wall, and then uses the response spectrum analysis. For these reasons, the existing analysis method cannot reflect the actual behavior of NPP structures. The input motion, boundary condition, and fluid effect of the model structure method are different from those of the real structure. Furthermore, this method is conservative for the modeling and analysis of a NPP structure. Therefore, the development of an effective seismic analysis method that could take into account the multi-physical interactions is demanded.

40.3.2 Proposed Seismic Analysis Method Using Static Analysis

If the ratio of the entire structure with target structures is less than 1/100, then target structure can be analyzed as an interpreted condition from the entire structure [2–4]. Two types of fluid tanks analysis methods (static analysis considering

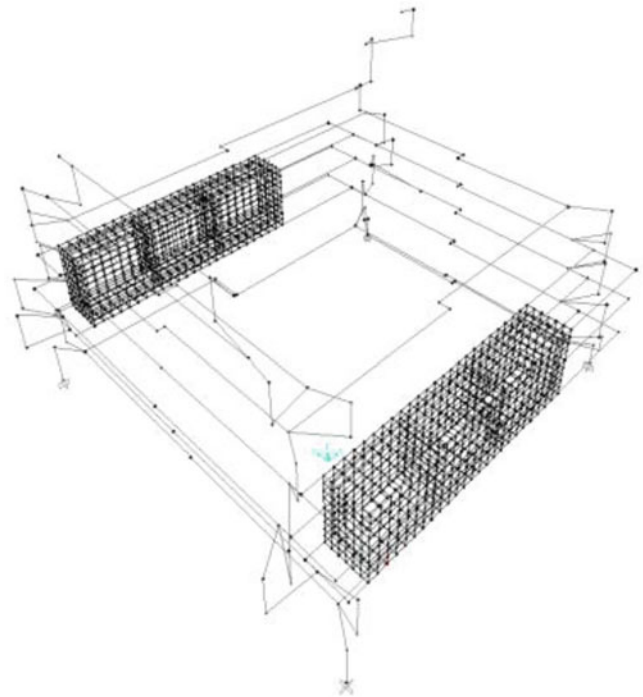


Fig. 40.3 The finite element model for simple analysis

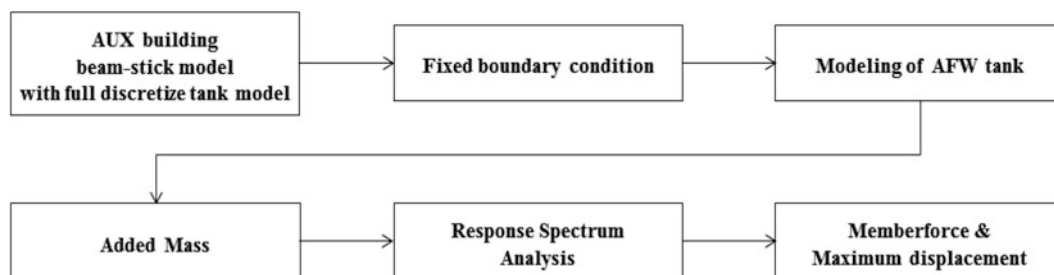


Fig. 40.4 Flow for the simple analysis scheme

Fig. 40.5 Flow for the proposed method 1 scheme

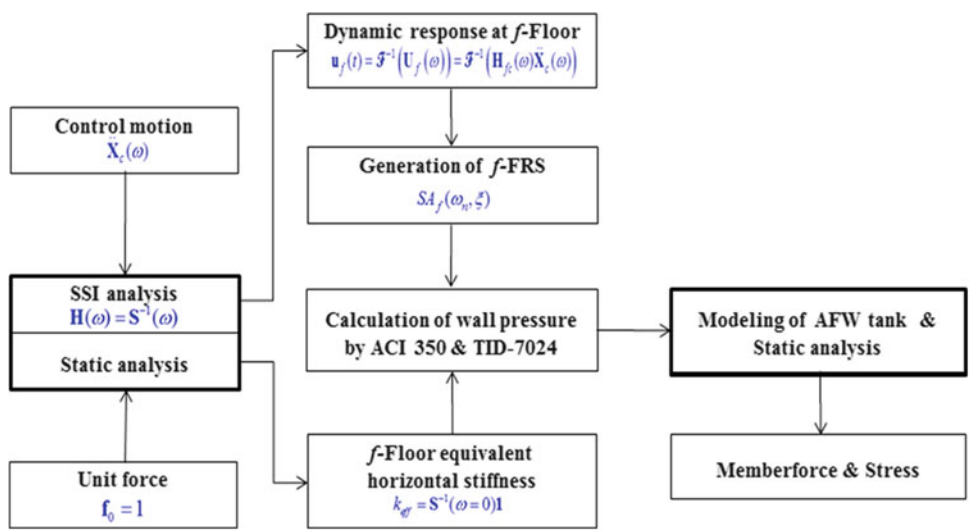
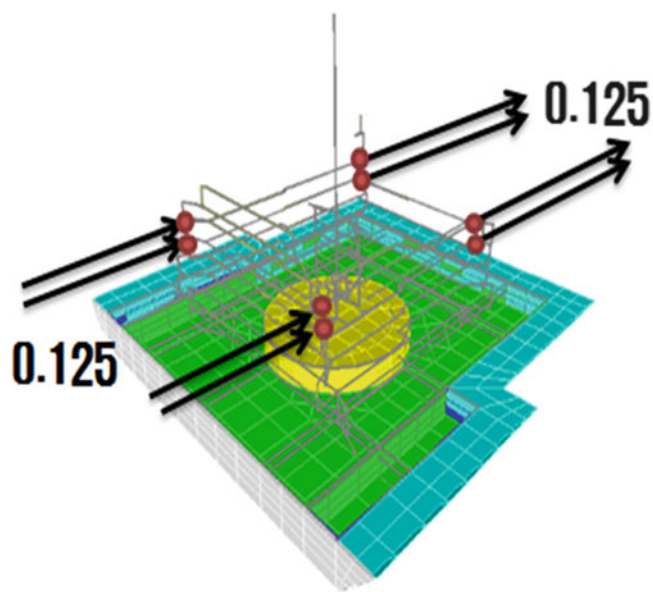


Fig. 40.6 The finite element model considered unit forces



the dynamic pressure and frequency domain analysis method considering dynamic mass and spring) have been proposed based on the above substructure method for an AFW tank. For this reason, the proposed methods can construct a FE model more simply than the existing analysis method. The sequence of proposed Method 1 is shown in Fig. 40.5.

In the proposed analysis methods, the applied fluid forces subjected to the tank wall were displaced to the fluid pressures in the ACI 350.3 & TID-7024. The control motion was the floor responses at aux building 100 ft, and it was computed by SASSI (A System for Analysis of Soil-Structure Interaction) analysis. The equivalent stiffness was considered as the constants identifying the AB-Fluid tank (structure-structure) interaction. Finally, static analysis is carried out. For this reason, the proposed analysis method is more advanced than the existing analysis method to account for the multi-physical interactions of soil-structure, fluid-structure, and structure-structure (Figs. 40.6 and 40.7; Tables 40.1 and 40.2).

40.3.3 Proposed Seismic Analysis Method Using Frequency Domain Analysis

Frequency domain analysis is not widely used in the commercial FE analysis programs. Thus, this study shows that a frequency domain analysis method has a good application for the hydro-dynamic analysis using KIESSI program [5]. The sequence of the proposed method 2 is shown in Fig. 40.8.

Fig. 40.7 The finite element model for the AFW tank considered dynamic pressures

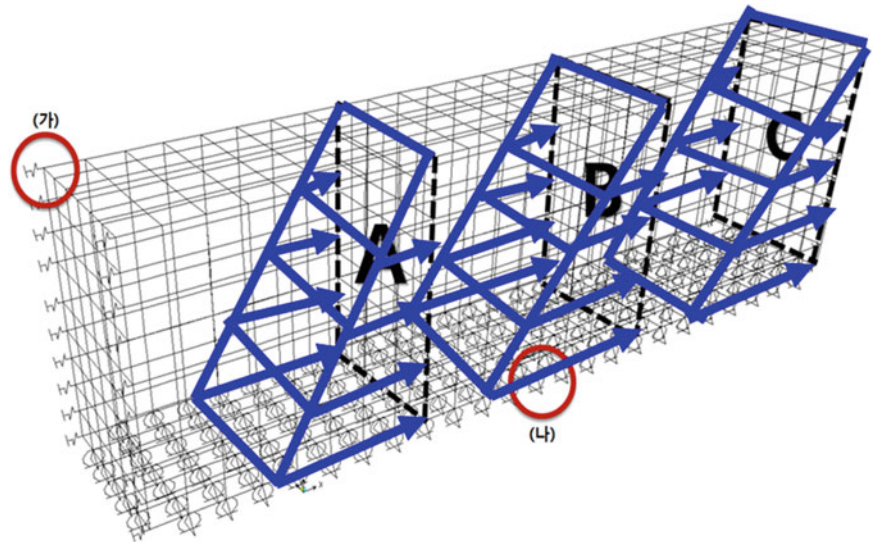


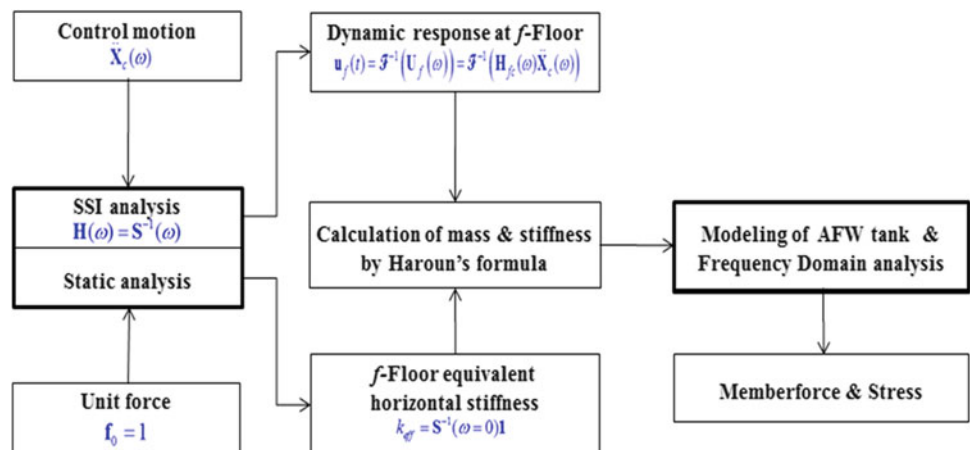
Table 40.1 Spectral acceleration

| Period [s] | | S_a [g] |
|------------|-------|-----------|
| T_i | 0.009 | 0.367 |
| T_c | 4.349 | 0.485 |

Table 40.2 Unit pressure subjected to the tank wall

| Height [ft] | Impulsive [kips/ft ²] | Convective [kips/ft ²] | Total pressure [kips/ft ²] |
|-------------|-----------------------------------|------------------------------------|--|
| 2.00 | 0.654 | 0.004 | 0.658 |
| 6.00 | 0.593 | 0.009 | 0.602 |
| 10.00 | 0.532 | 0.014 | 0.546 |
| 14.00 | 0.471 | 0.019 | 0.490 |
| 18.00 | 0.409 | 0.024 | 0.434 |
| 22.75 | 0.337 | 0.030 | 0.367 |
| 27.50 | 0.264 | 0.036 | 0.301 |
| 31.50 | 0.203 | 0.042 | 0.245 |
| 35.50 | 0.142 | 0.047 | 0.189 |

Fig. 40.8 Flow for proposed method 2 scheme



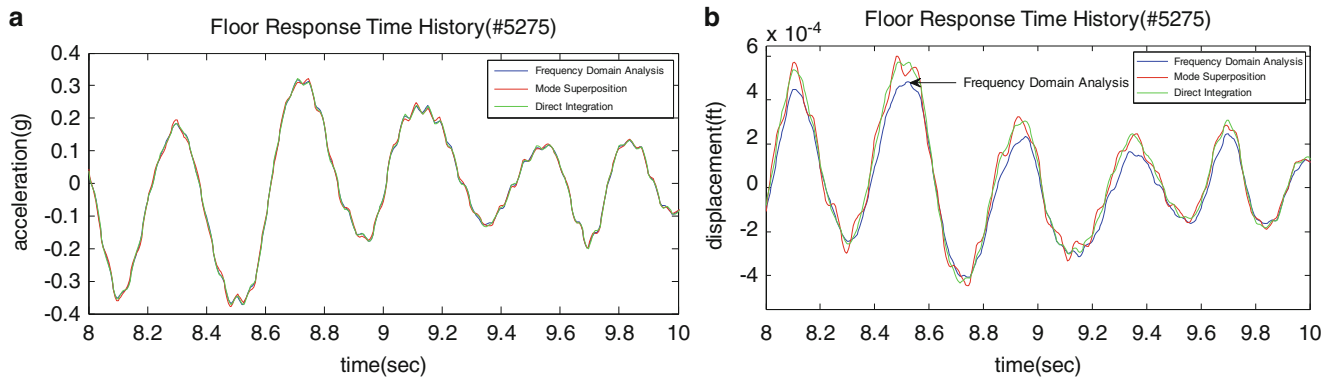
The background of the proposed method 2 is the same with the background of proposed method 1. However, in the proposed method 2, fluid is replaced with equivalent mass and spring damper system by using Haroun's method. The method 2 can find the final results of time history. Table 40.3 shows the constants of dynamic mass, spring stiffness, and equivalent height of the applied fluid.

Table 40.3 Hydro-dynamic properties

| Dynamic mass [kip] | Dynamic spring stiffness [kip/ft] | Equivalent height [ft] |
|--------------------|-----------------------------------|------------------------|
| m_i 60.77 | k_i 1.58e7 | h_i 14.25 |
| m_c 27.93 | k_c 29.15 | h_c 24.68 |

Table 40.4 Maximum displacement at a top node

| Direction | Simple analysis method | Proposed method 1 | Proposed method 2 |
|------------|------------------------|-------------------|-------------------|
| U_1 [ft] | 0.0010 | 0.0004 | 0.0005 |

**Fig. 40.9** Time history response at a top node. (a) Time history of acceleration ($8 \leq t \leq 10$). (b) Time history of displacement ($8 \leq t \leq 10$)

40.4 Conclusion

In order to evaluate the usability of the proposed analysis methods, the results of the proposed methods were compared with those of the existing analysis method. Table 40.4 shows the displacements at a top node obtained from the existing and proposed methods. The existing analysis method was found to be more conservative. In addition, compared with the mode superposition and the direct integration methods, accelerations obtained from the frequency domain analysis were in very good agreement with those of the methods shown in Fig. 40.9. However, there was a small difference in displacements as shown in Fig. 40.9. This causes the difference between the frequency and time domain analysis methods in addition to the difference between the applied damping theory (direct integration method—Rayleigh damping, mode superposition method—modal damping, and frequency domain analysis method—Hysteresis damping). The future study would further verify the difference between the proposed and the existing methods.

Acknowledgement This work was partly supported by the IT R&D program of MOTIE/KEIT(No. 10040909, Development of an Integrated Design Solution based on Codes and Field Data for the advancement of the Plant Industry) and the Human Resources Development of the Korea Institute of Energy Technology Evaluation and Planning (KETEP) grant funded by the Korea government Ministry of Knowledge Economy (No. 20104010100520).

References

1. Dey A, Gupta VK (1998) Response of multiply supported secondary systems to earthquakes in frequency domain. *Earthq Eng Struct Dyn* 27(2):187–201
2. Saady A (1992) Seismic analysis of multiply-supported mdof secondary system. PhD Thesis, McMaster University at Hamilton, Ontario, Canada
3. Yang YB, Huang WH (1998) Equipment-structure interaction considering the effect of torsion and base isolation. *Earthq Eng Struct Dyn* 27:155–171
4. Agrawal AK, Datta TK (1999) Seismic behavior of a secondary system on a yielding torsionally coupled primary system. *JSEE* 2:35–46
5. Korea Advanced Institute of Science & Technology (2012) KIESSI user's manual. Korea Advanced Institute of Science & Technology, Daejeon, Republic of Korea

Chapter 41

DEIM for the Efficient Computation of Contact Interface Stresses

M. Breidfuss, H. Irschik, H.J. Holl and W. Witteveen

Abstract The computational effort for the simulation of reduced order models containing contact stresses is determined by these nonlinear terms. Recent publications suggest the utilization of interpolation methods to overcome this bottleneck. The applicability of the Discrete Empirical Interpolation Method (DEIM) for the efficient computation of contact stresses is demonstrated. The modeling of a mechanical structure containing an interface using zero thickness elements is outlined first. This is followed by a reduction method using joint interface modes as extension to the well known Craig Bampton approach. The basic idea of interpolation methods and a summary of the applied DEIM algorithm is given. Finally the numerical example of a bolted cantilever is investigated for two loadcases and the results are discussed for different trial function bases. It is clearly shown that DEIM can be used to significantly improve the computational efficiency for this type of problems while keeping accuracy at an acceptable level.

Keywords DEIM • POD • Model Order Reduction • Joint Contact Consideration • Interpolation Method

41.1 Introduction

This contribution focuses on the efficient consideration of contact stresses within the framework of reduced order models for mechanical systems. Literature and current investigations of the authors clearly point out that the computational effort for the simulation of reduced order models containing contact stresses is determined by these nonlinear terms as the evaluation still takes place on the discretization of the full model. Furthermore a coordinate transformation from generalized coordinates to physical coordinates and the projection of the resulting stresses onto the generalized coordinates is necessary, which leads to an even higher computational effort involved for the interface stress computation compared to the full model.

Interpolation methods are an effective approach to lower the computational effort involved with the evaluation of parametrized functions defined on a spatial domain [6]. Furthermore in [2] the Discrete Empirical Interpolation Method (DEIM) is suggested to lower the computational effort for reduced order models containing nonlinear functions. In this case the former mentioned transformation and projection is only necessary for some few physical coordinates. The scaling of the interpolation functions is determined by collocation of function values and interpolated values at these so called interpolation points.

To demonstrate the applicability of DEIM for efficient computation of joint interface stresses the problem is formulated as single body involving self contact. The theory of zero thickness elements, see [4] and [5], is used to discretize the joint contact. The authors suggest a zero thickness element formulation leading to a contact stress equivalent force vector. This allows for a model order reduction following [3, 8] and fits into the DEIM formulation proposed by [2].

M. Breidfuss (✉) • H. Irschik • H.J. Holl
Johannes Kepler University Linz, Altenbergerstr. 69, 4040 Linz, Austria
e-mail: markus.breidfuss@jku.at

W. Witteveen
University of applied sciences Wels, Stelzhamerstr. 23, 4600 Wels, Austria

41.2 Problem Formulation

The body Ω with the surface Γ and the contact interface Γ_{jc} as depicted in Fig. 41.1a is investigated. As boundary conditions the displacement \mathbf{u}_d and the stresses \mathbf{t} are prescribed on Γ_d and Γ_t respectively which are disjunct surface regions of Γ . The dynamic equilibrium of a physical particle within the domain Ω at the position denoted by \mathbf{x} is given by

$$\rho \ddot{\mathbf{u}} - \text{div} \mathbf{S} = \mathbf{k} \quad \forall \mathbf{x} \in \Omega \quad (41.1a)$$

with the boundary conditions

$$\mathbf{u} = \mathbf{u}_d \quad \forall \mathbf{x} \in \Gamma_d \quad \text{and} \quad \mathbf{S} \mathbf{n} = \mathbf{t} \quad \forall \mathbf{x} \in \Gamma_t \quad (41.1b)$$

and the initial conditions for time $t = t_0 = 0$

$$\mathbf{u} = {}^0\mathbf{u} \quad \forall \mathbf{x} \in \Omega \quad \text{and} \quad \dot{\mathbf{u}} = {}^0\mathbf{v} \quad \forall \mathbf{x} \in \Omega \quad (41.1c)$$

where ρ denotes the mass density, \mathbf{u} the displacement, $\dot{\mathbf{u}} = \mathbf{v}$ the velocity, $\ddot{\mathbf{u}} = \mathbf{a}$ the acceleration, \mathbf{S} the Cauchy stress tensor, \mathbf{k} the imposed force density and \mathbf{n} the surface normal pointing outwards. The contact interface Γ_{jc} is interpreted as self contact of the body Ω with Γ_{jc}^- and Γ_{jc}^+ as the two contacting surfaces. Contact stresses will occur

$$\mathbf{S}^\pm \mathbf{n}^\pm = \mathbf{t}_{jc}^\pm \quad \forall \mathbf{x} \in \Gamma_{jc} \quad (41.1d)$$

where \mathbf{t}_{jc}^\pm describes the acting joint contact stresses on the two sides Γ_{jc}^\pm , see Fig. 41.1b.

41.3 Discretization

To obtain a finite element method (FEM) discretization of the contact problem Eq. (41.1), the principle of virtual work is applied. With the virtual displacements $\delta \mathbf{u}$ which are assumed to be small in relation to the body dimension and the according virtual strain tensor $\delta \boldsymbol{\epsilon}$ the resulting weak formulation of the dynamic equilibrium is given by

$$\begin{aligned} \delta W^\Omega = & \int_{\Omega} \rho \ddot{\mathbf{u}} \cdot \delta \mathbf{u} \, d\Omega + \sum_{i,j} \int_{\Omega} s_{ij} \delta \epsilon_{ij} \, d\Omega - \int_{\Gamma_t} \mathbf{S} \mathbf{n} \cdot \delta \mathbf{u} \, d\Gamma - \int_{\Gamma_{jc}^-} \mathbf{S}^- \mathbf{n}^- \cdot \delta \mathbf{u}^- \, d\Gamma \\ & - \int_{\Gamma_{jc}^+} \mathbf{S}^+ \mathbf{n}^+ \cdot \delta \mathbf{u}^+ \, d\Gamma - \int_{\Omega} \mathbf{k} \cdot \delta \mathbf{u} \, d\Omega = 0. \end{aligned} \quad (41.2)$$

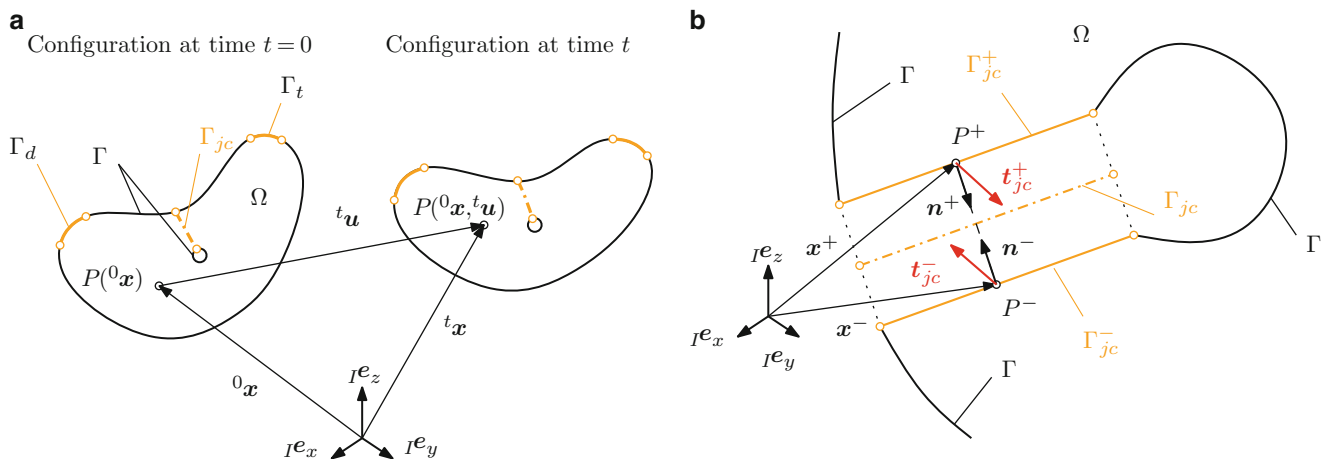


Fig. 41.1 Body Ω including joint interface in reference configuration and actual configuration at time t (a) and contact stresses within the joint interface Γ_{jc} for contact locations P^- and P^+ (b)

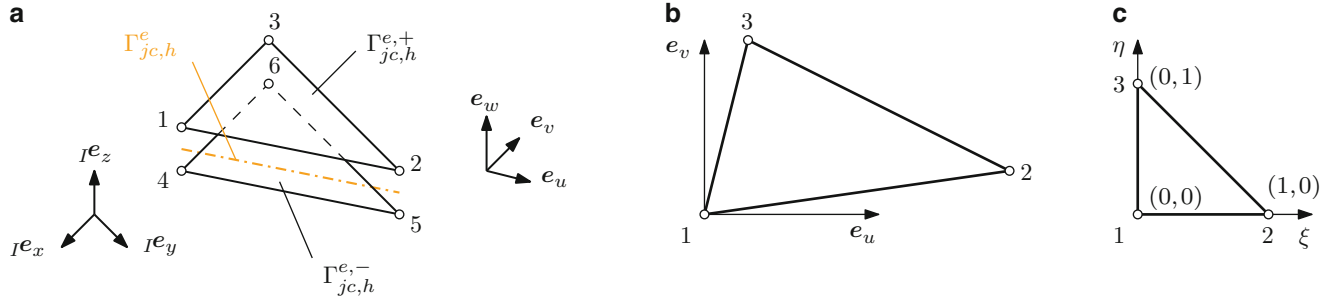


Fig. 41.2 Triangular shaped zero thickness element (a), arbitrary shaped triangle with local coordinate system (u, v) (b) and uniform triangle with natural coordinates (ξ, η) (c)

For a discretization Ω_h of the domain Ω with the nodes \mathbf{x}_h and the related nodal displacements \mathbf{u}_h Eq. (41.2) can be rewritten as sum over all elements $\Omega_h^e \subset \Omega_h$ and element surfaces $\Gamma_h^e \subset \Gamma_h$. The virtual work of a single element not adjacent to the contact interface Γ_{jc} is given by

$$\delta W^e = \int_{\Omega_h^e} \rho \ddot{\mathbf{u}} \cdot \delta \mathbf{u} \, d\Omega + \sum_{i,j} \int_{\Omega_h^e} s_{ij} \delta \epsilon_{ij} \, d\Omega - \int_{\Gamma_{i,h}^e} \mathbf{S} \mathbf{n} \cdot \delta \mathbf{u} \, d\Gamma - \int_{\Omega_h^e} \mathbf{k} \cdot \delta \mathbf{u} \, d\Omega = 0. \quad (41.3)$$

For each element the nodal displacement vector $\mathbf{u}_h^e \subset \mathbf{u}_h$ can be defined. By using the Matrix of element shape functions \mathbf{N}^e the displacement field $\mathbf{u}^e = \mathbf{N}^e \mathbf{u}_h^e$ and the virtual displacement field $\delta \mathbf{u}^e = \mathbf{N}^e \delta \mathbf{u}_h^e$ can be formulated for each element. Evaluation of the integrals, sum over all elements defined by Eq. (41.3) and implementation of the boundary conditions, see [1], but without consideration of the contact stresses at Γ_{jc}^- and Γ_{jc}^+ leads to the discretized equations of motion

$$\mathbf{M} \ddot{\mathbf{u}}_h + \mathbf{K} \mathbf{u}_h = \mathbf{f}_{ext}. \quad (41.4)$$

For an element adjacent to the contact surface Γ_{jc} the discretization Ω_h comprises a matching mesh $\Gamma_{jc,h}^-$ and $\Gamma_{jc,h}^+$ of the two sides Γ_{jc}^- and Γ_{jc}^+ . To handle the contact within the joint interface Γ_{jc} the theory of zero thickness elements is a straight forward technique as only small relative movement of the contact partner is expected. Several formulations can be found in literature, e.g. [4] and [5]. For this contribution the stress equivalent nodal force vector of an isoparametric, triangular shaped zero thickness element, depicted in Fig. 41.2a, is formulated. One surface triangle connects to the discretization $\Gamma_{jc,h}^-$ and the other one to the discretization $\Gamma_{jc,h}^+$.

For the nodal displacements of the element

$$\mathbf{u}_h^{e,+} = [\mathbf{u}_1^{eT} \ \mathbf{u}_2^{eT} \ \mathbf{u}_3^{eT}]^T \quad \text{and} \quad \mathbf{u}_h^{e,-} = [\mathbf{u}_4^{eT} \ \mathbf{u}_5^{eT} \ \mathbf{u}_6^{eT}]^T \quad (41.5)$$

a local coordinate system (u, v, w) where the \mathbf{e}_w vector is oriented in interface $\Gamma_{jc,h}^e$ normal direction as depicted in Fig. 41.2a is used. With these nodal displacements and the Matrix

$$\mathbf{N}^e = [\mathbf{N}_1 \ \mathbf{N}_2 \ \mathbf{N}_3] \quad \text{with} \quad \mathbf{N}_i = \text{diag}(N_i, N_i, N_i) \quad (41.6)$$

holding the shape functions $N_1 = 1 - \xi - \eta$, $N_2 = \xi$ and $N_3 = \eta$ where the natural coordinates of a uniform triangle $\xi = \xi(u, v)$ and $\eta = \eta(u, v)$ are depending on the coordinates u and v of the arbitrary shaped element, the displacement fields of both surface triangles

$$\mathbf{u}^{e,+} = \mathbf{N}^e \mathbf{u}_h^{e,+} \quad \text{and} \quad \mathbf{u}^{e,-} = \mathbf{N}^e \mathbf{u}_h^{e,-} \quad (41.7)$$

can be described. Both surface triangles are interpolated using the same shape function definition. With consideration of Newton's Third Law, the principle of actio and reactio

$$\mathbf{t}_{jc}^e = \mathbf{t}_{jc}^{e,+} = -\mathbf{t}_{jc}^{e,-} \quad (41.8)$$

illustrated in Fig. 41.1b, the virtual work of the zero thickness element is given by

$$\delta W^e = \delta W^{e,-} + \delta W^{e,+} = - \int_{\Gamma_{j_c,h}^{e,-}} \delta \mathbf{u}^{e,-} \cdot \mathbf{t}_{j_c}^{e,-} d\Gamma - \int_{\Gamma_{j_c,h}^{e,+}} \delta \mathbf{u}^{e,+} \cdot \mathbf{t}_{j_c}^{e,+} d\Gamma = \int_{\Gamma_{j_c,h}^{e,-}} \delta \mathbf{u}^{e,-} \cdot \mathbf{t}_{j_c}^e d\Gamma - \int_{\Gamma_{j_c,h}^{e,+}} \delta \mathbf{u}^{e,+} \cdot \mathbf{t}_{j_c}^e d\Gamma. \quad (41.9)$$

The contact stresses, e.g. for normal direction, depend on the gap function

$$\mathbf{g} = [\mathbf{u}^{e,+} - \mathbf{u}^{e,-}]^T \mathbf{e}_w = [\mathbf{N}^e \mathbf{u}_h^{e,+} - \mathbf{N}^e \mathbf{u}_h^{e,-}]^T \mathbf{e}_w = \begin{bmatrix} \mathbf{u}_h^{e,+} \\ \mathbf{u}_h^{e,-} \end{bmatrix}^T [\mathbf{N}^e - \mathbf{N}^e]^T \mathbf{e}_w \quad (41.10)$$

via the “constitutive” relation

$$\mathbf{t}_{j_c}^e = -t_n \mathbf{e}_w \quad \text{with} \quad t_n = \begin{cases} 0 & \text{if } g \geq 0, \\ c_n g & \text{if } g < 0 \end{cases} \quad (41.11)$$

with the penalty parameter c_n . For evaluation of the integral in Eq. (41.9) the triangular shaped interface $\Gamma_{j_c,h}^e$ depicted in Fig. 41.2b is projected onto a uniform triangle as depicted in Fig. 41.2c. The Jacobian \mathbf{J} of this transformation is given by

$$\begin{bmatrix} \frac{\partial}{\partial \xi} \\ \frac{\partial}{\partial \eta} \end{bmatrix} = \begin{bmatrix} \frac{\partial u}{\partial \xi} & \frac{\partial v}{\partial \xi} \\ \frac{\partial u}{\partial \eta} & \frac{\partial v}{\partial \eta} \end{bmatrix} \begin{bmatrix} \frac{\partial}{\partial u} \\ \frac{\partial}{\partial v} \end{bmatrix} = \mathbf{J} \begin{bmatrix} \frac{\partial}{\partial u} \\ \frac{\partial}{\partial v} \end{bmatrix}. \quad (41.12)$$

With this transformation the virtual work of the zero thickness element is given by

$$\delta W^e = - \int_0^1 \int_0^{1-\eta} [\delta \mathbf{u}^{e,+} - \delta \mathbf{u}^{e,-}] \cdot \mathbf{t}_{j_c}^e \det \mathbf{J} d\xi d\eta = - \int_0^1 \int_0^{1-\eta} \begin{bmatrix} \delta \mathbf{u}_h^{e,+} \\ \delta \mathbf{u}_h^{e,-} \end{bmatrix}^T [\mathbf{N}^e - \mathbf{N}^e]^T \mathbf{t}_{j_c}^e \det \mathbf{J} d\xi d\eta \quad (41.13)$$

where the stress equivalent nodal force vector of the zero thickness element is found

$$\mathbf{f}_{contact}^e = \int_0^1 \int_0^{1-\eta} [\mathbf{N}^e - \mathbf{N}^e]^T \mathbf{t}_{j_c}^e \det \mathbf{J} d\xi d\eta. \quad (41.14)$$

Finally Eq. (41.4) is extended with the nodal contact force vectors obtained from the zero thickness elements within the joint interface. The discretization of the contact problem Eq. (41.1) is given by

$$\mathbf{M} \ddot{\mathbf{u}}_h + \mathbf{K} \mathbf{u}_h = \mathbf{f}_{ext} + \mathbf{f}_{contact}. \quad (41.15)$$

41.4 Model Order Reduction

An approximation of the nodal displacements \mathbf{u}_h in Eq. (41.15) is given by

$$\mathbf{u}_h \approx \Phi \mathbf{q} \quad (41.16)$$

with the matrix Φ holding the displacement trial functions or modes φ_i and the according generalized coordinates \mathbf{q} . As described in [3] a mode base

$$\Phi_{classic} = [\Psi_{CM} \Phi_{NM}] \quad (41.17)$$

consisting of Constraint Modes Ψ_{CM} and Fixed Boundary Normal Modes Φ_{NM} is defined. As proposed by [8] for structures containing joints the classic mode base Eq. (41.17) is extended by a set of Joint Interface Modes Φ_{JIM} which account for the local deformation at the interface. The resulting transformation matrix is given by

$$\Phi = [\Psi_{CM} \ \Phi_{NM} \ \Phi_{JIM}]. \quad (41.18)$$

Substituting (41.16) and (41.18) into Eq. (41.15) and premultiplying with Φ^T leads to the reduced equations of motion

$$M_{red} \ddot{\mathbf{q}} + \mathbf{K}_{red} \mathbf{q} = \mathbf{f}_{red} + \Phi^T \mathbf{f}_{contact}(\Phi \mathbf{q}) \quad (41.19)$$

where $M_{red} = \Phi^T \mathbf{M} \Phi$ denotes the reduced mass matrix, $\mathbf{K}_{red} = \Phi^T \mathbf{K} \Phi$ denotes the reduced stiffness matrix and $\mathbf{f}_{red} = \Phi^T \mathbf{f}_{ext}$ denotes the projected vector of external forces.

The computational effort is dominated by the last term of the right hand side of Eq. (41.19). The evaluation of the nonlinear contact forces still takes place on the physical coordinates of the unreduced model and additionally requires a transformation from generalized to physical coordinates and a projection of the contact forces onto the generalized coordinates. The computational effort due to the nonlinear term is reduced using a procedure discussed in the next section.

41.5 Interface Stress Computation

41.5.1 POD

The Proper Orthogonal Decomposition (POD) is a method to construct a low dimensional set of ℓ basis vectors \mathbf{t}_i which approximate the collection of k snapshots \mathbf{t}_j^* in an optimal sense, see [7]. The resulting basis vectors are a solution to the minimization problem

$$\min_{\mathbf{t}_1, \dots, \mathbf{t}_\ell} \sum_{j=1}^k \left\| \mathbf{t}_j^* - \sum_{i=1}^{\ell} \langle \mathbf{t}_j^*, \mathbf{t}_i \rangle \mathbf{t}_i \right\|^2 \quad \text{with } \langle \mathbf{t}_i, \mathbf{t}_j \rangle = \delta_{ij} \text{ for } i, j = 1, \dots, \ell \quad (41.20)$$

where $\langle \cdot, \cdot \rangle$ denotes the inner product of two vectors.

41.5.2 Stress Interpolation

Evaluation of Eq. (41.14) using a numerical integration scheme requires the knowledge of the contact stress vector \mathbf{t}_{jc}^e at the integration points. The vector containing the discretized contact stress values in normal direction at these locations for each element within the discretized interface $\Gamma_{j,c,h}$ is denoted by \mathbf{t}_n . It is assumed that an approximation for the discretized joint contact stresses is given by

$$\mathbf{t}_n \approx \mathbf{T}_n \mathbf{p}_n \quad (41.21)$$

with a base \mathbf{T}_n of orthonormal stress trial functions or stress modes $\mathbf{t}_{n,i}$ and the according generalized coordinates \mathbf{p}_n . The stress mode equivalent nodal forces are computed for each element using Eq. (41.14). Formally integration over the element domain, transformation to global coordinates and sum over all elements to achieve the contact force vector $\mathbf{f}_{contact}$ in Eq. (41.15) can be expressed using the linear operator \mathbf{A} . An approximation of the nonlinear term in Eq. (41.19) is given by

$$\Phi^T \mathbf{f}_{contact}(\Phi \mathbf{q}) \approx \Phi^T \mathbf{A} \mathbf{T}_n \mathbf{p}_n. \quad (41.22)$$

with unknown generalized coordinates \mathbf{p}_n . The POD method is used to construct a valid base \mathbf{T}_n with the help of several contact stress distribution samples

$$\mathbf{t}_{n,i}^* \text{ with } i = 1, \dots, k \quad (41.23)$$

obtained from k solutions $\mathbf{u}_{h,i}^*$ of the discretized system Eq. (41.15) under different loading conditions. The computation of \mathbf{p}_n is briefly outlined in the following subsection.

41.5.3 DEIM

The Discrete Empirical Interpolation Method (DEIM) proposed by [2] is an effective method to compute the unknown generalized coordinates \mathbf{p}_n in Eq. (41.22). Formally this is achieved by a permutation matrix \mathbf{P} which is used to extract certain entries of the discretized contact stress vector \mathbf{t}_n . For these entries the contact stresses computed using constitutive relations, e.g. Eq. (41.11), are assumed to be equal to the interpolated contact stresses

$$\mathbf{P}^T \mathbf{t}_n = \mathbf{P}^T \mathbf{T}_n \mathbf{p}_n. \quad (41.24)$$

If $\mathbf{P}^T \mathbf{T}_n$ is invertible, the generalized coordinates \mathbf{p}_n can be expressed by the contact stresses at the locations denoted by the permutation matrix

$$\mathbf{p}_n = [\mathbf{P}^T \mathbf{T}_n]^{-1} \mathbf{P}^T \mathbf{t}_n. \quad (41.25)$$

The remaining entries of the contact stress vector \mathbf{t}_n are interpolated using the base \mathbf{T}_n holding the orthonormal interpolation functions. According to [2] the DEIM algorithm ensures the regularity of $\mathbf{P}^T \mathbf{T}_n$ by selecting the so called interpolation indices defining \mathbf{P} from a given POD base \mathbf{T}_n . First step of this algorithm is the selection of a unit vector \mathbf{e}_{\wp_1} to achieve

$$\left| \mathbf{e}_{\wp_1}^T \mathbf{t}_{n,1} \right| = \|\mathbf{t}_{n,1}\|_{\infty} \quad (41.26)$$

where $\|\cdot\|_{\infty}$ denotes the maximum norm of a vector and \wp_1 denotes the index of the largest absolute value of $\mathbf{t}_{n,1}$. With $\mathbf{T}_{n,1} = [\mathbf{t}_{n,1}]$, $\mathbf{P}_1 = [\mathbf{e}_{\wp_1}]$ and $\wp_1 = [\wp_1]$ the DEIM algorithm repeats for $i = 2, \dots, \ell$ as follows:

1. Determine \mathbf{c}_i from

$$(\mathbf{P}_{i-1}^T \mathbf{T}_{n,i-1}) \mathbf{c}_i = \mathbf{P}_{i-1}^T \mathbf{t}_{n,i} \quad (41.27)$$

2. Evaluate

$$\mathbf{r}_i = \mathbf{t}_{n,i} - \mathbf{T}_{n,i-1} \mathbf{c}_i \quad (41.28)$$

3. Select a unit vector \mathbf{e}_{\wp_i} where \wp_i denotes the index of the largest absolute value of \mathbf{r}_i to achieve

$$\left| \mathbf{e}_{\wp_i}^T \mathbf{r}_i \right| = \|\mathbf{r}_i\|_{\infty} \quad (41.29)$$

4. Assign

$$\mathbf{P}_i = [\mathbf{P}_{i-1}, \mathbf{e}_{\wp_i}] \quad (41.30a)$$

$$\mathbf{T}_{n,i} = [\mathbf{T}_{n,i-1}, \mathbf{t}_{n,i}] \quad \text{and} \quad (41.30b)$$

$$\wp_i = [\wp_{i-1}, \wp_i] \quad (41.30c)$$

The vector containing the interpolation indices is denoted by $\wp = \wp_{\ell}$. According to [2] the permutation matrix constructed in the last iteration is a valid choice $\mathbf{P} = \mathbf{P}_{\ell}$ for the permutation matrix in Eq. (41.25).

41.6 Numerical Example

41.6.1 Model Description

The DEIM method for computation of joint interface contact stresses is applied to the model of a bolted cantilever beam for two loading conditions depicted in Fig. 41.3. The first loadcase *LC1* is a tip load in vertical direction, the second loadcase *LC2* additionally considers a torsional moment.

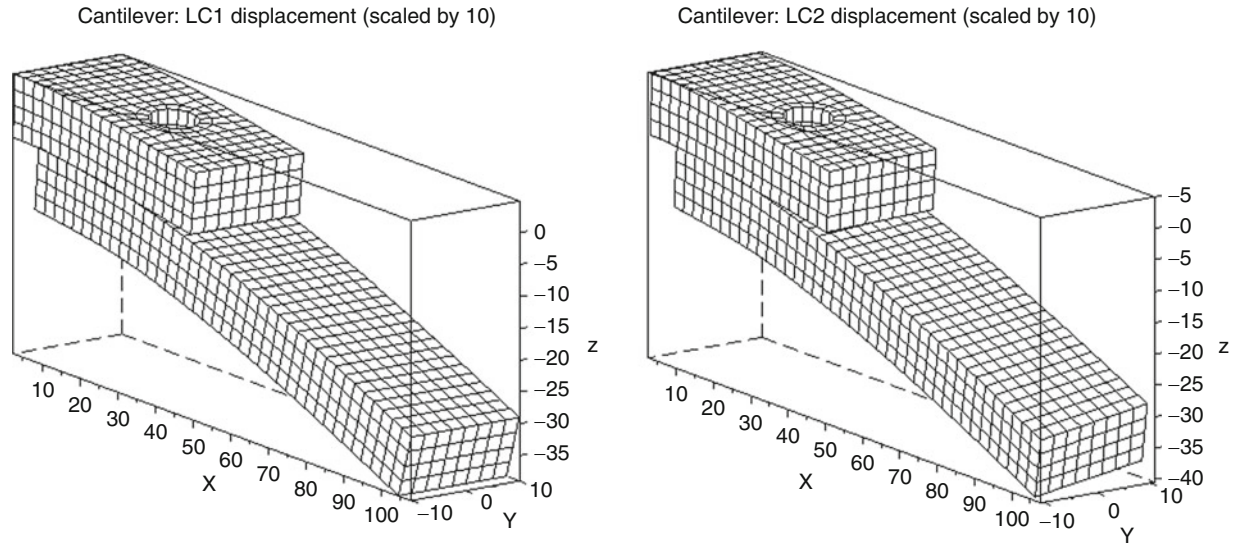


Fig. 41.3 Resulting displacement of the two substructures (the bolt model is hidden) for *LC1* (left) and *LC2* (right)

The structure itself consists of two substructures with rectangular shaped cross section ($a = 10$ mm, $b = 20$ mm) connected by a single bolt and an overall length of $l = 110$ mm. All structural components are modeled using a linear elastic material with Young's Modulus $E = 210,000$ N/mm², Poisson ratio $\nu = 0.29$ and density $\rho = 7,820$ kg/m³.

The discretization Ω_h of the full model contains 1,834 elements and 2,780 nodes. The CHEXA, CBEAM, RBE2 and RBE3 element formulations of the commercial FEM software package MSC Nastran are used to generate the system matrices in Eq. (41.4). The joint interface is modeled by zero thickness elements to obtain the contact force vector of the full model in Eq. (41.15). A convergence study regarding the meshsize of the full model is not within the scope of this contribution.

The results of the reduced order model Eq. (41.19) with the nonlinear term substituted by the DEIM based approximation Eq. (41.22) are computed in combination with 2 different types of contact stress trial function bases referenced in Eq. (41.21). These contact stress trial function bases are obtained using the POD snapshot method according to [7]:

1. Type 1 (SM id 1) based on a defined set of $r < k$ snapshots Eq. (41.23) (analogous to middle column of Fig. 41.4)
2. Type 2 (SM id 2) based on a defined set of k snapshots Eq. (41.23) (analogous to all columns of Fig. 41.4)

For the investigations within the context of this contribution the inertia effects and the contact shear stresses are neglected. To obtain and postprocess the solution of the resulting equations the software package Scilab is utilized.

The relative error of the gap function in surface normal direction as well as the relative error of the contact stresses in surface normal direction are chosen as evaluation criteria. While the first quantity expresses the influence of the contact stresses onto the structure, the second quantity illustrates whether the computed contact stresses are useful for subsequent computations, e.g. shear stresses due to friction. For a vector \mathbf{y} the relative error vector is given by

$$\mathbf{e}_{rel} = \frac{\mathbf{y} - \mathbf{y}_{ref}}{\|\mathbf{y}_{ref}\|_{\infty}} \quad (41.31)$$

where $\|\cdot\|_{\infty}$ denotes the maximum norm of a vector and \mathbf{y}_{ref} denotes the reference values obtained from the full model. For computation of the gap function relative error the maximum penetration is used as reference value.

41.6.2 Reference Solution

The parameterization of the contact model Eq. (41.11) is based on a permitted penetration under certain loading conditions. This is checked with solutions obtained from the full model. The resulting values of the gap function and the contact stresses depicted in Fig. 41.5 are comparable with solutions obtained using a commercial FEM code, e.g. ABAQUS in combination with a penalty approach based contact model.

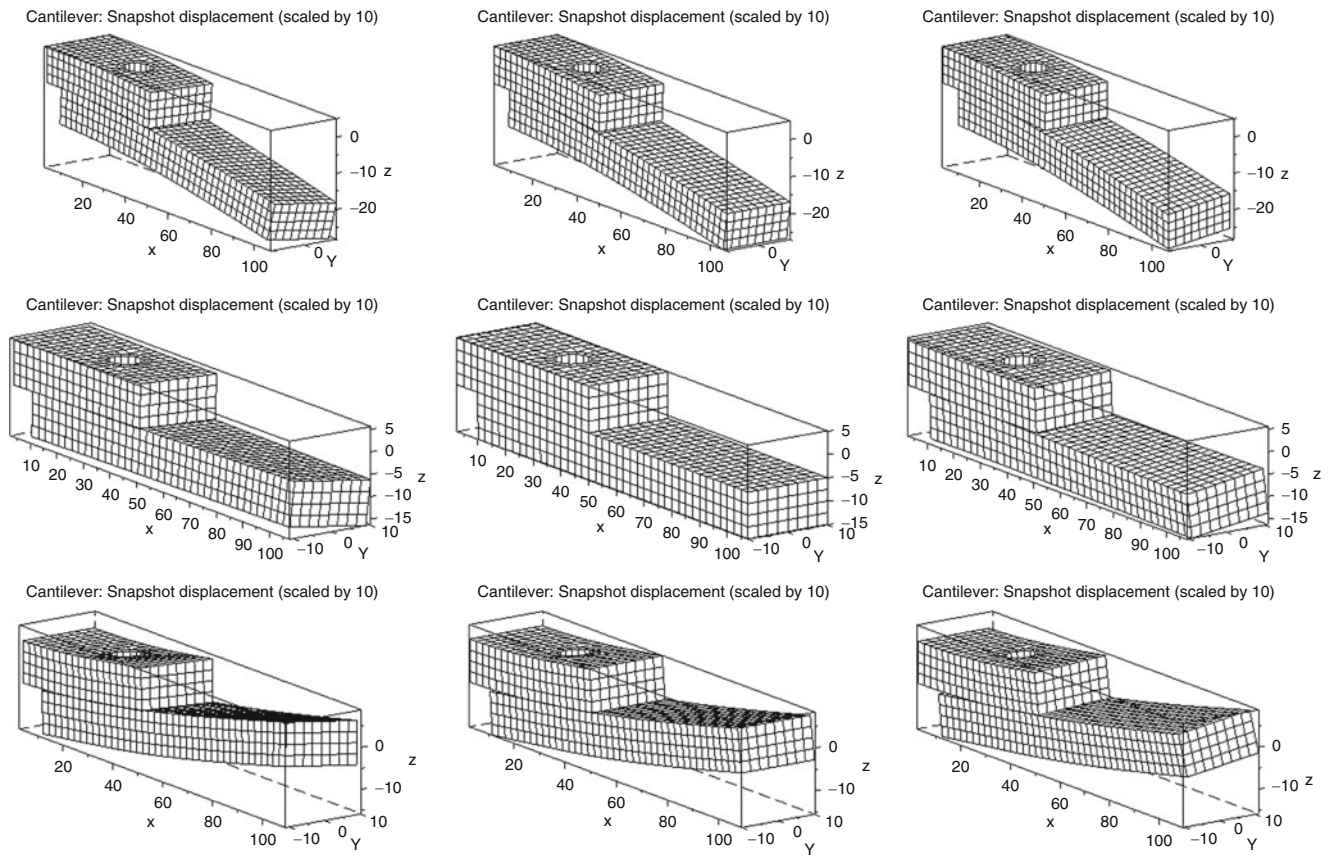


Fig. 41.4 Snapshots for obtaining the different contact stress trial function bases

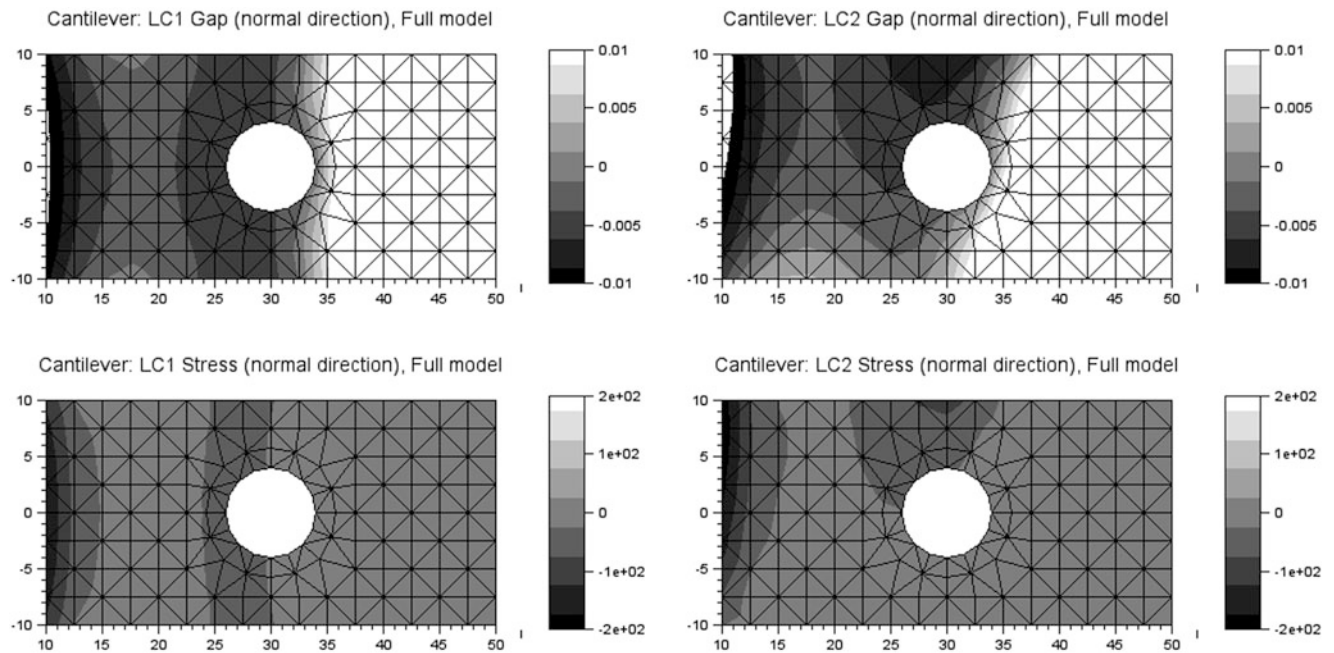


Fig. 41.5 Gap function values (*top row*) and contact stress values (*bottom row*) obtained from solutions of the full model

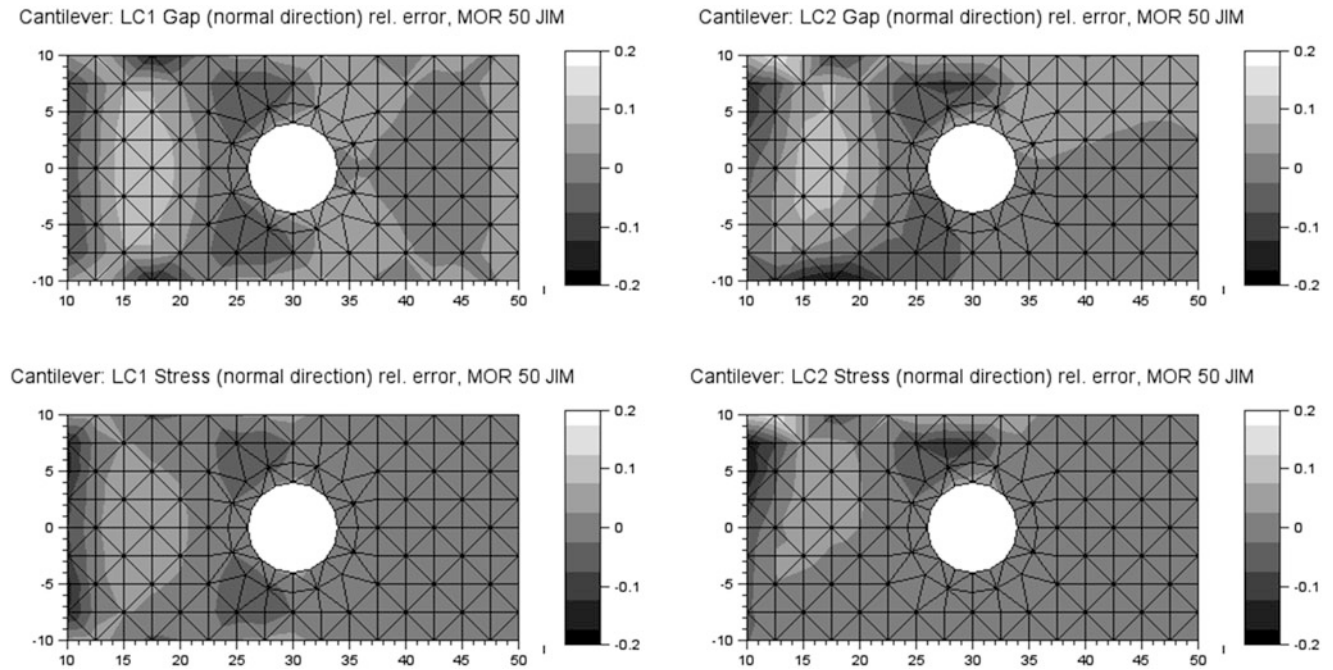


Fig. 41.6 Evaluation of the reduced model utilizing 50 JIMs with node based contact stress computation: gap function relative error values (*top row*) and contact stress relative error values (*bottom row*)

During Model Order Reduction (MOR) in Eq. (41.19) the number of JIM in Eq. (41.18) is increased until the error of the solution is sufficiently small. This is achieved with 50 JIM, the contact stresses are still computed for each node of the joint interface discretization. The resulting relative error values of the gap function and contact stresses are depicted in Fig. 41.6. The largest absolute relative error value is well below 0.2.

41.6.3 Results

The results utilizing stress trial function base type 1 are investigated first. The relative error of the results is depicted in Fig. 41.7. *LC1* in combination with only $\ell = 16$ trial functions already shows the applicability of the DEIM method for problems containing joint interfaces. The number of operations necessary to obtain these results decreases by a factor 10 compared to the reduced model with node based contact stress computation.

As the stress trial function base does not include the influence of the torsional moment a physical meaningful solution cannot be obtained for *LC2*. This clearly shows the importance of a well suited trial function base as the torsional moment can be interpreted as perturbation of *LC1*. This aspect is even more critical in case of a dynamic simulation without a priori knowledge about the vibrational behavior. The same conclusion is deduced when utilizing a different number of stress modes.

The results utilizing stress trial function base type 2 are investigated next, the relative error values of the results are depicted in Fig. 41.8. For almost all locations the absolute relative error value of the resulting contact stresses drops below 0.2 when using the DEIM approach in combination with only $\ell = 16$ stress trial functions. It can be concluded that these results show an higher error than those of the reduced model with node based contact stress computation depicted in Fig. 41.6. But if this error level is tolerable the number of operations necessary to obtain a solution decreases by a factor 10 compared to the reduced model with node based contact stress computation.

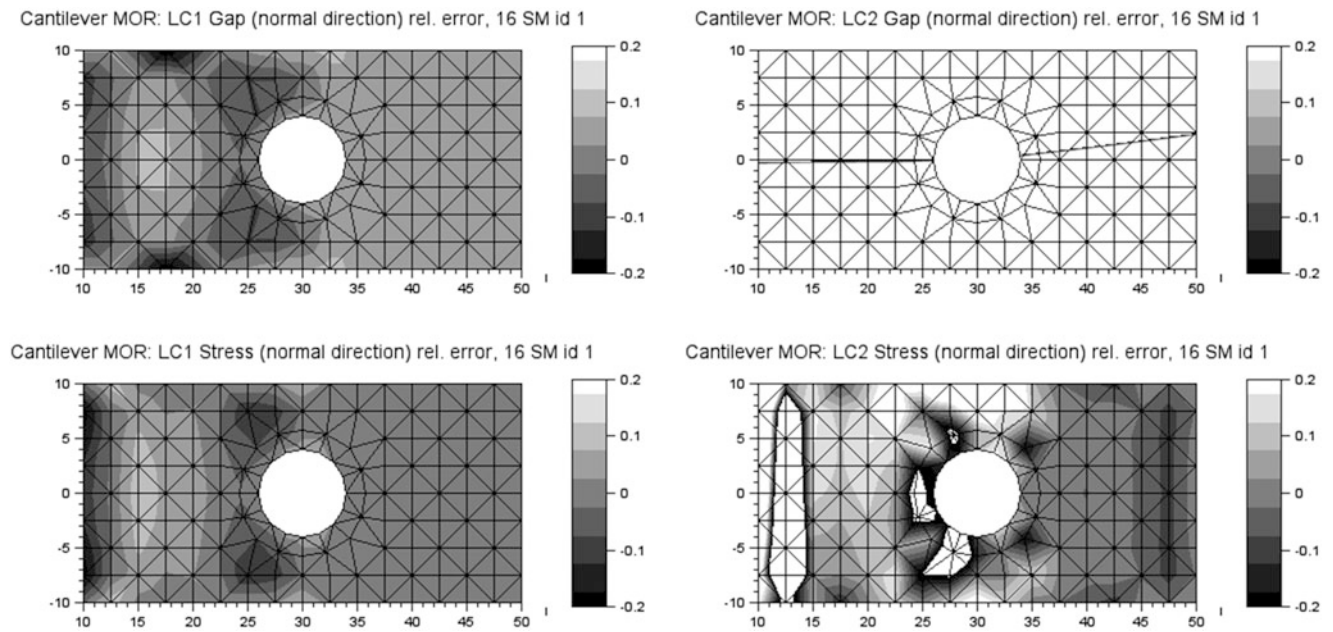


Fig. 41.7 Reduced model utilizing 50 JIMs and DEIM with 16 type 1 trial functions: gap function relative error values (*top row*) and contact stress relative error values (*bottom row*)

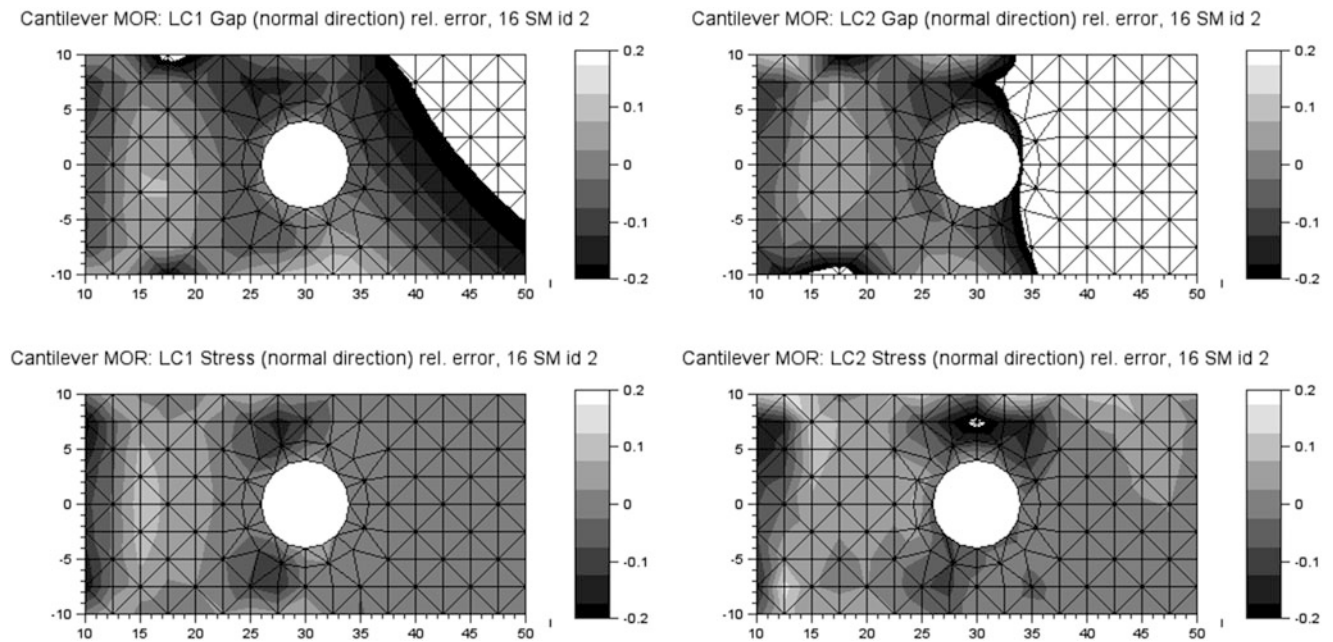


Fig. 41.8 Reduced model utilizing 50 JIMs and DEIM with 16 type 2 trial functions: gap function relative error values (*top row*) and contact stress relative error values (*bottom row*)

41.7 Conclusion

The results show that the Discrete Empirical Interpolation Method (DEIM) proposed by [2] can be applied to significantly lower the computational effort involved for joint interface contact stress computation within the framework of reduced order models for mechanical systems.

The results also illustrate that obtaining the required stress trial function base from simulations of the full system can lead to wrong results for a different loading of the structure which is not considered in the stress trial function base. This emphasizes the need for a trial function base covering the whole space of acting interface stresses.

Acknowledgements Support of the authors by the K2 Austria Center of Competence in Mechatronics (ACCM) and the Engineering Center Steyr (MAGNA Powertrain) is gratefully acknowledged. The authors would also like to acknowledge some fruitful discussions with Professor D.J. Rixen, P. Tiso and R. Dedden during the stay of one author at Delft University of Technology, PME.

References

1. Bathe K-J (1996) Finite element procedures. Prentice Hall, Upper Saddle River
2. Chaturantabut S, Sorensen DC (2010) Nonlinear model reduction via discrete empirical interpolation. *SIAM J Sci Comput* 32(5):2737–2764
3. Craig RR, Bampton MCC (1968) Coupling of substructures for dynamic analyses. *AIAA J* 6(7):1313–1319
4. Geisler J, Willner K (2007) Modeling of jointed structures using zero thickness interface elements. *PAMM* 7(1):4050009–4050010
5. Mayer M, Gaul L (2005) Modeling of contact interfaces using segment-to-segment-elements for fe vibration analysis. In: Proceedings of IMAC-XXIII: conference and exposition on structural dynamics, 2005
6. Nguyen NC, Patera AT, Peraire J (2008) A best points interpolation method for efficient approximation of parametrized functions. *Int J Numer Meth Eng* 73(4):521–543
7. Volkwein S (2010) Model reduction using proper orthogonal decomposition. <http://www.uni-graz.at/imawww/volkwein/POD.pdf>, September 2010
8. Witteveen W, Irschik H (2009) Efficient mode based computational approach for jointed structures: Joint interface modes. *AIAA J* 47(1): 252–263

Chapter 42

Amplitude Dependency on Dynamic Properties of a Rubber Mount

C.B. Nel and J. van Wyngaardt

Abstract An industrial rubber mount was characterized by using an electro-dynamic Shaker which allowed different excitation levels. This elastomeric mount was bolted between a rigid body mass and the base of the test assembly, which was firmly bolted to the Shaker table. Linear guide bearings along two shafts guided the moving mass in the vertical plane with minimal friction. Vibration responses with phase differences were measured at the base plate and the rigid body mass in the vertical direction. An FFT Analyzer was used to measure the time and frequency domain signals for a range of excitation amplitudes (0.01–4 mm) at a forced frequency of 27 Hz. The data was used to compute the dynamic characteristics of the mount by solving appropriate mathematical equations of motion. Bump tests were also done and the time domain response signals analyzed at different amplitudes, and the dynamic characteristics were calculated with different mathematical equations. A load-deflection testing machine was used to characterize the static stiffness properties, which were compared to the different dynamic stiffness properties. The dynamic properties for the forced excitation Shaker approach were compared to the Bump test approach. Amplitude dependency on dynamic stiffness and damping ratio were also investigated.

Keywords Stiffness • Damping • Rubber • Shaker • Bump test

42.1 Introduction

Previous work that has been done indicate that in general rubber dynamic properties depend on static preload, vibration amplitude, temperature and excitation frequency [1]. Strong amplitude dependence on the dynamic characteristics during cyclic loading of elastomers was found present by several researchers [2–5].

Rubber mount stiffness and damping properties were also determined by impact tests [1]. An optimization approach to mounting characterization was used to determine engine rubber mount dynamic properties *in situ* at a front wheel drive vehicle based on measured natural frequencies, and measured responses when the engine was running [6].

Amplitude dependency of the dynamic characteristics of engine rubber mounts was investigated because of different excitation levels caused by multiple engine operational conditions at vehicles [6, 7]. These dynamic stiffness coefficients and mount loss factors were obtained by measuring the load-deflection properties of an individual mount by using a dynamic testing machine, comprising a hydraulic actuator, a load cell and digital read-out instrumentation. Other researchers also used servo controlled hydraulic actuators, and some used electromagnetic Shakers for excitation to do experimental characterization of dynamic properties of rubber mounts [2–4, 8–10].

C.B. Nel (✉) • J. van Wyngaardt

Department of Mechanical Engineering, North-West University, Private Bag X6001, Potchefstroom 2520, South Africa
e-mail: carlbnel@netactive.co.za; johannvw1@gmail.com

42.2 Mathematical Model

A rigid body mass m , which is supported by a spring element k and viscous damping element c which represents the equivalent rubber mount comprising three rubber mounts arranged in parallel, and firmly bolted on the base of an electrodynamic Shaker as shown in Fig. 42.1, is considered [11]:

When $y(t)$ denotes the displacement of the base of the Shaker table, and $x(t)$ the rigid body mass displacement from equilibrium position at time t , then the relative displacement of the spring element will be $(x - y)$ and the relative velocity of the two ends at the damper $(\dot{x} - \dot{y})$.

The response of a viscous damped system under harmonic motion of the base can be described by the following equation of motion:

$$m\ddot{x} + c(\dot{x} - \dot{y}) + k(x - y) = 0 \quad (42.1)$$

with Y the displacement amplitude of the Shaker base and ω the forced frequency

$$y(t) = Y \sin(\omega t) \quad (42.2)$$

Equation (42.1) becomes

$$m\ddot{x} + c\dot{x} + kx = ky + c\dot{y} = kY \sin(\omega t) + c\omega Y \cos(\omega t) \quad (42.3)$$

Also

$$x(t) = X \sin(\omega t - \phi) \quad (42.4)$$

where the amplitude ratio is given by

$$\frac{X}{Y} = \left[\frac{k^2 + (c\omega)^2}{(k - m\omega^2)^2 + (c\omega)^2} \right]^{1/2} \quad (42.5)$$

and the phase angle

$$\phi = \tan^{-1} \left[\frac{mc\omega^3}{k(k - m\omega^2) + (c\omega)^2} \right] \quad (42.6)$$

The response X represents the amplitude of excitation and ϕ represents the phase angle between these X and Y displacement vectors.

The displacement amplitudes X and Y can also be written as

$$X = \frac{\ddot{X}}{\omega^2} \quad (42.7)$$

and

$$Y = \frac{\ddot{Y}}{\omega^2} \quad (42.8)$$

where \ddot{X} and \ddot{Y} are the corresponding acceleration amplitudes.

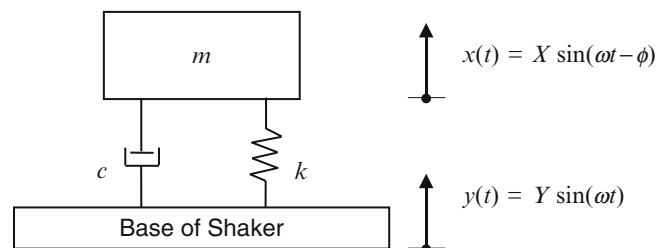
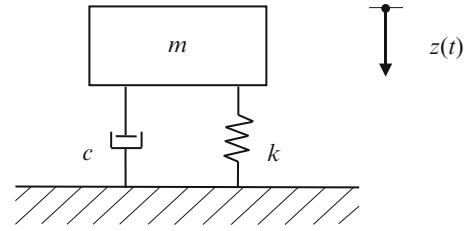


Fig. 42.1 Shaker test representation

Fig. 42.2 Bump test representation

The critical damping coefficient

$$c_c = 2\sqrt{km} \quad (42.9)$$

The damping ratio ζ is defined as the ratio between the actual damping coefficient c and the critical damping coefficient c_c as

$$\zeta = \frac{c}{c_c} \quad (42.10)$$

Figure 42.2 represents the same rigid body mass which is supported by the same equivalent rubber mount, but here the mount is firmly attached to a rigid foundation [11]:

When $z(t)$ denotes the displacement of the rigid body mass at time t due to an impact mallet load applied at an initial static equilibrium position, the system's frequency of the damped vibration ω_d is then excited as for a Bump test. This frequency for free vibration can be described as

$$\omega_d = \frac{1}{\tau_d} \quad (42.11)$$

where τ_d denotes the periodic time of the damped vibration between two successive acceleration amplitudes \ddot{z}_1 and \ddot{z}_2 for one complete cycle in the time domain response signal.

Also the acceleration ratio in the logarithmic decrement time domain response signal [9] is expressed as

$$\frac{\ddot{z}_1}{\ddot{z}_2} = e^{\zeta\omega_n\tau_d} \quad (42.12)$$

with the natural frequency

$$\omega_n = \frac{\omega_d}{\sqrt{1-\zeta^2}} \quad (42.13)$$

By solving Eqs. (42.12) and (42.13) simultaneously, the damping ratio ζ as well as the natural frequency ω_n can be determined, when the two acceleration magnitudes and the periodic time of the damped vibration are known, which could be obtained from a measured time domain response signal.

The dynamic stiffness coefficient

$$k = m\omega_n^2 \quad (42.14)$$

The average displacement amplitude z is related to the two successive acceleration amplitudes \ddot{z}_1 and \ddot{z}_2 which is defined as

$$z = \frac{(\ddot{z}_1 + \ddot{z}_2)}{2\omega_n^2} \quad (42.15)$$

The static stiffness k_s of the rubber mount

$$k_s = \frac{F}{z_s} \quad (42.16)$$

with F the additional vertical compression load applied at the mass above the mount, and z_s the corresponding static displacement experienced by the mount.

42.3 Computer Implementation

The mathematical models for the forced excitation Shaker approach as well as the Bump test mallet input approach were implemented in computer programs in a Matlab environment and the measured data as recorded with an FFT Analyzer and then used for the input data.

With the measured amplitudes of the two acceleration signals as well as the phase difference between these two signals at a certain forced frequency, the dynamic stiffness and damping properties for the Shaker approach were determined, where Eqs. (42.5) and (42.6) were simultaneously solved.

Equations (42.12), (42.13) and (42.14) were used to determine the dynamic stiffness and damping properties for the Bump test approach at different successive response amplitudes, while Eq. (42.16) was used to determine the static stiffness.

42.4 Experimental Characterization

For the forced excitation Shaker approach, the mount was characterized by using a Ling Dynamic Systems V724 electrodynamic Shaker with a DPA4 amplifier, and a SPC4 signal controller which allowed different excitation levels. The test assembly at the vibrator is shown in Fig. 42.3. Linear bearings along two polished shafts guided a moving mass with minimal friction. The mount was bolted between this mass and the base of the test assembly. The base of the test assembly was firmly bolted to the Shake table. A mass was of 10.41 kg was used to characterize the mount. This mass was placed on top of the mount to determine the dynamic stiffness and damping properties in the vertical direction for different excitation amplitudes at a forced frequency of 27 Hz (approximately two times larger than the natural frequency, depending on the stiffness).

Two CTC acceleration meters coupled to a Diagnostics Instruments 2200 FFT Analyzer were used to measure the acceleration signals simultaneously at the base and at the mass. As an example, Fig. 42.4 shows two measured time domain acceleration signals, in this case at a relative excitation amplitude of 0.1 mm, that were used to attain the amplitudes \dot{X} and \dot{Y} as well as the phase angle φ . These tests were performed over a range of relative excitation amplitudes, which varied between 0.01 and 4 mm at a forced frequency of 27 Hz.

For the Bump test approach, the equivalent rubber mount was characterized by using a rubber mallet to apply the impact load which allowed different response levels. The test assembly is shown in Fig. 42.5. The base of the rubber mount assembly was firmly bolted to a rigid table. The same mass of 10.41 kg as for the Shaker approach was also placed on top of the rubber mount to determine the dynamic stiffness properties in the vertical direction, for different response amplitudes.

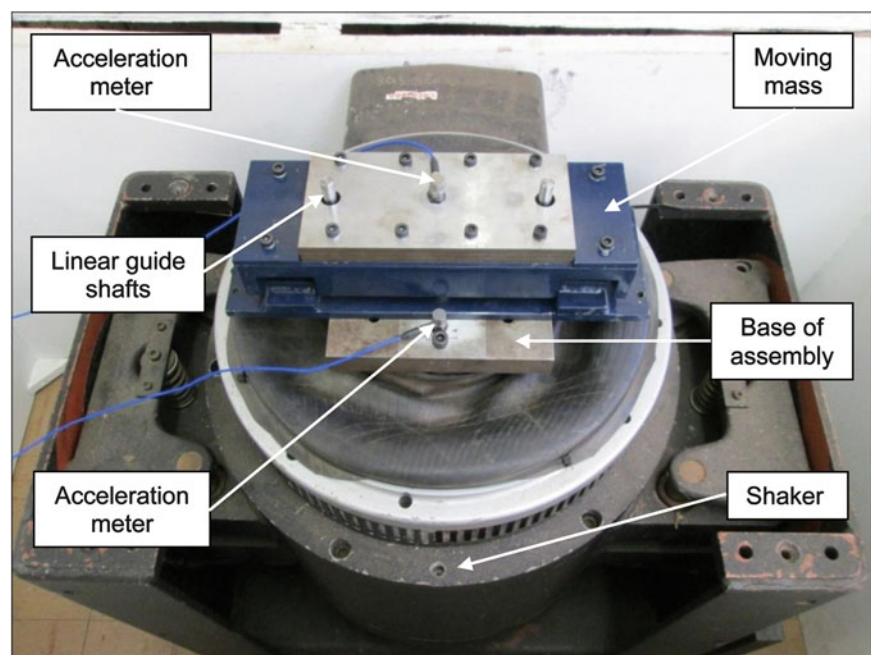


Fig. 42.3 Ling dynamic systems V724 Shaker test setup with rubber mount assembly

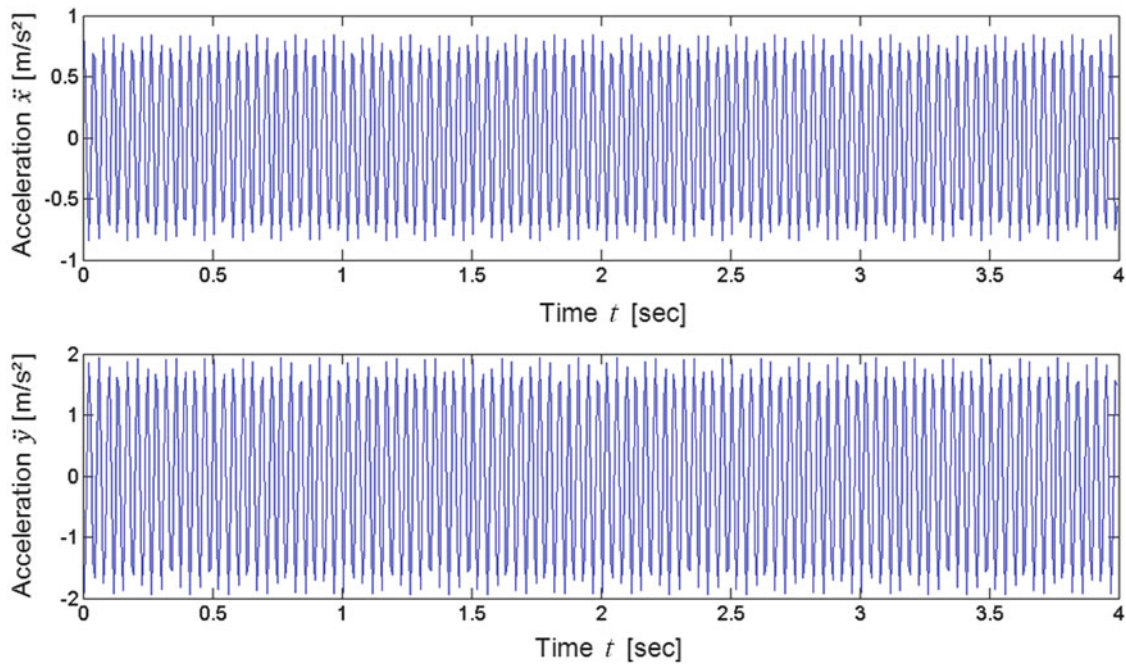


Fig. 42.4 Measured time domain acceleration signals with \ddot{x} and \ddot{y} (Shaker test approach)

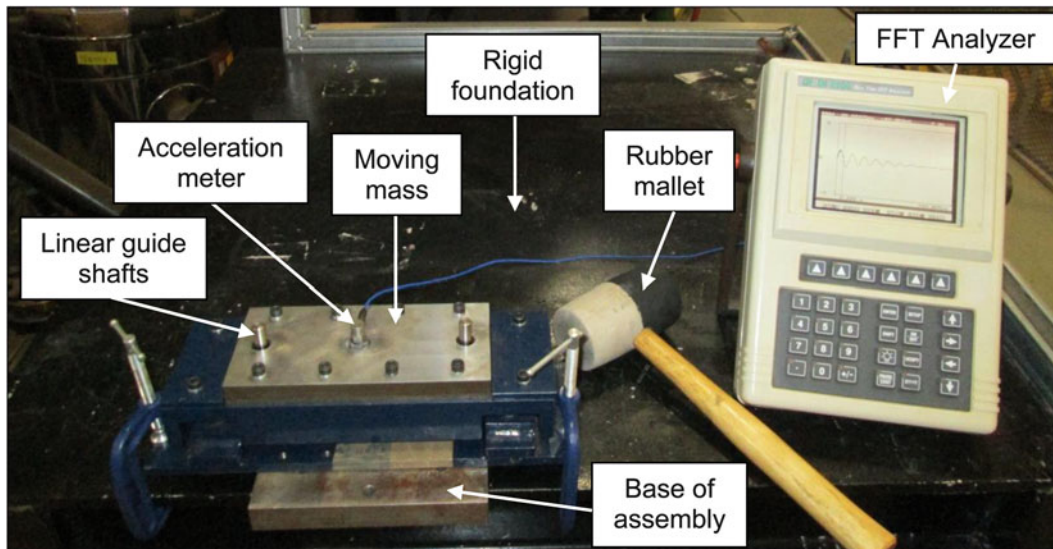


Fig. 42.5 Bump test experimental setup with rubber mount assembly

A CTC acceleration meter coupled to a Diagnostics Instruments 2200 FFT Analyzer was used to measure the time domain response acceleration signal at the moving mass. As an example, Fig. 42.6 shows a measured time domain logarithmic decrement acceleration signal, and in this case the two indicated acceleration data points resulted in an average displacement response amplitude of 3 mm. This signal was then also used to obtain the periodic time of damped vibration τ_d between these two successive acceleration amplitudes \ddot{z}_1 and \ddot{z}_2 as indicated. Several bump tests were performed in order to attain the same range of response amplitudes, which varied between 0.01 and 4 mm.

A MTS Landmark Servo hydraulic Test System as shown in Fig. 42.7 was used to measure static load-deflection properties in the vertical direction of the equivalent rubber mount. The same range of amplitudes for the dynamic tests was used to characterize the static stiffness of the mount, which varied between 0.01 and 4 mm.

The load-deflection curve is shown in Fig. 42.8.

Fig. 42.6 Measured time domain acceleration signal with \ddot{z}_1 and \ddot{z}_2 (Bump test approach)

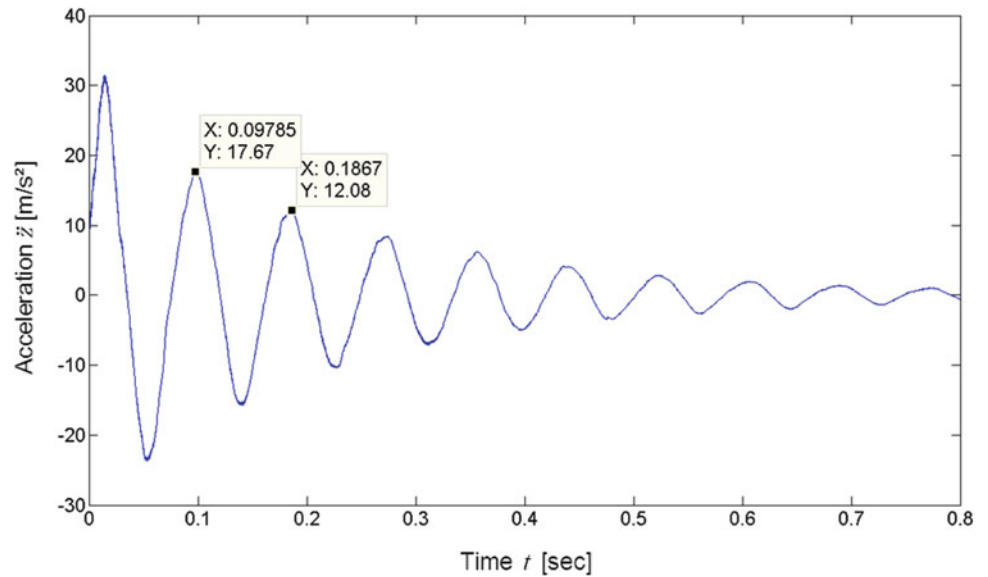
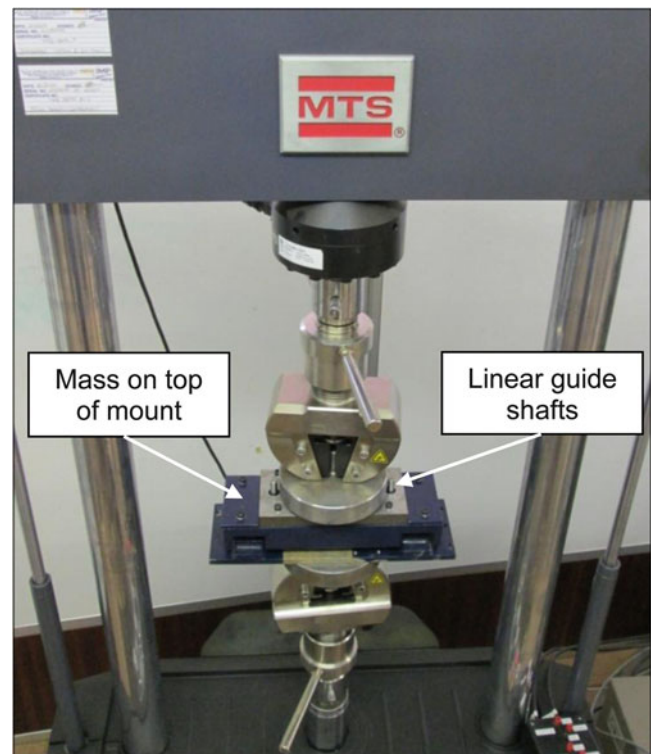


Fig. 42.7 Static load-deflection test setup



42.5 Results

Figure 42.9 shows a graphical representation of the rubber mount stiffness obtained from the different tests performed. The dynamic stiffness is a maximum for the lowest excitation amplitude of 0.01 mm. The dynamic stiffness magnitude decreases significantly up to a displacement amplitude of approximately 0.5 mm, and from there it decreases gradually to the largest amplitude at 4 mm for the Shaker approach. The stiffness magnitudes from the Bump test approach varied slightly compared to those magnitudes obtained from the Shaker approach, while the static stiffness magnitudes varied at an average of approximately 20 % lower compared to those magnitudes obtained from the Shaker approach.

A graphical representation of the damping ratio ζ is shown in Fig. 42.10. The damping ratio is a maximum for the smallest excitation amplitude of 0.01 mm and decreases significantly up to a displacement amplitude of approximately 0.25 mm, and

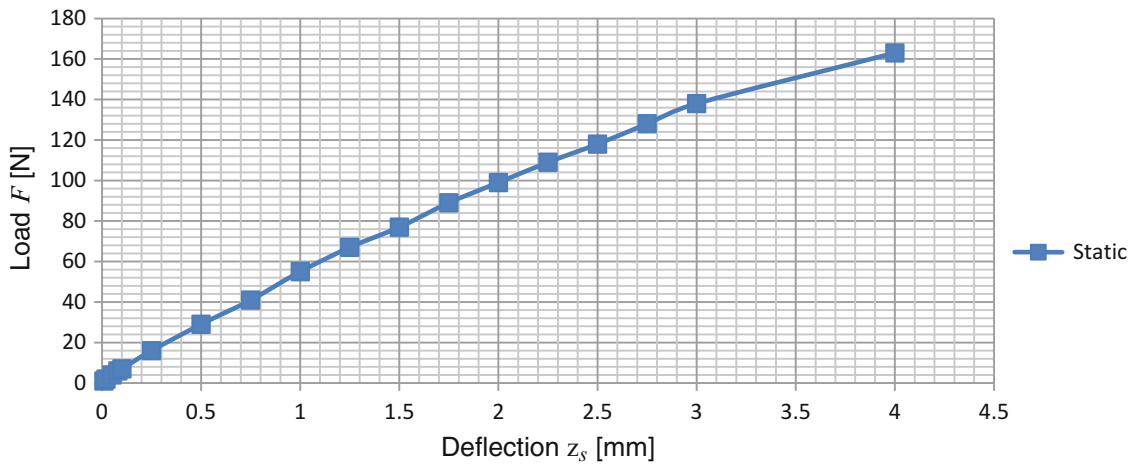


Fig. 42.8 Static load-deflection properties of the rubber mount for different amplitudes

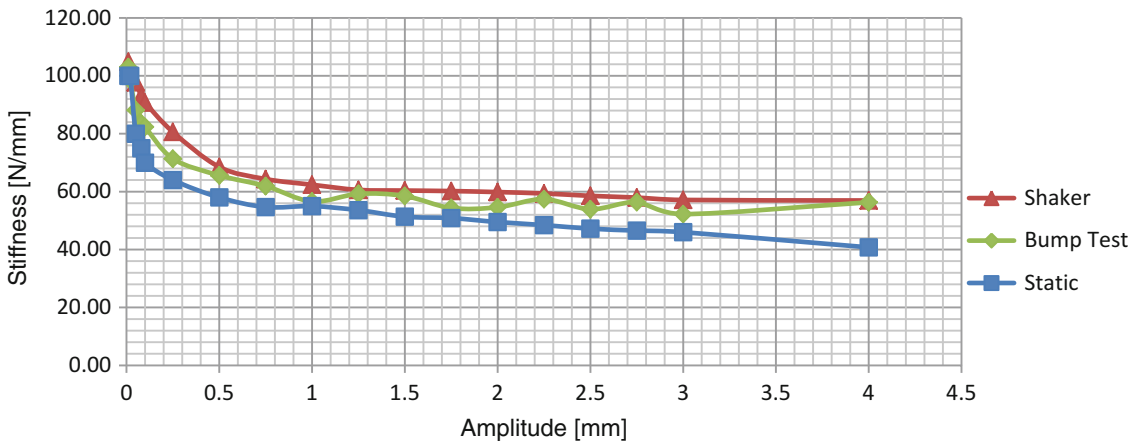


Fig. 42.9 Dynamic stiffness properties of the rubber mount for different amplitude excitations

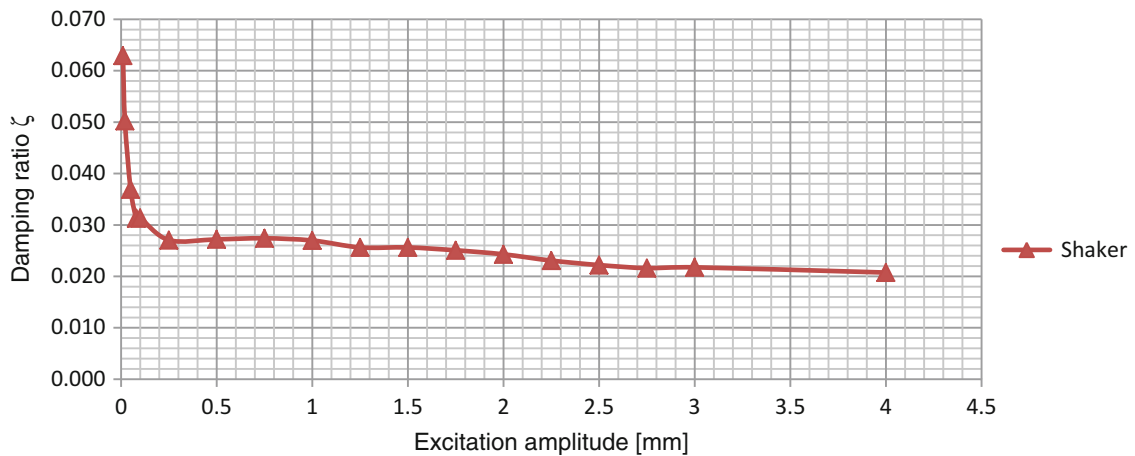


Fig. 42.10 Damping ratio properties of the rubber mount for different amplitude excitations

from there it decreases gradually to the largest amplitude at 4 mm. The damping ratio properties obtained from the Bump test approach were neglected in the graphical representation due to the presence of Coulomb damping caused by bearing friction between the guide shafts and the linear guide bearings that increased the damping ratio magnitudes significantly under the impact test condition.

42.6 Conclusions

Strong displacement amplitude dependency on the dynamic stiffness and damping properties of a rubber mount system was obtained. These dynamic properties for the forced vibration Shaker approach were compared to the free vibration Bump impact test approach, and a good correlation between them was obtained. It was found that the dynamic stiffness and also damping ratio magnitudes decreased when the displacement amplitudes increased. These dynamic stiffness magnitudes were also compared with the static magnitudes for corresponding displacement amplitudes, and it was found that the static stiffness values were an average of approximately 20 % lower. Future work will be done to investigate the frequency dependency on these rubber mount system properties.

References

1. Lin TR, Farag NH, Pan J (2005) Evaluation of frequency dependent rubber mount stiffness and damping by impact test. *Appl Acoust* 66: 829–844
2. Austrell P, Olsson AK (2012) Considering amplitude dependence during cyclic loading elastomers using an equivalent viscoelastic approach. *Polymer Test* 31:909–915
3. De-Wei S, Zhi-Gang C, Guang-Yu Z, Eberhard P (2011) Modeling and parameter identification of amplitude- and frequency-dependent rubber isolator. *J Cent South Univ Technol* 18:672–678
4. Colgate JE, Chang CT, Chiou YC, Liu WK, Keer LM (1995) Modelling of a hydraulic engine mount focusing on response to sinusoidal and composite excitations. *J Sound Vib* 3(184):503–528
5. Nel CB, Heyns PS (1995) An optimisation approach to mounting characterisation. *Proceedings of noise and vibration*, University of Pretoria, South Africa, November 1995
6. Nel CB (2000) Optimisation of engine mount systems at front-wheel-drive vehicles for multiple operational conditions, ISMA21. Katholieke Universiteit Leuven, Belgium
7. Nel CB, Heyns PS (1996) Experimental verification of an optimisation program for a front wheel drive engine mountsystem, ISMA21. Katholieke Universiteit Leuven, Belgium
8. Kim G, Singh R (1992) Resonance, isolation and shock control characteristics of automotive nonlinear hydraulic enginemounts. *ASME* 44:165–180
9. Singh R, Kim G, Ravindra PV (1992) Linear analysis of automotive hydro-mechanical mount with emphasis on decoupler characteristics. *J Sound Vib* 158(2):219–243
10. Richards CM, Singh R (2011) Characterization of rubber isolator nonlinearities in the context of single- and multi-degree-of-freedom experimental systems. *J Sound Vib* 247(5):807–834
11. Rao SS (2004) *Mechanical vibrations*, 4th edn. Prentice Hall, Pearson

Chapter 43

Model Order Reduction for Geometric Nonlinear Structures with Variable State-Dependent Basis

Johannes B. Rutzmoser and Daniel J. Rixen

Abstract Nonlinear model order reduction based on subspace projection is driven by the exploitation of the structure of the nonlinearity or by analyzing data generated from the nonlinear model. In the proposed approach the one way coupling of bending and stretching in geometrically nonlinear beam or shell elements is considered for a nonlinear projectional framework that is able to consider inertia effects of both, bending and stretching motion. The method increases accuracy in comparison to static condensation approaches, however at the cost of higher computational efforts.

Keywords Model reduction • Geometric nonlinearity • Static condensation • Variable basis • Structural dynamics

43.1 Introduction

The trend to more advanced, more detailed and more comprehensive simulation models drives the demand on efficient and model order reduction (MOR) techniques. While the properties of reduction methods for linear time invariant systems are well known and established [1], efficient nonlinear MOR is still an open question and thus an active research topic.

Basically two approaches are used in nonlinear MOR: the data-driven branch and the branch exploiting the properties of the mathematical structure of the nonlinearity. In the former approach, the strategy is to first generate representative data of the states of the system by a simulation of the full degrees of freedom (dof) model, second to extract the principal components of the states utilizing a singular value decomposition and third to project the dynamic equations on the subspace spanned by the most important principal component vectors. This method, known as Proper Orthogonal Decomposition (POD), is applied successfully in many fields of applications [4]. However the drawback is the necessity to simulate the full-dof system and the need on generating representative data.

In the latter approach, the structure of the nonlinearity or the information like linear modes or modal derivatives is exploited and used for either projection or condensation methods. In the field of structural dynamics with large deformations, the structure of geometric nonlinearities is well known and can be used for different approaches like e.g. [2, 3, 5, 7]. As these reduction methods are tailored to geometric nonlinearity, they are not characterized by generality as the POD is but have the advantage to avoid full scale and thus expensive computations.

In this paper a reduction method is proposed pertaining to the second category. A projectional framework is described exploiting the structure of the governing equations of geometrically nonlinear beam or shell elements using a nonlinear transformation which can be interpreted as a projection on a nonlinear subspace, or better, a manifold. The results outperform the static condensation approach in all cases in terms of accuracy, but on the cost of higher computational efforts.

This paper is organized as follows: After this introduction the general projection framework commonly used in MOR is shortly recalled (Sect. 43.2). As alternative strategy, the static condensation method is explained (Sect. 43.3) and subsequently transformed to the projectional framework as a projection approach with variable basis (Sect. 43.4). Numerical experiments are performed on three differently hinged beams showing the practicability of the projectional method (Sect. 43.5).

J.B. Rutzmoser (✉) • D.J. Rixen
Technische Universität München, Boltzmannstraße 15 D-85748 Garching, Germany
e-mail: johannes.rutzmoser@tum.de; rixen@tum.de

43.2 Projection Methods

Consider the differential equation of a nonlinear structural dynamics system

$$M\ddot{x} + D\dot{x} + f(x) = F(t) \quad (43.1)$$

with mass matrix M , damping matrix D , nonlinear stiffness function $f(x)$ and the time dependent external forcing $F(t)$. Now consider the linear transformation

$$x = Vz \quad (43.2)$$

with the new variable z . x is bound to the vector space spanned by the column vectors of V . Assuming V has less columns than rows, x is reduced to the subspace spanned by V . Inserting (43.2) in (43.1) transforms the latter equation to this subspace. As not every point in the displacement vector space can be captured, the equation produces an error, considered with the residual r :

$$MV\ddot{z} + DV\dot{z} + f(Vz) = F(t) + r \quad (43.3)$$

Taking into account, that the dynamics of (43.3) can only be described in the subspace spanned by V , the residual should not have an influence to the dynamics, i.e. the residual should be made orthogonal to the column space of V resulting in the projected version of equation (43.1)

$$V^T r = 0 \quad (43.4)$$

$$V^T M V \ddot{z} + V^T D V \dot{z} + V^T f(Vz) = V^T F(t) \quad (43.5)$$

with the matrices $V^T M V$ and $V^T D V$ being the reduced mass and stiffness matrix living in the subspace spanned by the column vectors of V . A wise choice of the column vectors of V reduces the differential equation (43.1) without losing important aspects of the dynamics of the system. Thus, the main questions in projectional model order reduction is the choice of V . For a nonlinear system a common strategy for choosing the column vectors of V is the POD method as mentioned in Sect. 43.1. In the subsequent part of the paper damping is not considered but can be handled according to the projection framework shown above.

43.3 Static Condensation Method

The axial strain of an Euler-Bernoulli beam expressed in the nonlinear Green-Lagrange strain measure gives [6]

$$\varepsilon_x = \frac{du}{dx} - z \frac{d^2w}{dx^2} - \frac{1}{2} \left(\frac{du}{dx} - z \frac{d^2w}{dx^2} \right)^2 - \frac{1}{2} \left(\frac{dw}{dx} \right)^2 \quad (43.6)$$

with the coordinate x along the beam axis, the transversal coordinate z with its origin in the centroid of the cross sectional area, the transversal deflection w and the axial displacement u . The von Kármán kinematic assumption states that axial deformations and curvature is small compared to the bending rotation. Stated as

$$\frac{1}{2} \left(\frac{du}{dx} - z \frac{d^2w}{dx^2} \right)^2 = 0 \quad (43.7)$$

gives the quadratic strain equation

$$\varepsilon_x = \frac{du}{dx} - z \frac{d^2w}{dx^2} - \frac{1}{2} \left(\frac{dw}{dx} \right)^2 \quad (43.8)$$

Applying a linear constitutive law for the stress-strain relation and proceeding with finite-element method yields the governing equation for the geometrically nonlinear Euler-Bernoulli beam. The degrees of freedom can be partitioned in membrane (m) and bending (b) parts with the membrane displacement u_i of node i and the transversal displacements and rotations w_i of node i as follows:

$$M_{m,ij} \ddot{u}_j + K_{m,ij}^{(1)} u_j + K_{mb,ijk}^{(2)} w_j w_k = F_{m,i} \quad (43.9)$$

$$M_{b,ij} \ddot{w}_j + K_{b,ij}^{(1)} w_j + K_{bm,ijk}^{(2)} w_j u_k + K_{b,ijkl}^{(3)} w_j w_k w_l = F_{b,i} \quad (43.10)$$

Neglecting acceleration in the membrane direction

$$M_{m,ij} \ddot{u}_j = 0 \quad (43.11)$$

the membrane displacement can be expressed using Eq. (43.9) as

$$u_j = -(K_{m,ij}^{(1)})^{-1} (K_{mb,ikl}^{(2)} w_k w_l - F_{m,i}) \quad (43.12)$$

Inserted in (43.10) gives the condensed equation for the transversal displacement:

$$M_{b,ij} \ddot{w}_j + K_{b,ij}^{(1)} w_j - K_{bm,ijk}^{(2)} w_j \left(K_{m,ik}^{(1)} \right)^{-1} \left(K_{mb,lno}^{(2)} w_n w_o - F_{m,l} \right) + K_{b,ijkl}^{(3)} w_j w_k w_l = F_{b,i} \quad (43.13)$$

Rearranging the arrays yields a final cubic equation for the transversal displacement:

$$M_{b,ij} \ddot{w}_j + K_{b,ij}^{(1)} w_j + \tilde{K}_{b,ijkl}^{(3)} w_j w_k w_l = F_{b,i} + \tilde{W}_{bm,ijk} w_j F_{m,k} \quad (43.14)$$

with the first and third order stiffness matrices $K_{b,ij}^{(1)}$ and $\tilde{K}_{b,ijkl}^{(3)}$ and the force transformation matrix $\tilde{W}_{bm,ijk} w_j$ projecting external membrane forces onto the bending dofs. The condensed equation reflects the additional stiffening at higher deformations due to membrane effects. For a static equilibrium position for any given transversal force vector F_b , Eq. (43.14) gives the same result as (43.9) with (43.10).

As the membrane displacement is directly coupled to the transversal displacement by (43.12) and can be obtained in a postprocessing step, the error made in the condensed equation is the negligence of the acceleration of the membrane dofs as stated in (43.11).

43.4 Projection Method with Variable Basis

As both approaches, the projection method (Sect. 43.2) and the static condensation method (Sect. 43.3) have successfully been applied on various systems [3, 5, 7], the combination of both ideas, the static condensation approach and the projection approach, results in a projection not on a linear subspace but on a manifold in physical space.

Consider the nonlinear transformation

$$x = g(z) \quad (43.15)$$

where the physical variable $x = (x_1 \ x_2)^T$ is expressed by a nonlinear function of the reduced variable z . The transformation $g(z)$ can be chosen, such that a partitioned nonlinear system of structure

$$M \ddot{x} + K x + f(x) = F(t) \quad (43.16)$$

$$\begin{pmatrix} M_{11} & M_{12} \\ M_{21} & M_{22} \end{pmatrix} \begin{pmatrix} \ddot{x}_1 \\ \ddot{x}_2 \end{pmatrix} + \begin{pmatrix} K_{11} & K_{22} \\ K_{21} & K_{22} \end{pmatrix} \begin{pmatrix} x_1 \\ x_2 \end{pmatrix} + \begin{pmatrix} f_1(x_1, x_2) \\ f_2(x_1) \end{pmatrix} = \begin{pmatrix} F_1(t) \\ F_2(t) \end{pmatrix} \quad (43.17)$$

is projected on a manifold, where the stiffness terms acting on the dofs x_2 are all zero:

$$K_{21} x_1 + K_{22} x_2 + f_2(x_1) = 0 \quad (43.18)$$

The condition for the projection is then

$$g(z) = \begin{pmatrix} z \\ -K_{22}^{-1} (K_{21}z + f_2(z)) \end{pmatrix} \quad (43.19)$$

with $z = x_1$. If the acceleration term

$$M_{21} \ddot{x}_1 + M_{22} \ddot{x}_2 = 0 \quad (43.20)$$

is set to zero, this projection is equivalent to static condensation, i.e. the elimination of x_2 in Eq. (43.17). This would be equivalent to the method exposed in Sect. 43.3. As we are in a projection framework, negligence of the mass is not demanded as the inertia forces are projected on the subspace as well.

In order to obtain the full projected differential equation, the first and second time derivative of the position x in terms of the reduced variable z is needed:

$$\dot{x} = \frac{\partial g}{\partial z} \frac{dz}{dt} = \frac{\partial g}{\partial z} \dot{z} \quad (43.21)$$

$$\ddot{x} = \frac{\partial^2 g}{\partial z^2} \dot{z} \dot{z} + \frac{\partial g}{\partial z} \ddot{z} \quad (43.22)$$

Inserted in the second order differential equation (43.16) gives

$$M \frac{\partial g}{\partial z} \ddot{z} + M \frac{\partial^2 g}{\partial z^2} \dot{z} \dot{z} + Kg(z) + f(g(z)) = F(t) + r \quad (43.23)$$

with the residual r induced by the approximation through projection. As the system has to stay by definition on the manifold spanned by the transformation $g(z)$, the only allowed motion of the system is along the tangential subspace spanned by the jacobian $\frac{\partial g}{\partial z}$. Thus a force perpendicular to this subspace will pull the state away from the permitted manifold, a force acting inside this subspace will influence the dynamics. Consequently the residual is required to be orthogonal to the tangential subspace of the manifold resulting in the projected reduced order differential equation:

$$\left(\frac{\partial g}{\partial z} \right)^T r = 0 \quad (43.24)$$

$$\left(\frac{\partial g}{\partial z} \right)^T M \frac{\partial g}{\partial z} \ddot{z} + \left(\frac{\partial g}{\partial z} \right)^T M \frac{\partial^2 g}{\partial z^2} \dot{z} \dot{z} + \left(\frac{\partial g}{\partial z} \right)^T Kg(z) + \left(\frac{\partial g}{\partial z} \right)^T f(g(z)) = \left(\frac{\partial g}{\partial z} \right)^T F(t) \quad (43.25)$$

Applying the transformation (43.19) onto the system (43.9) and (43.10) using (43.25) above gives for the variable $z = w$ the reduced projected framework

$$\left(\hat{M}_{m,ijkl}^{(3)} z_k z_l + M_{b,ij} \right) \ddot{z}_j + M_{m,ijkl}^{(3)} z_j \dot{z}_k \dot{z}_l + K_{b,ij}^{(1)} z_j + \tilde{K}_{b,ijkl}^{(3)} z_j z_k z_l = \tilde{W}_{bm,ijk} z_j F_{m,k} \quad (43.26)$$

with the arrays $\tilde{K}_{b,ijkl}^{(3)}$ and $\tilde{W}_{bm,ijk}$ being identical to the arrays used in (43.14). The main difference to the static condensation is the inclusion of the acceleration term of the membrane movement and a convective term $M_{m,ijkl}^{(3)} z_j \dot{z}_k \dot{z}_l$ due to the changing basis. Note that the mass matrix is a function of state. This causes additional computational effort when using an explicit time integration scheme as the linear systems has to be solved for \ddot{z} in every time step.

It is further possible to reduce the system by assuming a reduction basis for z

$$z = \Phi \eta \quad (43.27)$$

which can be performed on top of the nonlinear transformation (43.19) without loosing the main properties of this approach:

$$x = g(\Phi\eta) \quad (43.28)$$

A reasonable reduction matrix Φ can be obtained by well known linear reduction methods e.g. modal truncation, Krylov subspaces or balanced truncation. The subspace spanned by the column vectors of Φ is guided as tangent space along the manifold, i.e. if Φ spanned a modal basis around the equilibrium point, η were a vector of the modal coordinates along the manifold.

43.5 Numerical Results

The approach was tested on a straight beam with rectangular cross sectional area and the properties like plastic shown in Table 43.1. A nonlinear finite element beam model with 10 elements in three different setups shown in Fig. 43.1 was investigated.

All numerical experiments were performed with a sinusoidal load and the undeformed configuration at $t = 0$. The proposed approach is compared to the static condensation approach taking the full FE model as reference.

An intuitive view on the results is given in Fig. 43.2 showing the snapshots of 0.9 seconds simulation of the fixed-free beam as described in Fig. 43.1a. The sinusoidal forcing of 1.5 Hz is applied at the tip. The lowest eigenfrequencies of the bending modes are $\omega_{b,1} = 0.404$ Hz, $\omega_{b,2} = 2.53$ Hz, $\omega_{b,3} = 7.09$ Hz and $\omega_{b,4} = 13.9$ Hz, the lowest eigenfrequencies of the in-plane modes are $\omega_{m,1} = 125$ Hz, $\omega_{m,2} = 378$ Hz and $\omega_{m,3} = 641$ Hz. As the in-plane modes are of higher frequency than the bending modes, the condensation of the membrane dofs seems legitimate. Nonetheless, the large deflection causes a dynamics in horizontal direction, especially at the tip of the beam, which is not reflected in the static condensation approach. The difference of the transversal tip displacement over time is shown in Fig. 43.3. The displacement is given relative to the length l of the beam, i.e. a relative displacement of 1 means the beam having a vertical tip displacement of the beam's length.

In the simply supported setup, see Fig. 43.4, the difference between the static condensation approach and the projection approach is also remarkable. Here as in the fixed-free setup, the non symmetric supports cause a motion in membrane direction whose inertia effects are not reflected in static condensation resulting in a divergence from the reference full dof model.

As it is to be expected the static condensation approach in the pinned-pinned setup, see Fig. 43.5, is a sufficient approximation as nonlinear stiffening in bending occurs but almost no in-plane displacement is present.

In general, the softer and heavier the beam in its boundary conditions is, the more inertia effects in membrane direction are to be expected. Those inertia effects are included in the projection method, but not in the basic condensation approach. As an eigenfrequency is a measure of the relation between stiffness and inertia for a given modal displacement, supposedly systems with low eigenfrequencies undergoing large displacements are good candidates of the projection framework. Consequently, stiff systems with high eigenfrequencies will barely profit from the projection method.

Table 43.1 properties of the geometrically nonlinear beam

| Property | Symbol | Value |
|------------------------|--------|--------------------------------------|
| Length | l | 2 m |
| Height | h | 1 cm |
| Width | w | 2 cm |
| Cross sectional area | A | 2 cm ² |
| Area moment of inertia | I | 1,667 mm ⁴ |
| Young's modulus | E | 1 $\frac{\text{kN}}{\text{mm}^2}$ |
| Density | ρ | 1,000 $\frac{\text{kg}}{\text{m}^3}$ |

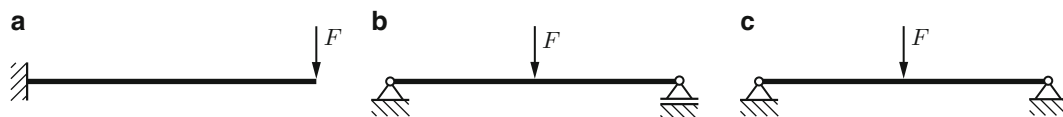


Fig. 43.1 Three types of supports and load cases for the geometrically nonlinear beam model: (a) fixed-free, (b) simply supported, (c) pinned-pinned

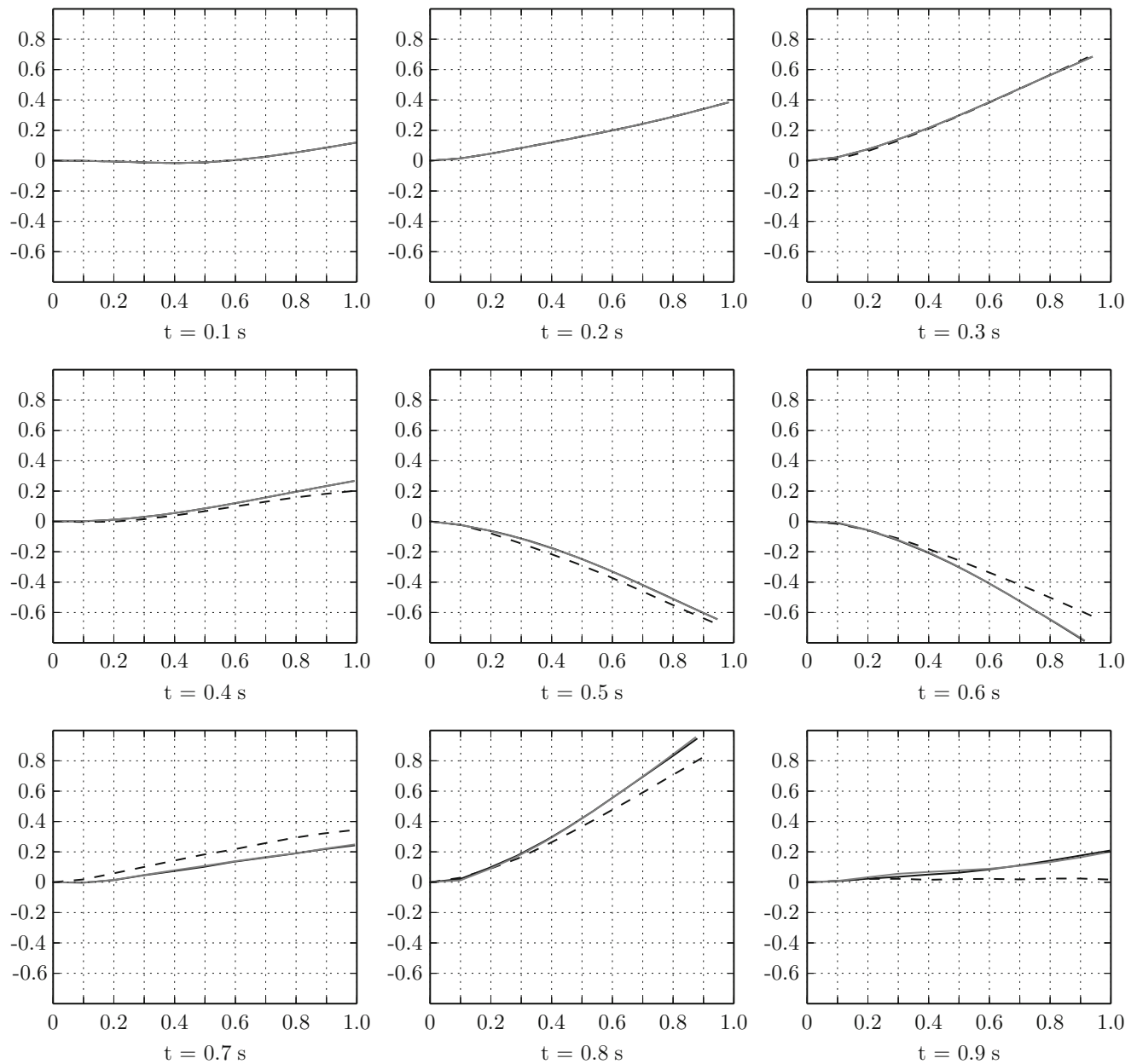


Fig. 43.2 Snapshots of the fixed-free beam (Fig. 43.1a) under sinusoidal load at the right tip. The projected approach (*grey*) follows the reference simulation (*black*, mostly covered by the *grey* line) better than the statically condensed model (*dashed*)

43.6 Conclusions

A new reduction method combining the static condensation approach and the projection approach was presented. The projection exceeds the theory of subspace projections, as the dynamics is described on a manifold defined by the static condensation condition stating that the stiffness forces acting in membrane direction are zero. This approach in comparison to static condensation considers membrane dynamic effects which are of high importance when larger membrane displacements occur. For deformations with small membrane displacements the static condensation approach holds as well as the proposed projection approach.

The field of nonlinear transformation for model order reduction that can be interpreted as a projection on a manifold is a topic which the authors is not known to be explored yet. Various topics have to be investigated, especially efficient integration schemes for the nonlinear mass matrix. The good approximation quality in the academic examples gives reason to assume a good approximation also in industry applications.

Fig. 43.3 Relative transversal tip displacement (displacement over beam length) of the fixed beam shown in Fig. 43.1a with sinusoidal load (amplitude: 10 N, frequency: 1.5 Hz)

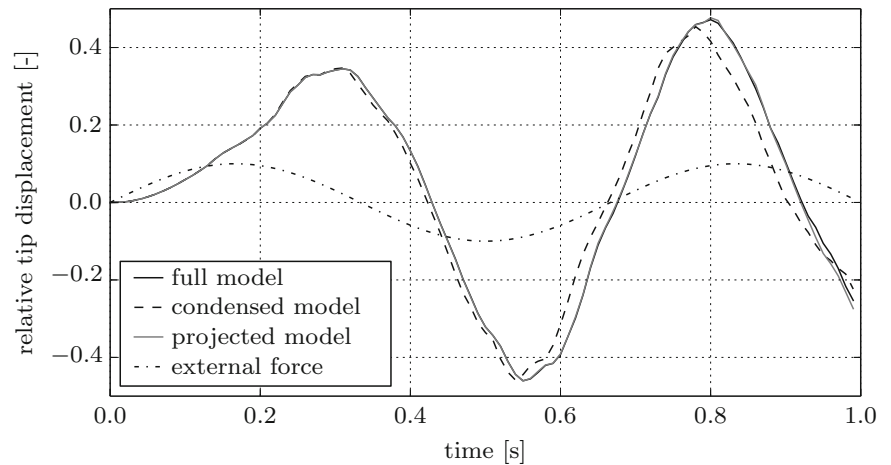


Fig. 43.4 Relative displacement of the point of force application the simply supported beam as shown in Fig. 43.1b with sinusoidal load (amplitude: 10 N, frequency: 3 Hz)

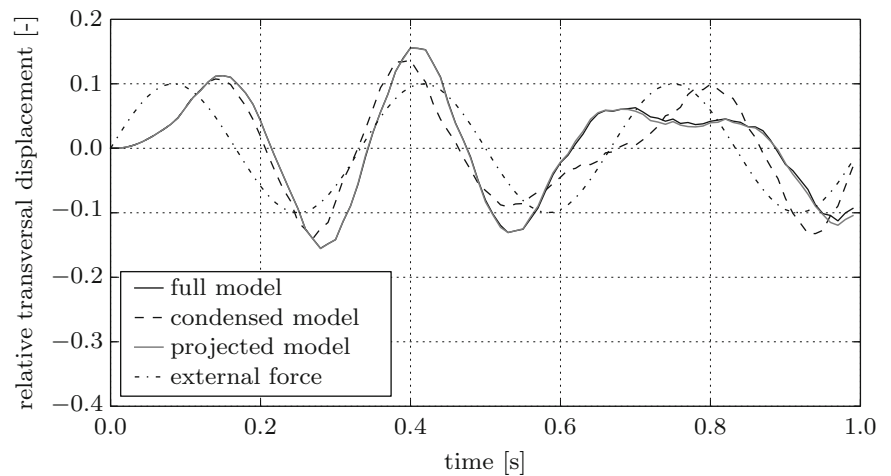
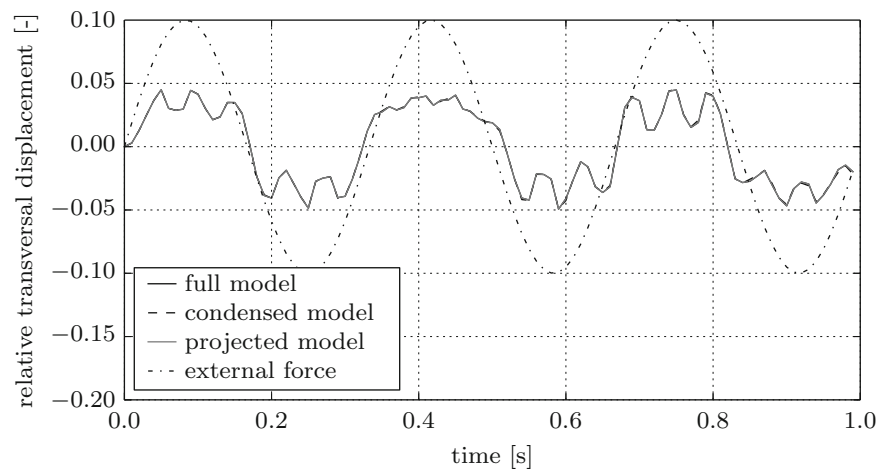


Fig. 43.5 Relative displacement of the point of force application of the pinned-pinned beam as shown in Fig. 43.1c with sinusoidal load (amplitude: 100 N, frequency: 3 Hz)



References

1. Besselink B, Tabak U, Lutowska A, van de Wouw N, Nijmeijer H, Rixen DJ, Hochstenbach ME, Schilders WHA (2013) A comparison of model reduction techniques from structural dynamics, numerical mathematics and systems and control. *J Sound Vib* 332(19):4403–4422
2. Idelsohn SR, Cardona A (1985) A load-dependent basis for reduced nonlinear structural dynamics. *Comput Struct* 20(1):203–210
3. Idelsohn SR, Cardona A (1985) A reduction method for nonlinear structural dynamic analysis. *Comput Meth Appl Mech Eng* 49(3):253–279
4. Kerschen G, Golinval J-C, Vakakis AF, Bergman LA (2005) The method of proper orthogonal decomposition for dynamical characterization and order reduction of mechanical systems: an overview. *Nonlinear Dynam* 41(1–3):147–169

5. Mignolet MP, Przekop A, Rizzi SA, Michael Spottswood S (2013) A review of indirect/non-intrusive reduced order modeling of nonlinear geometric structures. *J Sound Vib* 332(10):2437–2460
6. Reddy JN (2004) *Nonlinear finite element analysis*. Oxford University Press, New York
7. Tiso P, Rixen DJ (2011) Reduction methods for mems nonlinear dynamic analysis. In: *Nonlinear modeling and applications*, vol 2, p 53–65. Springer

Chapter 44

Stochastic Iwan-Type Model of a Bolted Joint: Formulation and Identification

X.Q. Wang and Marc P. Mignolet

Abstract This paper focuses on the development of a stochastic model of a bolted joint tested experimentally at Sandia National Lab under harmonic excitation and for which the dissipation per cycle and stiffness have been measured at various amplitudes of loading. The applicability of various Iwan-type models for the representation of the measured data is assessed and uncertainty is introduced in one of these models to duplicate the joint to joint variability observed in the test data. The specificities of the uncertainty model and the identification of its parameters are discussed in details.

Keywords Joints • Dissipation • Stiffness • Iwan model • Uncertainty modeling

44.1 Introduction

Joints are intrinsic components of assembled structures and thus their mechanical modeling is of primary importance in many engineering applications, e.g. automotive, aerospace, etc. Achieving this modeling has been and remains very challenging because of the complexity of the contact between the various surfaces, the occurrence of microslip, etc. This physical complexity is also reflected by a sensitivity to the exact conditions of the assembly and thus in a variability from sample to sample of otherwise identical joints. This situation naturally calls in for the formulation of uncertainty models of joints and such efforts have been carried out in the past, e.g. see [1] for a review and [2,3] for some recent references.

The present investigation is part of this undertaking and focuses more specifically on the development of a stochastic model of a particular bolted joint tested at Sandia National Lab [3]. The incorporation of the uncertainty within an Iwan model framework is justified and detailed using the experimental data on dissipation and stiffness reported in Chap. 12 of [3]. The process is expected to apply equally well to a broad range of joints.

44.2 Sandia Bolted Joint Data

Figure 44.1 depicts the leg section bolted joints tested at Sandia National Lab on which the present investigation focuses, see Chap. 12 of [3] for full details. Three nominally identical bottom parts (denoted by A, B, and C) and three nominally identical top components (denoted by 1, 2, and 3) were machined. All nine combinations were assembled then tested on a shaker (see Fig. 44.1b) under harmonic loading conditions. The stiffness (secant stiffness) of the joints and their dissipation were measured at five different force amplitudes (100 lbs, 200 lbs, 300 lbs, 400 lbs, and 500 lbs) and this data is presented in Fig. 44.2.

X.Q. Wang • M.P. Mignolet (✉)

SEMTE, Faculties of Mechanical and Aerospace Engineering, Arizona State University, 501 E. Tyler Mall, Tempe, AZ 85287-6106, USA
e-mail: marc.mignolet@asu.edu

Fig. 44.1 (a) Finite element model of the leg section bolted joint, (b) leg section being tested, (c) leg section interface (highlighted in black)

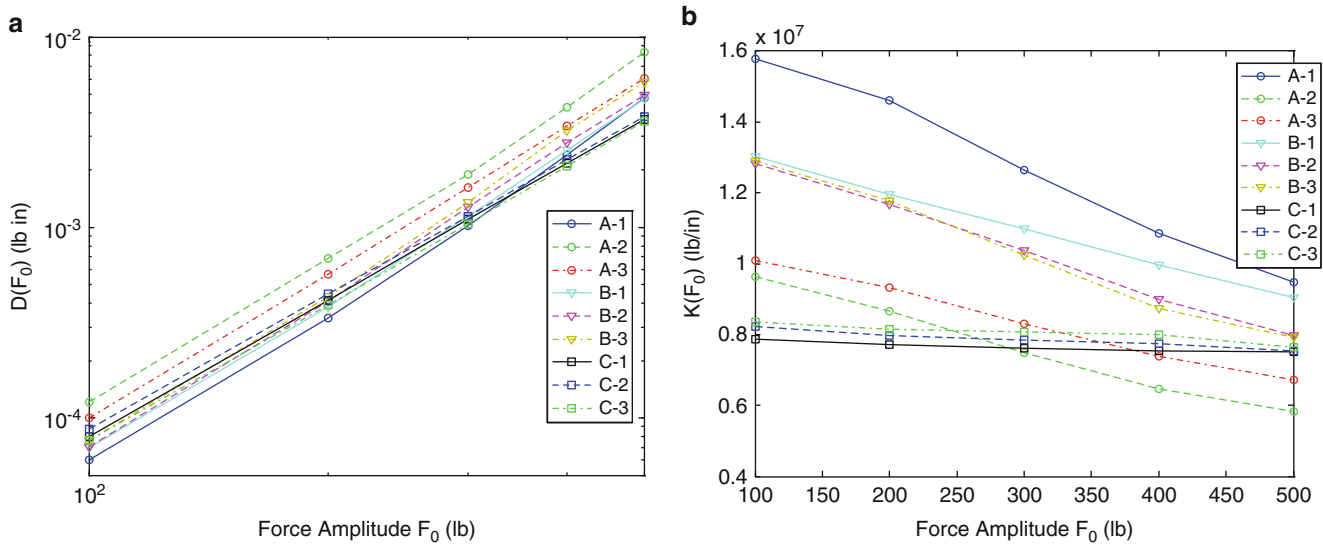
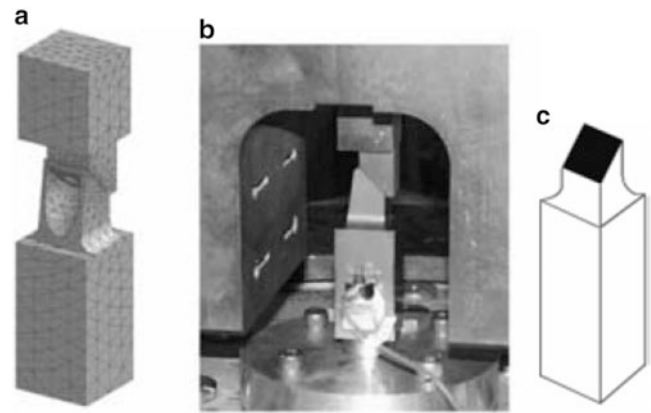


Fig. 44.2 (a) Energy dissipation per cycle and (b) stiffness vs. amplitude of harmonic force applied for the nine nominally identical samples (from Chap. 12 of [3])

44.3 Iwan Models

The Iwan model is a phenomenological model of yielding and microslip in which the physical process is represented by the sticking-slipping of a parallel array of Jenkins elements, see Fig. 44.3 and [3] for a detailed description of the model properties. A brief review of the key relations of this model is presented below.

Denote by $\rho(\phi)$ the distribution (appropriately normalized, see [3]) of Jenkins elements slipping under a displacement ϕ , it can be shown (e.g. see [3]) that

$$F(t) = \int_0^\infty \rho(\phi) [u(t) - x(t, \phi)] d\phi \tag{44.1}$$

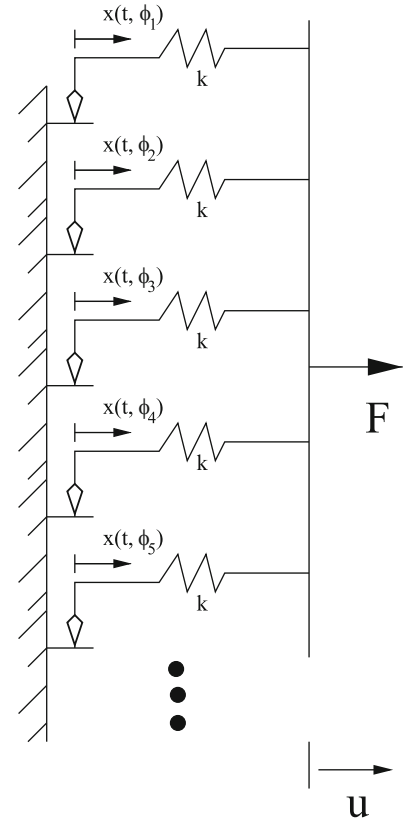
with

$$\dot{x}(t, \phi) = \dot{u}(t) \text{ if } \|u(t) - x(t, \phi)\| = \phi \text{ and } \dot{u}(u(t) - x(t, \phi)) > 0 \tag{44.2}$$

and 0 otherwise. Under an oscillatory displacement $u(t) = u_0 \sin t$, the maximum applied force F_0 is

$$F_0 = \int_0^{u_0} \phi \rho(\phi) d\phi + u_0 \int_{u_0}^{\phi_{\max}} \rho(\phi) d\phi \tag{44.3}$$

Fig. 44.3 Iwan Model representation (from [3])



where ϕ_{\max} denotes the displacement at which macroslip occurs. The dissipation of the entire system under the harmonic motion is obtained as

$$D = \int_0^{u_0} 4 [u_0 - \phi] \phi \rho(\phi) d\phi. \tag{44.4}$$

Further, proceeding with two differentiations of Eqs. (44.3) and (44.4) with respect to u_0 yields

$$\frac{\partial^2 F_0}{\partial u_0^2} = -\rho(u_0) \tag{44.5}$$

and

$$\frac{\partial^2 D}{\partial u_0^2} = 4 u_0 \rho(u_0). \tag{44.6}$$

The 4-parameter Iwan model is a simplification of the general one above in which the distribution $\rho(\phi)$ is expressed as

$$\rho(\phi) = R \phi^\chi [H(\phi) - H(\phi - \phi_{\max})] + S \delta(\phi - \phi_{\max}) \tag{44.7}$$

where $H()$ and $\delta()$ are the Heaviside and Dirac delta functions. Introducing Eq. (44.7) in Eqs. (44.3) and (44.4) leads to

$$F_0 = K_T u_0 - \frac{R u_0^{\chi+2}}{(\chi + 1)(\chi + 2)} \tag{44.8}$$

where $K_T = S + R \phi_{\max}^{\chi+1}/(\chi + 1)$ and

$$D = \frac{4 R u_0^{\chi+3}}{(\chi + 3)(\chi + 2)}. \tag{44.9}$$

Finally, the stiffness, i.e. secant stiffness, is defined as

$$K = \frac{F_0}{u_0} = K_T - \frac{R u_0^{\chi+1}}{(\chi+1)(\chi+2)} \quad (44.10)$$

44.4 Iwan-Type Modeling of the Sandia Joint Data: Strategy

The large variability observed in the experimental measurements of Fig. 44.2 demonstrates that the modeling of this physical joint must be carried out within an uncertainty framework. Given the global character of the measurements (total dissipation, overall joint stiffness), a phenomenological model, such as the Iwan model described above, is a particularly convenient basis to achieve this task. In proceeding with this effort, it must first be assessed whether the differences observed between samples (the curves of Fig. 44.2 here) originate from variations in the values of the parameters of the model (i.e. aleatoric uncertainty) or from changes in the features/physics of the model (i.e. epistemic uncertainty).

Considering first the 4-parameter model of Eqs. (44.7), (44.8), (44.9), and (44.10), aleatoric uncertainty is associated with variations from sample to sample of the parameters χ , K_T , R , ϕ_{\max} and thus would be observed when a good matching of each sample by the model predictions is achieved but requires different values of these parameters for different samples. To assess this possibility, a least squares fit of the data of Fig. 44.2 was carried out by Eqs. (44.8), (44.9), and (44.10) with the parameters χ , K_T , R (ϕ_{\max} is not observable since the macroslip load was not recorded) selected to minimize

$$\varepsilon = a \sum_i \left[\log(D_i) - \log(\widehat{D}_i) \right]^2 + b \sum_i \left[K_i - \widehat{K}_i \right]^2 \quad (44.11)$$

where \widehat{D}_i and \widehat{K}_i are the measured values of dissipation and stiffness at load level $F_{0,i}$ and D_i and K_i are their predicted counterparts based on values of χ , K_T , R .

Varying the relative magnitudes of a and b emphasizes more or less dissipation vs. stiffness and was found to produce significantly different approximations, see Fig. 44.4 for $b=0$ and Fig. 44.5 for $a=0$ both for sample B-2. Thus, the 4-parameter model cannot predict accurately the behavior of that sample and in fact of most others (as already pointed out in [3]). Accordingly, there exists epistemic uncertainty with respect to the 4-parameter Iwan model.

Introducing epistemic uncertainty requires the broadening of the model considered, i.e. features of the general Iwan model would need to be included (as suggested by the black arrows in Fig. 44.6) or, more drastically, a different joint formulation should be adopted (the red arrows in Fig. 44.6). In the first of these options, the dissipation and stiffness would be correctly

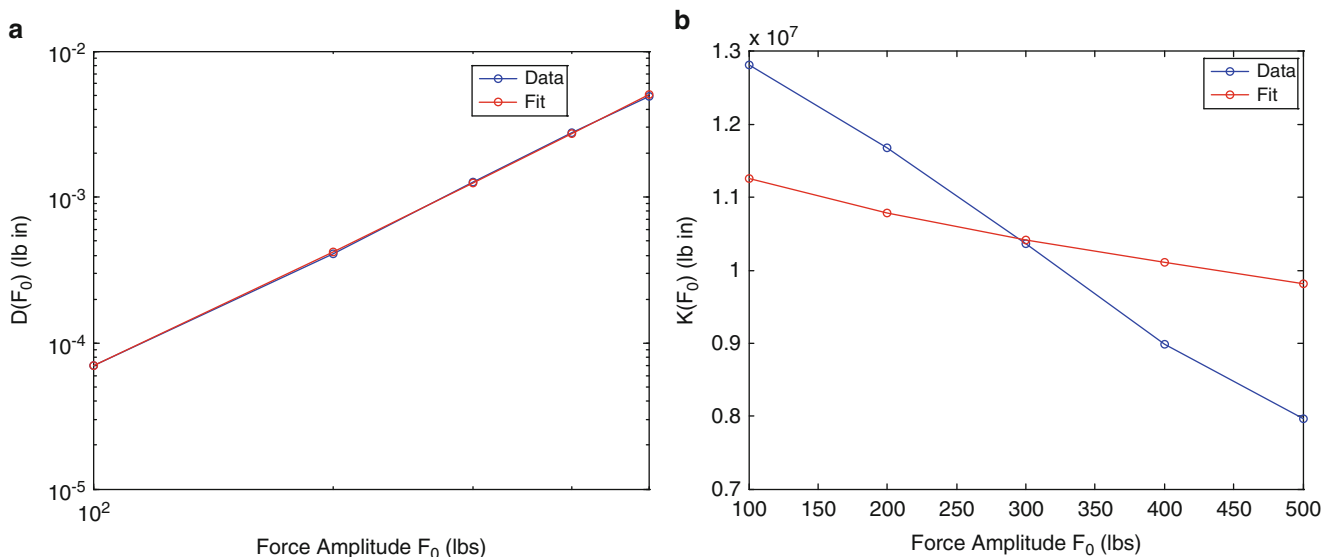


Fig. 44.4 (a) Energy dissipation per cycle and (b) stiffness vs. amplitude of harmonic force applied for the B-2 sample. Data and curve fit from Eq. (44.11) with $b=0$

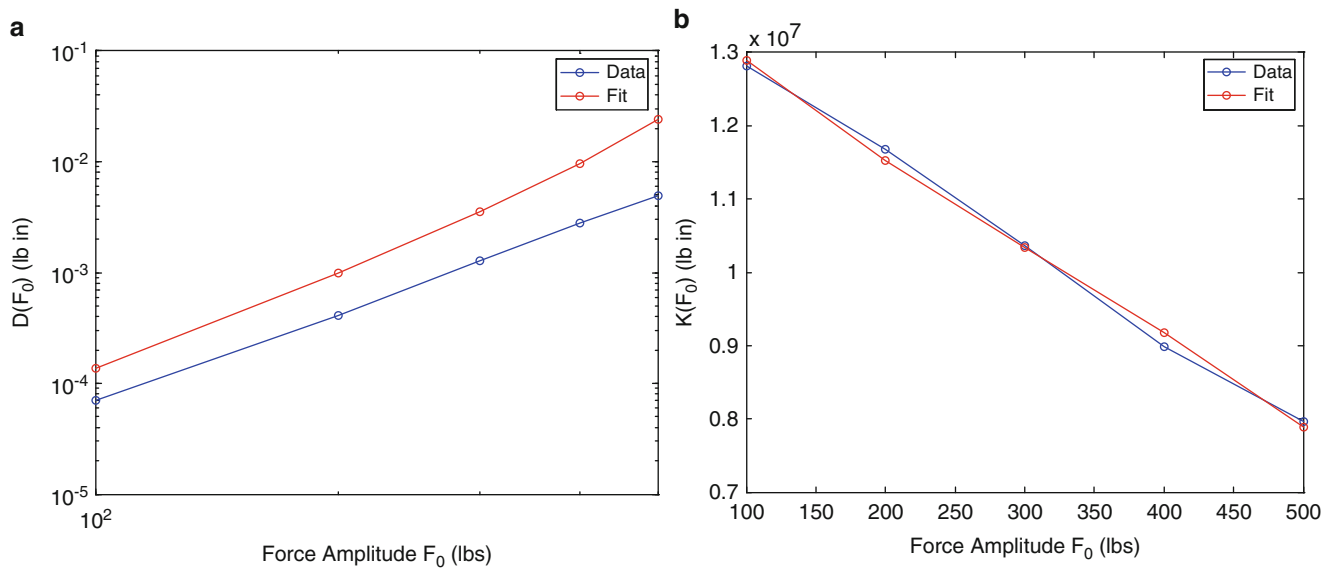
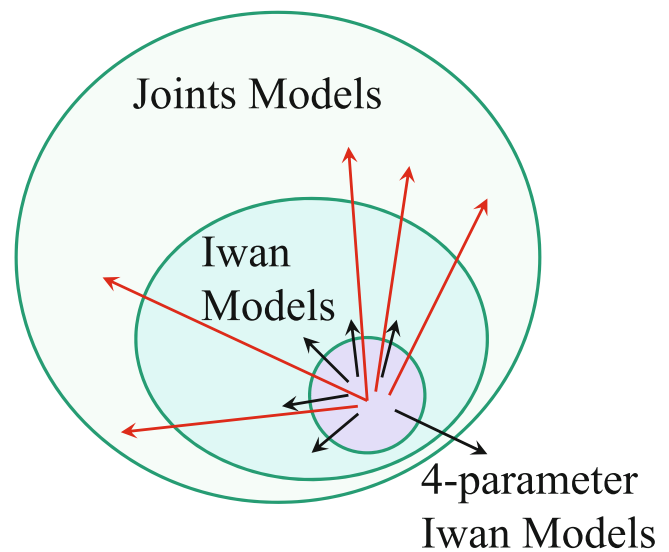


Fig. 44.5 (a) Energy dissipation per cycle and (b) stiffness vs. amplitude of harmonic force applied for the B-2 sample. Data and curve fit from Eq. (44.11) with $a = 0$

Fig. 44.6 Introduction of epistemic uncertainty in 4-parameter Iwan models



predicted by Eqs. (44.3) and (44.4) for each sample but with distributions $\rho(\phi)$ which differ from the power law of Eq. (44.7). Such distributions may take the form of the sum of a *parametrized* function and deviations around it. These deviations could be continuous, as depicted in Fig. 44.7a, modeled as a random process indexed by ϕ and possibly characterized by a zero mean and an autocorrelation function (with an assumed probability distribution), or other probabilistic model. The deviations around the parametrized function could also be discontinuous, as depicted in Fig. 44.7b, to model discrete slip events that may take place. Such deviations could be modeled for example through a Poisson process characterized by the probability of occurrence.

In the above models, variations of behavior from joint to joint are accounted for by variations in the continuous and/or discontinuous deviations in $\rho(\phi)$ as random samples of a common process and possibly by differences in the values of the parameters in the function, as aleatoric uncertainty.

Is any of these two Iwan models applicable to the data of Fig. 44.2? Key to answer this question is to recognize that there exist, within the Iwan model construct, one-to-one mappings between the dissipation $D(\phi)$ and the distribution $\rho(\phi)$, Eq. (44.6), and the stiffness $K(\phi)$ and $\rho(\phi)$, Eq. (44.5). Then, the dissipation $D(\phi)$ and stiffness $K(\phi)$ are tightly related quantities under this model assumption. Thus, an accurate fitting of the dissipation data by an Iwan model, 4-parameter or general, should result in a similar matching of the stiffness data if the joint behavior is indeed described by such a model. This is

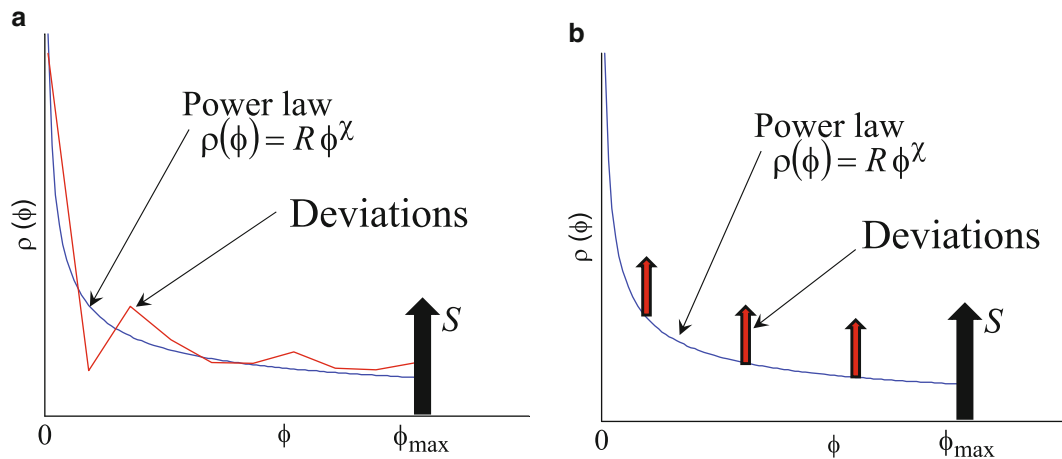
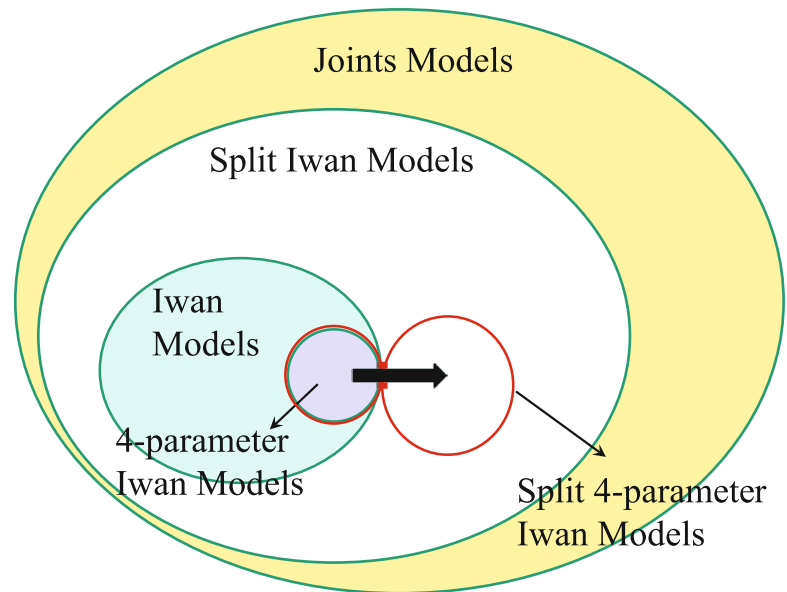


Fig. 44.7 Epistemic deviations from 4-parameter Iwan model within the general Iwan formulation. (a) Continuous deviations. (b) Discontinuous deviations

Fig. 44.8 Joint model evolution



clearly not the case for sample B-2, see Figs. 44.4 and 44.5, and others, which suggests that an Iwan model is not applicable here and a more general joint model should be sought as depicted in the red arrows of Fig. 44.6.

In seeking an appropriate model, note that the matching of the dissipation and stiffness data by 4-parameter Iwan models in Figs. 44.4 and 44.5 is good to very good *if done independently of each other*, i.e. as in Figs. 44.4a and 44.5b. This observation suggests the introduction of an ad-hoc joint model in which the dissipation and stiffness are approximated by Iwan models with *separate* distributions $\rho_D(\phi)$ and $\rho_K(\phi)$. Such models will be referred to here as “split Iwan models”. In fact, it would appear from Figs. 44.4a and 44.5b that the distributions $\rho_D(\phi)$ and $\rho_K(\phi)$ can each be represented by power laws of the form of Eq. (44.7) leading to “split 4-parameter Iwan models”. The joint modeling evolution carried out in this section is depicted by the arrows in Fig. 44.8.

44.5 Iwan-Type Modeling of the Sandia Joint Data: Detailed Uncertain Modeling

A separate curve fitting of the dissipation and stiffness data by the 4-parameter model of Eqs. (44.7), (44.8), (44.9), and (44.10) was achieved for each of the nine tested samples and a good to very good match was achieved in all cases suggesting that only aleatoric uncertainty must be introduced on the corresponding split 4-parameter Iwan model. For the ensuing discussion, presented in Table 44.1 are the values of the two sets of parameters χ , K_T , R identified.

Table 44.1 Identification results—split 4-parameter Iwan model

| Sample | χ_D | K_{TD} | R_D | $F_{\max,D}$ | χ_K | K_{TK} | R_K | $F_{\max,K}$ |
|--------|----------|----------|--------|--------------|----------|----------|---------|--------------|
| 1 | -0.509 | 1.54E7 | 3.44E8 | 2.10E3 | -0.544 | 2.00E7 | 6.22E8 | 5.89E2 |
| 2 | -0.622 | 9.80E6 | 5.07E7 | 2.67E3 | -0.685 | 1.38E7 | 6.37E7 | 6.65E2 |
| 3 | -0.646 | 1.05E7 | 3.72E7 | 4.01E3 | -0.553 | 1.25E7 | 2.65E8 | 6.96E2 |
| 4 | -0.577 | 1.33E7 | 1.16E8 | 3.08E3 | -0.617 | 1.67E7 | 1.71E8 | 8.62E2 |
| 5 | -0.548 | 1.25E7 | 1.51E8 | 2.69E3 | -0.531 | 1.58E7 | 5.10E8 | 6.13E2 |
| 6 | -0.520 | 1.26E7 | 2.31E8 | 2.05E3 | -0.633 | 1.75E7 | 1.68E8 | 6.42E2 |
| 7 | -0.729 | 9.07E6 | 7.90E6 | 2.61E4 | -0.933 | 1.08E7 | 4.53E5 | 7.64E8 |
| 8 | -0.773 | 9.71E6 | 5.33E6 | 3.68E4 | -0.462 | 8.64E6 | 1.59E8 | 4.27E3 |
| 9 | -0.722 | 9.52E6 | 9.18E6 | 2.35E4 | -0.061 | 8.51E6 | 1.24E10 | 1.65E3 |

The next stage of the model development is the selection/estimation of the probability density functions of these parameters. With enough data, these probability density functions or their joint could be determined nonparametrically, e.g. with the use of kernel-based methods (e.g. see [4–6] and discussion below). A more likely situation, as is the case here, is that only limited data will be available and a choice of parametrized distributions will be necessary. While physical arguments (e.g. positiveness of the simulated values) are helpful in this selection process, they are not restrictive enough to lead to a unique distribution and various choices are possible. Useful strategies to pick appropriate distributions include in particular expansion-type representations (e.g. polynomial chaos [7,8]) and maximum entropy concepts. The entropy of the distribution $p(x)$ of a random variable X defined over the domain Ω is expressed as

$$S_p = - \int_{\Omega} p(x) \ln [p(x)] dx. \quad (44.12)$$

The entropy is a measure of spread and thus its maximization under physical conditions leads to a distribution that extends as far as possible encompassing a broad range of behaviors. Many of the classical distributions correspond to a maximum of the entropy:

- the uniform distribution is obtained under the constraint that the domain Ω is bounded, $\Omega \equiv [a,b]$
- the Gaussian distribution corresponds to an unbounded domain on both positive and negative sides and imposed mean and standard deviation
- the exponential distribution results by imposing $\Omega \equiv [0,\infty)$ and the mean value.

In some instances, it is not only required that the domain be $\Omega = [0,\infty)$ but also that the distribution be a flat zero to exclude the occurrence of the lower bound. If the mean is additionally imposed, the resulting distribution is that of a Gamma random variable (see for example [9] for the matrix extension). These distributions are denoted here as $U(a,b)$, $N(\mu,\sigma)$, $\text{Exp}(\lambda)$, and $\text{Gamma}(a)$, respectively.

Since the parameters (one for the dissipation and one for the stiffness modeling) χ must be larger than -1 , it is proposed that $\chi + 1$ be represented in terms of Gamma random variables. A similar modeling of the two stiffnesses K_T is also proposed, that is

$$\chi_D = \bar{\chi}_D X_1 - 1 \quad \chi_K = \bar{\chi}_K X_2 - 1 \quad K_{T,D} = \bar{K}_{T,D} X_3 \quad K_{T,K} = \bar{K}_{T,K} X_4 \quad (44.13)$$

where X_i is distributed as $\text{Gamma}(a_i)$ with a_i , $\bar{\chi}_D$, $\bar{\chi}_K$, $\bar{K}_{T,D}$, and $\bar{K}_{T,K}$ positive deterministic parameters. Note here that the mean and variance of the parameter X_i are both equal to a_i .

Note that the above stochastic modeling has explicitly assumed that the random powers χ dissipation and stiffnesses K_T were independent variables. The modeling of the power law constants R_D and R_K must be carried out carefully, consistently with the available information on the forces that the joints can sustain before macro slip and the representations of Eqs. (44.8), (44.9), and (44.10). To this end, note from Eq. (44.10) that a zero stiffness would be obtained for a displacement

$$u_{\max} = \left[\frac{(\chi + 1) K_T}{R} \right]^{1/(\chi+1)} \quad (44.14)$$

for which the force is maximum and equal to, see Eq. (44.8),

$$F_{\max} = \frac{[(\chi + 1) K_T]^{(\chi+2)/(\chi+1)}}{(\chi + 2) R^{1/(\chi+1)}}. \quad (44.15)$$

Table 44.2 Mean and standard deviation of the parameters χ and K_T , offset \bar{F}_{\max} , and mean of the variable Y for both dissipation and stiffness 4-parameter Iwan models

| | Mean (χ) | Std. dev (χ) | Mean (K_T) | Std. dev (K_T) | \bar{F}_{\max} | Mean (Y) |
|-------------|-----------------|---------------------|----------------|--------------------|------------------|--------------|
| Dissipation | -0.616 | 0.096 | 1.16E7 | 2.18E6 | 2.04E3 | 7.24E2 |
| Stiffness | -0.620 | 0.144 | 1.45E7 | 3.73E6 | 5.80E2 | 9.79E1 |

Since none of the nine samples has experienced macro slip at or before the 500 lbs loading, each of the nine samples must have parameters for which the corresponding F_{\max} values exceed this limit. This is indeed the case, see Table 44.1. This observation suggests that the distribution of the parameter R should be such that the F_{\max} stays consistently above 500 lbs. Given that Eq. (44.15) involves all three parameters χ , K_T , R , the distribution of R cannot be independent of χ , K_T . This issue can be sidestepped by proceeding first with a modeling of F_{\max} which guarantees the property, i.e.

$$F_{\max} = \bar{F}_{\max} + Y \quad (44.16)$$

where \bar{F}_{\max} is larger than 500 lbs and Y is a positive random variable. The variable R is then selected to satisfy Eq. (44.15), i.e.

$$R = \frac{[(\chi + 1) K_T]^{(\chi+2)}}{[(\chi + 2) F_{\max}]^{(\chi+1)}} \quad (44.17)$$

The positiveness of Y is sufficient to ensure the satisfaction of the physical constraints and thus an appropriate maximum entropy distribution for that variable would be the exponential one. In fact, selecting \bar{F}_{\max} to be the lowest experimental F_{\max} value (see Table 44.1) gives Y values with mean and standard deviations approximately equal which is a distinguishing feature of the exponential distribution. Accordingly, the stochastic modeling was completed by introducing

$$F_{\max,D} = \bar{F}_{\max,D} + Y_D \quad \text{and} \quad F_{\max,K} = \bar{F}_{\max,K} + Y_K \quad (44.18)$$

where $\bar{F}_{\max,D}$ and $\bar{F}_{\max,K}$ are positive deterministic variables and Y_D and Y_K are exponentially distributed random variables with parameters λ_D and λ_K .

The values of the 12 parameters of the uncertain model are readily determined from the statistics of χ , K_T , and F_{\max} given in Table 44.2 extracted from the data of Table 44.1 for the six A and B samples.

44.6 Stochastic Parameter Identification and Uncertainty Bands

When the number of random samples is small, it is generally suggested that an identification of the deterministic parameters of a stochastic model is better achieved by using the maximum likelihood approach vs. the moments derived from the samples. To clarify this procedure, denote by \underline{X} the random vector of measurements, composed here of the five dissipation values D_i dissipations and stiffnesses K_i , i.e. $\underline{X} = [D_1 \dots D_5 \ K_1 \dots K_5]$. Further, let $\underline{x}^{(i)}$ be the vector of measured values of these dissipations for sample i , i.e. $\underline{x}^{(i)} = [\hat{D}_1^{(i)} \dots \hat{D}_5^{(i)} \ \hat{K}_1^{(i)} \dots \hat{K}_5^{(i)}]$ consistently with Eq. (44.11).

In the maximum likelihood framework, the 12 deterministic parameters of the model stacked in the vector $\underline{\theta}$ will be chosen to maximize the likelihood function

$$L = \prod_{i=1}^M p_{\underline{X}} \left(\underline{x}^{(i)}; \underline{\theta} \right) \quad (44.19)$$

where $p_{\underline{X}} \left(\underline{x}; \underline{\theta} \right)$ denotes the probability density function of the random vector \underline{X} . A first approach to evaluating L is to approximate $p_{\underline{X}} \left(\underline{x}; \underline{\theta} \right)$ by a joint Gaussian approximation, i.e.

$$p_{\underline{X}}^G(\underline{x}; \underline{\theta}) = \frac{1}{(2\pi)^{p/2} \sqrt{\det(K_{\underline{X}\underline{X}})}} \exp \left[-\frac{1}{2} \left(\underline{x} - \underline{\mu}_{\underline{X}} \right)^T K_{\underline{X}\underline{X}}^{-1} \left(\underline{x} - \underline{\mu}_{\underline{X}} \right) \right] \quad (44.20)$$

where $p = 10$ here is the number of components of the random vector \underline{X} and $\underline{\mu}_{\underline{X}}(\underline{\theta})$ and $K_{\underline{X}\underline{X}}(\underline{\theta})$ denote its mean vector and covariance matrix determined from the model of Eqs. (44.8), (44.9), (44.10), (44.13), (44.16), and (44.17) with the parameter values in $\underline{\theta}$ by a Monte Carlo simulation.

A more refined estimate of $p_{\underline{X}}(\underline{x}; \underline{\theta})$ can be obtained by the kernel density estimation technique (see [4,5] for theoretical discussions and [6] for an application). According to this methodology, the probability density function is estimated as

$$p_{\underline{X}}^K(\underline{x}; \underline{\theta}) = \frac{1}{M} \sum_{i=1}^M \prod_{l=1}^p \left\{ \frac{1}{h_l} K \left(\frac{y_l^{(i)} - y_l}{h_l} \right) \right\} \quad (44.21)$$

where y_l and $y_l^{(i)}$ are the l th components of the vectors \underline{y} and $\underline{y}^{(i)}$ defined as

$$\underline{y} = \Xi^T \left(\underline{x} - \underline{\mu}_{\underline{X}} \right) \quad \text{and} \quad \underline{y}^{(i)} = \Xi^T \left(\underline{x}^{(i)} - \underline{\mu}_{\underline{X}} \right) \quad (44.22)$$

in which Ξ is the matrix obtained by stacking by columns the normalized eigenvectors of the covariance matrix $K_{\underline{X}\underline{X}}(\underline{\theta})$. Further, $K(\cdot)$ denotes the kernel and h_l denotes coefficients related to it. For the Gaussian kernel, one has

$$K(u) = \frac{1}{\sqrt{2\pi}} \exp(-u^2/2); \quad h_l = \sqrt{\Lambda_{ll}} \left[\frac{4}{M(2+p)} \right]^{1/(4+p)} \quad (44.23)$$

in which Λ_{ll} is the l th eigenvalue of $K_{\underline{X}\underline{X}}(\underline{\theta})$.

Once the identification of the parameters has been performed, the stochastic modeling is complete and samples of the predicted dissipation and stiffness can be computed from which any desired statistic can be obtained. A particularly useful tool is the band of uncertainty generated by specific percentiles of the response. For example, shown in Fig. 44.9 are the bands of uncertainty on dissipation and stiffness corresponding to the interval 5th–95th percentiles, i.e. the zones in which the predicted values of dissipation and stiffness will fall in with a 90 % probability and excluding the 5 % smallest and largest. Also shown on Fig. 44.9 are the original nine measurements sets, i.e. of Fig. 44.2 and note that these curves all belong within the band of uncertainty as might be expected.

44.7 Summary

This paper focused on the development of a stochastic model of a bolted joint tested experimentally at Sandia National Lab under harmonic excitation and for which the dissipation per cycle and stiffness have been measured at various amplitude of loading. The construction of such a stochastic model requires first a deterministic model that captures appropriately the behavior of each sample and the 4-parameter Iwan model of Eq. (44.7) was initially assessed for this task. However, the disparate matching of the dissipation and stiffness data by its best predictions, see Figs. 44.4 and 44.5, demonstrated the need to generalize the model and two extensions were suggested within the general Iwan model framework, see Fig. 44.7. A property of these models was next highlighted which suggests however that a good matching of the data within that class of models may not be achievable. Accordingly, a “split” Iwan model was proposed in which dissipation and stiffness data are each modeled separately.

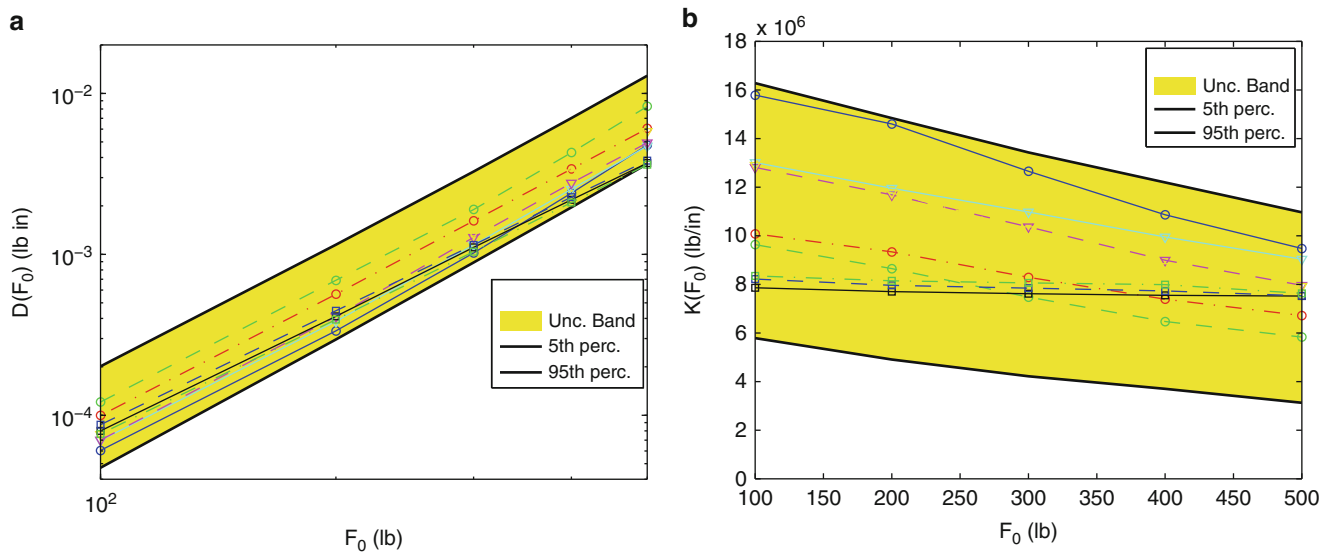


Fig. 44.9 5th–95th percentiles bands of uncertainty on (a) dissipation per cycle and (b) stiffness vs. amplitude of harmonic force for the split 4-parameter Iwan model with parameters determined from Table 44.2. Also shown are the nine measurement sets

The randomization of this split Iwan model was next discussed and the selection of statistical distributions and identification of the parameters from the available experimental data were described in details. The availability of such a stochastic model permits the prediction of the statistics, including band of uncertainty, on the predicted behavior, dissipation and stiffness, of the joints.

References

1. Ibrahim RA, Pettit CL (2005) Uncertainties and dynamic problems of bolted joints and other fasteners. *J Sound Vib* 279:857–936
2. Dohnal F, Mace BR, Ferguson NS (2009) Joint uncertainty propagation in linear structural dynamics using stochastic reduced basis methods. *AIAA J* 47:961–969
3. Segalman DJ, Gregory DL, Starr MJ, Resor BR, Jew MD, Lauffer JP, Ames NM (2009) Handbook on dynamics of jointed structures. Sandia Report SAND2009-4164
4. Bowman AW, Azzalini A (1997) Applied smoothing techniques for data analysis. Oxford University Press, Oxford
5. Terrell GR, Scott DW (1992) Variable kernel density estimation. *Ann Stat* 20:1236–1265
6. Soize C (2011) A computational inverse method for identification of non-Gaussian random fields using the Bayesian approach in very high dimension. *Comput Meth Appl Mech Eng* 200:3083–3099
7. Soize C, Ghanem R (2004) Physical systems with random uncertainties: chaos representation with arbitrary probability measure. *SIAM J Sci Comput* 26:395–410
8. Sakamoto S, Ghanem R (2002) Polynomial chaos decomposition for the simulation of non-Gaussian nonstationary stochastic processes. *J Eng Mech* 128:190–201
9. Soize C (2005) A comprehensive overview of a non-parametric probabilistic approach of model uncertainties for predictive models in structural dynamics. *J Sound Vib* 288:623–652